Green Chemistry and Sustainable Technology

Seema Garg
Amrish Chandra *Editors*

Green Photocatalytic Semiconductors

Recent Advances and Applications

Springer

Green Chemistry and Sustainable Technology

Series Editors

Liang-Nian He
State Key Lab of Elemento-Organic Chemistry, Nankai University, Tianjin, China

Pietro Tundo
Department of Environmental Sciences, Informatics and Statistics, Ca' Foscari University of Venice, Venice, Italy

Z. Conrad Zhang
Dalian Institute of Chemical Physics, Chinese Academy of Sciences, Dalian, China

Aims and Scope

The series Green Chemistry and Sustainable Technology aims to present cutting-edge research and important advances in green chemistry, green chemical engineering and sustainable industrial technology. The scope of coverage includes (but is not limited to):

- Environmentally benign chemical synthesis and processes (green catalysis, green solvents and reagents, atom-economy synthetic methods etc.)
- Green chemicals and energy produced from renewable resources (biomass, carbon dioxide etc.)
- Novel materials and technologies for energy production and storage (bio-fuels and bioenergies, hydrogen, fuel cells, solar cells, lithium-ion batteries etc.)
- Green chemical engineering processes (process integration, materials diversity, energy saving, waste minimization, efficient separation processes etc.)
- Green technologies for environmental sustainability (carbon dioxide capture, waste and harmful chemicals treatment, pollution prevention, environmental redemption etc.)

The series Green Chemistry and Sustainable Technology is intended to provide an accessible reference resource for postgraduate students, academic researchers and industrial professionals who are interested in green chemistry and technologies for sustainable development.

More information about this series at http://www.springer.com/series/11661

Seema Garg · Amrish Chandra
Editors

Green Photocatalytic Semiconductors

Recent Advances and Applications

Springer

Editors
Seema Garg
Department of Chemistry
Amity Institute of Applied Sciences
Amity University
Noida, Uttar Pradesh, India

Amrish Chandra
Amity Institute of Pharmacy
Amity University
Noida, Uttar Pradesh, India

ISSN 2196-6982 ISSN 2196-6990 (electronic)
Green Chemistry and Sustainable Technology
ISBN 978-3-030-77370-0 ISBN 978-3-030-77371-7 (eBook)
https://doi.org/10.1007/978-3-030-77371-7

© The Editor(s) (if applicable) and The Author(s), under exclusive license to Springer Nature Switzerland AG 2022
This work is subject to copyright. All rights are solely and exclusively licensed by the Publisher, whether the whole or part of the material is concerned, specifically the rights of translation, reprinting, reuse of illustrations, recitation, broadcasting, reproduction on microfilms or in any other physical way, and transmission or information storage and retrieval, electronic adaptation, computer software, or by similar or dissimilar methodology now known or hereafter developed.
The use of general descriptive names, registered names, trademarks, service marks, etc. in this publication does not imply, even in the absence of a specific statement, that such names are exempt from the relevant protective laws and regulations and therefore free for general use.
The publisher, the authors and the editors are safe to assume that the advice and information in this book are believed to be true and accurate at the date of publication. Neither the publisher nor the authors or the editors give a warranty, expressed or implied, with respect to the material contained herein or for any errors or omissions that may have been made. The publisher remains neutral with regard to jurisdictional claims in published maps and institutional affiliations.

This Springer imprint is published by the registered company Springer Nature Switzerland AG
The registered company address is: Gewerbestrasse 11, 6330 Cham, Switzerland

Preface

In modern era, the speedy industrial development and population progression has led to surge in the environmental pollution and grave energy crisis. With the developing chaos, the demand of environmental remediation, pollution control techniques, and alternative energy supply employing green technique have attracted broad research interests. Moreover, the need is felt to reduce the consumption of natural resources and raise awareness of the great impact of our consumerism so that the developed technologies, products, and materials are environmentally harmonious and sustainable. Photocatalysis is a green and efficient process to solve the environmental pollution problems, solar energy conversion, and in the sustainable production of fuels using conversion of CO_2 and water. Photocatalytic materials have been utilized in other fields also viz. self-cleaning surfaces, green chemistry, green engineering, food packaging, and biomedical and medical applications.

This book comprises a detailed emphasis on design and synthesis of photocatalytic materials, their mechanism and effective parameters with kinetics study for photocatalytic oxidation. Effective ways have been discussed in the book to enhance the photocatalytic activity of the material via the formation of nanomaterial and nanocomposites, doping, hybrid material, polymers, and rare earth elements. The book further elaborates the role of metal nanoparticles, oxygen vacancy, singlet oxygen generation, and advanced laser methods for enhancing photocatalytic activity. Approach to recover the photocatalytic material via immobilization has also been taught. Reducing environmental impact of leather industries, a potential route for environmental remediation and fouling mitigation, p type nanomaterials and separation of oily emulsion from aqueous effluents have been elaborated in the book chapters. Water splitting and CO_2 reduction for hydrogen generation and fuel production using photocatalytic processes with band gap engineering and the role of hybridized nanomaterials have been described in enhancing the photocatalytic activity.

This book brings to light much of the recent research in the development of such semiconductor photocatalytic systems. The book will thus be of relevance to researchers in the field of: material science, environmental science and technology, photocatalytic applications, newer methods of energy generation, and conversion and industrial applications.

The book has structured into five sections for ease of comprehension:

1. **Introductory Section** comprises of the first three chapters: Chap. 1 of the book describes the principles and mechanisms of heterogeneous photocatalysis, including the formation of photogenerated charge carriers, the role of different reactive species, and the effect of key parameters on the efficiency. Chapter 2 provides the state-of-the-art research activities targeting basic principles involved in the photocatalytic reactions, role of nanomaterials in optimization of process and mechanism and kinetics of photocatalytic oxidation. Chapter 3 elaborately showcases recent advances in the development of novel multifunctional nanostructured photocatalyst for water remediation via numerous approached. Moreover, a concise summary of the present challenges and an outlook for the designing and synthesis of nanostructured photocatalyst in the field of water remediation is provided.
2. **Nanomaterials and Nanocomposites Section** covers the next five chapters (Chaps. 4–8): Chap. 4 presents an overview of state-of-the-art graphene as well as functionalized graphene-based nanocomposites and their photocatalytic activity for degradation of organic pollutants. The goal of this study is to provide the latest and advance analysis in the area of developing nanotechnology for photocatalytic application. Chapter 5 discusses the state-of-the-art synthesis of 2D material-based polymer nanocomposites. The focus is on the recent advances in photocatalytic applications of polymer nanocomposites based on 2D materials including graphene, 2D transitional metal dichalcogenides (TMDs), and transition metal oxides (TMOs). Chapter 6 gives a brief overview of the progress in bismuth-carbon nanocomposites as promising visible light-driven photocatalysts. The fundamental structural features of bare bismuth-based photocatalysts and their historical background are highlighted in detail. Chapter 7 focuses on synthesis of new photoactive catalysts from Europium diphthalocyanine molecules. It has been dissolved in dimethylformamide and transferred to aqueous dispersion of detonation nanodiamonds, forming diphthalocyanine-diamond complexes. Chapter 8 presents non-conventional hybrid coatings with heterogeneous surface energy distribution, superhydrophobic, and photocatalytic properties. Hybrid coatings are prepared by incorporating photocatalyst particles into the hydrophobic poly (perfluorodecyl acrylate) fluoropolymer matrix.
3. **Photocatalytic Activity Enhancement Section** carries Chaps. 9–15: Chap. 9 focuses on rare earth doped photocatalysis. For this matter, photocatalysis driven by ultraviolet (UV) and visible light both has been covered. The luminescence and the upconversion phenomena have been discussed in case of several materials as a possibility to utilize low energy photons. Chapter 10 illustrates the synthesis of catalytic complexes of photosensitizer Radachlorin with polyvinylpyrrolidone and detonation nanodiamonds and characterization by optical absorption spectroscopy, luminescence excitation, dynamic light

scattering, and viscometry methods. Chapter 11 discusses the mechanisms and applications of photocatalytic activity of nanocomposites composed of metal-based nanomaterials. Chapter 12 discusses self-doped titania photocatalysts, including defect types, synthesis methods, and their applications for photocatalytic degradation of organic compounds and solar energy conversion. Antimicrobial properties of defective titania and other semiconductors have also been presented, confirming that these photocatalysts are highly promising as effective, green, and cheap materials. Chapter 13 provides an up-to-date review of recent development of perovskites and its related materials, including titanate-based, tantalite-based, niobium-based, ferrites, and others, showing a remarkably fast development and promising results in photocatalytic performance particularly in solar light-driven applications. Chapter 14 presents the laser processing techniques advantages through the functional property's enhancement of different photoactive materials such as complex stoichiometry inorganic perovskites (BiFeO3-based materials) or binary oxides (TiO_2, WO_3, ZnO). Chapter 15 discusses sol-gel, dip-coating, polymer assisted hydrothermal discharge, photo-etching, electrophoretic deposition, cold plasma discharge, RF magnetron sputtering, and spray pyrolysis. Characterization techniques used for studying various properties of immobilized catalyst have also been discussed in brief.

4. Environmental Remediation Section comprises of Chaps. 16–19: Chap. 16 describes recent advancement in photocatalytic process along with other similar green technologies such as nanotechnology, non-thermal plasma treatment, and ozone-based technologies with specific emphasis to reduce environmental impacts of leather production and processing. Chapter 17 outlines the importance of integration of nanophotocatalysts with the membrane matrix to ensure higher photodegradation of pollutant, enhanced water flux with reduced fouling of the membrane. Chapter 18 deals with the synthesis, characterization, and photocatalytic activity of nickel oxide nanoparticles, where the solution combustion method makes use of nickel nitrate as an oxidizer and oxalic acid as fuel for the synthesis. Chapter 19 overviews the conventional techniques for elimination of oils from aqueous effluents and focuses on the limitations of the conventional processes. The chapter illustrates the importance of using photocatalytic membrane, the future aspects of membrane technology, and promising solutions associated with membrane modification methods using photocatalytic and/or hydrophilic nanomaterials and nanocomposite to enhance the permeate quality and water flux.
5. **Water Splitting and CO_2 Reduction Section** covers seven chapters (Chaps. 20 –26): Chap. 20 focuses on the usage of heterogeneous photocatalytic methods for producing valuable products from CO_2 under UV and visible light irradiation. The chapter elaborates the main parts as electron structure of CO_2 and photoexcitation of such molecule; UV light and visible light-assisted CO_2 photoactivation in the gas phase over TiO_2 based and other catalysts; liquid phase CO_2 activation and the designing and upscaling techniques for CO_2 converting photoreactors. Chapter 21 gives a comprehensive view of

different production methods and electrode materials for photocatalytic water splitting toward hydrogen production. The covered topics include different metal oxides, metal chalcogenides, and different shapes of nanocomposites, which are used for photoelectrocatalytic hydrogen production. Also, the advantages and disadvantages of the selected materials and methods for hydrogen evolution from water splitting are discussed along with their challenges and prospects. Chapter 22 gives an overview on the designing of heterojunctions for enhancing PEC water splitting performance. Along with the heterojunction synthesis, recent progress in the heterojunction-based PEC system and the working mechanism behind the charge separation with future directions for PEC water splitting has also been discussed in the chapter. Chapter 23 provides the bandgap engineering of semiconductor photocatalysts through atomic doping, alloying, and hybridization to alter electronic structures and enhance the light absorption, charge transfer, and surface reactions in the photocatalytic processes. Furthermore, the current progresses in the band gap engineering of quantum dots, metal oxides, organic semiconductors, 2D hybrid materials for photocatalytic, and photoelectrocatalytic water splitting have been discussed and summarized. Finally, the challenges and perspectives for future research to develop highly efficient bandgap engineered heterostructures for water splitting have been proposed. Chapter 24 describes key aspects of materials used as solid photocatalysts for hydrogen evolution from aqueous phases including metal oxides, metal sulfides, and carbon-based semiconductors. An overview of the mechanisms and reaction pathways of hydrogen formation by heterogeneous photocatalysis, both for photo-reforming of organic substrates and water splitting, is given. Chapter 25 focuses on potential application areas, which is limited to solar fuels and solar cells as they represent two of the most studied fields of green photocatalytic semiconductors. Chapter 26 describes in detail the nanohybrid materials including metal oxides, carbon-based materials, metal sulfides, metal-organic frameworks, and transition metal phosphides as well as bandgap tuning based on these structures, which affect the efficiency of photocatalysis.

The book is a one stop solution for university students, researchers, and engineers who wish to initiate research in photocatalysis or to enhance their know how of the various applications of photocatalysis.

Noida, India

Seema Garg
Amrish Chandra

Contents

Part I Introductory Section

Part II Nanomaterials and Nanocomposites

Part III Photocatalytic Activity Enhancement

Part IV Environmental Remediation

Part V Water Splitting and CO2 Reduction

Part I
Introductory Section

Chapter 1
Photocatalysis: Introduction, Mechanism, and Effective Parameters

Máté Náfrádi, Gábor Veréb, Daniele Scheres Firak, and Tünde Alapi

Abstract The widely investigated heterogeneous photocatalysis offers an environmentally friendly, efficient, and versatile solution for several environmental problems. Among others, the removal of harmful organic pollutants and the generation of H_2 via water splitting are well-known and most widely studied applications. The process is based on the charge separation caused by the excitation of semiconductor photocatalyst via photon absorption. Due to the intensive development of material science, in addition to the well-known TiO_2 and ZnO, several new semiconductor materials have been designed and synthesized to increase the efficiency of heterogeneous photocatalysis and utilization of solar and/or visible light. This chapter describes the principles and mechanisms of heterogeneous photocatalysis, including the formation of photogenerated charge carriers, the role of different reactive species, and the effect of key parameters on the efficiency.

Keywords Advanced oxidation processes · Photogenerated charge carriers · Green photochemistry · Reaction parameters · Matrix effect

1.1 Introduction

1.1.1 Heterogeneous Photocatalysis for Environmental Applications

In the past decades, humanity started to face numerous emerging environmental problems, mainly related to transport, industrial, and agricultural activities. These problems require efficient and urgent solutions. The pollution of air and water with non-biodegradable pollutants may have unforeseeable consequences to the envi-

---

M. Náfrádi · D. S. Firak · T. Alapi (✉)
Faculty of Sciences, University of Szeged, Dóm tér 7., Szeged 6720, Hungary
e-mail: alapi@chem.u-szeged.hu

G. Veréb
Faculty of Engineering, University of Szeged, Moszkvai Blvd 9, Szeged 6725, Hungary

S. Garg and A. Chandra (eds.), *Green Photocatalytic Semiconductors*,
Green Chemistry and Sustainable Technology,
https://doi.org/10.1007/978-3-030-77371-7_1

ronment and may even endanger human health and life. These pollutants may be organic (e.g., pesticides, pharmaceuticals, hydrocarbons, dyes) or inorganic compounds, like heavy metals (e.g., chromium, mercury, lead), or other dissolved inorganic ions (e.g., nitrite, nitrate, arsenic) [1, 2]. The effect of these pollutants varies, several of them show toxic, carcinogenic, mutagenic, or have endocrine-disrupting effects (EDCs). They can accumulate in the ecosystem, so emissions below the limit values can also pose serious risks.

Advanced oxidation processes (AOPs) have been extensively investigated in the past decades, as they are a promising technique to solve and prevent many environment-related problems. The most well-known application of AOPs is the removal of trace amounts of organic, non-biodegradable pollutants, as classic biological-physical wastewater treatment methods are generally not adequate for this task [3]. AOPs are generally based on the in situ formation of reactive species that are able to oxidize many non-biodegradable pollutants. Some AOPs, like ozonation, Fenton-process, gamma-radiolysis combined with other methods (e.g., UV, O_3, H_2O_2) have been already established in water treatment plants, while many others are still many are still under further development [4]. One of the widely researched AOPs is heterogeneous photocatalysis.

Another serious issue is the excessive use of carbon-based fuels, which is responsible for the probably most well-known environmental problem of the last decades: global warming caused by the increased release of CO_2 and other greenhouse gases. Burning hydrocarbons and coal also contributes to the pollution of air with gaseous and solid pollutants, resulting in several environmental and health problems, like the formation of smog in densely populated and industrial areas. Another aspect of the problem is that reserves of coal and hydrocarbons are finite, and the search for accessible and cheap renewable substitutes is ongoing in the research field of alternative energies.

The fundamentals of green chemistry have been laid down in the 1990s, promoting environmentally friendly chemical processes. The principles of green chemistry aim primarily at the prevention of environmental and health hazards: the use of the least harmful chemicals, low waste production, and energy consumption [5, 6]. Since even today these principles are still not accomplished in many cases, and due to already occurred environmental damage, cost-effective solutions are still needed to reduce these problems. The use of catalysts is one of the key elements of green chemistry. Catalysts are materials used to increase reaction rates by introducing new reaction pathways with lower activation energies. Heterogeneous photocatalysis is a field of heterogeneous catalysis, in which a photochemical reaction is accelerated or initiated thanks to the presence of photocatalysts (generally semiconductors) and photons with appropriate energy to activate them. In the activated semiconductor particles, conduction band electrons $\left(e_{cb}^{-}\right)$ and valence band holes $\left(h_{vb}^{+}\right)$ are formed and initiate redox reactions with species adsorbed on the catalyst surface. In the presence of water and dissolved oxygen, the formation of different reactive species takes place, often leading to the formation of a highly reactive and non-selective oxidant, hydroxyl radical ($HO^{\bullet}$), which generally has an important role [7].

1.1.2 A Brief History of Heterogeneous Photocatalysis

The first mentions of photocatalytic reactions date back to the start of the twentieth century [8, 9], but they received wider attention after Fujishima and Honda displayed photocatalytic water splitting to produce hydrogen using a TiO_2 electrode [10]. Ever since, heterogeneous photocatalysis has received widespread scientific attention, thanks to the wide range of application possibilities. The number of studies investigating the mechanisms of photocatalysis, developing new photocatalytic materials, or otherwise incorporating photocatalytic materials into their work, is steadily growing. Many disciplines are related to the research of heterogeneous photocatalysis (Fig. 1.1). The application possibilities of heterogeneous photocatalysis seem limitless—they have been applied during selective oxidation/ reduction in organic synthesizes, environmental application, self-cleaning surfaces, healthcare applications, and cancer treatment [11].

As mentioned earlier, photocatalytic processes can offer solutions to many problems, especially using the Sun as a light source, but they still face a number of challenges. A “perfect” photocatalyst needs to have several properties: it must be highly photoactive, chemically and biologically inert, withstand photocorrosion, non-toxic, inexpensive, and it must have the ability to be activated by solar light. TiO_2 meets most of these requirements, except it is primarily active in the UV region. Other photocatalytic materials often suffer from problems, like low stability or high production costs [12]. In the past decades, the modification of TiO_2 (or other effective photocatalyst) and the synthesis of new photoactive semiconductors are the keys to the application of heterogeneous photocatalytic processes under visible light irradiation. Efficient reduction of TiO_2’s bandgap (below 2.5 eV), synthesis of new photocatalysts, enhancement of their photonic efficiency and/or activity are still great challenges [13].

Among these photoactive semiconductors, pristine metal-oxides such as TiO_2 and ZnO are often referred to as first-generation photocatalysts because they were

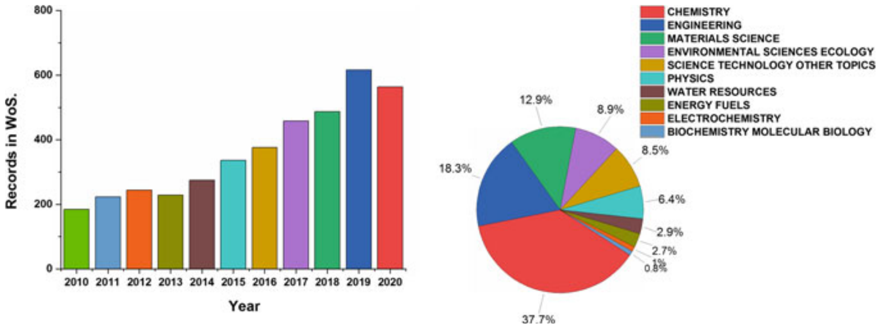

Fig. 1.1 Number of publications containing “heterogeneous photocatalysis” in the abstract, keywords, or title from 2010 to 2020, and their distribution among different fields of sciences. Data from Web of Science

the first semiconductors to be studied and applied in photocatalytic applications. These photocatalysts usually have bandgaps with energies higher than 3.1 eV (the wavelength of activating photons is lower than 400 nm) and therefore cannot be activated efficiently with solar irradiation—only 3–5% of the solar spectrum is in this range. Furthermore, the recombination of the charge carriers is a recurrent phenomenon in these first-generation photocatalysts, critically lowering their photonic efficiencies [12, 14–17].

Aiming to increase the sensitivity of these photocatalysts toward longer wavelengths as well as to reduce the recombination rate of the charge carriers, first-generation photocatalysts have been modified via several processes including elemental doping with metal and non-metal elements [18], dye sensitization [19], mesoporous structures [20], and creation of heterojunctions [12], giving rise to the second generation of photocatalysts. The doping process has received great attention and is considered an effective strategy to increase the efficiency of photocatalytic processes and extend light absorption [21]. In elemental doping, impurities are intentionally added to the structure of semiconductors [21]. The addition of phosphorous atoms to the structure of silicon semiconductors is one example of the addition of donor atoms, forming the n-type semiconductors (*n* represents the additional negative charge transferred by the donor atom). Similarly, the addition of acceptor, such as boron in silicon, results in p-type semiconductors [21, 22]. These modifications aim at better spectral sensitivity and photoactivity under exposure to sunlight. However, metal doping, for instance, can generate additional recombination or non-active absorption centers [15]. The incorporation of carbon nanotubes and graphene to semiconductors can increase adsorption sites for the substrates, serve as electron acceptors or channels to avoid charge carriers' recombination, and can induce the sensitization toward photons with higher wavelengths [12].

Another issue that has to be solved (especially when the photocatalyst is suspended in an aqueous solution) is the separation of the semiconductors from the media, which usually requires extra equipment and energy, increasing the cost of photocatalytic processes. To overcome this obstacle, photocatalysts have been immobilized into solid substrates or combined with co-catalysts, resulting in the third generation of photocatalysts [16] (immobilization methods are discussed later, in Sect. 1.5.1).

Among the several possible uses of heterogeneous photocatalysis, its potential in environmental applications is particularly notable. The application possibilities are numerous: the purification of water and air, degradation of hazardous waste, disinfection, cost-effective catalytic synthesis, and the production of hydrogen as a renewable, environmentally friendly fuel (Fig. 1.2). Another green aspect can be the use of recycled materials and waste during the production of photocatalytic materials, as it reduces both production costs and the amount of discarded waste. The metals needed for the synthesis of semiconductors, like zinc and titanium, might come from industrial wastes such as blast furnace slag [23], while catalyst supports, templates [24], and even dopants [25] can be produced from agricultural wastes [26]. The recently very popular g-C_3N_4 catalysts and other carbon-based photocatalytic materials can also be synthesized from organic waste [27, 28].

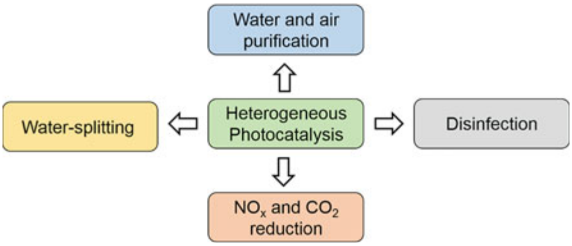

Fig. 1.2 Main environmental applications of heterogeneous photocatalysis

Biological materials can be used as size or shape controlling agents to enhance the synthesis of catalysts and even as additives to enhance the photocatalytic activity [29, 30].

A potential drawback of heterogeneous photocatalysis is the possibility of the release of catalyst particles into the environment. There are studies about the (eco)toxicity of nanoparticles in the environment, and the problem is even more complicated with photoactive materials [31]. The problem becomes more complex with the countless new nanomaterials with different chemical structures, particle sizes, and photoactivity [32].

1.2 Formation of Charge Carriers and Reactive Oxygen Species

Photocatalysis can be defined as the change in the rate of a chemical reaction or the initiation of this reaction in the presence of a catalyst excited by radiation with suitable wavelengths. In the case of photocatalysis, the formation of charge carriers with relative high reduction/oxidative potentials takes place, and these charge carriers are able to promote nonspontaneous reactions—or those with a positive change in Gibbs free energy—such as water splitting and the degradation of pollutants in water or air [17]. In a typical catalytic process, the kinetics of the reactions change, while thermodynamic parameters and reaction products are typically not altered.

Semiconductors are materials with conductivity in the range between metals and insulators, and in which the density of electric charge carriers is altered by external factors or agents—such as temperature and exposure to radiation [33]. When photons act as one of those agents, semiconductors can promote or accelerate reactions and the phenomenon of photocatalysis takes place; therefore, semiconductors activated by an absorbed photon are known as photocatalysts.

The formation of charge carriers is possible due to the semiconductors' electronic structure, characterized by a filled valence band and an empty conduction band separated in energy levels by a given bandgap. In the absence of an external stimulus—or the exposure to irradiation—electrons occupy the valence band. When the photocatalyst is exposed to radiation, photons with an energy equal to or greater than the energy of the bandgap (E_{bg}) are able to transfer electrons from the valence to the conduction band, leaving positive charges (or holes) behind [22]. Initially, the electron in the conduction band and the hole in the valence band—which will be herein represented as e^-_{cb} and h^+_{vb}, respectively—are not free charge carriers nor free entities, but together consist the so-called exciton, which is a quasiparticle stabilized in semiconductors by electrostatic Coulombic forces—the attraction between e^-_{cb} and h^+_{vb} and repulsion between different electrons in the conduction band. The exciton is an energy carrier, since it was formed by the absorption of a photon, but not a charge carrier. The separation of the energy carriers into free charge carriers occurs when enough excitons are formed—or enough electrons occupy the conduction band—so that the Coulombic attraction between e^-_{cb} and h^+_{vb} is exceeded by repelling forces [13, 34]. Most of these charge carriers undergo recombination processes in the semiconductor bulk or surface [22, 35], but a few of them can migrate to the surface of the photocatalyst, where they initiate oxidative and reductive reactions [36]. The recombination processes can be radiative, with the subsequent release of heat, or consist of non-radiative relaxation processes that propagate vibrational motions through the lattice of the semiconductor [13, 37].

The oxidation is initiated by the h^+_{vb}, a powerful oxidant with reduction potentials (vs. NHE) varying from +1.0 to +3.5 V depending on the material of the semiconductor, its properties, and the pH of the medium, as represented in Fig. 1.3 [38]. Similarly, reductive mechanisms are initiated by the e^-_{cb}, which can have reduction potentials (vs. NHE) in the range of +0.5 to −1.5 V. The following chart represents the electrochemical reduction/oxidation of species in various photocatalysts, with reduction potentials expressed versus the normal hydrogen electrode (NHE) [17, 38].

The fast recombination of the charge carriers is the main limitation of photocatalytic processes. It occurs in the timeframe of nanoseconds in the absence of

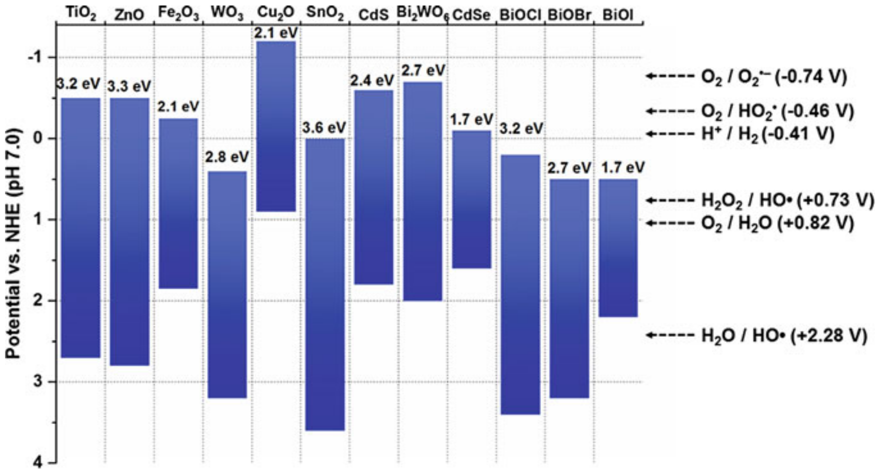

Fig. 1.3 Bandgap energies of several different semiconductors

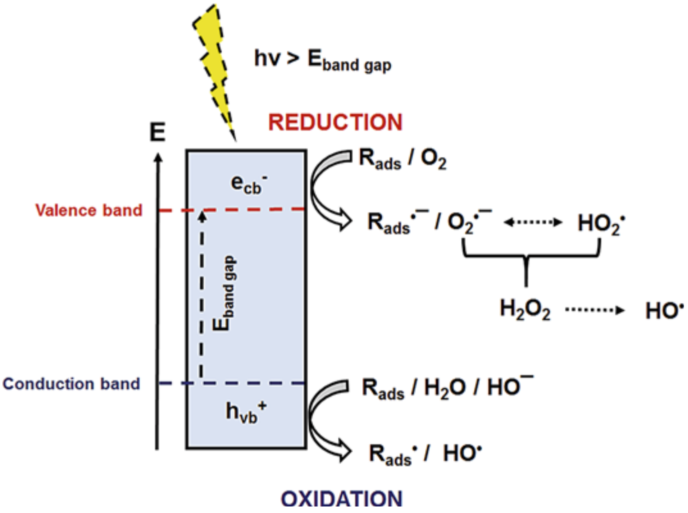

Fig. 1.4 Formation of reactive species in O_2 containing aqueous suspension of TiO_2 photocatalyst

suitable electron donors and/or acceptors, which must be adsorbed on the surface of the photocatalysts. The h_{vb}^+ can be trapped either by chemisorbed substrates or by surface oxygen/hydroxyl groups, depending on the pH of reaction media. The transfer of electrons from chemisorbed species to h_{vb}^+ occurs through an inelastic direct charge transfer pathway, while other substrates that interact weakly with the surface of the semiconductors can also undergo redox processes through indirect electron transfer mechanisms that depend on the capture of the charge carrier by surface atoms of the photocatalyst. Those mechanisms are particularly relevant to the oxidation of organic compounds in the liquid phase [39, 40]. A representation of the charge carriers formation and their reaction with adsorbed species in a general photocatalyst structure is given in Fig. 1.4.

The nature of the electron donor or acceptor is modified according to the reaction medium (aqueous or gaseous phase) and with the chemical environment (pH, presence of ions, etc.). In aqueous media, water molecules can donate electrons to the h_{vb}^+ (1.2), while dissolved oxygen acts as an electron acceptor (1.7). The products of these reactions are various Reactive Oxygen Species (ROS), which can initiate chain-reaction mechanisms and promote several processes such as the degradation of organic compounds (including alkanes, alkenes, PCBs, phenols, aromatic carboxylic acids, dyes, pesticides, etc.) as well as the reductive deposition of heavy metals (such as Cr^{6+}, Pt^{4+}, etc.) to the surface. In the same manner, in the gas phase, molecules such as CO_2 can accept the e_{cb}^- and suffer reductive processes to form formic acid, methanol, etc., while adsorbed water molecules will react with the h_{vb}^+. The mechanisms underlying the formation of reduction products of CO_2 are debatable, most of the authors suppose a series of one-electron transfer reactions [17].

The following reactions (1.1–1.11) show the reaction of charge carriers with electron donors or acceptors. Photogenerated charge carriers can react with adsorbed substances or be trapped in various ways by surface or subsurface groups of the photocatalyst. R_{ads} represents a chemisorbed organic species, $\mathrm{Ti}^{4+}-\mathrm{O}^{2-}-\mathrm{Ti}^{4+}$ a subsurface oxygen, $\mathrm{Ti}^{4+}-\mathrm{OH}^{-}$ is a surface hydroxil group of the $\mathrm{TiO_2}$ photocatalyst.

$$\text{Photocatalyst} + h\nu \rightarrow \mathrm{e}^{-}_{\mathrm{CB}} + \mathrm{h}^{+}_{\mathrm{VB}} \tag{1.1}$$

$$\mathrm{h}^{+}_{\mathrm{VB}} + \mathrm{H_2O} \rightarrow \mathrm{HO}^{\bullet} + \mathrm{H}^{+} \tag{1.2}$$

$$\mathrm{h}^{+}_{\mathrm{VB}} + R_{\mathrm{ads}} \rightarrow R^{\bullet +} \tag{1.3}$$

$$\mathrm{h}^{+}_{\mathrm{VB}} + \mathrm{Ti}^{4+}-\mathrm{O}^{2-}-\mathrm{Ti}^{4+} \rightarrow \mathrm{Ti}^{4+}-\mathrm{O}^{\bullet -}-\mathrm{Ti}^{4+} \tag{1.4}$$

$$\mathrm{Ti}^{4+}-\mathrm{O}^{\bullet -}-\mathrm{Ti}^{4+} + R \rightarrow \mathrm{Ti}^{4+}-\mathrm{O}^{2-}-\mathrm{Ti}^{4+} + \mathrm{R}^{\bullet +} \tag{1.5}$$

$$\mathrm{h}^{+}_{\mathrm{VB}} + \mathrm{Ti}^{4+}-\mathrm{OH}^{-} \rightarrow \mathrm{Ti}^{4+}-\mathrm{OH}^{\bullet} \tag{1.6}$$

$$\mathrm{e}^{-}_{\mathrm{CB}} + \mathrm{O_2} \rightarrow \mathrm{O_2}^{\bullet -} \tag{1.7}$$

The $\mathrm{HO}^{\bullet}$ is the main active species in the degradation of substrates in the aqueous phase. This statement is endorsed by its high reduction potential ($\mathrm{HO}^{\bullet}$, H^{+}/$\mathrm{H_2O}$, $E^0 = +2.80$ V) and its high reaction rates with numerous substances [41]. In photocatalytic reactions, the formation of $\mathrm{HO}^{\bullet}$ is determined by the nature of the photocatalyst. For instance, $\mathrm{TiO_2}$ occurs in three main crystal phases, known as anatase, rutile, and brookite; among those, only anatase and rutile are widely used as photocatalyst. The formation of mobile $\mathrm{HO}^{\bullet}$ which can diffuse 7.5 µm in water is reported in anatase, whereas only superficial $\mathrm{HO}^{\bullet}$ (1.6) is reported in rutile [42, 43].

$\mathrm{HO}^{\bullet}$ can also be formed in an aqueous solution via formation of $\mathrm{O_2}^{\bullet -}$ (1.7 and 1.8). In the case of $\mathrm{TiO_2}$, beside the reaction with molecular $\mathrm{O_2}$ (1.7), the $\mathrm{e}^{-}_{\mathrm{cb}}$ can be trapped by Ti^{4+}. The formed Ti^{3+} sites can act as a reductive agent and initiate the following mechanism (1.8–1.11) [44]:

$$\mathrm{Ti}^{3+} + \mathrm{O_2} \rightarrow \mathrm{Ti}^{4+} + \mathrm{O_2}^{\bullet -} \tag{1.8}$$

$$\mathrm{O_2}^{\bullet -} + \mathrm{HO_2}^{\bullet} + \mathrm{H}^{+} \rightarrow \mathrm{H_2O_2} + \mathrm{O_2} \tag{1.9}$$

$$\mathrm{H_2O_2} + h\nu \rightarrow 2\mathrm{HO}^{\bullet} \tag{1.10}$$

$$\mathrm{H_2O_2} + \mathrm{Ti}^{3+} \rightarrow \mathrm{Ti}^{4+} + \mathrm{HO}^{\bullet} + \mathrm{OH}^{-} \tag{1.11}$$

$\mathrm{HO}^{\bullet}$ react mainly through three different pathways: one-electron abstraction, hydrogen atom abstraction, and addition to double bonds. The one-electron abstraction generally happens in the presence of inorganic ions or easily oxidized

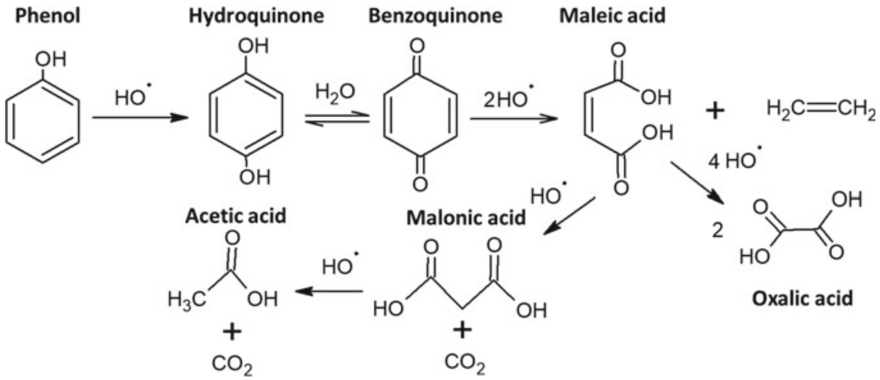

Fig. 1.5 HO• initiated transformation of phenol

organic compounds, hydrogen atom abstraction takes place mostly in the presence of saturated hydrocarbons, aldehydes, alcohols, and carboxylic acids, while the addition to double bonds is one of the main mechanisms for the degradation of unsaturated and aromatic organic compounds [44, 45]. Because the direct transfer of electrons requires the rearrangement of charged reaction centers, this is rarely observed. It can occur between HO• and metals through intermediate complexes [45]. Due to its electrophilic character, HO• readily reacts with the C=C bond and aromatic ring, as Fig. 1.5 shows, in the case of the phenol as a model substrate.

Enhanced reaction rates are usually observed in the gas phase due to the absence of solvation effects. Similar HO•-based reactions take place in the gas phase as well as under tropospheric conditions. It is known that tropospheric aerosol particles contain carboxylic acids such as oxalic, malonic, and succinic acid. These organic compounds originate from reactions between HO• radicals and aromatic compounds [46].

In the case of the gas phase removal of contaminants, the relative contribution of HO• (either from adsorbed water or surface −OH groups) and the role of charge transfer reactions and/or other reactive particles in the transformation of organic or inorganic substances strongly depend on the chemical properties of the pollutant, on its chemical structure and on the surface properties of the photocatalyst. During the transformation of toluene in the gas phase, the dominant role of HO• was confirmed [47]; however, HO• radicals have a minor contribution to the transformation of chlorinated compounds. In the case of perchloroethylene, for instance, the inhibition effect of water–vapor [48] and the consequences of the modification of the TiO_2 surface [49] indicated a significant contribution of direct charge transfer and reaction with superoxide anion radical ($O_2^{\bullet-}$) [50]. $O_2^{\bullet-}$ has been observed during several photo-assisted reactions, especially in sensitized processes, in which singlet oxygen and $O_2^{\bullet-}$ radicals are the main active species [51]. $O_2^{\bullet-}$ is formed by the direct transfer of electrons from the conduction band to O_2 molecules adsorbed on the surface of photocatalysts [52, 53]. It may act as an oxidant ($O_2^{\bullet-}$, $2H^+/H_2O_2$, $E^0 = +0.94$ V), although the intermediate species formed during the reduction of superoxide (i.e., O_2^{2-}) are very unstable [54–56].

The $O_2^{\bullet -}$ reacts by disproportionation, one-electron transfer, nucleophilic substitution, and deprotonation [57]. The main characteristic of $O_2^{\bullet -}$ is its ability to act as a strong Brønsted base. As a consequence, mechanisms involving this radical should not play an important role in protic solvents. The $O_2^{\bullet -}$ can attack positively charged compounds or centers due to its powerful nucleophilicity [54, 57]. This reaction is particularly relevant in the presence of alkyl halides, whose mechanism is schematically represented in reaction 1.13 [57]. Superoxide radicals can react through outer- or inner-sphere electron transfer mechanisms as shown in reactions 1.14 and 1.15 [57].

$$O_2^{\bullet -} + H^+ \rightleftharpoons HO_2^{\bullet}\ (pk_a = 4.8) \tag{1.12}$$

$$O_2^{\bullet -} + RX \rightarrow [O_2^{\bullet -} \ldots R \ldots X \rightleftharpoons O_2 \ldots R \ldots X^-] \rightarrow RO_2^{\bullet} + X^- \tag{1.13}$$

$$O_2^{\bullet -} + R \rightleftharpoons O_2 + R^{\bullet -} \tag{1.14}$$

$$R + O_2^{\bullet -} \rightleftharpoons R - O_2^{\bullet -} \rightarrow O_2 + R^{\bullet -} \tag{1.15}$$

The $O_2^{\bullet -}$ plays a major role in the formation of hydrogen peroxide, (1.9) [52]. Despite having a high reduction potential (H_2O_2, $2H^+/2H_2O$, $E^0 = +1.77$ V), the direct oxidation of substrates by hydrogen peroxide is considered irrelevant. Most probably, the hydrogen peroxide reacts with photogenerated charges on the surface of photocatalysts or with $O_2^{\bullet -}$ [54], resulting in $HO^{\bullet}$ formation (reactions 1.16 and 1.17).

$$H_2O_2 + e^-_{CB} \rightarrow HO^{\bullet} + HO^- \tag{1.16}$$

$$H_2O_2 + O_2^{\bullet -} \rightarrow HO^{\bullet} + HO^- + O_2 \tag{1.17}$$

Besides hydrogen peroxide, singlet oxygen is another non-radical oxidative species whose presence is reported in most photo-assisted systems associated with the formation of $O_2^{\bullet -}$. Singlet oxygen is formed after the oxidation of $O_2^{\bullet -}$ by photogenerated holes [58, 59]; however, the relevance of singlet oxygen in oxidation mechanisms is questionable due to its low reduction potential (${}^1O_2/O_2^{\bullet -}$, $E^0 = +0.65$ V) and short half-life in aqueous media (2 μs) [59, 60]. Table 1.1 presents the values for the reduction potential of the most important ROS observed during photocatalytic processes relative to the standard hydrogen electrode system as compiled by Buettner [61].

All the previously described ROS have been detected during photocatalysis, and one of the preferred techniques for this purpose applies the electron paramagnetic resonance (EPR) spectroscopy. These short-lived ROS can only be detected using spin-trapping techniques, which consist of reacting the radicals with a spin-trapping agent to form an organic adduct with higher stability. The most used spin-trapping agents are nitroxides, such as the 5,5-dimethyl-1-pyrroline-N-oxide (abbreviated as DMPO) and the 2,2,6,6-tetramethyl-piperidine-1-oxyl (known as TEMPO) [62]. TEMPO is a specific spin-trapping agent used to identify the singlet oxygen during

Table 1.1 Redox couples and reduction potential of ROS relative to the standard hydrogen electrode (SHE)

Couple	E^0 (V)
$O_2, H^+/HO_2^\bullet$	−0.46
$O_2/O_2^{\bullet-}$	−0.33
$H_2O_2, H^+/H_2O, HO^\bullet$	+0.32
$^1O_2/O_2^{\bullet-}$	+0.65
$O_2^{\bullet-}, 2H^+/H_2O_2$	+0.94
$HO^\bullet, H^+/H_2O$	+2.31
$HO_2^\bullet, H^+/H_2O_2$	+1.06

photocatalysis; DMPO can detect most of the radicals present in a photocatalytic system, although it has been shown that a few radicals are unstable and transformed to DMPO-OH (the adduct formed between DMPO and $HO^\bullet$ radicals). This conversion particularly occurs in aqueous solutions and was observed in the presence of carbonate radicals and $O_2^{\bullet-}$ [63, 64].

Besides EPR, the presence of oxidative species can be inferred with the addition of scavenger agents, which are species able to react quickly and specifically with the radicals and charge carriers, therefore quenching their effect in photocatalytic reactions. For instance, carboxylate or carboxyl groups can coordinate with the metals present on the surface of photocatalysts, thus forming inner-sphere complexes that favor the transfer of electrons directly from the ligand molecule to the valence band of the photocatalyst or photogenerated holes [65]. For this reason, oxalate and formic acid have been applied in mechanistic investigations of photocatalytic systems to act as hole traps [66]. Other scavenger species widely applied in mechanistic investigations are alcohols such as *tert*-butanol (TBA) and methanol. The elevated second-order rate constant of the reaction between TBA and $HO^\bullet$ ($k_{TBA+HO^\bullet} = 6 \times 10^8\ M^{-1}\ s^{-1}$ [67]), along with the lower rate constant between TBA and other radical species [67], allows for a high selectivity for $HO^\bullet$ radicals [65, 68, 69]. Other scavenger agents have been applied in mechanistic investigations to verify the presence of singlet oxygen and $O_2^{\bullet-}$, such as azide ion and parabenzoquinone, respectively [68].

1.3 Application of Heterogeneous Photocatalysis

1.3.1 Removal of Pollutants from Aqueous and Gaseous Media

Heterogeneous photocatalysis has great potential for removing hardly biodegradable organic contaminants from waters, such as pesticides, pharmaceuticals, and other persistent organic substances [11, 70]. This process has shown great potential for the transformation and the mineralization of organic pollutants from aqueous or gaseous media via radical reactions. Only in a few cases is an intermediate formed (e.g., cyanuric acid during the conversion of atrazine) for which heterogeneous photocatalysis is not suitable for further oxidation and degradation [71, 72]. Chlorinated molecules easily lose the Cl^- during photocatalytic processes, while from organophosphorus compounds phosphate ion is produced [71]. From nitrogen-containing molecules usually NO_3^- and NH_4^+ ions are formed. During the degradation of compounds containing azo groups, the formation of N_2 was reported [73]. The byproducts of the degradation of organic compounds in photocatalysis are highly dependent on the oxidation state of the atoms in the compound. For instance, when the nitrogen atom is at the oxidation state of −3, as in amino groups, it evolves to NH_4^+ with the same oxidation state for the nitrogen atom. Subsequently, the NH_4^+ can be oxidized to NO_3^-. In azo groups, however, the oxidation state of the nitrogen atom is +1, thus the formation of N_2 is favored [71, 73].

The photocatalytic removal of volatile organic compounds (VOCs) in gas phase follows a similar mechanism. In gas phase, $HO^•$ is usually originated from the water–vapor and oxygen content of the air [17]. Another possible use in the gas phase is the reduction of inorganic pollutants, like CO_2, SO_2, and NO_x. The photocatalytic reduction of CO_2 has especially great interest nowadays since this process can be used to remove the most well-known greenhouse gas while enabling the production of useful products (CH_4, CO, methanol) [17, 74–76]. Besides VOCs, the highly toxic NO_x compounds (mainly NO and NO_2) are among the most widespread anthropogenic air pollutants. Heterogeneous photocatalysis offers a way to degrade NO_x to less harmful nitric acid, although the method is still under constant development [17, 77]. The gas phase applications of heterogeneous photocatalysis have been widely investigated in the last two decades, and several methods were applied, from indoor air purifiers to self-cleaning building materials (glass, concrete) with photocatalysts as surface coatings or mixed into the components [78, 79].

1.3.2 Photocatalytic Water Splitting

In the field of green chemistry and alternative energy sources, hydrogen is considered a promising alternative to replace fossil fuels due to its close to unlimited reserves in the form of water and zero emissions of harmful products. Although its cheap production and implementation in practice are still not solved, its application is steadily growing in certain areas [80]. Photocatalytic and photo-electrocatalytic water splitting to produce H_2 has received widespread attention, especially if they can be initiated by solar light, which could theoretically make the process have close to zero operating costs. During photocatalytic water splitting, the reaction of e^-_{cb} with H^+ produces H_2, while h^+_{vb} contributes to the formation of O_2 [81]. In the case of photo-electrocatalytic processes, an external circuit is used to transport the

e^-_{cb} to a cathode (e.g., Pt), where reduction reactions can take place [82]. Several photocatalysts, like TiO_2, ZnO, CdS, WO_3, or carbon-based photocatalysts [12, 38, 83, 84] have been investigated for their potential in water splitting. Considering the generally low efficiency of the method, several directions were taken to improve it, like adding doping agents (typically cations as V^{4+}, Mo^{5+}, and Ru^{3+}, or anion as N, F^-, S^{2-}) or introducing electron trapping centers (typically noble metals as Au, Ag, Pt, Pd) to improve the separation of photogenerated charges.

The fast recombination of photogenerated charges is the main reason for the low efficiency, while another reason is the backward reaction resulting in H_2O formation, which can be hindered via the addition of electron mediators [81]. The addition of sacrificial electron donors (organic acids, or inorganic ions like I^- or S^{2-}) to react with h^+_{vb} and promote the formation of H_2 via reduced charge recombination is also possible [81]. To achieve effective photocatalytic H_2 production, the exact reaction mechanisms still need further studies. A suitable, visible light active photocatalyst is still a great challenge for material science to undertake due to the generally low photostability and conduction band potential of visible light active catalysts [12, 38].

1.3.3 Photocatalytic Disinfection

Application of heterogeneous photocatalysis for disinfection was reported at first in 1988 by Matsunaga et al., who employed TiO_2 to inactivate *L. acidophilus*, *S. cerevisiae,* and *E. coli*. Since then, photocatalysis has been largely applied in disinfection systems, and the gram-negative bacteria *E. coli* is by far the most studied organism in these applications since it is an indicator of fecal contamination in water, non-pathogenic to humans, and it is easily cultivated in academic laboratories [85]. Similarly, due to its elevated stability, high efficiency, and low toxicity, TiO_2 is the most investigated semiconductor in disinfection systems.

The application of photocatalysts for disinfection has been investigated in several fields, including in the food industry [86], healthcare [87], and it is especially effective in indoor air cleaning [88]. There are also several applications of photocatalytic surfaces in the production of self-cleaning glasses and in medical devices that prevent hospital-acquired infections [89]. Considering that solar disinfection systems are widely recognized for inactivating pathogenic microorganisms in water, photocatalytic materials have been also investigated to improve the degradation efficiency in these already well-established systems [71].

The disinfection effect is more pronounced the more intense the contact between the microorganism and the surface [89, 90]. In these conditions, the direct photocatalytic damage of a microorganism structure can be caused by interfacial charge transfers between the photocatalyst and the external cell membrane, and therefore, the inactivation depends on the components of the membrane. These components include phospholipids and lipo-polysaccharides that, in the case of *E. coli*, have been proven to react directly with the h_{vb}^{+} of TiO_2 [90, 91]. Other damages inflicted to cell structures can be caused by the exposure to radiation directly in the DNA structure that happens mostly in the UVC range of the solar spectrum, and also by ROS formed during photocatalysis—especially the $HO^{\bullet}$ [92]—or during the interaction of radiation and specific intracellular structures [71, 85]. The inactivation mechanism in photocatalytic processes is therefore extremely complex and includes several steps resulting not only from the presence of a photocatalyst but also from the irradiation itself. These steps can include the formation of ROS, DNA and RNA attack by either the direct absorption of light or the attack of internally formed ROS, chain reactions, and other mechanisms that will ultimately lead to cell mutation, membrane ruptures, loss of organelle functions, etc. [85, 90].

The use of the TiO_2/UV process has been proved to inactivate several pathogenic microorganisms, like bacteria, algae, and viruses [93]. TiO_2, in its pure or modified form, has been used widely, but other photocatalytic materials, carbon-based semiconductors, like g-C_3N_4, have also been recently applied with promising results [94]. Photocatalytic treatment of wastewater not only offers a solution for the removal of harmful organic contaminants but also inactivates many pathogens in the effluent [93]. The long sterilization period (60 h) are also feasible [95].

1.4 Improving the Efficiency of Photocatalysis

1.4.1 Combination with Other Methods

The efficiency of each method can be improved by their appropriate combination. Sonophotocatalysis is a process derived from the combination of sonochemical treatment with photocatalysis. The ultrasound exposure alone results in $HO^{\bullet}$ and $H^{\bullet}$ formation. Its combination with heterogeneous photocatalysis results in synergistic increases in the $HO^{\bullet}$ formation rate [96]. Combining photocatalysis with ozonation may also result in synergistic effects. Ozone is a potent but selective oxidant. In the presence of a photocatalyst, it also acts as an electron acceptor and $HO^{\bullet}$ source, inhibits recombination of excitons, and dramatically increases the rate of $HO^{\bullet}$ formation. [97]. Photocatalytic pretreatment can remove several toxic organic contaminants, so its use can significantly increase the efficiency of biological water treatment [98].

Another possibility of the combination is the application of photocatalysts in membrane reactors (PMRs—photocatalytic membrane reactors). PMRs can be categorized into two main groups: PMRs using suspended photocatalysts and PMRs applying photocatalytic material-modified membranes [99–101]. When suspended catalysts are applied in PMRs, the photocatalytic decomposition of the organic pollutant is the main process, which is followed by membrane separation for the recovery of the nanoparticles. This application provides a high surface area for the photocatalytic processes—compared to immobilized catalysts—resulting in high decomposition efficiency. The separation of the nanoparticles by membrane filtration results in excellent photocatalyst recovery, which is beneficial both from economic and environmental aspects. However, significant fouling of the membrane caused by a high amount of nanoscaled photocatalytic material can result in high energy requirements [100, 101].

This immobilization of photocatalytic nanoparticles in/on the membrane materials promises significant beneficial properties since the immobilized photocatalysts can enhance the hydrophilicity of the surface, which is important to suppress the adhesion of hydrophobic contaminants. These contaminants could quickly form serious water barriers on the membrane surfaces, being responsible for reduced water flux, decreased membrane lifespan, and increased energy consumption [99, 102–105]. In addition, immobilized photocatalytic nanoparticles can be used in self-cleaning membranes, which can be purified without the addition of chemicals. These membranes are also promising to suppress biofouling by preventing biofilm formation. The main disadvantages of these kinds of PMRs are the lower photocatalytic activity compared to the suspension method and technical difficulties, like providing continuous irradiation of the membrane surface and ensuring a good dispersion of the immobilized particles while also maintaining the porosity of the membranes [99–101, 105].

1.4.2 Photosensitization of Semiconductors

As briefly mentioned in the previous paragraphs, the nature of the reductive/oxidative species formed in photo-assisted processes relies on the electronic structure of the semiconductors. In recent years, different substances and compounds have been added to semiconductors to modify or interfere with their electronic structure. The purpose of these modifications is always to harvest photons with lower energy, thus increasing the efficiency of photocatalysts under solar irradiation.

The first observation of the so-called photosensitization process was published by O'Regan and Grätzel in 1991, who reported that TiO_2 could be modified with a dye to generate an electrical output. This was therefore the first mention of the Grätzel solar cell, which has inspired works in the field of photovoltaic cells ever since [16, 106–109].

Visible light initiated photocatalysis can be available in combination with TiO_2 and a sensitizing dye, coordination complexes of metals (e.g., ruthenium), or short bandgap semiconductors [110]. Organic dyes and several metal-complexes can effectively absorb light in the visible range of the electromagnetic spectrum; thus, they can be used as a photosensitizer. The dye can undergo photolysis or sensitize the semiconductor and thereby inject an electron into its conduction band (Fig. 1.6). However, Terenin and Akimov proposed that sensitization occurs by energy

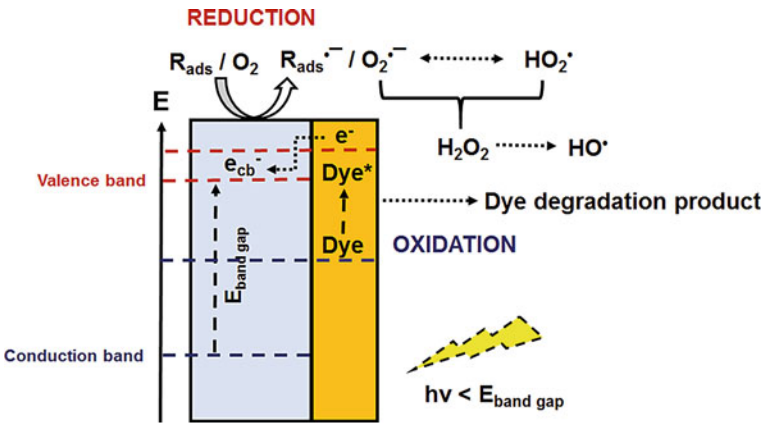

Fig. 1.6 Schematic figure of the photosensitization process (dye is adsorbed on the photocatalyst particle)

transfer from the excited dye molecule to surface-trapped electrons, and not electron transfer to the conduction band of the semiconductor [111].

To increase the absorption range of photocatalysts, inter-particle electron transfer pathways can be promoted by coupling two different semiconductors, such as TiO_2 with other visible-active photocatalyst, such as CdS [16] or WS_2 [112]. In these cases, the conduction band potential of the visible-active catalyst must be higher than that of TiO_2 (Fig. 1.7).

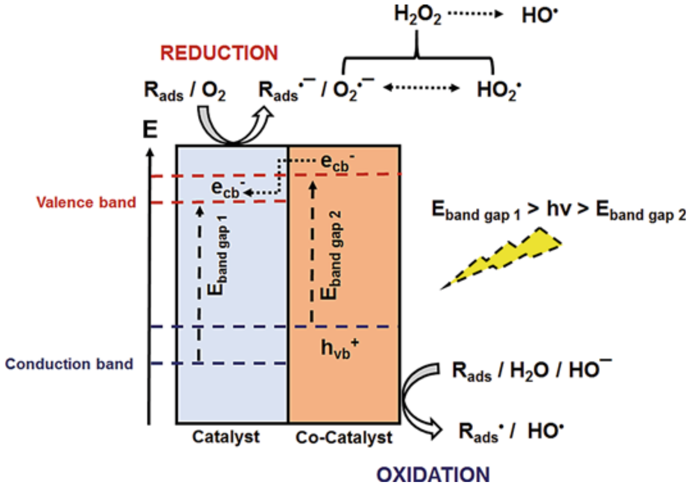

Fig. 1.7 Simplified depiction of the processes taking place in the case of a wide bandgap catalyst with a co-catalyst activated by visible light

1.5 Effective Parameters

1.5.1 Reactor Design

In the design of reactors for heterogeneous photocatalysis, the most important considerations are the mass transfer of target molecules to catalyst surface and maximizing the illuminated catalyst surface area. The photocatalysts are applied generally in two different ways: suspended in slurry reactors or immobilized as coatings. According to the light source and reaction chamber orientation, reactors can be classified as immersion, external and distributive types. The light for irradiation is distributed from the light source to the catalyst employing reflectors or optical fiber. Optical fiber reactors have the advantages of a fixed-bed reactor configuration while achieving a slurry system's equivalent efficiencies.

Suspended catalysts are always better in terms of photocatalytic efficiency due to their larger surface area and faster mass transport, but the high recovery and separation costs of nanoparticles hinder the practical application [11]. The immobilization of the catalyst is a cost-efficient way in terms of instrumentation and operating costs but significantly reduces photocatalytic activity. Due to the decrease in the surface area available to light, in this case, the fouling of the catalyst is more prominent [113]. Several immobilization methods already exist, and the most common ones are thermal, sol–gel methods, but the deposition of vapors and electrophoretic deposition has also been investigated thanks to their potential to create thin catalyst films. The most widely used supports are glass, silica-based materials, different polymers, and carbon-based materials (like activated carbon). Several other, less common supports have also been experimented with, like clays, sand, fibers, ceramic paper, and zeolites [114, 115]. The immobilization of the catalyst is a key element in terms of practical applications and finding the best method for different photocatalysts and reactor setups is an important challenge to overcome.

1.5.2 Light Intensity

The intensity of the light is another critical parameter, as the increased amounts of photons absorbed by the catalyst increase the formation of excitons. This theoretically leads to better photocatalytic activity, but the beneficial effect of higher photon fluxes is limited. Photochemical reactions are generally characterized by quantum yields or quantum efficiencies. The comparison to standard photocatalytic reactions (e.g., phenol degradation with TiO_2 P25) [116] is another possibility. The *quantum yield* (Φ) stands for the ratio of events (transformation of substrates or formation of products) and absorbed photons (1.18). Several factors complicate the determination of Φ in heterogeneous systems. During photocatalytic reactions polychromatic light is generally used, therefore, the exact quantification of photons via actinometry might be imprecise. Another issue is the reflection of photons by the photocatalyst particles, as it reduces the number of photons absorbed, resulting in a significantly lower *apparent quantum yield* (Φ_{app}) [117].

$$\Phi = \frac{\text{amount of transformed substrates or formed products}}{\text{amount of photons absorbed by the photocatalyst}} \tag{1.18}$$

$$\Phi_{\mathrm{app}} = \frac{\text{amount of transformed substrates or formed products}}{\text{amount of photons reaching the reactor}} \tag{1.19}$$

According to Hermann, due to the generally low Φ of photocatalytic reactions, the use of very high intensities is not recommended. In the case of complete surface coverage and precise determination of effective photon flux, high value can be reached (Φ = 30–40%), but in the case of trace pollutants, Φ is generally lower than 1% [72]. In many cases, the light intensity has a negligible effect [11, 14], but relatively high intensity can also promote charge carriers' recombination [118]. The effect of irradiation intensity also depends on the wavelength, the type of photocatalyst and reactants [113].

The light source is a dominant part of the reactor. The intensity of the light depends on the type of the light source, the electric power input, and the efficiency of the conversion of electrical energy into light. The utilization of solar radiation is advantageous because the cost of electricity can be avoided; however, highly efficient solar photocatalysis systems require complex design. The primary design consideration in solar photoreactors concerning the irradiation source is whether to use non-concentrated or concentrated sunlight [119].

As artificial light devices, UV lamps [120], lasers [121], or light-emitting diodes (LEDs) can be applied [122]. In most cases, conventional UV lamps are used. The efficiency of fluorescent lamps is limited by energy loss incurred in photon energy conversion and heat loss. Due to their intensive development and several advantageous properties, there has been an increased interest in applying LED light sources in the field of water treatment, even in the case of heterogeneous photocatalysis. UV LED reactors can fall under any immersion, external or distributive types and the various configurations reported in the literature [119].

1.5.3 Reaction Temperature

In homogeneous systems, higher temperature usually increases the reaction rate [123], but this effect is more complicated in photocatalytic heterogeneous systems since increasing temperatures hinders the adsorption of substrates on the catalyst surface and favor the recombination of charge carriers [11]. In gas phase at low temperatures, typically below 0 °C, the efficiency is also decreased due to the slow desorption of products [71]. In aqueous phase, the most favorable temperature range has been determined to fall between 20 and 80 °C, although it also depends on other reaction conditions and the goal of the application [11].

As a result of the relationship between temperature and adsorption, non-Arrhenius behaviors—or processes in which the rate constant is not linearly increased with the increase of temperature—are described during the heterogeneous photocatalysis conversion of many organic compounds, particularly in gas phase catalysis [44]. Examples of this behavior can be found in studies of volatile organic compounds abatement, such as trichloroethylene, benzene [124], *tert*-butyl ether, and *tert*-butyl alcohol [125] over TiO_2. This phenomenon is attributed to changes in the adsorption rate over the catalysts, which markedly decreases with the increase of temperature in solid/gas systems [124, 125].

1.5.4 Catalyst Load

The concentration of the photocatalyst directly influences the surface available for the adsorption of reactants and for photon absorption. Increasing the catalyst loading increases the reaction rates, but only up to a given concentration; therefore, the determination of the optimal loading has great importance [11]. In slurry reactors, above a given catalyst concentration, the efficiency does not change or even reduces due to increased light scattering and reduced penetration depth of the photons [14]. The role of aggregation also increases at higher catalyst loadings and leads to the reduction of photocatalytic efficiency [113]. The optimal catalyst concentration also depends on the reactor size and design [118].

In the case of immobilized catalysts, the optimal catalyst coating thickness must be determined. A thin film results in partial absorption of photons, while an overly thick one results in areas where unreactive dark zones are found, thus resulting in a waste of photocatalyst material [78].

1.5.5 Initial Concentration of the Reactant

Since photocatalytic reactions are generally described to occur on the surface of the catalyst (1.20), the role of adsorption is highly important.

$$A_{\mathrm{ads}} + B_{\mathrm{ads}} \rightarrow C_{\mathrm{ads}} \tag{1.20}$$

The reaction rates of photocatalytic processes are generally described by the Langmuir–Hinshelwood (L–H) kinetics. According to the L–H model (1.21), the concentration of substrates and their interactions with the surface determine the reaction rate:

$$r_0 = \frac{k \times K \times c_0}{1 + K \times c_0} \tag{1.21}$$

where r_0 is the initial reaction rate, c_0 is the initial concentration, k is the reaction rate constant, and K is the apparent equilibrium constant [126].

Another frequently mentioned kinetic model is the Eley–Rideal (E-R) mechanism. In contrast to the L–H model, which requires the pre-adsorption of substrates for the reactions to occur, the E-R model suggests one reactant (e.g., $HO^•$) is adsorbed while the other is in the solution/gas phase; therefore, the reaction only requires proximity to the surface of the catalyst [127]. This model can be useful to explain some experimental results, for instance, the similar transformation rate of coumarin with negligible adsorption (<1%), and 3-carboxy-coumarin with significant adsorption ($\sim$30%) on TiO_2 surface [128]. The reaction with $HO^•$ can take place in the aqueous phase, as $HO^•$ is reported to desorb from the surface of anatase phase TiO_2 and react with pollutants in solution [42].

At low reactant concentrations, the concentration increases the reaction rates, as the limiting factor is not the formation rate of excitons and reactive radicals. Above a given concentration, the reaction rates do not increase further, due to the limited number of photons or active sites available. The accumulation and adsorption of products formed during the photocatalytic reaction might also affect the efficiency, as it can block the active sites of the catalyst, leading to the poisoning of the catalyst particles [113].

The optimal concentration of the reactants must be determined individually, as it highly depends on their chemical structure. At higher concentrations, the adsorbed reactants might absorb the light and decrease the efficiency of photocatalytic processes [14]. We might conclude that heterogeneous photocatalysis is especially useful to transform reactants present in a low concentration (like trace amount of pollutants).

1.5.6 Electron Acceptors and Donors

The most important electron acceptor is O_2; on the one hand, it prevents the recombination of photogenerated charges, and on the other hand, it also plays a role in the formation of reactive particles. The presence of dissolved O_2 is highly important in an aqueous medium, but generally, there is no significant difference between reaction rates determined in air or O_2 saturated suspensions [78]. The role of O_2 is also crucial for the mineralization of organic pollutants [11] due to the formation of organic peroxyl radicals. The addition of electron acceptors, like H_2O_2, $S_2O_8^{2-}$, BrO_3^-, CCl_4, or dissolved ions (e.g., Ag^+) leads to improved charge separations and $HO^•$ formation, resulting in higher photocatalytic efficiency. The reactive species formed from these additives may also contribute to the photocatalytic process. In some cases, however, these electron acceptors may also act as radical scavengers, lowering the overall efficiency. Above the optimal concentration, the $HO^{\bullet}$ and h_{vb}^{+} scavenging effect of H_2O_2 exceed its positive effect as electron acceptor [113]. The addition of electron acceptors also makes the photocatalytic system quite complicated, and unexpected changes might occur; for instance, in the case of Ag^{+} or Fe^{3+} addition, they might even change the catalyst by precipitating in their metallic form [129].

Electron donors are especially employed in the case of H_2 generation via water splitting. Several organic electron donors have been employed, like alcohols and organic acids. In the case of CdS-based photocatalysts, the use of sulfite and sulfide ions has been proved to be beneficial to H_2-production [129].

1.5.7 Effect of Matrices

In the aqueous phase, the pH of the matrix is one of the key parameters, as it has a complex effect on heterogeneous photocatalysis. The pH affects the surface charge of the catalyst particles; above the point of zero charge (PZC), the catalyst becomes negatively charged, while at lower pH it becomes positively charged. This affects the adsorption of substrates on the surface due to electrostatic interactions. The aggregation of suspended catalyst particles also depends on pH, as particle–particle interactions result in lowered surface area and a loss of photocatalytic activity. The optimal pH range greatly depends on the catalyst, the reactants, and the goal of the application [11, 113].

Matrices may contain dissolved or floating microscopic organic components, which generally decrease the efficiency of photocatalytic processes. Suspended solids reduce the efficiency of all photochemical processes due to increased light scattering/reflectance.

Dissolved organic compounds often act as a scavenger of $HO^{\bullet}$ and/or h_{vb}^{+}, resulting in lower mineralization efficiency [11]. Their adsorption on the catalyst surface can increase the aggregation of suspended particles and occupy adsorption sites otherwise available for target compounds [130]. To solve this issue, there have been efforts to produce photocatalytic materials that show selectivity to the substrates. Coatings with selectively adsorbing materials [131] and molecular printing [132] increase the selectivity of photocatalysis for the removal of pollutants, while the adsorption of ions on TiO_2 has been used to increase its efficiency in CO_2 reduction and increase the formation of useful products like CH_4 [133].

The presence of inorganic ions has complex and varied effects. Adsorbed inorganic ions affect the surface charge of the catalysts and dramatically change adsorption properties and reaction mechanisms [134]. They may occupy adsorption sites and even displace surface −OH groups, resulting in reduced hole trapping and decreasing photocatalytic activity [135]. There are, however, special cases in which inorganic ions appear to enhance photocatalytic activities, like fluoride ions (F^{-}).

These ions replace the surface Ti–OH groups of TiO_2 with Ti–F groups, and significantly increase the transformation of organic pollutants. However, for those compounds where adsorption is required for degradation, a negative effect was observed [136, 137]. The effect even highly depends on the crystal structure, as increased efficiency of phenol degradation was observed on fluorinated anatase, while reduced transformation rates on rutile [138, 139].

The most frequent anions in natural waters are Cl^-, HCO_3^-, PO_4^{3-}, SO_4^{2-}, and NO_3^-. During the transformation of organic pollutants, both positive and negative effects have been reported. They may scavenge $HO^•$ or react with h_{vb}^+ to form reactive species, such as $Cl^•$, $CO_3^{•-}$, $PO_4^{•-}$ and $SO_4^{•-}$. These are much more selective species toward organic substances than $HO^•$; therefore, their effect on the transformation rate depends on the chemical structure and reactivity of the substrate [140].

Other ions, like Fe^{3+} or NO_3^-, have the potential to increase the efficiency of photocatalytic processes by enhancing charge separation and promoting $HO^•$ formation [113]. NO_3^- and NO_2^- may react with e_{cb}^- to form N_2, and this can be utilized to remove these ions as they are harmful in drinking water reserves, although the method still needs further development [141]. Cations like Fe^{3+} and Al^{3+} generally have a negative impact on the efficiency, while the most abundant cations in natural matrices, Na^+, Ca^+, and Mg^{2+} rarely affect that [140].

Reducing the matrix effect is a major challenge in large-scale applications of heterogeneous photocatalysis for water treatment.

1.6 Conclusions

Photocatalysis is one of the promising alternatives for environmentally friendly green solutions in water treatment, air cleaning, and energy production. Researchers with different backgrounds are involved in its development and concentrate their efforts on producing new photocatalytic materials that can cut costs and have adequate quantum efficiencies for the various applications. One of the prominent topics in this field is the heterogeneous photocatalysis driven by sunlight. Besides finding the proper materials for this application, researchers have to find cheap alternatives for catalysts manufacturing. The complexity of factors affecting photocatalysis efficiency and operation cost poses a significant challenge for implementing systems, especially those including removing pollutants from waters having complex matrix.

Acknowledgements Authors thanks for the support of the János Bolyai Research Scholarship of the Hungarian Academy of Sciences, the new national excellence program of the Ministry for Innovation and Technology (ÚNKP-20-5-SZTE 639) and the National Research, Development and Innovation Office (NKFIH, project number FK 132742).

References

1. Sousa JCG, Ribeiro AR, Barbosa MO, Pereira MFR, Silva AMT (2018) A review on environmental monitoring of water organic pollutants identified by EU guidelines. J Hazard Mater 344:146–162
2. Hassan I, Bream AS, El-Sayed A, Yousef AM (2017) International journal of advanced research in biological sciences assessment of disinfection by-products levels in aga surface water plant and its distribution system, Dakhlia Egypt. Int J Adv Res Biol Sci 4(4):37–43
3. Zhang Y, Geißen SU, Gal C (2008) Carbamazepine and diclofenac: removal in wastewater treatment plants and occurrence in water bodies. Chemosphere 73(8):1151–1161
4. Miklos DB, Remy C, Jekel M, Linden KG, Drewes JE, Hübner U (2018) Evaluation of advanced oxidation processes for water and wastewater treatment—a critical review. Water Res 139:118–131
5. Speight JG (1996) Green chemistry: designing chemistry for the environment. Energy Sources 18(7):833–834 (Review of: Anastas PT, Williamson TC, ACS symposium series No. 626. American Chemical Society, Washington, DC, $89.95, ISBN 0-8412-3399-3)
6. de Marco BA, Rechelo BS, Tótoli EG, Kogawa AC, Salgado HRN (2019) Evolution of green chemistry and its multidimensional impacts: a review. Saudi Pharm J 27(1):1–8
7. Zhang J, Nosaka Y (2013) Quantitative detection of OH radicals for investigating the reaction mechanism of various visible-light TiO2 photocatalysts in aqueous suspension. J Phys Chem C 117(3):1383–1391
8. Baly ECC, Heilbron IM, Barker WF (1921) CX.—photocatalysis, Part I. The synthesis of formaldehyde and carbohydrates from carbon dioxide and water. J Chem Soc Trans 119:1025–1035
9. Goodeve CF, Kitchener JA (1938) The mechanism of photosensitisation by solids. Trans Faraday Soc 34:902–908
10. Fujishima A, Honda K (1972) Electrochemical photolysis of water at a semiconductor electrode. Nature 238(5358):37–38
11. Ahmed SN, Haider W (2018) Heterogeneous photocatalysis and its potential applications in water and wastewater treatment: a review. Nanotechnology 29(34):13
12. Cao S, Yu J (2016) Carbon-based H2-production photocatalytic materials. J Photochem Photobiol C Photochem Rev Elsevier B.V. 27:72–99
13. Kubacka A, Fernández-García M, Colón G (2012) Advanced nanoarchitectures for solar photocatalytic applications. Chem Rev 112:1555–1614
14. Anwer H, Mahmood A, Lee J, Kim KH, Park JW, Yip ACK (2019) Photocatalysts for degradation of dyes in industrial effluents: opportunities and challenges. Nano Res 12:955–972 (Tsinghua University Press)
15. Emeline AV, Kuznetsov VN, Ryabchuk VK, Serpone N (2012) On the way to the creation of next generation photoactive materials. Environ Sci Pollut Res 19(9):3666–3675
16. Serpone N, Emeline AV (2012) Semiconductor photocatalysis—past, present, and future outlook. J Phys Chem Lett 3:673–677
17. Schreck M, Niederberger M (2019) Photocatalytic gas phase reactions. Chem Mater Am Chem Soc 31:597–618
18. Asahi R, Morikawa T, Irie H, Ohwaki T (2014) Nitrogen-doped titanium dioxide as visible-light-sensitive photocatalyst: designs, developments, and prospects. Chem Rev 114 (19):9824–9852
19. Xu J, Li Y, Peng S, Lu G, Li S (2013) Eosin Y-sensitized graphitic carbon nitride fabricated by heating urea for visible light photocatalytic hydrogen evolution: the effect of the pyrolysis temperature of urea. Phys Chem Chem Phys 15(20):7657–7665
20. Linares N, Silvestre-Albero AM, Serrano E, Silvestre-Albero J, García-Martínez J (2014) Mesoporous materials for clean energy technologies. Chem Soc Rev 43(22):7681–7717
21. Shao W, Wang H, Zhang X (2018) Elemental doping for optimizing photocatalysis in semiconductors. Dalton Trans 47(36):12642–12646

22. Colinge JP, Colinge CA (2002) Physics of Semiconductor devices. Kluwer Academic Publishers, Springer International Publishing, p 436
23. Zheng H, Okabe TH (2008) Recovery of titanium metal scrap by utilizing chloride wastes. J Alloys Compd 461(1–2):459–466
24. Yang L, Li X, Wang Z, Shen Y, Liu M (2017) Natural fiber templated TiO2 microtubes via a double soaking sol-gel route and their photocatalytic performance. Appl Surf Sci 420:346–354
25. Wang S, Wang H, Zhang R, Zhao L, Wu X, Xie H et al (2018) Egg yolk-derived carbon: achieving excellent fluorescent carbon dots and high performance lithium-ion batteries. J Alloys Compd 746:567–575
26. Rodríguez-Padrón D, Luque R, Muñoz-Batista MJ (2020) Waste-derived materials: opportunities in photocatalysis. Top Curr Chem 378(1):1–28
27. Colmenares JC, Lisowski P, Bermudez JM, Cot J, Luque R (2014) Unprecedented photocatalytic activity of carbonized leather skin residues containing chromium oxide phases. Appl Catal B Environ 150–151:432–437
28. Babar S, Gavade N, Shinde H, Gore A, Mahajan P, Lee KH et al (2019) An innovative transformation of waste toner powder into magnetic g-C3N4-Fe2O3 photocatalyst: sustainable e-waste management. J Environ Chem Eng 7(2)
29. Garg S, Yadav M, Chandra A, Sapra S, Gahlawat S, Ingole PP et al (2018) Facile green synthesis of BiOBr nanostructures with superior visible-light-driven photocatalytic activity. Materials 11(8)
30. Garg S, Yadav M, Chandra A, Sapra S, Gahlawat S, Ingole PP et al (2018) Biofabricated BiOI with enhanced photocatalytic activity under visible light irradiation. RSC Adv 8 (51):29022–29030
31. Hund-Rinke K, Simon M (2006) Ecotoxic effect of photocatalytic active nanoparticles (TiO2) on algae and daphnids. Environ Sci Pollut Res 13(4):225–232
32. Friehs E, AlSalka Y, Jonczyk R, Lavrentieva A, Jochums A, Walter JG et al (2016) Toxicity, phototoxicity and biocidal activity of nanoparticles employed in photocatalysis. J Photochem Photobiol C Photochem Rev 29:1–28
33. IUPAC (2009) IUPAC compendium of chemical terminology
34. Yu PY, Cardona M (1996) Optical properties. In: Fundamentals of semiconductors. Springer, Berlin, Heidelberg, pp 234–331
35. Yu PY, Cardona M (1996) Fundamentals of semiconductors. Fundamentals of semiconductors. Springer, Berlin, Heidelberg
36. Bhattacharyya S, Kundu S, Bramhaiah K (2020) Carbon-based nanomaterials: in the quest of alternative metal free photocatalysts for solar water splitting. Nanoscale Advances
37. Zhang L, Mohamed HH, Dillert R, Bahnemann D (2012) Kinetics and mechanisms of charge transfer processes in photocatalytic systems: a review. J Photochem Photobiol C Photochem Rev 13(4):263–276
38. Fajrina N, Tahir M (2019) A critical review in strategies to improve photocatalytic water splitting towards hydrogen production. Int J Hydrogen Energy 44(2):540–577
39. Montoya JF, Atitar MF, Bahnemann DW, Peral J, Salvador P (2014) Comprehensive kinetic and mechanistic analysis of TiO2 photocatalytic reactions according to the direct-indirect model: (II) experimental validation. J Phys Chem C 118(26):14276–14290
40. Montoya JF, Peral J, Salvador P (2014) Comprehensive kinetic and mechanistic analysis of TiO2 photocatalytic reactions according to the direct-indirect model: (I) theoretical approach. J Phys Chem C 118(26):14266–14275
41. Mitroka S, Zimmeck S, Troya D, Tanko JM (2010) How solvent modulates hydroxyl radical reactivity in hydrogen atom abstractions. J Am Chem Soc 132(9):2907–2913
42. Nosaka Y, Nosaka A (2016) Understanding hydroxyl radical (•OH) Generation processes in photocatalysis. ACS Energy Lett 1(2):356–359
43. Kim W, Tachikawa T, Moon GH, Majima T, Choi W (2014) Molecular-level understanding of the photocatalytic activity difference between anatase and rutile nanoparticles. Angew Chem Int Ed 53(51):14036–14041

44. Gligorovski S, Strekowski R, Barbati S, Vione D (2015) Environmental implications of hydroxyl radicals (•OH). chemical reviews. Chem Rev 115(24):13051–13092
45. Wojnárovits L, Takács E (2014) Rate coefficients of hydroxyl radical reactions with pesticide molecules and related compounds: a review. Radiat Phys Chem 96:120–134
46. Ervens B, Gligorovski S, Herrmann H (2003) Temperature-dependent rate constants for hydroxyl radical reactions with organic compounds in aqueous solutions. Phys Chem Chem Phys 5(9):1811–1824
47. Maira AJ, Yeung KL, Soria J, Coronado JM, Belver C, Lee CY et al (2001) Gas-phase photo-oxidation of toluene using nanometer-size TiO2 catalysts. Appl Catal B Environ 29 (4):327–336
48. Linsebigler AL, Lu G, Yates JT (1995) Photocatalysis on TiO2 surfaces: principles, mechanisms, and selected results. Chem Rev 95(3):735–758
49. Ollis DF, Al-Ekabi Hussain (1993) Photocatalytic purification and treatment of water and air. In: Proceedings of the 1st international conference on TiO2 photocatalytic purification and treatment of water and air. Elsevier Science Ltd., pp 365–373
50. Hegedus M, Dombi A, Kiricsi I (2001) Photocatalytic decomposition of tetrachloroethylene in the gas phase with titanium dioxide as catalyst. React Kinet Catal Lett 74(2):209–215
51. Pelaez M, Falaras P, Likodimos V, O'Shea K, de la Cruz AA, Dunlop PSM et al (2016) Use of selected scavengers for the determination of NF-TiO2 reactive oxygen species during the degradation of microcystin-LR under visible light irradiation. J Mol Catal A Chem 425:183–189
52. Schneider J, Matsuoka M, Takeuchi M, Zhang J, Horiuchi Y, Anpo M et al (2014) Understanding TiO2 photocatalysis: mechanisms and materials. Chem Rev 114(19):9919–9986
53. Gaya UI, Abdullah AH (2008) Heterogeneous photocatalytic degradation of organic contaminants over titanium dioxide: a review of fundamentals, progress and problems. J Photochem Photobiol C Photochem Rev 9(1):1–12
54. Petri BG, Watts RJ, Teel AL, Huling SG, Brown RA (2011) Fundamentals of ISCO using hydrogen peroxide. In: In situ chemical oxidation for groundwater remediation, vol 3, 1st edn. Springer Science+Business Media, New York, pp 33–88
55. Pignatello JJ, Oliveros E, MacKay A (2006) Advanced oxidation processes for organic contaminant destruction based on the fenton reaction and related chemistry. Crit Rev Environ Sci Technol 36(1):1–84
56. Krumova K, Cosa G (2016) Chapter 1: Overview of reactive oxygen species. In: Singlet oxygen: applications in biosciences and nanosciences, pp 1–21
57. Hayyan M, Hashim MA, Alnashef IM (2016) Superoxide ion: generation and chemical implications. Chem Rev Am Chem Soc 116:3029–3085
58. Daimon T, Hirakawa T, Kitazawa M, Suetake J, Nosaka Y (2008) Formation of singlet molecular oxygen associated with the formation of superoxide radicals in aqueous suspensions of TiO2 photocatalysts. Appl Catal A Gen 340(2):169–175
59. Nosaka Y, Daimon T, Nosaka AY, Murakami Y (2004) Singlet oxygen formation in photocatalytic TiO2 aqueous suspension. Phys Chem Chem Phys 6(11):2917–2918
60. Guo X, Li Q, Zhang M, Long M, Kong L, Zhou Q et al (2015) Enhanced photocatalytic performance of N-nitrosodimethylamine on TiO2 nanotube based on the role of singlet oxygen. Chemosphere 120:521–526
61. Buettner GR (1993) The pecking order of free radicals and antioxidants: lipid peroxidation, α-tocopherol, and ascorbate. Arch Biochem Biophys 300(2):535–543
62. Brustolon M, Giamello E (2009) Electron paramagnetic resonance: a practitioner's toolkit. Wiley, Hoboken, New Jersey, p 539
63. Bačić G, Spasojević I, Šećerov B, Mojović M (2008) Spin-trapping of oxygen free radicals in chemical and biological systems: new traps, radicals and possibilities. Spectrochim Acta Part A Mol Biomol Spectrosc 69(5):1354–1366

64. Bonini MG, Miyamoto S, Di MP, Augusto O (2004) Production of the carbonate radical anion during xanthine oxidase turnover in the presence of bicarbonate. J Bio Chem 279 (50):51836–51843
65. Yunfu S, Pignatello JJ (1995) Evidence for a surface dual hole-radical mechanism in the titanium dioxide photocatalytic oxidation of 2,4-D. Environ Sci Technol 29(8):2065–2072
66. Mendive CB, Bredow T, Schneider J, Blesa M, Bahnemann D (2015) Oxalic acid at the TiO2/water interface under UV(A) illumination: surface reaction mechanisms. J Catal 322:60–72
67. Lutze HV, Bircher S, Rapp I, Kerlin N, Bakkour R, Geisler M et al (2015) Degradation of chlorotriazine pesticides by sulfate radicals and the influence of organic matter. Environ Sci Technol 49(3):1673–1680
68. Rodríguez EM, Márquez G, Tena M, Álvarez PM, Beltrán FJ (2015) Determination of main species involved in the first steps of TiO2 photocatalytic degradation of organics with the use of scavengers: the case of ofloxacin. Appl Catal B Environ 178:44–53
69. Chen L, Zhao C, Dionysiou DD, O'Shea KE (2015) TiO2 photocatalytic degradation and detoxification of cylindrospermopsin. J Photochem Photobiol A Chem 307–308:115–122
70. Rammohan G, Nadagouda M (2013) Green photocatalysis for degradation of organic contaminants: a review. Curr Org Chem 17(20):2338–2348
71. Malato S, Fernández-Ibáñez P, Maldonado MI, Blanco J, Gernjak W (2009) Decontamination and disinfection of water by solar photocatalysis: recent overview and trends. Catal Today 147(1):1–59
72. Herrmann JM (2010) Fundamentals and misconceptions in photocatalysis. J Photochem Photobiol A Chem 216(2–3):85–93
73. Herrmann JM, Lacroix M (2010) Environmental photocatalysis in action for green chemistry. Kinet Catal 51(6):793–800
74. Shehzad N, Tahir M, Johari K, Murugesan T, Hussain M (2018) A critical review on TiO2 based photocatalytic CO2 reduction system: strategies to improve efficiency. J CO2 Utilization 26(November 2017):98–122
75. Ghadimkhani G, de Tacconi NR, Chanmanee W, Janakyab C, Rajeshwar K (2013) Efficient solar photoelectrosynthesis of methanol from carbon dioxide using hybrid CuO-Cu2O semiconductor nanorod arrays. Chem Commun 49(13):1297–1299
76. Janáky C, Hursán D, Endrödi B, Chanmanee W, Roy D, Liu D et al (2016) Electro- and photoreduction of carbon dioxide: the twain shall meet at copper oxide/copper interfaces. ACS Energy Lett 1(2):332–338
77. Zouzelka R, Rathousky J (2017) Photocatalytic abatement of NOx pollutants in the air using commercial functional coating with porous morphology. Appl Catal B Environ 217:466–476
78. Spasiano D, Marotta R, Malato S, Fernandez-Ibañez P, Di Somma I (2015) Solar photocatalysis: materials, reactors, some commercial, and pre-industrialized applications. A comprehensive approach. Appl Catal B Environ 170–171:90–123
79. Boonen E, Beeldens A (2014) Recent photocatalytic applications for air purification in Belgium. Coatings 4(3):553–573
80. Staffell I, Scamman D, Velazquez Abad A, Balcombe P, Dodds PE, Ekins P et al (2019) The role of hydrogen and fuel cells in the global energy system. Energy Environ Sci 12(2):463–491
81. Ni M, Leung MKH, Leung DYC, Sumathy K (2007) A review and recent developments in photocatalytic water-splitting using TiO2 for hydrogen production. Renew Sustain Energy Rev 11(3):401–425
82. Zhao W, Wang Z, Shen X, Li J, Xu C, Gan Z (2012) Hydrogen generation via photoelectrocatalytic water splitting using a tungsten trioxide catalyst under visible light irradiation. Int J Hydrogen Energy 37(1):908–915
83. Kundu S, Bramhaiah K, Bhattacharyya S (2020) Carbon-based nanomaterials: in the quest of alternative metal-free photocatalysts for solar water splitting. Nanoscale Advances
84. Janáky C, Rajeshwar K, De Tacconi NR, Chanmanee W, Huda MN (2013) Tungsten-based oxide semiconductors for solar hydrogen generation. Catal Today 199(1):53–64

85. Valero P, Giannakis S, Mosteo R, Ormad MP, Pulgarin C (2017) Comparative effect of growth media on the monitoring of *E. coli* inactivation and regrowth after solar and photo-Fenton treatment. Chem Eng J 313:109–120
86. Chawengkijwanich C, Hayata Y (2008) Development of TiO2 powder-coated food packaging film and its ability to inactivate *Escherichia coli* in vitro and in actual tests. Int J Food Microbiol 123(3):288–292
87. Wong MS, Chu WC, Sun DS, Huang HS, Chen JH, Tsai PJ et al (2006) Visible-light-induced bactericidal activity of a nitrogen-doped titanium photocatalyst against human pathogens. Appl Environ Microbiol 72(9):6111–6116
88. Vohra A, Goswami DY, Deshpande DA, Block SS (2006) Enhanced photocatalytic disinfection of indoor air. Appl Catal B Environ 64(1–2):57–65
89. Foster HA, Ditta IB, Varghese S, Steele A (2011) Photocatalytic disinfection using titanium dioxide: spectrum and mechanism of antimicrobial activity. Appl Microbiol Biotechnol 90 (6):1847–1868
90. Pulgarin C, Kiwi J, Nadtochenko V (2012) Mechanism of photocatalytic bacterial inactivation on TiO2 films involving cell-wall damage and lysis. Appl Catal B Environ 128:179–183
91. Nadtochenko V, Denisov N, Sarkisov O, Gumy D, Pulgarin C, Kiwi J (2006) Laser kinetic spectroscopy of the interfacial charge transfer between membrane cell walls of *E. coli* and TiO2. J Photochem Photobiol A Chem 181(2–3):401–407
92. Veréb G, Manczinger L, Bozsó G, Sienkiewicz A, Forró L, Mogyorósi K et al (2013) Comparison of the photocatalytic efficiencies of bare and doped rutile and anatase TiO2 photocatalysts under visible light for phenol degradation and E. coli inactivation. Appl Catal B Environ 129:566–574
93. Zhang Z, Gamage J (2010) Applications of photocatalytic disinfection. Int J Photoenergy
94. Gong M, Xiao S, Yu X, Dong C, Ji J, Zhang D et al (2019) Research progress of photocatalytic sterilization over semiconductors. RSC Adv 9(34):19278–19284
95. Rincón AG, Pulgarin C (2004) Bactericidal action of illuminated TiO2 on pure Escherichia coli and natural bacterial consortia: post-irradiation events in the dark and assessment of the effective disinfection time. Appl Catal B Environ 49(2):99–112
96. Selli E (2002) Synergistic effects of sonolysis combined with photocatalysis in the degradation of an azo dye. Phys Chem Chem Phys 4(24):6123–6128
97. Augugliaro V, Litter M, Palmisano L, Soria J (2006) The combination of heterogeneous photocatalysis with chemical and physical operations: a tool for improving the photoprocess performance. J Photochem Photobiol C Photochem Rev 7(4):127–144
98. Sarria V, Kenfack S, Guillod O, Pulgarin C (2003) An innovative coupled solar-biological system at field pilot scale for the treatment of biorecalcitrant pollutants. J Photochem Photobiol A Chem 159(1):89–99
99. Nascimbén Santos É, László Z, Hodúr C, Arthanareeswaran G, Veréb G (2020) Photocatalytic membrane filtration and its advantages over conventional approaches in the treatment of oily wastewater: a review. Asia Pac J Chem Eng 15(5)
100. Zhang W, Ding L, Luo J, Jaffrin MY, Tang B (2016) Membrane fouling in photocatalytic membrane reactors (PMRs) for water and wastewater treatment: a critical review. Chem Eng J 302:446–458
101. Molinari R, Lavorato C, Argurio P (2017) Recent progress of photocatalytic membrane reactors in water treatment and in synthesis of organic compounds. A review. Catal Today 281:144–164
102. Padaki M, Surya Murali R, Abdullah MS, Misdan N, Moslehyani A, Kassim MA et al (2015) Membrane technology enhancement in oil-water separation. A review. Desalination 357:197–207
103. Liu Q, Huang S, Zhang Y, Zhao S (2018) Comparing the antifouling effects of activated carbon and TiO2 in ultrafiltration membrane development. J Colloid Interface Sci 515:109–118

104. Veréb G, Kálmán V, Gyulavári T, Kertész S, Beszédes S, Kovács G et al (2019) Advantages of TiO2/carbon nanotube modified photocatalytic membranes in the purification of oil-in-water emulsions. Water Sci Technol Water Supply 19(4):1167–1174
105. Nascimben Santos E, Ágoston Á, Kertész S, Hodúr C, László Z, Pap Z et al (2020) Investigation of the applicability of TiO2, BiVO4, and WO3 nanomaterials for advanced photocatalytic membranes used for oil-in-water emulsion separation. Asia Pac J Chem Eng 15(5)
106. Hagfeldt A, Grätzel M (1995) Light-induced redox reactions in nanocrystalline systems. Chem Rev 95(1):49–68
107. Kamat PV, Tvrdy K, Baker DR, Radich JG (2010) Beyond photovoltaics: semiconductor nanoarchitectures for liquid-junction solar cells. Chem Rev 110(11):6664–6688
108. Silva SS, Magalhães F, Sansiviero MTC (2010) Nanocompósitos semicondutores ZnO/TiO2. Testes fotocatalíticos. Quim Nova 33(1):85–89
109. Zhang Z, Yates JT (2012) Band bending in semiconductors: chemical and physical consequences at surfaces and interfaces. Chem Rev 112(10):5520–5551
110. Pei D, Luan J (2012) Development of visible light-responsive sensitized photocatalysts. Int J Photoenergy 2012
111. Terenin A, Akimov I (2017) On the mechanism of the optical sensitization of semiconductors by organic dyes. Zeitschrift für Physikalische Chemie 217(1)
112. Jing D, Guo L (2007) WS2 sensitized mesoporous TiO2 for efficient photocatalytic hydrogen production from water under visible light irradiation. Catal Commun 8(5):795–799
113. Ahmed S, Rasul MG, Brown R, Hashib MA (2011) Influence of parameters on the heterogeneous photocatalytic degradation of pesticides and phenolic contaminants in wastewater: a short review. J Environ Manage 92(3):311–330
114. Shan AY, Ghazi TIM, Rashid SA (2010) Immobilisation of titanium dioxide onto supporting materials in heterogeneous photocatalysis: a review. Appl Catal A Gen 389(1–2):1–8
115. Veréb G, Ambrus Z, Pap Z, Mogyorósi K, Dombi A, Hernádi K (2014) Immobilization of crystallized photocatalysts on ceramic paper by titanium(IV) ethoxide and photocatalytic decomposition of phenol. React Kinet Mech Catal 113(1):293–303
116. Serpone N (1997) Relative photonic efficiencies and quantum yields in heterogeneous photocatalysis. J Photochem Photobiol A Chem 104(1–3):1–12
117. Serpone N, Salinaro A (1999) Terminology, relative photonic efficiencies and quantum yields in heterogeneous photocatalysis, Part I: suggested protocol (Technical report). Pure Appl Chem 71(2):303–20
118. Ibhadon AO, Fitzpatrick P (2013) Heterogeneous photocatalysis: recent advances and applications. Catalysts 3(1):189–218
119. Tokode O, Prabhu R, Lawton LA, Robertson PKJ (2015) UV LED sources for heterogeneous photocatalysis. Handb Environ Chem 35:159–179
120. Kuo WS, Ho PH (2001) Solar photocatalytic decolorization of methylene blue in water. Chemosphere 45(1):77–83
121. Yahaya AH, Gondal MA, Hameed A (2004) Selective laser enhanced photocatalytic conversion of CO2 into methanol. Chem Phys Lett 400(1–3):206–212
122. Eskandarian MR, Choi H, Fazli M, Rasoulifard MH (2016) Effect of UV-LED wavelengths on direct photolytic and TiO2 photocatalytic degradation of emerging contaminants in water. Chem Eng J 300:414–422
123. Gaya UI (2014) Heterogeneous photocatalysis using inorganic semiconductor solids. Heterogen Photocatalysis Using Inorg Semicond Solids 9789400777:1–213
124. Doucet N, Bocquillon F, Zahraa O, Bouchy M (2006) Kinetics of photocatalytic VOCs abatement in a standardized reactor. Chemosphere 65(7):1188–1196
125. Preis S, Kachina A, Santiago NC, Kallas J (2005) The dependence on temperature of gas-phase photocatalytic oxidation of methyl tert-butyl ether and tert-butyl alcohol. Catal Today 101(3–4):353–358

126. Emeline AV, Kuznetsov VN, Ryabchuk VK, Serpone N (2013) Heterogeneous photocatalysis: basic approaches and terminology. In: New and future developments in catalysis: solar photocatalysis. Elsevier B.V., pp 1–47
127. Ollis DF (2018) Kinetics of photocatalyzed reactions: five lessons learned. Frontiers Chem 6
128. Náfrádi M, Farkas L, Alapi T, Hernádi K, Kovács K, Wojnárovits L et al (2020) Application of coumarin and coumarin-3-carboxylic acid for the determination of hydroxyl radicals during different advanced oxidation processes. Radiat Phys Chem 1:170
129. Schneider J, Bahnemann DW (2013) Undesired role of sacrificial reagents in photocatalysis. J Phys Chem Lett 4(20):3479–3483
130. Zhu M, Wang H, Keller AA, Wang T, Li F (2014) The effect of humic acid on the aggregation of titanium dioxide nanoparticles under different pH and ionic strengths. Sci Total Environ 487(1):375–380
131. Xue Y, Chang Q, Hu X, Cai J, Yang H (2020) A simple strategy for selective photocatalysis degradation of organic dyes through selective adsorption enrichment by using a complex film of CdS and carboxylmethyl starch. J Environ Manage 274
132. Yuan Q, Zhang D, Yu P, Sun R, Javed H, Wu G et al (2020) Selective adsorption and photocatalytic degradation of extracellular antibiotic resistance genes by molecularly-imprinted graphitic carbon nitride. Environ Sci Technol 54(7):4621–4630
133. Li X, Bi W, Wang Z, Zhu W, Chu W, Wu C et al (2018) Surface-adsorbed ions on TiO2 nanosheets for selective photocatalytic CO2 reduction. Nano Res 11(6):3362–3370
134. Wang Q, Chen C, Zhao D, Wanhong M, Zhao J (2008) Change of adsorption modes of dyes on fluorinated TiO2 and its effect on photocatalytic degradation of dyes under visible irradiation. Langmuir 24(14):7338–7345
135. Burns RA, Crittenden JC, Hand DW, Selzer VH, Sutter LL, Salman SR (1999) Effect of inorganic ions in heterogeneous photocatalysis of TCE. J Environ Eng 125(1):77–85
136. Park H, Choi W (2004) Effects of TiO2 surface fluorination on photocatalytic reactions and photoelectrochemical behaviors. J Phys Chem B 108(13):4086–4093
137. Vohra MS, Kim S, Choi W (2003) Effects of surface fluorination of TiO2 on the photocatalytic degradation of tetramethylammonium. J Photochem Photobiol A Chem 160 (1–2):55–60
138. Xu Y, Lv K, Xiong Z, Leng W, Du W, Liu D et al (2007) Rate enhancement and rate inhibition of phenol degradation over irradiated anatase and rutile TiO2 on the addition of NaF: new insight into the mechanism. J Phys Chem C 111(51):19024–19032
139. Lv K, Lu CS (2008) Different effects of fluoride surface modification on the photocatalytic oxidation of phenol in anatase and rutile TiO2 suspensions. Chem Eng Technol 31(9):1272–1276
140. Kudlek E, Dudziak M, Bohdziewicz J (2016) Influence of inorganic ions and organic substances on the degradation of pharmaceutical compound in water matrix. Water (Switz) 8 (11)
141. Shand M, Anderson JA (2013) Aqueous phase photocatalytic nitrate destruction using titania based materials: routes to enhanced performance and prospects for visible light activation. Catal Sci Technol 3(4):879–899

Chapter 2
Optimization of Process, Mechanism and Kinetics Study for Photocatalytic Oxidation

Tejendra K. Gupta, Sucheta Sengupta, and Manoj Raula

Abstract Photocatalysis is the fastest growing and popular technological advancement used in various fields of science and technology, such as treatment of wastewater for the degradation of organic pollutants, self-cleaning surfaces, anti-fouling coating and photocatalytic water-splitting. Additional advantages for the photocatalytic oxidations are easier to use, cost-effective and environmentally benign. Nanomaterials, such as TiO_2, ZnO, Fe_2O_3, NiO and many more, are extensively used as photocatalyst for various applications as mentioned earlier. Nanomaterials play an important role in the advancement of innovative methods to produce new products and to reformulate new materials with enhanced performance, also consume less energy and materials and reduce the environmental dangers. A better understanding about the kinetics and mechanism of the photocatalytic oxidation is required to comprehend about this newly developed technique. This chapter aims to provide the state-of-the-art research activities targeting basic principles involved in the photocatalytic reactions, role of nanomaterials in optimization of process and mechanism and kinetics of photocatalytic oxidation.

Keywords Metal oxides · Photocatalytic oxidation · Kinetics · Mechanisms · Optimization

---

T. K. Gupta (✉) · M. Raula (✉)
Amity Institute of Applied Sciences, Amity University, Sector-125, Noida 201313, India
e-mail: tkgupta@amity.edu

M. Raula
e-mail: mraula@amity.edu

S. Sengupta
Amity Institute of Advanced Research and Studies (Materials and Devices), Amity University, Sector-125, Noida 201313, India

S. Garg and A. Chandra (eds.), *Green Photocatalytic Semiconductors*,
Green Chemistry and Sustainable Technology,
https://doi.org/10.1007/978-3-030-77371-7_2

2.1 Introduction

A large range of organic matters generated from agricultural overspills, industrial wastes and chemicals are the major water pollutants [1]. Their stability, toxic nature for natural decomposition and tenacity in the environment have become the cause of much concern to the civilizations and regulatory authorities everywhere in the globe [1, 2]. Development of suitable techniques for the degradation of contaminated particles from the wastewaters containing toxic or non-biodegradable compounds is highly necessary. Among the processes, several methods have been suggested and some advancement has also been done for the elimination of the organic pollutants. However, many organic chemicals are toxic and these methods are not adaptable to microbial degradation. Researchers have shown interest, and they have started the rigorous studies on heterogeneous photocatalysis, after the discovery of the photo-induced splitting of water on the surface of TiO_2 electrodes [3]. Two-dimensional semiconductor materials have been found to be active heterogeneous photocatalysts in a number of environmentally important reactions. Among them, TiO_2, ZnO, Fe_2O_3, NiO and many more are extensively used as photocatalyst for wastewater treatment. Photocatalysis with two-dimensional semiconductor materials can be used in organic synthesis to catalyse the reactions like oxidation reactions and reduction reactions, C–C bond formation or cyclization [4, 5]. Titanium dioxide (TiO_2) has been found to be the two-dimensional semiconductor material with the highest photocatalytic activity, non-toxic nature, highly stable in aqueous solutions and relatively cost-effective. A variety of aromatic and aliphatic substances and compounds containing halogen, oxygen, nitrogen or sulphur substitutions could be oxidized via using photocatalysis process [6]. In photocatalysis process, the photons with sufficient energy are absorbed by the photocatalyst and then the electrons are excited from the valence band to the conduction band which generates electron–hole pairs and induces the chemical reactions [7]. In photocatalytic reduction reaction of nitrobenzene, the electrons in conduction band reduce the nitrobenzene to aniline, and at the same time, alcohol is oxidized to aldehyde [8].

These photocatalytic reactions have several advantages such as high energy input at mild reaction conditions, the use of the less energetic substrates and the less amount of by-products formation; however, these photocatalytic reactions currently have less importance in the chemical industry. The main issues are the limited availability of scalable technical equipment for the reactions and less knowledge of the reaction mechanisms and kinetics which make the optimization and scaling-up highly challenging [4]. According to data available on the Web of Science database, almost seventy thousand research articles have been published from 2009 to 2019 on photocatalysis which includes “photocatalytic” as the keyword [9].

Therefore, in this chapter, the kinetics of photo-oxidation reaction and the effect of the reaction parameters on the rate and optimization of reaction parameters with respect to efficiency and productivity are discussed in detail.

2.2 Mechanism and Kinetic Study of Photocatalytic Oxidation

Photocatalytic oxidation (PCO) is a fascinating substitute for wet degradation of organic compounds with several advantages like easy operation, high efficiency, consumption of less amount of energy and nominal secondary pollution. In a typical photocatalytic oxidation reaction, suspensions of semiconductor nanomaterials prepared in desired solvent are irradiated using UV–Vis light and then the excitation of electrons takes place from valence band to conduction band [10, 11]. This excitation forms oxidizing sites (hole) in the valence band and a reducing sites (electron) in the conduction band which is shown in Fig. 2.1 and in Eq. (2.1) [10, 11]. This photo-oxidation process degrades the organic compounds into harmless reaction products like carbon dioxide and water [12]. For example, in TiO_2, which is the most common photocatalysts, the photodegradation process of the organic dye can be schematically described in Fig. 2.1 [13].

Once the photocatalytic surfaces are irradiated with light, a charge separation process immediately follows due to the absorption of the irradiated light as shown in Fig. 2.1. The photoexcited electron goes to conduction band which eventually reacts with the O_2 or H^+ ions present in the solution and reduces them [7]. Subsequently, the positive hole generated in the valence band will oxidize H_2O or organic dyes present in the solution [7, 10–17]. The chemical reactions involved during the oxidation of the organic dyes with TiO_2 as an example can be summarized as follows [7, 10–13]:

$$\mathrm{TiO_2} + hv \rightarrow \mathrm{TiO_2}(\mathrm{e^-} + \mathrm{h^+}) \tag{2.1}$$

$$\mathrm{OH^-} + \mathrm{h^+} \rightarrow \mathrm{HO^\bullet} \tag{2.2}$$

$$\mathrm{H_2O} + \mathrm{h^+} \rightarrow \mathrm{HO^\bullet} + \mathrm{H^+} \tag{2.3}$$

$$\mathrm{HO^\bullet} + \text{Organic Compounds} \rightarrow \mathrm{CO_2} + \mathrm{H_2O} \tag{2.4}$$

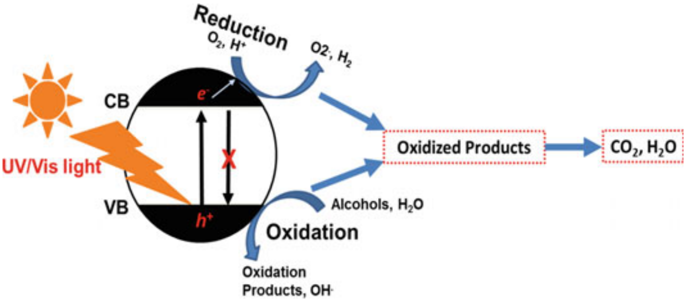

Fig. 2.1 Photocatalytic degradation of organic dyes using semiconductors

Table 2.1 Band gaps for the different semiconductors

Number	Semiconductors	Band gap (eV)
1	TiO_2	3.2
2	ZnO	3.2
3	Fe_2O_3	2.0
4	SnO_2	3.9
5	ZnS	3.7
6	CdS	2.5

Similarly, other semiconductors, viz. ZnO, Fe_2O_3, SnO_2, ZnS and CdS, also follow similar mechanisms and effectively catalysed the photodegradation of organic dyes [7, 15, 17]. These semiconductor nanomaterials absorb different wavelengths of the electromagnetic spectrum depending on the band gap of the semiconductors. The band gaps of the commonly used semiconductor nanoparticles are listed in Table 2.1 [7, 15, 17].

The semiconductor materials initiate the photocatalysed decolourization of a dye in a solution by the photoexcitation and form an electron–hole pair on the surface of catalyst (Eqs. 2.1, 2.5). The high oxidation potential of the hole (h^+_{VB}) in the catalyst allows the direct oxidation of the dye to reactive intermediates as shown in Eqs. (2.2, 2.6) [7, 12, 13, 15, 17]:

$$(MO/MO_2) + hv \rightarrow (MO/MO_2)\left(e^-_{CB} + h^+_{VB}\right) \tag{2.5}$$

$$h^+_{VB} + Dye \rightarrow Dye^{\bullet +} \rightarrow \text{Oxidation of the dye} \tag{2.6}$$

The hydroxyl radical ($OH^{\bullet}$) is the other reactive intermediate which is also responsible for the photocatalytic degradation. This hydroxyl radical can either be formed by the decomposition of water (Eq. 2.3) or be formed by the reaction of the hole with OH^- (Eq. 2.4). The OH• radical is highly strong and non-selective oxidant ($E_0 =$ +3.06 V) which mineralizes the several organic chemicals partially or completely [14]:

$$h^+_{VB} + H_2O \rightarrow H^+ + HO^{\bullet} \tag{2.7}$$

$$h^+_{VB} + HO^- \rightarrow HO^{\bullet} \tag{2.8}$$

$$HO^{\bullet} + Dye \rightarrow \text{Degradation of the dye} \tag{2.9}$$

2.2.1 Photo-oxidation of Commercial and Azo Dyes in Aqueous Solutions

The photocatalytic degradation of methyl orange (MO), Rhodamine 6G (R6G), Rhodamine B, crystal violet, etc., and organic dyes are well studied employing heterogeneous photocatalytic process using different semiconductors [16, 18, 19, 20] such as titanium dioxide (TiO_2), zinc oxide (ZnO), stannic oxide (SnO_2), zinc sulphide (ZnS) and cadmium sulphide (CdS). Rhodamine B is a very important basic dye extensively used to dye wool, cotton, silk and papers where dazzling shades of fluorescent effects are required. Methyl orange (MO) is another important azo dye extensively used in foodstuffs, textiles, pulp and paper and leather industries. The release of these complex dyes and their products in the environment is generally related to toxicity problems [18–20]. Thus, environment-friendly decolourization of these dyes is necessary. That can be achieved easily by using the process of photo-oxidation using above-mentioned semiconductors.

2.2.1.1 Mechanism of Photo-oxidation of Rhodamine B

The degradation pathway of Rhodamine B is depicted in Fig. 2.2. Photo-oxidation of Rhodamine B degrades into various organic subunits, such as aldehydes, acids or alcohols. Eventually, all these organic subunits degrade into H_2O, CO_2, CH_4, etc. [15]. Das et al. [15] identified the intermediate products using GC–MS and FT-IR spectroscopic study. The reaction mixtures contain products such as adipic acid, phthalic acid, 2-hydroxypropanoic acid, glutaric acid, propane-1,2,3-triol, formic acid, butane-1,3-diol, acetic acid and 2-dihydroxy acetic acid. Some of them are less harmful to the environment and further brake down to the low molecular weight acids and then finally to CO_2 and H_2O achieving complete mineralization [15].

2.2.1.2 Mechanism of Photo-oxidation of Methyl Orange

Similarly, the photo-oxidation of methyl orange azo dye is found to follow the steps as mentioned in Fig. 2.3. He et al. [21] were able to identify all the intermediate stages as highlighted as A, B, C, D, E, F and G intermediates of the methyl orange azo dye as shown in Fig. 2.3. Finally, the intermediate products will degrade into smaller fragments which will further degrade into H_2O, CO_2, etc.

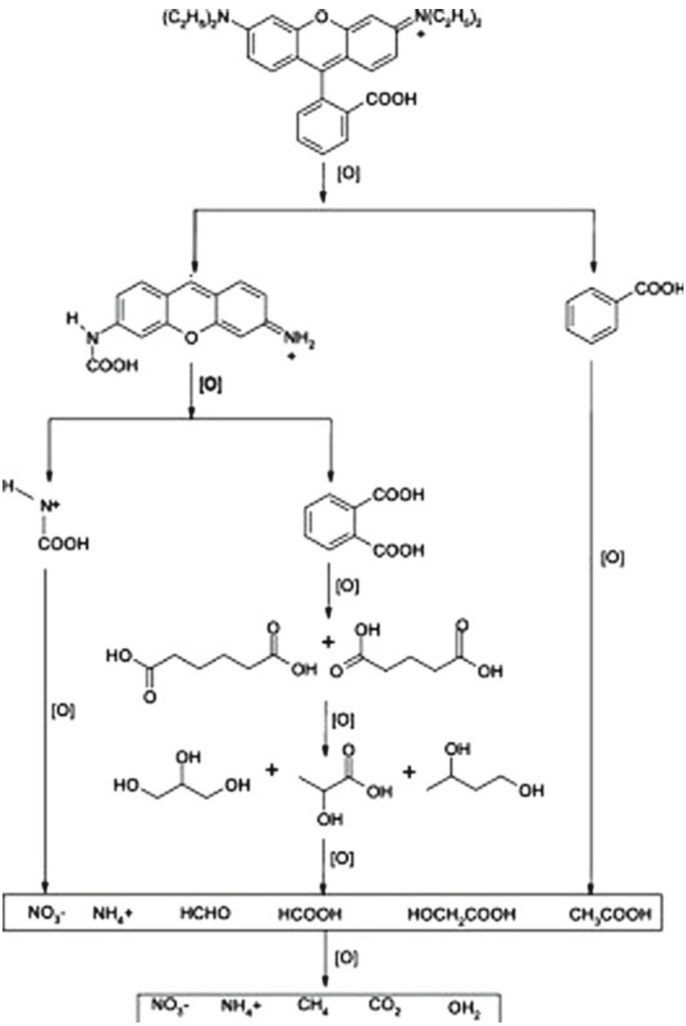

Fig. 2.2 Pathways of degradation of Rhodamine B upon photo-oxidation. Reprinted with the permission from [15]

2.2.2 *Destruction of Volatile Organic Compounds (VOCs) in Indoor Air via Photocatalytic Oxidation Process*

Volatile organic compounds (VOCs) are the well-known pollutants, which are produced from various sources, such as combustion by-products, office equipment, construction materials and consumer products. Aldehydes, aromatics, alcohols, halocarbons and esters are the main components containing VOCs which is identified in the indoor air. Photocatalytic oxidation (PCO) can be a promising method

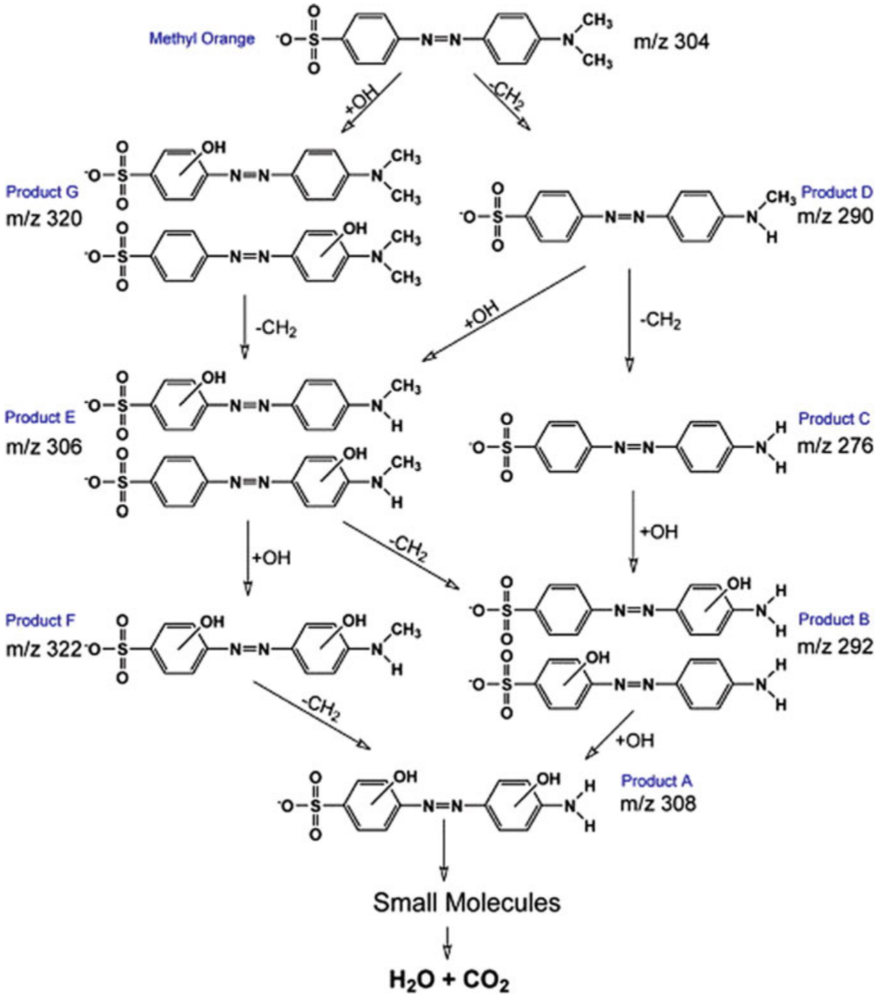

Fig. 2.3 Pathways of degradation of methyl orange azo dye upon photo-oxidation. Reprinted with the permission from [21]

for removing the VOCs. The examples of VOCs include formaldehyde, 1-butanol, ethanol, hexane, acetone, toluene, benzene, trichloroethylene and methyl ethyl ketone. The chemical pollutants can be decomposed by PCO which is performed using photocatalyst, ultraviolet (UV) light and oxygen. Among different types of photocatalysts, TiO_2 has been the most encouraging candidate owing to its high stability, low cost, ease of synthesis and the excellent capability to degrade various compounds as mentioned above [11, 22–24].

In the presence of air or oxygen, UV-irradiated TiO_2 can degrade many organic contaminants completely.

The TiO_2 can be activated by UV light and can be written as:

$$TiO_2 + hv \rightarrow TiO_2(h^+ + e^-) \quad (2.10)$$

In this reaction, h^+ and e^- are called strong oxidizing and reductive agents, respectively, and these oxidative and reductive reactions are expressed as

Oxidative reaction:

$$OH^- + h^+ \rightarrow OH \quad (2.11)$$

Reductive reaction:

$$O_2(ads) + e^- \rightarrow O^- \quad (2.12)$$

During the degradation process of organic substances and compounds, the oxidation of adsorbed water or adsorbed OH^- forms the hydroxyl radical ($OH^\bullet$) which is the primary oxidant. The presence of oxygen can inhibit the recombination of hole–electron pairs. For a complete photocatalytic oxidation reaction, the final products formed during the reactions are CO_2 and H_2O [11, 22–24].

$$OH^{\cdot} + \text{Pollutant} + O_2 \rightarrow \text{Products } (CO_2;\ H_2O;\ \text{etc.}) \quad (2.13)$$

2.2.3 Photocatalytic Oxidation of Water

Artificial photosynthetic devices have shown great attention as future clean energy systems [25]. Development of an effective and robust catalyst for oxidation of water to evolve O_2 (Eq. 2.14) is crucial to yield a breakthrough for constructing an artificial photosynthetic device [26–29].

$$2H_2O \xrightarrow{\text{Water Oxidation Catalyst}} O_2 + 4H^+ + 4e^- \quad (2.14)$$

Over the last decade, considerable advancements have been done for the development of manganese, ruthenium and iridium complexes as catalysts for water oxidation [26–29]. The molecular characteristics of these catalysts have been studied which provide hints for development of an effective catalyst and to gain clues to reveal the mechanism of O_2 evolution catalysed at the photosynthetic oxygen evolving complex (OEC). The active site of such OECs is known to consist of oxo clusters, such as tetramanganese-oxo cluster [30]. For the development of an artificial photosynthetic device, it is essential to understand the catalytic aspect in photo- and/or photoelectro-driven water oxidation [31].

Popular examples of water oxidation catalysts include cobalt oxide, manganese oxide (which are driven by visible light) [16], nickel oxide (from 1st transition series) and other metal oxides of 1st transition series like TiO_2, Cu_2O, Fe_2O_3 [27–29]. Cobalt oxide is most promising and prominent water oxidation catalysts, and its activity is defined through turnover frequencies (TOFs) [16, 27, 29]. Co_3O_4 has become spinal-type water oxidation catalysts, and it is highly advanced and promising, due to low cost and stable structure [31].

Manganese oxide (MnO_x) is extensively accepted as favourable catalyst for water oxidation as well. In photosystem II (PSII), Mn_4CaO_5 clusters turn solar energy into chemical energy [30]. More focus has been given to manganese oxide due its environmental factor and redox reactivity for the photocatalytic water oxidation [30].

The photocatalytic oxidation of water using various semiconductor catalysts, such as MnO_x, was explored in the presence of a photosensitizer ($[Ru(bpy)_3]^{2+}$) and a two-electron acceptor ($Na_2S_2O_8$) in aqueous buffer solution (Fig. 2.4). In the $[Ru(bpy)_3]^{2+}$ $-S_2O_8^{2-}$ system, $[Ru(bpy)_3]^{2+}$ is capable to absorb visible light and electron–hole pairs are generated on the catalyst surface. The electrons which are excited were banished by the sacrificial electron acceptor $S_2O_8^{2-}$ by further oxidation of $[Ru(bpy)_3]^{2+}$ to $[Ru(bpy)_3]^{3+}$ and reduction of $S_2O_8^{2-}$ to SO_4^{2-} and a sulphate radicals ($SO_4^{\bullet -}$). Therefore, the formed radical can further oxidize the $[Ru(bpy)_3]^{2+}$ to give $[Ru(bpy)_3]^{3+}$. Then, the holes of $[Ru(bpy)_3]^{3+}$ molecule are donated to the catalyst and are reverted back to $[Ru(bpy)_3]^{2+}$; at this site, water molecules are oxidized to form oxygen molecules at the surface [30].

2.2.4 Photocatalytic Reduction of Nitrobenzene

Hakki et al. [32–34] have reported the reduction of nitrobenzene in ethanol which also gives quinolines as one of the products and also discussed the kinetics of the

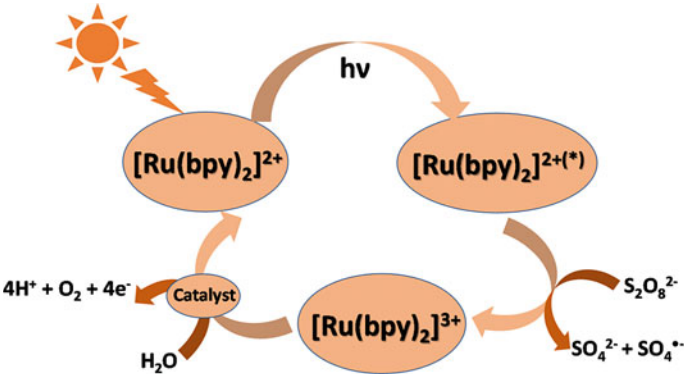

Fig. 2.4 Photocatalytic cycle of water oxidation using the $Na_2S_2O_8$ and $[Ru(bpy)_3]^{2+}$ system in the presence of various semiconductor photocatalysts

whole reaction up to quinolones. The experiments were carried out in the photoLAB Batch-S system (Peschl Ultraviolet) equipped with 25 ml four identical reactors arranged around a 20 W (radiant flux) LED lamp. In this experiment, the TiO_2 photocatalyst suspended into ethanol and nitrobenzene is used. The light intensity is varied from 4 to 100 μmol L^{-1} s^{-1}, and it is measured and verified by the ferrioxalate actinometer [6].

The kinetics and the effect of the reaction parameters of the photocatalytic reduction reaction of nitrobenzene in ethanol are studied using TiO_2 as a photocatalyst with varying the intensity of light from 4 to 100 μmol L^{-1} s^{-1} and catalyst concentration from 0.25 to 12.5 g L^{-1} [6].

Figure 2.5 shows the complete reaction mechanism of photocatalytic reduction reaction of nitrobenzene in ethanol. During photocatalytic reduction, nitrobenzene is reduced to aniline, via intermediates such as nitrosobenzene and phenylhydroxylamine. The concentration of these intermediates is very low, and therefore, they can be observed qualitatively but not quantitatively. Simultaneously, the oxidation of ethanol also takes place to acetaldehyde in the two consecutive one-electron transfer reactions, via an alcohol radical. For complete reduction of nitrobenzene, stoichiometric balance is necessary, so for this, three equivalent molecules of ethanol are oxidized to provide the electrons. Till 40 min of irradiation, nitrobenzene is completely reduced, and after this, the colour of the suspension changes from white to light blue, which is because of the well-known incomplete reduction of the TiO_2 surface by trapping of electrons which are generated from photoradiation as Ti(III), since an electron acceptor is no longer available [6]. After the reduction up to aniline and acetaldehyde, these reactions give condensation products which are easily observable. These such reactions are acid-catalysed, and when they progress over TiO_2 due to its acidic surface groups, they are faster in the presence of an added acid [32]. In the first step, condensation of acetaldehyde with aniline takes place to give ethylideneaniline. After that, a Povarov reaction of ethylvinylether (formed from acetaldehyde and ethanol) with ethylidenaniline takes place and gives 4-ethoxy-1,2,3,4-tetrahydroquinaldine [35].

Ethanol can be eliminated and form 1,2-dihydroquinaldine, and the following oxidation, reduction or disproportionation reactions lead to quinaldine and 1,2,3,4-tetrahydroquinaldine. The intermediates formed in the above reaction can be determined using GC–MS and further verified and quantified using GC-FID [32, 35, 36]; in this reaction, the intermediates nitrosobenzene and phenylhydroxylamine formed are reactive and can condense with other intermediates or aniline to form azoxybenzene or azobenzene.

The reduction rate of nitrobenzene as a function of the light intensity is shown in Fig. 2.6 in which the rate of the reaction increases almost linearly at low light intensity, and when the light intensity is high, the rate of the reaction increasingly shows diminishing returns. Similar behaviour is generally seen for other types of photocatalytic reactions. At higher light intensity, the changes in the reactions may be due to the increase in charge carrier recombination at higher light intensity [37–41].

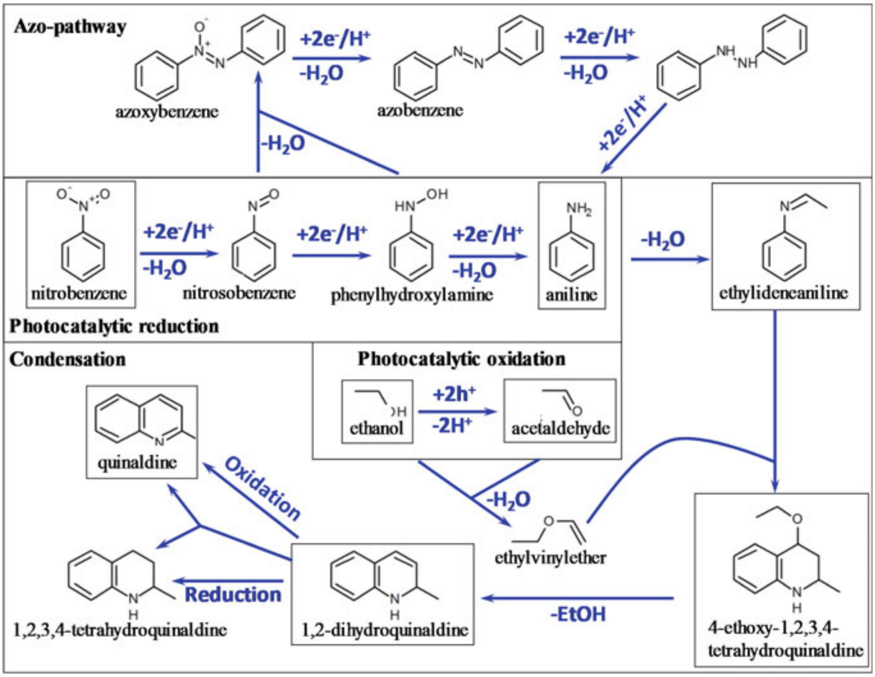

Fig. 2.5 Mechanism of reduction of nitrobenzene in ethanol in the presence of photo-light reaction. Few steps of photocatalytic reaction are represented by blue arrows, and other major intermediates or products are represented by black box. Reprinted with the permission from [6]

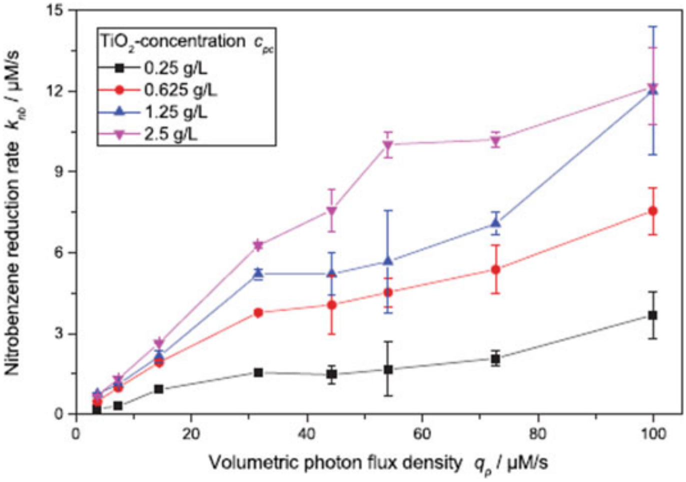

Fig. 2.6 Reduction rate dependence (k_{nb}) of the nitrobenzene reduction rate on the volumetric photon flux density (q_{p}) for different $\mathrm{TiO_2}$ photocatalyst concentrations. Reprinted with the permission from [6]

2.2.5 Photocatalytic Reduction of Nitrogen Containing Organic Substances

Serious chemical contaminants are the nitrogen containing organic substances which are found in a wide range of aquatic environments. They are most common ingredients of various detergents, biocides, explosives, synthetic dye, lubricants, industrial solvents and wasted foods and drugs, all of which could be significant sources of water pollution. In a study by Kim et al. [42], the kinetics and mechanism of the photocatalytic degradation of a series of $(CH_3)_nNH_{4-n}{}^+$ $(0 \leq n \leq 4)$ were studied systematically in an UV-illuminated aqueous suspensions of TiO_2 at pH ranges of 3–11. In the photocatalytic oxidation reaction of organic substances and compounds, all the elements present in a molecule can be mineralized to inorganic species such as carbon to carbon dioxide, hydrogen to water, sulphurs to sulphates, halogens to halide ions and phosphorus to phosphates, respectively. Nitrogen-containing compounds are the unique compounds due to their photocatalytic degradation properties which leads to the two main inorganic species such as ammonium $(NH_4{}^+)$ vs nitrate $(NO_3{}^-)$. The relative concentration of these two product ions depends upon the molecular structure of the substrates, the oxidation state of nitrogen, pH value, the illumination time and the adsorption behaviour of the substrates during photocatalysts [42]. In this work, photocatalytic degradation study of $(CH_3)_nNH_{4-n}{}^+$ $(0 \leq n \leq 4)$ has been carried out and the kinetics of photocatalytic degradation of formation of intermediates and products were discussed at a different pH. All the substrate samples are prepared in TiO_2 suspensions, and pH of each sample is maintained by adding hydrochloric acid and sodium hydroxide. Xe arc lamp is used as a light source for photo-irradiation [42]. The kinetics of photocatalytic degradations of $(CH_3)_4N^+$ at various pH is discussed and described successfully by the first-order kinetics. There is no effect of pH on the molecular charges of $(CH_3)_4N^+$, but the rate of degradation is affected strongly by change in pH. The unexpected drastic decrease in degradation rate was found at pH-7, and this decrease may be due to the particle aggregation and surface area reduction.

2.2.6 Photocatalytic Degradation of Pesticide Derivatives

Pesticides are another type of organic pollutants in water system, and these pesticides can come from various sources such as agricultural runoff, industrial effluents and chemical spills [2]. Their toxicity in the environment and persistence have been the cause of much concern to the society worldwide. Qamar et al. [1] have reported the photocatalytic degradation of two types of pesticide derivatives such as daminozide and triclopyr (as shown in Fig. 2.7a, b) in the aqueous TiO_2 suspensions.

The change in the substrate concentration and reduction of total organic carbon (TOC) were monitored by UV spectroscopic techniques with respect to the

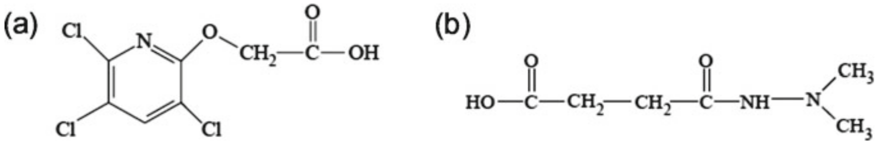

Fig. 2.7 Chemical structure of **a** triclopyr and **b** daminozide pesticide derivatives [1]

irradiation time. The kinetics of degradation were also studied under the different conditions such as pH of the reaction, concentrations of catalyst and substrate, types of TiO_2 and in the presence of electron acceptors like ammonium persulphate, potassium bromate, hydrogen peroxide and in addition to molecular oxygen [1]. Study reveals that the degradation rates were strongly influenced by all the above conditions. The kinetic study shows that the pesticide derivative triclopyr degraded very fast as compared to daminozide. TiO_2 can photocatalyse efficiently these pesticides and their derivatives in the presence of radiation and oxygen [1].

In this study, it was found that the Degussa P25 type TiO_2 photocatalyst was more efficient as compared with other types of TiO_2 photocatalyst. The addition of the electron acceptors can also enhance the degradation rate of the pollutants. These results obtained from this study clearly show the importance of selecting the optimum degradation parameters to achieve a high degradation rate, which is highly essential for any of the practical application of photocatalytic oxidation reaction processes.

2.3 Optimization of the Reaction Conditions

The optimization of the reaction conditions for the above-mentioned photocatalytic oxidations was important to obtain optimal results. For the optimization of the reaction conditions, the variation of reaction parameters, such as pH of the solution, catalyst concentration, concentration of dyes, irradiation time and wavelength of the irradiation light, should be monitored [7, 12-15, 17]. For example, Kansal et al. [12] showed the degradation of the methyl orange and Rhodamine 6G in various pH mediums, such as 2, 4, 8, and 10 pH at fixed dye concentration (25 mg/l), and catalyst loading of 1 g/l for 4 and 3 h for MO and R6G dyes, respectively, using various photocatalysts, such as ZnO, TiO_2, ZnS, SnO_2 and CdS [12]. The results reported by Kansal et al. prove that ZnO shows high photocatalytic activity as compared to the others, especially TiO_2 for both the dyes under similar degradation conditions [12]. The photocatalytic efficiency of various catalysts towards the degradation of MO and R6G at different pH values also varies to great extents as well. The degradation efficiency for both the dyes was higher in the pH range 8–10 [12]. Similar variation in the pH of the solution is also reported by Yaras et al. [43] for the cationic dyes Basic Blue 3 [BB3] and Basic Yellow 28 [BY28] in water. These two dyes also degrade higher in higher rates in the higher pH. Photocatalytic water oxidation reactions also heavily depend on the pH, amount of catalyst and time of photo-irradiation as well [30].

2.4 Conclusion

We are able to highlight all possible oxidation process in water or air under the influence of light irradiation. Semiconductor nanomaterials serve as the catalytic site for the photo-oxidation process. This photocatalytic oxidation process is found to be very helpful in destroying or degrading various organic impurities such as organic dyes in water as waste or organic volatile substances present in air. Photocatalytic water oxidation is another important and immersing field which will facilitate us in mimicking the photosynthesis by plants and will help us to obtain O_2 from water. A detailed understanding of the optimization, kinetics and mechanisms of the above-mentioned photo-oxidation reactions will help us further in designing new photo-oxidation reactions.

Acknowledgements T. K. Gupta, S. Sengupta and M. Raula are grateful to the Amity University, Noida, India, for their constant support and encouragement in this COVID-19 pandemic. This chapter has been written during COVID-19 pandemic; therefore, support of the family members and kids is highly appreciable.

Conflict of Interest None declared.

References

1. Qamar M, Muneer M, Bahnemann D (2006) Heterogeneous photocatalysed degradation of two selected pesticide derivatives, triclopyr and daminozid in aqueous suspensions of titanium dioxide. J Environ Manage 80:99–106
2. Dowd R, Anderson M, Johnson M (1988) Proceedings of the Second National Outdoor Action Conference on Aquifer Restoration. Ground Water Monit Geophys Methods 1365–1379
3. Fujishima A, Honda K (1972) Electrochemical photolysis of water at a semiconductor electrode. Nature 238:37–38
4. Bloh JZ, Marschall R (2017) Heterogeneous photoredox catalysis: reactions, materials, and reaction engineering. Eur J Org Chem 2085–2094
5. Friedmann D, Hakki A, Kim H, Choi W, Bahnemann D (2016) Heterogeneous photocatalytic organic synthesis: state-of-the-art and future perspectives. Green Chem 18:5391–5411
6. Patzsch J, Berg B, Bloh JZ (2019) Kinetics and optimization of the photocatalytic reduction of nitrobenzene. Front Chem 7:289
7. Schneider J, Matsuoka M, Takeuchi M, Zhang J, Horiuchi Y, Anpo M, Bahnemann DW (2014) Understanding TiO2 photocatalysis: mechanisms and materials. Chem Rev 114:9919–9986

8. Flores S, Rios-Bernij O, Valenzuela M, Córdova I, Gómez R, Gutiérrez R (2007) Photocatalytic reduction of nitrobenzene over titanium dioxide: by-product identification and possible pathways. Top Catal 44:507–511
9. Zhang Z, Bai L, Li Z, Qu Y, Jing L (2019) Review of strategies for the fabrication of heterojunctional nanocomposites as efficient visible-light catalysts by modulating excited electrons with appropriate thermodynamic energy. J Mater Chem A 7:10879–10897
10. Dahl M, Liu Y, Yin Y (2014) Composite titanium dioxide nanomaterials. Chem Rev 114:9853–9889
11. Lee KM, Abd Hamid SB, Lai CW (2015) Mechanism and kinetics study for photocatalytic oxidation degradation: a case study for phenoxyacetic acid organic pollutant. J Nanomaterials (Article ID 940857, 10 pages)
12. Kansal S, Singh M, Sud D (2007) Studies on photodegradation of two commercial dyes in aqueous phase using different photocatalysts. J Hazard Mater 141:581–590
13. Sheikh MUD, Naikoo GA, Thomas M, Bano M, Khan F (2016) Solar-assisted photocatalytic reduction of methyl orange azo dye over porous TiO2 nanostructures. New J Chem 40:5483–5494
14. Daneshvar N, Salari D, Khataee A (2004) Photocatalytic degradation of azo dye acid red 14 in water on ZnO as an alternative catalyst to TiO2. J Photochem Photobiol A Chem 162:317–322
15. Das M, Bhattacharyya KG (2014) Oxidation of Rhodamine B in aqueous medium in ambient conditions with raw and acid-activated MnO2, NiO, ZnO as catalysts. J Mol Catal A Chem 391:121–129
16. Jiao F, Frei H (2010) Nanostructured cobalt and manganese oxide clusters as efficient water oxidation catalysts. Energy Environ Sci 3:1018–1027
17. Mahadik M, Shinde S, Rajpure K, Bhosale C (2013) Photocatalytic oxidation of Rhodamine B with ferric oxide thin films under solar illumination. Mater Res Bull 48:4058–4065
18. Al-Qaradawi S, Salman SR (2002) Photocatalytic degradation of methyl orange as a model compound. J Photochem Photobiol A Chem 148:161–168
19. Wang Y (2000) Solar photocatalytic degradation of eight commercial dyes in TiO2 suspension. Water Res 34:990–994
20. Zhang F, Zhao J, Zang L, Shen T, Hidaka H, Pelizzetti E, Serpone N (1997) Photoassisted degradation of dye pollutants in aqueous TiO2 dispersions under irradiation by visible light. J Mol Catal A Chem 120:173–178
21. He Y, Grieser F, Ashokkumar M (2011) The mechanism of sonophotocatalytic degradation of methyl orange and its products in aqueous solutions. Ultrason Sonochem 18:974–980
22. Malayeri M, Haghighat F, Lee C-S (2019) Modeling of volatile organic compounds degradation by photocatalytic oxidation reactor in indoor air: a review. Build Environ 154:309–323
23. Salvadó-Estivill I, Hargreaves DM, Li Puma G (2007) Evaluation of the intrinsic photocatalytic oxidation kinetics of indoor air pollutants. Environ Sci Technol 41:2028–2035
24. Zhao J, Yang X (2003) Photocatalytic oxidation for indoor air purification: a literature review. Build Environ 38:645–654
25. Lewis NS (2007) Toward cost-effective solar energy use. Science 315:798–801
26. Eisenberg R, Gray HB (2008) Preface on making oxygen. Inorg Chem 47:1697–1699
27. Hunter BM, Gray HB, Muller AM (2016) Earth-abundant heterogeneous water oxidation catalysts. Chem Rev 116:14120–14136
28. Limburg B, Bouwman E, Bonnet S (2016) Rate and stability of photocatalytic water oxidation using [Ru (bpy) 3] 2+ as photosensitizer. ACS Catal 6:5273–5284
29. Singh A, Spiccia L (2013) Water oxidation catalysts based on abundant 1st row transition metals. Coord Chem Rev 257:2607–2622
30. Menezes PW, Indra A, Littlewood P, Schwarze M, Göbel C, Schomäcker R, Driess M (2014) Nanostructured manganese oxides as highly active water oxidation catalysts: a boost from manganese precursor chemistry. Chemsuschem 7:2202–2211

31. Deng X, Tüysüz H, (2014) Cobalt-oxide-based materials as water oxidation catalyst: recent progress and challenges. ACS Catal 4:3701–3714
32. Hakki A, Dillert R, Bahnemann DW (2013) Arenesulfonic acid-functionalized mesoporous silica decorated with titania: a heterogeneous catalyst for the one-pot photocatalytic synthesis of quinolines from nitroaromatic compounds and alcohols. ACS Catal 3:565–572
33. Hakki A, Dillert R, Bahnemann DW (2013) Factors affecting the selectivity of the photocatalytic conversion of nitroaromatic compounds over TiO2 to valuable nitrogen-containing organic compounds. Phys Chem Chem Phys 15:2992–3002
34. Hirakawa H et al (2015) One-pot synthesis of imines from nitroaromatics and alcohols by tandem photocatalytic and catalytic reactions on degussa (Evonik) P25 titanium dioxide. ACS Appl Mater Interfaces 7:3797–3806
35. Park KH, Joo HS, Ahn KI, Jun K (1995) One step synthesis of 4-ethoxy-1, 2, 3, 4-tetrahydroquinoline from nitroarene and ethanol: a TiO2 mediated photocatalytic reaction. Tetrahedron Lett 36:5943–5946
36. Selvam K, Swaminathan M (2011) Cost effective one-pot photocatalytic synthesis of quinaldines from nitroarenes by silver loaded TiO2. J Mol Catal A Chem 351:52–61
37. Mills A, O'Rourke C, Moore K (2015) Powder semiconductor photocatalysis in aqueous solution: an overview of kinetics-based reaction mechanisms. J Photochem Photobiol A Chem 310:66–105
38. Nosaka Y, Nosaka AY (2018) Langmuir-Hinshelwood and light-intensity dependence analyses of photocatalytic oxidation rates by two-dimensional-ladder kinetic simulation. J Phys Chem C 122:28748–28756
39. Satuf ML, Brandi RJ, Cassano AE, Alfano OM (2008) Photocatalytic degradation of 4-chlorophenol: a kinetic study. Appl Catal B Environ 82:37–49
40. Upadhya S, Ollis DF (1998) A simple kinetic model for the simultaneous concentration and intensity dependencies of TCE photocatalyzed destruction. J Adv Oxid Technol 3:199–202
41. Valencia S, Catano F, Rios L, Restrepo G, Marín J (2011) A new kinetic model for heterogeneous photocatalysis with titanium dioxide: case of non-specific adsorption considering back reaction. Appl Catal B Environ 104:300–304
42. Kim S, Choi W (2002) Kinetics and mechanisms of photocatalytic degradation of (CH3) n NH4-n+(0 ≤ n ≤ 4) in TiO2 suspension: the role of OH radicals. Environ Sci Technol 36:2019–2025
43. Yaraş A, Arslanoğlu H (2019) Utilization of paper mill sludge for removal of cationic textile dyes from aqueous solutions. Sep Sci Technol 54:2555–2566

Chapter 3
Design and Synthesis of Nanostructured Photocatalysts for Water Remediation

Mahima Sharma, Subhasha Nigam, and Monika Joshi

Abstract The presence of pollutants in aquatic environment evoked a major challenge among the whole scientific community. Meanwhile, solar energy-driven nanostructured photocatalysts are considered as most promising materials for water remediation as it utilizes natural sunlight as a source of energy and produces fewer or no toxic by-products. The nanostructured materials as photocatalysts are gaining tremendous interest due to their unique properties, such as high surface area, tuneable band gap, and strong oxidation ability. But the comparatively low photocatalytic efficiency remains a crucial drawback for the practical industrial application of the nanostructured photocatalysts. To solve this issue, various approaches have been utilized for the designing of advanced multifunctional photocatalysts. Predominantly, combing a semiconductor material with metal or semiconductor to form a nanocomposite photocatalyst has become a viable approach for designing of multifunctional highly efficient photocatalyst. Herein, we have elaborately showcased recent advances in the development of novel multifunctional nanostructured photocatalyst for water remediation via numerous approaches. Moreover, a concise summary of the present challenges and an outlook for the designing and synthesis of nanostructured photocatalyst in the field of water remediation are provided.

Keywords Photocatalysis · Nanomaterials · Water remediation · Synthesis

---

M. Sharma · M. Joshi (✉)
Amity Institute of Nanotechnology, Amity University, Noida, Uttar Pradesh 201313, India
e-mail: mjoshi@amity.edu

S. Nigam
Amity Institute of Biotechnology, Amity University, Noida, Uttar Pradesh 201313, India

S. Garg and A. Chandra (eds.), *Green Photocatalytic Semiconductors*,
Green Chemistry and Sustainable Technology,
https://doi.org/10.1007/978-3-030-77371-7_3

3.1 Introduction

Water is the most essential, precious, and abundant natural resources for all life on the earth. But only <1% of water resources have reliable access of clean and affordable water for human consumption [1]. The anthropogenic activities like rapid industrialization, unplanned urbanization, and population growth are the main cause for deterioration of water quality [2]. So, water pollution produced by physical, chemical, and biological pollutants of water has become a key environmental concern for society, public authorities, and industries [3]. The domestic, sewage, and industrial activities are persistently linked with the discharge of a bevy amount of numerous hazardous contaminants like diverse dyestuffs, heavy metal ions, oils, and other toxic carcinogenic organic and inorganic pollutants [4]. The utmost issue of these wastewater with environmental concerns is their high chemical oxygen demand (COD), biological oxygen demand (BOD), total dissolved solids, and total suspend solids (TSS) [5]. Thus, the elimination of these wastewater is mandatory before they are released into aquatic ecosystems due to its intense color, low biodegradability, and high toxicity [6]. The release of these industrial wastewater in water reservoirs without treatment or with improper treatment using conventional methods adversely affects the plant, aquatic life, and humans. Therefore, it is prerequisite to develop environmentally acceptable water remediation technology for the conservation of water resources and environment [7].

Nanotechnology offers the potential for the development of an alternate technologies for the wastewater treatment. Various methods, such as biological treatment, coagulation, membrane filtration, ion exchange, photocatalysis, and adsorption, have been employed to treat wastewater [7–10]. Among these, photocatalysis has proved to be most promising method for wastewater treatment, because the method utilizes natural resources such as water and sunlight to produce reactive oxygen species ($^{\circ}OH$ and $^{\circ}O_2^{-}$) for complete mineralization of hazardous compounds present in wastewater [11]. Recently, semiconductor oxide as photocatalyst like titanium dioxide (TiO_2), zinc oxide (ZnO), zinc sulfide (ZnS), tungsten trioxide (WO_3), copper oxide (CuO), etc., has attained focus for degradation of pollutants [12–15].

3.2 Different Types of Pollutants

Water is contaminated by numerous undesirable foreign substances like physical substance, chemicals, biological species, domestic, sewage and industrial wastes etc. These pollutants degrade the quality of the water and make it unacceptable for its best utilizations. Water pollutants can be categorized into below-mentioned three types, according to their form of existence in water (Fig. 3.1).

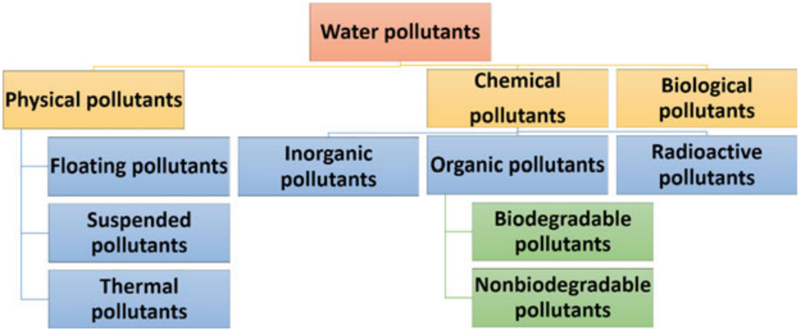

Fig. 3.1 Types of water pollutants

i. Physical pollutants
ii. Chemical pollutants
iii. Biological pollutants.

3.2.1 Physical Pollutants

The physical pollutants cause alteration in pH, temperature, odor, turbidity, and thermal and electrical characteristics of water [16]. Physical pollutants can be further classified into three categories.

3.2.1.1 Floating Substances

The floating substance includes leaves, foam, wood, etc. Foam is produced by soaps, surfactants, detergents, untreated wastewater etc.

3.2.1.2 Suspended Substances

The suspended substance includes sand, rubber, metal pieces, paper, carcasses, silt, sewage, pulp, etc.

3.2.1.3 Thermal Effects

It is primarily due to the release of heated water from different industries and thermal power plants. This heated water escalates the degradation of organic substances and lowers the dissolved oxygen level in water.

3.2.2 Chemical Pollutants

Chemical pollutants are usually most detrimental to human and aquatic ecosystems and can be classified into following three categories.

3.2.2.1 Inorganic Pollutants

Inorganic pollutants include acids, inorganic salts, minerals, metallic compounds, alkalies, chlorine, phosphates, sulfates, nitrates, sulphites, bicarbonates, trace elements, etc. In these pollutants, excessive amount of heavy metal ions is noticed due to industrial and sewage wastes. These heavy metal ions are nonbiodegradable in nature [17].

3.2.2.2 Organic Pollutants

The organic pollutants can also be categorized as biodegradable and non-biodegradable pollutants [18].

i. Biodegradable organic pollutants
   It includes sugar, fats, proteins, and other organic substances, found in domestic, sewage, and industrial wastewater. These pollutants can be oxidized in anaerobic or aerobic conditions.
ii. Nonbiodegradable organic pollutants
   It includes dyes, pesticides, insecticides, paints, herbicides, plastics, fungicides, etc., that contaminate the water reservoirs by numerous human activities. They are toxic and not degraded by the microbes. So, they remain in the aquatic ecosystems for long periods.

3.2.2.3 Radioactive Pollutants

It includes radioactive elements like 137Cs, 238U, 14C, 45Ca, 32P, 60Co, 248Pu, 35S, 235U, 31I etc. These pollutants are explained as release of high energy or radioactive materials into the water reservoirs by nuclear power plants and medical, agricultural, and industrial activities [19].

3.2.3 Biological Pollutants

Biological pollution is generated by domestic, sewage and industrial wastes, and excretory products of man and animals. Biological pollutants include pathogenic forms of algae, bacteria, virus, protozoa, etc. [20].

3.3 Different Methods Used for Water Remediation

Industrial, domestic, and sewage waste contain various pollutants like dyes, heavy metal ions, and other organic and inorganic toxic compounds. To provide sustainable environment for human, plants, and aquatic flora and fauna, wastewater treatment is essential. Various methods were employed for the wastewater treatment. Comparison of wastewater treatment methods is presented in Table 3.1.

3.3.1 Physical Method

3.3.1.1 Membrane Filtration

Membrane filtrations like ultrafiltration, reverse osmosis, and nanofiltration have received remarkable attention for water reuse, chemical recovery, and removal of dyes and heavy metal ions present in wastewater [22]. This method is resistant for microbial attack, temperature, and chemical environment. The limitations of this method are expensiveness, membrane fouling, and formation of secondary waste streams which have to be further treated [23].

i. Ultrafiltration
   Ultrafiltration uses semipermeable membrane for the separation of suspended solids in the influences of pressure gradient [24]. These unique membrane characteristics enable ultrafiltration to allow passage of low molecular weight solutes and solvents, while retaining molecules that have size bigger than pore size of membrane [25]. Salahi et al. prepared polyethersulfone ultrafiltration hollow fiber membranes via phase inversion induced by dry-jet wet spinning process [26]. This membrane was studied for the separation of oil from oily wastewater. This membrane effectively removed the chemical oxygen demand (COD), total organic carbon (TOC), turbidity, total suspended solids (TSS), and oil and grease content (OGC).
ii. Reverse osmosis method
   Reverse osmosis method involves a semipermeable membrane between two distinct concentrations of solution that exist on either side of membrane. By applying the pressure greater than osmatic pressure, flow will be started from high concentration zone to low concentration zone [27]. As membrane is sensitive to fouling, so this method can be employed for wastewater after prior pre-treatment. This method is applicable for broad range of pH. The removal of dyes and heavy metal ions by this method is majorly affected by pressure [28]. Bunani et al. investigated the performances of brackish water reverse osmosis (AK-BWRO) and seawater reverse osmosis (AD-SWRO) membranes at 10 bar as applied pressure [29]. These RO membranes were used for reuse of secondary treated urban wastewater in agricultural irrigation.

Table 3.1 Comparison of wastewater treatment methods [21]

Methods	Advantages	Disadvantages
Ultrafiltration	• Low driving force • Small space requirement • High packing capacity	• Prone to membrane fouling • Biodegradation of membrane material
Nanofiltration	• Easy operation • Low energy consumption	• Prone to membrane fouling • Expensive
Reverse osmosis	• Efficient rejection rate • Accounts for more than 20% of world desalination capacity	• High power consumption
Adsorption	• Effective • Low cost	• Low reusability capacity
Coagulation-flocculation	• Simple • Applicable to large-scale wastewater treatment • Improved sludge settling	• High chemical consumption • Production of toxic sludge in large quantity • Sludge disposal problem
Ion exchange	• Selective heavy metal removal	• Expensive • Fouling of resin
Chemical precipitation	• Simple to use • Can be adapted to handle large quantity of wastewater	• High chemical requirement • Sludge disposal problem
Chemical oxidation	• Does not increase volume of sludge • Rapid process for removal	• Expensive • Problems in sludge disposal • Formation of by-products
Electrochemical	• Rapid process • Nonchemical requirement	• High cost of electricity • Formation of by-products
Photocatalysis	• Non-toxicity • No foul smells • No sludge formation	• Utilization of expensive catalysts
Biological	• Noninvasive removal of pollutants • Completely mineralizes the toxic pollutants into non-toxic end products without any requirement of rigorous monitoring	• Process takes longer time for the removal of pollutants

iii. Nanofiltration method

Nanofiltration method has unique characteristics between reverse osmosis and ultrafiltration [30]. Removal of dyes and heavy metal ions is based on electrical (Gibbs-Donnan) and steric effects. A Donnan potential is formed between anion in semipermeable membrane of nanofiltration and co-anions (ions with same charge polarity as nanofiltration membrane's ions) in wastewater [31]. The separation process involves surface charge and small pores of nanofiltration membrane. This method is also applicable for broad range of pH. Garcia-Ivars et al. used three nanofiltration membrane, i.e., TFC-SR2, NF-270, and MPS-34 for removing trace pharmaceutically active compounds in wastewater from wastewater treatment plants [32].

3.3.1.2 Adsorption

Adsorption is an effective and reliable wastewater treatment method, in which contaminants are transferred from liquid form to solid form. It can be operating in wide range of physical, biological, and chemical processes. Various organic and inorganic contaminants are eliminated from aqueous medium by adsorption method [33]. Various low-cost and eco-friendly adsorbents like coconut shell, bagasse, rice husk, and industrial sludge were utilized for removal of dyes and heavy metal ions from wastewater [34]. Samanta et al. investigated the role of main constituents of coconut fibers on absorption of anionic (acid and reactive) and cationic (basic) dyes [35]. Zhang et al. fabricated the MnO_2 nanowires/polyurethane (PU) foam composites using hydrothermal method [36]. The hydrophobicity–oleophilicity was enhanced by chemical modification using silane coupling agent (KH 570). This nanocomposite exhibited the excellent oil recoverability and absorbent regenerability. Son et al. developed a magnetic biochar by pyrolysis of waste marine macro-algae as a feedstock, and biochar was then doped with iron oxide particles to impart magnetism for efficient removal of copper heavy metal [37].

3.3.1.3 Coagulation–Flocculation

The coagulation includes the destabilization of colloidal particles by the addition of coagulants (alum, ferric chloride, polyelectrolyte, guar gum, etc.), which leads to agglomeration of smaller particles [38]. For further enhancement in particle size, coagulation method is followed by flocculation to produce large flocs, which can easily settle down at bottom [39]. This method is simple and economically viable, but it has low removal efficiency and generates large amount of sludge. GilPavas et al. used $Al_2(SO_4)_3$ as coagulant for the industrial textile wastewater treatment [40].

3.3.1.4 Ion Exchange

In ion exchange, mobile ions present in external solution are exchanged for similarly charged ion that is electrostatically attached to immobile solid matrix [41]. Various synthetic organic resins (AV-17, AP-2, etc.), cereal grain-based products (soya parley, cellulose xanthate, etc.), and chelating agents (chitin, chitosan, etc.) were utilized for removal of different dyes and heavy metal ions from aqueous medium [42]. Regeneration of ion exchanger is possible using alkali or acids after saturation of resins. The disadvantages of this method are expensiveness, fouling of resin, clogging of resin owing to hardness of precipitated water and oxidation of resin by organic brighteners and oxidizing agents [3]. Sharma et al. synthesized polyacrylamide Zr(IV) vanadophosphate (PAM/ZVP) nanocomposite as an ion exchange for the degradation of congo red dye [43].

3.3.2 Chemical Method

3.3.2.1 Chemical Precipitation

Chemical precipitation includes the generation of a separable solid part from a solution with the use of chemicals [44]. Many chemicals like soda ash, lime, caustic soda, etc., were employed for the precipitation of heavy metal ions and dyes as insoluble carbonates, hydroxides, fluorides, and sulfides. Disadvantages of this method involve excessive sludge formation and requirement of large amount of chemicals [3]. Huang et al. studied the simultaneous removal of the total ammonia nitrogen, phosphate, and fluoride from wastewater by chemical precipitation method [45].

3.3.2.2 Chemical Oxidation

Chemical oxidation facilitates the decontamination of various pollutants present in the industrial and domestic wastewater. The oxidizing agents utilized are hydrogen peroxide (H_2O_2), ozone (O_3), chlorine (Cl_2), etc.

i. Oxidation by ozone
   Ozone (O_3) is a rapid and effective oxidizing agent for the water and wastewater because of its high instability compared to another oxidizing agents like hydrogen peroxide and chlorine [46]. It can easily degrade phenols, pesticides, aromatic and chlorinated hydrocarbons, and chemical oxygen demand (COD) level of wastewater [47]. Main advantage of this method is that ozone is applied in gaseous state and it does not increase volume of sludge and wastewater. Disadvantages associated with method are high cost, and continuous supply of ozone is needed as it has short life span. Guo et al.

investigated the sulfamethoxazole degradation using ultrasound (US), ozone (O_3), and ultrasound/ozone oxidation process [48].

ii. Oxidation by chlorine
The application of chlorine as disinfecting agent is extensively known; recently chlorine is used for the treatment of textile dyeing industry wastewater by in situ formation of chlorine using electrolysis of chlorine containing salts exist in the wastewater [49]. It can also be used in gaseous form for the water and wastewater treatment. But the main drawback of this method is the discharge of aromatic amines, which are aromatic in nature. Stange et al. used the chlorination, ozonation, and UV treatment for the removal of antibiotic-resistant bacteria and antibiotic resistance genes from drinking water [50].

iii. Oxidation by Fenton's reagent
Hydrogen peroxide in combination with ultraviolet (UV) radiation is known as Fenton's reagent. UV radiation dissociates the hydrogen peroxide into two hydroxyl (°OH), and these radicals have strong oxidation capacity that can easily oxidize the organic pollutants [51]. Main disadvantage of this method is generation of sludge as a result of flocculation of reagent and pollutants [52].

3.3.2.3 Electrochemical

Electrochemical is an efficient method for the removal of organic and inorganic pollutants without formation of sludge. This is a chemical process taken place under the influence of electrolytic potential [53]. When the applied electrochemical potential passes through an ion exchange membrane, oxidation–reduction happens at electrodes. High cost of electricity limits its application. Jiang et al. treated the explosive wastewater by electrochemical method using Ti/IrO_2 as the anodic electrode [54].

3.3.2.4 Photocatalysis

The photocatalysis is the chemical process which starts the reaction by ultraviolet, visible, or sunlight in the presence of catalyst (photocatalyst) that adsorbs the light and is involved in the degradation of reaction pollutants [55]. Figure 3.2 and Eqs. (3.1)–(3.4) illustrate the basic reaction mechanism of a photocatalyst to produce the reactive oxygen species, which can remove pollutants in the following steps: (i) photons with a specific energy ($h\upsilon$) are absorbed by the photocatalyst; (ii) the absorbed photons with energy ($h\upsilon$) greater than the band gap energy (E_g) of photocatalyst lead to the generation of electrons (e^{-}s) in the conduction band and corresponding holes (h^{+}s) in the valence band; and (iii) generated electron–hole (e^{-}–h^{+}) pairs will migrate to the surface of photocatalyst for oxidation of pollutant.

Fig. 3.2 Schematic diagram illustrating the principle of photocatalytic process

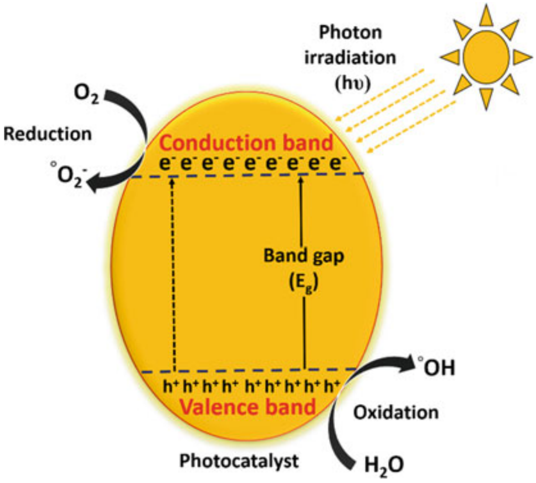

Excitation: Photon:

$$(h\upsilon) + \text{Photocatalyst} \rightarrow e^-_{CB} + h^+_{VB} \quad (3.1)$$

Oxidation of water:

$$H_2O + h^+_{VB} \rightarrow H^+ + {}^\circ OH \quad (3.2)$$

Reduction of adsorbed oxygen:

$$O_2 + e^-_{CB} \rightarrow {}^\circ O_2{}^- \quad (3.3)$$

Oxidation of pollutant:

$${}^\circ O_2{}^- + {}^\circ OH + \text{Pollutant} \rightarrow CO_2 + H_2O + \text{Intermediates} \quad (3.4)$$

The catalyst like zinc oxide (ZnO), copper oxide (CuO), and titanium dioxide (TiO_2) was employed for the removal of pollutants into carbon oxide (CO_2) and water (H_2O) [7]. Degradation is initiated by the generation of reactive oxygen species (hydroxyl radicals and superoxide radicals, etc.). Intensity of light, structure of dye, pH, and temperature affects the degradation of pollutants. The major advantages of this method are non-toxicity, no foul smell, and no sludge formation. The disadvantage is the utilization of expensive catalysts for wastewater treatment. Baladi et al. synthesized Dy_2ZnMnO_6 nanoparticles as a double perovskite [56]. The photocatalytic performance of the prepared product was examined by decolorization of three dyes including eriochrome black T, methyl orange, and methyl violet under UV irradiation. Covei et al. prepared the thin film heterostructures based on TiO_2 as n-type semiconductor and copper zinc tin sulfide (Cu_2ZnSnS_4) as p-type semiconductor, and this film was tested for the methylene blue dye removal under visible and solar light [57]. Ali et al. used the bismuth-TiO_2 nanotube composites as photocatalyst for the treatment of industrial wastewater [58].

3.3.3 Biological Method

Biological method has promising advantages over conventionally available methods due to its cost-effectiveness and environment-friendliness [59]. This method can completely mineralize the toxic pollutants into non-toxic end products without any requirement of rigorous monitoring. The noninvasive removal of pollutants occurs via metabolic potential of microorganism or biosorption [60]. This method can be aerobic, anaerobic, or combination of both. Algae, fungi, and bacteria are the main microorganism groups that were used for treatment of wastewater. The major drawbacks that limit its application include the fact that process can take longer time for the removal of pollutants. Hülsen et al. used purple phototrophic bacteria for domestic wastewater treatment [61].

3.4 Nanotechnology and Nanomaterials for Wastewater Treatment

Nanotechnology is the technology which works at nanoscale and has applications in the almost all fields of real world. Nanotechnology involves the fabrication, alteration, and application of biological, chemical, and physical systems at scales varying from individual atoms or molecules to submicron sizes and the amalgamation of the resultant nanostructures into larger system. They display distinctive physicochemical properties than their respective bulk counterparts of their small size.

3.4.1 Nanomaterials as Photocatalysis

During past decades, the removal of numerous hazardous contaminants using photocatalysis has been recommended as a viable solution for detoxification of water [4]. Much consideration has been done to the photocatalytic removal of pollutants with TiO_2 nanoparticles under UV since conventional treatment methods

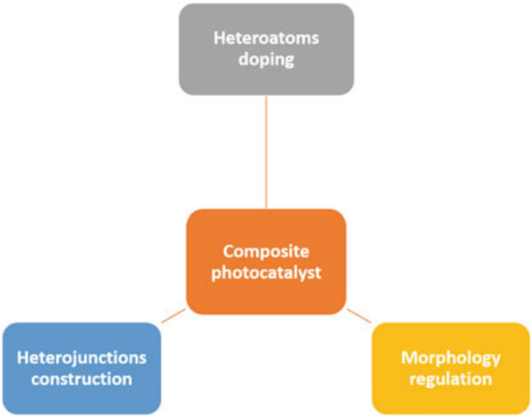

Fig. 3.3 Schematic illustration of different synthesis approaches for composite photocatalysts

are not efficient in removing the pollutants [62]. However, it remains a challenge to synthesize an efficient visible light-assisted photocatalyst only created on an single semiconductor photocatalyst. Thus, it is important to find an effective way to improve the functioning of semiconductor photocatalysts. Nowadays, a numerous of multifunctional composite have been prepared for different water remediation applications [7]. There have been several studies reporting the preparation of composite semiconductor photocatalysts via numerous approaches. Figure 3.3 illustrated the different synthesis approaches for composite photocatalysts for the water remediation.

3.4.1.1 Heteroatoms Doping

Recently, the scheme of incorporating heteroatoms into the lattice of semiconductor photocatalysts has been utilized for the regulation of band gap of semiconductor photocatalysts so as to improve their degradation efficiency under visible light [63]. The generally employed dopants in semiconductor photocatalysts are classified as the metallic cations and the non-metallic anions [64].

i. Metallic cation doing
   The most utilized metallic cation dopants for semiconductor photocatalysts are transition metal ions like Cu^{2+}, Mo^{5+}, Fe^{3+}, Zn^{2+}, Mn^{2+}, etc. [65]. Usually, the redox energy states of these utilized metallic cations remain within the band gap energy states of individual semiconductor photocatalysts; thus, incorporation of those metallic ions will form intra-band energy state near either conduction band or valance band of a semiconductor photocatalyst. Subsequently, the red shift in band gap energy absorption of a metallic cation-doped semiconductor photocatalyst [66]. Additionally, the doped metallic cations can act as an e^{-}–h^{+} pairs trapper for controlling the concentration of e^{-}–h^{+} pairs.

ii. Non-metallic anion doing

The doping semiconductor photocatalysts by non-metallic anion have been recognized to be an alternative way to control the intrinsic electronic properties of semiconductor photocatalysts, which lead to formation of several heteroatomic energy levels. These non-metallic anion-doped semiconductor photocatalysts demonstrate enhanced photocatalytic efficiency under sunlight [67]. Numerous non-metallic elements, like carbon, nitrogen, fluorine, phosphorus, and sulfur, were used as substitute for the oxygen in oxygen containing semiconductor photocatalysts such as TiO_2 and ZnO [68, 69]. The nitrogen doping leads to improved visible light response of photocatalyst due to the narrowing of p states of nitrogen of nitrogen-doped photocatalyst by overlapping with 2p states of oxygen, comparable atomic radii of oxygen and nitrogen, and high stability [70].

3.4.1.2 Heterojunction Construction

Construction of heterojunction in photocatalyst is another approach for improving photocatalytic efficiency of semiconductor photocatalysts. Heterojunction photocatalysts are developed interface between two semiconductor photocatalysts with the uneven band structure [71]. The heterojunction photocatalysts are classified as conventional and new generation photocatalysts.

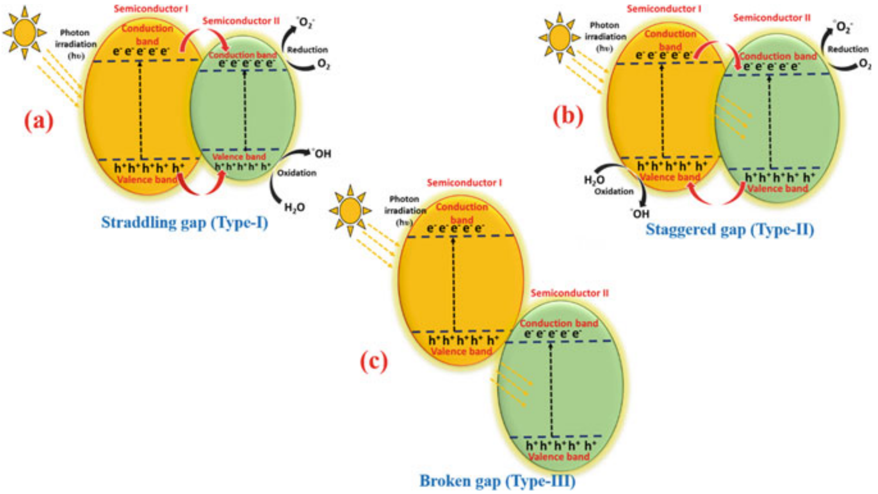

Fig. 3.4 Three different types of heterojunctions photocatalysts: **a** Type-I, **b** Type-II, and **c** Type-III

i. Conventional heterojunction photocatalysts

   The conventional heterojunction photocatalysts are classified into following three types (Fig. 3.4) [72]:

   a. Straddling gap (Type-I)

      In type-I, the valance band and conduction band of semiconductor II are higher and lower than the valance band and conduction band of semiconductor I, respectively [73]. Thus, photoexcited e^{-}s and h^{+}s transfer to the conduction and valance band of semiconductor II. The reactive oxygen species are generated on the surface of semiconductor II.

   b. Staggered gap (Type-II)

      In the type-II heterojunction photocatalyst, the valance band and conduction band of semiconductor II are lower than the valance band and conduction band of semiconductor I. Thus, photoexcited e^{-}s will transfer to the conduction band of semiconductor I to the semiconductor II, and corresponding h^{+}s will transfer from valance band of semiconductor II to the semiconductor I to inhibit the recombination of e^{-}–h^{+} pairs. It is the most effective way to improve the photocatalytic efficiency of the photocatalyst [74]. Various type-II heterogenous photocatalysts have been synthesized for the water remediation. For example, Sharma et al. successfully prepared multifunctional mesoporous CuO/ZnO-tetarpods heterojunction photocatalyst using a two-step synthesis approach [7]. The result demonstrated that the heterojunction photocatalyst has a type-II band structure and displayed enhanced photocatalytic efficiency for the removal of methyl orange and crystal violet dyes present in wastewater.

   c. Broken gap (Type-III)

      In the type-III heterojunction photocatalyst, the energy band gap of the two semiconductor photocatalysts will not overlap, so there is no migration or separation of e^{-}s and h^{+}s between semiconductor I and semiconductor II [73].

ii. New generation of heterojunction photocatalysts

   There are certain drawbacks of type-II heterojunction photocatalysts, like weak redox capacity and suppressed migration of e^{-}s and h^{+}s due to electrostatic repulsion [75]. To overcome these drawbacks, new generation of heterojunction photocatalysts has been synthesized like p–n, surface, Z-scheme, and the semiconductor/carbon heterojunction photocatalysts.

   a. p–n heterojunction photocatalysts

      The p–n heterojunction photocatalysts are designed by combining a p-type and n-type semiconductors to improve the photocatalytic efficiency of photocatalysts. When the p–n heterojunction photocatalysts are illuminated by a light source, then e^{-}–h^{+} pairs will be created in the related semiconductor photocatalysts [76]. Though, photoexcited e^{-}s and h^{+}s will migrate to the conduction band of n-type semiconductor and valence band of p-type semiconductor, respectively, because of the internal electric field. Additionally, separation of the photoexcited e^{-}–h^{+} pairs is much more effectual in the p–n heterojunction photocatalysts compared than conventional type-II heterojunction photocatalysts because of the combing effect of the internal electric field and band arrangement [77].

b. Surface heterojunction photocatalysts
A surface heterojunction photocatalysts are designed on the heterojunction between two crystal facets of a single semiconductor surface. As reported before, a surface heterojunction can be created between two crystal facets of a single semiconductor [73]. This heterojunction photocatalyst is much cheaper than p–n heterojunction photocatalyst as it utilized a single semiconductor.

c. Z-scheme heterojunction
Z-scheme heterojunction is designed using two types of semiconductors and e^{-} donor/acceptor pair. In the process of photocatalysis process, the photoexcited e^{-}/h^{+} will transfer from one semiconductor to another semiconductor through the e^{-} donor/acceptor pair [73]. So, e^{-}/h^{+} will accumulate on another semiconductor photocatalysts with higher redox potentials for more efficient spatial separation of e^{-}–h^{+} pairs.

d. Semiconductor/carbon heterojunction photocatalysts
The unique properties of the carbonaceous nanomaterials such as large surface area, excellent conductivity, and high chemical stability make them excellent candidate for designing novel photocatalysts for water remediation [78]. The widely employed nanomaterials which are used with combination of semiconductor photocatalysts are graphene oxide, carbon nanotubes, and carbon dots. Various reports have shown the preparation of semiconductor/carbon heterojunction photocatalysts by combining graphene oxide with semiconductor photocatalyst like graphene oxide/ZnO, graphene oxide TiO_2, etc., for the treatment of different industrial wastewater [62]. For example, Sharma et al. prepared graphene oxide/ZnO nanocomposite using hydrothermal method and ZnO nanostructures by green synthesis (lemon and honey) approach [5]. The prepared nanocomposite was used for the removal of methylene blue dye.

3.4.1.3 Morphology Modification

Morphological modification of photocatalysts also affects the photocatalytic efficiency. In this section, we will briefly discuss the designing of different nanocomposite photocatalysts with morphologies of zero, one, two, and three dimensions.

i. Zero-dimensional photocatalyst

The zero-dimensional photocatalyst is described as spherically shaped materials within the dimensions in the nanoscale. These photocatalysts have properties like high surface area, high chemical stability, easy to synthesize, and functionalized for various applications [79]. Nowadays, these photocatalysts are synthesized by different chemical methods like hydrothermal, sol–gel, etc.

ii. One-dimensional photocatalyst

The one-dimensional photocatalysts have unique characteristics like high surface area, long aspect ratio, easy to synthesize, and functionalized [80]. One-dimensional photocatalysts with different morphologies such as wire, rod, belt, and tube have been prepared by mainly electrospinning and hydrothermal method.

iii. Two-dimensional photocatalyst

The two-dimensional photocatalysts (nanosheets) have distinctive properties such as high surface area and tuneable structures [81]. Sheet like nanophotocatalyst have been synthesized widely by hydrothermal approach.

iv. Three-dimensional photocatalyst

Nowadays, three-dimensional photocatalysts designed due to their exceptional properties include high specific surface area, excellent adsorption capacity, high chemical stability, excellent mass transfer capacity, and large number of active sites, which make these photocatalysts as promising materials for effective photodegradation of pollutants in water [82]. These photocatalysts have been prepared by sol–gel, template method, in situ assembly, etc.

3.5 Synthesis of Photocatalyst

The photocatalytic activity of the photocatalysts greatly influenced by its preparation method. Various techniques including physical, chemical, and biological methods have been used to synthesize nano photocatalyst. Photocatalytic material can be prepared in the form of powders, fibers, and films by these methods. In this section, we briefly discuss the major methods which are widely used for the synthesis of nano photocatalyst.

3.5.1 Physical Methods

In physical techniques, the photocatalyst is deposited onto the substrate directly in gas phase without any chemical change from precursor to photocatalyst. The substrate can be glass, alumina, metal, zeolite, silicon, fluorine tin oxide-coated glass or any porous material. Electron beam lithography and sputtering are the most used techniques under this category [83]. In these methods, the obtained photocatalyst is in the form of film. Various semiconducting photocatalysts like TiO_2, ZnO, SnO_2, etc., with variety of shapes including spheres, rods, and wires can be synthesized using this technique. The morphology and shape of the catalyst can be controlled by controlling temperature and pressure conditions. The major advantages of these methods are formation of pure thin films with uniform shape and size. Additionally, the photocatalyst can be easily restored after wastewater treatment. These techniques require expensive and highly complex system. Therefore, they are not extensively used for the synthesis of photocatalyst.

3.5.2 Chemical Methods

These methods are widely used for the preparation of photocatalyst. Major chemical methods include sol–gel process, chemical deposition method, hydrothermal, spray pyrolysis, and microwave technique [84]. Majorly semiconducting nanostructured material with or without doping of metal nanoparticles has been synthesized using this technique. The main advantages of the method are that it includes simple operation, low cost, and high yield of the photocatalyst. The brief discussion of few chemical methods is as follows.

3.5.2.1 Sol–Gel Method

Sol–gel synthesis process is one of the most popular methods used for the synthesis of photocatalyst. The methods have certain salient features like low processing temperature, homogeneity of the finally produced material, and formation of the complex structures or composite nanomaterials [85]. Doping of metal nanoparticles on semiconducting matrix is widely used in photocatalysis process to reduce the band gap of semiconducting nanostructures. Sol–gel method has an advantage that it is easy incorporation of dopant in semiconducting matrix during synthesis process. The method offers simple, fastest, and low cost for photocatalyst synthesis [86]. In this method, variety of photocatalyst with different shape, size, and morphology can be synthesized by controlling pH, temperature, reaction time, concentration of solvent, and aging temperature. TiO_2, ZnO, Ag-doped TiO_2, and Au–TiO_2 nano photocatalysts are few examples which have been synthesized using sol–gel technique.

3.5.2.2 Chemical Vapor Deposition Method

Chemical vapor deposition (CVD) technique is one of the reliable techniques for the growth of nano photocatalyst. The method involves deposition of atoms or molecules on the substrate in their vapor phase. The obtained catalyst is in the form of film, composite supported. The method is capable to control high quality thin film on the substrate. The main advantage of this technique includes controlled and uniform morphology and narrow particle size distribution of the photocatalyst [87]. No post-annealing treatment of the photocatalyst is required in this method. Metal, semiconductor nanostructures and their composites with high purity and high performance as photocatalyst can be prepared using this technique. Recently, TiO_2 thin film as photocatalysts on the surface of polymeric materials for water filter application has been deposited using CVD method.

3.5.2.3 Solvothermal/Hydrothermal Method

Solvothermal is defined a chemical reaction, when the solvent is heated around their boiling point with autogenous pressure. The process takes place in a steel vessel containing Teflon line known as autoclave under constant temperature and pressure. Organic, inorganic, and water can be used as a solvent in this method. If water is used as a solvent, the method is termed as hydrothermal method [83]. The shape, size, and the surface area of the photocatalyst mainly depend on the temperature and pressure condition. Photocatalysts synthesis using this process usually involves formation of crystal nucleation followed by its subsequent growth [88]. Therefore, by controlling the parameters like temperature, pH, and solvent concentrations, the final catalyst could be fabricated with desired particle sizes and morphologies [85]. Variety of metal, semiconductor nanoparticles, and their composites for photocatalytic applications has been synthesized using this method. The method is widely used by industries for the preparation of nano photocatalyst.

3.5.2.4 Spray Pyrolysis

The method is a one step and scalable process which is widely used by industries for the preparation of photocatalyst. In this method, the ionic solution of the desired catalyst is sprayed over heated substrate [89]. The method provides flexibility of choosing precursors and solvents; therefore, it is considered as an economically viable solution for the industries. The photocatalysts synthesized by this technique are more thermally stable compared with the other reported chemical methods. Two or more metal nanoparticles, two or more metal oxides like Al-doped CeO_2, Cu-doped $Ce_xZr_{1-x}O_2$, Sn-doped ZnO, Ag/TiO_2, and their heterojunctions can be easily synthesized using this method [90].

3.5.3 Biological or Eco-Friendly Method

Most of the chemical and physical methods have complex synthesis protocols and require very high temperature and pressure conditions. Additionally, these methods require toxic chemicals as a reducing agent, which interns increases the cost of the photocatalyst and sometimes some toxic chemicals are also deposited on the surface of the photocatalyst [62]. On the other hand, biological methods have emerged as a novel root for the synthesis of photocatalyst because of its ease of the eco-friendly approach, economic viability, and possibility of readily covering large surface areas. The method generally involves the non-toxic natural sources known as microbes as a reducing and capping agent. Microbes of few nanometers to micrometers are termed as nano factories, meaning generators of nanoparticles. The green synthesis of nanoparticles is considered as economically viable solution as they use microbes to produce nanomaterials as part of their metabolism and which reproduce very quickly [91]. Plant extracts, fungi, yeast, and bacteria are some of the famous natural sources which are widely used for the preparation of photocatalyst. A brief discussion of various green agents is discussed in detail below.

3.5.3.1 Synthesis of Photocatalyst Using Bacteria

Synthesis of metal and metal oxide nanoparticles using bacterial extract is considered as green, eco-friendly, and economical biological method for the synthesis of photocatalytic nanoparticles. Cyanobacteria have huge potential for the large-scale synthesis of nanoparticles with variety of shape and size due to being a sustainable resource for various metabolic product [92]. Prokaryotic bacteria have been extensively researched for the synthesis of nanoparticles as they can easily survive in harsh environmental conditions and easy to manipulate. Some of the researches also report the degradation of dyes and heavy metals present in wastewater using cyanobacteria.

3.5.3.2 Synthesis of Photocatalyst Using Fungi

Recently, the use of fungi for the synthesis of metal nano photocatalyst is another popular method. The prevention and handling of fungi is easy compared with another microorganism. Moreover, most of the fungi secrete large quantities of enzymes, which is a potential candidate as reducing agent for biosynthesis [93]. Compared to bacteria, fungi secret more protein which results in higher amount of nanoparticles synthesis. However, the genetic manipulation of some specific enzymes for over expression is much more difficult than in prokaryotes. Metal nanoparticles like Ag and Au and other semiconducting photocatalysts like ZnO and TiO_2 are some of the photocatalysts which have been synthesized using fungi.

3.5.3.3 Synthesis of Photocatalyst Using Plant Extract

The synthesis of nanoparticles using plant extracts and their metabolites has been widely used for the preparation of metal and semiconducting nanoparticles and their hybrids. Different parts of the plants including leave, stem, fruits accumulate biomolecules like protein, enzyme, and carbohydrates which are responsible for the reduction of metal into nanoparticles [94]. The plant phytochemicals (flavonoids, alkaloids, terpenoids, and amides) with antioxidant properties are responsible for the synthesis of stable metal and metal oxide nanoparticles. In this method, the shape, size, and stability of the nanoparticles can be controlled by controlling the pH and concentration of the plant extract [95]. The major advantage of the plant-assisted nanoparticle synthesis process is the kinetics of this method. It is abundantly higher than other biosynthesis method. Additionally, it can be considered as an environment-friendly and cheap process for photocatalyst synthesis as the stable nanostructures can be formed without the utilization of intermediate base compounds [91]. Recently, nanoparticles like ZnO, TiO_2, and their hybrid composite have been synthesized using plant extract which are widely used for photocatalytic applications.

3.5.3.4 Synthesis of Photocatalyst Using Yeast

The synthesis of nanoparticles using yeast is another simple and cost-effective approach for the synthesis of nanoparticles. Yeast secretors of extracellular enzymes and number of species growth rate are fast, which help to keep the culturing process simple at laboratory scale [96]. They can produce metal nanoparticles and nanostructure via reducing enzyme intracellularly or extracellularly. The synthesis of photocatalytic nanoparticles using yeast has limited investigations.

3.6 Summary and Prospects

In summary, to address the worldwide major concerned problem of water pollution, several photocatalysis procedures depended on various photocatalysts have been designed. Numerous attempts have been done to further enhance the photocatalytic efficiency of the semiconductors-based photocatalysts. In this chapter, the recent advances in the designing and synthesis of nanostructured photocatalysts for water remediation are presented, including the most adapted approaches for narrowing the band gap of semiconductor photocatalysts, to supress the fast recombination of the photoexcited $e^{-}–h^{+}$ pairs, to improve the visible light response of photocatalysts. Furthermore, the nanostructured photocatalysts with several morphologies were also summarized. Although remarkable designing and synthesis of nanostructured photocatalysts has been attained, there are still many drawbacks yet to be addressed for improvement in the real-time industrial application implementation of the photocatalysts. Thus, a few possible prospects for the recent development of nanostructured photocatalysts for the water remediation are suggested based on the current studies: (i) the current synthesis approaches are relative complex, expensive, and utilize harmful chemicals, so a more simple, effective, and eco-friendly method is expected; (ii) the mechanism of the nanostructured semiconductor photocatalysts is still unclear, couple of them are implausible, and consequently, much more attention is required for the basic analyses of the their catalytic mechanisms; and (iii) the real-time industrial applications are inadequate, and therefore, novel nanostructured photocatalysts with enhanced reusability are recommended. Conclusively, we anticipate that this chapter can offer some beneficial support for the design and synthesis of next generation of nanostructured photocatalysts for the water remediation.

Acknowledgements The authors are grateful to the Directors of Amity Institute of Biotechnology, Amity Institute of Nanotechnology, Amity University Uttar Pradesh.

References

1. Kamali M, Persson KM, Costa ME, Capela I (2019) Sustainability criteria for assessing nanotechnology applicability in industrial wastewater treatment: current status and future outlook. Environ Int 125:261–276. https://doi.org/10.1016/j.envint.2019.01.055
2. De Gisi S, Lofrano G, Grassi M, Notarnicola M (2016) Characteristics and adsorption capacities of low-cost sorbents for wastewater treatment: a review. Sustain Mater Technol 9:10–40. https://doi.org/10.1016/j.susmat.2016.06.002
3. Crini G, Lichtfouse E (2019) Advantages and disadvantages of techniques used for wastewater treatment. Environ Chem Lett 17:145–155. https://doi.org/10.1007/s10311-018-0785-9
4. Mangalam J, Kumar M, Sharma M, Joshi M (2019) High adsorptivity and visible light assisted photocatalytic activity of silver/reduced graphene oxide (Ag/rGO) nanocomposite for wastewater treatment. Nano Struct Nano Objects 17:58–66. https://doi.org/10.1016/j.nanoso.2018.11.003
5. Sharma M, Sondhi H, Krishna R et al (2020) Assessment of GO/ZnO nanocomposite for solar-assisted photocatalytic degradation of industrial dye and textile effluent. Environ Sci Pollut Res 27:32076–32087. https://doi.org/10.1007/s11356-020-08849-3
6. Behl K, SeshaCharan P, Joshi M et al (2020) Multifaceted applications of isolated microalgae Chlamydomonas sp. TRC-1 in wastewater remediation, lipid production and bioelectricity generation. Bioresour Technol 304:122993. https://doi.org/10.1016/j.biortech.2020.122993
7. Sharma M, Poddar M, Gupta Y et al (2020) Solar light assisted degradation of dyes and adsorption of heavy metal ions from water by CuO–ZnO tetrapodal hybrid nanocomposite. Mater Today Chem 17:100336. https://doi.org/10.1016/j.mtchem.2020.100336
8. Hube S, Eskafi M, Hrafnkelsdóttir KF et al (2020) Direct membrane filtration for wastewater treatment and resource recovery: a review. Sci Total Environ 710:136375. https://doi.org/10.1016/j.scitotenv.2019.136375
9. Santana-Viera S, Padrón MET, Sosa-Ferrera Z, Santana-Rodríguez JJ (2020) Quantification of cytostatic platinum compounds in wastewater by inductively coupled plasma mass spectrometry after ion exchange extraction. Microchem J 157:104862. https://doi.org/10.1016/j.microc.2020.104862

10. Yu M, Wang J, Tang L et al (2020) Intimate coupling of photocatalysis and biodegradation for wastewater treatment: mechanisms, recent advances and environmental applications. Water Res 175:115673. https://doi.org/10.1016/j.watres.2020.115673
11. Li J, Cui W, Chen P et al (2020) Unraveling the mechanism of binary channel reactions in photocatalytic formaldehyde decomposition for promoted mineralization. Appl Catal B Environ 260:118130. https://doi.org/10.1016/j.apcatb.2019.118130
12. Hojamberdiev M, Czech B, Göktaş AC et al (2020) SnO2@ZnS photocatalyst with enhanced photocatalytic activity for the degradation of selected pharmaceuticals and personal care products in model wastewater. J Alloys Compd 827:154339. https://doi.org/10.1016/j.jallcom.2020.154339
13. Bahmani M, Dashtian K, Mowla D et al (2020) UiO-66(Ti)-Fe3O4-WO3 photocatalyst for efficient ammonia degradation from wastewater into continuous flow-loop thin film slurry flat-plate photoreactor. J Hazard Mater 393:122360. https://doi.org/10.1016/j.jhazmat.2020.122360
14. ur Rehman A, Aadil M, Zulfiqar S et al (2020) Fabrication of binary metal doped CuO nanocatalyst and their application for the industrial effluents treatment. Ceram Int. https://doi.org/10.1016/j.ceramint.2020.11.064
15. Franco P, Sacco O, De Marco I et al (2020) Photocatalytic degradation of eriochrome black-T azo dye using Eu-doped ZnO prepared by supercritical antisolvent precipitation route: a preliminary investigation. Top Catal 63:1193–1205. https://doi.org/10.1007/s11244-020-01279-y
16. Walczykowski P, Jenerowicz A, Orych A (2013) A review on remote sensing methods of detecting physical water pollutants
17. Borah P, Kumar M, Devi P (2020) Chapter 2—types of inorganic pollutants: metals/metalloids, acids, and organic forms. In: Devi P, Singh P, Kansal SK (eds) Inorganic pollutants in water. Elsevier, pp 17–31
18. Rasalingam S, Peng R, Koodali RT (2014) Removal of hazardous pollutants from wastewaters: applications of TiO_2-SiO_2 mixed oxide materials. J Nanomater 2014:617405. https://doi.org/10.1155/2014/617405
19. Natarajan V, Karunanidhi M, Raja B (2020) A critical review on radioactive waste management through biological techniques. Environ Sci Pollut Res 27:29812–29823. https://doi.org/10.1007/s11356-020-08404-0
20. Rani P, Kumar V, Singh PP et al (2020) Highly stable AgNPs prepared via a novel green approach for catalytic and photocatalytic removal of biological and non-biological pollutants. Environ Int 143:105924. https://doi.org/10.1016/j.envint.2020.105924
21. Srivastava S, Agrawal SB, Mondal MK (2016) Characterization, isotherm and kinetic study of phaseolus vulgaris husk as an innovative adsorbent for Cr(VI) removal. Korean J Chem Eng 33:567–575. https://doi.org/10.1007/s11814-015-0165-0
22. Ezugbe EO, Rathilal S (2020) Membrane technologies in wastewater treatment: a review. Membranes (Basel) 10. https://doi.org/10.3390/membranes10050089
23. Wan Ikhsan SN, Yusof N, Aziz F, Nurasyikin M (2017) A review of oilfield wastewater treatment using membrane filtration over conventional technology. Malaysian J Anal Sci 21:643–658. https://doi.org/10.17576/mjas-2017-2103-14
24. Bhattacharjee C, Saxena VK, Dutta S (2017) Fruit juice processing using membrane technology: a review. Innov Food Sci Emerg Technol 43:136–153. https://doi.org/10.1016/j.ifset.2017.08.002
25. Chao G, Shuili Y, Yufei S et al (2018) A review of ultrafiltration and forward osmosis: application and modification. IOP Conf Ser Earth Environ Sci 128:12150. https://doi.org/10.1088/1755-1315/128/1/012150
26. Salahi A, Mohammadi T, Mosayebi Behbahani R, Hemmati M (2015) Asymmetric polyethersulfone ultrafiltration membranes for oily wastewater treatment: synthesis, characterization, ANFIS modeling, and performance. J Environ Chem Eng 3:170–178. https://doi.org/10.1016/j.jece.2014.10.021

27. Hailemariam RH, Woo YC, Damtie MM et al (2020) Reverse osmosis membrane fabrication and modification technologies and future trends: a review. Adv Colloid Interface Sci 276:102100. https://doi.org/10.1016/j.cis.2019.102100
28. Umar M, Roddick F, Fan L (2015) Recent advancements in the treatment of municipal wastewater reverse osmosis concentrate—an overview. Crit Rev Environ Sci Technol 45:193–248. https://doi.org/10.1080/10643389.2013.852378
29. Bunani S, Yörükoğlu E, Yüksel Ü et al (2015) Application of reverse osmosis for reuse of secondary treated urban wastewater in agricultural irrigation. Desalination 364:68–74. https://doi.org/10.1016/j.desal.2014.07.030
30. Mulyanti R, Susanto H (2018) Wastewater treatment by nanofiltration membranes. IOP Conf Ser Earth Environ Sci 142:12017. https://doi.org/10.1088/1755-1315/142/1/012017
31. Abdel-Fatah MA (2018) Nanofiltration systems and applications in wastewater treatment: review article. Ain Shams Eng J 9:3077–3092. https://doi.org/10.1016/j.asej.2018.08.001
32. Garcia-Ivars J, Martella L, Massella M et al (2017) Nanofiltration as tertiary treatment method for removing trace pharmaceutically active compounds in wastewater from wastewater treatment plants. Water Res 125:360–373. https://doi.org/10.1016/j.watres.2017.08.070
33. Burakov AE, Galunin EV, Burakova IV et al (2018) Adsorption of heavy metals on conventional and nanostructured materials for wastewater treatment purposes: a review. Ecotoxicol Environ Saf 148:702–712. https://doi.org/10.1016/j.ecoenv.2017.11.034
34. Afroze S, Sen TK (2018) A review on heavy metal ions and dye adsorption from water by agricultural solid waste adsorbents. Water Air Soil Pollut 229:225. https://doi.org/10.1007/s11270-018-3869-z
35. Samanta AK, Basu G, Mishra L (2018) Role of major constituents of coconut fibres on absorption of ionic dyes. Ind Crops Prod 117:20–27. https://doi.org/10.1016/j.indcrop.2018.02.080
36. Zhang T, Kong L, Dai Y et al (2017) Enhanced oils and organic solvents absorption by polyurethane foams composites modified with MnO2 nanowires. Chem Eng J 309:7–14. https://doi.org/10.1016/j.cej.2016.08.085
37. Son E-B, Poo K-M, Chang J-S, Chae K-J (2018) Heavy metal removal from aqueous solutions using engineered magnetic biochars derived from waste marine macro-algal biomass. Sci Total Environ 615:161–168. https://doi.org/10.1016/j.scitotenv.2017.09.171
38. Teh CY, Budiman PM, Shak KPY, Wu TY (2016) Recent advancement of coagulation-flocculation and its application in wastewater treatment. Ind Eng Chem Res 55:4363–4389. https://doi.org/10.1021/acs.iecr.5b04703
39. Zhang H, Yang L, Zang X et al (2019) Effect of shear rate on floc characteristics and concentration factors for the harvesting of Chlorella vulgaris using coagulation-flocculation-sedimentation. Sci Total Environ 688:811–817. https://doi.org/10.1016/j.scitotenv.2019.06.321
40. GilPavas E, Dobrosz-Gómez I, Gómez-García MÁ (2017) Coagulation-flocculation sequential with Fenton or Photo-Fenton processes as an alternative for the industrial textile wastewater treatment. J Environ Manage 191:189–197. https://doi.org/10.1016/j.jenvman.2017.01.015
41. Luo T, Abdu S, Wessling M (2018) Selectivity of ion exchange membranes: a review. J Memb Sci 555:429–454. https://doi.org/10.1016/j.memsci.2018.03.051
42. Levchuk I, Rueda Márquez JJ, Sillanpää M (2018) Removal of natural organic matter (NOM) from water by ion exchange—a review. Chemosphere 192:90–104. https://doi.org/10.1016/j.chemosphere.2017.10.101
43. Sharma G, Kumar A, Naushad M et al (2016) Polyacrylamide@Zr(IV) vanadophosphate nanocomposite: ion exchange properties, antibacterial activity, and photocatalytic behavior. J Ind Eng Chem 33:201–208. https://doi.org/10.1016/j.jiec.2015.10.011
44. Rajasulochana P, Preethy V (2016) Comparison on efficiency of various techniques in treatment of waste and sewage water—a comprehensive review. Resour Technol 2:175–184. https://doi.org/10.1016/j.reffit.2016.09.004

45. Huang H, Liu J, Zhang P et al (2017) Investigation on the simultaneous removal of fluoride, ammonia nitrogen and phosphate from semiconductor wastewater using chemical precipitation. Chem Eng J 307:696–706. https://doi.org/10.1016/j.cej.2016.08.134
46. Krishnan S, Rawindran H, Sinnathambi CM, Lim JW (2017) Comparison of various advanced oxidation processes used in remediation of industrial wastewater laden with recalcitrant pollutants. IOP Conf Ser Mater Sci Eng 206:12089. https://doi.org/10.1088/1757-899x/206/1/012089
47. Deng Y, Zhao R (2015) Advanced oxidation processes (AOPs) in wastewater treatment. Curr Pollut Reports 1:167–176. https://doi.org/10.1007/s40726-015-0015-z
48. Guo W-Q, Yin R-L, Zhou X-J et al (2015) Sulfamethoxazole degradation by ultrasound/ozone oxidation process in water: kinetics, mechanisms, and pathways. Ultrason Sonochem 22:182–187. https://doi.org/10.1016/j.ultsonch.2014.07.008
49. Bartolomeu M, Neves MGPMS, Faustino MAF, Almeida A (2018) Wastewater chemical contaminants: remediation by advanced oxidation processes. Photochem Photobiol Sci 17:1573–1598. https://doi.org/10.1039/C8PP00249E
50. Stange C, Sidhu JPS, Toze S, Tiehm A (2019) Comparative removal of antibiotic resistance genes during chlorination, ozonation, and UV treatment. Int J Hyg Environ Health 222:541–548. https://doi.org/10.1016/j.ijheh.2019.02.002
51. Zhang M, Dong H, Zhao L et al (2019) A review on Fenton process for organic wastewater treatment based on optimization perspective. Sci Total Environ 670:110–121. https://doi.org/10.1016/j.scitotenv.2019.03.180
52. Tagg A, Harrison J, Ju-Nam Y et al (2017) Fenton's reagent for the rapid and efficient isolation of microplastics from wastewater. Chem Commun 53:372–375. https://doi.org/10.1039/C6CC08798A
53. Martínez-Huitle CA, Panizza M (2018) Electrochemical oxidation of organic pollutants for wastewater treatment. Curr Opin Electrochem 11:62–71. https://doi.org/10.1016/j.coelec.2018.07.010
54. Jiang N, Zhao Q, Xue Y et al (2018) Removal of dinitrotoluene sulfonate from explosive wastewater by electrochemical method using Ti/IrO2 as electrode. J Clean Prod 188:732–740. https://doi.org/10.1016/j.jclepro.2018.04.030
55. Dong S, Feng J, Fan M et al (2015) Recent developments in heterogeneous photocatalytic water treatment using visible light-responsive photocatalysts: a review. RSC Adv 5:14610–14630. https://doi.org/10.1039/C4RA13734E
56. Baladi M, Soofivand F, Valian M, Salavati-Niasari M (2019) Sonochemical-assisted synthesis of pure Dy2ZnMnO6 nanoparticles as a novel double perovskite and study of photocatalytic performance for wastewater treatment. Ultrason Sonochem 57:172–184. https://doi.org/10.1016/j.ultsonch.2019.05.022
57. Covei M, Perniu D, Bogatu C, Duta A (2019) CZTS-TiO2 thin film heterostructures for advanced photocatalytic wastewater treatment. Catal Today 321–322:172–177. https://doi.org/10.1016/j.cattod.2017.12.003
58. Ali I, Han G-B, Kim J-O (2019) Reusability and photocatalytic activity of bismuth-TiO2 nanocomposites for industrial wastewater treatment. Environ Res 170:222–229. https://doi.org/10.1016/j.envres.2018.12.038
59. Azubuike CC, Chikere CB, Okpokwasili GC (2016) Bioremediation techniques–classification based on site of application: principles, advantages, limitations and prospects. World J Microbiol Biotechnol 32:180. https://doi.org/10.1007/s11274-016-2137-x
60. Timková I, Sedláková-Kaduková J, Pristaš P (2018) Biosorption and bioaccumulation abilities of actinomycetes/streptomycetes isolated from metal contaminated sites. Separations 5. https://doi.org/10.3390/separations5040054
61. Hülsen T, Barry EM, Lu Y et al (2016) Domestic wastewater treatment with purple phototrophic bacteria using a novel continuous photo anaerobic membrane bioreactor. Water Res 100:486–495. https://doi.org/10.1016/j.watres.2016.04.061

62. Sharma M, Behl K, Nigam S, Joshi M (2018) TiO2-GO nanocomposite for photocatalysis and environmental applications: a green synthesis approach. Vacuum 156:434–439. https://doi.org/10.1016/j.vacuum.2018.08.009
63. Yu Z, Chen X-Q, Kang X et al (2018) Noninvasively modifying band structures of wide-bandgap metal oxides to boost photocatalytic activity. Adv Mater 30:1706259. https://doi.org/10.1002/adma.201706259
64. Liu G, Wang L, Yang HG et al (2010) Titania-based photocatalysts—crystal growth, doping and heterostructuring. J Mater Chem 20:831–843. https://doi.org/10.1039/B909930A
65. Benjwal P, De B, Kar KK (2018) 1-D and 2-D morphology of metal cation co-doped (Zn, Mn) TiO2 and investigation of their photocatalytic activity. Appl Surf Sci 427:262–272. https://doi.org/10.1016/j.apsusc.2017.08.226
66. Venkataswamy P, Jampaiah D, Kandjani AE et al (2018) Transition (Mn, Fe) and rare earth (La, Pr) metal doped ceria solid solutions for high performance photocatalysis: effect of metal doping on catalytic activity. Res Chem Intermed 44:2523–2543. https://doi.org/10.1007/s11164-017-3244-5
67. Mittal A, Mari B, Sharma S et al (2019) Non-metal modified TiO2: a step towards visible light photocatalysis. J Mater Sci Mater Electron 30:3186–3207. https://doi.org/10.1007/s10854-018-00651-9
68. Shayegan Z, Lee C-S, Haghighat F (2018) TiO2 photocatalyst for removal of volatile organic compounds in gas phase—a review. Chem Eng J 334:2408–2439. https://doi.org/10.1016/j.cej.2017.09.153
69. Kumari V, Mittal A, Jindal J et al (2019) S-, N- and C-doped ZnO as semiconductor photocatalysts: a review. Front Mater Sci 13:1–22. https://doi.org/10.1007/s11706-019-0453-4
70. Wang W, Tadé MO, Shao Z (2018) Nitrogen-doped simple and complex oxides for photocatalysis: a review. Prog Mater Sci 92:33–63. https://doi.org/10.1016/j.pmatsci.2017.09.002
71. He R, Xu D, Cheng B et al (2018) Review on nanoscale Bi-based photocatalysts. Nanoscale Horizons 3:464–504. https://doi.org/10.1039/C8NH00062J
72. Su Q, Li Y, Hu R et al (2020) Heterojunction photocatalysts based on 2D materials: the role of configuration. Adv Sustain Syst 4:2000130. https://doi.org/10.1002/adsu.202000130
73. Low J, Yu J, Jaroniec M et al (2017) Heterojunction photocatalysts. Adv Mater 29:1601694. https://doi.org/10.1002/adma.201601694
74. Yaw CS, Ruan Q, Tang J et al (2019) A Type II n-n staggered orthorhombic V2O5/monoclinic clinobisvanite BiVO4 heterojunction photoanode for photoelectrochemical water oxidation: fabrication, characterisation and experimental validation. Chem Eng J 364:177–185. https://doi.org/10.1016/j.cej.2019.01.179
75. Mosleh S, Dashtian K, Ghaedi M, Amiri M (2019) A Bi2WO6/Ag2S/ZnS: Z-scheme heterojunction photocatalyst with enhanced visible-light photoactivity towards the degradation of multiple dye pollutants. RSC Adv 9:30100–30111. https://doi.org/10.1039/c9ra05372g
76. Meng S, Zhang J, Chen S et al (2019) Perspective on construction of heterojunction photocatalysts and the complete utilization of photogenerated charge carriers. Appl Surf Sci 476:982–992. https://doi.org/10.1016/j.apsusc.2019.01.246
77. Li X, Shen R, Ma S et al (2018) Graphene-based heterojunction photocatalysts. Appl Surf Sci 430:53–107. https://doi.org/10.1016/j.apsusc.2017.08.194
78. Ashouri R, Ghasemipoor P, Rasekh B et al (2019) The effect of ZnO-based carbonaceous materials for degradation of benzoic pollutants: a review. Int J Environ Sci Technol 16:1729–1740. https://doi.org/10.1007/s13762-018-2056-5
79. Raj AM, Balachandran M (2020) Coal-based fluorescent zero-dimensional carbon nanomaterials: a short review. Energy Fuels 34:13291–13306. https://doi.org/10.1021/acs.energyfuels.0c02619
80. Samadi M, Zirak M, Naseri A et al (2019) Design and tailoring of one-dimensional ZnO nanomaterials for photocatalytic degradation of organic dyes: a review. Res Chem Intermed 45:2197–2254. https://doi.org/10.1007/s11164-018-03729-5

81. Zhao Y, Zhang S, Shi R et al (2020) Two-dimensional photocatalyst design: a critical review of recent experimental and computational advances. Mater Today 34:78–91. https://doi.org/10.1016/j.mattod.2019.10.022
82. Jiang W, Zhu Y, Zhu G et al (2017) Three-dimensional photocatalysts with a network structure. J Mater Chem A 5:5661–5679. https://doi.org/10.1039/C7TA00398F
83. Hernández-Ramírez A, Medina-Ramírez I (2015) Photocatalytic semiconductors: synthesis, characterization, and environmental applications
84. Varshney G, Kanel SR, Kempisty DM et al (2016) Nanoscale TiO2 films and their application in remediation of organic pollutants. Coord Chem Rev 306:43–64. https://doi.org/10.1016/j.ccr.2015.06.011
85. Ge J, Zhang Y, Heo YJ, Park SJ (2019) Advanced design and synthesis of composite photocatalysts for the remediation of wastewater: a review
86. Tseng TK, Lin YS, Chen YJ, Chu H (2010) A review of photocatalysts prepared by sol-gel method for VOCs removal. Int J Mol Sci 11:2336–2361. https://doi.org/10.3390/ijms11062336
87. Li Puma G, Bono A, Krishnaiah D, Collin JG (2008) Preparation of titanium dioxide photocatalyst loaded onto activated carbon support using chemical vapor deposition: a review paper. J Hazard Mater 157:209–219. https://doi.org/10.1016/j.jhazmat.2008.01.040
88. Yang G, Park SJ (2019) Conventional and microwave hydrothermal synthesis and application of functional materials: a review. Materials (Basel) 12. https://doi.org/10.3390/ma12071177
89. Rahemi Ardekani S, Sabour Rouh Aghdam A, Nazari M et al (2019) A comprehensive review on ultrasonic spray pyrolysis technique: mechanism, main parameters and applications in condensed matter. J Anal Appl Pyrolysis 141:104631. https://doi.org/10.1016/j.jaap.2019.104631
90. Bogovic J, Rudolf R, Friedrich B (2016) The controlled single-step synthesis of Ag/TiO2 and Au/TiO2 by ultrasonic spray pyrolysis (USP). JOM 68:330–335. https://doi.org/10.1007/s11837-015-1417-5
91. Nagajyothi PC, Prabhakar Vattikuti SV, Devarayapalli KC et al (2020) Green synthesis: photocatalytic degradation of textile dyes using metal and metal oxide nanoparticles-latest trends and advancements. Crit Rev Environ Sci Technol 50:2617–2723. https://doi.org/10.1080/10643389.2019.1705103
92. Menon S, Rajeshkumar S, Kumar V (2017) A review on biogenic synthesis of gold nanoparticles, characterization, and its applications. Resour Technol 3:516–527. https://doi.org/10.1016/j.reffit.2017.08.002
93. Agarwal H, Venkat Kumar S, Rajeshkumar S (2017) A review on green synthesis of zinc oxide nanoparticles—an eco-friendly approach. Resour Technol 3:406–413. https://doi.org/10.1016/j.reffit.2017.03.002
94. Basnet P, Inakhunbi Chanu T, Samanta D, Chatterjee S (2018) A review on bio-synthesized zinc oxide nanoparticles using plant extracts as reductants and stabilizing agents. J Photochem Photobiol B Biol 183:201–221. https://doi.org/10.1016/j.jphotobiol.2018.04.036
95. Ahmed S, Annu, Chaudhry SA, Ikram S (2017) A review on biogenic synthesis of ZnO nanoparticles using plant extracts and microbes: a prospect towards green chemistry. J Photochem Photobiol B Biol 166:272–284. https://doi.org/10.1016/j.jphotobiol.2016.12.011
96. Mohd Yusof H, Mohamad R, Zaidan UH, Abdul Rahman NA (2019) Microbial synthesis of zinc oxide nanoparticles and their potential application as an antimicrobial agent and a feed supplement in animal industry: a review. J Anim Sci Biotechnol 10:57. https://doi.org/10.1186/s40104-019-0368-z

Part II
Nanomaterials and Nanocomposites

Chapter 4
Graphene-Based Nanocomposites for Photocatalytic Applications: Emphasis on Environmental Remediation

Hema Bhandari, Diwan S. Rawat, and Seema Garg

Abstract Graphene is one of the most promising and potential materials in the field of nanotechnology due to its high specific surface area, unique planar structure, better conductivity and extraordinary chemical stability. It is considered as an extremely potential material for development of various nanocomposites for enormous applications. The optical and electrical properties of graphene are enhanced by preparation of its composites with inorganic nanomaterials, polymers or using functionalized graphene such as graphene oxide and reduced graphene oxide. Superior and controllable optical properties of graphene-based nanocomposites make them excellent photocatalysts. Nanocomposites based on graphene exhibit suppressed electron–hole pair recombination rates and diminish energy gaps due to valence band-level and conduction band-level modifications, leading to the better adsorption of light radiation and enhancement in the photocatalytic performance of nanocomposites. This chapter will present an overview of state-of-the-art graphene as well as functionalized graphene-based nanocomposites and their photocatalytic activity for degradation of organic pollutants. In this chapter, various strategies will be demonstrated to synthesize graphene-based nanocomposites. The effect of various components such as inorganic nanoparticles, polymeric materials and graphene analogue on photocatalytic activity of nanocomposites will be reported. The goal of this study is to provide the latest and advance analysis in the area of developing nanotechnology for photocatalytic application.

H. Bhandari (✉)
Department of Chemistry, Maitreyi College, University of Delhi, Delhi 110021, India
e-mail: hbhandari@maitreyi.du.ac.in

D. S. Rawat
Department of Chemistry, University of Delhi, New Delhi 110007, India

S. Garg
Department of Applied Science, Amity University, Noida, Uttar Pradesh, India

S. Garg and A. Chandra (eds.), *Green Photocatalytic Semiconductors*,
Green Chemistry and Sustainable Technology,
https://doi.org/10.1007/978-3-030-77371-7_4

Keywords Graphene · Nanocomposites · Photocatalysts · Metal oxides · Conducting polymers · Biopolymers

4.1 Introduction

Carbon is the fourth most abundant element on the earth. The catenation behaviour of carbon allows it to develop a variety of allotropes having a wide range of dimensions such as zero-dimensional fullerenes, one-dimensional carbon nanotubes and three-dimensional graphite. Among the various existing allotropes of carbon, an attractive two-dimensional carbon allotrope, graphene is known as a sparkling rising star, especially, since the Nobel Prize for Physics in 2010. Considering its planar structure, graphene can also be arranged to form 3D graphite, turned to form one-dimensional carbon nanotube and enfolded up into zero-dimensional fullerenes with the introduction of pentagons. Therefore, graphene is known as the basic building block of all dimensional carbon allotropes. It has single-, bi-, or multi-layered of sp^2 hybridized carbon atoms settled in a six-membered ring. Graphene is the potential material in the field of nanotechnology as it has a unique band structure in which the conduction band and valence band just close each other, making an exactly zero bandgap semiconductor. It is a two-dimensional single sheet sp^2 hybridized of carbon atoms organized in a hexagonal close-packed honeycomb like a crystal lattice. Due to its large surface area, better conductivity, excellent charge carrier mobility, superior chemical stability, greater mechanical strength, thermal and optical properties of graphene, it is found to be a suitable candidate for the preparation nanocomposites for extensive range of applications in various areas such as in photonics supercapacitors [1], electronics [2] biosensing [3] solar cell [4, 5] and photocatalyst [6]. Graphene-based nanocomposites have been employed for a wide range of applications especially as a photocatalyst for environmental remediation over the past decade. The use of photocatalysts for the degradation of pollutants such as dyes, chemicals and toxic heavy metals has emerged as an effective method for wastewater treatment [7]. Use of photo catalysts based on graphene-based nanocomposites offers significant advantages. (i) Due to its unique 2D structure, graphene is used as the support to increase the specific surface area of the photocatalyst, (ii) incorporation of semiconductors in graphene matrix could enhance the performance of photocatalysts by increasing the charge separation and inhibit the recombination of photogenerated electron and hole pairs, (iii) the strong π–π interaction between graphene and organic molecules helps the absorption of organic molecules. Therefore, these significant features of graphene-based nanocomposites show that they can be used as a potential photocatalytic material for remediation of environmental pollution [8, 9].

Graphene derivatives such as graphene oxide (GO) and reduced graphene oxide (rGO) are semiconducting in nature, and they have the ability to degrade pollutants from wastewater photocatalytically. Moreover, graphene derivatives show narrow band gap and behave as charge transfer media. Therefore, when these derivatives are incorporated with inorganic materials such as metal/metal oxide nanoparticles, they can prevent agglomeration of nanoparticles by providing better dispersion within the composites and increase the photocatalytic efficiency of the material. Graphene oxide (GO) is one of the most extensively employed graphene precursors due to its 2D open pore structure and the presence of numerous oxygen-containing functional groups such as carboxyl, epoxy, carbonyl and hydroxyl. This property allows the development of highly compatible graphene-based nanocomposites with strong interactions between graphene and other material [10]. This chapter presents the recent advances in the synthesis of graphene-based nanocomposites and their photocatalytic applications.

4.2 Approaches for Synthesis of Graphene and Graphene Derivatives

Graphene can be synthesized from a variety of materials which includes hydrocarbon and other carbonaceous gases. Various methodological approaches have been developed over the years, and these methods are most commonly used for the synthesis of graphene such as chemical exfoliation of graphite [11], thermal decomposition epitaxial growth on electrically insulated surfaces [12], chemical vapour deposition method [13, 14], chemical methods [15] and microwave synthesis [16].

In the chemical exfoliation method, solution dispersed graphite is exfoliated by using large alkali ions between the graphite layers. The chemical vapour deposition method is also found to be the most remarkable method synthesis of graphene in large scale. Beside these methods, other methods have also been employed by several researchers; for example, Dato and co-workers [17] reported synthesis of graphene sheets using substrate-free gas phase method in which graphene sheets were synthesized by passing liquid ethanol droplets into an argon plasma. Kosynkin et al. reported [18] synthesis of graphene nanoribbons by unzipping of carbon nanotubes.

Similarly, there are various methods available for the synthesis of derivatives of graphene (i.e. graphene oxide and reduced graphene oxide). The known methods for synthesis of graphene oxide were proposed by Brodie [19] and Staudenmaier [20] which involves the use of strong acids such as nitric or sulphuric acid and potassium chlorate. While the well-known Hummers method involves a mixture of concentrated H_2SO_4, $NaNO_3$ and $KMnO_4$, in which, high yield of product was achieved in a short duration of time [21]. Figure 4.1 shows the structure of graphene oxide and reduced graphene oxide and their synthesis. The modern developments for synthesis of GO are based on Hummers oxidation and exfoliation of graphite [22]. One of the most developed techniques to obtain graphene oxide with greater yields is single-layer powder following a modified Hummer's method [23–25] which involve the initial oxidation of graphite to water-dispersible graphite

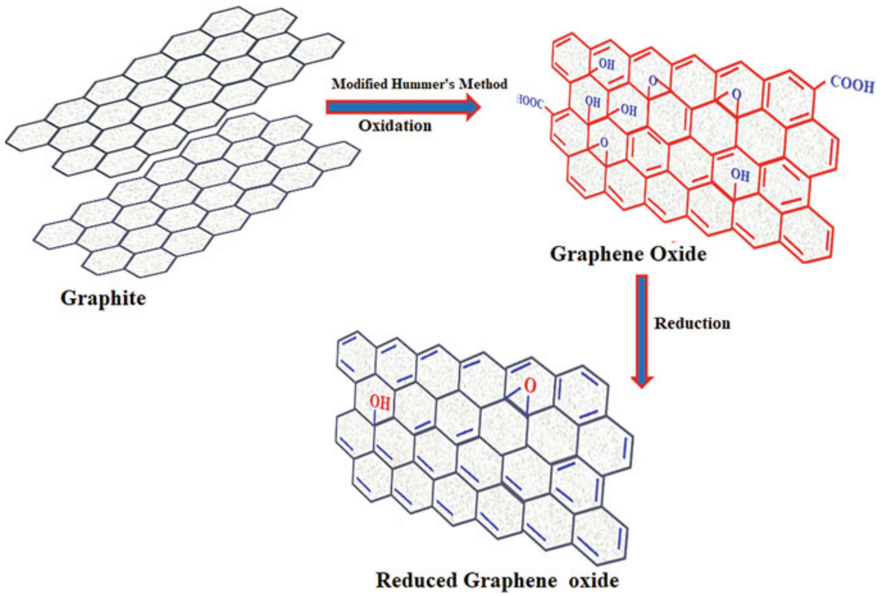

Fig. 4.1 Illustration of the structure of graphene oxide and reduced graphene oxide and their synthesis

oxide, which results in enhancement in the interlayer spacing between the oxygen-containing graphene layers.

The hydrophilic properties of graphene oxide sheets are greater due to the presence of oxygen-containing functional groups in it and render them prone to swelling quickly and therefore easy to be dispersed in water. This process must be followed by mechanical or chemical exfoliation of graphite oxide to graphene oxide sheets and the final reduction to graphene. Furthermore, the reduction of graphite oxide by thermal or chemical method leads to the formation of reduced graphene oxide. Singh et al. [26] demonstrated the detailed review of known methods of synthesis of graphene oxide by oxidation of graphite. The synthesis of graphene and graphene nanostructure in good yield was carried out by chemical exfoliation of graphite; this method is more fruitful and favourable than the other methods. In another work, Alkhouzaam and co-workers [27] also developed modified Hummers method to prepare graphene oxide particles with high oxidation degree. Similarly, Alam et al. [28] demonstrated the preparation of graphene oxide by modified Hummers method, where the concentration of $NaNO_3$ had been reduced and the concentration of oxidizing agents such as $KMnO_4$ was increased. The reaction was carried out in a 9:1 (by volume) mixture of H_2SO_4/H_3PO_4. That modification was carried out to achieve high yield and minimize the evolution of the toxic gas while using a varied proportion of $KMnO_4$ and H_2SO_4 as those required by Hummers method. In order to maintain the pH of the solution, the authors introduced $K_2S_2O_8$

to the reaction system. Reduced graphene oxide (rGO) was thereafter extracted by thermal modification of GO.

4.3 Approaches for the Synthesis of Graphene-Based Nanocomposites

A variety of nanoparticles have been used for the synthesis of graphene and functional graphene oxide-based nanocomposites. They mainly include metal oxides (i.e. TiO_2, ZnO, Cu_2O, Fe_2O_3 and SiO_2, V_2O_5), metal sulphides (e.g. CdS), metal oxyhalide (BiOI) and polymers (insulating polymers, biopolymers and conducting polymers). The widely used preparation methods are in situ growth [29], microwave-assisted method, [30] sol–gel technique [31–33], electrochemical deposition [34] and hydrothermal and/or solvothermal method [35].

Table 4.1 shows the synthesis method of graphene-based nanocomposites for photocatalytic application. The following paragraphs deal with a more detailed illustration of the widely used synthesis methods for the fabrication of graphene-based nanocomposites that have been performed by many researchers.

4.3.1 In Situ Growth Approach

In situ growth method is a conventional route for the preparation of GO-based metal oxide nanocomposite on a higher scale. A variety of graphene-based metal oxide nanocomposites have been prepared using these methods. The most common precursors of graphene and metal compounds are functional graphene oxide and metal salts, respectively. In this method, the salt is mixed with GO and then converted to the corresponding oxide leading to the formation of graphene oxide/metal oxide composite. After reduction of GO, graphene-based metal composites were obtained. The presence of oxygen-containing functional groups on graphene can act as the heterogeneous nucleation sites and anchor metal oxide nanoparticles [36]. In in situ growth approach, a definite weight % of GO is dissolved in ethanol and then mixed with metal salt under continuous magnetic stirring. This solution is then sonicated for proper mixing at ambient temperature for about 20–24 h to make complete reduction of the precursors. In situ method has been widely employed for preparation of ZnO/graphene nanocomposites-based photocatalytic [37–39]. Similarly, Lambert et al. [40] also described the in situ synthesis of graphene oxide/TiO_2 nanocomposites by the hydrolysis of TiF_4 in the presence of aqueous dispersions of GO. Similarly, in situ deposition method was also employed by He and co-workers [41] to carry out the coating of graphene foam with BiOI. For the preparation of GOF–BiOI nanocomposite, Bi^{3+} ions were first deposited on the surface of the graphene oxide foam under electrostatic attraction, and they then

Table 4.1 Some reported photocatalysts based on graphene/inorganic nanocomposites

Photocatalyst (nanocomposites)	Preparation method	Photocatalytic application	References
ZnO/graphene oxide	Solvothermal method	Photodegradation of methylene blue (MB)	[47]
GO-$BiPO_4$	Self-assembly	Photodegradation of MB	[49]
SiO_2/Cu_2O/graphene	Self-assembly method	Photodegradation of MB, rhodamine B (RhB), reactive black B (RBB)	[50]
Graphene-Ag	Electrochemical synthesis	Photodegradation of MB and Congo red (CR)	[64]
GO foam-supported BiOI	In situ deposition approach	Phenol removal	[41]
Graphene-TiO_2 nanorod hybrid composite	One-step in situ synthesis	Photodegradation of MB	[114]
rGO/ZnO	One-pot hydrothermal synthesis	Photodegradation of MB	[115]
Graphene oxide/ZnO	Two-step sol–gel deposition method	Degradation of basic fuchsin (BF) dye	[116]
rGO/ZnO	Hydrothermal methods	Photodegradation azure B dye	[117]
GO-ZnO	One-pot sol–gel synthesis	Photodegradation of MB	[118]
Graphene oxide Fe_2O_3	In situ method	Photodegradation of RhB and 4-nitrophenol	[119]
Fe_2O_3/reduced graphene oxide	Hydrothermal method	Photodegradation Rh B	[120]
rGO-V_2O_5	Hydrothermal method	Photodegradation of MB	[121]
rGO-TiO_2	Ex situ synthesis methods	Photodegradation of antibiotics antibiotic-resistant bacteria and their associated genes	[74]
rGO/CdS-TiO_2 nanocomposite	Modified hydrothermal method	Photocatalytic degradation of RhB, crystal violet dyes	[83]
TiO_2/Ag/rGO nanocomposite	Hydrothermal methods	Photodegradation of MB	[81]
Fe_2O_3/graphene/CuO	Solvothermal method	Photodegradation of MB	[77]
Nitrogen-doped graphene ZnO/$CoFe_2O_4$	Hydrothermal method	Photodegradation of methyl orange (MO) and malachite green (MG)	[80]
Ag_2S-MgO/GO	Sol–gel method	Photodegradation of RhB	[85]

(continued)

Table 4.1 (continued)

Photocatalyst (nanocomposites)	Preparation method	Photocatalytic application	References
rGO-ZnO/ $ZnFe_2O_4$	Co-precipitation-calcination process	Photodegradation of tetracycline	[79]
Z-scheme CdS/ rGO/BiOI	In situ synthesis method	Photodegradation of chlorinated paraben	[122]
Au/PdO-rGO	Sonochemical and deposition–precipitation	Photodegradation of tetrodotoxin	[123]

grew into nanoplates in situ. To achieve the in situ growth of bismuth oxy iodide, the concentration of Bi^{3+}, I^{-} and graphene was quite adjusted which leads to the uniform distribution of small plates of BiOI on the graphene oxide foams.

In another work, Sang et al. [42] demonstrated facile method for the synthesis of rGO/TiO_2 nanocomposites by assembling of graphene oxide (GO) on the surface of TiO_2 nanobelt followed by an in situ photocatalytic reduction using water–ethanol solvent mixtures. GO nanosheets are tightly wrapped around the surface of the TiO_2 nanobelts through an aggregation process and are then reduced in situ under UV light irradiation to form rGO/TiO_2 nanobelt surface heterostructures. Therefore, in situ approach is the most wide and convenient method for preparation of graphene-based photocatalysts at greater yield.

4.3.2 Sol–Gel Method

Sol–gel method is a wet chemical technique mostly used in the synthesis of graphene-based semiconductor nanocomposites. It is based on the phase transformation of a sol obtained from organometallic or metallic alkoxides precursors. For example, in order to prepare TiO_2/graphene nanocomposites, tetrabutyl titanate was dispersed in graphene-containing absolute ethanol solution which gradually formed a sol with continuous stirring, which after drying and post-heat treatment changed into TiO_2/graphene nanocomposites. Wojtoniszak et al. [43] and Zhang et al. [44] used a similar strategy to prepare the TiO_2/graphene nanocomposite via the hydrolysis of titanium(IV) butoxide in GO-containing ethanol solution.

4.3.3 Hydrothermal/Solvothermal Method

The hydrothermal/solvothermal technique is a unique method for the development of graphene-based photocatalysts. This method is a very low-cost method that is facile, environmental friendly which involves the incorporation of inorganic nanoparticles on the graphene oxide sheets, where GO is reduced to graphene simultaneously with or without reducing agents. This method involves synthesis of composites generally in an autoclave under high temperatures and pressures. Aqueous solution is used in hydrothermal method while in non-aqueous solution is used in solvothermal method.

Shi et al. introduced [45] hydrothermal method for the synthesis of graphene-TiO_2 nanocomposites. The schematic diagram for formation of rGO/TiO_2 nanocomposites using hydrothermal method is shown in Fig. 4.2a; in this method, reduction of graphene oxide to reduced graphene oxide was carried out using dextran as reducing agent and surface modifier. Then the TiO_2 nanoparticles were successfully prepared from a water soluble precursor, peroxotitanium acid and attached to reduced graphene oxide/dextran matrix due to hydrogen bond and van der Waals interactions. Recently, Liu et al. [46] demonstrated the hydrothermal method for preparation TiO_2 nanorods inserted graphene oxide-based photocatalysts. The synthesized nanocomposites showed remarkable photodegradation ability especially for dyes such as methylene blue, rhodamine B, methylorange and Congo red.

In another work, Atchudan and co-workers [47] prepared ZnO/graphene oxide nanocomposites by simple solvothermal process as shown in Fig. 4.2b.

Similarly, Moussa and co-workers [48] synthesized reduced graphene oxide/ZnO nanocomposites using solvothermal method. This method was also found to be a cost-effective and facile method for the preparation of graphene-based metal oxide nanocomposites.

4.3.4 Self-assembly Method

Lv and co-workers [49] demonstrated the synthesis of photocatalyst based on graphene oxide/$BiPO_4$ nanocomposites using two-phase self-assembly method. In this method, the pre-synthesized toluene solution of oleylamine-capped $BiPO_4$ nanocrystals (OM-$BiPO_4$ NCs) was mixed with aqueous solution of GO and stirred for 12 h. The self-assembly of OM-$BiPO_4$ NCs on the GO nanosheets occurs at the water/toluene interface. The removal of the oleylamine molecules from $BiPO_4$ to the surface of OM-GO-$BiPO_4$ nanocomposites was carried out by acetic acid so as to make the GO-$BiPO_4$ nanocomposite readily dispersed in water for practical photocatalytic application.

Nguyen et al. [50] demonstrated the synthesis of mesoporous SiO_2/Cu_2O-graphene nanocomposites using self-assembly method. Schematic diagram in Fig. 4.3 exhibits the procedure for synthesis of SiO_2/Cu_2O/graphene nanocomposite using self-assembly method. In this method, the mixture of Cu_2O, cetyltrimethylammonium bromide (CTAB) and tetraethyl orthosilicate (TEOS) was sonicated and stirred for about 6–7 h. The pH value of the solution was adjusted with the addition of NH_4OH until reaching pH 9.5–10. SiO_2/Cu_2O-graphene dispersion was transferred to an autoclave for a hydrothermal reaction at 100 °C for

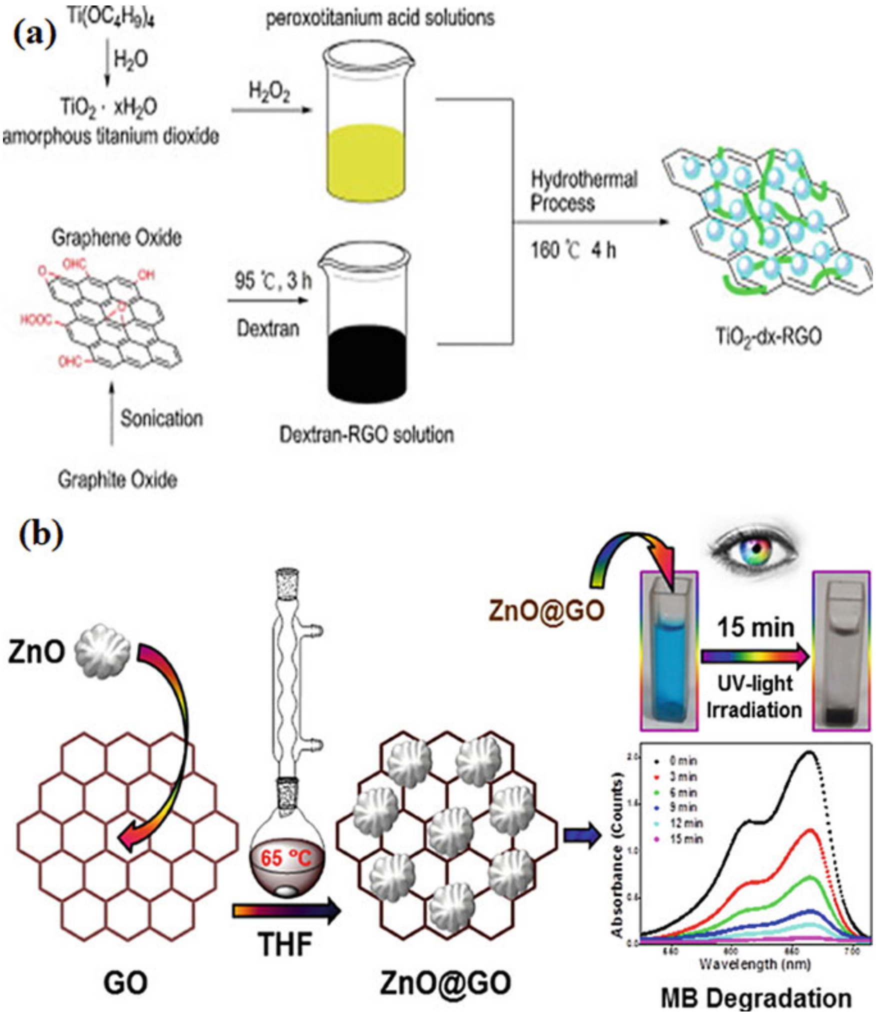

Fig. 4.2 Illustration of the **a** hydrothermal (Shi et al. [45]) and **b** solvothermal synthesis for the synthesis of rGO/TiO_2 and GO/ZnO nanocomposites. Reprinted with permission from Ref. [47]

24 h, the mixture was filtered and washed with distilled water and 95% ethanol twice followed by calcined at 550–550 °C for 8 h. The authors suggested that the mesoporous structure of the silica nanoparticles plays a major role in increasing the photodegradation effect as well as the surface of the graphene sheets.

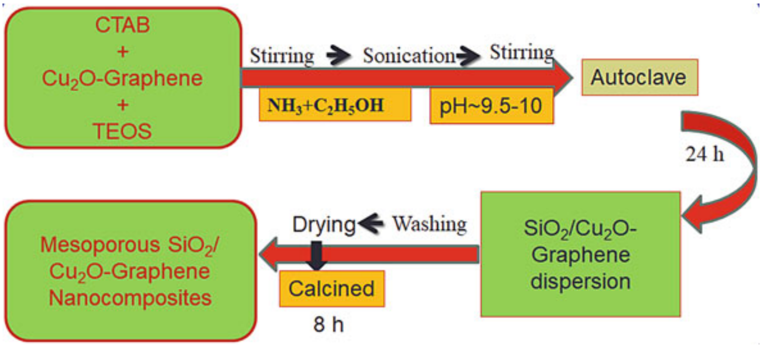

Fig. 4.3 Schematic diagram for the preparation of SiO_2/Cu_2O/graphene nanocomposite. Adapted with permission from Ref. [50]

4.3.5 *In Situ Polymerization*

In situ polymerization method is used for the preparation of GO-based polymer nanocomposite on a larger scale. This method has been employed to develop polymers such as polyaniline, polypyrrole and polymethyl methacrylate in situ on a graphene oxide matrix. For example, in order to synthesize graphene-based polyaniline, aniline is used as a precursor, which is then immersed in the mixture of dopant (HCl solution) and graphene solution. The polymerization is carried with the addition of oxidant (ammonium persulfate). Ameen et al. [51] synthesized polyaniline/graphene nanocomposites using in situ oxidative polymerization. Similar method has been used by Mitra et al. [52] for the synthesis of reduced graphene oxide/polyaniline nanocomposites for photodegradation of organic dyes. Similarly, graphene-based nanocomposites can also be prepared using other polymers by in situ oxidative polymerization [53]. Therefore, in order to incorporate inorganic nanoparticles in graphene-polymer matrix, in situ oxidative polymerization was found to be a more facile, controllable and scalable method [54].

4.4 Graphene-Based Inorganic Nanocomposite

The textile and printing industries consume a large quantity of toxic organic dyes that are settled into the waters. The organic dyes, which remain in the effluents and cannot be degraded by ordinary wastewater treatment methods. Persistence of the health hazardous organic dyes in the water system leads to severe environmental pollution and risk to living organisms. There are various techniques available for decontamination of wastewater which include coagulation, precipitation, advanced oxidation, adsorption, membrane filtration and photocatalytic processes, etc. Among these techniques, photocatalysis is one of the most efficient methods for wastewater treatment. This method effectively degrades organic or inorganic pollutants using low-cost photocatalytic materials that can be modified to utilize inexhaustible solar light to further increase the degradation process.

Therefore, water treatments by using graphene-based inorganic nanocomposites in the photocatalytic degradation of dyes such as methylene blue (MB), malachite green (MG), methyl orange (MO) rhodamine B (RhB), rhodamine 6G (Rh6G), reactive black 5 (RB5), Congo red (CR) became very important due to the danger of dyes as environmental pollutants [55, 56]. There are various metal oxides such as ZnO [57], Fe_2O_3 [58], TiO_2 [59], WO_3 [60] and V_2O_5 [61] have been explored as heterogeneous photocatalysts in the last three decades. These photocatalysts showed some unique properties such as large specific surface area and greater numbers of active surface sites which favour the absorption of pollutants and facilitate photogenerated charge carriers to react with pollutants. Under the influence of photo-irradiation, these nanomaterials generate photogenerated charge carriers such as electrons (e^-) and hole pairs (h^+), which are responsible for the reduction and oxidation of decontaminants on their surfaces. These charge carriers combined with oxygen or water molecules present on the surfaces of the photocatalysts to produce reactive oxygen species, and these species further link with organic molecules and change them to CO_2 and H_2O as a result of photocatalytic degradation [62]. However, these inorganic nanomaterials are not so efficient for photocatalytic degradation of organic pollutants as these photocatalysts are not ideal when they are used alone. This is due to the rapid recombination of photogenerated electrons and holes, which leads to their consumption. Various graphene-based photocatalyst materials have been incorporated to improve their photodegradation performance. Graphene-based inorganic nanocomposites were found to be potential materials for photocatalytic degradation of organic pollutants. The pollutants such as organic dyes, heavy metals and pathogenic microorganism can efficiently be degraded or inactivated by using these nanocomposites. The interaction of graphene or graphene derivatives with inorganic nanomaterials such as metal and metal oxide nanoparticles can improve the photodegradation efficiency of nanocomposites towards various pollutants which enhance the surface area of graphene and reduce the electron–hole pair recombination, hence improving the photocatalytic activity of the semiconductor due to the synergistic effect between the graphene and inorganic nanoparticles.

Recently, Chandu and co-workers [63] reported in situ synthesis of reduced graphene oxide sheets decorated with silver nanoparticles using custard apple leaf extract as an effective reducing and stabilizing agent which showed remarkable photocatalytic performance up to 96% for methylene blue in 2 h under sunlight. In another work, Khan et al. [64] also investigated the photocatalytic performance graphene-Ag nanocomposites. The authors reported that the organic dyes such as methylene blue and Congo red could remarkably be degraded using this nanocomposite under visible light irradiation. The authors investigated that the hydrophilic nature of Ag nanoparticles is helpful in enhancement of photocatalytic performance of graphene. Recently, Yaqoob and co-workers [65] reviewed graphene oxide-based ZnO photocatalyst for dye photo-oxidation. The authors suggested that GO/ZnO nanocomposites can support the charge separation, light absorption, charge transportation and photo-oxidation performance of dyes. Raizada et al. [66] reviewed graphene-based ZnO composites photocatalyst for wastewater treatment, and Posa et al. [67] demonstrated photocatalytic performance of graphene/ZnO nanocomposites for degradation of methyl orange dye. The authors investigated that the photocatalytic performance of ZnO nanoparticles was enhanced by incorporation of GO. This was attributed to the enhanced visible light absorption and decreased electron–hole pair recombination with the incorporation of GO with ZnO. Therefore, a number of studies have been carried out to demonstrate photocatalytic degradation of organic dyes from wastewater using graphene-based ZnO nanocomposites [68–70]. Furthermore, GO-based ZnO nanocomposites were also reported by Wu and co-workers [71] for the photocatalytic inactivation of bacteria such as *Escherichia coli* K-12. The authors demonstrated that GO-ZnO composite had excellent VLD photocatalytic bacterial inactivation activity, which was attributed to the strong interaction of ZnO nanoparticles in GO matrix. The authors described that GO acts as a photosensitizer and facilitated the charge separation and transfer, thus boosted the massive production of reactive oxygen species which was identified as the major reactive species from the conduction band of ZnO and resulted in a significant improvement in bacterial inactivation efficiency.

Similarly, TiO_2 was also found to be one of the most widely used photocatalysts for environmental remediation due to its band gap of 3.2 eV, and it is usually active under UV light irradiation. Graphene-based TiO_2 nanocomposites have widely been reported by many researchers [55, 72–74] for photocatalytic degradation of synthetic dyes.

Gu et al. [72] demonstrated the photodegradation activity of methylene blue using reduced graphene//TiO_2 nanocomposite. Figure 4.4 shows the proposed photocatalytic mechanism of rGO/TiO_2 nanocomposite during a UV light irradiation. The authors investigated that the photocatalytic activity of TiO_2 nanoparticles was enhanced by incorporation of graphene oxide. Similarly, photocatalysts based on graphene-TiO_2 nanocomposites have also been employed by Karaolia et al. [74] for removal of antibiotics, antibiotic-resistant bacteria and their associated genes. Zhang and co-workers [55] evaluated the photocatalytic performance of rGO-SnO_2 and rGO-TiO_2 composites for degrading rhodamine B under visible light irradiation. The rGO-SnO_2 composite showed a better photocatalytic activity than rGO-TiO_2. The authors concluded that the excellent photocatalytic performance of the composite materials was associated with the good electrical conductivity and effective charge separation because of the presence of rGO.

Recently, He et al. [41] demonstrated the synthesis of graphene oxide foam coated with bismuth oxyiodide (GOF-BiOI) which exhibited a higher photocatalytic activity than BiOI and GO-modified BiOI for the oxidation of phenol under visible light. The remarkable photocatalytic activity of GOF-BiOI was due to the electron trapping role of graphene oxide foam, which effectively suppress charge recombination.

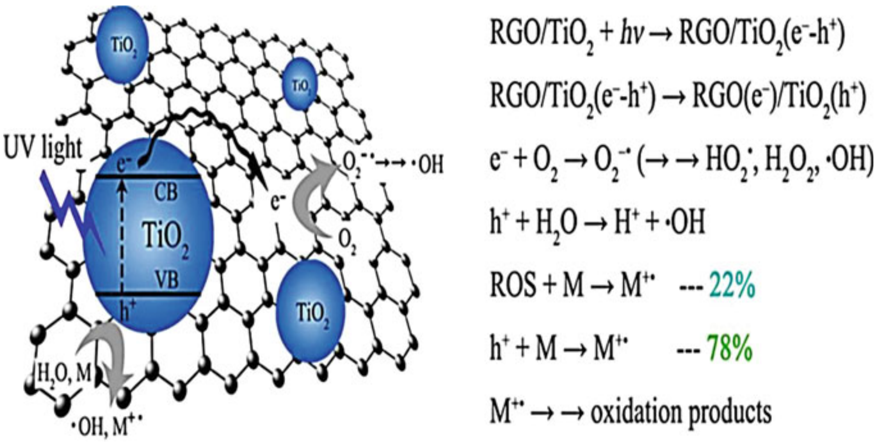

Fig. 4.4 Proposed photocatalytic mechanism of the reduced graphene//TiO_2 nanocomposite on UV light irradiation. Adapted with permission from Ref. [72]

Teo et al. [75] introduced iron oxide nanoparticles in reduced graphene oxide sheets to develop magnetically separable and reusable rGO/Fe_3O_4 nanocomposites. The synthesized rGO/Fe_3O_4 nanocomposite was found to be super-paramagnetic in nature at room temperature which exhibited better adsorption properties and remarkable photocatalytic activity towards the degradation of methylene blue as compared to rGO and pristine Fe_2O_3. Furthermore, rGO/Fe_3O_4 exhibited good sustainability even after eight cycles of methylene blue photodegradation as shown in Fig. 4.5; hence, the remarkable photocatalytic activity could be attributed to the synergistic effect that arises between the rGO and Fe_3O_4 which significantly reduces the charge recombination. Moreover, the magnetically separable rGO/Fe_3O_4 could be reused for several photodegradation experiment cycles to elucidate their sustainability.

Moreover, some researchers have developed graphene-based mixed metal oxides hybrid nanocomposite for photocatalytic degradation of organic pollutants. For example, Benjwal and co-workers [76] reported the synthesis of reduced graphene oxide (rGO) metal oxide-based binary (rGO-TiO_2/rGO-Fe_3O_4) and ternary (rGO-Fe_3O_4-TiO_2) nanocomposites by one-step solvothermal process. Those nanocomposites had been used to photocatalytic degradation of methylene blue and adsorption of arsenic. It was found that the ternary (rGO-Fe_3O_4-TiO_2) nanocomposite revealed the highest dye degradation efficiency ($\sim$100% within 5 min). As compared to binary nanocomposite, this is due to the synergetic effect of graphene and metal oxide nanoparticles which enhanced the surface area of rGO-Fe_3O_4-TiO_2 nanocomposites.

Similarly, Nuengmatcha et al. [77] demonstrated the photocatalytic property of graphene-based mixed metal oxides hybrid nanocomposite, i.e. Fe_2O_3/graphene/CuO nanocomposites, which not only exhibited an excellent photocatalytic

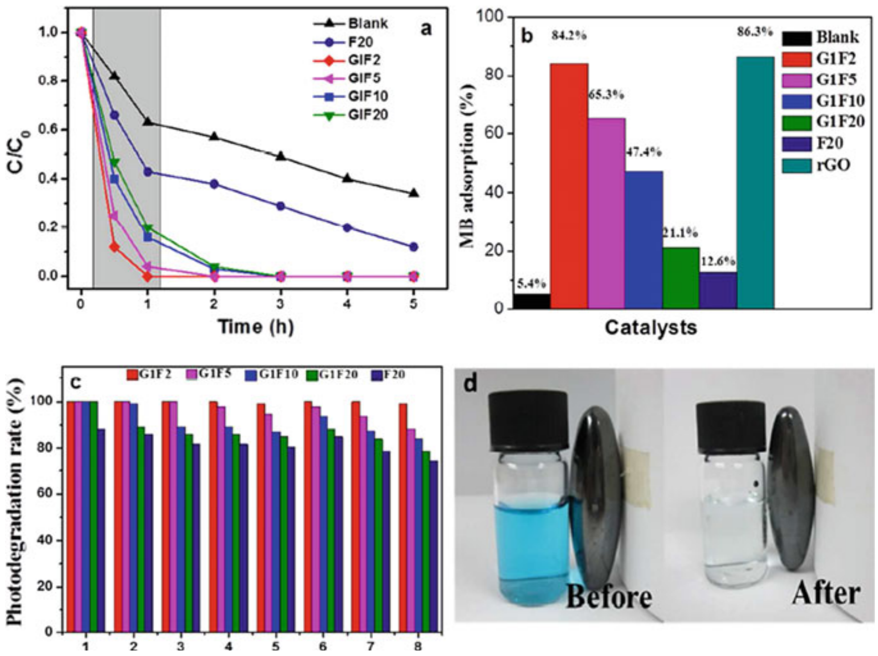

Fig. 4.5 **a** Photocatalytic degradation of methylene blue using different photocatalysts nanocomposite under sunlight irradiation, **b** adsorption of MB by different catalysts after 12 h stirring, **c** photodegradation efficiency (%) of MB solution for eight cycles in the presence of rGO/Fe_3O_4 nanocomposites and Fe_3O_4 and (**d**). Photographic images showing methylene blue before and after degradation by rGO/Fe_3O_4 and recovery by applying an external magnet G1F2, G1F5, G1F10, G1F20 and F20 indicate weight ratio of GO: $FeSO_4$ were 1:2, 1:5, 1:10, 1:20 and 500 mg $FeSO_4$, respectively, for the preparation of rGO/Fe_2O_3 nanocomposites. Reprinted with permission from Ref. [75]

property for degradation of methylene blue under visible light but also showed high stability and recyclability.

Recently, Zhang and co-workers [78] developed the water-dispersible ZnO/$C_OFe_2O_4$/graphene nanocomposites photocatalyst for the organic dye degradation. The results showed that the nanocomposites had good water dispersibility, convenient magnetic separation and high photocatalytic activity. Similarly, Wei et al. [79] synthesized reduced graphene-based ZnFe mixed metal oxide (rGO-ZnO/$ZnFe_2O_4$) using co-precipitation–calcination process. The nanocomposite exhibited higher photocatalytic performance and stability for the degradation of tetracycline (100% photodegradation in 120 min.) under visible light irradiation. Moreover, the photocatalyst could easily be separated from reaction mixture by applying an external magnetic field.

In another work, Chandel et al. [80] developed nitrogen doped graphene-based ZnO/$ZnFe_2O_4$ (ZnO/ZF/NG) and ZnO/$CoFe_2O_4$ (ZnO/CF/NG) photocatalysts for degradation of toxic dyes such as methyl orange (MO) and malachite green (MG).

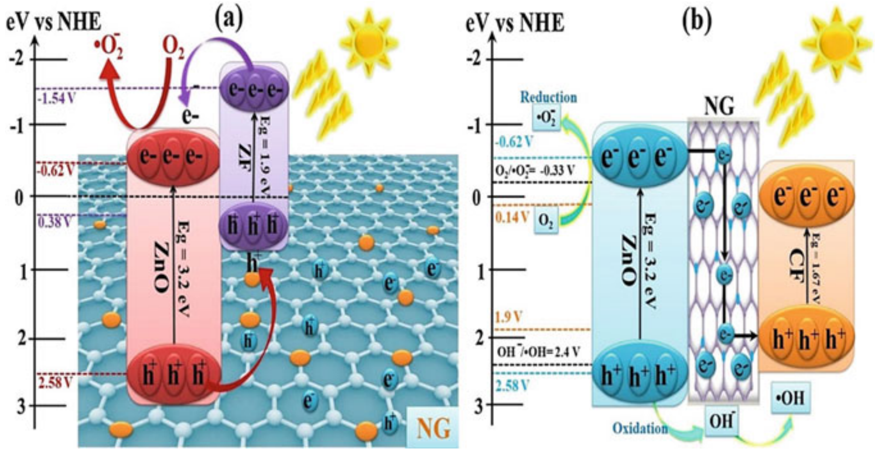

Fig. 4.6 Proposed mechanistism of photocatalytic degradation of pollutants using **a** ZnO/ZF/NG and **b** ZnO/CF/NG nanocomposites [80]. Adapted with permission from Ref. [80]

The materials showed superior photocatalytic performance and recyclability. The authors proposed the mechanistic view of photocatalytic degradation of pollutants using ZnO/ZF/NG and ZnO/CF/NG nanocomposites as represented in Fig. 4.6.

Under visible light irradiation, mixed metal oxide ($ZnFe_2O_4$) becomes excited which leads to generation of electrons and holes, while another metal oxide such as ZnO cannot be excited due to the wide band gap. Hence, part of the photogenerated electrons in the conduction band of mixed metal oxide ($ZnFe_2O_4$) transfer to the conduction band of ZnO since the conduction band potential of $ZnFe_2O_4$ (−1.54 eV) is more negative than that of ZnO (−0.31 eV). The other part of the photogenerated electrons quickly transfers to the surface of rGO due to the ultra-high electron mobility that rGO has, and this process significantly inhibits the rapid recombination of photogenerated electrons and holes in $ZnFe_2O_4$. Hence, ternary nanocomposites based on ZnO/ZF/NG and ZnO/CF/NG showed higher photocatalytic performance for degradation of toxic dyes by generating reactive species such as electrons, holes, hydroxyl radicals and superoxides as indicated in Fig. 4.6.

Vasilaki et al. [81] demonstrated another ternary nanocomposites based on silver nanoparticles (Ag) loaded TiO_2/reduced graphene oxide. The photocatalytic performance of the hybrid nanocomposite was evaluated for removal of methylene blue dye under visible light irradiation. The results showed that TiO_2/Ag/rGO nanocomposite showed complete decolourization of dye; hence, it presented remarkably increased photocatalytic activity as compared to the TiO_2/Ag, TiO_2/rGO composites and bare TiO_2. Therefore, reduced graphene oxide had enhanced the overall photocatalytic activity of metal/metal oxide nanoparticles towards visible light [82].

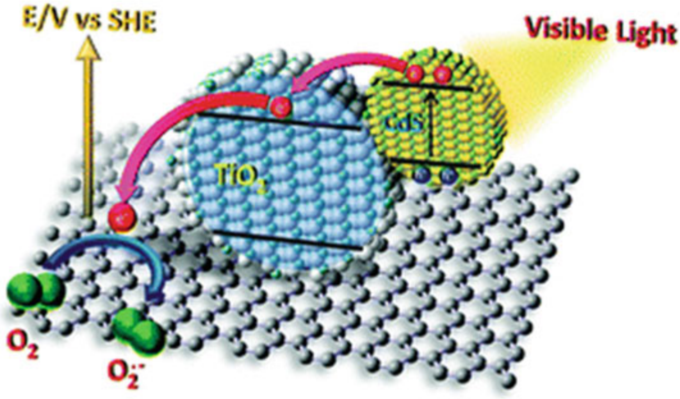

Fig. 4.7 Schematic diagram showing photocatalytic activity of ternary nanocomposite based on rGO/CdS-TiO_2 photocatalyst. Reprinted with permission from Ref. [83]

Dutta and co-workers [83] developed a ternary nanocomposite based on rGO/CdS-TiO_2 photocatalyst, in which TiO_2 presents at the interface of rGO and CdS in the composite and thus creates a barrier that impedes the direct interaction between rGO and CdS. This leads to a relatively higher bandgap value for CdS in nanocomposite, hence shows better photocatalytic activity by suppressing charge recombination process. Moreover, rGO in the nanocomposite also supports rapid dye degradation through higher dye adsorption and rapid internal electron transfer (CdS → TiO_2 → rGO) in the nanocomposite matrix as indicated by the schematic diagram in Fig. 4.7.

Beside TiO_2 and ZnO nanomaterials, some other metal oxides such as CuO have also been incorporated with graphene matrix for photocatalytic applications. Gusain et al. [84] demonstrated the use of rGO-CuO nanocomposites for photocatalytic conversion of CO_2 into methanol under visible light irradiation. The improved photocatalytic activity of CuO in rGO-CuO nanocomposites was due to the slow recombination of charge carriers and efficient charge transfer of photogenerated electrons through the rGO sheet.

Recently, Wang et al. [85] developed a ternary photocatalyst based on Ag_2S-MgO/GO nanocomposites using the sol–gel method. The synthesized nanocomposites exhibited excellent photocatalytic activity for rhodamine B decontamination.

Similarly, Nguyen et al. [50] investigated the photocatalytic activity of mesoporous SiO_2/Cu_2O-graphene nanocomposite which exhibited a remarkable photocatalytic degradation of organic dyes such as methylene blue, rhodamine B and reactive black B. Moreover, the results showed that the mesoporous SiO_2/Cu_2O-graphene composite was much more effective photocatalyst. The mesoporous SiO_2/Cu_2O-graphene nanocomposite showed the significantly greater photodegradation value of around 89.27% for rhodamine B, 68.62% for methylene blue and 84.07% for reactive black B as compared to Cu_2O-graphene, Cu_2O-graphene-TiO_2

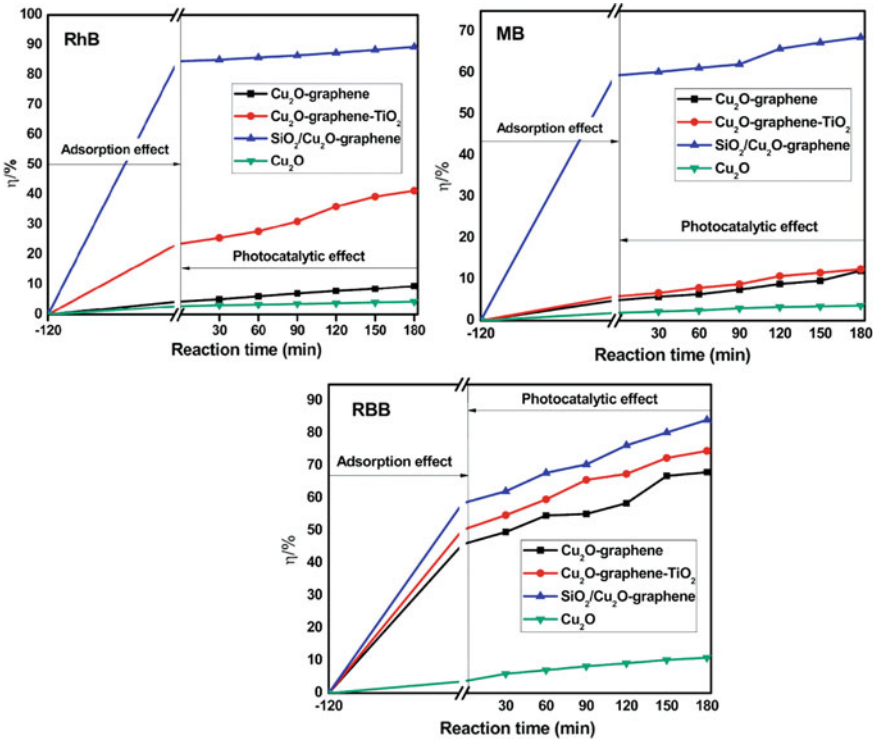

Fig. 4.8 Degradation efficiency of different composites (0.05 g weight) with various dyes (MB, RBh and RBB concentration 200 ppm) under visible light. Adapted with permission from Ref. [50]

composites and bare Cu_2O nanoparticles under the same experimental condition as shown in Fig. 4.8.

The authors also suggested that the photocatalytic degradation performance of the mesoporous SiO_2/Cu_2O-graphene composite was influenced by two factors: the adsorption capacity due to the mesoporous structure and the decomposition effect through catalysis. The valence band of the SiO_2 is higher than that of Cu_2O. Therefore, the photogenerated electrons of SiO_2 transfer to the valence band of Cu_2O and then shift to the graphene surface to join the reduction reaction. Simultaneously, the photogenerated holes of Cu_2O also transfer to the graphene surface to participate in oxidation reactions, and this whole process leads to the suppression of electron–hole recombination and enhancement of photocatalytic degradation.

4.5 Graphene-Based Polymer Nanocomposites

The design of graphene-based polymer nanomaterials for photocatalytic applications is one of the most promising routes in the field of wastewater treatment technology. The combination of graphene or functionalized graphene with polymeric materials leads to the formation of highly durable and stable composite for practical applications. Development of graphene-based polymer nanocomposites has been the topic of increasing interest in both academic and industrial point of view due to their multifunctional applications in different fields. Polymer nanocomposites based on graphene and graphene analogue such as graphene oxide and reduced graphene oxide have been used to enhance the mechanical and chemical properties of polymers. A variety of polymers such as poly(vinyl alcohol) [86], polystyrene [87], unsaturated polyester [88], etc., have been successfully used to develop nanocomposites with graphene or graphene analogue for various practical applications. The following paragraphs deal with a more detailed illustration of the widely used graphene nanocomposites based on variety of polymers such as insulating polymers, biopolymers and conducting polymers that have been developed by many researchers for photocatalytic application for environmental remediation.

4.5.1 Graphene-Based Insulating Polymers Nanocomposite

The development of graphene-based insulating polymer nanocomposites for photocatalytic applications has been found to be one of the most promising routes in the field of environmental remediation. Incorporation of photoactive polymers in graphene matrix can strongly improve the photocatalytic performance of nanocomposite by enhancing the separation and transfer of photogenerated charges. Ussia et al. [89] developed a hybrid nanocomposite based on graphene and photoactive polyporphyrins polymer, which was found to be highly efficient polymer-based nanocomposites for degradation of methylene blue under visible light irradiation.

Recently, Hussien et al. [90] developed graphene-filled polymethyl methacrylate (PMMA) nanocomposites using facile casting method, and the results showed that the nanocomposites based on graphene-PMMA exhibited the most effective activity in amoxicillin photodegradation under visible radiation at 30 min due to decrease in electron–hole recombination. Table 4.2 reveals some reported graphene-based insulating polymer nanocomposites for photocatalytic application.

Recently, Sundaran and co-workers [91] reported a reduced graphene oxide-titanium dioxide (rGO-TiO_2) loaded polyurethane (PU) nanofibrous membrane for photocatalytic templates in water purification. The authors demonstrated that the thermal and mechanical properties of the polyurethane membrane were enhanced by incorporation of rGO-TiO_2 nanocomposites. Moreover, the photocatalytic activity of polyurethane membrane was found to increase with an increase

Table 4.2 Some reported graphene-based insulating polymer nanocomposites for photocatalytic application

Photocatalyst (nanocomposites)	Preparation methods	Photocatalytic application	References
Graphene-PMMA	Casting method	Photodegradation of amoxicillin antibiotic	[90]
PU/rGO–TiO_2	Chemical deposition	Photodegradation of MB	[91]
P25/graphene/polyacrylamide hydrogels	Chemical synthesis route	Photodegradation of MB	[93]
Poly(vinyl alcohol)/poly (acrylic acid)/TiO_2/graphene oxide	Radical polymerization and condensation reaction	Photodegradation of organic pollutants	[95]
Poly(vinylidene fluoride) (PVDF)/GO/ZnO	Immersion-precipitation phase transformation	Photodegradation of MB	[92]
Poly(vinylidene difluoride-co-trifluoroethylene)/ GO/TiO_2	Electrospinning method	Photodegradation of MB	[96]
AgO-CoO-CdO/poly(alanine)-chitosan-rGO	Chemical method	Photocatalytic degradation of dyes	[97]
Cu_2O/3D-rGO/nano-chitosan composites	In situ reduction synthesis	Photodegradation of RhB	[98]
rGO/chitosan/Ag	Self-assembly process	Photodegradation of RhB	[100]

in rGO-TiO_2 loading and PU/rGO-TiO_2 nanofibrous membrane showed 95% of degradation against methylene blue dye. Similarly, Zhang and co-workers [92] reported a nanocomposite photocatalyst composed of zinc oxide as photocatalyst, graphene oxide as dispersant and poly(vinylidene fluoride) (PVDF) membrane as carrier.

The synthesized nanocomposites PVDF/GO/ZnO showed remarkable photocatalytic degradation of methylene blue (86.84%) under xenon lamp irradiation which was found to be an efficient material for wastewater purification. Furthermore, the authors demonstrated the effect ZnO and GO on the structure and photocatalytic activity of PVDF/GO/ZnO ternary nanocomposite membranes. Due to the strong hydrophilic nature of the carboxyl group, the addition of graphene oxide enhanced the dispersibility of ZnO in PVDF membranes. Figure 4.9 shows synergistic effects of ZnO, GO and PVDF in PVDF/GO/ZnO-based nanomembrane on photodegradation mechanism of methylene blue.

Moztahida et al. [93] demonstrated photocatalytic degradation of methylene blue using P25/graphene/polyacrylamide hydrogels which showed remarkable photocatalytic activity for degradation of methylene blue as shown in Fig. 4.10. Furthermore, the authors investigated that rGO not only improved the adsorption capacity of the hydrogel by increasing the surface area but also enhanced the

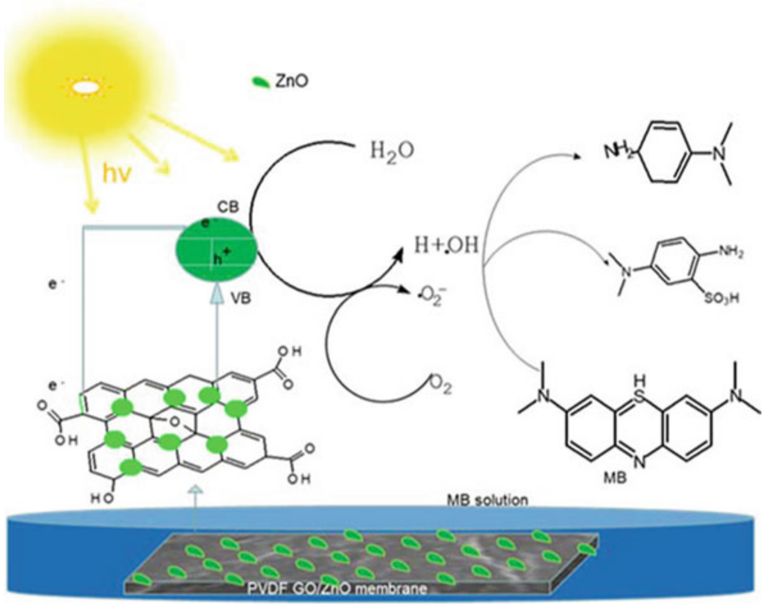

Fig. 4.9 Schematic diagram of photodegradation adsorption and proposed mechanism of PVDF/GO/ZnO nanocomposite membrane for methylene blue. Reprinted with permission from Ref. [92]

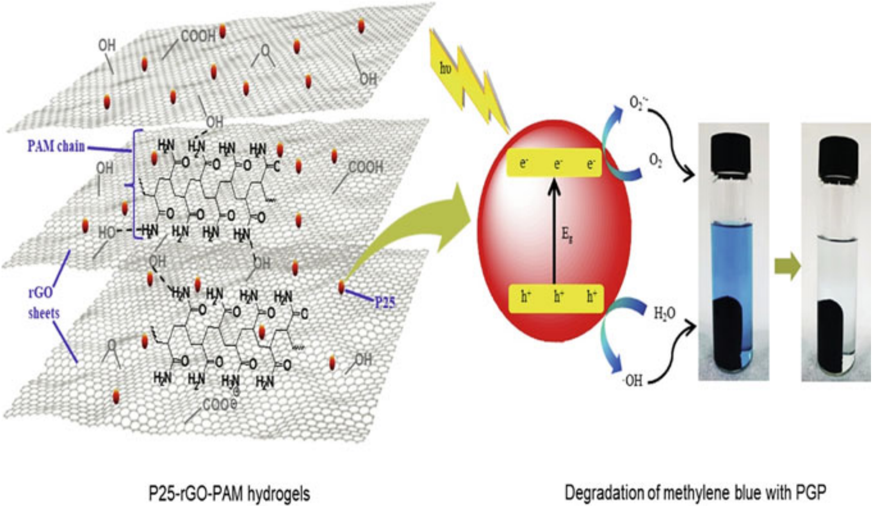

Fig. 4.10 Schematic diagram showing photodegradation of methylene blue with P25/graphene/polyacrylamide hydrogels. Reprinted with permission from Ref. [93]

photocatalytic performance synergistically by inhibiting the recombination of electron–hole pairs.

Ni and co-workers also developed [94] ternary nanocomposite-based photocatalyst which involved reduced graphene oxide-based polystyrene ceria nanocomposites for photodegradation of methylene blue. While Moon and co-workers [95] developed graphene oxide/insulating polymers-based nanocomposites containing four components, the researchers developed a photocatalyst based on poly(vinyl alcohol)/poly(acrylic acid)/TiO_2/graphene oxide nanocomposite using radical polymerization and condensation reaction. The nanocomposites exhibited superior photocatalytic activity for degradation of organic pollutants from wastewater.

Some researchers have demonstrated the photocatalytic performance of graphene-based insulating copolymer nanocomposites. For example, Almeida et al. [96] investigated the photocatalytic performance of poly(vinylidene difluoride-co-trifluoroethylene) (P(VDF-TrFE)) copolymer fibrous membranes/titanium dioxide/graphene oxide (TiO_2/GO) nanocomposite. The presence of the TiO_2/GO increases the photocatalytic efficiency of the nanocomposite membrane towards the degradation of methylene blue (MB) when compared with the membranes prepared with pristine TiO_2 in UV–visible range. The significant photocatalytic activity shown by these nanocomposites was explained on the basis of rapid electron transport and the suppressed recombination of electron–hole pairs due to improved ionic interaction between titanium and carbon combined with the superior electric properties of the polymer, such as high polarization and dielectric constant in addition with low dielectric loss. Some researchers have developed graphene-based biopolymers for photocatalytic degradation of organic dyes. Recently, Zhang et al. [97] developed AgO-CoO-CdO/poly(alanine)-chitosan-reduced graphene nanocomposite-based photocatalyst for degradation of organic dyes from wastewater.

Chitosan is biodegradable and biocompatible non-toxic polymer, and the nanocomposites based on graphene with chitosan have also been reported for photodegradation of organic pollutants. Similarly, Zhang et al. [98] also reported the photodegradation of rhodamine B dye using cuprous oxide/3D-rGO/chitosan nanocomposites. The photocatalytic performance of the synthesized nanocomposites for degradation of rhodamine B dye under visible light was found to be enhanced by 68.2 and 46.8% when Cu_2O/3D-rGO/nano-chitosan composite was used compared with the pristine Cu_2O and Cu_2O/3D-rGO nanocomposite. The superior photocatalytic performance shown by Cu_2O/3D-rGO/nano-chitosan compared to the pristine Cu_2O and Cu_2O/3D-rGO nanocomposite was due to high porosity from 3D-rGO, an efficient charge transfer from Cu_2O to rGO. Moreover, the greater adsorption ability of nano-chitosan also played an important role for enhancing the photocatalytic activity of nanocomposite.

Recently, Samuel and co-workers also [99] reported the photodegradation performance of a new hybrid adsorbent material based on graphene oxide-chitosan and $Cu_3(btc)_2$ (btc = benzene-1,3,5-tricarboxylic acid) which showed 98% degradation of methylene blue within 60 min under UV irradiation. The higher adsorption ability was due to the presence of chitosan biopolymer in nanocomposites. In another studies, nanocomposites based on reduced graphene oxide/chitosan/silver hydrogel were reported by Jiao and co-workers [100] for degradation of organic dyes under UV light irradiation. The authors investigated that the photocatalytic performance of the nanocomposites was mainly due to presence of silver nanoparticle on rGO sheets, whereas the chitosan molecule was incorporated to facilitate the gelation process of the graphene oxide sheets.

In another work, Ahmad et al. [101] also developed biodegradable polymer-graphene oxide composite based on cellulose/polypyrrole-graphene oxide. Fluorescence spectra showed that the incorporation of graphene into the polymer matrix remarkably enhanced charge separation and reduced recombination of charge carrier which in turn favours the photocatalytic performance of the composite.

4.5.2 Graphene-Based Conducting Polymers Nanocomposites

Conducting polymers such as polyaniline, polypyrrole and poly (3,4-ethylenedioxythiophene) have an extended π-electron conjugated system over a large number of monomer units show high charge carriers mobility expressed through high absorption coefficients that varied from visible light to near infrared region, due to which they can be used as photosensitizers for semiconductor materials, increasing their photocatalytic activity under ultraviolet as well as sunlight irradiation. Photocatalysts based on conducting polymer hybrid composite with graphene or functionalized graphene have become one of the potential techniques for degradation of organic pollutants especially for wastewater remediation [102–104] (Table 4.3).

These polymers show high hole transport ability and stability, slow charge recombination rate and fast charge carrier separation. However, when these polymers are incorporated with graphene molecules, the photodegradation ability of the composite was found to be enhanced. Thekkayil and co-workers demonstrated [105] photocatalytic activity of graphene oxide/polyaniline composite. Moreover, it was suggested that polymerizing monomers such as aniline with graphene oxide leads to generation of some remarkable bonding between polyaniline and graphene oxide. The composite has partial hydrogen bonding between imine of polyaniline and the oxygen-containing functional group of graphene oxide sheet, which shows enhanced photocatalytic performance as compared to pristine polyaniline due to efficient photogenerated electron–hole pairs and charge separation.

Ameen et al. [51] reported graphene/polyaniline-based nanocomposites for degradation of rose Bengal dye (RB). The prepared graphene/polyaniline nanocomposites showed a remarkable degradation of RB dye by ~56% within 3 h under light illumination. Mitra and co-workers [52] investigated photodegradation of organic dyes such as malachite green, rhodamine B and Congo red using

Table 4.3 Some reported graphene-based conducting polymer nanocomposites for photocatalytic application

Photocatalysts (nanocomposites)	Preparation methods	Photocatalytic applications	References
Graphene/polyaniline	In situ polymerization	Photodegradation of RB (Rose Bengal dye)	[51]
Rgo/polyaniline	In situ polymerization	Photodegradation of malachite green, Rh B and Congo red (CR)	[52]
rGO/CuI/polyaniline	Self-assembly approach	Photodegradation of RhB	[124]
rGO-$ZnFe_2O_4$-polyaniline	In situ polymerization	Photodegradation of RhB	[125]
NiO/polyaniline/rGO	Interfacial polymerization/ solvothermal process	Photodegradation of MB	[107]
rGO/polyaniline/ZnO	In situ polymerization	Photodegradation of MB	[108]
PANI/SnS_2/N-doped rGO	In situ polymerization	Photocatalytic reduction of Cr(VI)	[111]
PEDOT/GO/MnO_2	Template-free solution method	Photodegradation of MB	[113]
Graphene-polyaniline-$BiVO_4$	Sonochemical technique	Photodegradation of MB, RhB	[109]
$BiVO_4$-GO-TiO_2-polyaniline	One-pot hydrothermal method	Photodegradation of MB and phenol	[110]

reduced graphene-based polyaniline photocatalyst. The composite showed uniform distribution polyaniline in rGO sheet as shown in TEM image (Fig. 4.11), and it exhibited remarkably enhanced activity towards the degradation of cationic and anionic dyes in comparison with polyaniline or rGO. The superior activity of the polyaniline/rGO composite was explained by the improvement of charge separation due to incorporation of rGO in the polyaniline matrix. The authors explained the photodegradation mechanism of rGO/polyaniline composite. As shown in Fig. 4.11, the authors suggested that in the presence of visible light, polyaniline gets electrons flow downhill from the conduction band (CB) of polyaniline to the Fermi level (FL) of rGO, resulting in the suppression in the charge pair recombination process. As rGO shows a higher reduction potential than $O_2/{\bullet}O_2^-$ (+0.07 V). Hence, the electrons present at the surface of rGO can easily react with dissolved O_2 to produce a superoxide radical anion $({\bullet}O)_2^-$, which in turn produces hydrogen peroxide in the presence of water. Photo-oxidation and photoreduction of hydrogen peroxide take place with electrons and holes at the catalyst surfaces, resulting in the formation of oxidant species •OH radicals, which degrade the dye molecules to colourless products.

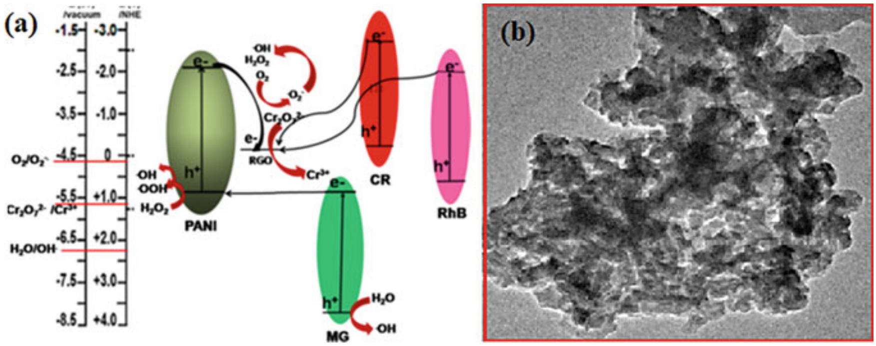

Fig. 4.11 **a** Schematic diagram showing proposed mechanism of the visible light-driven charge transfer process of the photogenerated electrons and holes in the reduced graphene oxide/ polyaniline composite and **b** TEM image of rGO/PANI composite. Adapted with permission from Ref. [52]

Furthermore, some researchers have developed polyaniline-based ternary nanocomposites. For example, Miao et al. [106] developed reduced graphene oxide/ polyaniline/Cu_2O composite hydrogel with a 3D porous network in which polyaniline acts as an electron donor and a hole conductor, whereas graphene oxide acts as an electron acceptor on photoexcitation with UV–visible light. Therefore, their composites with inorganic materials such as metal oxide additionally increase the degradation rate due to the synergistic effects by reducing recombination losses. The authors investigated that the photocatalytic performance of the nanocomposites based on graphene oxide/polyaniline/Cu_2O was found to be 97.91% in 20 min under UV–visible light irradiation. In addition, it was suggested that both LUMO and HOMO of polyaniline are present at a higher energy level as compared to Cu_2O, resulting in the facile electron transfer from LUMO of polyaniline to conduction band of Cu_2O, while the hole transfer between valence bands of Cu_2O moves to the HOMO of polyaniline. Therefore, this charge transfer suppresses the recombination of the photogenerated electrons–hole pairs. In another work reported by Ahuja and co-workers [107] on photocatalyst based on NiO/polyaniline/rGO composites, the synthesized composite exhibited remarkable photocatalytic degradation of methylene blue dye. The photodegradation efficiency of the nanocomposites for degradation of methylene blue was reported as 98% within 11 min, whereas polyaniline/rGO, polyaniline and rGO exhibited an extended time duration to degrade 97, 84 and 32% of methylene blue, respectively.

Similarly, Wu and co-workers [108] also reported photocatalytic performance of ternary nanocomposites photocatalyst based on rGO/polyaniline/ZnO nanocomposite. The nanocomposites showed enhanced photocatalytic performance for the photodegradation of methyl orange with a maximum degradation efficiency of almost 100% within 60 min under UV light irradiation compared to pure ZnO. This improvement is due to the presence of rGO which effectively enhances the ability to transfer the photo-excited electrons and the specific surface area of material;

moreover, the role of conducting polymer such as polyaniline is to increase the absorption of light and adsorption of dyes.

Similarly, Biswas et al. [109] demonstrated photodegradation performance of polyaniline/bismuth vanadate/graphene oxide for methylene blue and rhodamine B dyes. These improvements in photocatalytic degradation performance and photocatalytic stability were due to the formation of a heterojunction free electron between polyaniline and $BiVO_4$/graphene oxide.

In another work, Zhao and co-workers [110] developed a quaternary system by inclusion of TiO_2 nanoparticles in polyaniline/bismuth vanadate/graphene oxide matrix to enhance the photocatalytic activity of the nanocomposite. Therefore, nanocomposites photocatalyst based on four components materials exhibited remarkable photodegradation of methylene blue and phenol under visible light irradiation.

Beside photodegradation of organic dyes from wastewater, graphene-based polyaniline nanocomposites were also investigated for photodegradation of heavy metals from contaminated water. Zhang et al. [111] developed a ternary photocatalyst based on N-doped reduced graphene oxide/polyaniline/SnS_2 nanocomposite. The photocatalytic experiments demonstrated that the synthesized ternary nanocomposite prepared under the optimum conditions (N-doped rGO/polyaniline/SnS_2 2%) exhibited remarkably higher photocatalytic activity than SnS_2 nanoplates, polyaniline/SnS_2 and N-doped rGO composites in the reduction of aqueous Cr(VI) under the irradiation of visible light. Figure 4.12 shows a schematic diagram for photocatalytic activity of ternary nanocomposite based on N-doped rGO/polyaniline/SnS_2 for reduction of Cr(VI) ions. The photocatalytic performance of SnS_2 was increased by incorporation of N-doped rGO and conducting polymer,

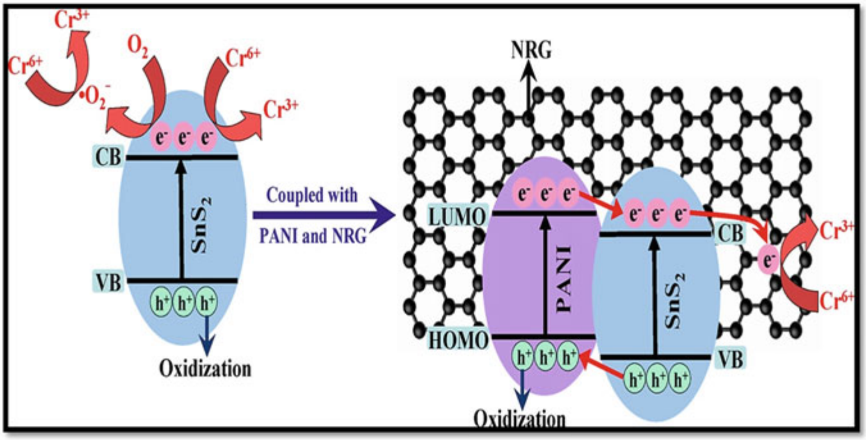

Fig. 4.12 Schematic diagram for photocatalytic activity of ternary nanocomposite based on N-doped rGO/polyaniline/SnS_2 for reduction of Cr(VI) ions. Reprinted with permission from Ref. [111]

polyaniline as shown in Fig. 4.12, in which polyaniline acts as a transporter of photogenerated electrons and holes, while rGO acts as a receptor which can accept the electrons on photoexcitation with visible light due to which highly toxic Cr(VI) ions get easily reduced Cr(III) ions.

Beside polyaniline, some researchers have incorporated other conducting polymers such as polypyrrole and poly(3,4-ethylenedioxythiophene) in graphene matrix. Recently, Ahmad et al. [112] developed graphene oxide-based polypyrrole/CdS nanocomposites for photodegradation of organic pollutants such as rhodamine B, reactive blue 171 dyes and toluene. Similarly, Zhang et al. demonstrated [113] the photocatalytic performance based on nanocomposite of poly(3,4-ethylenedioxythiophene)/graphene oxide (PEDOT/GO), poly(3,4-ethylenedioxythiophene)/MnO_2 (PEDOT/MnO_2), and poly(3,4-ethylenedioxythiophene)/graphene oxide/MnO_2 (PEDOT/GO/MnO_2) for photodegradation of methylene blue. The photocatalytic performance of pure PEDOT and nanocomposites was found to be in the order of PEDOT/GO/MnO_2 > PEDOT/MnO_2 > PEDOT/GO > pure PEDOT. Among pure PEDOT and nanocomposites, PEDOT/GO/MnO_2 nanocomposites exhibited the highest photodegradation efficiency under different light sources. This phenomenon has been explained on the basis of hydrogen bonding between surface hydroxyl groups of MnO_2 and the nitrogen atoms present in methylene blue molecules. Furthermore, graphene oxide is an excellent electron acceptor and transporter which could reduce the recombination of charge carriers and increase the photocatalytic performance of nanocomposites. Hence, the synergetic effects between PEDOT, MnO_2 and graphene oxide would be combined together to enhance the catalytic activity of nanocomposites.

4.6 Conclusions

In this chapter, the great interest and advantages of using different nanomaterials such as inorganic nanoparticles (metal, metal oxide, metal sulphide, etc.) and polymers (insulating, biopolymers and conducting polymers) as a support with graphene and functionalized graphene for the development of highly efficient photocatalyst has been presented. The inherent properties of graphene such as large surface area, greater electron mobility, high thermal conductivity and good mechanical strength can be enhanced by the development of different nanocomposite hybrid materials with graphene which have opened up new pathways to develop high-performance photocatalysts. On the basis of research carried out in the field of graphene-based photocatalyst nanocomposites in last few decades, it was observed that graphene oxide is believed to be a better starting material than pure graphene for the development of nanocomposite with semiconductor photocatalysts. This chapter provides new insights into the development and application of graphene-based nanocomposite for environmental remediation. Various preparative routes such as sol–gel, in situ growth, hydrothermal/solvothermal, self-assembly and in situ polymerization have been explained to develop the high-performance graphene-based semiconductor photocatalyst which have exhibited potential applications in photodegradation of organic contaminants, photocatalytic hydrogen generation and photocatalytic reduction of toxic hazardous elements into non-toxic ions. Incorporation of different inorganic materials such as metals, metal oxide, metal sulphides, metal oxyhalide and polymers into the graphene matrix can improve the properties like adsorption capacity, extended light absorption range and increase charge separation properties which enhance the overall photocatalytic performance of the nanocomposite. In this chapter, graphene-based binary, ternary and quaternary nanocomposites systems have been reported, and it was observed that a ternary and quaternary system was employed to enhance the photocatalytic performance of graphene-based nanocomposites. In order to achieve recyclable and reusable graphene-based nanocomposites photocatalysts, some magnetic nanomaterials such as Fe_2O_3 nanoparticles have been incorporated in the functional graphene matrix. Incorporation of polymers in graphene-metal nanocomposites is used to prevent aggregation and release of nanoparticles from composite matrix. Additionally, use of conducting polymers in graphene-based nanocomposites offers enhanced photocatalytic performance of the nanocomposite. Moreover, nanocomposites based on graphene oxide modified with biodegradable and non-toxic biopolymers such as chitosan and cellulose hybrid nanomaterials were exhibited enhancing the adsorption ability for the contaminants. This study demonstrates that graphene-based nanocomposites are very promising candidate for development of high-performance photocatalysts for environmental remediation.

References

1. Gao Y (2017) Graphene and polymer composites for supercapacitor applications: a review. Nanoscale Res Lett 12:387
2. Zheng D, Hu H, Liu X, Hu S (2015) Application of graphene in elctrochemical sensing. Curr Opin Colloid Interface Sci 20:383–405
3. Syama S, Mohanan PV (2019) Comprehensive application of graphene: emphasis on biomedical concerns. Nano Micro Lett 11:6
4. Mahmoudi T, Wang Y, Hahn Y-B (2018) Graphene and its derivatives for solar cells application. Nano Energy 47:51–56
5. Díez-Pascual AM, Luceño Sánchez JA, Peña Capilla R, García Díaz P (2018) Recent developments in graphene/polymer nanocomposites for application in polymer solar cells. Polymers 10:217
6. Li X, Yu J, Wageh S, Al-Ghamdi AA, Xie J (2016) Graphene in photocatalysis: a review. Small 12:6640
7. Zhang S, Li B, Wang X, Zhao G, Hu B, Lu Z, Wen T, Chen J, Wang X (2020) Recent developments of two-dimensional graphene-based composites in visible-light photocatalysis for eliminating persistent organic pollutants from wastewater. Chem Eng J 390:124642
8. Nasrollahzadeh M, Nezafat Z, Gorab MG, Sajjadi M (2020) Recent progresses in graphene-based (photo)catalysts for reduction of nitro compounds. Mol Catal 484:110758

9. Prasad C, Liu Q, Tang H, Yuvaraja G, Long J, Rammohan A, Zyryanov GV (2020) An overview of graphene oxide supported semiconductors based photocatalysts: properties, synthesis and photocatalytic applications. J Mol Liq 297:111826
10. Xiang Q, Yu J (2013) Graphene-based photocatalysts for hydrogen generation. J Phys Chem Lett 4:753
11. Niyogi S, Bekyarova E, Itkis ME, McWilliams JL, Hamon MA, Haddon RC (2006) Solution properties of graphite and grapheme. J Am Chem Soc 128(24):7720–7721
12. Juang Z-Y, Wu C-Y, Lo C-W, Chen W-Y, Huang C-F, Hwang J-C, Chen F-R, Leou K-C, Tsai C-H (2009) Synthesis of graphene on silicon carbide substrates at low temperature. Carbon 47(8):2026–2031
13. Reina A, Jia XT, Ho J, Nezich D, Son H, Bulovic V, Mildred Dresselhaus S, Kong J (2009) Large area, few-layer graphene films on arbitrary substrates by chemical vapor deposition. Nano Lett 9(1):30–35
14. Wu T, Jiang Y, Zhang X (2015) The synthesis of CVD single crystal graphene growth on copper substrate. J Funct Mater 46:16037–16043
15. Park S, Ruoff RS (2009) Chemical methods for the production of graphenes. Nat Nanotechnol 4:217–224
16. Xin GQ, Hwang W, Kim N, Cho SM, Chae H (2010) A graphene sheet exfoliated with microwave irradiation and interlinked by carbon nanotubes for high-performance transparent flexible electrodes. Nanotechnology 21(40)
17. Dato A, Radmilovic V, Lee Z, Phillips J, Frenklach M (2008) Substrate-free gas-phase synthesis of graphene sheets. Nano Lett 8:2012
18. Kosynkin DV, Higginbotham AL, Sinitskii A, Lomeda JR, Dimiev A, Price BK, Tour JM (2009) Longitudinal unzipping of carbon nanotubes to form graphene nanoribbons. Nature 458:872
19. Brodie BC (1860) Sur le poids atomique du graphite. Ann Chim Phys 59:466–472
20. Staudenmaier L (1898) Verfahren zur Darstellung der Graphitsäure. Eur J Inorg Chem 31 (2):1481–1487
21. Hummers WS, Offeman RE (1958) J Am Chem Soc 80(6):1339–1339
22. Marcano DC, Kosynkin DV, Berlin JM, Sinitskii A, Sun Z, Slesarev A et al (2010) Improved synthesis of graphene oxide. ACS Nano 4:480
23. Chen J, Li Y, Huang L, Li C, Shi G (2015) High-yield preparation of graphene oxide from small graphite flakes via an improved Hummers method with a simple purification process. Carbon 81:826–834
24. Zaaba NI, Foo KL, Hashim U, Tan SJ, Liu WW, Voon CH (2017) Synthesis of graphene oxide using modified hummers method: solvent influence. Procedia Eng 184:469
25. Bezerra de Araujo CM, Filipe Oliveira do Nascimento G, Rodrigues Bezerra da Costa G, Santos da Silva K, Salgueiro Baptisttella AM, Ghislandi MG, Alves da Motta Sobrinho M (2019) Adsorptive removal of dye from real textile wastewater using graphene oxide produced via modifications of hummers method. Chem Eng Commun 206(11):1375–1387
26. Singh RK, Kumar R, Sing DP (2016) Graphene oxide: strategies for synthesis, reduction and frontier applications. RSC Adv 6:64993
27. Alkhouzaam A, Qiblawey H, Khraisheh M, Atieh M, Al-Ghouti M (2020) Synthesis of graphene oxides particle of high oxidation degree using a modified Hummers method. Ceram Int 46:23997
28. Alam SN, Sharma N, Kumar L (2017) Synthesis of graphene oxide (GO) by modified Hummers method and its thermal reduction to obtain reduced graphene oxide (rGO). Graphene 6
29. Gui D, Liu C, Chen F, Liu J (2014) Appl Surf Sci 307:172
30. Xu G, Jiang F, Ren Z, Yang L (2015) Ceram Int 41:10680
31. He HY (2015) Mater Sci Semicond Process 31:200
32. Durmus Z, Kurt BZ, Durmus A (2019) Synthesis and characterization of graphene oxide/zinc oxide (GO/ZnO) nanocomposite and its utilization for photocatalytic degradation of basic fuchsin dye. Chem Select 4:271

33. Wang CC, Shieu FS, Shih HC (2020) Enhanced photodegradation by RGO/ZnO core-shell nanostructures. J Environ Chem Eng 8:103589
34. Li Y, Wang D, Li W, He Y (2015) J Alloys Compd 648:942
35. Zhao X, Zhang J, Zhang J, Gong C, Gu X, Ma Z, Zhou J, Yu L, Zhang Z (2015) Construction of spongy antimony-doped tin oxide/graphene nanocomposites using commercially available products and its excellent electrochemical performance. J Power Sources 294:223
36. Li N, Liu G, Zhen C, Li F, Zhang LL, Cheng HM (2011) Adv Funct Mater 21:1717
37. Bhirud A, Sathaye S, Waichal R, Park C, Jand Kale B (2015) In situ preparation of N–ZnO/graphene nanocomposites: excellent candidate as a photocatalyst for enhanced solar hydrogen generation and high performance supercapacitor electrode. J Mater Chem A 3:17050
38. Anand K, Singh O, Singh RC (2013) Different strategies for the synthesis of graphene/ZnO composite and its photocatalytic properties. Appl Phys A 116(3)
39. Rattan S, Kumar S, Goswamy JK (2020) In-situ one pot synthesis of graphene-ZnO nanohybrid and its application to UV light detection. Mater Res Express 7:015058
40. Lambert TN, Chavez CA, Hernandez-Sanchez B, Lu P, Bell NS, Ambrosini A, Friedman T, Boyle TJ, Wheeler DR, Huber DL (2009) Synthesis and characterization of titania−graphene nanocomposites. J Phys Chem C 113:19812
41. He R, Lou Z, Gui J, Tang B, Xu D (2020) Room-temperature synthesis of BiOI/graphene oxide foam composite for phenol removal under visible light. Appl Surface Sci 504:144370
42. Sang Y, Zhao Z, Tian J, Hao P, Jiang H, Liu H, Claverie JP (2014) Enhanced photocatalytic property of reduced graphene oxide/TiO_2 nanobelt surface heterostructures constructed by an in situ photochemical reduction method. Small 10:3775
43. Wojtoniszak M, Zielinska B, Chen XC, Kalenczuk RJ, Borowiak-Palen E (2012) J Mater Sci 47(7):3185
44. Zhang XY, Li HP, Cui XL, Lin YH (2010) Graphene/TiO_2 nanocomposites: synthesis, characterization and application in hydrogen evolution from water photocatalytic splitting. J Mater Chem 20:2801
45. Shi M, Shen J, Ma H, Li Z, Lu X, Li N, Ye M (2012) Preparation of graphene-TiO_2 composite by hydrothermal method from peroxotitanium acid and its photocatalytic properties. Colloids Surf A Physicochemical Eng Aspects 405:30
46. Liu Y, Yu Z, Peng Y, Shao L, Li X, Zeng H (2020) A novel photocatalytic self-cleaning TiO2 nanorods inserted graphene oxide-based nanofiltration membrane. Chem Phys Lett 749:137424
47. Atchudan R, Nesakumar T, Edison JI, Perumal S, Karthikeyan D, Lee YR (2016) Facile synthesis of zinc oxide nanoparticles decorated graphene oxide composite via simple solvothermal route and their photocatalytic activity on methylene blue degradation. J Photochem Photobiol B Biol 162:500
48. Moussa H, Girot E, Mozet K, Alem H, Medjahdi G, Schneider R (2016) ZnO rods/reduced graphene oxide composites prepared via a solvothermal reaction for efficient sunlight-driven photocatalysis. Appl Catal B Environ 185:11
49. Lv H, Shen X, Ji Z, Qiu D, Zhu G, Bi Y (2013) Synthesis of graphene oxide-$BiPO_4$ composites with enhanced photocatalytic properties. Appl Surface Sci 284:308
50. Nguyen DCT, Yeon Cho K, Won-Chun OH (2017) Synthesis of mesoporous SiO_2/Cu_2O–graphene nanocomposites and their highly efficient photocatalytic performance for dye pollutants. RSC Adv 7:29284
51. Ameen S, Seo HK, Akhtar MS, Shin HS (2012) Novel graphene/polyaniline nanocomposites and its photocatalytic activity toward the degradation of rose Bengal dye. Chem Eng J 210:220
52. Mousumi Mitra M, Ahamed ST, Ghosh A, Mondal A, Kargupta K, Ganguly S, Banerjee D (2019) Polyaniline/reduced graphene oxide composite-enhanced visible light-driven photocatalytic activity for the degradation of organic dyes. ACS Omega 4:1623

53. Oliveira HPD, Sydlik SA, Swager TM (2013) Supercapacitors from free-standing polypyrrole/graphene nanocomposites. J Phys Chem C 117:10270
54. Wu H, Lin S, Chen C, Liang W, Liu X, Yang HA (2016) New ZnO/rGO/polyaniline ternary nanocomposite as photocatalyst with improved photocatalytic activity. Mater Res Bull 83:434
55. Zhang J, Xiong Z, Zhao XS (2011) Graphene–metal–oxide composites for the degradation of dyes under visible light irradiation. J Mater Chem 21:3634
56. Khan F, Khan MS, Kamal S, Arshad M, Ahmad SI, Nami SAA (2020) Recent advances in graphene oxide and reduced graphene oxide based nanocomposites for the photodegradation of dyes. J Mater Chem C
57. Ahmed MA, El-Katori EE, Gharni ZH (2013) Photocatalytic degradation of methylene blue dye using Fe_2O_3/TiO_2 nanoparticles prepared by sol–gel method. J Alloys Compd 553:19
58. Singh P, Sharma K, Hasija V, Sharma V, Sharma S, Raizada P, Singh M, Saini AK, Bandegharaei AH, Thakur VK (2019) Systematic review on applicability of magnetic iron oxides–integrated photocatalysts for degradation of organic pollutants in water. Mater Today Chem 14:100186
59. Khan A, Sajjad L, Shamaila S, Tian B, Chen F, Zhang J (2010) Comparative studies of operational parameters of degradation of azo dyes in visible light by highly efficient WOx/TiO_2 photocatalyst. J Hazard Mater 177:781
60. Hayat K, Gondal MA, Khaled MM, Yamani ZH, Ahmed S (2011) Laser induced photocatalytic degradation of hazardous dye (Safranin-O) using self synthesized nanocrystalline WO_3. J Hazard Mater 186:1226
61. Jayaraj SK, Sadishkumar V, Arun T, Thangadurai P (2018) Enhanced photocatalytic activity of V2O5 nanorods for the photodegradation of organic dyes: a detailed understanding of the mechanism and their antibacterial activity. Mater Sci Semicond Process 85:122
62. Nagajyothi PC, Prabhakar Vattikuti SV, Devarayapalli KC, Yoo K, Shim J, Sreekanth TVM (2020) Green synthesis: photocatalytic degradation of textile dyes using metal and metal oxide nanoparticles-latest trends and advancements. Crit Rev Environ Sci Technol 50 (24):2617–2723
63. Chandu B, Kurmarayuni CM, Kurapati S et al (2020) Green and economical synthesis of graphene–silver nanocomposite exhibiting excellent photocatalytic efficiency. Carbon Lett 30:225
64. Khan ME, Khan MM, Cho MH (2015) Biogenic synthesis of a Ag–graphene nanocomposite with efficient photocatalytic degradation, electrical conductivity and photoelectrochemical performance. New J Chem 39:8121
65. Yaqoob AA, Mohd Noor NHB, Serrà A, Nasir M, Ibrahim M (2020) Advances and challenges in developing efficient graphene oxide-based ZnO photocatalysts for dye photo-oxidation. Nanomaterials 10:932
66. Raizada P, Sudhaik A, Singh P (2019) Photocatalytic water decontamination using graphene and ZnO coupled photocatalysts: a review. Mater Sci Energy Technol 2:509
67. Posa VR, Annavaram V, Koduru JR, Ammireddy VR, Somala AR (2016) Graphene-ZnO nanocomposite for highly efficient photocatalytic degradation of methyl orange dye under solar light irradiation. Korean J Chem Eng 33:456
68. Worajittiphon P, Pingmuang K, Inceesungvorn B, Wetchakun N, Phanichphant S (2015) Enhancing the photocatalytic activity of ZnO nanoparticles for efficient rhodamine B degradation by functionalised graphene nanoplatelets. Ceram Int 41:1885
69. Ameen S, Akhtar MS, Seo HK, Shin HS (2013) Advanced ZnO-graphene oxide nanohybrid and its photocatalytic applications. Mater Lett 100:261
70. Qin J, Zhang X, Yang C, Cao M, Ma M, Liu R (2017) ZnO microspheres-reduced graphene oxide nanocomposite for photocatalytic degradation of methylene blue dye. Appl Surf Sci 392:196
71. Wu D, An T, Li G, Wang W, Cai Y, Yip HY, Zhao H, Wong PK (2015) Mechanistic study of the visible-light-driven photocatalytic inactivation of bacteria by graphene oxide-zinc oxide composite. Appl Surf Sci 358:137

72. Gu L, Wang J, Cheng H, Zhao Y, Liu L, Han X (2013) One-step preparation of graphene-supported anatase TiO2 with exposed 001 facets and mechanism of enhanced photocatalytic properties. ACS Appl Mater Interfaces 5(8):3085
73. Velasco-Hernández A, Esparza-Muñoz RA, de Moure-Flores FJ, Santos-Cruz J, Mayén-Hernández SA (2020) Synthesis and characterization of graphene oxide—TiO2 thin films by sol-gel for photocatalytic applications. Mater Sci Semicond Process 114:105082
74. Karaolia P, Michael-Kordatou I, Hapeshi E, Drosou C, Bertakis Y, Christofilos D, Armatas GS, Sygellou L, Schwartz T, Xekoukoulotakis NP, Fatta-Kassinos D (2018) Removal of antibiotics, antibiotic-resistant bacteria and their associated genes by graphene-based TiO_2 composite photocatalysts under solar radiation in urban wastewaters. Appl Catal B Environ 224:10–824
75. Teo PS, Pandikumar A, Lim HN, Huang NM, Chia CH (2014) Magnetically separable reduced graphene oxide/iron oxide nanocomposite materials for environmental remediation Catal. Sci Technol. https://doi.org/10.1039/C4CY00806E
76. Benjwal P, Kumar M, Chamoli P, Kamal KK (2015) Enhanced photocatalytic degradation of methylene blue and adsorption of arsenic(III) by reduced graphene oxide (rGO)–metal oxide (TiO_2/Fe_3O_4) based nanocomposites. RSC Adv 5:73249
77. Nuengmatcha P, Porrawatkul P, Chanthai S, Sricharoen P, Limchoowong N (2019) Enhanced photocatalytic degradation of methylene blue using Fe2O3/graphene/CuO nanocomposites under visible light. J Environ Chem Eng 7(6):103438
78. Zhang L, Hu X, Zhu L, Jin X, Feng C (2019) Water-dispersible ZnO/$C_OFe_2O_4$/graphene photocatalyst and their high-performance in water treatment. Fullerenes Nanotubes Carbon Nanostruct 27(11):873–877
79. Wei Y, Liang J, Yao Y et al (2019) Synthesis of visible light-driven graphene based ZnFe mixed metal oxide for efficient degradation of tetracycline. J Mater Sci Mater Electron 30:8931
80. Chandel N, Sharma K, Sudhaik A, Raizada P, Hosseini-Bandegharaei A, Thakur VK, Singh P (2020) Magnetically separable ZnO/$ZnFe_2O_4$ and ZnO/$CoFe_2O_4$ photocatalysts supported onto nitrogen doped graphene for photocatalytic degradation of toxic dyes. Arab J Chem 13:4324
81. Vasilaki E, Georgaki I, Vernardou D, Vamvakaki M, Katsarakis N (20145) Ag-loaded TiO_2/reduced graphene oxide nanocomposites for enhanced visible-light photocatalytic activity. Appl Surface Sci 353:865
82. Khalid NR, Ahmed E, Ahmad M, Niaz NA, Ramzan M, Shakil M, Iqbal T, Majid A (2016) Microwave-assisted synthesis of Ag-TiO_2/graphene composite for hydrogen production under visible light irradiation. Ceram Int 42:8257
83. Dutta S, Sahoo R, Ray C, Sarkar S, Jana J, Negishi Y, Pal T (2015) Biomolecule-mediated CdS-TiO_2-reduced graphene oxide ternary nanocomposites for efficient visible light-driven photocatalysis. Dalton Trans 44:193
84. Gusain R, Kumar P, Sharma OP, Jain SL, Khatri OP (2016) Reduced graphene oxide-CuO nanocomposites for photocatalytic conversion of CO_2 into methanol under visible light irradiation. Appl Catal B Environ 181:352
85. Wang H, Li G, Fakhri A (2020) Fabrication and structural of the Ag2S-MgO/graphene oxide nanocomposites with high photocatalysis and antimicrobial activities. J Photochem Photobiol B Biol 207:111882
86. Dhanasekar M, Jenefer V, Nambiar RB, Babu SG, Selvam SP, Neppolian B, Bhat SV (2018) Ambient light antimicrobial activity of reduced graphene oxide supported metal doped TiO_2 nanoparticles and their PVA based polymer nanocomposite films. Mater Res Bull 97:238
87. Hong Y, Bao S, Xiang X, Wang X (2020) Concentration-dominated orientation of phenyl groups at the polystyrene/graphene interface. ACS Macro Lett 9(6):889
88. Divakaran N, Kale MB, Senthil T, Mubarak S, Dhamodharan D, Wu L, Wang J (2020) Novel unsaturated polyester nanocomposites via hybrid 3D POSS-modified graphene oxide reinforcement: electro-technical application perspective. Nanomaterials 10:260

89. Ussia M, Bruno E, Spina E, Vitalini D, Pellegrino G, Ruffino F, Privitera V, Carroccio SC (2018) Freestanding photocatalytic materials based on 3D graphene and polyporphyrins. Sci Rep 8:5001
90. Hussien MSA, Mohammed MI, Yahia IS (2020) Multifunctional applications of graphene-doped PMMA nanocomposite membranes for environmental photocatalytic. J Inorg Organomet Polym 30:2708
91. Sundaran SP, Reshmi CR, Sagitha P, Athiyanathil S (2020) Polyurethane nanofibrous membranes decorated with reduced graphene oxide-TiO_2 for photocatalytic templates in water purification. J Mater Sci 55:5892
92. Zhang D, Dai F, Zhang P, An Z, Zhao Y, Chen L (2019) The photodegradation of methylene blue in water with PVDF/GO/ZnO composite membrane. Mater Sci Eng C 96:684–692
93. Moztahida M, Lee DS (2020) Photocatalytic degradation of methylene blue with P25/graphene/polyacrylamide hydrogels: optimization using response surface methodology. J Hazard Mater 400:123314
94. Ni X, Zhang J, Hong L, Yang C, Li Y (2019) Reduced graphene oxide@ceria nanocomposite-coated polymer microspheres as a highly active photocatalyst. Colloids Surfaces A Physicochemical Eng Aspects 567:161
95. Moon YE, Jung G, Yun J, Kim H (2013) Poly(vinyl alcohol)/poly(acrylic acid)/TiO_2/graphene oxide nanocomposite hydrogels for pH-sensitive photocatalytic degradation of organic pollutants. Mater Sci Eng B 178:1097
96. Almeida NA, Martins PM, Teixeira S et al (2016) TiO2/graphene oxide immobilized in P (VDF-TrFE) electrospun membranes with enhanced visible-light-induced photocatalytic performance. J Mater Sci 51:6974
97. Zhang J, Ding E, Xu S, Li Z, Fakhri A, Gupta VK (2020) Production of metal oxides nanoparticles based on poly-alanine/chitosan/reduced graphene oxide for photocatalysis degradation, anti-pathogenic bacterial and antioxidant studies. Int J Biol Macromol 164:1584
98. Zhang Z, Zhai S, Wang M, Ji H, He L, Ye C, Wang C, Fang S, Zhang H (2016) Photocatalytic degradation of rhodamine B by using a nanocomposite of cuprous oxide, three-dimensional reduced graphene oxide, and nanochitosan prepared via one-pot synthesis. J Alloys Compd 659:101
99. Samuel MS, Suman S, Venkateshkannan, Selvarajan E, Mathimani T, Pugazhendhi A (2020) Immobilization of Cu3(btc)2 on graphene oxide-chitosan hybrid composite for the adsorption and photocatalytic degradation of methylene blue. J Photochem Photobiol B Biol 204:111809
100. Jiao T, Zhao H, Zhou J, Zhang Q, Luo X, Hu J, Peng Q, Yan X (2015) Self-assembly reduced graphene oxide nanosheet hydrogel fabrication by anchorage of chitosan/silver and its potential efficient application toward dye degradation for wastewater treatments. ACS Sustain Chem Eng 3(12):3130
101. Ahmad N, Sultana S, Azam A, Sabir S, Khan MZ (2017) Novel bio-nanocomposite materials for enhanced biodegradability and photocatalytic activity. New J Chem 41:10198
102. Mitra M, Ghosh A, Mondal A, Kargupta K, Ganguly S, Banerjee D (2017) Facile synthesis of aluminium doped zinc oxide polyaniline hybrids for photoluminescence and enhanced visible light assisted photo-degradation of organic contaminants. Appl Surf Sci 402:418
103. Eskizeybek V, Sarı F, Gülce H, Gülce A, Avcı A (2012) Preparation of the new polyaniline/ZnO nanocomposite and its photocatalytic activity for degradation of methylene blue and malachite green dyes under UV and natural sun lights irradiations. Appl Catal B 119–120:197–206
104. Ghaly HA, El-Kalliny AS, Gad-Allah TA, Abd El-Sattar NE, Souaya ER (2017) Stable plasmonic Ag/AgCl-polyaniline photoactive composite for degradation of organic contaminants under solar light. RSC Adv 7:12726
105. Thekkayil R, Gopinath P, Jon H (2014) Enhanced photocatalytic activity of polyaniline through noncovalent functionalization with graphite oxide. Mater Res Express 1:045602

106. Miao J, Xie A, Li S, Huang F, Cao J, Shen Y (2016) A novel reducing graphene/polyaniline/cuprous oxide composite hydrogel with unexpected photocatalytic activity for the degradation of Congo red. Appl Surf Sci 360:594
107. Ahuja P, Ujjain SK, Arora I, Samim M (2018) Hierarchically grown NiO-decorated polyaniline-reduced graphene oxide composite for ultrafast sunlight-driven photocatalysis. ACS Omega 3:7846
108. Wu H, Lin S, Chen C, Liang W, Liu X, Yang H (2016) A new ZnO/rGO/polyaniline ternary nanocomposite as photocatalyst with improved photocatalytic activity. Mater Res Bull 83:434
109. Biswas MRUD, Cho KY, Na JD, Oh W-C (2019) Highly electro-conductive graphene-decorated PANI-$BiVO_4$ polymer-semiconductor nanocomposite with outstanding photocatalytic performance. Mater Sci Eng B 251:114469
110. Zhao J, Biswas MRUD, Oh WC (2019) A novel $BiVO_4$-GO-TiO_2-PANI composite for upgraded photocatalytic performance under visible light and its non-toxicity. Environ Sci Pollut Res 26:11888
111. Zhang F, Zhang Y, Zhang G, Yang Z, Dionysiou DD, Zhu A (2018) Exceptional synergistic enhancement of the photocatalytic activity of SnS2 by coupling with polyaniline and N-doped reduced graphene oxide. Appl Catal B Environ 236:53
112. Ahmad N, Sultana S, Sabir S, Zain Khan MZ (2020) Exploring the visible light driven photocatalysis by reduced graphene oxide supported Ppy/CdS nanocomposites for the degradation of organic pollutants. J Photochem Photobiol A Chem 386:112129
113. Zhang L, Jamal R, Zhao Q, Wang M, Abdiryim T (2015) Preparation of PEDOT/GO, PEDOT/MnO_2, and PEDOT/GO/ MnO_2 nanocomposites and their application in catalytic degradation of methylene blue. Nanoscale Res Lett 10:148
114. Sun M, Li W, Sun S, He J, Zhang Q, Shi Y (2015) One-step in situ synthesis of graphene-TiO2 nanorod hybrid composites with enhanced photocatalytic activity. Mater Res Bull 61:280–286
115. Liu S, Sun H, Suvorova A, Wang S (2013) One-pot hydrothermal synthesis of ZnO-reduced graphene oxide composites using Zn powders for enhanced photocatalysis. Chem Eng J 229:533–539. ISSN 1385–8947
116. Durmus Z, Kurt BZ, Durmus A (2019) Synthesis and characterization of graphene oxide/zinc oxide (GO/ZnO) nanocomposite and its utilization for photocatalytic degradation of basic fuchsin dye. Chem Select 4(1):271–278
117. Rabieh S, Nassimi K, Bagheri M (2016) Synthesis of hierarchical ZnO–reduced graphene oxide nanocomposites with enhanced adsorption–photocatalytic performance. Mater Lett 162:28
118. Azarang M, Shuhaimi A, Yousefi R, Jahromi SP (2015) One-pot sol-gel synthesis of reduced graphene oxide uniformly decorated zinc oxide nanoparticles in starch environment for highly efficient photodegradation of Methylene Blue. RSC Adv 528:21888
119. Guo S, Zhang G, Guo Y, Yu JC (2013) Graphene oxide-Fe_2O_3 hybrid material as highly efficient heterogeneous catalyst for degradation of organic contaminants. Carbon 60:437
120. Feng Y, Yao T, Yang Y, Zheng F, Chen P, Wu J, Xin B (2018) One-step preparation of Fe_2O_3/reduced graphene oxide aerogel as heterogeneous Fenton-like catalyst for enhanced photo-degradation of organic dyes. Chem Select 3:9062
121. Aawani E, Memarian N, Dizaji HR (2019) Synthesis and characterization of reduced graphene oxide–V2O5 nanocomposite for enhanced photocatalytic activity under different types of irradiation. J Phys Chem Solids 125:8
122. Ma N, Chen A, Bian Z, Yang Y, Wang H (2019) In situ synthesis of a cadmium sulfide/reduced graphene oxide/bismuth Z-scheme oxyiodide system for enhanced photocatalytic performance in chlorinated paraben degradation. Chem Eng J 359:530
123. Fakhri A, Naji M (2017) Degradation photocatalysis of tetrodotoxin as a poison by gold doped PdO nanoparticles supported on reduced graphene oxide nanocomposites and evaluation of its antibacterial activity. J Photochem Photobiol B Biol 167:58

124. Wang X, Zhang J, Zhang K, Zou W, Chen S (2016) Facile fabrication of reduced graphene oxide/CuI/PANI nanocomposites with enhanced visible-light photocatalytic activity. RSC Adv 6:44851–44858

125. Feng J, Hou Y, Wang X, Quan W, Zhang J, Wang Y, Li L (2016) In-depth study on adsorption and photocatalytic performance of novel reduced graphene oxide-$ZnFe_2O_4$-polyaniline composites. J Alloys Compd 681:157–166

Chapter 5
Polymer Nanocomposite Films Based on Two-Dimensional Materials for Photocatalytic Applications

Jyoti Gupta, Prachi Singhal, and Sunita Rattan

Abstract 2D material-based polymer nanocomposites are potential contenders for the development of photocatalytic structure for ecological remediation. It is a tactical way in the direction of the advancement of innovative photocatalytic materials involving synergistic combination of the distinctive properties of 2D nanostructures along with the outstanding advantages offered by polymer. The exclusive properties of 2D materials which make them promising photocatalytic materials include their tunable atomic thickness, larger surface-to-volume ratio, superior electron mobility and high light absorption capacity. Further, the band gap of 2D materials can be altered through various modifications to extend the photo-response range from UV (∼390 nm) to visible light (∼480 nm). Combination of polymers with 2D materials address the challenges confronted by 2D materials related to stability, agglomeration, and recovery issues. Polymers help in immobilization, provide chemical, mechanical and environmental stability to photocatalytic material, simplify the recovery of photocatalytic material which overall reduces the commercial cost of the material. The chapter recaps the state-of-the-art construction of 2D material-based polymer nanocomposites. The emphasis is on the recent innovations in photocatalytic functions of 2D material/polymer nanostructures involving graphene, 2D transitional metal dichalcogenides (TMDs), and transition metal oxides (TMOs).

Keywords Atomically thin two-dimensional materials · Polymer · Photocatalytic applications

---

J. Gupta · P. Singhal · S. Rattan (✉)
Amity Institute of Applied Sciences, Amity University, Sector 125, Noida,
Uttar Pradesh 201313, India
e-mail: srattan@amity.edu

S. Garg and A. Chandra (eds.), *Green Photocatalytic Semiconductors*,
Green Chemistry and Sustainable Technology,
https://doi.org/10.1007/978-3-030-77371-7_5

5.1 Introduction

Rapid industrialization and constantly increasing population are responsible for worsening the problem of environmental pollution. Organic contaminants such as dyes, the common byproduct contaminants including other industrial contaminants in the industrial sector in water, could be a terrible hazard to human health. Traditional practices of organic contaminant degradation include adsorption technique, filtration, membrane separation, coagulation, flocculation, ion exchange, oxidation, biodegradation, and microbial treatment. But the degradation efficiency obtained is still insufficient through these techniques. For partial or complete conversion of organic dyes (into non-harmful products), recently the most sustainable way out is photocatalytic oxidation, one of the advanced techniques which constitutes a green, sustainable, and economical chemical processes [1, 2].

The photocatalytic oxidation phenomenon includes photochemical reactions decomposing organic contaminants into carbon dioxide (CO_2) and water or non-toxic byproducts, under the presence of sunlight illumination and a photocatalyst. The utilization of efficient photocatalysts to directly convert the sunlight energy into chemical energy is a long-term solution to address the current environmental challenges. Photocatalyst, mostly metal oxides or sulfides as semiconductors owing to their typical structure, produces electron–hole pairs upon sunlight illumination (abundant natural energy resource) with an appropriate wavelength, followed by their movement toward photocatalyst surface and generates hydroxy radicals and other superoxide anions which have high oxidizing power and capable of oxidizing organic pollutants into harmless substances [3, 4].

Conventional photocatalysts such as TiO_2, CdS, Ag, etc. among many others pose challenges in terms of efficiency and economics that remain to be overcome. Different photocatalytic materials were described such as metal oxides-based semiconductors, sulfides, nitrides, and silver-based materials applied for various photocatalytic phenomenon such as selective organic synthesis, [5] splitting water [6, 7] as well as degradation of organic pollutants [8]. The intrinsic drawbacks of the conventional semiconductors as (a) large bandgap energy can respond to ultraviolet (UV) light of higher energy, which account for only $\sim 4.0\%$ in the solar spectrum, (b) lower photo-generated carrier separation and migration efficiency, (c) insufficient active sites and the relatively delayed catalytic kinetics, photocatalytic redox reactions scarcely occurred even on reaching the photo-induced carriers to the exterior side of the catalyst. Therefore, it is considerable to concern the design of semiconductors for obtaining high efficiency photocatalytic activity. Photocatalysis phenomenon is gazing at innovative materials, exploring strategies to enhance photo absorbance, charge carrier lifetimes, stability, etc.

In recent decades, upcoming two-dimensional (2D) material-based photocatalyst system has generated new opportunity in the field of photocatalysis because of their fascinating properties as tunable structure, surface area, etc. that are absent in the corresponding bulk counterparts [3, 4]. The large defect-free surface of 2D inorganic material sheets plays a crucial role in minimizing the charge recombination and thus strengthening the photocatalytic efficacy. Intense exploration activities have been devoted for the optimization of 2D material-based photocatalytic material to achieve high absorptivity of visible light, less charge recombination, narrowing band gap, etc. A significant approach to get an optimized and high-performance photocatalytic material is the growth of coupled structure formed by the blending various 2D materials to attain a typical product with synergistic blending between constituent properties. Unusually strong electronic coupling is possible between 2D inorganic nanosheets and other hybridized components of 2D material-based nanocomposites as all the component ions of these materials are exposed on the interfacial surfaces.

Further, combination of 2D nanoheterostructures with polymer substrates significantly improves the photocatalytic action (PA) of the fabricated photocatalyst. The immobilization of the 2D nanoheterostructures catalyst in a specific polymer substrate provide environmental stability, chemical inertness and resistance to ultraviolet radiations, mechanical stability, reusability, low cost, ease of availability, etc. Further, use of conjugated polymers, which exhibits unique conjugation mechanism, remarkable charge-transporting properties, high thermal and photochemical stability, photosensitizing property, helps in lowering band gap and widening the absorbing range of photocatalytic material toward visible light. Thus, 2D material/polymer nanocomposite is developed as a photocatalytic material through optimization which provides a chance of facile separation and reuse of material, also reduces the cost of procedure and eliminates post treatment separation process.

This chapter will focus on 2D material-based polymer nanocomposite photocatalysts and their application for the photocatalytic decomposition of waste-water organic pollutants. It also focuses on the impact of various factors such as concentration of dyes, pH, light intensity, and contact time [9–12].

This review will specifically focus on polymer nanocomposites photocatalyst containing most popular 2D structure as graphene oxide (GO), reduced graphene oxide (RGO), two-dimensional metal dichalcogenides (MoS_2, WS_2, $MoSe_2$, WSe_2 etc.) and two-dimensional metal oxides (ZnO nanosheets, TiO_2 nanosheets, WO_3, CeO_2, MoO_3 etc.) for good photocatalytic degradation of organic pollutants under the UV or visible light.

5.2 Characteristics of an Efficient Photocatalytic Material

The basic technical requirements for an efficient photocatalyst are (a) low recombination rate of electron and hole (e^-h^+) pairs, (b) lesser bandgap energies, (c) unconstrained movement of charge carriers, (d) higher surface area, (e) higher number of exposed active locations and (f) have ability to efficiently yield and utilize photons in the visible range to create electron–hole pairs. Further, it should be cost effective, prerequisites to energy efficient and operationally feasible.

Conventional photocatalysts reported in literature such as ZnO, TiO_2 have some shortcomings as (a) increased band gap, making the materials appropriate for mainly absorption in UV range instead of visible range [13]; (b) only having the capacity to catalyze either reduction or oxidation reaction at a time, leading to their unsuitability for dual function overall water splitting catalysts [14]; (c) their higher charge recombination rates in bulk medium and on the surface, resulting in lower activity [15]; and (d) inaccessibility of active sites lying in bulk material [16].

Therefore, 2D materials such as transition metal oxides (TMOs), transition metal dichalcogenides (TMDs), graphene derivatives have been investigated as new and more efficient photocatalytic materials. For example, visible light-driven TMOs, such as WO_3, MoO_3 and V_2O_5, have narrower band gap ranging from 2.6 to 3.0 eV, thus can absorb in visible range and thus promotes higher absorption. Further, their better electron transport properties enhance charge separation in TMOs. But the problem lies in the band gap, not suitable for effective photocatalytic redox reactions due to their low CB positions, resulting in ineffective consumption of photo-induced electrons. Thus, hybrid structures involving combination of different 2D materials are needed.

5.3 Two-Dimensional (2D) Nanosheet Materials

The 2D nanosheets are highly anisotropic crystalline structures having thickness in the range of subnanometer to few nanometer and lateral dimension in micrometers range. Depending upon the synthesis method of 2D materials, these consist of 1–10 stacked monolayers.

5.3.1 2D Materials for Photocatalytic Applications

The layered 2D materials are reported as promising photocatalyst alternatives as sheet-like structure possess exceptional electrical, thermal, and mechanical properties; maximize the light absorption with ultrafast transfer of photo-induced charges and more surface-active spots for the development of multijunctions [17–19]. The coupled structures enhance light absorption capability and results in narrower bandgap energy [20, 21].

First known example of 2D material is graphene that exhibits a sp^2 bonded hexagonal packed lattice that exhibits many interesting characteristics as exceptional mechanical strength, superior thermal conductivity, outstanding transparency, a huge specific surface area, and excellent charge transport [22–24]. Graphene and other graphene modifications (e.g., GO and RGO) have stimulated curiosity in the fabrication of high-performance graphene-based composite materials to induce some positive effects on the PA of catalysts by creating synergies among carbon and the semiconductor [25–27].

Beside graphene derivative, some other 2D material nanosheets with semiconducting nature can be used for photocatalytic active components for hybrid photocatalysts nanostructures. The 2D nanosheet-based hybrid photocatalysts reported in literature can be classified broadly into following five categories as shown in Fig. 5.1—(a) TMO nanosheet-based photocatalysts, (b) layered double hydroxide (LDH) nanosheet-based photocatalysts, (c) TMD nanosheet-based photocatalysts, (d) g-C_3N_4 nanosheet-based photocatalysts, and (e) other types of 2D nanosheet-based photocatalysts including black phosphorus, metal carbide (MXene), bismuth oxyhalide, and boron nitride. The exposed active site of 2D photocatalyst, fast charge transfer phenomenon and strong electronic coupling are the advantages of 2D nanosheets as illustrated in Fig. 5.1. The present chapter will focus on TMOs nanosheet-based photocatalysts, TMD-based photocatalysts and graphene-based photocatalysts.

5.3.2 2D Transition Metal Oxides (TMO's)

TMOs are made up of transition metal and oxygen atoms, where oxygen atoms are bounded with central transition metal. Different types of crystal structure are found for TMOs such as monoxide (NiO), di-oxide (MnO_2), tri-oxide (WO_3) perovskite ($LaNiO_3$), spinel ($NiCo_2O_4$), etc. It was first attempted in 1990s to exfoliate TMOs

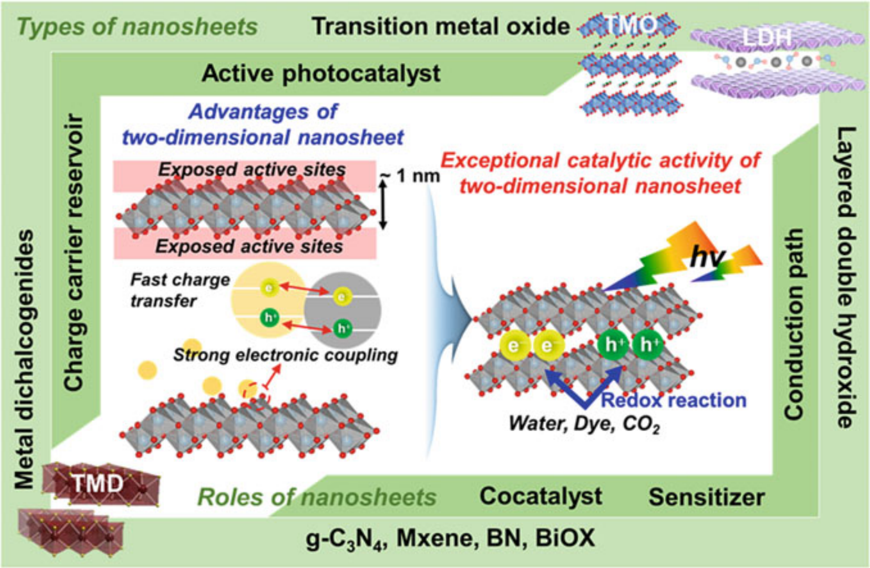

Fig. 5.1 Classification of 2D nanosheets and their advantages. Adapted with permission from Ref. [28]. Copyright 2019 Elsevier B.V.

to form flexible 2D TMOs which display excellent characteristics for various technical applications [29]. Some of the 2D TMOs include Mn, Ta, Rh oxides. Some of the TMOs as molybdenum oxide (MoO_3), vanadium oxide (V_2O_5), tungsten oxide (WO_3), etc. exist naturally in layered formed and can be easily exfoliated to 2D TMOs. Other includes perovskites, which can also be stacked in 2D layered form through bottom-up synthesis techniques. The high surface area, high chemical and photochemical stability, tunable electronic structure, and exceptional physiochemical, optical properties of 2D TMOs facilitate their photocatalytic action. Polarizable oxygen ions provide non-uniform charge distribution responsible for exceptional surface and interfacial properties and help in coulombic interactions with neighboring ions. These polarizable groups can change the stoichiometry followed by change in electronic properties, i.e., bandgap structure can be tuned such as TMO's semiconductors can have sizable band gaps such as WO_3: 2.6 eV, MoO_3: 3.2 eV, etc. [30]. Transition metal cations can adopt different charge states and thus binding configurations can be altered. The interfacial properties of 2D TMOs are desirable for coulombic interactions when coupled with other semiconducting materials to fabricate a multijunction semiconducting material. 2D TMOs have rich and reversible acid–base redox property, helpful in photocatalytic activities [31–34].

Some examples of the 2D TMOs explored for photocatalytic applications include TiO_2, MnO_2, TaO_3, $Ca_2Nb_3O_{10}$, ZnO, Bi_2WO_6, WO_3, $NaBiO_3$, $SnNb_2O_6$ etc. used for hydrogen–water splitting, CO_2 conversion under effective consumption of solar radiation and efficient photocatalytic decomposition of organic contaminants such as dyes, phenol, etc. [6, 35–44].

5.3.3 2D Transition Metal Dichalcogenides (TMD's)

TMDs are made up of hexagonal metal atoms (M) and two layers of chalcogen layers (X) with a MX_2 stoichiometry. Various types of combination of transition metal (Mo, W, Nb, Re, Ni, or V) and chalcogenides (S, Se, or Te) create 40 different categories. Hexagonal packed layer of transition metal is sandwiched between chalcogen layers. Each layer has thickness $\sim$ 6–7 A°. Sandwitched layer is coupled with weak van der walls forces, whereas intralayer is coupled with covalent bonds. TMDs such as cadmium sulfide (CdS) and zinc sulfide (ZnS) are the two most reported materials [44–48]. CdS (2.4 eV) provides better results as compared to other TMO-based photocatalysts. Generally used TMDs (MoS_2, $MoSe_2$, WS_2, and WSe_2) undergo transition from indirect in the bulk and direct in the monolayer as shown in Fig. 5.2 [49].

TMDs provide band gap in wide range 1–2 eV, more suitable for photocatalytic degradation under UV–visible light [50] as depicted in Fig. 5.2. Figure depicts the potential level of CB and VB of TMOs and TMDs, which are favorable for the photocatalytic action.

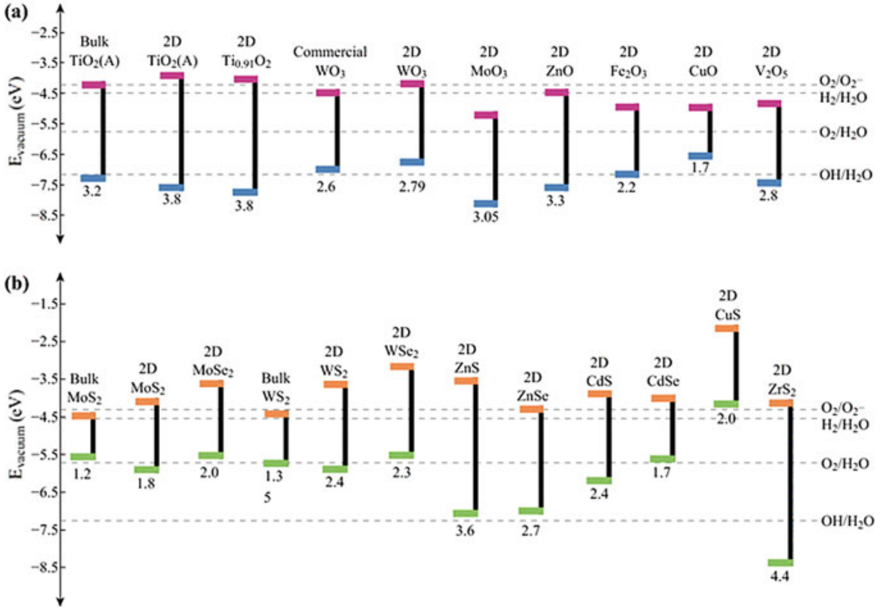

Fig. 5.2 Band structure of some **a** TMOs; **b** TMDs for photocatalytic applications. Adapted with permission [51]. Copyright © 2017, Springer Nature, Haque et al.

5.3.4 *Graphene and Graphene Derivatives (GO and RGO)*

Graphene sheet (GS) represents a honeycomb-like structure consisting of *sp*₂-hybridized C-atoms with exceptional opto-electrical properties, still directly its use as photocatalytic material is restricted owing to its zero band gap, but capable of acting as competent co-catalyst in fabrication of photocatalytic material. Extended π–π conjugation of GS prevents the recombination of photogenerated $e^{-}h^{+}$ pair that further enhances the adsorption of dye molecule [52, 53].

Graphene derivatives also exhibit many advantages over 2D GS which promote the photocatalytic efficiency further. The advantages include improved hydrophilic character, the possibility of optimizing the band gap by adjusting oxygen functionalities, unique electrical properties, better adsorption of positively charged entities, providing reactive centers for photodegradation, etc. [54, 55]. The oxygen functionalities of GO and RGO also help in uniform distribution of other photocatalytic elements on them which proves to be beneficial for the fabrication of graphene-based nanocomposite photocatalytic materials. For example, NiO@PANI/RGO nanocomposites were reported as photocatalytic material involving the influence of oxygen containing functional groups on GO surface on PA [56].

Hence, coupled structures of semiconductor photocatalysts with 2D graphene derivatives accelerates the photocatalytic action (PA) due to the synergistic influences of the constituents and proves to be better photocatalytic materials.

5.4 Factors Effecting the Photocatalytic Activity of 2D Material

2D photocatalyst with thickness reduced to atomic-scale and increase exposed surface area shows variation in structural characteristics such as bond angle and bond length, defect in atomic arrangements, etc. [57–59]. These variations result in modified material for efficient photocatalytic applications with superior intrinsic physiochemical properties over the bulk counterpart. Major intrinsic changes include quantum confinement effect (QCE) and density of states (DOS) [60]. QCE leads to change in VB and CB potential variation and wider band gap suitable for carrying out the required redox reactions at the catalyst surface. Further, enhanced DOS aids the speedy transfer of photo-induced charges and thus reduces the rate of charge recombination.

5.5 Challenges

TMOs, TMDs or graphene are considered as competent 2D structures for photocatalytic functions. However, they suffer from number of intrinsic drawbacks that limit their PE and their practical applications as efficient photocatalyst. For example, it is challenging to enhance the thin 2D material stability and to control its structure and defect density during the synthetic procedure. The electron–hole pair (e^-h^+) recombination is still significant in 2D materials with respect to the photocatalytic application and redox potentials are insufficient for the dye decomposition. The 2D materials can be oxidized easily through the photogenerated holes which lead to the deterioration of the photocatalytic material [61–64].

To clear off the shortcomings, 2D materials can be coupled with other semiconductors to obtain optimized structure for maximum utilization of solar energy. Coupling of 2D materials to form heterojunctions proves to be an effective means of enhancing the photocatalytic activity by promoting charge carrier separation and extending visible light absorption range.

5.6 Methods to Increase the Photocatalytic Efficiency (PE) of 2D Structures

Light harvesting, charge separation and interfacial catalysis reactions are three main crucial factors which must be adjusted to enhance the PA of 2D material-based photocatalysts.

1. Light harvesting: Most of the reported photocatalyst have band gap suitable for excitation through UV light with higher energy, which accounts for a narrow portion of the solar light (while visible light accounts for 52%) (Fig. 5.3). Thus, one important tactic to improve the PA includes the modification of bandgap positions of 2D semiconductors to below 3 eV, which tune absorption scale of the photocatalyst toward visible portion of the sunlight.
2. Charge separation and transfer: After illumination by light radiation, the photogenerated electrons (e^-) and holes (h^+) will move to the exterior side of semiconductors. However, most of the photo-induced e^-h^+ are recombined during migration process that largely restricting the further enhancement of photocatalytic performance. Heterojunction design with other components exhibited as a realistic approach to reduce charge recombination rate. Moreover, photocatalytic action could also be improved by the assembly of nanoscale units into 3D functional architectures, which are beneficial in terms of enhancing light adsorption and carrier and transfer.

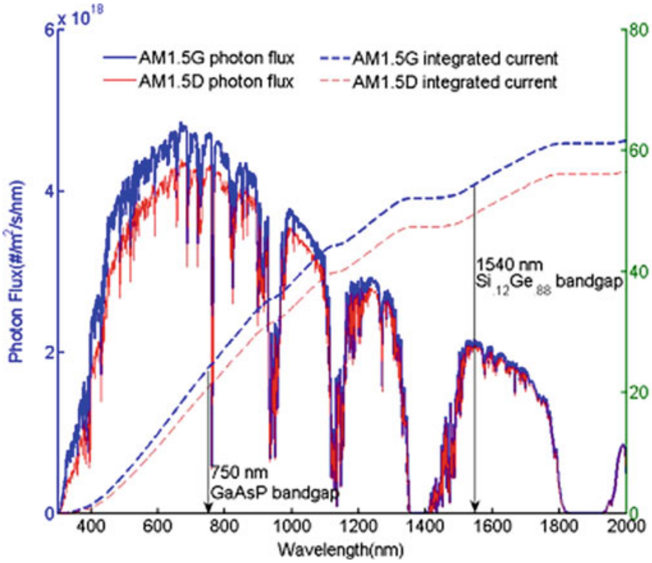

Fig. 5.3 Solar spectrum (red) and photon flux curve (in blue) versus wavelength and optical band gap. Reproduced with permission from Ref. [65]. Copyright @ 2016 Elsevier B.V.

3. Surface reactive sites: Owing to insufficient reactive sites and the relatively delayed catalytic kinetics of semiconductors, photocatalytic redox reactions hardly occurred even when the photo-generated carriers reach to the surface of catalyst. Therefore, it is significant to concern the design of semiconductors with high efficiency by increasing the reactive sites at surface of 2D materials.

2D materials allow achieving these crucial features to enable high photocatalytic efficiency (PE) through different procedures such as doping, surface sensitization, coupling, improving electrical conductivity, increasing electrocatalytic reactive sites, increasing photostability, constructing nanostructure (Fig. 5.4). All these modifications can be simultaneously achieved through *fabrication of multijunction in the form 2D material-based nanohybrid structures.*

5.7 Two-Dimensional (2D) Nanosheet-Based Hybrid Nanostructure Materials

Hybrid nanostructure fabrication provides the most feasible way to optimize the crucial constraints and to investigate highly efficient photocatalytic materials [66–70]. 2D materials with thickness ranging in few nanometers, large lateral dimensions, diverse and tunable chemical structure are most efficient building units for development of hybrid nanostructures. Coupling 2D materials with other semiconductor materials by forming well-matched heterogeneous junctions can synergistically improve the PE of the fabricated materials. The exposed interfacial surfaces of 2D nanosheets are great advantage because they provide a strong electronic coupling [71, 72]. Apart from this, the exfoliation of nanosheets shows extra advantage of defect-free surface which helps in minimizing the charge recombination centers and improves the photocatalytic action [69, 70].

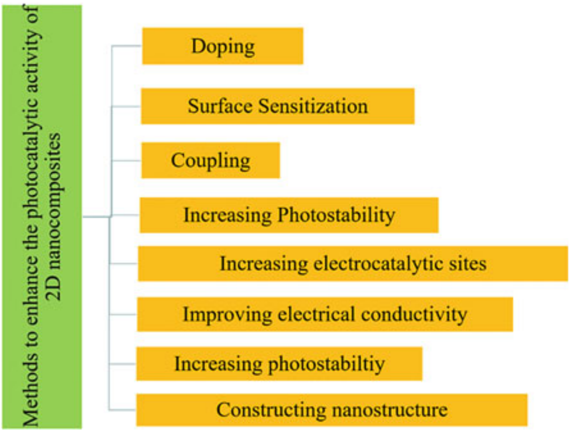

Fig. 5.4 Approaches for advanced photocatalytic activity of 2D nanocomposites

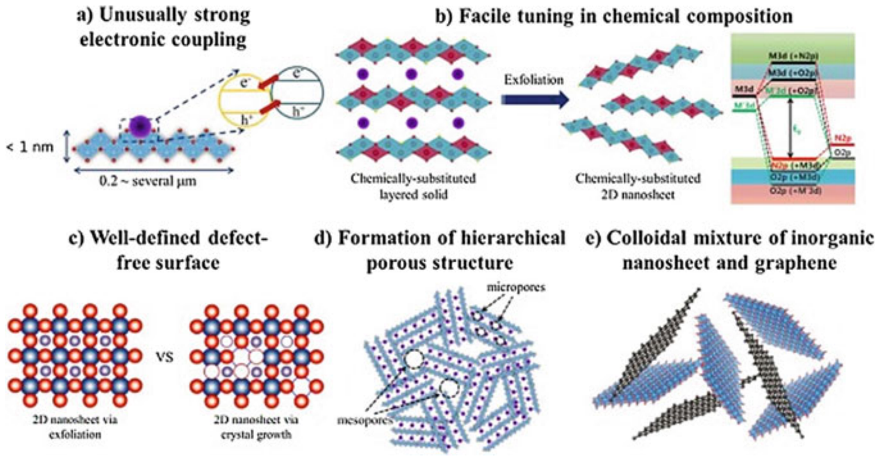

Fig. 5.5 Unique and beneficial features of 2D inorganic nanostructures as fundamental units for hybrid photocatalytic structures. Reproduced with permission from Ref. [73]. Copyright 2019 Elsevier B.V.

Figure 5.5 has shown the exfoliated nanosheets that have anisotropic 2D structure with large surface area and atomic level thickness. The chemical reaction and electronic coupling between hybridized species occur at inadequate interfacial regions [74, 75]. The heterostructures of thin 2D nanosheets with other nanomaterials can persuade extraordinarily strong electronic coupling and provides required opto-electronic properties. This type of coupling tunes the electronic structures which result in optimization of their functionalities.

Figure 5.5b represents diverse electro-optical properties achieved in 2D nanosheets due to wide spectrum of chemical compositions and their crystal structure [76–78]. Chemical substitution is a controlled way to achieve various chemical compositions in 2D nanosheets. The layered material is chemically substituted in 2D nanosheets for exfoliation process [79–81]. Chemical substitution also provides significant modification in interband states of electronic structure and bandgap energy [82–84]. This chemical modification also improves the electronic connection between the blended species and optimizes the electrochemical and catalytic functionalities of the resulting hybrid materials.

Well-defined defect-free surface is another advantage of exfoliated 2D nanosheets. Generally, large number of surface defects creates during nanocrystal formation. The surface defects are main cause of charge recombination; hence, the photocatalytic efficacy is reduced [85, 86]. Exfoliated 2D nanosheets can be simply modified by changing the layered structure of the pure host material without notable creation of surface defects as shown in Fig. 5.5c [87, 88]. This defect-free nature of exfoliated 2D nanosheets is highly important for photocatalytic activities. As seen from Fig. 5.5d, the hybridization of 2D nanosheets played a vital part in forming the micropores and mesopores structure [89–91]. The hybridized species are selected with appropriate size and bonding nature between hybrid species. This pore structure of 2D nanosheets heterostructure photocatalyst improves the photocatalytic activity. From Fig. 5.5e, the graphene and 2D nanosheets can easily mixed and form colloidal solution as they behave similarly in chemical nature and morphologically [92, 93]. Graphene improves the electrochemical and catalytic activities of 2D nanosheets.

Further, polymers, significantly conducting polymers such as polyaniline (PANI), polyacetylene (Pac), polythiophene (Pth), poly (3, 4-ethylenedioxythiophene) (PEDOT), etc. have also been studied which influences the PA of the photocatalytic nanocomposite materials [94]. The conducting polymers exhibit unique conjugation mechanism, remarkable charge-transporting properties, high thermal and photochemical stability, and they act as organic photosensitizers also. Further, polymer matrix enhances mechanical strength and recyclability of the photocatalytic material. Moreover, the low cost and flexibility of the photocatalyst design constitute appealing features. The merging of the excellent ability of conjugated polymers to absorb in visible light, with exceptional charge transfer characteristics of 2D GS-based materials (GS, GO, and RGO) and semiconductor moieties represents the cutting-edge on water treatment technology [95]. However, the majority of the reported work centered on polymers as PANI, PPy, or PTh, but recent work reported the synthesis of donor–acceptor conjugated polymer-based conducting microporous polymers (CMP) with bandgap energy ranging from 2.95–1.94 eV [96].

Some scientists also make positive use of the insulating polymer for supporting photocatalysts in the form of film, but the work is limited to small reactors [97].

5.8 Mechanism of Action: Photocatalytic Decomposition of Organic Pollutants in 2D Heterostructures

The heterostructure photocatalyst has the property of semiconductors such as electronic band structure consisting of a fully filled VB and unoccupied CB with intrinsic band gap and light absorption capacity which totally depends upon the intrinsic band gap or bandgap energy. The factors important for designing photocatalytic materials involve bandgap energy and band structure. *The photocatalytic reaction to occur needs appropriate band structure with CB and VB positions located in between redox potentials of reactants and products* [98–100].

The basic process of photocatalytic operation is illustrated in Fig. 5.6. In the photocatalytic process, (a) photocatalyst is illuminated by a source of light with appropriate energy and intensity; (b) after irradiation, e^- move from VB to CB, creating h^+ in the VB; (c) some of the photo-induced charge carriers drift to the surface of semiconductor, the energy is released in the form of heat or photons [101]. The electron-accepting species pull out the available electrons in conduction band and generate radical anions; (d) the photo-induced holes in VB with potential lower than that of OH^-/H_2O may interact with surface-bound H_2O or OH^- to

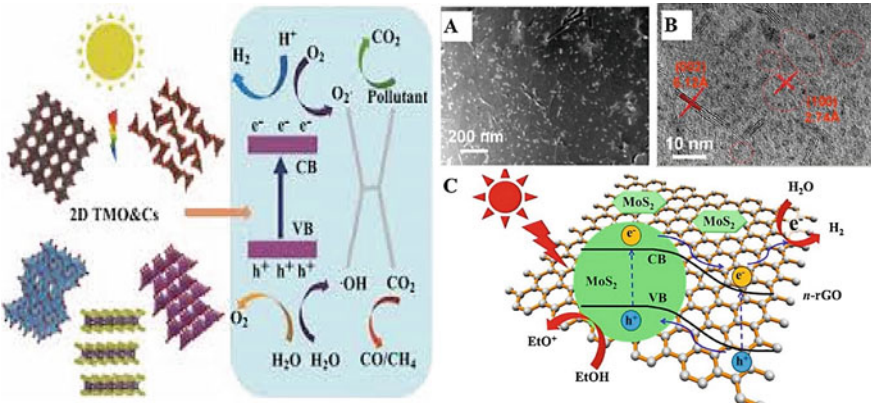

Fig. 5.6 Photocatalytic mechanism pathway of 2D TMDs and TMOs. Adapted with permission [51]. Copyright © 2017, Springer Nature, Haque et al.

produce hydroxyl radicals ($OH^{\bullet}$). The $OH^{\bullet}$ and radical anions act as primary oxidizing species in the photocatalytic oxidation processes while removing the organic compounds such as dyes, pesticides, phenols [102–107]. Therefore, the following parameters must be considered for efficient photocatalytic action on the surface of photocatalyst.

- A source of light with energy in the visible or UV spectrum, or solar energy.
- To generate the (holes) h^+ and (electrons) e^- pairs, a semiconductor catalyst must be capable of absorbing light energy equal to or greater than its bandgap energy cited in [6, 108, 109]

Numerous kinds of hybrid structures for photocatalytic applications are investigated and reported as shown in Fig. 5.7. Z-scheme-based hybrid structure is demonstrated as effective hybrids which constitutes of different semiconducting photocatalytic material with a mediator shuttling the charge carriers [110]. Mediator with redox property plays a major role encouraging the coupling among e^- of one semiconductor and h^+ of an added semiconductor. This reduces the e^-h^+ recombination of each semiconductor and performs photocatalytic activity without use of any sacrificial agents.

Three types of redox mediator such as redox ionic couple, noble metal nanoparticle, and conductive nanosheet are used in Z scheme photocatalyst systems [111–113]. For example, redox mediators are Au noble metal nanoparticles which can help in internal charge transfer between hybridized CdS and g-C_3N_4 materials. In this similar way, Fe^{2+}/Fe^{3+} ions in solution act as redox couple for transferring charge between hybridized material. This process boosts the photocatalytic activity [114]. Like the metal nanoparticles, conductive nanosheets such as RGO act as redox mediator to construct the Z scheme photocatalyst which improves the PA such as H_2 production and O_2 generation [115].

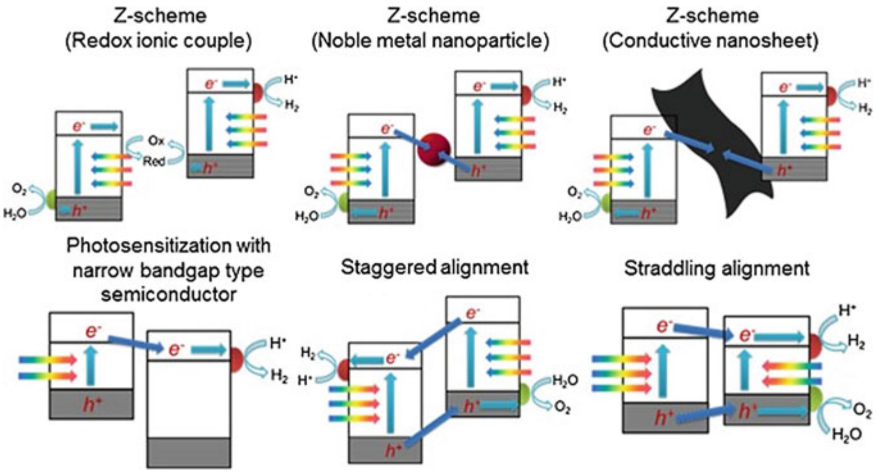

Fig. 5.7 Various types of band structure in 2D materials. Reproduced with permission from Ref. [28]. Copyright 2019 Elsevier B.V.

As observed from Fig. 5.7, the photosensitization of wide bandgap photocatalyst can also be achieved by hybridization with narrow bandgap semiconductor [116–118]. In this process, light is absorbed at lower bandgap photocatalytic structure and chase the internal charge transfer phenomenon from narrow bandgap to wide bandgap photocatalyst under visible light. It leads to separation of electrons (e^{-}) and holes (h^{+}). The life span of charge is increased via the transfer of electrons from narrow bandgap to wide bandgap. The type with type I-straddling band and type II-staggered alignments are other hybrid scheme that improves charge separation and photocatalytic activity [119, 120].

5.9 2D Material-Based Polymer Nanocomposites as Photocatalysts

5.9.1 2D Transition Metal Oxide (TMO)-Based Polymer Nanocomposites

2D TMO-based nanocomposites have been focused for photocatalytic functions as interfacial synergy acting between 2D TMOs and polymer surface, resulting in change in electronic structure beneficial for photocatalytic applications. Nanocomposites facilitate transfer of charge and broaden photo-responsive range for photocatalytic applications.

2D TMO-based photocatalysts were reported with enhanced PA and extended photo response to visible region PTh/TiO_2-Cu nanocomposite, g-C_3N_4/F-TiO_2, etc.

[121, 122]. Photocatalytic Z scheme configurations have been fabricated through coupling 2D materials along with polymer, resulting in appropriate band structures and tendency for degradation of contamination on light exposure. Kaur et al. [123] designed 2D TMO-based photocatalytic material by hybridizing them with polythiophene (PTh). PTh is an excellent conducting polymer with small band gap of ~2.0 eV, which results in photogeneration of electrons on exposure to visible light. Kaur et al. suggest through computational investigation the appearance of discrete band levels in PTh-TMO complex, resulting in interfacial transfer of charge from PTh to TMO CB and restricts charge recombination. Merkulov et al. demonstrated PANI/TiO_2-based photocatalysts, used for degradation of various organic contaminants as pharmaceuticals and pesticides under UV light irradiation [124]. This heterostructure is carried out for photocatalytic degradation under different water bodies: double distilled water, river, and lake. Sulcotrione is showing best photocatalytic action with degradation up to 93.8% under the presence of TiO_2/PANI among all the pollutant. Xu et al. have presented PANI/bismuth oxyhalide photocatalyst in which PANI has improved separation of photo-induced e^- and h^+ and broadens the range of light absorption [125]. PANI will not only widens the light absorption region but also enhances the photocatalytic decomposition efficacy. PANI/$Bi_{12}O_{17}C_{12}$ will decomposed the ciprofloxacin (CIP) higher degradation efficiency as compared to pristine $Bi_{12}O_{17}Cl_2$. Simultaneously, it degraded the RhB than pristine $Bi_{12}O_{17}C_{12}$. Hence, TMO-based polymer nanocomposites not only widen the light response region but also enhanced the PE. The photocatalytic mechanism of PANI/$Bi_{12}O_{17}C_{12}$ is explained in Fig. 5.8. The photo-generated electrons instantly transferred to the $Bi_{12}O_{17}C_{12}$ CB which is having favorable more negative CB position than lowest unoccupied molecular orbital of PANI, resulting into improved PA.

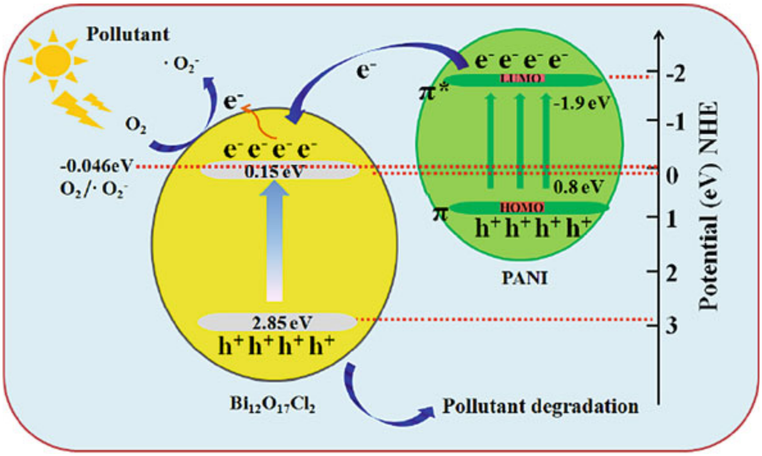

Fig. 5.8 Photocatalytic mechanism for PANI/$Bi_{12}O_{17}C_{12}$ composite under visible light. Reproduced with permission from Ref. [125]. Copyright @ 2018 Elsevier B.V.

The PANI/TiO_2-graphene hydrogel photocatalyst is prepared for photodegradation of organic pollutants [126]. Xu et al. have presented the PANI/gray-TiO_2 photocatalyst for photocatalytic decomposition of RhB [127]. Deng et al. performed single crystal TiO_2 (MS–TiO_2) with PANI for PA [128]. PANI has increased the PA of TiO_2 up to 99.8% in 120 min for RhB and 99.5% in 150 min for MB. Wu et al. have synthesized zinc oxide/reduced graphene oxide (rGO)/PANI and performed the photocatalytic activity on MO (methyl orange) pollutants [129]. Remita et al. reported 1D poly(diphenylbutadyne) (PDPB) which exhibits superior PE for removal of MO and phenol molecules in comparison to simple conjugated PTh, PPy, PANI, etc. polymers [130]. B-BT-1,4-E/TiO_2 nanocomposites were fabricated using conjugated polymer B-BT-1,4-E (poly benzothiadiazole) which showed outstanding PA for CIP (ciprofloxacin) degradation [131] (Table 5.1).

5.9.2 2D Transition Metal Dichalcogenide (TMD)-Based Polymer Nanocomposites

2D heterostructures is synthesized based on monolayer transition metal dichalcogenides (TMDs) and some other 2D nanosheets or other nanomaterials. 2D layered TMD polymer hybrid nanostructures are most important photocatalytic material because of increased number of reaction sites for photocatalytic decomposition of organic dyes and fast transfer of photogenerated excitons.

For example, MoS_2/PANI hybrid structure is used by Saha et al. for degradation of 4-CP and MB. The positive synergistic combination of PANI and MoS_2 enables the transfer of electrons form LUMO of PANI to CB of MoS_2, thus enhancing charge separation and efficient photocatalytic degradation of dyes. Conducting polymer polyaniline (PANI)/BiS_3 heterostructure is synthesized by chemisorption method for photodegradation of methylene blue aqueous solution. BiS_3 is prepared in various weight percentage form (1, 2, 5 and 10 wt%) [146]. The solar-light-driven semiconductor photocatalyst ZnO-MoS_2-RGO is developed by Kumar et al. for the removal of organic dyes from waste-water [147]. 2D MoS_2/RGO nanosheets are synthesized by Zhang et al. by using simple one-step hydrothermal method. In this MoS_2/rGO nanoheterostructure, MoS_2 clusters were strongly intertwined with some RGO sheets. On increasing the amount of RGO, crystalline behavior of MoS_2 is slightly changed by reducing the diameter of crystal which resulted in a large surface area of the hybrid photocatalyst [148]. Jo et al. have presented MoS_2 nanosheets supported TiO_2/g-C_3N_4 semiconductor photocatalyst for the decay of MB in visible range [149]. The photocatalyst displayed improved PA in comparison to other photocatalyst. The exfoliated-hexagonal-WS_2 nanostructure investigated for photo-decomposition of dyes solution with 4 ppm aqueous concentration [150]. The photocatalytic response of 2D/2D BiOCl/WS_2 (BWX) hybrid nanosheets was explored for the photo-decomposition of Malachite Green (MG) and photoreduction of Cr(VI) ion under visible irradiation. Nearly

Table 5.1 2D TMO-based nanocomposites for organic photodegradation

Photocatalyst	Light irradiation	Pollutants	Initial conc. of dye solution, amount of photocatalyst, irradiation time, percentage degradation (%)	References
GR–TiO_2	150 W high-pressure Xe lamp	MB	(1 mg L^{-1}) 180 min	[132]
RGO–SnO_2	350 W Xe lamp	MB	(2.7×10^{-5} M) 360 min	[133]
RGO@ZnO	Simulated solar light	RhB	120 min	[134]
RGO–ZnO	12 W UV lamp	MB	(5.0×10^{-5} M) 130 min	[135]
GR–TiO_2	UV light, 100 W mercury lamp	MO	(10^{-4} mol L^{-1}) 240 min	[136]
RGO–TiO_2–ZnO	300 W Xe lamp	MB	(0.3 mg L^{-1}) 120 min	[137]
α-Fe_2O_3 nanoplate/ graphene composites	Xe light (350 W) irradiation	RhB under		[138]
GO–TiO_2	Visible light 1000 W Xe lamp	MO	(12 mg L^{-1}) 180 min	[139]
RGO–ZnO	UV light	MB	(5 mg L^{-1}) 260 min	[140]
TiO_2 nanosheet/ graphene composite	UV light	RhB	30 ml of 5×10^{-5} mol/L concentration of RhB 30 mg of photocatalyst; 98% degradation after 1 h	[141]
g-C_3N_4/ surface-fluorinated TiO_2 nanosheets	50 W 410 nm LED light irradiation	Methylene blue	100 mL 10 mg/L aqueous solution of MB and 0.1 g photocatalyst 30% g-C_3N_4/F-TiO_2 shows 13.9 times degradation than that of commercial Degussa P25 TiO_2	[142]
TiO_2 nanosheet arrays on carbon fibers	300 W xenon lamp (UV source)	MO	Initial concentration 5 mg L^{-1} Almost complete degradation after 45 min	[143]

(continued)

Table 5.1 (continued)

Photocatalyst	Light irradiation	Pollutants	Initial conc. of dye solution, amount of photocatalyst, irradiation time, percentage degradation (%)	References
Black phosphorus @ TiO_2 hybrid	UV (4 W, 365 nm, visible light (150 W Xe lamp, 420 nm)	Black 5, RhB	Rho B concentration = 3 mg/L, pH 5.5, photocatalyst samples (1 g/L) 92% after ~1 h	[144]
GO/fluorinated TiO_2 nanosheets	UV light irradiation (250 W 365 nm Hg lamp)	MB under	100 mL 10 mg L^{-1} aqueous solution of MB and 0.1 g photocatalysts 96% MB degradation, showing superior catalytic activity to commercial Degussa P25 and pure TiO_2	[145]

98.4% of the MG degradation was achieved over BiOCl/WS_2 (2%) photocatalyst in 45 min of irradiation. BiOCl/WS_2 (2%) hybrid nanosheet catalyst indicated maximum quantum efficiency (EQE) in both the UV and visible regimes [151]. As illustrated in Fig. 5.9, PANI/Bi_2S_3 polymer nanocomposite is used as photocatalytic material under visible light illumination. Bi_2S_3 VB and CB are positioned at +1.3 and −0.1 eV versus NHE, respectively [152], whereas the bandgap potentials of PANI are more negative and positioned at −1.9 and +0.8 eV NHE [153]. The band structure of PANI and Bi_2S_3 is favorable for charge carrier transfer. The photogenerated electrons instantly drift to the Bi_2S_3 CB from the LUMO of PANI, while the holes drift from the VB of Bi_2S_3 to PANI HOMO lowering the charge coupling rate. The holes from VB of Bi_2S_3 with favorable band position (more positive than the standard oxidation potential of O_2/H_2O (1.23 eV vs. NHE [35]) have tendency to combine with H_2O to produce oxygen O_2 and hydrogen ions (H^+). Similarly, the CB potential of Bi_2S_3 is favorable for the conversion of O_2 into hydrogen peroxide (H_2O_2) [154, 155]. Thus, photogenerated electrons and holes results in production of production of $OH^\cdot$ radicals and superoxide anion radicals (O^{-2}) through secondary reactions resulting into photo-decomposition of MB dye molecules. The nanostructures have been evaluated for their PA on MB under visible light illumination. Ninefold increase has been observed in the photocatalytic action of Bi_2S_3/polyaniline nanocomposite. The interfacial coupling between constituents PANI and Bi_2S_3 significantly suppress the recombination of photo-induced e^-h^+ and results in improved PA of the nanocomposites.

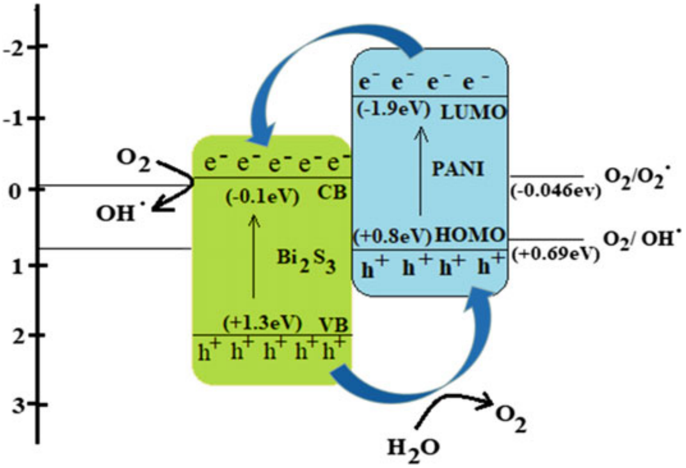

Fig. 5.9 Probable photocatalytic degradation mechanism for PANI/Bi_2S_3 nanocomposite under visible light

Hou et al. synthesized triple-junction C_3N_4/N-doped graphene/MoS_2 which showed a high PA on MB oxidation and reduction of Cr(VI), under visible light [156]. Some other example of TMD-based nanoheterostructures are mentioned in Table 5.2.

5.9.3 2D Graphene-Based Polymer Nanocomposites

In current era, 2D graphene-based materials have been emerged as an efficient contender for photocatalytic applications for the purpose of environmental remediation. A range of 2D graphene and reduced graphene-based composites have been reported in literature for the photocatalytic decay of organic toxins [166–169]. In the last 10 years, ~6000 research papers on 2D GS-based nanocomposites were on Scopus search engine [170].

Thus, the design of 2D GS-based hybrid nanocomposites for photocatalytic applications is one of the favorable ways for the organic pollutant degradation. 2D GS-based hybrid photocatalytic nanocomposite materials includes graphene derivatives with metal oxides, metal–metal oxides, salts, metals, etc. The combination of GS GO or RGO with photoactive materials aims to enhance the PA of the formulated systems by boosting the separation and transfer of photo-generated charges, which constitutes a critical step in photocatalytic reactions. Figure 5.10 represents of various semiconductors coupling at graphene nanosheet surface.

2D graphene-based polymer ternary nanocomposites gained immense attention as photocatalytic materials owing to the unique synergistic combination of the constituent properties. For example, $ZnFe_2O_4$/GR/PANI-based photocatalytic

Table 5.2 2D TMD-based nanocomposites for organic degradation

Photocatalyst	Light irradiation	Pollutants	Initial conc. of dye solution, amount of photocatalyst, irradiation time, percentage degradation (%)	References
MoS_2/TiO_2	Xenon lamp	MB	Time—90 min	[157]
RGO–SnS_2	500 W Xe lamp	Rh B phenol	(10 mg L^{-1}), 120 min (10 mg L^{-1}) 240 min	[158]
RGO–MoS_2	Visible light, 5 W white LED	MB	(60 mg L^{-1}) 60 min	[159]
SnS_2 nanosheets/TiO_2 nanofibers	UV light Visible light	Rh B MO	*kapp* for RhB solution = 0.035 min^{-1}	[160]
SnS_2 nanosheets/ graphene	Visible light Visible light	RhB phenol	12.5 mg of photocatalyst added in 25 mL of an MB (0.01 mM), Rh B (0.01 mM), aqueous solution with maximum of 99% degradation	[161]
P-doped ZnO nanosheets/ MoS_2 layers	Sunlight	MB and RhB	40 mg of the photocatalysts with different MoS_2 loading levels in 40 mL MB aq. solution with of 10 mg/L^{-1}. 95% degradation reported within six minutes with rate constant of 1.413 min^{-1}	[162]
SnS_2 nanosheets/ g-C_3N_4 nanosheets	Visible light irradiation	RhB	100 mL of aq. solution with conc. of 10 mg L^{-1} can remove ~99.8% of RhB after only 20 min of irradiation	[163]
Ultrathin $MoSe_2$ nanosheets/ graphene	Visible light 300-W Xe lamp	photodegradation of organic dyes	15 mg of $MoSe_2$ nanospheres powder used with 20 mL of aq. solutions of RhB (50–100 mg L^{-1}). The maximum adsorption capability of RhB on $MoSe_2$ reached 133 mg g^{-1} in 5 min	[164]
Copper-doped SnS_2 nanosheet-RGO junctions	Visible light irradiation	Photodegradation of MO	10 mg of the photocatalysts used with 20 mL of a 25 ppm aqueous solution of MO, 60% degradation before 30 min	[165]

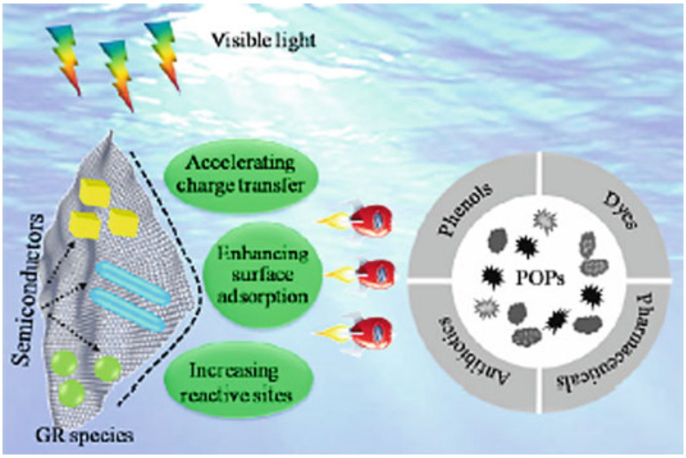

Fig. 5.10 Schematic for 2D graphene-based nanocomposites used for photocatalytic applications. Adapted with permission from Ref. [171] Zhang et al. Copyright @ 2020 Elsevier B.V.

material showed enhanced degradation action on rhodamine B dye [172]. Zhang et al. explored PEDOT/GR/MnO_2 nanocomposite with 7 h of reported time for complete photocatalytic decomposition of MB [173]. PANI@TiO_2/GS nanocomposite was reported showed degradation of methylene blue within 180 min [174].

Significant research work has been reported in this field to develop 2D graphene polymer ternary nanocomposite-based photocatalytic material with optimized material design with the aim to exploit the advantage of constituents' synergistic action. Biswas et al. described the use of bismuth vanadate/graphene oxide/polyaniline ($BiVO_4$/GO/PANI) as visible range photocatalysts, with enhanced electron–hole pair separation efficiency due to coupling at interface of the components [175]. PANI/GR hybrids were fabricated as photocatalyst for decomposition of dyes as MO, RhB, etc. In the PANI/GR NCs GR aids in charge transport through its 2D pi-conjugated structure, photo-induced electrons transit from PANI LUMO level to the CB of GR and thus can be rapidly transferred through 2D network of GR and can participate in degradation redox reactions at the exterior side of the photocatalyst. Further, PANI/GR-based photocatalytic material is synthesized and used for decomposition of RB dye. Mechanism of action involved adsorption of dye, π–π^* stacking of dye molecules and graphene results into enhanced absorption, followed by photoexcitation of electrons in PANI (Fig. 5.11) [176].

The improved PA of the PANI/GR hybrids results from the enhanced e^-h^+ separation and formation of radicals by 2D GSs. Ternary PANI/SnS_2/RGO composite was developed by Zhang et al. which exhibits enhanced PA with facilitated charge transfer due to conductive character of RGO and PANI. Further, redox reactions on RGO and PANI inhibit the photo-corrosion of the semiconductor (Fig. 5.12) [177].

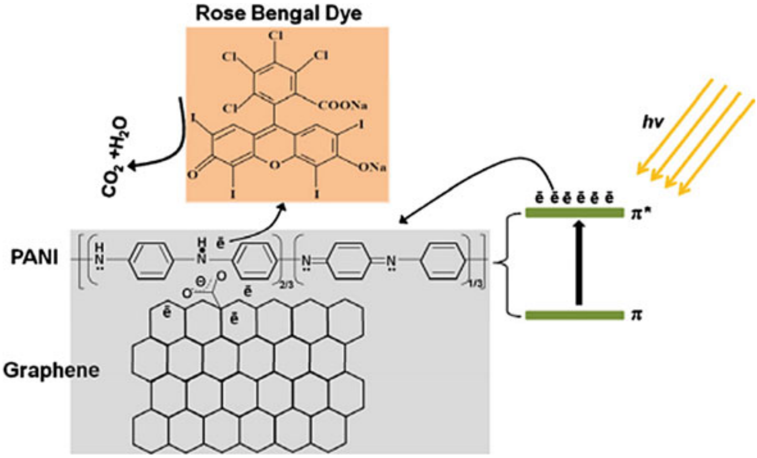

Fig. 5.11 Scheme representing photocatalytic RB dye decomposition by PANI/Gr nanocomposites. Reproduced with permission from Ref. [176]. Copyright @ 2012 Elsevier B.V.

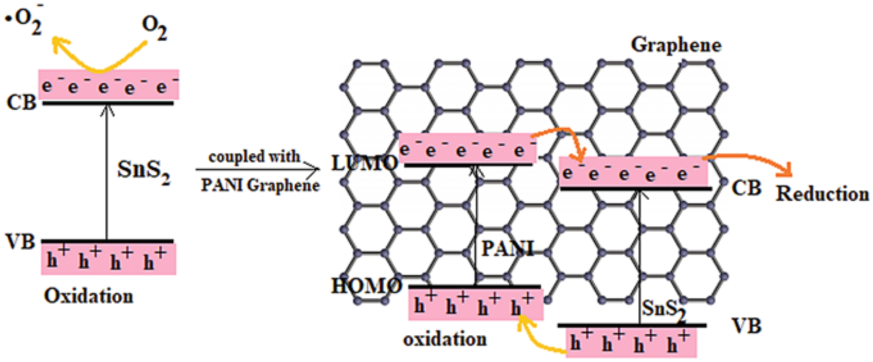

Fig. 5.12 Mechanisms of photocatalytic reduction of Cr(VI) by PANI/SnS_2/NRG composite and SnS_2

Ahuja et al. developed visible light active ternary NiO@PANI/RGO nanocomposites hierarchically structured, i.e., PANI/RGO matrix is intercalated by NiO nanoparticles, showed PA in UV–Vis extended light absorption range with 98% methylene blue (MB) decomposition within 11 min with 0.086 min^{-1} as rate constant [56]. The NiO@PANI/RGO ternary nanocomposites showed effective sunlight utilization due to decreased band gap of 1.9 eV, in comparison to 2.6 and 2.3 eV reported for PANI and PANI/RGO, respectively. Even the ternary nanocomposites reported to maintain consistent PA after 10 cycles.

Adsorption and photocatalytic applications of GN@PANI and CuO/GN@PANI were explored. It was observed that CuO/GN@PANI nanocomposites with low band gap and better charge separation are better adsorbent and photocatalyst than GN@PANI nanocomposites. Some other examples of graphene-based hybrid polymer nanostructures are mentioned in Table 5.3.

Table 5.3 Various Graphene-based polymer nanostructures used in different photocatalytic reactions

Photocatalyst	Light irradiation	Pollutants	Initial conc. of dye solution, amount of photocatalyst, irradiation time, percentage degradation (%)	References
PANI/RGO (RGO—5 wt%)	Visible light	MG RhB CR	Ci—1.7 × 10^{-5} M, V = 50 ml, pH—7, mC—10 mg for each dye. Contact time—15 min for MG, 30 min for RhB and 40 min for CR 99.68% (MG) 99.35% (RhB) 98.73% (CR)	[81]
Reduced graphene oxide/ CuI/PANI	24 visible light wavelength	RhB MO	50 ml RhB or MO (1 × 10^{-5} mol L^{-1}) Complete degradation of RhB after 50 min Complete degradation of MO after 70 min	[178]
PANI/ conjugated graphene	41 visible light	MO, MB, RhB	100% degradation of MO, MB and RhB in 40, 140 and 100 min, respectively	[170]
PANI/graphene oxide	42 300 W Xenon lamp	Rose Bengal dye	50 ml of 20 ppm dye 100 mg dye 95% degradation on 300 min	[179]
MnO_2/PEDOT/ GO	FSL MW1-Y-15 (λ = 254 nm)	MB	92.7% degradation in 420 min	[180]
NiO/PANI/ RGO	Sunlight	MB	8 mg photocatalyst was mixed with the MB solution (10^{-5} M) 98% degradation within 11 min	[56]
CuO/ GN@PANI	104 W visible light	2-Chloro phenol	0.03 g (1.6 cm) of the thin film was hanged in the 150 mL 2-CP solution of 25 mg/L concentration under continuous stirring condition	[181]
GO/PTh composites	4.2 W LED light with CREE XM-L2 lamp	MB	10 mg of photocatalyst 100 MB with conc. 28.2 mg/L	[182]

(continued)

Table 5.3 (continued)

Photocatalyst	Light irradiation	Pollutants	Initial conc. of dye solution, amount of photocatalyst, irradiation time, percentage degradation (%)	References
PTh-WSe_2/NG	300-W Xe lamp	MB	0.05 g of photocatalyst in 50 ml of 1 × 10^{-4} mol/L Completely degraded after 120 min	[183]
PEDOT ZnO@GQDs nanocomposites	UV light source	Rhodamine 6G	50 mg photocatalyst in 50 ml of 10^{-5} M aq. solution of dye The sunlight-irradiated R6G degraded about 85.2% at 300 min then with UV irradiated which was only 69.3% in 500 min	[184]

The chapter delivers a review of photocatalytic materials centered on 2D nanosheet/polymer nanocomposites. 2D TMOs, TMDs and graphene have inherent advantages of having readily tunable electronic structure and diverse physio-chemical properties that enable limitless opportunities for the coupling hybrids in the field of development of efficient and optimized photocatalysts. Further, with advances in polymer chemistry, and the intrinsic merit of band gap engineering with conjugated polymers, designing of 2D nanosheet/polymer nanocomposites plays a significant role in practical photocatalytic applications.

References

1. Zou ZJ, Ye K, Sayama H (2001) Direct splitting of water under visible light irradiation with an oxide semiconductor photocatalyst. Nature 414(6864):625–627. https://doi.org/10.1038/414625a
2. Li Y, Wang H, Xie L, Liang Y, Hong G, Dai HJ (2011) MoS_2 nanoparticles grown on graphene: an advanced catalyst for the hydrogen evolution reaction. Am Chem Soc 133:7296–7299. https://doi.org/10.1021/ja201269b
3. Boyjoo Y, Sun H, Liu J, Pareek VK, Wang S (2017) A review on photocatalysis for air treatment: from catalyst development to reactor design. Chem Eng J 310:537–559
4. Zhang Y, Sivakumar M, Yang S, Enever K, Ramezanianpour M (2018) Application of solar energy in water treatment processes: A review. Desalination 428:116–145
5. Schultz DM, Yoon TP (2014) Solar synthesis: prospects in visible light photocatalysis. Science 343:1239176
6. Kudo A, Miseki Y (2009) Heterogeneous photocatalyst materials for water splitting. Chem Soc Rev 38:253–278
7. Martin DJ, Liu GG, Moniz SJA, Bi YP, Beale AM, Ye JH, Tang JW (2015) Efficient visible driven photocatalyst, silver phosphate: performance, understanding and perspective. Chem Soc Rev 44:7808–7828

8. Di J, Xia JX, Yin S, Xu H, Xu L, Xu YG, He MQ, Li HM (2014) Preparation of sphere-like g-C3N4/BiOI photocatalysts via a reactable ionic liquid for visible-light-driven photocatalytic degradation of pollutants. J Mater Chem A 2:5340–5351
9. Jia J, Wu Y, Ding Z, Li X (2016) Preparation and characterization of carbon nanotubes/chitosan composite foam with enhanced elastic property. Carbohyd Polym 136:1288–1296
10. Rajesh R, Hariharasubramanian A, Sethilkumar A, Ravichandran YD (2012) Radical scavenging and antioxidant activity of hibiscus rosasinensis extract. Int J Pharm Pharm Sci 4 (4):716–720
11. Guirguis OW, Moselhey MTH (2012) Thermal and structural studies of poly (vinyl alcohol) and hydroxypropyl cellulose blends. Nat Sci 4(1):57–67
12. Gupta J, Singhal P, Rattan S (2020) Chitosan/Nanographite platlets (NGPs)/ Tungsten trioxide (WO3) Nanocomposites for visible light driven photocatalytic applications. Springer Proc Phys Book 256:23–34
13. Lee YY, Jung HS, Kang YT (2017) A review: effect of nanostructures on photocatalytic CO_2 conversion over metal oxides and compound semiconductors. J Carbon Dioxide Util 20:163–177
14. Wang Q, Hisatomi T, Suzuki Y, Pan Z, Seo J, Katayama M, Minegishi T, Nishiyama H, Takata T, Seki K (2017) Particulate photocatalyst sheets based on carbon conductor layer for ffficient Z-Scheme pure-water splitting at ambient pressure. J Am Chem Soc 139:1675–1683
15. Hisatomi T, Kubota J, Domen K (2014) Recent advances in semiconductors for photocatalytic and photoelectrochemical water splitting. Chem Soc Rev 43:7520–7535
16. Su T, Shao Q, Qin Z, Guo Z, Wu Z (2018) Magnetic switch of permeability for polyelectrolyte microcapsules embedded with Co@ Au nanoparticles. ACS Catal 8:2253–2276
17. Li Y, Li YL, Sa B, Ahuja R (2017) Review of two-dimensional materials for photocatalytic water splitting from a theoretical perspective. Catal Sci Technol 7:545–559
18. Acar C, Dincer I, Naterer GF (2016) Review of photocatalytic water-splitting methods for sustainable hydrogen production. Int J Energy Res 40:1449–1473
19. Tewari VK, Zhang Y (2015) Modeling, characterization, and production of nanomaterials. Woodhead Publishing, Cambridge, UK, pp 477–524
20. Peng R, Ma Y, Huang B, Dai Y (2019) Two-dimensional Janus PtSSe for photocatalytic water splitting under the visible or infrared light. J Mater Chem A 7:603–610
21. Wang J, Waters JL, Kung P, Kim KM, Kelly JT, McNamara LE, Hammer NI, Pemberton BC, Schmehl RH, Gupta A (2017) A facile electrochemical reduction method for improving photocatalytic performance of α-Fe_2 O_3 photoanode for solar water splitting. ACS Appl Mater Interfaces 9:381–390
22. Novoselov KS, Geim AK, Morozov SV, Jiang D, Zhang Y, Dubonos SV, Grigorieva IV, Firsov AA (2004) Electric field effect in atomically thin carbon films. Science 306 (5696):666–669
23. Geim AK, Novoselov KS (2007) The rise of graphene. Nat Mater 6(3):183–191
24. Geim AK (2009) Graphene: status and prospects. Science 324(5934):1530–1534
25. Li Q, Guo B, Yu J, Ran J, Zhang B, Yan H, Gong J (2011) Highly efficient visible-lightdriven photocatalytic hydrogen production of CdS-cluster-decorated graphene nanosheets. J Am Chem Soc 133:1078–10884
26. Jia L, Wang DH, Huang YX, Xu AW, Yu HQ (2011) Highly durable N-doped graphene/CdS nanocomposites with enhanced photocatalytic hydrogen evolution from water under visible light irradiation. J Phys Chem C 115:11466–11473
27. Zhang H, Lv X, Li Y, Wang Y, Li J (2010) P25-graphene composite as a high performance photocatalyst. ACS Nano 4:380–386
28. Jo YK, Lee JM, Son S, Hwang SJ (2019) 2D Inorganic nanosheet-based hybrid photocatalysts:design, applications, and perspective. J Photochem Photobio C Photochem Rev 40:150–190
29. Rao CNR, Raveau B (1998) Transition metal oxides. Wiley–VCH, New York
30. Fierro JLG (ed) (2006) Metal oxides: chemistry and applications. CRC Press, Boca Raton

31. Jackson SD, Hargreaves JSJ (2009) Metal oxide catalysis. Wiley–VCH, Weinheim, Germany
32. Cox PA (2010) Transition metal oxides: an introduction to their electronic structures and properties. Oxford University Press, New York
33. Gong Y, Zhou MF, Andrews L (2009) Spectroscopic and theoretical studies of transition metal oxides and dioxygen complexes. Chem Rev 109:6765–6808
34. Payne DJ (2008) The electronic structure of post–transition metal oxides. Ph.D. thesis, University of Oxford, Oxford, UK
35. Pârvulescu VI, Marcu V (2006) Surface and nanomolecular catalysis (Richards R (ed)). CRC Press, Boca Roton, Florida
36. Anpo M, Dohshi S, Kitano M, Hu Y, Takeuchi M, Matsuoka M (2005) The preparation and characterization of highly efficient titanium oxide-based photofunctional materials. Ann Rev Mater Res 35:1–27
37. Krol RV, Liang Y, Schoonman J (2018) Solar hydrogen production with nanostructured metal oxides. J Mater Chem 18:2311–2320
38. Somorjai GA, Frei H, Park JY (2009) Advancing the frontiers in nanocatalysis, biointerfaces, and renewable energy conversion by innovations of surface techniques. J Am Chem Soc 131:16589–16605
39. Youngblood WJ, Lee SHA, Maeda S, Mallouk SE (2009) Visible light water splitting using dye-sensitized oxide semiconductors. Acc Chem Res 42:1966–1973.
40. Zhang H, Chen G, Bahnemann DW (2009) Photoelectrocatalytic materials for environmental applications. J Mater Chem 19:5089–5121
41. Kitano M, Hara M (2009) Bismuth-doped oxide glasses as potential solar spectral converters and concentrators. J Mater Chem 20:627–630
42. Valdés A, Brillet J, Grätzel M, Gudmundsdótti H, Hansen HA, Jónsson H, Klüpfel P, Kroes GJ, Formal FL, Man IC, Martins RS, Nørskov JK, Rossmeisl J, Sivula K, Vojvodic A, Zäch M (2012) Solar hydrogen production with semiconductor metal oxides: new directions in experiment and theory. Phys Chem Chem Phys 14:49–70
43. Kubacka A, Fernández-García M, Colón GM (2012) Advanced nanoarchitectures for solar photocatalytic applications. Chem Rev 112:1555–1614
44. Kumar B, Llorente M, Froehlich J, Dang T, Sathrum A, Kubiak CP (2012) Photochemical and photoelectrochemical reduction of CO_2. Annu Rev Phys Chem 63:541–569
45. Hu JS, Ren LL, Guo YG, Liang HP, Cao AM, Wan LJ, Bai CL (2005) Mass production and high photocatalytic activity of ZnS nanoporous nanoparticles. Angew Chem Int Ed 117 (8):1295–1299
46. Reber JF, Meier K (1984) Photochemical production of hydrogen with zinc sulfidesuspensions. J Phys Chem 88(24):5903–6591. https://doi.org/10.1021/j150668a032
47. Sathish M, Viswanathan B, Viswanath R (2006) Alternate synthetic strategy for the preparation of CdS nanoparticles and its exploitation for water splitting. Int J Hydrog Energy 31(7):891–898. https://doi.org/10.1016/j.ijhydene.2005.08.002
48. Yin H, Wada Y, Kitamura T, Yanagida S (2001) Photoreductive dehalogenation of halogenated benzene derivatives using ZnS or CdS nanocrystallites as photocatalysts. Environ Sci Technol 35(1):227–231. https://doi.org/10.1021/es001114d
49. Mak KF, Lee C, Hone J, Shan J, Heinz TF (2010) Atomically thin MoS_2: a new direct-gap semiconductor. Phys Rev Lett 105 (13):136805
50. Kalantar–zadeh K, Ou KZ, Daeneke T, Strano MS, Pumera M, Gras SL (2015) Two-dimensional transition metal dichalcogenides in biosystems. Adv Funct Mater 25(32):5086
51. Haque F, Daeneke T, Kalantar–zadeh K (2018) Two-Dimensional transition metal oxide and chalcogenide-based photocatalysts. Nano Micro Lett 10:23
52. Ling V, Siong E, Tai XH, Lee KM, Juan JC, Lai CW (2020) Unveiling the enhanced photoelectrochemical and photocatalytic properties of reduced graphene oxide for photodegradation of methylene blue dye. RSC Adv 10:37905

53. Liu X, Wang Z, Wu Z, Liang Z, Guo Y, Xue Y, Tian J, Cui H (2019) Integrating the Z-scheme heterojunction into a novel Ag_2O@rGO@reduced TiO_2 photocatalyst: Broadened light absorption and accelerated charge separation co-mediated highly efficient UV/visible/NIR light photocatalysis. J Colloid Interface Sci 538:689–698
54. Singh M (2018) Boron doped graphene oxide with enhanced photocatalytic activity for organic pollutants. J Photochem Photobiol A 364:130–139
55. Jin Y (2020) Band gap of reduced graphene oxide tuned by controlling functional groups. J Mater Chem C 8(14):4885–4894
56. Ahuja P, Ujjain SK, Arora I, Samim M (2018) Hierarchically grown NiO-decorated polyaniline-reduced graphene oxide composite for ultrafast sunlight-driven photocatalysis. ACS Omega 3(7):7846–7855. https://doi.org/10.1021/acsomega.8b00765
57. Deng DH, Novoselov KS, Fu Q, Zheng NF, Tian ZQ, Bao XH (2016) Catalysis with two-dimensional materials and their heterostructures. Nat Nanotechnol 11:218–230
58. Sun YF, Gao S, Lei FC, Xiao C, Xie Y (2015) Ultrathin two-dimensional inorganic materials: new opportunities for solid state nanochemistry. Acc Chem Res 48:3–12
59. Zhang XD, Xie Y (2013) Recent advances in free-standing two-dimensional crystals with atomic thickness: design, assembly and transfer strategies. Chem Soc Rev 42:8187–8199
60. Ramalingam G, Kathirgamanathan P, Ravi G, Elangovan T, Kumar BA, Manivannan N, Kasinathan K (2020) Quantum confinement effect of 2D nanomaterials, quantum dots—fundamental and applications. Faten Divsar IntechOpen. https://doi.org/10.5772/intechopen.90140
61. Luo B, Liu G, Wang L (2016) Recent advances in 2D materials for photocatalysis. Nanoscale 8(13):6904–6920. https://doi.org/10.1039/c6nr00546b
62. Li Y, Gao C, Long R, Xiong Y (2019) Photocatalyst design based on two-dimensional materials. Mater Today Chem 11:197–216. https://doi.org/10.1016/j.mtchem.2018.11.002
63. Yaqoob AA, Noor NH, Serrà A, Ibrahim ANM (2020) Advances and challenges in developing efficient graphene oxide-based ZnO photocatalysts for dye photo-oxidation. Nanomaterials (Basel) 10(5):932. https://doi.org/10.3390/nano10050932
64. Wang H, Liu X, Niu P, Wang S, Shi J, Li L (2020) Porous two-dimensional materials for photocatalytic and electrocatalytic applications. Matter 2:1377–1413
65. Zhao X, Li D, Zhang T, Conrad B, Wang L, Soeriyadi AH, Barnett A (2017) Short circuit current and efficiency improvement of SiGe solar cell in a GaAsP-SiGe dual junction solar cell on a Si substrate. Solar Energy Mater Solar Cells 159:86–93
66. Qin D, Zhou Y, Wang W, Zhang C, Zeng G, Huang D, Wang L, Wang H, Yang Y, Lei L, Chenab S, Heab D (2020) Recent advances in two-dimensional nanomaterials for photocatalytic reduction of CO_2: insights into performance, theories and perspective. J Mater Chem A 8:19156–19195
67. Liang Q, Li Z, Huang ZH, Kang F, Yang QH (2015) Holey graphitic carbon nitride nanosheets with carbon vacancies for highly improved photocatalytic hydrogen production. Adv Funct Mater 25:6885–6892
68. Allen MR, Thibert A, Sabio EM, Browning ND, Larsen DS, Osterloh FE (2010) Evolution of physical and photocatalytic properties in the layered titanates $A_2Ti_4O_9$ (A=K, H) and in nanosheets derived by chemical exfoliation. Chem Mater 22:1220–1228
69. Dong X, Cheng F (2015) Recent development in exfoliated two-dimensional g-C_3N_4 nanosheets for photocatalytic applications. J Mater Chem A 3:23642–23652
70. Singh AK, Mathew K, Zhuang HL, Hennig RG (2015) Computational screening of 2D materials for photocatalysis. J Phys Chem Lett 6:1087–1098
71. Jo YK, Kim IY, Gunjakar JL, Lee JM, Lee NS, Lee SH, Hwang SJ (2014) Unique properties of 2D layered titanate nanosheets as a building block for the optimization of the photocatalytic activity and photostability of TiO_2-based nanohybrids. Chem Eur J 32:10011–10019
72. Kim IY, Jo YK, Lee JM, Wang L, Hwang SJ (2014) Unique advantages of exfoliated 2D nanosheets for tailoring the functionalities of nanocomposites. J Phys Chem Lett 5:4149–4161

73. Ballard DGH, Rideal GR (1983) Flexible inorganic films and coatings. J Mater Sci 18:545–561
74. Ghosh HN (2007) Effect of strong coupling on interfacial electron transfer dynamics in dyesensitized TiO_2 semiconductor nanoparticles. J Chem Sci 119:205–215
75. Wieckowsi A (1999) Interfacial electrochemistry: theory, experiment, and applications. CRC Press
76. Wang QH, Kalantar-Zadeh K, Kis A, Coleman JN, Strano MS (2012) Electronics and optoelectronics of two-dimensional transition metal dichalcogenides. Nat Nanotechnol 7:699–712
77. Sasaki N, Ebina Y, Kakada T, Sasaki S (2004) Electronic band structure of titania semiconductor nanosheets revealed by electrochemical and photoelectrochemical studies. J Am Chem Soc 126:5851–5858
78. Baugher BWH, Churchill HO, Yang Y, Jarillo-Herrero P (2013) Intrinsic electronic transport properties of high-quality monolayer and bilayer MoS_2. Nano Lett 13:4212–4216
79. Kim SJ, Kim IY, Patil SB, Oh SM, Lee NS, Hwang SJ (2014) Composition-tailored 2D Mn1xRuxO2 nanosheets and their reassembled nanocomposites: Improvement of electrode performance upon Ru substitutio. Chem Eur J 20:5132–5140
80. Dong X, Osada M, Ueda H, Ebina Y, Kotani Y, Ono K, Ueda S, Kobayashi K, Takada K, Sasaki T (2009) Synthesis of Mn-substituted titania nanosheets and ferromagnetic thin films with controlled doping. Chem Mater 21:4366–4373
81. Asai R, Nemoto H, Jia Q, Saito K, Iwase A, Kudo A (2014) A visible light responsive rhodium and antimony-codoped $SrTiO_3$ powdered photocatalyst loaded with an IrO_2 cocatalyst for solar water splitting. Chem Commun 50:2543–2546
82. Liu Y, Zhou W, Liang Y, Cui W, Wu P (2015) Tailoring band structure of TiO_2 to enhance photoelectrochemical activity by codoping S and Mg. J Phys Chem C 119:11557–11562
83. Lee JM, Jin HB, Kim IY, Jo YK, Hwang JW, Wang JK, Kim MG, Kim YR, Hwang SJ (2015) A crucial role of Rh substituent ion in photoinduced internal electron transfer and enhanced photocatalytic activity of $CdS/Ti_{(5.2\text{-}x)/6}Rh_{x/2}O_2$ nanohybrids. Nanohybrids 11:5771–5780
84. Wang F, Li W, Gu S, Li H, Wu X, Liu X (2016) Samarium and nitrogen co-doped Bi_2WO_6 photocatalysts: Synergistic effect of Sm^{3+}/Sm^{2+} redox centers and N-doped level for enhancing visible-light photocatalytic activity. Chem Eur J 22:12859–12867
85. Xu J, Teng Y, Teng Y (2016) Effect of surface defect states on valence band and charge separation and transfer efficiency. Sci Rep 6:32457
86. Zhao H, Pan F, Li Y (2017) A review on the effects of TiO_2 surface point defects on CO_2 photoreduction with H_2O. J Materiomics 3:17–32
87. Kim IY, Park S, Kim H, Park S, Ruoff RS (2014) Hwang strongly-coupled freestanding hybrid films of graphene and layered titanate nanosheets: An effective way to tailor the physicochemical and antibacterial properties of graphene film. J Adv Funct Mater 24:2288–2294
88. Pan L, Zou JJ, Wang S, Huang ZF, Yu A, Wang L, Zhang X (2013) Quantum dot self decorated TiO_2 nanosheets. Chem Commun 49:6593–6595
89. Kaur J, Gravagnuolo AM, Maddalena P, Altucci C, Giardina P, Gesuele F (2017) Green synthesis of luminescent and defect-free bio-nanosheets of MoS_2: Interfacing two-dimensional crystals with hydrophobins RSC Adv 7:22400–22408
90. Xingfu Z, Zhaolin H, Yiqun F, Su C, Weiping C, Nanping X (2008) Microspheric organization of multilayered ZnO nanosheets with hierarchically porous structures J Phys Chem C 112:11722–11728
91. Wang C, Zhao Y, Liu J, Gong P, Li X, Zhao Y, Yue G, Zhou G (2016) Highly hierarchical porous structures constructed from NiO nanosheets act as Li ion and O_2 pathways in long cycle life, rechargeable Li-O_2 batteries. Chem Commun 52:11772–11774
92. Park SK, Lee J, Bong S, Jang B, Seong KD, Piao Y (2016) Scalable synthesis of few layer MoS_2 incorporated into hierarchical porous carbon nanosheets for high-performance Li and Na-ion battery anodes. Appl Mater Interfaces 8:19456–19465

93. Hoffmann MR, Martin ST, Choi W, Bahnemann DW (1995) Environmental applications of semiconductor photocatalysis. Chem Rev 95:69–96
94. Keshavarzi N, Cao S, Antonietti M (2020) A new conducting polymer with exceptional visible-light photocatalytic activity derived from barbituric acid polycondensation. Adv Mater 32(16):1907702
95. Liras M, Barawi M, Víctor A (2019) Hybrid materials based on conjugated polymers and inorganic semiconductors as photocatalysts: from environmental to energy applications. Chem Soc Rev 48:5454–5487
96. Sprick RS, Jiang JX, Bonillo B, Ren SJ, Ratvijitvech T, Guiglion P, Zwijnenburg MA, Adams DJ, Cooper AI (2015) Bimodal heterogeneous functionality in redox-active conjugated microporous polymer toward electrocatalytic oxygen reduction and photocatalytic hydrogen evolution. J Am Chem Soc 137:3265–3270
97. Das S, Mahalingam H (2019) Reusable floating polymer nanocomposites photocatalyst for the efficient treatment of dye wastewater under scaled-up conditions in batch and recirculation mode. J Chem Technol Biotechnol 94:2597–2608
98. Hagfeldt A, Grätzel M (1995) Light-induced reactions in nanocrystalline systems. Chem Rev 95:49–68
99. Anne M, Dulay M T (1993) Heterogeneous Photocatalysis Chem Rev 93(1): 341–357
100. Zhang H, Chen G, Bahnemann DW (2009) Photoelectrocatalytic materials for environmental applications. J Mater Chem 19(29):5089–5121
101. Pelaez M, Nolan NT, Pillai SC, Seery MK, Falaras P (2012) A review on the visible light active titanium dioxide photocatalysts for environmental applications. Appl Catal B 125 (33):331–349. https://doi.org/10.1016/j.apcatb.2012.05.036
102. Akpan U, Hameed B (2009) Parameters affecting the photocatalytic degradation of dyes using TiO_2-based photocatalysts: a review. J Hazard Mater 170(2):520–529. https://doi.org/10.1016/j.jhazmat.2009.05.039
103. Meng X, Zhang Z, Li X (2015) Synergetic photoelectrocatalytic reactors for environmental remediation: a review. J Photochem Photobiol C 24:83–101. https://doi.org/10.1016/j.jphotochemrev.2015.07.003
104. Soltani N, Elias S, Hussein MZ (2012) Visible light-induced degradation of methylene blue in the presence of photocatalytic ZnS and CdS nanoparticles Int J Mol Sci 13(12):12242–12258
105. Torres–Martínez CL, Kho R, Mian OI, Mehra RK (2001) Efficient photocatalytic degradation of environmental pollutants with mass-produced ZnS nanocrystals. J Colloid Interface Sci 240(2):525–532
106. Pouretedal HR, Norozi A, Keshavarz MH, Semnani A (2009) Nanoparticles of zinc sulfide doped with manganese, nickel and copper as nanophotocatalyst in the degradation of organic dyes. J Hazard Mater 162(2–3):674–681
107. Zhou P, Yu J, Jaroniec M (2014) All-solid-state Z-scheme photocatalytic systems. Adv Mater 26:4920–4935
108. Maeda K (2013) Z-scheme water splitting using two different semiconductor photocatalysts. ACS Catal 3:1486–1503
109. Bard AJ (1979) Photoelectrochemistry and heterogeneous photocatalysts at semiconductors. J Photochem 10:59–75
110. Zheng D, Pang C, Wang X (2015) The function-led design of Z-scheme photocatalytic systems based on hollow carbon nitride semiconductors. Chem Commun 51:17467–17470
111. Iwase A, Yoshino S, Takayama T, Ng YH, Amal R, Kudo A (2016) Water splitting and CO_2 reduction under visible light irradiation using Z-scheme systems consisting of metal sulfides, CoOx-loaded $BiVO_4$ and a reduced graphene oxide electron mediator. J Am Chem Soc 138:10260–10264
112. Zhang Z, Wang W, Wang L, Sun S (2012) Enhancement of visible-light photocatalysis by coupling with narrow-band-gap semiconductor. Appl Mater Interfaces 4:593–597
113. Georgieva J, Armyanov S, Valova E, Poulios I, Sotiropoulos S (2007) Enhanced photocatalytic activity of electrosynthesised tungsten trioxide/ titanium dioxide bi-layer coatings under ultraviolet and visible light illumination. Electrochem Commun 9:365–370

114. Hou Y, Li XY, Zhao QD, Quan X, Chen GH (2009) Fabrication of Cu_2O/TiO_2 nanotube heterojunction arrays and investigation of its photoelectrochemical behavior. Appl Phys Lett 95:093108
115. Walter MG, Warren EL, Mckone JR, Boettcher SW, Mi Q, Santori EA, Lewis NS (2010) Fabrication of Cu_2O/TiO_2 nanotube heterojunction arrays and investigation of its photoelectrochemical behavior Chem Rev 110:6446–6473
116. Wang H, Zhang L, Chen Z, Hu J, Li S, Wang Z, Liu J, Wang X (2014) Semiconductor heterojunction photocatalysts: design, construction, and photocatalytic performances. Chem Soc Rev 43:5234–5244
117. Wojtyła S, Baran T (2017) Photosensitization and photocurrent switching effects in wide band gap semiconductors J Inorg Organomet Polym 27:436–445
118. Zhang Y, Zhang N, Tang ZR, Xu YJ (2012) Enhanced photocatalytic hydrogen-production performance of graphene-$Zn_{(x)}Cd_{(1\text{-}x)}S$ composites by using an organic S source. ACS Nano 6(11):9777–9789
119. Dong, Fan & Ni, Zilin & Li, Peidong & Wu, Zhongbiao. (2015) New J Chem 39. https://doi.org/10.1039/C5NJ00351B
120. Rahimi K, Yazdani A (2018) Improving photocatalytic activity of ZnO nanorods: a comparison between thermal decomposition of zinc acetate under vacuum and in ambient air. Mater Sci Semicond Process 80:38–43
121. Ruess R, Ringleb R, Nonomura K, Vlachopoulos N, Wittstock G, Schlettwein D (2019) Diverging surface reactions at TiO_2- or ZnO-based photoanodes in dye-sensitized solar cells. Phys Chem Chem Phys 21:13047–13057
122. Ansaria O, Sajid MK, Ansaria SJ, Cho MH (2015) Polythiophene nanocomposites for photodegradation applications. J Saudi Chem Soc 19:494–504
123. Kaur Z, Komal N, Gupta K, Kumar S, Tikoo V, Singhal KB, Goel N (2019) Time-dependent DFT and experimental study on visible light photocatalysis by metal oxides of Ti, V and Zn after complexing with a conjugated polymer. New J Chem. https://doi.org/10.1039/c8nj04729d
124. Merkulov DVŠ, Despotovi VN, Bani ND, Armakovi SJ, Fincur NL, Lazerevi MJ, Cetojevic–Simin DD, Orcic DZ, Radoicic MB, Šaponjic ZV (2018) Photocatalytic decomposition of selected biologically active compounds in environmental waters using TiO_2/polyaniline nanocomposites kinetics, toxicity and intermediates assessment. Environ Pollut 239:457–465
125. Xu Y, Ma Y, Ji X, Huang S, Xia J, Xie M, Yan J, Xu H, Li H (2019)Conjugated conducting polymer PANI decorated $Bi_{12}O_{17}C_{12}$ photocatalyst with extended light response range and enhanced photoactivity. Appl Surf Sci 464:552–561
126. Chen F, An W, Li Y, Liang Y, Cui W (2018) Fabricating 3D porous PANI/TiO_2–graphene hydrogel for the enhanced UV-light photocatalytic degradation of BPA. Appl Surf Sci 27:123–132
127. Xu S, Han Y, Xu Y, Meng H, Xu J, Wu J, Xu Y, Zhan X (2017) Fabrication of polyaniline sensitized grey-TiO_2 nanocomposites and enhanced photocatalytic activity. Sep Purif Technol 184:248–256
128. Deng Y, Tang L, Zeng G, Dong H, Yan M, Wang J, Hu W, Wang J, Zhou Y, Tang J (2016) Enhanced visible light photocatalytic performance of polyaniline modified mesoporous single crystal TiO_2 microsphere. Appl Surf Sci 387:882–893
129. Wu H, Lin S, Chen C, Liang W, Liu X, Yang H (2016) A new ZnO/rGO/polyaniline ternary nanocomposite as photocatalyst with improved photocatalytic activity. Mater Res Bull 83:434–441
130. Ghosh MS, Kouame NA, Ramos L, Remita S, Dazzin A, Deniset-Besseau A, Beaunier B, Goubard F, Aubert PH, Remita H (2015) Conducting polymer nanostructures for photocatalysis under visible light. Nat Mater 14:505–511
131. Xiang Y, Wang X, Zhang X, Hou H, Dai K, Huang Q, Chen H (2018) Enhanced visible light photocatalytic activity of TiO_2 assisted by organic semiconductors: a structure optimization

strategy of conjugated polymers. J Mater Chem A 6(1):153–159. https://doi.org/10.1039/c7ta09374h

132. Zhou K, Zhu Y, Yang X, Jiang X, Li C (2011) Preparation of graphene–TiO_2 composites with enhanced photocatalytic activity. New J Chem 35:353–359. https://doi.org/10.1039/C0NJ00623H
133. Seema H, Kemp KC, Chandra V, Kim KS (2012) Graphene–SnO_2 composites for highly efficient photocatalytic degradation of methylene blue under sunlight. Nanotechnology 23:355705. https://doi.org/10.1088/0957-4484/23/35/355705
134. Wang J, Tsuzuki T, Tang B, Hou X, Sun L, Wang X (2012) Reduced graphene Oxide/ZnO composite: reusable adsorbent for pollutant management. ACS Appl Mater Interfaces 4:3084–3090. https://doi.org/10.1021/am300445f
135. Zhou X, Shi T, Zhou H (2012) Hydrothermal preparation of ZnO-reduced graphene oxide hybrid with high performance in photocatalytic degradation. Appl Surf Sci 258:6204–6211. https://doi.org/10.1016/j.apsusc.2012.02.131
136. Liu X, Cong R, Cao L, Liu S, Cui H (2014) The structure, morphology and photocatalytic activity of graphene–TiO_2 multilayer films and charge transfer at the interface. New J Chem 38:2362–2367. https://doi.org/10.1039/C3NJ01003A
137. Raghavan N, Thangavel S, Venugopal G (2015)) Enhanced photocatalytic degradation of methylene blue by reduced graphene-oxide/titanium dioxide/zinc oxide ternary nanocomposites. Mater Sci Semicond Process 30:321–329. https://doi.org/10.1016/j.mssp.2014.09.019
138. Han S, Hu L, Liang Z, Wageh S, Al–Ghamdi AA, Chen Y, Fang X (2014) One-Step hydrothermal synthesis of 2D hexagonal nanoplates of α-Fe_2O_3/graphene composites with enhanced photocatalytic activity adv funct mater 24:5719–5727
139. Chen C, Cai W, Long M, Zhou B, Wu Y, Wu D (2010) Synthesis of visible-Light Responsive Graphene Oxide/TiO_2 composites with p/n Heterojunction. Feng Y ACS Nano 4:6425–6432. https://doi.org/10.1021/nn102130m
140. Lv T, Pan L, Liu X, Lu T, Zhu G (2011) Enhanced photocatalytic degradation of methylene blue by ZnO-reduced graphene oxide composite synthesized via microwave-assisted reaction. J Alloys Compd 509:10086–10091
141. Sun J, Zhang H, Guo LH, Zhao L (2013) Two-dimensional interface engineering of a Titania–Graphene nanosheet composite for improved photocatalytic activity. Acs Appl Mater Inter 5:13035–13041
142. Dai K, Lu L, Liang C, Liu Q, Zhu Q (2014) Heterojunction of facet coupled g-C_3N_4/surface-fluorinated TiO_2 nanosheets for organic pollutants degradation under visible LED light irradiation. Appl Catal B Environ 156:331–340
143. Guo W, Zhang F, Lin C, Wang ZL (2012) Direct growth of TiO_2 nanosheet arrays on carbon fibers for highly efficient photocatalytic degradation of methyl orange. Adv Mater 24:4761–4764
144. Lee HU, Lee SC, Won J, Son BC, Choi S, Kim Y, Park SY, Kim HS, Lee YC, Lee J (2015) Stable semiconductor black phosphorus (BP)@titanium dioxide (TiO_2) hybrid photocatalysts. Sci Rep 5
145. Dai K, Lu L, Liu Q, Zhu G, Liu Q, Liu Z (2014) Graphene oxide capturing surface-fluorinated TiO_2 nanosheets for advanced photocatalysis and the reveal of synergism reinforce mechanism. Dalton Trans 5(43):2202–2210
146. Sharma S, Khare N (2018) Sensitization of narrow band gap Bi_2S_3 hierarchical nanostructures with polyaniline for its enhanced visible-light photocatalytic performance. Colloid Polym Sci 296:1479–1489
147. Oshima T, Ishitani S, Maeda K (2014) Non-sacrificial water photo-oxidation activity of lamellar calcium niobate induced by exfoliation. Adv Mater Interfaces 1:1400131
148. Zhang L, Sun L, Liu S, Huang Y, Xu K, Ma K (2016) Effective charge separation and enhanced photocatalytic activity by the heterointerface in MoS_2/reduced graphene oxide composites. RSC Adv 6:60318–60326

149. Jo WK, Adinaveen T, Vijaya JJ, Selvam VV (2016) Synthesis of MoS_2 nanosheet supported Z-scheme TiO_2/g-C_3N_4 photocatalysts for the enhanced photocatalytic degradation of organic water pollutants. RSc Adv 6:10487–10497
150. Koyyadaa G, Prabhakar SV, Jaesool SS, Veerenda S, Junga CJ (2019) Enhanced solar light-driven photocatalytic degradation of pollutants and hydrogen evolution over exfoliated hexagonal WS_2 platelets. 109:246–254
151. Ashrafa W, Bansala S, Singh V, Barmanb S, Khanuja M (2020) BiOCl/WS_2 hybrid nanosheet (2D/2D) heterojunctions for visible-light-driven photocatalytic degradation of organic/inorganic water pollutants. RSC Adv 10:25073–25088
152. Lee WPC, Tan LL, Sumathi S, Chai SP (2018) Copper-doped flower-like molybdenum disulfide/bismuth sulfide photocatalysts for enhanced solar water splitting. J Hydrogen Energy 43:748–756
153. Zhang H, Zong R, Zhu Y (2009) Photocorrosion suppression of ZnO nanoparticles via hybridization with graphite-like carbon and enhanced photocatalytic activity. J Phys Chem C 113:4605–4611
154. Ye L, Su Y, Lin X, Xie H, Zhang C (2014) Recent advances in BiOX (X = Cl, Br and I) photocatalysts: synthesis, modification, facet effects and mechanisms. Environ Sci Nano 1:90–112
155. Kim J, Lee CW, Choi W (2010) Platinized WO_3 as an environmental photocatalyst that generates OH radicals under visible light. Sci Technol 44:6849–6854
156. Liu Y, Shi Y, Liu X, Li H (2017) A facile solvothermal approach of novel Bi_2S_3/TiO_2/RGO composites with excellent visible light degradation activity for methylene blue. Appl Surf Sci 396:58–66
157. Hou Y, Wen Z, Cui S, Guo X, Chen J (2013) Constructing 2D Porous Graphitic C_3N_4 nanosheets/nitrogen-doped graphene/layered MoS_2 ternary nanojunction with enhanced photoelectrochemical activity. Adv Mater 25(43):6291–6297. https://doi.org/10.1002/adma.201303116
158. Teng W, Wang YM, Lin Q, Zhu H, Tang YB, Li XY (2019) Synthesis of MoS_2/TiO_2 Nanophotocatalyst and its enhanced visible light driven photocatalytic performance. J Nanosci Nanotechnol 19:3519–3527
159. Chen P, Su S, Liu H, Wang Y (2013) Interconnected Tin disulfide nanosheets grown on graphene for Li-Ion storage and photocatalytic applications. ACS Appl Mater Interfaces 5:12073–12082. https://doi.org/10.1021/am403905x
160. Yan X, Ye K, Zhang T, Xue C, Zhang D, Ma C, Weia J, Yang G (2017) Formation of three-dimensionally ordered macroporous TiO_2@nanosheet SnS_2 heterojunctions for exceptional visible-light driven photocatalytic activity. New J Chem 41:8482–8489
161. Chauhan H, Soni K, Kumar M, Deka S (2016) Tandem photocatalysis of graphene-stacked SnS_2 nanodiscs and nanosheets with efficient carrier separation. ACS Omega 1(1):127–137. https://doi.org/10.1021/acsomega.6b00042
162. Liu Y, Xie S, Li H, Wang X (2014) A highly efficient sunlight driven ZnO nanosheet photocatalyst: synergetic effect of P-doping and MoS_2 Atomic Layer Loading. Chem Cat Chem 6:2522–2526
163. Zhang Z, Huang J, Zhang M, Yuan L, Dong M (2015) Ultrathin hexagonal SnS_2 nanosheets coupled with g-C_3N_4 nanosheets as 2D/2D heterojunction photocatalysts toward high photocatalytic activity. Appl Catal B Environ 163:298–305
164. Jiang Q, Lu Y, Huang Z, Hu J (2017) Facile solvent-thermal synthesis of ultrathin $MoSe_2$ nanosheets for hydrogen evolution and organic dyes adsorption.Appl Surf Sci 402:277–285
165. An X, Yu JC, Tang J (2014) Biomolecule-assisted fabrication of copper doped SnS_2 nanosheet–reduced graphene oxide junctions with enhanced visible-lightphotocatalytic activity. J Mater Chem A 2:1000–1005
166. Zhang R, Wan W, Li D, Dong F, Zhou Y (2017) Three dimensional MoS_2/reduced graphene oxide aerogel as a macroscopic visible-light photocatalyst. Chin J Catal 38:313–320
167. Li X, Yu J, Wageh S, Al–Ghamdi AA, Xie J (2016) Graphene in photocatalysis: a review Small 12:6640−6696

168. Luo W, Zafeiratos S (2017) A brief review of the synthesis and catalytic applications of graphene-coated oxides. Chem Cat Chem 9:2432–2442
169. Li X, Shen R, Ma S, Chen X, Xie J (2018) Graphene-based heterojunction photocatalysts. Appl Surf Sci 430:53–107
170. Neelgund GM, Bliznyuk VN, Oki A (2016) Photocatalytic activity and NIR laser response of polyaniline conjugated graphene nanocomposite prepared by a novel acid-less method. Appl Catal B 187:357–366
171. Zhang S, Li B, Wang X, Zhao G, Hu B, Lu Z, Wang X (2020) Recent developments of two-dimensional graphene-based composites in visible- light photocatalysis for eliminating persistent organic pollutants from wastewater. Chem Eng J 124642. https://doi.org/10.1016/j.cej.2020.124642
172. Feng J, Hou Y, Wang X, Quan W, Zhang J, Wang Y, Li L (2016) In-depth study on adsorption and photocatalytic performance of novel reduced graphene oxide ZnFe2O4-polyaniline composites. J Alloys Compd 681:157–166. https://doi.org/10.1016/j.jallcom.2016.04.146
173. Grimm NB, Faeth SH, Golubiewski NE, Redman CL, Wu J, Bai X, Briggs JM (2008) Global change and the ecology of cities. Science 319:756–760. https://doi.org/10.1126/science.1150195
174. Umar R, Ansari MO, Parveen N, Oves M, Barakat MA, Alshahri A, Khan MY, Cho MH (2016) Facile route to a conducting ternary polyaniline@TiO_2/GN nanocomposite for environmentally benign applications: photocatalytic degradation of pollutants and biological activity. RSC Adv 6:111308–111317. https://doi.org/10.1039/c6ra24079h
175. Biswas MRUD, Ho BS, Oh WC (2019) Eco-friendly conductive polymer-based nanocomposites, $BiVO_4$/graphene oxide/polyaniline for excellent photocatalytic performance. Polym Bull. https://doi.org/10.1007/s00289-019-02973-y
176. Ameen S, Seo HK, Akhtar SM, Shin HS (2012) Novel graphene/polyaniline nanocomposites and its photocatalytic activity toward the degradation of rose Bengal dye. Chem Eng J 210:220–228. https://doi.org/10.1016/j.cej.2012.08.035
177. Zhang F, Zhang Y, Zhang G, Yang Z, Dionysiou DD, Zhu A (2018) Exceptional synergistic enhancement of the photocatalytic activity of SnS_2 by coupling with polyaniline and N-doped reduced graphene oxide. Appl Catal B Environ 236:53–63. https://doi.org/10.1016/j.apcatb.2018.05.002
178. Wang X, Zhang J, Zhang K, Zou W and Chen S. (2016) Facile fabrication of reduced graphene oxide/CuI/PANI nanocomposites with enhanced visible-light photocatalytic activity. RSC Adv 6:44851
179. Vadivel S, Theerthagiri J, Madhavan J, Maruthamani D (2016) Synthesis of polyaniline/graphene oxide composite via ultrasonication method for photocatalytic applications. Mater Focus 5:393–397
180. Zhang L, Jamal R, Zhao Q (2015) Preparation of PEDOT/GO, PEDOT/MnO_2, andPEDOT/GO/MnO_2 nanocomposites and their application in catalytic degradation of methylene blueNanoscale. Res Lett 10:148
181. Ansari O, Kumar R, Alshahrie A, Abdel–wahab S, Sajith VK, Ansari S, Jilani A, Barakat MA, Darwesh R (2019) Anion selective pTSA doped polyaniline@ graphene oxide-multiwalled carbon nanotube composite for Cr (VI) and Congo red adsorption. Compos Part B Eng 175:107092.
182. Liu Y, Yin H, Xu C, Zhuge X, Wan J (2019) Polythiophene-tungsten selenide/nitrogen-doped graphene oxide nanocomposite for visible light-driven photocatalysis. Nanopart Res 21:210.
183. Yu Y, Yang Q, Yu X, Lu Q, Hong X (2017) Chem Select 2 (20): 5578
184. Khan S, Narula AK (2018) Synthesis of the ternary photocatalyst based on ZnO sensitized graphene quantum dot reinforced with conducting polymer exhibiting photocatalytic activity. J Mater Sci Mater Electron 29(8):6337–6349

Chapter 6
Photocatalyst Composites from Bi-based and Carbon Materials for Visible Light Photodegradation

Nikita Sharma, Zsolt Pap, Seema Garg, and Klara Hernadi

Abstract This chapter gives a brief overview of the progress in bismuth-carbon nanocomposites as promising visible-light-driven photocatalysts. The fundamental structural features of bare bismuth-based photocatalysts and their historical background is highlighted. The composites of BiOX with carbon nanotubes are discussed in detail. Overview of some composites with other carbon nanomaterials, such as activated carbon, graphene, and g-C_3N_4, are also discussed. Based on this, significant roles played by these carbon nanomaterials are reviewed as well. The important examples are collected, compared and analyzed thoroughly. The introduction of carbon nanomaterials has a pronounced effect on the photocatalytic performance of bare bismuth-based metal oxides owing to the synergetic effect that exists between carbon nanostructures and bismuth-related photocatalysts, besides the effect on their morphological, structural and optical properties.

N. Sharma · Z. Pap · K. Hernadi (✉)
Department of Applied and Environmental Chemistry, University of Szeged, Rerrich Béla 1, Szeged 6720, Hungary
e-mail: hernadi@chem.u-szeged.hu

Z. Pap
e-mail: pzsolt@chem.u-szeged.hu

N. Sharma
Advanced Materials and Intelligent Technologies Higher Education and Industrial Cooperation Centre, University of Miskolc, Miskolc 3515, Hungary

Z. Pap
Nanostructured Materials and Bio-Nano-Interfaces Centre, Institute for Interdisciplinary Research on Bio-Nano-Sciences, Babeş–Bolyai University, Treboniu Laurian 42, 400271 Cluj-Napoca, Romania

S. Garg
Department of Chemistry, Amity Institute of Applied Sciences, Amity University, Sector-125, Noida, Uttar Pradesh 201313, India

K. Hernadi
Institute of Physical Metallurgy, Metal Forming and Nanotechnology, University of Miskolc, Miskolc-Egyetemváros, C/1 108, Miskolc 3515, Hungary

S. Garg and A. Chandra (eds.), *Green Photocatalytic Semiconductors*,
Green Chemistry and Sustainable Technology,
https://doi.org/10.1007/978-3-030-77371-7_6

Keywords Bismuth-based · Carbonaceous materials · Photocatalytic degradation · Composites · Layered structure

6.1 Introduction

The abundance of solar energy points to the potential applications of fuel generation and environmental remediation by photocatalytic materials. For long, this has been a hot topic for researchers across the globe. Figure 6.1 shows the growing number of publications in the field of photocatalysis. Over three decades, the total number of publications in the field of photocatalysis reached more than 50,000, if the keyword "photocatalytic" is used on web of science (searched on 9 November 2020), out of which nearly 10,000 publications were reported for visible-light-driven photocatalysts (inside picture), using keyword "visible-light" and "photocatalytic". Till now, many different types of photocatalysts have been developed and several advances have been made to understand their course of action. However, substantial challenges are still on the way. Among those, the major challenge is to find their practical use in industries, thus cutting down the overall cost in comparison to the existing technology. This chapter aims to provide a novel perspective of one such class of visible light-driven photocatalyst (of bismuth family) and their composites with popular carbon nanostructures.

The "bismuth" class of photocatalyst came into attention when different strategies were being adopted including, developing novel materials using visible light as

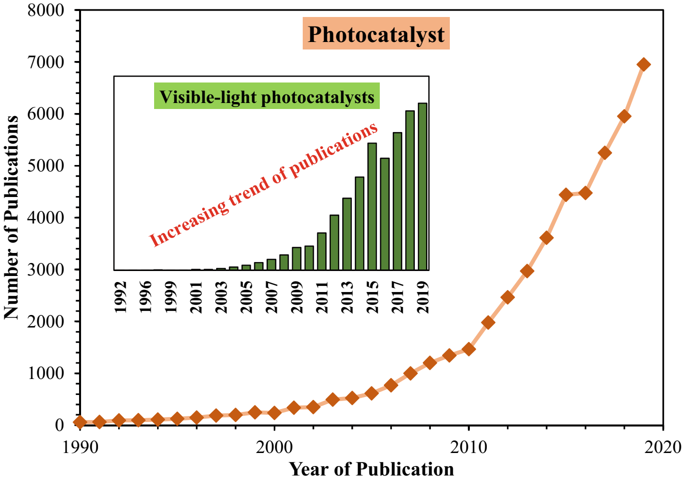

Fig. 6.1 Number of publications in the field of photocatalysis over three decades. *Source* web of science; keywords: "photocatalytic" and "visible-light photocatalytic", search date: 9 November 2020

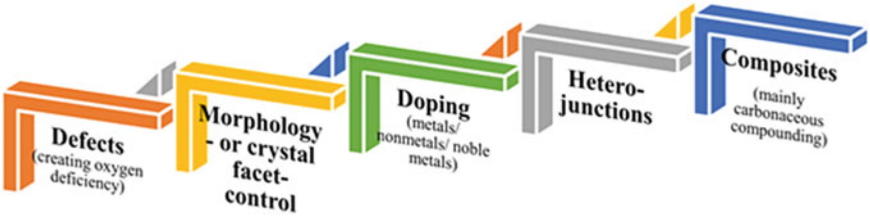

Fig. 6.2 Different strategies adopted for enhancing the photocatalytic activity of a photocatalyst

source of irradiation. The aim was for improving the photocatalytic performance by widening the absorption of light, maximizing the charge transfer phenomena at the surface, suppressing the recombination process by efficient charge separation and enhancing surface redox reactions. The practical applications of these materials are still too low, as stated previously, due to easy recombination of charge carriers which resulted in decrease in photocatalytic efficiency. Therefore, here came the need for adopting other strategies investigated for achieving enhanced photocatalytic performance, as shown in Fig. 6.2. For instance, Niu and coworkers highlighted the key points on introducing oxygen vacancies in BiOCl crystal structure that helped in the removal of bacteria (*E. coli* and *S. aureus*) and RhB dye under simulated sunlight with (010) and (001) exposed facets [66]. The prepared BiOCl experienced reduction in band gap by forming impurity energy levels that promoted visible light absorption and also acted as trapping sites for electrons, thus boosting charge separation [18, 88, 106]. To get into the details of each one of these is beyond the scope of this chapter. Therefore, the most popular and widely used approach which is “composite” formation, is discussed here.

6.2 Photocatalysts from “Bismuth” Family

Bismuth-based photocatalysts have reported several positive characteristics, such as high stability, low cost, efficient photocatalytic response, abundance in nature, and non-toxicity [114]. The increasing popularity of these materials can be seen in Fig. 6.3, which shows the total number of articles published on using Bi-based photocatalysts in almost two decades.

As a result of this, these novel and high-performance photocatalytic materials have found various applications, for example, in degrading organic pollutants, water splitting, photocatalytic removal of heavy metal ions and hazardous gas, and photo reduction, and oxidation of air pollutants [114]. The bismuth-based semiconductors have reported good UV and visible light photocatalytic activity due to their narrow band gap, typically less than 3.0 eV. The band gap energy values of these have been shown in Fig. 6.4 [100]. In their band structure, the valence band consist of hybrid orbitals of Bi 6s and O 2p, unlike TiO_2 which consists of only O

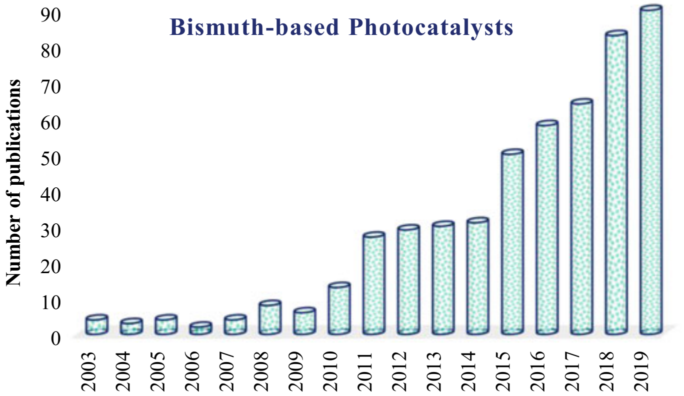

Fig. 6.3 Rising trend in number of publications on bismuth-based photocatalysts. *Source* web of science, keywords: "bismuth" and "photocatalytic"

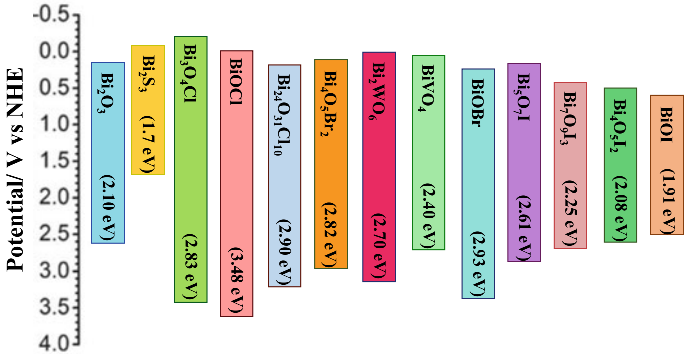

Fig. 6.4 Band gap energy values of various bi-based photocatalysts

2p orbitals. The presence of this well-dispersed Bi 6s orbitals reported the increased mobility of photogenerated charge carriers and reduction in band gap [37]. A study done by Rengaraj et al. revealed that Bi–O sites act as electron trapping sites in the case of TiO_2 doped with Bi^{3+} for the degradation of methyparathion, an endocrine disruptor, under UV-A radiation. The degradation efficiency reached almost 97% within 2 h [70].

Synthesis methods like sol–gel, hydro/solvo-thermal, microwave irradiation, micro-emulsion, precipitation, sonochemical, chemical vapor deposition have been used to obtain higher photocatalytic activity for these bismuth-related nanostructures. Different synthetic methods result in different photocatalytic yields for the nanocomposite [40]. Likewise, different synthesis conditions also results in difference in photocatalytic performance. For instance, one of the studies done by our

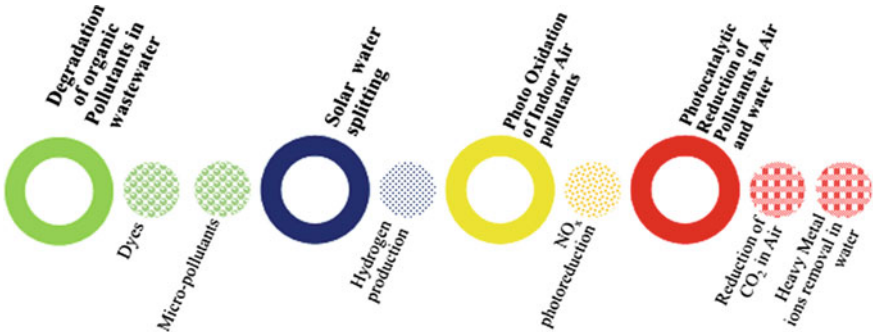

Fig. 6.5 Different applications of bi-based photocatalysts

research group investigated the influence of hydrothermal crystallization parameters (time and temperature) on the final properties of BiOX [5]. Recently, combination of these methods have also been used. For example, in the study by Yang and Zhang, BiOCl/BiOBr composite was prepared by using microwave-assisted co-precipitation method (MWAC) and the composite was quite stable even after 5 cycles [110]. However, the downfall of using microwave-assisted method is uncontrolled growth of crystal structure and size [75]. Due to the stability of Bi^{3+} than Bi^{5+}, most of the work is focused on Bi^{3+} containing compounds which include Sillen-structured (BiOX: X = Cl, Br, I), Aurivilius-structured (Bi_2MO_6; M = Mo, W) and Scheelite-structured ($BiVO_4$, Bi_2S_3). These can be classified into different categories, namely bismuth chalcogenides (binary sulfides or oxides), bismuth oxyhalides, bismuth vanadate, and other bismuth-related nanoparticles (multi-component oxides). These compounds mainly have layered structure with mainly platelets-type of morphology [100]. Such class of photocatalysts has been tested on a wide range of organic pollutants ranging from azo dyes (Rhodamine B, Methyl Orange, Methylene Blue) to toxic gases (acetaldehyde, bisphenol A, nitric oxide) for determining their photocatalytic activity under visible light [32]. They have found a number of applications ranging from eliminating toxic organic pollutants to solar water splitting and CO_2 photoreduction, as shown in Fig. 6.5. In subsequent sections, only the most widely studied Bi-family members including BiOX (X = Cl, Br, I), Bi_2WO_6 and $BiVO_4$ are discussed and also their carbon-based composite structures.

Bismuth Oxyhalides (BiOX) are one of the promising candidates among visible light photocatalyst and are extensively studied. Their outstanding photocatalytic activity is attributed to their unique layered structure. This layered structure is beneficial for the transfer of electrons to the photocatalyst surface along the layered network since the recombination of charge carriers could be suppressed by transferring electrons to a layered host [58]. BiOX has open-layered crystalline structure and belongs to a family of multicomponent metal oxyhalides which crystallizes into tetragonal matlockite structure (PbFCl-type structure). This was first determined by Bannister in 1935 [4]. Their crystal structure consists of Bi_2O_2 slabs interleaved by

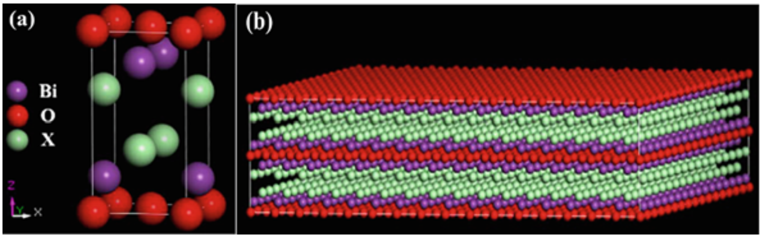

Fig. 6.6 Structural representation of BiOX (X: Cl, Br, I) **a** single-crystal cell **b** 2-D layered structure with a two-layer thickness. Reprinted from Ref. [19] with permission from Elsevier

double halogen atom slabs forming a layered structure, as shown in Fig. 6.6. In each [X–Bi–O–Bi–X] layer, a bismuth atom is surrounded by four oxygen and four halogen atoms. Such arrangement of layers provides large enough space to polarize the related atoms and orbitals, generating static internal electric fields. This promotes the separation and migration of photogenerated electron–hole pairs, one of the important factors in photocatalysis. The intralayer atoms are held together by strong covalent bonding whereas the weak interlayer is held by Van der Waals interaction. The presence of such kind of bonding leads to highly anisotropic structural, optical, electrical, and mechanical properties. Their layered structure bestow them with fascinating physicochemical properties including high chemical and optical stability, chemical inertness, and resistance towards corrosion, apart from its low cost and abundance in nature. BiOX has found potential applications for hydrogen evolution by solar water splitting, indoor-gas purification, photocatalytic wastewater treatment, selective oxidation of alcohol, photodegradation of volatile organic compounds (VOC), and recently, in nitrogen fixation. The first work of BiOX was reported for BiOCl in 2006 by Zhang et al. [107]. They synthesized irregular BiOCl nanoplates which effectively degraded methyl orange under UV light. Not only did the BiOCl photocatalysts performed better than commercial P25 TiO_2 but also reported high stability even after 3 runs in comparison to P25.

It is interesting to note that the band gap energy value (*Eg*) for the three bismuth oxyhalides is variable [16, 17]. For BiOCl *Eg* is $\sim$3.3 eV, for BiOBr *Eg* is 2.7 eV and in case of BiOI, it is 1.8 eV. Due to their narrow band gap, they can be easily excited using visible light, except for BiOCl which is UV-active just like TiO_2 due to its large band gap ($Eg < 3.0$ eV). Although BiOCl is mainly active under UV light but with certain modifications it could be employed under visible light. For instance, the work by Wang and coworkers reported synthesis of modified BiOCl nanocomposites with PANI which showed superior photocatalytic activity for the degradation of methyl orange (MO) under visible light [89]. The composite showed synergetic effect between BiOCl conduction band maximum and π^* orbital of PANI due to the chemical interaction and around 67% of dye was removed within 210 min using visible light. Another work of extending BiOCl absorption range to visible region was reported by Cai et al. where they synthesized the composites of BiOCl and g-C_3N_4 [12]. These composites showed remarkable photocatalytic activity in the photodegradation of phenol and 4-chlorophenol under visible light. The superior photocatalytic performance is due to the effective separation of charge carriers by the introduction of g-C_3N_4 into BiOCl crystal structure.

As stated earlier, a number of synthesis methods are used and have also been reported for the fabrication of bismuth oxyhalides. Lin et al. used deposition–precipitation approach for the synthesis of BiOBr/AgBr composite for the degradation of methyl orange under visible light [31]. They reported $O_2^{\cdot -}$ as the main active species responsible for the photodegradation of methyl orange. Lately, a new greener approach towards BiOX synthesis have been followed. One such example is the synthesis of BiOBr using leaf extract of *Azadirachta indica* and comparing its photocatalytic efficiency with the chemical version of BiOBr using methyl orange and phenol as model pollutant [24].

Bismuth Vanadate ($BiVO_4$) is another famous class of metal oxide semiconductors under Bi-based photocatalysts which shares similar beneficial characteristics such as nontoxicity, good visible light harvesting property, and chemical corrosion resistance, that marks it as a good candidate for environmental applications [61]. The first report on use of $BiVO_4$ photocatalyst for solar oxidation was reported by Kudo et al. in 1988 [45]. Prior to this, it was mainly used as a yellow pigment due to its nontoxic nature and coloristic properties [8]. It has an advantage over toxic, expensive, and less stable organic pigments, for example, Cd- or Pb-based pigments [27]. However, its uncontrolled pigmentary color is a serious drawback [27]. Nowadays, the applications of $BiVO_4$ has wider spectrum ranging from gas sensors [26], temperature indictor [81] to photoanode material in photoelectrochemical cells [43, 68]. Based on its light absorption properties under UV and visible light, $BiVO_4$ is now widely used in degrading organic pollutants such as noxious dyes [20] and endocrine disruptors like bisphenol A [2]. A study reported the effective photodegradation of an endocrine disruptor, diethylstilbestrol, under visible light using $BiVO_4$ and persulfate system [55]. Li et al. reported the superior visible light photodegradation of methylene blue by ordered mesoporous monoclinic $BiVO_4$ using silica as a template [47]. Also, $BiVO_4$ with olive-like morphology was found to exhibit excellent visible light photocatalytic activity for phenol [39]. Recently, numerous encouraging results have also been reported for carbon dioxide reduction and oxygen evolution using $BiVO_4$ apart from degrading organic pollutants. The lamellar $BiVO_4$ prepared by Ke et al. demonstrate the best photocatalytic activity for oxygen evolution [42]. Other applications arise from its ferroelasticity [10], conductivity [7] and catalytic properties such as its use as a catalyst in oxidative dehydrogenation reactions [27].

$BiVO_4$ occurs in its natural form as a mineral pucherite with an orthorhombic crystal structure. However, when synthesized in laboratory, it crystallizes into either scheelite or zircon-type crystal structure. The scheelite structure has two crystal forms, monoclinic (distorted) and tetragonal phase while zircon-type has only tetragonal phase. Both the tetragonal phases differ only in their lattice parameters. The tetragonal zircon is obtained at low temperature while synthesis at high-temperature results in monoclinic phase. It was reported that the reversible phase transition occurs from monoclinic to tetragonal scheelite structure when

Fig. 6.7 Phase transition of $BiVO_4$ from monoclinic to tetragonal, and vice-versa, depending on temperature conditions. Reprinted from Ref. [67] with permission from 10th international conference on electrical and computer engineering

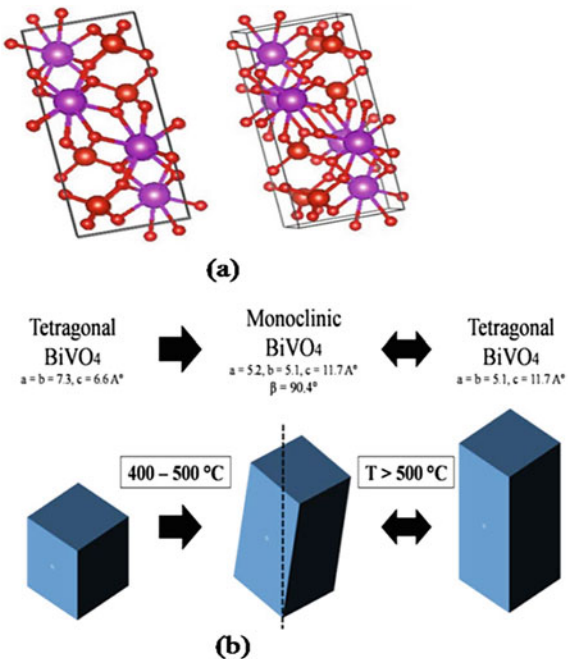

heated above 255 °C [9]. Similarly, the irreversible phase transition of tetragonal zircon-type structure to monoclinic scheelite structure occurs above 400–500 °C. It has been demonstrated by Noor et al. in Fig. 6.7 [67]. Therefore, it shows that the phase transition of $BiVO_4$ strongly depends on temperature, although in some cases mechanical treatment (for e.g. manual crushing of the powder) at room temperature also resulted in irreversible phase transition [9].

Out of all three polymorphs, monoclinic exhibits higher photocatalytic activity under visible light irradiation ($\lambda > 420$ nm) due to its narrow band gap energy (2.4 eV) [33] [62]. This visible light absorption is mainly due to the distortion in monoclinic structure [64, 84] and is associated with the transition from valence band (VB) formed by Bi 6s or a hybrid orbital of Bi 6s and O 2p to a conduction band (CB) of V 3d. On the other hand, in case of UV absorption by both tetragonal and monoclinic $BiVO_4$, the transition from O 2p to V 3d is responsible [69]. For that reason, it is crucial to control its crystal form in order to develop visible-light-driven photocatalysts [97].

The basic structure of $BiVO_4$ is composed of vanadium ions (VO_4) tetrahedron units coordinated by four oxygen atoms in V site and bismuth ions (BiO_8) polyhedron unit surrounded by eight oxygen atoms. These eight oxygen atoms are connected at Bi site through eight different VO_4 tetrahedral units. The basic unit cell of monoclinic $BiVO_4$ is represented in Fig. 6.8.

In this monoclinic structure, Bi and V atoms are alternatively arranged along the crystallographic axis exhibiting a layered structure. The bond lengths of V–O and Bi–O in tetragonal scheelite structure are equal while in monoclinic phase are different.

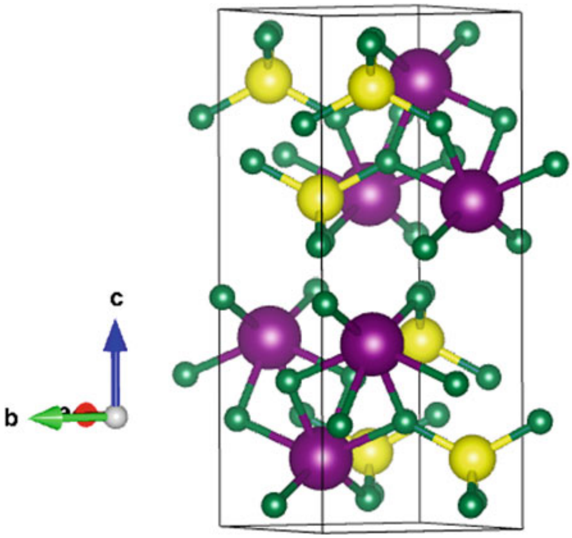

Fig. 6.8 Single unit crystal structure of monoclinic $BiVO_4$ (created using VESTA)

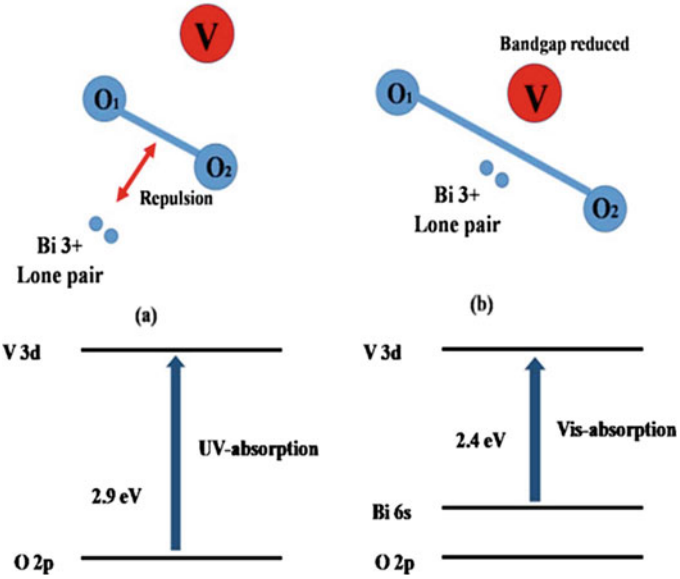

Fig. 6.9 Band gap structure of **a** pure tetragonal $BiVO_4$ (*left*) and **b** pure monoclinic $BiVO_4$ (*right*). Reprinted from Ref. [67] with permission from 10th international conference on electrical and computer engineering

As a result of this, the monoclinic $BiVO_4$ has narrower band gap energy value than tetragonal $BiVO_4$. Noor et al. explain this reduction in band gap of monoclinic phase via a graphical representation shown in Fig. 6.9, where, the higher bond lengths of O–O in monoclinic results in decrease in repulsion between O 2p electrons and lone pair electrons of Bi^{3+}, thereby resulting in reduced band gap energy.

Moreover, its photophysical and photocatalytic properties vary significantly depending on the crystal form and the type of synthesis [27, 97]. A variety of methods have also been reported for the synthesis of $BiVO_4$ including solid-state reaction, hydrothermal, sol–gel, aqueous solution, solvothermal, microemulsion, chemical precipitation, microwave irradiation, etc. Another alternative route for synthesizing $BiVO_4$ was by metalorganic decomposition technique to form thin films of $BiVO_4$ [22]. Through this method, control over the particle size can be achieved by slight change in thermal condition (duration). Depending on the type of synthesis, different phases can be obtained. Sometimes even the same crystal structure can show different photocatalytic behavior. For example, one study compared the photocatalytic efficiency of the monoclinic phase $BiVO_4$ prepared by two different methods and the results revealed that same crystal structure can show different photocatalytic activity, the one synthesized by an aqueous process at room temperature shows higher photocatalytic activity than the one prepared by conventional solid-state reaction [27]. Bhattacharya et al. prepared zircon structure $BiVO_4$ using co-precipitation method and found out that the method is sensitive to both pH and temperature of the solution from which the compound is precipitated [9]. Zhang et al. reported the synthesis of mixed-phase $BiVO_4$ (tetragonal and monoclinic) via hydrothermal method where they reported the dependence of morphology and phases on pH of the precursor solution. According to their report, in acidic condition (i.e., pH $\leq$ 3.8) a pure tetragonal phase was obtained while in alkaline medium (pH $\geq$ 8.5) a pure monoclinic phase was formed and in between this pH values (3.8–8.5) a mixture of these two phases was formed. In another study, monoclinic $BiVO_4$ with nanofibrous morphology was synthesized by hydrothermal method using a cationic surfactant cetyltrimethylammonium bromide (CTAB) as a template directing agent [102].

Bi_2MO_6: (M = Cr, Mo, W) types belong to Aurivillius family and its crystal structure falls under orthorhombic space group *Pca2(1)*. Unlike $BiVO_4$ band gap structure (as discussed previously), the valence band and conduction band for this family consist of hybridized Bi 6p, O 2p, and M nd orbitals (n = 3, 4, 5 for Bi2CrO6, Bi2MoO6, and $Bi2WO_6$, respectively) [60]. The predicted band gaps for Bi_2CrO_6, Bi_2MoO_6 and Bi_2WO_6 are 1.245 eV, 1.96 eV and 2.2 eV, respectively [60]. Since the band gap of Bi_2CrO_6 is very narrow, the recombination of charge carriers is easy and therefore, limits its applications in photocatalysis [60]. Bi_2WO_6, on the other hand, is the most widely studied due to its physical and chemical properties like pyroelectricity, piezoelectricity, ferroelectricity, etc. [15, 59]. Bi_2WO_6 has shown excellent visible-light induced-photocatalytic activity for degrading organic pollutants, water splitting (oxygen evolution) and certain toxic gases such as nitric oxide, bisphenol A, acetaldehyde [48]. The Bi_2WO_6 consists of layered structure with perovskite slabs interleaved with Bi_2O_2 layers and WO_6 units sharing the corner sites. The work done by Kudo and coworkers was the first on Bi_2WO_6 for photocatalytic oxygen evolution from $AgNO_3$ solution [44]. It has been known to show comparable activity to that of anatase TiO_2 but its instability at low pH limits its application in liquid phase [21]. However, its strong absorption ability for visible light and resistant to photocorrosion makes it suitable for photocatalysis and photoelectrocatalysis applications [33]. Different methods could be used to prepare Bi_2WO_6, such as solid-state reaction and hydrothermal process. In a study of Bi_2WO_6 synthesis via solid-state reaction (SSR), large particle size, and low surface area was obtained [109]. However, with hydrothermal synthesis, the advantage of smaller crystal size, narrower band gap, and higher surface area was obtained and these materials showed better photocatalytic activity than those prepared by SSR method [60, 87]. Furthermore, the control over morphology could be possible in hydrothermal treatment by regulating parameters like pH or use of shape-tailoring agents [41]. A number of model pollutants were successfully degraded using Bi_2WO_6 reaching more than 95% of removal efficiency in case of azo dyes and above 90% for endocrine disruptors like bisphenol A under visible light irradiation [35]. The removal of $CHCl_3$, acetaldehyde [83] and nitric oxide in air [36] has also been reported.

One of the most important and beneficial points for photocatalyst is to have organized hierarchical structures. This results in their high physicochemical properties and also provides various channels for diffusion of small molecules much faster to the reaction sites [92]. For instance, flower-like superstructure of Bi_2WO_6 was synthesized by Wang and coworkers which resulted in degradation of RhB upto 97% in only 60 min under visible light [108]. The interesting fact about their work is that they obtained this morphology without using surfactant or template, rather with facile hydrothermal treatment and the samples exhibited high surface area. The high photocatalytic activity of Bi_2WO_6 flower-like morphology than that of TiO_2 is due to its novel hierarchal transport pores. A wide range of morphologies for Bi_2WO_6 were obtained such as microspheres [48], nanoplates [105], hollow spheres, nest-like [14], flower-like [108], hollow tubes [54], nanocages [74].

6.3 Carbon-Nanostructures in Photocatalysis

Recombination is a very common and rapid phenomena that lower the performance of a photocatalyst. But when it is combined with a material which is conductive in nature, it boosts the overall photocatalytic efficiency by lowering the recombination rate [65]. Conductive carbon-based materials are a good choice and are well-known for ages for their high surface area, porous structure, high adsorption capacity, excellent electrical and thermal conductivity, and extremely high mechanical strength. The increasing popularity is also due to their chemical inertness, low cost as compared to other commercial polymeric agents, environmentally benign nature, thermal stability, and easy availability. For example, activated carbon is a very good adsorbent used for pollutant removal and can be obtained easily from waste material, such as by burning any kind of nut shells [73]. The obtained carbon has very high BET surface area, one of the vital aspects in heterogeneous photocatalysis. Carbonaceous-based materials are the most valuable material, in terms of its unique and novel properties and their diverse applications including wastewater treatment. Another significant feature of carbon is that it can be doped easily with a variety of metal oxide nanoparticles and therefore, is regarded as a promising material for pollutant removal. Additionally, their stability under acidic and basic conditions and easy recovery of metals is another interesting property. The cause of the enhanced performance by carbon-nanomaterials, when combined with semiconductors, takes place via 3 main mechanisms: (i) high adsorption, (ii) enhanced absorption of visible light, and (iii) easy separation of photogenerated charge carriers [11]. This resulted in the overall enhancement of their photocatalytic activity. Figure 6.10 gives the general visual representation of removal of organic pollutants by the use of different forms of carbon nanomaterials [28].

The introduction of carbon nanostructures can have significant impact on photocatalysts, as listed in Fig. 6.11 such as, it reduces the recombination of electron–hole pair, enhances the adsorption capacity, and prevents the agglomeration of particles, all of which are essential in photocatalysis. These are known to increase the dispersion of the photocatalysts owing to their high surface area.

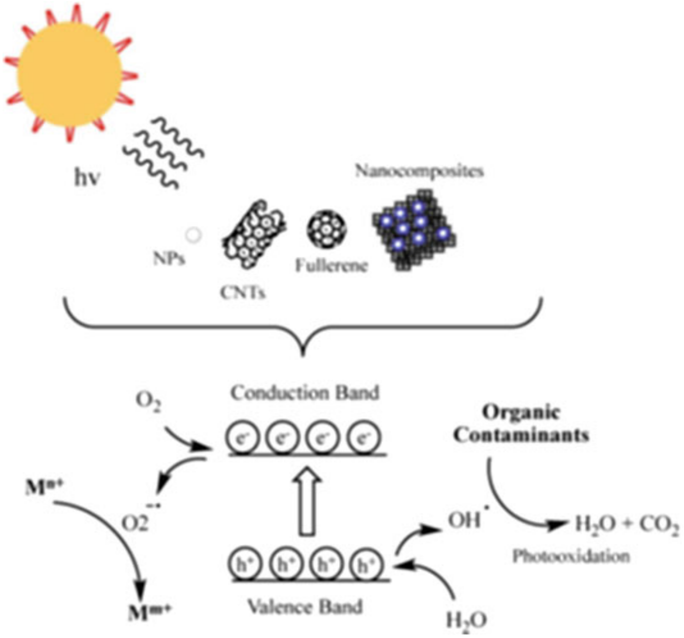

Fig. 6.10 Illustration of photocatalytic degradation mechanism of organic contaminants by different forms of C-nanostructures (Fernanda D. Guerra, https://pubmed.ncbi.nlm.nih.gov/30021974/. Licensed under CC BY)

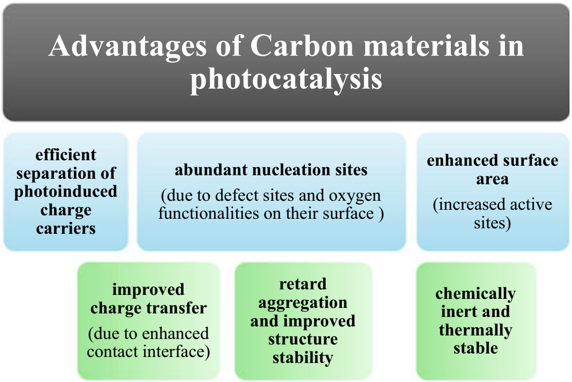

Fig. 6.11 Advantages of incorporating carbon nanomaterials to the semiconductor during photocatalysis

The carbon nanostructures play significant roles, such as (i) a support material for metal oxide nanoparticles (ii) as an adsorbent due to its high adsorption capacity towards pollutants and that increases active sites as well, (iii) acting as electron acceptor and transport channel due to its high electrical conductivity, preventing the recombination of photogenerated electron-holes (iv) as a co-catalyst (v) as a photosensitizer. A visual representation of the different roles played by C-nanostructure family (in photocatalysis) can be seen in Fig. 6.12. In a study of Tryba et al., TiO_2 coated with carbon layers experienced increase adsorption for phenol but lower photodecomposition as compared to bare TiO_2 [85]. This is because the activated carbon, here, merely acted as a support material for the TiO_2 deposition and did not participate in photodegradation process. Besides this, another important role played

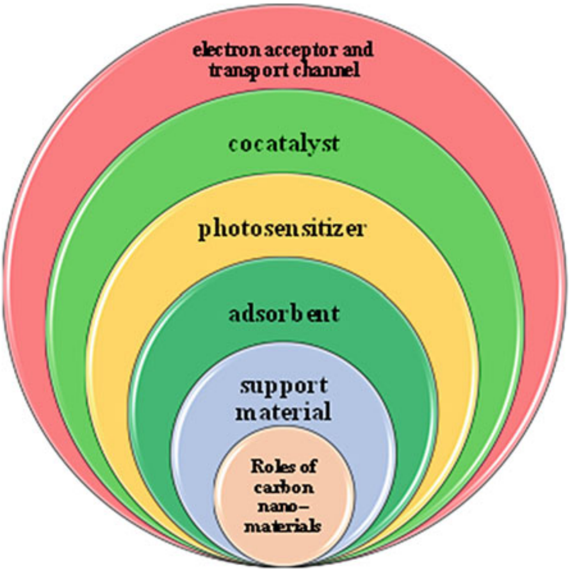

Fig. 6.12 Different roles played by carbon nanostructures in a semiconductor-carbon hybrid photocatalyst system

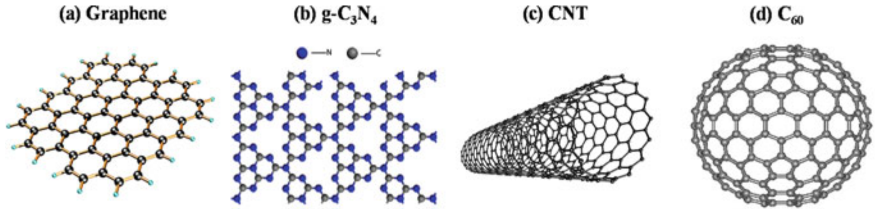

Fig. 6.13 Different forms of carbon nanomaterials

was the suppression of phase transformation from anatase to poorly photoactive rutile phase. In another study, Xian et al. described the dual roles played by graphene in the composite system of BiOBr–TiO_2-graphene. The 2-D graphene in the composite system served as both as an electron sink to capture the photogenerated electrons from semiconductor and as a conductive network to improve the migration of these electrons. In addition, the author reported random dispersion of graphene as evident by absence of any kind of shift in the absorption edge of the composite and no effect on their band gap energy.

Conventional carbon forms used in photocatalysis are activated carbon, graphite, and graphitized materials. Recently, carbon nanotubes (CNT), graphene (or graphene oxide GO), carbon nanofibers, C-60 (fullerenes), carbon quantum dots (CQD), and carbon nitride (g-C_3N_4) have expanded the list of carbonaceous materials under heterogeneous photocatalysis. Figure 6.13 shows the structure of different carbon nanomaterials used in photocatalytic applications. Such carbon nanostructures having different morphologies made a great impact as a promising material for diverse applications, particularly in environmental remediation. It has been reported to extend the absorption edge of bare semiconductor photocatalyst into visible region that led to the enhancement of photocatalytic response of the composite. In a further section, a brief summary of the general characteristics of these novel promising nanomaterials are discussed.

Graphene is a single-layer 2D graphite structure with fascinating electrical and structural properties. Although the study on it goes back to 1859 but the wide-scale research started in 2004 and for which Geim and Novoselov were awarded Nobel Prize in 2010. Since then it is in limelight. Some of its outstanding properties include large specific surface area, high charge mobility at room temperature, remarkable electrical conductivity that makes the transmission of electrons relatively easy, and excellent adsorption capacity, apart from its high strength. Its combination with a semiconductor would result in a composite structure with a great tendency to eliminate pollutants. Additionally, the pronounced adsorption of pollutants on its surface is another beneficial point that accelerates the photodegradation mechanism of adsorbed pollutants. Liang et al. reported the first study on photocatalytic CO_2 reduction [52]. Since then, it is greatly studied, particularly from the aspect of CO_2 photoreduction. Their introduction into composite system has resulted in high photocatalytic efficiency of the photocatalyst. Their large specific surface area and high chemical stability also plays significant role in

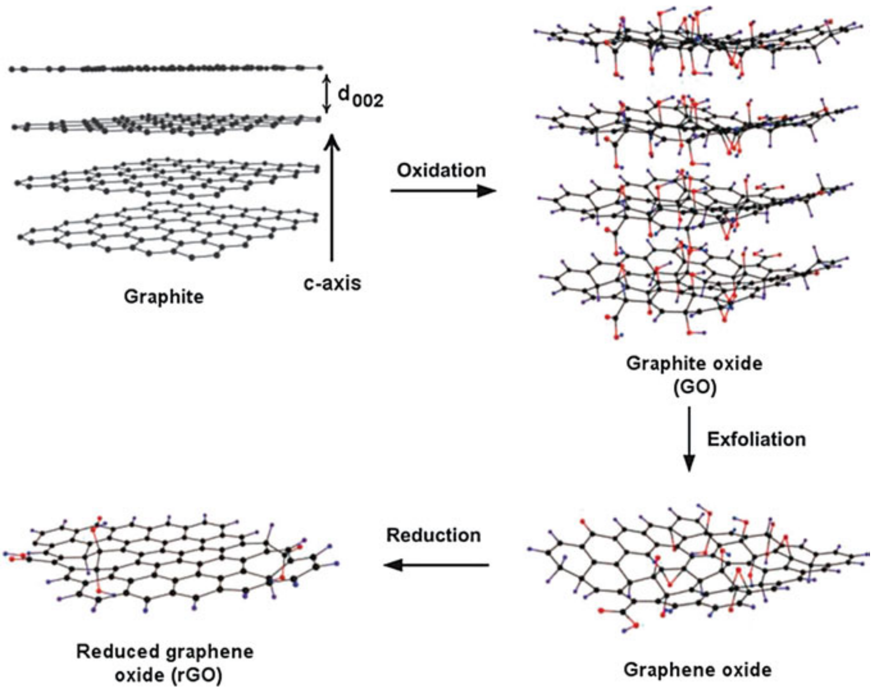

Fig. 6.14 Schematic representation for preparation of reduced graphene oxide from graphite. Reprinted from [3], Copyright 2011 Wiley–VCH Verlag GmbH & Co. KGaA, Weinheim

enhancing the photocatalytic efficiency of CO_2 reduction. The use of hollow and mesoporous nanostructures result in increase of surface area and as a result of this, large number of active sites are generated which further enhances the diffusion and adsorption of reactant molecules, resulting in enhanced photocatalytic activity [30].

Reduced-Graphene oxide (rGO), yet another sub-class of graphene is formed by reducing graphene oxide in various reductive conditions. Figure 6.14 shows synthesis of rGO from graphite [46]. It has also received much attention due to several oxygen functionalities present on its surface and its high surface area, that makes it suitable as an excellent support and electron acceptor [112]. It has similar properties as that of graphene. Due to the oxidation of graphite, several functional groups containing oxygen are introduced on its surface that makes them hydrophilic in nature. As a result of this, it is easily mixed in water and therefore, has much higher exposed area in aqueous solution. This has an advantage in solar water splitting applications.

Graphitic carbon nitrides (g-C_3N_4) has been extensively used in photocatalysis and are sometimes referred to as "metal-free visible light photocatalyst" [40]. The electronic properties differ markedly from graphene. g-C_3N_4 exists in seven different phases (α-C_3N_4, β-C_3N_4, cubic-C_3N_4, pseudocubic-C_3N_4, g-h-triazine, g-h-heptazine and g-o-triazine), out of which only polymeric graphitic-C_3N_4 is the most stable with highly ordered polymeric structure with pendant amino groups and tri-s-triazine (C_6N_7) as the building structural units. It has a narrow band gap of 2.7 eV, which is appropriate for excitation under visible light while graphene is a zero band gap conductor with excellent conductivity properties. Due to its high reduction ability, it has shown many effective results in photoreduction for H_2 production and CO_2 reduction. The tremendous surface properties of g-C_3N_4 makes it perfect as a support material for other photocatalysts [57] or as a photosentisizer in other cases. Besides its rich surface characteristics, g-C_3N_4 offers other beneficial features such as high specific surface area, good chemical stability even under harsh acidic conditions, good light absorption properties, and low-cost for photocatalytic CO_2 reduction [115, 116].

Activated Carbon, also sometimes called active carbon or activated charcoal, since long have been widely used as a support or adsorbent in case of removal of pollutants from air [38] or eliminating organic amides from aqueous solutions [82]. Owing to its large adsorption capacity, it is one of the common choices for adsorbents in industries as the intermediates produced after photodegradation process can be effectively adsorbed on its surface. Like with other carbon nanostructures, the combination of AC with semiconductor can suppress the recombination of electron/hole pairs to some extent. It is also the most preferred choice in the case of carbon-supported catalysts [72].

Carbon Nanotubes (CNT) are, yet, another group of promising materials in environmental remediation. These are grouped into two categories, namely, single-walled CNT (SWCNT) and multi-walled CNT (MWCNT). SWCNT consists of only the layer of graphene sheet while MWCNT is composed of multiple concentric layers of graphene. By virtue of their high specific surface area, hollow layered structure, and presence of delocalized π-electrons, CNT facilitated in enhancing light adsorption capacity and charge transportation phenomena. From past, numerous research and efforts have been put to increase the photocatalytic activity by using CNT, especially of the well-known TiO_2 and in many cases, visible-light response was obtained due to the beneficial properties imparted by CNT, such as serving as temporary electron reservoir [6]. Besides acting as electron sink, MWCNT, during photocatalysis process, could also act as a photosensitiszer, as reported by Wang et al., in which the photogenerated electrons from MWCNT are injected into the TiO_2 conduction band, on the other hand, the positively-charged MWCNT leaves a hole onto TiO_2 by scavenging the electrons from valence band of TiO_2. Although, MWCNT has resulted in increased performance of the photocatalysts, in several cases, however, this is valid only upto certain amount. This has been proven by a study done by Réti et al. where the author observed that increased MWCNT amount deteriorates the activity due to light-absorbing properties of MWCNT and their shadowing effect [71]. This study revealed that low amount of MWCNT proved beneficial for obtaining higher photocatalytic efficiency and MWCNT were considered to act as “conductive wires” that is responsible for transferring and storing electrons and, therefore, increases the lifetime of these charge carriers.

Table 6.1 Possible roles of different carbon nanostructures as summarized by Shaowen and coworkers in their review

Role of nano-carbons	Type of carbon nanostructure					
	CNT	Graphene	C60	CQD	Carbon fibers	Activated carbon
Supporting material	✓	✓	✖	✖	✓	✓
Increasing adsorption and active sites	✓	✓			✓	✓
Electron acceptor and transport channel	✓	✓	✓	✓	✓	✓
Cocatalyst	✓	✓	✓	✓	✖	✖
Photosensitization	✓	✓	✓	✓	✖	✖
Band gap narrowing effect	✓	✓	✖	✖	✖	✖
Photocatalyst	✓	✓	✓	✓	✖	✓

Source Ref. [13]

Shaowen et al. has interestingly summarized different roles of these carbon nanostructures during the photocatalytic process, shown in Table 6.1 [13]. As rightly quoted by him, particular carbon material can show multi-functional roles during the entire photocatalytic reaction while it may not be true for other specific carbon materials because of limitations of their texture and properties.

6.4 Nanocomposites of Bismuth/Carbon as Visible Light-Driven Photocatalysts (VLD)

This section deals with the following subjects: significant roles played by carbon nano-family in Bismuth/Carbon composite system and the effect of incorporation of these carbonaceous materials on bismuth family members. The strategy of forming "composite" materials proved successful in many cases and accounted for superior photocatalytic activity as compared to their pristine materials. This is mainly due to the efficient transfer and suppression of recombination of photogenerated electron–hole pairs which ultimately led to an increase in photocatalytic activity. For example, the advantage of incorporating carbon materials resulted in enhancement of photocatalytic reduction of CO_2, depicted in Fig. 6.15 [40]. Here, such examples of bismuth-carbon hybrid photocatalyst systems are discussed.

1. **BiOX/Carbon nanocomposites for visible light photodegeradation:**

Carbon materials have been reported to improve the dispersion and increase the surface active sites on semiconductor-carbon interface. Yin et al. reported that in the composite of BiOCl/MWCNT, the transfer of electrons was promoted by the introduction of MWCNT and suppressed the recombination of electron and holes.

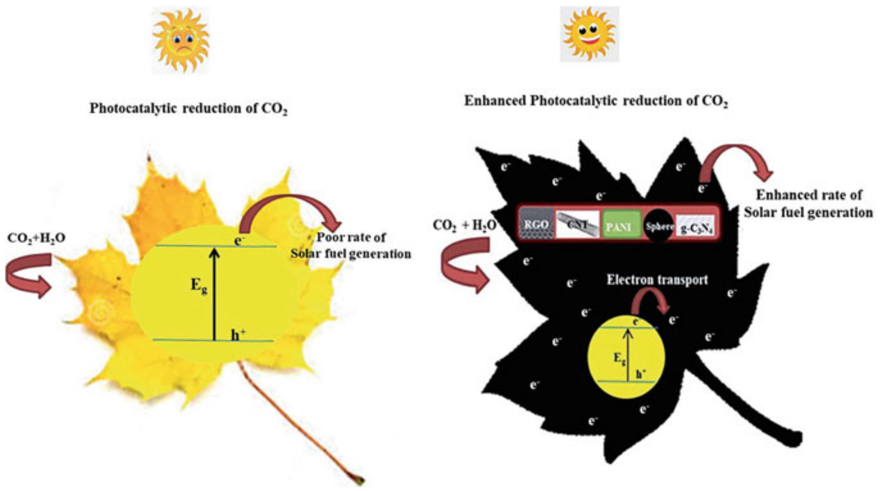

Fig. 6.15 The increased photoreduction of CO_2 by different carbon-based materials. Reprinted from [40] with permission from The Royal Society of Chemistry

Another significant observation was the structural stability of MWCNT, as evident by SEM images, even after being embedded into BiOCl crystal structure [101]. In another work, BiOI/MWCNT composite was synthesized and showed enhance photocatalytic activity for Acid Orange II (AOII) dye. The enhanced photocatalytic activity was attributed to the efficient transfer of electrons between BiOI and MWCNT. The composite also demonstrated high adsorption for AOII dye via π-π interaction between MWCNT surface and AOII [79]. Further, novel work was done by Weng et al. to form a composite of BiOX-carbon nanofiber (CF)/CNT [91]. Such type of hierarchal structure where there is a combination of “semiconductor-substrate”, was designed to maximize the recycling possibility of nanosheets from aqueous solution after photocatalytic process [29]. In the study, BiOX nanosheets were grown over carbon composite fiber embedded with CNT by ionic layer adsorption and reaction method. This prepared composite system of CNTs well aligned and embedded into CF matrix is confirmed through SEM and TEM images as shown in Figure 6.13. Figure 6.16a–f shows the morphology of the pure CF with smooth surface and CNT/CF composite with rough surface. Figure 6.16f shows the TEM images of the 30% CNT/CF composite fiber which confirms that CNT are aligned and embedded into CF matrix. This composite structure resulted in photodegradation for MO and exhibited excellent stability as well as recycled ability under simulated sunlight. The CFs were chosen as a substrate due to its flexibility and 1-D conductivity while CNTs for its ability to effectively store and transport the electrons. Furthermore, there exists a synergistic effect between the semiconductor and C, as reported by Guo et al., that retards the recombination of photogenerated electron-hole pairs, thereby, enhancing the photocatalytic performance [29]. Figure 6.17a, b shows the recycling tests done for MO

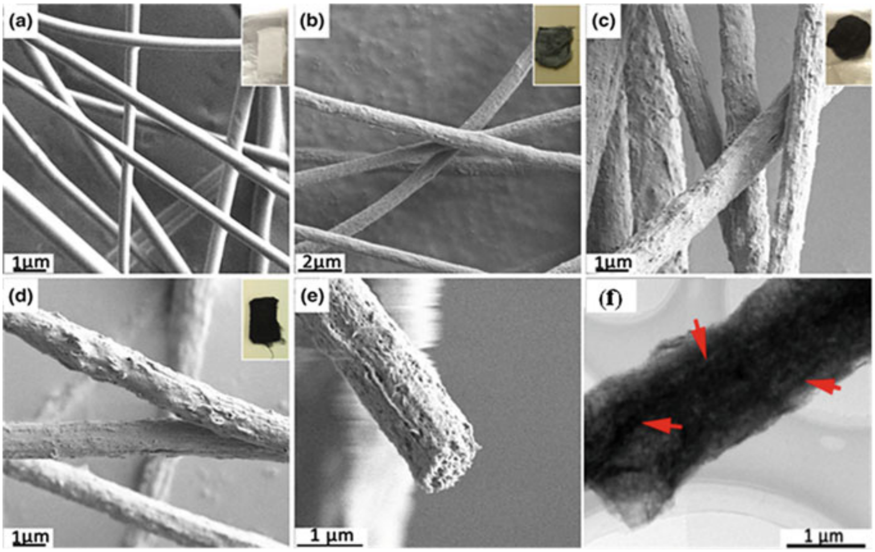

Fig. 6.16 SEM images of **a** pure CFs, **b–d** CNT/CF composite fibers and different amount of CNT (10%, 20%, 30%, respectively), **e** cross-sectional view of (**d**) and, **f** TEM image of sample (**d**). Red arrow marks CNTs. Reprinted from Ref. [91] with permission from Springer

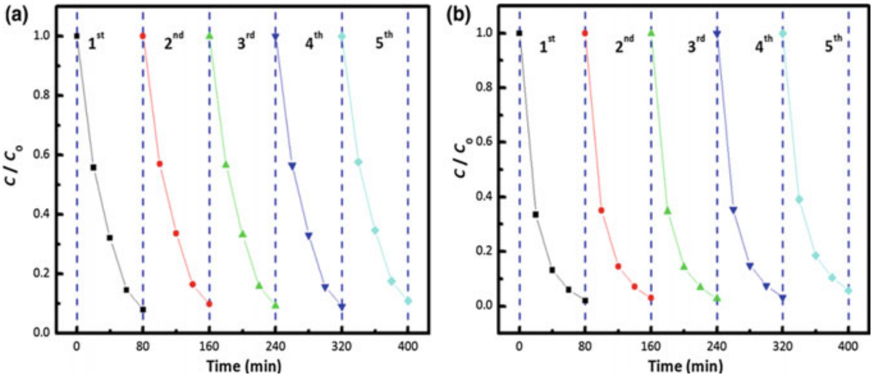

Fig. 6.17 Cycling graphs for MO photodegradation with **a** CNTs/CFs-BiOCl NSs, **b** CNTs/CFs-BiOI NSs. Reprinted from Ref. [91] with permission from Springer

dye and the results revealed that even after 5 consecutive tests, the photocatalytic performance of the composite remained the same suggesting the remarkable stability and recycling ability of the prepared composites. Both the carbon sources had the advantage of large surface area and stability under corrosive conditions, apart from their excellent conductive nature. Additionally, due to high adsorption

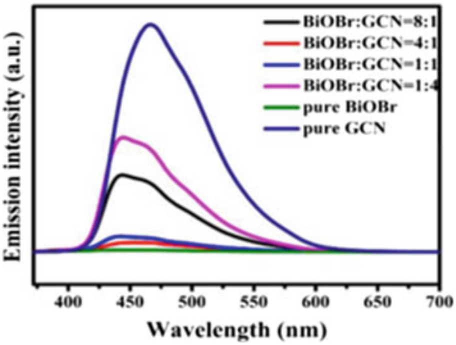

Fig. 6.18 Photoluminious spectra (PL) spectra of pure BiOBr, g-C_3N_4 and BiOBr/g-C_3N_4 composite (Jun Wun, https://www.frontiersin.org/articles/10.3389/fchem.2019.00649/full. Licensed under CC BY)

capacity for pollutants and excellent mechanical strength of CNTs, it is said to tailor the energy gaps of semiconductors through the covalent bonds [91]. In some reports, the effect of carbon nanomaterials on narrowing band gap energy of the composite has also been reported. For instance, the study by Wu et al. for the fabrication of BiOBr/g-C_3N_4 composites by hydrothermal method reported narrowing of band gap of BiOBr/g-C_3N_4 composite as compared to pure bulk BiOBr and C_3N_4 [93]. Furthermore, through photoluminescence (PL) spectra, it was evident that the electrons majorly originated from C_3N_4 and then transferred to the surface of BiOBr. The low intensity in case of composite indicates suppression of recombination of photogenerated carriers and no signal for pure BiOBr indicates no radiative recombination of charge carriers. This means that little electrons were provided by BiOBr separately. The PL spectra are shown in Figure 6.18. Also, the composites exhibited excellent photocatalytic activity for the degradation of bisphenol A in 120 min under visible light.

The study by Zhang et al. reported the enhanced photocatalytic degradation for RhB and NO by nanocomposites of BiOBr and graphene and graphite oxide [111]. The enhanced visible light absorption by nanocomposites was attributed to the increased surface area, pore volumes, and effective charge separation and transfer at the interface as compared to pristine BiOBr. Figure 6.19a, b illustrates the

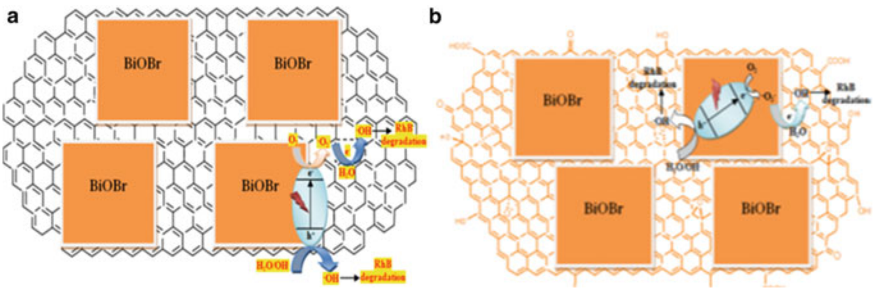

Fig. 6.19 Photocatalytic degradation mechanism of RhB by **a** BiOBr-GE and **b** BiOBr-GO nanocomposites. Reprinted from Ref. [111] with permission from Elsevier

photodegradation mechanism by BiOBr-GE and BiOBr-GO nanocomposites for RhB, respectively. After achieving some remarkable and positive results for green BiOBr synthesis [24], as mentioned under BiOX section, motivated by this, another study was performed to explore the combining effect of using plant extract and benefits of incorporating carbon nanostructures. This study included the impregnation of BiOI, synthesized by using plant extract, over activated carbon (AC) matrix [98]. The interesting results revealed that there exist multiple interfaces by the introduction of AC, which not only facilitated charge flow and transportation that led to reduced recombination rate of photogenerated charge carriers, but also subsequently, aided the formation of superoxide radical anions ($O_2^{\cdot -}$), one of the active species responsible for the superior performance.

Work by Shijie Li and coworkers reported excellent photodegradation for RhB, MO and 4-chlorophenol (CP) by BiOI/MWCNT composite, prepared solvothermally, with degradation efficiency of 98.3% (after 60 min.), 84.2% (after 180 min.), and 78.3% (after 180 min.), respectively, under visible light [50]. The enhanced photocatalytic performance is attributed to the strong coupling interface between MWCNT and BiOI that promoted the efficient separation of electron–hole pairs. The author reported the following significant findings by the incorporation of MWCNT: (a) higher surface areas of composites than pure BiOI (b) more adsorptive and reactive sites for organic pollutants (c) enhanced visible light absorption of BiOI (d) efficient charge transfer and separation (f) low recombination rate. However, this may not be true in every case. The magic of combining such fascinating materials may not always work. For instance, a study by our group reported the opposite trend observed in case of composites of BiOBr with MWCNT. We observed that addition of MWCNT in BiOBr did not lead to enhancement of photocatalytic activity of the composite, rather the samples without MWCNT showed the highest degradation efficiency for phenol under visible light. Therefore, in our case, MWCNT did not contribute in efficient charge separation and electron trapping phenomena. Other interesting fact witnessed was that the not-so reported facet (003) reported for the first time ever to play a significant role in enhancing the photocatalytic performance. The trend observed between different sample series in regard to overall photocatalytic efficiency of the composite system (BiOBr/MWCNT) for phenol photodegradation under visible light is shown in Fig. 6.20.

Other than MWCNT, composites with graphite oxide (GO) were also reported for the photodegradation of pollutants. For example, composite of BiOCl and graphite oxide synthesized via in-situ sol-gel method exhibited high photocatalytic activity for RhB [112]. The reason for enhanced activity was due to the nanosized interfacial contact of these nanofibers. Other novel works reported on BiOX composites with carbon nano family includes [1, 34, 53, 56, 77, 86, 90, 94, 101]. Recently, Singh et al. fabricated composites of BiOX (X = F, Cl, Br, I) with g-C_3N_4 and investigated their photocatalytic performance for a dye (Congo Red) and a fungicide (carbendazim) under natural sunlight [78]. The author confirmed the significant interaction between BiOX and g-C_3N_4 via a shift observed in the binding energies of the components. This intimate interaction between them can

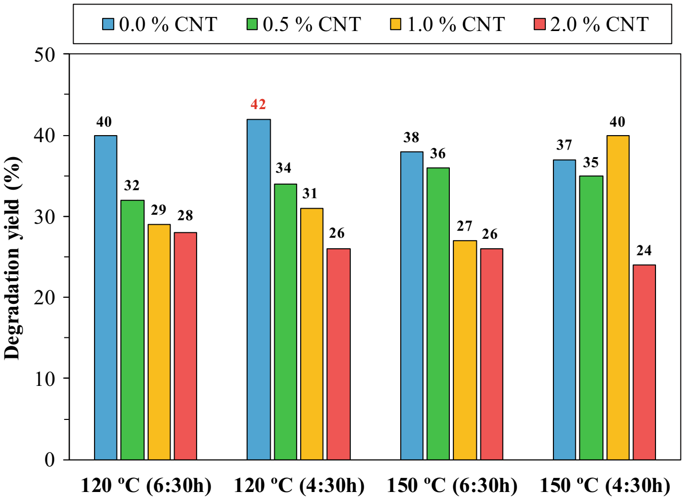

Fig. 6.20 Trend of different sample series of BiOBr/MWCNT composite system reflecting degradation efficiency for phenol under visible light irradiation. Reprinted from Ref. [76] with permission from Elsevier

boost the charge transfer during the photocatalytic process. Other than this, as expected, enhanced UV–Vis light absorption and relatively higher surface area of composites in comparison to bulk counterparts, was observed. The degradation efficiency of composites for Congo Red dye ranged from 92 to 79% for different BiOX in 90 min under natural sunlight. The increased photocatalytic performance was due to the presence of g-C_3N_4 into BiOX which resulted in generation of more charge carriers and at the same time, cause of suppressing the recombination phenomena. Figure 6.21 is a pictorial representation of addition of g-C_3N_4 and its impact on the photodegradation efficiency of BiOX/g-C_3N_4 composites.

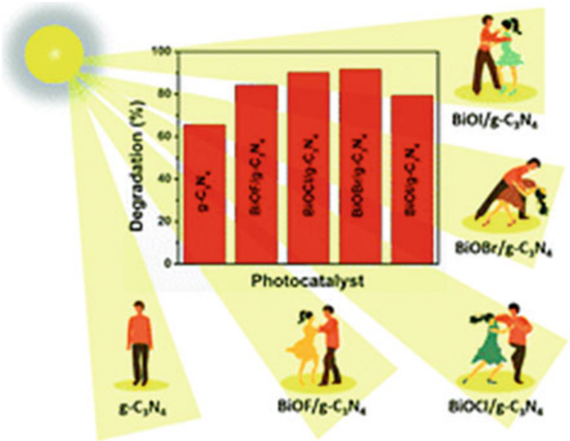

Fig. 6.21 Pictorial representation of photodegradation efficiency of BiOX/g-C_3N_4 composites. (Singh, https://pubs.rsc.org/en/content/articlepdf/2020/ma/d0ma00294a. Licensed under CC BY 3.0)

2. **Bi_2WO_6/Carbon nanocomposites for visible light photodegradation:**

The composites of Bi_2WO_6 with carbon nanofamily has also shown superior photocatalytic performance. The effect of carbon on Bi_2WO_6 could be seen through several studies reported. For instance, Ge et al. reported the composite of Bi_2WO_6 with g-C_3N_4 for the degradation of methyl orange under visible light [25]. On the other hand, Li et al. studied the highly selective photoreduction of CO_2 to CO by Bi_2WO_6/g-C_3N_4 composite [49]. In the study by Ge, red shift and strong absorption in visible-light region was observed after incorporating g-C_3N_4. However, significant effect of the doping amount of g-C_3N_4 on the catalytic activity was seen. The interfacial charge transfer and photocatalytic activity of the composite was lowered when the amount of g-C_3N_4 doping exceeded 70 wt%. Here, g-C_3N_4 played the role of a sensitizer and Bi_2WO_6 as a substrate. In another study, Bi_2WO_6 nanostructures were modified by carbon via hydrothermal synthesis, as reported by Li et al., where glucose was used as a source of carbon [51]. Parallel to the study of Ge, in this study also, the amount of carbon had a significant impact on the photocatalytic activity. In general, the glucose transforms to some carbonaceous species under hydrothermal conditions. Following this, glucose acted as a surfactant here and resulted in change of morphology after hydrothermal treatment, from 2-D plates to 3-D hierarchal structure, as shown in Fig. 6.22. However, beyond a certain increase in glucose content, agglomeration of nanoplates was seen. Photocatalytic activity of the C-modified Bi_2WO_6 decreased dramatically after adding excess amount of glucose due to thick coating of carbon formed that prevented the optical absorption of Bi_2WO_6.

Other significant work done on Bi_2WO_6 composite using activated carbon (AC) by Zuo and coworkers for eliminating microcystin under simulated sunlight [117]. The composite with 5% AC showed the highest photocatalytic performance with degradation efficiency reaching more than 90%. Similar study to investigate the role of activated carbon on the photocatalytic activity of Bi_2WO_6 was reported by Lopez et al. [63]. As discussed about the benefits of incorporating

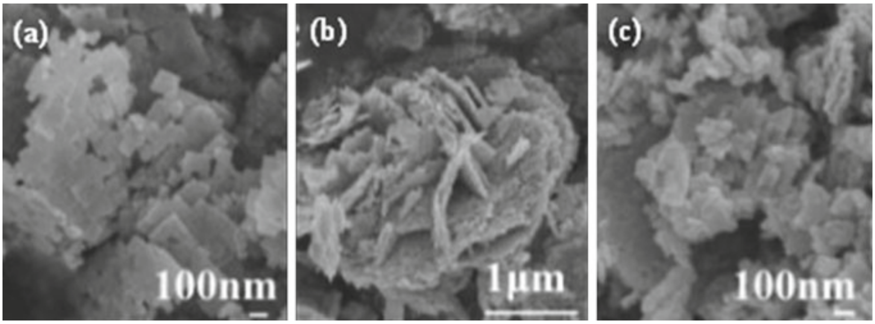

Fig. 6.22 SEM images of **a** pure Bi_2WO_6 **b** Bi_2WO_6/glucose, **c** aggregated 2-D nanoplates Bi_2WO_6/glucose (excess of glucose). Reprinted from Ref. [51] with permission from The Royal Society of Chemistry

two-dimensional layered structure graphene into composite system of photocatalysts in previous section, several works were reported on the composites with Bi_2WO_6 as well. Gao et al. prepared Bi_2WO_6/graphene composite via hydrothermal method for the decomposition of RhB under visible light [23]. The composite of Bi_2WO_6 and graphene offered higher conduction band position of Bi_2WO_6, thus, increasing the reduction ability. The composites of uniform Bi_2WO_6 nanoparticles with reduced graphene oxide (RGO) was fabricated by Juang et al. via a facile self-assembly approach [99]. They revealed some interesting facts about the dependence of energy levels of photogenerated charge carriers on the photocatalytic activity of the Bi_2WO_6/RGO composite. An upshift of valence and conduction band edge of catalyst was observed due to close interfacial contact and electronic interaction between Bi_2WO_6 and RGO. However, its influence on the photocatalytic reduction and oxidation reactions was different. There was significant enhancement in the photocatalytic reduction reactions because of upshift of conduction band edge and improved charge separation while a very slight improvement for the oxidation reactions in comparison to pure Bi_2WO_6 was found. Therefore, they concluded that the prime reason for the difference in the enhancement of photocatalytic activity for different reactions is based on the energy levels of photogenerated charge carriers. Figure 6.23 shows a schematic diagram of the proposed mechanism and photocatalytic efficiency of the prepared composites

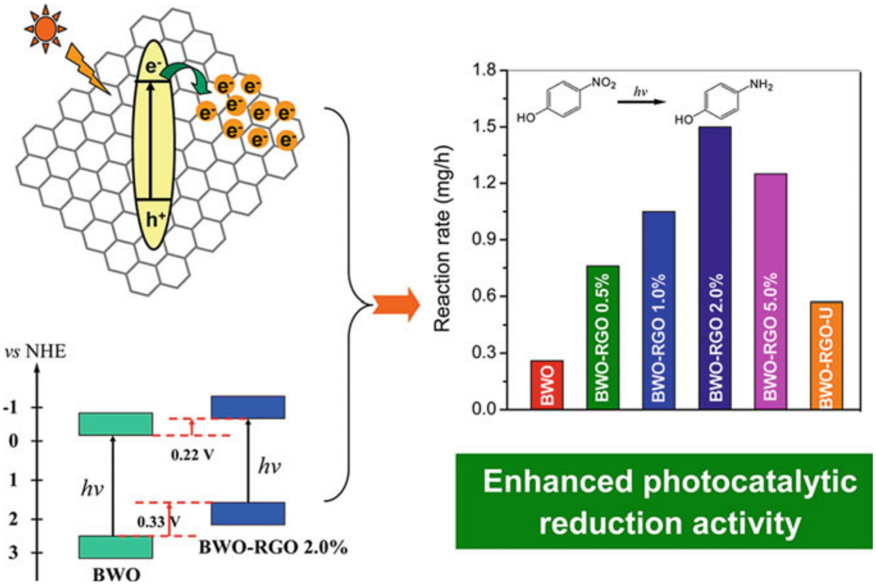

Fig. 6.23 Graphical representation of the effect of introducing graphene into Bi_2WO_6 showing upshift of valence and conduction band *(left)* and order of photocatalytic selective reduction of 4-NP by different Bi_2WO_6/RGO composites *(right)*. Reprinted from Ref. [99] with permission from The American Chemical Society

series. The composites of Bi_2WO_6 with MWCNT have also shown promising results. Longfei et al. synthesized Bi_2WO_6/MWCNT mesoporous composites to study the photodegradation of tetracycline [103]. As predicted, the performance of the composite was significantly enhanced after introduction of MWCNT as compared to pure Bi_2WO_6. The obvious reason for enhancement is because of efficient charge separation, thus facilitating charge transportation. Additionally, the adsorption of tetracycline on catalysts surface was enhanced due to large surface area of MWCNT and π-π electron coupling with the contaminant and MWCNT.

3. $BiVO_4$/Carbon nanocomposites for visible light photodegradation:

The composites of $BiVO_4$ with carbon nanostructures also seems to play an important role in removing pollutants and photoreduction applications. The $BiVO_4$/r-GO composite was fabricated by J. Sun et al. to study the photodegradation of acetaminophen under visible light [80]. The composites were synthesized in different morphologies including nanotubes, nanosheets, and nanoparticles, out of which nanosheets showed superior photocatalytic activity and relatively high stability, as shown in Fig. 6.24. Obviously, the interfacial contact between GO and nanosheets helped in the photodegradation process but to some extent, in this case, the morphology also contributed. Figure 6.25 explains the charge separation mechanism for BiVO4/r-GO composite. Similarly, another work was done on $BiVO_4$/graphene composite synthesized via single-step method [95]. Interestingly, leaf-like morphology was obtained and the outstanding performance, for RhB under visible light, is due to coupling with r-GO as well as rough surface of the leaf-like $BiVO_4$. The leaf-like morphology could be seen in SEM images shown in Fig. 6.26.

In a composite of $BiVO_4$ with MWCNT, the particles of MWCNT were tightly embedded within $BiVO_4$ [113]. However, some of them could be seen on the surface of $BiVO_4$ also. This growth mechanism of MWCNT on $BiVO_4$ is shown in Fig. 6.27. This is advantageous as it resulted in more active sites in addition to enhancement of optical properties as compared to pure $BiVO_4$. As expected, the

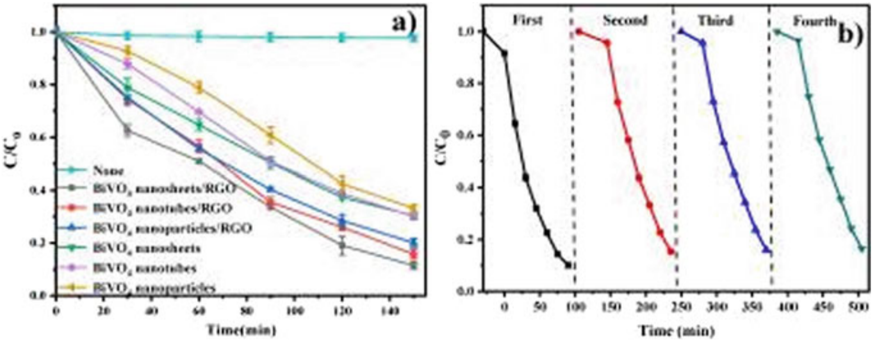

Fig. 6.24 **a** Photocatalytic degradation curves of acetaminophen under visible light irradiation and **b** stability curves for the sample BiVO4/r-GO nanosheets (Jing Sun, https://www.ncbi.nlm.nih.gov/pmc/articles/PMC6630799/. Licensed under CC BY 4.0)

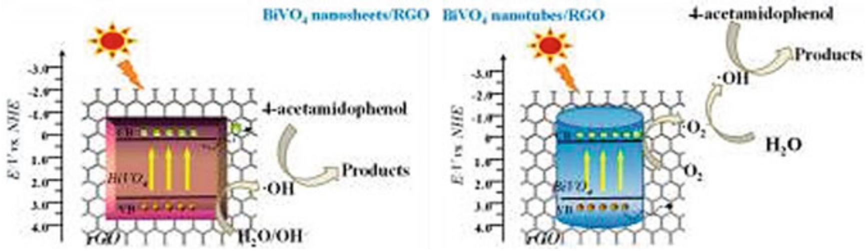

Fig. 6.25 Schematic diagram to show electron–hole separation in BiVO4/r-GO composite (Jing Sun, https://www.ncbi.nlm.nih.gov/pmc/articles/PMC6630799/. Licensed under CC BY 4.0)

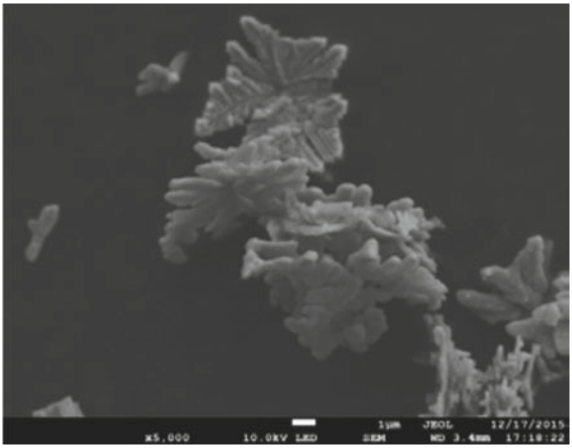

Fig. 6.26 SEM image of $BiVO_4$/r-GO composite with leaf-like morphology. Reprinted from Ref. [95] with permission from The Royal Society of Chemistry

high photocatalytic performance of the composite for RhB under visible light is because MWCNT is well embedded which enhanced the visible light absorption. Activated carbon fibers (ACF) have also been used with $BiVO_4$ for decomposing pollutants. For instance, Zhang et al. synthesized nanocomposite of $BiVO_4$/ACF to study the photodegradation of Reactive Black KN-B (RB5) under visible light [104]. The formation of heterojunction electric field between catalyst and ACF resulted in higher photocatalytic activity. Xuan and coworkers reported the synthesis of BiVO4/graphene nanocomposites where good dispersion of $BiVO_4$ on graphene sheet led to an improved photodegradation of RhB under visible light [96]. The presence of graphene provided the high mobility of charge carriers, therefore, facilitating the charge separation. However, with increase in graphene content, no enhancement in the photocatalytic activity of the nanocomposite was observed. Thus, in every case, the beneficial effect of such nanostructures could be seen only upto an optimal quantity, beyond this, the effect seems to be detrimental.

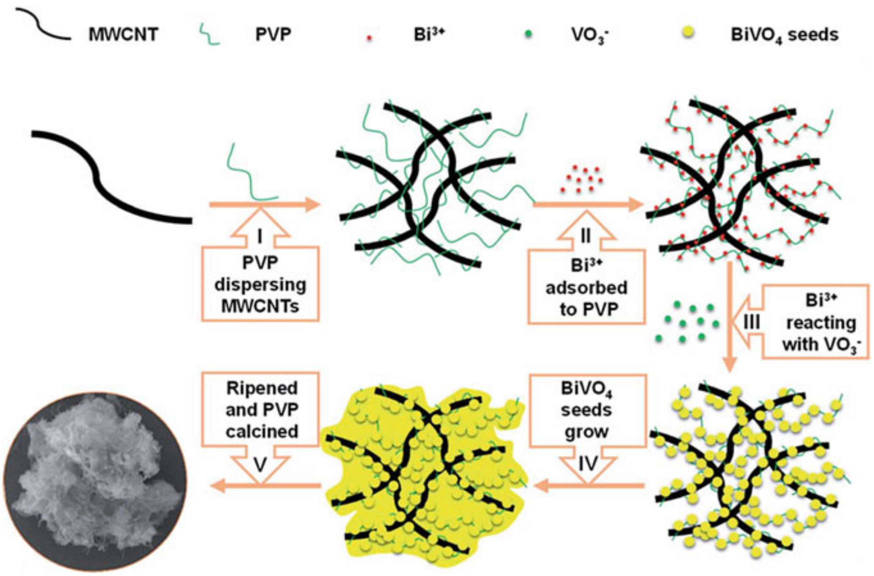

Fig. 6.27 Schematic diagram showing growth of MWCNT on $BiVO_4$ spheres (D. Zhao, https://pubs.rsc.org/en/content/articlepdf/2017/ra/c7ra04288d. Licensed under CC BY-NC 3.0)

In summary, the development of visible-light-driven photocatalysts is progressing significantly and group of "bismuth" family contributes to a great extent. The appropriate band gap energy of Bismuth-related photocatalysts is an added advantage. However, the high instability of photogenerated charge carriers, during the photocatalytic process, ends up in recombining with other processes and as a result, the adsorbed energy is lost in the form of heat which leads to lower photocatalytic efficiency. Bismuth/Carbon nanocomposites have emerged as promising materials and helped in solving such issues to some extent. The introduction of such nanostructures into semiconductor metal oxide has the benefit of providing high surface area support, besides the advantage of facilitating charge separation. This charge separation has been possible via one or more mechanism: lowering the recombination rate of charge carriers, availability of high adsorptive active sites, and in some cases, tuning band gap/photosensitization. Therefore, it could be concluded that the role of carbon nanostructures may vary depending on a number of factors. It is anticipated that with growing research on carbon-bismuth hybrid system, newer versions of such photocatalytic composites will evolve and be one of the powerful systems in the fields of energy and environmental protection.

References

1. Ai Z, Ho W, Lee S (2011) Efficient visible light photocatalytic removal of NO with BiOBr-graphene nanocomposites. J Phys Chem C 115(51):25330–25337. https://doi.org/10.1021/jp206808g
2. Bacha AUR, Nabi I, Cheng H, Li K, Ajmal S, Wang T, Zhang L (2020) Photoelectrocatalytic degradation of endocrine-disruptor bisphenol—a with significantly activated peroxymonosulfate by Co-BiVO4 photoanode. Chem Eng J 389(January):124482. https://doi.org/10.1016/j.cej.2020.124482
3. Bai H, Li C, Shi G (2011) Functional composite materials based on chemically converted graphene. Adv Mater 23(9):1089–1115. https://doi.org/10.1002/adma.201003753
4. Bannister FA (1935) The crystal-structure of the bismuth oxyhalides. Mineral Mag J Mineral Soc 24(149):49–58. https://doi.org/10.1180/minmag.1935.024.149.01
5. Bárdos E, Király AK, Pap Z, Baia L, Garg S, Hernádi K (2019) The effect of the synthesis temperature and duration on the morphology and photocatalytic activity of BiOX (X = Cl, Br, I) materials. Appl Surface Sci 479(November 2018):745–756. https://doi.org/10.1016/j.apsusc.2019.02.136
6. Bárdos E, Kovács G, Gyulavári T, Németh K, Kecsenovity E, Berki P, Hernádi K (2018) Novel synthesis approaches for WO3-TiO2/MWCNT composite photocatalysts- problematic issues of photoactivity enhancement factors. Catal Today 300:28–38. https://doi.org/10.1016/j.cattod.2017.03.019
7. Barreca D, Depero LE, Di Noto V, Rizzi GA, Sangaletti L, Tondello E (1999) Thin films of bismuth vanadates with modifiable conduction properties. Chem Mater 11(2):255–261. https://doi.org/10.1021/cm980725q
8. Benesh AH, Ave SA, Dak S (1989) United States patent, 191 Date of Patent: EQQEIQNQPEEE' DOQQMENTS, pp 2–5
9. Bhattacharya AK, Mallick KK, Hartridge A (1997) Phase transition in BiVO4. Mater Lett 30 (1):7–13. https://doi.org/10.1016/S0167-577X(96)00162-0
10. Bierlein JD, Sleight AW (1975) Ferroelasticity in BiVO4. Solid State Commun 16(1):69–70. https://doi.org/10.1016/0038-1098(75)90791-7
11. Bilgin Simsek E, Balta Z, Demircivi P (2019) Novel shungite based Bi 2 WO 6 carbocatalyst with high photocatalytic degradation of tetracycline under visible light irradiation. J Photochem Photobiol A Chem 380(January):111849. https://doi.org/10.1016/j.jphotochem.2019.05.012
12. Cai L (2015) Enhanced visible light photocatalytic activity of BiOCl by compositing with g-C3N4. Mater Res Innovations 19(5):392–396. https://doi.org/10.1179/1433075X15Y.0000000047
13. Cao S, Yu J (2016) Reviews carbon-based H_2-production photocatalytic materials. J Photochem Photobiol C : Photochem 27:72–99
14. Cao XF, Zhang L, Chen XT, Xue ZL (2011) Microwave-assisted solution-phase preparation of flower-like Bi 2WO6 and its visible-light-driven photocatalytic properties. CrystEngComm 13(1):306–311. https://doi.org/10.1039/c0ce00031k
15. Castro A, Bégué P, Jiménez B, Ricote J, Jiménez R, Galy J (2003) New Bi2Mo1-xWxO6 solid solution: mechanosynthesis, structural study, and ferroelectric properties of the x = 0.75 member. Chem Mater 15(17):3395–3401. https://doi.org/10.1021/cm030224r
16. Chang X, Gondal MA, Al-Saadi AA, Ali MA, Shen H, Zhou Q, Ji G (2012) Photodegradation of rhodamine B over unexcited semiconductor compounds of BiOCl and BiOBr. J Colloid Interface Sci 377(1):291–298. https://doi.org/10.1016/j.jcis.2012.03.021
17. Chang X, Huang J, Cheng C, Sui Q, Sha W, Ji G, Yu G (2010) BiOX (X = Cl, Br, I) photocatalysts prepared using NaBiO3 as the Bi source: characterization and catalytic performance. Catal Commun 11(5):460–464. https://doi.org/10.1016/j.catcom.2009.11.023

18. Cui D, Wang L, Xu K, Ren L, Weng L, Yu Y, Hao W (2018) Band-gap engineering of BiOCl with oxygen vacancies for efficient photooxidation properties under visible-light irradiation. J Mater Chem A 6(5):2193–2199. https://doi.org/10.1039/c7ta09897a
19. Di J, Xia J, Li H, Guo S, Dai S (2017) Bismuth oxyhalide layered materials for energy and environmental applications. Nano Energy 41(August):172–192. https://doi.org/10.1016/j.nanoen.2017.09.008
20. Dong P, Xi X, Zhang X, Hou G, Guan R (2016) Template-free synthesis of monoclinic BiVO4 with porous structure and its high photocatalytic activity. Materials 9(8):1–11. https://doi.org/10.3390/ma9080685
21. Fresno F, Portela R, Suárez S, Coronado JM (2014) Photocatalytic materials: recent achievements and near future trends. J Mater Chem A 2(9):2863–2884. https://doi.org/10.1039/c3ta13793g
22. Galembeck A, Alves OL (2002) Bismuth vanadate synthesis by metallo-organic decomposition: thermal decomposition study and particle size control. J Mater Sci 37(10):1923–1927. https://doi.org/10.1023/A:1015206426473
23. Gao E, Wang W, Shang M, Xu J (2011) Synthesis and enhanced photocatalytic performance of graphene-Bi 2WO6 composite. Phys Chem Chem Phys 13(7):2887–2893. https://doi.org/10.1039/c0cp01749c
24. Garg S, Yadav M, Chandra A, Sapra S, Gahlawat S, Ingole PP, Hernadi K (2018). Facile green synthesis of BiOBr nanostructures with superior visible-light-driven photocatalytic activity. Materials 11(8). https://doi.org/10.3390/ma11081273
25. Ge L, Han C, Liu J (2011) Novel visible light-induced g-C3N4/Bi2WO6 composite photocatalysts for efficient degradation of methyl orange. Appl Catal B 108–109:100–107. https://doi.org/10.1016/j.apcatb.2011.08.014
26. Golmojdeh H, Zanjanchi MA (2014) Ethanol gas sensor based on pure and La-doped bismuth vanadate. J Electron Mater 43(2):528–534. https://doi.org/10.1007/s11664-013-2921-4
27. Gotić M, Musić S, Ivanda M, Šoufek M, Popović S (2005) Synthesis and characterisation of bismuth(III) vanadate. J Mol Struct 744–747(SPEC. ISS.):535–540. https://doi.org/10.1016/j.molstruc.2004.10.075
28. Guerra FD, Attia MF, Whitehead DC, Alexis F (2018) Nanotechnology for environmental remediation: materials and applications. Molecules 23(7):1–23. https://doi.org/10.3390/molecules23071760
29. Guo W, Zhang F, Lin C, Wang ZL (2012) Direct growth of TiO_2 nanosheet arrays on carbon fibers for highly efficient photocatalytic degradation of methyl orange. Adv Mater 24 (35):4761–4764. https://doi.org/10.1002/adma.201201075
30. Gusain R, Kumar P, Sharma OP, Jain SL, Khatri OP (2016) Reduced graphene oxide-CuO nanocomposites for photocatalytic conversion of CO_2 into methanol under visible light irradiation. Appl Catal B 181:352–362. https://doi.org/10.1016/j.apcatb.2015.08.012
31. Haili LIN, Jing CAO, Bangde LUO, Benyan XU, Shifu C (2012) Visible-light photocatalytic activity and mechanism of novel AgBr/BiOBr prepared by deposition-precipitation. 57 (22):2901–2907. https://doi.org/10.1007/s11434-012-5260-6
32. He J, Wang W, Zhang L, Zou Z, Fu Z, Xu Z (2013) Morphology controlled synthesis and characterization of Bi 2WO6 photocatalysts. J Wuhan Univ Technol Mater Sci Ed 28 (2):231–234. https://doi.org/10.1007/s11595-013-0670-0
33. He R, Cao S, Zhou P, Yu J (2014) Recent advances in visible light Bi-based photocatalysts. Cuihua Xuebao/Chin J Catal 35(7):989–1007. https://doi.org/10.1016/s1872-2067(14)60075-9
34. He R, Cao S, Guo D, Cheng B, Wageh S, Al-Ghamdi AA, Yu J (2015) 3D BiOI-GO composite with enhanced photocatalytic performance for phenol degradation under visible-light. Ceram Int 41(3):3511–3517. https://doi.org/10.1016/j.ceramint.2014.11.003
35. Huang Y, Kou S, Zhang X, Wang L, Lu P, Zhang D (2020) Facile fabrication of Z-scheme BI2wo6/wo3 composites for efficient photodegradation of bisphenol a with peroxymonosulfate activation. Nanomaterials 10(4). https://doi.org/10.3390/nano10040724

36. Huang Yu, Ai Z, Ho W, Chen M, Lee S (2010) Ultrasonic spray pyrolysis synthesis of porous Bi2WO6 microspheres and their visible-light-induced photocatalytic removal of NO. J Phys Chem C 114(14):6342–6349. https://doi.org/10.1021/jp912201h
37. Huizhong AN, Yi DU, Tianmin W, Cong W, Weichang HAO, Junying Z (2008) Photocatalytic properties of BiOX (X =Cl, Br, and I). Rare Met 27(3):243–250
38. Ibusuki T, Takeuchi K (1994) Removal of low concentration nitrogen oxides through photoassisted heterogeneous catalysis. J Mol Catal 88(1):93–102. https://doi.org/10.1016/0304-5102(93)E0247-E
39. Jiang H, Dai H, Meng X, Ji K, Zhang L, Deng J (2011) Porous olive-like BiVO4: Alcoho-hydrothermal preparation and excellent visible-light-driven photocatalytic performance for the degradation of phenol. Appl Catal B 105(3–4):326–334. https://doi.org/10.1016/j.apcatb.2011.04.026
40. Kandy MM (2020) Carbon-based photocatalysts for enhanced photocatalytic reduction of CO_2 to solar fuels. SUT J Math 4(2):469–484. https://doi.org/10.1039/c9se00827f
41. Kása Z, Baia L, Magyari K, Hernádi K, Pap Z (2019). Innovative visualization of the effects of crystal morphology on semiconductor photocatalysts. Tuning the Hückel polarity of the shape-tailoring agents: the case of Bi 2 WO 6. CrystEngComm 21(8):1267–1278. https://doi.org/10.1039/c8ce01744a
42. Ke D, Peng T, Ma L, Cai P, Dai K (2009) Effects of hydrothermal temperature on the microstructures of BiVO4 and its photocatalytic O_2 evolution activity under visible light. Inorg Chem 48(11):4685–4691. https://doi.org/10.1021/ic900064m
43. Khan Z, Bhattu S, Haram S, Khushalani D (2014) SWCNT/BiVO4 composites as anode materials for supercapacitor application. RSC Adv 4(33):17378–17381. https://doi.org/10.1039/c4ra01273a
44. Kudo A, Hijii S (1999) H_2 or O_2 evolution from aqueous solutions on layered oxide photocatalysts consisting of Bi3+ with 6s2 configuration and d0 transition metal ions. Chem Lett 1103–1104. https://doi.org/10.1246/cl.1999.1103
45. Kudo A, Ueda K, Kato H, Mikami I (1998) Photocatalytic O_2 evolution under visible light irradiation on BiVO4 in aqueous $AgNO_3$ solution. Catal Lett 53(3):229–230. https://doi.org/10.1023/A:1019034728816
46. Kumar S, Kumar A, Bahuguna A, Sharma V, Krishnan V (2017) Two-dimensional carbon-based nanocomposites for photocatalytic energy generation and environmental remediation applications. Beilstein J Nanotechnol 8(1):1571–1600. https://doi.org/10.3762/bjnano.8.159
47. Li G, Zhang D, Yu JC (2008) Ordered mesoporous BiVO4 through nanocasting: a superior visible light-driven photocatalyst. Chem Mater 20(12):3983–3992. https://doi.org/10.1021/cm800236z
48. Li G, Zhang D, Yu JC, Leung MKH (2010) An efficient bismuth tungstate visible-light-driven photocatalyst for breaking down nitric oxide. Environ Sci Technol 44 (11):4276–4281. https://doi.org/10.1021/es100084a
49. Li M, Zhang L, Fan X, Zhou Y, Wu M, Shi J (2015) Highly selective CO_2 photoreduction to CO over g-C3N4/Bi2WO6 composites under visible light. J Mater Chem A 3(9):5189–5196. https://doi.org/10.1039/c4ta06295g
50. Li S, Hu S, Xu K, Jiang W, Liu J, Wang Z (2017) A novel heterostructure of BiOI nanosheets anchored onto MWCNTs with excellent visible-light photocatalytic activity. Nanomaterials 7(1):1–13. https://doi.org/10.3390/nano7010022
51. Li Y, Liu J, Huang X, Yu J (2010) Carbon-modified Bi2WO6 nanostructures with improved photocatalytic activity under visible light. Dalton Trans 39(14):3420–3425. https://doi.org/10.1039/b924584g
52. Liang YT, Vijayan BK, Lyandres O, Gray KA, Hersam MC (2012) Effect of dimensionality on the photocatalytic behavior of carbon-titania nanosheet composites: charge transfer at nanomaterial interfaces. J Phys Chem Lett 3(13):1760–1765. https://doi.org/10.1021/jz300491s

53. Liu H, Cao WR, Su Y, Chen Z, Wang Y (2013) Bismuth oxyiodide-graphene nanocomposites with high visible light photocatalytic activity. J Colloid Interface Sci 398:161–167. https://doi.org/10.1016/j.jcis.2013.02.007
54. Liu SJ, Hou YF, Zheng SL, Zhang Y, Wang Y (2013) One-dimensional hierarchical Bi2WO6 hollow tubes with porous walls: synthesis and photocatalytic property. CrystEngComm 15(20):4124–4130. https://doi.org/10.1039/c3ce40237a
55. Liu Y, Zhang Y, Guo H, Cheng X, Liu H, Tang W (2017) Persulfate-assisted photodegradation of diethylstilbestrol using monoclinic BiVO4 under visible-light irradiation. Environ Sci Pollut Res 24(4):3739–3747. https://doi.org/10.1007/s11356-016-8020-3
56. Liu Z, Xu W, Fang J, Xu X, Wu S, Zhu X, Chen Z (2012) Decoration of BiOI quantum size nanoparticles with reduced graphene oxide in enhanced visible-light-driven photocatalytic studies. Appl Surf Sci 259:441–447. https://doi.org/10.1016/j.apsusc.2012.07.063
57. Low J, Cheng B, Yu J, Jaroniec M (2016) Carbon-based two-dimensional layered materials for photocatalytic CO_2 reduction to solar fuels. Energy Storage Mater 3:24–35. https://doi.org/10.1016/j.ensm.2015.12.003
58. Lv Y, Yao W, Zong R, Zhu Y (2016) Fabrication of wide-range-visible photocatalyst Bi2WO6-x nanoplates via surface oxygen vacancies. Sci Reports 6(July 2015):1–9. https://doi.org/10.1038/srep19347
59. Mahanty S, Ghose J (1991) Preparation and optical studies of polycrystalline Bi2WO6. Mater Lett 11(8–9):254–256. https://doi.org/10.1016/0167-577X(91)90196-D
60. Meng X, Zhang Z (2016) Bismuth-based photocatalytic semiconductors: Introduction, challenges and possible approaches. J Mol Catal A: Chem 423:533–549. https://doi.org/10.1016/j.molcata.2016.07.030
61. Monfort O, Plesch G (2018) Bismuth vanadate-based semiconductor photocatalysts: a short critical review on the efficiency and the mechanism of photodegradation of organic pollutants. Environ Sci Pollut Res 25. https://doi.org/10.1007/s11356-018-2437-9
62. Munprom R, Salvador PA, Rohrer GS (2015) The orientation dependence of the photochemical reactivity of BiVO4. J Mater Chem A 3(5):2370–2377. https://doi.org/10.1039/c4ta06045h
63. Murcia-López S, Navío JA, Hidalgo MC (2013) Role of activated carbon on the increased photocatalytic activity of AC/Bi2WO6 coupled materials. Appl Catal A 466:51–59. https://doi.org/10.1016/j.apcata.2013.06.022
64. Nikam S, Joshi S (2016) Irreversible phase transition in BiVO4 nanostructures synthesized by a polyol method and enhancement in photo degradation of methylene blue. RSC Adv 6 (109):107463–107474. https://doi.org/10.1039/c6ra14700c
65. Niu J, Dai P, Wang K, Zhang Z, Zhang Q, Yao B, Yu X (2019) Enhanced visible-light photocatalytic activity of BiOI–MWCNT composites synthesised via rapid and facile microwave hydrothermal method. Mater Technol 34(9):506–514. https://doi.org/10.1080/10667857.2019.1586086
66. Niu S, Zhang R, Guo C (2020) Oxygen vacancy induced superior visible-light-driven photo-catalytic performance in the BiOCl homojunction. Mater Chem Front 4(8):2314–2324. https://doi.org/10.1039/d0qm00187b
67. Noor M, Al Mamun MA, Matin MA, Islam MF, Haque S, Rahman F, Hakim MA (2019) Effect of pH variation on structural, optical and shape morphology of BiVO4photocatalysts. In: ICECE 2018—10th international conference on electrical and computer engineering, pp 81–84. https://doi.org/10.1109/ICECE.2018.8636721
68. Park Y, Mc Donald KJ, Choi KS (2013) Progress in bismuth vanadate photoanodes for use in solar water oxidation. Chem Soc Rev 42(6):2321–2337. https://doi.org/10.1039/c2cs35260e
69. Rajalingam V (2015) Synthesis and characterization of BiVO4 nanostructured materials: application to photocataly. Université Du Maine 1–150. https://doi.org/10.1590/S0100-40422009000300005

70. Rengaraj S, Li XZ, Tanner PA, Pan ZF, Pang GKH (2006) Photocatalytic degradation of methylparathion—an endocrine disruptor by Bi3+-doped TiO_2. J Mol Catal A: Chem 247(1–2):36–43. https://doi.org/10.1016/j.molcata.2005.11.030
71. Réti B, Mogyorósi K, Dombi A, Hernádi K (2014) Substrate dependent photocatalytic performance of TiO_2/MWCNT photocatalysts. Appl Catal A 469:153–158. https://doi.org/10.1016/j.apcata.2013.10.001
72. Rodriguez-reinoso F (1998) The role of carbon materials catalysis * in heterogeneous. Nanotechnol Environ Remed Mater Appl 36(3):159–175. https://pubmed.ncbi.nlm.nih.gov/30021974/
73. Schrder E, Thomauske K, Oechsler B, Herberger S (2011) Activated Carbon from Waste Biomass. Prog Biomass Bioenergy Prod. https://doi.org/10.5772/20594
74. Shang M, Wang W, Xu H (2009) New Bi2WO6 nanocages with high visible-light-driven photocatalytic activities prepared in refluxing EG. Cryst Growth Des 9(2):991–996. https://doi.org/10.1021/cg800799a
75. Sharma K, Dutta V, Sharma S, Raizada P, Hosseini-Bandegharaei A, Thakur P, Singh P (2019) Recent advances in enhanced photocatalytic activity of bismuth oxyhalides for efficient photocatalysis of organic pollutants in water: a review. J Ind Eng Chem 78:1–20. https://doi.org/10.1016/j.jiec.2019.06.022
76. Sharma N, Pap Z, Garg S, Hernádi K (2019) Hydrothermal synthesis of BiOBr and BiOBr/CNT composites, their photocatalytic activity and the importance of early Bi6O6(OH)3(NO3)3·1.5H2O formation. Appl Surf Sci 495(July):143536. https://doi.org/10.1016/j.apsusc.2019.143536
77. Shenoy S, Sridharan K (2020) Bismuth oxybromide nanoplates embedded on activated charcoal as effective visible light driven photocatalyst. Chem Phys Lett 749(April):137435. https://doi.org/10.1016/j.cplett.2020.137435
78. Singh M, Kumar A, Krishnan V (2020) Influence of different bismuth oxyhalides on the photocatalytic activity of graphitic carbon nitride: a comparative study under natural sunlight. Mater Adv 1(5):1262–1272. https://doi.org/10.1039/d0ma00294a
79. Su M, He C, Zhu L, Sun Z, Shan C, Zhang Q, Xiong Y (2012) Enhanced adsorption and photocatalytic activity of BiOI-MWCNT composites towards organic pollutants in aqueous solution. J Hazard Mater 229–230:72–82. https://doi.org/10.1016/j.jhazmat.2012.05.061
80. Sun J, Wang C, Shen T, Song H, Li D, Zhao R, Wang X (2019) Engineering the dimensional interface of BiVO4–2D reduced graphene oxide (RGO) nanocomposite for enhanced visible light photocatalytic performance. Nanomaterials 9(6). https://doi.org/10.3390/nano9060907
81. Sun Y, Xie Y, Wu C, Zhang S, Jiang S (2010) Aqueous synthesis of mesostructured BiVO4 quantum tubes with excellent dual response to visible light and temperature. Nano Res 3(9):620–631. https://doi.org/10.1007/s12274-010-0022-8
82. Takeda N, Iwata N, Torimoto T, Yoneyama H (1998) Influence of carbon black as an adsorbent used in TiO_2 photocatalyst films on photodegradation behaviors of propyzamide. J Catal 177(2):240–246. https://doi.org/10.1006/jcat.1998.2117
83. Tang J, Zou Z, Ye J (2004) Photocatalytic decomposition of organic contaminants by Bi 2WO6 under visible light irradiation. Catal Lett 92(1–2):53–56. https://doi.org/10.1023/b:catl.0000011086.20412.aa
84. Tokunaga S, Kato H, Kudo A (2001) Selective preparation of monoclinic and tetragonal BiVO4 with scheelite structure and their photocatalytic properties. Chem Mater 13(12):4624–4628. https://doi.org/10.1021/cm0103390
85. Tryba B, Tsumura T, Janus M, Morawski AW, Inagaki M (2004) Carbon-coated anatase: adsorption and decomposition of phenol in water. Appl Catal B 50(3):177–183. https://doi.org/10.1016/j.apcatb.2004.01.003
86. Vadivel S, Theerthagiri J, Madhavan J, Santhoshini Priya T, Balasubramanian N (2016) Enhanced photocatalytic activity of degradation of azo, phenolic and triphenyl methane dyes using novel octagon shaped BiOCl discs/MWCNT composite. J Water Process Eng 10:165–171. https://doi.org/10.1016/j.jwpe.2015.12.001

87. Wang C, Zhang H, Li F, Zhu L (2010) Degradation and mineralization of bisphenol a by mesoporous Bi 2WO6 under simulated solar light irradiation. Environ Sci Technol 44 (17):6843–6848. https://doi.org/10.1021/es101890w
88. Wang H, Yong D, Chen S, Jiang S, Zhang X, Shao W, Xie Y (2018) Oxygen-vacancy-mediated exciton dissociation in biobr for boosting charge-carrier-involved molecular oxygen activation. J Am Chem Soc 140(5):1760–1766. https://doi.org/10.1021/jacs.7b10997
89. Wang Q, Hui J, Li J, Cai Y, Yin S, Wang F, Su B (2013) Photodegradation of methyl orange with PANI-modified BiOCl photocatalyst under visible light irradiation. Appl Surf Sci 283:577–583. https://doi.org/10.1016/j.apsusc.2013.06.149
90. Wang XJ, Wang Q, Li FT, Yang WY, Zhao Y, Hao YJ, Liu SJ (2013) Novel BiOCl-C3N4 heterojunction photocatalysts: In situ preparation via an ionic-liquid-assisted solvent-thermal route and their visible-light photocatalytic activities. Chem Eng J 234:361–371. https://doi.org/10.1016/j.cej.2013.08.112
91. Weng B, Xu F, Xu J (2014). Hierarchical structures constructed by BiOX (X = Cl, I) nanosheets on CNTs/carbon composite fibers for improved photocatalytic degradation of methyl orange. J Nanopart Res 16(12). https://doi.org/10.1007/s11051-014-2766-7
92. Wu Ju, Duan F, Zheng Y, Xie Y (2007) Synthesis of Bi2WO6 nanoplate-built hierarchical nest-like structures with visible-light-induced photocatalytic activity. J Phys Chem C 111 (34):12866–12871. https://doi.org/10.1021/jp073877u
93. Wu J, Xie Y, Ling Y, Dong Y, Li J, Li S, Zhao J (2019) Synthesis of flower-like g-C3N4/ BiOBr and enhancement of the activity for the degradation of bisphenol a under visible light irradiation. Front Chem 7(October):1–12. https://doi.org/10.3389/fchem.2019.00649
94. Xiang Q, Yu J, Jaroniec M (2012) Graphene-based semiconductor photocatalysts. Chem Soc Rev 41(2):782–796. https://doi.org/10.1039/c1cs15172j
95. Xiong S, Wu T, Fan Z, Zhao D, Du M, Xu X (2017) Preparation of a leaf-like BiVO4-reduced graphene oxide composite and its photocatalytic activity. J Nanomater 2017. https://doi.org/10.1155/2017/3475248
96. Xu X, Zou Q, Yuan Y, Ji F, Fan Z, Zhou B (2014) Preparation of BiVO4-graphene nanocomposites and their photocatalytic activity. J Nanomater 2014. https://doi.org/10.1155/2014/401697
97. Xu YH, Liu CJ, Chen MJ, Liu YQ (2011) A review in visible-light-driven BiVO4 photocatalysts. Int J Nanopart 4(2–3):268–283. https://doi.org/10.1504/IJNP.2011.040513
98. Yadav M, Garg S, Chandra A, Gläser R, Hernadi K (2020) Green BiOI impregnated 2-dimensional cylindrical carbon block: a promising solution for environmental remediation and easy recovery of the photocatalyst. Sep Purif Technol 240(January):116628. https://doi.org/10.1016/j.seppur.2020.116628
99. Yang J, Wang X, Zhao X, Dai J, Mo S (2015) Synthesis of uniform Bi2WO6-reduced graphene oxide nanocomposites with significantly enhanced photocatalytic reduction activity. J Phys Chem C 119(6):3068–3078. https://doi.org/10.1021/jp510041x
100. Ye L, Deng Y, Wang L, Xie H, Su F (2019) Bismuth-based photocatalysts for solar photocatalytic carbon dioxide conversion. Chemsuschem 12(16):3671–3701. https://doi.org/10.1002/cssc.201901196
101. Yin S, Di J, Li M, Fan W, Xia J, Xu H, Li H (2016) Synthesis of multiwalled carbon nanotube modified BiOCl microspheres with enhanced visible-light response photoactivity. Clean: Soil, Air, Water 44(7):781–787. https://doi.org/10.1002/clen.201500418
102. Yu J, Kudo A (2005) Hydrothermal synthesis of nanofibrous bismuth vanadate a b. Chem Lett 34(6):850–851. https://doi.org/10.1246/cl.2005.850
103. Yue L, Wang S, Shan G, Wu W, Qiang L, Zhu L (2015) Novel MWNTs-Bi2WO6 composites with enhanced simulated solar photoactivity toward adsorbed and free tetracycline in water. Appl Catal B 176–177:11–19. https://doi.org/10.1016/j.apcatb.2015.03.043
104. Zhang C, Han P, Lu X, Mao Q, Qu J, Li Y (2018) Preparation and photocatalytic activity characterization of activated carbon fiber-BiVO4 composites. RSC Adv 8(43):24665–24672. https://doi.org/10.1039/c8ra04659j

105. Zhang C, Zhu Y (2005) Synthesis of square Bi2WO6 nanoplates as high-activity visible-light-driven photocatalysts. Chem Mater 17(13):3537–3545. https://doi.org/10.1021/cm0501517
106. Zhang H, Zhao L, Wang L, Hao J, Meng X (2020) Fabrication of oxygen-vacancy-rich black-BiOBr/BiOBr heterojunction with enhanced photocatalytic activity. J Mater Sci 55 (24):10785–10795. https://doi.org/10.1007/s10853-020-04700-9
107. Zhang KL, Liu CM, Huang FQ, Zheng C, Wang WD (2006) Study of the electronic structure and photocatalytic activity of the BiOCl photocatalyst. Appl Catal B 68(3–4):125–129. https://doi.org/10.1016/j.apcatb.2006.08.002
108. Zhang L, Wang W, Chen Z, Zhou L, Xu H, Zhu W (2007) Fabrication of flower-like Bi2WO6 superstructures as high performance visible-light driven photocatalysts. J Mater Chem 17(24):2526–2532. https://doi.org/10.1039/b616460a
109. Zhang L, Zhu Y (2012) A review of controllable synthesis and enhancement of performances of bismuth tungstate visible-light-driven photocatalysts. Catal Sci Technol 2 (4):694–706. https://doi.org/10.1039/c2cy00411a
110. Zhang S, Yang J (2015) Microwave-assisted synthesis of BiOCl/BiOBr composites with improved visible-light photocatalytic activity. Ind Eng Chem Res 54(41):9913–9919. https://doi.org/10.1021/acs.iecr.5b02332
111. Zhang W, Dong F, Xiong T, Zhang Q (2014) Synthesis of BiOBr-graphene and BiOBr-graphene oxide nanocomposites with enhanced visible light photocatalytic performance. Ceram Int 40(7 Part A):9003–9008. https://doi.org/10.1016/j.ceramint.2014.01.112
112. Zhang Y, Park M, Kim HY, Park SJ (2016) In-situ synthesis of graphene oxide/BiOCl heterostructured nanofibers for visible-light photocatalytic investigation. J Alloy Compd 686:106–114. https://doi.org/10.1016/j.jallcom.2016.06.004
113. Zhao D, Wang W, Sun Y, Fan Z, Du M, Zhang Q, Xu X (2017) One-step synthesis of composite material MWCNT@BiVO4 and its photocatalytic activity. RSC Adv 7 (53):33671–33679. https://doi.org/10.1039/c7ra04288d
114. Zhao H, Tian F, Wang R, Chen R (2014) A review on bismuth-related nanomaterials for photocatalysis. Rev Adv Sci Eng 3(1):3–27. https://doi.org/10.1166/rase.2014.1050
115. Zhao Z, Sun Y, Dong F (2015) Graphitic carbon nitride based nanocomposites: a review. Nanoscale 7(1):15–37. https://doi.org/10.1039/c4nr03008g
116. Zhu J, Xiao P, Li H, Carabineiro SAC (2014) Graphitic carbon nitride: synthesis, properties, and applications in catalysis. ACS Appl Mater Interfaces 6(19):16449–16465. https://doi.org/10.1021/am502925j
117. Zuo X, Cao Y, Gong A, Ding S, Zhang T, Wang Y (2016) Removal of microcystins by highly efficient photo-catalyst Bi2WO6-activated carbon under simulated light. Water, Air, Soil Pollut 227(4). https://doi.org/10.1007/s11270-016-2798-y

Chapter 7
New Photocatalytic Materials Based on Complexes of Nanodiamonds with Diphthalocyanines of Rare Earth Elements

Vasily T. Lebedev, Gyula Török, Yuri V. Kulvelis, Marina A. Soroka, Vladimir A. Ganzha, Vera A. Orlova, Eduard V. Fomin, Larisa V. Sharonova, and Alexandr V. Shvidchenko

Abstract New photoactive catalysts have been synthesized from Europium diphthalocyanine molecules dissolved in dimethylformamide and transferred to aqueous dispersion of detonation nanodiamonds (~4.5 nm in size, positive ζ-potential ~30–40 mV), forming diphthalocyanine–diamond complexes. The weight ratio of diphthalocyanine to nanodiamonds was varied in the range C_R = 0.1–1.0%. The formation of complexes was detected by optical absorption, dynamic light scattering and Raman spectroscopy. The complexes remained stable in water and

---

V. T. Lebedev (✉) · Y. V. Kulvelis · M. A. Soroka · V. A. Ganzha · E. V. Fomin
Petersburg Nuclear Physics Institute Named By B.P.Konstantinov, NRC “Kurchatov Institute”, Gatchina, Leningrad, Russia
e-mail: lebedev_vt@pnpi.nrcki.ru

Y. V. Kulvelis
e-mail: kulvelis_yv@pnpi.nrcki.ru

M. A. Soroka
e-mail: soroka_ma@pnpi.nrcki.ru

V. A. Ganzha
e-mail: ganzha_va@pnpi.nrcki.ru

E. V. Fomin
e-mail: fomin_ev@pnpi.nrcki.ru

G. Török
Atomic Energy Research Institute, MTA, KFKI, Budapest, Budapest,, Hungary
e-mail: torok.gyula@energia.mta.hu

V. A. Orlova
V.G. Khlopin Radium Institute, Saint-Petersburg, Russia

L. V. Sharonova · A. V. Shvidchenko
Ioffe Institute, Saint-Petersburg, Russia
e-mail: sharonova@mail.ioffe.ru

A. V. Shvidchenko
e-mail: avshvid@mail.ioffe.ru

S. Garg and A. Chandra (eds.), *Green Photocatalytic Semiconductors*,
Green Chemistry and Sustainable Technology,
https://doi.org/10.1007/978-3-030-77371-7_7

demonstrated fractal-type self-assembly into chain-like structures at low fraction of molecular component (C_R = 0.1–0.2%). However, at critical concentration C_R * ~0.3% it was detected a transition to branched structures of diamond particles linked via hydrophobic molecules of diphthalocyanine. Dried complexes with Eu atoms settled on diamond carriers showed an intensive characteristic luminescence at wavelengths ~600 and 700 nm under X-ray irradiation (0.154 nm). The developed hybrid structures may serve as catalysts for singlet oxygen generation in surrounding media (air, water, biological tissues) for their cleaning and disinfection. It is assumed the advanced usage in photodynamic therapy and in processes with chemical photoreactions exploiting the activity of molecular oxygen by using light of long wavelength ~600–700 nm.

Keywords Catalyst · Diphthalocyanine · Nanodiamond · Complex · Singlet · Oxygen · Generation

7.1 Introduction

In global aspect, the problems of purification of natural water, industrial and domestic effluents play a key role for mankind, which requires new scientific approaches for saving and restoring fresh water resources. Presently, the tasks of chemical and radiation decomposition of organic matter into less toxic or safe components come to the fore. A high total volume of water resources to be cleaned makes it necessary to develop relevant ecologically clear technologies, e.g., using effective catalytic nanoparticles made of natural components.

For example, valuable results were achieved in the synthesis and photocatalytic applications of new green BiOBr nanoparticles for waste water treatment and recently developed bismuth semiconductor oxyhalide composites (BiOXs) [1]. It was realized a fast green synthesis of BiOBr nanostructures with high photocatalytic activity induced by visible light. There was shown also that plant leaf extracts as photocatalytic agents positively affect the natural biological activity in general, contributing to the restoration of the environment [2]. The results of the analysis of the problems of ecotoxicology and environmental safety are summarized in recent review devoted to BiOX (X = Cl, Br, I) nano(micro)structures and their photocatalytic applications [3]. In following researches, the temperature and synthesis duration effect on the morphology and photocatalytic activities of BiOX materials (X = Cl, Br, I) have been studied to create the basics for producing new industrial catalysts [4].

On the other hand, good opportunities removing aromatic organic compounds from water are opened up by new materials such as graphene nanocomposites [5] and heterogeneous photocatalysis based on TiO_2 particles immobilized on glass spheres [6]. For such objects, an analysis of photoactivity was carried out in connection with the leaching, regeneration of water systems [5, 6].

Along with these approaches, it seems crucially important to find profitable ways to generate active forms of molecular oxygen like in living nature where it is possible a process of photo excitation of molecules O_2. Normally, they are in triplet state but can be transferred into singlet state when they get extremely high chemical activity.

In living nature, singlet oxygen (*SO*) plays a substantial role in photochemical and photobiological processes of catalysis and synthesis [7]. On the other hand, *SO* molecules may initiate a photodegradation of organic molecules (polymers). It is applied in medicine (blood sterilization, photodynamic therapy) and sanitary (purification of water, air, surfaces) [8–10].

Studies of the chemical properties of *SO* have shown its high ability to oxidize substances that do not interact with oxygen in the ground energy state. But in singlet state, oxygen becomes a stronger electrophile than triplet and get an order of magnitude greater oxidative ability. Such excited oxygen quickly reacts with unsaturated carbon–carbon bonds, nucleophiles (sulfides, amines), anions [11]. The methods for producing singlet oxygen are especially important, primarily by optical pumping of photosensitizer molecules, which in turn are capable of exciting surrounding molecular oxygen existing normally in low-energy triplet state [12].

Reactions using *SO* are applied in therapy of viral diseases and for photodynamic inactivation of bacteria by UV irradiation [8–10]. Mechanisms of singlet oxygen formation as well as its chemical and physical properties are reviewed in detail [11–13]. Usually, a direct generation of *SO* in gas or liquid phase is not profitable because of low absorption of UV by oxygen irradiation. Therefore, various dyes (photosensitizers) with high cross section of light (UV) absorption are exploited in the processes of their primary excitation and following energy transfer to oxygen molecules which finally become in singlet state.

Among different ways of the generation of singlet oxygen, the processes using sensitizers are most attractive and prevalent in nature [14]. For biomedical applications, the ideal photosensitizer should be not toxic and fulfill several requirements including the presence of intense absorption band in red or near IR regions of spectrum, the absence of aggregation lowering quantum yield by *SO* generation. It is useful also if these substances are highly fluorescent for simultaneous diagnostics. At last, their life time in triplet state must be long to have intense photodynamic effect. Obviously, these requirements in general are common for other applications of sensitizers to solve sanitary, ecological and medical tasks.

During last decades, a search of effective photosensitizers is widened toward the applications of spread natural and synthetic dyes such as porphyrines [15]. These are molecular pigments containing a flat ring composed of four linked heterocyclic groups often captured a central metal atom. At the same time, most water-soluble porphyrines have not intense longwave absorption band. Therefore, their structural analogs, phthalocyanines (PC), are more suitable for application in photocatalytic processes.

These molecules with nitrogen bridges in the structure possess a stronger absorption ability shifted toward red edge of spectrum where a higher transparence of biological tissues promotes better photodynamic effect [16–19]. Introduction of diamagnetic atoms (Al, Ga, Zn, Si, etc.) into the molecules of PC allows to prepare effective fluorescent substances for diagnostics and photo-dynamic therapy (PDT), while the incorporated transition metals (Co, Fe, Mn, etc.) bring them a high catalytic activity in oxidation reactions although diminish luminescent properties [20, 21].

A combination of these useful properties (fluorescence, catalytic activity) is achieved in more complicated structures being macrocyclic ligands like PC bonded via the rare earth atom (metal tetrapyrrole double- and tripple-deckers) [22]. Such first synthesized structures [23–25] with lanthanides or actinides (Fig. 7.1) are very thermally and chemically stable and combine catalytic and magnetic properties with optical absorption at characteristic wavelengths depending on atomic number of metal atom as well as demonstrate luminescent properties under UV and X-ray irradiation [26].

These macrocyclic compounds, diphthalocyanines of lanthanides (DPC), are optically active materials which may serve as pigments and catalysts with redox potential [27]. Their use can be diversified for relevant applications for cleaning water resources by means of optical or X-ray excitation of these materials. A relaxation of PC or DPC molecules from exited states trigger a generation of chemically extra active singlet oxygen [28] in surrounding medium to cause a degradation of organic impurities. Especially antiviral and antibacterial activity of these materials seems attractive for medicine and sanitary [28].

For advanced applications of these molecular substances (DPC), it should be solved the key problem of deposition of molecules on nanocarriers to provide maximum interface and to prevent a coagulation and irreversible sedimentation of molecules losing catalytic activity in such a case. In this way, it seems a progress of heterogeneous catalysts is developing [29].

For these purposes, we proposed to link the active DPC molecules with diamond surface. The latter is highly stable, chemically inert and very suitable for modification by grafting various functional groups providing desirable interactions of diamonds with ions or molecules in solutions. This is the first step in the creation of new generation of photocatalysts promising a synergy of active DPC and diamond

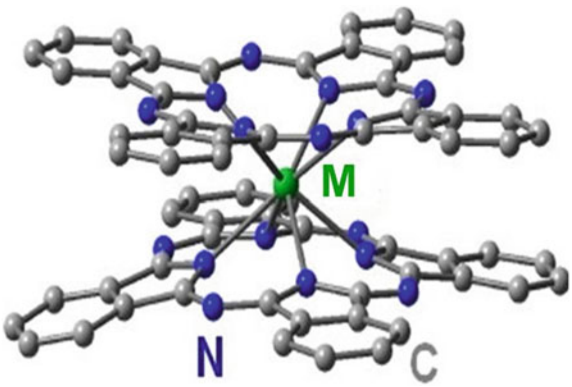

Fig. 7.1 Molecule of diphthalocyanine with metal atom coordinated with plane macrocyclic ligands

components for multiple applications (cleaning water and air, surfaces disinfection, PDT with UV and X-ray pumping). Use of DPC is considered as more profitable way as compared to putting into practice some other nanostructures.

For example, fullerenes may serve as photosensitizers for singlet oxygen generation with quantum yield higher than that for most dyes [30]. On the other hand, fullerenes remain very expensive substances insoluble in water that does not allow use them directly in aqueous solutions and it is needed a synthesis of water-soluble derivatives. Therefore, a search of the ways of the application of more profitable cheaper and easily synthesized substances still remains important.

In this work, the authors tried to create really new nanocatalysts with active macrocyclic DPC component associated with nanodiamonds which can amplify the quantum yield of photosensitizers because of semiconducting properties of diamonds carrying mobile charges on the facets and interior the volume of crystals [31].

7.2 Experimental

7.2.1 Samples

Active component of new catalyst, DPC with Europium, was chosen because of suitable optical absorption and luminescence spectra of Eu attached to ligands shows characteristic bands at short wavelengths $\lambda \sim 300$–400 nm and long wavelengths $\lambda \sim 600$–700 nm near red edge of visible diapason [26]. The latter band is really exploiting in PDT due to lower extinction of such light in biological tissues and media.

The synthesis of DPC with Europium has been performed using the methods developed by the authors [23–25]. The Eu-acetate salt was mixed with melted o-phthalonitrile in a quartz reactor flushed with argon current by heating at the enhanced temperatures 220–250 °C (proportion Salt:o-phthalonitrile = 1:6, melt intensively stirred for 1–2 min). Following reaction of the formation of DPC has taken a time within 25–30 min. Then, the temperature was raised up to 350–400 °C to ward off excess o-phthalonitrile condensed in the upper part of the reactor. Further, it was provided cleaning the final product from the residue of o-phthalonitrile and reaction byproducts. The chemical structure of the obtained DPC samples was confirmed by IR spectroscopy.

The other component was prepared from detonation nanodiamonds (DND) first milled and then chemically purified by etching in acids. To produce the diamonds with positive surface potential, the authors have applied the procedure similar the method [32]. The materials were treated by heating in hydrogen flow (500 °C) to get nanocrystals (DND Z^+) with grafted surface groups (CH_x, COH). This provided positive ζ-potential of particles in aqueous media ($\sim$30–40 mV) and allow obtain stable dispersions. In detail, the procedures of nanodiamonds preparations, formation their dispersions and gels, studies of chemical and physical properties of these materials are described in the papers [31, 33, 34].

To prepare the diamond complexes with DPC the original dispersion containing 0.35% wt. of DND Z^+ (size of particles 4.5 nm found by dynamic light scattering, see Fig. 7.3) was twice diluted and a small amount of the solution of DPC in dimethylformamide (DMF) was added. The DPC component is insoluble in water, while diamonds have a good solubility in both media (H_2O, DMF) as well as DMF is soluble in water unlimited. Then, the mixture was sonicated, cooled and stored two days. To find the upper limit of molecular component in complexes, we increased the amount of DPC till a saturation. Above this critical point, it was observed a sedimentation of DPC not associated with diamonds because of insolubility of DPC in water. After drying the saturated mixture, we found the maximum content of DPC in complexes $C_R = 12\%$ wt. The powder of composite was soluble in water where formed a stable dispersion. The data of optical absorption have shown the presence of DPC molecules in aqueous solution (Fig. 7.2). At wavelengths $\lambda \sim 300$–400 nm, 580–650 and $\lambda \sim 700$ nm, the characteristic bands corresponding to the coordination of Eu atom with PC ligands [26] are detected in spectrum (Fig. 7.2). This confirmed a formation of stable complexes DND-DPC since the DPC molecules are insoluble in water.

The formation of the complex was irreversible. Upon dissolution of the dry powder of the complex in DMF, no dissociation of the complex was observed with the transition of DPC molecules into solution. Since on the surface of DND Z^+ the attached H and OH groups dominate, we conclude a probable formation of complexes DND-DPC with these groups' participation.

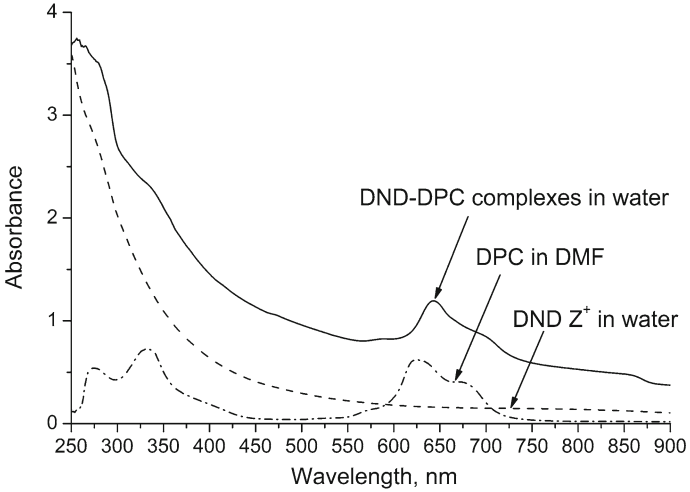

Fig. 7.2 Optical densities of DPC in DMF and aqueous solutions of DND Z^+ and DND-DPC complexes versus light wavelength

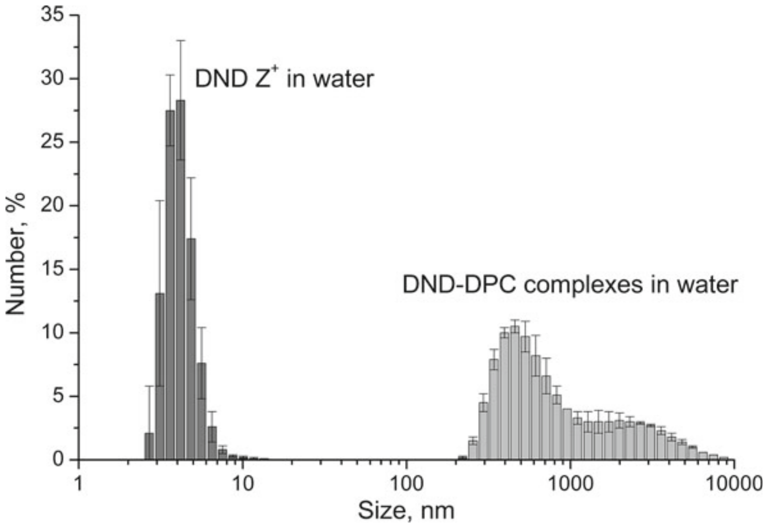

Fig. 7.3 Particle size distributions of DND Z^{+} and DND-DPC complexes in water obtained by dynamic light scattering

In aqueous solution, the complexes showed the aggregation at submicron and micron scales (Fig. 7.3). A bimodal distribution of complexes' clusters indicates the presence of particles with characteristic dimension of 400–500 nm and their aggregates of few microns in size.

The formation of complexes of diamonds with DPC molecules is a result of a number of different type interactions of components. In aqueous medium, hydrophobic DPC molecules via ligands prevail contact hydrophobic regions at diamond surface and possible hydrogen bonds between ligands and functional groups promotes in complexes formation. But the main factor for complexing responsible is electrostatic attraction between positively charged diamonds DND Z^{+} and electro-negative DPC molecules. Oppositely to this, the procedure of complexes preparation with negatively charged diamonds DND Z^{-} (with carboxyl groups on the surface) did not allow obtain complexes. In this case, the molecules did not show any association with diamonds, vice versa a sedimentation of molecules in the dispersion of DND Z^{-} was observed.

Along with discussed physical mechanisms, complexes formation is confirmed by Raman spectroscopy. Powder samples of DND Z^{+}, DPC and binary system after drying of aqueous dispersions were studied by Raman scattering (laser wavelength of 532 nm, radiation power of 6.25 mW spectral resolution of 1.5 cm^{-1}) (Figs. 7.4, 7.5). A typical spectrum with bands 1,320 and 1,628 cm^{-1} was observed for pristine DND Z^{+} (Fig. 7.4). The position of the C–C vibration band (1,321 cm^{-1}) really corresponds to small diamonds ($\sim$3 nm) according to the data [35], where the calculated and experimental spectra for diamonds of different sizes were compared. The 1,628 cm^{-1} band in the spectra for diamonds is attributed to partial sp^2 hybridization of carbon and the presence of single C=C bonds (precursors of graphitization), surface defects and functional groups (OH) on the diamond surface [36].

Comparatively to DND Z^+, the molecular DPC component demonstrates more complicated spectrum (Fig. 7.5, data 1) with a broad photoluminescence band (2,439 cm^{-1}) reflecting electronic transitions in Eu ions [37]. Lines in the range 1,700–600 cm^{-1} characterize stretching modes (1,590; 1,490 cm^{-1}) of benzene rings and isoindole groups, C=C ring bonds vibrations (1,322 cm^{-1}), in-plane deformation vibrations of C–H groups (1,000–1,200 cm^{-1}), out-of-plane vibrations of phthalocyanine rings (675–811 cm^{-1}). At low wavenumbers (100–200 cm^{-1}), the observed lines indicate sandwich structures [37].

Then we analyzed the spectra for binary system with DND Z^+ (Fig. 7.5, data 2) to find the indications of complexing when hydrophilic diamond serves as a carrier of water-insoluble DPC molecules to transfer them into aqueous media. In fact, the components' integration is revealed in DPC lines' intensity change and in their shift relative to the data for pure DPC (Fig. 7.5).

Due to complex formation, well-pronounced band for the pristine DPC (stretching vibrations of benzene rings, 1,590 cm^{-1}) weakens and merges with the neighboring band (1,490 cm^{-1}, vibrations of isoindole groups) which increases on the contrary (Fig. 7.5). The lines (1,112; 1,167 cm^{-1}) are shifted toward high wavenumbers, the band at 1,322 cm^{-1} (vibrations of C–C bonds) becomes more intense.

Along with the shift and redistribution of the band intensities for DPC molecules, a disappearance of molecular luminescence was observed. In sum, it proves DPC molecules are involving in complexes when components' interaction has the character of chemical bonding.

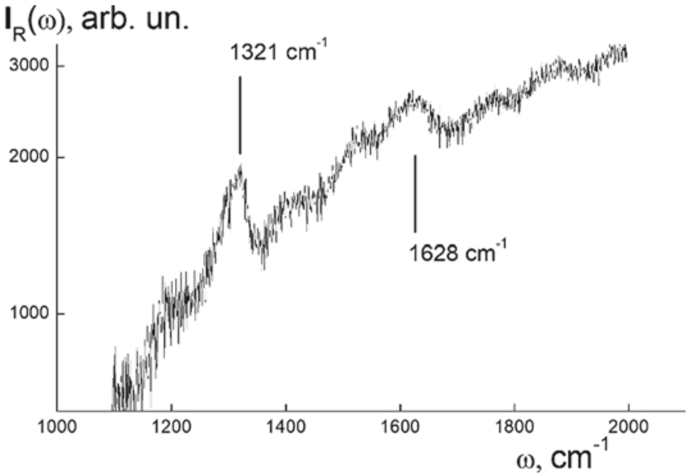

Fig. 7.4 Raman spectrum for DND Z^+ layer obtained after drying a diamond aqueous dispersion

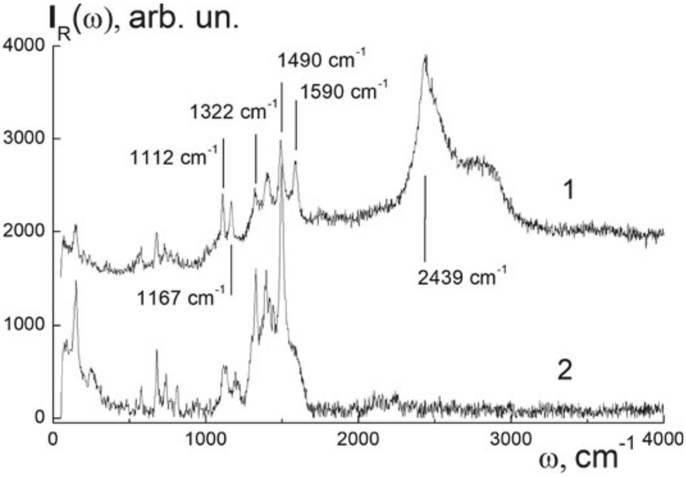

Fig. 7.5 Raman spectrum for DPC powder (1) and complex (2)

7.2.2 Neutron Scattering Experiments

These observations delivered mostly qualitative information on the formation of complexes. To recognize the structure of complexes in detail as dependent on the content of DPC, we carried out a series of neutron scattering experiments on complexes' aqueous solutions (Budapest Neutron Centre, Small Angle Neutron Diffractometer "Yellow submarine"). The set of samples included a control specimen (No 0) of pure aqueous dispersion of DND with concentration $C_{\mathrm{DND}} = 0.175\%$ wt. (Table 7.1). The other samples (No 1–7) have had the same content of diamonds and varied fracture of DPC, $C_{\mathrm{DPC}} = (1.8\text{–}18.0)10^{-4}\%$ wt. Relatively to diamonds, the amount of DPC covered the range $C_{\mathrm{R}} = C_{\mathrm{DPC}}/C_{\mathrm{DND}} = 0.1\text{–}1.0\%$ (Table 7.1).

Table 7.1 Aqueous solutions of complexes

Sample, no	C_{DPC}, $10^{-4}\%$ wt	C_{R}, % wt
0	0	0
1	1.8	0.1029
2	3.6	0.2057
3	5.4	0.3086
4	7.2	0.41s14
5	10.8	0.6171
6	14.4	0.8229
7	18.0	1.0286

Concentrations of DPC (C_{DPC}) and its mass fractions relatively to fixed amount of diamonds $C_{\mathrm{R}} = C_{\mathrm{DPC}}/C_{\mathrm{DND}}$

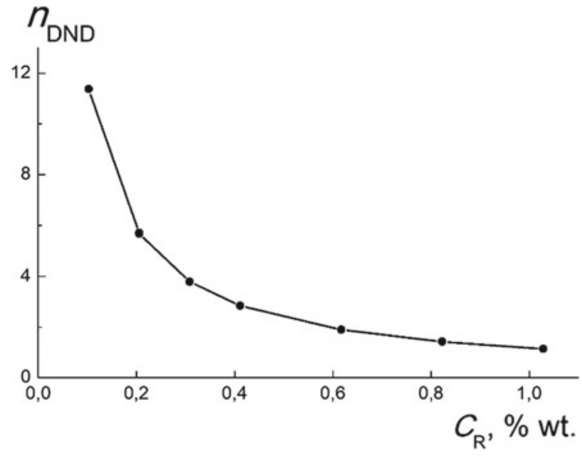

Fig. 7.6 Solutions of complexes, the number of diamond particles per DPC molecule depending on the mass fraction of DPC in the complexes

The goal was to find out how DPC molecules order ensembles of diamond particles in water. In the samples, neutron scattering occurred mainly on diamond particles with high contrast in light water, where the DPC molecules had a weak contrast and were practically not observed in scattering.

For the selected proportions of DPC to diamonds, $C_R = 0.1–1.0$ wt%, the numerical concentration of diamond particles (N_{DND}) was higher or comparable to that for DPC molecules (N_{DPC}). Figure 7.6 shows the calculated ratio $n_{DND} = N_{DND}/N_{DPC} = C_R \times 10^2 \quad (M_{DPC}/M_{DND})$, where $M_{DPC} = 1{,}176$, $M_{DND} = 1.01 \times 10^5$ are the molecular weights of DPC, Eu[$C_{64}H_{32}N_{16}$], and diamond particles having characteristic size of $d_P = 4.5$ nm.

At a minimum fraction of DPC ($C_R \sim 0.1\%$), we have the number of diamonds $n_{DND} \sim 12$ per a molecule in solution while at the upper edge of the concentration range ($C_R \sim 1.0\%$) it is only one particle, $n_{DND} \sim 1$. Hence, in the case of DPC deficiency each molecule can bind several diamond particles from a solution, or integrate into existing diamond structures. With comparable amounts of molecules and particles ($C_R \sim 1.0\%$), the formation of molecule-particle pairs is likely. The neutron scattering data on a series of samples with different DPC contents (Table 7.1), indeed, showed that the nature of the structuring of an ensemble of diamond particles varies depending on the amount of DPC in the system.

7.3 Results and Discussion

7.3.1 Neutron Scattering on Complexes in Solutions

Structural studies of aqueous diamond dispersion and complexes based on it (Table 7.1) were performed by the method of small-angle neutron scattering (SANS) (BNC, Budapest). Measurements on solution layers with a thickness of

$\delta = 0.1$ cm were carried out at room temperature in the range of momentum transfer $q = (4\pi/\lambda)\sin(\theta/2) = 0.2$–$4\ \mathrm{nm}^{-1}$, defined by the scattering angle (θ) and neutron wavelength ($\lambda = 0.382$ nm, $\Delta\lambda/\lambda \sim 0.1$).

To find the neutron scattering cross sections in absolute units, the scattering intensities I_E (q) from the cells filled with solutions were divided by the values of their neutron transmission Tr_T. Then we subtracted the background $I_\mathrm{CV}(q)$ measured for the empty quartz cell and normalized to its transmission relative to the initial neutron beam. The values $I_\mathrm{S}(q) = I_\mathrm{E}(q)/Tr_\mathrm{T}$-$I_\mathrm{CV}(q)$ were normalized to the data for light water $I_\mathrm{W}(q)$ obtained under the same conditions and multiplied by known differential cross section of water $\mathrm{d}\Sigma_\mathrm{W}/\mathrm{d}\Omega$ per cm^3 of volume [38].

As a result, the scattering cross sections of the samples were calculated $\sigma(q) = \mathrm{d}\Sigma/\mathrm{d}\Omega = [I_\mathrm{S}(q)/I_\mathrm{W}(q)]\mathrm{d}\Sigma_\mathrm{W}/\mathrm{d}\Omega$ per unit volume (cm^3) and per unit solid angle (Ω) (Fig. 7.5). The selected q-range corresponds to spatial scales $R \geq R_\mathrm{min} \sim 2\pi/q_\mathrm{max} \sim 1$ nm from the size of DPC molecule and diamond particles up to the distances $R \sim R_\mathrm{max} \sim 2\pi/q_\mathrm{min} \sim 40$ nm by an order of magnitude higher than the size of particle size. The scale available in the measurements in the upper limit $R \sim R_\mathrm{max}$ would be comparable with the distance between particles $R_\mathrm{int} \sim N_\mathrm{DND}{}^{-1/3}$ in the case of their uniform distribution at a given concentration of diamonds, $N_\mathrm{DND} \sim 10^{16}\ \mathrm{cm}^{-3}$. However, at the scales $R \leq R_\mathrm{max}$ the profiles of cross sections growing with decreasing momentum clearly indicate diamond aggregation (Fig. 7.7).

The behavior of the cross sections at small momenta $q \leq 0.4\ \mathrm{nm}^{-1}$ approaches the power law between the dependences, $\sigma(q) \sim 1/q^2$ and $\sigma(q) \sim 1/q$. The first is typical for coiled (Gaussian) and the second for straightened polymer like chains composed of small units (size $b \ll 1/q$) [39]. The role of the units here is played by the particles of size $d_\mathrm{P} \sim 4$ nm, capable of forming the chains of size $R \geq R_\mathrm{max}$ with the number of particles $\geq R_\mathrm{max}/d_\mathrm{P} \sim 10$.

Structures of this kind were detected in diamond dispersions [33, 34, 40, 41], where the neutron scattering showed momentum dependences $\sim q^{-\beta}$ with fractal indices $\beta \sim 2.3$–2.4 corresponding to branched chains of particles. In our case, this indicator is lower, since even at lower q-band edge, $q \leq 0.4\ \mathrm{nm}^{-1}$, we observe only small aggregates fragments close to linear chains. Above, at momenta $q \sim 1\ \mathrm{nm}^{-1}$, the profiles of the scattering curves have a peculiarity that is weakly pronounced wide peak, reflecting correlations between neighboring particles on scales of the order of their diameter. The region $q \geq 1\ \mathrm{nm}^{-1}$ relates mainly to scattering within individual particles. At the upper edge of the q-band, incoherent scattering predominates (mainly on water protons) with a constant cross section $\sigma_\mathrm{inc} \approx 0.8\ \mathrm{cm}^{-1}$.

Regarding scattering at small angles, it should be clarified that in pure diamond dispersion and the systems with the addition of DPC the measured cross sections, minus the incoherent background, mainly reflect the contribution of diamonds. Due to the high mass per unit volume ($\rho = 3.5\ \mathrm{g/cm}^3$), they also have a large scattering length density $K_\mathrm{DND} = 11.67 \times 10^{10}\ \mathrm{cm}^{-2}$ comparatively to DPC molecules having a similar parameter $K_\mathrm{DPC} = 2.36 \times 10^{10}\ \mathrm{cm}^{-2}$. In light water having very small

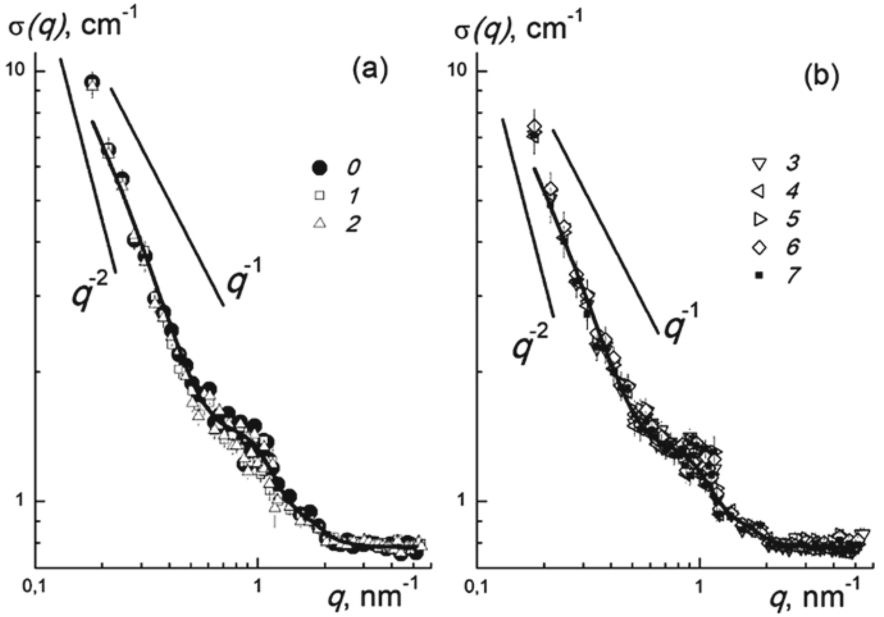

Fig. 7.7 Cross sections $\sigma(q)$ versus momentum transfer for aqueous dispersions: **a** diamond (0), **b** DPC-DND Z^+ complexes (1–7) with different DPC contents (Table 7.1). The data are approximated by the function (1). Straight lines represent the behavior of the cross sections $\sigma \sim 1/q^2$, $\sigma \sim 1/q$

scattering density $K_W = -0.56 \times 10^{10}\ \mathrm{cm}^{-2}$ the contrast factor for diamonds $\Delta K_{DND} = K_{DND} - K_W = 12.23 \times 10^{10}\ \mathrm{cm}^{-2}$ is four times higher than the same parameter for DPC molecules, $\Delta K_{DPC} = K_{DPC} - K_W = 2.92 \times 10^{10}\ \mathrm{cm}^{-2}$. The difference in cross sections between diamonds and DPC is proportional to the squared contrast factors. For a molecule of DPC, the cross section is only ~6% relative to a diamond of the same volume. Due to very low DPC content ($C_R \leq 1\%$) compared to diamonds, scattering directly from DPC molecules can be neglected and the data should be attributed to diamonds. As follows from a subsequent analysis of the data, these molecules contribute to the large-scale structuring of the diamond component.

7.3.2 Fractal Structures Formed by Diamonds

To obtain detail structural information, the data were corrected for a constant incoherent background, $\sigma_{inc} \approx 0.8\ \mathrm{cm}^{-1}$. In double logarithmic coordinates (Fig. 7.8), the coherent component of the cross sections $\sigma_S(q) = \sigma(q) - \sigma_{inc}$ varies linearly for momenta $q < 2\pi/d_P \sim 1\ \mathrm{nm}^{-1}$; therefore, the data were approximated

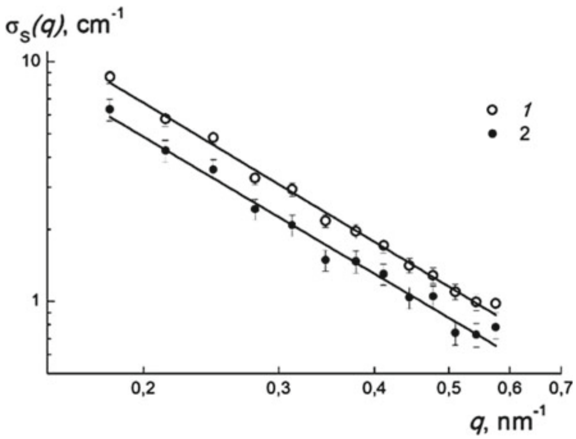

Fig. 7.8 Approximation of the cross sections $\sigma_S(q)$ by the power function of momentum transfer. Data for diamond dispersion (1) and a solution of complexes (2) (samples 0; 3) are presented

by the function $\sigma_S(q) = A_\beta/q^\beta$, where the parameter A_β is given by the scattering power, and the fractal index β by the geometry of the observed objects. Figure 7.8 illustrates the results of data approximation by this power function using the example of diamond dispersion and a solution of complexes.

For the samples, the dependences of the parameters $A_\beta(C_R)$ and $\beta(C_R)$ on the content of the molecular component in the complexes are plotted in Fig. 7.9. According to the data (Fig. 7.9), diamonds themselves and with the participation of DPC molecules form aggregates with exponents close to $\beta = 2$. This is observed usually for statistical coils being ideal Gaussian chains without excluded volume. But really statistical chains have an excluded volume, and the scattering from them is characterized by Flory index $\beta_F = 5/3$ [42]. In the initial dispersion of diamonds and solutions of complexes, the values $\beta(C_R) > \beta_F$. Hence, between the units in the chains there is a volume interaction of attraction. The increase of the fraction of DPC in the complexes does not lead to the collapse of chains observed in scattering. On the contrary, there is a slight decrease in the index $\beta \sim 1.8–1.9$, i.e., the chains become even slightly straightened. This is accompanied by a decrease in their scattering ability. The parameter A_β (C_R) lowers by ~25% (Fig. 7.9).

In this connection, it was important to find out whether we observed single chains of particles linked like in linear polymers or these structures are linear associates of small aggregates of particles when the aggregates the role of chain units. The data in Fig. 7.9 allowed us estimate the size of such effective units.

We compared the data to generally used model function $\sigma_A = \sigma_o/[1 + (q\xi)^2]^{\beta/2}$ with the asymptotic behavior $\sigma_A = (\sigma_o/\xi^\beta)/q^\beta$ for $(q\xi)^2 \gg 1$ [43]. The function describes the scattering on chain aggregates with fractal dimension β and correlation radius ξ. The forward cross section $\sigma_o = \sigma_A(q \rightarrow 0) = (\Delta K_{DND})^2\varphi v_a$ is proportional to the square of the contrast factor ΔK_{DND}, the volume fraction of diamonds φ and the dry volume of aggregate $v_a = (\pi/6)d_P{}^3 n_a$ composed of n_a units.

The correlation radius of the aggregate ξ is related to its gyration radius, $r_{ga} = (3\beta/2)^{1/2}\xi$. The latter depends on the size of units d_P, their number n_a in a chain and

Fig. 7.9 Approximation parameters: **a** $A_\beta(C_R)$ and **b** $\beta(C_R)$ depending on the mass fraction of DPC in complexes

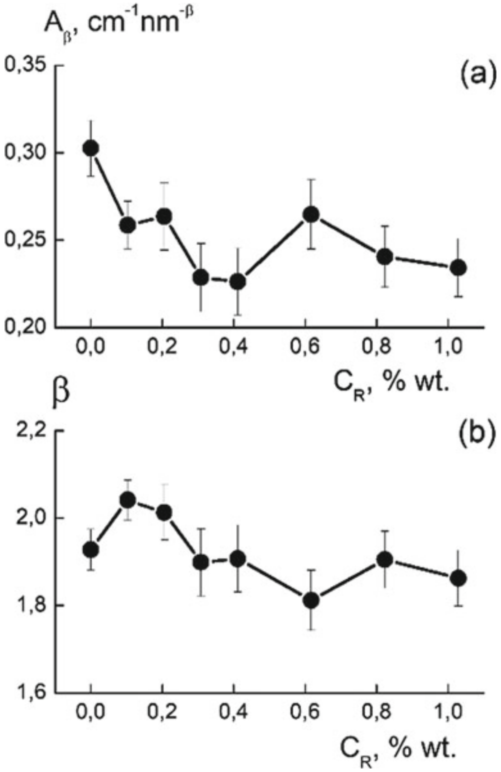

index β according to the formula $r_{ga} = d_P \cdot n_a^{1/\beta}\ [(1 + 2/\beta)\ (2 + 2/\beta)]^{-1/2}$ giving $r_{ga} = d_P \cdot n_a^{1/2}/\sqrt{6}$ for Gaussian chain [42].

The relationship between r_{ga} and n_a allowed us to calculate the parameter $A_\beta = \sigma_o/\xi^\beta = (\Delta K_{DND})^2\varphi(\pi/6)d_P^{3-\beta}(3\beta/2)^{\beta/2}[(1 + 2/\beta)\ (2 + 2/\beta)]^{\beta/2}$. For Gaussian chains, it is proportional to the size of units, $A_\beta = 3\pi\ (\Delta K_{DND})^2\varphi d_P$. In a simple case of chains like polymers, the size of units is directly equal to the diameter of diamond particle $d_P \sim 4.5$ nm known from previous DLS measurements. However, the observed structures can be more complicated, e.g., composed of small aggregates associated linearly. To check it, we have calculated the effective size of units from the data in Fig. 7.9. The obtained magnitudes of $d_{PEF} \sim 3.5$–4.5 nm are close to the size of diamonds (Fig. 7.10) and certify mainly the presence of single-diamond chains in the studied systems. Only a weak trend of lowering units' size is observed by the enrichment of systems with the molecular component as compared to original dispersion (Fig. 7.10).

These results have confirmed a formation of chain fragments in original dispersion and complexes solutions even at comparable numerical concentrations of diamonds and molecules ($C_R \sim 1\%$). However, the conclusion refers to the scales of tens of nanometers, on which chain fragments of diamond structures are visible. At the local level, the molecular component does not cause qualitative changes in

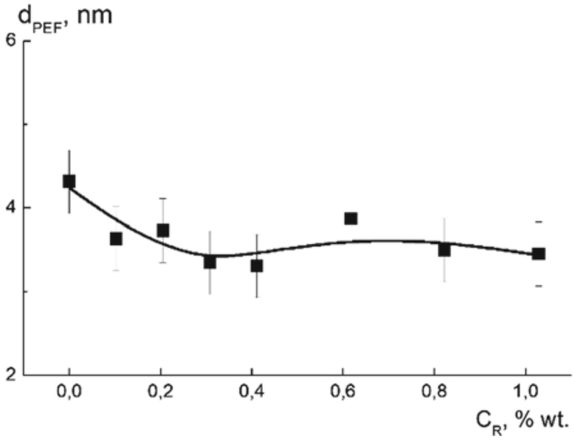

Fig. 7.10 Effective size $d_{\mathrm{PEF}}(C_{\mathrm{R}})$ of units forming chains in dispersion and complexes solutions with various proportions of DPC relatively to diamonds

the structure of the studied systems while at larger scales we found the effects of aggregation stimulated by DPC that is discussed below.

7.3.3 Features of Diamond Surface and Complexes Formation

The peculiarities of diamonds aggregation depend strongly on the structural features of their surface. The latter contribute to the scattering mostly at high momenta $q > 1\ \mathrm{nm}^{-1}$. Typical behaviors of cross sections in this q-region are shown in Fig. 7.11 for original dispersion and the solutions of complexes with DPC content $C_{\mathrm{R}} \sim 0.3\%$ wt. (sample 3).

At the upper edge of q-range, the data obey also exponential scattering function $\sigma(q) = A_D/q^D$ being again the asymptotic form of general scattering law while applied to fractal surfaces, $\sigma(q) = \sigma_{\mathrm{oc}}/[1 + (q\rho_{\mathrm{c}})^2]^{D/2}$ [44]. Here the parameter σ_{oc} is forward cross section, the length ρ_{c} shows the size of coherently scattering regions at the surface (crystal facets) and the index $3 < D \leq 4$ is defined by the fractal dimension of the crystalline surface $D_{\mathrm{S}} = 6 - D$. The combination of the quantities σ_{oc}, ρ_{c} and the exponent D determine the coefficient $A_D = (\sigma_{\mathrm{oc}}/\rho_{\mathrm{c}})^D$. From the approximation of the cross sections by the function A_D/q^D we found the characteristics $D(C_{\mathrm{R}})$ and $A_D(C_{\mathrm{R}})$ for the basic dispersion and solutions of the complexes (Fig. 7.12).

The results show that diamonds in dispersion have a developed fractal surface. This is evidenced by the parameter A_{D} which exceeds that of the solutions of the complexes, and the index $D \sim 3.5$ is lower than the value $D = 4$ for a smooth border (Fig. 7.12). Accordingly, the surface of the diamonds in the dispersion has a dimension of $D_{\mathrm{S}} = 6 - D \sim 2.5 > 2$ that is inherent defective borders. The formation of complexes with small amounts of DPC ($C_{\mathrm{R}} \leq 0.2\%$) did not disturb

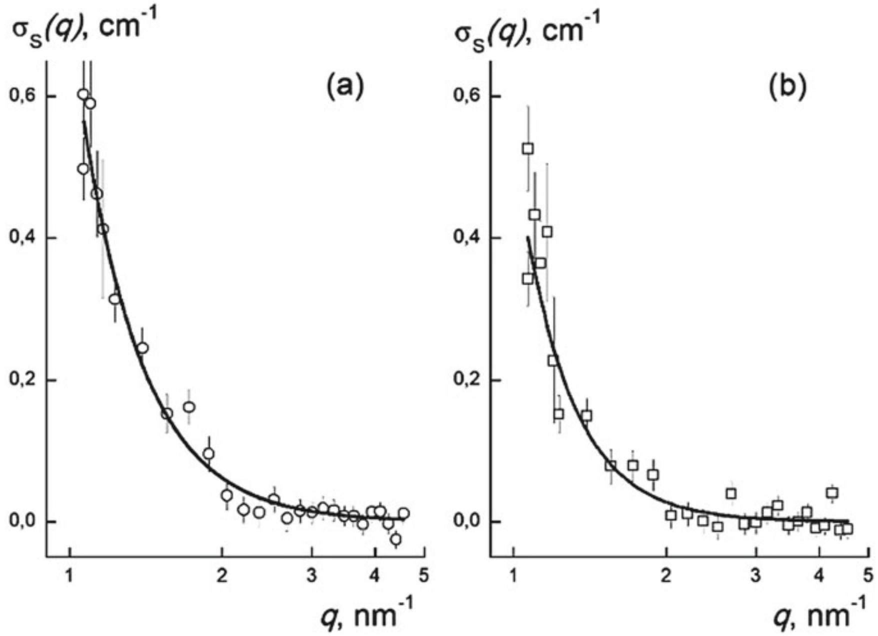

Fig. 7.11 Cross sections of dispersions versus momentum transfer: **a** diamond, **b** complexes (sample no 3). Fitting curves $\sigma(q) = A_D/q^D$ are shown

substantially the index in the scattering law, $D \sim 3.2$–3.5. For such values of the parameter D, the particle surface dimension remains within the range $D_S \sim 2.5$–2.8. However, the value of A_D decreased sharply (Fig. 7.12a). It means a reduction of surface visible in scattering and may be due to close contact of particles when they are bonded through DPC molecules.

The increase of the fraction of DPC in complexes ($C_R \geq 0.3\%$) caused the growth of the index up to the values $D \sim 3.8$ close to the limit $D = 4$ for a smooth surface ($D_S = 2$). Moreover, the factor $A_D(C_R)$ came down somewhat. Obviously, DPC molecules more actively attach to surface defects under the action of a high gradient of electric potential near them, and the surface is smoothed ($D_S \sim 2.2$). In addition, the dense crosslinking of defective fragments of the particles' surfaces through DPC molecules makes these fragments cease to contribute to scattering. The conclusion is confirmed by the analysis of the correlations between the characteristics of $D(C_R)$, $A_D(C_R)$. From the values of $A_D = (\sigma_{oc}/\rho_c)^D$, the correlation lengths $\rho_c = (\sigma_o/A_D)^{1/D}$ were found using the cross section of independently scattering particles, $\sigma_o = (\Delta K_{DND})^2\varphi(\pi/6)d_P^3$ (Fig. 7.13). At the distances $R \leq \rho_c \sim 1$ nm, the surface fragments scatter coherently, which really corresponds to the size of a diamond facet $\sim 2\rho_c \sim d_P/2$.

According to the data in Fig. 7.13, the structuring effect of the DPC on the diamond system is already evident at low molecular concentrations, $C_R \leq 0.3\%$.

Fig. 7.12 Fractal characteristics of diamond surface versus content of DPC regarding to diamonds amount: **a** $A_D(C_R)$, **b** and $D(C_R)$

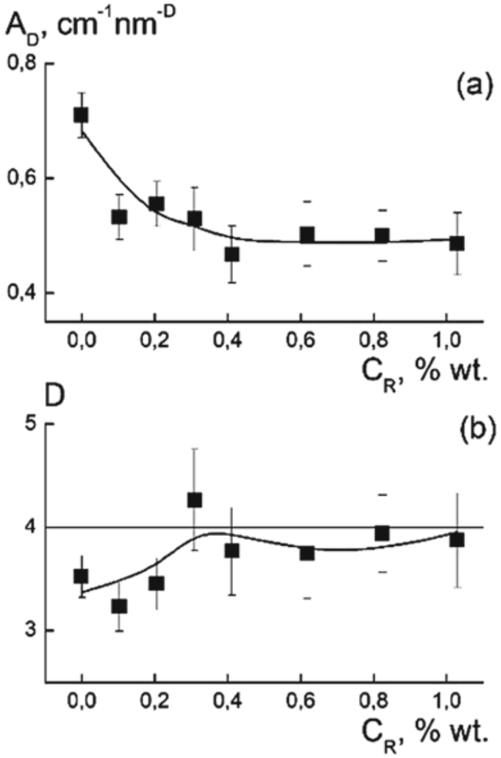

Fig. 7.13 Coherence length $\rho_c(C_R)$ for the scattering from the surface of diamonds

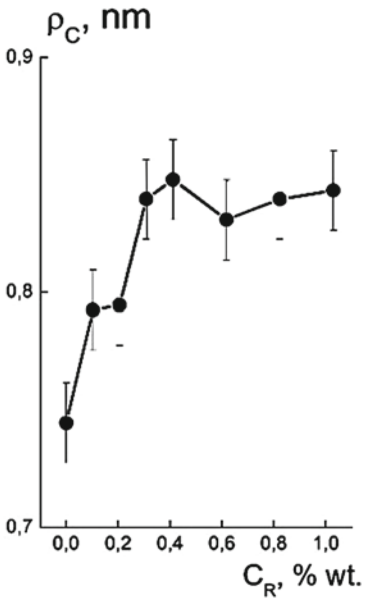

The introduction of DPC causes an increase in the correlation length $\Delta\rho_c/\rho_c \sim 10\%$ with reaching a plateau at $C_R > 0.3\%$.

While increasing the fraction of the molecular component $C_R = 0.3$–1.0% in the systems, their characteristics $D(C_R)$, A_D (C_R), $\rho_c(C_R)$ remain stable (Figs. 7.12, 7.13). It follows from the analysis that the area of the observed fractal surface of the particles should decrease significantly due to a decrease in the dimension $D_S = 6 - D$, following the change in the parameter D as the complex is enriched with the molecular component.

In the dispersion of diamonds with the diameter of $d_P \sim 4$ nm and the surface dimension of $D_S \sim 2.5$, the surface area of an individual particle is of $S_{pfr} \sim a$ $(\sqrt{\pi}d_P/a)^{Ds}$, where $a = 0.357$ nm is the diamond lattice constant. With a numerical concentration of particles in the NDND system of $\sim 1.5 \times 10^{16}$ cm^{-3}, the total area is of $S_t \sim 3$ m^2/cm^3. In the case of complexes ($C_R > 0.3\%$), the particles have the surface dimension of $D_S \sim 2.2$, which leads to the estimate of $S_t \sim 1.4$ m^2/cm^3. Thus, the fractal character of diamond surface is revealed in developed surface. Its area is by 2–4 times larger than this one $S_{SM} \sim 0.8$ m^2/cm^3 for smooth spheres of the indicated size at the same content in the solution.

7.3.4 Analysis of Scattering Centers Correlation

Further the data treatment on scales above and below the size of an individual particle we supplemented by a general analysis of the correlations between scattering centers at different scales (atoms within the particles, particles and aggregates). Using the ATSAS [45, 46] software package, the distribution functions of the distances between scattering centers G $(R) = R^2\gamma(R)$, where $\gamma(R)$ is the pair correlation function for centers at a distance R (Fig. 7.14), were reconstructed from the data for the cross sections.

In general, all the G(R) spectra represent a broad hump with additional local peaks (Fig. 7.14). The hump full width $\Delta R \sim 17$ nm indicates a characteristic size of diamond aggregates. Within them the distances between particles are distributed in the range of $R = 0$–17 nm. The radius of such aggregates $\sim \Delta R/2 \sim 2d_P$ is only twice diameter of a particle. Therefore, it is needed to take into account their discrete structure manifested in the spectra by local maxima. At small distances, the maximum at $R \sim 2$ nm $\sim d_P/2$ indicates atomic correlations inside the particles. The coordinates of the following maxima, $R_1 \sim 4$–5, $R_2 \sim 7$–8, $R_3 \sim 11$–12 and $R_4 \sim 13$–14 nm, are approximately multiple of particle's diameter, and this confirms their chain linking.

For the initial dispersion and complexes with a low fraction of the molecular component ($C_R \leq 0.2\%$), the correlation spectra differ little (Fig. 7.14, data 1–3). Hence, these numbers of molecules do not cause a significant change in the structure inherent in the base dispersion.

However, the increase in the fraction of molecules in complexes to $C_R \sim 0.3\%$ provoked a sharp effect of decrease in spectral intensity in the whole range of radii.

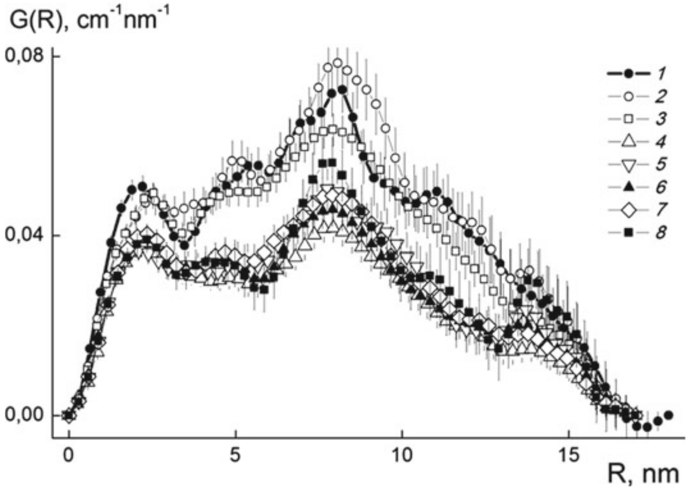

Fig. 7.14 Spectra of distances distribution between the scattering centers $G(R)$ in the diamond dispersion (1) and solutions of complexes (2–8) (Table 7.1)

Further enrichment of complexes with DPC up to the limit $C_R \sim 1\%$ did not make any substantial changes in spectra. Hence, DPC molecules deposited on a diamond surface upon reaching a critical concentration of $C_R^* \sim 0.3\%$ violate the initial conditions of aggregation. It means that original diamond structures have a finite capacity $C_R \leq C_R^* \sim 0.3\%$ for molecular component integration. Exceeding this threshold causes a restructuring of diamond ensembles. This is evident in the behavior of integral parameters obtained by the reconstruction of correlation spectra. Such parameters, forward cross section $\sigma_{oa} = \sigma\ (q \rightarrow 0)$ and aggregates gyration radius R_{ga}, are plotted in Fig. 7.15.

It is remarkable that in all the systems the aggregates are dimensionally stable ($R_{ga} \approx$ const) but have variable cross sections (Fig. 7.15). The gyration radius of aggregates $R_{ga} \sim 6$ nm is comparable to DND diameter and indicates the correlations of particles with environment within the nearest coordination spheres. Both parameters, σ_{oa} and R_{ga}, reflect the interactions of particles DND Z^+ via electrostatic forces, functional groups, hydrophobic fragments on diamond surfaces and adsorbed DPC molecules.

At low molecular fractions $C_R \leq 0.2\%$, the values of cross section $\sigma_{oa} \sim 8$–$9\ \text{cm}^{-1}$ are close to the data for basic dispersion. However, by reaching the critical concentration $C_R^* \sim 0.3\%$ the cross section comes down by $\sim 30\%$. However, a greater adding molecular component did not cause significant changes in the cross section (Fig. 7.15a).

The observed variations in cross section are defined by altering aggregation degree since the values of $\sigma_{oa}(C_R) = (\Delta K_{DND})^2 \varphi(\pi/6) d_P{}^3 n_a$ are proportional to aggregation numbers n_a. These numbers calculated from the σ_{oa} data have shown a drop from high initial level of $n_a \sim 35$ in basic dispersion and complexes solutions

Fig. 7.15 Parameters of aggregates versus fraction of molecular component in complexes: **a** forward cross sections $\sigma_{oa}(C_R)$, **b** gyration radii $R_{ga}(C_R)$

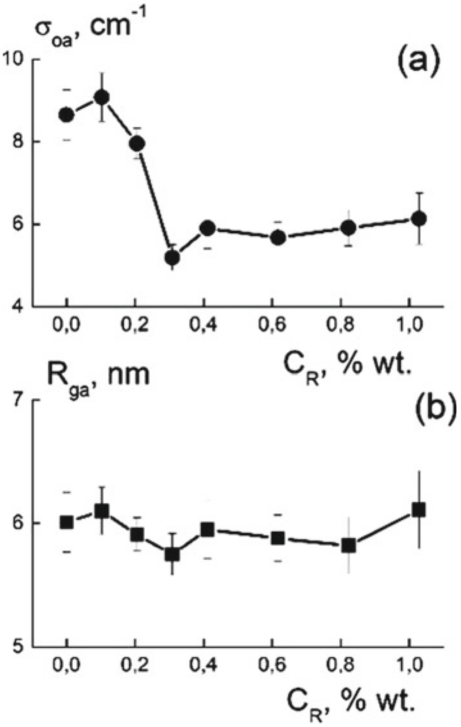

with little DPC amount to low level of $n_a \sim 24$ in the DPC enriched systems, $C_R* \geq 0.3\%$ (Fig. 7.16).

The aggregation numbers are large enough for the structures with small gyration radius $R_{ga} \sim 6$ nm. If such structures were Gaussian chains with the diameter of

Fig. 7.16 Aggregation numbers $n_a(C_R)$ depending on the concentration of DPC component in the systems

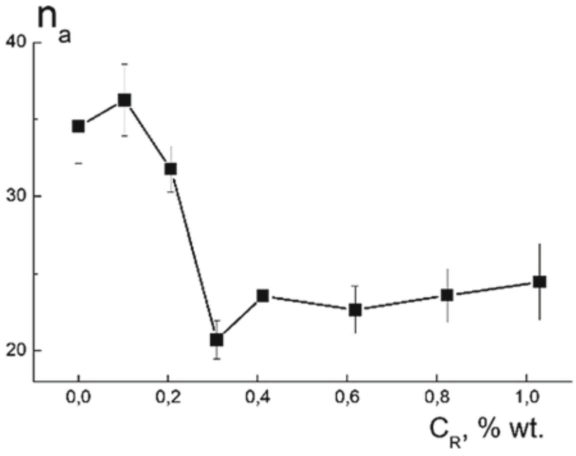

$h = \sqrt{6}R_{ga} \sim 15$ nm, the aggregation number $n_{ag} = (h/d_P)^2 \sim 14$ would be lower than experimental values. So, an aggregate is an interweaving of 2–3 Gaussian chains and its fractal dimension exceeding this one for a chain, $d_{AF} = \ln(n_a)/\ln(h/d_P) \sim 2.7$ and 2.4 for aggregation numbers $n_a \sim 35$ and $n_a \sim 24$. Indeed, in the case of the systems without or with low DPC content, the estimate of $d_{AF} \sim 2.7$ has confirmed the existence of very branched structures of high aggregation numbers. Meanwhile, in the systems enriched by molecular component the magnitude of $d_{AF} \sim 2.4$ has indicated lower branching in less dense aggregates.

7.3.5 Large-Scale Structures in Complexes Solutions

We considered above only a primary level of systems structural organization within the correlation radii of the entire order of a dozen particle diameters. Higher structural levels were discovered by the analysis of the neutron transmission through the samples when we measured the intensities (I_o, I) of the initial and passed beams and calculated the ratio $Tr_T = I/I_o$ (Fig. 7.17). The latter reflects not only absorption, but also integrated neutron scattering with momenta $q > q_B \sim 2\pi\theta_B/\lambda \sim 0.03$ nm^{-1}. Here the limit $q = q_B$ was set by the aperture of the straight beam $\Delta\Omega \sim \pi\theta_B{}^2 \sim 1 \times 10^{-5}$ steric rad. within the angles $0 < \theta < \theta_B \sim 2 \times 10^{-3}$ rad. To separate the effects of scattering in the samples, we compared their transmissions to similar parameter for pure water. The data for water were corrected for the volume of dissolved components that gave the transmission of solvent $Tr_W \approx 0.61$ (Fig. 7.17).

The transmissions for the samples $Tr_T \sim 0.6$ did not differ much from the data for water, since neutron departure from the beam happened mainly due to intense incoherent scattering from water protons (Fig. 7.17). The presence of diamonds in the basic dispersion reduced the transmission by only a small value $Tr_W - Tr_T \sim 0.005$ relative to water. With the introduction of DPC, the transmission decreased substantially, $Tr_W - Tr_T \sim 0.03$, at the concentration of $C_R{}^* \sim 0.3\%$ above which the effect remained almost unchanged. It should be clarified that the changes in transmission were not associated with the absorption of neutrons in diamonds and DPC in these diluted systems. Here the main role was played by integral scattering from the diamond and molecular components.

To highlight the contribution of these components to the total scattering, we found the ratio $Tr_S = Tr_T/Tr_W$ (Fig. 7.17). The values of $Tr_S(C_R) = \exp(-\Sigma_S\delta)$ for the solution layer with a thickness of $\delta = 1$ mm were determined by the integral of the scattering cross section for diamonds and DPC, $\Sigma_S = -\ln(Tr_S)/\delta = \int\sigma_S(q)d\Omega$, where the solid angle (Ω) is defined by the scattering angle $\theta_B \leq \theta \leq \pi$ (Fig. 7.18).

At the initial part of the curve (Fig. 7.18a), the integral $\Sigma_S(C_R \leq C_R{}^*)$ showed a gain proportional to the squared DPC concentration. The data were fitted by the function $\Sigma_S(C_R) = S_o + S_C C_R{}^2$ with the parameters $S_o = 0.075 \pm 0.001$ cm^{-1}, $S_C = 3.24 \pm 0.05$ cm^{-1} where the cross section S_o corresponds to basic diamond

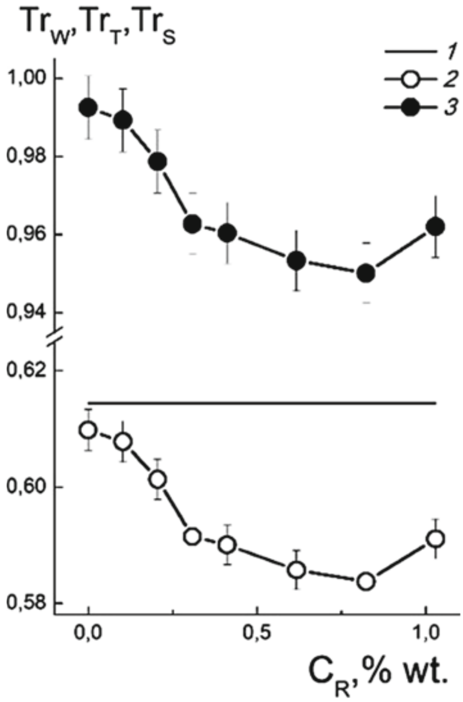

Fig. 7.17 Transmission data: water layer (1), value Tr_W adjusted for the total volume fraction of DND and DPC; magnitudes of $Tr_T(C_R)$ for samples (2) with different content of DPC; final transmissions $Tr_S(C_R)$ (3) related to dissolved components

dispersion and the coefficient S_C reflects the influence of DPC molecules on the structure of diamond ensembles.

Such a nonlinear effect testifies a crucial role of events when a diamond particle absorbs at least two DPC molecules while due to deficit of DPC it is more probable single molecule linking. A hydrophobic DPC molecule must be preferably screened by diamonds from surrounding water, e.g., be localized between diamonds and bind them. In this case, the DPC molecules help in formation of linear chains of diamonds although such formations are inherent in aqueous dispersion already. On the other hand, a particle associated with two DPC molecules play a role of link connecting at least three chain fragments. As a result, some star-shaped structures are formed (Fig. 7.19).

A parabolic growth of cross section integral shows a progressive formation of such branched structures due to the increase of DPC amount at $C_R < C_R^*$ until final assembly of diamonds into dense gel-like aggregates at $C_R \geq C_R^*$ when the integral of the cross section reached a plateau $\Sigma_S(C_R) \sim 0.4\text{–}0.5\ \text{cm}^{-1}$ (Fig. 7.18a). Since the value of $\Sigma_S(C_R)$ is proportional to characteristic mass of an aggregate, the increase of integral shows a gain of the number of arms $f_A \geq 3$ in star-shapes structures which trend to be integrated into gel droplets (Fig. 7.20).

In general, such formations can be described by the model of mass fractals with dimension $2 < D_f < 3$. These large structures with correlation length $L_A \geq 1/q_b$ induce the scattering mostly within aperture of straight beam, $q < q_b$. At the same

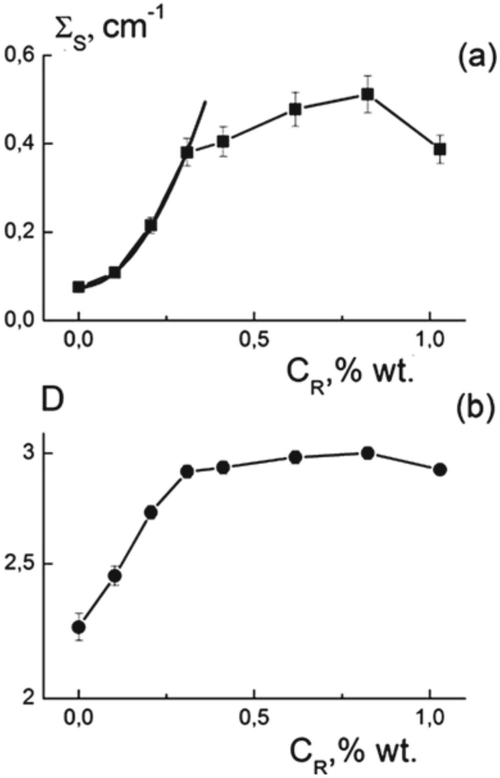

Fig. 7.18 Characteristics of aggregates versus content of DPC in complexes: **a** integral cross section $\Sigma_S(C_R)$, quadratic approximation of the data at low DPC is shown; **b** fractal dimension of aggregates D (C_R)

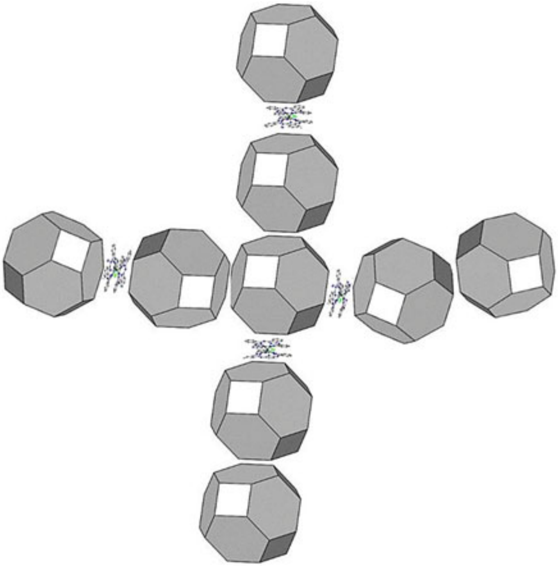

Fig. 7.19 Formation of junction centers due to the presence of two molecules at the diamond surface

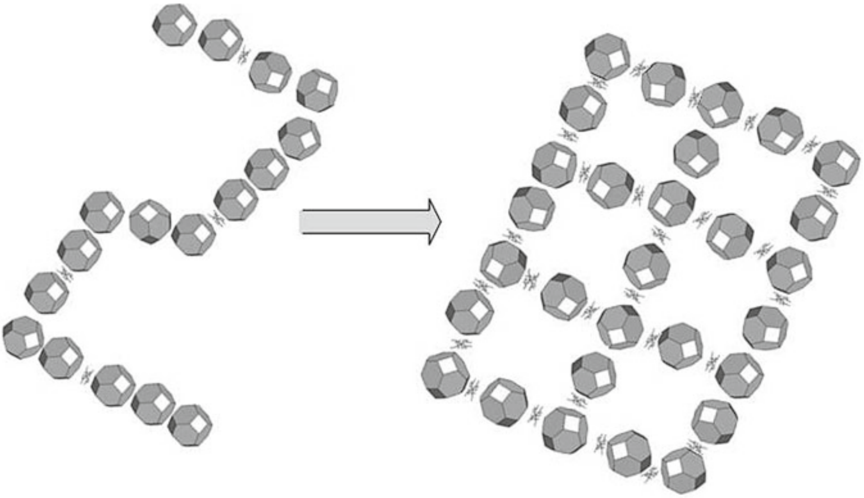

Fig. 7.20 Transformation of short-range order in diamonds arrangement from mostly linear chains to three-dimensional gel network

time, a formation of dense gel-like structures makes stronger the scattering abroad the apertures, $q > q_b$. To describe the scattering in this q-region the cross section, we used the exponent function $\sigma(q) = \sigma_o n_{FA}/(qL_A)^{Df}$. Here the parameter σ_o is the forward cross section for the system of diamonds scattering independently, $n_{FA} = (R_{GA}/r_{gd})^{Df}$ is the number of particles in fractal having dimension D_f and gyration radius $R_{GA} = (3D_f/2)^{1/2}L_A$ proportional to the correlation length. The aggregation number depends on the ratio of gyration radii of fractal and diamond particle, $r_{gd} = (3/5)^{1/2}(d_P/2)$. For such a model, there was calculated the integral cross section

$$\Sigma_S = (\sigma_o/r_{gd}^{Df})(3D_f/2)^{Df/2}\left(\lambda^2/2\pi\right)(D_f - 2)^{-1}\left[1/q_b^{Df-2} - 1/q_{max}^{Df-2}\right] \qquad (7.1)$$

over the interval $q_b \leq q \leq q_{max} = 4\pi/\lambda$.

Using the cross sections data (Fig. 7.18a), the fractal dimension of aggregates D (C_R) was calculated from (7.1) depending on the fraction of the molecular component in the systems. The results (Fig. 7.18b) show a linear growth in the $D_f(C_R)$ index with an increase in the DPC fraction at $C_R \leq C_R{}^*$ from the minimum $D_f(C_R) \sim 2.25$ in the initial diamond dispersion up to values close to the limit $D = 3$ in systems enriched molecular component.

Returning to the results discussed above, we can treat the parabolic increase of the integral cross section as a consequence of formation of dense fractal aggregates around the centers being diamond particles carrying two DPC molecules. The observed increase of the exponent D_f ($C_R \leq C_R$*) reflects a gain in the probability of sedimentation of DPC molecules on a diamond particle, $P_2 = (1/2)(N_{\mathrm{DPC}}/N_{\mathrm{DND}})^2\exp(-N_{\mathrm{DPC}}/N_{\mathrm{DND}}) \approx (1/2)(N_{\mathrm{DPC}}/N_{\mathrm{DND}})^2$ in the first approximation at $N_{DPC}/N_{\mathrm{DND}} \ll 1$. Such a molecule becomes a center of branching, and the number of centers enhances proportionally, $N_2 = P_2N_{\mathrm{DND}}$ at a constant concentration of diamond particles. A formation of new centers occurs if certain number of molecules ($\mathit{\Delta} n_{\mathrm{DPC}}$) is introduced to the system according to the condition $\mathit{\Delta} N_2 = N_{\mathrm{DPC}}\mathit{\Delta} n_{\mathrm{DPC}}/N_{\mathrm{DND}} = 1$. The issued magnitude of $\mathit{\Delta} n_{\mathrm{DPC}} = N_{\mathrm{DND}}/N_{\mathrm{DPC}} = (1/C_{\mathrm{R}})(M_{\mathrm{DPC}}/M_{\mathrm{DND}})$ will be of $\mathit{\Delta} n_{\mathrm{DPC}} \sim 17$ in most diluted system ($C_{\mathrm{R}} \sim 0.1\%$) while in more concentrated ($C_{\mathrm{R}} \sim 0.3\%$) it is needed $\mathit{\Delta} n_{\mathrm{DPC}} \sim 6$ molecules to create a center. As a result, there is a gain in the integral cross section, $\Delta\Sigma_{\mathrm{S}}(C_{\mathrm{R}}) = 2S_{\mathrm{C}}\cdot C_{\mathrm{R}}\mathit{\Delta} C_{\mathrm{R}} = 2S_{\mathrm{C}}(M_{\mathrm{DPC}}/M_{\mathrm{DND}})^2/N_{\mathrm{DND}} = 1.21 \times 10^{-15}\ \mathrm{cm}^{-1}$. Since the integral cross section was measured per cm^3 of sample's volume, we get corresponding cross section of single aggregate $\Sigma_2 = 1.21 \times 10^{-15}\ \mathrm{cm}^2$. The computed cross section

$$\Sigma_2 = (\Delta K_{\mathrm{DND}})^2 v_{\mathrm{p}}^2 n_2 \left(\lambda^2/2\pi\right)(3D_{\mathrm{f}}/2)^{Df/2} r_{\mathrm{g}}^{-Df} q_B^{2-Df}/(D_{\mathrm{f}} - 2) \tag{7.2}$$

includes the volume of particle $v_{\mathrm{p}} = (\pi/6)d_{\mathrm{P}}^3$ with diameter d_{P} and gyration radius $r_{\mathrm{g}} = (3/5)^{1/2}(d_{\mathrm{P}}/2)$ and the aggregation number n_2. To estimate this number, we used the fractal dimension $D_{\mathrm{f}} = 2.25$ for initial structures in basic dispersion.

Finally, from (7.2) we found the characteristics of an aggregate, its aggregation number $\mathrm{n}_2 \approx 218$ and gyration radius $R_{\mathrm{G2}} \approx 17$ nm. In the approximation of star-shaped structure with the number of the arms f_2 each of them is compose of $n_B = n_2/f_2$ particles we define the gyration radius of such formation, $R_{\mathrm{G2}}{}^2 = [(3f - 2)/f]r_{\mathrm{gb}}{}^2$ where an arm has a similar parameter $r_{\mathrm{gb}}{}^2 = n_{\mathrm{B}}d_{\mathrm{P}}{}^2/6$ [47]. So known characteristics n_2 and R_{G2} give the number of arms $f_2 \approx 5.3$ (functionality) with gyration radius $r_{\mathrm{gb}} \approx 10$ nm and the amount of particles $n_B \approx 41$. The estimated magnitudes of n_B and r_{gb} corresponds approximately to aggregation number $n_{\mathrm{a}} \approx 35$ gyration radius $R_{\mathrm{GA}} \approx 6$ nm found above for the structures in basic dispersion and solutions of complexes having low content of DPC (Figs. 7.15, 7.16).

Thus, the formation of DPC complexes with diamonds with an increase in the fraction of the molecular component leads to the transformation of fractal aggregates close in structure to linear chains into highly branched gel-like structures.

Comparing these conclusions with the results of the analysis of the correlations of diamond particles in dispersion and solutions of complexes, it is necessary to clarify that the formation and densification of the gel network leads to stretching of the chains connecting the junctions. With an increase in the numerical concentration of junctions (N_{J}), a characteristic distance between them (cell size) changes as $R_{\mathrm{J}} \sim N_{\mathrm{J}}{}^{-1/3}$.However, the contour length between the junctions $L_{\mathrm{CON}} \sim 2d_{\mathrm{P}}N_{\mathrm{DND}}/(f_{\mathrm{A}}N_{\mathrm{J}})$ is inversely proportional to the concentration of junctions. As a result, the ratio $R_{\mathrm{J}}/L_{\mathrm{CON}} \sim N_{\mathrm{J}}{}^{2/3}$ increases with the concentration of junctions.

Hence, for a Gaussian chain between junctions, the number of links n_A is proportional to the factor $1/N_{\mathrm{J}}{}^{4/3}$and decreases with increasing concentration of junctions. To a lesser extent, the concentration of units $n_A/v_J \sim 1/N_J^{1/3}$ in the cell volume $v_J \sim 1/N_J$ decreases. The estimates show that the transition of the systems to the gel state at submicron scales is associated with a decrease in the local concentration of diamond particles inside the cells of gel network in accordance with the neutron scattering data (Fig. 7.14) discussed above.

7.3.6 Optical Luminescence of Complexes by X-ray Irradiation

The analysis of neutron scattering data has enabled us to understand the mechanism of ordering diamond ensembles as a result of integration of hydrophobic DPC molecules which induce a qualitative transformation of these systems' self-assembly. In these transformed structures, the optically active molecules of DPC play the role of centers for structuring and simultaneously become the sources of luminescence under irradiation by X-rays (monochromatic beam, wavelength 0.154 nm, Cu K_α line). The spectrum presented in Fig. 7.21 shows the characteristic lines of Eu atoms and usual broad band of luminescence from nitrogen atoms with neighbor vacancies in diamond lattice [48–52].

These first synthesized complexes DND-DPC demonstrated the ability to be excited by X-rays and secondary produce optical radiation which may serve for a generation of singlet oxygen is surrounding air or water media that can be applied in relevant tasks of these media purification and biological disinfection.

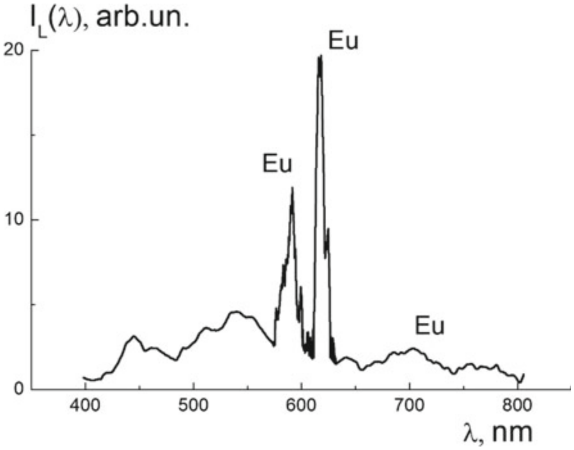

Fig. 7.21 Spectrum of DND-DPC complexes powder luminescence $I(\lambda)$ in optical diapason induced by X-ray irradiation. The characteristic peaks of Eu atoms are revealed on the broad band λ = 400–800 nm of the luminescence from diamonds

7.4 Summary

First prepared water-soluble complexes of hydrophobic electro-negative Europium diphthalocyanines with positively charged nanodiamonds have shown intensive self-assembly in aqueous solutions. In basic diamond dispersion, there was detected mainly low-dimensional formations of diamond particles trend to be associated into linear chains. However, even low amounts of diphthalocyanines caused substantial structural changes in the ensemble of diamonds. According to neutron scattering data, the systems integrated a critical mass of diphthalocyanines, $C_R \sim 0.3\%$ wt. relative to diamonds amount, showed a transition in the mode of short-range order from linear diamond chains to highly branched clusters with fractal dimension close to the upper limit $D_f \sim 3$. This transformation became a consequence of increased probability of two or more molecules to be settled on the surface of a particle which in this way obtain a function of a center of junction associating a number of diamond chains. As we found, a created center linked in average ~5 chains and such star-shaped cluster integrated totally ~200 particles. The new hybrid diamond-diphthalocyanine structures have shown stability because of irreversible binding molecules to diamond surfaces, and dried powders of complexes were not soluble in dimethylformamide oppositely to both components formed solutions in them before complexing. The obtained complexes carried magnetic Eu atoms firmly captured between ligands and demonstrated good luminescent properties under X-ray irradiation that can be applied for the creation of new effective photocatalysts for air and water purification and disinfection, further advanced applications in photodynamic therapy.

Acknowledgements The work was supported by Russian Fund for Basic Researches (gr. No 18-29-19008 mk). Authors thank engineers I. N. Ivanova and L. I. Lisovskaya for technical assistance.

References

1. Garg S, Yadav M, Chandra A, Sapra S, Gahlawat S, Ingole P, Todea M et al (2018) Facile green synthesis of BiOBr nanostructures with superior visible-light-driven photocatalytic activity. Materials 11(8):1273–1289
2. Garg S, Yadav M, Chandra A, Gahlawat S, Ingole PP, Pap Z, Hernadi K (2018) Plant leaf extracts as photocatalytic activity tailoring agents for BiOCl towards environmental remediation. Ecotoxicol Environ Saf 165:357–366
3. Garg S, Yadav M, Chandra A, Hernadi K (2019) A review on BiOX (X= Cl, Br and I) Nano-/microstructures for their photocatalytic applications. J Nanosci Nanotechnol 19(1):280–294
4. Bárdos E, Király AK, Pap Z, Baia L, Garg S, Hernádi K (2019) The effect of the synthesis temperature and duration on the morphology and photocatalytic activity of BiOX (X= Cl, Br, I) materials. Appl Surf Sci 479:745–756
5. Paixão MM, Gomes Vianna MT, Marques M (2018) Graphene and graphene nanocomposites for the removal of aromatic organic compounds from the water: systematic review. Mater Res Express **5**(1):012002. https://doi.org/10.1088/2053-1591/aaa047

6. Cunha D, Achete CA, Kuznetsov A, Yu Da, Hora Machado AE, Marques M (2018) Immobilized TiO_2 on glass spheres applied to heterogeneous photocatalysis: photoactivity, leaching and regeneration process. Peer J 6(3):4464–4482. https://doi.org/10.7717/peerj.4464
7. Politzer IR, Griffin GW, Laseter JL (1971) Singlet oxygen and biological systems. Chem Biol Interact 3(2):73–93
8. Wigginton KR, Menin L, Montoya JP, Kohn T (2010) Oxidation of virus proteins during UV254 and singlet oxygen mediated inactivation. Environ Sci Technol 44(14):5437–5443
9. Maisch T, Baier J, Franz B, Maier M, Landthaler M, Szeimies RM, Baumler W (2007) The role of singlet oxygen and oxygen concentration in photodynamic inactivation of bacteria. Proc Natl Acad Sci USA 104(17):7223–7228
10. Ragas X, He X, Agut M, Roxo-Rosa M, Gonsalves AR, Serra AC, Nonell S (2013) Singlet oxygen in antimicrobial photodynamic therapy: photosensitizer-dependent production and decay in *E. coli*. Molecules 18(3):2712–2725
11. Frimer AA (ed) (1985) Singlet O_2: vol. 4. CRC Press Inc., Boca Raton, Florida
12. Schweitzer C, Schmidt R (2003) Physical mechanisms of generation and deactivation of singlet oxygen. Chem Rev 103(5):1685–1757
13. Ogilby PR (2010) Singlet oxygen: there is indeed something new under the sun. Chem Soc Rev 39(8):3181–3209
14. Devasagayam TPA, Kamat JP (2002) Biological significance of singlet oxygen. Indian J Exp Biol 40(6):680–692
15. Hambright P (2000) Chemistry of water-soluble porphyrins. In: Kadish KM, Smith KM, Guilard R (eds) The porphyrin handbook, vol. 3, ch. 18. Academic Press, Amsterdam, pp 132–208
16. Olshevskaya VA, Savchenko AN, Zaitsev AV, Kononova EG, Petrovskii PV, Ramonova AA, Tatarskiy VV, Uvarov OV, Moisenovich MM, Kalinin VN, Shtil AA (2009) Novel metal complexes of boronated chlorin e6 for photodynamic therapy. J Organomet Chem 694:1632–1637
17. Rosenthal I (1991) Phthalocyanines as photodynamic sensitizers. Photochem Photobiol 53 (6):859–870
18. Lukyanets EA (1999) Phthalocyanines as photosensitizers in the photodynamic therapy of cancer. J Porphyrins Phthalocyanines 3(6/7):424–432
19. Bonnett R (1995) Photosensitizers of the porphyrin and phthalocyanine series for photodynamic therapy. Chem Soc Rev 24:19–33
20. Martynov AG, Gorbunova YG, Tsivadze AY (2014) Crown-substituted phthalocyanines—components of molecular ionoelectronic materials and devices. J Inorg Chem 59:1635–1664. https://doi.org/10.1134/S0036023614140046
21. Safonova EA, Polovkova MA, Martynov AG, Gorbunova YuG, Tsivadze AYu (2018) Crown-substituted naphthalocyanines: synthesis and supramolecular control over aggregation and photophysical properties. Dalton Trans 47:15226–15231. https://doi.org/10.1039/C8DT03661F
22. Buchler JW, Ng DKP (2000) Metal tetrapyrrole double- and triple-deckers with special emphasis on porphyrin systems. In: Kadish KM, Smith KM, Guilard R (eds) The porphyrin handbook, vol 3. Academic Press, Amsterdam, pp 246–294
23. Kirin IS, Moskalev PN, Makashev YuA (1965) Formation of unusual rare earth metal phthalocyanines. Zh Neorg Khim 10:1951–1953 (Russ.)
24. Moskalev PN, Mishin VYa, Rubtsov EM, Kirin IS (1976) Synthesis and thermal stability of diphthalocyanine complexes with lanthanides, hafnium, thorium, uranium. Zh Neorg Khim 21 (8):2259–2262 (Russ.)
25. Moskalev PN (1990) Sandwich-like coordination compounds of metals with phthalocyanine and porphyrines. Koordinats Khim 10:147–158 (Russ.)
26. Ziminov AV, Yuppe TA, Ramsh SM, Mezdrogina MM (2010) Spectral characteristics of europium phthalocyaninates with different axial ligands. Phys Solid State 52:1915–1918

27. Jiang J, Kasuga K, Arnold DP (2001) Sandwich-type phthalocyaninate and porphyrinate metal complexes. In: Nalwa HS (ed) Supramolecular photosensitive and electroactive materials. Academic Press, New York, pp 113–211
28. Kazuyuki I (2012) Functional singlet oxygen generators based on phthalocyanines. Coord Chem Rev 256(15–16):1556–1568. https://doi.org/10.1016/j.ccr.2012.03.022
29. Teoh WY, Scott JA, Amal R (2012) Progress in heterogeneous photocatalysis: from classical radical chemistry to engineering nanomaterials and solar reactors. J Phys Chem Lett 3(5):629–639. https://doi.org/10.1021/jz3000646
30. Arbogast JW, Darmanyan AP, Foote ChS, Diederich FN, Whetten RL, Rubin Y, Alvarez MM, Anz SJ (1991) Photophysical properties of sixty atom carbon molecule (C60). J Phys Chem 95(1):11–12. https://doi.org/10.1021/j100154a006
31. Vul AYa, Dideikin AT, Aleksenskiy AE, Baidakova MV (2014) Detonation nanodiamonds. Synthesis, properties and applications. In: Williams OA (ed) Nanodiamond. RSC Nanoscience and Nanotechnology, RSC Publishing, Cardiff
32. Williams O, Hees J, Dieker C, Jager W, Kirste L, Nebel CE (2010) Size-dependent reactivity of diamond nanoparticles. ACS Nano 4:4824–4830
33. Lebedev VT, Kulvelis YuV, Kuklin AI, Vul AYa (2016) Neutron study of multilevel structures of diamond gels. Condensed Matter 1(10):1–9. https://doi.org/10.3390/condmat1010010
34. Vul AYa, Eidelman ED, Aleksenskiy AE, Shvidchenko AV, Dideikin AT, Yuferev VS, Lebedev VT, Kulvelis YuV, Avdeev MV (2017) Transition sol-gel in nanodiamond hydrosols. Carbon 114:242–249
35. Koniakhin SV, Utesov OI, Terterov IN, Siklitskaya AV, Yashenkin AG, Solnyshkov D (2018) Raman spectra of crystalline nanoparticles: replacement for the phonon confinement model. J Phys Chem C 122:19219–19229. https://doi.org/10.1021/acs.jpcc.8b05415
36. Khomich AA, Власов ИИ, Shenderova OA, Poklonskaya ON, Dzeraviaha AN, Averin AA, Popovich AF, Khmelnitsky RA, Vyrko SA, Khomich AV (2017) On the nature of the “1630 cm^{-1}” band in the Raman spectra of diamonds. In: Proceedings of 12th international conference “interaction of radiation with solids”, section 1, 19–22 Sept 2017, Minsk, Belarus, pp. 78-80.
37. Belogorokhov IA, Tikhonov EV, Breusova MO, Pushkarev VE, Zoteev AV, Tomilova LG, Khokhlov DR (2007) Raman scattering in semiconductor structures based on mono- and threephtalocyanine molecules with erbium ions. Semiconductor Phys Technol 41(11):1381–1383 (Rus.)
38. Lindner P (2000) Water standard calibration at D11verified with polymer samples. J Appl Cryst 33:807–811
39. De Gennes P-G (1979) Scaling concepts in polymer physics. Cornell University Press, Ithaca
40. Avdeev MV, Rozhkova NN, Aksenov VL, Garamus VM, Willumeit R, Osawa EJ (2009) Aggregate structure in concentrated liquid dispersions of ultrananocrystalline diamond by small-angle neutron scattering. J Phys Chem C 113:9473–9479
41. Tomchuk OV, Volkov DS, Bulavin LA, Rogachev AV, Proskurnin MA, Korobov MV, Avdeev MV (2015) Structural characteristics of aqueous dispersions of detonation nanodiamond and their aggregatefractions as revealed by small-angle neutron scattering. J Phys Chem C 119:794–802
42. Grosberg AY, Khokhlov AR (1994) Statistical physics of macromolecules. AIP Press, New York
43. Teixeira J (1988) Small-angle scattering by fractal systems. J Appl Cryst 21:781–785. https://doi.org/10.1107/S0021889888000263
44. Bale HD, Schmidt PW (1984) Small angle X-Ray scattering investigation of submicroscopic porosity with fractal properties. Phys Rev Lett 53(53):596–599
45. Svergun DI, Feigin LA (1987) Structure analysis by small-angle X-Ray and neutron scattering. Plenum Press, New York, London
46. Svergun DI (1992) Determination of the regularization parameter in indirect-transformmethods using perceptual criteria. J Appl Crystallogr 25:495–503

47. Rawiso M (1999) De l'intensite a la structure en physico-chimie des polymeres. J Phys IV France 9:1–147–195
48. Matthews IG (1958) The fluorescence of diamonds excited by X-Rays. Proc Phys Soc 72:1074–1080
49. Zhou X, Sham T-K, Wu Y, Chong Y-M, Bello I, Lee S-T, Heigl F, Regier T, Blyth RIR (2007) X-ray excited optical luminescence from diamond thin films: the contribution of sp^2- and H-bonded carbon to the luminescence. J Am Chem Soc 129(6):1476–1477. https://doi.org/10.1021/ja064555r
50. Demchenko AP, Dekaliuk MO (2013) Novel fluorescent carbonic nanomaterials for sensing and imaging. Methods Appl Fluoresc 1(4):042001–042017. https://doi.org/10.1088/2050-6120/1/4/042001
51. Lu H-C, Cheng B-M (2011) Analysis of nitrogen defects in diamond with VUV photoluminescence. Anal Chem 83(17):6539–6544. https://doi.org/10.1021/ac200808n
52. Lu H-C, Lin M-Y, Chou S-L, Peng Y-C, Lo J-I, Cheng B-M (2012) Identification of nitrogen defects in diamond with photoluminescence excited in the 160–240 nm region. Anal Chem 84 (21):9596–9600. https://doi.org/10.1021/ac302545u

Chapter 8
Photoreactive Composite Coatings with Tunable Surface Wetting Properties and Their Application Possibilities

Mohamed M. Abdelghafour, Ágota Imre-Deák, László Mérai, and László Janovák

Abstract The self-cleaning surfaces play a crucial role in the present pandemic and global crisis. Self-cleaning property is mainly associated to superhydrophobic surfaces, from which the dust particles can be easily swept down by the rolling motion of droplets. The second type of self-cleaning surfaces is photocatalytic coatings that can induce the degradation of organic materials upon light-exposure. In this chapter, we present non-conventional hybrid coatings with heterogeneous surface energy distribution, superhydrophobic, and photocatalytic properties. Our hybrid coatings are prepared by incorporating photocatalyst particles into the hydrophobic poly(perfluorodecyl acrylate) (pPFDAc) fluoropolymer matrix. With adjusting the loading of particles into hybrid coatings, the surface roughness, the surface charge density, the surface energy, the wetting properties, and thus the bacterial adhesion capacity were controlled. We showed that the surface roughness and hydrophobicity increase with increasing loading of particles into the fluoropolymer binder. The investigated hybrid coatings presented superhydrophobic, photocatalytic, and antimicrobial properties with the increasing content of the photocatalyst particles. It was also presented that the surface wetting properties and thus the pollutant's adsorption on the photoreactive composites can be tuned by the polymer hydrophilicity and surface roughness. Therefore, at the *S*/*L* interface, the photocatalytic efficiency is dependent on the polarity of the subject model pollutants. Moreover, antibacterial activity and self-healing behaviors of these non-conventional hybrid layers with heterogeneous surface energy distribution are also presented and discussed in this chapter.

M. M. Abdelghafour · Á. Imre-Deák · L. Mérai · L. Janovák (✉)
Department of Physical Chemistry and Materials Science, University of Szeged, Rerrich Béla tér 1, Szeged 6720, Hungary
e-mail: janovakl@chem.u-szeged.hu

M. M. Abdelghafour
Department of Chemistry, Faculty of Science, Zagazig University, Zagazig 44519, Egypt

S. Garg and A. Chandra (eds.), *Green Photocatalytic Semiconductors*,
Green Chemistry and Sustainable Technology,
https://doi.org/10.1007/978-3-030-77371-7_8

Keywords Hybrid coatings · Heterogeneous surface · Superhydrophobic surface · Photocatalytic and antimicrobial coatings

8.1 The Importance of Self-Cleaning Photocatalytic Surfaces in Healthcare

As the common human pathogenic bacteria, such as the *Acinetobacter baumannii*, the methicillin-resistant *Staphylococcus aureus* (MRSA), or the *Pseudomonas aeruginosa* gain multidrug-resistance, the number and severity of nosocomial infections are increasing worldwide. To address this global issue, alternative healthcare solutions emerge, and in general, the emphasis is being put on prevention instead of post-infection treatment.

The most effective preventive measure against nosocomial infections is the provision of a sterile environment for patients with weakened immune-system in healthcare facilities. To fulfill this idea, the application of self-cleaning photocatalytic surfaces is a beneficial option. There are several examples of the utilization of such coatings in antimicrobial scenarios, even in the cosmetic-, food-, and textile industries. These composite systems can deal with a wide variety of pathogens, regardless of their Gram-positive or -negative nature. Moreover, there are studies in which the antimicrobial coatings effectively dealt with viruses and fungi.

The specific application possibilities include for example photoreactive wall paints and other photocatalyst coated surfaces in hospital wards. If visible-light-active semiconductor photocatalyst (e.g., noble metal-doped TiO_2) nanoparticles are incorporated in such coatings, the antimicrobial effect can be sufficient without applying special (e.g., high power-output UV) light sources: in this case the ambient light is utilized to prevent infections.

8.2 Photoreactive Surfaces

8.2.1 Second Generation of Photocatalyst Particles

Photocatalytic processes are such chemical reactions in which the role of the catalyst is taken by a light-excitable photocatalyst. During the illumination of the most commonly applied heterogeneous photocatalyst particles, reactive oxygen species with high oxidative potential are formed. These species include superoxide radicals ($O_2^{\cdot -}$), hydroxyl radicals ($HO\cdot$), and hydrogen peroxide (H_2O_2): with the help of these, the photocatalyst-containing surfaces can oxidize organic pollutants and eliminate microorganisms.

If a photocatalytic surface exhibits such behavior upon UV-illumination, it is called a first-generation self-cleaning surface. To elaborate on this kind of surface, photocatalyst particles with different excitation wavelengths (e.g., TiO_2 or ZnO) are applied. The most common candidate is TiO_2, which is widespread due to its cheapness and chemical inertness, but its application is limited by the relatively high band gap energy (E_g = 3.2 eV for the anatase polymorph) as only UV-photons ($\lambda > 388$ nm) can cause excitation. The photocatalytic applications of TiO_2 are limited due to the small quantum efficiency, which is the result of the high electron–hole recombination rate.

The already available extensive literature, covering various application-oriented and fundamental aspects of semiconductor photocatalysis, is still growing exponentially: the topics are generally ranging from size effects through enhanced absorption of light, to phenomena, related to crystalline properties [1]. However, the synthetic preparation procedures aiming for benign-by-design of nanomaterials attracted less attention. The synthesis of TiO_2 nanomaterials is extensively studied: the applied different synthetic strategies [2] mostly revolve around the variations of hydrothermal and sol–gel processes. Despite these efforts, the need for new, more sophisticated methods shows a growing tendency, as various new samples with improved specific-surface areas, physicochemical properties, and crystallinity are still being prepared. On the other hand, the development of more economical and greener synthetic methods is also popular as the shorter energy-payback time is of high importance at all fields, related to the application of solar energy. For instance, solution combustion synthesis [3, 4] is considered as an attractive approach where the crystalline nanoparticle formation is the result of the exothermic reaction alongside the release of different gases. Mechanochemical syntheses provide a quick, mild, and simple alternative to the more widespread methods, ensuring high reproducibility, as well [5]. Furthermore, dry milling (solvent-free mechanochemistry) can offer other second-to-none possibilities in the development of materials with advanced catalytic activity [5]. For instance, a composite of two different metal oxides (SnO_2 and ZnO) has been reportedly synthesized in a one-pot preparation process [6]. During the mechanochemical synthesis, the direct incorporation of the product ZnO particles into synthetic polymers is also possible, paving the way toward the preparation of future antibacterial composite coatings [7]. Despite the promising results, these methods possess limited control over the resulting particle morphology, size, and specific-surface area. To overcome these drawbacks, hard and soft templates can be utilized as a feasible solution. As it has already been presented in the literature [8–10], template syntheses provide samples with well-controlled size, shape, and nanostructure. On the other hand, anodized alumina or synthetic polymer templates were applied in most of these studies, which is not in line with the aspirations of mechanochemists to reduce the overall environmental footprint of the synthetic processes [11]. To overcome this contradiction, biopolymers can also be applied as excellent sacrificial templates: their application in semiconductor oxide photocatalyst syntheses promotes biomass utilization, as well [12]. Previously, we have reported the benign-by-design synthesis of nanocrystalline ZnO via an effective reactive dry milling route, using $Zn(NO_3)_2$ as metal salt precursor and different polysaccharides (e.g., a biomass-derived agar extracted from macroalgae) as sacrificial templates [13]. This method combined the advantages of mechanochemistry and template syntheses while employing a template from environment friendly sources. In our work, the achievability of the mechanochemical templating approach was studied, for a variety of photoactive nanomaterials. This investigation included the qualification of photocatalytic, photoelectrochemical, and antimicrobial properties of the mechanochemically obtained nanoparticles. The reactive dry milling method was applied to prepare ZnO, and TiO_2 as semiconductor oxide nanoparticles, besides using different polysaccharides (e.g., starch) as biotemplates. As it was found out during the study, the mechanochemically prepared nanoparticles possessed photoelectrochemical and photocatalytic performance similar to the widely applied commercial P25 TiO_2 of EVONIK, while ZnO displayed remarkable antimicrobial properties.

The bio-templated nanoparticle synthesis was carried out employing a ball mill instrument [13]. In a general scenario, the chosen quantity of metal salt precursors, namely titanium isopropoxide $Zn(NO_3)_2{\cdot}6H_2O$, was milled separately with the corresponding starch-quantities to reach the desired 1:4 = metal precursor: starch mass ratios (e.g., 2 g $Zn(NO_3)_2{\cdot}6H_2O$ was co-milled with 8 g starch) in a 125 cm^3 stainless steel recipient of a Retsch PM100 planetary ball mill at 350 rpm for 30 min (these are the optimized conditions), applying 18 stainless steel balls with a diameter of 1 cm. During the milling process, the slightly colored solids were transferred directly to a ceramic vessel and subsequently calcined for 4 h at 600 °C in air atmosphere. The temperature of calcination was chosen based on the preceding thermal decomposition experiments which evidenced that most organic materials were removed from the sample over 500 °C [13].

To identify the crystal phases in the resulting oxides and to examine the overall crystalline properties, XRD diffractograms were recorded (Fig. 8.1). The TiO_2 samples (Fig. 8.1a) were determined to be composed of 75% anatase and 25% rutile phases. It is important to highlight that this composition is almost identical to those of the most common benchmark semiconductor photocatalyst, EVONIK P25 TiO_2 [14]. According to the analyses of TiO_2 samples, the average size of the anatase crystallites in majority was proven to be 22 nm, while the minority phase rutile possessed crystallites with the size averaging 26 nm. Our findings supported the previous results of Luque and co-workers, as a well-defined wurtzite phase was featured in the prepared ZnO samples (JCPDS card No. 36–1451) (Fig. 8.1b). This oxide semiconductor displayed noteworthy crystalline properties with an estimated mean particle diameter of 44 nm (calculated from full profile fit).

To characterize the optical properties of the synthesized materials and the estimated band gaps of the synthesized materials, UV–VIS diffuse-reflectance spectroscopy (DR) was applied: the band gaps in question were determined to be 3.04 eV for TiO_2 and 3.22 eV for ZnO particles. These values agree well with previously published results [15]. TEM examinations were conducted to collect direct information on particle diameter and shape of the mechanochemically prepared nanomaterials (Fig. 8.2). The most important observation of the studies was that the synthesis resulted the formation of nanoporous, structured networks instead of the expected individual nanoparticles. The same could be experienced, not even in the case of ZnO, but in the case of TiO_2 nanostructures, as well (Fig. 8.2a, d).

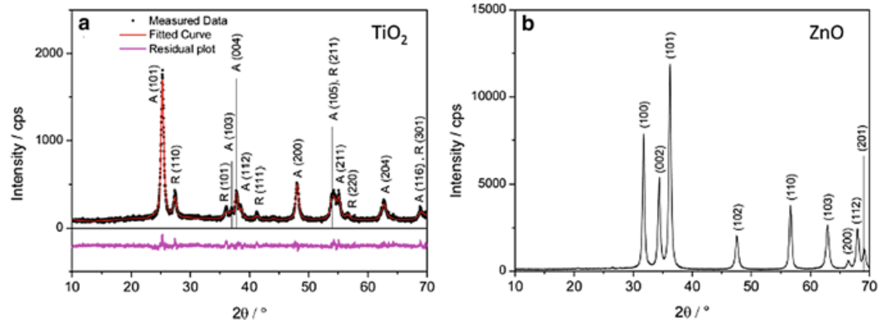

Fig. 8.1 XRD diffractograms of **a** TiO_2 and **b** ZnO samples. In figure **a**, the crystal facets were assigned to all reflections (A: anatase, R: rutile); the result of Rietveld refinement is also displayed [13]

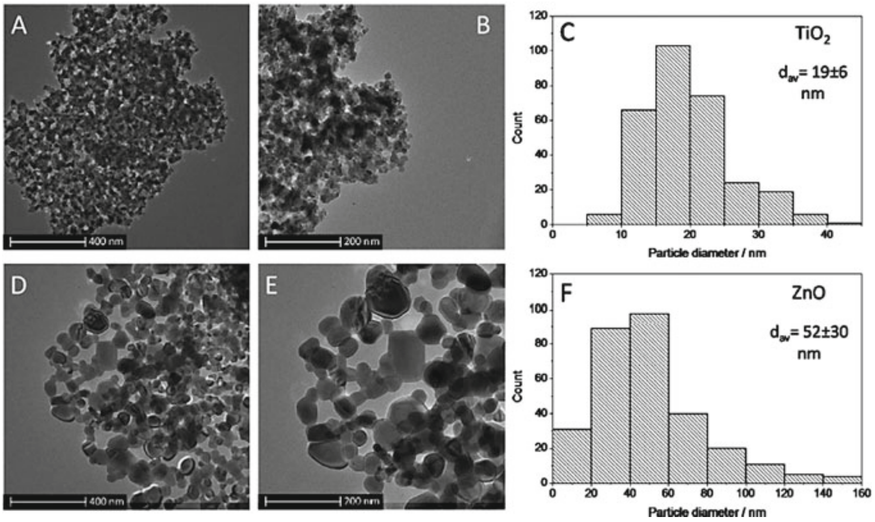

Fig. 8.2 **a, b** TEM images of TiO_2 and **d, e** ZnO with the corresponding distributions of particle sizes (**c, f**) [13]

The applicability of the synthesized nanomaterials was examined in two different scenarios of solar light utilization. The first scheme was a model photocatalytic environmental remediation process, applying ethanol vapor as a test material to mimic the photodegradation of different volatile organic compounds (VOCs) [16]. During the photodegradation of EtOH, sequences of chemical transformations occur on the surface of TiO_2 until reaching complete mineralization (which results in CO_2 and H_2O), including the generation of intermediates [16]. To monitor the photoreactivity of prepared materials under practically relevant environmental conditions, the EtOH vapor photooxidation tests were run in a circulatory reactor, besides maintaining a constant rate of gas mixture flow. The composition of the gas phase was anaylzed by gas chromatograph. Figure 8.3a displays the decomposed EtOH amounts as a function of the duration of irradiation, normalized by the catalyst surface area (30 and 15 m^2g^{-1} for TiO_2 and ZnO, according to BET measurement results). As Fig. 8.3a presents, both TiO_2 samples exhibited a similar efficiency, while ZnO outperformed not only the mechanochemically prepared TiO_2 but the commercial P25 photocatalyst particles, as well. To further qualify and quantify the photocatalytic efficiencies, the apparent first-order reaction rates (k_0) were calculated as the slope of $-\ln(c/c_0) = k't$ where c is the EtOH concentration at a given time, c_0 is the initial EtOH concentration, and t is the time of illumination. As the observed kinetics of the process was pseudo-first-order, the application of this approach was implementable. The apparent first-order reaction rates (k') were also normalized using the BET surface area to compare the specific photocatalytic activity of the different semiconductor catalyst.

The nearly equal values obtained for both tested titania samples evidence that after the peeling off of the obvious surface area, the other photocatalytic activity-affecting factors (for instance, phase composition and crystallinity) are basically the same for these two TiO_2 samples.

The antibacterial performance of the photocatalysts was subsequently studied applying a modified version of the ISO 27447:2009 standard method, during which the number of the surviving bacterial cells per cm^3 on the original inocula was calculated after different exposure times (0, 30, 60, 90, and 120 min). As Fig. 8.3b shows, the mechanochemically synthesized titania—similarly to the pure polymer binder material and P25—exhibited insignificant activity: this can be considered as the direct effect of irradiation. In contrast, bio-templated ZnO displayed significant antimicrobial activity, destroying all bacterial cells after 90 min. It is important to note that control experiments in dark environment were also performed, resulting in the finding, that in all cases, ~50% of the overall antimicrobial activity can be attributed to the irradiation. These observations prove that the biomass-templated

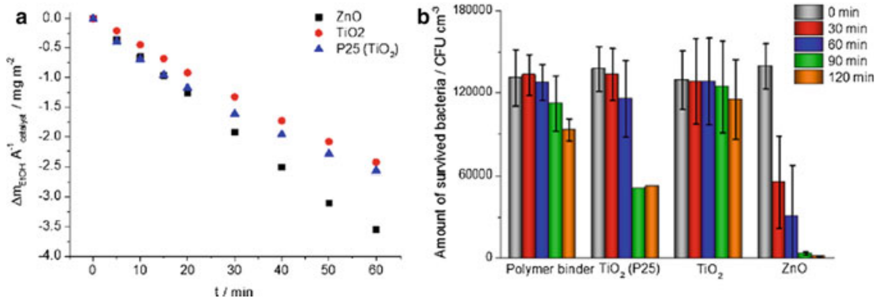

Fig. 8.3 **a** Surface area normalized photocatalytic activity of the semiconductor oxide nanomaterials during EtOH degradation tests. **b** Antibacterial performance comparison of the synthesized TiO_2 and ZnO samples, determined according to the standard ISO 27447:2009. The activity of the polymer matrix and the benchmark P25 TiO_2 particles is also displayed [13]

dry ball milling resulted in the formation ZnO nanoparticles, possessing the well-known remarkable antimicrobial character of ZnO nanomaterials.

The band gap energy can be adjusted to near-UV or visible range by doping the TiO_2 with different nonmetal elements, such as sulfur, phosphor, or nitrogen. As a result of the doping process, the electron system and the optical properties get affected beneficially.

These doped photocatalysts are called second-generation photocatalysts, and therefore, their composite surfaces are considered to be the second-generation photocatalytic surfaces. Second-generation catalysts can also be formed by introducing noble metal nanoparticles or nanodots to the surface of semiconductor particles. Besides tuning the absorbance into the visible range, these metals take the role of electron traps, hindering the charge recombination, thereby increasing the overall quantum efficiency.

The noble metal particles are also famous for their plasmonic nature, which also contributes to the photocatalytic utilization of visible light. The phenomenon of local plasmon resonance (LSPR) is the photoinduced collective oscillation of the valence electrons in the vicinity of the particle. This state can be achieved when the wavelength of the incoming photons matches the wavelength of the electron oscillations. As the energy of the exciting photons gets concentrated in this process, the phenomenon can be applied for the utilization of diffuse solar light. The resonant wavelength is particularly dependent on the composition, and the morphological properties of the noble metal nanoparticle, but the distance between the metal and photocatalyst surfaces also has a relevant contribution. A latter parameter can be controlled, for example, through the intercalation of the metal nanoparticles into non-swelling layered silicates or TiO_2 templates with mesopores. Another control opportunity is the formation of so-called nanophase reactors from biner mixtures on the surface of supporting particles. All in all, the band gap energy of the initially UV-active semiconductor photocatalyst particles can be lowered by modification with noble metal nanoparticles, which can lead to visible-light photoreactivity. This all means an opportunity to eliminate organic pollutants and microorganisms with the help of visible light. In the instance of TiO_2, Ag NPs are excellent functionalizing agents because the release of Ag^+ ions from such photocatalysts is proven to be far below the harmful level.

The release of metal ions can be easily quantified by ion-selective electrodes: in an experiment, a hybrid thin layer of polyacrylate-immobilized Ag–TiO_2 (124 cm^2 surface area, a total of 0.775 mg Ag NPs in 155 mg photocatalyst) was immersed into 100 ml deionized water. During the 1 week incubation period, only 1.4% of the total silver content got released and entered the liquid phase as Ag^+ ions [17, 18]. The immobilization of the particles with polymer also helps to avoid the release of nanoparticles into the environment.

8.2.2 Photocatalyst Immobilization, Nanohybrid Surfaces

During practical applications, it is of crucial importance to provide proper adhesion between the photocatalyst particles and everyday substrate materials, such as glass, textile, paper, ceramics, or wall and plastic surfaces. Thanks to the rapid development of the field, self-cleaning TiO_2-based coatings are now commercially available. In the laboratory environment, TiO_2 thin layers are achievable through routes like sol–gel methods, spray-pyrolysis, hydrothermal processes, magnetron cathode sputtering, or dip-coating techniques.

Polymer-based coatings are the state-of-the-art composites of this field, having the highest versatility. Polymers are esteemed photocatalyst binders as they have adjustable elasticity, low density, price, and excellent impact-resistance. Initially, the photocatalyst particles are distributed uniformly in such matrices: however, their surficial concentration increases as the polymer suffers photodegradation. As a result of this, the particles get uncovered, and a gradual increase in the photocatalytic efficiency is expected during application. The methods of photocatalytic activity quantification of such films are well described in the literature [17, 18].

8.3 Photoreactive Coatings with Lotus Leaf-Like Water Repellency and Self-Cleaning Characteristics

The leaf-like superhydrophobic coatings belong to the third generation of antimicrobial coatings. Recently, surfaces with water contact angle values exceeding 150° got increased attention. Water-repellent surfaces have many practical uses in our everyday life: enough to think about the lotus effect-based self-cleaning wall paintings or windows, but different water-repellent textiles are also commercially available.

The so-called lotus effect (the name is inspired by the water-repellent character of the lotus leaf) has two prerequisites: at first, a surface with low surface energy is needed (e.g., hydrophobic fluoropolymers), which have to possess hierarchical surface micro-/nano-roughness. Increasing the surface roughness of an initially hydrophobic surface ($\Theta > 90°$) can lead to the drastic increase of the contact angle, and even superhydrophobic character is achievable ($\Theta > 150°$) when a lotus leaf-like surface with hierarchical roughness is formed.

A cooperative effect of low surface free energy and the rough surface structure is completely crucial to attain suitable superhydrophobic surfaces. Superhydrophobic surface with $\sim 12\%$ ZnO material, which has photocatalytic properties, was synthesized using spherical layered double oxide (LDO) particles (with ~ 25 μm diameter). On the one hand, the application of spherical structured LDO particles ensures sufficient surface roughness, while with the synthesized low-energy 1H,1H-Perfluoro-n-decyl acrylate pPFDAc fluoropolymer binder content consisting of polyacrylate backbone with suspended perfluorodecyl functional groups, sufficiently low surface energy was attained [19].

To obtain spherical layered double oxide (LDO) particles, inorganic ZnMgAl layered double hydroxides (ZnMgAl-LDH LDH) were synthesized, [20] and to obtain the photocatalytically active calcinated form of spherical LDO, the resulting LDH powder sample was calcined at 600 °C for 2 h. The original LDH spherical morphology was still maintained after calcination. Moreover, a low-energy fluoropolymer binder material was used to lower the surface energy of the rough surface LDO photocatalyst particles (Fig. 8.4).

The LDO photocatalysts' band gap energies were determined using the Kubelka–Munk function from the diffuse-reflectance spectra of the samples. Figure 8.5 shows the Kubelka–Munk plot of the powdered LDO sample where the obtained band gap energy (Eg) values of the ZnO-containing LDO powder and Nanox ZnO (as reference) were 3.23, and 3.19 eV, respectively, and also the excitation wavelength was determined at $\lambda_g = 386$ nm.

Using this special morphology of the obtained LDO particles, they were incorporated into a low-energy hydrophobic fluoropolymer matrix. The initial poly (perfluorodecyl acrylate) pPFDAc fluoropolymer binder material with low surface energy has a relatively smooth surface with the Θ_w value which was 107.5°, which is the low-energy flat surface characteristics [21]. With adjusting the loading of LDO particles into hybrid layers, the surface morphology and roughness had changed. Figure 8.6 illustrates schematic diagrams and SEM photographs of the LDO/fluoropolymer photoreactive layers with increased LDO content.

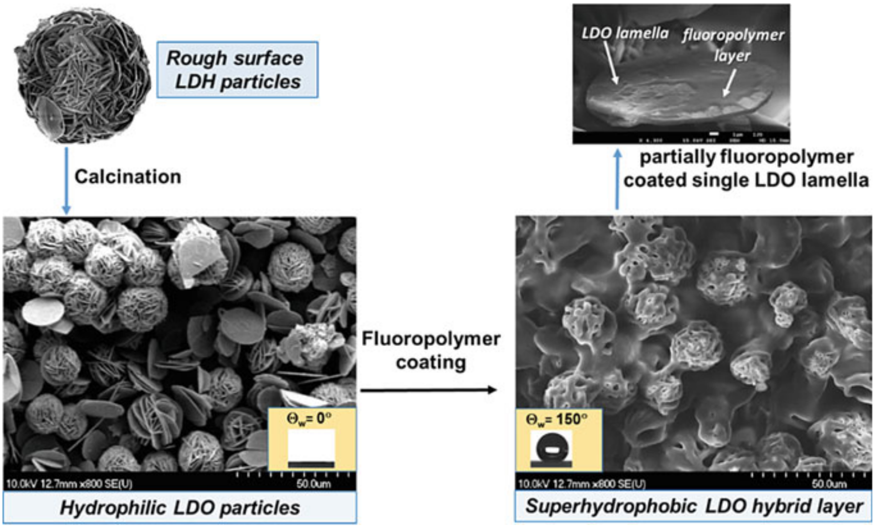

Fig. 8.4 Preparation of the photoreactive superhydrophobic hybrid surfaces containing LDO-based photocatalyst microparticles with corresponding SEM pictures [19]

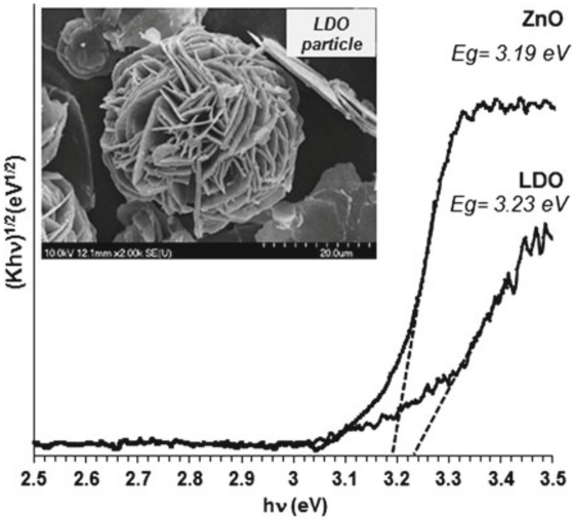

Fig. 8.5 Kubelka–Munk plot of the prepared LDO compare with the commercial semiconductor ZnO photocatalyst (Nanox) [19]

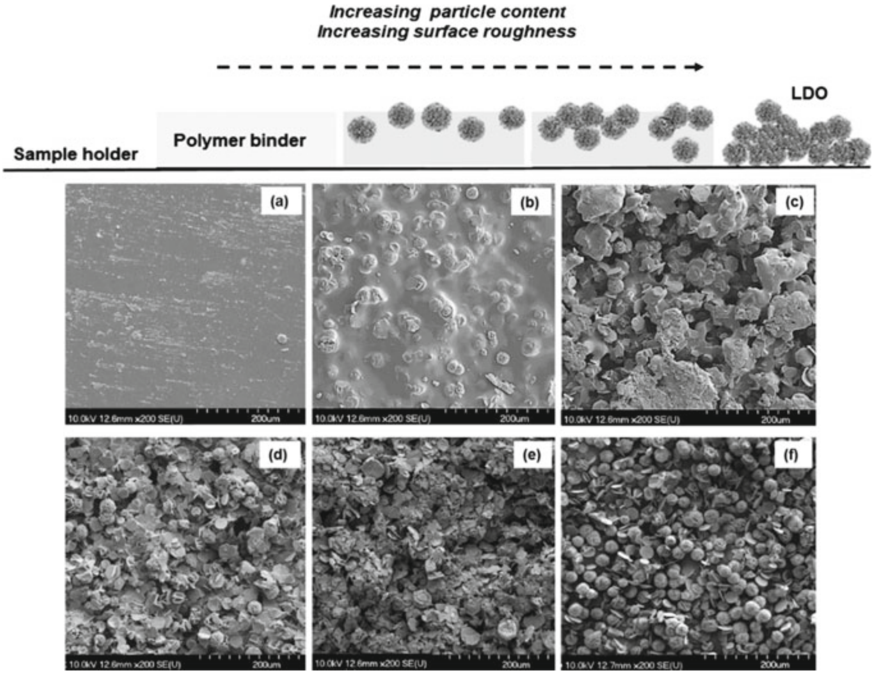

Fig. 8.6 Schematic diagram and SEM images of increasingly LDO-loading photoreactive LDO fluoropolymer layers. The nominal concentration of the LDO photocatalyst particles was: **a** 0, **b** 20, **c** 40, **d** 60, **e** 80, and **f** 100 wt% [19]

Figure 8.6a shows that the initial fluoropolymer layer (without LDO content) has relatively smooth surface with the roughness 0.002 ± 0.0002 µm (Fig. 8.7) and the contact angle of 105.6° ± 0.21°. Figure 8.6b–e demonstrate that the gradual increase in the LDO content contributes to a pronounced increase of the surface roughness of layers, and the SEM image Fig. 8.6f displays the well-separated spherical particles of 100% particle content by weight (pure LDO layer) with particle size ~25 µm. The addition of 25.3 ± 2.3 µm spherical LDO particles with structured surfaces increases the roughness to 8.78 ± 0.48 µm and 15.3 ± 2.04 µm for 60 and 80 wt% LDO, and the obtained contact angles were 149.1° and 156.3°, respectively. This indicates that the superhydrophobic hybrid layers were obtained (Fig. 8.7).

Due to ~ 12% ZnO content of the LDO particles, photooxidation measurements had evidenced photocatalytic efficiency of the reactive LDO particles containing layers. Figure 8.8 confirms that the most benzoic acid test molecule (~24% of the initial 0.17 g/L) can be degraded by the pure LDO particle thin photocatalyst layer after 240 min UV-A light ($\lambda_{\text{characteristic}} = 365$ nm) illumination time at 25.0 ± 0.5 °C.

The immobilization of particulate LDO photocatalyst in the low surface energy polymer matrix material resulted in a continuous decline in the rates of photocatalytic reactions, since the polymer partially covered the LDO photocatalyst particles (Fig. 8.4]. As shown in Fig. 8.8, for the pure polymer film and control measurement (the absence of sample film), photodegradation was not observable; so, self-photolysis may be excluded. The rate of photooxidation became more pronounced at 80 wt% LDO content. During the photocatalytic measurements, the composite layers photodegraded ~24% of the initial 0.17 g/L benzoic acid (test molecule) content from this LDO loading (80 wt% LDO content).

Comparing the wetting and photocatalytic properties (Fig. 8.8) of the hybrid layers, it can be concluded that the prepared hybrid layers have remarkable

Fig. 8.7 Surface roughness (R_q) and water contact angle (Θ_w) as a function of LDO content in hybrid thin layers ($T = 25 \pm 0.5$ °C). *Inset* topographies of surfaces with extreme roughness (rough and smooth). On top of the values of the contact angles, the photography of the liquid droplet on the hybrid layer is shown

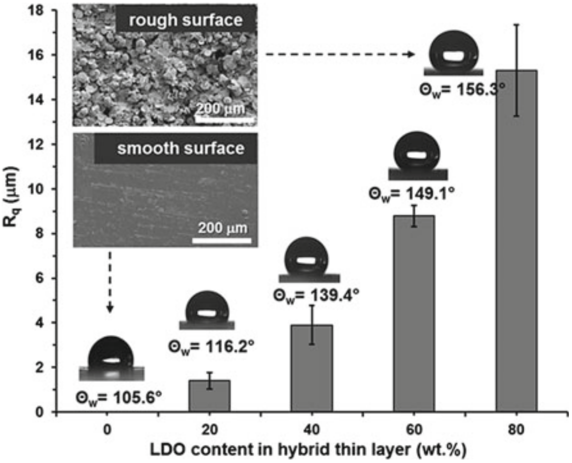

Fig. 8.8 Photocatalytic degradation of benzoic acid (as test molecule) as a function of illumination time under UV-A irradiation (λ_{max} = 365 nm) on LDO-containing fluoropolymer-based hybrid layers [19]

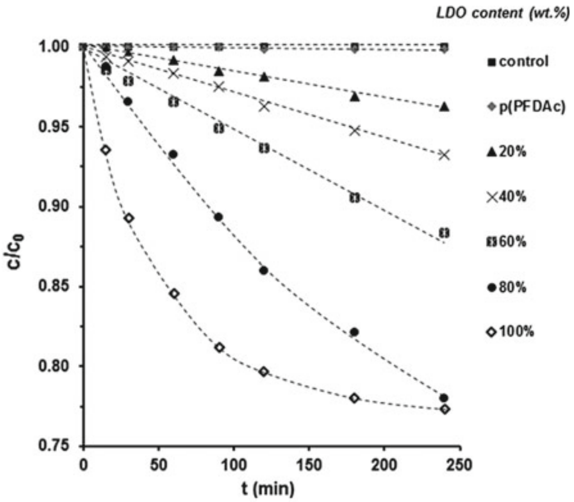

photoreactive characteristics between 80 and 90 wt% LDO loading, besides the substantial superhydrophobic (>150°) property as well.

As a result, the prepared composite rough surfaces exhibited both photocatalytic and superhydrophobic features (Fig. 8.9). The prepared layers were verified by water contact angle experiments as non-wettable. For water-based methylene-blue solution, almost spherical liquid droplets with $\Theta > 150°$ were observed, while organic (hexane) dye solution was scattered on the surface, and the layer has been stained by the applied Sudan IV molecules (Fig. 8.9). However, the interfacial dye molecules have been fully photodegraded after ~240 min of UV-A irradiation due to the LDO/fluoropolymer hybrid layer with ZnO photocatalyst material content.

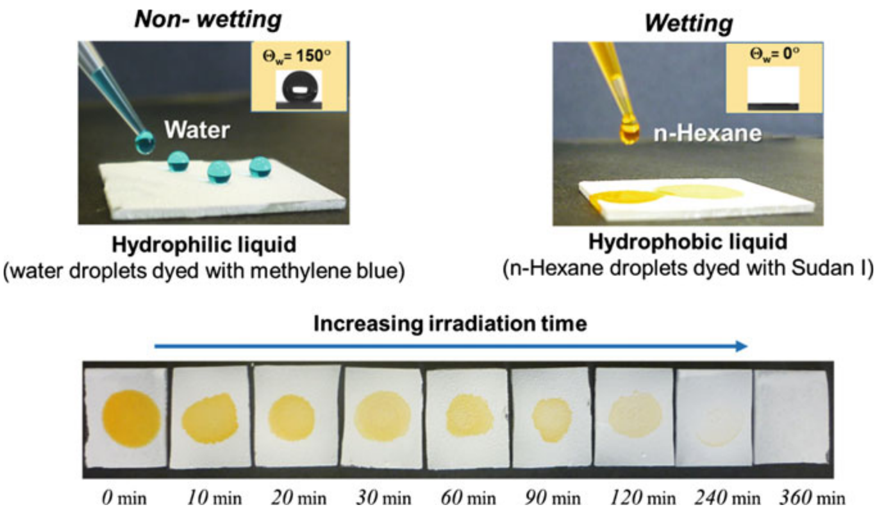

Fig. 8.9 Superhydrophobic and photocatalytic properties of the hybrid layer [19]

8.4 Adhesion and Inactivation of Gram-Positive and Gram-Negative Bacteria on Hybrid Photoreactive Coatings

There is a strong increasing trend toward infections due to bacteria (e.g., *S. aureus*, *P. aeruginosa*), and therefore, it is important to avoid transmission from human to human to optimize the efficacy of infection control. Bacteria, viruses, and fungi on many surfaces in water and in the air may be inactivated by antimicrobial material (and particularly composites) and may therefore be the key prevention method in healthcare facilities [22–24]. Various techniques are published applied related to the development of antimicrobial surfaces, but only a handful of them contains details on the structural and chemical property optimization in order to maximize antimicrobial activity [25–28]. Surfaces containing TiO_2 can eliminate numerous microorganisms due to their photocatalytic properties [29–31], as they generate strong oxidizing species upon UV-light illumination.

The first step toward bacterial colonization that affects human health [32] and the environment [33] is bacterial adhesion to surface of materials. The adhesion mechanism is driven by physical and chemical interactions between surface and microorganisms and is the first stage by attachment and survival, where nutrients on the surface will increase the amount of bacteria, colonize the surface, and form biofilms that are fundamental sources of more contamination [34, 35].

Different physicochemical properties of bacterial cells and material surfaces influence on bacterial adhesion to different material surfaces [36, 37] and also depend on surface characteristics like surface roughness, degree of hydrophobicity, and surface charge. Moreover, the surface charge of photocatalyst particles, e.g., TiO_2, is environmentally pH dependent [38].

Therefore, the surface charge of the bacteria and photocatalysts needs to be known and characterized, and it can be determined from streaming potential measurements.

Figure 8.10a displays the values of measured streaming potential for titration of 10 ml 1% TiO_2 suspensions with 1% sodium dodecyl sulfate (SDS) solution at pH = 4.5. In the beginning, positive streaming potential values were obtained for the aqueous TiO_2 suspension at this pH value, then the potential showed continuous decrease as the deprotonation of $TiOH^{2+}$ surface sites progressed, and the surface charge was lost concomitantly. Considering the amount of surfactant molecules, required for charge neutralization, the specific surface charge of TiO_2NPs at pH 4.5 was calculated to be +12.3 meq/100 g. Similar to pure TiO_2, the plasmonic Ag–TiO_2 particles with 0.5% Ag content were also examined, and a specific surface charge of +0.38 meq/100 g was obtained. Besides these determinations of specific surface charge at pH 4.5, 10 ml 1.09×10^7 cfu/ml *Escherichia coli* bacterial suspensions were titrated with 0.01% hexadecyl pyridinium chloride (HDPCl) solution at the same pH, as well. Figure 8.10b displays the values of potential streaming measured for suspension of *E. coli* bacteria. In this last case, the charge titration curve indicated the opposite tendency: the original bacterial suspension has negative streaming potential that showed continuous increase due to the increasing concentration of the cationic surfactant. The calculated specific surface charge of *E. coli* bacteria was—1.33 μeq/10^9 cfu. For other bacterial suspensions—3.19 μeq/10^9 cfu (*P. aeruginosa*) and—0.89 μeq/10^9 cfu (*MRSA*) values were determined.

The negative charge of the different GR− bacteria can be attributed to the presence of embedded polysaccharide chains embedded in peptidoglycan cell wall components [39, 40]. In the light of the determined specific surface charge values, 10 ml 1.09 × 10^9 cfu/ml *E. coli* bacterial suspension was titrated with 1% TiO_2 suspension. The result of this experiment is presented in Fig. 8.10c: as it was determined, 10^9 cfu *E. coli* bacteria can electrostatically adhere to (and can neutralize) 1.88 g of particulate TiO_2. The determined surface charge values of the applied photocatalyst (TiO_2 and Ag–TiO_2) and the studied bacteria are summarized in Table 8.1. One can imply from the results that *E. coli* and *P. aeruginosa* GR − bacteria possess higher specific surface charge values than the *S. aureus*, which belongs to the group of GR+ bacteria.

During microscopic experiments, the electrostatic interactions between the Ag–TiO_2 nanoparticles and the tested bacteria were also evidenced. *E. coli* bacterial suspensions were stained with LIVE/DEAD® BacLightTM kit, which contains different fluorescence dyes. The SYTO 9 (green emission) penetrates the bacterial cell wall and labels bacterial cells, both alive and dead, while propidium iodide (PI, red emission) cannot penetrate the cell wall of living bacterial cells, only when it is damaged. This results in the decrease in SYTO 9 stain fluorescence when both dyes are present during bacteria labeling experiments. In our experiments, bacterial adhesion on photocatalyst particles was observed with a Leica DM IL LED Fluo light microscope. In the case of *E. coli*, an initial green emission was observed, which could be attributed to the strong attachment of the living bacterial cells to the surface of spherical Ag–TiO_2 aggregates (Fig. 8.11a). However, after 120 min of

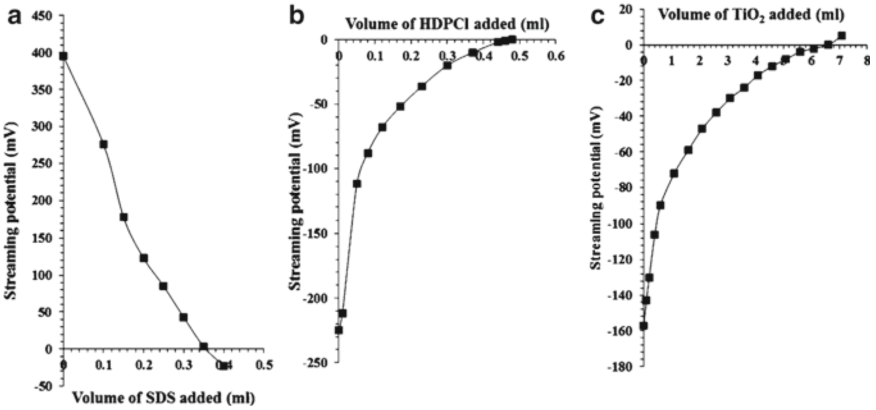

Fig. 8.10 **a** Specific surface charge value determinations of TiO_2, **b** *E. coli* bacteria, and **c** the quantification of adhered TiO_2 on the surface of *E. coli* at the electrostatic charge compensation point at pH = 4.5 (std. error: 2.0%) [38]

Table 8.1 Determined specific surface charge values of the studied photocatalyst nanoparticles and GR+ and GR− bacteria [38]

Photocatalysts or bacteria	Concentration	Measured surface charge (at c. e.p)[a]	Calculated surface charge[b] (Coulomb/ 10^9 cfu)	Electrostatically adhered TiO_2 (g/ 10^9 cfu)
TiO_2	1%	+12.3 meq/ 100 g		
Ag–TiO_2	1%	+0.38 meq/ 100 g		
E.coli (GR−)	1.06×10^7 cfu/ mL	−1.33 μeq/ 10^9 cfu	0.129	1.88
P.aeruginosa (GR−)	1.32×10^7 cfu/ mL	−3.19 μeq/ 10^9 cfu	0.308	2.55
MRSA (GR+)	1.09×10^7 cfu/ mL	−0.89 μeq/ 10^9 cfu	0.086	0.61

[a] Specified surface charge (c.e.p.) = $C_{\text{surfactant}} \times V_{\text{surfactant}}/m_{\text{TiO2 or bacteria}}$

[b] Calculated surface charge (coulomb/10^9 cfu) = ($n_{\text{added surfactant}}$ × Faraday constant)/number of bacteria

LED-light illumination, only the bacteria with the damaged membrane (Fig. 8.11b) can be seen on the surface of the photocatalyst particles, which was indicated by the detected red emission.

During the photocatalytic degradation mechanism, the irradiated photocatalyst particles generate extremely reactive oxygen species including hydrogen peroxide (H_2O_2), superoxide radical ion ($O_2^{\cdot -}$), or hydroxyl radical ($HO^{\cdot}$) [41, 42]. The presence of reactive radicals means that microorganisms can be inactivated via

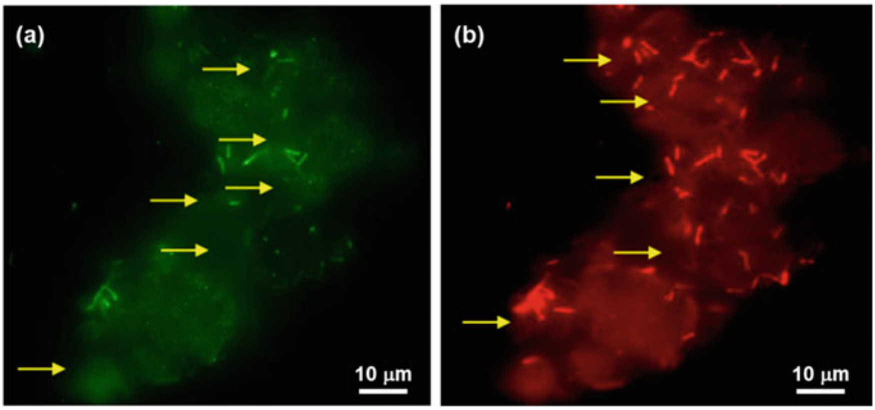

Fig. 8.11 Evaluation of the adhered *Escherichia coli* ATCC 29,522 bacteria at the aggregated Ag–TiO_2 photocatalyst particles by the help of a fluorescent microscope. The green emission correspond to living bacteria **a** whereas the red parts correspond to damaged bacteria **b** at the beginning (t = 0 min) and after 2 h of LED-light illumination

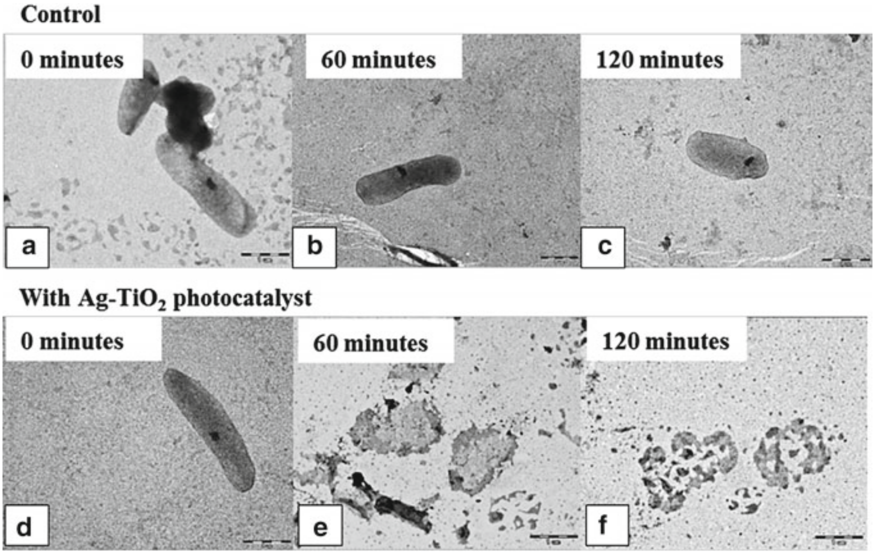

Fig. 8.12 TEM images representing the *E. coli* sacculi; **a** prior to illumination, **b** after 60 min and **c** 120 min of only visible LED-light illumination (λ = 405 nm) as control measurements, and in the presence of Ag–TiO_2 photocatalyst **d** after 0, **e** 60 and **f** 120 min illumination with the same light source [38]

photocatalyst particles by damaging the cell wall and their DNA [17, 18]. After 60 min of illumination, a significant degradation can be observed (Fig. 8.12e). The cell wall was totally degraded after 120 min of illumination, the formation of peptidoglycan cross-links was completely inhibited by the existence of free radicals that generated during the photocatalysis process (Fig. 8.12f). We have to note that without photocatalysts, no cell wall degradation was observed even after 120 min of LED-light illumination (Fig. 8.12b and c). According to these experimental results, the Ag–TiO_2 photocatalyst has proven the specific effect on the peptidoglycan layer in case of the bacteria under visible-light illumination.

8.5 Wetting-Regulation of Photocatalytic Coatings

8.5.1 Wetting-Regulation by Photocatalyst Loading and Roughness

After finding the most optimal photocatalyst particle for a specific coating application, one must consider the possibilities of immobilization and how they will affect the surfaces' affinity to the medium and the possible photocatalytic substrates and therefore the overall photocatalytic performance.

When it comes to the photocatalytic reaction at the S/L interface—specifically at the solid/water interfaces—one of the most influencing factors is the wettability of the solid surface, which affects not only the free-radical generation capability but the adsorption of the photocatalytic substrates (e.g., organic pollutants), as well.

In the case of photoreactive coatings, the main factors affecting wettability are the surface roughness, the surface free energy of the photocatalyst and the matrix material(s), and the composition of them (photocatalyst: matrix ratio).

The role of surface roughness is somewhat superior in these scenarios. As the Wenzel and Cassie-Baxter models imply [43], introducing roughness to a solid surface can emphasize its originally hydrophobic or hydrophilic nature. By this means, extreme wetting characteristics, such as superhydrophobicity ($\Theta > 150°$) or super hydrophilicity ($\Theta < 10°$), are achievable. As it was previously presented in the example of lotus leaf-like surfaces, these behaviors require hierarchical (micro- and nano-) morphology.

In the case of photoreactive coatings, the most obvious way to influence surface morphology is to appropriately choose the photocatalyst particle shape, size, loading, and preparation method. As it was presented earlier, the spray-coating is a cheap, simple, and scalable process, during which rough composite films can be built. Our approach to the adjustable photoreactivity was the optimization of this roughness through changing the photocatalyst content of the layers [44].

As Fig. 8.13 shows, the Ag/TiO_2 loading can influence the surface roughness of the spray-coated pPFDAc fluoropolymer layers, as well. As a result of this, the profilometrically determined R_q-values increased from 3.7 ± 0.9 µm to 15.2 ± 1.2 µm as the catalyst content was increased from 20 to 80%. These rough layers have significant porosity, as well: the porosity of the 80% Ag–TiO_2-containing film was determined to be 74.8% via X-ray micro-CT analysis. According to the EDX-SEM mapping of the surfaces, the spray-coating process provided a relatively homogenous distribution of the Ag–TiO_2 particles in the polymer matrix.

This homogeneity was also reflected in the low standard deviations of the contact angle measurements (Fig. 8.14). Besides the low deviations, the increasing photocatalyst nanoparticle content and roughness resulted in a strict increase of hydrophobicity up to 80% Ag–TiO_2. Despite this composition is superhydrophobic ($\Theta > 150°$), the further increase of photocatalyst content up to 100% results in superhydrophilic ($\Theta \sim 0°$) behavior that can be attributed to the low surface coverage of the fluoropolymer.

Nonsurprisingly, the increasing photocatalyst content of these films resulted in increased photodegradation efficiency in EtOH (g) visible-light photodegradation ($\lambda = 405$ nm) scenarios (Fig. 8.15a). To illustrate the photocatalytic performance of the superhydrophobic layer at the *S*/*L* interface, hydrophobic SUDAN IV in hexane solvent was decomposed. In this experiment, a dye solution drop was placed on the surface and the surface concentration of the dye molecule was monitored with the help of UV–VIS diffuse-reflectance spectroscopy. As Fig. 8.15b shows, the dye was rapidly decomposed by the superhydrophobic surface; however, the drops of aqueous methylene-blue (MB) solution did not spread on the surface, indicating the superhydrophobic character.

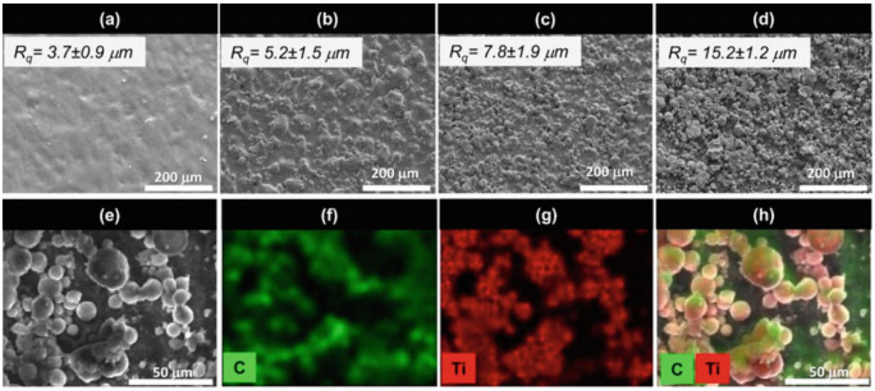

Fig. 8.13 Surface roughening by adding an Ag–TiO_2 filler to pPFDAc fluoropolymer shown in SEM images with the relevant Ag–TiO_2 content: **a** 0%, **b** 20%, **c** 40%, and **d** 80%. The surface roughness (*R*q) values profilometrically determined were also inserted. **e** SEM–EDX base image, and **f** elemental mapping for carbon, **g** titanium, and **h** carbon and titanium of the superhydrophobic surface with 80 wt% Ag–TiO_2 content [44]

Fig. 8.14 Measured Θ-values for Ag–TiO_2/pPFDAc hybrid layers with increasing of Ag–TiO_2 content. A reference to the eyes is a dotted line [44]

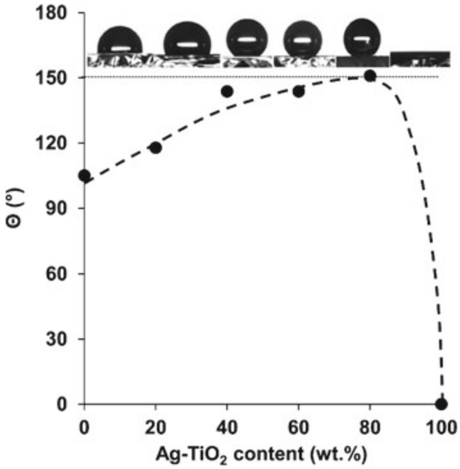

8.5.2 Regulation of Wetting and Photoreactivity of Composite Surfaces Through Adjusting Polymer Matrix Composition

Besides the presented Ag–TiO_2/fluoropolymer coatings have roughness- and photocatalyst content-dependent wettability and photoreactivity, the achievable wettability range is restricted to the hydrophobic regime due to the hydrophobic nature of the applied polymer binder (and the far super hydrophilic region, as well, thanks to the photocatalyst). To overcome this limitation, one can introduce other, hydrophilic polymer components to the composite matrix to expand the wetting regime, and thereby the range of applications.

To address this goal, we introduced the hydrophilic poly(2-hydroxyethyl acrylate) or pHEA to the Ag–TiO_2/pPFDAc films [45]. As Fig. 8.16 shows, the spray-coated pHEA-pFDAc surfaces exhibit wetting properties from slightly hydrophobic (Θ = 105.0°) to slightly hydrophilic (27°) as the pHEA content is increased in the polymer matrix. When surface roughness is introduced to the systems by the addition of 80 wt% Ag–TiO_2, the wetting properties drastically get highlighted and the achievable regime ranges from superhydrophobic (Θ = 150.9°) to superhydrophilic ($\Theta \sim 0.0°$).

SEM images of Fig. 8.17 indicate, that the initially smooth polymer surfaces non-surprisingly get decorated by micro- and nanostructures as the photocatalyst nanoparticles got introduced. The resulting porosity was measured via the X-ray micro-CT method and was proven to be 74.8%. This is in good accordance with the porosity data calculated from the profile thickness measurement results and the densities of the components (78.1%).

Since the prepared photocatalytic surfaces are porous, a preferable way to evaluate the changes in wettability is the exploitation of the phenomenon of contact angle hysteresis. In the light of this, the surface free-energy values of these coatings

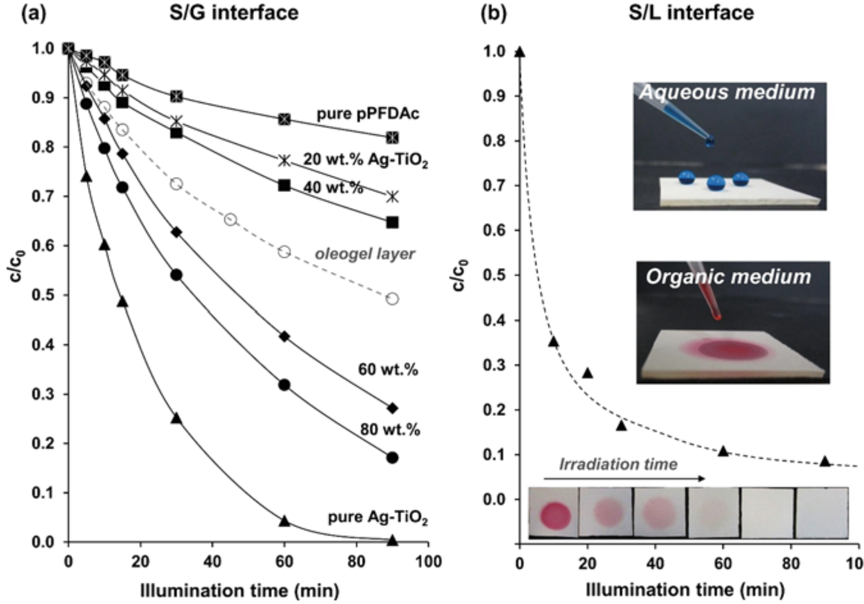

Fig. 8.15 **a** Photodegradation of EtOH vapor over Ag–TiO_2/polymer composite layers under blue LED-light illumination (λ_{max} = 405 nm); relative concentrations (c_0 = 0.36 mM) as the function of illumination time, **b** SUDAN IV photodegradation (c_0 = 20 mg l^{-1}) on roughened (80 wt% Ag–TiO_2) pPFDAc layers as a function of LED illumination time [44]

were calculated by applying the method of Chibowsky and Drelich [46, 47] throughout the measurement of advancing (Θ_{adv}) and receding (Θ_{rec}) contact angles. As Fig. 8.18 shows, the roughening increased the free energy of the initially hydrophilic pHEA surface and decreased the value of the hydrophobic pPFDAc, which both indicate the appearance of extreme wetting properties.

The roughness and porosity do not only affect photoreactivity by the means of wettability alteration: as the depth of penetration of UV and visible light in the case of porous TiO_2 films is maximized at a few micrometers [48], the provision of adequate porosity is crucial to ensure high photoreactivity.

Just like in the case of the previously presented systems, the photoreactivity of these surfaces turned out to be composition dependent, as well moreover, changing the pPFDAc to pHEA polymer matrix can drastically alter the affinity of the coating toward different pollutants and media. As it is illustrated by Fig. 8.19, the superhydrophilic Ag–TiO_2/pHEA layer effectively decomposes methylene blue from an aqueous solution besides showing lower reactivity toward the SUDAN IV, which is dissolved in abs. EtOH during visible-light illumination (blue LED, λ = 405 nm). However, the reactivity of superhydrophobic Ag–TiO_2/pPFDAc coating is the opposite. This indicates the wetting-regulated photoreactivity, which can be attributed to the different free-radical forming capabilities of the composite coatings. Fig. 8.20 shows the luminometrically determined maximum radical concentrations in H_2O_2-equal concentration units. These measurements evidenced the higher rate of ROS formation over the more hydrophilic—and therefore more wetted—layers in an aqueous medium, however, there are other efficiency-determining factors, as well.

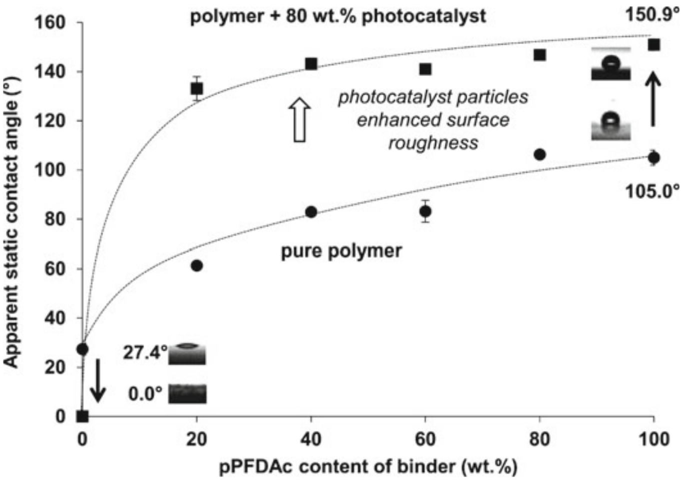

Fig. 8.16 Apparent static contact angles on initial smooth polyacrylate thin films and Ag–TiO_2–loaded rough polyacrylate composite layers as a function of the hydrophobic pPFDAc fluoropolymer content in the copolymer matrix (T = 25 ± 0.5 °C) [45]

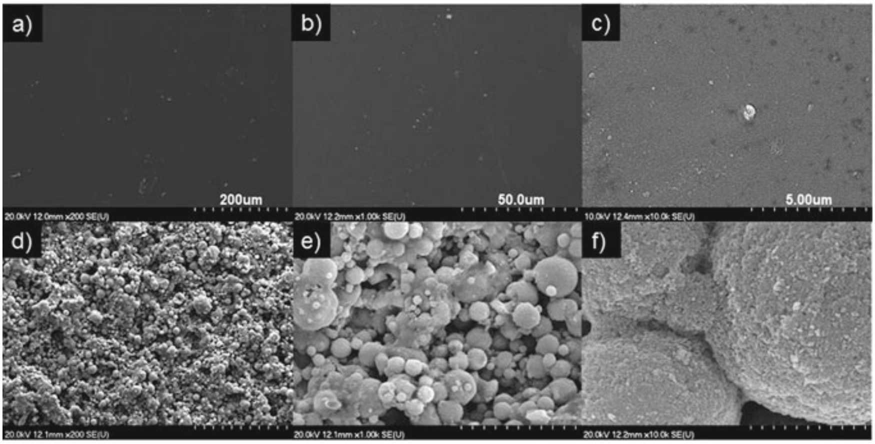

Fig. 8.17 **a–c** A smooth pPFDAc fluoropolymer film and **d–f** the 80 wt% Ag–TiO$_2$-containing pPFDAc film in SEM images, under different magnifications: 200× (**a, d**), 1000× (**b, e**), 10000× (**c, f**) [45]

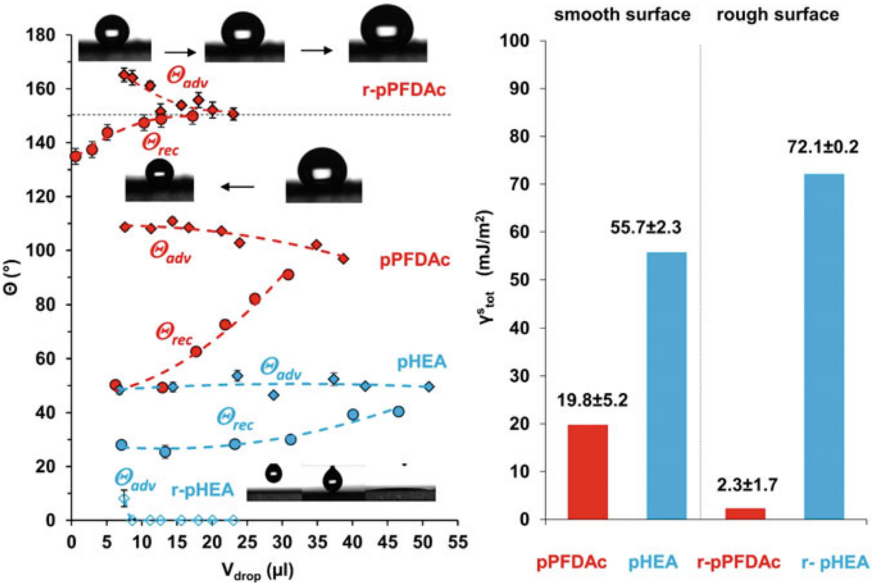

Fig. 8.18 **Left** dynamic (advancing and receding) contact angles and **right** the calculated total surface free-energy ($\gamma_{\mathrm{s\ tot}}$) values of smooth and roughened (*r*−) pPFDAc and pHEA-based composite layers [45]

Similar to the previously presented Ag–TiO_2/pPFDAc coatings with different photocatalyst nanoparticle content, these coatings also have a different affinity toward not just the medium but the decomposable substrate. As it was proved during S/G photocatalytic experiments (the visible-light-assisted decomposition of EtOH vapor), layers with higher hydrophobic pPFDAc content had higher decomposition-efficiency, which can be attributed to the different EtOH adsorption capabilities (Fig. 8.21).

8.5.3 Hydrophobization of Photocatalysts on Inorganic Base

In most photocatalytic surface scenarios, organic polymers are used to influence the wetting properties (preferably hydrophobic) of the originally hydrophilic semiconductor oxide photocatalysts. However, as these polymers (e.g., fluoropolymers) often have a high price and/or complicated production procedure, greener and cheaper solutions would be more preferred in photocatalyst hydrophobization.

To address this issue, one can seek potential hydrophobizing agents among inorganic materials, as well. The elemental sulfur can be a suitable candidate, as it is a cheap, abundant by-product of the oil and gas refinery. Besides its main usage

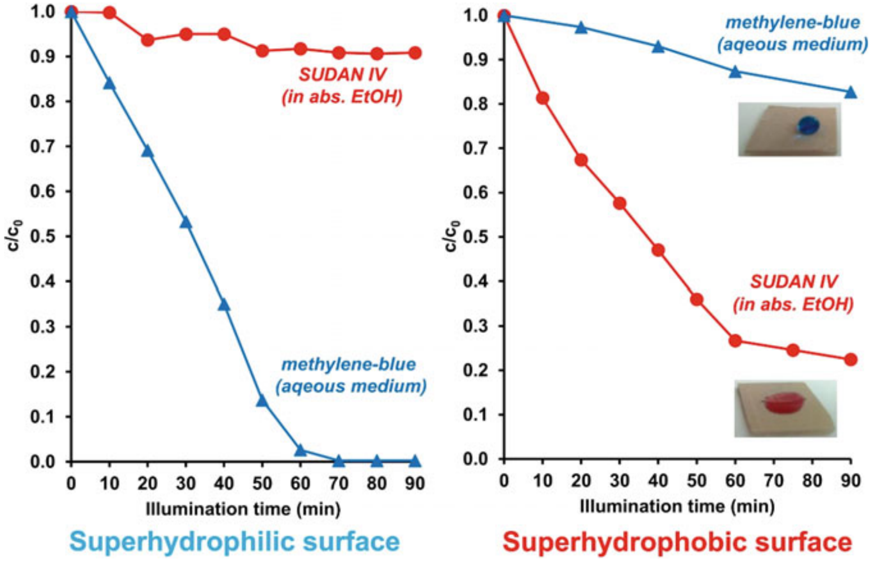

Fig. 8.19 **Left** Corresponding normalized concentration changes of MB ($c_0 = 2$ mg/l) and SUDAN IV ($c_0 = 2.5$ mg/l) dyes over a superhydrophilic and **right** over a superhydrophobic surface upon LED ($\lambda = 405$ nm) illumination. The inserted images show the drops of the aqueous and organic solutions on a superhydrophobic composite layer [45]

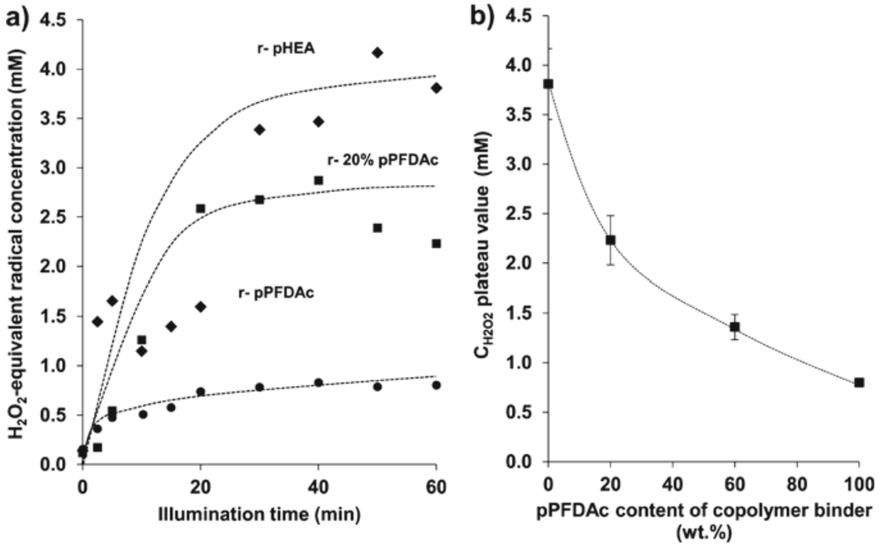

Fig. 8.20 Evolution of ROS on roughened (*r*−) pPFDAc and pHEA hybrid layers upon blue LED illumination (λ = 405 nm), **b** the measured maximum H_2O_2-equivalent radical concentrations as a function of the pPFDAc content of the polymer matrix

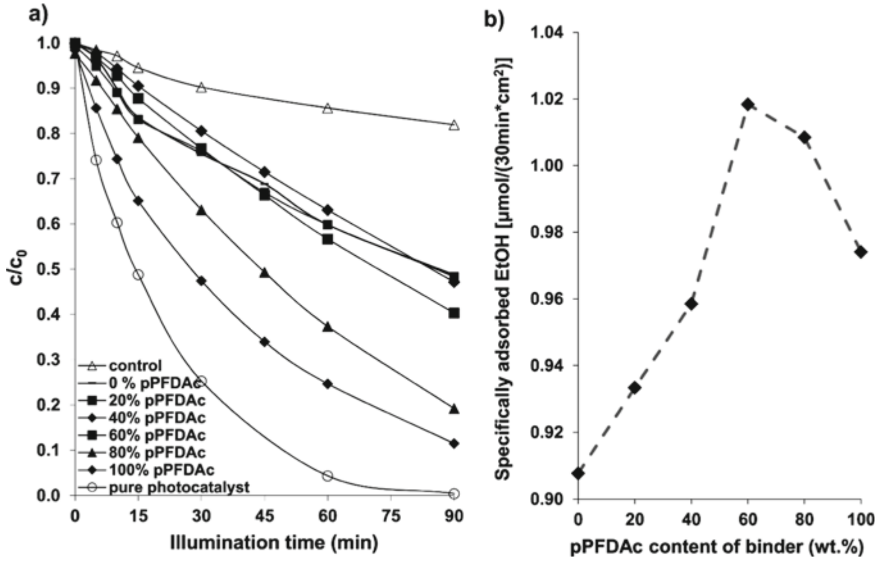

Fig. 8.21 **a** EtOH decomposition on Ag–TiO_2/polyacrylate hybrid layers upon LED-light illumination (λ = 405 nm; c_0 = 0.36 mM); relative concentrations as a function of illumination time (the composition of the polymer matrix is referred in the legends), **b** and the specifically adsorbed amounts of EtOH adsorbed by the particular layers in the 30 min dark period before the photocatalytic measurements [45]

(sulfuric acid production), elemental sulfur is applied for example in agricultural scenarios [49, 50] antibacterial materials [51] and as composite filler material in concrete and polymer matrices [52, 53].

The commercial elemental sulfur is particulate, with mean diameters usually falling within the micrometer regime. To achieve the hierarchical (micro- and nano-) surface roughness with sulfur particles, the primer particle size should be decreased to the colloidal or nano region. This is hardly manageable through top-down methods, like milling as sintering can occur and good control over the particle size is relatively difficult to achieve. In accordance with this, the most popular processes are bottom-up methods, which—at the downside cost of having lower yields—offer better controllability and most importantly, sulfur nanoparticles. Among bottom-up sulfur nanoparticle preparation techniques, the most well-known ones are the Weimar [54] and Raffo [55] solvent-precipitation methods, but sulfur nanoparticles can also be prepared, e.g., through the deposition of sulfur vapor on cold water [56].

Solvent-precipitation methods in general have negligible yields and require harmful organic solvents, such as CS_2 or benzene due to the low solubility of sulfur. However, the Raffo method is an exception with its possible maximum yield of 600 g/l colloidal elemental sulfur. Instead of physical dissolution, this process is based on the chemical dissolution of sulfur in a highly basic (pH $\sim$ 14) medium, which is a disproportionation reaction. As Eqs. 8.1–8.4 show, elemental sulfur particles are formed upon the reacidification of these mixtures. With the help of this method, sulfur nanoparticles were obtained with 4–40 nm mean diameters (Fig. 8.22) at a concentration of $\sim$0.9 g/l.

$$4\,\mathrm{S} + 6\,\mathrm{NaOH} = \mathrm{Na_2S_2O_3} + 2\mathrm{Na_2S} + 3\mathrm{H_2O} \tag{8.1}$$

$$\mathrm{Na_2S_2O_3} + \mathrm{H_2SO_4} = \mathrm{H_2S_2O_3} + \mathrm{Na_2SO_4} \tag{8.2}$$

$$x\,\mathrm{H_2S_2O_3} = y\,\mathrm{H_2O} + z\,\mathrm{SO_2} + \mathrm{H_2S}_m\mathrm{O_6} \tag{8.3}$$

$$\mathrm{H_2S}_m\mathrm{O_6} = \mathrm{H_2S}_{m-n}\mathrm{O_6} + \mathrm{S}_n(n > 5) \tag{8.4}$$

To prepare composites with Ag–TiO_2 nanoparticles, electrostatic interactions were utilized between the sulfur and the photocatalyst [57]. Despite sulfur is quite hydrophobic in nature, it has a slightly negative surface charge over pH = 2 in an aqueous medium [58]. On the contrary, TiO_2 has a point of zero charge (or PZC) at pH $\sim$ 6 [59], which means between 2 and 6 pH values, attractive electrostatic interactions can be observed between the two particles. This was evidenced during streaming potential measurement-assisted particle charge titrations (Fig. 8.23). To preferably strengthen the attraction between the negatively charged sulfur and the inorganic particles, a negligible amount of cationic polyelectrolyte (e.g., 0.1 g/l chitosan) can be applied, as well [53].

The spray-coated, photocatalyst, and sulfur nanoparticle-containing two-component composite films showed composition-dependent wettability.

Figure 8.24 shows that such surfaces have superhydrophilic behavior ($\Theta \sim 0°$) up to 60 wt% sulfur content, and then the measured contact angle values sharply rise toward the superhydrophobic region ($\Theta > 150°$), which is reached at 90 wt% sulfur content. This well-wetted nature despite the high amount of added hydrophobizing agent indicates a Wenzel-type surface characteristic [47], where the water droplets penetrate the porous structure of the layers. This was also evidenced during the measurement of advancing and receding contact angles: although the overall surface free energy was appeared to be very low ($\gamma_{tot} < 4$ mJ/m^2), the difference between the advancing and receding angles is very significant. This behavior is a result of the lack of immobilizing agents (polymers), as the particles in the spray-coated films become loosely adhered thanks to the low surface free energy of sulfur.

Despite the low mechanical stability, these composite films are superior to the polymer-hydrophobized photocatalysts, in terms of UV- and visible-light resistance. As it can be seen in Fig. 8.25, thanks to the 180 min blue LED illumination

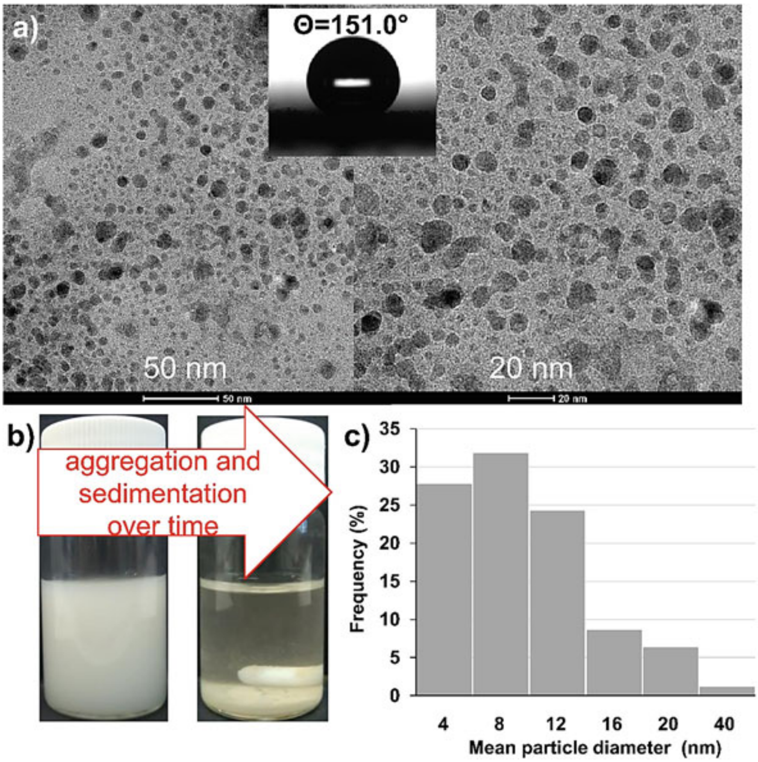

Fig. 8.22 **a** TEM images of precipitated sulfur nanoparticles and the wetting interaction between a spray-coated sulfur nanoparticle layer and a drop of deionized water, **b** aqueous dispersions of freshly prepared and 24 h old sulfur particles, **c** and the size distribution of precipitated sulfur nanoparticles, based on the images of **a** [57]

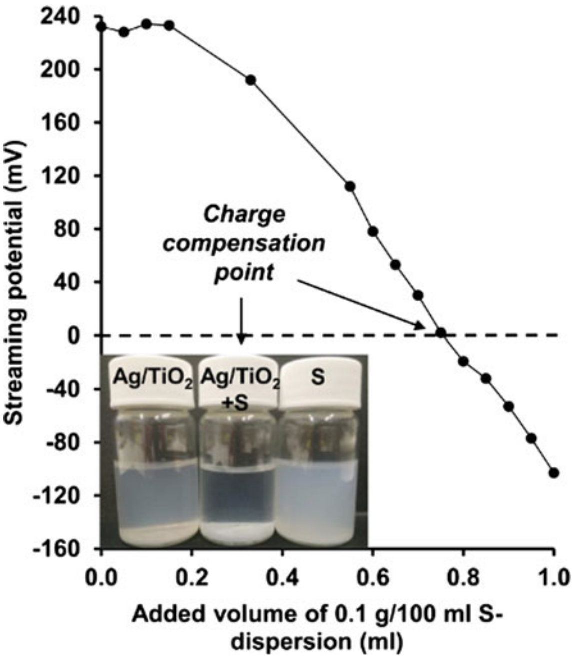

Fig. 8.23 Streaming potential values of the 0.01% Ag–TiO_2 nanoparticle dispersion upon the addition of 0.09% sulfur nanoparticle dispersion (pH = 5.00) [57]

(λ = 405 nm), the apparent surface free energy showed only a minor increase (γ_{tot} increased from 2.3 to 3.3 mJ/m^2). During two weeks of blue LED-light illumination, the sulfur-hydrophobized layers did not lose their wettability; however, a constant contact angle decline could be observed in the case of polymer-immobilized Ag–TiO_2 (Fig. 8.26). This stability is reflected in the photocatalytic performance, as well: as it can be seen in Fig. 8.27, the EtOH (g) photodegradation efficiency decreases only by 5% after a week-long LED illumination.

As sulfur is an abundant and cheap ingredient, these promising results may prospect a bright future to elemental sulfur in photocatalysis- and/or wetting-related applications.

8.6 Self-Healing Photoreactive Coatings

As it was demonstrated before (Fig. 8.26), the photostability of the binder material is vital in most coating scenarios, where the most suitable (mechanically stable) immobilizing agents for the photocatalyst particles are the different polymers. To address this issue of photoinstability, a potential approach is the utilization of the so-called self-healing behavior. Self-healing materials are capable of repairing themselves and regaining their physical or chemical properties upon damage without human intervention [60, 61].

Fig. 8.24 Characteristic apparent contact angles of Ag–TiO_2/S composite powders as a function of S-content. The inserted image with a drop of aqueous methylene-blue solution illustrates the water repellency of 90 wt% S-containing composite [57]

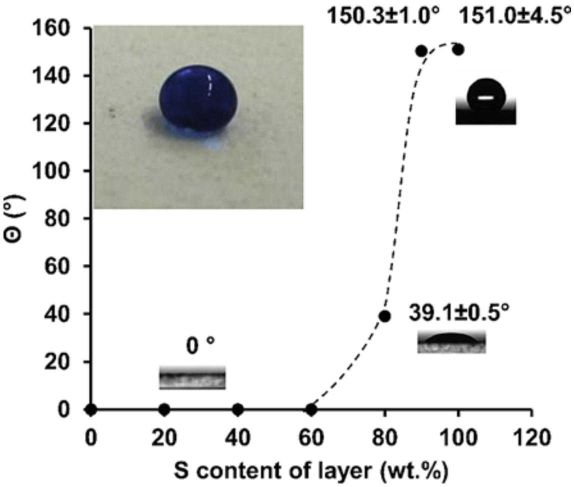

Fig. 8.25 Dynamic (advancing and receding) contact angles on sprayed (90 wt%) sulfur-hydrophobized, photoreactive Ag-TiO_2 films, with the corresponding total apparent surface free-energy ($\gamma_{s\ tot}$) values prior to and after 180 min blue LED-light illumination (λ = 405 nm) [57]

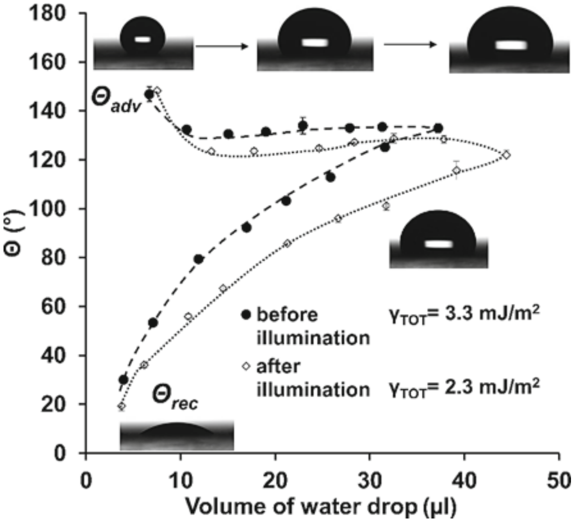

There are three main approaches to self-healing behavior in the case of polymer materials. The intrinsic self-healing is achieved as a result of the inherent reversibility of chemical bonding: these systems utilize interactions like, e.g., Diels–Alder reactions [62]. Apart from this, the most studied systems are the capsule-based (monomers are incorporated in capsules) [63] and the vascular surfaces (the repairing agent is transferred through channels to the place of damage) [64]. Recently, the photocatalysis-related applications of self-healing character also got into the focus of researchers [65, 66] and even TiO_2-related systems were prepared. Tu et al. reported the thermal repairability of photocatalytic TiO_2-containing fluoropolymer films [67]. In their work, the photoreactive coating was

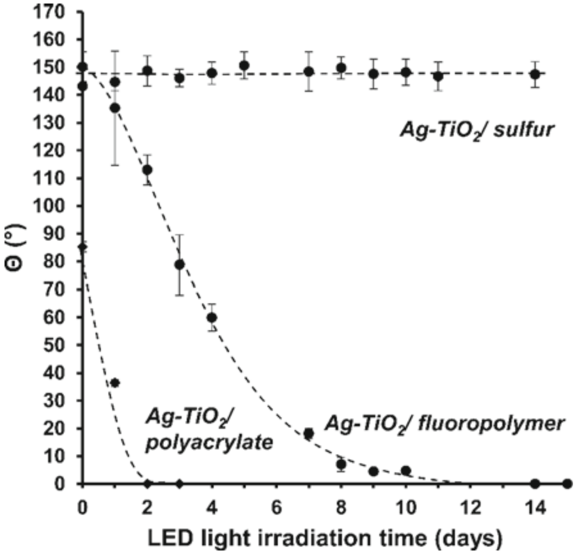

Fig. 8.26 Effect of long-term blue LED (λ = 405 nm) illumination on the wettability of different polymer-based and inorganic sulfur-containing superhydrophobic composites; contact angles as a function of irradiation time [57]

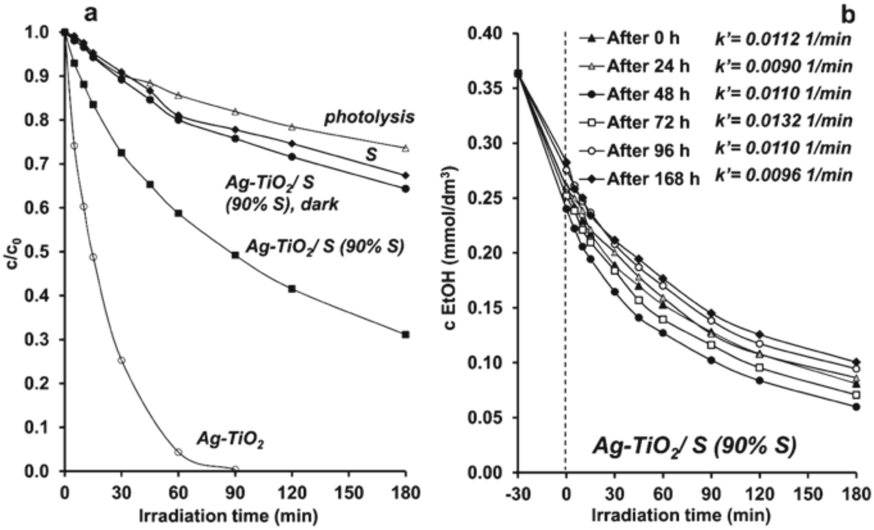

Fig. 8.27 **a** EtOH vapor photodegradation (c_0 = 0.36 mM) on pure Ag–TiO_2 and sulfur layers, and on Ag–TiO_2/S composite film (90 wt% S) upon LED-light illumination (λ = 405 nm) as a function of the time of illumination. The EtOH concentrations were also measured without any illumination for reference. **b** Change of EtOH concentration over Ag–TiO_2/S layers after 0, 24, 48, 72, 96, and 168 h continuous illumination [57]

sprayed over a PDMS elastomer film on wooden substrates. Upon thermal treatment, the PDMS could diffuse to the upper layers of the coating and take the place of the photodegraded fluoropolymer, which resulted in the regaining of the wetting properties.

Due to its easily tunable elasticity and chemical stability, PDMS itself is a favored material when it comes to the development of self-healing systems. Wang et al. reported the successful synthesis and characterization of superhydrophobic and self-healing propyl trichlorosilane-infused PDMS oleogel surfaces [68]. The key to the self-healing mechanism of these surfaces is the hydrolysis and polycondensation of the trichlorosilane molecules upon coming in contact with the ambient moisture. Originally, these silane molecules are dispersed in the PDMS-silicone oil oleogel matrix; however, they form a protective siloxane layer and grass-like structures (surface roughness) at the polymer/air interface. When mechanical or chemical damage is inflicted to this protective layer, it regenerates itself as the dispersed alkyl-trichlorosilane molecules come in contact with the moisture. By this means, the wetting properties could be regained many times, consecutively: theoretically, the trichlorosilane loading of the oleogel is the only limiting factor. Despite the promising results with this sophisticated self-healing mechanism, the range of possible applications is limited due to the complicatedness of the preparation process (inert atmosphere and glovebox required, only tested for bulk samples, etc.).

However,—as the results of our recent work prove—this approach toward self-healing behavior can also be implemented via the preparation of similar surfaces by spray coating [44]. In the case of our implementation, the hydrophobicity of these surfaces ($\Theta = 124.7 \pm 3.2°$) was less emphasized than the previously reported ones', as no grass-like surface protrusions were formed (Fig. 8.28).

This could mainly be attributed to the exclusion of inert atmosphere from the procedure, but the slightly different choice of ingredients could change the product quality, as well (PDMS starting material and silicone was of different quality, and dodecyl trichlorosilane was infused into the oleogel instead of propyl trichlorosilane). Although the surface appeared to be relatively rough, the hierarchical roughness was still missing to reach superhydrophobicity. This issue was solved upon the addition of 25 wt% Ag–TiO_2 photocatalyst to the spray-coated layers, which resulted in the formation of the desired hierarchical surface (Fig. 8.28), besides significant photodegradation efficiency toward gas-phase EtOH and keeping the self-healing behavior. As it was proved in this work, this principle of self-healing is applicable in the case of spray-coated photocatalytic coatings, as well. However, the main usage-limiting downside can be the mechanical stability, as we still deal with vulnerable gelous composite materials. In order to successfully apply similar systems in everyday practical applications, one must consider for example the interactions between the alkyl-trichlorosilane and the catalyst nanoparticles (e.g., surface functionalization, alteration of optical properties), as well [69, 70].

8.7 Monolithic Organic Photoreactive Coatings

In the preceding chapters, the effect of the photocatalyst loading and the matrix composition on the wetting properties and photoreactivity was discussed. The previously presented approaches to this matter showed that not only the hydrophobicity of the matrix but the roughness, provided by the photocatalyst particles, is also a crucial factor.

To make such rough, visible-light-active photoreactive surfaces or coatings more sophisticated, one can decide to prepare them on a monolithic base. To address this goal, a photoreactive conducting polymer (organic photovoltaic or OPV), such as poly(3-hexyltiophene) (P3HT) is required as a base material [71], which is needed to be roughened to adjust the wetting behavior. P3HT is an ideal candidate for these studies as it is the most studied OPV, visible-light-active, and relatively cheap, besides it is producible in higher amounts [72].

Based on our recent study, it is possible to prepare bifunctional, superhydrophobic, and visible-light photoreactive surfaces just by elaborating the surface roughness of initially hydrophobic P3HT layers [73]. This approach is based on the exploitation of the different solubility conditions of the polymer. The polymer segments of macromolecules in poor solvents (such as DMF) can get near each other and tend to form polymer globules to minimize the area of solvent/polymer contact interface. However, in better solvents (e.g., toluene), the segments of P3HT chains get further from each other, and the polymer coil takes an expanded state.

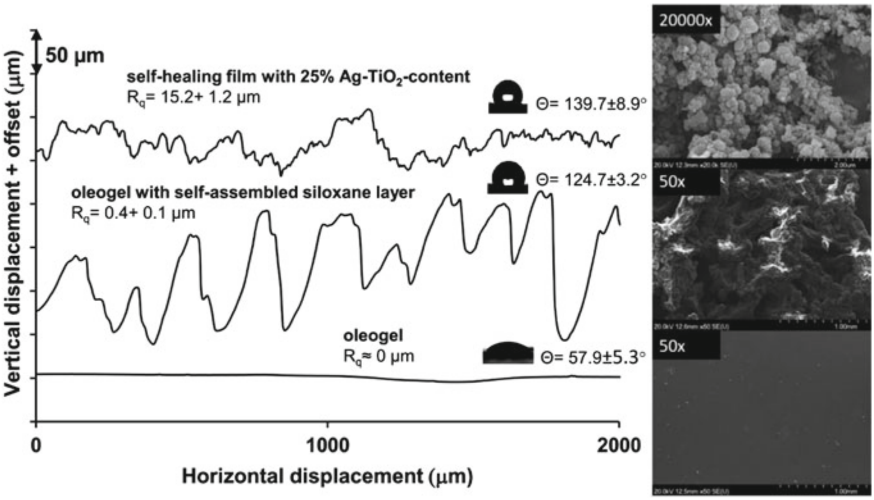

Fig. 8.28 Measured profilometric curves for orignal PDMS oleogel layer (soft) at t = 0 min and after formation of rough siloxane layer with the corresponding Θ values. Adding of 25% Ag–TiO_2 photocatalyst particles offered additional nano-roughness to the layer. The respective SEM images show the sample surfaces [44]

The results of filtration from such solutions can be utterly different: filtering a solution with good solvent leaves a smooth polymer layer on the filter, on the contrary, filtering a solution with poor solvent results a structured polymer film. The dissolution conditions and thereby the quality of the obtained polymer films can be adjusted by not just the solvent composition but mechanical treatment, such as ultrasonication, as well. The sonication process contributes to the decrease of particle size as the disaggregation of the larger polymer particles occurs. In this case, the morphological attributes of the obtained polymer films are influenced by the sonication power and time.

To illustrate this phenomenon, P3HT solutions (in toluene/DMF = 60: 40; *V: V*) were filtered through filter papers after certain sonication times. After 5 and 10 min of sonication, the solutions were dark and turbid, indicating the presence of particulate polymer with high dispersity. The complete dissolution was achieved after 30 min sonication, when the solutions became transparent and orange colored, without any presence of dispersed polymer particles. To characterize the influence of sonication on the surficial morphology of the prepared polymer layers, SEM images were taken. As Fig. 8.29a shows, 1 min sonication led to a coarse P3HT surface with micro-roughness; however, 5 and 10 min (b and c) of ultrasonic treatment led to the formation of hierarchical roughness. When the polymer was completely dissolved after 30 min ultrasonication, the resulting P3HT film was smooth (d). These images are in good accordance with the roughness values (R_q) of the surface profilometrically determined: after 30 min sonication, the R_q value was 0.23 ± 0.05 µm, while after 10 min, it was proven to be 7.85 ± 0.60 µm.

As it was proposed, the wetting properties were dependent on the roughness, as well. As Fig. 8.30 shows that the contact angle vs. sonication time data pairs give a maximum curve, indicating an optimal sonication time between 10 and 20 min to reach superhydrophobic character ($\Theta \sim 150°$), which can be attributed to the previously presented hierarchical roughness. This tendency toward superhydrophobicity is also reflected in the measured sliding angles, reaching a minimum value of 10° in the interval of 10–20 min sonication time.

The roughening of P3HT films resulted in increased photodegradation efficiency against EtOH (g) at the S/G interface (Fig. 8.31): during artificial solar light illumination (λ = 280–900 nm), the rough P3HT surface decomposed 38% of the initial EtOH concentration (0.36 mM), while the smooth surface decomposed 31% only. However, this increased performance is still negligible, compared to the one of the reference P25 TiO_2-containing layer (57%).

On the contrary, when the visible LED-light source is used (λ = 420–700 nm), the photocatalytic efficiency of TiO_2 drastically decreases, while the degradation efficiency of P3HT increases up to 44%.

Besides the quantification of photocatalytic and wetting properties, it is important to find out, whether the polymer itself is durable and resistant enough to withstand the ROS, formed during the photocatalytic processes. As Fig. 8.32 displays, under ambient conditions, the week-long LED-light illumination caused a minor mass decrease; however, the UV-illumination almost completely decomposed the initial polymer amount. These results proved the viability of monolithic, polymer-based superhydrophobic coatings in visible-light photocatalytic scenarios.

As a prospected research direction in this field, it would be interesting to prepare similar monolithic photoreactive coatings, e.g., via templating techniques [74] and top-down-, such as chemical [75], plasma [76], or laser [77] etching methods, which could give more control over the surface morphology and the wetting properties besides broadening the variety of coatable substrates.

8.8 Stimulus-Responsive Photocatalytic Composite Surfaces

The so-called stimulus-responsive materials have been attracting still increasing attention in the past decades. Stimulus responsivity means the ability of a material to alter its physical and/or chemical properties upon exposure to external effects, such as temperature change, light, pH, or magnetic field. This characteristic paves the way toward the development of smart materials. The potential in this field has already been widely acknowledged by giving the Nobel Prize in chemistry to

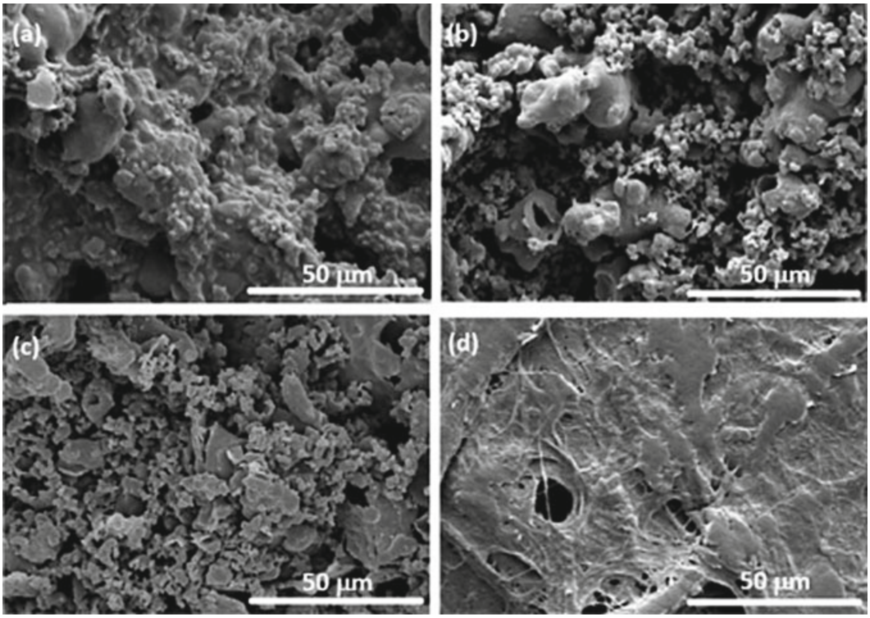

Fig. 8.29 SEM pictures of P3HT films that formed on filter papers after **a** 1 min, **b** 5 min, **c** 10 min, and **d** 30 min of sonication [73]

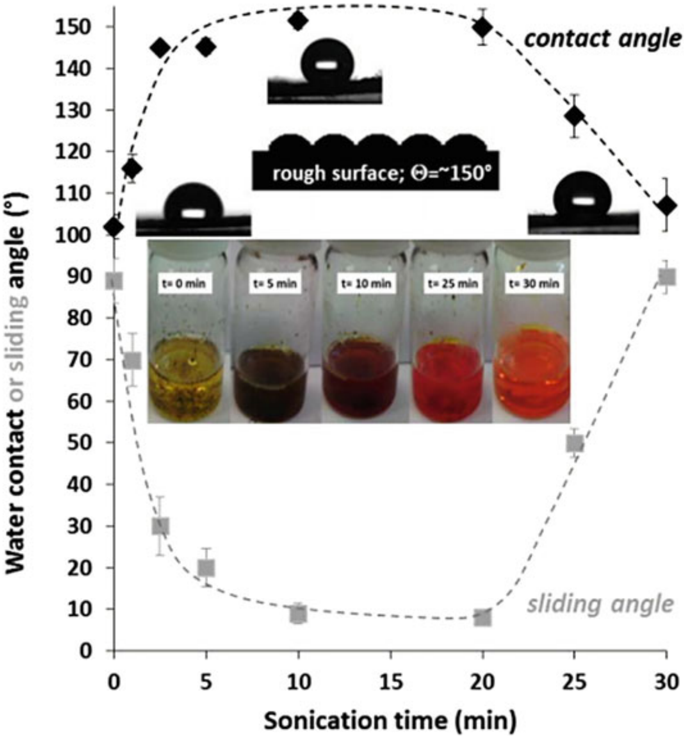

Fig. 8.30 Measured contact and sliding angle values of P3HT layers as a function of the duration of ultrasonication in 40/60 v/v% (toluene/DMF) mixture ($T = 25 \pm 0.5$ °C). The inserted photographs display the polymer dispersions after the corresponding sonication intervals [73]

Sauvage, Stoddart, and Feringa in 2016 "for the design and synthesis of molecular machines."

Stimulus-responsive materials have many examples that they even can be found in our everyday life: enough to think about liquid crystal displays and windows with electricity-adjusted transmittance. Also, an increasing number of drug formulation systems utilize stimulus-responsivity in many different ways in order to control the release of different active pharmaceutical ingredients (APIs) in a specific target organ and/or at a specific rate [78]. The amount of examples of stimulus-responsive materials for healthcare applications is numerous: there are drug-release systems, in which the release is controlled by the pH- or temperature-regulated swelling of the drug carrier [79], or magnetic field with the help of incorporated magnetic particles [80]. Stimulus-responsive materials became prevalent in other fields, as well, such as in analytical scenarios, where the responsive character can serve as a key mechanism in sensing physical amounts, like pH or temperature, [81] and at microfluidics, where they are at hand when it comes to creating miniaturized actuators for creating fluid motion through

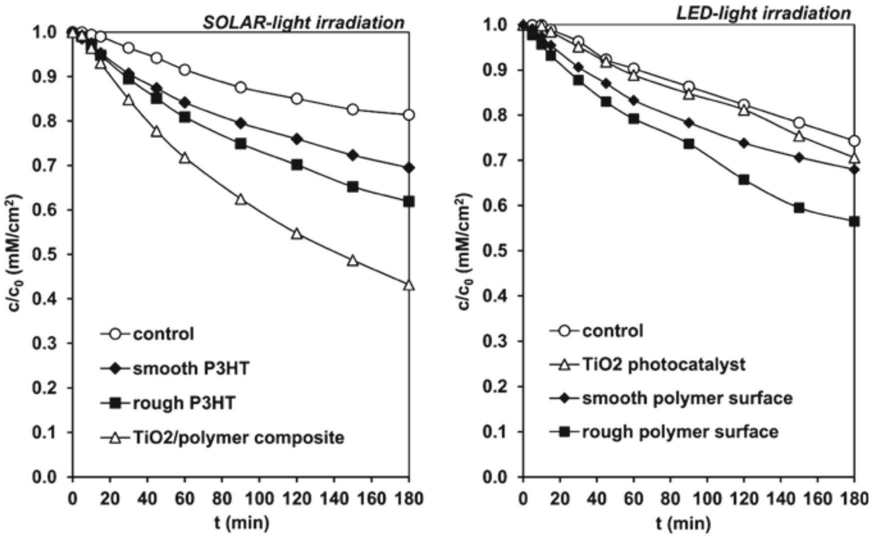

Fig. 8.31 Rate of EtOH vapor photodegradation on smooth and rough P3HT films, compared with P25 TiO_2; relative concentrations ($c_0 = 0.36$ mM) as a function of illumination time upon **a** simulated solar ($\lambda = 280$–900 nm) and **b** LED-light irradiation ($\lambda = 420$–700 nm) [73]

Fig. 8.32 Weights of the P3HT thin films (1 mg × cm^{-2} surface polymer content) as a function of the duration of irradiation, using solar- ($\lambda = 280$–900 nm) and visible-light (LED; $\lambda = 420$–700 nm) exposure. The inserted images represent the thin P3HT film during the irradiation process [73]

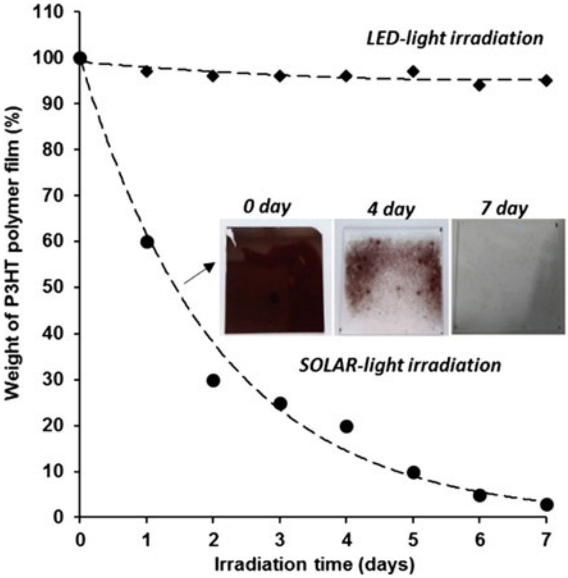

mechanical response or changing the surface wetting characteristics as a result of the external stimuli [82, 83].

We have already discussed how wettability can affect the catalytic performance of photoreactive coatings. In this vein, altering the surface wetting characteristics of macroscopic surfaces or particles by external stimuli real-time can open new possibilities toward not just liquid manipulation but heterogeneous photocatalysis, as well. There are not so many examples in the literature for changing wetting and/or adsorption—and therefore photocatalytic—properties of different surfaces by external stimuli. A promising way to elaborate such characteristics is the application of poly(*N*-isopropyl acrylamide) (pNIPAAm). The pNIPAAm polymer chains are miscible with water at room temperature, but these systems suffer phase separation over ~32 °C as a result of entropy-driven precipitation [84]. This lower critical solution temperature (LCST) can be adjusted to fulfill the requirements of specific tasks by adjusting the molecular length and its dispersity or copolymerization with different other monomers. pNIPAAm chains can be anchored to different substrate surfaces like silicon wafers [85], glass [82], or polymers [86], while their length can have monodisperse distribution if living polymerization methods, such as RAFT or ATRP are applied [86].

The thermoresponsive feature of these polymers is utilized in various fields: for example, one can find pNIPAAm-based drug-release systems with temperature responsivity [87] or pNIPAAm-functionalized sensing elements [88], but there are pNIPAAm-utilizing approaches at the field of catalysis, as well [89, 90]. Jia and their co-workers coated photoreactive Cu_2O particles with a shell of pNIPAAm chains, which gave the particles thermoresponsive photocatalytic behavior in methyl-orange degradation scenarios [91]. According to their mechanistic insights, not only the wetting of the coated particles gets affected by the temperature but over the LCST, the diffusion of the degradable model pollutant toward the catalyst surface also gets hindered in such systems. Despite the existing scenarios with thermoresponsive photocatalytic particles, this feature is barely implemented in the case of macroscopic photocatalytic surfaces.

Besides pNIPAAm-based systems, another promising approach to the stimulus-responsive wetting characteristics utilizes magnetic particles to influence surface structure—and therefore the wetting properties—real-time. The so-called magnetorheological elastomers are elastic polymers that can be deformed—and their mechanical properties can be altered—by a magnetic field. Lee et al. [92] and Sorokin et al. [93] dispersed carbonyl iron particles in poly(dimethylsiloxane) (PDMS). The incorporated particles then could be aligned in the direction of the external magnetic force-field lines to form needle-like surface structures which increased hydrophobicity. A different type of magnetic coatings utilizes magnetic grasses or pillars to alter wetting conditions [94]. Such pillars can form when magnetic particles (e.g., magnetite, iron, etc.) are dispersed in the uncured polymer matrix, and the magnetic field is introduced during the curing process, which leaves elongated magnetic polymer strains as a result. The pillars can be bent or stiffened by changing the direction and/or strength of the magnetic field, which alters the surface structure and the wetting properties in real-time, as well. In the study of

Yang et al., the authors prepared magnetic pillars of carbonyl iron and PDMS via a magnetic-field-assisted spray-coating process [95]. When no magnetic field was introduced, the pillars were aligned randomly and could be bent by the impacting water droplets, increasing the *S*/*L* contact surface and therefore adhesion. However, when a magnetic field is introduced perpendicularly to the substrate surface, the pillars stiffened and pinned the impacting droplets: this pinning contact between the droplet and the magnetic pillar forest resulted in the decreased contact area and adhesion, therefore seemingly more hydrophobic character. Thanks to the stimulus-responsive character, these coatings can be applied as liquid-manipulation tools: by the help of an electromagnet or permanent magnet, the water droplets can be picked up and released, and therefore, lossless liquid droplet transportation becomes achievable (Fig. 8.33). Considering the achievable broad contact angle ranges, this mechanism may have a bright future in heterogenous photocatalytic scenarios, as well.

In our first approach to stimulus-responsive photoreactive coatings, these magnetic pillar systems were enhanced with Ag–TiO_2 photocatalyst nanoparticles [96]. We applied Yang's optimal PDMS: carbonyl iron: toluene ratio (3 g PDMS: 4.5 g carbonyl iron: 9 ml toluene) in the spraying mixture [95] besides adding 6.3–16.7 wt% photocatalyst content in order to render the magnetic pillars photoreactive. As it can be seen in Fig. 8.34, the addition of the photocatalyst particles introduces roughness to the initially smoother pillars, which changes the wetting behavior, as well (from $\Theta = 56.5°$ up to 163.9°).

According to the measured contact and sliding angle data (Fig. 8.35), the apparent hydrophobicity of these pillar forests increases (increasing contact and decreasing sliding angles) with the increasing photocatalyst content (from 0 to 16.7 wt%) in the case of the magnetically stiffened state. When no magnetic field is introduced, the pillars are randomly aligned and the contact angles showed a slight decrease with increasing Ag–TiO_2 content: this is proposed to be the result of the decreasing pillar-density and/or the increasing contact area between the droplets and the pillars (as it can be seen in Fig. 8.35 and the SEM images of Fig. 8.34). However, it is important to highlight that this hydrophilicity is considered to be apparent as the material itself remains hydrophobic while the pillars "swallow" the droplets.

The presented wetting behavior expectedly affected the photocatalytic properties, as well during methylene-blue degradation tests ($\lambda = 405$ nm) on 16 wt% Ag–TiO2-containing pillars (2.6 × 7.6 cm^2 surface; 63.3 ± 1.3 mg/cm^2 specific mass) As it can be seen in Fig. 8.36, the more wetted randomly oriented pillars degraded 42.1 ± 3.5% of the initial methylene-blue concentration (2 mg/l), while the less-wetted magnetically stiffened (0.30 T) ones degraded only 24.4 ± 3.3%. It can be seen that the photodegradation efficiency of the randomly oriented pillars almost exceeds the corresponding value (52.0 ± 1.8%) of the magnetic particle-less Ag–TiO_2/PDMS- coating with the same polymer-to-catalyst ratio and specific mass.

This work proves that this easy to produce liquid-manipulation tool can be enhanced with real-time, magnetically tunable photoreactivity to fulfill specific needs.

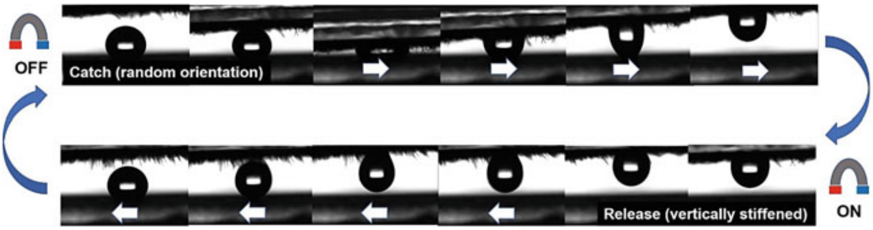

Fig. 8.33 CCD images of water droplet catch and release with 16.7 wt% Ag–TiO_2 content by magnetic grass coatings [96]

In our second approach to stimulus-responsive photoreactive coatings, the thermoresponsive pNIPAAm polymer was utilized. As it was introduced earlier, pNIPAAm is compatible with many kinds of surfaces; however, the presented beneficial adjustable elasticity and compatibility with other coating target surfaces made PDMS an ideal base-material candidate in this research, as well.

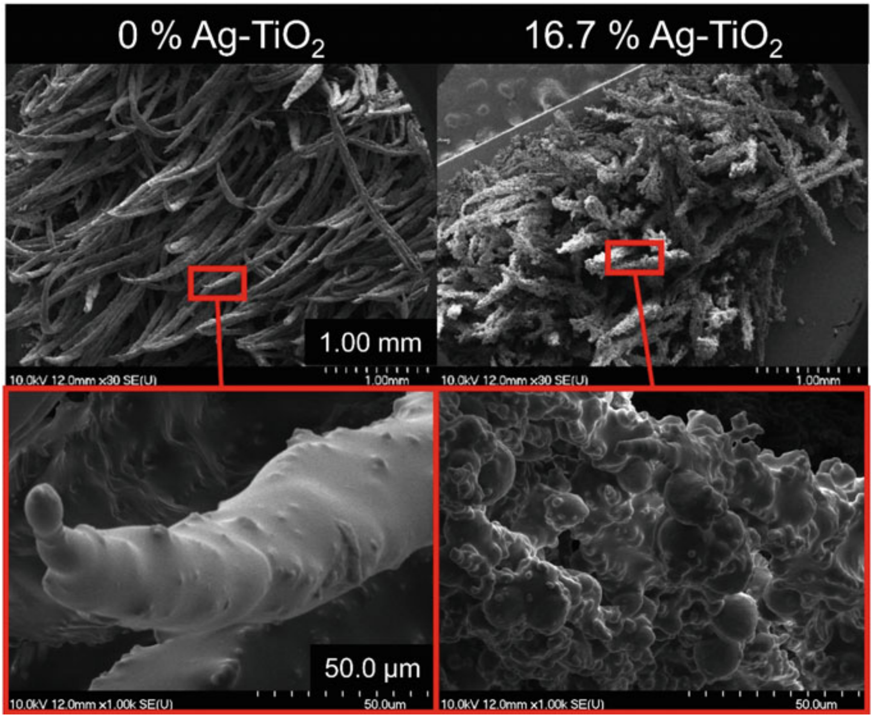

Fig. 8.34 SEM pictures of magnetic grasses cured under 0.35 T magnetic field with 0 and 16.7 wt % nominal Ag–TiO_2 content [96]

To enhance PDMS with thermoresponsive characteristics and visible-light photoreactivity, the polymer was grafted with pNIPAAm chains applying a previously published ARGET-ATRP method (activators regenerated by electron transfer—atom transfer radical polymerization) [85], which required 10-undecenyl 2-bromoisobutyrate as a surface initiator. As a photocatalyst, Ag–TiO$_2$ was introduced to these systems, as well. The initiator itself is integrated into the cross-linked PDMS network during the curing process (Fig. 8.37a), which affects cross-linking density and viscoelastic properties of the final products, as well. In Fig. 8.37b and c, the decreasing G′ and G″ values indicate more viscous characteristics as the initiator concentration is increased. This can be attributed to the significant cross-linking density decrease of the cured PDMS. The initiator content was limited to an 11: 0.5 PDMS-to-initiator mass ratio in the prepared photocatalytic layers to avoid mechanical instability and disintegration.

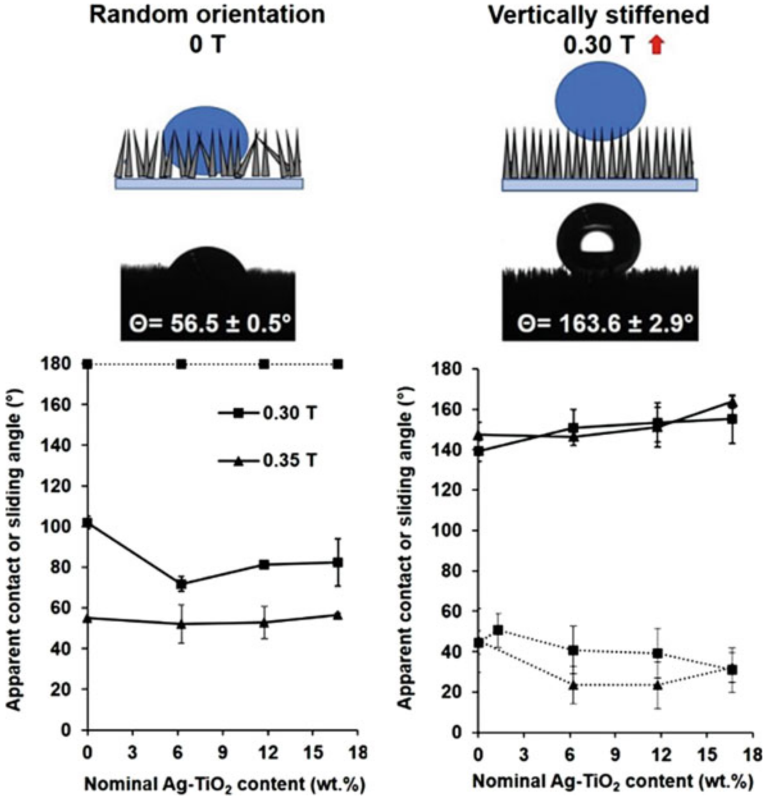

Fig. 8.35 Schematic illustrations of the two wetting states of Ag–TiO$_2$ -enhanced magnetic grass coatings with respective drop images on grass samples with 16.7 wt% Ag–TiO$_2$, prepared in 0.35 T magnetic field (top) and apparent water contact (continuous lines) and sliding angles (dotted lines) on magnetic grasses in the respective wetting states, cured under 0.30 T or 0.35 T magnetic fields as a function of the nominal Ag–TiO$_2$ content [96]

The pNIPAAm chains could be grown on both doctor blade-casted (80 µm thickness) and spray-coated (19 mg/cm^2 specific mass) PDMS films. To reach the optimal wetting and photocatalytic conditions, both the PDMS: initiator ratio (11: 0.13 or 11: 0.5) and the grafting monomer NIPAAm concentration (0–10 M) can be adjusted.

As Fig. 8.38 shows, the water contact angles have a decreasing tendency on these layers with increasing grafting pNIPAAm monomer concentration besides the aimed thermoresponsive wetting also can be observed. In Fig. 8.38 both initial (0 min) and quasi-equilibrial (1 min), contact angles are displayed: at 25 °C, the water droplets spread over the initially hydrophobic surface in 1 min as the surface pNIPAAm chains become hydrated, while over the LCST, (which is determined to be 34 °C via DSC) at 40 °C, the spreading does not occur due to the entropy-controlled precipitation of the polymer chains. The spreading itself is more complete at higher surface monomer concentration, and therefore, surfaces containing longer pNIPAAm chains have more spectacular wetting transitions and broader contact angle ranges to work with (up to 33.4° difference). Introducing Ag–TiO$_2$ photocatalyst nanoparticles to these layers also broaden the contact angle ranges by enhancing roughness and therefore the wetting nature both below and over LCST (up to 54.4° difference).

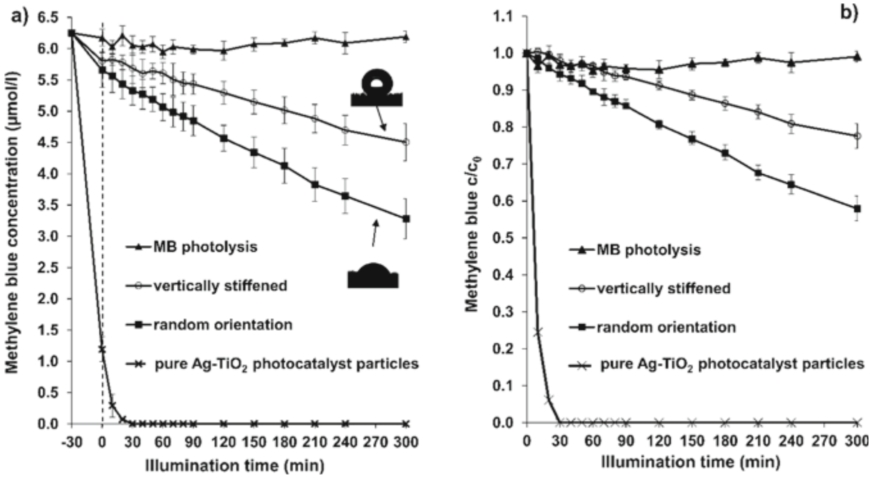

Fig. 8.36 **a** Absolute and **b** relative representation of the photodegradation of 2 mg/l methylene-blue (MB) model dye solution on the surface of 2.6 × 7.6 cm^2 magnetoresponsive thin film (63.3 ± 1.6 mg/cm^2 specific mass, 16.7 wt% Ag–TiO$_2$ content) with different grass orientations under LED-light illumination. The direct photolysis of MB solution and the photocatalytic efficiencies of the pure Ag–TiO$_2$ particles, and the non-magnetic composite samples are also provided as references [96]

The S/L-photocatalytic activity of these coatings also turned out to be stimulus-responsive. Figure 8.39 shows the characteristic photodegradation curves of methylene blue (c_0 = 2 mg/l) at 25 and 50 °C. While there is a 15.5% difference between the effectiveness of direct photolysis and the photodegradation of MB at 25 °C, this gap diminishes at 50 °C, indicating the temperature and wetting-regulated “turnoff” of photocatalytic activity.

While the particular practical field of application of these stimulus-responsive coatings with tunable photodegradation efficiency is yet to be found, they are prospected to take roles similar to photoreactive coatings with

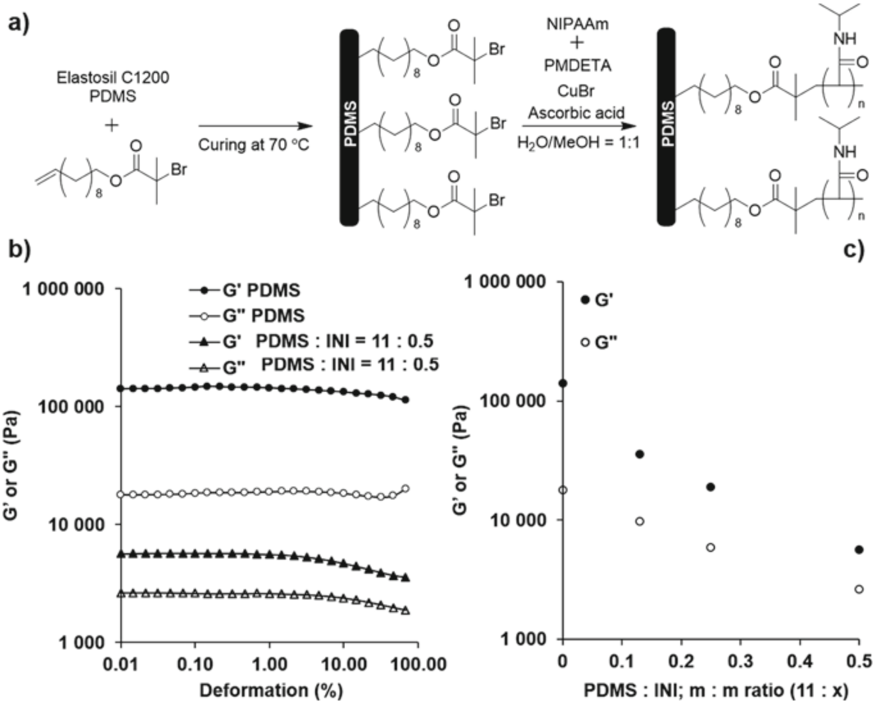

Fig. 8.37 **a** Schematic representation of the synthesis of PDMS-gr-pNIPAAm polymers, **b** characteristic storage (G′) /loss (G″) modulus versus deformation curves of bulk pure PDMS and PDMS: INI = 11: 0.5 (m: m) samples, **c** G′ and G″ values of PDMS-INI copolymers with different INI-content at 1% deformation

composition-dependent wetting. In this case, a single stimulus-responsive surface may be eligible to deal with a wide variety of pollutants with all kinds of polarities. Despite the very promising results in the field of stimulus-responsive photocatalytic coatings, further testing and optimization with other model pollutants are required (and in progress) to prove this idea.

8.9 Conclusion

During the illumination of the most commonly applied heterogeneous photocatalyst particles, reactive oxygen species with high oxidative potential are formed. If a photocatalytic surface exhibits such behavior upon UV-illumination, it is called a

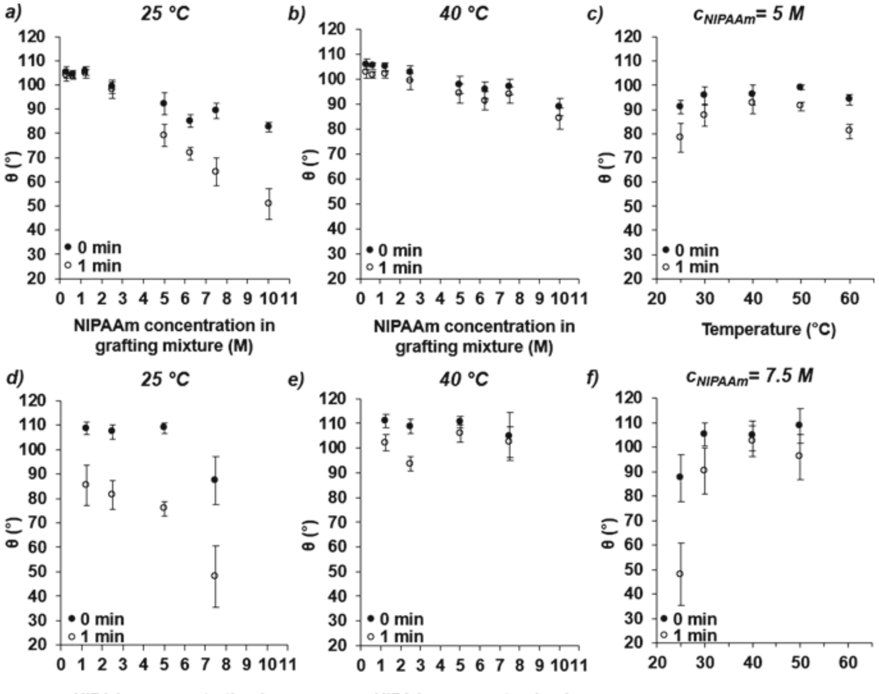

Fig. 8.38 **Top row** c.a. values, measured on doctor blade-casted PDMS-gr-pNIPAAm layers (PDMS: INI = 11: 0.13) as a function of NIPAAm concentration in the grafting mixture at **a** 25 °C, **b** 40 °C and as a **c** function of the temperature, measured on a PDMS-gr-pNIPAAm (PDMS: INI = 11: 0.13; 5 M NIPAAm) layer, **bottom row** c.a. values, measured on doctor blade-casted Ag–TiO_2/PDMS-gr-pNIPAAm layers (PDMS: INI = 11: 0.13) as a function of NIPAAm concentration in the grafting mixture at **d** 25 °C, **e** 40 °C and **f** as a function of the temperature, measured on a Ag–TiO_2/PDMS-gr-pNIPAAm (PDMS: INI = 11: 0.13; 7.5 M NIPAAm) layer

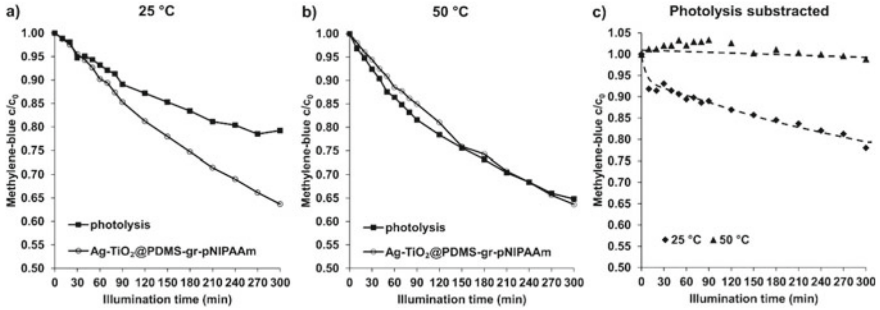

Fig. 8.39 Characteristic photodegradation curves of MB at the S/L interface upon blue LED-light (λ_{max} = 405 nm) illumination at **a** 25, **b** 50 °C, and **c** at both temperatures after the subtraction of photolyzed concentration; relative MB-concentration (c_0 = 2 mg/l) versus illumination time. The corresponding curves for MB photolysis and photodegradation with the help of Ag–TiO$_2$/PDMS-gr-pNIPAAm (PDMS: INI = 11: 0.13; 5 M NIPAAm) are both displayed

first-generation self-cleaning surface. However, the band gap energy can be tuned to the near-UV or visible range by doping conventional semiconductor photocatalysts with different nonmetal elements or plasmonic nanoparticles. These doped photocatalysts are called second-generation photocatalysts, and therefore, their composite surfaces are considered to be the second-generation photocatalytic surfaces. In this chapter, it was presented that these plasmonic photocatalyst particles are highly applicable for photocatalytic uses and the creation of antibacterial and self-cleaning surfaces. During practical applications, it is of crucial importance to provide proper adhesion between the photocatalyst particles and everyday substrate materials. The incorporation of semiconductor photocatalyst particles into a proper polymer-based matrix or binder material is supposed to result in antimicrobial and self-cleaning properties, which would extend the application fields of the raw materials. As it is well known from scientific literature, polymers are often used as photocatalyst binders, owing to their versatility and easily adjustable nature. For instance, the wettability of a polymer surface can easily be adjusted by changing the monomer composition, using hydrophilic and hydrophobic monomers in an adequate ratio. In conclusion, if polymeric materials are utilized for the immobilization of different photocatalysts, one can obtain multifunctional composite surfaces with adjustable characteristics. The wettability of a surface may be manipulated by altering surface charge excess, functionality, roughness, or topology all of these can be subjected to external stimuli. In a widely known approach, the wetting properties of a solid surface become tunable through its functionalization with poly(*N*-isopropyl acrylamide) (pNIPAAm). Based on this, poly(dimethylsiloxane) (PDMS) copolymer-based composite coatings with thermally adjustable wetting and visible-light photoreactivity were prepared. Besides the wetting characteristics, the photoreactivity of these composite surfaces was also proven to be temperature-dependent during visible-light photodegradation tests at S/L interface. Finally, it was also presented that these stimulus-responsive wetting and photocatalytic characteristics are also possible by the use of magnetorheological elastomers.

Acknowledgements The authors are thankful for the financial support through project GINOP-2.3.2-15-2016-00013. This chapter was also supported by the UNKP-20-5, UNKP-20-4, and UNKP-20-4-II New National Excellence Program of the Ministry for Innovation and Technology from the source of the National Research, Development and Innovation Fund and by the János Bolyai Research Scholarship of the Hungarian Academy of Sciences. L.J. acknowledges support from the Moroccan-Hungarian Joint Research project no. 2018-2.1.10-TÉT-MC-2018-00005.

References

1. Rajeshwar K, Thomas A, Janáky C (2015) Photocatalytic activity of inorganic semiconductor surfaces: myths, hype, and reality. J Phys Chem Lett 6:139–147. https://doi.org/10.1021/jz502586p
2. Chen X, Mao SS (2007) Titanium dioxide nanomaterials: synthesis, properties, modifications, and applications. Chem Rev 107:2891–2959. https://doi.org/10.1021/cr0500535
3. Rajeshwar K, de Tacconi NR (2009) Solution combustion synthesis of oxide semiconductors for solar energy conversion and environmental remediation. Chem Soc Rev 38:1984. https://doi.org/10.1039/b811238j
4. Thomas A, Janáky C, Samu GF et al (2015) Time- and energy-efficient solution combustion synthesis of binary metal tungstate nanoparticles with enhanced photocatalytic activity. Chemsuschem 8:1652–1663. https://doi.org/10.1002/cssc.201500383
5. Xu C, De S, Balu AM et al (2015) Mechanochemical synthesis of advanced nanomaterials for catalytic applications. Chem Commun 51:6698–6713. https://doi.org/10.1039/C4CC09876E
6. Dodd A, McKinley A, Saunders M, Tsuzuki T (2006) Mechanochemical synthesis of nanocrystalline SnO_2–ZnO photocatalysts. Nanotechnology 17:692–698. https://doi.org/10.1088/0957-4484/17/3/013
7. Díez-Pascual AM, Xu C, Luque R (2014) Development and characterization of novel poly (ether ether ketone)/ZnO bionanocomposites. J Mater Chem B 2:3065. https://doi.org/10.1039/c3tb21800g
8. Lakshmi BB, Dorhout PK, Martin CR (1997) Sol−gel template synthesis of semiconductor nanostructures. Chem Mater 9:857–862. https://doi.org/10.1021/cm9605577
9. Brezesinski T, Wang J, Polleux J et al (2009) Templated nanocrystal-based porous TiO_2 films for next-generation electrochemical capacitors. J Am Chem Soc 131:1802–1809. https://doi.org/10.1021/ja8057309
10. Weng C-C, Hsu K-F, Wei K-H (2004) Synthesis of arrayed, TiO_2 needlelike nanostructures via a polystyrene-block-poly(4-vinylpyridine) diblock copolymer template. Chem Mater 16:4080–4086. https://doi.org/10.1021/cm049367j
11. Kimling MC, Caruso RA (2012) Sol–gel synthesis of hierarchically porous TiO_2 beads using calcium alginate beads as sacrificial templates. J Mater Chem 22:4073. https://doi.org/10.1039/c2jm15720a
12. Liu Y, Goebl J, Yin Y (2013) Templated synthesis of nanostructured materials. Chem Soc Rev 42:2610–2653. https://doi.org/10.1039/C2CS35369E
13. Samu GF, Veres Á, SzP T, Janovák L, Dékány I, Yepez A, Luque R, Cs J (2016) Photocatalytic, photoelectrochemical, and antibacterial activity of benign-by-design mechanochemically synthesized metal oxide nanomaterials. Catal Today 284:3–10. https://doi.org/10.1016/j.cattod.2016.07.010

14. Ohtani B, Prieto-Mahaney OO, Li D, Abe R (2010) What is degussa (evonik) P25 crystalline composition analysis, reconstruction from isolated pure particles and photocatalytic activity test. J Photochem Photobiol A Chem 216:179–182. https://doi.org/10.1016/j.jphotochem.2010.07.024
15. Veres Á, Ménesi J, Janáky C et al (2015) New insights into the relationship between structure and photocatalytic properties of TiO_2 catalysts. RSC Adv 5:2421–2428. https://doi.org/10.1039/C4RA11489B
16. Sauer ML, Ollis DF (1996) Photocatalyzed oxidation of ethanol and acetaldehyde in humidified air. J Catal 158:570–582. https://doi.org/10.1006/jcat.1996.0055
17. Tallósy SP, Janovák L, Ménesi J et al (2014) LED-light activated antibacterial surfaces using silver-modified TiO_2 embedded in polymer matrix. J Adv Oxid Technol 17. https://doi.org/10.1515/jaots-2014-0101
18. Tallósy SP, Janovák L, Ménesi J et al (2014) Investigation of the antibacterial effects of silver-modified TiO_2 and ZnO plasmonic photocatalysts embedded in polymer thin films. Environ Sci Pollut Res 21:11155–11167. https://doi.org/10.1007/s11356-014-2568-6
19. Deák Á, Janovák L, Csapó E et al (2016) Layered double oxide (LDO) particle containing photoreactive hybrid layers with tunable superhydrophobic and photocatalytic properties. Appl Surf Sci 389:294–302. https://doi.org/10.1016/j.apsusc.2016.07.127
20. Deák Á, Janovák L, Tallósy SP et al (2015) Spherical LDH–Ag°-montmorillonite heterocoagulated system with a pH-dependent sol-gel structure for controlled accessibility of AgNPs immobilized on the clay lamellae. Langmuir 31:2019–2027. https://doi.org/10.1021/la504096t
21. Miwa M, Nakajima A, Fujishima A et al (2000) Effects of the surface roughness on sliding angles of water droplets on superhydrophobic surfaces. Langmuir 16:5754–5760. https://doi.org/10.1021/la991660o
22. Fu G, Vary PS, Lin C-T (2005) Anatase TiO_2 nanocomposites for antimicrobial coatings. J Phys Chem B 109:8889–8898. https://doi.org/10.1021/jp0502196
23. Peng C-C, Yang M-H, Chiu W-T et al (2008) Composite nano-titanium oxide-chitosan artificial skin exhibits strong wound-healing effect-an approach with anti-inflammatory and bactericidal kinetics. Macromol Biosci 8:316–327. https://doi.org/10.1002/mabi.200700188
24. Ye L, Pelton R, Brook MA et al (2013) Targeted disinfection of e. coli via bioconjugation to photoreactive TiO_2. Bioconjug Chem 24:448–455. https://doi.org/10.1021/bc300581t
25. Chen W-J, Chen Y-C (2010) Fe_3O_4 /TiO_2 core/shell magnetic nanoparticle-based photokilling of pathogenic bacteria. Nanomedicine 5:1585–1593. https://doi.org/10.2217/nnm.10.92
26. Brugnera MF, Miyata M, Zocolo GJ et al (2013) A photoelectrocatalytic process that disinfects water contaminated with *Mycobacterium kansasii* and *Mycobacterium avium*. Water Res 47:6596–6605. https://doi.org/10.1016/j.watres.2013.08.027
27. Rodríguez-Gattorno G, Santiago-Jacinto P, Rendon-Vázquez L et al (2003) Novel synthesis pathway of ZnO nanoparticles from the spontaneous hydrolysis of zinc carboxylate salts. J Phys Chem B 107:12597–12604. https://doi.org/10.1021/jp035788x
28. Dékány I, Turi L, Szücs A, Király Z (1998) Preparation of semiconductor and transition metal nanoparticles on colloidal solid supports. Colloids Surfaces A Physicochem Eng Asp 141:405–417. https://doi.org/10.1016/S0927-7757(97)00178-7
29. Gupta K, Singh RP, Pandey A, Pandey A (2013) Photocatalytic antibacterial performance of TiO_2 and Ag-doped TiO_2 against *S. aureus*. *P. aeruginosa* and *E. coli*. Beilstein J Nanotechnol 4:345–351. https://doi.org/10.3762/bjnano.4.40
30. Colon G, Ward BC, Webster TJ (2006) Increased osteoblast and decreasedStaphylococcus epidermidis functions on nanophase ZnO and TiO_2. J Biomed Mater Res Part A 78A:595–604. https://doi.org/10.1002/jbm.a.30789
31. Nataraj N, Anjusree GS, Madhavan AA et al (2014) Synthesis and anti-staphylococcal activity of TiO_2 nanoparticles and nanowires in ex vivo porcine skin model. J Biomed Nanotechnol 10:864–870. https://doi.org/10.1166/jbn.2014.1756

32. Klevens RM, Edwards JR, Richards CL et al (2007) Estimating health care-associated infections and deaths in U.S. hospitals, 2002. Public Health Rep 122:160–166. https://doi.org/10.1177/003335490712200205
33. Tsvetanova Z (2006) Study of biofilm formation on different pipe materials in a model of drinking water distribution system and its impact on microbiological water quality. In: Chemicals as intentional and accidental global environmental threats. Springer Netherlands, Dordrecht, pp 463–468
34. Hori K, Matsumoto S (2010) Bacterial adhesion: from mechanism to control. Biochem Eng J 48:424–434. https://doi.org/10.1016/j.bej.2009.11.014
35. Zupan J, Mavri J, Raspor P (2009) Quantitative cell wall protein profiling of invasive and non-invasive *Saccharomyces cerevisiae* strains. J Microbiol Methods 79:260–265. https://doi.org/10.1016/j.mimet.2009.09.003
36. Bayoudh S, Othmane A, Ponsonnet L, Ben Ouada H (2008) Electrical detection and characterization of bacterial adhesion using electrochemical impedance spectroscopy-based flow chamber. Colloids Surfaces A Physicochem Eng Asp 318:291–300. https://doi.org/10.1016/j.colsurfa.2008.01.005
37. Böhmler J, Ponche A, Anselme K, Ploux L (2013) Self-assembled molecular platforms for bacteria/material biointerface studies: importance to control functional group accessibility. ACS Appl Mater Interfaces 5:10478–10488. https://doi.org/10.1021/am401976g
38. Tallósy SP, Janovák L, Nagy E et al (2016) Adhesion and inactivation of gram-negative and gram-positive bacteria on photoreactive TiO_2/polymer and Ag–TiO_2/polymer nanohybrid films. Appl Surf Sci 371:139–150. https://doi.org/10.1016/j.apsusc.2016.02.202
39. Neuhaus FC, Baddiley J (2003) A continuum of anionic charge: structures and functions of *d*-alanyl-teichoic acids in gram-positive bacteria. Microbiol Mol Biol Rev 67:686–723. https://doi.org/10.1128/MMBR.67.4.686-723.2003
40. Weiss J, Victor M, Elsbach P (1983) Role of charge and hydrophobic interactions in the action of bactericidal/permeability-increasing protein of neutrophils on gram-negative bacteria. J Clin Invest 71:540–549. https://doi.org/10.1172/JCI110798
41. Fujishima A, Honda K (1972) Electrochemical photolysis of water at a semiconductor electrode. Nature 238:37–38. https://doi.org/10.1038/238037a0
42. Martra G, Coluccia S, Marchese L et al (1999) The role of H_2O in the photocatalytic oxidation of toluene in vapour phase on anatase TiO_2 catalyst. Catal Today 53:695–702. https://doi.org/10.1016/S0920-5861(99)00156-X
43. Alberto G, Meloni S, Chinappi M et al (2012) Cassie-Baxter and Wenzel states on a nanostructured surface: phase diagram, metastabilities, and transition mechanism by atomistic free energy calculations. Langmuir 28:10764–10772. https://doi.org/10.1021/la3018453
44. Mérai L, Varga N, Deák Á et al (2019) Preparation of photocatalytic thin films with composition dependent wetting properties and self-healing ability. Catal Today 328:85–90. https://doi.org/10.1016/j.cattod.2018.10.015
45. Merai L, Deak A, Sebok D et al (2018) Photoreactive composite coating with composition dependent wetting properties. Express Polym Lett 12:1061–1071. https://doi.org/10.3144/expresspolymlett.2018.93
46. Drelich J (2013) Guidelines to measurements of reproducible contact angles using a sessile-drop technique. Surf Innov 1:248–254. https://doi.org/10.1680/si.13.00010
47. Chibowski E (2003) Surface free energy of a solid from contact angle hysteresis. Adv Colloid Interface Sci 103:149–172. https://doi.org/10.1016/S0001-8686(02)00093-3
48. Wahl A, Augustynski J (1998) Charge carrier transport in nanostructured anatase TiO_2 films assisted by the self-doping of nanoparticles. J Phys Chem B 102:7820–7828. https://doi.org/10.1021/jp9814000
49. Fuentes-Lara L, Medrano-Macías J, Pérez-Labrada F et al (2019) From elemental sulfur to hydrogen sulfide in agricultural soils and plants. Molecules 24:2282. https://doi.org/10.3390/molecules24122282

50. Ellis MA, Ferree DC, Funt RC, Madden LV (1998) Effects of an apple scab-resistant cultivar on use patterns of inorganic and organic fungicides and economics of disease control. Plant Dis 82:428–433. https://doi.org/10.1094/PDIS.1998.82.4.428
51. Roy Choudhury S, Roy S, Goswami A, Basu S (2012) Polyethylene glycol-stabilized sulphur nanoparticles: an effective antimicrobial agent against multidrug-resistant bacteria. J Antimicrob Chemother 67:1134–1137. https://doi.org/10.1093/jac/dkr591
52. Dugarte M, Martinez-Arguelles G, Torres J (2018) Experimental evaluation of modified sulfur concrete for achieving sustainability in industry applications. Sustainability 11:70. https://doi.org/10.3390/su11010070
53. Mérai L, Rajkumar T, Janovák L et al (2020) Sulfur nanoparticles transform montmorillonite into an inorganic surfactant applicable in thermoplastics processing. Polym Test 85:106419. https://doi.org/10.1016/j.polymertesting.2020.106419
54. Weimarn PPv (1926) Über Schwefellösungen von allen Farben des Spektrums. Kolloidchem Beihefte 22:38–62. https://doi.org/10.1007/BF02556771
55. Gilbert B (1965) GMELINS HANDBUCH DER ANORGANISCHEN CHEMIE. SCHWEFEL, 8. Auflage, System-Nummer 9, Teil B -Lieferung 3, 1963, Verlag Chemie, GMBH, Weinheim/Bergstrasse, West Germany. Isr J Chem 3:121–121. https://doi.org/10.1002/ijch.196500033
56. Gutbier A (1926) Thermische Kolloidsynthesen. Zeitschrift für Anorg und Allg Chemie 152:163–179. https://doi.org/10.1002/zaac.19261520118
57. Lantos E, Mérai L, Deák Á et al (2020) Preparation of sulfur hydrophobized plasmonic photocatalyst towards durable superhydrophobic coating material. J Mater Sci Technol 41:159–167. https://doi.org/10.1016/j.jmst.2019.04.046
58. Steudel R (2003) Aqueous sulfur sols. Top Curr Chem 230:153–166. https://doi.org/10.1007/b12113
59. Zeng M (2013) Influence of TiO_2 surface properties on water pollution treatment and photocatalytic activity. Bull Korean Chem Soc 34:953–956. https://doi.org/10.5012/bkcs.2013.34.3.953
60. Wang S, Urban MW (2020) Self-healing polymers. Nat Rev Mater 5:562–583. https://doi.org/10.1038/s41578-020-0202-4
61. Bekas DG, Tsirka K, Baltzis D, Paipetis AS (2016) Self-healing materials: a review of advances in materials, evaluation, characterization and monitoring techniques. Compos Part B Eng 87:92–119. https://doi.org/10.1016/j.compositesb.2015.09.057
62. Postiglione G, Turri S, Levi M (2015) Effect of the plasticizer on the self-healing properties of a polymer coating based on the thermoreversible Diels-Alder reaction. Prog Org Coatings 78:526–531. https://doi.org/10.1016/j.porgcoat.2014.05.022
63. Zhang H, Yang J (2014) Development of self-healing polymers via amine–epoxy chemistry: I. Properties of healing agent carriers and the modelling of a two-part self-healing system. Smart Mater Struct 23:065003. https://doi.org/10.1088/0964-1726/23/6/065003
64. Hamilton AR, Sottos NR, White SR (2010) Self-healing of internal damage in synthetic vascular materials. Adv Mater 22:5159–5163. https://doi.org/10.1002/adma.201002561
65. Huang Z, Gurney RS, Wang T, Liu D (2018) Environmentally durable superhydrophobic surfaces with robust photocatalytic self-cleaning and self-healing properties prepared via versatile film deposition methods. J Colloid Interface Sci 527:107–116. https://doi.org/10.1016/j.jcis.2018.05.004
66. Zhu H, Wu L, Meng X et al (2020) An anti-UV superhydrophobic material with photocatalysis, self-cleaning, self-healing and oil/water separation functions. Nanoscale 12:11455–11459. https://doi.org/10.1039/D0NR01038C
67. Tu K, Wang X, Kong L, Guan H (2018) Facile preparation of mechanically durable, self-healing and multifunctional superhydrophobic surfaces on solid wood. Mater Des 140:30–36. https://doi.org/10.1016/j.matdes.2017.11.029
68. Wang L, Urata C, Sato T et al (2017) Self-healing superhydrophobic materials showing quick damage recovery and long-term durability. Langmuir 33:9972–9978. https://doi.org/10.1021/acs.langmuir.7b02343

69. Almeida AR, Carneiro JT, Moulijn JA, Mul G (2010) Improved performance of TiO_2 in the selective photo-catalytic oxidation of cyclohexane by increasing the rate of desorption through surface silylation. J Catal 273:116–124. https://doi.org/10.1016/j.jcat.2010.05.006
70. Yang C, Yang C (2014) Preparation of TiO2 particles and surface silanization modification for electronic ink. J Mater Sci Mater Electron 25:3285–3289. https://doi.org/10.1007/s10854-014-2015-y
71. Kleinschmidt AT, Root SE, Lipomi DJ (2017) Poly(3-hexylthiophene) (P3HT): fruit fly or outlier in organic solar cell research? J Mater Chem A 5:11396–11400. https://doi.org/10.1039/C6TA08317J
72. Meitzner R, Faber T, Alam S et al (2019) Impact of P3HT materials properties and layer architecture on OPV device stability. Sol Energy Mater Sol Cells 202:110151. https://doi.org/10.1016/j.solmat.2019.110151
73. Janovák L, Dernovics Á, Mérai L et al (2018) Microstructuration of poly(3-hexylthiophene) leads to bifunctional superhydrophobic and photoreactive surfaces. Chem Commun 54:650–653. https://doi.org/10.1039/C7CC07671A
74. Qing Y, Long C, An K et al (2019) Sandpaper as template for a robust superhydrophobic surface with self-cleaning and anti-snow/icing performances. J Colloid Interface Sci 548:224–232. https://doi.org/10.1016/j.jcis.2019.04.040
75. Kim J-H, Mirzaei A, Kim HW, Kim SS (2018) Facile fabrication of superhydrophobic surfaces from austenitic stainless steel (AISI 304) by chemical etching. Appl Surf Sci 439:598–604. https://doi.org/10.1016/j.apsusc.2017.12.211
76. Ko T-J, Park SJ, Kim M-S et al (2020) Single-step plasma-induced hierarchical structures for tunable water adhesion. Sci Rep 10:874. https://doi.org/10.1038/s41598-019-56787-z
77. Ta VD, Dunn A, Wasley TJ et al (2016) Laser textured superhydrophobic surfaces and their applications for homogeneous spot deposition. Appl Surf Sci 365:153–159. https://doi.org/10.1016/j.apsusc.2016.01.019
78. Abdo GG, Zagho MM, Khalil A (2020) Recent advances in stimuli-responsive drug release and targeting concepts using mesoporous silica nanoparticles. Emergent Mater 3:407–425. https://doi.org/10.1007/s42247-020-00109-x
79. Jiang H, Ochoa M, Waimin JF et al (2019) A pH-regulated drug delivery dermal patch for targeting infected regions in chronic wounds. Lab Chip 19:2265–2274. https://doi.org/10.1039/C9LC00206E
80. Zahn D, Weidner A, Saatchi K et al (2019) Biodegradable magnetic microspheres for drug targeting, temperature controlled drug release, and hyperthermia. Curr Dir Biomed Eng 5:161–164. https://doi.org/10.1515/cdbme-2019-0041
81. Seo J, Song M, Jeong J et al (2016) Broadband pH-sensing organic transistors with polymeric sensing layers featuring liquid crystal microdomains encapsulated by di-block copolymer chains. ACS Appl Mater Interfaces 8:23862–23867. https://doi.org/10.1021/acsami.6b08257
82. Saitoh T, Suzuki Y, Hiraide M (2002) Preparation of poly(*N*-isopropylacrylamide)-modified glass surface for flow control in microfluidics. Anal Sci 18:203–205. https://doi.org/10.2116/analsci.18.203
83. Bakarich SE, Gorkin R, Panhuis MIH, Spinks GM (2015) 4D printing with mechanically robust, thermally actuating hydrogels. Macromol Rapid Commun 36:1211–1217. https://doi.org/10.1002/marc.201500079
84. Zhang S, Wang J, Zhang X et al (2019) Tunable multi-stage wettability and adhesion force on polymer brushes triggered by temperature and pH. Sci China Mater 62:597–603. https://doi.org/10.1007/s40843-018-9357-9
85. Shivapooja P, Ista LK, Canavan HE, Lopez GP (2012) ARGET–ATRP synthesis and characterization of pnipaam brushes for quantitative cell detachment studies. Biointerphases 7:32. https://doi.org/10.1007/s13758-012-0032-z
86. Xiong X, Wu Z, Pan J et al (2015) A facile approach to modify poly(dimethylsiloxane) surfaces via visible light-induced grafting polymerization. J Mater Chem B 3:629–634. https://doi.org/10.1039/C4TB01600A

87. Kim YS, Kim MA, Lee C-M (2019) Controlled drug release from PNIPAM-incorporated melanin nanovesicles by photo-stimulation. Mater Technol 34:639–644. https://doi.org/10.1080/10667857.2019.1611055
88. Choe A, Yeom J, Shanker R et al (2018) Stretchable and wearable colorimetric patches based on thermoresponsive plasmonic microgels embedded in a hydrogel film. NPG Asia Mater 10:912–922. https://doi.org/10.1038/s41427-018-0086-6
89. Yu W, Lou L-L, Li S et al (2017) Highly efficient and durable platinum nanocatalysts stabilized by thiol-terminated poly(*N*-isopropyl acrylomide) for selective hydrogenation of halonitrobenzene to haloaniline. RSC Adv 7:751–757. https://doi.org/10.1039/C6RA24773C
90. Zhang L, Zhang S, He B et al (2008) TiO_2 nanoparticles functionalized by a temperature-sensitive poly(*N*-isopropylacrylamide) (PNIPAM): synthesis and characterization. Zeitschrift für Naturforsch B 63:973–976. https://doi.org/10.1515/znb-2008-0809
91. Jia H, Roa R, Angioletti-Uberti S et al (2016) Thermosensitive Cu_2O-PNIPAM core–shell nanoreactors with tunable photocatalytic activity. J Mater Chem A 4:9677–9684. https://doi.org/10.1039/C6TA03528K
92. Lee S, Yim C, Kim W, Jeon S (2015) Magnetorheological elastomer films with tunable wetting and adhesion properties. ACS Appl Mater Interfaces 7:19853–19856. https://doi.org/10.1021/acsami.5b06273
93. Sorokin VV, Sokolov BO, Stepanov GV, Kramarenko EY (2018) Controllable hydrophobicity of magnetoactive elastomer coatings. J Magn Magn Mater 459:268–271. https://doi.org/10.1016/j.jmmm.2017.10.074
94. Huang Y, Stogin BB, Sun N et al (2017) A switchable cross-species liquid repellent surface. Adv Mater 29:1604641. https://doi.org/10.1002/adma.201604641
95. Yang C, Wu L, Li G (2018) Magnetically responsive superhydrophobic surface. In situ reversible switching of water droplet wettability and adhesion for droplet manipulation. ACS Appl Mater Interfaces 10:20150–20158. https://doi.org/10.1021/acsami.8b04190
96. Mérai L, Deák Á, Sebők D et al (2020) A stimulus-responsive polymer composite surface with magnetic field-governed wetting and photocatalytic properties. Polymers (Basel) 12:1890. https://doi.org/10.3390/polym12091890

Part III
Photocatalytic Activity Enhancement

Chapter 9

Rare Earth Doped Luminescent Materials as Photocatalysts for Enhanced Photocatalytic Reactions

Boglárka Hampel, Klara Hernadi, and Zsolt Pap

Abstract The present book chapter focuses on rare earth doped photocatalysis. For this matter, it is essential to cover photocatalysis driven by ultraviolet (UV) and visible light as well. The luminescence and the upconversion phenomena will be discussed in case of several materials as a possibility to utilize low energy photons. Rare earth metals and their fluorides happen to be one of the most suitable upconverting materials because of their energy level setup. These materials can be used for photocatalytic purposes, as they can convert near-infrared (NIR) light to UV/visible light. In order to benefit the NIR light, it is necessary to form composites with these materials and UV or visible-light active photocatalysts, so the upconverted light could be used by them.

Keywords Luminescence · Upconversion · Photocatalysis · Near-infrared light · Rare earth ions

---

B. Hampel · K. Hernadi · Z. Pap (✉)
Department of Applied and Environmental Chemistry, University of Szeged,
Rerrich Béla sqr. 1, Szeged 6720, Hungary
e-mail: pzsolt@chem.u-szeged.hu

B. Hampel · Z. Pap
Nanostructured Materials and Bio-Nano-Interfaces Center, Institute for Interdisciplinary
Research on Bio-Nano-Sciences, Babeş–Bolyai University, Treboniu Laurian str. 42,
400271 Cluj-Napoca, Romania

K. Hernadi
Institute of Physical Metallurgy, Metal Forming and Nanotechnology, University of Miskolc,
HU-3515 Miskolc-Egyetemváros, C/1 108, Miskolc, Hungary

S. Garg and A. Chandra (eds.), *Green Photocatalytic Semiconductors*,
Green Chemistry and Sustainable Technology,
https://doi.org/10.1007/978-3-030-77371-7_9

9.1 Photocatalysis in all Wavelength Ranges. Overview of the UV-, Visible- and NIR-Light-Active Photocatalysts

If one types the word ‘photocatalysis’ in Google©, there are almost 4 million results, so it can be safely said that this is an increasingly researched area, especially in the past 15 years, which is illustrated in Fig. 9.1 as well.

It started back in 1972, when a research team used TiO_2 for hydrogen production purpose, using UV light [1]. After this, plenty of studies appeared in this field. After almost 50 years, TiO_2 is still the most studied photocatalyst, because it is rather cheap, not toxic for the environment, stable, and the photogenerated holes are extremely oxidizing [2]. The major drawback of titanium-dioxide is that it can be excited only by UV light. Therefore, attempts were made in order to extend the spectrum of light in which TiO_2 can be used [3]. This includes forming composites with noble metals, such as Ag [4–6], Au [7–9], Pd [10–12], Pt [13–15], or even non-metallic elements: S [16, 17], N [18, 19] or by coupling it to semiconductors of

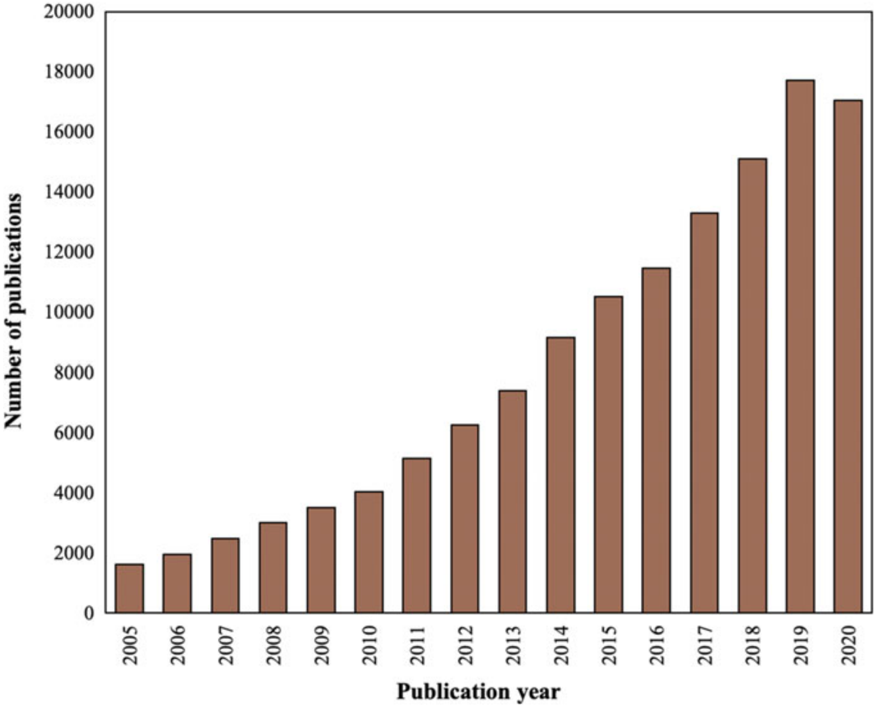

Fig. 9.1 Comparing the number of publications in the past 15 years: it is clear that more and more published papers appear every year studying photocatalysis (information acquired using the Web of Science Core Collection, December 2020, search parameters: *TOPIC: (Photocata*) Timespan: 2005–2020.*)

narrower bandgap [20]. According to studies, metal ion (Fe^{2+}, Cu^{2+}) implantation and dye sensitization have proved to be the most effective methods for expanding titania-based photocatalysts in visible light [21].

It is worth mentioning that there is photocatalysis in UV light beyond titania. ZnO was successfully used in photocatalysis as a substitute for titanium-dioxide [22–24]. Another prosperous candidate is ZrO_2 [24–26]. Reduced graphene oxide (rGO) with its zero bandgap and fast internal electron transport is a newly trending co-photocatalyst [27]. It has been used along with $NaTaO_3$ [28], ZnO [29, 30], V_2O_5 [31].

As the UV light is only ~5% of the sunlight, it was reasonable to broaden the set of photocatalysts in order to achieve more, which are active in higher wavelengths as well. One of the most popular visible-light-driven photocatalyst is CdS [32]; however, the photogenerated electron–hole pairs have high recombination rate [27]. Therefore, composites were formed with Ni nanosheets [33], MoS_2 [34], ZnO [35], graphene [36], etc. There is a series of oxides, which proved to be suitable for visible-light photocatalysis, such as WO_3 [37], CuO [38], Ag_2O [39], Bi_2WO_6 [40], or $BiVO_4$ [41]. Before moving on to the next thought, it is essential mentioning the carbon-based materials: carbon quantum dots [42], carbon nanodots [43], graphitic carbon nitride [44], carbon nanotubes [45], graphene [46], and carbon nanospheres as template [47–51].

The third light range for photocatalysis is the near-infrared (NIR) light. This area is not as well studied, as the previous two, it still has some challenges for the researchers [3]. It has to be highlighted that most photocatalysts do not have activity in NIR light, although the structure of composites allows to absorb the NIR light, convert it to shorter wavelengths, and use that for photocatalysis [52]. For this upconversion process, lanthanides and lanthanide fluorides are the most fitting, because the setup of their energy level [53] $NaYF_4$ being the most commonly used one [54]. The carbon quantum dots while gaining more popularity do have upconversion properties also [55].

In Fig. 9.2, a comparison of the published papers concerning photocatalysis in visible and near-infrared light in the past 10 years can be seen. The reason why the UV photocatalysis is not presented in the chart is that there are far more publications on this topic. If all three sections would be presented on one diagram, then it would be harder to interpret, since the numbers for UV overshadows the others. In Fig. 9.2, the number of the published articles from 2010 to 2020 about near-infrared photocatalysis is presented in the inner circle, while the external are the ones about visible light. It can be seen that the visible-light-driven photocatalysis is still much more researched then the NIR. This gave the motivation to study photocatalysis under NIR light and upconversion luminescence materials.

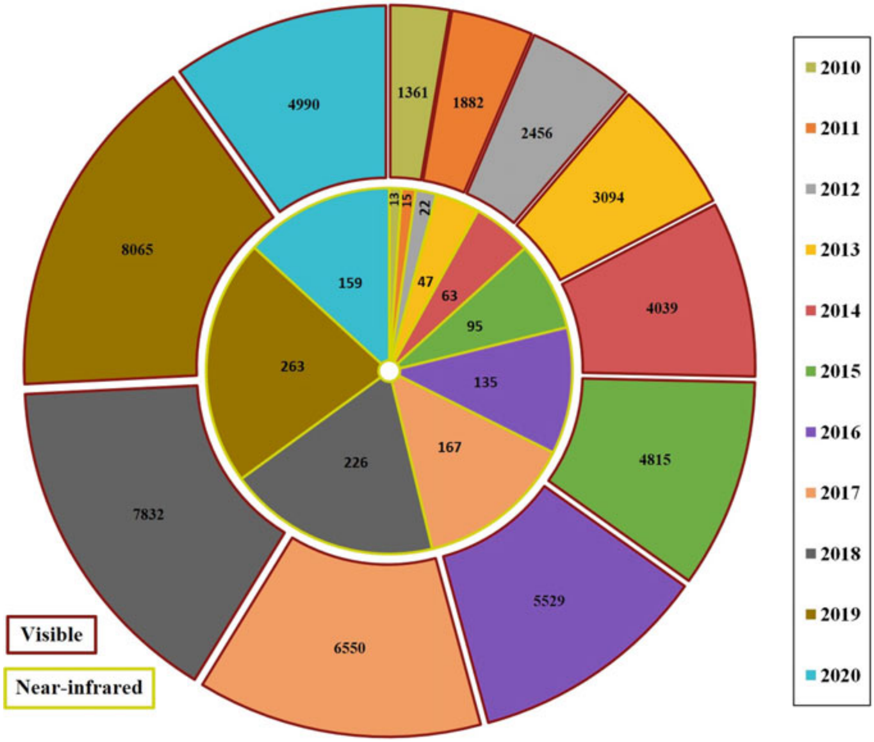

Fig. 9.2 Comparing the published papers concerning photocatalysis in *visible* and *near-infrared* light in the past 10 years (information acquired using the Web of Science Core Collection, July 29, 2020, search parameters: *TOPIC: (photocatal*) AND TOPIC: (visible) Timespan: 2010–2020. Indexes: SCI-EXPANDED, SSCI, A&HCI, CPCI-S, CPCI-SSH, BKCI-S, BKCI-SSH, ESCI, CCR-EXPANDED, IC*. and *TOPIC: (Photocatal*) AND TOPIC: (Near-infrared) Timespan: 2010–2020. Indexes: SCI-EXPANDED, SSCI, A&HCI, CPCI-S, CPCI-SSH, BKCI-S, BKCI-SSH, ESCI, CCR-EXPANDED, IC.*)

9.2 General Summary of Luminescence Materials

Luminescence occurs when an atom or molecule emits radiation, after absorbing photons, radiation, chemical, or biochemical reactions [56]. This phenomenon is provoked by the movement of the electrons within the material from higher energy levels to lower ones, resulting the emission of light without giving off heat. The two main types of luminescence are: fluorescence and phosphorescence. The difference between these two is the delay between the absorption and emission of light. In case of fluorescence, the endurance of the light emission is relatively short, 10^{-6}–10^{-8} s, while for phosphorescence is 10^{-6} s and longer (sometimes even minutes, hours) [57]. Stokes law states that emitted light is always of longer wavelength than the absorbed one [58]. The photoluminescent materials generally follow this. In some cases, the emitted photon has higher energy than the absorbed one, this happens to be the anti-Stokes shift, which appears in three ways: simultaneous two-photon absorption (STPA), second-harmonic generation (SHG), and upconversion [59]. Among these, the upconversion will be discussed in detail.

9.2.1 Energy Transfer Mechanism of the Upconversion Materials

Typically, upconversion is a nonlinear optical process, when two or more photons are absorbed in a row, which results in real intermediate energy states and luminescence is emitted with a wavelength shorter than the absorbed light, and therefore, it can be considered as an anti-Stokes mechanism [54]. There are five main upconversion mechanisms, which are presented in Fig. 9.3: excited-state absorption (ESA), energy transfer upconversion (ETU), cooperative sensitization upconversion (CSU), cross-relaxation (CR), and photon avalanche (PA).

Excited-state absorption (*ESA*): the sequential absorption of pump photons by a single ground-state ion. In Fig. 9.3, a three-level system is presented, where the ion is excited from ground state (G) to E1 level. During this, another pump photon has the possibility to promote the ion from E1 level to the higher-lying E2 level. This results the upconversion, before it sets back to the ground state [60]. Therefore, the upconversion will take place from the E2 level. Highly adequate ESA occurs when the lanthanide ion has a ladder-like arrangement of the energy states. Only a few lanthanide ions like Er^{3+}, Ho^{3+}, Tm^{3+}, and Nd^{3+} have such energy level structures [61].

Energy transfer upconversion (*ETU*): is very similar to ESA, as they both operate with sequential absorption of two photons. The difference between them is that ETU process requires two neighboring ions: Ion1 as a sensitizer, while Ion2 as an activator (Fig. 9.3). As it is illustrated in Fig. 9.3, the sensitizer ion absorbs the pump photons, which excites it from the ground state to the metastable E1 energy level. Ion1 successively transfers this harvested energy to the ground state and to the excited state E1 level of Ion2, exciting Ion2 to its upper emitting state E2, while

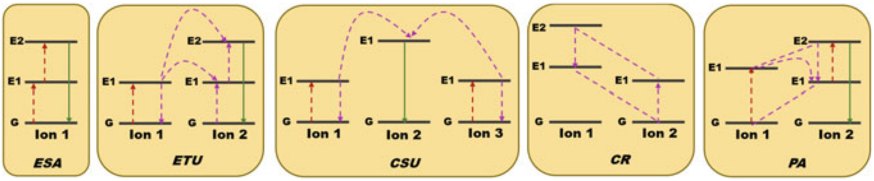

Fig. 9.3 Possible mechanisms of the upconversion processes, from left to right: excited-state absorption (**ESA**), energy transfer upconversion (**ETU**), cooperative sensitization upconversion (**CSU**), cross-relaxation (**CR**), and photon avalanche (**PA**). The red, violet, and green lines represent photon excitation, energy transfer, and emission processes

the sensitizer ion relaxes back again to the ground state [62]. The efficiency of ETU process strongly depends on the concentration of the sensitizer and activator ions, as it determinates the average distance between the neighboring ions.

Cooperative sensitization upconversion (*CSU*): involves the presence of three ion centers. As shown in Fig. 9.3, Ion1 and Ion3 act as sensitizers: after absorbing pump photons, they both are excited to the excited state E1. Both Ion1 and Ion3 will interact with Ion2 (activator) and will excite it to the higher state E1 by transferring the absorbed energy simultaneously and cooperatively. The excited Ion2 can emit the upconverted photon by relaxing back to the ground state [54]. Although CSU has lower efficiency then ESA or ETU, it provides opportunity to gain high-resolution imagining, which is not possible from any other upconverting process.

Cross-relaxation (*CR*): energy transfer process between two ions. This occurs from ion–ion interaction, where Ion1 transfers a part of its absorbed energy to Ion2. The process is shown is Fig. 9.3, and it can be described as follows: E2 (Ion1) + G (Ion2) → E1 (Ion1) + E1 (Ion2). In this process, Ion1 and Ion2 can either be the same or different, and Ion2 in some cases can be in excited form. The CR efficiency depends on the dopant concentration. This process is responsible for ‘concentration quenching mechanism’ of emission; however, it can be used for tuning emission color of upconversion materials, as well as for composing efficient photon avalanche mechanism [60].

Photon avalanche (*PA*): requires a certain threshold of excitation power. If the pump intensity is below the threshold upconversion luminescence barely appears, while if it is above it, then stronger upconverted luminescence occurs. PA process is a circle, including ESA for excitation light and CR that produces feedback. The process starts with the population of the E1 level of Ion2 by non-resonant weak ground-state absorption, which is followed by the ESA process populating the emitting E2 level. After this comes a CR process: E2 (Ion2) + G (Ion1) → E1 (Ion2) + E1 (Ion1), both ions occupy the intermediate level E1. The two ions easily populate level E2, to launch cross-relaxation and increase the E2 level population by ESA, which produces upconversion emission [63].

9.2.2 The Categories of the Rare Earth Ions in the Upconverting Process

A typical upconversion material consists of two components: an inorganic host matrix and doping ions. Most of these materials include trivalent rare earth ions (Pr^{3+}, Nd^{3+}, Er^{3+}, Tm^{3+}, Yb^{3+}), which act as active components [64]. The reason why these ions pay such important role is due to their relevant electronic states in their inner 4f shell. The outer 5 s and 6p shells participate in the bonding; however, the f states are insensitive to the nature of the host lattice, resulting a great number of excited f states. These states lead to upconversion, as their lifetime is long enough to be part of the process. Generally, inorganic crystals do not show upconversion luminescence at room temperature. Accordingly, lanthanide dopants are added in low concentration to the host lattice, in the role of localized luminescence center. After excitation, the dopant ion radiates to a higher energetic state, which is the result of the non-radiative transfer of the energy from another dopant ion. The activator is the ion that emits the radiation, while the donator of the energy is the sensitizer [65].

9.2.2.1 Activators

The upconversion process requires multiple metastable levels which is why the lanthanides are used most of the times. The lanthanides, from lanthanum to lutetium, fill the 4f shell and their most stable oxidation state is as trivalent ions (Ln^{3+}). Most of lanthanide ions have more than one excited 4f energy level, except La^{3+}, Ce^{3+}, Yb^{3+} and Lu^{3+}. Hypothetically, all lanthanides could be used for upconversion, yet for efficient upconversion process there is one more condition. The energy difference between each excited level and its lower-lying intermediate level (ground level) shall be close enough to promote photon absorption and energy transfer. The most frequently used activators are Er^{3+}, Tm^{3+}, and Ho^{3+}, because of their ladder-like arranged energy levels [65].

9.2.2.2 Sensitizers

The concentration of the doping ion is crucial. Operating with high doping level may cause the quenching of excitation energy. Therefore, the concentration of the activator has to be low and precisely adjusted. Nevertheless, if the doping level is too low, the absorption of the pump light is also low, which results in low emission luminescence efficiency. Thus, sensitizers are essential because they are strongly absorbing and provide efficient energy transfer to the activator. Yb^{3+} is the most widely used sensitizer for Er^{3+} and Tm^{3+}. Yb^{3+} has a very simple energy level structure, with only one 4f level. The separation energy between the ground and excited states of Yb^{3+} corresponds to the transient states of Er^{3+}, and this promotes the efficient energy transfer between the two ions [65].

9.2.2.3 Host Materials

Choosing the host material is just as important step as choosing the dopant ions. The lattice of the host material determines the distance between the dopant ions, their relative spatial position, coordination numbers, and the type of anions surrounding the dopant. The two most important properties of the host material are: low phonon energy and small lattice mismatch to the dopant ions [66]. Heavy halides, like chlorides, bromides, and iodides show low phonon energies, but they are hygroscopic and of limited use. Oxides have high chemical stability, but their phonon energies are relatively high. By contrast, fluorides show low phonon energies and high chemical stability, that is why they are the most frequently used as host materials for upconversion [67]. Among these the most widely used are Na^+ and Ca^{2+} fluorides, particularly, hexagonal $NaYF_4$ (β-$NaYF_4$) appears to be the most efficient one [53].

9.3 Photocatalysis in NIR Light in Detail

As mentioned beforehand, photocatalysis is an increasingly researched area. However, the most studied light ranges are the UV and visible. A new approach to utilize more of the sunlight is developing composite systems, which show photocatalytic activity in near-infrared light, which makes up ~44% of the sunlight.

Since most of the photocatalysts do not have photocatalytic activity in near-infrared light, this is an indirect realization of photocatalysis [27]. During the process, the NIR light is converted to UV or visible light, which is utilized for the degradation. The upconversion process takes place as described in Sect. 2.1. The presence of an UV or visible-light active photocatalyst is essential beside the upconverting nanoparticle, because the actual photocatalysis will be performed by them [53]. The schematic illustration of the mechanism of NIR photocatalysis is presented in Fig. 9.4. In brief, the upconverting nanoparticle converts the NIR light to UV or visible light. The photocatalyst uses this upconverted light to oxidize organic pollutants.

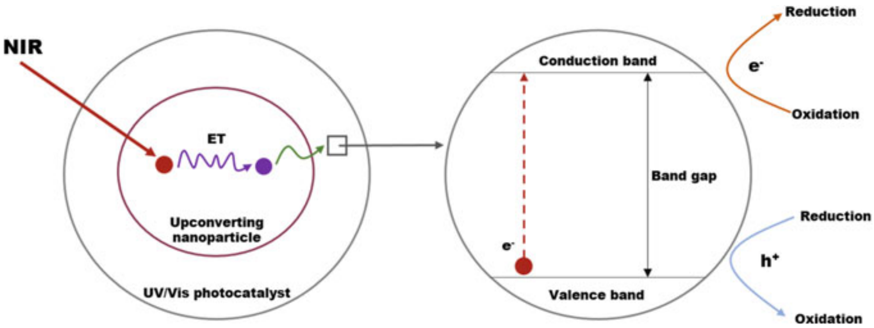

Fig. 9.4 Mechanism of the near-infrared photocatalysis based on upconverting nanoparticle and UV or visible-light active photocatalyst (**ET* energy transfer)

9.3.1 *Formation of Composites, Which Contain Upconverting Materials to Achieve Upconversion Photocatalysis*

9.3.1.1 Composites with TiO_2

Many oxides have been used for photocatalysis. Among these ***TiO_2*** is the most studied candidate. Our research group has dedicated much research on TiO_2 based photocatalysts [68–71]. Rare earth materials were used to prepare photocatalysts: lanthanide-doped $NaYF_4$, TiO_2, and gold nanoparticles were present in the composites. $NaYF_4$ was present as a host material, where Yb^{3+}, Er^{3+} and Tm^{3+} ions were in the role of sensitizer and activators. This upconverting material and TiO_2 were prepared via solvothermal crystallization, while Au nanoparticles by chemical reduction. The photocatalytic activity was investigated by the degradation of rhodamine B under UV and visible-light irradiation. Results show that the formation of these composites was beneficial, as the highest decomposition efficiencies were almost 90% after the two-hour experiment.

Other researchers studied TiO_2 and rare earth containing materials as well. The core–shell structure is widely used, as this formation of composites promotes the process of upconversion photocatalysis. If the upconverting material is the core, then it is protected from surface quenching and the energy transfer could be increased [72]. The photocatalytic activity of TiO_2 was improved via forming core–shell composites with $NaYF_4$:Yb, Tm, and CdS quantum dots [73]. The CdS quantum dots were deposited on the surface of TiO_2 shell, while $NaYF_4$:Yb, Tm was the core. The photocatalytic activity was investigated in white light, visible, and near-infrared light: under any irradiation, the composite had better activity than the pure TiO_2, what can be contributed to the fact that the quantum dots can extend the absorption region of TiO_2 and the upconversion effect of $NaYF_4$:Yb, Tm. Double core–shell structures were also prepared. One way of this is the double core structure which is presented in the following. First a core–shell structure was prepared as follows: $NaYF_4:Yb^{3+}$, Tm^{3+} was prepared as a core, then $NaYF_4:Yb^{3+}$, Nd^{3+} was prepared as a shell covering it, and lastly TiO_2 became the second shell of this core–shell structure [74]. This system may seem complicated at first, but has 4.4 times as high degradation rate constant of rhodamine B under 980 nm laser irradiation than $NaYF_4:Yb^{3+}$, Tm^3-TiO_2. Another way to the double core–shell structure is a double-shell formation of composites. β-$NaYF_4:Yb^{3+},Tm^{3+}/Er^{3+}$ nanocrystals were present as a core, SiO_2 as a mid-shell and TiO_2 as the outer shell [75]. These structures were applied in the photocatalytic degradation of rhodamine B. β-$NaYF_4:Yb^{3+},Tm^{3+}$ or β-$NaYF_4:Yb^{3+},Er^{3+}$ based catalysts had similar activity in NIR light, both of them decomposed all of the pollutant, by contrast those materials which did not contain these upconverting materials showed no photocatalytic activity under NIR light at all.

Rare earth ions were also used as doping materials for TiO_2. Researchers reported Er^{3+} and/or Yb^{3+} doped TiO_2 photocatalysts [76]. Their results reveal that the presence of these doping ions reduces the recombination rate of the photogenerated electron–hole pairs of titania. This leads to a better photocatalytic activity of TiO_2 for the degradation of phenol under the irradiation of sunlight. Other interesting results can be found about gadolinium-doped TiO_2. Gd^{3+} and Gd_2O_3 loading was studied on titania [77]. The presence of these dopants may lead to lattice disorientation and surface oxygen vacancy in TiO_2. Furthermore, particle agglomeration was inhibited by Gd^{3+} ions, due to the 4f electrons, which lead to visible-light response. These materials showed great photocatalytic activity for the degradation of methyl orange and rhodamine B. La-doped TiO_2 was prepared, so better photocatalytic activity could be reached [78]. Visible and solar light were used as the irradiation source, while the NO elimination was investigated. La-TiO_2 had better activity than pure titania due to the relatively narrow bandgap and that this material can boost the electron–hole separation, while La^{3+} can have synergistic effects and capture photoinduced electrons.

9.3.1.2 Composites with ZnO

$NaYF_4$ being the most suitable candidate as a host material, and it has been used with ***ZnO*** as well. One study reports that two types of composites were prepared from β-$NaYF_4$:Yb^{3+},Tm^{3+} and ZnO: one by a two-step high thermolysis method and the other by physical mixing [79]. While $NaYF_4$:Yb^{3+},Tm^{3+} or ZnO by themselves did not show any photocatalytic activity for the degradation of rhodamine B under near-infrared light, the composite and the physical mixture had 65% and 35% degradation rate, respectively. The contrast between the two degradation rates is due to the difference between their energy transfers. In the composite prepared with the thermolysis method, the ZnO is attached closely to $NaYF_4$, so the energy transfer between them takes place easier than in the physical mixture, that is why this composite had higher photocatalytic activity. Core–shell nanoparticle design was used with ZnO, too. $NaYF_4$:Yb, Tm@ZnO composite was synthetized, where ZnO represented the shell, while $NaYF_4$ is the core [80]. This composite was used for the photocatalytic degradation of methylene blue under 980 nm NIR irradiation. The core of this composite upconverted the near-infrared light and successfully transferred it to ZnO, which benefiting this energy decomposed almost 70% of the methylene blue. Another way of enhancing the photocatalytic activity of ZnO is by rare earth doping.

One research group prepared different rare earth (La, Nd, Sm, and Dy) doped ZnO [81]. Results show that Nd doping proved to be the most favorable through the photocatalytic degradation of rhodamine B and methylene blue. Another study confirms that Nd doping is the most beneficial for ZnO [82]. In this case beside, Nd, Eu, and Ce were tested along with ZnO. The photocatalytic activity was investigated by the degradation of phenol under visible light. All the rare earth doped zinc oxides showed better activity than pure ZnO or commercial TiO_2, because of the high charge separation efficiency and OH radical generation ability.

9.3.1.3 Composites with CuO

As ***copper-oxide*** is a promising visible-light-driven photocatalyst, some studies can be found about coupling it to rare earth containing materials to utilize the upconverted light. Combining Cu_2O with $NaYF_4$:Yb,Tm, a composite film was prepared by a simple electrodeposition process [83]. The results demonstrate that this film is capable to collect the near-infrared light, as $NaYF_4$:Yb,Tm converts it to visible photons, which excite the electrons of Cu_2O. This way the as-prepared composites may be suitable for upconversion photocatalysis. The core–shell design of the composites appears again: $NaYF_4$:Yb, Tm core was covered with a thin shell of Cu_2O [84]. Two methods were used to combine the two components: physical mixture and synthesis of composites. The photocatalytic activity of the prepared samples was investigated by the degradation of methylene-blue aqueous solution under NIR irradiation. The composite proved to be better for photocatalytic applications, since the energy transfer between Tm^{3+} and Cu_2O is more efficient than in the physical mixture. Another interesting study reports that CuO was combined to $NaYF_4$:Yb,Tm/TiO_2 composite to increase the photocatalytic activity in visible light [85]. The as-prepared composites showed excellent photocatalytic activity for the degradation of methylene blue, and moreover, it presented up to 60% recyclability.

9.3.1.4 Composites with CeO_2

The last presented oxide is ***cerium dioxide***. A research group developed a method to deposit a CeO_2 layer on $NaYF_4$:Yb,Tm upconverting nanoparticles [86]. The as-prepared core–shell particles were tested for photocatalytic activity. Results showed that these photocatalysts had good activity for the degradation of methyl orange under NIR light. In addition, this $NaYF_4$:Yb,Tm@CeO_2 was further coated with ZnO, building a semiconductor heterojunction structure on the upconverting nanoparticle. In this structure, the separation of the photogenerated electrons and holes was improved, and in this way, the photocatalytic activity was also enhanced under near-infrared light.

Rare earth metal doping was used on CeO_2 as well. The effect of Gd and Sm on CeO_2 was studied [87]. The photocatalytic activity was tested for the degradation of methylene blue under natural sunlight. Sm-doped cerium dioxide had the highest photocatalytic activity, which can be explained by the fact that the presence of the rare earth metals caused the change of Ce^{4+} to Ce^{3+} and oxygen vacancy defects. Sm doping was the most beneficial for these changes. Another research was made on La^{3+} doped CeO_2 [88]. The doping ratio was varied from 10 to 50%. The results demonstrated that the 10% doping rate was the most favorable for the photocatalytic degradation of methylene blue under visible-light irradiation.

9.3.1.5 Composites with CdS

Since ***CdS*** is a promising visible-light active photocatalyst as well, it was successfully applied in upconversion photocatalysis. Core–shell composites were prepared containing $NaYF_4$:Yb,Er core and cubic CdS shell [89]. This material proved to have good photocatalytic activity toward methyl orange and carbendazim degradation under NIR irradiation because of the energy transfer between the components. A significant amount of energy can be transferred from Er^{3+} ions to CdS, which improved the photocatalytic degradation. Other studies report about core–shell composite of $NaYF_4$:Yb,Tm and CdS [90, 91]. The results were similar to the previous study: the composite always had higher photocatalytic activity than pure CdS for the degradation of rhodamine B and methylene blue under NIR and visible-NIR light.

Researchers obtained photocatalysts of rare earth (La^{3+}, Eu^{3+}, Er^{3+}, Gd^{3+}) doped CdS-TiO_2 composites [92]. The photocatalytic activity was investigated under visible-light irradiation, and the order of the composites regarding of the doping ion is: $La^{3+} > Eu^{3+} > Er^{3+} > Gd^{3+}$. The reason why rare earth ions improve the photocatalytic activity is because they are incorporated into the TiO_2, which cannot be excited with visible light. This way the electrons of CdS are excited by the visible light which can be transferred to TiO_2, where the rare earth ion may act as an effective electron-trapped agent.

9.3.1.6 Composites with $BiVO_4$

Among the visible-light-active photocatalysts, ***$BiVO_4$*** has recently shown promising results. As for the near-infrared light-driven photocatalysis, composites were formed with bismuth vanadate and different rare earth containing upconversion materials. One research presents photocatalytic systems of $BiVO_4$ and $NaYbF_4$:Tm^{3+} [93]. This composite system had good photocatalytic activity toward crystal violet and sulfathiazole degradation under 980 nm NIR irradiation. The key in the process is that the Yb^{3+} ions can absorb the NIR irradiation and get excited, and then, through energy transfer, Tm^{3+} ions get excited and upon their relaxation emit the upconverted energy in the UV and/or visible region. Since the electrons of $BiVO_4$ can be excited by ~500 nm light, they can absorb the upconverted irradiation and through the photogenerated charge carriers can decompose the pollutant.

As a host material, CaF_2 was combined with $BiVO_4$ as well. One study reports the preparation of CaF_2:Yb@$BiVO_4$ composite for the degradation of methylene blue under near-infrared light via one-step energy transfer process [94]. The results were promising, as the composite had 80% degradation rate after the 7 h experiment and the recycling experiments proved high stability of the photocatalyst. CaF_2 was also doped with Er^{3+}, Tm^{3+}, and Yb^{3+} ions and utilized in the preparation of composites with bismuth vanadate [95]. The photocatalytic activity of the as-prepared composite was investigated under NIR light for the decomposition of methyl orange, and it was found that the composite had eight times higher activity than the pure CaF_2.

Doping $BiVO_4$ with rare earth metals is another way of achieving upconversion photocatalysis. A core–shell material was prepared via doping $BiVO_4$ with Er^{3+} and Yb^{3+} ions, where this doped material was present as the shell and pure $BiVO_4$ was the core [96]. The rare earth ions were incorporated in the layers of $BiVO_4$ that is why the doping promoted the upconversion emissions of visible light. $BiVO_4$:Er^{3+}, Yb^{3+} had higher charge transport ability and lower recombination rate of the photogenerated charge carriers than pure $BiVO_4$. Another study can be found about Yb^{3+} doped $BiVO_4$ [97]. The presence of Yb^{3+} ion helped the transformation of monoclinic $BiVO_4$ to tetragonal phase, which improved its photocatalytic activity for the degradation of methylene blue under visible-light irradiation. Using this information, more attempts were made, so that the photocatalytic activity could be further improved. Tri-doped materials were synthetized containing Er^{3+}/Tm^{3+}, Yb^{3+}, Y^{3+}, and $BiVO_4$ [98]. The photocatalytic activity was enhanced even more by the presence of all three rare earth ions. This can be due to the cooperative luminescence process, what can transfer extra UV or visible photons from the near-infrared range.

9.3.1.7 Composites with Bi_2WO_6

As the different lanthanide-doped $NaYF_4$ is the most popular upconverting material, there is no surprise that it was utilized in the preparation of composites with ***Bi_2WO_6*** as well. The core shell material was prepared as follows: the active core was consisted of Yb^{3+}, Gd^{3+}, and Tm^{3+} doped $NaYF_4$, while the inert shell was Bi_2WO_6 [99]. Designing these composites can be considered as a successful attempt, since they had higher (94% decomposition rate) photocatalytic activity than the components separately.

Bi_2WO_6 was doped with various rare earth ions. Different amount of Yb^{3+} ion was doped on Bi_2WO_6, and the improved photocatalytic activity can be explained with the increased surface area, the decreased bandgap energy, and the lower recombination rate of the electron–hole pairs [100]. Another study presents Ce^{3+}, Nd^{3+}, Pr^{3+}, or Sm^{3+} doped Bi_2WO_6 [101]. Results showed that Nd^{3+} doping into Bi_2WO_6 was the most beneficial to the photocatalytic degradation of rhodamine B as it decreased 99.8% of it. This is due to the smaller crystallite size, larger surface area, and lower bandgap than the other candidates. In addition, Nd^{3+} doped Bi_2WO_6 had excellent recyclability, since it did not show loss in activity after six cycles. Tm^{3+} and Yb^{3+} co-doped Bi_2WO_6 was formed under different synthesis conditions [102]. The photocatalytic activity was tested with the degradation of rhodamine B under visible and near-infrared light irradiation. The results proved that the doping was favorable, as the doped Bi_2WO_6 had higher photocatalytic activity than pure Bi_2WO_6 or commercial Degussa P25, which can be attributed to the successful energy transfer between Tm^{3+}/Yb^{3+} and Bi_2WO_6 and the decreased recombination rate of the photogenerated electron–hole pairs.

9.3.1.8 Composites Containing Plasmonic Noble Metal Nanoparticles

Among the noble metal nanoparticles ***Au*** had been studied the most for upconversion photocatalysis. This, beside increasing the lifetime of electron–hole pairs, is due to the surface plasmon resonance (SPR) exhibited by gold nanoparticles. This SPR-induced hot electrons can be directly induced from gold nanoparticles to the conduction band of a semiconductor [103]. Using this information, researchers attempted to achieve composites by combining SPR and upconversion effects. One study presents the design of a composite-containing TiO_2, upconverting Yb^{3+} and Er^{3+} doped $NaYF_4$, and plasmonic gold nanoparticles [104]. Results showed that by employing SPR and upconversion effects together, the solar light utilization can be improved. Rare earth vanadates and gold nanoparticle composites had been studied as well. Au nanoparticles were deposited onto $NdVO_4$, which resulted great photocatalytic activity for the degradation of methyl orange under solar light [105]. $GdVO_4$:Eu and Au core–shell nanoparticles were synthetized [106]. It was found that these materials had high surface area, and they integrate SPR and fluorescence which suggests that it may be potential in photocatalytic applications.

The aforementioned localized plasmon resonance appears not only for the gold nanoparticles but for ***Ag*** nanoparticles, too. Yb^{3+}, Er^{3+}, and Tm^{3+} doped $NaYF_4$ core and TiO_2 shell were integrated with Ag nanoparticles [107]. The as-prepared composites showed great photocatalytic activity under UV, visible, or near-infrared light for the methyl orange degradation, moreover, had excellent stability. SnO_2 was coated on the surface of Yb^{3+} and Tm^{3+} doped $NaYF_4$ and further decorated with silver nanoparticles [108]. The results were similar to the previous study, as the composite had superior photocatalytic activity in UV, visible, NIR, and simulated solar light than the components separately due to the SPR and upconversion effects.

9.4 Conclusions

It is important mentioning that photocatalysis does not consist only of TiO_2 or UV light. Therefore, this chapter provides information about photocatalysis in all wavelength ranges. The UV and visible-light-driven photocatalysts are discussed in brief, as the essence of this chapter is photocatalysis under near-infrared light and the rare earth doped luminescence materials.

The energy transfer mechanisms of upconversion are presented in this chapter before detailing the photocatalysis in near-infrared light. In short, upconversion is a nonlinear optical process, when two or more photons are absorbed in a row. This results in real intermediate energy states, and luminescence is emitted with a wavelength shorter than the absorbed light. Photocatalysis under near-infrared light is an indirect realization of photocatalysis since most of the photocatalyst do not have photocatalytic activity in this light range. During the process, the NIR light is converted to UV or visible light, which is utilized for the degradation. The presence of an UV or visible-light-active photocatalyst is essential beside the upconverting nanoparticle, because the actual photocatalysis will be performed by them.

After interpreting photocatalysis in NIR light in detail, some scientific results were presented of composites which contain upconverting materials. The most frequently used upconverting host materials are fluorides, as they show low phonon energies and high chemical stability. Among these the most widely used are Na^+ and Ca^{2+} fluorides, particularly, hexagonal $NaYF_4$ (β-$NaYF_4$) appears to be the most efficient one. These fluorides are usually doped with at least one lanthanide ion. Generally, the composites are formed in core–shell structure, as this formation promotes the process of upconversion photocatalysis: the upconverting material is the core than it is protected from surface quenching and the energy transfer could be increased. Rare earth ions were also used as doping materials. This book chapter presents composites containing rare earth materials and the following photocatalyst: TiO_2, ZnO, CuO, CeO_2, CdS, $BiVO_4$, Bi_2WO_6, or plasmonic noble metal nanoparticles.

Materials reviewed in this chapter are excellent candidates to amplify photocatalytic application in a broad range of irradiation, thus enhancing the environmentally benign harvesting of each component of sunlight.

Bibliography

1. Fujishima A, Honda K (1972) Electrochemical photolysis of water at a semiconductor electrode. Nature 238:37–38
2. Fujishima A, Rao TN, Tryk DA (2000) Titanium dioxide photocatalysis. J Photochem Photobiol C Photochem Rev 1:1–21
3. Xu Z, Quintanilla M, Vetrone F, Govorov AO, Chaker M, Ma D (2015) Harvesting lost photons: plasmon and upconversion enhanced broadband photocatalytic activity in core@shell microspheres based on lanthanide-doped $NaYF_4$, TiO_2, and Au. Adv Funct Mater 25:2950–2960. https://doi.org/10.1002/adfm.201500810
4. Xin B, Jing L, Ren Z, Wang B, Fu H (2005) Effects of simultaneously doped and deposited Ag on the photocatalytic activity and surface states of TiO_2. J Phys Chem B 109:2805–2809. https://doi.org/10.1021/jp0469618
5. Liu R, Wang P, Wang X, Yu H, Yu J (2012) UV- and visible-light photocatalytic activity of simultaneously deposited and doped Ag/Ag(I)-TiO_2 photocatalyst. J Phys Chem C 116:17721–17728. https://doi.org/10.1021/jp305774n
6. Sung-Suh HM, Choi JR, Hah HJ, Koo SM, Bae YC (2004) Comparison of Ag deposition effects on the photocatalytic activity of nanoparticulate TiO_2 under visible and UV light irradiation. J Photochem Photobiol A Chem 163:37–44. https://doi.org/10.1016/S1010-6030(03)00428-3
7. Tian Y, Tatsuma T (2005) Mechanisms and applications of plasmon-induced charge separation at TiO_2 films loaded with gold nanoparticles. J Am Chem Soc 127:7632–7637. https://doi.org/10.1021/ja042192u
8. Ansari SA, Khan MM, Ansari MO, Cho MH (2015) Gold nanoparticles-sensitized wide and narrow band gap TiO_2 for visible light applications: a comparative study. New J Chem 39:4708–4715. https://doi.org/10.1039/c5nj00556f

9. Yoshida T, Misu Y, Yamamoto M, Tanabe T, Kumagai J, Ogawa S, Yagi S (2020) Effects of the amount of Au nanoparticles on the visible light response of TiO_2 photocatalysts. Catal Today 352:34–38. https://doi.org/10.1016/j.cattod.2019.12.035
10. Fodor S, Kovács G, Hernádi K, Danciu V, Baia L, Pap Z (2017) Shape tailored Pd nanoparticles' effect on the photocatalytic activity of commercial TiO_2. Catal Today 284:137–145. https://doi.org/10.1016/j.cattod.2016.11.011
11. Yan J, Li X, Jin B, Zeng M, Peng R (2020) Synthesis of TiO_2/Pd and TiO_2/PdO hollow spheres and their visible light photocatalytic activity. Int J Photoenergy 2020. https://doi.org/10.1155/2020/4539472.
12. Hariharan D, Thangamuniyandi P, Selvakumar P, Devan U, Pugazhendhi A, Vasantharaja R, Nehru LC (2019) Green approach synthesis of Pd@TiO_2 nanoparticles: characterization, visible light active picric acid degradation and anticancer activity. Process Biochem 87:83–88. https://doi.org/10.1016/j.procbio.2019.09.024
13. Kovács G, Fodor S, Vulpoi A, Schrantz K, Dombi A, Hernádi K, Danciu V, Pap Z, Baia L (2015) Polyhedral Pt vs. spherical Pt nanoparticles on commercial titanias: is shape tailoring a guarantee of achieving high activity? J Catal 325:156–167. https://doi.org/10.1016/j.jcat.2015.02.008.
14. Qiu H, Ma X, Sun C, Zhao B, Chen F (2020) Surface oxygen vacancies enriched Pt/TiO_2 synthesized with a defect migration strategy for superior photocatalytic activity. Appl Surf Sci 506:145021. https://doi.org/10.1016/j.apsusc.2019.145021
15. Zielinska-Jurek A, Wei Z, Janczarek M, Wysocka I, Kowalska E (2019) Size-controlled synthesis of Pt particles on TiO_2 surface: physicochemical characteristic and photocatalytic activity. Catalysts 9:1–18
16. Ohno T, Mitsui T, Matsumura M (2003) Photocatalytic activity of S-doped TiO_2 photocatalyst under visible light. Chem Lett 32:364–365. https://doi.org/10.1246/cl.2003.364
17. Huang Z, Gao Z, Gao S, Wang Q, Wang Z, Huang B, Dai Y (2017) Facile synthesis of S-doped reduced TiO_2-x with enhanced visible-light photocatalytic performance. Cuihua Xuebao/Chin J Catal 38:821–830. https://doi.org/10.1016/S1872-2067(17)62825-0
18. Wang J, Tafen DN, Lewis JP, Hong Z, Manivannan A, Zhi M, Li M, Wu N (2009) Origin of photocatalytic activity of Nitrogen-doped TiO_2 nanobelts. J Am Chem Soc 131:12290–12297. https://doi.org/10.1021/ja903781h
19. Zhou L, Cai M, Zhang X, Cui N, Chen G, Zou GY (2020) In-situ nitrogen-doped black TiO_2 with enhanced visible-light-driven photocatalytic inactivation of microcystis aeruginosa cells: synthesization, performance and mechanism. Appl Catal B Environ 272:119019. https://doi.org/10.1016/j.apcatb.2020.119019
20. Morikawa T, Asahi R, Ohwaki T (2005) Visible-light photocatalyst-nitrogen-doped titanium dioxide. R&D Rev Toyota CRDL 40:45–50
21. Ni M, Leung MKH, Leung DYC, Sumathy K (2007) A review and recent developments in photocatalytic water-splitting using TiO_2 for hydrogen production. Renew Sustain Energy Rev 11:401–425. https://doi.org/10.1016/j.rser.2005.01.009
22. Daneshvar N, Salari D, Khataee AR (2004) Photocatalytic degradation of azo dye acid red 14 in water on ZnO as an alternative catalyst to TiO_2. J Photochem Photobiol A Chem 162:317–322. https://doi.org/10.1016/S1010-6030(03)00378-2
23. Bica BO, de Melo JVS (2020) Concrete blocks nano-modified with zinc oxide (ZnO) for photocatalytic paving: performance comparison with titanium dioxide (TiO_2). Constr Build Mater 252:119120. https://doi.org/10.1016/j.conbuildmat.2020.119120
24. Neppolian B, Choi HC, Sakthivel S, Arabindoo B, Murugesan V (2002) Solar/UV-induced photocatalytic degradation of three commercial textile dyes. J Hazard Mater 89:303–317. https://doi.org/10.1016/S0304-3894(01)00329-6
25. Basahel SN, Ali TT, Mokhtar M, Narasimharao K (2015) Influence of crystal structure of nanosized ZrO_2 on photocatalytic degradation of methyl orange. Nanoscale Res Lett 10. https://doi.org/10.1186/s11671-015-0780-z

26. Karunakaran C, Senthilvelan S (2005) Photocatalysis with ZrO_2: oxidation of aniline. J Mol Catal A Chem 233:1–8. https://doi.org/10.1016/j.molcata.2005.01.038
27. Sang Y, Liu H, Umar A (2015) Photocatalysis from UV/Vis to near-infrared light: towards full solar-light spectrum activity. ChemCatChem 7:559–573. https://doi.org/10.1002/cctc.201402812
28. Fu Z, Zhang S, Fu Z (2019) Hydrothermal preparation of $NaTaO_3$/rGO composite photocatalyst to enhance UV photocatalytic activity. Results Phys 15:102669. https://doi.org/10.1016/j.rinp.2019.102669
29. Nazari A (2019) Preparation of electroconductive, antibacterial, photoactive cotton fabric through green synthesis of ZnO/reduced graphene oxide nanocomposite. Fibers Polym 20:2618–2624. https://doi.org/10.1007/s12221-019-9180-9
30. Ngaloy RT, Fontanilla AM, Soriano MSR, Pascua CS, Matsushita Y, Agulo IJA (2019) Highly efficient photocatalysis by zinc oxide-reduced graphene oxide (ZnO-rGO) composite synthesized via one-pot room-temperature chemical deposition method. J Nanotechnol 2019. https://doi.org/10.1155/2019/1895043
31. Aawani E, Memarian N, Dizaji HR (2019) Synthesis and characterization of reduced graphene oxide–V2O5 nanocomposite for enhanced photocatalytic activity under different types of irradiation. J Phys Chem Solids 125:8–15. https://doi.org/10.1016/j.jpcs.2018.09.028
32. Cheng L, Xiang Q, Liao Y, Zhang H (2018) CdS-Based photocatalysts. Energy Environ Sci 11:1362–1391. https://doi.org/10.1039/c7ee03640j
33. Han G, Jin YH, Burgess RA, Dickenson NE, Cao XM, Sun Y (2017) Visible-light-driven valorization of biomass intermediates integrated with H_2 production catalyzed by ultrathin Ni/CdS nanosheets. J Am Chem Soc 139:15584–15587. https://doi.org/10.1021/jacs.7b08657
34. Han B, Liu S, Zhang N, Xu YJ, Tang ZR (2017) One-dimensional CdS@MoS_2 core-shell nanowires for boosted photocatalytic hydrogen evolution under visible light. Appl Catal B Environ 202:298–304. https://doi.org/10.1016/j.apcatb.2016.09.023
35. Ma D, Shi JW, Zou Y, Fan Z, Ji X, Niu C (2017) Highly Efficient Photocatalyst based on a CdS quantum dots/ZnO nanosheets 0D/2D heterojunction for hydrogen evolution from water splitting. ACS Appl Mater Interfaces 9:25377–25386. https://doi.org/10.1021/acsami.7b08407
36. Wu J, Bai S, Shen X, Jiang L (2010) Preparation and characterization of graphene/CdS nanocomposites. Appl Surf Sci 257:747–751. https://doi.org/10.1016/j.apsusc.2010.07.058
37. Dong P, Hou G, Xi X, Shao R, Dong F (2017) WO_3-based photocatalysts: morphology control, activity enhancement and multifunctional applications. Environ Sci Nano 4:539–557. https://doi.org/10.1039/c6en00478d
38. Fodor S, Baia L, Focşan M, Hernádi K, Pap Z (2019) Designed and controlled synthesis of visible light active copper(I)oxide photocatalyst: From cubes towards the polyhedrons—with Cu nanoparticles. Appl Surf Sci 484:175–183. https://doi.org/10.1016/j.apsusc.2019.03.288
39. Li G, Wang Y, Mao L (2014) Recent progress in highly efficient Ag-based visible-light photocatalysts. RSC Adv 4:53649–53661. https://doi.org/10.1039/c4ra08044k
40. Fu H, Pan C, Yao W, Zhu Y (2005) Visible-light-induced degradation of rhodamine B by nanosized Bi_2WO_6. J Phys Chem B 109:22432–22439. https://doi.org/10.1021/jp052995j
41. Tan HL, Amal R, Ng YH (2017) Alternative strategies in improving the photocatalytic and photoelectrochemical activities of visible light-driven $BiVO_4$: a review. J. Mater. Chem. A 5:16498–16521. https://doi.org/10.1039/c7ta04441k
42. Lim SY, Shen W, Gao Z (2015) Carbon quantum dots and their applications. Chem Soc Rev 44:362–381. https://doi.org/10.1039/c4cs00269e
43. Li H, Kang Z, Liu Y, Lee ST (2012) Carbon nanodots: Synthesis, properties and applications. J Mater Chem 22:24230–24253. https://doi.org/10.1039/c2jm34690g
44. Zheng Y, Liu J, Liang J, Jaroniec M, Qiao SZ (2012) Graphitic carbon nitride materials: Controllable synthesis and applications in fuel cells and photocatalysis. Energy Environ Sci 5:6717–6731. https://doi.org/10.1039/c2ee03479d

45. Akhavan O, Abdolahad M, Abdi Y, Mohajerzadeh S (2009) Synthesis of titania/carbon nanotube heterojunction arrays for photoinactivation of *E. coli* in visible light irradiation. Carbon N. Y. 47:3280–3287, doi:https://doi.org/10.1016/j.carbon.2009.07.046.
46. Zhang H, Lv X, Li Y, Wang Y, Li J (2010) P25-graphene composite as a high performance photocatalyst. ACS Nano 4:380–386. https://doi.org/10.1021/nn901221k
47. Gyulavári T, Veréb G, Pap Z, Réti B, Baan K, Todea M, Magyari K, Szilágyi IM, Hernadi K (2019) Utilization of carbon nanospheres in photocatalyst production: From composites to highly active hollow structures. Materials (Basel) 12. https://doi.org/10.3390/ma12162537
48. Bakos LP, Justh N, Hernádi K, Kiss G, Réti B, Erdélyi Z, Parditka B, Szilágyi IM (2016) Core-shell carbon nanosphere-TiO_2 composite and hollow TiO_2 nanospheres prepared by atomic layer deposition. J Phys Conf Ser 764. https://doi.org/10.1088/1742-6596/764/1/012005
49. Justh N, Bakos LP, Hernádi K, Kiss G, Réti B, Erdélyi Z, Parditka B, Szilágyi IM (2017) Photocatalytic hollow TiO_2 and ZnO nanospheres prepared by atomic layer deposition. Sci Rep 7:2–10. https://doi.org/10.1038/s41598-017-04090-0
50. Réti B, Mogyorósi K, Dombi A, Hernádi K (2014) Substrate dependent photocatalytic performance of TiO_2/MWCNT photocatalysts. Appl Catal A Gen 469:153–158. https://doi.org/10.1016/j.apcata.2013.10.001
51. Réti B, Major Z, Szarka D, Boldizsár T, Horváth E, Magrez A, Forró L, Dombi A, Hernádi K (2016) Influence of TiO_2 phase composition on the photocatalytic activity of TiO_2/MWCNT composites prepared by combined sol-gel/hydrothermal method. J Mol Catal A Chem 414:140–147. https://doi.org/10.1016/j.molcata.2016.01.016
52. Qin W, Zhang D, Zhao D, Wang L, Zheng K (2010) Near-infrared photocatalysis based on YF_3:Yb^{3+}, Tm^{3+}/TiO_2 core/shell nanoparticles. Chem Commun 46:2304–2306. https://doi.org/10.1039/b924052g
53. Kumar A, Reddy KL, Kumar S, Kumar A, Sharma V, Krishnan V (2018) Rational design and development of lanthanide-doped $NaYF_4$@CdS-Au-RGO as quaternary plasmonic photocatalysts for harnessing visible-near-infrared broadband spectrum. ACS Appl Mater Interfaces 10:15565–15581. https://doi.org/10.1021/acsami.7b17822
54. Lingeshwar Reddy K, Balaji R, Kumar A, Krishnan V (2018) Lanthanide doped near infrared active upconversion nanophosphors: fundamental concepts, synthesis strategies, and technological applications. Small 14:1–27. https://doi.org/10.1002/smll.201801304
55. Yu H, Shi R, Zhao Y, Waterhouse GIN, Wu LZ, Tung CH, Zhang T (2016) Smart utilization of carbon dots in semiconductor photocatalysis. Adv Mater 28:9454–9477. https://doi.org/10.1002/adma.201602581
56. Kalyani TN, Swart H, Dhoble SJ (2017) Principles and applications of organic light emitting diodes (OLEDs). Woodhead publishing series in electronic and optical materials. ISBN 9781437778236.
57. Wouterlood FG, Boekel AJ (2009) Fluorescence microscopy in the neurosciences. Encycl Neurosci 253–260. https://doi.org/10.1016/B978-008045046-9.00666-5.
58. Valeur B, Berberan-Santos MN (2011) A brief history of fluorescence and phosphorescence before the emergence of quantum theory. J Chem Educ 88:731–738. https://doi.org/10.1021/ed100182h
59. Gamelin DR, Güdel HU (2000) Design of luminescent inorganic materials: new photophysical processes studied by optical spectroscopy. Acc Chem Res 33:235–242. https://doi.org/10.1021/ar990102y
60. Chen G, Qiu H, Prasad PN, Chen X (2014) Upconversion nanoparticles: design, nanochemistry, and applications in theranostics. Chem Rev 114:5161–5214. https://doi.org/10.1021/cr400425h
61. Auzel F (2004) Upconversion and anti-stokes processes with f and d ions in solids. Chem Rev 104:139–173. https://doi.org/10.1021/cr020357g
62. Shyichuk A, Câmara SS, Weber IT, Carneiro Neto AN, Nunes LAO, Lis S, Longo RL, Malta OL (2016) Energy transfer upconversion dynamics in YVO_4:Yb^{3+},Er^{3+}. J Lumin 170:560–570. https://doi.org/10.1016/j.jlumin.2015.07.005.

63. Joubert MF (1999) Photon avalanche upconversion in rare earth laser materials. Opt Mater (Amst) 11:181–203. https://doi.org/10.1016/S0925-3467(98)00043-3
64. Wang R, Zhang F (2014) NIR luminescent nanomaterials for biomedical imaging. J Mater Chem B 2:2422–2443. https://doi.org/10.1039/c3tb21447h
65. Wang F, Liu X (2009) Recent advances in the chemistry of lanthanide-doped upconversion nanocrystals. Chem Soc Rev 38:976–989. https://doi.org/10.1039/b809132n
66. Zhang F (2017) Photon upconversion nanomaterials, vol 3. Springer, Berlin. ISBN 9783662455968.
67. Gong G, Xie S, Song Y, Tan H, Xu J, Zhang C, Xu L (2018) Synthesis of lanthanide-ion-doped NaYF 4 RGB up-conversion nanoparticles for anti-counterfeiting application. J Nanosci Nanotechnol 18:8207–8215. https://doi.org/10.1166/jnn.2018.15801
68. Hampel B, Kovács G, Czekes Z, Hernádi K, Danciu V, Ersen O, Girleanu M, Focşan M, Baia L, Pap Z (2018) Mapping the photocatalytic activity and ecotoxicology of Au, Pt/TiO$_2$ composite photocatalysts. ACS Sustain Chem Eng 6:12993–13006. https://doi.org/10.1021/acssuschemeng.8b02465
69. Tóth Z-R, Pap Z, Danciu V, Cosoveanu V, Baia L, Kovács G (2018) Detailed investigation of phenol degradation on Au/TiO$_2$ composite materials. J Nanosci Nanotechnol 19:407–413. https://doi.org/10.1166/jnn.2019.15793
70. Hampel B, Pap Z, Sapi A, Szamosvolgyi A, Baia L, Hernadi K (2020) Application of TiO$_2$–Cu composites in photocatalytic degradation different pollutants and hydrogen production. Catalysts 10:1–20. https://doi.org/10.3390/catal10010085
71. Bárdos E, Kovács G, Gyulavári T, Németh K, Kecsenovity E, Berki P, Baia L, Pap Z, Hernádi K (2018) Novel synthesis approaches for WO$_3$-TiO$_2$/MWCNT composite photocatalysts- problematic issues of photoactivity enhancement factors. Catal Today 300:28–38. https://doi.org/10.1016/j.cattod.2017.03.019
72. Zhang Y, Hong Z (2013) Synthesis of lanthanide-doped NaYF$_4$@TiO$_2$ core-shell composites with highly crystalline and tunable TiO$_2$ shells under mild conditions and their upconversion-based photocatalysis. Nanoscale 5:8930–8933. https://doi.org/10.1039/c3nr03051b
73. Xu J, Shi Y, Chen Y, Wang Q, Cheng J, Li P (2019) Enhanced photocatalytic activity of TiO$_2$ in visible and infrared light through the synergistic effect of upconversion nanocrystals and quantum dots. Mater Res Express 6. https://doi.org/10.1088/2053-1591/aaf1f2
74. Huang H, Li H, Wang Z, Wang P, Zheng Z, Liu Y, Dai Y, Li Y, Huang B (2019) Efficient near-infrared photocatalysts based on NaYF$_4$:Yb^{3+}, T^{m3}+@NaY$_F$4:Y^{b3}+, Nd3+@T$_i$O2 core@shell nanoparticles. Chem Eng J 361:1089–1097. https://doi.org/10.1016/j.cej.2018.12.174
75. Wang W, Huang W, Ni Y, Lu C, Xu Z (2014) Different upconversion properties of β-NaYF$_4$: Yb^3+, ^{Tm}3+/^{Er}3+ in affecting the near-infrared-driven photocatalytic activity of high-reactive T$_i$O2. ACS Appl Mater Interfaces 6:340–348. https://doi.org/10.1021/am404389g
76. Fang X, Chen X, Zhu Z (2017) Optical and photocatalytic properties of Er^{3+} and/or Yb^{3+} doped TiO$_2$ photocatalysts. J Mater Sci Mater Electron 28:474–479. https://doi.org/10.1007/s10854-016-5545-7
77. Wu D, Li C, Zhang D, Wang L, Zhang X, Shi Z, Lin Q (2019) Enhanced photocatalytic activity of Gd^{3+} doped TiO$_2$ and Gd$_2$O$_3$ modified TiO$_2$ prepared via ball milling method. J Rare Earths 37:845–852. https://doi.org/10.1016/j.jre.2018.10.011
78. Huang Y, Cao JJ, Kang F, You SJ, Chang CW, Wang YF (2017) High selectivity of visible-light-driven la-doped TiO$_2$ photocatalysts for NO removal. Aerosol Air Qual. Res. 17:2555–2565. https://doi.org/10.4209/aaqr.2017.08.0282
79. Guo X, Song W, Chen C, Di W, Qin W (2013) Near-infrared photocatalysis of β-NaYF$_4$: Yb^3+, ^{Tm}3+@ZnO composites. Phys Chem Chem Phys 15:14681–14688. https://doi.org/10.1039/c3cp52248b

80. Zhang J, Zhao S, Xu Z, Zhang L, Zuo P, Wu Q (2019) Near-infrared light-driven photocatalytic NaYF $_4$:Yb, Tm@ZnO core/shell nanomaterials and their performance. RSC Adv 9:3688–3692. https://doi.org/10.1039/c8ra07861k
81. Alam U, Khan A, Ali D, Bahnemann D, Muneer M (2018) Comparative photocatalytic activity of sol-gel derived rare earth metal (La, Nd, Sm and Dy)-doped ZnO photocatalysts for degradation of dyes. RSC Adv 8:17582–17594. https://doi.org/10.1039/c8ra01638k
82. Sin JC, Lam SM, Lee KT, Mohamed AR (2014) Preparation of rare earth-doped ZnO hierarchical micro/nanospheres and their enhanced photocatalytic activity under visible light irradiation. Ceram Int 40:5431–5440. https://doi.org/10.1016/j.ceramint.2013.10.128
83. Jia H, Zheng SH, Xu C, Chen WB, Wang JC, Liu XF, Qiu JR (2015) Near-infrared light-induced photocurrent from a (NaYF$_4$:Yb-Tm)/(Cu$_2$O) composite thin film. Adv Energy Mater 5:1–7. https://doi.org/10.1002/aenm.201401041
84. Zhang J, Qiao B, Liang Z, Zuo P, Wu Q, Xu Z, Piao L, Zhao S (2018) Near-infrared light-induced photocatalysis of NaYF$_4$:Yb, Tm@Cu$_2$O core-shell nanocomposites. Opt Mater (Amst) 84:89–93. https://doi.org/10.1016/j.optmat.2018.06.053
85. Mavengere S, Jung SC, Kim JS (2018) Visible light photocatalytic activity of NaYF$_4$:(Yb, Er)-CuO/Ti$_O$2 composite. Catalysts 8:1–15. https://doi.org/10.3390/catal8110521
86. Cui C, Tou M, Li M, Luo Z, Xiao L, Bai S, Li Z (2017) Heterogeneous semiconductor shells sequentially coated on upconversion nanoplates for NIR-light enhanced photocatalysis. Inorg Chem 56:2328–2336. https://doi.org/10.1021/acs.inorgchem.6b03079
87. Chinnu MK, Anandan P, Arivanandhan M, Venkatesan A, Kumar RM, Jayavel R (2018) Effect of rare earth doping on the enhancement of photocatalytic performance of ceria nanocrystals under natural sunlight. J Mater Sci Mater Electron 29:9564–9572. https://doi.org/10.1007/s10854-018-8991-6
88. Singh K, Kumar K, Srivastava S, Chowdhury A (2017) Effect of rare-earth doping in CeO$_2$ matrix: correlations with structure, catalytic and visible light photocatalytic properties. Ceram Int 43:17041–17047. https://doi.org/10.1016/j.ceramint.2017.09.116
89. Balaji R, Kumar S, Reddy KL, Sharma V, Bhattacharyya K, Krishnan V (2017) Near-infrared driven photocatalytic performance of lanthanide-doped NaYF$_4$@CdS core-shell nanostructures with enhanced upconversion properties. J Alloys Compd 724:481–491. https://doi.org/10.1016/j.jallcom.2017.07.050
90. Feng P, Pan Y, Ye H (2018) Core-shell structured NaYF$_4$:Yb, Tm@CdS composite for enhanced photocatalytic properties. RSC Adv 8:35306–35313. https://doi.org/10.1039/c8ra06800c
91. Li C, Wang F, Zhu J, Yu JC (2010) NaYF4:Yb, Tm/CdS composite as a novel near-infrared-driven photocatalyst. Appl Catal B Environ 100:433–439. https://doi.org/10.1016/j.apcatb.2010.08.017
92. Peng S, Huang Y, Li Y (2013) Rare earth doped TiO$_2$-CdS and TiO$_2$-CdS composites with improvement of photocatalytic hydrogen evolution under visible light irradiation. Mater Sci Semicond Process 16:62–69. https://doi.org/10.1016/j.mssp.2012.06.019
93. Ullah S, Ferreira-Neto EP, Hazra C, Parveen R, Rojas-Mantilla HD, Calegaro ML, Serge-Correales YE, Rodrigues-Filho UP, Ribeiro SJL (2019) Broad spectrum photocatalytic system based on BiVO$_4$ and NaYbF$_4$:Tm^{3+} upconversion particles for environmental remediation under UV-vis-NIR illumination. Appl Catal B Environ 243:121–135. https://doi.org/10.1016/j.apcatb.2018.09.091
94. Liu X, Di W, Qin W (2017) Cooperative luminescence mediated near infrared photocatalysis of CaF$_2$:Yb@BiVO$_4$ composites. Appl Catal B Environ 205:158–164. https://doi.org/10.1016/j.apcatb.2016.12.027
95. Huang S, Zhu N, Lou Z, Gu L, Miao C, Yuan H, Shan A (2014) Near-infrared photocatalysts of BiVO$_4$/CaF$_2$:Er^{3+}, Tm^{3+}, Yb^{3+} with enhanced upconversion properties. Nanoscale 6:1362–1368. https://doi.org/10.1039/c3nr05266d
96. Shan L, Liu Y (2016) Er3+, Yb3+ doping induced core-shell structured BiVO$_4$ and near-infrared photocatalytic properties. J Mol Catal A Chem 416:1–9. https://doi.org/10.1016/j.molcata.2016.02.013

97. Huang J, Tan G, Zhang L, Ren H, Xia A, Zhao C (2014) Enhanced photocatalytic activity of tetragonal $BiVO_4$: Influenced by rare earth ion Yb^{3+}. Mater Lett 133:20–23. https://doi.org/10.1016/j.matlet.2014.06.123
98. Obregón S, Colón G (2015) On the origin of the photocatalytic activity improvement of $BIVO_4$ through rare earth tridoping. Appl Catal A Gen 501:56–62. https://doi.org/10.1016/j.apcata.2015.04.032
99. Anwer H, Park JW (2019) Near-infrared to visible photon transition by upconverting $NaYF_4$: Yb^{3+}, Gd^{3+}, Tm^{3+}@Bi_2WO_6 core@shell composite for bisphenol A degradation in solar light. Appl Catal B Environ 243:438–447. https://doi.org/10.1016/j.apcatb.2018.10.074
100. Jinyun H, Yunpeng Z, Yanwu W (2020) Rare Earth Ion Yb^{3+} Doping of Bi_2WO_6 with Excellent Visible-light Photocatalytic Activity. J Wuhan Univ Technol Mater Sci Ed 35:348–355. https://doi.org/10.1007/s11595-020-2263-z
101. Zhang X, Wang M, Jia X, Cao K, Zhang M (2019) Synthesis and enhanced photocatalytic activity of rare earth ion (Ce^{3+}, Nd^{3+}, Pr^{3+} or Sm^{3+}) doped Bi_2WO_6 microspheres for rhodamine B degradation. ChemistrySelect 4:12785–12793. https://doi.org/10.1002/slct.201903621
102. Shen Z, Li H, Hao H, Chen Z, Hou H, Zhang G, Bi J, Yan S, Liu G, Gao W (2019) Novel Tm^{3+} and Yb^{3+} co-doped bismuth tungstate up-conversion photocatalyst with greatly improved photocatalytic properties. J Photochem Photobiol A Chem 380:111864. https://doi.org/10.1016/j.jphotochem.2019.111864
103. Cushing SK, Li J, Meng F, Senty TR, Suri S, Zhi M, Li M, Bristow AD, Wu N (2012) Photocatalytic activity enhanced by plasmonic resonant energy transfer from metal to semiconductor. J Am Chem Soc 134:15033–15041. https://doi.org/10.1021/ja305603t
104. Wang Y, Zhu Y, Yang X, Shen J, Zhu J, Qian S, Li C (2017) Plasmonic Au decorated single-crystal-like TiO_2-$NaYF_4$ mesoporous microspheres for enhanced broadband photocatalysis. Chin J Chem 35:949–956. https://doi.org/10.1002/cjoc.201600771
105. Chang M, Wang M, Shu M, Zhao Y, Ding B, Huang S, Hou Z, Han G, Lin J (2019) Enhanced photoconversion performance of $NdVO_4$/Au nanocrystals for photothermal/photoacoustic imaging guided and near infrared light-triggered anticancer phototherapy. Acta Biomater 99:295–306. https://doi.org/10.1016/j.actbio.2019.08.026
106. Chen M, Wang JH, Luo ZJ, Cheng ZQ, Zhang YF, Yu XF, Zhou L, Wang QQ (2016) Facile synthesis of flower-shaped Au/$GdVO_4$: Eu core/shell nanoparticles by using citrate as stabilizer and complexing agent. RSC Adv 6:9612–9618. https://doi.org/10.1039/c5ra23958c
107. Gao Y, Shi C, Feng J, Zhao G, Yu H, Bi Y, Ding F, Sun Y, Xu Z (2017) Synergistic effect of upconversion and plasmons in $NaYF_4$:Yb^{3+}, Er^{3+}, Tm^{3+}@TiO_2–Ag composites for MO photodegradation. RSC Adv 7:54555–54561. https://doi.org/10.1039/c7ra09368c
108. Tian Q, Yao W, Wu W, Liu J, Wu Z, Liu L, Dai Z, Jiang C (2017) Efficient UV-Vis-NIR responsive upconversion and plasmonic-enhanced photocatalyst based on lanthanide-doped $NaYF_4$/SnO_2/Ag. ACS Sustain Chem Eng 5:10889–10899. https://doi.org/10.1021/acssuschemeng.7b02806

Chapter 10
Enhancement of Singlet Oxygen Generation of Radachlorin® Conjugated with Polyvinylpyrrolidone and Nanodiamonds in Aqueous Media

Yuri V. Kulvelis, Vasily T. Lebedev, Natalia P. Yevlampieva, Daniil S. Cherechukin, and Elena B. Yudina

Abstract Catalytic complexes of photosensitizer Radachlorin® (sodium salts of chlorin e_6, chlorin p_6, purpurin 5) with polyvinylpyrrolidone (PVP) and detonation nanodiamonds (DND) have been synthesized and studied by optical absorption spectroscopy, luminescence excitation, dynamic light scattering and viscometry methods. Binary complexes PVP-Radachlorin® demonstrated electrostatic and donor–acceptor binding of Radachlorin® with PVP detected by spectrophotometric titration when Q-band (~ 650 nm) displayed bathochromic shift and enhancement with isosbestic point indicating a single type of binding sites. Similar changes in luminescence emission spectra in binary complexes were observed earlier at higher polymer contents. The yield of singlet oxygen under UV-irradiation (405 nm) of Radachlorin® increased in PVP-Radachlorin® complex. Dynamic light scattering and viscometry confirmed the stability of complexes and no agglomeration. Ternary complexes DND-PVP-Radachlorin® provided a generation of singlet oxygen by UV-irradiation exciting diamonds which do not emit but transfer the energy to surrounding molecules. The results allow develop effective catalysts for chemical and medical applications as well as for disinfection, active filtration and cleaning

---

Y. V. Kulvelis (✉) · V. T. Lebedev
Petersburg Nuclear Physics Institute Named By B.P.Konstantinov, NRC "Kurchatov Institute", Gatchina, Leningrad distr, Russia
e-mail: kulvelis_yv@pnpi.nrcki.ru

V. T. Lebedev
e-mail: lebedev_vt@pnpi.nrcki.ru

N. P. Yevlampieva · D. S. Cherechukin
Saint Petersburg State University, Saint Petersburg, Russia
e-mail: n.yevlampieva@spbu.ru

D. S. Cherechukin
e-mail: st054874@student.spbu.ru

E. B. Yudina
Ioffe Institute, Saint Petersburg, Russia
e-mail: yudina@mail.ioffe.ru

S. Garg and A. Chandra (eds.), *Green Photocatalytic Semiconductors*,
Green Chemistry and Sustainable Technology,
https://doi.org/10.1007/978-3-030-77371-7_10

air, water, surfaces. Novel catalytic complexes based on chemically inert diamonds are resistant to the singlet oxygen and profitable for long-term usage.

Keywords Catalyst · Complex · Polymer · Nanodiamond · Singlet oxygen · Photodynamic therapy · Photosensitizer

10.1 Introduction

Progress of photocatalytic methods for solving tasks of water and air cleaning, efficient disinfection and medical applications in photodynamic therapy makes it necessary to extend a variety of new substances possessing high activity induced by UV or X-ray radiation [1–5]. In many cases, such substances are hybrid structures involving nanoparticles, quantum dots and molecular components [6–8].

Among most promising objects are the structures which can produce a generation of singlet oxygen in surrounding media as a result of optical, UV or X-ray excitation of these structures being able to transfer the energy to molecular oxygen existing normally in triplet state. This is especially profitable method for the enhancement of molecular oxygen chemical activity in aqueous media without its ionization while it exists a problem to achieve the highest quantum yield of singlet oxygen via photosensitizer excitation by external irradiation [9, 10]. Actually, it is important to search possible ways to achieve a gain in photosensitizers' efficiency by means of complexes formation with polymers and nanoparticles. Some attempts in synthesis of such structures promise really significant improvement in their functional properties, especially in quantum yield, solubility in aqueous media, etc.

A deposition of molecular catalysts on nanocarriers may solve some problems of improving their efficiency, e.g., provide maximal interface between catalyzer and surrounding medium, prevent irreversible coagulation of catalyst and at last stimulate its activity due to the interaction with the surface of carriers [11]. Moreover, the carriers may play the role of converters of X-rays energetic and highly penetrating water media and biological tissues when such a radiation is absorbed with secondary emission of optical quants for excitation of sensitizers then serving for generation of singlet oxygen [12]. It is requested also that these carriers associated with sensitizer molecules would be chemically stable in aggressive media saturated with singlet oxygen.

A search of candidates for durable and effective carriers allowed us choose polyvinylpyrrolidone and nanodiamonds as most suitable components to prepare binary and triple complexes with Radachlorin® being a good photosensitizer and then to test optical and photocatalytic properties of such new structures. The main component of Radachlorin® is the compound chlorin e6 (short notation below e6) belonging to the class of chlorins (Fig. 10.1).

Primarily, the aim of our work was devoted to the development of the methods of complexes preparation and then the determination their stability conditions as defined by the composition and the characteristics of components. In following

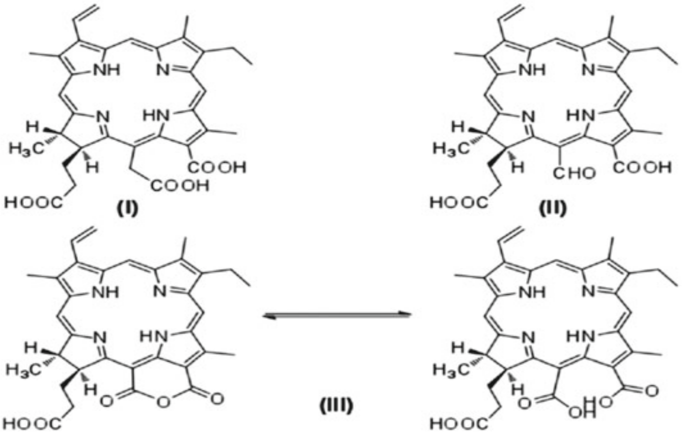

Fig. 10.1 Chemical structure of representatives of the class of chlorins (Radachlorin® composition): chlorin e6 (I), purpurin 5 (II) and purpurin 18 - chlorin p6 (III)

experiments, we studied physical and chemical features of complexes in aqueous solutions in relation to their structure and optical properties by the activation using UV.

The e6 and its derivatives, salts and complexes are of practical interest as effective photosensitizers (PS) and these objects are intensively studied [13–18]. This is associated not only with finding ways to improve the efficiency of PS, but with widening the PDT method to treat various types of cancer, large and deeply located tumors [9]. The e6 (Fig. 10.1I) as a derivative of chlorophyll satisfies the properties of medical PS.

The compound e6 is already used in practical PDT as a part of Radachlorin® and Photolon® preparations. Due to its availability, the e6 is a convenient object for modification. Therefore, numerous publications are dedicated to the second-generation of PS based on e6. The chemical structure of e6 allows relatively simple ways to modify it by replacing the peripheral groups of the macrocycle. This makes it possible to alter both the absorption spectrum of e6 derivatives and the Stokes shift of the luminescence [13, 15–17]. The luminescence intensity and the Stokes shift of e6 and its derivatives in aqueous media are influenced by pH, ionic strength and ionic composition, as well as the magnitude and sign of the total charge of molecules [17, 18]. So, the cationic and anionic salt forms of chlorins differ in luminescent properties; e.g., the study [18] showed the effect of the structure of peripheral substituents in the macrocycle on the photo-induced antitumor activity of e6. It has been established that positive charging e6 macrocycle due to the terminal groups reduces the intracellular accumulation of PS and photo-induced cytotoxic effect on tumor cells of various origins. On the other hand, negatively charged peripheral groups of e6 derivatives in aqueous media enhance the effectiveness of such compounds as PS for PDT. Thus, the sign of the charge of amphiphilic chlorines in water is important for their antitumor activity. Unfortunately, it was not possible to obtain a significant increase in the efficiency of e6 as PS by covalent grafting terminal groups of different chemical structures. However, the properties of PS can be improved by their non-covalent modification, i.e., through complexing this dye with carbon nanoparticles and biocompatible polymers. Biologically inert carbon nanoparticles soluble in aqueous media are desirable for biomedical applications by their multifunctionality, including the field of PDT [19]. Fullerenes and their derivatives are also of particular interest for PDT because of their ability to generate singlet oxygen, super-oxides, oxygen radical anions.

However, fullerenes weakly absorb light in the red spectral range being most important for PDT. A formation of complexes of fullerenes with dyes that absorb red light was the subject of studies [20–22]. These successful works have enabled to create stable non-covalent complexes of water-soluble fullerene derivatives with dyes, which absorb light and transfer either excitation or electron to the fullerene. Finally, there was created a new PS for PDT (Photosens® preparation) based on a complex of water-soluble fullerene derivatives with xanthene dyes and a water-soluble phthalocyanine derivative [20–22].

It was reported also a formation of complex of cationic fullerene derivative C_{60} with e6 in aqueous and ethanol solutions [23] due to the electrostatic interaction of the components. The efficiency of complexation and the structure of the complexes depended on the polarity of the medium. The presence of fullerene in binary complexes caused a decrease of luminescence of e6 as in the case with other dyes [20–22]. Luminescence quenching was associated with the efficient transfer of electron from the dye in excited singlet state to fullerene cage [23]. Thus, fullerene derivatives in aqueous solutions mainly quench a luminescence of dyes and a generation of singlet oxygen by them. Therefore, such systems need a third component to increase efficiency, which was actually implemented in the case of the Photosens® preparation. This is necessary also as far as a formation of complex in aqueous medium leads to an aggregation when several molecules of dye associate with a fullerene derivative. The fullerene components are partially hydrophobic and their molecules trend to be assembled in aquatic environment. Along this, large macrocyclic tetrapyrrole PS molecules (Fig. 10.1), like many other cyclic compounds with conjugated bonds, even those that dissolve well in water, are characterized by a formation of various associates, dynamic or stable aggregates in solutions [24, 25]. For example, the aggregation of porphyrin molecules is accompanied by an energy transfer between macrocycles that leads to not radiative deactivation of the triplet excited state. So, the effectiveness of porphyrins as PS is significantly reduced [24]. In this case, linking biocompatible polymers with PS molecules (Fig. 10.1) may serve for their better dispersion in aqueous media to prevent the aggregation.

The choice of biocompatible synthetic polymers, which aqueous solutions of can be stored for a long time without changing initial properties, is not large. Therefore, studies carried out in this direction concerned a limited number of polymers [26]. These include polyvinyl alcohol, polyvinylpyrrolidone (PVP), polyethylene oxide (PEO) and its copolymers (e.g., Pluronic), carboxymethylcellulose. When studying joint solutions of these non-luminescent polymers with PS, it was found that polymers improve the stability, molecular dispersion of aqueous solutions of dyes and increase their luminescent properties.

For a number of PS-polymer systems at certain ratios of components in solutions, there was experimentally shown the increase in PS absorption, intensity of luminescence and phosphorescence of singlet oxygen [27–29]. In particular, it was demonstrated for porphyrin series: Dimegin (3,8-di (1-methoxy-ethyl) deuteroporphyrin IX), Photoditazine® (N-methyl-di-D-glucamine salt of chlorin e6), tetrafluorophenyl porphyrin (tetracesium salt of 5,10,15,20-tetrakis [4- (1′-carba-closo-dodecar-boran-1′-yl)tetrafluorophenyl] porphyrin) [28]. The gain in photosensitizing activity of these PSs due to the presence of polymers was detected [28]. Such "polymer effect" was explained by a formation of complexes of amphiphilic polymers with PS and preventing the aggregation of PS molecules. The toxicological tests showed a possibility to reduce by an order the therapeutic dose of porphyrin PS by its complexing with biocompatible polymers.

Complexation between PS and polymers was studied for Radachlorin®-PVP system as an example, where, at a certain ratio of components in solution, the increase in PS absorption in the red spectral range and the amplification of singlet oxygen phosphorescence were observed [30–32]. Radachlorin® contains mostly e6 (80–90%) forming non-covalent inclusion complex with PVP that prevents e6 aggregation in aqueous media [30–32].

Despite a number of publications devoted to the e6-PVP binary systems [27–32], their results are rather difficult to compare, since the studies are performed in different concentration ranges of components, by varying their proportions in different solvents, pH values and ionic strengths of solutions, degrees of PVP polymerization. For example [32], a multicomponent phosphate buffer was used and the measurements were carried out mainly in water with addition of various low molecular electrolytes. The concentration range where it was recorded a complexation between PVP and e6 was also different, and the weight ratio between the components varied from 1:1 to 1:10.

In our work with e6-PVP complexes and ternary systems with detonation nanodiamonds (DND), we have chosen the conditions closest to physiological ones (the aqueous medium 0.15 M NaCl (0.9% NaCl), pH 6.2).

10.2 Experimental

10.2.1 Samples and Methods

In the first part of the study, we prepared the complexes of sensitizer Radachlorin® (e6) with polyvinylpyrrolidone (PVP) by mixing their aqueous solutions containing NaCl (0.9 wt.%, isotonic solution) at ambient temperature with the following sonication. The e6 component is produced by "RADAPHARM LLC," (Radachlorin®, content of e6 ~90%) and the polymer is manufactured by

Shanghai Yuking Water Soluble Materials Tech. Co. Ltd. (trademark PVPK-17 (EP 8.0), molecular weight $M_W = 9000$). The PVP powder was dissolved in deionized water or isotonic aqueous solvent (0.15 M NaCl) during 24 h by periodic mixing.

Since e6 belongs to the dyes, we used mostly optical methods to study the complexes of e6 with PVP and DND in solutions and carry out the measurements of electron absorption and luminescence spectra in combination with viscometry and dynamic light scattering (DLS). The spectrophotometer UNICO 2800 UV/VIS (UNICO, USA) has served for spectra recording in the range of wavelengths 190–1100 nm for the samples in quartz cells (thickness 10 mm). The luminescence data were registered by fluorimeters Shimadzu RF-6000 (Japan) and Fluorolog-3 (Horiba Jobin Yvon, Israel) (cells of 4 and 10 mm) delivered by Centre for optical and laser materials research, St. Petersburg State University. The optical data were treated as dependent on the hydrodynamic properties characterizing possible self-assembly of molecular systems and dispersions at submicron scale. To examine these properties at ambient temperature (298 K), we carried out the measurements of intrinsic viscosity and Huggins' constant of the samples on the viscometer Lovis-200 M/ME ("Anton Paar", Austria) by Heppler's method using the capillary inclined by the angle of 50°. The structuring solutions was tested by dynamic light scattering ("Photocor Complex," wavelength of incident light 445 nm, St. Petersburg State University, Centre for diagnostics of functional materials for medicine, pharmacology and nanoelectronics).

10.3 Results and Discussions

10.3.1 Binary Complexes of Sensitizer with Polymer

10.3.1.1 Light Absorption and Luminescence

Preliminarily we have measured the electron absorption spectra of e6 sensitizer as a main component at different contents in aqueous solutions, $C_{e6} = (0.299–0.820)10^{-5}$ g/cm^3 (Fig. 10.2). These data are in agreement with known spectra of this sensitizer [14].

In the visible range, the sensitizer demonstrates two characteristic absorption bands at 403 and 650 nm (Soret and Q-band) (Fig. 10.2). The positions of their maxima are dependent on molecular environment, pH, ionic strength of solution. Hence, watching the shift of the bands may give the information on the interactions of sensitizer with polymer (PVP) in solution. On the other hand, the excitation of e6 at the wavelength of its absorption maximum indices a high luminescence in the red region (Fig. 10.3). A bathochromic Stokes shift $\sim$15 nm is seen for the maximum of its luminescence spectrum (665 nm) relative to the absorption spectrum (Fig. 10.2).

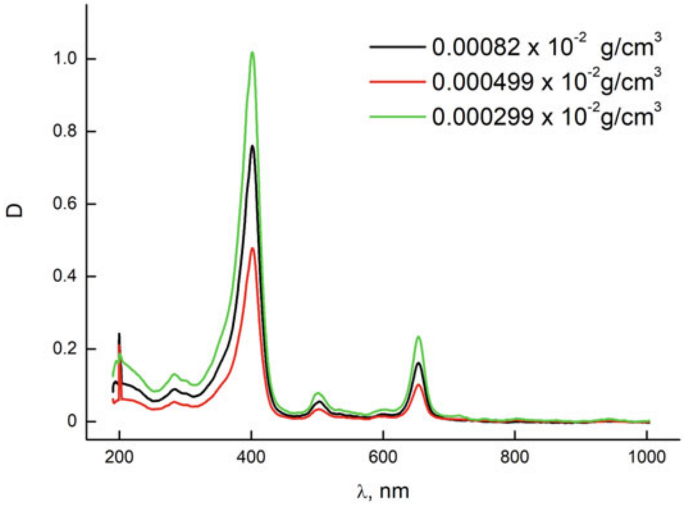

Fig. 10.2 Absorption spectra (optical density D vs light wavelength λ) of isotonic solutions at different concentrations of e6 sensitizer

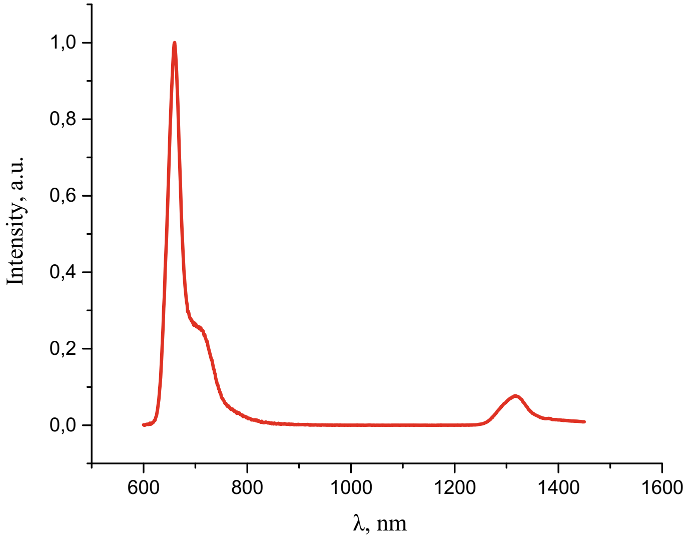

Fig. 10.3 Luminescence spectrum of e6 upon excitation at the wavelength of 405 nm in isotonic solution (0.15 M NaCl), concentration of 1.5×10^{-5} g/cm^3

The spectral and hydrodynamic properties of combined solutions of e6 and PVP were studied at 298 K in different concentration ranges. We tested the stability of the e6-PVP system in the range of polymer concentration from 0.003 to 10×10^{-2} g/cm^3 with a variation of the weight proportion e6:PVP in the range (1:1)–(1:50).

The effect of e6 binding with polymer was detected by the method of spectrophotometric titration (SPT) at the fixed e6 concentration (0.0015 wt.% = 2.54×10^{-5} M, molecular weight of 590 g/mol) and ambient temperature. SPT results at the constant concentration of e6 and by consistently changing the content of the polymer in their mixed solution are presented in Fig. 10.4. In the spectra of optical absorption, we observed mainly the changes in the Q-band ($\sim$650 nm) which demonstrated a bathochromic shift and a sharp growth of amplitude. A single crossing point of spectra confirmed one type centers of binding. From the results of SP-titration, we computed the binding parameters for e6 and PVP. These are the concentrations of e6 free and bonded (C_{FREE}, C_B) and a molar ratio of bonded e6 to PVP, $r = C_B/C_{PVP}$ (Fig. 10.5).

The plotted Scatchard isotherm $r/C_{FREE} = f(r)$ has revealed the behavior inherent in not cooperative binding. The resulting binding curve $r(C_{FREE})$ achieved the saturation level of r = 0.0037 that is one bound molecule of e6 per 270 chain units of PVP (Fig. 10.5). Since a PVP chain is of molecular weight $M_{PVP} \sim 9000$ and involves $\sim$80 units, it takes 3–4 chains to bind a molecule of e6. However, such association is not strong as far as at a given parameter *r* the amount of free sensitizer exceeded the bound fraction by 3 times (screening effect by counterions).

In following experiments, the luminescence in aqueous–salt solutions of pure e6 (0.0015 wt.%.) was recorded. Similar measurements were performed for complex e6-PVP at the excess of the polymer (C_{e6} = 0.0015 wt.%., C_{PVP} = 0.426 wt.%.) to guarantee the maximum degree of sensitizer binding (Fig. 10.6). We found that the excitation by radiation (wavelength 405 nm) has induced a luminescence corresponding to Q-band of absorption. The presence of PVP caused the shift and

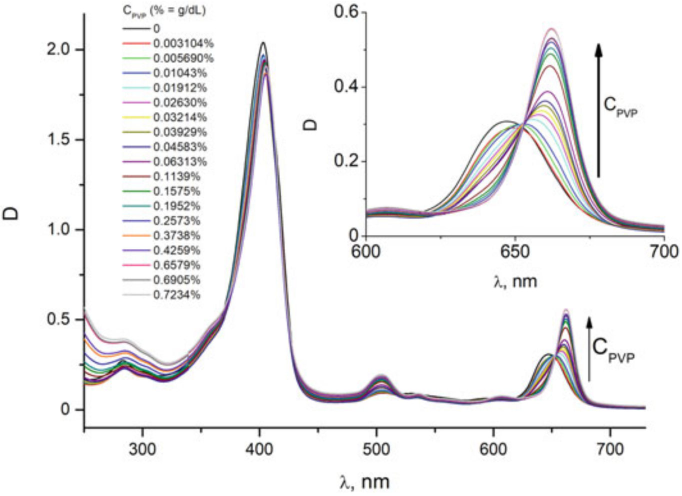

Fig. 10.4 Measurements of optical density $D(\lambda)$ vs light wavelength (λ). Change in the absorption spectrum of e6 (content 1.5×10^{-5} g/cm^3) by a sequential increase of PVP concentration, $C_{PVP} = 0.0{-}0.7234 \times 10^{-2}$ g/cm^3, in mixed solutions (0.15 M NaCl)

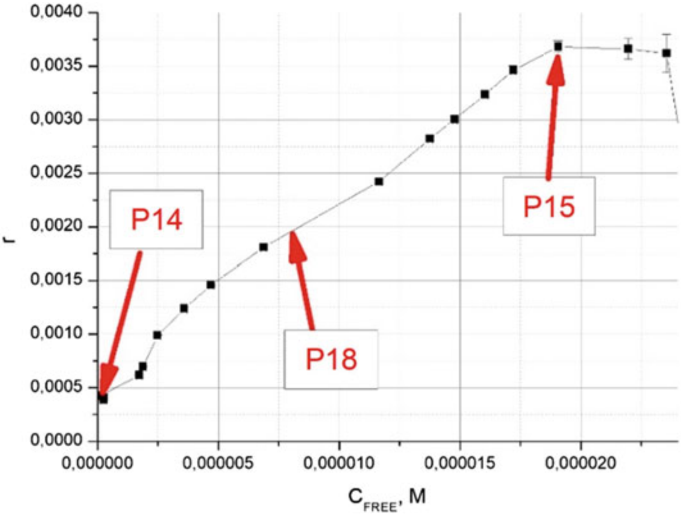

Fig. 10.5 Binding curve: bound e6 amount relative to PVP content vs. molar concentration of free e6. Characteristic samples P14, P18, P15 with low, intermediate and high fraction of free e6 molecules are indicated (weight ratios of components e6:PVP = 1:50; 1:25; 1:10)

substantial increase of peak's amplitude. Worth to mention, in medical procedures the UV radiation penetrate tissues weakly, but it can be generated by some scintillators excited by X-rays. Then, following luminescence of e6 will transfer molecular oxygen to an excited singlet state.

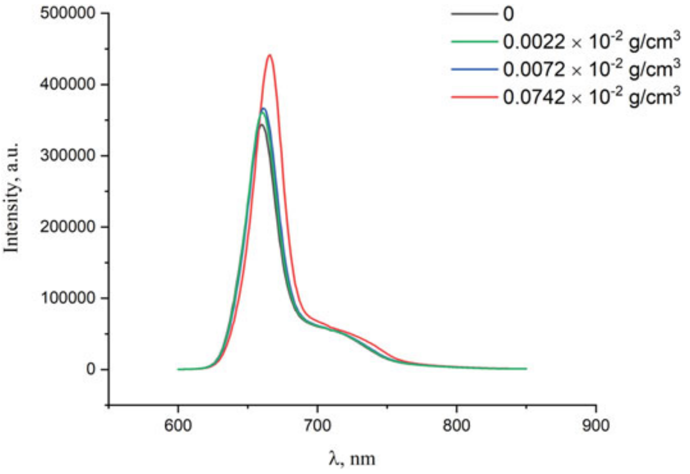

Fig. 10.6 Main band shift in the luminescence spectrum for e6-PVP complex (luminescence excited at $\lambda = 405$ nm). Variation in the PVP content, $C_{PVP} = 0.0–0.0742 \times 10^{-2}$ g/cm^3, at the fixed e6 concentration of 1.5×10^{-5} g/cm^3

A fixed concentration of e6 in this study was chosen two or more times lower than in the works cited above. A weight ratio of the e6:PVP components was varied from 1:1 to 1:50. From the data presented in Fig. 10.4 (in more detail in the inset), it is seen that starting from a cert ain "threshold" of polymer concentration $\sim 0.01 \times 10^{-2}$ g/cm^3 (ratio e6:PVP $\sim$1:6), the Q-band of the absorption spectrum of e6 (650 nm) changes quite sharply. Its bathochromic shift by 10 nm with a substantial increase in intensity is found, while the intensity of the main absorption band decreases insignificantly.

A shift of the Q-band in the spectrum of e6 (Fig. 10.6) depends on the ratio e6:PVP and increases with the PVP amount. Similar changes in the absorption were detected in the systems based on e6 derivatives and PVP of different molecular weights (5000–25,000 g/mol) [28, 33]. A convincing explanation for this phenomenon has been found. The reason for the observed changes is in the nature of e6 as an amphiphilic compound (Fig. 10.1). In aqueous media even at micromolar concentrations $\sim 10^{-5}$–10^{-6} M, it forms associates to minimize interaction of hydrophobic parts of molecules with a solvent. In [26–28], using a combination of spectral methods and ^{1}H NMR, it was shown that a bathochromic shift of the Q-band in the spectrum is associated with a destruction of e6 associates due to the interaction of PVP with hydrophobic parts of e6 molecules. The increase in the absorption at $\lambda \sim 665$ nm (Fig. 10.4) is explained by a growth of the number of the e6 molecules non-interacting with each other in solution. The authors [30–32] showed that e6-PVP complexes are stable due to dye encapsulation by the polymer. The interactions of the components in e6-PVP complex are electrostatic and donor–acceptor type, depending on environmental conditions [32]. The dipole–dipole interactions of the components and the formation of hydrogen bonds between them were noted [28, 31].

The spectra (Fig. 10.4) are recorded in the solutions (0.15 M NaCl) where e6 may carry a negative charge, but PVP under these conditions should be neutral. However, due to the donor–acceptor interaction of PVP with e6, polymer coils may become partially charged. In this case, the aggregation begins in the solution, if the ionic strength of the solvent is not enough to compensate electrostatic interactions of charged objects.

The interaction of e6 with PVP affects the luminescent properties of the dye (Fig. 10.6, Shimadzu RF-6000). It is observed a shift of the main luminescence band in the e6-PVP solutions at the constant amount of dye while varying the weight ratio e6:PVP from 1:1.5 to 1:50 (Fig. 10.6).

In the solutions of complexes, the emission spectrum maximum demonstrates a bathochromic shift in comparison with e6 solution. The effect grows with the polymer concentration, as does the luminescence intensity. This confirmed the interaction of the electronic systems of PVP and e6. The intensity increase is explained by disaggregation (monomerization) of e6 molecules due to their encapsulation by the polymer. In general, these data are consistent with the results previously published, although we used the region of lower (micromolar) dye concentrations for the formation of complexes.

In these experiments, a special interest is associated with the detection of the phosphorescence of singlet oxygen in e6 aqueous solutions, but it is complicated by the fact that the second-order maximum in the luminescence spectra of the dye falls on the same λ-range (Fig. 10.3). To record the luminescence of singlet oxygen $^1O_2$, the KS19 filter was used to isolate its radiation. The e6 luminescence was excited at $\lambda = 405$ nm. The recorded spectra of $^1O_2$ in solutions of e6 and e6-PVP in 0.15 M NaCl (Figs. 10.7, 10.8) have a maximum at $\lambda = 1271$ nm in accordance with the data [18, 23, 31–34]. Spectra (Fig. 10.7) demonstrate that the presence of PVP stimulates the luminescence of $^1O_2$ comparative to initial solution of e6 of the same concentration fixed in the experiment. The data presented in Fig. 10.8 were obtained when the fraction of e6 was varied from 0.0007 to 0.00758 10^{-2} g/cm^3 and the weight ratio e6:PVP was changed from 1:1.5 to 1:56.

The spectra in Figs. 10.7, 10.8 display a generation of singlet oxygen in aqueous solutions of e6 and complexes e6-PVP when the data are dependent on the dye concentration. The fluorescence peak has the highest amplitude at low dye concentrations $\sim(0.0015–0.0018) \times 10^{-2}$ g/cm^3 when its molecules are mostly disaggregated (Fig. 10.9, data 1). The presence of polymer in weight proportion e6: PVP from 1:2 to 1:56 (Fig. 10.9, data 2) stimulates a disaggregation of e6 molecules which cause a generation of singlet oxygen in mixed solution. In Fig. 10.9 (data 2) four points on the curve near the maximum correspond to the ratio e6:PVP in the range from 1:47 to 1:50.

Summarizing the spectral data, we conclude PVP complexing with e6 that is revealed in a bathochromic shift of the dye main luminescence band. This stimulates the emission from the dye and a following generation of singlet oxygen in the environment. Such polymer-dye complexes are stable over time in various solvents, including aqueous ones. Meanwhile, the solutions of e6-PVP are multicomponent and contain also free PVP and unbound dye molecules. The latter may violate the stability of systems by changing conditions.

All the spectral phenomena considered above are dependent on the concentration of PVP which serves as a regulator enhancing the activity of e6 being PDT

Fig. 10.7 Luminescence spectra of singlet oxygen in solutions of e6-PVP at fixed content of e6 and by variation of PVP amount in aqueous solution (0.15 M NaCl), $C_{PVP} = 0$ (*1*), 0.022 (*2*), 0.037 (*3*) and 0.074 × 10^{-2} g/cm^3 (*4*)

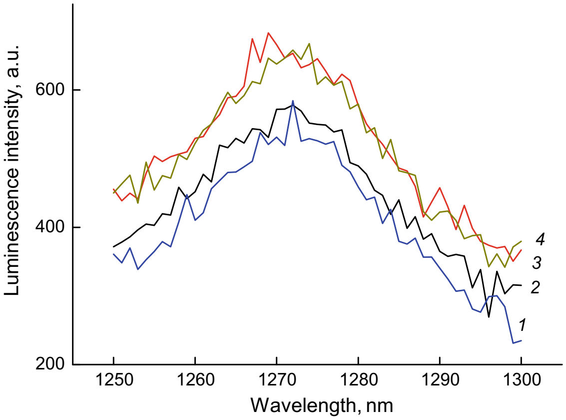

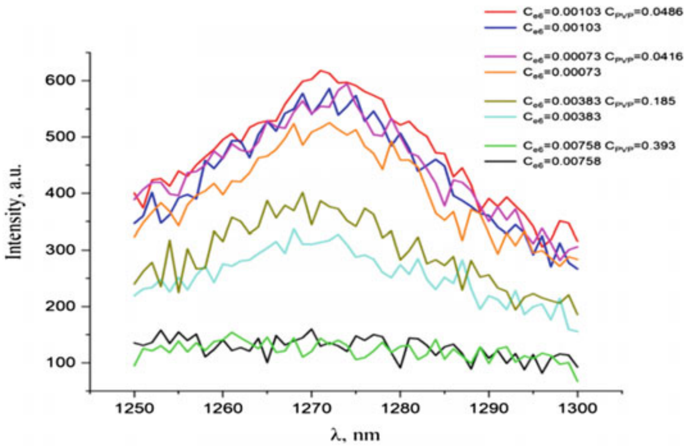

Fig. 10.8 Luminescence spectra of singlet oxygen in aqueous solutions (0.15 M NaCl) of e6 and complexes e6-PVP with different fractions of components in units of 10^{-2} g/cm^3

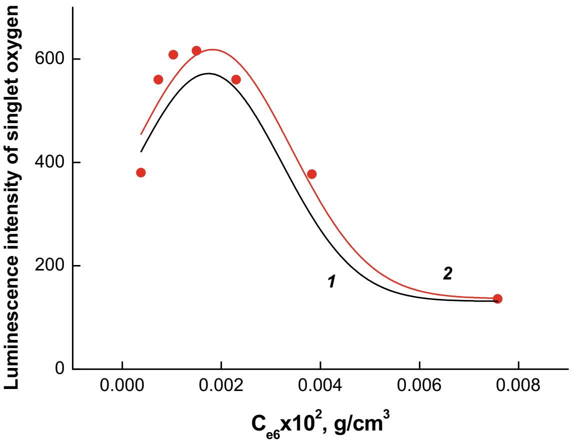

Fig. 10.9 Dependence of singlet oxygen luminescence intensity on the concentration of e6 (1) and e6-PVP complexes (2) in aqueous solutions (0.15 M NaCl)

sensitizer. Indeed, the intensity of luminescence of e6 increases in the concentration range where complexation occurs between the components.

For the chosen solvent (0.15 M NaCl) and the dye concentration ~1 × 10^{-5} g/cm^3, complexation begins at the weight ratio e6: PVP = 1:6. In this work, we discovered most favorable range of dye concentrations and optimal proportion e6: PVP for singlet oxygen generation in aqueous system (0.15 M NaCl). We found rather narrow range of e6 concentrations (0.0015–0.0018) × 10^{-2} g/cm^3 and desirable e6:PVP weight ratio interval from 1:47 to 1:50. Presently, such data are not demonstrated in the literature which may be due to real problems in the determination of complexes formation conditions and some difficulties in recording luminescence spectra of singlet oxygen.

The obtained results showed a significance of application of biocompatible PVP to gain a therapeutic activity of e6 along with a reduction of its dose in PDT practice that is relevant in pharmacology (Photolon®, Belarus). Our results are in agreement with the data obtained for other sensitizers (Photoditazine®, pure chlorine e6) by using PVP of different molecular weights and varying exciting radiation characteristics [28, 31, 32, 35–37].

10.3.1.2 Hydrodynamic Properties of Complexes e6-PVP

Since the medical aspects of PS complexes applications in solutions require reliable knowledge of their stability limits, it was important to test the hydrodynamic behaviors of these multicomponent systems at the concentrations exceeded than that used in spectroscopy. In polymer solutions, the main hydrodynamic parameters are viscosity characteristics and particles' dimensions estimated from translational diffusion coefficients in dynamic light scattering experiments (DLS). For the tests, we prepared the systems P14, P15, P18 having a weight ratio of components e6: PVP = 1:50; 1:10; 1:25. As mentioned above, in these systems, only a part of e6 molecules is involved in the complex with PVP, while some of them remain free (Fig. 10.5). The fraction of e6 molecules bound to PVP was estimated from spectrophotometric titration data (Fig. 10.4). The data analysis showed that for the ratio e6: PVP = 1:10, a part of free e6 molecules is higher than at the proportion e6: PVP = 1:50. This is a result of e6 monomerization in the presence of PVP when more dye molecules are disaggregated at higher amounts of polymer in the solutions. In solutions P14, P15 and P18 at a given temperature (T) and solvent viscosity η_s, the intrinsic viscosity $[\eta] = \lim_{c\to 0}(\eta_{sp}/c)$, the coefficients of translational diffusion $D_o = \lim_{c\to 0} D_t$ and hydrodynamic radii of particles $R_h = k_B T/6\pi\eta_s D_o$ were measured, where k_B is Boltzmann constant.

The viscosity measurements (298 K, Fig. 10.10) show clearly linear concentration dependences of the reduced viscosity (η_{sp}/c) in two-component solutions of P14 and P18, and the data for them are close to each other. The $[\eta]$ values for the complexes are somewhat higher than similar parameter for pure PVP. The slopes of the dependencies in Fig. 10.10 (Huggins' constants) for PVP and complexes P14, P18 complexes are different also. These deviations indicate some changes in the thermodynamic quality of the solvent for polymer in the presence of e6. On the other hand, from the data one may conclude about complexes stability in solution. The latter is supported by the increase of $[\eta]$ in the systems with complexes comparative to pure polymer. Thus, viscometry is sensitive to changes of PVP conformation even at a low content of e6, as in solutions of P14 and P18 (Fig. 10.10).

Worth to note that the $[\eta]$ values obtained for P14 and P18 complexes confirm the absence of large aggregates in solutions. On the other hand, the P15 solution is unstable and exfoliates at the polymer concentrations above 1×10^{-2} g/cm^3. Therefore, it was possible to make evaluative measurements only after it was diluted to low polymer concentrations. This indicated an insufficient amount of

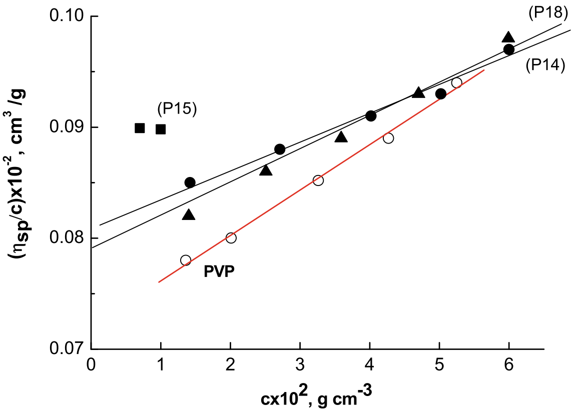

Fig. 10.10 Concentration dependence of reduced viscosity (η_{sp}/c) at 25 °C for PVP and complexes P14, P18, P15 in aqueous solutions (0.15 M NaCl), obtained at different weight ratios e6:PVP (r = 1/2500 (P14), r = 1/500 (P18) and r = 1/270 (P15))

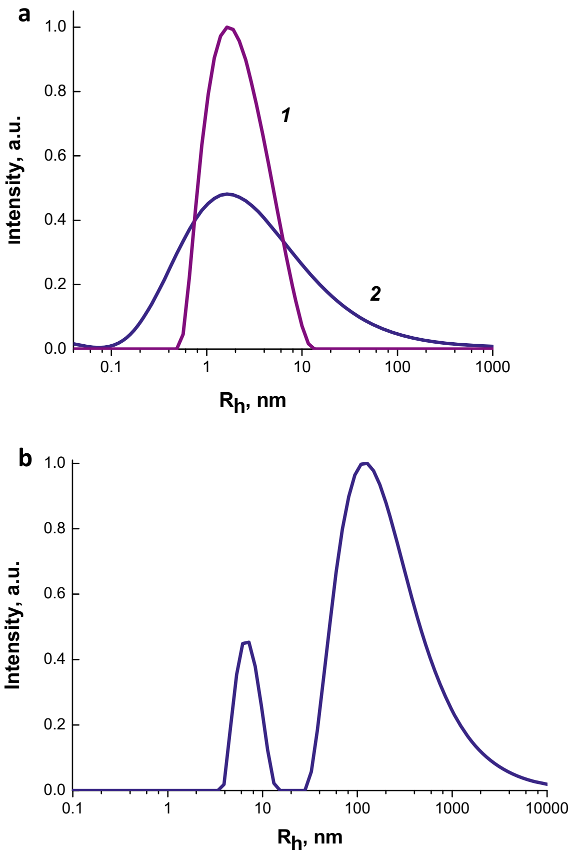

Fig. 10.11 Normalized volume fractions of particles vs. hydrodynamic radii: **a** data for PVP (1) and P14 (r = 1/2500) (2) at PVP concentration of 2 × 10^{-2} g/cm^3 in aqueous solution (0.15 M NaCl) (scattering angle 90°), **b** similar data for P15 (r = 1/270) in the same solvent at PVP concentration of 0.33 × 10^{-2} g/cm^3 (scattering angle 60°)

polymer to stabilize e6 and the beginning of aggregation of complex particles in the P15 solution. The same result was obtained by the DLS data for the P15 solution (Fig. 10.11).

The DLS results for P14 (Fig. 10.11a) comparative to pure PVP indicate the absence of large aggregates of complex in the solution, while there is broadening in size distribution of particles in P14 solution against spectrum for PVP. Oppositely to this, the P15 solution demonstrates qualitatively different distribution (Fig. 10.11b). In addition to particles having the hydrodynamic radius $R_h \sim 2$ nm corresponding to PVP, the aggregates with $R_h \sim 100$ nm and larger particles appear.

Both methods showed the absence of large particles in the solutions of P14 and P18, which demonstrated stability and can be characterized as molecularly dispersed systems. On the other hand, the P15 system revealed a substantial instability due to the lack of PVP.

Finally, taking into account all the data obtained for the solutions containing e6-PVP complexes, we declare the condition of their stability at the concentrations $\sim(1–10) \times 10^{-2}$ g/cm^3 when per one e6 molecule should be $\sim$500 chain units of PVP (5–6 macromolecules of molecular weight $M_{PVP} = 9000$ g/mol).

Obviously, a large excess of polymer seems to be not satisfactory, and other ways are desirable to provide optimal state of e6 in aqueous solutions. For this purpose, we used the third component being detonation nanodiamonds (DNDs) having a small diameter $d_P \sim 4–5$ nm and carrying regulated positive or negative charge in aqueous media as dependent on the treatment [38–40]. DNSs as biologically inert carbon particles are currently attractive for applications in medicine and biotechnology [41, 42]. In recent years, interest in them has especially grown, since synthesis methods were developed that made them commercially available [43]. Since the duration of the formation of the diamond phase during detonation synthesis is very short, really large particles are not formed. According to X-ray diffraction analysis and electron microscopy data DNDs are rather uniform and have a size of 4–5 nm [43]. Unlike other carbon nanoparticles, for example fullerenes, DNDs are partially hydrophilic and form stable aqueous suspensions, where the size of aggregates depends on pH factor. The reason for this is the presence of various functional groups (H, OH, COOH) on the surface of nanoparticles modified by annealing. By changing the processing method, it is possible to obtain both positively or negatively charged DNDs [38, 44]. The unique hydrophilic surface of DND allows both covalent and non-covalent binding of various biologically active compounds to DND [41–43]. There are various ways to stabilize aqueous DND suspensions, including those using biocompatible polymers [40, 43]. Our following work is devoted to search optimal conditions to obtain stable optically active binary and ternary complexes, e6-DND and e6-PVP-DND, with advanced luminescent properties.

10.3.2 Binary and Ternary Complexes of Dyes with DND

10.3.2.1 Luminescence of e6-DND in Aqueous Solutions

First of all, the special tests of the effect of DND on the spectral-luminescent properties of e6 were carried out by introducing DND hydrosol into e6 aqueous solution (concentration 0.00149 × 10^{-2} g/cm^3). The results showed that DNDs quench e6 luminescence, and if the DND amount in the solution doubles, e6 luminescence intensity also decreases by about a factor of two (Fig. 10.12). Noteworthy, there is a small hypsochromic shift (2–5 nm) of main e6 luminescence band in the presence of DND, which is larger, the more DND particles are in the solution.

Similar result was obtained earlier [23] when the effect of fullerene derivative on the luminescence of e6 was detected. In the presence of carbon particles, these authors found also e6 luminescence quenching with a bathochromic rather than hypsochromic shift (as in our case) of e6 luminescence band. As a strong π-electron acceptor, fullerene molecule causes an effective transfer of an electron from the excited singlet state of e6 to itself that explains luminescence weakening. At the same time, the probability of non-radiative transitions (responsible for the generation of singlet oxygen) increases. The authors [23] concluded that a formation of non-fluorescent static complexes of e6 with carbon nanoparticles should gain the efficiency of PS based on such complexes.

The performed studies of partial effects of PVP and DND on e6 luminescence enabled us to create ternary complexes with finely regulated optical and hydrodynamic properties in aqueous solutions.

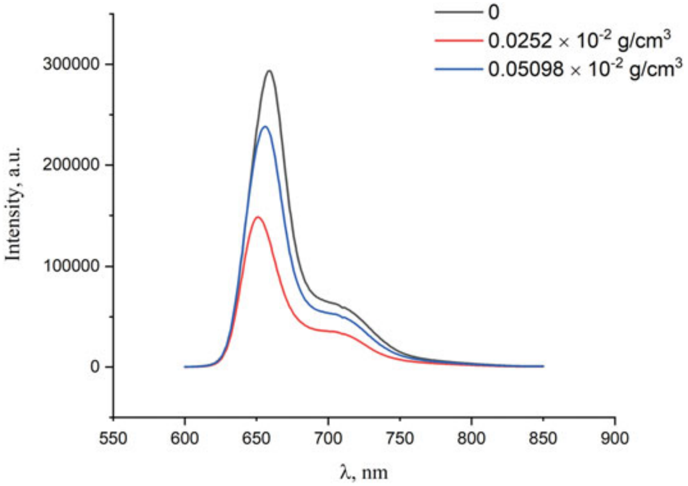

Fig. 10.12 Luminescence spectra of e6-DND aqueous solutions by varying DND content at fixed dye concentration, $C_{e6} = 0.00149 \times 10^{-2}$ g/cm^3

10.3.2.2 Ternary Systems E6-PVP-DND, Hydrodynamic Properties

The particles of PVP and DND have comparable sizes, $2R_h \sim 4$ nm, $d_P \sim 4.5$ nm, while the diamond particles are rigid and heavy and have molecular weight per one particle $M_{DND} \sim 1.0 \cdot 10^5$ g/mol by one order in magnitude higher than that for PVP, $M_{PVP} = 9000$ g/mol. Therefore, in aqueous systems with equal molar contents of PVP and DND, the number of diamond particles will be ten times lower than the amount of polymer chains. It was taken into account, and the mixtures of PVP and DND with desirable proportion of components were prepared initially. The e6 was introduced to prepared mixed solutions. We varied both the proportion between the numbers of PVP molecules and DND particles, $R = N_{PVP}/N_{DND}$, and the ratio of molar concentrations of e6 and PVP chain units, $r_o = C_{e6}/C_{PVP}$ (Table 10.1). The stability of the solutions of ternary complexes was tested by viscometry (Table 10.1).

Among ternary compositions with different parameters R and r_o, only the complex e6-PVP-DND-1 is stable in aqueous solution (0.15 M NaCl) (Table 10.1). Its parameters, intrinsic viscosity [η] and Huggins' constant k', as well as altering in [η] with temperature increase correspond to the molecular disperse system differing from the pure PVP (Table 10.1). Meanwhile, the system with e6-PVP-DND-2 exfoliates over time. Moreover, measurements of e6-PVP-DND-3 was almost impossible to carry out, because DNDs precipitated after the first dilution of the system.

While DLS in solutions of binary complexes e6-PVP showed mainly the presence of particles with the size of PVP molecules (Fig. 10.11), the ternary system e6-PVP-DND-1 exhibited the particles having the sizes ~4.5 and ~34 nm (Fig. 10.13) corresponding to PVP and complexes based on DNDs associated with the polymer.

Earlier [40], stable aqueous colloids of PVP-DND were examined by neutron scattering. It was shown that DND particles transferred from initial hydrosol to aqueous PVP solution formed stable aggregates of several particles surrounded by hydrophilic polymer. The average size of DND aggregates upon their stabilization by PVP in isotonic solvent was of 30–40 nm [40]. It is apparent in our case that the

Table 10.1 Hydrodynamic characteristics of PVP and ternary complexes e6-PVP-DND in aqueous solutions (0.15 M NaCl) at 25 and 37 °C: intrinsic viscosity [η], Huggins' constant *k*'

Sample	Composition R // (r_0)	[η] × 10^{-2}, cm^3 g^{-1}, 25 °C	k', 25 °C	[η] × 10^{-2}, cm^3 g^{-1}, 37 °C	k', 37 °C
PVP	–	0.072 ± 0.006	0.79 ± 0.05	0.066 ± 0.008	0.96 ± 0.05
e6-PVP-DND-1	10 // (1/2100)	0.081 ± 0.005	0.35 ± 0.05	0.078 ± 0.005	0.36 ± 0.05
e6-PVP-DND-2	0.5 // (1/3500)	0.126 ± 0.007	1.55 ± 0.09	0.127 ± 0.007	1.57 ± 0.09
e6-PVP-DND-3	0.3 //(1/200)	~0.05	~47	~0	>4000

*R is the number of PVP molecules per DND particle; $r_o = C_{e6}/C_{PVP}$ (both molar concentrations), and r_o shows the number of PVP chain units per e6 molecule

Fig. 10.13 DLS data for the complex e6-PVP-DND-1 in aqueous solutions (0.15 M NaCl): **a** reciprocal relaxation time 1/τ vs squared scattering vector q^2, linear approximation corresponds to complexes hydrodynamic radius R_h = 34 nm; **b** volume fractions of the objects observed in solution vs their radii (scattering angle 90°)

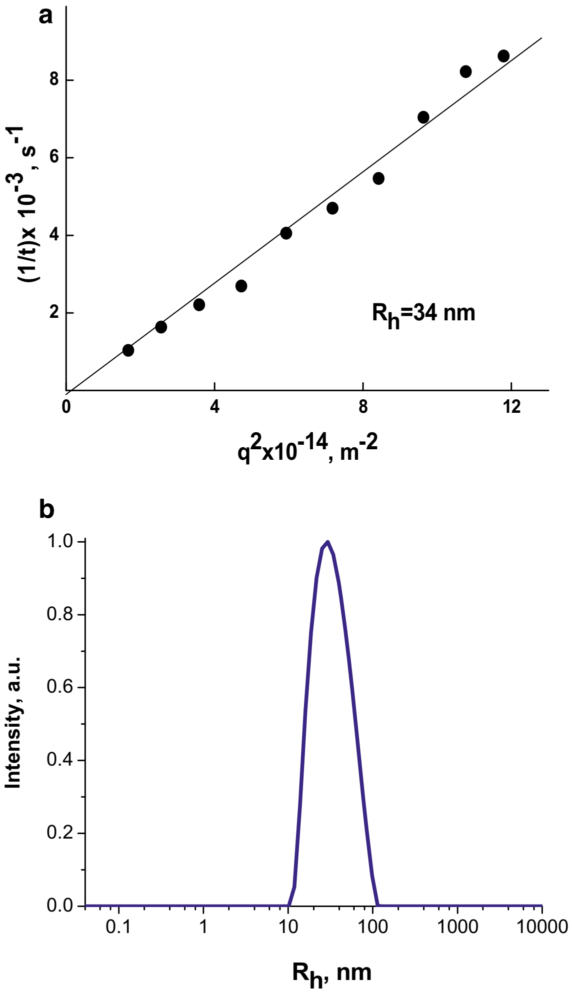

observed large particles in the complex e6-PVP-DND-1 are just similar hybrid particles, since aqueous colloid solutions of PVP-DND were prepared according to the procedure [40].

As we established, the particles of e6-PVP-DND-1 are stable and involved in diffusive motion in solution, as evidenced from linear dependence (Fig. 10.13) of reciprocal relaxation time on squared scattering vector modulus, $1/\tau \sim q^2$. This is confirmed also by normal course and slope of the dependence $\eta_{sp}/c = f(c)$ for the complex e6-PVP-DND-1.

From the medical point of view, such particles having diameter ~70 nm should not be hazardous for intravenous injection into the body and promise good prospects for biomedical applications [42].

Both hydrodynamic methods have shown very different behaviors of ternary complexes in solutions comparative to binary structures and demonstrated greatly enhanced degree of components' integration. The integration of DND into binary complexes caused substantial altering their optical properties.

10.3.2.3 Optical Absorption and Luminescence in Solutions of Ternary Complexes

The study of absorption spectra of stable ternary systems e6-PVP-DND in aqueous colloid solutions (0.15 M NaCl) showed a number of differences from binary systems. Figure 10.14 shows the Q-band of the absorption spectrum of e6 shifted first hypsochromically, by the increase of the concentration of PVP, C_{PVP} = (0.0–0.033) × 10^{-2} g/cm^3, and fixing a ratio for PVP/DND content, C_{DND} = (0.0–0.066) × 10^{-2} g/cm^3. Such opposite effect comparative to the data for binary complexes e6-PVP (Fig. 10.6) was observed in aqueous e6-DND systems (Fig. 10.12) shows a hypsochromic shift increasing with DND concentration. It seems, in the case of the lack of PVP in the system, most of dye molecules form complexes with the diamond surface directly since preferable molecular binding with PVP is limited. Larger amount of PVP makes the effect of Q-band splitting when both hypsochromic and bathochromic components are detected. At higher concentrations, only a single band is observed again but bathochromically shifted (Fig. 10.14). This bathochromic shift characterizes e6 binding to PVP in the presence of DND. However, in this case, it was impossible to calculate binding characteristics because of too large spectral contribution of light scattering on DND particles.

A shift of the Q-band towards lower wavelengths at low contents of DND and PVP can be explained by the fact of the interaction of e6 with the PVP-DND complex and with pure PVP proceeds in different ways. In comparison with the data for e6-PVP solutions (Fig. 10.6), the absorption in ternary systems in the Q-band range is halved. From the spectral data in Fig. 10.14, it follows that interesting results could be expected for those ratios of the components of ternary systems in solutions where a bathochromic shift of the Q absorption band of e6 is observed.

To study the luminescence in ternary systems, we prepared two series of the samples (P34-P39; P40-43). In the first series, P34 → P39, the concentration of DND increases with the sample number, while the concentration of PVP and e6 remains constant; i.e., the molar ratio of C_{e6}/C_{PVP} is kept constant. In the second series of samples P39, P40-P43 the amount of DND and PVP in the solution increases with the sample number, while the concentration of e6 is fixed (0.0015%); i.e., the C_{e6}/C_{PVP} ratio decreases. In contrast to the first series, in the second one, the weight ratio C_{PVP}/C_{DND} is kept constant. Luminescence spectra for the series 34–39 and 39, 40–43 are shown in Figs. 10.15 and 10.16, respectively.

While DND amount increases in e6-PVP-DND complexes, the luminescence intensity comes down (Fig. 10.15). In the spectra for P34-P39 series, the position of

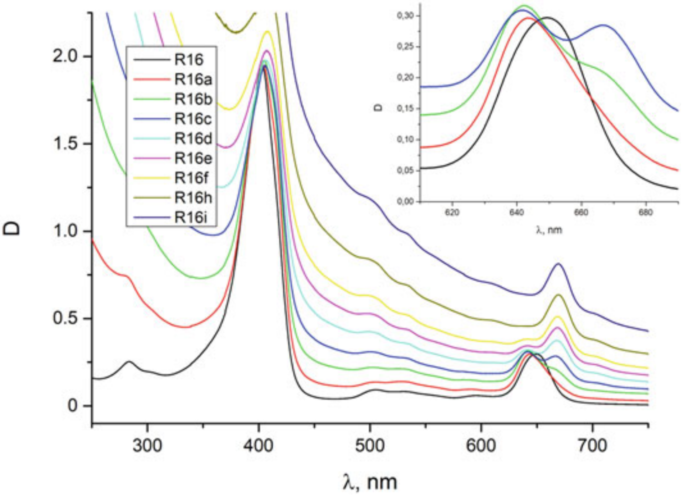

Fig. 10.14 Absorption spectra D(λ) of e6-PVP-DND aqueous solutions (0.15 M NaCl) at fixed e6 content $C_{e6} = 0.0015 \times 10^{-2}$ g/cm^3 when polymer $C_{PVP} = (0.0–0.033) \times 10^{-2}$ g/cm^3 and DND $C_{DND} = (0.0–0.066) \times 10^{-2}$ g/cm^3 fractions increased consequently (data R16, R16a-i) keeping PVP/DND ratio fixed. Inset shows the data at wavelengths $\lambda = 600–700$ nm

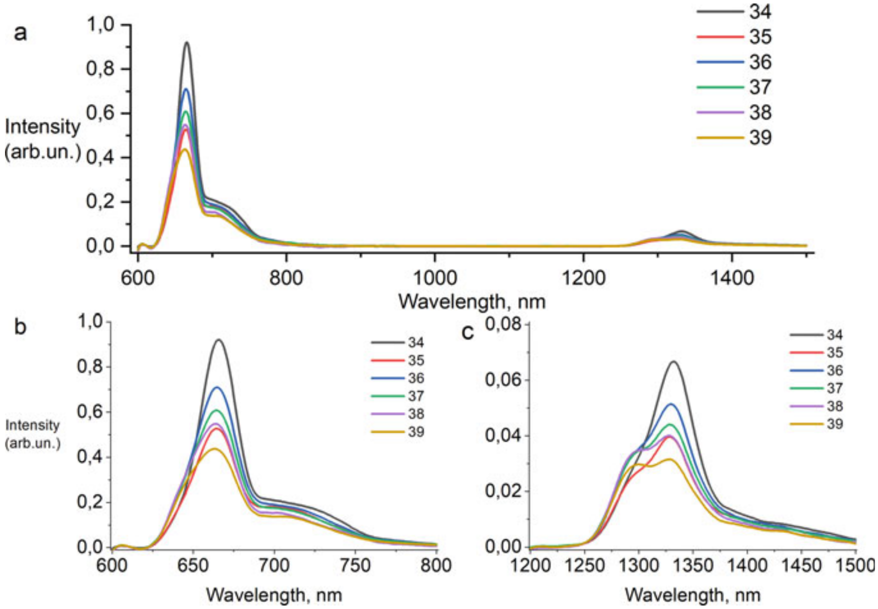

Fig. 10.15 Luminescence spectra of complexes e6-PVP-DND (samples 34–39) in aqueous solutions (0.15 M NaCl) at fixed concentrations of PVP and e6 (C_{e6}/C_{PVP} = const), by varying DND content: **a** data at wavelengths $\lambda = 600–1500$ nm; **b**, **c** data at $\lambda = 600–800$ nm and 1200–1500 nm. DND concentrations in the samples 34–39: 0; 0.005; 0.010; 0.015; 0.020; 0.025 wt.%

main peak approximately does not change. In the solutions of ternary complexes P35-P39, the maximum of luminescence band practically coincides with that for binary complex P34 and with the data for e6 and e6-PVP complexes of different compositions (Fig. 10.6). The profiles of spectra for the sample P34 (Fig. 10.15) and e6-PVP binary complex (Fig. 10.6) are quite similar. The position of luminescence peak (λ = 665 nm, Fig. 10.15) does not depend on DND concentration in the series P35-P39 and well corresponds to luminescence maximum observed for binary e6-PVP complexes with the same polymer concentration.

However, in the spectra of ternary systems P35-P39 (Fig. 10.15) there is a significant change of the second-order luminescence peak profile at $\lambda \sim 1300$ nm in comparison with P34. In this range, the ternary complexes display the overlap of luminescence bands with maxima at $\lambda < 1300$ nm and at $\lambda > 1300$ nm. Remarkable, the increase in DND concentration (P38, P39) makes the first peak stronger. According to previous measurements, the maximum of luminescence of singlet oxygen lies at 1271 nm, and such effect can indicate a stimulation of singlet oxygen generation by DNDs integrated into the complexes. At the same e6 concentration in aqueous solution (0.15 M NaCl) and in the composition of e6-PVP, no similar peculiarities were observed in dye luminescence. Probably, DNDs integrated into binary complexes somehow activates the dye luminescence revealed in solutions of ternary e6-PVP-DND systems. Taking into account that DNDs as themselves are weak luminophores, this can be mostly attributed to the interaction of dye, DND and polymer.

In the spectra of the second series of samples P40-P43, P39 (Fig. 10.16), it can be seen that more amount of PVP in solution makes greater bathochromic shift of the main luminescence maximum of e6. Similar changes of luminescence was observed in binary systems; i.e., the role of PVP and the mechanism of its interaction with the dye are similar in binary and ternary systems. At the same time, the spectra in Fig. 10.16 clearly showed a tendency towards a separation of two contributions of luminescence in the range around 1300 nm with an increase of DND fraction in ternary systems with respect to e6.

10.3.2.4 Singlet Oxygen Generation in the Solutions of Ternary Complexes

The luminescence in the 1200–1300 nm range was investigated in more detail using a special KS19 filter to isolate the second-order contribution of e6 luminescence in the band around 1340 nm, highlighting the singlet oxygen luminescence region. In solutions of binary systems e6-PVP without DND, the luminescence spectra in the range 1200–1300 nm with excitation at a wavelength of 405 nm are presented by a single symmetric peak with a maximum at 1270 nm (Fig. 10.17, data 1).

However, the ternary complexes e6-PVP-DND showed the spectra which differ strongly from the data for binary systems. This is illustrated by the data for complexes with zero, intermediate and maximum amounts of DND (samples 34, 43, 39).

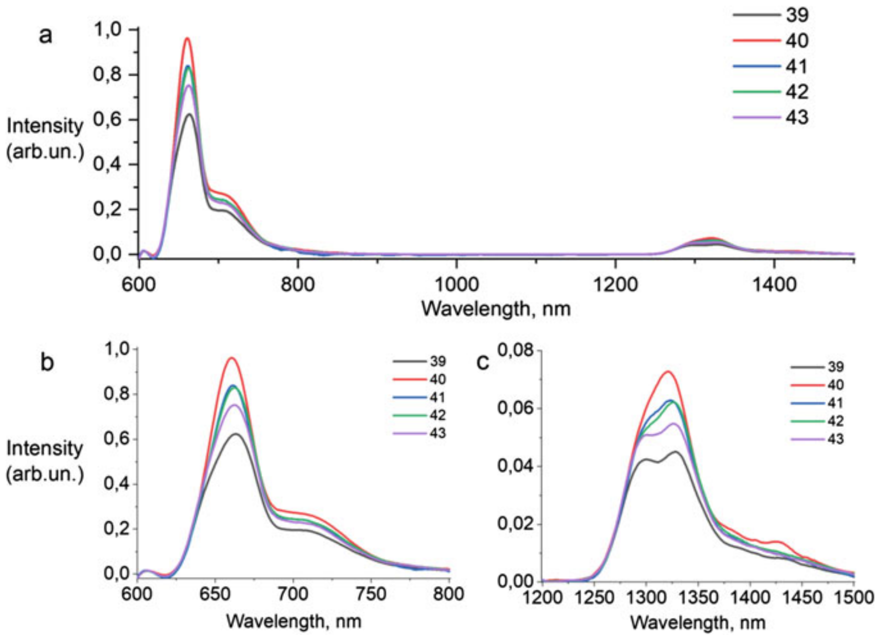

Fig. 10.16 Luminescence spectra of complexes e6-PVP-DND (samples P40-P43, P39) in aqueous solutions (0.15 M NaCl) at fixed e6 concentration and by varying the amounts of PVP and DND, but keeping a constant ratio C_{PVP}/C_{DND}: **a** data at wavelengths λ = 600–1500 nm; **b**, **c** data at λ = 1200–1500 nm, λ = 600–800 nm. PVP concentrations: 0.015; 0.031; 0.045; 0.060; 0.075 wt.% (samples 40–43, 39). DND concentrations: 0.005; 0.011; 0.015; 0.020; 0.025 wt.% (samples 40–43, 39)

The additional emission band is detected in the spectra (maximum at 1214 nm) (Fig. 10.17, data 2, 3). The appearance of a new emission band in the spectrum of e6-PVP-DND systems and the enhancement of the radiation intensity with DND concentration can be considered as the evidence of complexation between the components and the ability of DND to emit actively by binding with the polymer and the dye. Oppositely to this, the amplitude of the main band with a maximum at 1270 nm related to singlet oxygen does not demonstrate a gain at larger amounts of DND. On the other hand, this broadened band has much greater integral intensity that can be treated as stimulation of singlet oxygen formation due to presence of diamonds.

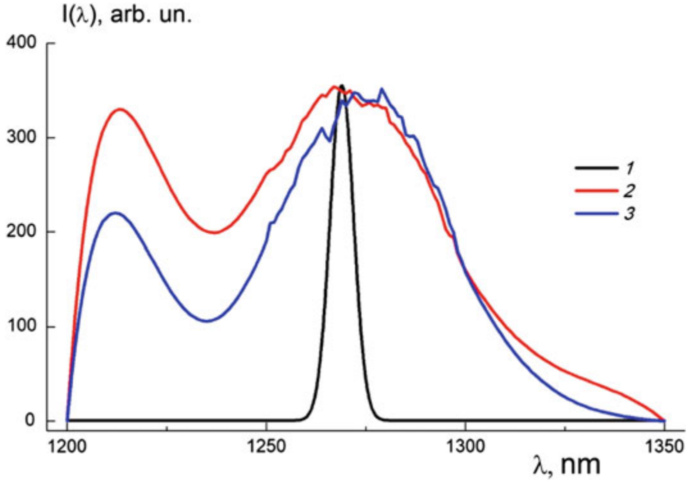

Fig. 10.17 Emission spectra of singlet oxygen luminescence of binary e6-PVP (1) and ternary e6-PVP-DND complexes (2, 3) in aqueous medium. Samples 34 (1), 39 (2) and 43 (3) with the weight proportions of components: e6:PVP:DND = 0.0015:0.076:0; 0.0015:0.075:0.025; 0.0015:0.075:0.011

10.4 Conclusions

First prepared ternary complexes e6-PVP-DND have shown specific optical properties indicating the crucial role of diamonds in the generation of singlet oxygen when UV radiation excites diamonds which may transfer the energy to dye molecules in non-radiative way or directly to surrounding water molecules since DND ability to emit radiation is depressed due to surface defects (black diamonds).

On the other hand, dye molecules may excite the diamonds also and stimulate their action onto water molecules. Such a combined effect can stimulate the generation of singlet oxygen and enhance the therapeutic effect of PDT procedures.

In general, these principles can be used for the creation of new hybrid nanocatalysts carrying macrocyclic dyes assuming wide areas of application, e.g., in theranostics, for disinfection against viruses and bacteria, active filtration and cleaning air, water, surfaces, etc. Chemically inert diamonds are more resistant to the attack of singlet oxygen and should provide longer action of such photocatalysts.

Acknowledgements The work was supported by the Russian Foundation for Basic Research (grant no 18-29-19008).

References

1. Klán P, Wirz J (2009) Photochemistry of organic compounds: from concepts to practice. Wiley-Blackwell, Oxford
2. Kyle DJ, Osmond CB, Arntzen CJ (eds) (1987) Photoinhibition. Elsevier, Amsterdam
3. Caughey WS, Acad NY (eds) (1979) Biochemical and clinical aspects of oxygen. Academic Press, New York
4. Dougherty TJ, Gomer CJ, Henderson BW, Jori G, Kessel D, Korbelik M, Moan J, Peng Q (1998) Photodynamic therapy. J National Cancer Inst 90(12):889–905
5. Dolmans DE, Fukumura D, Jain RK (2003) Photodynamic therapy for cancer. Nat Rev Cancer 3:380–387
6. Larue L, Mihoub A, Youserf Z, Colombeau L, Acherar S, André JC, Arnoux P, Baros F, Vermandel M, Frochot C (2018) Using X-rays in photodynamic therapy: an overview. Photochem Photobiol Sci 17(11):1612–1650
7. Ostroverkhov P, Semkina A, Naumenko V, Plotnikova E, Yakubovskaya R, Vodopyanov S, Abakumov A, Majouga A, Grin M, Chekhonin V, Abakumov M (2018) HSA—coated magnetic nanoparticles for MRI-guided photodynamic cancer therapy. Pharmaceutics 10(4): 284
8. Kulvelis YV, Trounov VA, Lebedev VT, Orlova DN, Gelfond ML (2009) Synthesis and structural investigation of ferrofluids with porphyrins and prospects of their application in photodynamic therapy. J Surf Investig 3(3):379–386
9. Benov L (2015) Photodynamic therapy: current status and future directions. Medical Princ Prac 24(s1):14–28
10. Bonneau S, Vever-Bizet C (2008) Tetrapyrrole photosensitisers, determinants of subcellular localisation and mechanisms of photodynamic processes in therapeutic approaches. Expert Opin Ther Patents 18(9):1011–1025
11. Colpani GL, Odorick Dal`Toé AT, Zanetti M, Zeferino RCF, Silva LL, Muneron de Mello JM, Fiori MA (2019) Photocatalytic adsorbents nanoparticles. In: Edebali S (ed) Adv Sorp Process Appl 63–86. IntechOpen
12. Chen X, Song J, Chen X, Yang H (2019) X-ray-activated nanosystems for theranostic applications. Chem Soc Rev 48(11):3073–3101
13. Macdonald IJ, Dougherty TJ (2001) Basic principles of photodynamic therapy. J Porphyrins Phthalocyanines 5(2):105–129
14. Sternberg ED, Dolphin D, Brückner C (1998) Porphyrin-based photosensitizers for use in photodynamic therapy. Tetrahedron 54(17):4151–4202
15. Kiesslich T, Gollmer A, Maisch T, Berneburg M, Plaetzer K (2013) A comprehensive tutorial on in vitro characterization of new photosensitizers for photodynamic antitumor therapy and photodynamic inactivation of microorganisms. BioMed Res Int 2013:1–17
16. Uzdensky AB, Dergacheva OY, Zhavoronkova AA, Reshetnikov AV, Ponomarev GV (2004) Photodynamic effect of novel chlorin e6 derivatives on a single nerve cell. Life Sci 74(17): 2185–2197
17. Jinadasa R, Hu X, Vicente M, Smith KM (2011) Syntheses and cellular investigations of 17^3-, 15^2-, and 13^1-amino acid derivatives of chlorin e_6. J Med Chem 54(21):7464–7476
18. Brusov SS, Efremenko AV, Lebedeva VS, Shchepelina EYu, Ponomarev PhV, Feofanov AV, Mironov AF, Grin MA (2015) Influence of positive charge in the structure of photosensitizers of chlorine series on the photoinduced anticancer activity. Russ J Biother 14(4):87–92
19. Lucky SS, Soo KC, Zhang Y (2015) Nanoparticles in photodynamic therapy. Chem Rev 115(4):1990–2042
20. Barinov AV, Goryachev NS, Poletaeva DA, Rybkin AYu, Kornev AB, Troshin PA, Schimitt FJ, Renger G, Eichler HJ, Kotelnikov AI (2012) Photodynamic activity of hybrid nanostructure on the basis of polycationic fullerene derivative and xanthene dye eosine Y. Nanotechnol. Russia. 7(7–8):409–414

21. Kotel'nikov AI, Rybkin AY, Goryachev NS, Belik AYu, Troshin PA (2016) Spectral properties and photodynamic activity of complexes of polycationic derivative of fullerene C60 with xanthene dye fluorescein. Opt Spectrosc 120(3):379–385
22. Belik AYu, Rybkin AYu, Voronov II, Goryachev NS, Volyniuk D, Grazulevicius JV, Troshin PA, Kotelnikov AI (2017) Non-covalent complexes of polycationic fullerene C_{60} derivative with xanthene dyes—spectral and photochemical properties in water and in liposomes. Dye Pigment 139:65–72
23. Goryachev NS, Belik AYu, Rybkin AYu, Mikhailov PA, Kraevaya OA, Troshin PA, Kotelnikov AI (2019) Investigation of the spectral properties of noncovalent complexes of a polysubstituted water-soluble derivative of the C_{60} fullerene and chlorin e6 in polar solvents. Opt Spectrosc 126(6):629–633
24. Charlesworth P, Truscott TG, Kessel D, Medforth CJ, Smith KM (1994) Photophysical studies of substituted porphyrins. J Chem Soc Faraday Trans 90(8):1073–1076
25. Serra VV, Andrade SM, Neves MG, Cavaleiro JA, Costa SM (2010) J-aggregate formation in bis-(4-carboxyphenyl)porphyrins in water: pH and counterion dependence. New J Chem 34(12):2756–2757
26. Arif U, Haider S, Khan N, Alghyamah AA, Jamila N, Khan MI, Almasry WA, Kang I-K (2019) Biocompatible polymers and their potential biomedical applications: a review. Cur Pharm Design 25(34):3608–3619
27. Chin WWL, Heng PWS, Thong PSP, Bhuvaneswari R, Hirf W, Kuenzel S, Soo KC, Olivo M (2008) Improved formulation of photosensitizer chlorin e6 polyvinylpyrrolidone for fluorescence diagnostic imaging and photodynamic therapy of human cancer. Eur J Pharm Biopharm 69(3):1083–1093
28. Solov'eva AB, Aksenova NA, Glagolev NN, Melik-Nubarov NS, Ivanov AV, Volkov VI, Chernyak AV (2012) Amphiphilic polymers in photodynamic therapy. Russ J Phys Chem B 6(3):433–440
29. Saboktakin MR, Tabatabee RM (2014) The novel polymeric systems for photodynamic therapy technique. Int J Biol Macromol 65:398–414
30. Paul S, Selvam S, Heng PWS, Chan LW (2013) Elucidation of monomerization effect of PVP on chlorin e6 aggregates by spectroscopic, chemometric, thermodynamic and molecular simulation studies. J Fluoresc 23(5):1065–1076
31. Hädener M, Gjuroski I, Furrer J, Vermathen M (2015) Interactions of polyvinylpyrrolidone with chlorin e6-based photosensitizers sudied by NMR and electronic absorption spectroscopy. J Phys Chem B 119(36):12117–12128
32. Gjuroski I, Furrer J, Vermathen M (2018) How does the encapsulation of porphyrinic photosensitizers into polymer matrices affect their self-association and dynamic properties? Chem Phys Chem 19(9):1089–1102
33. Isakau HA, Parkhats MV, Knyukshto VN, Dzhagarov BM, Petrov EP, Petrov PT (2008) Toward understanding the high PDT efficacy of chlorin e6–polyvinylpyrrolidone formulations: Photophysical and molecular aspects of photosensitizer–polymer interaction in vitro. J Photochem Photobiol B 92(3):165–174
34. Caughey WS (ed) (1979) Biochemical and clinical aspects of oxygen. Academic Press
35. Gorokh YuA, Aksenova NA, Solov'eva AB, Ol'shevskaya VA, Zaitsev AV, Lagutina MA, Luzgina VN, Mironov AF, Kalinin VN (2011) The influence of amphiphilic polymers on the photocatalytic activity of water-soluble porphyrin photosensitizers. Russ J Phys Chem A 85(5):871–875
36. Aksenova NA, Zhientaev TM, Brilkina AA, Dubasova LV, Ivanov AV, Timashev PS, Melik-Nubarov NS, Solovieva AB (2013) Polymers as enhancers of photodynamic activity of chlorin photosensitizers for photodynamic therapy. Photon Lasers Med 2(3):189–198
37. Zhientaev TM, Boltaev UT, Solov'eva AB, Aksenova NA, Glagolev NN, Cherhjak AV, Melik-Nubarov NS (2014) Complexes of chlorin e6 with pluronics and polyvinylpyrrolidone: structure and photodynamic activity in cell culture. Photochem Photobiol 90(1):171–182
38. Aleksenskiy AE, Eydelman ED, Vul' AYa (2011) Deagglomeration of detonation nanodiamonds. Nanosci Nanotechnol Lett 3(1):68–74

39. Bradac C, Rastogi ID, Cordina NM, Garcia-Bennett A, Brown LJ (2018) Influence of surface composition on the colloidal stability of ultra-small detonation nanodiamonds in biological media. Diam Relat Mater 83:38–45
40. Kulvelis YuV, Shvidchenko AV, Aleksenskii AE, Yudina EB, Lebedev VT, Shestakov MS, Dideikin AT, Khozyaeva LO, Kuklin AI, Török Gy, Rulev MI, Vul AYa (2018) Stabilization of detonation nanodiamonds hydrosol in physiological media with poly(vinylpyrrolidone). Diam Relat Mater 87:78–89
41. Chen M, Pierstorff ED, Lam R, Li S-Y, Huang H, Osawa E, Ho D (2009) Nanodiamond-mediated delivery of water-insoluble therapeutics. ACSNano 3(7):2016–2022
42. Chen C, Wang H (eds) (2016) Biomedical applications and toxicology of carbon nanomaterials. Wiley-VCH, Weinheim
43. Vul' A, Shenderova O (eds) (2014) Detonation nanodiamonds. Science and applications. Pan Stanford, Singapore
44. Williams OA, Hees J, Dieker C, Jäger W, Kirste L, Nebel CE (2010) Size-dependent reactivity of diamond nanoparticles. ACS Nano 4(8):4824–4830

Chapter 11
The Role of Metals in Nanocomposites for UV and Visible Light-Active Photocatalysis

Vikas, Ruchi Singh, Arti Sharma, Ashish Kumar Dhillon, and Soumik Siddhanta

Abstract Photocatalysis has emerged as a promising tool to perform various applications such as water splitting, inert molecular excitation, harnessing solar energy for chemical as well as biochemical activities, and developing various photocatalytic devices. The driving force behind the synthesis using light is that it is reliable, abundant, and a green source of energy. In the past decade, there is an immense increase in interest in exploring the use of metal nanoparticles in photocatalysis. Among many nanoparticle systems exploited for catalysis, plasmonic photocatalysts are one of the most intensely investigated due to their potential applications in energy materials. The shift of interest has been taking place to utilize the electromagnetic properties of metal or plasmonic nanoparticles than their traditional use as co-catalyst in various chemical processes. Photocatalysis consists of the direct conversion of light energy into chemical energy and thus reducing energy consumption. Metal nanoparticles (Ag, Au, Pd, or Pt) photocatalyst is very efficient, for example, in transforming renewable solar energy to chemical energy. Apart from catalytic applications, these nanocomposites are perceived to be environment-friendly, an attribute, which is becoming more relevant in recent times. This book chapter mainly discusses the mechanisms and applications of photocatalytic activity of nanocomposites composed of metal-based nanomaterials.

Keywords Metal nanoparticles · Photocatalysis · Nanocomposites · Plasmonics · Solar energy

---

Vikas, Ruchi Singh, Arti Sharma, Ashish Kumar Dhillon. These authors have contributed equally.

Vikas · R. Singh · A. Sharma · A. K. Dhillon · S. Siddhanta (✉)
Department of Chemistry, Indian Institute of Technology, New Delhi 110016, India
e-mail: soumik@iitd.ac.in

S. Garg and A. Chandra (eds.), *Green Photocatalytic Semiconductors*,
Green Chemistry and Sustainable Technology,
https://doi.org/10.1007/978-3-030-77371-7_11

11.1 Introduction

Photocatalysis is the best way of utilizing and converting the abundantly available solar energy into chemical energy. Due to its application in various fields such as wastewater treatment and hydrogen generation, it has been in consideration of various research groups for many years. TiO_2 is the most widely used photocatalyst used for environment cleaning and hydrogen energy generation, but it has a wide energy gap and can only use 4% of the total solar radiation. Many methods were employed to increase the bandgap of $TiO_{2,}$ such as through metal ion and non-metal ion doping. However, it results in problems such as thermal instability, photo-corrosion, and fast electron–hole recombination. Therefore, to make proper use of sunlight, many materials have been developed that could use a wide range of visible light. Coinage metal photocatalysts such as Ag, Au, and Pt show localized surface plasmon resonance (LSPR), which allows them to absorb photons in the visible region.

11.1.1 Surface Plasmons in Photocatalysis

Semiconductors are the main part of the photocatalysis process [1] in which semiconductors absorb photons of the incident light to generate holes and electrons, which initiates various processes like oxidation, reduction, and photocatalysis. Various emerging areas utilizing photocatalysis are water splitting [2], self-cleaning surface, air purification, wastewater treatment, and carbon dioxide reduction which are showing considerable promise and becoming key players in the environment and energy industries [3]. When the light of suitable wavelength falls on the surface of a simple semiconductor material, the photons of the incident radiation get absorbed on the surface. As a result, a generation of electrons and holes takes place, and they occur within the material or near the surface. To bring about the redox reaction, these holes and electrons need to be transferred to the surface [1].

There are a few drawbacks of semiconductor-based photocatalysis, such as low efficiency and the lack of suitable photocatalyst material, which show a good response to visible light. In a homogenous semiconductor photocatalyst, migration is random. So, there are plenty of chances of recombination of the excited species such as electrons and holes. This is responsible for the low efficiency of photocatalytic materials. Secondly, there are some materials like ZnO or TiO_2 [4] which are high-performance photocatalytic materials and have a bandgap which is large enough to absorb light in the UV region instead of the visible region. On the other hand, there are low-performance photocatalytic materials like Fe_2O_3 or CdS, which fail to maintain photoactivity for longer periods of time [5, 6].

To avoid these pressing problems presented by simple semiconductor photocatalysis materials, plasmonic photocatalysis comes into the picture [7]. In plasmonic photocatalysis, noble metals, like silver, and gold, with sizes less than

100 nm are dispersed or conjugated along with semiconductor photocatalysts. As a result, there is a significant enhancement of the photoactivity in both UV and visible light. There are two additional factors that are imposed by the plasmonic photocatalysis on the semiconductor photocatalysts, which are the creation of Schottky junction and the generation of localized surface plasmon resonance (LSPR) and both enhance the photocatalytic activities of the metal–semiconductor nanocomposites.

11.1.2 Schottky junction effect

The Schottky junction effect arises because of the physical contact or creation of a junction between the plasmonic nanoparticles and the semiconductor material [8]. When the light of a particular wavelength falls on this composite, the metallic nanoparticles build up an internal electric field or space charge, which is opposite to that of the electric field of the incident light inside the photocatalyst and close to the junction or metal–semiconductor interface (Fig. 11.1a). As a result, the electrons and the holes move in a direction opposite to each other at the Schottky junction. Additionally, a metallic surface produces a rapid rate of charge transfer also acts as a center for trapping charges, and therefore holds additional locations for photoreactions. These factors combine to reduce the electron–hole recombination and thus results in the enhancement of the efficiency of the photocatalysts.

11.1.3 Localized Surface Plasmon Resonance (LSPR)

As discussed earlier, LSPR is the combined oscillation of the free electrons of metal nanoparticles, which is in phase with the variable electric field of the incident radiation (Fig. 11.2a). This phenomenon leads to various effects in the metal nanoparticle–semiconductor composites. Surface plasmon resonance phenomenon (SPR) is a physical process associated with particles having a size in the range of 1–100 nm, showing unique optical properties. These unusual properties of nanoparticles are quite different from that of the bulk properties of the material. SPR phenomenon occurs when plane-polarized light falls on thin metal films with total internal reflection conditions [9] (Fig. 11.2c). SPR is linked with noble metals like Au, Ag, Pt, and Cu, etc. [10]. In the case of noble metals, the outmost s-orbital contains one electron, and when the light of suitable electromagnetic radiation falls on the surface, these free surface electrons can easily interact and absorb the photons of the incident light, and the energy is thus transferred to these free electrons forming surface plasmons. When the frequency of the incident light is in resonance with the frequency of the coherent oscillation of these free electrons in nanoparticles, it gives rise to localized surface plasmons. SPR is a bulk phenomenon while LSPR is associated only with nanoscale dimensions or

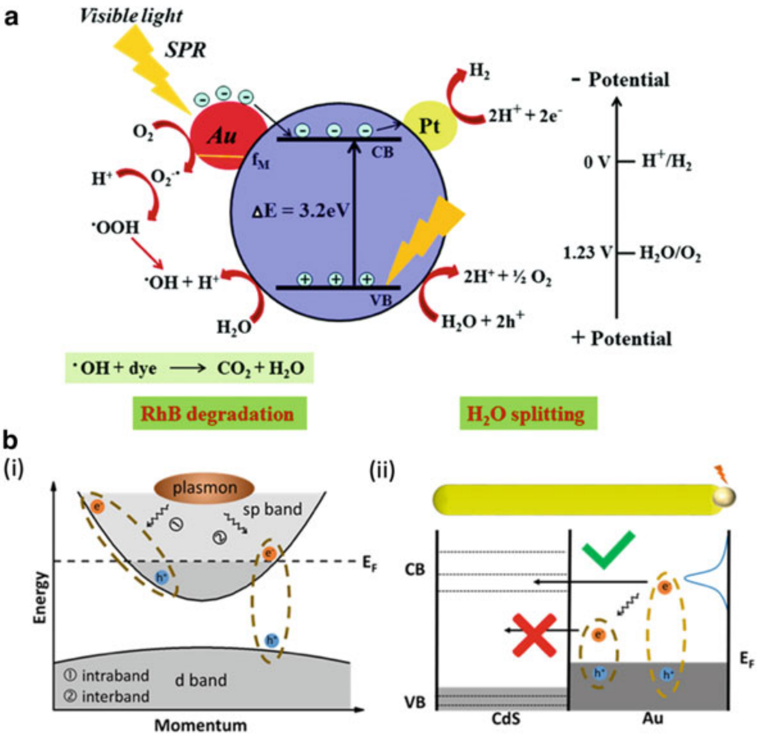

Fig. 11.1 **a** Diagrammatic representation of plasmonic photocatalysis using TiO_2. Figures reprinted from [6] with permission. Copyright (2018) Royal Society of Chemistry. **b** (i) Hot electron generation at metal–semiconductor interface showing interband and intraband transitions. (ii) Hot electron/carrier transfer and plasmonic decay at metal nanoparticle–semiconductor interface. Figure reprinted from [13] with permission. Copyright (2020) American Chemical Society

nanoparticles. When the frequency of the incident electromagnetic wave is comparable or equal to the plasmon frequency, this phenomenon is known as localized surface plasmon resonance or LSPR, and the frequency is known as the resonant frequency. The plasmon resonance of the metallic nanoparticle can be tailored by changing the shape, size, and nearby environment of the nanoparticles, and the resonance wavelength can be brought to the visible or near-UV range [11] (Fig. 11.2d). By doing so, the plasmonic semiconductor hybrid photocatalyst can respond to a broad range of radiation, whether it is in UV or in the visible range. So, the downside of the TiO_2-type semiconductor [4] now can be resolved by combining it with the metallic nanoparticles. Better enhancement can be seen in the absorption and the scattering processes when the size of the metal nanoparticle is smaller than the wavelength of the light used. There are processes such as damping, which is also seen in the case of metal nanoparticles and can reduce the absorption or scattering of light. In smaller metal nanoparticles, damping is more pronounced.

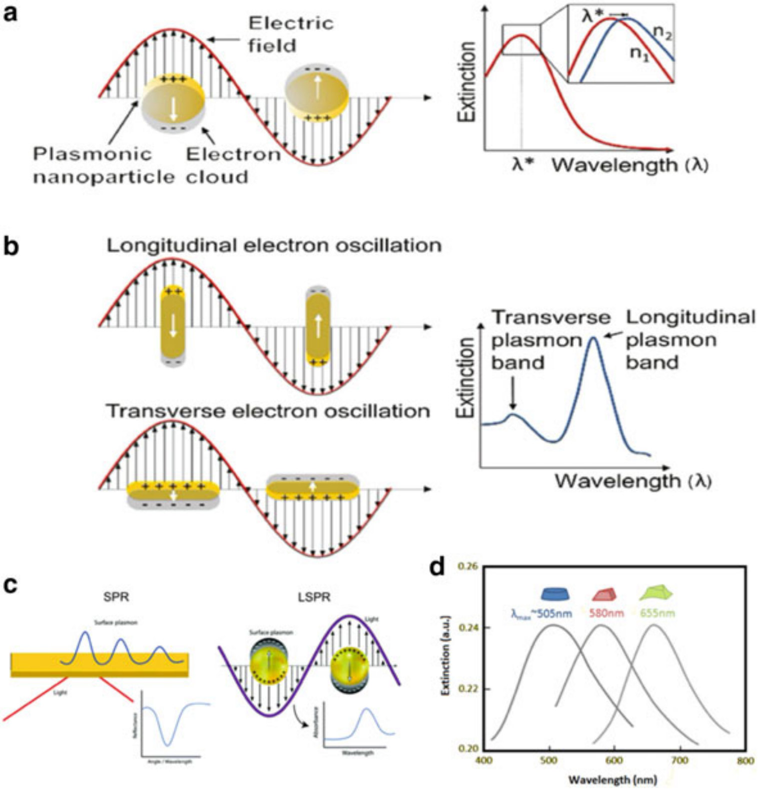

Fig. 11.2 **a** Origin of LSPR in plasmonic nanoparticles. LSPR can detect interactions through shift in the resonance wavelength (right). **b** Generation of transverse and longitudinal plasmon modes in anisotropic nanoparticles such as gold nanorods. Reprinted with permission from [11]. Copyright (2018) De Gruyter. **c** Generation of SPR on a thin metallic film, as compared to LSPR on a nanoparticle. Reprinted with permission from [8]. Copyright (2020) Royal Society of Chemistry. **d** The effect of the shape of the nanomaterials on the plasmon resonance. Reprinted with permission from [10]

There is also an additional factor which is responsible for the tuning of the plasmonic resonance frequency which is known as coupling. Coupling occurs due to the interaction of the surface plasmons of closely spaced nanoparticles. As the distance between the two nanoparticles increases, the coupling decreases, and after a certain distance, it completely vanishes. This coupling can create hotspot regions on the surface of the nanoparticles consisting of strong electromagnetic field. In most cases, coupling leads to a redshift for longitudinal surface plasmons and a blue shift for the transverse surface plasmons [12] (Fig. 11.2b).

We can also enhance the absorption of visible light for Fe_2O_3-type semiconductor photocatalysts, which typically have low bandgaps. The light gets absorbed very near to the surface with a penetration depth of around 10 nm due to the strong absorption by the material. Consequently, the distance between the excited electrons and holes to the surface gets shortened. As a result, electrons or holes have to travel a lesser distance to reach the surface, which further reduces the probability of recombination. Metallic LSPR itself builds up a local intense electric field, which enhances many photocatalytic reactions as it permits the excitation of a large number of electrons and holes. LSPR also heats up the surrounding environment to enhance the rate of redox reaction as well as mass transfer. Sometimes this effect also polarizes the nonpolar species for enabling good absorption. Apart from these, there are numerous impacts of surface plasmons on semiconductor photocatalyst as noble metals can show their own catalytic effect just like Pt metal, which can act as a surface for hydrogen evolution. A type of quantum tunneling effect can also be seen. Although Schottky junction is not a direct type of plasmonic or resonance effect, it is an outcome of the combination of noble metal nanoparticles with the semiconductor surface. So, it can be regarded as an intrinsic property of plasmonic photocatalysis. The structure and configuration of the metallic nanoparticles–semiconductor duo also play a major role in the photocatalytic process [13]. For better efficiency, we can use noble metal nanoparticles of various shapes and the semiconductor material as thin films to achieve maximum surface area and good electron transfer property.

11.1.4 Hot Electron Transfer

Hot electrons are generated when a source with high-energy photon radiation strikes the surface of the semiconductor material. The energy from the photons may shift to the surface electrons of the semiconductor, resulting in the excitation of the electron from the valence band and forming an electron-hole pair. If this excited electron has enough energy to leave the valence band and cross over to the conduction band, then it becomes a hot electron. Hot electrons have characteristics of high temperature and have high mobility. Therefore, it can easily leave the surface and transfer to the surrounding material [14]. This kind of generation of a hot electron is an intrinsic characteristic of the metal nanoparticles. In a classic plasmonic metal, there are two types of bonds, one being the s-p band and the other being the d band. The incident light responds to the metal nanoparticles in two different ways and results in two types of excited charge carriers resulting from interband and intraband transitions (Fig. 11.1b). The intraband transitions are capable of generating electrons of high energy having energy above the Fermi level. The hot electron generation is a type of quantum effect and comes into light due to the non-conservation of linear momentum of an excited electron near the surface and in the hotspot. The quantum efficiency of these hot electrons depends upon two factors, the first one is the initial population level of hot electrons or holes having sufficient energy for transfer to the surrounding material. The second is the transfer efficiency of hot electrons. In small-sized nanoparticles, the transfer rate is fast because the electrons have to travel a lesser distance to come to the surface. For bulk material, the process is quite slow, and a higher probability of recombination occurs. The selectivity of the material system is very important. For gold nanoparticles, the interband transitions are more predominant because it satisfies both momentum and energy conservation criteria. Silver nanoparticles can produce hot electrons more coherently than gold because of the longer electron mean free path. Also, the hot electrons with lower energy value fraction are lower in the case of silver nanoparticles. A sharper plasmon resonance will create a large number of hot electrons with high energy. Also, the quantum effect is more pronounced in nanoparticles with a longer mean free path. The energy of the hot electron contains a wide distribution range between 1 and 4 eV for gold and silver nanoparticles [15]. Hot electrons are transferred to the adjacent semiconductor only if the energy of the electrons is greater than the Schottky junction barrier. These electrons can still be injected into the semiconductor through tunneling. This plasmon-induced hot electron transfer phenomenon depends on the size of the nanoparticles and the area that is in contact with the semiconductor. The decrease in the particle size can enhance the initial distribution of hot electrons, reduce the energy barrier of electron transfer, and increase the rate of hot electron transfer. This can enhance the quantum efficiency of the catalyst. However, there are many drawbacks in the electron transfer process in the case of the photolytic application. The bands of semiconductors and nanoparticles should be in proper alignment and have effective coupling to ensure high efficiency. Therefore, proper physical contact between the metal nanoparticles and semiconductors is required. After the migration of the hot electron, hot holes are still left behind in the metal nanoparticles, which must be immediately compensated to regain a suitable LSPR.

11.2 Systematic Naming of Plasmonic Photocatalysts

The different combinations of metal nanoparticle–semiconductor photocatalysts give rise to different properties that can be harnessed for various applications. These combinations can be shown by specific notation [5, 7]. We mark metal nanoparticle as M and semiconductor material, which can act as substrate as S.

a. M/S—here M represents metal nanoparticle and S represents semiconductor surface with spherical shape but not of nano-dimension. M is partially embedded in S. Some part of the metal nanoparticle is exposed to the surrounding area or solution. "/" represents the surface of metal nanoparticle which is in contact with the semiconductor material. An example of such a conjugate is Au/TiO_2.
b. M-S—it represents a combo in which metal nanoparticle M is fused with the thin film of semiconductor S. "-" represents the thin film surface of semiconductor photocatalyst such as Au–Fe_2O_3.

c. M(S—it means that metal nanoparticle M is totally covered within the semiconductor surface, S. No part of metallic nanoparticle M is exposed to surroundings. “(” represents the encapsulation such as Ag(TiO$_2$.
d. M@S is also called a core@shell structure, where M is the core and S acts as a shell around the metallic nanoparticle. In this case, the metal nanoparticle M is fully covered from all the sides by the semiconductor material S, such as in Ag@SiO$_2$. Here, M@S is different from M(S, as in the former case, S acts as a shell around the nanoparticle, while in the latter, S acts as substrate support.

11.3 Strategies to Increase the Efficiency of Metal-Enhanced Photocatalysis

The photocatalytic efficiency depends upon factors like absorption of light, and how the electron–hole pair are separated, and their correspond migration toward the catalytic surface. This step is not trivial for the metal-induced photocatalyst because of the presence of the unique electronic properties of these metal absorbers. The maximum efficiency we can get with plasmonic metal nanostructures is only 8% in spite of the perfect absorption. However, this limit can be exceeded by transforming the electronic density of states of absorbers. Several attempts have been made to increase the metallic nanoparticle efficiency, such as morphology control, nanostructure construction, and catalytic decoration [16].

11.3.1 Light-Harvesting and Achieving Broadband Absorption

For better utilization of solar energy, it is necessary to harvest a wide range of wavelengths including the visible region. This strategy is also applicable to the plasmonic photocatalysts. For example, if TiO$_2$ is introduced with gold nanorods (NRs), the longer wavelengths of light from the visible spectrum and beyond can be harvested. The LSPR of gold NRs splits into two peaks, longitudinal and transverse, and the resonance frequency of the longitudinal axis greatly depends upon the aspect ratio (length divided by the width of the nanorod). This happens because of the difference in the charge accumulation at both the axes. Charge accumulation is directly proportional to the restoring force, which in turn is smaller for the longitudinal axis due to less electronic charge displacement. The longer wavelength of light can be harvested by changing the aspect ratios of these nanorods. When the aspect ratio of these gold NRs is decreased, there is an overlap between the longitudinal and transverse plasmon resonance, and the shape changes from the rod to almost spherical [17]. In this way, not only the transverse component helps in harvesting the light but also the longitudinal component. Another example is Au

NC/C–TiO_2 (Fig. 11.3a). It is capable of harvesting visible light over a broader range of sunlight for both photocatalytic aerobic oxidation of isopropanol and photo-electrocatalysts. Experimental studies such as electromagnetic field simulations and electron paramagnetic resonance confirm that the increased efficiency of this photocatalyst is due to the plasmon-photon coupling, which is enhanced at the interface between gold nanocluster and C–TiO_2. It results in the generation of high-energy hot electrons and hence increases photocatalytic efficiency [18]. The shape of gold nanoparticles also affects the efficiency of these photocatalysts. The decrease in the photocatalytic activity is in the following order—gold nanospheres > nanorods > nanostars. It is probably due to the difference in the charge carriers trapping for different geometries [19]. Light-harvesting is enhanced not only by LSPR but also by interband transitions. Cu possesses a low interband transition than Au, so it should have more photocatalytic activity. However, the ease by which copper gets oxidized restricts its application [16].

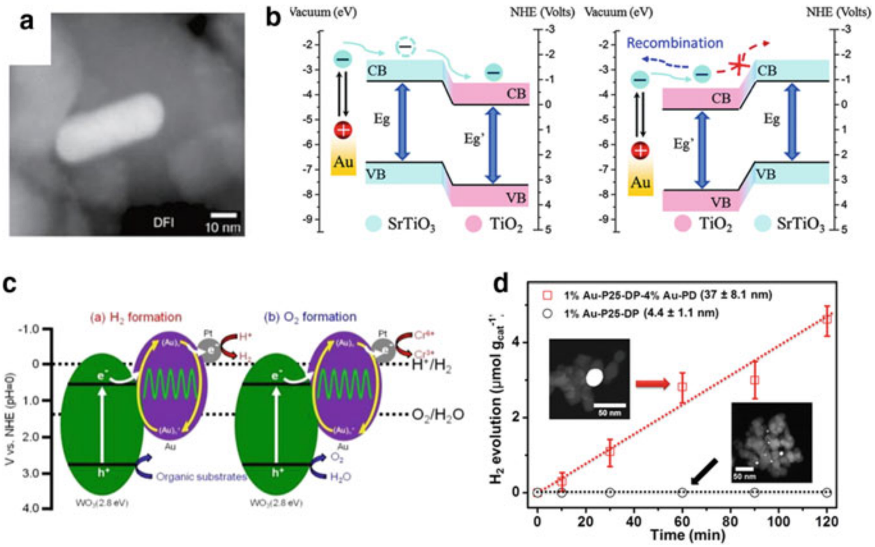

Fig. 11.3 **a** A HAADF-STEM image of Au nanorod/TiO_2 catalyst. Reprinted with permission from [16]. Copyright (2013) Wiley-VCH. **b** Example of a charge transfer process across a metal-semiconductor composite. Reprinted with permission from [20]. Copyright (2014) Royal Society of Chemistry. **c** Reaction mechanism of production of H_2 and O_2 over Pt/Au/WO_3. Reprinted with permission from [23]. Copyright (2013) American Chemical Society. **d** Differential H_2O reduction over two different photocatalysts prepared using deposition–precipitation (DP) and photodeposition (PD). Reprinted with permission from [26]. Copyright (2014) American Chemical Society

11.3.2 Enhancing Charge Separation

Reduction in charge separation leads to decrease in the performance of the photocatalyst due to ultrafast decay of the hot electrons from the semiconductor to the metallic nanoparticles. The lifetime of these hot electrons is considerably shorter (around 10^{-3} ns). For Au/TiO_2 nanocomposites, the combination of these hot electrons takes place just after 1.5 ns [16]. The separation of charge carrier can be enhanced by loading gold nanoparticles onto a composite of anatase/rutile TiO_2 [20]. This method is very efficient in reducing the rate of electron-hole recombination. Another example is the multicomponent junction Au–$SrTiO_3$–TiO_2 [21]. In this, gold nanoparticles are irradiated with visible light, and the photoelectrons produced are transported with the support of $SrTiO_3$–TiO_2 junction (Fig. 11.3b). The driving force for this whole process is the generation of potential difference through the different band energy levels. It results in the prevention of electron–hole recombination and also backward charge transfer to the gold nanoparticles [21]. Another type of nanostructure is Au@CdS/$SrTiO_{3,}$ which reduces the ultrafast decay of the photoelectrons by strong coupling with CdS quantum dots and by a Schottky junction with $SrTiO_3$ nanoparticles [22]. Another method of boosting the efficiency of the photocatalyst is through interface designing. Plasmon-induced interfacial charge separation aids in the decaying of the plasmons and thereby helps in the direct excitation of the electrons from the metal to the strongly coupled acceptor. This concept was applied to increase the quantum efficiency of Se–Au NRs nanostructures [23]. Thus, we could see that the efficiency of the metal–semiconductor composites can be increased by proper designing of the structure and by interface engineering (Fig. 11.3b).

11.3.3 Decoration with Co-catalyst

Co-catalysts have a major role in increasing the efficiency of the photocatalyst. It provides more charge separation and a greater number of active sites for the surface reactions [16]. Generally, group VIII, IB, IIB, and P block metal elements act as co-catalysts. One such example of such a photocatalyst is Pt/Au/WO_3, used in water splitting. In this system, the migration of electrons from the gold surface to the platinum surface takes place where it induces the reduction of H^+ ions to H_2 gas (Fig. 11.3c). Firstly, gold nanoparticles are placed on the WO_3 surface by colloid photo-absorption, and then platinum is placed on the gold surface by ordinary photo-absorption [24]. TiO_2 nanofibres with Au and Pt co-catalysts were used in the generation of $H_{2,}$ which is done by applying a dual-beam radiation. First, the radiation of 420 nm is applied to excite the impurity or defects present in the TiO_2; subsequently, the second beam of radiation of wavelength 550 nm is passed to excite the Au surface plasmon resonance. Due to this, the activity of H_2 generation increases by a factor of 2.5 [25]. Similarly, O_2 evolution is done using iridium co-catalyst loaded on plasmonic nanoparticles with TiO_2 nanowires. This technique improves the lifetime of the hot electrons and enhances the rate of kinetics of the chemical reaction [26]. Decoration of the co-catalyst on the metal–semiconductor composites is considered a difficult process as it requires a proper preparation strategy to load the co-catalyst on the active site. Sometimes, the high work function of the plasmonic nanoparticles decreases the effect of the co-catalyst [16].

11.3.4 Particle Size Effect

The size of the nanoparticles plays a significant role in improving the efficiency of the photocatalysts. The performance of the photocatalyst can be enhanced by strengthening the LSPR. For instance, in photocatalyst Au/TiO_2, different sized Au particles were synthesized by a single-step ($SS–Au/TiO_2$) and multi-step photo-deposition ($MS–Au/TiO_2$) methods. It was observed that Au particles synthesized using the multi-step photo-deposition method showed larger LSPR than the single-step photodeposition method. The photocatalytic H_2 formation shown by the $MS–Au/TiO_2$ is four times more than the $SS–Au/TiO_2$. Wei et al. [27] adopted two different methods for preparing heterostructure $Au–TiO_2$ nanoparticles with sizes 4.4 ± 1.7 nm and 67 ± 17 nm, respectively. It was observed that larger Au particles show a greater hydrogen production than the smaller Au particles. The low electron density of smaller nanoparticles results in weaker intensity of the LSPR. Therefore, transferred electrons are inadequate in bringing them to the energy level higher than the hydrogen potential. However, the opposite trend is also observed in the case of gold nanoparticles of different sizes loaded on fluorine-doped titanium oxide nanocrystalline film. It was found that the rate of water oxidation increases with the decreasing size of the nanoparticle. The above contradicting result has no satisfactory explanation, and it needs further study and understanding [16].

11.3.5 Plasmonic Photocatalyst Composed of Silver and TiO_2 Nanoparticles

TiO_2 is classically used as photocatalyst due to its ability to absorb photons in the visible region. Its application has been extended to various areas of photocatalysis, such as self-cleaning surfaces and photochemical super hydrophilicity. However, it uses only 4% of the total solar energy to convert it into chemical energy. Due to this reason, multiple methods have been employed by the researchers to enhance the photocatalytic activity. It was found that improving the quantum yield, suppressing the electron-hole combination, and extending the bandgap to the visible region can increase the photocatalytic activity of TiO_2. A new approach based on silver nanoparticles improves the photocatalytic activity of TiO_2. Ag nanoparticles show an intense LSPR band near the UV visible region. The enhanced near-field effect could boost the excitation of electron–hole pairs present in the TiO_2. However, when silver nanoparticles come in contact with the TiO_2, it forms silver oxide layer at the interface of Ag–TiO_2. To prevent the oxidation of silver nanoparticles, a thin layer of SiO_2 is fabricated between the Silver and TiO_2. Further studies show that the thickness of the layer must be kept very low as the electrons present in the conduction band of the Ag nanoparticles can be affected by the SiO_2 surface [18]. The efficiency of the photocatalyst decreases with increasing thickness of the SiO_2. TiO_2-based plasmonic metal–semiconductor has also contributed to the enhanced photocatalytic activity, such as the enhancement in the water splitting performance compared to that of only TiO_2. The increased efficiency is due to the formation of electron–hole pairs near the surface of the semiconductor. Moreover, these electron–hole pairs help in separating the charge carriers so that they could move toward the surface and perform photocatalytic reactions [7].

11.3.6 Plasmonic Photocatalysts Based on Silver Nanoparticles and Silver Halide Nanoparticles

As we have discussed earlier, the photocatalytic efficiency of noble–metal nanoparticles can be increased by placing them in direct contact with the semiconductor surface. Silver halides are rarely used as a photocatalysts because of their unstable nature in sunlight. However, AgCl can photocatalyze O_2 production from water in the presence of silver ions in solution. Due to the strong LSPR shown by the silver nanoparticles, the plasmonic photocatalyst Ag/AgCl shows strong absorption in the visible region. It was found that the photodecomposition of methyl orange dye using Ag/AgCl is about eight times greater than Ag/N–TiO_2. However, the Ag/AgCl photocatalyst is sensitive to sunlight due to the presence of point defects and electron traps. The stability of the Ag/AgCl photocatalyst in the visible region is because of the electrons generated from the photogeneration process, and the holes are migrated to the AgCl surface where they oxidize the Cl^- ions. Later, the electrons are transferred to the oxygen present in the solution to form superoxide and other reactive species, as shown in Fig. 11.4a [7].

11.3.7 Plasmonic Photocatalyst Composed of Silver Nanoparticles Based Composite Semiconductors

Plasmonic photocatalysts composed of different semiconductors can enable effective charge separation of electrons and holes. One such example of the composite photocatalyst is Ag/AgBr/WO_3.H_2O (Fig. 11.4b). In this composite photocatalyst,

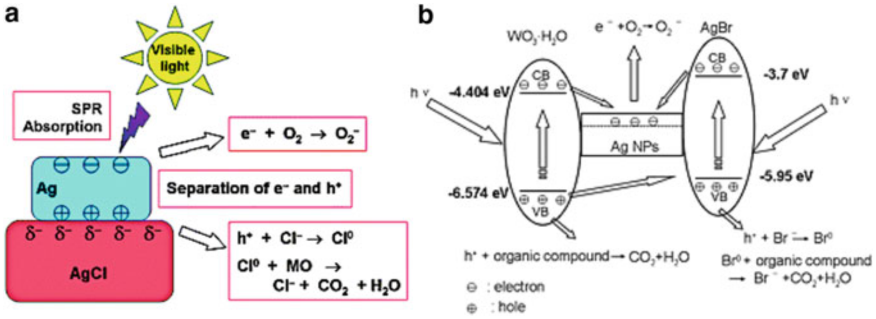

Fig. 11.4 **a** A schematic of the mechanism of photooxidation of methyl orange by Ag@AgCl. **b** The mechanism of photogeneration of electron–hole pairs and their migration and reactions in plasmonic nanoparticle–semiconductor composite. Reprinted with permission from [6]. Copyright (2012) Royal Society of Chemistry

the valence band and conduction band of AgBr lie at −5.95 eV and −3.7 eV, respectively. In comparison, the valence band and conduction band of WO_3•H_2O lie at −6.574 eV and −4.404 eV, respectively. Moreover, the electrons, after photogeneration, get transferred to the Ag nanoparticles and thereby increase the charge separation between electrons and the holes. Due to the combined properties of both plasmonic nanoparticle and the semiconductor composite, the material shows higher absorption in the visible region. The high photocatalytic activity is evaluated on E. coli bacteria. It was found that E. coli bacteria were photo-catalytically destroyed by composite photocatalyst in just 20 min in contrast to other photocatalysts. Other examples of plasmonic Ag nanoparticles and composite semiconductor photocatalyst are Ag/AgBr/BiOBr, Ag/AgBr/Al_2O_3, TiO_2–Ag/AgBr and Ag/AgCl/TiO_2 [7].

11.3.8 Plasmonic Photocatalyst Composed of Carbon and Ag Nanoparticles

Coupling of the plasmonic nanoparticles with carbon (Ag@C) helps in covering and protecting the silver nanoparticles, and these composites are typically synthesized by employing a hydrothermal process. It is found that the high photocatalytic efficiency of Ag@C aids in the photodecomposition of the aqueous tetra-ethylated rhodamine blue dye and gaseous acetaldehyde under visible light. Further study reveals that TiO_2C@Ag nanofibers increase the photocatalytic activity more than that of pure TiO_2 and TiO_2@C nanofibers because of the higher light absorption in the visible region. The photosynergistic effect between the Ag, TiO_2, and carbon is the reason behind the high absorption capacity and high charge separation between electron–hole pairs [7].

11.3.9 Plasmonic Photocatalyst Containing Graphene and Ag Nanoparticles

Graphene has been under consideration for the fabrication of photocatalysts due to its unusual properties such as high electron mobility and high conductivity. Coupling of graphene with photocatalysts has added new properties such as high dye adsorption capacity, extended light absorption range, and increased charge separation. Thus, the overall catalytic efficiency is significantly increased due to the introduction of graphene [28]. A new type of plasmonic photocatalyst that has emerged is Ag/AgCl/GO. Where GO (graphene oxide) is used as a carrier for the plasmonic photocatalyst (Ag/AgCl). GO uses a large portion of the visible light and hence helps in making highly efficient photocatalysts and is four times more effective than bare Ag/AgCl. The high photocatalytic efficiency is due to the effective charge transfer from the Ag nanoparticles to the graphene layer. Further, it reduces the rate of recombination of charge carriers [7].

11.3.9.1 Plasmonic Photocatalysts Composed of Au and Cu Nanoparticles

Gold nanoparticles are very stable, and it shows very high absorption cross section in the visible region and large scattering due to LSPR. The color of Au nanoparticles strongly depends upon the shape, size, and morphology. Larger sized nanoparticle absorbs radiation of larger wavelength because of higher electromagnetic retardation. Nanorods also show higher absorption of radiation than spherical nanoparticles because it shows oscillations in two axes, longitudinal and transverse. The greater the aspect ratio of the nanorods, the larger is the absorption of the wavelength [7]. Au nanoparticles loaded with a metal oxide such as TiO_2 have drawn the attention of researchers in recent years. When visible light falls on the Au/TiO_2, the LSPR of the Au particles gets excited and results in the interfacial transfer of an electron to the conduction band of TiO_2. Au/TiO_2 surface activity can be enhanced by surface modification without affecting the LSPR. Recent works have been done on alloying the gold nanoparticles with copper, and it was found that the alloying with copper increases the photocatalytic activity by 30% compared to that of Au/TiO_2 when employed for alcohol oxidation. A very thin layer of Cu between Au/TiO_2 increases the photocatalytic activity for the conversion of amines into aldehydes [29].

11.4 Applications of Metal-Semiconductor Hybrid Photocatalysts

11.4.1 Solar Water Splitting

Around the Globe, the pre-eminent dependence on fossil fuels and the way they intensify global warming and air pollution has affected our economy. Thus, as an alternative to fossil fuels, solar energy has emerged as a promising way to generate renewable energy with minimal impact on the environment [30]. It has attracted much interest as it is a non-exhaustible natural source and provides clean fuel. The efficient splitting of water into oxygen and usable hydrogen could be the type of industrial photosynthesis that provides environment-friendly, cost-effective, clean fuel whose only waste product is water.

Generally, water splitting is the process in which water is broken into its key constituents, i.e., hydrogen and oxygen gases. This can be done by various methods and techniques, but in this chapter, we will show only the metal-induced photocatalysis of water in the presence of visible light. The overall process of water splitting into hydrogen and oxygen gases is a non-spontaneous reaction that requires free energy of 237 kJ/mol (calculated using Nernst equation at standard conditions) [31].

$$2H_2O \rightarrow 2H_2 + O_2 \quad (\Delta G^\circ = 237\ \mathrm{kJ/mol}) \tag{11.1}$$

During water splitting, a photon of energy greater than its bandgap is absorbed by a semiconductor upon which the electrons get excited from their filled valence band to the empty conduction band. This produces an exciton (i.e., a pair of electron and hole) as the initial step of photocatalysis. Then these electrons and holes diffuse into the semiconductor surface and participate in the "hydrogen evolution reaction (HER) and oxygen evolution reactions (OER)," [32] shown with Eqs. 11.2 and 11.3, respectively.

$$2H^+ + 2e^- \rightarrow H_2 \tag{11.2}$$

$$2H_2O + 4H^+ \rightarrow 4H^+ + O_2 \tag{11.3}$$

The two most commonly used and verified approaches for water splitting are (11.2) one-step photoexcitation and (11.3) two-step photoexcitation systems (Fig. 11.5a). Both these approaches have different setups and photocatalysts, but the basic process occurring in both these approaches are similar. The overall water splitting mainly depends upon the collective effect of the primary steps, i.e., light absorption, charge transfer, and surface reaction. Both of these one and two-step photocatalytic reactions of water splitting can be achieved by using the semiconductor material with minor modification under visible light.

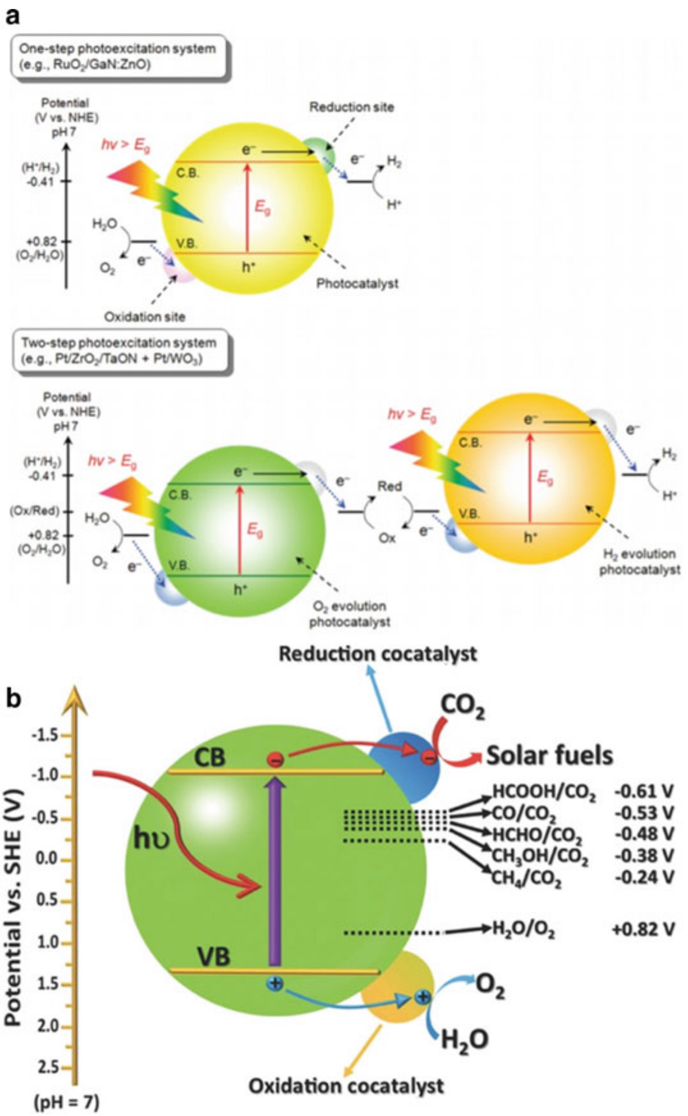

Fig. 11.5 **a** Photocatalytic water-splitting occurs through two different mechanisms—one-step and two-step. Reprinted with permission from [33]. Copyright (2010) American Chemical Society. **b** Cartoon representation of photocatalytic CO_2 reduction using a semiconductor material conjugated with co-catalysts. Reproduced with permission from [36]. Copyright (2018) Wiley

The four basic processes that occur are (1) the absorption of the incident photon by metal nanoparticles [33] because of their SPR effect, (2) ejection of electrons from the metal nanoparticles to the empty conduction band of the semiconductor, (3) the electron-deficient nanoparticle return back to their original metallic state by oxidizing H_2O–O_2, (4) transfer of electrons from the conduction band of the semiconductor to the metal oxide nanoparticles which is acting as a co-catalyst where reduction of H^+ to H_2 occurs.

The one-step photoexcitation process is an example of water splitting in which both the catalytic sites on which oxidation and reduction take place are present on the same single semiconductor photocatalyst. In this process, the excitons diffuse at the surface of the semiconductor and involve in the HER and OER, and the main necessary condition here is that the band edge should surmount the H^+/H_2 and O_2/H_2O potentials. Therefore, in overall water splitting, four photons are utilized.

The two-step photoexcitation process involves the two different photocatalysts that make H_2 and O_2 evolve separately. This technique is somewhat like the idea of natural photosynthesis and is named the Z-scheme. The photogenerated holes in oxygen evolutions photocatalysts (OEP) oxidize the H_2O to O_2, whereas the electrons in hydrogen evolutions photocatalysts (HEP) reduce the H^+ to $H_{2,}$ and the photocatalytic cycle is completed by an aqueous or solid-state mediator. In water-splitting by this approach, eight photons are utilized [32]. Due to the difference in photon utilized, the efficiency of the one-step photocatalysis is more than that of the two-step photocatalysis process. However in the two-step photocatalysis process, we can employ a wide variety of semiconductors due to the use of two different photocatalysts. So, in order to utilize the maximum amount of solar energy, one should attain the overall water splitting at low energy irradiation because as the wavelength increases, the available number of photons in the solar spectrum increases [34]. In the future, one can think of the setup of a water-splitting reactor that can separate H_2 and O_2 and also conceptualize a solar hydrogen chemical plant for generating renewable energy.

11.4.2 Utilization of CO_2 for Solar Fuels

In this era of growing consumption of fossil fuels, the enormous emission of CO_2 is a significant source of environmental pollution, which is a matter of global concern. The heat trapped by the accumulation of CO_2 in the atmosphere is responsible for the increase in the earth's surface temperature [35]. To mitigate this problem, we require environment-friendly and renewable sources of energy with minimum CO_2 emission. Solar energy emerges as the big contender as it is bountiful and can enable the photolytic reduction of CO_2 to solar fuels and reduce the concentration of CO_2 in the atmosphere.

In recent times, various semiconductors have been developed, which can facilitate CO_2 reduction such as TiO_2, Fe_2O_3, CdS, and g–C_3N_4. But these semiconductors suffer from low photoconversion efficiency due to their large bandgap, which requires UV light for excitation. Only 5% UV and 45–50% visible light are available from the solar spectrum, so modifications are needed to increase the efficiency of the catalysts. Photocatalytic reduction of CO_2 is similar to the conversion of solar energy into fuels, just like natural photosynthesis (Fig. 11.5b).

The reduction of CO_2 by photocatalysis [36] can be completed in four steps: (1) the adsorption of the CO_2 on the semiconductor, (2) absorption of incident photon energy to generate the electron–hole pair, (3) the separation of electron–hole pair and their transfer to the photocatalytic surface, and (4) the reduction of CO_2. The surface modification of semiconductors provides a large specific surface area and, consequently, a greater number of surface-active sites, which improves the ability of CO_2 adsorption. The other approach to modify the surface is to make the surface of semiconductor alkaline since CO_2 is acidic in nature and therefore can be easily chemisorbed.

Another modification that is required for the utilization of solar radiation is to reduce the bandgap of the semiconductor, which is done by doping the semiconductor with metals or non-metals. Attaching plasmonic nanoparticles to the surface of the semiconductor can increase the efficiency of electron-hole pair generation by implanting "hot electrons" from nanoparticles to the semiconductor, thus triggering the photocatalytic reaction [36]. The electron–hole pairs that are generated are very prone to recombination to create useless heat, so to use them in the proper direction, they must be separated from each other. Specifically, for this function, co-catalysts like metals on carbon material such as graphene and carbon nanotubes are introduced that reduces the possibility of recombination by accepting the electrons in the photocatalyst. As the CO_2 molecules are highly stable, the electrons having sufficient reduction potential can stimulate the reduction of CO_2 [37].

$$
\begin{array}{ll}
CO_2 + 2H^+ + 2e^- \rightarrow HCOOH & E^\circ = -0.61\ \text{V versus NHE at pH} = 7 \\
CO_2 + 2H^+ + 2e^- \rightarrow CO + H_2O & E^\circ = -0.53\ \text{V versus NHE at pH} = 7 \\
CO_2 + 8H^+ + 8e^- \rightarrow CO + H_2O & E^\circ = -0.24\ \text{V versus NHE at pH} = 7
\end{array}
$$

As the production of CH_4 and CH_3OH requires multiple electrons [38], it is desirous to rack-up electrons at the particular site. However, doping can curb the growth of particles and limit the size. Additionally, over-doping can lead to the introduction of crystal defects, which will ultimately reduce performance. Metal doping suffers from photo-corrosion, which reduces its durability; hence, doping with non-metals is preferably used for ensuring high photostability.

The plasmonic nanoparticles can harvest visible light for photocatalysis because of their SPR effect and the presence of high-energy hot electrons, which can be transferred directly to the semiconductor and help in achieving a visible light-catalyzed reduction of CO_2 [36]. Plasmonic nanoparticles provide other advantages due to their photostability, and by adjusting their shape and size, we can tune the light absorption ability. Additionally, only a minute amount of materials is required for improving the efficiency and induces a local electrical field that is beneficial for exciton separation. Heterojunction construction using semiconductors ensures fast exciton separation and also provides distinct sites for oxidation and reduction for enhanced photocatalytic CO_2 reduction.

In the future, metal and non-metal incorporation will be gradually replaced by carbon-based materials due to their extraordinary properties such as high resistance to corrosion, high electrical conductivity, large surface area, and lesser costs.

Further work needs to be done on ensuring the reproducibility of the photocatalysts and promoting the selectivity for the formation of different hydrocarbon fuels [37].

11.4.3 Activation of Inert (C–H) Bond

In today's world, one of the widely used fuel is "Natural Gas," which contains a huge number of hydrocarbons that remain unused. Hydrocarbons can generally be classified into two types: saturated and unsaturated, where the later ones are less stable and subject to the attack of reagents. But in contrast, saturated hydrocarbons, usually alkanes, contain C–C and C–H single bonds, which are highly stable [39]. There is almost no or negligible difference in the order of reactivity of various carbon–hydrogen bonds, due to which it is very difficult to target a specific bond. Over the last few decades, chemists have developed various methods in which the introduction of transition metal into the C–H bond takes place, which is known as "oxidative addition." However, only less than half of the hydrocarbons are reactive, and the reaction does not take place in a single step. The main drawback is that it requires the same equivalents of both hydrocarbon and metal, and the two are completely consumed. So modified photocatalysts that activate the C–H bond by utilizing the visible light are preferably used. As the C–H bond is highly stable, it can be activated using a heteroatom radical-mediated process such as the Hofmann–Loffler–Freytag and Barton reactions [39]. However, the generation of heteroatom radical species is difficult as it requires high energy. Therefore, we are particularly restricted to modified metal-induced photocatalysis. It provides an easy route for selective functionalization-controlled activation of inert C–H bonds. The very first step is to absorb the visible light by the photocatalyst, and the photocatalytic reduction of a compound takes place which contains a bond between heteroatoms such as N-alkoxy phthalimide. The photolytic cleavage of the N–O bond provides the O and N radicals, which can abstract a hydrogen atom to reform a strong OH and NH bond. The radical species perform the activation of inert C–H bond by 1,5 HAT process (1, 5 hydrogen atom transfer) [40] and the newly formed carbon radical can be trapped and reacted with various radical acceptors in a controlled and selective manner to form new C–C bonds. These photogenerated O and N radicals open new opportunities to develop the reactions which can directly convert N–H bond to N radical and may provide an easier and cost-effective path for C–H bond activation.

11.4.4 Nitrogen Fixation

Every living organism utilizes nitrogen in one way or another to synthesize amino acids, biomolecules, and proteins. Despite having a huge reserve of nitrogen in the earth's atmosphere, it cannot be directly utilized by the organisms due to its molecular form, which has high ionization energy, negative electron affinity, and strong nonpolar N–N triple bond. However, there is an industrial process that converts N_2 and H_2 into NH_3 by using Fe as a catalyst [41]. The main drawback of this reaction is that a large amount of energy is required, and a large amount of CO_2 is released into the atmosphere. Taking inspiration from natural nitrogenase, the photolytic reduction of N_2 utilizes water as a solvent and uses cost-effective semiconductors and solar energy to drive the reaction. But the efficiency is very low due to the poor interfacial charge transfer as the maximum excitons try to recombine among themselves rather than transfer to the nitrogen molecule. Another hurdle is that the reduction potential of the reduced or protonated form of high-energy nitrogen intermediate cannot be energetically accessed by the conventional semiconductors [41].

$$\begin{array}{ll} \mathrm{N_2 + 1e^- \rightarrow N_2^-} & \text{reduction potential}(-4.2\ \text{V vs. NHE}) \\ \mathrm{N_2 + H^+ + 1e^- \rightarrow N_2H} & \text{reduction potential}(-3.2\ \text{V vs. NHE}) \end{array}$$

To overcome these problems, chemists have proposed the implantation of oxygen vacancies on the semiconductor, which can adsorb and activate the N_2 molecules due to the availability of localized electrons in large quantities [42]. The presence of defects on the surface in the form of oxygen vacancies is able to trap the excitons and prohibit their recombination, thus helping in the transfer of these species to the adsorbates. The semiconductors consisting of semimetals that are responsive to visible light are selected because of their suitable energy band position and a layered structure [43]. The oxygen vacancy mediates the activation of N_2 by transferring electrons to the antibonding orbitals of N_2 to produce high-energy intermediates where the extent of activation is checked by the N–N bond length. The overall reaction proceeds as:

$$\mathrm{2N_2(g) + 6H_2O(1) \rightarrow 4NH_3(g) + 3O_2(g)} \quad (\lambda > 420\ \text{nm})$$

The overall mechanism consists of adsorption and activation of N_2 by oxygen vacancies (OV’s), and the protonation of each successive intermediate occurs through hydrogenation by associative mechanism and results in the formation of NH_3 or its derivatives. The presence of metals which can show SPR effect can further enhance these processes [42], through hot electron injection and plasmon-induced resonance-free energy transfer. Surface plasmon of metals can enable a wide range of photon adsorption, and the hot electrons help in the charge separation and the photolytic reduction of N_2. To utilize the full potential of solar energy, such surface modifications of photoelectrodes can be adopted for N_2 fixation in the future.

11.4.5 Photocatalysis for Green Organic Synthesis

In the twenty-first century, the main challenge for scientists is to reduce the environmental impact of chemical reactions by performing them using renewable energy sources through pollution-free techniques. Most of the organic synthesis methods require catalysts at high temperatures to yield higher yields. One of the major limitations is that they produce undesirable by-products at such high temperatures [44]. In the last decade, chemists focused on the development of heterogeneous catalysts and also innovating new photocatalysts. The direct photocatalysts based on metal–incorporated semiconductors involve the same mechanism discussed earlier [45]. However, there still exists problems of exciton recombination, reduced quantum yield, and energy lost during charge transfer. The plasmonic metal nanoparticles, which use their LSPR effect, involve the harvesting of light, charge transfer to the surface adsorbate, and the subsequent photocatalytic activity on the surface [46]. Basically, the charge transfer follows two principal mechanisms: direct and indirect. In the direct mechanism, the charge transfer occurs through the plasmon-mediated charge scattering. Whereas, in the indirect mechanism, the energetically excited charge carriers favor the transfer to the acceptor orbitals (LUMO) of the absorbate. Here a few reactions are discussed which utilized the plasmonic metal nanoparticles mediated photocatalysis:

(a) **Photocatalytic selective Oxidation: alcohol to aldehyde**

Upon visible light irradiation, LSPR generation on the metal nanoparticles produces energetic electrons on the surface that are captured by the pre-adsorbed O_2 molecules to form O_2^- species (Fig. 11.6a). As the ($-CH_2-$) group of benzyl alcohol has an active α-hydrogen, the electrochemically polarized metal nanoparticles readily abstract the α-hydrogen from the surface adsorbed benzyl alcohol to form the metal-hydrogen (M–H) surface species [46]. After this, the O_2^- species utilizes the M–H hydrogen to form water as a by-product. Meanwhile, the adsorbed benzyl alcohol releases the electrons that are captured by the electron-deficient metal nanoparticles to restore the catalytic activity. Finally, the benzylic alcohol radical automatically releases the hydrogen of the hydroxy group to form the C–O bond, and the final product is desorbed from the surface.

(b) **Photocatalytic selective Reduction: Nitrobenzene to azobenzene**

The photoreduction process occurs in the solution phase, which requires a solvent that can perform both as a hydrogen donor and the solvent. The main photo-catalytically active center for these reactions is the metal–hydrogen surface species (M–H) (Fig. 11.6b). As the metal nanoparticles are irradiated by visible light, the energetically excited electrons generated through LSPR are able to abstract hydrogen from the solvent (isopropyl alcohol) to form the active photocatalytic center [45]. Thereafter, the M–H species combines with the N–O bond of the nitrobenzene to yield the HO–M species. The interaction of high-energy electrons with the electrophilic nitro group favors the cleavage of the N–O bond.

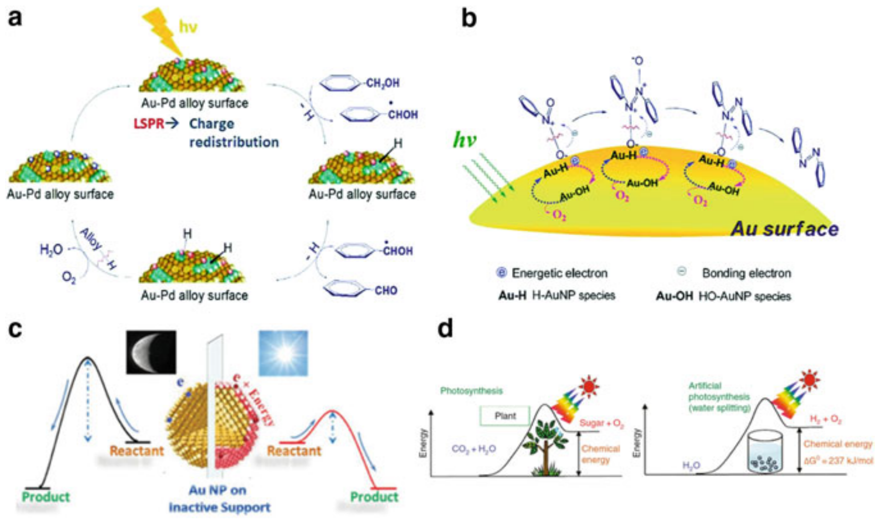

Fig. 11.6 **a** Visible light-driven mechanism of oxidation of aromatic alcohol on gold–palladium alloy nanoparticles. **b** Schematic showing mechanism of reductive coupling of nitrobenzene. Reprinted with permission from [45]. Copyright (2015) Royal Society of Chemistry. **c** Development of gold insulator-based photocatalysts. Reprinted with permission from [43]. Copyright (2013) Royal Society of Chemistry. **d** Natural versus artificial photosynthesis. Reprinted with permission from [50]. Copyright (2008) Royal Society of Chemistry

Then the HO–M species transfers hydrogen to the nitrogen atom and releases oxygen gas to transform into the original state to recycle the photocatalytic activity of the material.

These are a few of the reactions demonstrated, and photocatalysis has a wide range of applications such as degradation of volatile organic compounds. More interesting discoveries are waited for trailing the environmental remediation and eco-friendly chemical transformations.

11.5 Photocatalysis in the UV Range

The absorption by coinage metals shows localized surface plasmon resonance in the visible region, whereas it is debatable whether absorption by other metals in the UV–Visible range is attributed to LSPR or interband transition [47]. In particular, gold nanoparticles are significant as they can absorb visible light via surface plasmon resonance (SPR) to enhance photocatalytic reactivity [48]. In addition, supported Au nanoparticles can also absorb ultraviolet (UV) via electron interband transitions from 5d to 6s [49, 50].

11.5.1 Solar Water Splitting

The water-splitting photocatalysis is an example of artificial photosynthesis and indeed its challenging. The two essential processes that take place during photosynthesis are the production of oxygen by oxidation of water and reduction of carbon dioxide (Fig. 11.6d). The reduction and oxidation processes for water splitting can be achieved using semiconductor photocatalysts consisting of transition metal oxides. Semiconductors due to their unique electronic properties can act as sensitizers for the light-induced redox reactions. The electronic structure of semiconductors consists of filled valence band and an empty conduction band. When they are irradiated by light of frequency equal or greater than their bandgap, electrons from valence band (VB) get promoted to conduction band which leads to the formations of electron–hole pairs. The electrons in the conduction band facilitate the reduction of water to form hydrogen, whereas the holes in VB's are responsible for the oxidation of water to produce oxygen. For the production of hydrogen gas, the redox potential of conduction band should be more negative than redox potential of H_2/H_2O (0 V vs. NHE), and for the production of oxygen, the oxidation potential of valence band should be more positive than O_2/H_2O (1.23 V). Thus, the bandgap should be larger than 1.23 eV to perform water splitting. Semiconductor photocatalysts consisting of stable oxides and having metal cations (Ti^{4+},Zr^{4+},Ta^{5+},W^{6+}) with d_0 configurations [51] and metal cations with d_{10} configurations have their valence band which consists of O 2p orbitals, which are more positive(3 eV) than oxidation potential of water. This results in wider bandgaps, and due to their wider bandgaps, they respond to only UV light [52]. Nitrides and oxynitride can often be used for the photocatalysis of water splitting because they harvest solar light very efficiently [53].

11.5.2 CO_2 Photoreduction

CO_2 can be converted into various useful chemicals like HCOOH, HCHO, and CH_3OH and hydrocarbons like methane and so on. In 1978, Halmann did pioneering work on photocatalytic reduction of CO_2 [54]. Then, in 1979 it was demonstrated by Inoue et al. that CO_2 could be photoelectrically reduced to produce organic compounds by using semiconducting photocatalyst [55]. Among various useful chemicals produced by $CO_{2,}$ HCOOH is highly desirable because it acts as a raw material for H_2 production and is also widely used in chemical and energy industries as a fuel [56]. Here we discuss the photocatalytic reduction of CO_2 to HCOOH using Cu–Zn nanoparticle-loaded $SrTiO_3$. Copper has unique properties like its high abundance, nontoxicity, and brilliant finish. The alloy Cu–Zn can convert CO_2 into HCOOH selectively in aqueous medium at room temperature. Cu–Zn nanoparticle-loaded $SrTiO_3$ acts as an efficient photocatalyst that can selectively convert CO_2 into HCOOH under UV radiation. It was observed that under UV irradiation, HCOOH is produced as the major product while methane and CO are also produced, their production was limited, and a negligible amount of H_2 was also detected. This highlights the selectivity of the Cu–Zn co-catalyst for CO_2 reduction.

The reason for the selectivity of Cu–Zn alloy electrode is based on two factors:

(1) CO_2 reduction pathways
(2) The state of the catalyst surface.

By studying numerous CO_2 reduction pathways, it was analyzed that HCOOH formation is initiated by a CO_2 radical, which has weak adsorption on the catalyst surface [57]. Due to this weak adsorption of CO_2 anion radical, the transfer of one electron to CO_2 takes place, whereas a CO_2 anion radical show hydrogenation, thereby forming $HCOO^-$. Here in the Cu–Zn based system, the adsorption of a CO_2 anion radical on the Zn surface is weak. Therefore, the major product of CO_2 reduction is HCOOH. On the other hand, when the catalyst surface shows high adsorption for a CO_2 anion radical, it leads to the formation of CO. Furthermore, if metal possesses weak adsorption for CO radical, it will desorb from the surface of metal which results in the production of CO. But, if the metal surface has enough adsorption strength to stabilize CO radical on its surface, then the formation of CH_4 or CH_3OH takes place. When both Cu and Zn are combined at an atomic scale, adsorption of both CO_2 anion radical and CO radicals gets decreased, which leads to the formation of HCOOH as a major product [58].

11.5.3 Activation of Inert molecules—the Cases of N_2 and CH_4

The first reported conversion of N_2 into NH_3 under UV radiations was given by Schrauzer et al. in 1977 [59]. CH_4 is the type of hydrocarbon which are the highly stable and are widely distributed in nature. The high abundance of methane is one of the promising factors that compel us to use this hydrocarbon as an alternative for fuel and chemical industry [60]. It has always been of interest to convert CH_4 into useful hydrocarbons and hydrogen. But it is challenging due to its inert nature or high stability and high-energy requirements for the conversion processes. Various schemes have been employed for the photolytic oxidation of CH_4. The photocatalytic oxidation of CH_4 over Ag decorated Zn nanocatalyst was reported by Yi et al. [61]. It shows how the reduction in particle size of zinc to the nanoscale can increase the activity of the oxidation of methane in sunlight and how the photocatalytic activity for the oxidation process can be enhanced further by decorating with silver. This additional enhancement is attributed to the LSPR effects.

11.6 Conclusions and Future Outlook

The world today is facing challenges in solving the energy crisis issues in the form of greenhouse effect, excess carbon dioxide emissions, global rise in temperature, etc. Additionally, there are challenges such as mitigating the projected energy crisis and finding alternative energy sources that are clean and renewable. Efforts to address these problems require harnessing of emergent and green chemistry, which can be further accentuated by advanced photocatalysts that can provide an energy-efficient way of chemical conversion. Among all existing sources, hydrogen, due to its high-energy capacity and environmental friendliness, is one of the most popular choices. Thus, photocatalytic processes such as water splitting come as a solution that will contribute to solving the energy crisis and environmental issues through a sustainable and environment-friendly way. Such photocatalyst needs to be good absorbers of sunlight and needs to have high stability and favorable band structures. The incorporation of plasmonic entities has greatly influenced the catalytic activity due to the generation of hot electrons, hotspots and enhanced electromagnetic field, among others. In today's scenario, the photoreduction of carbon dioxide can be the most promising solution since it can be executed just by using sunlight. We are aware that coal is a national treasure; thus, controlling CO_2 emissions is one of the largest technical challenges faced by the fossil energy industry. Photocatalysts also play an important role in the catalytic conversion of CO_2 and other inert molecules, which is of utmost importance as it will help us decrease environmental-related problems and provide scope for renewable sources of energy, i.e., green and clean energy. In all these applications of photocatalysts, the role of metals and plasmonic materials has resulted in some fundamental breakthroughs which have captured our imagination and have thrown light into the mechanism of charge transfer. Further work is needed to fully realize the potential and address several problems which are affecting semiconductors-based photocatalysis such as charge transport and rapid recombination. Several of these mechanisms have been discussed in this chapter, and with the advent of advanced spectroscopies, both steady-state and ultrafast, would help in investigating the charge separation and transport at the semiconductor heterojunction-based photocatalysts, thus giving more clear ideas about solving the low efficiencies and enabling the fabrication of highly energy-efficient photocatalysts.

References

1. Serpone N, Emeline A (2012) Semiconductor photocatalysis—past, present, and future outlook. J Phys Chem Lett 3(5):673–677. https://doi.org/10.1021/jz300071j
2. Ingram D, Linic S (2011) Water splitting on composite plasmonic-metal/semiconductor photoelectrodes: evidence for selective plasmon-induced formation of charge carriers near the semiconductor surface. J Am Chem Soc 133(14):5202–5205. https://doi.org/10.1021/ja200086g

3. Zhang F, Wang X, Liu H, Liu C, Wan Y, Long Y et al (2019) Recent advances and applications of semiconductor photocatalytic technology. Appl Sci-Basel 9(12). https://doi.org/10.3390/app9122489
4. Hashimoto K, Irie H, Fujishima A (2005) TiO_2 photocatalysis: a historical overview and future prospects. Japanese J Appl Phys Part 1-Regular Papers Brief Commun Rev Papers 44 (12):8269–85. https://doi.org/10.1143/JJAP.44.8269
5. Zhang X, Chen YL, Liu RS, Tsai DP (2013) Plasmonic photocatalysis. Rep Prog Phys 76 (4):046401. https://doi.org/10.1088/0034-4885/76/4/046401
6. Khore S, Kadam S, Naik S, Kale B, Sonawane R (2018) Solar light active plasmonic Au@ TiO_2 nanocomposite with superior photocatalytic performance for H-2 production and pollutant degradation. New J Chem 42(13):10958–10968. https://doi.org/10.1039/c8nj01410h
7. Wang P, Huang B, Dai Y, Whangbo MH (2012) Plasmonic photocatalysts: harvesting visible light with noble metal nanoparticles. Phys Chem Chem Phys 14(28):9813–9825. https://doi.org/10.1039/c2cp40823f
8. Cushing SK, Li J, Meng F, Senty TR, Suri S, Zhi M et al (2012) Photocatalytic activity enhanced by plasmonic resonant energy transfer from metal to semiconductor. J Am Chem Soc 134(36):15033–15041. https://doi.org/10.1021/ja305603t
9. Masson J (2020) Portable and field-deployed surface plasmon resonance and plasmonic sensors. Analyst 145(11):3776–3800. https://doi.org/10.1039/d0an00316f
10. Sui M, Kunwar S, Pandey P, Lee J (2019) Strongly confined localized surface plasmon resonance (LSPR) bands of Pt, AgPt, AgAuPt nanoparticles. Sci Rep 9(1):16582. https://doi.org/10.1038/s41598-019-53292-1
11. Hammond JL, Bhalla N, Rafiee SD, Estrela P (2014) Localized surface plasmon resonance as a biosensing platform for developing countries. Biosensors (Basel) 4(2):172–188. https://doi.org/10.3390/bios4020172
12. Xavier J, Vincent S, Meder F, Vollmer F (2018) Advances in optoplasmonic sensors—combining optical nano/microcavities and photonic crystals with plasmonic nanostructures and nanoparticles. Nanophotonics 7(1):1–38. https://doi.org/10.1515/nanoph-2017-0064
13. Tseng YH, Chang IG, Tai Y, Wu KW (2012) Effect of surface plasmon resonance on the photocatalytic activity of Au/TiO_2 under UV/visible illumination. J Nanosci Nanotechnol 12 (1):416–422. https://doi.org/10.1166/jnn.2012.5376
14. Liu Y, Chen Q, Cullen DA, Xie Z, Lian T (2020) Efficient hot electron transfer from small Au nanoparticles. Nano Lett 20(6):4322–4329. https://doi.org/10.1021/acs.nanolett.0c01050
15. Park JY, Kim SM, Lee H, Nedrygailov II (2015) Hot-electron-mediated surface chemistry: toward electronic control of catalytic activity. Acc Chem Res 48(8):2475–2483. https://doi.org/10.1021/acs.accounts.5b00170
16. Liu L, Zhang X, Yang L, Ren L, Wang D, Ye J (2017) Metal nanoparticles induced photocatalysis. Natl Sci Rev 4(5):761–780. https://doi.org/10.1093/nsr/nwx019
17. Liu L, Ouyang S, Ye J (2013) Gold-nanorod-photosensitized titanium dioxide with wide-range visible-light harvesting based on localized surface plasmon resonance. Angew Chem Int Ed Engl 52(26):6689–6693. https://doi.org/10.1002/anie.201300239
18. Awazu K, Fujimaki M, Rockstuhl C, Tominaga J, Murakami H, Ohki Y et al (2008) A plasmonic photocatalyst consisting of silver nanoparticles embedded in titanium dioxide. J Am Chem Soc 130(5):1676–1680. https://doi.org/10.1021/ja076503n
19. Golabiewska A, Malankowska A, Jarek M, Lisowski W, Nowaczyk G, Jurga S et al (2016) The effect of gold shape and size on the properties and visible light-induced photoactivity of Au–TiO_2. Appl Catal B-Environ 196:27–40. https://doi.org/10.1016/j.apcatb.2016.05.013
20. Tsukamoto D, Shiraishi Y, Sugano Y, Ichikawa S, Tanaka S, Hirai T (2012) Gold nanoparticles located at the interface of anatase/rutile TiO_2 particles as active plasmonic photocatalysts for aerobic oxidation. J Am Chem Soc 134(14):6309–6315. https://doi.org/10.1021/ja2120647
21. Liu L, Li P, Wang T, Hu H, Jiang H, Liu H et al (2015) Constructing a multicomponent junction for improved visible-light photocatalytic performance induced by Au nanoparticles. Chem Commun (Camb) 51(11):2173–2176. https://doi.org/10.1039/c4cc08556f

22. Yu S, Kim YH, Lee SY, Song HD, Yi J (2014) Hot-electron-transfer enhancement for the efficient energy conversion of visible light. Angew Chem Int Ed Engl 53(42):11203–11207. https://doi.org/10.1002/anie.201405598
23. Wu K, Chen J, McBride JR, Lian T (2015) Charge transfer. Efficient hot-electron transfer by a plasmon-induced interfacial charge-transfer transition. Science 349(6248):632–635. https://doi.org/10.1126/science.aac5443
24. Tanaka A, Hashimoto K, Kominami H (2014) Visible-light-induced hydrogen and oxygen formation over Pt/Au/WO_3 photocatalyst utilizing two types of photoabsorption due to surface plasmon resonance and band-gap excitation. J Am Chem Soc 136(2):586–589. https://doi.org/10.1021/ja410230u
25. Zhang Z, Li A, Cao SW, Bosman M, Li S, Xue C (2014) Direct evidence of plasmon enhancement on photocatalytic hydrogen generation over Au/Pt-decorated TiO_2 nanofibers. Nanoscale 6(10):5217–5222. https://doi.org/10.1039/c3nr06562f
26. Hung S, Xiao F, Hsu Y, Suen N, Yang H, Chen H et al (2016) Iridium oxide-assisted plasmon-induced hot carriers: improvement on kinetics and thermodynamics of hot carriers. Adv Energy Mater 6(8). https://doi.org/10.1002/aenm.201501339
27. Qian K, Sweeny B, Johnston-Peck A, Niu W, Graham J, DuChene J et al (2014) Surface plasmon-driven water reduction: gold nanoparticle size matters. J Am Chem Soc 136 (28):9842–9845. https://doi.org/10.1021/ja504097v
28. Zhang L, Mohamed H, Dillert R, Bahnemann D (2012) Kinetics and mechanisms of charge transfer processes in photocatalytic systems: a review. J Photochem Photobiol C-Photochem Rev 13(4):263–276. https://doi.org/10.1016/j.jphotochemrev.2012.07.002
29. Sato Y, Naya S, Tada H (2015) A new bimetallic plasmonic photocatalyst consisting of gold (core)-copper(shell) nanoparticle and titanium(IV) oxide support. Apll Mater 3(10). https://doi.org/10.1063/1.4923098
30. Tachibana Y, Vayssieres L, Durrant J (2012) Artificial photosynthesis for solar water-splitting. Nat Photonics 6(8):511–518. https://doi.org/10.1038/nphoton.2012.175
31. Walter MG, Warren EL, McKone JR, Boettcher SW, Mi Q, Santori EA et al (2010) Solar water splitting cells. Chem Rev 110(11):6446–6473. https://doi.org/10.1021/cr1002326
32. Chen S, Takata T, Domen K (2017) Particulate photocatalysts for overall water splitting. Nat Rev Mater 2(10). https://doi.org/10.1038/natrevmats.2017.50
33. Tanaka A, Teramura K, Hosokawa S, Kominami H, Tanaka T (2017) Visible light-induced water splitting in an aqueous suspension of a plasmonic Au/TiO_2 photocatalyst with metal co-catalysts. Chem Sci 8(4):2574–2580. https://doi.org/10.1039/c6sc05135a
34. Maeda K, Domen K (2010) Photocatalytic water splitting: recent progress and future challenges. J Phys Chem Lett 1(18):2655–2661. https://doi.org/10.1021/jz1007966
35. Wei L, Yu C, Zhang Q, Liu H, Wang Y (2018) TiO_2-based heterojunction photocatalysts for photocatalytic reduction of CO_2 into solar fuels. J Mater Chem A 6(45):22411–22436. https://doi.org/10.1039/c8ta08879a
36. Low J, Cheng B, Yu J (2017) Surface modification and enhanced photocatalytic CO_2 reduction performance of TiO_2: a review. Appl Surf Sci 392:658–686. https://doi.org/10.1016/j.apsusc.2016.09.093
37. Ran J, Jaroniec M, Qiao SZ (2018) Cocatalysts in semiconductor-based photocatalytic CO. Adv Mater 30(7). https://doi.org/10.1002/adma.201704649
38. Ola O, Maroto-Valer M (2016) Synthesis, characterization and visible light photocatalytic activity of metal based TiO_2 monoliths for CO_2 reduction. Chem Eng J 283:1244–1253. https://doi.org/10.1016/j.cej.2015.07.090
39. Bergman RG (2007) Organometallic chemistry: C–H activation. Nature 446(7134):391–393. https://doi.org/10.1038/446391a
40. Hu X, Chen J, Xiao W (2017) Controllable remote C–H bond functionalization by visible-light photocatalysis. Angewandte Chemie-Internat Edn 56(8):1960–1962. https://doi.org/10.1002/anie.201611463

41. Li H, Shang J, Ai Z, Zhang L (2015) Efficient visible light nitrogen fixation with BiOBr nanosheets of oxygen vacancies on the exposed 001 facets. J Am Chem Soc 137(19):6393–6399. https://doi.org/10.1021/jacs.5b03105
42. Li C, Wang T, Zhao ZJ, Yang W, Li JF, Li A et al (2018) Promoted fixation of molecular nitrogen with surface oxygen vacancies on plasmon-enhanced TiO. Angew Chem Int Ed Engl 57(19):5278–5282. https://doi.org/10.1002/anie.201713229
43. Dong X, Zhang W, Sun Y, Li J, Cen W, Cui Z et al (2018) Visible-light-induced charge transfer pathway and photocatalysis mechanism on Bi semimetal@defective BiOBr hierarchical microspheres. J Catal 357:41–50. https://doi.org/10.1016/j.jcat.2017.10.004
44. Sarina S, Waclawik E, Zhu H (2013) Photocatalysis on supported gold and silver nanoparticles under ultraviolet and visible light irradiation. Green Chem 15(7):1814–1833. https://doi.org/10.1039/c3gc40450a
45. Xiao Q, Jaatinen E, Zhu H (2014) Direct photocatalysis for organic synthesis by using plasmonic-metal nanoparticles irradiated with visible light. Chem Asian J 9(11):3046–3064. https://doi.org/10.1002/asia.201402310
46. Peiris S, McMurtrie J, Zhu H (2016) Metal nanoparticle photocatalysts: emerging processes for green organic synthesis. Catal Sci Technol 6(2):320–338. https://doi.org/10.1039/c5cy02048d
47. Chen H, Shao L, Li Q, Wang J (2013) Gold nanorods and their plasmonic properties. Chem Soc Rev 42(7):2679–2724. https://doi.org/10.1039/c2cs35367a
48. Lan J, Zhou X, Liu G, Yu J, Zhang J, Zhi L et al (2011) Enhancing photocatalytic activity of one-dimensional $KNbO_3$ nanowires by Au nanoparticles under ultraviolet and visible-light. Nanoscale 3(12):5161–5167. https://doi.org/10.1039/c1nr10953g
49. Zhu H, Chen X, Zheng Z, Ke X, Jaatinen E, Zhao J et al (2009) Mechanism of supported gold nanoparticles as photocatalysts under ultraviolet and visible light irradiation. Chem Commun 48:7524–7526. https://doi.org/10.1039/b917052a
50. Zhu H, Ke X, Yang X, Sarina S, Liu H (2010) Reduction of nitroaromatic compounds on supported gold nanoparticles by visible and ultraviolet light. Angewandte Chemie-Inter Edn 49(50):9657–9661. https://doi.org/10.1002/anie.201003908
51. Kudo A, Miseki Y (2009) Heterogeneous photocatalyst materials for water splitting. Chem Soc Rev 38(1):253–278. https://doi.org/10.1039/b800489g
52. Kudo A (2007) Photocatalysis and solar hydrogen production. Pure Appl Chem 79(11):1917–1927. https://doi.org/10.1351/pac200779111917
53. Kato H, Asakura K, Kudo A (2003) Highly efficient water splitting into H_2 and O_2 over lanthanum-doped $NaTaO_3$ photocatalysts with high crystallinity and surface nanostructure. J Am Chem Soc 125(10):3082–3089. https://doi.org/10.1021/ja027751g
54. Halmann M (1978) Photoelectrochemical reduction of aquesous carbon-dioxide on p-type Gallium-phosphide in liquid junction solar-cells. Nature 275(5676):115–116. https://doi.org/10.1038/275115a0
55. Inoue T, Fujishima A, Konishi S, Honda K (1979) Photoelectrocatalytic reduction for carbon-dioxide in aqueous suspensions of semiconductor powders. Nature 277(5698):637–638. https://doi.org/10.1038/277637a0
56. Johnson TC, Morris DJ, Wills M (2010) Hydrogen generation from formic acid and alcohols using homogeneous catalysts. Chem Soc Rev 39(1):81–88. https://doi.org/10.1039/b904495g
57. Kortlever R, Shen J, Schouten K, Calle-Vallejo F, Koper M (2015) Catalysts and reaction pathways for the electrochemical reduction of carbon dioxide. J Phys Chem Lett 6(20):4073–4082. https://doi.org/10.1021/acs.jpclett.5b01559
58. Yin G, Abe H, Kodiyath R, Ueda S, Srinivasan N, Yamaguchi A et al (2017) Selective electro- or photo-reduction of carbon dioxide to formic acid using a Cu–Zn alloy catalyst. J Mater Chem A 5(24):12113–12119. https://doi.org/10.1039/c7ta00353f
59. Schrauzer G, Guth T (1977) Photolysis of water and photoreduction of nitrogen in titanium-dioxide. J Am Chem Soc 99(22):7189–7193. https://doi.org/10.1021/ja00464a015

60. Holmen A (2009) Direct conversion of methane to fuels and chemicals. Catal Today 142(1–2): 2–8. https://doi.org/10.1016/j.cattod.2009.01.004
61. Chen X, Li Y, Pan X, Cortie D, Huang X, Yi Z (2016) Photocatalytic oxidation of methane over silver decorated zinc oxide nanocatalysts. Nat Commun 7:12273. https://doi.org/10.1038/ncomms12273

Chapter 12
The Role of Oxygen Vacancy and Other Defects for Activity Enhancement

Marcin Janczarek, Maya Endo-Kimura, Tharishinny Raja-Mogan, and Ewa Kowalska

Abstract Titania (titanium(IV) oxide; TiO_2) has been intensively studied for both fundamental and applied photocatalysis because of high photocatalytic activity, abundance, low costs, and stability. However, the inability of working under visible-light irradiation and recombination of charge carriers limit its broad commercialization. Accordingly, various methods of titania modification have been proposed, including the preparation of defect-rich titania samples. This chapter has focused on this aspect, discussing self-doped titania photocatalysts, including defect types, synthesis methods, and their applications for photocatalytic degradation of organic compounds and solar energy conversion. Additionally, more complex photocatalysts, such as self-doped titania co-modified with other elements (metals and nonmetals) and novel structures of titania, i.e., inverse opal photonic crystals with introduced defects, have also been discussed. Finally, antimicrobial properties of defective titania and other semiconductors have been presented, confirming that these photocatalysts are highly promising as effective, green, and cheap materials.

Keywords Defective titania · Surface vacancies · Ti^{3+} · Photonic crystals · Antimicrobial properties · Vis-responsive photocatalysts · Titania modification · Cancer therapy

12.1 Introduction

Over the past 40 years, titanium dioxide (TiO_2; titania) has been of great interest, because of its exceptional properties as an efficient photocatalyst in various redox reactions. Although titania has been widely investigated and even commercially

---

M. Janczarek
Institute of Chemical Technology and Engineering, Faculty of Chemical Technology, Poznan University of Technology, Berdychowo 4, 60-965 Poznan, Poland

M. Endo-Kimura · T. Raja-Mogan · E. Kowalska (✉)
Institute for Catalysis (ICAT), Hokkaido University, Sapporo N21 W20, 001-0021, Japan
e-mail: kowalska@cat.hokudai.ac.jp

S. Garg and A. Chandra (eds.), *Green Photocatalytic Semiconductors*,
Green Chemistry and Sustainable Technology,
https://doi.org/10.1007/978-3-030-77371-7_12

used (e.g., as self-cleaning coatings), there are two main shortcomings that limit its broader applications, i.e., light sensitivity only in the UV range of irradiation (λ 400 nm; depending on polymorphic form), and charge carriers' recombination (typical for all semiconductors). Accordingly, the properties of titania have been improved by various methods [1, 2], including surface modification [3], doping [4], heterojunction formation with other semiconductors [5, 6] and nano-architecture design of advanced morphology, e.g., faceted nanoparticles [7, 8], nanotubes [9], and inverse opal structures (photonic crystals) [10]. The introduction of external species to titania structure and the interaction between modifier/dopant and titania brings many challenges, such as intrinsic stability and real possibility of commercialization of designed visible-light active photocatalysts. Another method, i.e., the defect engineering of semiconductors, has also been proposed and recognized as a promising direction to improve the photocatalytic efficiency. First, numerous studies have shown that the introduction of defects, such as oxygen vacancies or Ti^{3+} species, can shift the photoabsorption properties into visible-light region of irradiation, and thus, even unmodified titania has been described as "self-modified/doped titania" [11, 12]. Furthermore, oxygen vacancies can affect also the charge transport [13] and surface properties of titania [14]. The influence of the presence of these defects on various properties of photocatalyst is still under debate.

12.2 The Character of Defect Disorder in Titania

The defect disorder in titania might be described by the presence of three types of ionic defects: (i) oxygen vacancies, (ii) titanium interstitial (e.g., hydrogen or nonmetal dopants), and (iii) substitutional impurity (e.g., metal or nonmetal dopants) [14–16]. The formation of intrinsic defects can be described using the Kröger–Vink notation by the following example of defect equilibria (12.1) and (12.2) [15, 17]:

$$\mathrm{O}_\mathrm{O}^{x} \leftrightarrow \mathrm{V}_\mathrm{O}^{\bullet\bullet} + 2\mathrm{e}' + \frac{1}{2}\mathrm{O}_2 \tag{12.1}$$

$$\mathrm{Ti}_\mathrm{Ti}^{x} + 2\mathrm{O}_\mathrm{O}^{x} \leftrightarrow \mathrm{Ti}_{i}^{\bullet\bullet\bullet} + 3\mathrm{e}' + \mathrm{O}_2 \tag{12.2}$$

where

$\mathrm{O}_\mathrm{O}^{x}$	O^{2-} ion in the oxygen lattice site,
$\mathrm{V}_\mathrm{O}^{\bullet\bullet}$	oxygen vacancy,
e'	Ti^{3+} ion in the titanium lattice site (quasi-free electron),
$\mathrm{Ti}_\mathrm{Ti}^{x}$	Ti^{4+} ion in the titanium lattice site,
$\mathrm{Ti}_{i}^{\bullet\bullet\bullet}$	Ti^{3+} in the interstitial site.

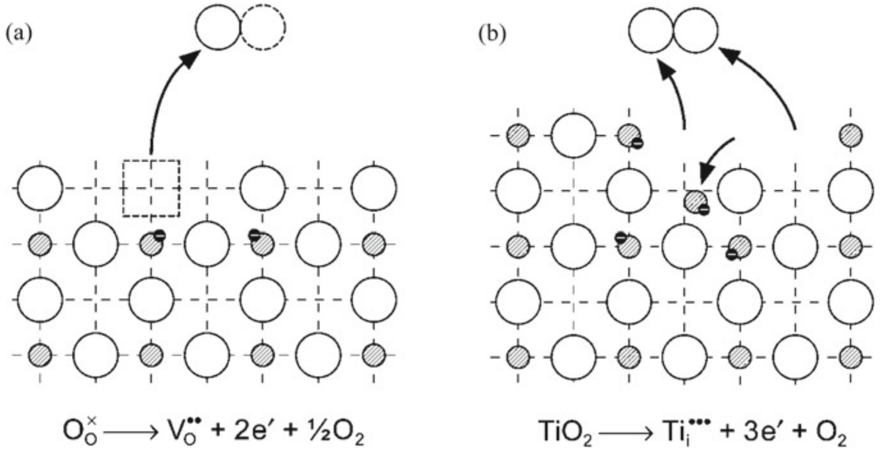

Fig. 12.1 Formation of doubly ionized oxygen vacancy (**a**) and trivalent titanium interstitial (**b**): large and small circles represent lattice oxygen and titanium ions, respectively; black circles denote electrons, and the square represents an empty lattice site. Reprinted with permission from [18]. Copyright 2011, American Chemical Society

The formation of doubly ionized oxygen vacancy and trivalent titanium interstitial is shown in Fig. 12.1a and b, respectively.

The relationships between oxygen vacancies and Ti^{3+} are complex, and three basic cases could be distinguished: (i) the electric charges of Ti^{3+} species in TiO_2 might be balanced by oxygen vacancies → Ti^{3+} and oxygen vacancies appear/disappear simultaneously, (ii) besides Ti^{3+} and oxygen vacancies a certain amount of structural defects are present → inequalities between Ti^{3+} and oxygen vacancies occur, (iii) electric charges of Ti^{3+} species in TiO_2 are balanced by protons → Ti^{3+} that has no direct connection with oxygen vacancies [12]. Furthermore, it is necessary to underline that the ionic defects are responsible for the formation of donor and acceptor levels in the electronic structure of titania (Fig. 12.2) [19]. It has been stated that the introduced localized oxygen vacancy states at energies from 0.75 to 1.18 eV below the conduction band minimum of titania [20].

Fig. 12.2 Band model of TiO_2 with the indication of the energy levels of intrinsic lattice defects. Reprinted with permission from [19]. Copyright 2008, American Chemical Society

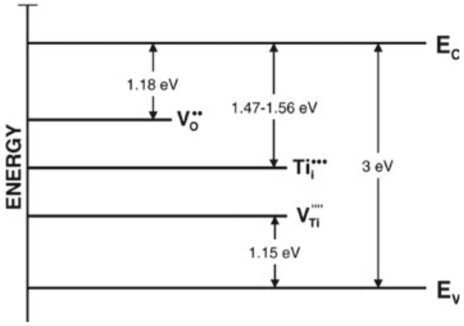

Furthermore, oxygen vacancies might also influence the electron-hole recombination phenomenon, changing chemical rates that depend on charge transfer from either electrons or holes [21].

12.3 Methods of Defects' Introduction and the Properties of Defective Materials

Modification of defect disorder can be conducted by: (i) changes of the titanium-to-oxygen ratio and related concentration of point defects (self-modified titania), and (ii) incorporation of higher- and lower-valence ions, forming donors and acceptors, respectively [18]. It is important to state that the excess of electrons located on oxygen vacancy states affects the surface adsorption and reactivity of key adsorbates, such as O_2 and H_2O on titania [22]. Furthermore, theoretical calculations show that a high vacancy concentration could induce a vacancy band of electronic states just below the conduction band. Therefore, the development of controllable synthesis of titania with oxygen vacancies with the possible adjustment of its intrinsic properties important for photocatalytic applications is of great importance [23].

12.3.1 Self-Modified Titania

The first group of methods to obtain defected titania without introducing additional species is to reduce titania to form oxygen-deficient, non-stoichiometric titania (TiO_{2-x}). The most commonly used reductant is hydrogen (H_2). Hydrogen reacts with the lattice oxygen to form oxygen vacancies in titania, and simultaneously one oxygen vacancy leaves behind two excess electrons. The mentioned electrons might locate at titanium positions (forming Ti^{3+}) or remain at the positions of oxygen vacancies [12]. For example, Liu et al. treated titania powder with hydrogen gas at high temperatures and estimated the photocatalytic properties of prepared materials [24]. They observed the improvement of photocatalytic activity for phenol degradation. An optimal H_2-treatment temperature was found to be between 500 and 600 °C. According to EPR studies, it was observed that first oxygen vacancies were generated, and then with an increase in temperature above 450 °C also Ti^{3+} defects were formed. It was concluded that both oxygen vacancies and Ti^{3+} were attributed to the enhancement of photocatalytic activity [24].

The hydrogenated titania (black samples) exhibiting solar-induced photocatalytic activity (related to methylene blue and phenol degradation, and hydrogen generation with Pt-particles presence as co-catalyst) was also prepared by Chen et al. [25]. They applied H_2-thermal treatment in high-pressure hydrogen system (20 bar) at 200 °C for 5 days. In this case, the presence of mid-gap electronic states in the lattice disordered titania structure was indicated as the main reason of observed photocatalytic behavior [25, 26]. In another study, Wei et al. synthesized hydrogenated (001)-facets-dominated anatase nanosheets [27]. These materials showed higher UV–visible and visible-light irradiation-induced photocatalytic activity than pristine TiO_2. The presence of both oxygen vacancies and Ti^{3+} was detected. It was proposed that these defects induced the adsorption of O^- species on the titania surface, resulting in a significant bandgap narrowing [27], as also confirmed by the work of Naldoni et al. [28]. Sinhamahapatra et al. applied modified method to prepare black titania, called as magnesiothermic reduction of titania under H_2 (5%)/ Ar atmosphere [29]. They observed outstanding photocatalytic activity of prepared samples (visible-light-induced hydrogen generation) due to the extended absorption of visible light, optimal band position, the presence of an appropriate amount of oxygen vacancies and Ti^{3+} and hindered charge carriers' recombination. It has been proposed that surface defects and/or oxygen vacancies might be considered as one of the property factors, acting as electron donors to enhance donor density and improving the charge transfer in black titania [29–31].

However, different observation was made by Leshuk et al. for black titania, prepared by high-temperature hydrogenation (up to 450 °C) under 20 bar H_2 for 24 h [32]. The deterioration of photocatalytic activity under sunlight irradiation during degradation of methylene blue was observed for hydrogenated samples with an increase in H_2-treatment temperature, despite strong visible-light absorption. It was proposed that a decrease in activity was caused by the presence of vacancy defects confined to the core of titania crystals rather than to their surface, and, in that case, they could behave as trap states and charge recombination centers [32]. Therefore, the proper conditions for hydrogenation of titania (temperature, H_2 pressure, treatment time) are very important to adjust the proper ratio between surface and core defects, such as oxygen vacancies.

Other approach for the preparation of self-doped titania to avoid the high-temperature requirement and excessive energy consumption in H_2-gas hydrogenation is to apply mild sources of hydrogen, such as $NaBH_4$ [33]. Xing et al. successfully prepared self-doped titania nanoparticles (NPs) by a simple one-step solvothermal method with $NaBH_4$ added as a reductant [34]. Self-modified titania samples have shown a good visible-light photocatalytic activity for phenol degradation, which could be directly correlated with the concentration of Ti^{3+} and oxygen vacancies. In another work, Fang et al. obtained self-doped TiO_2 samples also through $NaBH_4$ reduction step [35]. The high photocatalytic activity for degradation of Rhodamine B under visible-light irradiation was reported. It has been proposed that as the consequence of visible-light irradiation of photocatalyst, the electron is excited to the impurity level resulting from the presence of Ti^{3+} and oxygen vacancies. The life of the photoinduced electron in the oxygen vacancy trap is longer than that in conduction band, and thus leading to reduction of oxygen and formation of superoxide radical, what enhances photocatalytic activity [34]. However, it should be pointed out that application of dyes for vis-activity testing is not recommended due to possible dye-sensitization of semiconductors [36], and thus vis-response should also be confirmed for colorless compounds.

Interesting and economic synthetic approach to obtain self-modified titania was applied by Xing et al. via low-temperature vacuum-activated method [37]. The photocatalysts possessed higher visible-light activity in degradation of methyl orange and phenol than commercially available unmodified Degussa P25 titania (P25 is probably the most investigated titania, composed of anatase, rutile, and amorphous phase, with one of the highest photocatalytic activities among titania samples, and thus commonly used as a reference sample [38–40]). It was confirmed (by EPR method) that three types of oxygen vacancy states existed in the bandgap of vacuum-activated titania, i.e., O_V^{++}, $[O_V{\cdot}Ti^{3+}]^+$, and $[O_V{\cdot}Ti^{3+}]^0$, as shown in Fig. 12.3. It was found that neutral $[O_V{\cdot}Ti^{3+}]^0$ has been readily transformed to $[O_V{\cdot}Ti^{3+}]^+$ in the presence of O_2 and light irradiation. This transformation might move up the oxygen vacancy color center, resulting in a decrease in the visible-light response and color decay [37].

In another research, Xia et al. prepared vacuum-treated titania nanocrystals [41]. It was proposed that the long-wavelength optical absorption was caused by the existence of oxygen vacancies and Ti^{3+} defects, and also possible surface structural disorders. Both oxygen vacancies and Ti^{3+} defects influenced the photocatalytic activities in methylene blue decomposition and hydrogen generation. Interestingly, it was found that oxygen vacancies positively influenced the decomposition of methylene blue but harmed the photocatalytic hydrogen generation. Accordingly, it was proposed that the vacuum-induced formation of Ti^{3+} could be associated with the formation of oxygen vacancies as [41]:

$$2\mathrm{O}_\mathrm{O}^{x} + \mathrm{Ti}_\mathrm{Ti}^{x} \leftrightarrow 2\mathrm{V}_\mathrm{O}^{\bullet\bullet} + 3\mathrm{e}' + \mathrm{Ti}_\mathrm{Ti}' + \mathrm{O}_2 \quad (12.3)$$

where

Ti_Ti' Ti^{3+} in the lattice titanium position.

Since superoxide ions are generated at oxygen vacancy sites in the photocatalyst through reaction (12.4) [41]:

$$\mathrm{O}_2 + \mathrm{V}_{O}^{\bullet\bullet} + e' \rightarrow \mathrm{O}_{2(\mathrm{v})}^{\bullet\bullet} \quad (12.4)$$

where

$\mathrm{O}_{2(\mathrm{v})}^{\bullet\bullet}$ the superoxide ion generated in the oxygen vacancy sites,

the amount of superoxide ion generation is highly affected by the availability of oxygen vacancy sites in titania. Dong et al. have postulated that the enhanced photocatalytic activity of vacuum-activated P25 is attributed to the high separation efficiency of photogenerated electron–hole pairs, caused by decreasing the ratio of bulk and surface oxygen vacancies [42].

Katal et al. applied different synthesis strategies to generate surface oxygen vacancies using vacuum [43]. They transformed Degussa P25 titania pellets by

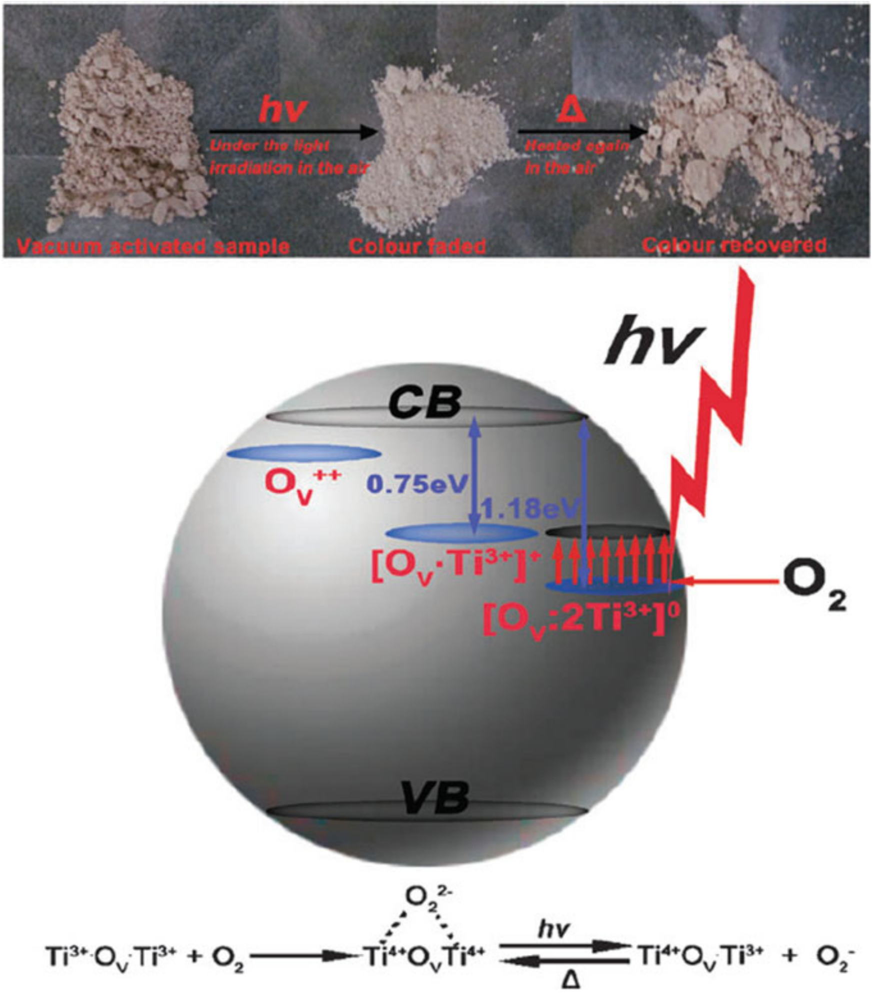

Fig. 12.3 Band structure model and color changing for vacuum-activated TiO_2 and the illustration of its photosensitive property in the air. Reprinted with permission from [37]. Copyright 2011, The Royal Society of Chemistry

sintering at different temperatures (500–800 °C) under vacuum conditions. The color of pellets changed from white to black due to the presence of both oxygen vacancies and Ti^{3+}, corresponding to the bandgap narrowing. It was found that the density of oxygen vacancy influenced the solar light-induced photocatalytic activity, tested for acetaminophen degradation. Furthermore, it has been found that the density of surface oxygen vacancies can be optimized; i.e., the density higher than the optimum value has a negative effect on photocatalytic activity [43].

12.3.2 Modification of TiO_2 by Metal and Nonmetal Elements

Modification of titania by metal and nonmetal elements might also introduce both types of defects. For example, interesting correlations were reported for nitrogen doping of TiO_2 by Batzill et al., where $Ti^{3+}$and oxygen vacancies occurred simultaneously with nitrogen doping, as confirmed by DFT calculations [44]. Similarly, Huang et al. observed for N-doped titania nanowire arrays, obtained by annealing of titania under H_2 and NH_3 atmosphere, the presence of substitutional N and Ti^{3+} doping, resulting in enhanced water oxidation induced by visible light [45]. In contrast, other research reports showed that titania annealing in NH_3 gas atmosphere resulted not only in nitrogen doping but also the introduction of oxygen vacancies. It has been postulated that the visible-light activity of these materials is originated from a synergistic effect of substitutional N species and oxygen vacancies [46].

Another nonmetal element showing successful synergistic effect with defects was sulfur. Yang et al. showed that S–TiO_{2-x} material with a core-shell structure, prepared through post-thermal treatment in H_2S atmosphere, exhibited a large number of oxygen vacancies in the shell zone [47]. Next, a disordered layer becomes accessible to sulfur ions S^{2-}, occupied the oxygen vacancies site, enhancing visible-light absorption properties. Feng et al. prepared boron-doped titania with disordered surface layers [48]. They reported that the introduction of interstitial B not only led to the formation of a stable Ti^{3+} and oxygen vacancies, but also generated structural disorders in the surface layer. These changes caused the substantial variations in the density of states: New mid-gap states were formed, accompanied by a significant reduction of the bandgap. It has been stated that these structures promote photogenerated electron mobility and provide shallow trapping sites (B–O–Ti^{3+}) to decrease a charge carriers recombination effect [48].

Modification with metals has also been proposed for defective titania samples. For example, Liu et al. prepared Cu(II)–TiO_2@Ti^{3+} structure [49]. The visible-light photocatalytic activity was introduced by the presence of Ti^{3+} and grafted Cu(II) oxide (amorphous nanoclusters), and the recombination of electron–hole pairs was inhibited at the isolated Ti^{3+} band. Furthermore, it was reported that the presence of Ti^{3+} did not significantly narrow the bandgap but led to the formation of isolated states between the forbidden gap. These isolated states have various electric levels from 0.3 to 0.8 eV below the conduction band minimum, resulting in the broad visible-light absorption of the Ti^{3+} self-doped TiO_2 (Fig. 12.4) [49].

Plasmonic photocatalysts (wide-bandgap semiconductors modified with deposits of noble metals) were also investigated for defective titania samples (Ti^{3+}) by Bielan et al. [50]. Defective titania (confirmed by EPR) was prepared by the hydrothermal method assisted with the annealing process, and then nanoparticles (NPs) of noble metals (Pt and Cu) were deposited on its surface by co-precipitation method with the assistance of $NaBH_4$ (that could also work as reducing agent, as discussed above). It was confirmed that co-modification (Pt and Ti^{3+}) significantly

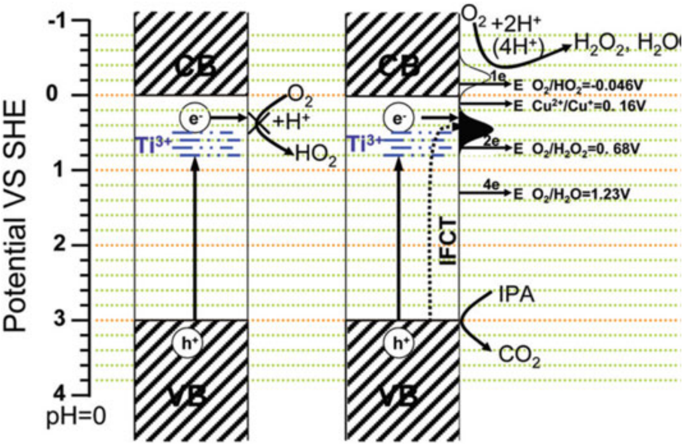

Fig. 12.4 Photocatalytic mechanism proposed for Cu(II)–TiO_2@Ti^{3+} photocatalyst. Reprinted with permission from [49]. Copyright 2011, American Chemical Society

improved vis-activity for phenol degradation, resulting from both bandgap narrowing and plasmonic photocatalysis, as shown in Fig. 12.4. However, under UV/vis irradiation much lower activity for defective platinum-modified sample was observed than that for non-defective one (Pt/TiO_2). It is not surprising since it has been known that thought doped titania (not only self-doped but also nonmetal-doped) samples exhibit vis-response, dopants are also as recombination centers, and thus a decrease in UV-activity is the main shortcoming of doped titania samples (Fig. 12.5).

12.4 Advanced Structures—Photonic Crystals with Defects

Photonic crystals (PCs) have been identified as promising materials to harvest light at longer wavelengths region (visible light and IR) due to the spatial periodicity of refractive index owning to high dielectric medium (backbone of PCs) and low dielectric medium (air and water). The periodicity causes prevention of light pathways at certain frequency resulting in the appearance of photonic bandgap (PBG), where at the edges of this particular wavelength, slow photons (reduced group velocity of photons) are formed and could be utilized efficiently for better photoabsorption [51–53]. In most of the cases, two-dimensional and three-dimensional PCs have been explored theoretically and experimentally. In this regard, inverse opal PCs (IO–PCs) are known as three-dimensional PC obtained as the exact replica of the template (opal) structure, possessing plenty of advantages such as large surface area, excellent mass transfer, and tunable porosity [54–56].

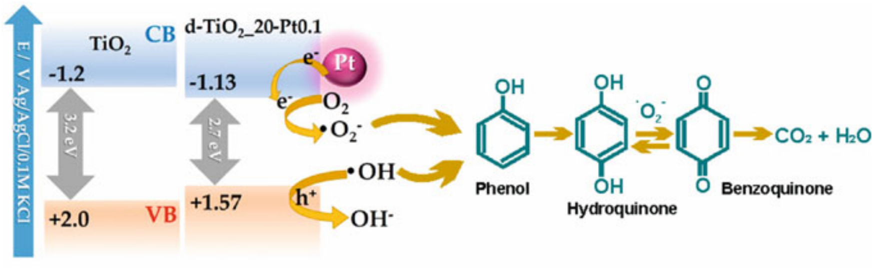

Fig. 12.5 Energy diagram showing the position of valence and conduction bands of bare and defective titania samples co-modified with Pt NPs (d-TiO_2_20-Pt0.1) with the schematic illustration of phenol degradation mechanism; reprinted from [50] (open-access article distributed under the Creative Commons Attribution License)

It is well known that the utilization of PCs is recognized as efficient pathway to enhance photocatalytic performance due to their photonic effect apart from enlarged surface area and efficient mass transfer [57, 58]. Self-doped titania PCs have also been prepared and explored for various applications, e.g., surface-enhanced Raman scattering (SERS) [59], photoelectrochemical bioanalysis and sensors [60, 61], gas sensors [62], and photocatalysis [63, 64]. The idea of introducing oxygen vacancies/surface defects within the structure of PCs-based materials has been investigated by many methods, such as hydrogenation [65], microwave-assisted reduction [66], utilizing reducing agents with subsequent calcination [67], noble metals deposition [63], and annealing [68].

An interesting finding has been reported by Rahul et al., which strongly indicates on the importance of precursor choice to obtain self-doped (Ti^{3+}) titania PCs. In brief, Ti^{3+} has been only detected when titanium butoxide was used as the titania precursor, whereas no significant trace of reduced titania was observed (by X-ray photoelectron spectroscopy) when titanium isopropoxide was used to infiltrate the opal template [69]. A different approach has been taken by Xin and Lu, in which titanium isopropoxide has been utilized to form titania IO structure, the Ti^{3+} defects have been formed by subsequent reduction of IO by H_2 to form black titania IO with enhanced photocatalytic activity for dye degradation [64].

Defective titania-based PCs have been successfully applied for solar energy conversion. For example, enhanced photocurrent density in photoelectrochemical (PEC) water splitting has been achieved by hydrogenated titania nanotube PCs in comparison with pristine titania nanotube PC (without defects) [65]. It has been proposed that enhanced activity results from the presence of oxygen vacancies, which have narrowed bandgap and provided better charge carrier separations. Similarly, self-doped (Ti^{3+}) titania nanotube PC structure, obtained by reducing agent during microwave treatment, exhibited about tenfold amplified performance in PEC water splitting as compared to non-doped structures [66].

As already discussed, titania could not drive photocatalytic reactions under visible-light irradiation without the assistance of vis-responsive materials/elements, such as noble metals. It should be noted that even though the utilization of IO PCs could extend the optical pathway to longer wavelengths, the photoabsorbing material should be able to capture these slow photons. In this sense, self-defects might be helpful to narrow the electronic bandgap of titania, which enables the absorption of visible light coupling with the slow photons' effects from the PC, thus resulting in high vis-response, as proven by Qi et al. (without the aid of other co-catalysts) [70].

PCs-based plasmonic photocatalysts have also been recognized as promising materials with enhanced photocatalytic activity due to magnification of visible-light harvesting ability (localized surface plasmon resonance (LSPR)) by slow photon effect [52, 53]. Accordingly, further enhancement in photocatalytic performance has been expected when three factors; i.e., slow photons, plasmonic absorption and oxygen vacancies are implemented for better light harvesting, enhanced charge carriers' separation, and migration. Accordingly, hydrogen treated (to introduce defects) Au/3D-ordered macroporous-titania photocatalyst has been investigated [71]. Indeed, an obvious amplification in hydrogen evolution during photocatalytic water splitting has been observed as compared to the similar structure without oxygen vacancies. Another plasmonic material—MoO_{3-x} of wide light absorption ability and with Mo^{5+} species as oxygen vacancies, incorporated into titania IO PC, has also been investigated [72]. As expected, higher photocatalytic activity has been observed for photochemical water splitting and dye photodegradation than that for the sample without Mo^{5+} species, suggesting the synergetic effects between oxygen vacancies and photonic and plasmonic properties.

Apart from that, the deposition of noble metals on the surface of PCs could also be a promising way to induce the oxygen vacancies due to enhanced metal–PCs support interactions. In this sense, it has been reported that the loading of Pt NPs has increased the Ti^{3+} content in Pt/PC-titania photocatalyst, causing remarkable photocatalytic activity, probably because of the combination between slow photons effect (from PC) and intensified light absorption (oxygen vacancies and Pt) [63].

In summary, the combination of unique characteristics from both PCs and oxygen vacancies/surface defects could significantly enhance the photocatalytic activity, as exemplary shown in Table 12.1.

12.5 Antimicrobial and Biomedical Applications of Defective Oxides

Although the study of defective metal oxides is quite new, it has already been investigated for antimicrobial and biomedical applications, due to the attractive costs (in comparison with metal/nonmetal modification), simple preparation and improved light absorption in visible light and even NIR range [28, 73]. For example, oxygen-deficient metal oxides, such as titania (TiO_2, e.g., black titania), zinc oxide (ZnO), magnesium oxide (MgO), and tungsten oxide (WO_3), have been

Table 12.1 Combination of unique characteristics from both PCs and oxygen vacancies/surface defects could significantly enhance the photocatalytic activity

PCs	Oxygen vacancies introduction method	Photocatalytic tests	Findings	References
Au–Pt/Ti^{3+} IO–TiO_2	Titanium butoxide precursor and thermal treatment	Water splitting; simulated solar light	Enhanced H_2 production	[69]
H–TiO_2 NTPCs	Annealing in the presence of H_2	PEC water splitting	Twofold enhanced photocurrent density	[65]
MWR–TiO_2 NTPCs	Ethylene glycol reduction in microwave	PEC water splitting	10-fold enhanced photocurrent density	[66]
Pt_x/PC–TiO_2	Deposition of Pt nanoparticle	CO_2 reduction; $\lambda = 320–780$ nm	3.2-fold enhanced activity	[63]
IOPC–TZS	Vacancies in IO	Photodegradation of Rhodamine B	27-fold enhanced activity as compared to P25	[76]
black TiO_2 IO	Reduction of IO with H_2	Photodegradation of Rhodamine B; $\lambda > 400$ nm	Enhanced activity	[68]
Ti^{3+} doped TiO_2 IOs	Vacuum heating	Photodegradation of acid orange 7	Enhanced activity	[70]
Hydrogen-treated Au/TiO_2–3DOM	Hydrogen treatment	Water splitting; 300 W Xe lamp	3.4-fold enhanced activity	[71]
IO-TiO_2-MoO_{3-x}	Presence of Mo^{5+}	Photodegradation of Rhodamine B; water splitting; 300 W Xe lamp	Enhanced activity	[72]
N-doped mesoporous IO	Incorporation of nitrogen atoms	photodegradation of methylene blue	4.9-fold enhanced activity	[77]

H–TiO_2 NTPCs—hydrogenated-TiO_2 nanotube PC; IOPC–TZS—Ternary inverse opal TiO_2–$ZrTiO_4$–SiO_2 PC; MWR–TiO_2 NTPCs—self-doped through ethylene reduction in a microwave process TiO_2 nanotube PC; 3DOM—three-dimensionally ordered microporous structure examined for antimicrobial purposes. One of the advantages of defective titania is the improved surface adsorption and reactivity (e.g., for O_2 and H_2O), derived from the formation of donor levels by the oxygen vacancies in TiO_2 (unpaired electrons or Ti^{3+} centers) [74]. For instance, the enhanced cytotoxicity for microorganisms has been revealed for oxygen-deficient P25, i.e., higher bactericidal activity than that of pristine P25 under UV–A illumination, probably due to enhanced generation of hydroxyl radicals (·OH) [75].

It should be pointed out that oxygen vacancies introduced into the bandgap might also improve the electrical conductivity of titania [78]. Therefore, Carlson et al. have developed the point-of-use water disinfection device using black titania nanotubes (synthesized by annealing in H_2 atmosphere) under applied electric potential in the absence of irradiation, confirming higher bactericidal activity of defect-rich titania than that for the reference sample (less oxygen defects) [78].

In addition to titania photocatalysts, ZnO has also been regarded as an efficient antimicrobial agent. It has been proposed that the bactericidal activity of ZnO is attributed to reactive oxygen species (ROS) even in the absence of light, due to the oxygen vacancies [79]. For example, Xu et al. have found that an increase in the oxygen vacancies results in an increase in the bactericidal activity in the dark [80]. It has been proposed that this activity correlates with generated hydrogen peroxide (H_2O_2) on the oxygen vacancy in the surface layer of ZnO. Interestingly, it has also been found that oxygen-deficient ZnO nanowires (NWs) exhibit higher antimicrobial activity in the dark for various microorganisms (*Escherichia coli*, methicillin-resistant *Staphylococcus aureus* (MRSA) and *Cryptococcus neoformans* (fluconazole-resistant fungus)) than oxygen-deficient flat ZnO film, indicating that both morphology and surface composition are responsible for the activity (Fig. 12.6) [81].

Similarly, the bactericidal activity of MgO is also oxygen vacancy-dependent and the cell toxicity of MgO is attributed to the lipid peroxidation in the liposomal membrane [82]. Moreover, the defective WO_3@carbon shows enhanced ROS generation by the promoted interfacial charge transfer on the surface of defective WO_3, resulting in an efficient visible-light-driven bactericidal activity [83].

Black titania has also been proposed for other biological applications, i.e., in the field of the cancer therapy due to its unique NIR absorption ability, since UV and visible light do not penetrate the skin and thus cannot be used for the noninvasive medical treatment. It has been proposed that the bandgap narrowing, which is attributed to the oxygen vacancies in the disordered surface layers, could be responsible for the shift in the absorption from UV to NIR region [28]. Indeed, the black titania with chitosan thermogels and polyethylene glycol exhibits excellent therapeutic effect on tumors due to both photothermal therapy and ROS effect under NIR laser irradiation, as shown in Fig. 12.7 [84, 85]. Moreover, it has been shown by Han et al. that in addition to the photothermal effect, the black titania exhibits tumor sonodynamic therapeutic effect under ultrasonication, due to enhanced charge carriers separation [86].

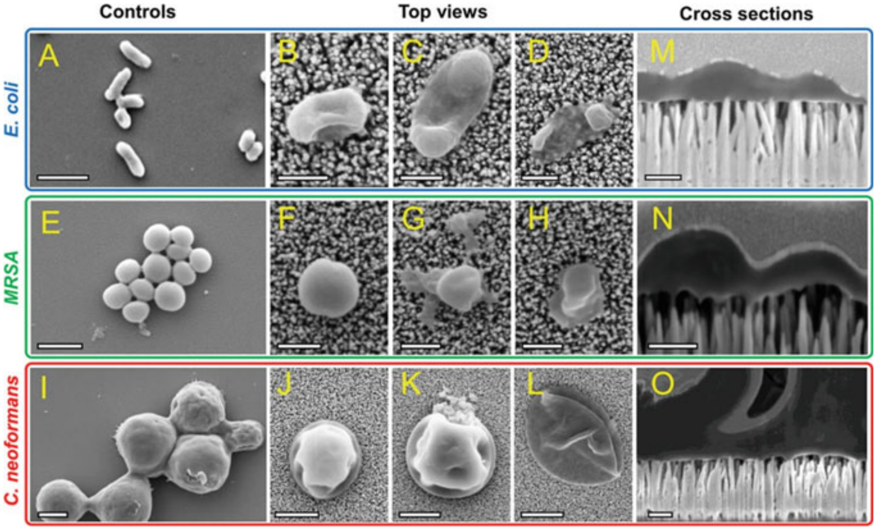

Fig. 12.6 SEM images of the interaction between microbial cells and ZnO nanowires. Top view (A–L) and cross section (M–O) with control glass (A, E, I) and ZnO nanowires (others). Scale bars for top views are 2 μm (A, I, J–L), 500 nm (B–H), and 1 μm (E). Scale bars for cross sections are 200 nm. Reprinted with permission from [81]. Copyright 2015, American Chemical Society

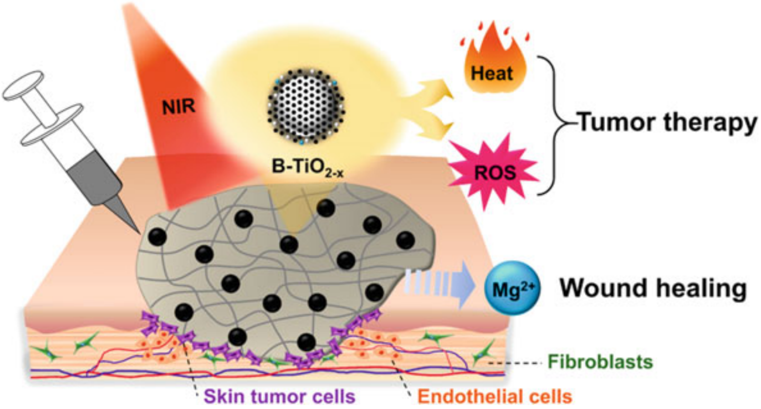

Fig. 12.7 Schematic mechanism of skin tumor treatment by black titania–chitosan matrix. Reprinted with permission from [84]. Copyright 2019, American Chemical Society

12.6 Concluding Remarks

During the last decade, the number of papers about the role of oxygen vacancies and/or Ti^{3+} ions in photocatalytic processes has constantly increased. The presence of these defects in the photocatalyst (mainly TiO_2) structure is favorable for introducing visible-light-induced activity and also can positively influence charge transport issues, such as an inhibition of electrons–holes recombination effect. Indeed, various studies have confirmed enhanced activity for environmental purification, solar energy conversion, antimicrobial purposes, and even for cancer treatment. However, there are still many challenges to properly design efficient photocatalytic materials based on defective structure. The main difficulty is to find the optimal concentration of oxygen vacancies/Ti^{3+} species so as not to lead to a decrease in photocatalytic activity. Other problematic issue is to properly identify the nature and local structure of these defects, which is the base to perform a valuable interpretation of results. Therefore, to eliminate all mentioned gaps, the need for more intensive research in this field still exists.

References

1. Schneider J, Matsuoka M, Takeuchi M, Zhang J, Horiuchi Y, Anpo M, Bahnemann DW (2014) Understanding TiO_2 photocatalysis: mechanisms and materials. Chem Rev 114:9919–9986
2. Pelaez M, Nolan NT, Pillai SC, Seery MK, Falaras P, Kontos AG, Dunlop PSM, Hamilton JWJ, Byrne JA, O'Shea K, Entezari MH, Dionysiou DD (2012) A review on the visible light active titanium dioxide photocatalysts for environmental applications. Appl Catal B: Environ 125:331–349
3. Herrmann J-M, Disdier J, Pichat P (1986) Photoassisted platinum deposition on TiO_2 powder using various platinum complexes. J Phys Chem 90:6028–6034
4. Ohno T, Akiyoshi M, Umebayashi T, Asai K, Mitsui T, Matsumura M (2004) Preparation of S-doped TiO_2 photocatalysts and their photocatalytic activities under visible light. Appl Catal A 265:115–121
5. Endo-Kimura M, Janczarek M, Bielan Z, Zhang D, Wang K, Markowska-Szczupak A, Kowalska E (2019) Photocatalytic and antimicrobial properties of Ag_2O/TiO_2 heterojunction. Chem Eng 3:3
6. Janczarek M, Endo M, Zhang D, Wang K, Kowalska E (2018) Enhanced photocatalytic and antimicrobial prformance of cuprous oxide/titania: the effect of titania matrix. Mater 11:2069
7. Janczarek M, Kowalska E, Ohtani B (2016) Decahedral-shaped anatase titania photocatalyst particles: synthesis in a newly developed coaxial-flow gas-phase reactor. Chem Eng J 289:502–512
8. Wei Z, Kowalska E, Verrett J, Colbeau-Justin C, Remita H, Ohtani B (2015) Morphology-dependent photocatalytic activity of octahedral anatase particles prepared by ultrasonication-hydrothermal reaction of titanates. Nanoscale 7:12392–12404
9. Kowalski D, Kim D, Schmuki P (2013) TiO_2 nanotubes, nanochannels and mesosponge: self-organized formation and applications. Nano Today 8:235–264
10. Wang KL, Janczarek M, Wei ZS, Raja-Mogan T, Endo-Kimura M, Khedr TM, Ohtani B, Kowalska E (2019) Morphology- and crystalline composition-governed activity of titania-based photocatalysts: overview and perspective. Catalysts 9

11. Kuznetsov VN, Serpone N (2009) On the origin of the spectral bands in the visible absorption spectra of visible-light-active TiO_2 specimens analysis and assignment. J Phys Chem C 113:15110–15123
12. Su J, Zou X, Chen JS (2014) Self-modification of titanium dioxide materials by Ti^{3+} and/or oxygen vacancies: new insights into defect chemistry of metal oxides. RSC Adv 4:13979–13988
13. Jing L, Xin B, Yuan F, Wang B, Fu H (2006) Effects of surface oxygen vacancies on photophysical and photochemical processes of Zn-doped TiO_2 nanoparticles and their relationships. J Phys Chem B 110:17860–17865
14. Nowotny J (2008) Titanium dioxide-based semiconductors for solar-driven environmentally friendly applications: impact of point defects on performance. Energy Environ Sci 1:565–572
15. Nowotny J, Alim MA, Bak T, Idris MA, Ionescu M, Prince K, Sahdan MZ, Sopian K, Teridi MAM, Sigmund W (2015) Defect chemistry and defect engineering of TiO_2-based semiconductors for solar energy conversion. Chem Soc Rev 44:8424–8442
16. Naldoni A, Altomare M, Zopellaro G, Liu N, Kment S, Zboril R, Schmuki P (2019) Photocatalysis with reduced TiO_2: from black TiO_2 to cocatalyst-free hydrogen production. ACS Catal 9:345–364
17. Nowotny MK, Bak T, Nowotny J (2006) Electrical properties and defect chemistry of TiO_2 single crystal. I. Electr Cond J Phys Chem B 110:16270–16282
18. Bak T, Nowotny J, Sucher NJ, Wachsman E (2011) Effect of crystal imperfections on reactivity and photoreactivity of TiO_2 (rutile) with oxygen, water, and bacteria. J Phys Chem C 115:15711–15738
19. Nowotny MK, Sheppard LR, Bak T, Nowotny J (2008) Defect chemistry of titanium dioxide. Application of defect engineering in processing of TiO_2-based photocatalysts. J Phys Chem C 112:5275–5300
20. Zuo F, Wu T, Zhang Z, Borchardt D, Feng P (2010) Self-doped Ti^{3+} enhanced photocatalyst for hydrogen production under visible light. J Am Chem Soc 132:11856–11857
21. Wang J, Liu P, Fu X, Li Z, Han W, Wang X (2009) Relationship between oxygen defects and the photocatalytic property of ZnO nanocrystals in nafion membranes. Langmuir 25:1218–1223
22. Thompson TL, Yates JT (2005) TiO_2-based photocatalysis: surface defects, oxygen and charge transfer. Top Catal 35:197–210
23. Pan X, Yang MQ, Fu X, Zhang N, Xu YJ (2013) Defective TiO_2 with oxygen vacancies: synthesis, properties and photocatalytic applications. Nanoscale 5:3601–3614
24. Liu H, Ma HT, Li XZ, Li WZ, Wu M, Bao XH (2003) The enhancement of TiO_2 photocatalytic activity by hydrogen thermal treatment. Chemosphere 50:39–46
25. Chen X, Liu L, Yu PY, Mao SS (2011) Increasing solar absorption for photocatalysis with black hydrogenated titanium dioxide nanocrystals. Science 331:746–750
26. Liu L, Yu PY, Mao SS, Shen DZ (2013) Hydrogenation and disorder in engineered black TiO_2. Phys Rev Lett 111:065505
27. Wei W, Yaru N, Chunhua L, Zhongzi X (2012) Hydrogenation of TiO_2 nanosheets with exposed 001 facets for enhanced photocatalytc activity. RSC Adv 2:8286–8288
28. Naldoni A, Allieta M, Santangelo S, Marelli M, Fabbri F, Cappeli S, Bianchi CL, Psaro R, Dal Santo V (2012) Effect of nature and location of defects on bandgap narrowing in black TiO_2 nanoparticles. J Am Chem Soc 134:7600–7603
29. Sinhamahapatra A, Jeon JP, Yu JS (2015) A new approach to prepare highly active and stable black titania for visible light-assisted hydrogen production. Energy Environ Sci 8:3529–3544
30. Wang G, Wang H, Ling Y, Tang Y, Yang X, Fitzmorris RC, Wang C, Zhang JZ, Li Y (2011) Hydrogen-treated TiO_2 nanowire arrays for photoelectrochemical water splitting. Nano Lett 11:3026–3033
31. Hu YH (2012) A highly efficient photocatalyst—hydrogenated black TiO_2 for the photocatalytic splitting of water. Angew Chem Int Ed 51:12410–12412
32. Leshuk T, Parviz R, Everett P, Krishnakumar H, Varin RA (2013) Photocatalytic activity of hydrogenated TiO_2. ACS Appl Mater Interfaces 5:1892–1895

33. Fang W, Xing M, Zhang J (2017) Modifications on reduced titanium dioxide photocatalysts: a review. J Photochem Photobiol C: Photochem Rev 32:21–39
34. Xing M, Fang W, Nasir M, Ma Y, Zhang J, Anpo M (2013) Self-doped Ti^{3+}-enhanced TiO_2 nanoparticles with a high-performance photocatalysis. J Catal 297:236–243
35. Fang W, Xing M, Zhang J (2014) A new approach to prepare Ti^{3+} self-doped TiO_2 via $NaBH_4$ reduction and hydrochloric acid treatment. Appl Catal B 160–161:240–246
36. Yan X, Abe R, Ohno T, Toyofuku M, Ohtani B (2008) Action spectrum analyses of photoinduced superhydrophilicity of titania thin films on glass plates. Thin Solid Films 516:5872–5876
37. Xing M, Zhang J, Chen F, Tian B (2011) An economic method to prepare vacuum activated photocatalysts with high photo-activities and photosensitivities. Chem Commun 47:4947–4949
38. Wang KL, Wei ZS, Ohtani B, Kowalska E (2018) Interparticle electron transfer in methanol dehydrogenation on platinum-loaded titania particles prepared from P25. Catal Today 303:327–333
39. Markowska-Szczupak A, Wang KL, Rokicka P, Endo M, Wei ZS, Ohtani B, Morawski AW, Kowalska E (2015) The effect of anatase and rutile crystallites isolated from titania P25 photocatalyst on growth of selected mould fungi. J Photochem Photobiol B-Biol 151:54–62
40. Ohtani B, Prieto-Mahaney OO, Li D, Abe R (2010) What is Degussa (Evonik) P25? Crystalline composition analysis, reconstruction from isolated pure particles and photocatalytic activity test. J Photochem Photobiol Chemi 216:179–182
41. Xia T, Zhang Y, Murowchick J, Chen X (2014) Vacuum-treated titanium dioxide nanocrystals: optical properties, surface disorder, oxygen vacancy, and photocatalytic activities. Catal Today 225:2–9
42. Dong G, Wang X, Chen Z, Lu Z (2018) Enhanced photocatalytic activity of vacuum-activated TiO_2 induced by oxygen vacancies. Photochem Photobiol 94:472–483
43. Katal R, Salehi M, Farahani MHDA, Panah-Masudy S, Ong SL, Hu J (2018) Preparation of a new type of black TiO_2 under a vacuum atmosphere for sunlight photocatalysis. ACS Appl Mater Interfaces 10:35316–35326
44. Batzill M, Morales EH, Diebold U (2006) Influence of nitrogen doping on the defect formation and surface properties of TiO_2 rutile and anatase. Phys Rev Lett 96:026103
45. Hoang S, Berglund SP, Hahn NT, Bard AJ, Mullins CB (2012) Enhancing visible light photo-oxidation of water with TiO_2 nanowire arrays via cotreatment with H_2 and NH_3: synergistic effects between Ti^{3+} and N. J Am Chem Soc 134:3659–3662
46. Chen Y, Cao X, Lin B, Gao B (2013) Origin of the visible-light photoactivity of NH3-treated TiO_2: Effect of nitrogen doping and oxygen vacancies. Appl Surf Sci 264:845–852
47. Yang C, Wang Z, Lin T, Yin H, Lu X, Wan D, Xu T, Zheng C, Lin J, Huang F, Xie X, Jiang M (2013) Core-shell nanostructured “black” rutile titania as excellent catalyst for hydrogen production enhanced by sulfur doping. J Am Chem Soc 135:17831–17838
48. Feng N, Liu F, Huang M, Zheng A, Wang Q, Chen T, Cao G, Xu J, Fan J, Deng F (2016) Unravelling the efficient photocatalytic activity of boron-induced Ti^{3+} species in the surface layer of TiO_2. Sci Rep 6:34765
49. Liu M, Qiu X, Miyauchi M, Hashimoto K (2011) Cu(II) oxide amorphous nanoclusters grafted Ti^{3+} self-doped TiO_2: an efficient visible light photocatalyst. Chem Mater 23:5282–5286
50. Bielan Z, Sulowska A, Dudziak S, Siuzdak K, Ryl J, Zielinska-Jurek A (2020) Defective TiO_2 core-shell magnetic photocatalyst modified with plasmonic nanoparticles for visible light-induced photocatalytic activity. Catalysts 10:672
51. Yablonovitch E (1993) Photonic Band-Gap Structures. J Opt Soc America Opt Phy 10:283–295
52. Raja-Mogan T, Lehoux A, Takashima M, Kowalska E, Ohtani B (2021) Slow photon-induced enhancement of photocatalytic activity of gold nanoparticle-incorporated titania in-verse opal. Chem Lett. https://doi.org/10.1246/cl.200804

53. Raja-Mogan T, Ohtani B, Kowalska E (2020) Photonic crystals for plasmonic photocatalysis. Catalysts 10:827
54. Chiang CC, Tuyen LD, Ren CR, Chau LK, Wu CY, Huang PJ, Hsu CC (2016) Fabrication of titania inverse opals by multi-cycle dip-infiltration for optical sensing. Photonics Nanostruct-Fundam Appl 19:48–54
55. Li X, Yu JG, Jaroniec M (2016) Hierarchical photocatalysts. Chem Soc Rev 45:2603–2636
56. Likodimos V (2018) Photonic crystal-assisted visible light activated TiO_2 photocatalysis. Appl Catal B Environ 230:269–303
57. Wu M, Liu J, Jin J, Wang C, Huang SZ, Deng Z, Li Y, Su BL (2014) Probing significant light absorption enhancement of titania inverse opal films for highly exalted photocatalytic degradation of dye pollutants. Appl Catal B Environ 150:411–420
58. Ye J, He JH, Wang S, Zhou XJ, Zhang Y, Liu G, Yang YF (2019) Nickel-loaded black TiO_2 with inverse opal structure for photocatalytic reduction of CO_2 under visible light. Sep Purif Technol 220:8–15
59. Zhou WM, Wang J, Wang XG, Li JF, Li Y, Wang CW (2020) Ag loaded TiO_2 nanotube photonic crystals self-doped Ti^{3+} periodically by anodization process and their performance of surface enhanced Raman scattering. Opt Mater 99
60. Fu BH, Wu WL, Gan LY, Zhang ZH (2019) Bulk/surface defects engineered TiO_2 nanotube photonic crystals coupled with plasmonic gold nanoparticles for effective in vivo near-infrared light photoelectrochemical detection. Anal Chem 91:14611–14617
61. Wu WL, Zhang ZH (2017) Defect-engineered TiO_2 nanotube photonic crystals for the fabrication of near-infrared photoelectrochemical sensor. J Mater Chem B 5:4883–4889
62. Su J, Zou XX, Zou YC, Li GD, Wang PP, Chen JS (2013) Porous titania with heavily self-doped Ti_3+ for specific sensing of CO at room temperature. Inorg Chem 52:5924–5930
63. Jiao JQ, Wei YC, Chi KB, Zhao Z, Duan AJ, Liu J, Jiang GY, Wang YJ, Wang XL, Han CC, Zheng P (2017) Platinum nanoparticles supported on TiO_2 photonic crystals as highly active photocatalyst for the reduction of CO_2 in the presence of water. Energ Technol 5:877–883
64. Xin LL, Liu XF (2015) Black TiO_2 inverse opals for visible-light photocatalysis. RSC Adv 5:71547–71550
65. Meng M, Zhou SH, Yang L, Gan ZX, Liu KL, Tian FS, Zhu Y, Li CY, Liu WF, Yuan HL, Zhang Y (2018) Hydrogenated TiO_2 nanotube photonic crystals for enhanced photoelectrochemical water splitting. Nanotech 29:155401
66. Zhang ZH, Yang XL, Hedhili MN, Ahmed E, Shi L, Wang P (2014) Microwave-assisted self-doping of TiO_2 photonic crystals for efficient photoelectrochemical water splitting. ACS Appl Mater Interfaces 6:691–696
67. Liu SM, Zhou L, Zhang JL, Lei JY (2019) Controllable synthesis of inverse opal TiO_{2-x} photonic crystals and their photoelectric properties. Chem Asian J 14:322–327
68. Zeng Y, Wang WJ, Ling FR, Yao JQ (2020) Terahertz wave modulation properties of thermally processed BST/PZT ferroelectric photonic crystals. Photonics Res 8:1002–1010
69. Rahul TK, Mohan M, Sandhyarani N (2018) Enhanced solar hydrogen evolution over in situ gold-platinum bimetallic nanoparticle-loaded Ti^{3+} self-doped titania photocatalysts. ACS Sustain Chem Eng 6:3049–3059
70. Qi DY, Lu LJ, Xi ZH, Wang LZ, Zhang JL (2014) Enhanced photocatalytic performance of TiO_2 based on synergistic effect of Ti^{3+} self-doping and slow light effect. Appl Catal B Environ 160:621–628
71. Chang Y, Xuan Y, Quan HY, Zhang H, Liu SX, Li ZC, Yu K, Cao JL (2020) Hydrogen treated Au/3DOM–TiO_2 with promoted photocatalytic efficiency for hydrogen evolution from water splitting. Chem Eng J 382:122869
72. Lv C, Wang LL, Liu XG, Zhao L, Lan XF, Shi JS (2020) An efficient inverse opal (IO)–TiO_2–MoO_{3-x} for photocatalytic H_2 evolution and RhB degradation—the synergy effect of IO structure and plasmonic MoO_{3-x}. Appl Surf Sci 527:146726
73. Osorio-Vargas PA, Pulgarin C, Sienkiewicz A, Pizzio LR, Blanco MN, Torres-Palma RA, Petrier C, Rengifo-Herrera JA (2012) Low-frequency ultrasound induces oxygen vacancies

formation and visible light absorption in TiO_2 P-25 nanoparticles. Ultrason Sonochem 19:383–386

74. Benabbou AK, Derriche Z, Felix C, Lejeune P, Guillard C (2007) Photocatalytic inactivation of *Escherischia coli*—effect of concentration of TiO_2 and microorganism, nature, and intensity of UV irradiation. Appl Catal B Environ 76:257–263
75. Qin YK, Guo XP, Tou FY, Pan H, Feng JN, Xu J, Chen B, Liu M, Yang Y (2017) Cytotoxicity of TiO_2 nanoparticles toward *Escherichia coli* in an aquatic environment: effects of nanoparticle structural oxygen deficiency and aqueous salinity. Environ Sci-Nano 4:1178–1188
76. Wu YT, Li X, Liu CQ, Chang XJ, Hu XF (2020) Studies on the active radicals in synthesized inverse opal photonic crystal and its effect on photocatalytic removal of organic pollutants. J Mol Liq 320:114414
77. Ha SJ, Kim DH, Moon JH (2015) N-doped mesoporous inverse opal structures for visible-light photocatalysts. RSC Adv 5:77716–77722
78. Carlson K, Elliott C, Walker S, Misra M, Mohanty S (2016) An effective, point-of-use water disinfection device using immobilized black TiO_2 nanotubes as an electrocatalyst. J Electrochem Soc 163:H395–H401
79. Prasanna VL, Vijayaraghavan R (2015) Insight into the mechanism of antibacterial activity of ZnO: surface defects mediated reactive oxygen species even in the dark. Langmuir 31:9155–9162
80. Xu XL, Chen D, Yi ZG, Jiang M, Wang L, Zhou ZW, Fan XM, Wang Y, Hui D (2013) Antimicrobial mechanism based on H_2O_2 generation at oxygen vacancies in ZnO crystals. Langmuir 29:5573–5580
81. Elbourne A, Cheeseman S, Wainer P, Kim J, Medvedev AE, Boyce KJ, McConville CF, Van Embden J, Crawford RJ, Chapman J, Truong VK, Della Gaspera E (2020) Significant enhancement of antimicrobial activity in oxygen-deficient zinc oxide nanowires. ACS Appl Bio Mater 3:2997–3004
82. Krishnamoorthy K, Manivannan G, Kim SJ, Jeyasubramanian K, Premanathan M (2012) Antibacterial activity of MgO nanoparticles based on lipid peroxidation by oxygen vacancy. J Nanopart Res 14:1063
83. Wang R, Zhang WT, Zhu WX, Yan LZ, Li SH, Chen K, Hu N, Suo YR, Wang JL (2018) Enhanced visible-light-driven photocatalytic sterilization of tungsten trioxide by surface-engineering oxygen vacancy and carbon matrix. Chem Eng J 348:292–300
84. Wang XC, Ma B, Xue JM, Wu JF, Chang J, Wu CT (2019) Defective black nano-titania thermogels for cutaneous tumor-induced therapy and healing. Nano Lett 19:2138–2147
85. Mou J, Lin TQ, Huang FQ, Chen HR, Shi JL (2016) Black titania-based theranostic nanoplatform for single NIR laser induced dual-modal imaging-guided PTT/PDT. Biomaterials 84:13–24
86. Han XX, Huang J, Jing XX, Yang DY, Lin H, Wang ZG, Li P, Chen Y (2018) Oxygen-deficient black titania for synergistic/enhanced sonodynamic and photoinduced cancer therapy at near iInfrared-II biowindow. ACS Nano 12:4545–4555

Chapter 13
Efficient Visible-Light-Driven Perovskites Photocatalysis: Design, Modification and Application

Noor Haida Mohd Kaus, Mohd Lokman Ibrahim,
Saifullahi Shehu Imam, Salma Izati Sinar Mashuri,
and Yogesh Kumar

Abstract Perovskite-based photocatalysts are oxides with the general formula ABO_3 are interesting materials that remained essential in solving a great deal of energy and environmental remediation challenges. Recent key issues for high-efficiency solar or visible light photocatalysis are the effectiveness in rapid transport to the semiconductor surface and the separation of photo-generated electron-hole pairs; thus, substantial efforts have been made to design and develop new generation of perovskite-based photocatalyst systems to improve their possible use. The present article provides an up-to-date review of recent development of perovskites-and its related materials, including titanate-based, tantalite-based, niobium-based, ferrites and others, demonstrating a remarkably rapid development and promising results in photocatalytic performance particularly in visible light-driven applications. Furthermore, the review also includes modification strategies that are commonly employed to improve the photocatalytic performance of perovskites. Finally, the summary of recent developments of perovskites-based photocatalysis for viable applications.

N. H. Mohd Kaus (✉)
School of Chemical Sciences, Universiti Sains Malaysia, 11800 Penang, Malaysia
e-mail: noorhaida@usm.my

M. L. Ibrahim · S. I. S. Mashuri
School of Chemistry and Environment, Faculty of Applied Science, UiTM Shah Alam, Selangor, Malaysia
e-mail: mohdlokman@uitm.edu.my

S. S. Imam
Department of Pure and Industrial Chemistry, Bayero University, P.M.B 3011 Kano, Nigeria
e-mail: ssimam.chm@buk.edu.ng

Y. Kumar
Department of Physics, ARSD College, University of Delhi, New Delhi 110021, India
e-mail: ykumar@arsd.du.ac.in

S. Garg and A. Chandra (eds.), *Green Photocatalytic Semiconductors*,
Green Chemistry and Sustainable Technology,
https://doi.org/10.1007/978-3-030-77371-7_13

Keywords Perovskites · Photocatalysis · Material science · Visible-light · Water remediation · Semiconductor

13.1 Introduction

Visible-light-induced chemical transformations or photocatalytic is a procedure of significantly speed up reactions in the presence of a photocatalyst (single-electron redox mediator) which absorbs photon energy from light irradiation to generate photoinduced electrons and holes pairs. In particular, the photocatalysis transpire through single-electron pathways, utilizing visible-light response of organic reactions for the applications of wastewater treatment and environmental protection [12, 114, 163]. This procedure is environmentally and ecologically friendly, green and produced clean energy as opposed to conventional organic reactions [83]. The process particularly refers to heterogeneous photocatalysis that has remarkable interest nowadays and mainly focuses on perovskites semiconductors that possess distinctive electronic and optical properties, as well as the ability to photogenerated electron-hole pairs [24, 152] with higher stability and potential recyclability [42, 83, 183]. Mostly semiconductors with wide band gaps i.e. TiO_2, ZnO, etc. will restrict its applicability to ultraviolet (UV) wavelengths, reflecting just 5% of the universe's available solar light energy. Moreover, the rapid recombination of photogenerated electron-hole pairs results in a rapid dissemination of energy that decreases the performance of photocatalyst [89, 121].

Some conventional approaches to prevail over the drawbacks listed compasses the extension of the absorption to the spectrum of visible range [22, 86], and decreasing the recombination rate of the photogenerated electrons and holes [38, 156]. The solutions explored to boost photocatalytic performance include the construction of appropriate band gaps [77, 170], the employment of nanosized architechtures [183, 172, 174, 168], the implementation of interface design and facet-engineered surface [13, 52], utilization of dopants, as well as metal and non-metal co-catalysts [6, 95, 111], surface modification [54, 199] and the heterostructure construction [16, 189, 69, 101].

Amongst the most photocatalytic materials, perovskite-based catalytic (PCB) materials are auspicious photocatalytic materials with fascinating controllable physico-chemical and optoelectronic properties, such as electron mobility, redox performance, structural flexibility, efficient photocatalytic performance, long charge carrier lifetimes, excellent charge carrier mobilities, high absorbance coefficients, and uncomplicated bandgap engineering with facile fabrication route [126, 193, 194, 7, 106]. The complete replacement of cation A or B by other metals leads to variant interesting properties and alteration of the surface facets to create catalytic activity enhancement [73, 113, 127, 94]. As opposed to other visible-light active inorganic semiconductors, perovskite-type catalytic materials exhibited facile and effortless materials construction, application, and permit simple alteration of their semiconductor bandgap. In our study, we present a concise review to the current findings and noteworthy properties of perovskite materials, accompanied by the enhancement techniques and their recent representative applications for improved photocatalytic properties.

13.2 Overview and Design of Perovskites-Based Photocatalysts

Perovskites are materials having similar crystalline unit cell as calcium titanate ($CaTiO_3$), that was first discovered by Aleksevich von Perovski in 1839 [18, 118]. They have general chemical formula ABX_3, where ‘A’ and ‘B’ are cations of different ionic radii (A larger than B), and ‘X’ which is a halogen or oxygen anion, holds ‘A’ and ‘B’ together through an ionic bond [44, 65, 191]. Such different anions and various cations form oxide perovskites and halide perovskites, both of which have BX_6 octahedra in their crystal structures, with ‘A’ cation located in the interstitial voids of the neighbouring octahedra (Fig. 13.1).

The catalytic activity of the perovskites is primarily attributed to the transition metal ion at the B-site, while their thermal endurance is mainly due to the rare earth ion at the A-site [5]. As a result of their photoelectric [141], luminescent [187], magnetic [9], and electrical properties [82], perovskites are used in the areas of biological imaging, ionic conductors, sensing, photocatalytic, electro-catalytic, information sensing and other numerous technological applications [191].

Among the perovskite materials, the perovskite oxide with the formula ABO_3 is a typical structure in inorganic chemistry [79]. It has demonstrated outstanding potential in the development of solid oxide fuel cells [207], solar cells [206], and ferroelectrics [40]. Various oxide perovskites such as titanates [109], ferrites [37], and tantalates [98] are photocatalytically active. The flexibility in the composition and structure of the oxide perovskites greatly influences their photocatalytic performance [143, 193, 194].

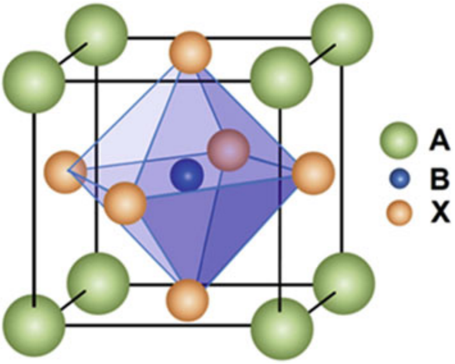

Fig. 13.1 ABX_3 perovskite unit cell (Reproduced with permission from Ref. [118])

Previously, perovskite materials were usually prepared using the traditional solid-state reaction method, but the produced materials are mostly heterogeneous, impure, have low light absorption in the visible region, are very sensitive to temperature changes, and the excited states have short lifetimes [2, 47]. To overcome these defects, alternative methods, including sol–gel [36], freeze-drying [88], combustion synthesis [92], electrospinning method [35], sonochemical method [110], coprecipitation method [81], microemulsion method [5], glycine-nitrate route [167] and microwave-assisted method [162] have been introduced. According to Tanaka and Misono [161], the main strategies of designing perovskite catalysts for the enhancement of their catalytic activity are; (1) selection of B-site elements which principally determine its catalytic activity, (2) valency and vacancy control by the selection of A-site elements, (3) synergistic effects of mainly B-site elements, (4) enhancement of surface area via formation of fine particles or dispersion on supports, and (5) addition of precious metals with their regeneration.

The efficiency of the catalyst, including perovskite materials during photocatalytic reactions, depends on three steps: (a) photon absorption and generation of charge carriers, (b) separation and transfer of charge carriers to the active sites of the surface, and (c) consumption of photogenerated charge carriers on the active sites during redox reaction [120]. Since most perovskites have a wide bandgap, several strategies have been employed to improve their visible light absorption and enhance the separation of photogenerated charge carriers. According to Moniruddin et al. [118], the key strategies include (a) bandgap engineering to achieve suitable band edge position, (b) enhancing the separation of charge carriers by changing particle size and crystal nanostructure, (c) improving visible absorption via the use of plasmonic metal nanoparticles (Ag or Au), (d) formation of heterojunctions to enhance separation of charge carriers, and (e) introduction of ferroelectric material to capitalize on its polarization field towards photoexcited charge separation. Specifically, various photo-active perovskites catalysts will be discussed in the following sub-sections.

13.2.1 Titanite Perovskites

One of the classified perovskite with general formula of $MTiO_3$ (M = Sr, Ba, Ca, Mn, Fe, Co, Ni, Pb, Cd) known as titanate perovskites [74]. They are promising photocatalysts with structural simplicity and flexibility [125]. Although most titanates are only active under UV light because of their wide bandgap, however, those containing transition metal oxides with d^0 and d^{10} orbitals, including Co^{2+}, Fe^{2+}, Ni^{2+}, Zn^{2+}, Pb^{2+}, and Cd^{2+}, would favour narrowing of the bandgap [21]. In general, titanates remain attractive materials in photocatalysis due to their high thermal stability and excellent resistance to photocorrosion [4, 100].

Among the titanate perovskites, $SrTiO_3$ happens to be the most widely studied titanate [164]. It is an n-type semiconductor posseseses an indirect bandgap between 3.1 and 3.7 eV, having a basic framework of Ti–O polyhedron as TiO_2, and remarkable charge transport properties [47, 166, 200]. Furthermore, $SrTiO_3$ is cheap, less toxic, and easily doped to control its electrical properties [45, 173]. Although some narrow bandgap titanates such as $NiTiO_3$ (2.10 eV) and $CoTiO_3$ (2.28 eV) are visible light active, their conduction band is below the water oxidation potential. This limitation makes them unpopular [2]. Fortunately, despite its wide bandgap, the band edge for $SrTiO_3$ straddles the water splitting redox potential [74].

13.2.2 Tantalate Perovskites

Tantalates perovskites have the general formula $ATaO_3$ (A = Li, Na, K), and the bandgap of lithium, sodium and potassium tantalates was found to be 4.7, 4.0 and 3.6 eV, respectively [67, 122]. Although the tantalates are only active under UV light, however, they are interesting photocatalysts due to their good quantum yield, structural feasibility and environment-friendly nature [3, 41, 184]. Moreover, the respective Ta 5d orbital was placed at a negative site as compared to titanates. This could make the tantalates paramount during a photocatalytic reaction [15].

The high photocatalytic activity of tantalates has been related to their layered structure with a corner-shared framework of TaO_6, allowing easy transport and separation of photogenerated charge carriers [208]. $NaTaO_3$ is the most active tantalates perovskite [153], nevertheless it needs to be modified to extend their photodetection to the visible region to harness more solar energy [164].

13.2.3 Vanadate Perovskites

Vanadate perovskites have the general formula RVO_3 [177]. Among the vanadate perovskites, $AgVO_3$ is an efficient photocatalyst with favourable morphology and nanocrystalline nature [150]. It has two crystalline phases of α-$AgVO_3$ and β-$AgVO_3$, both of which have an intense absorption in the visible light region and are strongly dependent on temperature [50, 182]. At higher temperatures beyond 200 °C, α-$AgVO_3$ phase starts to convert into β-$AgVO_3$, and the process reaches completion at 300 °C [80]. Due to its more narrow bandgap, larger structural and chemical stability, β-$AgVO_3$ has gained more attention and wider application than α-$AgVO_3$ [81]. Although the CB potential of $AgVO_3$ is suitable for O_2 evolution and degradation of volatile organic compounds (VOCs), it is not sufficient for H_2 evolution [26].

13.2.4 Niobate Perovskites

Niobate perovskites can be identified as $ANbO_3$ (A = Na, K, Ag, Cu) [47]. Although they are only active under UV light due to their wide bandgaps (>3 eV), they can induce both photocatalytic water splitting and oxidative degradation of organic contaminants [208].

Among the niobate perovskites, sodium vanadate ($NaNbO_3$) and potassium vanadate ($KNbO_3$) are less toxic and environmentally friendly materials and have attracted considerable interest [56]. They are both indirect bandgap semiconductors, with $NaNbO_3$ having a bandgap of 3.4 eV, while $KNbO_3$ has a slightly narrow bandgap of 3.1 eV [78]. Band structure calculation revealed that the mobilities of both charge carriers are higher in $KNbO_3$ than in $NaNbO_3$ [151]. This, in addition to better light absorption, resulted in higher photocatalytic performance by $KNbO_3$ compared to $NaNbO_3$ [151].

13.2.5 Ferrite Perovskites

Ferrite perovskites have been identified as $AFeO_3$ (A = Bi, La, Gd, etc.), with their original bandgap in the visible area [74, 164]. Among the ferrite perovskites, $BiFeO_3$ photocatalyst is now parallel with the famous TiO_2-based photocatalysts [43]. Apart from its narrow bandgap, other interesting features of $BiFeO_3$ are non-toxic nature, high chemical stability, and the coexistence of ferromagnetic and ferroelectric behaviours at room temperature [64].

13.2.6 Bismuthate Perovskites

Bismuthate perovskites have the general formula $MBiO_3$ (M = Li, Na, K, Ag), and bandgap in the order $NaBiO_3$ (2.53 eV) > $KBiO_3$ (2.04 eV) > $LiBiO_3$ (1.63 eV) > $AgBiO_3$ (0.87 eV) [132, 159]. They consist of Bi^{5+} with 6 s empty orbital, contributing to both the valence band top and the conduction band bottom [204]. Such a feature can narrow the bandgap and vary the band edge positions, leading to improved photocatalytic performance [97, 96].

Despite the narrow bandgap of $AgBiO_3$, the large radius of Ag^+ and the strong contact between Ag atoms and O atoms hinders the free transfer of Ag^+ ions. However, due to small ionic radii of Li^+, Na^+, or K^+ and the weak interaction with $[BiO_6]$ octahedrons, Li^+, Na^+, or K^+ ions may easily transfer in the tunnelled or layered space to harness solar energy [204].

13.2.7 Cobaltite Perovskites

Cobaltite perovskites have the general formula $ACoO_3$ (A = Gd, Sm, La, Pr, Eu, etc.) [51]. Among them, $LaCoO_3$ is considered as a promising catalytic material, as lanthanum (La) plays a vital role in the catalytic performance due to its partly occupied 4f levels [66, 115]. At the same time, the cobalt (Co) is considered active due to its mixed-valence state, excellent electrochemical behaviour, high electrical and ionic conductivities [49, 66]. However, partial visible light-harvesting ability, a short lifetime and recombination of photogenerated charge carriers limits its practical application [66].

13.2.8 Nickelate Perovskites

Nickelate perovskites have the general formula $RNiO_3$ (R = La, Pr, Nd, etc.), and $LaNiO_3$ has attracted considerable attention in multiple fields [63, 140]. As a result of its outstanding optoelectronic properties, inexpensiveness, suitable bandgap (1.9 eV) and non-toxic nature, $LaNiO_3$ has been deemed as an interesting and hopeful visible light photocatalyst for wastewater purification [188]. However, the conduction band position of $LaNiO_3$ is below the H^+/H_2 potential, and therefore electrons in the conduction band of $LaNiO_3$ could not be used for H_2 evolution [175].

13.2.9 Antimonate Perovskites

Antimonate perovskites have the general formula $ASbO_3$ (A = K, Ag, Cs, etc.), and $AgSbO_3$ has been reported as a promising material with positive response towards visible light [71]. The two main polymorphs of $AgSbO_3$ are the pyrochlore and ilmenite phases. The ilmenite $AgSbO_3$ phase was reported to show better photocatalytic performance towards the degradation of organic compounds under visible light irradiation than the pyrochlore $AgSbO_3$ phase [148]. However, the ilmenite $AgSbO_3$ phase is metastable and transforms into the stable pyrochlore $AgSbO_3$ phase by heat treatment under appropriate conditions [72].

The conduction band bottom of $AgSbO_3$ mainly consists of hybridized Ag 5 s and Sb 5 s orbitals, while the valence band top consists of hybridized Ag 4d and O 2p orbitals. The hybridization of orbitals leads to a continuous dispersion in a relatively wide energy range, resulting in high photocatalytic performance [90].

13.2.10 Chromite Perovskites

Chromite perovskites have the general formula $RCrO_3$ (R = La, Ce, Pr, Nd, Sm, Eu, Gd, Tb, etc.) [139]. Among the chromite perovskites, $LaCrO_3$ has been extensively examined due to its wide application in various fields, including photocatalysis [149]. It is a p-type visible light active perovskite photocatalyst with a bandgap of 2.6 eV [124]. The Cr-sites on the $LaCrO_3$ surface are better adsorption centres for atomic oxygen than Mn in $LaMnO_3$ or Fe in $LaFeO_3$ [169]. Such a feature in $LaCrO_3$ endows more favourable properties for photocatalytic applications [124].

13.2.11 Others

Apart from the above-discussed oxide perovskites, other oxide perovskites such as zirconates ($RZrO_3$ (R = Ca, Sr, and Ba)) [76], cerates ($RCeO_3$ (R = Ca, Sr, and Ba)) [28] and stannates [$RSnO_3$ (R = Ca, Sr, and Ba)] [201] also exists. However, they are barely used as photocatalysts, possibly due to their wide bandgaps [62, 70, 201].

13.3 Design and Modification Strategies

Solid-state technique is conventionally used to synthesize perovskites in the presence of basic salts at high thermal condition [39, 165]. Nevertheless, this method restricts the control of the particles dimension and its crystallinity [53]. On that account, an alternative method recently employed for the fabrications of tantalate perovskites, for instance, hydrothermal, [23, 25, 68, 84, 108]. solvothermal [29, 129] and polymerized complex method [178] to ensure the possibility of tuning the particle size with high surface area. It is interesting to note that, several modification strategies along with the alternative method are necessary to produce effective PCB with high photocatalytic performance. For example, the modification strategies particularly in defect engineering, doping and co-doping, sensitization, facet control and others.

The light absorption ability of the perovskite-based catalyst (PCB) was found to be enhanced when compared particularly with common wide band gap semiconductors (e.g., TiO_2), significant to the efficacy of photon and its carrier conversion. It is relevant to extend the duration of these carriers to further enhanced the photocatalytic performance. A befitting band gap is mostly crucial to optimize the absorption of light by the photocatalyst. Practically, the greater absorption in the visible range, the effectiveness of light absorption can be enhanced by tuning the band gap to be narrower [23, 25] The construction of the band structures is vital in modulating the optical and electronic properties of perovskite nanostructures for achieving multifunctional the efficacy and efficiency [123].

In particular, the perovskite material has a direct band gap for the whole visible light range, therefore, the charge carriers were effectively generated at lower energies in particularly for photocatalytic application [123, 17]. Among all, PBC has been reported perspicuous approach for tuning the band gap, by simply adjusting the defects of crystal structure, including the vacancy, impurity and the interstitial atoms. It can be useful strategy for improving its performance [128, 197, 196] and lead to reduction in band gap value, thus improving the light absorption within visible range, subsequently possessed higher photocatalytic activity [10, 48].

13.4 Design and Modification Strategies

One of the internal influences that profoundly impact the performance of the photocatalyst is its configuration and modification in the physical structure and composition. To be an ideal photocatalyst, the material should have narrow band gap, high charge separation efficiency and a reasonable absorption efficiency under visible light. Many photocatalytic materials suffer from wide band gap energy which couldn’t be stimulated by visible light (Zheng et al. 2015) and high recombination rate [57].

Conventional solid-state technique is commonly for synthesize perovskites perovskite materials at high temperatures [39, 165]. However, this approach limits regulation of crystallinity and particle size [53]. On that basis, for the manufacture of tantalate perovskites, hydrothermal technique currently used as an alternative strategy [23, 25, 29, 68, 84, 108, 129] and polymerized complex method [178] has been reported to ensure the possibility of tuning the particle size with better surface area. It is important to note that several modification strategies, along with the alternative method, are required to produce successful perovskite-based catalyst (PBC) with high photocatalytic efficiency. Several techniques have been developed to address these limitations, such as defect engineering, doping, heterojunction, sensitization, and other greener technique, i.e. integrated carbon-based material or biopolymers [111].

The light absorption ability of the perovskite-based catalyst was improved compared to typical large band gap semiconductors (e.g., TiO_2), as reported by Jiang and co-worker (2018). This improvement leading to the enhance the efficiency of photon to electron mobility. They proposed that it is important to increase the lifespan of these carriers to boost the overall performance of photocatalysts. An appropriate band gap is fundamentally crucial for optimizing the absorption of photocatalysts. In general, since the visible light range is greater, the absorption efficiency can also be enhanced by modulating the band gap to lower values [23, 25]. To achieve multifunctional efficacy and effectiveness, the engineering of band structures is crucial in tuning the optical properties and electronic states of perovskite nanostructures [123].

Some researcher reported the perovskite material has a direct band gap through the visible spectrum, so the charge carriers have been produced efficiently at lower energies, particularly for photocatalytic application [123, 17]. Relevant approach for tuning the band gap, by simply tuning the crystal structure defects, including the vacancy, impurity, and interstitial atoms, has been documented among the advanced features of different photocatalysts. According to [197, 196, 128], a proper tuning mechanism can be useful to enhance its efficiency and contribute to decreases in the value of the band gap, thereby increasing the light absorption in the visible spectrum and consequently allowing greater photocatalytic performance [10, 48].

13.4.1 Defect Engineering

The improvement in light absorption, catalytic efficiency, charge transfer and stability can be constructed by defect engineering. The defects were graded according to the defects and atomic structures of the semiconductor. In theory, structural discrepancies of photocatalysts can be classified into four such as point defects [146], line defects [131], planar defects [97, 96], and volume defects [99]. In addition, many photocatalysis with cation vacancies have been established by many researchers, and therefore significant to monitor the development of defects in perovskite materials by generating vacancies and self-doping.

For instance, one of the perovskites reported by Liu and Solhberg, [100] called strontium titanate, have been designed by defect engineering. $SrTiO_3$, a semiconductor of simple cubic and n-type with superior physical properties with bandgap between 3.1 and 3.3 eV. Despite the advantages, its wide optical bandgap restricts its capacity to absorb light, leaving most of the energy from solar light unused. Strategies to increase the photocatalytic potential of $SrTiO_3$ by controlling its bandgap to allow use of a wider visible and solar spectrum range. In this example, introducing defect or doping technique was done for the tuning of the $SrTiO_3$ bandgap.

Xie and co-workers [181] constructed self-doped $SrTiO_3$ through one-step combustion technique. The samples were treated with argon, Ti^{3+} ion vacancies and oxygen (O_2) were injected into the lattice, serving as a template to activate water molecules, helping to restore the efficacy of artificial photosynthesis. This study was able to show that these oxygen deficiencies are accommodated by inducing the gap that enables photoexcitation within the visible light region from the defect band to the conduction band, consequently encourage the adsorption for reduction of CO_2 under visible light irradiation.

In another study investigated by Luo et al. [107], they stated that the link between strontium titanate surface and its photocatalytic behaviour on CO_2 reduction. As reported, the surface of TiO_2-terminated surface is in low pH, so the electronic properties of the two Sr and Ti surfaces experienced significant different, where the Sr 4d orbital is more negative than the Ti 3d orbital in the conduction band, resulting in greater SrO-terminated surface reduction potential. The study indicates that $SrTiO_3$ surface-Ti-rich had the greatest potential for reducing CO_2.

Kwak and Kang [87] have attempted to comprehend the effect of the Ca: Ti ratio towards $CaTiO_3$ and its potential efficiency. They reported a s the molar ratio of Ti in the catalyst extends up, a reaction between the reactive sites and carbon dioxide molecules occur. Nevertheless, it is reported that an excess of Ti will prohibit both metals from having a synergistic impact. $CaTiO_3$ encapsulated basalt fibre was recorded as an assisted material to create the highest numbers of oxygen vacancies on the planes {001} and sufficient pores size that allowed facilitating of CO_2 as indicated by Im et al. [61]. The fiber consisting of large amounts of SiO_2 with impurities of CaO, Al_2O3, and Fe_2O_3 [27] having a role as photosensitizer to enhance photocatalytic efficiency [30, 61].

In a separate approach, Hou et al. [55] disclosed the presence of nitrogen and oxygen vacancy are able to modulate the electronic bandgap NaTaON, thereby increasing the absorption of visible light. As these vacancies able to shifts the absorption of visible light from the UV region, resulting in a reduction in the 2.18 eV bandgap. The heterojunction also increased the separation of charged and improved the durability of the materials, thus improved the activity of CO_2 reduction.

13.4.2 Doping or Co-doping

Doping or co-doping, which is modulated by the inclusion of a foreign element in photocatalysts, is another alteration technique. Metal impurities are introduced into the lattice of perovskite as foreign atoms in the doping technique. Doping modifies the band gap and the material's atomic composition, thus making it possible to employ the visible light. In addition, Huang et al. [57] stated the additional energy levels can be added that help trap excitons in separate carriers while avoiding recombination. Many researchers utilized metallic elements and non- metallic elements doped perovskite [14, 102, 144, 192, 198] to modulate the band composition and electronic behaviour of studied photocatalysts.

The assortment of modifications has been investigated to broaden the photocatalyst bandgap and thus expand their photo-response to the visible light field, as reported by Samsudin and Abd Hamid [136] utilising noble metal deposition or known as doping. In other work, the significant observation by Anzai et al. [8] stated that the photocatalyst Ag-doped $CaTiO_3$ showed a higher generation rate and greater CO formation selectivity. In this study, Ag nanoparticles serve as unique active site within $CaTiO_3$ that reduced the production of H_2, and subsequently increased the creation of CO in water splitting.

Furthermore, by co-doping with La and Cr rare-earth metal, Wang et al. [172, 174, 168] successful modified hollow $CaTiO_3$ cubes to reduce the bandgap and boost their light-harvesting. In contrast to the small bandgap of pristine $CaTiO_3$, the hollow cubes exhibited stronger photocatalytic activity. This was primarily due to the improved photon interactions in La/Cr co-doping as well as the shorter charge transport paths. Another series of La/Cr perovskite compounds co-doped with $ATiO_3$, of which A 1⁄4 Ca, Sr and Ba were studied by Lu et al. [105] to see the differences in crystal structure as well as their optical and physicochemical properties. Critical structural contortions can be found for $Ca_{0.9}La_{0.1}Ti_{0.9}$–$Cr_{0.1}O_3$, indicating that Cr is responsible for the apparent light photoactivity. Lu et al. [105] discovered that the divergence away from the bond angle of Ti–O–Ti contributed to low catalytic efficiency as visible light absorption deteriorates. However, the existence of Ti–O–Ti bond angle ensures optimum overlap between Ti 3d orbitals and O 2p orbitals, resulting in broad band distribution and raised in charge movement for effective H_2 generations under visible light illumination.

Huang et al. [58] explored the properties of $BaTiO_3$ perovskite structure, by adjusting the concentrations of dopant elements such as selenium, tellurium and sulfur. These dopants substantially minimize the energy gap of $BaTiO_3$, thereby increasing absorption of the catalyst in the visible region. The catalytic properties of potassium tantalate, $KTaO_3$, studied by Chen et al. [23, 25] was doped with carbon and evaluated in the H_2 generation under sunlight illumination. From the observation, carbon-doped $KTaO_3$ demonstrated improved efficiency in the H_2 generation rate relative to the parent materials. In contrast, Krukowska et al. [84] investigated the role of lanthanides for $KTaO_3$-doped material and its efficiency towards generation of H_2. Synergistic results found between ion-doped perovskites of $KTaO_3$ and lanthanides and have strengthened the formation of H_2.

Depending on the crystallographic orientation, $BiFeO_3$ a perovskite oxide in rhombohedral unit cell and space group of *R3c* has known to be readily visible light active with a direct bandgap between 2.2 and 2.7 eV [138, 186]. In addition, doped or pristine ferrites materials are extensively studied in photocatalysis. For example, Yang and co-workers (2019) used Gd-doped $BiFeO_3$ as an efficient catalyst in generating H_2 in water splitting application. Meanwhile, Satar et al. [137] suggested that the band gap of $BiFeO_3$ decreased substantially in the presence of yttrium doped, increasing the percentage degradation of cationic dye, MB under sunlight irradiation. The authors claim, changes in performance are primarily due to electrons and holes being effectively produced, separated, and migrated.

13.4.3 Heterojunction

Heterojunction is another technique to improve the performance of the photocatalytic by increasing the efficiency of charge separation. Several studies conducted by Dutta et al. [33] and Ola and Maroto-Valer [121] showed, by bridging the semiconductor with metals or non-metals, heterostructures are produced that introduce new energy states that help to separate photogenerated charges and thereby preventing the electron from recombining. Ruzimuradov et al. [134], for instance, developed lanthanum- and N-co-doped strontium titanate-heterostructured macroporous monolithic materials with a bi-continuous morphology of titanium dioxide in visible light-active condition.

A number of works reported [11, 75] based on the effect of p-type coupled with n-type materials to form a p–n heterojunction photocatalyst in addition to doping. In specific, the efficacy of CO_2 reduction in the presence of $BiFeO_3$–ZnO p–n heterojunction has been investigated by Karamian and Sharifnia [75]. The author reported that the composite showed higher optical responses in the visible light spectrum with higher performance in charge separation. This is largely due to the existence of the p–n heterojunction that has supplied the CO_2 photoconversion with an excess of energetic electrons.

In another study, Bagvand et al. [11] investigated the role of ZnS for the production of n-type photocatalyst of $BiFeO_3$ and its efficiency effect by controlling ZnS and ZnO molar ratios. The findings demonstrated the highest efficiency of photocatalytic CO_2 reduction at the equivalent molar ratio of both ZnO, ZnS and $BiFeO_3$ in the experiments. They claim that p–n structure will produce localized electrical field that contributes to the transition in the opposite direction of charge carriers, leading to a reduction of the recombination rate.

13.4.4 Sensitization and Facet Defect

Another strategy in crafting heterojunction for improved photocatalyst efficiency is facet engineering. Facet engineering is a potent approach to intensify the crystal's photocatalytic efficiency by inducing the creation of the facet defect by modulating the environment in which the crystal is being formed. The variation of surface energy of facets will affect the photocatalytic behaviour. There are several types of facets of the semiconductor lattice. Studies by Liu et al. [103] detected facets {110} and {101} possess low surface energy and stable, while the {001} facet has the greatest surface energy and highly reactive, respectively.

Interesting research finding by Yu et al. [190] has shown that {101} and {001} facets of high-energy TiO_2 nanocrystals exhibit different band configurations, and these co-exposed {101} and {001} facets of nanocrystals establish unique surface heterojunctions within single particles of TiO_2 that are advantageous for the rapid transfer of photo-induced electrons. In addition, building 3D/2D heterojunctions between two contact semiconductors with profound and broad facet-dependent contact areas will provide more effective gap and improved the efficiency as claimed by Cao et al. [20]. Through efficient synthesis of TiO_2/g-C3N4 heterojunction composites with a simple calcination route it resulted the photo-generated holes appear to stay in the TiO_2 valence band, while the electrons initially transfer from the conduction band of TiO_2 to the valence band of g-C3N4, which further excited the g-C3N4 VB [190].

Dye sensitization and reactive facet exposure have recently become a successful way to extend the spectrum of light reaction and prolong the lifespan of photogenerated electrons and holes. Owing to its greatest π-conjugated framework, good thermal stability, and better absorption on visible irradiation, metalloporphyrin is known as one of outstanding photosensitizer. Most of the studies by several researchers involved metalloporphyrin sensitized metal composites [85, 116, 154, 183, 104, 197, 196, 46], has been shown to effectively increase the photocatalytic activity of certain semiconductor materials. Furthermore, metalloporphyrin processes suitable energy levels as one form of organic semiconductor and can comprise effective Z-scheme heterojunction hybrid photocatalysts with n-type TiO_2. This hybrid system will prevent the possibility of recombination of photogenerated charge carriers and boost photocatalytic activity through heterojunction interfaces as claimed by Low et al. [104].

Another study from Jeyalakshmi et al. [68], the team reported that sensitization of cobalt(II) tetraphenylporphyrin controls the electronic configuration in La changed perovskite of $NaTaO_3$, adjusting the bandgap to be narrow bandgap. No major change in the crystal structure of the pristine $NaTaO_3$ nanocubes were observed, but an absorption shift to 330 nm was observed. In addition, sensitization increased the ability to minimize CO_2 and decreased the recombination rate of the charge carrier. After longer irradiation, the material has been shown to be chemically stable. In other works, Zhong et al. [202] reported the effect of exposed catalyst crystal facets on water splitting using CdSe quantum dot (QD) sensitized $BaTiO_3$ nanocubes. They reported that CdSe QDs located on anisotropic planes of (230) and (001) of 30-face cubic of barium titanate exhibited higher efficiency compared to isotropic (001) facets of 6-face cubic of similar perovskite.

13.4.5 Others

Another alternative and practical modification, by involving carbon-based materials due to their appropriate function, large surface areas, good conductivity and chemical stability, as described by Sun et al. [155], Wang et al. [172, 174, 168], Tan et al. [160]. Thus, the electron transfer of p–n heterojunctions is predicted to be strongly promoted to achieve enhanced photocatalytic behaviour when coated with a carbon film. Besides, the conductive carbon layer will also prevent p–n heterojunction nanostructure accumulation, which is helpful for the increased the stability of p–n heterojunctions.

Zhou et al. [203] reported the production of $ATiO_3$ hierarchical structure in 3D utilizing the natural green leaves that aimed to decrease the emission of carbon dioxide in the presence of A: 1⁄4 Sr, Ca and Pb. The porous network provided by leave vein has a wide surface area that enhances gas diffusion, thus improving overall efficiency. Furthermore, with a similar 3D structure, worked with numerous cocatalysts, such as Pt, Cu, NiOx, Au, Ag and RuO_2. The highest evolution of CO and CH_4 among all gold (Au) was observed, followed by Cu and Ag under visible light illumination.

Shi and co-workers [142] have been investigating the impact of the manufacturing approach on the catalytic efficiency of $NaNbO_3$ through a solid-state reaction and hydrothermal. Different morphologies were observed from those reactions. Smooth and straight nanowires produced from hydrothermal reaction while bulk particles in homogenous sizes were formed by solid-state reaction. The two methods provided perovskite with a similar bandgap of 3.4 eV and the activity was examined under UV illumination by the generation of CH4. The homogeneous nanowires with increased crystallinity and greater surface area showed better CH4 behaviour relative to pristine $NaNbO_3$ [142]. Further combination of $NaNbO_3$ nanowires with g-C3N4 steered to greater performance compared to pristine $NaNbO_3$ or g-C3N4 for reduction of carbon dioxide. The overlap of $NaNbO_3$ and C3N4 coordinated band structures increased the efficiency of photocatalytics [142].

By using rGO carbon derivative as an electron separator and transporter to improve H_2 photocatalytic performance in water splitting, Humera et al. [60] further enhanced the production of $LaFeO_3$. The analysis shows that the integration of rGO was able to improve the efficiency of the studied material. In addition, several researchers team like Moniruddin et al. [117] and Dong et al. [31] stated the calcination temperature and the concentration of precursors play a crucial role in improving the photocatalytic perovskite performance. The study of Moniruddin et al. [117] found the size of $SrTiO_3$ is greatly increased with heating temperatures up to 800 °C. The H_2 production rate increases as the temperature rises. It can be seen that with increasing precursor concentration in EtOH at 800 °C, the H_2 production rate reduces simultaneously as the size of $SrTiO_3$ decreases.

The effect on the size and structure of $CaTiO_3$ by changing the temperature, molar ratio of water to ethanol and reaction time was successfully studied by Dong et al. [31]. The shape varies from inhomogeneous structure to microspheres with longer reaction time and temperature elevation. The morphology of microspheres demonstrated greater photocatalytic activity as opposed to randomly aggregated nanosheets [31]. The growth in photocatalytic activity is largely due to the greater redox potential of $CaTiO_3$. The synergistic impact of morphology and visible facets in a photocatalytic system is therefore crucial to determine the efficiencies of photocatalyst [202].

13.5 Application of Perovskite Photocatalyst

13.5.1 Water Purification

Water purification is the process of discarding contaminants from water such as algae, bacteria, fungi, viruses as well as parasites as in a biological group, meanwhile in the chemical group consists of organic pollutants, inorganic pollutants, toxic metals and suspended solids. Conventional purification processes use filtration and adsorption to remove the impurities from water sources. However, there are several problems encountered, such as producing secondary waste, needing extra treatment to unclog the filter and the pollutant not completely degraded. Therefore, photocatalysis provides new insight into the water purification process. Due to the ability of photocatalyst in degrading pollutants, it overcomes all the drawbacks of conventional processes.

Figure 13.2 shows the basic mechanism of water purification by the photocatalysis process. The general photocatalysis process by perovskite photocatalyst describe as following (i) the photon from light source hit the perovskite photocatalyst surface and produce electrons and holes; the light energy must overcome the band gap in order to produce electrons and holes (ii) electron travel to the conductive band (CB), simultaneously hole travelled to valence band (VB) (iii) holes react with water molecules to produce hydroxyl ions and hydrogen ions. Further reaction of hydroxyl ions with holes produce hydroxyl radicals which are an active species to degrade the pollutants (iv) simultaneously, electrons react with electrophilic oxygen to form superoxide radical anions also one of active species. When superoxide reacts with hydrogen ions, create hydroperoxyl radicals. Two hydroperoxyl radicals react, forming the hydrogen peroxide. Hydrogen peroxide acts as fuel in producing an abundance of hydroxyl ions and hydroxyl radicals. Therefore, most of the pollutants can be degraded when they react with these active species and usually produce oxygen, carbon dioxide, water among the end products.

When light source hit the perovskite photocatalyst surface,

Perovskite photocatalyst + $hv \rightarrow h^+ + e^-$ (*perovskite photocatalyst*)

At CB,

$$h^+ + H_2O \rightarrow OH^- + H^+$$

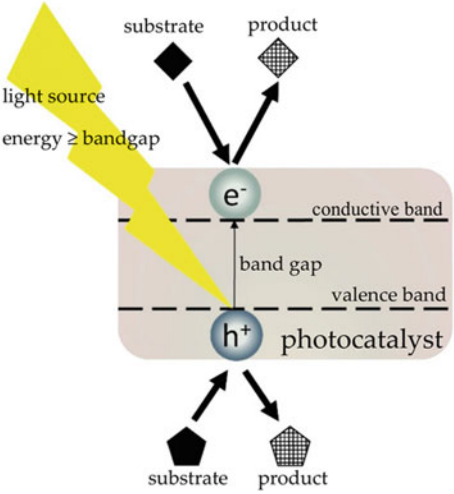

Fig. 13.2 Basic mechanism of perovskite photocatalysis [112]

$$h^+ + OH^- \rightarrow {}^{\bullet}OH$$

Simultaneously, at VB,

$$e^- + O_2 \rightarrow O_2^{\bullet -}$$

$$O_2^{\bullet -} + H^+ \rightarrow HO_2^{\bullet}$$

$$HO_2^{\bullet} + HO_2^{\bullet} \rightarrow H_2O_2 + O_2$$

$$H_2O_2 + O_2^{\bullet -} \rightarrow {}^{\bullet}OH + OH^- + O_2$$

$$H_2O_2 + e^- \rightarrow {}^{\bullet}OH + OH^-$$

Therefore, after generate the active species,

The pollutants + specific active species → degradation products

Absalan et al. [1] synthesis to degrade bromophenol blue wastewater. The band gap was found at 3.80 eV required visible light of 410 W halogen lamp. In 120 min, 0.05 mol perovskite photocatalyst dosage successfully degraded 82% of 10.5^{-14} mol/L bromophenol blue solution. The reaction was repeated for 3 cycles to prove the stability of that perovskite photocatalyst. Due to high crystallinity and highly photoinduced, $CoTiO_3$ creates electrons at CB and holes at VB after obtaining the required light source. At the surface, the same mechanism as previously stated in general perovskite photocatalysis was observed in degradation of bromophenol blue solution. Meanwhile, Fig. 13.3 shows the mechanism of $BaBiO_3$ perovskite photocatalyst in degradation of Rhodamine B wastewater. 0.5 g/L of perovskite photocatalyst is able to tackle 5 mg/L of Rhodamine B solution by both discoloration (83%) and mineralization (80%) within 240 min and shows high stability for 4 cycles of reaction under visible light (450 W Xenon lamp). Active species generated by excitation of $BaBiO_3$ (2.02 eV band gap) such as holes, hydroxyl and superoxide radicals, break the aromatic rings to form smaller molecular weight and intermediates, which further reaction produce the end products such as CO_2, NH_4^+ and water. It proves that perovskite photocatalyst can enhance the charge mobility in the crystalline network due to high crystallinity, the low particle size promotes short diffusion length of the charge carrier to reach the photocatalyst surface and reduce the electron-hole recombination [59].

Doped-perovskite photocatalysis for water purification shows a different mechanism. Usually, the doping acts as an electron trapper to avoid electron-hole recombination. Therefore, the electron acceptor such as diffuse oxygen can easily trap electrons to produce superoxide radicals and other active species to degrade pollutants. It is observed by Wang et al. [176, 171], 91.4% of 48 mg/L rhodamine B wastewater degraded within 120 min under visible light (300 W Xenon lamp) by Bi/BiOCl/$ZnSn(OH)_6$ doped-perovskite photocatalyst. Figure 13.4 two-part energy level for Bi/BiOCl and $ZnSn(OH)_6$; Firstly, light energy hit BiOCl to produce electrons at CB and holes at VB. Due to Fermi level of Bi is lower than CB of

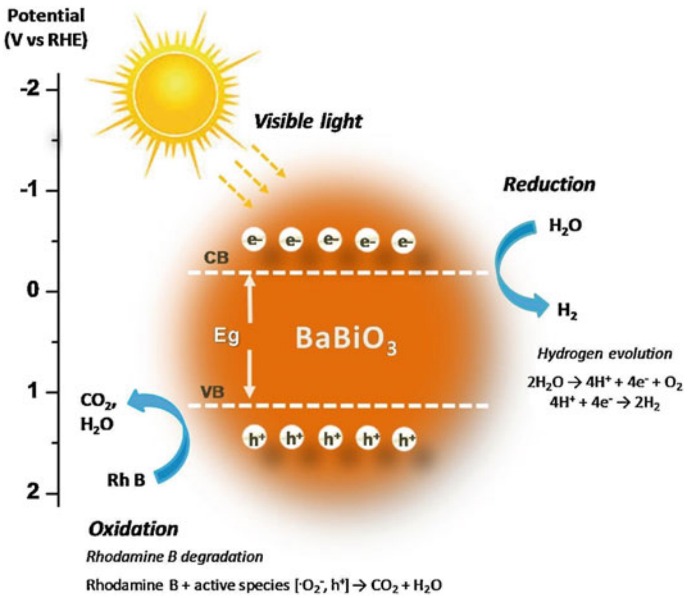

Fig. 13.3 Mechanism of $BaBiO_3$ perovskite photocatalyst in Rhodamine B wastewater degradation and hydrogen production [59]

BiOCl, the electron trap at Bi-metal instead. Then, the electrons transfer to $ZnSn(OH)_6$ and react with diffuse oxygen to produce superoxide. The superoxide further reacts and produce hydroxyl radicals to degrade Rhodamine B molecules partly into water and CO_2. Interestingly, at dopant, due to the accumulated electrons, the same mechanism also applied to produce hydroxyl radicals and able to degrade Rhodamine B. Next, the holes created by perovskite photocatalyst act as powerful active species to directly degrade Rhodamine B molecules. Aligned with Safari et al. [135], the methylene blue molecules purified by photogenerated holes and superoxide anion radicals produced by Gd-doped $NiTiO_3$. The doping of gadolinium (Gd) ion helps in improving the porosity of $NiTiO_3$ perovskite photocatalyst by decreasing the perovskite size, improving the specific surface area and reducing the recombination of electron-hole. Thus, it enhanced the production of holes and superoxide anion radicals. Therefore, the degradation of methylene blue achieved 88.64% within 120 min.

$$\mathrm{Gd}^{3+} + \mathrm{e}^- \rightarrow \mathrm{Gd}^{2+}\,(\text{electron trapping step})$$

$$\mathrm{Gd}^{2+} + \mathrm{O}_{2(\mathrm{ads})} \rightarrow \mathrm{Gd}^{3+} + \mathrm{O}^{\bullet -}_{2(\mathrm{ads})}\,(\text{electron transferring step})$$

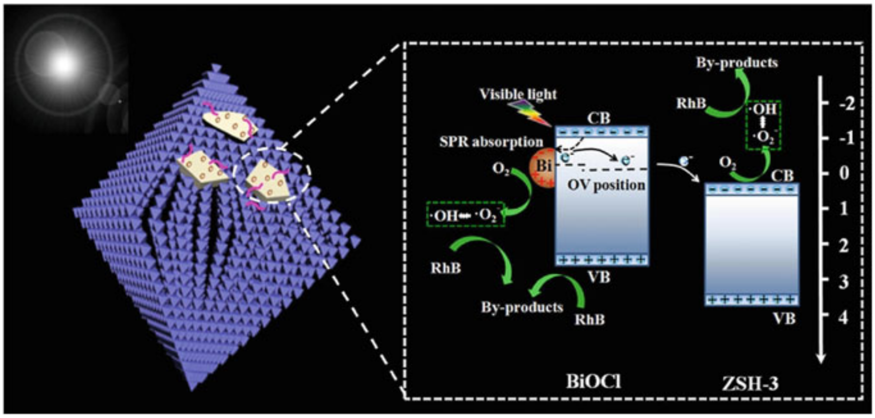

Fig. 13.4 Doped-perovskite photocatalyst [176, 171]

$$O^{\bullet -}_{2(ads)} + H^{+}_{(ads)} \rightarrow HO^{\bullet}_{2(ads)}$$

$$HO^{\bullet}_{2(ads)} + H^{+}_{(ads)} + e^{-} \rightarrow H_2O_2$$

$$H_2O_{2(ads)} + e^{-} \rightarrow {}^{\bullet}OH_{(ads)} + OH^{-}_{(ads)}$$

13.5.2 *Bacteria Disinfection and Air Purification*

Bacteria is a unicellular microorganism from prokaryote group. It can be divided into two types: gram-positive and gram-negative. Gram-positive bacteria have a thick cell wall made of peptidoglycan, meanwhile gram-negative bacteria have a cell wall made from outer membrane and thin peptidoglycan layer. Bacteria disinfection is physical or chemical treatment to reduce bacteria amount until obtaining desired concentration. Bacteria disinfection by photocatalysis can be achieved when the light source hits the perovskite photocatalyst to generate electrons and holes. In the CB, there are two paths to deactivate the bacteria. Powerful active species in deactivating bacteria is superoxide radicals which produce when electrons react with oxygen. In the presence of water molecules, superoxide radicals can react with it to create another active species, hydroxyl radicals to deactivate the bacteria. Meanwhile, at VB, the holes itself have the ability to deactivate the bacteria directly.

At CB,

$$e^- + O_2 \rightarrow O_2^{\bullet -}$$

$$O_2^{\bullet -} + \text{bacteria} \rightarrow \text{deactivated bacteria}$$

$$O_2^{\bullet -} + H_2O \rightarrow {}^{\bullet}OH$$

$$^{\bullet}OH + \text{bacteria} \rightarrow \text{deactivated bacteria}$$

Simultaneously at VB,

$$h^+ + \text{bacteria} \rightarrow \text{deactivated bacteria}$$

The study by Shi et al. [145] found that $CuBi_2O_4/Bi_2MoO_6$, a perovskite photocatalyst (Bi_2MoO_6) with heterojunction p-type semiconductor ($CuBi_2O_4$), disinfect *Escherichia coli* (*E. coli*) almost completely within 4 h under visible light. Figure 13.5 shows the mechanism of photocatalytic disinfection that produces the active species such as holes, superoxide radicals, and hydroxyl radicals to inactivate *E. coli*. The band gap of perovskite photocatalyst is 2.72 eV can highly absorb 420 nm visible light and create the holes after the electrons excite to CB. At CB of perovskite photocatalyst, the electrons accumulate and follow the same paths as the stated general mechanism to produce superoxide radical and hydroxyl radicals for bacteria deactivation. Concurrently, the holes accumulate at p-type semiconductor attack the cell membrane and cause the inactivation of *E. coli*. The large specific surface area of $CuBi_2O_4/Bi_2MoO_6$ provides a more reactive site and reaction interface between photocatalyst and the bacteria. Hence, slow recombination rate,

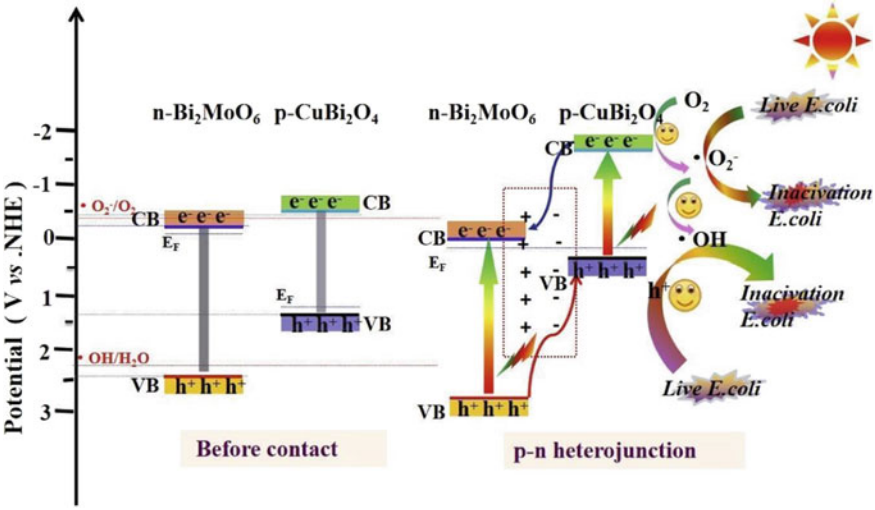

Fig. 13.5 Photocatalytic disinfection mechanism of *E. coli* by $CuBi_2O_4/Bi_2MoO_6$ [145]

high efficiency for separation, high utilization rate of light and large specific surface area are the valuable characteristics for photocatalyst during photo-disinfection. Meanwhile, Li et al. [93], study the application of perovskite photocatalyst for both gram-positive and gram-negative under the same factors. Under 400 nm visible light (300 W Xenon lamp) irradiation, *E. coli* gram-negative and *Staphylococcus aureus* (*S. aureus*) gram-positive were successfully degraded by Pb–$BiFeO_3$/rGO. The complete inactivation of *E. coli* within 30 min, meanwhile *S. aureus* achieved 99.7% degradation within 90 min. Gram-positive is more highly resistant due to their cell wall structure, made up of 3D spatial network structure composed of many layers of teichoic acids and peptidoglycan compare to gram-negative bacteria consists of single layer scattered structure only.

Air purification is a process to kill airborne pathogens that can cause airborne disease to humans or animals such as allergies, influenza, flu and measles. The treatment reaction must be able cut-off the spread routes of pathogens either via aerosol or contaminated fluid. The perovskite photocatalyst, $La_{0.9}MnO_3$ demonstrates high oxidative ability towards influenza A virus. The illustration in Fig. 13.6 shows hemagglutinin and neuraminidase, the amino acid residue of envelope proteins on influenza virus oxidized by $La_{0.9}MnO_3$. The oxidative species might penetrate the virus and damage the genetic materials. In 15 min, almost 76% of the virus has been disinfected. Therefore, prefer features of perovskite photocatalyst as air purifier utilize visible light despite of UV light due to its carcinogenic potential to humans and animals, able to self-disinfecting the airborne pathogens without requiring external energy sources and working continuously, less harsh and also high stability.

13.5.3 Photocatalytic Hydrogen and Oxygen Production

Hydrogen energy is the latest renewable energy discovered by scientists in this century. In the meantime, it was developed for the purpose of hydrogen vehicles that use internal combustion engines and fuel cells that are still under progress and expected extensive study. The benefits of this approach are low greenhouse gas emissions and can obtain by various fuel sources. For energy storage, gives economic benefits due to efficient remote power systems and also reduction in production and operational costs compared to fossil fuel energy.

Photocatalytic hydrogen evolution requires electrons as major active species. Water splitting is a reversible process in hydrogen and oxygen production, so photocatalyst is introduced in the reaction in order to produce an abundance of hydrogen gas that can be collected.

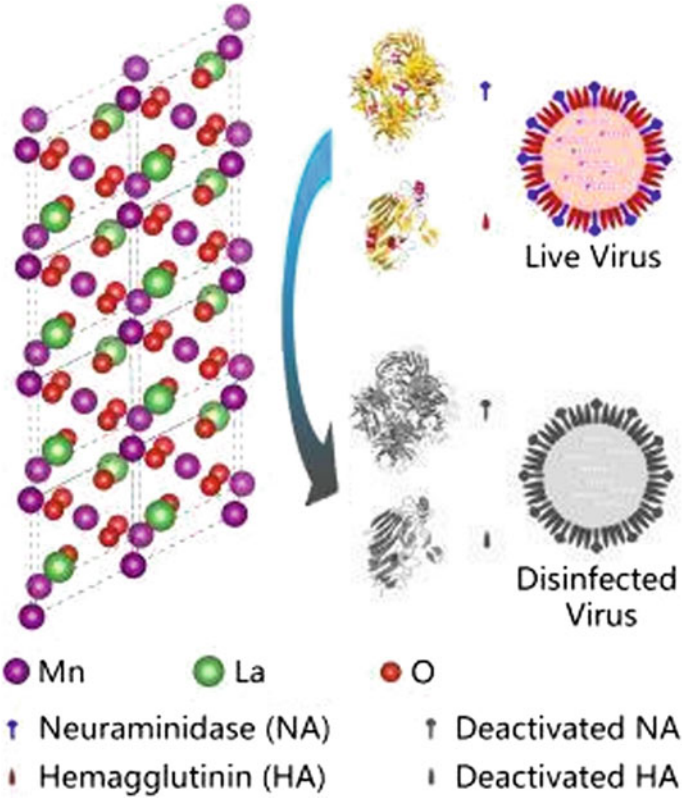

Fig. 13.6 Deactivation of amino acids residue of envelope proteins influenza A virus by $La_{0.9}MnO_3$ perovskite photocatalyst [179]

Water splitting by exert energy

$$2H_2O + \text{energy} \rightleftarrows 2H_2 + O_2$$

In presence of photocatalyst, at CB, water molecules reduce to form hydrogen gas

$$2H_2O + 2e^- \rightarrow H_2 + 2OH^-$$

And water molecules oxidize to form oxygen gas

$$2H_2O + 4h^+ \rightarrow O_2 + 4H^+ + 4e^-$$

Existing research recognizes the critical role played by perovskite photocatalyst in hydrogen and oxygen production. $BaBiO_3$ produces 61 μmol g^{-1} h^{-1} hydrogen gas in 3 h under irradiated 450 W Xenon visible lamp. The water molecule is reduced to produce hydrogen gas, meanwhile it is oxidized to form oxygen gas as shown in Fig. 13.3.

Water molecule reduction to form hydrogen gas

$$2H_2O \rightarrow 4H^+ + 4e^- + O_2$$

$$4H^+ + 4e^- \rightarrow 2H_2$$

This perovskite photocatalyst synthesis with slow and good crystal growth with a less formation of defects. The defects can act as a recombination center. Thus, the high crystallinity promotes better electrons and holes mobility in the crystal network to reach the surface. Next, the particle is small in size to decrease the diffusion length of photogenerated charges transfer to the surface, short distance directly related to low resistance. It also implies low probability for electron-hole pair recombination. Furthermore, small particles contribute to high surface area and increase the adsorption capacity between perovskite photocatalyst and water molecules. Hence, the stable photocatalytic hydrogen evolution must be attributed to high crystallinity, low particle size, low recombination of electron-hole and low resistance to improve the hydrogen production.

13.5.4 Photocatalytic Reduction of CO_2

Almost 77% of carbon dioxide emission mainly contributed by transportation, electricity and industry was reported by the United States Environmental Protection Agency (EPA) due to large consumption of limited fossil fuels. Therefore, the endeavour to convert CO_2 into chemical fuels such as carbon monoxide, methane and methanol to solve the global energy and environmental issues. Photocatalysis has been recognized as one of promising strategies to tackle this problem. As artificial photosynthesis, photocatalysts utilize solar energy to combine with CO_2 and H_2O to produce the chemical fuels and carbon monoxide as shown in Fig. 13.7.

As shown in Fig. 13.8, there are two paths for CO_2 reduction either as CO or CH_4 can be achieved simultaneously during photocatalytic reactions. The influence of H^+ ion amounts towards CO_2 molecules play an important role for the end product yields. When the light reaches $SrTiO_3$ perovskite photocatalyst, the electrons excite to CB leaving the holes on VB. The active species on VB react with H_2O to produce H^+. Meanwhile, the electrons at CB transfer to the dopant, Pt and react with H^+ to produce CO and CH_4.

$$CO_2 + 2H^+ + 2e^- \rightarrow CO + H_2O \left(E^\theta = -0.53\ \mathrm{V}\right)$$

$$CO_2 + 8H^+ + 8e^- \rightarrow CH_4 + 2H_2O\left(E^\theta = -0.24\ \mathrm{V}\right)$$

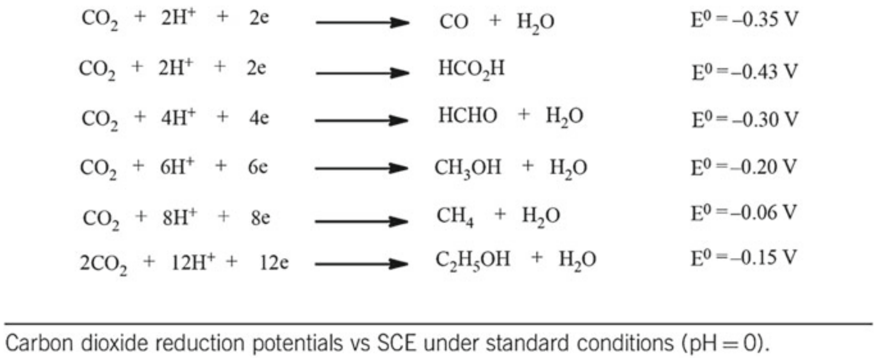

$CO_2 + 2H^+ + 2e \rightarrow CO + H_2O \quad E^0 = -0.35\ V$

$CO_2 + 2H^+ + 2e \rightarrow HCO_2H \quad E^0 = -0.43\ V$

$CO_2 + 4H^+ + 4e \rightarrow HCHO + H_2O \quad E^0 = -0.30\ V$

$CO_2 + 6H^+ + 6e \rightarrow CH_3OH + H_2O \quad E^0 = -0.20\ V$

$CO_2 + 8H^+ + 8e \rightarrow CH_4 + H_2O \quad E^0 = -0.06\ V$

$2CO_2 + 12H^+ + 12e \rightarrow C_2H_5OH + H_2O \quad E^0 = -0.15\ V$

Carbon dioxide reduction potentials vs SCE under standard conditions (pH = 0).

Fig. 13.7 List of carbon dioxide reduction reactions produce different chemical fuel products [185]

Meanwhile, the morphology of perovskite photocatalysts influences light harvesting. The 3D ordered macroporous (3DOM) morphology of $SrTiO_3$ perovskite photocatalyst improves the light absorption by slowing the light source from reaching Pt/$SrTiO_3$ and separating the charge carriers. Next, the alkali earth metal, Sr in the $SrTiO_3$ helps the adsorption and initiate activity for CO_2 reactant due to high alkalinity of Sr. The Pt dopant helps to separate the photogenerated charges by transferring the electrons and react directly with H^+ ions. Therefore, perovskite photocatalyst shows potential in CO_2 reduction by undergoing artificial photosynthesis.

13.5.5 Application of Visible-Light-Driven Perovskite as Photovoltaic Solar Cell (PSCs)

Current global power demand is increasing significantly every year aligned with the improvement of the technologies and industries need. Nowadays it was reported that the energy usage is 16TW globally and expected to increase up to 30TW in 2050 [133]. Therefore, a lot of research has been done since then with only one purpose to find an alternative source that can add-on to the current or conventional source of energy such as petroleum-based fuel. Among the various sources of energy, solar energy was found to be the most significant and promising since it is easily and readily available. This is possible by converting the solar energy to electricity. Therefore, using photovoltaic solar cells for power generation seems to be a promising way as they convert the sunlight directly into electricity.

Nowadays, the market was dominated by the crystalline silicon solar cells. However, the production of the solar cells is costly due to the expensive raw materials. Because of that, most of the researchers come up with new ideas of utilizing PV technology that has low efficiency and cost manufacturing. Despite all

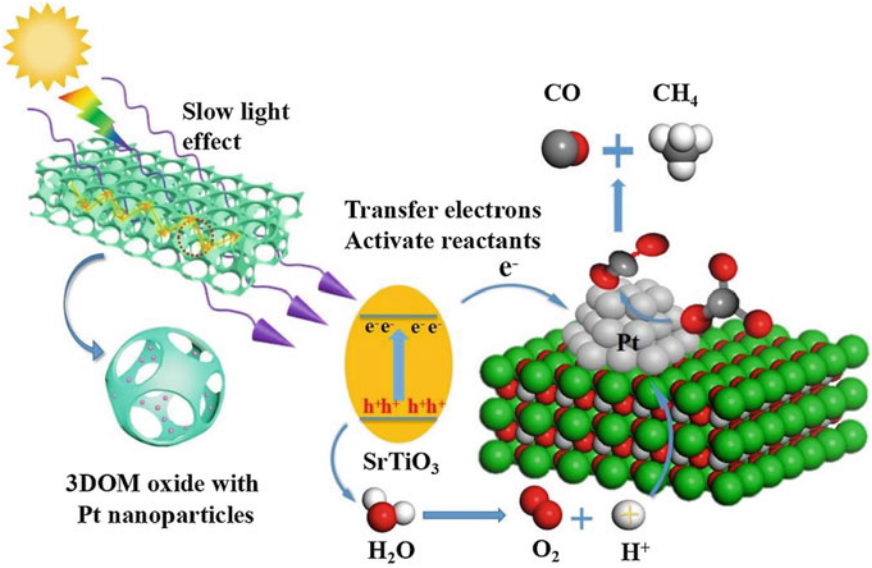

Fig. 13.8 The mechanism of Pt doped $SrTiO_3$ perovskite photocatalyst in carbon dioxide reduction into carbon monoxide and methane [180]

the facts, poor device stability and short lifetime are creating interferences in the path of commercialization of PSCs, the perovskite materials are gaining huge attention among the researchers because of their excellent PV performance, cheap raw material, and requires of easy processing parameters [205]. Furthermore, it also does not entail any complicated processing conditions, since it can be created by using simple low-cost methods such as screen printing, dual-source evaporation, spin and dip coatings techniques which can be developed on flexible substrate.

Si et al. [147] have studied the fundamentals on the absorption of PSCs. It was found that the perovskite layer tends to absorb UV and visible light bands, meanwhile, the electrode layer favours to absorb IR bands. Interestingly, plasmonic was used to create hot spots in active layer via light-flow-circulating and nonlinear absorption mechanisms so that, the light can be localized through perovskite material. Si et al. [147] also reported that the absorption of IR-band has been extended to 58.2% when the plasmonic was used in the materials.

Figure 13.9a, b shows the mesoscopic architecture and the planar heterojunction structure of PSCs, respectively. Recently, the mesoporous materials have been studied and applied as PSCs due to their high porosity and large specific surface area up to 1000 m^2/g [205]. It potentially increases the light response of photosensitize material and improves the effectiveness of the instrument.

Basically, a solar cell consists of metal electrode layer, a hole transport layer as Hole Transporting Material (HTM), a perovskite layer, a porous oxide layer, a dense electron transport layer as Electron Transporting Material (ETM), and

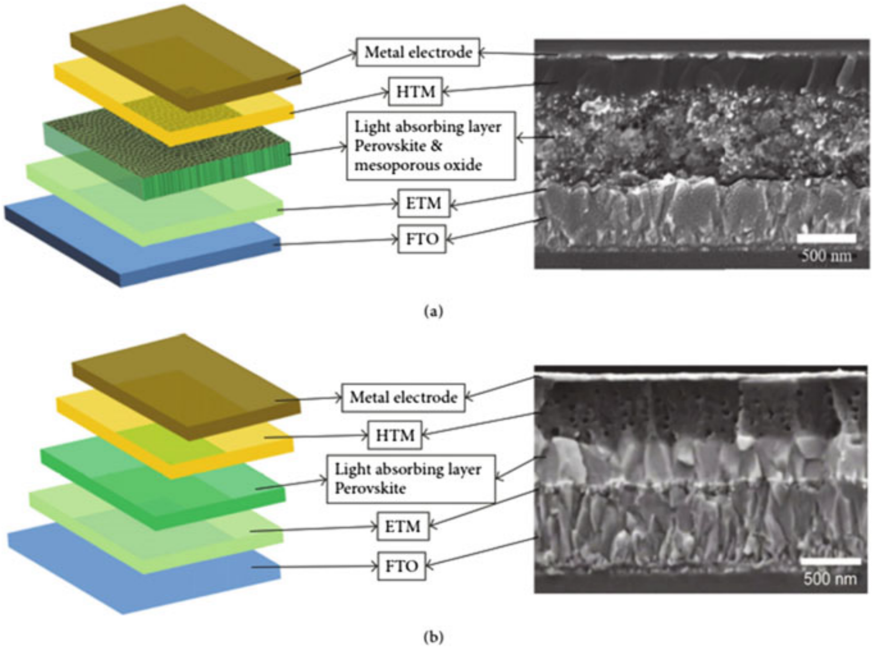

Fig. 13.9 Schematic diagram and SEM section image of **a** mesoscopic architecture PSCs and **b** planar heterojunction structure PSCs (adapted from [205]

Flourine-doped Tin Oxide (FTO) electrode. This structure arrangement not just effective to decrease the recombination rate of electrons and holes, but also provides the necessary diffusion length for the accumulation of electrons and holes effectively [34]. The TiO_2 layer in the middle layer plays a significant function such as conducting the electrons, blocking the holes and inhibits the electron-hole pairs recombination in the FTO conductive substrate. Thus, it contributes to improve the photoelectric conversion efficiency of the studied materials. Furthermore, other than TiO_2, materials like ZnO, Al_2O_3, and ZrO_2 are typically used. Meanwhile, the function of hole transport layer is to accept the generated holes and transfer them to the surface of the metal electrodes. Commonly, the hole transport material and counter electrode materials are Spiro-OMeTAD (2,2’,7,7’-Tetrakis [N,N-di (4-methoxyphenyl)amino]-9,9’-spirobifluorene) and noble metals, such as Au, Ag, and Pt, respectively.

Based on Fig. 13.9b, the distinction from the mesoscopic structure is that the planar structure has no porosity of materials between the two layers of the electron transport and the hole transport, as a result, the electron-hole pairs can be parted effectively. Additionally, it contributes enlightenment the mechanisms of light absorption and electron-hole separation, thus, enhance the versatility of device optimization for the development of highly effective and advanced coated perovskite solar cells.

Latest research by Ren et al. [130] they studied power conversion efficiency and efficient light capture and prepared the ultraviolet-ozone assisted strategy on the TiO_2 interface for perovskite solar cells. Interestingly, the modified perovskite PSCs with ultraviolet ozone TiO_2 efficiently suppress the decomposition of perovskite films under light illumination. They found that this device has better performance and remarkable stability as compared to the pristine perovskite solar cells.

13.5.6 Application of Visible-Light-Driven Perovskite as Photocatalytic Nitrogen Fixation

Ammonia (NH_3) is an essential and important substance in the present-day industry as the major component of production of many types of chemicals such as fertilizers and bleaching agents for the cleaning process. Conventionally it has been produced in big scale industries via Haber-Bosch reaction, which requires very high temperature ranging from 400 to 500 °C and pressure ranging from 15 to 25 Mpa [195]. Recently, numbers of research papers reported on the new and advanced techniques which are simpler and environmentally friendly known as nitrogen fixation. Previously, biological nitrogen fixation was introduced and applied in many applications. During this process, the nitrogen gas from the environment will be activated by the organism to produce NH_3 at ambient temperature and pressure, for example of the organism is nitrogenase enzymes which catalyze the reduction of N_2 to NH_3 [19]. Recently, artificial solar-powered nitrogen fixation was introduced, where the concept is by using the energy from light source such photons to excite electron which will be used to create radicals. This can be divided into two major steps; step (i) semiconductor is excited under light irradiation producing photogenerated electrons excited to the CB leaving holes in the VB. Step (ii) the photogenerated holes oxidize water to O_2 while the photogenerated electrons reduce N_2 to NH_3. Figure 13.10 shows the mechanism for the production of NH_3 by using the photocatalytic N_2 fixation technique.

Fig. 13.10 Propose mechanism for the photocatalytic N_2 reduction [195]

As reported by Li et al. [91], the bismuth molybdate nanosheet with oxygen vacancies can be prepared via NaOH etching treatment at room temperature. The function of oxygen vacancies is to boost the photocatalytic nitrogen fixation to produce ammonia under the visible light source at room temperature and ambient pressure. They found that the oxygen vacancies had improved the photogenerated charge carrier separation and improve the capability of the materials for the N_2 adsorption and activation. As a result, production of ammonia was increased up to 800 μmol g^{-1} h^{-1}. Furthermore, these materials also show a good tolerance to the oxygen in the N_2 source for the replacement of pure N_2 with air under simulated solar conditions. The pictorial illustration of relaxed slab model of BMO sample and the Vo–BMO–OH sample surfaces and the schematic representation of photocatalytic N_2 fixation process under visible light illumination is shown in Fig. 13.11.

Wang et al. [176, 171], reported the importance of oxygen vacancies with abundant localized electrons, where it can assist or improve the ability of the material to capture and activate N_2. They proved that the bismuth oxybromide-based semiconductor that they have prepared produced higher NH_3 generation with rate up to 1.38 mmol h^{-1} g^{-1} under visible-light-induced OVs. It also resulted in the stable photoreduction of atmospheric N_2 into NH_3 in pure water, which serves as both solvent and proton source. Figure 13.12 shows that the photocatalytic N_2 fixation of the Bi_5O_7Br–NT can be divided into 4 major steps; (i) under visible light irradiation, part of the O will escape in the form of O_2 from the surface of Bi_5O_7Br–NT creating sufficient surface OVs, (ii) the N_2 is chemisorbed and activated on the OV sites, (iii) the excited electrons s injected into the activated N_2 and reduce it to NH_3 and the last step (iv) the photoinduced OVs would be refilled by seizing O atoms from water, leading to a good recovery to the original stable OV-free composition.

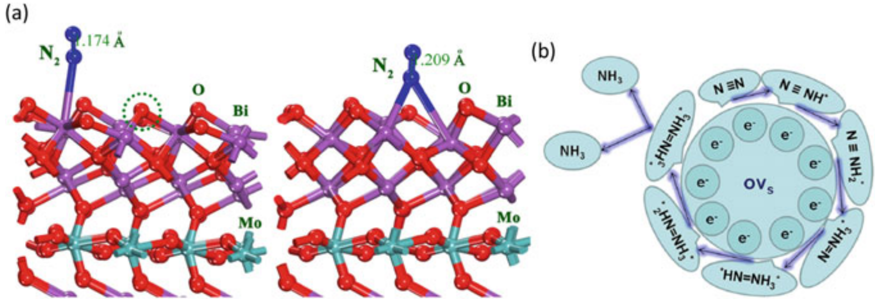

Fig. 13.11 Illustration of **a** the pictorial views of a relaxed slab model for the BMO sample and the Vo–BMO–OH sample surfaces, and **b** the schematic illustration of the photocatalytic N_2 fixation process on the Vo–BMO–OH sample under visible light illumination [91]

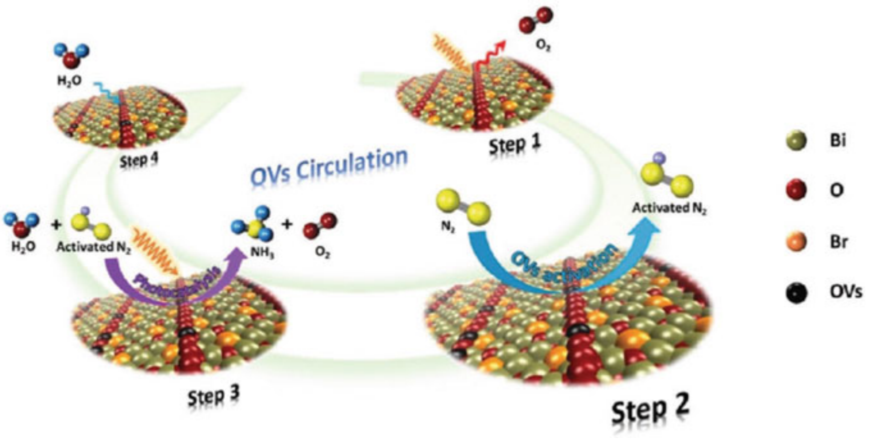

Fig. 13.12 Schematic illustration of the photocatalytic N_2 fixation model in which water serves as both the solvent and photon source as well as the reversible creation of light-induced OVs [176, 171]

13.5.7 Application of Visible-Light-Driven Perovskite Photocatalyst for Anti-fogging Glass

Fog or fogging phenomenon is the formation of small water droplets from the water condensation on the surface of glasses, goggles, camera lenses and binoculars. This is possible due to high surface tension resulting in a single droplet of water. Here, anti-fog or antifogging is very useful to avoid or to reduce the fogging phenomena, it can be done by reducing the surface tension and altering the degree of wetting by introduction of antifogging film, resulting in the super hydrophilic, non-scattering film or water instead of droplets.

Takata et al. [158], reported that they prepared the antifogging glass by coating the glass with the TiO_2 layer. It was observed that the TiO_2 has super hydrophilic properties which is very likely attracted to water other than common ability such as anti-bacterial, anti-pollution and deodorant materials. They mentioned that when the surface of TiO_2 is irradiated with UV-light could decrease the contact angle (CA) and reaches almost zero with time as illustrated in Fig. 13.13 where the incident light will not be diffracted. This finding also aligned with the statement reported by Duan et al. [32] stated that the super hydrophilic TiO_2 film reduces the CA 150° (hydrophobic TiO_2) to less than 5° (hydrophilic TiO_2). When the TiO_2 coated glass expose to the condensed water, the droplets will create or form very thin water film and become transparent, automatically, due to the self-cleaning effect it will repel oil layer and when exposed to the light source it activated and catalyzed the degradation of any possible bacteria and fungi, etc. Because of that ability, it was known that the TiO_2 has vast application as antifogging and also the antibacterial or self-cleaning assisted material.

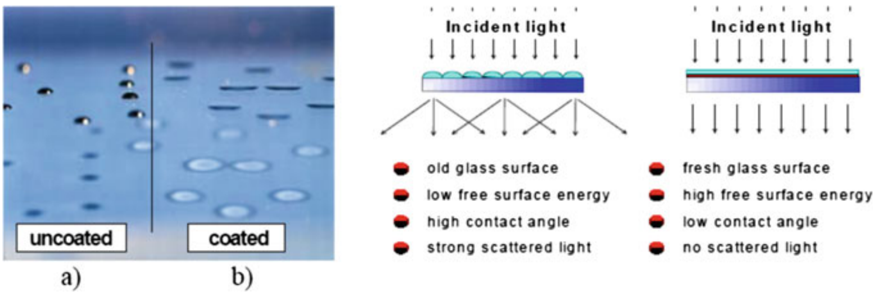

Fig. 13.13 Illustration of water drops on a glass surface **a** uncoated side: hydrophobic (CA = 65°) and **b** coated side: hydrophilic (CA < 10°)

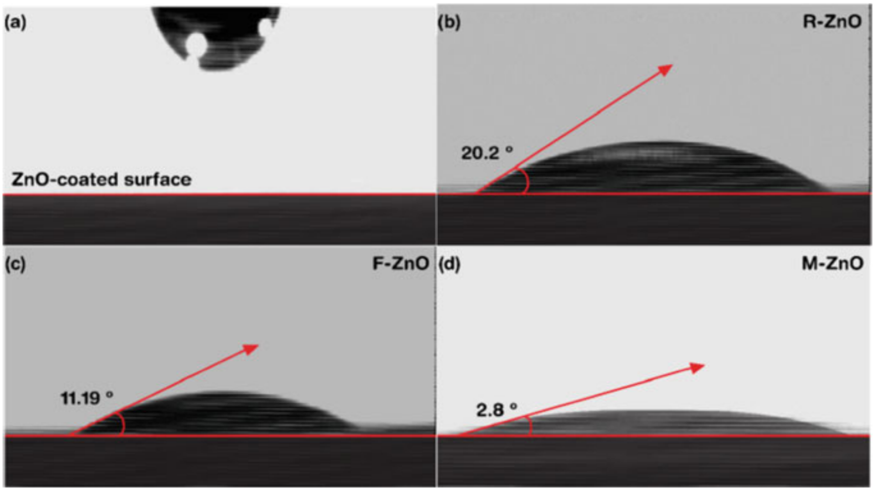

Fig. 13.14 Contact angle measurement (CA) of **a** water drop before contact to the ZnO-coated surface; **b** nanorods ZnO, **c** microflowers ZnO, and **d** porous microspheres ZnO [119]

Nundy et al. [119] studied the performance of the super hydrophilic ZnO microstructure coating for photovoltaic and glazing applications. They reported on the wettability and photovoltaic behaviour can be affected by the different structures of ZnO by affecting the CA of each structure as shown in Fig. 13.14. From this Figure, we can see that the hydrophilic surfaces for nanorods ZnO with higher CA and super hydrophilicity of microflower and microsphere ZnO with lesser CA, respectively. This is due to the changes of crystallinity and microstructural during the synthesis of ZnO. Thus, microstructure ZnO is good for the many antifogging and photovoltaic applications.

According to Takagi et al. [157], there are numbers of application of TiO_2 that has been studied as the sterilizer, cleaner, decomposer, and antifogging agent. This is because of the TiO_2 that has high oxidizing power when it is irradiated by solar light. They also studied the sputter deposition technique to apply the TiO_2 film on the surface of the glass or any targeted clean surface. Based on our previous studies, a lot of research papers were discussed on the potential of photocatalyst as an antifogging agent by increasing the wettability and reducing the contact angle of the surfaces especially TiO_2 and ZnO. However, best in our knowledge, studies on the perovskite structure of photocatalyst as potential antifogging glass is not yet reported or discussed elsewhere. This will become a good opportunity for the researchers to study, evaluate and conduct research on the application of perovskite photocatalyst as the antifogging agent.

13.6 Conclusion

This chapter revealed the theory of perovskite-based photocatalyst for various environmental remediation applications specifically under visible light and solar irradiation. Moreover, the different type of perovskite materials together with its advantages is thoroughly discussed. Its unique characteristic enables it to incorporate with other metal and non-metal nanomaterials and such modification strategies leads to an improve ability of perovskite-based photocatalyst especially in harvesting of visible or solar light and prolong the life span of the charge carriers has been further explained. The promising outcome of the fabrication perovskite materials and its development pathway for various applications for energy conversion and other environmental applications. Hence, the perovskite-based photocatalysts are a versatile material in terms of its recurrent development that enable performance enhancement and its practicality towards environment protection in the time ahead.

References

1. Absalan Y, Alabada R, Ryabov M, Tolstoy V, Butusov L, Nikolskiy V, Kopylov V, Gholizadeh M, Kovalchukova O (2020) Removing organic harmful compounds from the polluted water by a novel synthesized cobalt(II) and titanium(IV) containing photocatalyst under visible light. Environ Nanotechnol Monit Manag 14:
2. Adnan MAB, Arifin K, Minggu LJ, Kassim MB (2018) Titanate-based perovskites for photochemical and photoelectrochemical water splitting applications: a review. Int J Hydrogen Energy 43(52):23209–23220
3. Ahmad T, Farooq U, Phul R (2018) Fabrication and photocatalytic applications of perovskite materials with special emphasis on alkali-metal-based niobates and tantalates. Ind Eng Chem Res 57(1):18–41
4. Alammar T, Hamm I, Wark M, Mudring A-V (2015) Low-temperature route to metal titanate perovskite nanoparticles for photocatalytic applications. Appl Catal B 178:20–28
5. Aman D, Zaki T, Mikhail S, Selim S (2011) Synthesis of a perovskite $LaNiO_3$ nanocatalyst at a low temperature using single reverse microemulsion. Catal Today 164(1):209–213

6. Anandan S, Ohashi N, Miyauchi M (2010) ZnO-based visible-light photocatalyst: band-gap engineering and multi-electron reduction by co-catalyst. Appl Catal B Environ 100:502–509
7. Andrei V, Reuillard B, Reisner E (2020) Bias-free solar syngas production by integrating a molecular cobalt catalyst with perovskite–$BiVO_4$ tandems. Nat Mater19
8. Anzai A, Fukuo N, Yamamoto A, Yoshida H (2017) Highly selective photocatalytic reduction of carbon dioxide with water over silver-loaded calcium titanate. Catal Commun 100:134–138
9. Arun B, Akshay V, Mutta GR, Venkatesh C, Vasundhara M (2017) Mixed rare earth oxides derived from monazite sand as an inexpensive precursor material for room temperature magnetic refrigeration applications. Mater Res Bull 94:537–543
10. Asahi R, Morikawa T, Ohwaki T, Aoki K, Taga Y (2001) Visible-light photocatalysis in nitrogen-doped titanium oxides. Science 293:269–271
11. Bagvand N, Sharifnia S, Karamian E (2018) A visible-light-active $BiFeO_3$/ZnS nanocomposite for photocatalytic conversion of greenhouse gases. Korean J Chem Eng 35:1735–1740
12. Bahnemann D (2004) Photocatalytic water treatment: solar energy applications. Sol Energy 77:445–459
13. Bai S, Wang L, Li Z, Xiong Y (2017) Facet-engineered surface and interface design of photocatalytic materials. Adv Sci 4:1–26
14. Bai S, Zhang N, Gao C, Xiong Y (2018) Defect engineering in photocatalytic materials. Nano Energy 53:296–336
15. Bajorowicz B, Reszczyńska J, Lisowski W, Klimczuk T, Winiarski M, Słoma M, Zaleska-Medynska A (2015) Perovskite-type $KTaO_3$—reduced graphene oxide hybrid with improved visible light photocatalytic activity. RSC Adv 5(111):91315–91325
16. Balachandran S, Swaminathan M (2012) Facile fabrication of heterostructured $Bi2O_3$-ZnO photocatalyst and its enhanced photocatalytic activity. J Phys Chem C 116:26306–26312
17. Brenner TM, Egger DA, Kronik L, Hodes G, Cahen D (2016) Hybrid organic–inorganic perovskites: low-cost semiconductors with intriguing charge-transport properties. Nat Revi Mater 1:1–16
18. Bresolin B-M, Park Y, Bahnemann DW (2020) Recent progresses on metal halide perovskite-based material as potential photocatalyst. Catalysts 10(6):709
19. Burgess BK, Lowe DJ (1996) Mechanism of molybdenum nitrogenase. Chem Rev 96:2983–3011
20. Cao XR, Tian GH, Chen YJ, Zhou J, Zhou W, Tian CG, Fu HG (2014) Hierarchical composites of TiO_2 nanowire arrays on reduced graphene oxide nanosheets with enhanced photocatalytic hydrogen evolution performance. J Mater Chem A 2:4366–4374
21. Carrasco-Jaim OA, Mora-Hernandez J, Torres-Martínez LM, Moctezuma E (2019) A comparative study on the photocatalytic hydrogen production of $ATiO_3$ (A = Zn, Cd and Pb) perovskites and their photoelectrochemical properties. J Photochem Photobiol, A 371:98–108
22. Chai J, Shen J, Zhang X, Ng YH, Huang J, Guo W, Lin C, Lai Y (2019) Light-driven sustainable hydrogen production utilizing TiO_2 nanostructures: a review. Small Methods 3:1–24
23. Chen K, Schünemann S, Song S, Tüysüz H (2018) Structural effects on optoelectronic properties of halide perovskites. Chem Soc Rev 47:7045–7077
24. Chen S, Huang D, Xu P, Xue W, Lei L, Cheng M, Wang R, Liu X, Deng R (2020) Semiconductor-based photocatalysts for photocatalytic and photoelectrochemical water splitting: will we stop with photocorrosion? J Mater Chem A 8:2286–2322
25. Chen Z, Xing P, Chen P, Chen Q, Wang Y, Yu J, He Y (2018) Synthesis of carbon doped $KTaO_3$ and its enhanced performance in photocatalytic H_2 generation. Catal Commun 109:6–9
26. Chouhan N, Liu R-S, Zhang J (2017) Photochemical water splitting: materials and applications. CRC Press

27. Déak T, Czigány T (2009) Chemical composition and mechanical properties of basalt and glass fibers: a comparison. Text Res J 79:645–651
28. Demin A, Gorbova E, Brouzgou A, Volkov A, Tsiakaras P (2020) Sensors based on solid oxide electrolytes. Solid Oxide-Based Electrochemical Devices, pp 167–215. Elsevier
29. Ding Z, Guo S, Wu X, Fida H (2018) One-step synthesis of spherical $NaTaO_3$ and graphene spherical $NaTaO_3$ nanoparticles with enhanced photocatalytic activity for NO purification. Funct Mater Lett 11(4):1850070
30. Do JY, Im Y, Kwak BS, Park S-M, Kang M (2016) Preparation of basalt fiber@perovskite $PbTiO_3$ core-shell composites and their effects on CH_4 production from CO_2 photoreduction. Ceram Int 42:5942–5951
31. Dong W, Song B, Meng W, Zhao G, Han G (2015) A simple solvothermal process to synthesize $CaTiO_3$ microspheres and its photocatalytic properties. Appl Surf Sci 349:272–278
32. Duan Z, Zhu Y, Ren P, Jia J, Yang S, Zhao G, Xie Y, Zhang J (2018) Non-UV activated superhydrophilicity of patterned Fe-doped TiO_2 film for anti-fogging and photocatalysis. Appl Surf Sci 452:165–173
33. Dutta SK, Mehetor SK, Pradhan N (2015) Metal semiconductor heterostructures for photocatalytic conversion of light energy. J Phys Chem Lett 6:936–944
34. Edri E, Kirmayer S, Cahen D, Hodes G (2013) High open circuit voltage solar cells based on organic-inorganic lead bromide perovskite. J Phys Chem Lett 4:897–902
35. Fan H-T, Xu X-J, Ma X-K, Zhang T (2011) Preparation of $LaFeO_3$ nanofibers by electrospinning for gas sensors with fast response and recovery. Nanotechnology 22(11):
36. Feldhoff A, Arnold M, Martynczuk J, Gesing TM, Wang H (2008) The sol-gel synthesis of perovskites by an EDTA/citrate complexing method involves nanoscale solid state reactions. Solid State Sci 10(6):689–701
37. Feng Y-N, Wang H-C, Luo Y-D, Shen Y, Lin Y-H (2013) Ferromagnetic and photocatalytic behaviors observed in Ca-doped $BiFeO_3$ nanofibres. Am Inst Phy
38. Frank AJ, Willner I, Goren Z, Degani Y (1987) Improved charge separation and photosensitized H_2 evolution from water with TiO_2 particles on colloidal SiO_2 carriers. J Am Chem Soc 109:3568–3573
39. Fresno F, Jana P, Renones P, Coronado JM, Serrano DP, de la Pena O'Shea VA (2017) CO_2
40. Fu Q, Wang X, Li C, Sui Y, Han Y, Lv Z, Song B, Xu P (2016) Enhanced photocatalytic activity on polarized ferroelectric $KNbO_3$. RSC Adv 6(110):108883–108887
41. Fujiwara T, Sasahara A, Happo N, Kimura K, Hayashi K, Onishi H (2020) Single-crystal model of highly efficient water-splitting photocatalysts: a $KTaO_3$ wafer doped with calcium cations. Chem Mater 32(4):1439–1447
42. Gao C, Wang J, Xu H, Xiong Y (2017) Coordination chemistry in the design of heterogeneous photocatalysts. Chem Soc Rev 46:2799–2823
43. Gao T, Chen Z, Huang Q, Niu F, Huang X, Qin L, Huang Y (2015) A review: preparation of bismuth ferrite nanoparticles and its applications in visible-light induced photocatalyses. Rev Adv Mater Sci 40(2):97–109
44. Garba ZN, Zhou W, Zhang M, Yuan Z (2020) A review on the preparation, characterization and potential application of perovskites as adsorbents for wastewater treatment. Chemosphere 244:125474
45. García-López E, Marcì G, Megna B, Parisi F, Armelao L, Trovarelli A, Boaro M, Palmisano L (2015) $SrTiO_3$-based perovskites: preparation, characterization and photocatalytic activity in gas-solid regime under simulated solar irradiation. J Catal 321:13–22
46. Gomathi Devi L, Nithya PM (2018) Photocatalytic activity of Hemin (Fe(III) porphyrin) anchored $BaTiO_3$ under the illumination of visible light: synergetic effects of photosensitization, photo-Fenton and photocatalysis processes. Inorg Chem Front 5:127–138
47. Grabowska E (2016) Selected perovskite oxides: characterization, preparation and photocatalytic properties—a review. Appl Catal B 186:97–126

48. Guan M, Xiao C, Zhang J, Fan S, An R, Guan M, Xiao C, Zhang J, Fan S, An R et al (2013) Vacancy associates promoting solar-driven photocatalytic activity of ultrathin bismuth oxychloride nanosheets. J Am Chem Soc 135:10411–10417
49. Gundeboina R, Perala V, Muga V (2020) Perovskite material-based photocatalysts. Revolution of Perovskite, pp 251–287. Springer
50. Guo J, Liang J, Yuan X, Jiang L, Zeng G, Yu H, Zhang J (2018) Efficient visible-light driven photocatalyst, silver (meta) vanadate: synthesis, morphology and modification. Chem Eng J 352:782–802
51. Gutiérrez Seijas J, Prado-Gonjal, JS, Ávila Brande D, Terry I, Morán E, Schmidt R (2017) Microwave-assisted synthesis, microstructure, and magnetic properties of rare-earth cobaltites. Inorg Chem 56(1):627–633
52. Han X, Kuang Q, Jin M, Xie Z, Zheng L (2009) Synthesis of titania nanosheets with a high percentage of exposed (001) facets and related photocatalytic properties. J Am Chem Soc 131:3152–3153
53. He Y, Zhu Y, Wu N (2004) Synthesis of nanosized $NaTaO_3$ in low temperature and its photocatalytic performance. J Solid State Chem 177:3868–3872
54. Hong RY, Li JH, Chen LL, Liu DQ, Li HZ, Zheng Y, Ding J (2009) Synthesis, surface modification and photocatalytic property of ZnO nanoparticles. Powder Technol 189:426–432
55. Hou J, Cao S, Wu Y, Liang Fi, Ye Li, Lin Z, Sun L (2016) Perovskite-based nanocubes with simultaneously improved visible-light absorption and charge separation enabling efficient photocatalytic CO_2 reduction. Nano Energy 30:59–68
56. Huan Y, Shen H, Zhu Y, Li M, Li H, Wang Z, Hao Y, Wei T (2019) Enhanced ferro-photocatalytic performance for $ANbO_3$ (A = Na, K) nanoparticles. Math Biosci Eng 16: 4122–4134
57. Huang F, Yan A, Zhao H (2016) Influences of doping on photocatalytic properties of TiO_2 photocatalyst. In: Cao W (ed) Semiconductor photocatalysis—materials, mechanisms and applications. InTech, Rijeka
58. Huang HC, Yang C-L, Wang M-S, Ga Ma X (2019) Chalcogens doped $BaTiO_3$ for visible light photocatalytic hydrogen production from water splitting Spectrochim. Acta, Part A 208:65–72
59. Huerta-Flores AM, Sánchez-Martínez D, Hernández-Romero MDR, Zarazúa-Morín ME, Torres-Martínez LM (2019) Visible-light-driven $BaBiO_3$ perovskite photocatalysts: effect of physicochemical properties on the photoactivity towards water splitting and the removal of rhodamine B from aqueous systems. J Photochem Photobiol, A 368:70–77
60. Humera S, Sara M, Muhammad S, Muhammad Azhar K, Muhammad S, Muhammad Farooq W (2018) Rare earth substituted nanocrystalline $LaFeO_3$ perovskites and their composites with reduced graphene oxide for enhanced photocatalytic and other potential applications Mater. Res Express 5:065062
61. Im Y, Park SM, Kang M (2017) Effect of Ca/Ti ratio on the core-shell structured CaTiO Bull. Korean Chem Soc 38:397–400
62. Ishii T, Anzai A, Yamamoto A, Yoshida H (2020) Calcium zirconate photocatalyst and silver cocatalyst for reduction of carbon dioxide with water. Appl Catal B: Environ 119192
63. Iwasaki T, Shimamura Y, Makino Y, Watano S (2016) Mechanochemically assisted synthesis and visible light photocatalytic properties of lanthanum nickel oxide nanoparticles. Optik 127(20):9081–9087
64. Jaffari ZH, Lam S-M, Sin J-C, Zeng H (2019) Boosting visible light photocatalytic and antibacterial performance by decoration of silver on magnetic spindle-like bismuth ferrite. Mater Sci Semicond Process 101:103–115
65. Jamal M, Bashar M, Hasan AM, Almutairi ZA, Alharbi HF, Alharthi NH, Karim MR, Misran H, Amin N, Sopian KB (2018) Fabrication techniques and morphological analysis of perovskite absorber layer for high-efficiency perovskite solar cell: a review. Renew Sustain Energy Rev 98:469–488

66. Jayapandi S, Lakshmi D, Premkumar S, Packiyaraj P, Anitha K (2018) Augmented photocatalytic and electrochemical activities of Ag tailored $LaCoO_3$ perovskite semiconductor. Mater Lett 218:205–208
67. Jeyalakshmi V, Mahalakshmy R, Ramesh K, Rao PV, Choudary NV, Thirunavukkarasu K, Krishnamurthy KR, Viswanathan B (2018) Metal oxides as photo catalysts: modified sodium tantalate as catalyst for photo reduction of carbon dioxide. Mol Catal 451:105–113
68. Jeyalakshmi V, Tamilmani S, Mahalakshmy R, Bhyrappa P, Krishnamurthy KR, Viswanathan B (2016) Sensitization of La modified $NaTaO_3$ with cobalt tetra phenyl porphyrin for photo catalytic reduction of CO_2 by water with UV–visible light. J Mol Catal A: Chem 420:200–207
69. Jin J, Yu J, Guo D, Cui C, Ho WA (2015) Hierarchical Z-scheme CdS-WO_3 photocatalyst with enhanced CO_2 reduction activity. Small 11:5262–5271
70. Kadi MW, Mohamed RM (2019) Synthesis of $BaCeO_3$ nanoneedles and the effect of V, Ag, Au, Pt doping on the visible light hydrogen evolution in the photocatalytic water splitting reaction. J Sol-Gel Sci Technol 91(1):138–145
71. Kako T, Kikugawa N, Ye J (2008) Photocatalytic activities of $AgSbO_3$ under visible light irradiation. Catal Today 131(1–4):197–202
72. Kako T, Ye J (2010) Synergistic effect of different phase on the photocatalytic activity of visible light sensitive silver antimonates. J Mol Catal A: Chem 320(1–2):79–84
73. Kamat PV (2015) All Solution-Processed Lead Halide Perovskite-$BiVO_4$ tandem assembly for photolytic solar fuels production. J Am Chem, Soc, p 137
74. Kanhere P, Chen Z (2014) A review on visible light active perovskite-based photocatalysts. Molecules 19(12):19995–20022
75. Karamian E, Sharifnia S (2018) Enhanced visible light photocatalytic activity of $BiFeO_3$–ZnO pn heterojunction for CO_2 reduction. J Mater Sci Eng B 238–239:142–148
76. Khaliullin SM, Zhuravlev V, Bamburov V (2017) Solution-combustion synthesis of $MZrO_3$ zirconates (M = Ca, Sr, Ba) in open reactor: thermodynamic analysis and experiment. Int J Self Propag High Temp Synth 26(2):93–101
77. Khan MM, Ansari SA, Pradhan D, Ansari MO, Han DH, Lee J, Cho MH (2014) Band gap engineered TiO_2 nanoparticles for visible light induced photoelectrochemical and photocatalytic studies. J Mater Chem A 2:637–644
78. Khorrami GH, Kompany A, Zak AK (2015) Structural and optical properties of (K, Na) NbO_3 nanoparticles synthesized by a modified sol–gel method using starch media. Adv Powder Technol 26(1):113–118
79. Kong J, Yang T, Rui Z, Ji H (2019) Perovskite-based photocatalysts for organic contaminants removal: current status and future perspectives. Catal Today 327:47–63
80. Kong X, Guo Z, Zeng C, Huang J, Cao L, Li L, Yin L, Wen P, Feng Q, Xu Z (2015) Soft chemical in situ synthesis, formation mechanism and electrochemical performances of 1D bead-like $AgVO_3$ nanoarchitectures. J Mater Chem A 3(35):18127–18135
81. Konta R, Kato H, Kobayashi H, Kudo A (2003) Photophysical properties and photocatalytic activities under visible light irradiation of silver vanadates. Phys Chem Chem Phys 5 (14):3061–3065
82. Kostopoulou A, Brintakis K, Nasikas NK, Stratakis E (2019) Perovskite nanocrystals for energy conversion and storage. Nanophotonics 8(10):1607–1640
83. Kou J, Lu C, Wang J, Chen Y, Xu Z, Varma RS (2017) Selectivity enhancement in heterogeneous photocatalytic transformations. Chem Rev 117:1445–1514
84. Krukowska A, Trykowski G, Lisowski W, Klimczuk T, Winiarski MJ, Zaleska-Medynska A (2018) Monometallic nanoparticles decorated and rare earth ions doped $KTaO_3/K_2Ta_2O_6$ photocatalysts with enhanced pollutant decomposition and improved H_2 generation. J Catal 364:371–381
85. Kurumisawa Y, Higashino T, Nimura S, Tsuji Y, Iiyama H, Imahori H (2019) Renaissance of fused porphyrins: substituted methylene-bridged thiophene-fused strategy for high-performance dye-sensitized solar cells. J Am Chem Soc 141:9910–9919

86. Kusiak-Nejman E, Morawski AW (2019) TiO_2/graphene-based nanocomposites for water treatment: a brief overview of charge carrier transfer, antimicrobial and photocatalytic performance. Appl Catal B Environ 253:179–186
87. Kwak BS, Kang M (2015) Photocatalytic reduction of CO_2 with H_2O using perovskite Ca x Tiy O_3. Appl Surf Sci 337:138–144
88. Lee SH, Kim H-J, Nam JW, Jung H, Kang SK, Lee K-Y (2004) Preparation of $LaCoO_3$ with high surface area for catalytic combustion by spray-freezing/freeze-drying method. Studies in surface science and catalysis, pp 463–468. Elsevier
89. Lettmann C, Hildenbrand K, Kisch H, Macyk W, Maier WF (2001) Visible light photodegradation of 4-chlorophenol with a coke-containing titanium dioxide photocatalyst. Appl Catal B Environ 32:215–227
90. Li G, Wang W, Yang N, Zhang W (2011) Composition dependence of $AgSbO_3$/$NaNbO_3$ composite on surface photovoltaic and visible-light photocatalytic properties. Appl Phys A 103(1):251–256
91. Li G, Yang W, Gao S, Shen Q, Xue J, Chen K, Li Q (2021) Creation of rich oxygen vacancies in bismuth molybdate nanosheets to boost the photocatalytic nitrogen fixation performance under visible light illumination. Chem Eng J 404:
92. Li Y, Yao S, Wen W, Xue L, Yan Y (2010) Sol–gel combustion synthesis and visible-light-driven photocatalytic property of perovskite $LaNiO_3$. J Alloy Compd 491(1–2):560–564
93. Li Y, Zhao J, Zhang G, Zhang L, Ding S, Shang E, Xia X (2019) Visible-light-driven photocatalytic disinfection mechanism of Pb-$BiFeO_3$/rGO photocatalyst. Water Res 161:251–261
94. Li J, Xu L, Wang T, Song J, Chen J, Xue J, Dong Y (2016) 50-Fold EQE improvement up to 6.27% of solution-processed all-inorganic perovskite $CsPbBr_3$ QLEDs via surface ligand density control. Adv Mater 29
95. Liqiang J, Yichun Q, Baiqi W, Shudan L, Baojiang J, Libin Y, Wei F, Honggang F, Jiazhong S (2006) Review of photoluminescence performance of nano-sized semiconductor materials and its relationships with photocatalytic activity. Sol Energy Mater Sol Cells 90:1773–1787
96. Liu J, Chen S, Liu Q, Zhu Y, Zhang J (2013) Correlation of crystal structures and electronic structures with visible light photocatalytic properties of $NaBiO_3$. Chem Phys Lett 572:101–105
97. Liu M, Jing D, Zhou Z, Guo L (2013) Twin-induced one-dimensional homojunctions yield high quantum efficiency for solar hydrogen generation. Nat Commun 4:2278
98. Liu X, Lv J, Wang S, Li X, Lang J, Su Y, Chai Z, Wang X (2015) A novel contractive effect of $KTaO_3$ nanocrystals via La^{3+} doping and an enhanced photocatalytic performance. J Alloy Compd 622:894–901
99. Liu F, Shi R, Wang Z, Weng Y, Chen Y (2019) Direct Z-scheme hetero-phase junction of black/red phosphorus for photocatalytic water splitting. Angew Chem Int Ed 58:11791
100. Liu X, Sohlberg K (2014) Theoretical calculations on layered perovskites: implications for photocatalysis. Complex Metals 1(1):103–121
101. Liu G, Wang L, Yang HG, Cheng HM, Lu GQ (2010) Titania-based photocatalysts-crystal growth, doping and heterostructuring. J Mater Chem 20:831–843
102. Liu Y, Xiao C, Li Z, Xie Y (2016) Vacancy engineering for tuning electron and phonon structures of two-dimensional materials. Adv Energy Mater 6(23):1600436
103. Liu L, Jiang Y, Zhao H, Chen J, Cheng J, Yang K et al (2016) Engineering coexposed {001} and {101} facets in oxygen-deficient TiO_2 nanocrystals for enhanced CO_2 photoreduction under visible light. ACS Catal 6(2):1097–1108
104. Low J, Yu J, Jaroniec M, Wageh S, Al-Ghamdi AA (2017) Heterojunction photocatalysts. Adv Mater 29(20):1601694
105. Lu L, Ni S, Liu G, Xu X (2017) Structural dependence of photocatalytic hydrogen production over La/Cr co-doped perovskite compound $ATiO_3$ (A = Ca, Sr and Ba). Int J Hydrogen Energy 42:23539–23547

106. Luo J (2014) Water photolysis at 12.3% efficiency via perovskite photovoltaics and Earth-abundant catalysts. Science 345:1593–1596
107. Luo C, Zhao J, Li Y, Zhao W, Zeng Y, Wang C (2018) Photocatalytic CO_2 reduction over $SrTiO_3$: correlation between surface structure and activity. Appl Surf Sci 447:627–635
108. Ly T, Wen J, Marks LD (2018) Kinetic growth regimes of hydrothermally synthesized potassium tantalate nanoparticles. Nano Lett 18:5186–5191
109. Maeda K (2014) Rhodium-doped barium titanate perovskite as a stable p-type semiconductor photocatalyst for hydrogen evolution under visible light. ACS Appl Mater Interfaces 6(3):2167–2173
110. Mai L, Xu L, Gao Q, Han C, Hu B, Pi Y (2010) Single β-$AgVO_3$ nanowire H_2S sensor. Nano Lett 10(7):2604–2608
111. Marschall R, Wang L (2014) Non-metal doping of transition metal oxides for visible-light photocatalysis. Catal Today 225:111–135
112. Mashuri SIS, Ibrahim ML, Kasim MF, Mastuli MS, Rashid U, Abdullah AH, Islam A, Asikin-Mijan N, Tan YH, Mansir N, Kaus NHM, Hin T-YY (2020) Photocatalysis for organic wastewater treatment: from the basis to current challenges for society. Catalysts 10 (11):1260
113. Mathies F, Unger E, Universität H, Physik I, Chemie I, Adlershof I, Zentrum H, Straße BT (2020) Advances in inkjet-printed metal-halide perovskitephotovoltaic and optoelectronic devices florian. Energy Technol 8
114. Matsuoka M, Kitano M, Takeuchi M, Tsujimaru K, Anpo M, Thomas JM (2007) Photocatalysis for new energy production recent advances in photocatalytic water splitting reactions for hydrogen production. Catal Today 122:51–61
115. Michel CR, Lopez-Alvarez MA, Martínez-Preciado AH, Carbajal-Arízaga GG (2019) Novel UV sensing and photocatalytic properties of $DyCoO_3$. J Sens 2019
116. Min KS, Kumar RS, Lee JH, Kim KS, Lee SG, Son YA (2019) Synthesis of new TiO_2/porphyrin-based composites and photocatalytic studies on methylene blue degradation. Dyes Pigm 160:37–47
117. Moniruddin M, Afroz K, Shabdan Y, Bizri B, Nuraje N (2017) Hierarchically 3D assembled strontium titanate nanomaterials for water splitting application. Appl Surf Sci 419:886–892
118. Moniruddin M, Ilyassov B, Zhao X, Smith E, Serikov T, Ibrayev N, Asmatulu R, Nuraje N (2018) Recent progress on perovskite materials in photovoltaic and water splitting applications. Mater Today Energy 7:246–259
119. Nundy S, Ghosh A, Mallick TK (2020) Hydrophilic and superhydrophilic self-cleaning coatings by morphologically varying ZnO microstructures for photovoltaic and glazing applications. OCS Omega 5:1033–1039
120. Nuraje N, Asmatulu R, Kudaibergenov S (2012) Metal oxide-based functional materials for solar energy conversion: a review. Curr Inorg Chem 2(2):124–146
121. Ola O, Maroto-Valer MM (2015) Review of material design and reactor engineering on TiO_2 photocatalysis for CO_2 reduction. J Photochem Photobiol C Photochem Rev 24:16–42
122. Onishi H (2019) Sodium tantalate photocatalysts doped with metal cations: why are they active for water splitting? Chemsuschem 12(9):1825–1834
123. Ou Q, Bao X, Zhang Y, Shao H, Xing G, Li X (2019) Band structure engineering in metal halide perovskite nanostructures for optoelectronic applications. Nano Mater Sci 1:268–287
124. Paramanik L, Reddy KH, Sultana S, Parida K (2018) Architecture of biperovskite-based $LaCrO_3$/$PbTiO_3$ p–n heterojunction with a strong interface for enhanced charge anti-recombination process and visible light-induced photocatalytic reactions. Inorg Chem 57(24):15133–15148
125. Paramanik L, Parida K (2020) Efficient perovskite titanate photocatalysts for oxygen evolution reactions. Mater Today: Proc
126. Park S, Chang WJ, Lee CW, Park S, Ahn HY, Nam KT (2017) Photocatalytic hydrogen generation from hydriodic acid using methylammonium lead iodide in dynamic equilibrium with aqueous solution. Nat Energy 2:1–8

127. Park B, Philippe B, Zhang X, Rensmo H, Boschloo G, Johansson EMJ (2015) Bismuth based hybrid perovskites $A_3Bi_2I_9$ (a: methylammonium or cesium) for solar cell application. Adv Mater 27:6806–6813
128. Ran C, Xu J, Gao W, Huang C, Dou S (2018) Defects in metal triiodide perovskite materials towards high-performance solar cells: origin, impact, characterization, and engineering. Chem Soc Rev 47:4581–4610
129. Rao MP, Nandhini VP, Wu JJ, Syed A, Ameen F, Anandan S (2018) Synthesis of N-doped potassium tantalate perovskite material for environmental applications. J Solid State Chem 258:647–655
130. Ren Z, Wang N, Wei P, Cui M, Li X, Qin C (2020) Ultraviolet-ozone modification on TiO_2 surface to promote both efficiency and stability of low-temperature planar perovskite solar cells. Chem Eng J 393:124731
131. Ren P, Song M, Lee J, Zheng J, Li D (2019) Edge dislocations induce improved photocatalytic efficiency of colored TiO_2. Adv Mater Inter 1901121
132. Rokesh K, Sakar M, Do TO (2020) Calcium bismuthate ($CaBiO_3$): a potential sunlight-driven perovskite photocatalyst for the degradation of emerging pharmaceutical contaminants. ChemPhotoChem
133. Roy P, Sinha NK, Tiwari T, Khare A (2020) A review on perovskite solar cells: evolution of architecture, fabrication techniques, commercialization issues and status. Sol Energy 198:665–668
134. Ruzimuradov O, Hojamberdiev M, Fasel C, Riedel R (2017) Fabrication of lanthanum and nitrogen—Co-doped $SrTiO_3$–TiO_2 heterostructured macroporous monolithic materials for photocatalytic degradation of organic dyes under visible light. J Alloys Compd 699:144–150
135. Safari S, Ahmadian SMS, Amani-Ghadim AR (2020) Visible light photocatalytic activity enhancing of $MTiO_3$ perovskites by M cation (M = Co, Cu, and Ni) substitution and Gadolinium doping. J Photochem Photobiol, A 394:112461
136. Samsudin EM, Abd Hamid SB (2017) Effect of band gap engineering in anionic-doped TiO_2 photocatalyst. Appl Surf Sci 391:326–336
137. Satar NSA, Adnan R, Lee HL, Hall SR, Kobayashi T, Kassim MHM, Kaus NHM (2019) Facile green synthesis of ytrium-doped $BiFeO_3$ with highly efficient photocatalytic degradation towards methylene blue. Ceram Int 45(13):15964–15973
138. Satar NSA, Aziz AW, Yaakob MK, Yahya MZA, OH Hassan OH, Kudin TIT, Mohd Kaus NH (2016) Experimental and first-principles investigations of lattice strain effect on electronic and optical properties of biotemplated $BiFeO_3$ nanoparticles. J Phys Chem C 120 (45):26012–26020
139. Schmidt R, Prado-Gonjal J, Ávila D, Amador U, Morán E (2014) Electron microscopy of microwave-synthesized rare-earth chromites. arXiv:14095607
140. Shamblin J, Heres M, Zhou H, Sangoro J, Lang M, Neuefeind J, Alonso J, Johnston S (2018) Experimental evidence for bipolaron condensation as a mechanism for the metal-insulator transition in rare-earth nickelates. Nat Commun 9(1):1–7
141. Shi Z, Guo J, Chen Y, Li Q, Pan Y, Zhang H, Xia Y, Huang W (2017) Lead-free organic–inorganic hybrid perovskites for photovoltaic applications: recent advances and perspectives. Adv Mater 29(16):1605005
142. Shi H, Wang T, Chen J, Zhu C, Ye J, Zou Z (2011) Photoreduction of carbon dioxide over $NaNbO_3$ nanostructured photocatalysts. Catal Lett 141(4):525–530
143. Shi R, Waterhouse GI, Zhang T (2017) Recent progress in photocatalytic CO_2 reduction over perovskite oxides. Solar Rrl 1(11):1700126
144. Shi R, Zhao Y, Waterhouse G, Zhang S, Zhang T (2019) Defect engineering in photocatalytic nitrogen fixation. ACS Catal 9:9739–9750
145. Shi H, Fan J, Zhao Y, Hu X, Zhang X, Tang Z (2020) Visible light driven $CuBi_2O_4$/Bi_2MoO_6 p-n heterojunction with enhanced photocatalytic inactivation of *E. coli* and mechanism insight. J Hazard Mater 381:121006
146. Shintaro I, Namhoon K, Elif E, Sakae T, Tatsumi I (2015) Photocatalytic reaction centers in two-dimensional titanium oxide crystals. J Am Chem Soc 137:239

147. Si H, Liao Q, Zhang Z, Li Y, Yang X, Zhang G, Kang Z, Zhang Y (2016) An innovative design of perovskite solar cells with Al_2O_3 inserting at ZnO/perovskite interface for improving the performance and stability. Nano Energy 22:223–231
148. Singh J, Uma S (2009) Efficient photocatalytic degradation of organic compounds by ilmenite $AgSbO_3$ under visible and UV light irradiation. J Phys Chem C 113(28):12483–12488
149. Situmeang RTM (2019) Pectins as emulsifying agent on the preparation, characterization, and photocatalysis of nano-$LaCrO_3$. Pectins-extraction, purification, characterization and applications. IntechOpen
150. Sivakumar V, Suresh R, Giribabu K, Narayanan V (2015) $AgVO_3$ nanorods: synthesis, characterization and visible light photocatalytic activity. Solid State Sci 39:34–39
151. Su T-M, Qin Z-Z, Ji H-B, Jiang Y-X, Huang G (2016) Recent advances in the photocatalytic reduction of carbon dioxide. Environ Chem Lett 14(1):99–112
152. Suk J, Gyu H, Sung J (2012) Heterojunction semiconductors: a strategy to develop efficient photocatalytic materials for visible light water splitting. Catal Today 185:270–277
153. Sun J, Chen G, Li Y, Jin R, Wang Q, Pei J (2011) Novel (Na, K) TaO_3 single crystal nanocubes: molten salt synthesis, invariable energy level doping and excellent photocatalytic performance. Energy Environ Sci 4(10):4052–4060
154. Sun WJ, Li J, Mele G, Zhang ZQ, Zhang FX (2013) Enhanced photocatalytic degradation of rhodamine B by surface modification of ZnO with copper (II) porphyrin under both UV–vis and visible light irradiation. J Mol Catal A: Chem 366:84–91
155. Sun L, Li R, Zhan W, Wang F, Zhuang Y, Wang X, Han X (2019) Rationally designed double-shell dodecahedral microreactors with efficient photoelectron transfer: N-Doped-C-Encapsulated ultrafine In_2O_3 nanoparticles. Chem A Eur J 25:3053–3060
156. Tachikawa T, Tojo S, Kawai K, Endo M, Fujitsuka M, Ohno T, Nishijima K, Miyamoto Z, Majima T (2004) Photocatalytic oxidation reactivity of holes in the sulfur- and carbon-doped TiO_2 powders studied by time-resolved di use reflectance spectroscopy. J Phys Chem B 108:19299–19306
157. Takagi K, Makimoto T, Hiraiwa H, Negishi T (2001) Photocatalytic, antifogging mirror. J Vac Sci Technol, A 19:2931
158. Takata Y, Hidaka S, Cao JM, Nakamura T, Yamamoto H, Masuda M, Ito T (2005) Effect of surface wettability on boiling and evaporation. Energy 30:209–220
159. Takei T, Haramoto R, Dong Q, Kumada N, Yonesaki Y, Kinomura N, Mano T, Nishimoto S, Kameshima Y, Miyake M (2011) Photocatalytic activities of various pentavalent bismuthates under visible light irradiation. J Solid State Chem 184(8):2017–2022
160. Tan Y, Shu Z, Zhou J, Li T, Wang W, Zhao Z (2018) One-step synthesis of nanostructured g-C_3N_4/TiO_2 composite for highly enhanced visible-light photocatalytic H_2 evolution. Appl Catal B 230:260–268
161. Tanaka H, Misono M (2001) Advances in designing perovskite catalysts. Curr Opin Solid State Mater Sci 5(5):381–387
162. Tang P, Tong Y, Chen H, Cao F, Pan G (2013) Microwave-assisted synthesis of nanoparticulate perovskite $LaFeO_3$ as a high active visible-light photocatalyst. Curr Appl Phys 13(2):340–343
163. Taylor P, Yunus IS, Kurniawan A, Adityawarman D, Indarto A (2012) Nanotechnologies in water and air pollution treatment. Environ Technol Rev 1:136–148
164. Teh YW, Chee MK, Kong XY, Yong S-T, Chai S-P (2020) An insight into perovskite-based photocatalysts for artificial photosynthesis. Sustain Energy Fuels 4(3):973–984
165. Teramura K, Okuoka S-I, Tsuneoka H, Shishido T, Tanaka T (2010) Photocatalytic reduction of CO_2 using H_2 as reductant over $ATaO_3$ photocatalysts (A = Li, Na, K). Appl Catal B 96:565–568
166. Terranova U, Viñes F, de Leeuw NH, Illas F (2020) Mechanisms of carbon dioxide reduction on strontium titanate perovskites. J Mater Chem A 8(18):9392–9398

167. Vidal K, Morán-Ruiz A, Larrañaga A, Porras-Vázquez J, Slater P, Arriortua M (2015) Characterization of LaNi0. 6Fe0. 4O3 perovskite synthesized by glycine-nitrate combustion method. Solid State Ionics 269:24–29
168. Wang X, Bai L, Liu H, Yu X, Yin Y, Gao CA (2018) Unique disintegration-reassembly route to mesoporous titania nanocrystalline hollow spheres with enhanced photocatalytic activity. Adv Funct Mater 28:1–8
169. Wang Y, Cheng H-P (2013) Oxygen reduction activity on perovskite oxide surfaces: a comparative first-principles study of $LaMnO_3$, $LaFeO_3$, and $LaCrO_3$. J Phys Chem C 117 (5):2106–2112
170. Wang F, DiValentin C, Pacchioni G (2012) Rational band gap engineering of WO_3 photocatalyst for visible light water splitting. Chem Cat Chem 4:476–478
171. Wang S, Hai X, Ding X, Chang K, Xiang Y, Meng X, Yang Z, Chen H, Ye J (2017) Light-switchable oxygen vacancies in ultrafine Bi_5O_7Br nanotubes for boosting solar-driven nitrogen fixation in pure water. Adv Mater 29:1701774
172. Wang F, He X, Sun L, Chen J, Wang X, Xu J, Han X (2018) Engineering an N-doped TiO_2@N-doped C butterfly-like nanostructure with long-lived photo-generated carriers for efficient photocatalytic selective amine oxidation. J Mater Chem A 6:2091–2099
173. Wang N, Kong D, He H (2011) Solvothermal synthesis of strontium titanate nanocrystallines from metatitanic acid and photocatalytic activities. Powder Technol 207(1–3):470–473
174. Wang R, Ni S, Liu G, Xu X (2018) Hollow $CaTiO_3$ cubes modified by La/Cr co-doping for efficient photocatalytic hydrogen production. Appl Catal B 225:139–147
175. Wang Z, Su B, Xu J, Hou Y, Ding Z (2020) Direct Z-scheme $ZnIn_2S4/LaNiO_3$ nanohybrid with enhanced photocatalytic performance for H_2 evolution. Int J Hydrogen Energy 45 (7):4113–4121
176. Wang H, Yuan X, Wu Y, Zeng G, Tu W, Sheng C, Deng Y, Chen F, Chew JW (2017) Plasmonic Bi nanoparticles and BiOCl sheets as cocatalyst deposited on perovskite-type $ZnSn(OH)_6$ microparticle with facet-oriented polyhedron for improved visible-light-driven photocatalysis. Appl Catal B 209:543–553
177. Wang F, Zhang J, Yuan P, Yan Q, Zhang P (2000) Magnetic and transport properties of vanadate $PrVO_3$. J Phys: Condens Matter 12(13):3037
178. Wei S, Xu X (2018) Boosting photocatalytic water oxidation reactions over strontium tantalum oxynitride by structural laminations. Appl Catal B 228:10–18
179. Weng D, Lei C, Wu TT, Sun R, Shen M, Lu Y (2015) Spontaneous and continuous anti-virus disinfection from nonstoichiometric perovskite-type lanthanum manganese oxide. Prog Nat Sci 25(3):191–196
180. Wu X, Wang C, Wei Y, Xiong J, Zhao Y, Zhao Z, Liu J, Li J (2019) Multifunctional photocatalysts of Pt-decorated 3DOM perovskite-type $SrTiO_3$ with enhanced CO_2 adsorption and photoelectron enrichment for selective CO_2 reduction with H_2O to CH_4. J Catal 377:309–321
181. Xie K, Umezawa N, Zhang N, Reunchan P, Zhang Y, Ye J (2011) Self-doped $SrTiO_3–\delta$ photocatalyst with enhanced activity for artificial photosynthesis under visible light. Energy Environ Sci 4:4211–4219
182. Xu J, Hu C, Xi Y, Wan B, Zhang C, Zhang Y (2012) Synthesis and visible light photocatalytic activity of β-$AgVO_3$ nanowires. Solid State Sci 14(4):535–539
183. Xu C, Ravi Anusuyadevi P, Aymonier C, Luque R, Marre S (2019) Nanostructured materials for photocatalysis. Chem Soc Rev 48:3868–3902
184. Xu D, Shi W, Song C, Chen M, Yang S, Fan W, Chen B (2016) In-situ synthesis and enhanced photocatalytic activity of visible-light-driven plasmonic $Ag/AgCl/NaTaO_3$ nanocubes photocatalysts. Appl Catal B 191:228–234
185. Yan Y, Gu J, Zeitler EL, Bocarsly AB (2015) Photoelectrocatalytic reduction of carbon dioxide. In: Peter S, Elsje AQ, Katy A (eds) Carbon dioxide utilisation. Elsevier, Oxford, pp 211–233

186. Yang Y, Kang L, Li H (2019) Enhancement of photocatalytic hydrogen production of $BiFeO_3$ by Gd^{3+} doping. Ceram Int 45:8017–8022
187. Yao J-S, Ge J, Han B-N, Wang K-H, Yao H-B, Yu H-L, Li J-H, Zhu B-S, Song J-Z, Chen C (2018) Ce^{3+} -doping to modulate photoluminescence kinetics for efficient $CsPbBr_3$ nanocrystals based light-emitting diodes. J Am Chem Soc 140(10):3626–3634
188. Yao S, Zheng R, Li R, Chen Y, Zhou X, Luo J (2019) Construction of Z-scheme $LaNiO_3$/SnS_2 composite for boosting visible light photodegradation of tetracycline. J Taiwan Inst Chem Eng 100:186–193
189. Yu ZB, Xie YP, Liu G, Lu GQ, Ma XL, Cheng HM (2013) Self-assembled CdS/Au/ZnO heterostructure induced by surface polar charges for efficient photocatalytic hydrogen evolution. J Mater Chem A 1:2773–2776
190. Yu J, Low J, Xiao W, Zhou P, Jaroniec, M (2014) Enhanced photocatalytic CO_2-reduction activity of anatase TiO_2 by coexposed {001} and {101} facets. J Am Chem Soc 136 (25):8839–8842. https://doi.org/10.1021/ja5044787
191. Zeng Z, Xu Y, Zhang Z, Gao Z, Luo M, Yin Z, Zhang C, Xu J, Huang B, Luo F (2020) Rare-earth-containing perovskite nanomaterials: design, synthesis, properties and applications. Chem Soc Rev 49(4):1109–1143
192. Zhang N, Gao C, Xiong Y (2019) Defect engineering: a versatile tool for tuning the activation of key molecules in photocatalytic reactions. J Energy Chem 37:43
193. Zhang G, Liu G, Wang L, Irvine JTS (2016) Inorganic perovskite photocatalysts for solar energy utilization. Chem Soc Rev 45:5951–5984
194. Zhang G, Liu G, Wang L, Irvine JT (2016) Inorganic perovskite photocatalysts for solar energy utilization. Chem Soc Rev 45(21):5951–5984
195. Zhang G, Sewell CD, Zhang P, Mi H, Lin Z (2020) Nanostructured photocatalysts for nitrogen fixation. Nano Energy 71:104645
196. Zhang J, Wang A, Zhao W, Li C, Chen X, Wang Y, Zhu W, Zhong Q (2018) Influence of metal-porphyrins on the photocatalysis of graphitic carbon nitride. Dyes Pigm 153:241–247
197. Zhang H, Zhang X, Yang G, Zhou X (2018) Point defect effects on photoelectronic properties of the potential metal-free C2N photocatalysts: insight from first-principles computations. J Phys Chem C 122:5291–5302
198. Zhang S, Zhao Y, Shi R, Waterhouse G, Zhang T (2019) Photocatalytic ammonia synthesis: recent progress and future. Energy Chem 1:100013
199. Zheng Z, Huang B, Lu J, Wang Z, Qin X, Zhang X, Dai Y, Whangbo MH (2012) Hydrogenated titania: synergy of surface modification and morphology improvement for enhanced photocatalytic activity. Chem Commun 48:5733–5735
200. Zheng Z, Huang B, Qin X, Zhang X, Dai Y (2011) Facile synthesis of $SrTiO_3$ hollow microspheres built as assembly of nanocubes and their associated photocatalytic activity. J Colloid Interface Sci 358(1):68–72
201. Zhong F, Zhuang H, Gu Q, Long J (2016) Structural evolution of alkaline earth metal stannates $MSnO_3$ (M = Ca, Sr, and Ba) photocatalysts for hydrogen production. RSC Adv 6 (48):42474–42481
202. Zhong D, Liu W, Tan P, Zhu A, Liu Y, Xiong X, Pan J (2018) Insights into the synergy effect of anisotropic {001} and {230}facets of $BaTiO_3$ nanocubes sensitized with CdSe quantum dots for photocatalytic water reduction. Appl Catal B 227:1–12
203. Zhou H, Guo J, Li P, Fan T, Zhang D, Ye J (2013) Leaf-architectured 3D hierarchical artificial photosynthetic system of perovskite titanates towards CO_2 photoreduction into hydrocarbon fuels. Sci Rep 3:1667
204. Zhou W-L, Zhao Z-Y (2016) Electronic structures of efficient $MBiO_3$ (M = Li, Na, K, Ag) photocatalyst. Chin Phys B 25(3):037102
205. Zhou D, Zhou T, Tian Y, Zhu X, Tu Y (2018) Perovskite-based solar cells: materials, methods, and future perspectives. J Nanomater 1–12
206. Zhu L, Shao Z, Ye J, Zhang X, Pan X, Dai S (2016) Mesoporous $BaSnO_3$ layer based perovskite solar cells. Chem Commun 52(5):970–973

207. Zhu Y, Zhou W, Shao Z (2017) Perovskite/carbon composites: applications in oxygen electrocatalysis. Small 13(12):1603793

208. Zlotnik S, Tobaldi DM, Seabra P, Labrincha JA, Vilarinho PM (2016) Alkali niobate and tantalate perovskites as alternative photocatalysts. Chem Phys

Chapter 14
Advanced Laser Methods for Synthesizing Photocatalysts

Florin Andrei, Athanasios Tiliakos, Monica Scarisoreanu,
and Nicu D. Scarisoreanu

Abstract The global demand for energy is steadily increasing in the past decades, leading to a rise of the uses of conventional energy sources which are causing serious environmental problems such as the greenhouse effect and pollution of the water and air supplies. Therefore, numerous alternatives to minimize the impact of environmental pollution have been tracking down and developed. In the quest for sustainable growth in all fields of human activity, the water and air purification by efficient catalysts which can be activated by natural sunlight is now a primary goal of the worldwide research activity. Employing laser-based methods such as laser pyrolysis (LP) or pulsed laser deposition (PLD) to obtain new or modified photocatalysts can contribute to these efforts, due to the fact that the native advantages of these techniques allow the use of several efficient strategies (sensitization, structural strain engineering, metal/non-metal doping) to enhance photocatalytic activity of different materials. In this chapter, the laser processing techniques advantages are presented through the functional property's enhancement of different photoactive materials such as complex stoichiometry inorganic perovskites ($BiFeO_3$-based materials) or binary oxides (TiO_2, WO_3, ZnO). The tuning process of the photocatalysts active in visible light for complete degradation of the persistent organic pollutant or the effect of the structural strain on the photoelectrochemical water splitting performance is detailed for both laser pyrolysis (LP) or pulsed laser deposition (PLD) produced oxide nanomaterials.

F. Andrei · A. Tiliakos · M. Scarisoreanu · N. D. Scarisoreanu (✉)
National R&D Institute for Lasers, Plasma and Radiation Physics (INFLPR), 409 Atomistilor Street, P.O. Box MG-36, 077125 Măgurele, Ilfov, Romania
e-mail: nicu.scarisoreanu@inflpr.ro

A. Tiliakos
National R&D Institute for Cryogenic and Isotopic Technologies (ICSI), 4 Uzinei Street, Râmnicu Vâlcea, P.O. Râureni, P.O. Box 7, 240050 Vâlcea, Romania

F. Andrei
Laboratory of Chemical Technology and Catalysis, Department of Organic Chemistry, Biochemistry and Catalysis, Faculty of Chemistry, University of Bucharest, 4-12, Blv. Regina Elisabeta, 030018 Bucharest, Romania

S. Garg and A. Chandra (eds.), *Green Photocatalytic Semiconductors*,
Green Chemistry and Sustainable Technology,
https://doi.org/10.1007/978-3-030-77371-7_14

Keywords Environmental pollution · Laser pyrolysis (LP) · Pulsed laser deposition (PLD) · Inorganic perovskites ($BiFeO_3$-based materials) · Binary oxides (TiO_2, WO_3, ZnO)

14.1 Introduction

Photocatalysis is an advanced oxidation process with a vast potential in contributing to the solution of energy generation and environmental pollution problems. The photocatalytic process is based on harvesting of sunlight—probably the cleanest and most sustainable of the available energy sources—and its conversion to chemical energy. Photocatalytic materials, generally referred to as photocatalysts, are typically semiconductors capable of absorbing photons of energy at least equal to the band gap (E_g) of the respective material. As an effect of the absorption process, electrons (e^-) from the valence band (VB) are promoted to the conduction band (CB), leaving behind positive holes (h^+). These photogenerated charge carriers migrate towards the surface of the material where the chemical reaction takes place. Depending on the reaction type, the photocatalytic mechanism is different. For example, in the case of photocatalytic water splitting, water reduction is a two-electron transfer process ($2H_2O + 2e^- \rightleftarrows H_2 + 2HO^-$), while the transfer of four electrons is required for water oxidation ($2H_2O \rightleftarrows 4e^- + O_2 + 4H^+$) [1–3]. From the thermodynamical point of view, water decomposition into H_2 and O_2 is a non-spontaneous reaction requiring an excess of energy (theoretical value of 1.23 eV per electron transfer) to take place. However, in practice, it was observed that an even higher energy is necessary for the reaction to occur, in order to avoid energy losses associated with charge carrier transfer and recombination, as well as induced kinetic losses [4, 5]. A schematic representation of the photocatalytic water splitting process is presented in Fig. 14.1.

The photodegradation of pollutants in aqueous solution can be viewed similarly to the water splitting process. Photogenerated electrons react with the adsorbed oxygen molecules on the photocatalyst surface, leading to the formation of highly reactive radicals (dioxide radical and its protonated hydroperoxyl form: O_2^- ($O_2^\bullet$), HO_2 ($HOO^\bullet$), respectively); then, positive holes react with the adsorbed water molecules and hydroxyl radicals ($^\bullet OH$) are formed. All these produced radicals interact with the pollutants, oxidizing them to other less toxic or non-toxic compounds, like CO_2 and H_2O [6].

Perhaps the most widely used photocatalyst, titanium dioxide (TiO_2), a semiconductor which is activated by light, can either mineralize organic molecules or oxidize inorganics in the presence of water and oxygen, thus helping to alleviate environmental pollution [7–22].

The electromagnetic spectrum corresponding to sunlight extends over a wide range of wavelengths, from the ultraviolet (UV) at 250 nm to the infrared (IR) at 2500 nm, equivalent to an energy range starting from 4.9 to 0.5 eV, respectively. It is comprised mainly from IR (ca. 49.4%) and visible (ca. 42.3%) radiation, with the

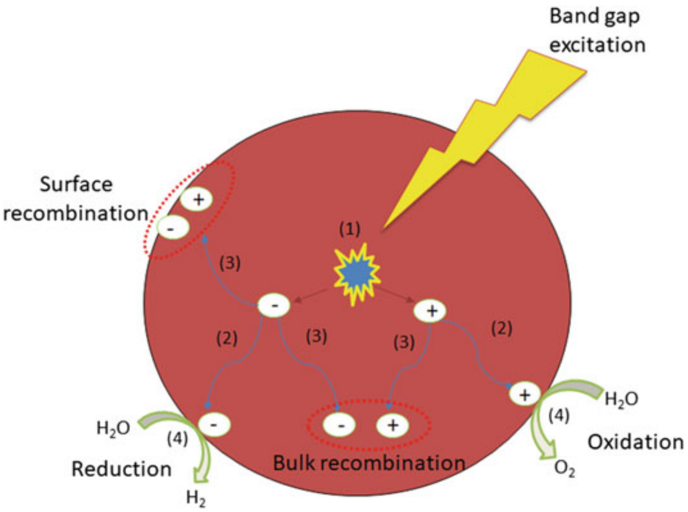

Fig. 14.1 Photocatalytic water splitting process

UV part corresponding to only a small portion (ca. 8%) [23]. Thus, for efficient photocatalysis by sunlight, it is recommended to employ semiconductors with band gap values between 2.0 and 2.2 eV, with the positions of band maxima being a crucial factor for the efficiency of the process [4].

Although photocatalysis poses as a highly efficient process, there can still be issues concerning photocatalytic materials, with the most common of them being related to [24]:

- overly high band gap values;
- short lifetime of the photogenerated charge carriers and their rapid recombination;
- photo-corrosive effects.

In general, photocatalytic activity can be enhanced by increasing the absorbance of sunlight by the photocatalyst and by limiting the recombination rate of free charge carriers. Several efficient strategies to enhance photocatalytic activity are listed below [25, 26]:

- sensitization;
- photoelectrochemical (PEC) enhancement;
- oxygen vacancies and structural strain engineering;
- metal and/or non-metal doping;
- stratified photocatalysts;
- morphological optimization.

Nanoparticle properties (phase composition and morphology, particle size distribution and shape, porosity distribution) are determined by the employed synthesis method. There have been several conventional methods for synthesizing TiO_2: sol–gel [8, 15, 27], hydrothermal [11, 18], chemical vapour deposition (CVD) [28] and combustion flame [29]. To these, advanced laser-based methods have been added offering greater versatility: pulsed laser deposition (PLD) [12], matrix-assisted pulsed laser evaporation (MAPLE) [30] and laser pyrolysis (LP)/laser-induced chemical vapour deposition (LCVD) [31–49]. Especially the latter laser methods offer the possibility of synthesizing a wide range of nanomaterials: TiO_2 and TiC; SnO and SnO_2; ZnO; Fe and Fe_2O_3; as well as Fe coated in polymer nanotubes, carbon nanotubes (CNTs), or turbostratic carbon). The major advantage of laser pyrolytic methods is that the process of doping is performed in a single step, within the main LP reactor during synthesis (Fig. 14.6).

14.1.1 Simple Metal Oxides Photocatalysts Prepared by Conventional Methods

14.1.1.1 Titanium Oxide (TiO_2)

The photoelectrochemical activity of TiO_2 photoanode was discovered in 1972 by Fujishima et al. They have tested a n-type TiO_2 semiconductor for the water photodecomposition reaction under UV irradiation [50]. Additionally to the photocatalysis, in a photoelectrochemical process, the redox reactions take place at different materials surface. For example, the water oxidation occurs at the anode (e.g. TiO_2), while the hydrogen is formed at the cathode surface (e.g. Pt wire). In order to improve the free charge carriers separation, an external electrical bias can be applied [51]. Since then, TiO_2 has become one of the most studied photocatalyst due to its high resistance to chemical and photocorossion, non-toxicity and high activity. Under UV light irradiation photoanodes based on TiO_2 show excellent results with the photocurrent value of 2.5 mA/cm^2 at 1.23 V versus RHE. The Incident-Photo-to-Current-Efficiency (IPCE) in the UV region is ~95%, but it is almost 0 under visible light irradiation, because TiO_2 has typically a large band gap of ca. 3.0–3.2 eV. A small value of the onset potential (0.1 V vs. RHE) was reported for this type of photocatalyst. The onset potential can be defined as the potential where the photocurrent starts to increase. The Solar-to-Hydrogen (STH) conversion efficiency is ~1.63% with a measured volume of mixed gas (H_2 and O_2) of ~0.47 mL/h. The photocatalyst still shows high stability after 16 h of reaction [52]. The addition of Si to TiO_2 and the decreasing of pH value are lowering the photocurrent density. The IPCE under Vis irradiation is still under 1%. Also, the onset potential increases around 3 times leading to a higher energy consumption.

One way to improve the absorption properties under visible radiation is to use a dye-sensitizer. A detailed studied was recently published by Wang et al. concerning the dye-sensitizer TiO_2 effect. They have used an anthraquinone dye to harvest the visible light on the surface of TiO_2 semiconductor and 2,2,6,6-tetramethylpiperidin-1-yl)oxyl for oxidative transformation. They have successfully tested the prepared photocatalyst under visible irradiation for oxidation of amines to imines with both high selectivities (up to 97%) and conversions (up to 98%) [53]. Choi et al. have reported photocatalysts based on organic dye-sensitized TiO_2 for solar hydrogen production and photodegradation of different organic pollutants under visible radiation. They have used several branched organic dyes with numerous carboxylate anchoring groups for light harvesting and triethanolamine and ethylenediaminetetra-acetic acid as electrons donor [54].

A detailed study concerning the doping of TiO_2 photocatalysts was recently reported by Khlyustova et al. They have demonstrated that by integrating different dopants into the TiO_2 structure the photocatalytic activity can be rigorously improved. For example, when using Al and Cu as dopants, the photocatalytic activity is increased up to 70%, while for Mo and W dopants it increases to 96% [55]. Also, other studies related to C-doped TiO_2 [56, 57], S-doped TiO_2 [58, 59] and N-doped TiO_2 [60, 61] with smaller band gap values than pristine TiO_2 are reported in literature.

14.1.1.2 Zinc Oxide (ZnO)

ZnO is a widely used photocatalyst, its physical and chemical properties, as well as band gap value being similar to the TiO_2 semiconductor. Lu et al. have reported a micro/nanoarchitecture prepared by solvothermal method with excellent photodegradation efficiency of methyl orange under UV radiation. The high photocatalytic efficiency was correlated to the high specific surface area of ZnO semiconductor (>180 m^2/g) and stability against particles aggregation [62]. Numerous studies concerning the morphology of ZnO semiconductor are reported in literature and its effect on the photodegradation of different organic dyes (e.g.: rhodamine B, methylene blue) are detailed [63, 64]. One way to improve the photocatalytic activity of ZnO is by combining with CdS. Bulk CdS has a band gap value of 2.4 eV at room temperature and it possesses higher affinity for electrons than ZnO. By irradiating the ZnO/CdS composite, electrons from the VB of CdS are expelled into its CB. After ca. 18 picoseconds the electrons found in the CB of CdS are transferred to the CB of ZnO. This process can further improve the photocatalytic activity [65]. Also, the doping of ZnO is an effective way to lower the band gap value and to improve the separation of the free charge carriers leading to an enhanced photocatalytic activity. Numerous dopants, both metallic and non-metallic are integrated in the ZnO structure increasing the global efficiency of the photocatalytic process [66].

14.1.1.3 Tungsten Trioxide (WO_3)

WO_3 is a suitable n-type semiconductor used for the photocatalytic applications. Although it has the capability to absorb approximately 12% of the solar light with a band gap energy value of about 2.5–2.8 eV, it presents several limitations which influence the generation and separation of free charge carriers, as well as their transport to the photocatalytic reaction process. An impressive number of dopants were used to modify the physico-chemical properties of WO_3 in order to improve its photocatalytic activity [67]. For example, it was demonstrated that by doping WO_3 with Fe^{3+} the separation of charge carriers is improved as well as the stability of the material. Further loading of Fe-doped WO_3 with Pt leads to a photocatalyst which is able to rapidly oxidize ethylene [68]. Al-doped WO_3 prepared by hydrothermal method on FTO glass shows a photocurrent density 1.3 times higher than pristine WO_3. Al atoms increase the electron conductivity and mobility leading to an increase of the global photoelectrochemical activity [69]. Mo-doped WO_3 prepared by the same method was successfully studied for the photodegradation of rhodamine B under visible light radiation (420 nm). The highest efficiency was obtained in a strong alkaline solution (pH = 12) [70].

14.1.2 Perovskites-Based Photocatalysts Prepared by Conventional Methods

14.1.2.1 Bismuth Vanadate ($BiVO_4$)

$BiVO_4$ is a promising perovskite material with great photocatalytic activity due to its narrow band gap (2.3–2.5 eV), non-toxicity and high photocorrosion stability. It shows three crystal structures: monoclinic scheelite structure, tetragonal scheelite structure and tetragonal zircon structure. The highest photocatalytic efficiency is generally obtained for the monoclinic structure due to its smaller band gap value compared to the others structures. However, the main issue of the bare $BiVO_4$ is correlated to the fast recombination of the free charge carriers which limits the global efficiency of the photocatalytic process [71, 72]. Kudo et al. have synthesized $BiVO_4$ through a long-term process at room temperature with different crystal structure: monoclinic ($E_g = 2.4$ eV) and tetragonal ($E_g = 2.9$ eV). Under UV irradiation, the photocatalytic activities for oxygen evolution reaction are comparable for both structures. When perovskites were irradiated with visible light, the highest efficiency was obtained for the monoclinic structure [73]. Monoclinic $BiVO_4$ with different morphologies, sizes and specific surface areas were prepared by hydrothermal method. They were tested for the photodegradation of methylene blue under visible irradiation and the highest photocatalytic performance was obtained for $BiVO_4$ flower-like photocatalyst. In contrast to other studied morphologies, it shows the smallest band gap value (2.14 eV) [74]. Regmi et al. have reported a study where they have synthesized a monoclinic-tetragonal Fe-doped $BiFeO_3$ structure by using microwave hydrothermal method. The photocatalytic activity over photodegradation of ibuprofen (>70% after 1 h under visible irradiation) is clearly increased compared to undoped $BiVO_4$, the highest performance being obtained for the sample doped with 1 wt% Fe [75]. Similar performance (75%) was reported for Cu-doped $BiVO_4$ tested for the photodegradation of ibuprofen, while almost entire methylene blue was oxidated over this type of photocatalyst [76]. S-doped $BiVO_4$ prepared by the surfactant-free hydrothermal method was tested for the photooxidation of methylene blue under visible irradiation. In just only 25 min, 100% of the organic dye was eliminated [77]. Also, rhodamine B was almost completely photo-oxidized over Mo-doped $BiVO_4$, while in the same experimental conditions, pristine $BiVO_4$ shows a photoconversion of ca. 40% [78].

14.1.2.2 Bismuth Ferrite ($BiFeO_3$)

$BiFeO_3$ is one of the most studied materials which present multiferroic properties at room temperature. It has distorted rhombohedral structure with high transition ferroelectric Curie temperature (1103 K) [79], while the Neel temperature for the antiferromagnetic ordering is $\sim$643 K [80]. The ferroelectric order is due to the 6 s lone pair electron of Bi^{3+}, while the unpaired Fe spins are responsible for the magnetic ordering [81]. The structure of $BiFeO_3$ is rhombohedrally distorted along [111] direction. The Bi^{3+} cations are strongly displaced in relation to the FeO_6 octahedra and this is leading to the formation of ferroelectric effect with the highest spontaneous polarization when it is oriented along [111] direction [82].

$BiFeO_3$ is among the most studied perovskite-type photocatalyst, especially for the water photolysis and organic dyes decomposition despite the fact that it has a relative high band gap value (ca. 2.7 eV) [83]. Liu et al. have reported the preparation of single-phase $BiFeO_3$ nanoparticles by a simple chemical coprecipitation of bismuth and iron nitrates. Excellent efficiency was obtained when the photocatalyst was used for the organic dye decolorization under UV irradiation (>92% for methyl orange) [84]. Single crystalline $BiFeO_3$ nanosheets and nanowires were prepared through hydrothermal synthesis starting from Bi^{3+} and Fe^{3+} precursors. They were tested for the degradation of rhodamine B under UV irradiation with acceptable photocatalytic activity after 3 h (66% for nanosheets; 60% for nanowires). The slightly higher efficiency obtained for the nanosheet morphology can be correlated to the lower band gap value (2.075 for nanosheets; 2.1 for nanowires). Further, the authors have tested the degradation of rhodamine B over the same catalysts, but under ultrasonic wave vibrations. Interesting was the fact that under these conditions, BFO samples show higher degradation rate of rhodamine B (59% for nanosheets and 92% for nanowires after 1 h). An even higher performance was obtained under simultaneous irradiation and ultrasonic wave vibration conditions, with a degradation of rhodamine B of 71% for nanosheets and 97% for nanowires. The authors have demonstrated that the internal

Fig. 14.2 Photocatalytic and piezoelectric processes

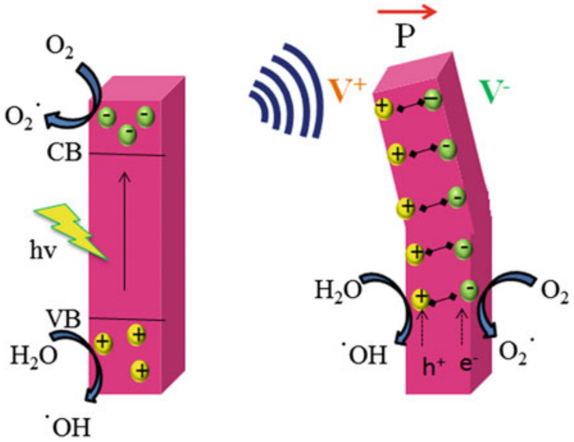

piezoelectric effect is responsible for enhanced efficiency, which ensures a better electrical transport property of charge carriers to the BFO-electrolyte interface, limiting the recombination of these species [85]. A schematic representation of photocatalytic and piezoelectric processes is presented in Fig. 14.2. As in the case of other photocatalysts, numerous dopants were used to modify $BiFeO_3$ structure and thus its photocatalytic performance, as Haruna et al. have presented in a recently published review [86].

14.1.2.3 Lanthanum Ferrite ($LaFeO_3$)

Alongside $BiFeO_3$, $LaFeO_3$ perovskite is also widely used in the field of photocatalysis, it presenting a lower band gap value (ca. 2.07 eV) compared to $BiFeO_3$ [87, 88]. Ismael et al. have reported the preparation of $LaFeO_3$ through a sol–gel method showing excellent photocatalytic activity under visible light irradiation. They have tested thus prepared photocatalyst for the photodegradation of rhodamine B and 4-chlorophenol and have correlated the high activity to the high specific surface area and the good separation of charge carriers [89]. Also, $LaFeO_3$ was prepared by a similar sol–gel method with ca. 1.86 eV band gap energy and the effect of vacuum microwave calcination temperature on the photocatalytic degradation of methylene blue and methyl orange dyes under visible irradiation was studied by Shen et al. They have observed that the vacuum microwave calcination can reduce the separation of the photogenerated charge carriers leading to an improvement of the photocatalytic performances [90]. B-doped $LaFeO_3$ shows excellent photocatalytic activity for the degradation of phenol with a conversion of ca. 87.9% under simulated solar light [91]. The photoelectrochemical performance of $LaFeO_3$ thin film photocathodes prepared by sol–gel on F-doped SnO_2 substrates was tested by Wang et al. At an applied potential of 0.6 V versus RHE, they have obtained a photocurrent density of ca. $-4.82\ \mu A/cm^2$. This value can be further increased in absolute value (ca. −19.6 μA/cm^2) by integrating a thin layer of Au between the substrate and the perovskite material. The layer of Au ensures an improved light harvesting, better charges separation and enhanced electrical conductivity [92]. A detailed study concerning the metal doping of $LaFeO_3$ photocathodes was reported by Diez-Garcia et al. They have used different contents of Mg^{2+} and Zn^{2+} for Fe^{3+} substitution leading to an improvement of the photoelectrochemical efficiency of the water reduction [93].

14.1.3 General Aspects Concerning Laser Devices

The laser was built for the first time by Maiman in 1960 [94]. Even from the beginning, the name "LASER" itself, has given a lot of information about this device which is based on Light Amplification by Stimulated Emission of Radiation. The main difference between a light emitted by a commercial source and a laser can be highlighted by the fact that the laser light has monochromacity (only one wavelength), directionality, coherence and high intensity. A laser device is made of three important components, as can be seen in Fig. 14.3. The gain medium (laser medium) is responsible for the population inversion, process that is closely related to the stimulated emission of light (laser effect). The wavelength of the laser light is given by the nature of the laser medium. The pump source ensures the required energy for the population inversion to take place. Last, but not least, the optical

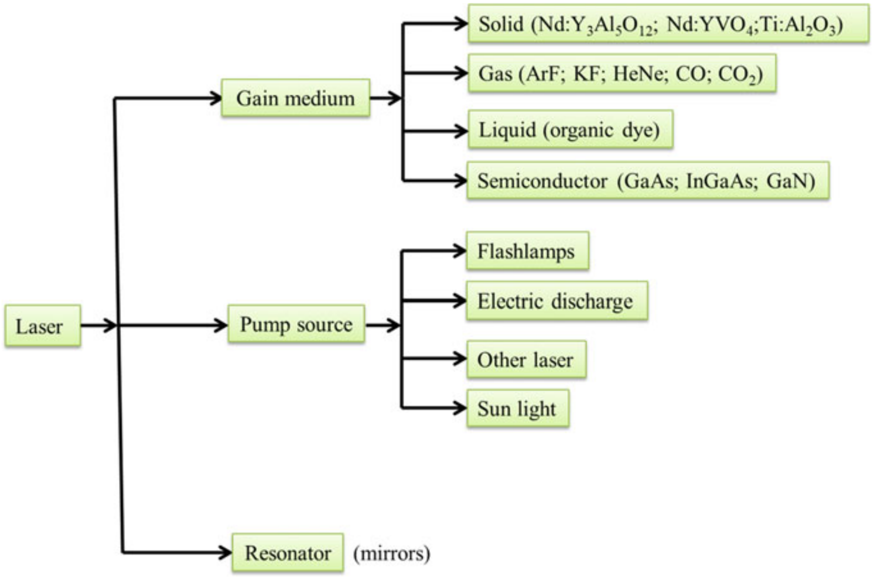

Fig. 14.3 General aspects concerning the components of a laser device

resonator acts as light amplifier and it is generally composed by mirrors with different partial reflectivities.

Laser devices are widely used in numerous application fields, especially for medical and biomedical applications, welding/cutting/joining and for material processing [95]. In the next sections, different laser-based techniques used for the preparation of different photocatalysts will be presented in detail.

14.2 Laser Pyrolysis

In the frame of sustainable growth, the water and air purification by efficient catalysts which can be activated by natural sunlight is now the goal of researchers. Titanium dioxide (TiO_2) is widely studied at the international level, but fundamentally limited by its low absorption efficiency of sunlight (4%) and by the rapid recombination of electron-hole pairs. In order to solve this problem, we propose four solutions: (i) doping of TiO_2 with metallic/non-metallic ions, (ii) coating of TiO_2 nanoparticles, (iii) coupling with other semiconductors or (iv) by decorating them with noble metals, where metal-titania composites become advantageous due to resonant plasmonic effect (SPR). This chapter will provide information about how the TiO_2-based nanoparticles with photocatalytic properties can be correlated to experimental conditions using a fast, single-step method—laser pyrolysis (LP). LP is a versatile and reproducible technique in controlling the morphological and structural properties of the resulted products. A wide range of the experimental parameters can be varied: power density, the pressure in the reaction chamber, the flow of gas/vapour introduced into the reaction. Optical, morphological and structural characterizations of titania-based nanoparticles synthesized by LP have been performed, as well as their organic pollutant photodegradation efficiency evaluation, under UV and Vis range, the main purpose being to obtain photocatalysts active in visible light for complete degradation of the pollutant. The aim of this chapter is to assess the photocatalytic activity of modified titania nanoparticles synthesized by LP. These nanomaterials with predictable properties were obtained by introduction of different degree of V dopant in the TiO_2 lattice or by coupling with SnO_2 or by loading them with noble metal (Ag). The structural, morphological and optical properties of nanopowders were characterized using X-ray diffraction (XRD), transmission electron microscopy (TEM), energy-dispersive X-ray spectroscopy (EDX), Raman spectroscopy and UV–V is diffuse reflectance spectroscopy (DRS) techniques and correlated with their photodegradation efficiency of different organic pollutant (Fig. 14.4).

Some examples of the Ag/SnO_2/V-modified TiO_2 catalysts used for different pollutant degradation studies along with their preparation technique are given in Table 14.1.

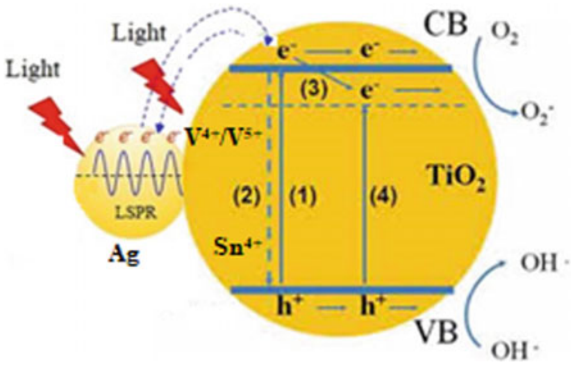

Fig. 14.4 Pictorial representation of the band gap when modified TiO_2

Table 14.1 Studies on Ag/SnO_2/V-modified TiO_2 assisted photodegradation of different pollutant

Catalyst	Pollutant used for analysis	Techniques for preparation of TiO_2-based catalysts	Ref.
TiO_2–Ag particles	P-nitrophenol	Sol–gel method	[5]
TiO_2/Ag nanosponge composite	RhB and salicylic acid	Sol–gel method	[6]
Ag/TiO_2	Rhodamine B	Photodeposition	[7]
Ag/P25, Ag@CuO NPs	Phenol and acetic acid	Radiolytic reduction	[8]
Ag@TiO_2 NPs	Methyl Orange	Hydrothermal method	[9]
Ag-loaded TiO_2	Methylene blue	Pulsed laser ablation	[10]
TiO_2/Ag/SnO_2 composites	Methylene blue	One-step reduction	[11]
Silver-doped TiO_2 nanoparticles	Lomefloxacin	Liquid impregnation method	[12]
SnO_2/TiO_2 nanoparticles	Methylene Blue, Rhodamine B and phenol	Sol–gel method	[13]
SnO_2–TiO_2 composite	Rhodamine B	Chemical precipitation	[14]
Sn-doped TiO_2 nanoparticles and TiO_2–SnO_2 nanocomposites	Methylene blue	Sol–gel method	[15]
TiO_2-doped with SnO_2 thin films	Methylene blue	Sol–gel method	[16]
SnO_2/TiO_2 nanotube	Textile dye effluent	Hydrothermal preparation followed by chemical precipitation	[17]
SnO_2 particles	Congo red	Precipitation and calcination pathways	[18]
V–TiO_2 nanoparticles	NO_2 reduction	Gas-phase condensation	[19]
Vanadium-doped TiO_2 nanoparticles	Methyl orange	Sol–gel method	[20]
Vanadium-doped TiO_2 nanoparticles	Alkyd resin (Photochromic properties)	Wet chemical method	[21]
Vanadium-doped TiO_2	Methylene blue	Sol–gel method	[22]

14.2.1 Materials and Methods

Three types of TiO_2 nanopowders were studied. All these samples were obtained by the laser pyrolysis method using the following precursors: $TiCl_4$ (Aldrich 98% purity), $SnCl_4$ (Aldrich 98% purity), $VOCl_3$ (Aldrich 99% purity), Air (Siad 99.99% purity), C_2H_4 (Siad 99.5% purity), $AgNO_3$ (Aldrich 97% purity) and Ar (Siad 99.98% purity).

14.2.2 Laser Pyrolysis-The Synthesis Method

The laser pyrolysis method is based on the resonant transfer of energy between the CO_2 laser radiation and the absorption band of a reactant or sensitizer. The CO_2 laser was first developed in 1964 by Patel and colleagues working Bell Labs in the USA [96]. It was soon observed a significant increase in the laser power and efficiency with the addition of nitrogen and helium. This made it possible to achieve very high-power continuous wave (1, 10 kW), and 20–30% efficiency. The CO_2 laser emits in the spectral range 9–11 μm (middle infrared) in over 100 individual rotational vibration lines. The most intense lines are found at 10.6 μm line 10P (20) and at 9.6 μm line 9P (20) [97]. Gas lasers use a gas or a mixture of gases as the active medium. Common examples of gas lasers are those with HeNe, CO_2, argon or excimers. The main scheme of such a laser is presented in Fig. 14.5.

There is a wide variety of constructive configurations. For example, the gas can flow through the laser tube or can be used in closed mode; the electric discharge can be in direct current, in alternating current or in radio frequency. Gas lasers emit over 6000 laser lines into gases and vapours from more than 140 different species (atoms and molecules) [98].

Titanium tetraisopropoxide (TTIP) or $TiCl_4$ is mainly used as precursors for the production of TiO_2 via laser pyrolysis [37, 38]. Doped nanoparticles can be easily obtained through LP in one-step reaction, which is a major advantage of this technique in contrast to other chemical methods where, generally, a few reaction steps are required.

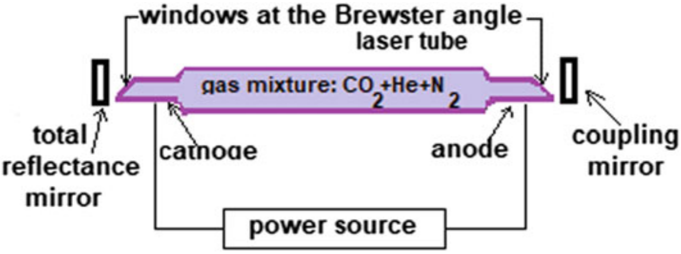

Fig. 14.5 Diagram of the CO_2 laser

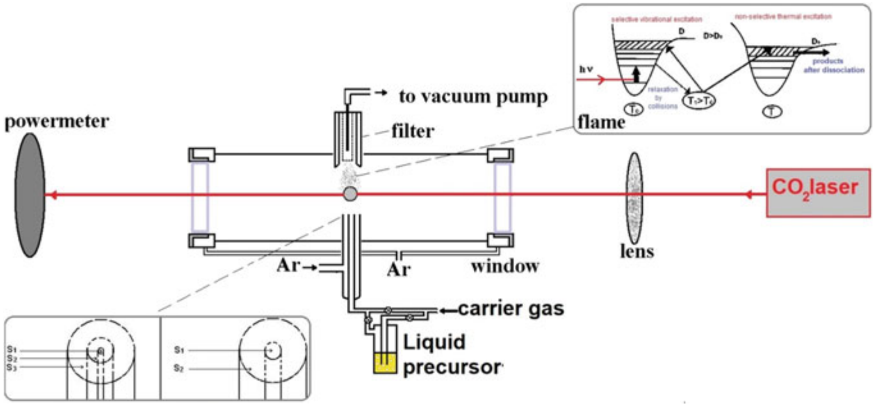

Fig. 14.6 Schematic setup of a LP system

Generally, pyrolysis in the gas phase takes place in the small volume defined by the interpenetration between gas and radiation, place where a flame usually appears (see Fig. 14.6). The visible emission is attributed primarily to the thermal effect, resulting from the emission of hot, newly formed particles. Being a well-defined reaction in volume (no contact with the walls of the enclosure) no chemical contamination occurs ensuring a high purity of the powder obtained. Due to the high temperatures during the reaction (700–2000 °C) corroborated with high heating/cooling speeds (10^5–10^6 °C/sec) the obtained particles have small size (5–25 nm).

Until now, our best results regarding TiO_2-based materials are: (i) TiO_2 nanospheres, decorated with Au, Ag and Pt nanoparticles by chemical impregnation reveal a rapidly and complete degradation of MO pollutant and a good biocompatibility with human lung cell [31]; (ii) TiO_2 nanoparticles with majority anatase phase (reaching values of 97%) whose photocatalytic properties were tested, yielding a 45% efficiency higher than the current industry standard Degussa P25 [46]; (iii) interstitial N-doped-TiO_2 (0.7–0.9 at%)—obtained both by varying the doping level and the nature of the oxidizing agent in order to improve the properties of absorption in the visible range for photocatalytic applications [37, 48]; (iv) substitutional Fe-doped TiO_2 nanoparticles with varied doping level (0.1–0.5 at%)/(7–25 at%)—the displacement to the visible of absorption peak succeeded, from ~380 nm at 533 nm (for photocatalytic applications) [36, 40]; (v) improve the photocatalytic properties of TiO_2 by doping with S and/or C coverage. The results have shown the visible light absorption improvement by narrowing the band gap up to 2.7 eV (versus 3.2 eV in the literature corresponding to anatase phase) [41]; (vi) TiO_2 nanocomposites with photocatalytic properties as well as magnetic in order to recover their properties in magnetic field after the process of photodegradation, by carrying out new architectures of the core/shell—Fe/TiO_2/SiO_2 [38].

In the present study, TiO_2-based nanoparticles were obtained by laser pyrolysis method using the following precursors: $TiCl_4$—titanium tetrachloride (as precursor for Ti), air (as oxidizing agent), C_2H_4—ethylene (as sensitizing), $VOCl_3$ (as precursor for V), $SnCl_4$ (as precursor for Sn) and $AgNO_3$ for decoration of TiO_2 NP with metallic Ag particles. The introduction of ethylene as sensitive was necessary because none of precursors not absorb CO_2 laser radiation The synthesis experimental parameters are strictly controlled by using electronic-assisted equipments (mass flow controllers, pressure controller): flow reactants: ΦAr = 1500–2000 sccm, $\Phi_{\mathrm{Air}\rightarrow\,\mathrm{TiCl_4}} = 150-300$ sccm, Φ_{C2H4} = 30–50 sccm, ΦAir supplementary = 200 sccm and ΦAr window = 2500 sccm, the total pressure (P = 450 mbar) and the laser power (400 W). The doping process of the titania nanoparticles was performed using the following precursors and varying their proportion: $\Phi_{\mathrm{Air}\rightarrow\mathrm{AgNO_3}} = 150$ sccm, $\Phi_{\mathrm{C_2H_4}\rightarrow\mathrm{VOCl_3}} = 5-30$ sccm and $\Phi_{\mathrm{Ar}\rightarrow\mathrm{SnCl_4}} = 0-30$ nm. The precursors enter in the reaction chamber through a system of three concentric nozzles, to not react chemically before encountering the laser radiation, as shown in Fig. 14.6. The following parameters were maintained constant for each of the three types of experiments: the flows of Ar for windows flushing (ΦAr window = 1750 sccm), the total pressure (P = 450/850 mbar) and the laser power (450 W). The nanoparticles formed in the pyrolysis flame are collected on a ceramic filter; the mean productivity for the powder is about 1.5 g/h.

14.2.3 Characterization Methods

Energy-dispersive X-ray spectroscopy coupled to a Scanning Electron Microscope (SEM) (FEI Co., model Quanta Inspect S, at 15 kV in high vacuum) was used to study the elemental composition of TiO_2-based nanopowders.

An X-ray diffractometer Panalytical X'Pert MPD theta-theta was used to evaluate the crystalline phases of the samples and the topography of the sample was analysed by High-Resolution Transmission Electron Microscopy (HRTEM) in a TECNAI F30 G2 S-TWIN.

The optical properties of TiO_2-based samples were measured by Diffuse Reflectance (DR) spectra using a UV–VIS spectrophotometer, Analytik Yena Specord, 200 Plus. The values of optical band gap for some samples are estimated from the Tauc plots of diffuse reflectance UV–VIS data converted into absorbance by Kubelka-Munk function.

The surface morphology and particle size of nanostructured of TiO_2 powders were characterized using transmission electron microscopy TEM, high-resolution transmission electron microscopy (HRTEM), and selected area electron diffraction (SAED) measurements using JEM ARM 200F analytical microscope (Jeol, Japan). The preparation of samples for the test was performed by dispersing the powders on Cu grids with an amorphous carbon support layer, after a light grinding of the powders. This grinding aims to break down the particle aggregates into submicron aggregates, transparent to the electron beam, and does not affect the morphology of the nanometer particles.

14.2.4 Evaluation of Photocatalytic Performance

14.2.4.1 Photocatalytic Degradation of Methanol

The experimental procedure consisted in dispersing in a uniform layer 0.05 g of photocatalyst in powder form on an area of about 3.6 cm^2. This photoactive surface was subsequently exposed to simulated sunlight. Methanol (5 μL) was injected into the photoreactor with a volume of about 120 cm^3 so that the concentration at the beginning of the experiment in the gas phase is 123 μmoles. The temperature inside the photoreactor was maintained constant, 18 °C, with a cryostat. The AM 1.5 solar light (1000 W/m^2) was provided by a Peccell L01 solar simulator. For each test 200 μL gas samples were taken from the photoreactor at 20 min and analysed with two gas chromatographs equipped with FID (Agilent 7890A) and TCD detection (Buck Scientific, model 910). The total time of a photocatalytic test was 180 min.

14.2.4.2 Photocatalytic Degradation of Methyl Orange

The UV photocatalytic activity was measured in a photoreactor coupled to 6 × 6 W fluorescent lamps (λ_{max} = 365 nm, irradiation time ~2.25 h). The concentration of the dissolved oxygen in the photoreactor containing the photocatalyst suspension and the pollutant was kept constant by continuously purging air during the reaction process. A JASCO-V650 (Tokio, Japan) spectrophotometer (λ = 297 nm) was used to measure the concentration of the organic dye. The slope of the curve ln (C0/Ct) versus irradiation time was used to calculate the photocatalytic rate constants considering a first-order kinetics, where C defines MO concentration, C0—initial concentration, Ct—final concentration.

14.2.5 Results and Discussion

14.2.5.1 EDX Measurements

EDX quantitative analysis indicates a good correlation between the precursors used and the elemental concentration of samples (at. %). The presence of the dopant and degree of this which modifies the structure of TiO_2 is presented in Table 14.2 together with calculated crystallite size and phases proportion of titania. The samples were named according to the degree of doping given by the EDS results.

Table 14.2 TiO_2-based samples crystallographic parameters

Sample	Degree of doping	TiO_2—phases proportion		Mean crystallite size	
	(at%)	A (%)	R (%)	Da (nm)	Dr (nm)
TiO_2:V	V (at%)				
TiO_2:V-0	0	87	13	18	26
TiO_2:V-1	1.0	83	17	19	29
TiO_2:V-6	6.3	67	33	20	27
TiO_2:V-8	8.6	68	32	19	20
TiO_2–SnO_2	Sn (at%)				
TiO_2–SnO_2–0	0	100	0	20	–
TiO_2–SnO_2–3	2.7	83	17	17	10
TiO_2–SnO_2–5	4.8	77	23	16	8
TiO_2@NM	Ag (at%)				
P25	–	84	16	22	31
TiO_2	–	87	13	35	38
TiO_2@Ag	0.05	76	23	36	28

14.2.5.2 X-ray Diffraction

XRD was carried out to characterize the crystalline phase of the powders. All samples show the characteristic phases of TiO_2 -anatase (JCPDS 00-021-1271) and rutile (JCPDS 00-021-1276), only in the case of TiO_2–SnO_2 samples could be identified for the sample with highest Sn content the formation of the crystalline phase of SnO_2–cassiterite (JCPDS 00-041-1445). Neither shifts can be seen in the anatase and rutile XRD peaks for the vanadium or silver containing samples, meaning that the doping degree is very low or absent. These superposed diffractograms (shown in Fig. 14.7) allow a direct comparison between the pure TiO_2–SnO_2–0 sample (containing a single phase: TiO_2 anatase) with the highest sample content Sn–TiO_2–SnO_2–5, where all three phases are present due to the presence of tin who favours the formation of the rutile phase. The crystallite size was calculated from the most intense peaks for each powder, respectively (101) at $2\theta = 25.4°$ for anatase and (110) at $2\theta = 27.5°$ for rutile, using Scherrer's equation and the results are presented in Table 14.2.

Increasing doping degree of TiO_2 with Ag, Sn and V leads to the transformation of the anatase phase into rutile in all three cases (see Table 14.2). Khatun et al. explain this in the case of V, the increase of the doping level leads to the increase of the V^{4+} phase to the detriment of V^{5+} also observing a decrease of the band gap value, simultaneously [99].

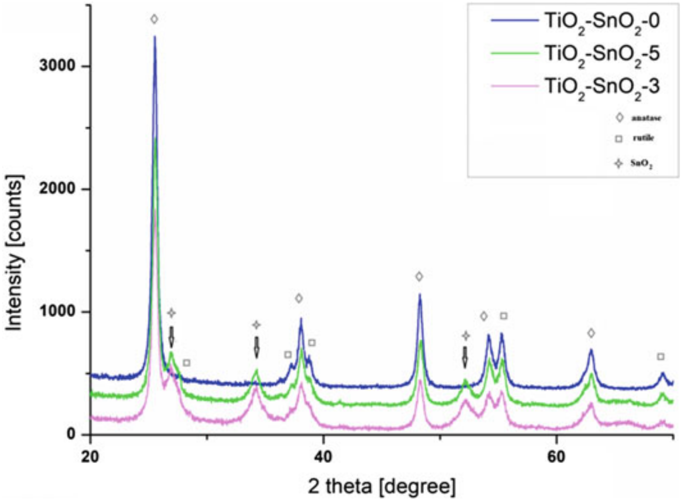

Fig. 14.7 X-ray superposed diffractograms of TiO_2–SnO_2 samples obtained by LP

14.2.5.3 TEM Analysis

TiO_2@Ag

Spherical nanoparticles of TiO_2 with dimensions 30–50 nm are presented in Fig. 14.8. Due to the small amount of Ag, the silver nanoparticles could not be distinguished on the TiO_2 surface for the TiO_2@Ag sample but the diffraction rings from de SAED measurements, presented as an inset in the figure, confirm its presence—Pt (111) and the anatase (101) and rutile (110) planes.

TiO_2–SnO_2

The anatase titania phase nanoparticles for the sample TiO_2–SnO_2–0 are shown in Fig. 14.9 and the corresponding insets-SAED and HRTEM confirms this. The images are in concordance with the XRD results, which show the 100% anatase phase.

The introduction of tin leads to decrease the crystallinity of TiO_2–SnO_2–3 sample, nanoparticles appear to be embedded in an amorphous carbon matrix (Fig. 14.10). Diffraction rings are less intense compared to the previous sample TiO_2–SnO_2–0 (without tin content).

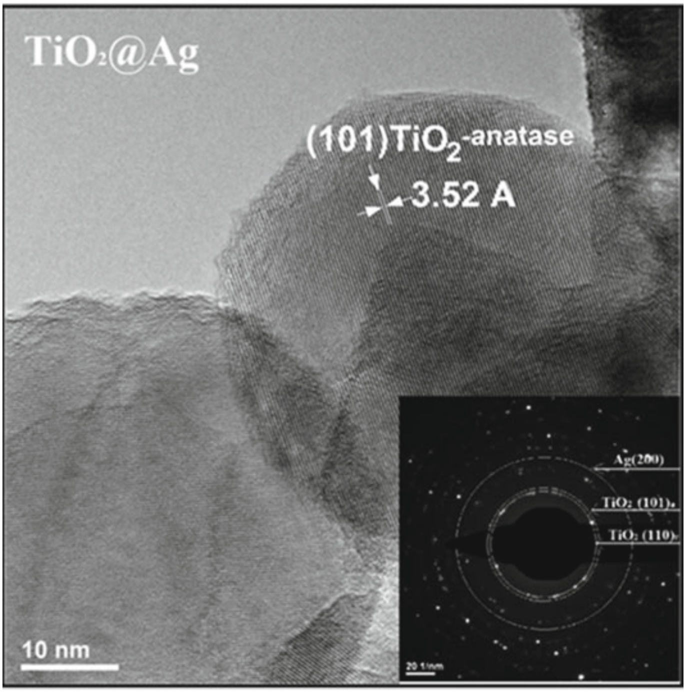

Fig. 14.8 HRTEM images of TiO_2@Ag together with their corresponding SAED-inset

The increase of the Sn content in sample TiO_2–SnO_2–5 continue the trend of lowering crystallinity, the HRTEM image presented in Fig. 14.11 showed the TiO_2 nanoparticle covered in the carbon layer.

TiO_2:V

The TiO_2:V-0- reference sample is TiO_2 powder obtained by laser pyrolysis without the addition of vanadium (Fig. 14.12) The crystals of anatase are observed, which are partially faceted and more spheroidal, fact that constitutes a specific morphological characteristic for the powders obtained by laser pyrolysis. SAED image, presented as inset in the figure indicates a high degree of crystallinity of the sample containing anatase phase in major proportion.

The TEM image shows nanoparticles with different shapes and sizes, easily aggregated in the sample TiO_2:V-1. By introducing vanadium, the crystallinity of the powder decreases (see the SAED/EDS image shown by the inset in Fig. 14.13.).

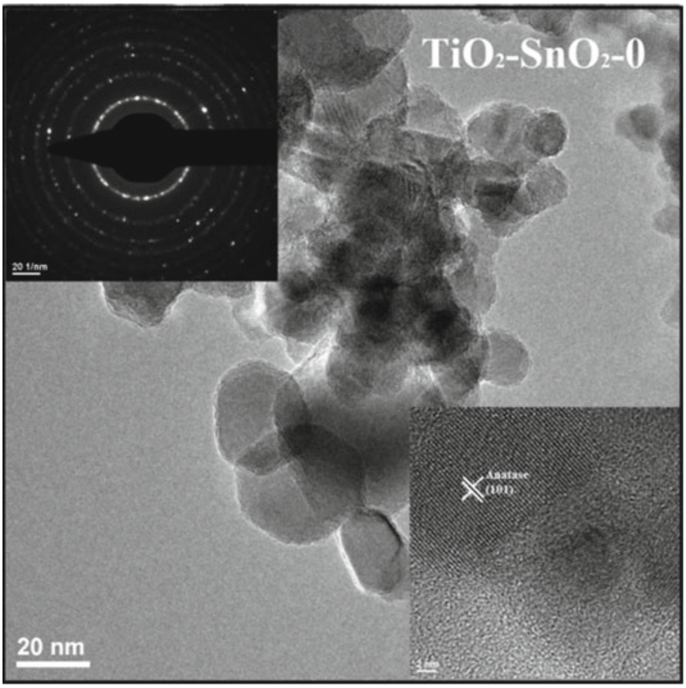

Fig. 14.9 TEM images of TiO_2–SnO_2–0 and SAED/HRTEM presented as inset

14.2.5.4 Evaluation of Photocatalytic Performance

Photocatalytic Degradation of MO

TiO_2@Ag

In Fig. 14.14, TiO_2@Ag sample shows an enhanced photoactivity as compare with pure TiO_2 sample against the water-soluble Methyl orange azo dye, used by many other researchers as a benchmark dye in photodegradation experiments. The presence of Ag on the titania photocatalyst drastically decreased the MO concentration. In our experiments, for photodegradation of MO ($c_0 = 125$ μM or 41.25 mg/l) under UV light we found rate constants of 18.55×10^{-3} and 9.6×10^{-3} min^{-1} for TiO_2@Ag and TiO_2 samples, respectively, whereas the corresponding rates for visible light irradiation were slightly lower, 14.56×10^{-3} and 1.8×10^{-3} min^{-1} (see Table 14.3). The explanation for the MO photodegradation on the synthesized composite materials under V is light irradiation can be based on the SPR effect of noble metal nanoparticles, deposited on the TiO_2 surface in which the electron gets transferred from metal NPs surface to the conduction band of TiO_2.

Among the as-synthesized photocatalysts, TiO_2@Ag shows the highest activity for MO photodegradation under UV or VIS light, the rate constant value is more

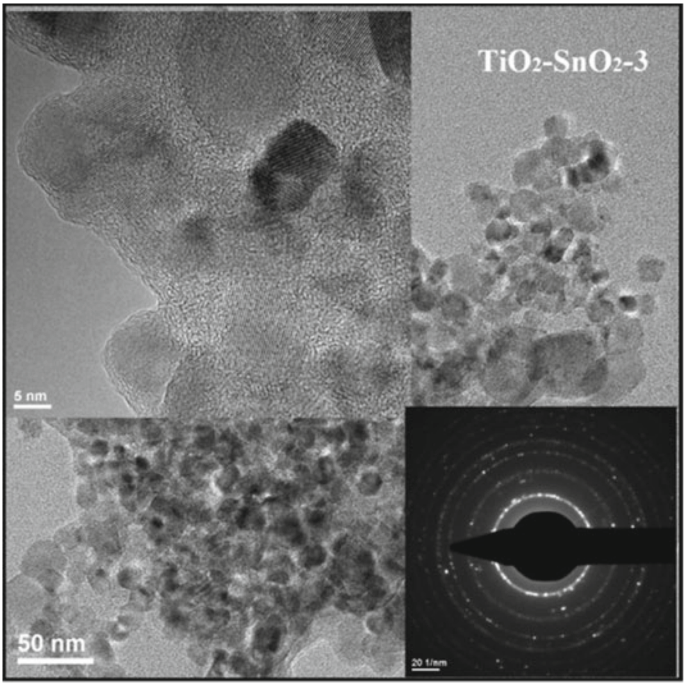

Fig. 14.10 TEM images of TiO_2–SnO_2–3 and SAED/HRTEM presented as inset

Fig. 14.11 HRTEM image of TiO_2–SnO_2–5

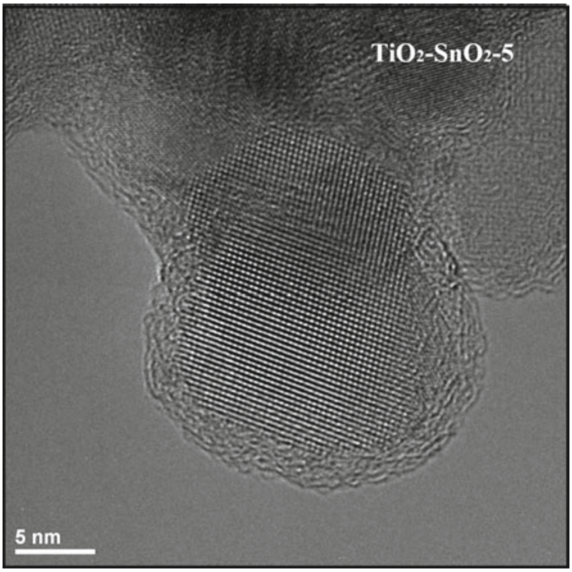

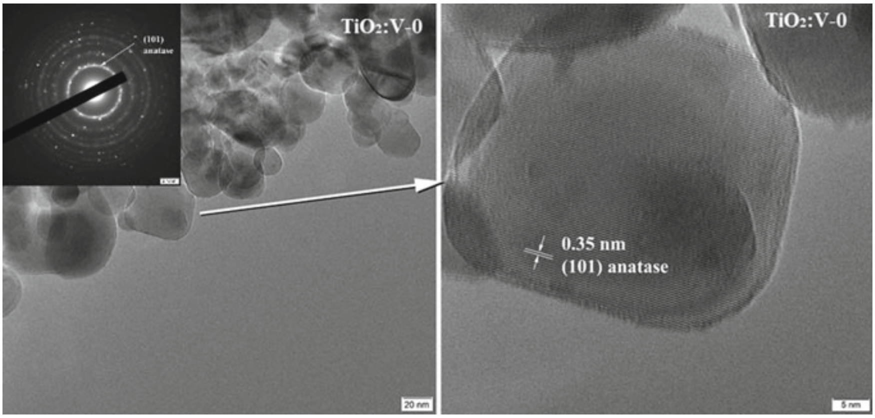

Fig. 14.12 HRTEM image of TiO_2:V-0- reference sample and inset-corresponding SAED

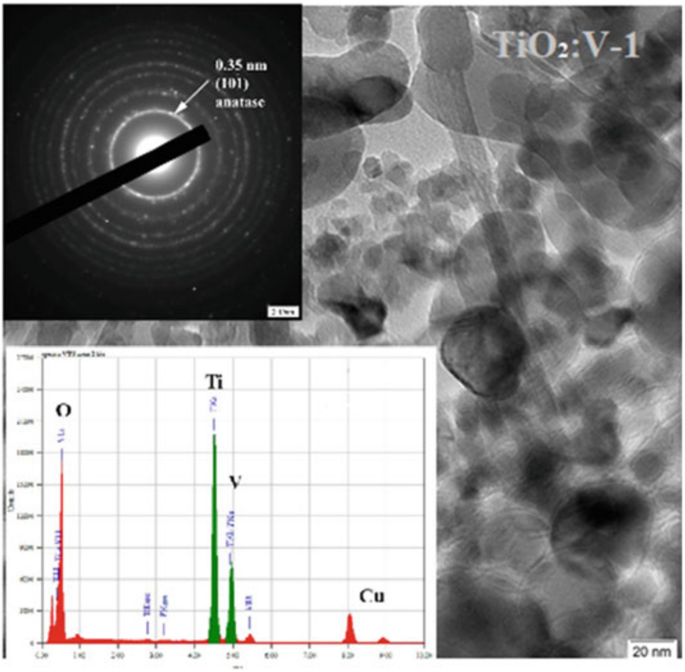

Fig. 14.13 TEM image of TiO_2:V-1 sample and SAED/EDS presented as inset

than 2 times higher than that obtained TiO_2, and 3 times higher than that for P25 photocatalyst. In a previous study, we obtained a slightly better result, achieving total photodegradation of MO in visible light by a similar procedure [31].

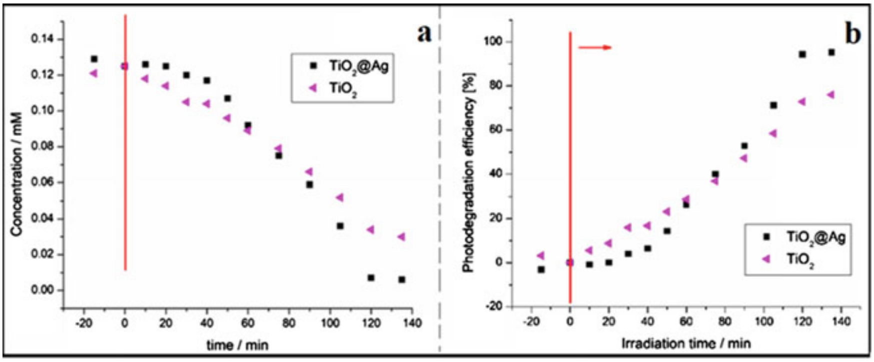

Fig. 14.14 Photodegradation of MO for the sample TiO_2@Ag as compare with bare sample

TiO_2–SnO_2

Figure 14.15 shows the degradation of methylene blue for two hundred minutes in the case of TiO_2–SnO_2 type photocatalyst, and Table 14.3 collates the dye removed per specimen under UV irradiation. In the first part of the experiment, the free tin sample TiO_2–SnO_2–0 shows the highest photoactivity, but in the end, it decreases, highlighting the influence of the tin on the reaction yield. After the finishing of the irradiation process, TiO_2–SnO_2–3 and TiO_2–SnO_2–5 show a higher efficiency for MO degradation as compared with P25.

Improving the photocatalytic properties of titania by the introduction of tin content is attributed by the better separation of electrons and holes by coupling TiO_2 with SnO_2 [100].

TiO_2:V

The results of photocatalytic tests for the formation of CO_2 from CH_3OH–H_2O mixtures on TiO_2:V samples, prepared by laser pyrolysis, exposed to simulated sunlight are presented in Fig. 14.16 (in comparison are represented the results

Table 14.3 Photodegradation efficiency and band gap energy values

Samples	Rate constant k × 10^{-3} (min^{-1})		Band gap energy (eV)
	UV	VIS	
P25	6.54	0.19	3.25
TiO_2	9.6	1.8	3.08
TiO_2@Ag	18.55	14.56	2.90
TiO_2–SnO_2–0	7.08	–	3.22
TiO_2–SnO_2–3	6.65	–	3.04
TiO_2–SnO_2–5	9.16	–	3.05

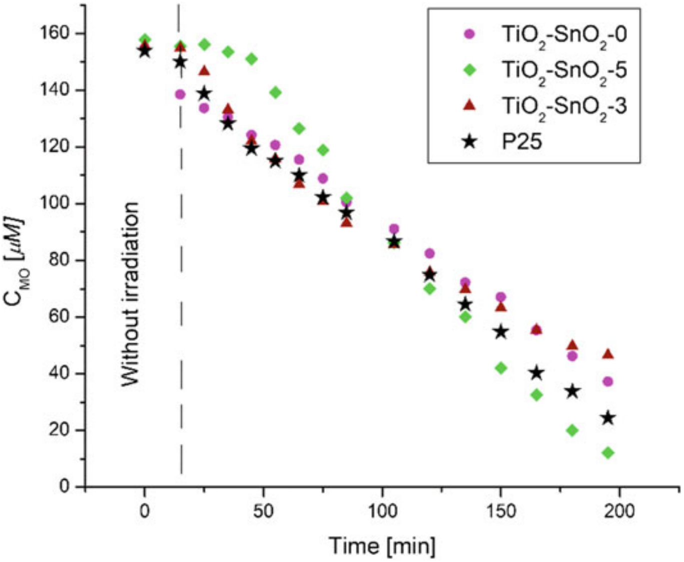

Fig. 14.15 Photodegradation of MO for **TiO_2–SnO_2** photocatalysts as compare with P25 sample

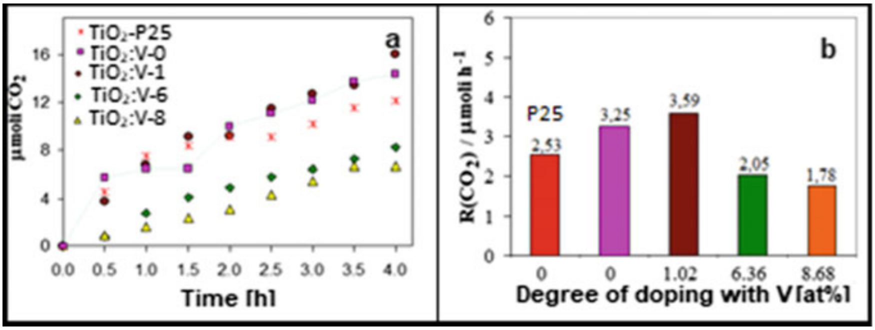

Fig. 14.16 Photodegradation of CH_3OH for TiO_2:V photocatalysts as compare with P25 sample

obtained for pure TiO_2 obtained by LP and commercial reference material-P25). The photomineralization activity of CH_3OH is relevant for depollution processes.

Figure 14.16a, b can be seen that (i) the preparation process of TiO_2 nanoparticles by laser pyrolysis improves the photocatalytic activity of CO_2 production and (ii) the addition of a small amount of vanadium to the TiO_2 matrix (1.02 at.%) has a good result on catalytic activity. The highest CO_2 formation rate of 3.59 μmol h^{-1} was measured on the TiO_2:V-1 sample, which has the lowest V content of all the analysed samples. The factors that determine this type of behaviour by adding vanadium to the TiO_2 matrix are (i) improving the absorption of light radiation by extending it in the visible range, (ii) separating electrons and gaps generated at the interface of crystalline domains, (iii) CH_3OH adsorption and of the degraded intermediates formed (formaldehyde and formic acid). In a similar study for MB photodegradation using V-doped TiO_2 nanoparticles obtained by flame spray pyrolysis Thian et al. reported that the optimal V concentration is 0.5% above this level decreasing the photocatalytic activity due to V^{4+} ions which steadily become the recombination centres of photogenerated electrons and holes [101].

14.3 Pulsed Laser Deposition

Since 1970, when pulsed laser deposition (PLD) technique was discovered [102], it became one of the most important laser-based technique for the material processing, mainly as thin films. The experimental setup of PLD is presented in Fig. 14.17. In this technique, the surface of a material target positioned in a sealed vacuum chamber is hitted by a high energy pulsed laser, leading to the melting and vapourization of the material. Further, the vapours are ionized with the formation of a high temperature plasma plume. Parallel to the material target is positioned a substrate which is able to collect the material particles through a condensing process. In this way, the desired material can be grown onto a substrate via PLD technique.

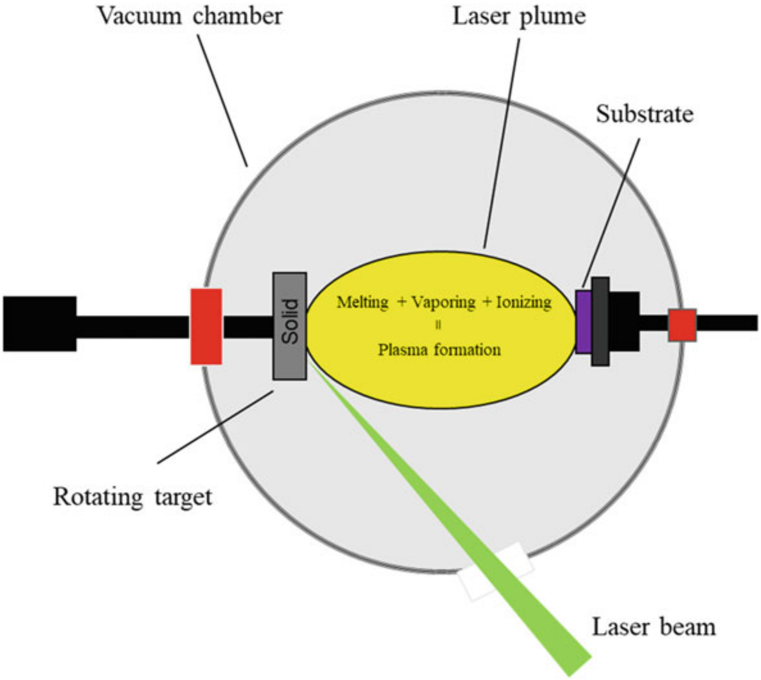

Fig. 14.17 PLD experimental setup

This technique presents the following advantages [103, 104]:

- The process efficiency, as well as its control and flexibility, are improved due to the laser radiation which can be focused on very small spot sizes;
- The thin film growing is performed in a sealed reactor and in this way the external contamination is avoided. Also, the deposition process can occur in both reactive or inert gasses;
- It ensures a precise stoichiometric transfer for all kinds of materials (complex stoichiometry, organo-metallic compounds);
- It provides high deposition rates (1–5 Å/pulse) with excellent control of the parameters involved in the process.

These advantages make this technique a widely used one for the thin films fabrication. Further, for this chapter, the preparation by PLD of different materials with potential applications on the photocatalysis field will be presented.

14.3.1 Simple Stoichiometry Metal Oxides Photocatalysts Prepared by PLD

14.3.1.1 TiO_2

TiO_2 was prepared by PLD using both excimer (KF) and solid-state (Nd:YAG) lasers on different substrates, in Table 14.4 being resumed the experimental conditions used for the preparation of various simple oxides thin films. Lin et al. have grown TiO_2 on conductive ITO substrates by using an excimer KF laser with a laser fluence of 1.8 J/cm^2. They have prepared TiO_2 films by using three deposition temperatures (room temperature, 600 and 800 °C) and different partial pressures (0.33; 1 mbar). The photoelectrochemical properties of TiO_2/FTO photoanodes were tested in a three-electrode system which is one of the most utilized systems for the evaluation of PEC performance. A slightly alkaline electrolyte solution was used for PEC tests (pH = 9). The flat band potential (V_{fb}) is strongly dependent on the experimental conditions of the deposition process and it increases (in absolute vacuum energy scale) with lowering the partial pressure inside the deposition chamber at 600 °C. This modification of V_{fb} was correlated by the authors to the induced oxygen vacancies in TiO_2 structure. At low deposition temperature (e.g. 600 °C), TiO_2/FTO films show high porosity which leads to a higher IPCE and hence, a better PEC performance [105]. Gyorgy et al. have reported the preparation of TiO_2 on Si substrates by PLD, starting from a metallic Ti target, under controlled oxygen pressure. The deposition temperature was 500 °C and the laser fluence 3 J/cm^2. They have demonstrated the semiconductor behaviour of grown TiO_2 films, which make them possible candidates for the utilization as photocatalysts [106]. Daghrir et al. have reported the growing of TiO_2 on Ti grinds by ablating a high purity TiO_2 target, under oxygen pressure and different substrate temperatures (400

Table 14.4 Experimental conditions for different oxides-based thin films prepared by PLD

Material	Substrate	Gain medium	λ (nm)/ν (Hz)/Laser fluence (J/cm^2)	Partial pressure (mbar)	T$_S$ (°C)	Application	Ref.
TiO_2	ITO	KF	248/n.s./1.8	0.33 (Ar: O_2 = 50:50)	600	PEC studies	[105]
TiO_2	ITO	KF	248/n.s./1.8	1 Ar: O_2 = 50:50	800	PEC studies	[105]
TiO_2	Si	Nd: YAG	266/3/3	10^{-4}–10^{-1} (O_2)	500	Semiconductor studies	[106]
TiO_2	Ti	KrF	248/30/4.5	1.3×10^{-3} (O_2)	400 600	PEC studies (ChD)	[107]
TiO_2	Sapphire	KrF	248/10/n.s.	3.5×10^{-4} (O_2)	400	PC studies (MBD)	[108]
TiO_2/ TiN/ TiO_2	SiO_2	KrF	248/n.s./n.s.	3.0×10^{-2} (N_2 for TiN) 1.4×10^{-2} (O_2 for TiO_2)	150	PC studies (MBD)	[109]
TiO_2	Modified SiO_2	KrF	248/5/n.s.	0.24 (O_2)	675–750	PEC studies (WS)	[110]
WO_3	Si and SiO_2	KrF	248/20/4.5	1.5×10^{-2} (O_2)	RT	PC studies (MBD)	[111]
WO_3	FTO	KrF	248/10/n.s.	1.3×10^{-1} (O_2)	400	PEC studies (WS)	[112]
TiO_2/ WO_3	Quartz	KrF	248/10/3 (TiO_2) 1.3 (WO_3)	0.27 (O_2)	500	PC studies (MBD)	[113]
ZnO	Si	Nd: YAG	1064/10/n.s.	2 (O_2)	n.s	PC studies (RbD)	[114]
ZnO	FTO	Nd: YAG	355/n.s./n.s.	8.5×10^{-4} (O_2)	n.s	PEC studies (WS)	[115]

T$_s$—the substrate temperature; ITO—indium tin oxide; FTO—fluorine-doped tin oxide; PC—photocatalytic (without external applied bias); PEC—photoelectrochemical (with external applied bias); ChD—chlortetracycline degradation; MBD—methylene blue degradation; WS—water splitting; RbD—rhodamine B degradation; n.s.—not specified

and 600 °C). They have tested TiO_2/Ti thin films for the photoelectrochemical degradation of chlortetracycline and obtained a very high photocatalytic activity (ca. 98% degradation) [107]. The photocatalytic degradation of methylene blue over TiO_2 thin films grown on Al_2O_3 (sapphire) substrates via PLD was studied by Yamaki et al. They have demonstrated that the experimental laser parameters used for the TiO_2 deposition are crucial for the physico-chemical properties of the final material. Also, the authors have mentioned that the photocatalytic efficiency can be improved by choosing the correct PLD experimental conditions [108]. Also, the photocatalytic degradation of methylene blue was successfully evaluated over a heterostructure based on TiO_2/TiN/TiO_2 prepared by PLD, starting from a ceramic target of TiN [109]. Rahman et al. have demonstrated the preparation of TiO_2/Si via PLD with high degree of control of films morphology as well as defects content, which are extremely important parameters for the photoelectrochemical performance [110].

14.3.1.2 WO_3

WO_3 thin films were grown on Si and SiO_2 from a compressed target chemically prepared starting from metallic tungsten and boric acid. The deposition process was performed at room temperature under oxygen pressure with a laser fluence of 4.5 J/cm^2 and a laser frequency of 20 Hz. The complete formation of WO_3 was ensured by annealing of thin film at 600 °C. Excellent photodegradation efficiency of methylene blue was obtained over prepared WO_3 films this behaviour being correlated to the high specific surface area which can improve the interaction between the organic dye and the catalytic active sites [111]. Fàbrega et al. have reported the preparation of monoclinic WO_3/FTO thick films through PLD using an excimer KF laser. The deposition temperature was set to 400 °C and the oxygen pressure during the deposition process was 0.13 mbar. Their photoelectrochemical water splitting activity was tested in acid electrolyte and the authors have reported a value of the photocurrent density of ca. 2.4 mA/cm^2 [112]. Also, multilayer TiO_2/WO_3 thin films prepared by PLD on different substrates were tested for the photodegradation of methylene blue under visible light irradiation [113]. We have grown WO_3 on commercial Pt/TiO_2/SiO_2/Si by PLD using a Nd-YAG laser which emits at 355 nm. Two different WO_3 film's thicknesses (330 nm and 1100 nm, respectively) were obtained by varying the number of laser pulses. The films were tested in acid electrolyte for the photoelectrochemical oxygen generation from water. No major differences in the I versus V curves were observed, the maximum value of the photocurrent density being ca. 30 mA/cm^2 at 1.59 V versus RHE (Fig. 14.18).

14.3.1.3 ZnO

ZnO has been grown on Si by PLD using a solid-state Nd-YAG laser emitting at 1064 nm. The band gap of the resulting films is ca. 3.25 eV. ZnO thin films were immersed in a solution of rhodamine B and were left for 6 h under sunlight irradiation, the concentration of the organic dye being spectrometrically analysed at every hour. After the first two hours, only 30% of the organic dye was eliminated. After other two hours, the percentage increases to ca. 82%, in the final ca. 91% of rhodamine B being oxidized. The authors have mentioned that the photocatalytic performance can be further increases by adjusting the PLD experimental parameters [114]. A detailed study concerning the photoelectrochemical properties of ZnO thin films prepared by PLD was reported by Wolcott et al. [115].

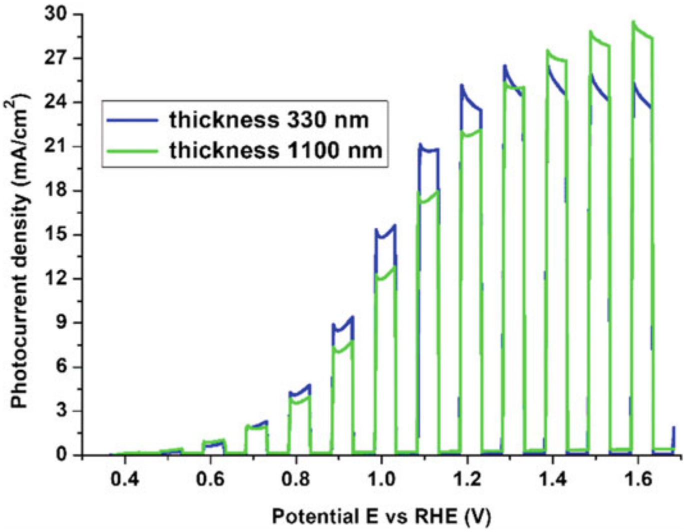

Fig. 14.18 Potentiodynamic measurements performed for WO_3 films

14.3.2 Perovskites-Based Photocatalysts Prepared by PLD

Perovskites materials having ABO_3 structure are of great interest in the photocatalytic field, especially due to their photocorossion stability and optical properties. Table 14.5 presented the experimental PLD parameters for obtaining different perovskite-based thin films with potential applications in photocatalysis.

14.3.2.1 $BiVO_4$

Bare $BiVO_4$ and Li-doped $BiVO_4$ were grown on ITO/YSZ substrates by PLD technique. The deposition temperature was 600 °C with a laser fluence of 1.8 J/cm^2. The thin films were used as photoanodes in a three-electrode configuration and their photoelectrochemical water splitting performances was studied. It was demonstrated that the Li doping of $BiVO_4$ improves the global efficiency of the reaction [116]. A very complex study related to photoelectrochemical activity of single layer $BiVO_4$/FTO and multiple layer $BiVO_4/SnO_2$/FTO, $BiVO_4/WO_3/SnO_2$/FTO thin films prepared by PLD was reported by Lopez et al. [117].

14.3.2.2 $BiFeO_3$

Both pristine $BiFeO_3$ and doped $BiFeO_3$ were grown by PLD on different types of substrates with numerous applications in photocatalysis, ferroelectric and

Table 14.5 Experimental conditions for different perovskite-based thin films prepared by PLD

Material	Substrate	Gain medium	λ (nm)/ ν (Hz)	P_{O2} (mbar)	T_S (°C)	Film thickness (nm)	Ref.
$BiVO_4$	ITO/YSZ	KrF	248/5	2×10^{-2}	600	n.s.	[116]
$BiVO_4$	FTO	KrF	248/10	2.6×10^{-1}	300	n.s.	[117]
Li-doped $BiVO_4$	ITO/YSZ	KrF	248/5	2×10^{-2}	600	n.s.	[116]
$BiFeO_3$	$SrRuO_3$/ $SrTiO_3$	KrF	248/10	2.6×10^{-1}	680	n.s.	[118]
$BiFeO_3$	Pt/TiO_2/ SiO_2/Si	Nd: YAG	355/2.5	7×10^{-2}	450	300	[119, 120]
$BiFeO_3$	$SrTiO_3$	Nd: YAG	355/2.5	10^{-2}	580	70	[119, 120]
$BiFeO_3$	Nb-doped $SrTiO_3$	KrF	248/5	4×10^{-2}– 4×10^{-1}	670	30–80	[121]
Ca- and Mn-doped $BiFeO_3$	$SrRuO_3$/ $SrTiO_3$	KrF	248/5	3×10^{-2}	700	n.s.	[122]
Sm-doped $BiFeO_3$	$SrTiO_3$	KrF	248/5	2.6×10^{-1}	600–670	n.s.	[123]
Ba-doped $BiFeO_3$	Nb-doped $SrTiO_3$	KrF	248/5	6.6×10^{-2}	650	ca. 80	[124]
Pr-doped $BiFeO_3$	Pt/SiO_2	Nd: YAG	355/5	n.s	n.s	ca. 200	[125]
Nb- and V-doped $BiFeO_3$	Pt/TiO_2/ SiO_2/Si	KrF	248/5	10^{-1}	690	150	[126]
$LaFeO_3$	$SrTiO_3$	KrF	248/10	4×10^{-5}	700	65	[127]
$LaFeO_3$	$SrTiO_3$	KrF	248/4	2×10^{-1}	670	32–53	[128]
$LaFeO_3$	$LaAlO_3$	KrF	248/10	4×10^{-5}	700	65	[127]
$LaFeO_3$	$GdScO_3$	KrF	248/5	1.3×10^{-1}	700	100	[129]
$LaFeO_3$	$SrTiO_3$	KrF	248/1	3.5×10^{-1}	540	20	[130]
Sr-doped $LaFeO_3$	Si	Nd: YAG	266/10	5×10^{-2} (air)	570	150–170	[131]

photovoltaic fields, as can be seen in Table 14.5. The intense research studies on $BiFeO_3$ have started after a large ferroelectric polarization (60 μC/cm^2) in thin films of $BiFeO_3$ prepared by PLD has been reported [132]. In the bulk form, the ferroelectric polarization is much lower because of the high oxygen vacancies content which leads to high dielectric losses An acceptable value of the ferroelectric polarization (20 μC/cm^2) was reported for bulk $BiFeO_3$ [133, 134]. Yun et al. have reported a giant ferroelectric polarization (ca. 150 μC/cm^2) for $BiFeO_3$ deposited on Pt/TiO_2/SiO_2/Si substrates by PLD with a solid-state Nd:YAG laser emitting at 355 nm [119, 120]. A high spontaneous polarization can improve the photocatalytic activities, because it can minimize the recombination of the free charge carriers, the effect being illustrate in Fig. 14.2. A detailed study concerning the effect of the ferroelectric properties on the photoelectrochemical water splitting activity of $BiFeO_3$ thin films prepared by PLD was reported by Song et al. They have obtained a value of the photocurrent density of 0.080 mA/cm^2 at 0 V versus Ag/AgCl [118]. Also, the unassisted photoelectrochemical water splitting over epitaxial $BiFeO_3$ thin films prepared by PLD was studied by Ji et al. [135]. As already discussed, PLD is a versatile laser-based technique which permits an excellent control and transfer of complex stoichiometries, and hence, numerous single- and co-doped $BiFeO_3$ perovskites were successfully grown on different substrates. Among the most used $BiFeO_3$ dopants are Ca, Mn [122], Sm [123], Ba [124], Pr [125] and Nb [126].

Y-Doped $BiFeO_3$

Recently, a detailed study related to the influence of the dopant concentration, as well as the structural strain of Y-doped $BiFeO_3$ (Y-BFO) thin films on the photoelectrochemical water splitting activity was reported by our group [136]. Starting from a $Bi_{0.957}Y_{0.03}FeO_3$ ceramic target, films with thickness in the range of 20–80 nm were deposited on conductive Nb-doped $SrTiO_3$ (001) substrates via PLD. Independently on the thickness, all the films show very well crystalized perovskites phase with no additional secondary phases, as can be observed in the obtained diffractograms presented in Ref. [136].

It was observed a clear tendency of decreasing the photocurrent density value with the increased film thickness. The highest value at 1.4 V versus RHE (0.72 mA/cm^2) was obtained for the thinnest Y-BFO film (22 nm) and it decreases with the increase of the film thickness. The same trend was obtained for the structural strain, the thinnest film showing the most strained structure. Also, the sample with the smallest thickness shows the higher absorbed photon-to-current conversion efficiency (APCE) [136].

Y-Doped $BiFeO_3$ Heterostructures

Using the same PLD experimental setup, bi-layer heterostructures based on BFO/Y-BFO were fabricated. Two different types of heterostructures were prepared by varying the dopant concentration of the material targets. Hence, the following ceramic targets were used for the deposition experiments: (1) $Bi_{0.957}Y_{0.03}FeO_3 \rightarrow$ Y-BFO3; (2) $Bi_{0.955}Y_{0.05}FeO_3 \rightarrow$ Y-BFO5 and (3) $BiFeO_3 \rightarrow$ BFO. They were grown on Nb-STON and Pt/Si substrates in sealed chamber without opening the reactor between the deposition processes. In this way, the contamination and the formation of undesired interfaces are avoided. The used laser was an excimer ArF with emission at 193 nm with a laser frequency of 5 Hz and the pressure inside the chamber was 0.13 mbar. For all the samples BFO was deposited on the top. The experimental conditions for the preparation of thins films are presented in Table 14.6.

Table 14.6 Experimental conditions for BFO/Y-BFO heterostructures prepared by PLD

Sample	Substrates	d_{t-c} (cm)	T_S (°C)	N_{pls}
(1) BFO/Y-BFO$_3$	PtSi	4	600	(500/500) × 3
(2) BFO/Y-BFO$_3$	STON	4	700	(500/500) × 3
(3) BFO/Y-BFO$_3$	STON	4	700	(1000/1000) × 3
(4) BFO/Y-BFO$_5$	STON	4	700	1000/1000
(5) BFO/Y-BFO$_5$	STON	4	700	(1000/1000) × 2
(6) BFO/Y-BFO$_5$	STON	4	700	1000/1000/1000

d_{t-c} (cm)—the distance between the substrate and the target; T_S (°C)—the substrate temperature; N_{pls}—the number of pulses (e.g. (500/500) × 3 represents a series of 500 pulses of Y-BFO deposited on STON and 500 pulses deposited on Y-BFO/STON, repeated 3 times)

Y (3%) Doped BiFeO$_3$ Heterostructures

A very important factor for the photoelectrochemical performance is the choice of the collecting substrate. Figure 14.19 presented the effect of the substrate on the potentiostatic measurements of the BFO/Y-BFO$_3$ heterostructures. Independently on the applied potential, when using STON substrate, the photocurrent density is much higher compared to PtSi substrates. For a more detailed analysis of these results, additional characterisations of the obtained thin films, especially on the growing mechanisms and the conductivity of the substrates. Nevertheless, at 0 V versus Ag/AgCl, the highest value of the photocurrent density is ca. 0.4 mA/cm^2, while by increasing the applied potential to 0.4 V versus Ag/AgCl it increases almost three times. Also, the photocurrent's spikes are diminished by increasing the external applied potential, meaning that the recombination of the charge carriers is decreased. By increasing the thickness of the film, the progenerated current decreases as well, as can be observed in Fig. 14.20. This behaviour probably is correlated to the structural strain, which decreases with the increase of the film thickness.

Y (5%) Doped BiFeO$_3$ Heterostructures

The photoelectrochemical water splitting activity of heterostructures based on BFO/Y-BFO$_5$ was tested in an strong alkaline solution of NaOH (pH = 13). Figure 14.21 presented the potentiodynamic measurements under dark conditions obtained for different BFO/Y-BFO$_5$ thin films with different thicknesses. All the samples are catalitically inactive for the water splitting reaction without irradiation, the current being zero.

The photocurrent increases under light irradiation with a maximum photocurrent density of ca. 0.8 mA/cm^2 at 1.8 V versus RHE. It decreases with the increase of the film thickness, as can be observed in Fig. 14.22.

All the tested samples show excellent stability for 900 s in strong alkaline solution under an applied potential of 0.4 V versus Ag/AgCl, the results being presented in Fig. 14.23.

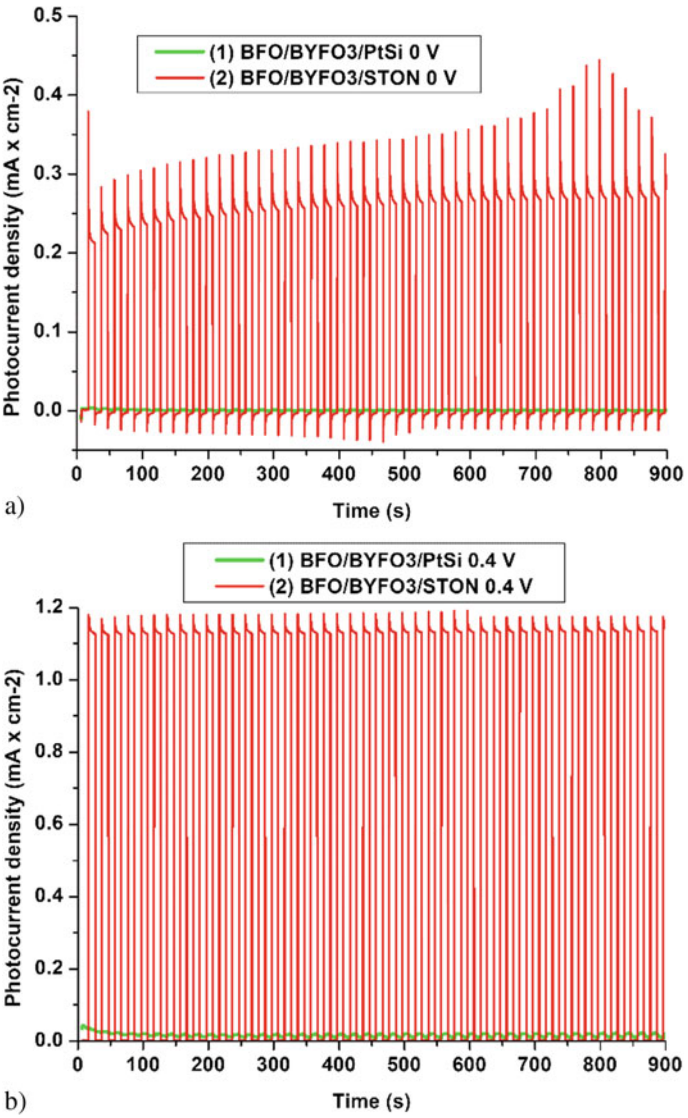

Fig. 14.19 Potentiostatic measurements obtained for BFO/Y-BFO_3 heterostructures grown on different substrates: **a** under 0 V versus Ag/AgCl; **b** under 0.4 V versus Ag/AgCl

$KBiFe_2O_5$

$KBiFe_2O_5$ (KBFO) was grown on STON substrates via PLD using an excimer laser emitting at 193 nm. The oxygen pressure inside the chamber was 0.13 mbar. Table 14.7 presented the experimental conditions for thin films preparation.

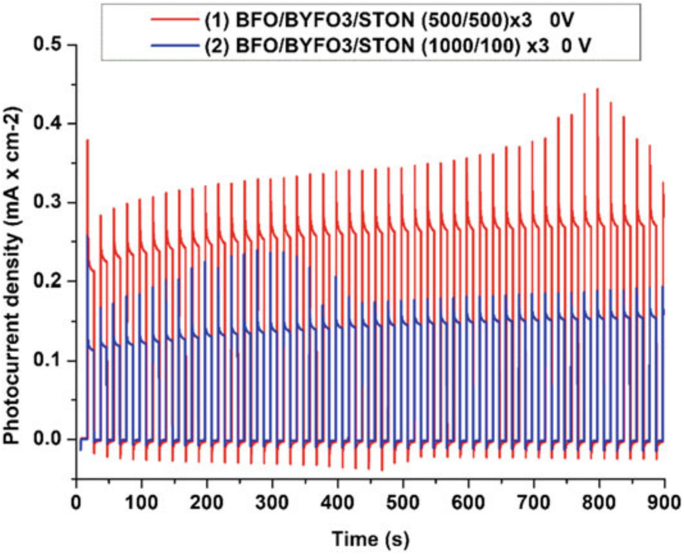

Fig. 14.20 Potentiostatic measurements obtained for BFO/Y-BFO$_3$ heterostructures with different thicknesses at 0 V versus Ag/AgCl

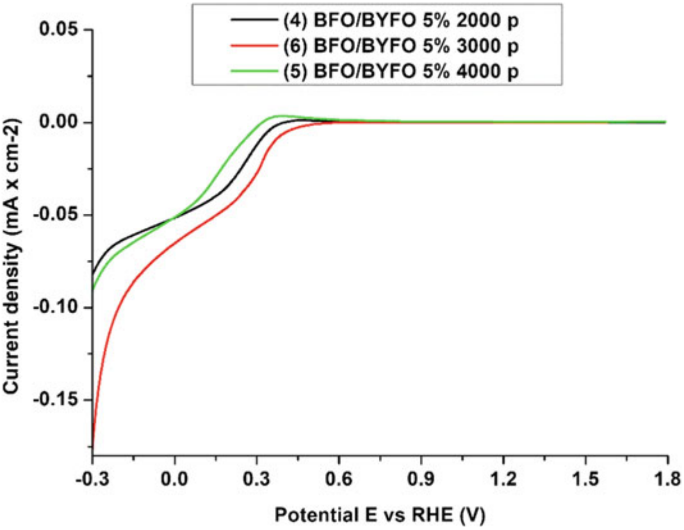

Fig. 14.21 Potentiodynamic measurements obtained for BFO/Y-BFO$_5$ heterostructures without irradiation

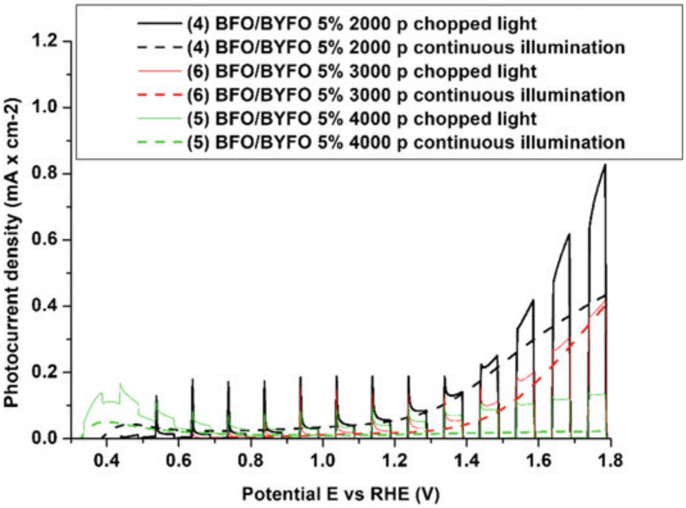

Fig. 14.22 Potentiodynamic measurements obtained for BFO/Y-BFO$_5$ heterostructures with 404 nm irradiation

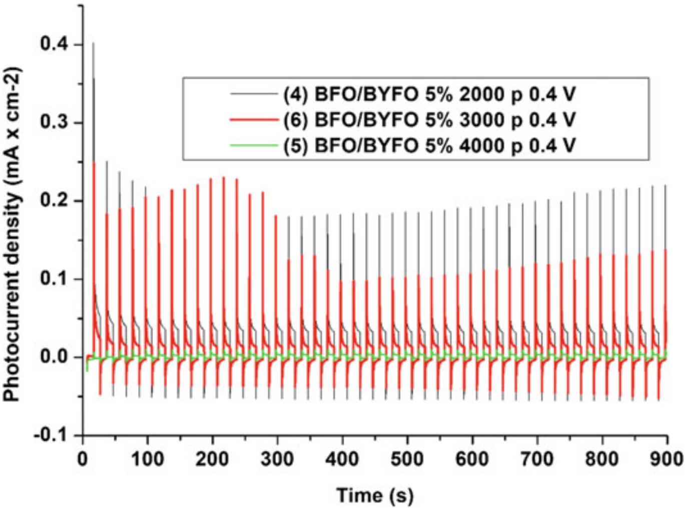

Fig. 14.23 Potentiostatic measurements obtained for BFO/Y-BFO$_5$ heterostructures with different thicknesses at 0.4 V versus Ag/AgCl

The photoelectrochemical measurements for water splitting reaction were performed using a three-electrode system connected to a sealed quartz cell. For studying of the photoelectrochemical activity, the samples based on KBFO grown on STON were used as working electrodes, the counter electrode was made of Pt

Table 14.7 Experimental conditions for KBFO/STON thin films prepared by PLD

Sample	Substrates	d_{t-c} (cm)	T_S (°C)	N_{pls}
(1) KBFO	STON	4	700	3000
(2) KBFO	STON	4	700	12,300
(3) KBFO	STON	4	700	15,000
(4) KBFO	STON	4	700	15,000

and the reference electrode was Ag/AgCl (Ag/AgCl 3.5 M KCl). The electrical contact for working electrode was made by contacting a conductive wire on the back of the STON substrate with silver paste. The external field was applied using a Methrom AutoLAb model PGSTAT 302 N and the measurements were recorded with NOVA software. All measurements were performed in strong alkaline solution of NaOH (0.1 M; pH = 13 pH). Before measurements, the back and the sides of KBFO samples were electrically insulated with a noncorrosive resin to avoid the short circuit. The samples were irradiated with a laser diode (405 nm) having an output power of ~5 mW.

The potentiodynamic measurements were performed in the applied potential range of −0.4–2 V versus RHE to study the influence of the film thickness for both HER and OER. As can be seen in Fig. 14.24, all samples show both cathodic and anodic photocurrents. The photoelectrochemical properties of KBFO films are strongly dependent on the film thickness, with the photocurrent density J_{ph} increasing with the thickness of the films. The KBFO/STON film having 104 nm shows at 2 V versus RHE a maximum value of the photogenerated current of ~0.085 mA/cm^2. Similar values of J_{ph} were reported for the photodegradation of methylene blue (MB) under visible light irradiation using poly-crystalline KBFO prepared via citrate combustion technique [137]. This value is much higher compared to the thinnest sample (30 nm) which shows the maximum J_{ph} of ~0.019 mA/cm^2 at 2 V versus RHE.

The same trend is observed for the values of the onset potential as a function of KBFO films thickness as can be seen in Fig. 14.25. A negative onset potential value of −0.152 V was recorded for 30 nm KBFO sample. Increasing the film thickness, the onset potential is shifted to higher values, more precisely 0.189 V for 80 nm and 0.367 V for 104 nm, respectively.

The potentiostatic measurements were performed to study the stability of the KBFO/STON samples under strong alkaline conditions. As can be seen in Fig. 14.26 all the samples show excellent stability at an external applied potential of 1.4 V versus RHE during 900 s. In the case of the thickest sample, the peaks are very sharp indicating a high recombination of the free charge carriers [138].

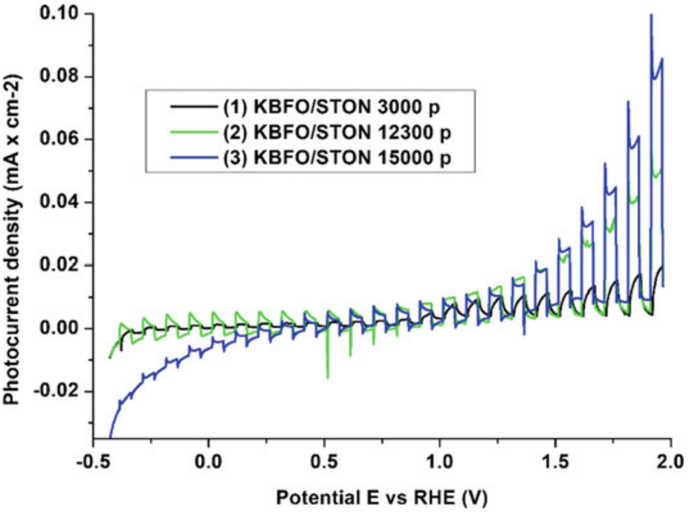

Fig. 14.24 Potentiodynamic measurements under chopped irradiation for KBFO/STON thin films having different thicknesses

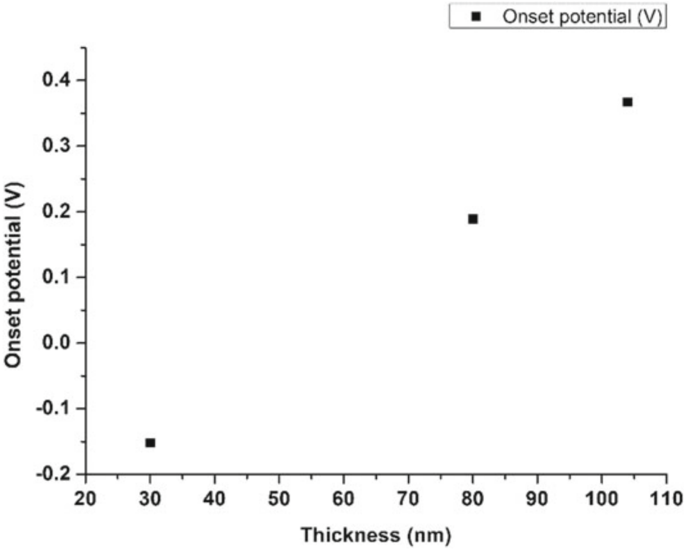

Fig. 14.25 Onset potential versus KBFO thickness

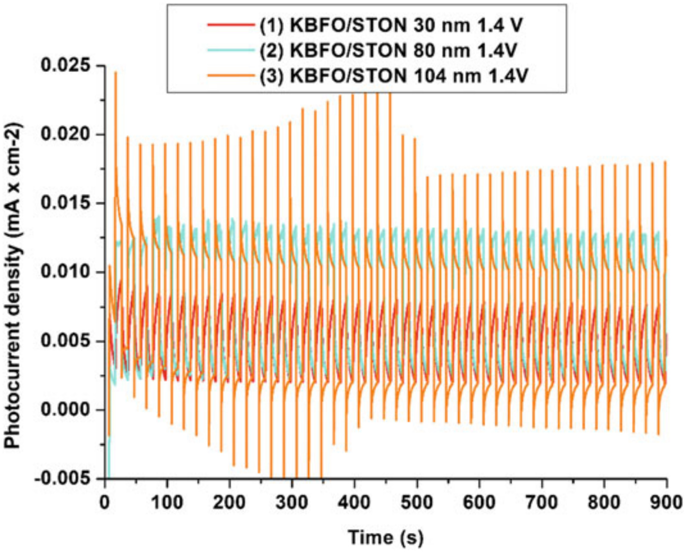

Fig. 14.26 Potentiostatic measurements under chopped irradiation for KBFO/STON thin films having different thicknesses

14.4 Conclusions

It was proven here that the laser-based material processing techniques, namely laser pyrolysis and pulsed laser deposition, are versatile and reproducible techniques in controlling the physical and chemical properties of the resulted nanostructures (nanopowders, thin films). Having the possibility to vary a wide range of the experimental parameters such as laser power density, the working gas pressure in the reaction chamber, the flow of gas/vapour introduced into the reaction, laser fluence or deposition temperature, makes these techniques suitable for tailoring or enhancing certain functional proprieties of different oxide materials. Synthesizing, the laser pyrolysis and pulsed laser deposition techniques have the following intrinsic advantages:

- fast, single-step methods with high accuracy in controlling different experimental parameters.
- the material processing is performed in a sealed reactor and in this way the external contamination is avoided. Also, the obtaining process can occur in both reactive or inert gasses;
- precise stoichiometric transfer for all kinds of materials (complex stoichiometry, organo-metallic compounds);
- high production rates (up to kg/h nanopowder rate production for LP, 1–10 Å/pulse thin film growth for PLD) with excellent control of the functional properties of the resulted nanomaterials.

The following conclusions can be drawn from the analysis of the three series of TiO_2-based nanopowders (decorated with Ag, coupled with SnO_2 and doped with V) produced by LP technique:

- photocatalytic degradation of MO in an aqueous solution is influenced by factors such as morphology (the best result was obtained for the TiO_2@Ag sample as compared with all the TiO_2–SnO_2 samples) and degree of doping (the efficiency of degradation increases by increasing the doping level with tin).
- for the degradation of CH_3OH, titania doped with vanadium presents an improvement of the photocatalytic properties up to a degree of an optimum level (1.02 at.%), beyond that the efficiency of degradation of pollutant decreased.
- all three categories of samples present improved photocatalytic properties (by loading, coupling, or doping process) as compare with pure TiO_2 or P25 commercial sample, demonstrating de versatility of LP method for obtaining titania-modified photocatalysts with high visible light photocatalytic activity.

Using Pulsed Laser Deposition technique both simple and complex stoichiometry oxide materials can be processed into thin films form with tailored functional properties. Employing doping or structural strain engineering strategies, it is possible to surpass the performances of the host materials. Thus, simple stoichiometry oxides such as TiO_2, ZnO or WO_3 thin films have been deposited for achieving superior photoelectrochemical water splitting efficiency. For example, a maximum value of the photocurrent density of 30 mA/cm^2 at 1.59 V versus RHE has been obtained for WO_3/Pt/Si (100) thin films. Moreover, the possibility to engineer the crystalline structure of complex stoichiometry materials such as ABO_3-type perovskites, for enhancing the photoelectrochemical water splitting activity adds a new dimension to the extended possibilities of this material processing technique.

References

1. Benck JD, Hellstern TR, Kibsgaard J, Chakthranont P, Jaramillo TF (2014) Catalyzing the hydrogen evolution reaction (HER) with molybdenum sulfide nanomaterials. ACS Catal 4:3957–3971. https://doi.org/10.1021/cs500923c
2. Kim B, Kim JS, Kim H, Park I, Seong WM, Kang K (2019) Amorphous multinary phyllosilicate catalysts for electrochemical water oxidation. J Mater Chem A 7:18380–18387. https://doi.org/10.1039/C9TA05599A
3. Hu C, Zhang L, Gong J (2019) Recent progress made in the mechanism comprehension and design of electrocatalysts for alkaline water splitting. Energy Environ Sci 12:2620–2645. https://doi.org/10.1039/C9EE01202H
4. Navarro Yerga RM, Alvarez-Galván MC, Vaquero F, Arenales J, Fierro JLG (2013) Hydrogen production from water splitting using photo-semiconductor catalysts. In: Renewable Hydrogen Technologies, Elsevier, pp 43–61, ISBN 978–0-444-56352-1
5. Linsebigler AL, Lu G, Yates JT (1995) Photocatalysis on TiO_2 surfaces: principles, mechanisms, and selected results. Chem Rev 95:735–758. https://doi.org/10.1021/cr00035a013

6. Chiu Y-H, Chang T-FM, Chen C-Y, Sone M, Hsu Y-J (2019) Mechanistic insights into photodegradation of organic dyes using heterostructure photocatalysts. Catalysts 9:430. https://doi.org/10.3390/catal9050430
7. Lee MS, Hong S-S, Mohseni M (2005) Synthesis of photocatalytic nanosized TiO_2–Ag particles with sol–gel method using reduction agent. J Mol Catal Chem 242:135–140. https://doi.org/10.1016/j.molcata.2005.07.038
8. Yu D-H, Yu X, Wang C, Liu X-C, Xing Y (2012) Synthesis of natural cellulose-templated TiO_2/Ag nanosponge composites and photocatalytic properties. ACS Appl Mater Interfaces 4:2781–2787. https://doi.org/10.1021/am3004363
9. Albiter E, Valenzuela MA, Alfaro S, Valverde-Aguilar G, Martínez-Pallares FM (2015) Photocatalytic deposition of Ag nanoparticles on TiO_2: metal precursor effect on the structural and photoactivity properties. J Saudi Chem Soc 19:563–573. https://doi.org/10.1016/j.jscs.2015.05.009
10. Méndez-Medrano MG, Kowalska E, Lehoux A, Herissan A, Ohtani B, Bahena D, Briois V, Colbeau-Justin C, Rodríguez-López JL, Remita H (2016) Surface modification of TiO_2 with Ag nanoparticles and CuO nanoclusters for application in photocatalysis. J Phys Chem C 120:5143–5154. https://doi.org/10.1021/acs.jpcc.5b10703
11. Zhang Y, Fu F, Li Y, Zhang D, Chen Y (2018) One-step synthesis of Ag@TiO_2 nanoparticles for enhanced photocatalytic performance. Nanomaterials 8:1032. https://doi.org/10.3390/nano8121032
12. Zhou R, Lin S, Zong H, Huang T, Li F, Pan J, Cui J (2017) Continuous synthesis of Ag/TiO_2 nanoparticles with enhanced photocatalytic activity by pulsed laser ablation. J Nanomater 2017:1–9. https://doi.org/10.1155/2017/4604159
13. Zhang Z, Ma Y, Bu X, Wu Q, Hang Z, Dong Z, Wu X (2018) Facile One-step synthesis of TiO_2/Ag/SnO_2 ternary heterostructures with enhanced visible light photocatalytic activity. Sci Rep 8:10532. https://doi.org/10.1038/s41598-018-28832-w
14. Kulkarni RM, Malladi RS, Hanagadakar MS, Doddamani MR, Bhat UK (2016) Ag-TiO_2 nanoparticles for photocatalytic degradation of lomefloxacin. Desalination Water Treat 57:16111–16118. https://doi.org/10.1080/19443994.2015.1076352
15. Hassan SM, Ahmed AI, Mannaa MA (2019) Preparation and characterization of SnO_2 Doped TiO_2 nanoparticles: effect of phase changes on the photocatalytic and catalytic activity. J Sci Adv Mater Devices 4:400–412. https://doi.org/10.1016/j.jsamd.2019.06.004
16. Toloman D, Pana O, Stefan M, Popa A, Leostean C, Macavei S, Silipas D, Perhaita I, Lazar MD, Barbu-Tudoran L (2019) Photocatalytic activity of SnO_2–TiO_2 composite nanoparticles modified with PVP. J Colloid Interface Sci 542:296–307. https://doi.org/10.1016/j.jcis.2019.02.026
17. Nithyadevi D, Rajendrakumar RT (2013) Synthesis, characterization and photocatalytic properties of TiO_2–SnO_2 composite nanoparticles. Adv Mater Res 678:373–377. https://doi.org/10.4028/www.scientific.net/AMR.678.373
18. Vinod VTP, Miroslav Č (2015) Visible-light-driven SnO_2/TiO_2 nanotube nanocomposite for textile effluent degradation. https://doi.org/10.1039/C4RA13434F
19. Rossi G, Pasquini L, Catone D, Piccioni A, Patelli N, Paladini A, Molinari A, Caramori S, O’Keeffe P, Boscherini F (2018) charge carrier dynamics and visible light photocatalysis in vanadium-doped TiO_2 nanoparticles. Appl Catal B Environ 237:603–612. https://doi.org/10.1016/j.apcatb.2018.06.011
20. Zhou W, Liu Q, Zhu Z, Zhang J (2010) Preparation and properties of vanadium-doped TiO_2 photocatalysts. J Phys Appl Phys 43:035301. https://doi.org/10.1088/0022-3727/43/3/035301
21. Songara S, Patra MK, Manoth M, Saini L, Gupta V, Gowd GS, Vadera SR, Kumar N (2010) Synthesis and studies on photochromic properties of vanadium doped TiO_2 nanoparticles. J Photochem Photobiol Chem 209:68–73. https://doi.org/10.1016/j.jphotochem.2009.11.001
22. Lin W-C, Lin Y-J (2012) Effect of vanadium(IV)-doping on the visible light-induced catalytic activity of titanium dioxide catalysts for methylene blue degradation. Environ Eng Sci 29:447–452. https://doi.org/10.1089/ees.2010.0350

23. Buch J, Hammond B (2020) Photobiomodulation of the visual system and human health. Int J Mol Sci 21:8020. https://doi.org/10.3390/ijms21218020
24. Moroz P, Boddy A, Zamkov M (2018) Challenges and prospects of photocatalytic applications utilizing semiconductor nanocrystals. Front Chem 6. https://doi.org/10.3389/fchem.2018.00353
25. Djurišić BA, Hang Leung Y, Ng AMC (2014) Strategies for improving the efficiency of semiconductor metal oxide photocatalysis. Mater Horiz 1:400–410. https://doi.org/10.1039/C4MH00031E
26. Basics and advanced developments in photocatalysis—a review. Int J Hydrol 2. https://doi.org/10.15406/ijh.2018.02.00122
27. Sangchay W (2016) The self-cleaning and photocatalytic properties of TiO_2 doped with SnO_2 thin films preparation by sol–gel method. Energy Procedia 89:170–176. https://doi.org/10.1016/j.egypro.2016.05.023
28. Bessergenev VG, Khmelinskii IV, Pereira RJF, Krisuk VV, Turgambaeva AE, Igumenov IK (2002) Preparation of TiO_2 films by CVD method and its electrical, structural and optical properties. Vacuum 64:275–279. https://doi.org/10.1016/S0042-207X(01)00318-9
29. Kammler HK, Mädler L, Pratsinis SE (2001) Flame synthesis of nanoparticles. Chem Eng Technol 24:583–596. https://doi.org/10.1002/1521-4125(200106)24:6%3c583:AID-CEAT583%3e3.0.CO;2-H
30. Caricato AP, Manera MG, Martino M, Rella R, Romano F, Spadavecchia J, Tunno T, Valerini D (2007) Uniform thin films of TiO_2 nanoparticles deposited by matrix-assisted pulsed laser evaporation. Appl Surf Sci 253:6471–6475. https://doi.org/10.1016/j.apsusc.2007.01.113
31. Scarisoreanu M, Ilie AG, Goncearenco E, Banici AM, Morjan IP, Dutu E, Tanasa E, Fort I, Stan M, Mihailescu CN et al (2020) Ag, Au and Pt decorated TiO_2 biocompatible nanospheres for UV & Vis photocatalytic water treatment. Appl Surf Sci 509:145217. https://doi.org/10.1016/j.apsusc.2019.145217
32. Ilie AG, Scarisoreanu M, Dutu E, Dumitrache F, Banici A-M, Fleaca CT, Vasile E, Mihailescu I (2018) Study of phase development and thermal stability in as synthesized TiO_2 nanoparticles by laser pyrolysis: ethylene uptake and oxygen enrichment. Appl Surf Sci 427:798–806. https://doi.org/10.1016/j.apsusc.2017.08.041
33. Morjan IP, Morjan I, Ilie A, Scarisoreanu M, Gavrila L, Dumitrache F, Vasile E, Turcu R, Miron C (2017) The study of nitrogen inclusion in carbon nanotubes obtained by catalytic laser-induced chemical vapour deposition (C-LCVD). Appl Surf Sci 425:440–447. https://doi.org/10.1016/j.apsusc.2017.06.296
34. Gavrila-Florescu L, Dumitrache F, Balas M, Fleaca CT, Scarisoreanu M, Morjan IP, Dutu E, Ilie A, Banici A-M, Locovei C et al (2017) Synthesis of Fe-based Core@ZnO shell nanopowders by laser pyrolysis for biomedical applications. Appl Phys A 123:802. https://doi.org/10.1007/s00339-017-1416-1
35. Scarisoreanu M, Fleaca C, Morjan I, Niculescu A-M, Luculescu C, Dutu E, Ilie A, Morjan I, Florescu LG, Vasile E et al (2017) High photoactive TiO_2/SnO_2 nanocomposites prepared by laser pyrolysis. Appl Surf Sci 418:491–498. https://doi.org/10.1016/j.apsusc.2016.12.122
36. Kuncser VE, Schinteie GA, Kuncser AC, Leca A, Scarisoreanu M, Morjan I, Filoti G (2017) Physical mechanisms of exchange coupling effects in nanoparticulate diluted magnetic oxides obtained by laser pyrolysis. J Phys Chem C 121:9063–9069. https://doi.org/10.1021/acs.jpcc.7b01500
37. Wang J, Tapio K, Habert A, Sorgues S, Colbeau-Justin C, Ratier B, Scarisoreanu M, Toppari J, Herlin-Boime N, Bouclé J (2016) Influence of nitrogen doping on device operation for TiO_2-based solid-state dye-sensitized solar cells: photo-physics from materials to devices. Nanomaterials 6:35. https://doi.org/10.3390/nano6030035
38. Fleaca CT, Scarisoreanu M, Morjan I, Luculescu C, Niculescu A-M, Badoi A, Vasile E, Kovacs G (2015) Laser oxidative pyrolysis synthesis and annealing of TiO_2 nanoparticles embedded in carbon-silica shells/matrix. Appl Surf Sci 336:226–233. https://doi.org/10.1016/j.apsusc.2014.11.106

39. Dutu E, Dumitrache F, Fleaca CT, Morjan I, Gavrila-Florescu L, Morjan IP, Sandu I, Scarisoreanu M, Luculescu C, Niculescu A-M et al (2015) Metallic tin-based nanoparticles synthesis by laser pyrolysis: parametric studies focused on the decreasing of the crystallite size. Appl Surf Sci 336:290–296. https://doi.org/10.1016/j.apsusc.2014.12.092
40. Scarisoreanu M, Morjan I, Fleaca C-T, Morjan IP, Niculescu A-M, Dutu E, Badoi A, Birjega R, Luculescu C, Vasile E et al (2015) Synthesis and optical properties of TiO_2-based magnetic nanocomposites. Appl Surf Sci 336:335–342. https://doi.org/10.1016/j.apsusc.2014.12.125
41. Scarisoreanu M, Morjan I, Alexandrescu R, Fleaca CT, Badoi A, Dutu E, Niculescu A-M, Luculescu C, Vasile E, Wang J et al (2014) Enhancing the visible light absorption of titania nanoparticles by S and C doping in a single-step process. Appl Surf Sci 302:11–18. https://doi.org/10.1016/j.apsusc.2014.01.135
42. Morjan IP, Alexandrescu R, Morjan I, Luculescu C, Vasile E, Osiceanu P, Scarisoreanu M, Demian G (2013) Effect of the manufacturing parameters on the structure of nitrogen-doped carbon nanotubes produced by catalytic laser-induced chemical vapor deposition. J Nanopart Res 15:2045. https://doi.org/10.1007/s11051-013-2045-z
43. Scarisoreanu M, Alexandrescu R, Morjan I, Birjega R, Luculescu C, Popovici E, Dutu E, Vasile E, Danciu V, Herlin-Boime N (2013) Structural evolution and optical properties of C-coated TiO_2 nanoparticles prepared by laser pyrolysis. Appl Surf Sci 278:295–300. https://doi.org/10.1016/j.apsusc.2013.01.052
44. Alexandrescu R, Morjan I, Dumitrache F, Scarisoreanu M, Fleaca CT, Morjan IP, Barbut AD, Birjega R, Prodan G (2013) Development of TiO_2 and TiO_2/Fe-based polymeric nanocomposites by single-step laser pyrolysis. Appl Surf Sci 278:305–312. https://doi.org/10.1016/j.apsusc.2012.12.094
45. Alexandrescu R, Morjan I, Dumitrache F, Birjega R, Fleaca C, Morjan I, Scarisoreanu M, Luculescu CR, Dutu E, Kuncser V et al (2012) Laser processing issues of nanosized intermetallic Fe–Sn and metallic Sn particles. Appl Surf Sci 258:9421–9426. https://doi.org/10.1016/j.apsusc.2012.01.159
46. Alexandrescu R, Morjan I, Scarisoreanu M, Birjega R, Fleaca C, Soare I, Gavrila L, Ciupina V, Kylberg W, Figgemeier E (2010) Development of the IR laser pyrolysis for the synthesis of iron-doped TiO_2 nanoparticles: structural properties and photoactivity. Infrared Phys Technol 53:94–102. https://doi.org/10.1016/j.infrared.2009.10.004
47. Morjan I, Alexandrescu R, Scarisoreanu M, Fleaca C, Dumitrache F, Soare I, Popovici E, Gavrila L, Vasile E, Ciupina V et al (2009) Controlled manufacturing of nanoparticles by the laser pyrolysis: application to cementite iron carbide. Appl Surf Sci 255:9638–9642. https://doi.org/10.1016/j.apsusc.2009.04.125
48. Alexandrescu R, Scarisoreanu M, Morjan I, Birjega R, Fleaca C, Luculescu C, Soare I, Cretu O, Negrila CC, Lazarescu N et al (2009) Preparation and characterization of nitrogen-doped TiO_2 nanoparticles by the laser pyrolysis of N_2O-containing gas mixtures. Appl Surf Sci 255:5373–5377. https://doi.org/10.1016/j.apsusc.2008.08.046
49. Alexandrescu R, Dumitrache F, Morjan I, Sandu I, Savoiu M, Voicu I, Fleaca C, Piticescu R (2004) TiO_2 nanosized powders by $TiCl_4$ laser pyrolysis. Nanotechnology 15:537–545. https://doi.org/10.1088/0957-4484/15/5/023
50. Fujishima A, Honda K (1972) Electrochemical photolysis of water at a semiconductor electrode. Nature 238:37–38. https://doi.org/10.1038/238037a0
51. Abe R (2010) Recent progress on photocatalytic and photoelectrochemical water splitting under visible light irradiation. J Photochem Photobiol C Photochem Rev 11:179–209. https://doi.org/10.1016/j.jphotochemrev.2011.02.003
52. Wang G, Wang H, Ling Y, Tang Y, Yang X, Fitzmorris RC, Wang C, Zhang JZ, Li Y (2011) Hydrogen-treated TiO_2 nanowire arrays for photoelectrochemical water splitting. Nano Lett 11:3026–3033. https://doi.org/10.1021/nl201766h
53. Wang Z, Lang X (2018) Visible light photocatalysis of dye-sensitized TiO_2: the selective aerobic oxidation of amines to imines. Appl Catal B Environ 224:404–409. https://doi.org/10.1016/j.apcatb.2017.10.002

54. Choi SK, Yang HS, Kim JH, Park H (2012) Organic dye-sensitized TiO_2 as a versatile photocatalyst for solar hydrogen and environmental remediation. Appl Catal B Environ 121–122:206–213. https://doi.org/10.1016/j.apcatb.2012.04.011
55. Khlyustova A, Sirotkin N, Kusova T, Kraev A, Titov V, Agafonov A (2020) Doped TiO_2: the effect of doping elements on photocatalytic activity. Mater. Adv. 1:1193–1201. https://doi.org/10.1039/D0MA00171F
56. Khan SUM, Al-Shahry M, Ingler WB (2002) Efficient photochemical water splitting by a chemically modified N-TiO_2. Science 297:2243–2245. https://doi.org/10.1126/science.1075035
57. Sakthivel S, Kisch H (2003) Daylight photocatalysis by carbon-modified titanium dioxide. Angew Chem Int Ed 42:4908–4911. https://doi.org/10.1002/anie.200351577
58. Umebayashi T, Yamaki T, Itoh H, Asai K (2002) Band gap narrowing of titanium dioxide by sulfur doping. Appl Phys Lett 81:454–456. https://doi.org/10.1063/1.1493647
59. Umebayashi T, Yamaki T, Yamamoto S, Miyashita A, Tanaka S, Sumita T, Asai K (2003) Sulfur-doping of rutile-titanium dioxide by ion implantation: photocurrent spectroscopy and first-principles band calculation studies. J Appl Phys 93:5156–5160. https://doi.org/10.1063/1.1565693
60. Irie H, Washizuka S, Yoshino N, Hashimoto K (2003) Visible-light induced hydrophilicity on nitrogen-substituted titanium dioxide films. Chem Commun 1298–1299. https://doi.org/10.1039/B302975A
61. Di Valentin C, Pacchioni G, Selloni A, Livraghi S, Giamello E (2005) Characterization of paramagnetic species in N-doped TiO_2 powders by EPR spectroscopy and DFT calculations. J Phys Chem B 109:11414–11419. https://doi.org/10.1021/jp051756t
62. Lu F, Cai W, Zhang Y (2008) ZnO hierarchical micro/nanoarchitectures: solvothermal synthesis and structurally enhanced photocatalytic performance. Adv Funct Mater 18:1047–1056. https://doi.org/10.1002/adfm.200700973
63. Wang L, Chang L, Zhao B, Yuan Z, Shao G, Zheng W (2008) Systematic investigation on morphologies, forming mechanism, photocatalytic and photoluminescent properties of ZnO nanostructures constructed in ionic liquids. Inorg Chem 47:1443–1452. https://doi.org/10.1021/ic701094a
64. Yan H, Hou J, Fu Z, Yang B, Yang P, Liu K, Wen M, Chen Y, Fu S, Li F (2009) Growth and photocatalytic properties of one-dimensional ZnO nanostructures prepared by thermal evaporation. Mater Res Bull 44:1954–1958. https://doi.org/10.1016/j.materresbull.2009.06.014
65. Johar MA, Afzal RA, Alazba AA, Manzoor U (2015) Photocatalysis and bandgap engineering using ZnO nanocomposites. Adv Mater Sci Eng 2015:1–22. https://doi.org/10.1155/2015/934587
66. Mirzaeifard Z, Shariatinia Z, Jourshabani M, Rezaei Darvishi SM (2020) ZnO photocatalyst revisited: effective photocatalytic degradation of emerging contaminants using S-doped ZnO nanoparticles under visible light radiation. Ind Eng Chem Res 59:15894–15911. https://doi.org/10.1021/acs.iecr.0c03192
67. Kalanur SS (2019) Structural, optical, band edge and enhanced photoelectrochemical water splitting properties of tin-doped WO_3. Catalysts 9:456. https://doi.org/10.3390/catal9050456
68. Liu X, Zhai H, Wang P, Zhang Q, Wang Z, Liu Y, Dai Y, Huang B, Qin X, Zhang X (2019) Synthesis of a WO_3 photocatalyst with high photocatalytic activity and stability using synergetic internal Fe^{3+} doping and superficial Pt loading for ethylene degradation under visible-light irradiation. Catal Sci Technol 9:652–658. https://doi.org/10.1039/C8CY02375A
69. Li W, Zhan F, Li J, Liu C, Yang Y, Li Y, Chen Q (2015) Enhancing photoelectrochemical water splitting by aluminum-doped plate-like WO_3 electrodes. Electrochim Acta 160:57–63. https://doi.org/10.1016/j.electacta.2015.01.095
70. Li N, Teng H, Zhang L, Zhou J, Liu M (2015) Synthesis of Mo-doped WO_3 nanosheets with enhanced visible-light-driven photocatalytic properties. RSC Adv 5:95394–95400. https://doi.org/10.1039/C5RA17098B

71. Huang H, Liu L, Zhang Y, Tian N (2015) Novel $BiIO_4/BiVO_4$ composite photocatalyst with highly improved visible-light-induced photocatalytic performance for rhodamine B degradation and photocurrent generation. RSC Adv 5:1161–1167. https://doi.org/10.1039/C4RA12916D
72. Hu Y, Fan J, Pu C, Li H, Liu E, Hu X (2017) Facile synthesis of double cone-shaped $Ag_4V_2O_7/BiVO_4$ nanocomposites with enhanced visible light photocatalytic activity for environmental purification. J Photochem Photobiol Chem 337:172–183. https://doi.org/10.1016/j.jphotochem.2016.12.035
73. Kudo A, Omori K, Kato H (1999) A novel aqueous process for preparation of crystal form-controlled and highly crystalline $BiVO_4$ powder from layered vanadates at room temperature and its photocatalytic and photophysical properties. J Am Chem Soc 121:11459–11467. https://doi.org/10.1021/ja992541y
74. Fan H, Wang D, Wang L, Li H, Wang P, Jiang T, Xie T (2011) Hydrothermal synthesis and photoelectric properties of $BiVO_4$ with different morphologies: an efficient visible-light photocatalyst. Appl Surf Sci 257:7758–7762. https://doi.org/10.1016/j.apsusc.2011.04.025
75. Regmi C, Kshetri YK, Kim T-H, Pandey RP, Lee SW (2017) Visible-light-induced Fe-doped $BiVO_4$ photocatalyst for contaminated water treatment. Mol Catal 432:220–231. https://doi.org/10.1016/j.mcat.2017.02.004
76. Regmi C, Kshetri YK, Pandey RP, Kim T-H, Gyawali G, Lee SW (2019) Understanding the multifunctionality in Cu-doped $BiVO_4$ semiconductor photocatalyst. J Environ Sci 75:84–97. https://doi.org/10.1016/j.jes.2018.03.005
77. Guo M, Wang Y, He Q, Wang W, Wang W, Fu Z, Wang H (2015) Enhanced photocatalytic activity of S-doped $BiVO_4$ photocatalysts. RSC Adv 5:58633–58639. https://doi.org/10.1039/C5RA07603J
78. Tian X, Zhu Y, Zhang W, Zhang Z, Hua R (2019) Preparation and photocatalytic properties of Mo-doped $BiVO_4$. J Mater Sci Mater Electron 30:19335–19342. https://doi.org/10.1007/s10854-019-02295-9
79. Eerenstein W, Mathur ND, Scott JF (2006) Multiferroic and magnetoelectric materials. Nature 442:759–765. https://doi.org/10.1038/nature05023
80. Fischer P, Polomska M, Sosnowska I, Szymanski M (1980) Temperature dependence of the crystal and magnetic structures of $BiFeO_3$. J Phys C Solid State Phys 13:1931–1940. https://doi.org/10.1088/0022-3719/13/10/012
81. Kotnala RK, Shah J (2015) Chapter 4—ferrite materials: nano to spintronics regime. In: Buschow KHJ (ed) Handbook of magnetic materials, Elsevier, vol 23, pp 291–379
82. Chu Y-H, Martin LW, Holcomb MB, Ramesh R (2007) Controlling magnetism with multiferroics. Mater Today 10:16–23. https://doi.org/10.1016/S1369-7021(07)70241-9
83. Alexe M, Hesse D (2011) Tip-enhanced photovoltaic effects in bismuth ferrite. Nat Commun 2:256. https://doi.org/10.1038/ncomms1261
84. Liu Z, Qi Y, Lu C (2010) High efficient ultraviolet photocatalytic activity of $BiFeO_3$ nanoparticles synthesized by a chemical coprecipitation process. J Mater Sci Mater Electron 21:380–384. https://doi.org/10.1007/s10854-009-9928-x
85. Mushtaq F, Chen X, Hoop M, Torlakcik H, Pellicer E, Sort J, Gattinoni C, Nelson BJ, Pané S (2018) Piezoelectrically enhanced photocatalysis with $BiFeO_3$ nanostructures for efficient water remediation. iScience 4:236–246. https://doi.org/10.1016/j.isci.2018.06.003
86. Haruna A, Abdulkadir I, Idris SO (2020) Photocatalytic activity and doping effects of $BiFeO_3$ nanoparticles in model organic dyes. Heliyon 6:e03237. https://doi.org/10.1016/j.heliyon.2020.e03237
87. Li S, Jing L, Fu W, Yang L, Xin B, Fu H (2007) Photoinduced charge property of nanosized perovskite-type $LaFeO_3$ and its relationships with photocatalytic activity under visible irradiation. Mater Res Bull 42:203–212. https://doi.org/10.1016/j.materresbull.2006.06.010
88. Li F, Liu Y, Liu R, Sun Z, Zhao D, Kou C (2010) Preparation of Ca-doped $LaFeO_3$ nanopowders in a reverse microemulsion and their visible light photocatalytic activity. Mater Lett 64:223–225. https://doi.org/10.1016/j.matlet.2009.10.048

89. Ismael M, Wark M (2019) Perovskite-type $LaFeO_3$: photoelectrochemical properties and photocatalytic degradation of organic pollutants under visible light irradiation. Catalysts 9:342. https://doi.org/10.3390/catal9040342
90. Shen H, Xue T, Wang Y, Cao G, Lu Y, Fang G (2016) Photocatalytic property of perovskite $LaFeO_3$ synthesized by sol–gel process and vacuum microwave calcination. Mater Res Bull 84:15–24
91. Wu H, Hu R, Zhou T, Li C, Meng W, Yang J (2015) A novel efficient boron-doped $LaFeO_3$ photocatalyst with large specific surface area for phenol degradation under simulated sunlight. CrystEngComm 17:3859–3865. https://doi.org/10.1039/C5CE00288E
92. Wang P, He Y, Mi Y, Zhu J, Zhang F, Liu Y, Yang Y, Chen M, Cao D (2019) Enhanced photoelectrochemical performance of $LaFeO_3$ photocathode with au buffer layer. RSC Adv 9:26780–26786. https://doi.org/10.1039/C9RA05521E
93. Díez-García MI, Gómez R (2017) Metal doping to enhance the photoelectrochemical behavior of $LaFeO_3$ photocathodes. Chemsuschem 10:2457–2463. https://doi.org/10.1002/cssc.201700166
94. Maiman TH (1960) Stimulated optical radiation in ruby. Nature 187:493–494. https://doi.org/10.1038/187493a0
95. Dutta Majumdar J, Manna I (2011) Laser material processing. Int Mater Rev 56:341–388. https://doi.org/10.1179/1743280411Y.0000000003
96. Omi T, Numano K (2014) The role of the CO_2 laser and fractional CO_2 laser in dermatology. LASER Ther 23:49–60. https://doi.org/10.5978/islsm.14-RE-01
97. Guţu I, Julea T, Drăgănescu V, Dumitraş D, Milhailescu IN, Medianu R (1986) Development of a high power gas transport CO_2 laser with with cylindrical geometry. Opt Laser Technol 18:308–312. https://doi.org/10.1016/0030-3992(86)90056-3
98. Beck R, Englisch W, Gürs K (1980) Table of laser lines in gases and vapors. Springer Series in Optical Sciences; 3rd ed.; Springer-Verlag: Berlin Heidelberg. ISBN 978–3–662–13497–9
99. Khatun N, Anita Rajput P, Bhattacharya D, Jha SN, Biring S, Sen S (2017) Anatase to rutile phase transition promoted by vanadium substitution in TiO_2: a structural, vibrational and optoelectronic study. Ceram Int 43:14128–14134. https://doi.org/10.1016/j.ceramint.2017.07.153
100. Shifu C, Lei C, Shen G, Gengyu C (2006) The preparation of coupled SnO_2/TiO_2 photocatalyst by ball milling. Mater Chem Phys 98:116–120. https://doi.org/10.1016/j.matchemphys.2005.08.073
101. Tian B, Li C, Gu F, Jiang H, Hu Y, Zhang J (2009) Flame sprayed V-doped TiO_2 nanoparticles with enhanced photocatalytic activity under visible light irradiation. Chem Eng J 151:220–227. https://doi.org/10.1016/j.cej.2009.02.030
102. Karlov NV, Krokhin ON, Lukishova SG (2010) History of quantum electronics at the moscow lebedev and general physics institutes: nikolaj basov and alexander prokhorov. Appl Opt 49:F32–F46. https://doi.org/10.1364/AO.49.000F32
103. Eason R (2007) Pulsed laser deposition of thin films: applications-led growth of functional materials. John Wiley & Sons. ISBN 978–0–470–05211–2
104. Morintale E. Constantinescu CD, Dinescu M (2010) Thin films development by pulsed laser-assisted deposition. Ann Univ Craiova Phys 20
105. Lin H, Rumaiz AK, Schulz M, Wang D, Rock R, Huang CP, Shah SI (2008) Photocatalytic activity of pulsed laser deposited TiO_2 thin films. Mater Sci Eng B 151:133–139. https://doi.org/10.1016/j.mseb.2008.05.016
106. György E, Pino AP del, Sauthier G, Figueras A, Alsina F, Pascual J (2007) Structural, morphological and local electric properties of TiO_2 thin films grown by pulsed laser deposition. J Phys Appl Phys 40:5246–5251. https://doi.org/10.1088/0022-3727/40/17/035
107. Daghrir R, Drogui P, El Khakani MA (2013) Photoelectrocatalytic oxidation of chlortetracycline using Ti/TiO_2 photo-anode with simultaneous H_2O_2 production. Electrochim Acta 87:18–31. https://doi.org/10.1016/j.electacta.2012.09.020

108. Yamaki T, Sumita T, Yamamoto S, Miyashita A (2002) Preparation of epitaxial TiO_2 films by PLD for photocatalyst applications. J Cryst Growth 237–239:574–579. https://doi.org/10.1016/S0022-0248(01)01959-5
109. Kawasaki H, Ohshima T, Yagyu Y, Suda Y, Khartsev SI, Grishin AM (2008) TiO_2/TiN/TiO_2 heat mirrors by laser ablation of single TiN target. J Phys Conf Ser 100:012038. https://doi.org/10.1088/1742-6596/100/1/012038
110. Rahman MA, Bazargan S, Srivastava S, Wang X, Abd-Ellah M, Thomas JP, Heinig NF, Pradhan D, Leung KT (2015) Defect-rich decorated TiO_2 nanowires for super-efficient photoelectrochemical water splitting driven by visible light. Energy Environ Sci 8:3363–3373. https://doi.org/10.1039/C5EE01615K
111. Fendrich M, Popat Y, Orlandi M, Quaranta A, Miotello A (2020) Pulsed laser deposition of nanostructured tungsten oxide films: a catalyst for water remediation with concentrated sunlight. Mater Sci Semicond Process 119:105237. https://doi.org/10.1016/j.mssp.2020.105237
112. Fàbrega C, Murcia-López S, Monllor-Satoca D, Prades JD, Hernández-Alonso MD, Penelas G, Morante JR, Andreu T (2016) Efficient WO_3 photoanodes fabricated by pulsed laser deposition for photoelectrochemical water splitting with high faradaic efficiency. Appl Catal B Environ 189:133–140. https://doi.org/10.1016/j.apcatb.2016.02.047
113. Shinguu H, Bhuiyan MMH, Ikegami T, Ebihara K (2006) Preparation of TiO_2/WO_3 multilayer thin film by PLD method and its catalytic response to visible light. Thin Solid Films 506–507:111–114. https://doi.org/10.1016/j.tsf.2005.08.312
114. Yudasari N, Kennedy DS, Suliyanti MM (2019) Pulse laser deposition (PLD) technique for ZnO photocatalyst fabrication. J Phys Conf Ser 1191:012009. https://doi.org/10.1088/1742-6596/1191/1/012009
115. Wolcott A, Smith WA, Kuykendall TR, Zhao Y, Zhang JZ (2009) Photoelectrochemical study of nanostructured ZnO thin films for hydrogen generation from water splitting. Adv Funct Mater 19:1849–1856. https://doi.org/10.1002/adfm.200801363
116. Zhou C, Sanders-Bellis Z, Smart TJ, Zhang W, Zhang L, Ping Y, Liu M (2020) Interstitial lithium doping in $BiVO_4$ thin film photoanode for enhanced solar water splitting activity. Chem Mater 32:6401–6409. https://doi.org/10.1021/acs.chemmater.0c01481
117. Murcia-López S, Fàbrega C, Monllor-Satoca D, Hernández-Alonso MD, Penelas-Pérez G, Morata A, Morante JR, Andreu T (2016) Tailoring multilayered $BiVO_4$ photoanodes by pulsed laser deposition for water splitting. ACS Appl Mater Interfaces 8:4076–4085. https://doi.org/10.1021/acsami.5b11698
118. Song J, Kim TL, Lee J, Cho SY, Cha J, Jeong SY, An H, Kim WS, Jung Y-S, Park J et al (2018) Domain-engineered $BiFeO_3$ thin-film photoanodes for highly enhanced ferroelectric solar water splitting. Nano Res 11:642–655. https://doi.org/10.1007/s12274-017-1669-1
119. Yun KY, Ricinschi D, Kanashima T, Noda M, Okuyama M (2004) Giant ferroelectric polarization beyond 150 MC/Cm^2 in $BiFeO_3$ thin film. Jpn J Appl Phys 43:L647–L648. https://doi.org/10.1143/JJAP.43.L647
120. Béa H, Bibes M, Barthélémy A, Bouzehouane K, Jacquet E, Khodan A, Contour J-P, Fusil S, Wyczisk F, Forget A et al (2005) Influence of parasitic phases on the properties of $BiFeO_3$ epitaxial thin films. Appl Phys Lett 87:072508. https://doi.org/10.1063/1.2009808
121. Ravalia A, Vagadia M, Trivedi P, Solanki PS, Asokan K, Ojha S, Thakur OP, Choudhary RJ, Phase DM, Kuberkar DG (2013) Role of oxygen in multiferroic behavior of $BiFeO_3$ films grown on 0.2% Nb doped $SrTiO_3$. Solid State Commun 169:10–13. https://doi.org/10.1016/j.ssc.2013.06.020
122. Pei W, Chen J, You D, Zhang Q, Li M, Lu Y, Fu Z, He Y (2020) Enhanced photovoltaic effect in Ca and Mn Co-doped $BiFeO_3$ epitaxial thin films. Appl Surf Sci 530:147194. https://doi.org/10.1016/j.apsusc.2020.147194
123. Wang H, Huang J, Sun X, Jian J, Liu J, Wang H (2020) Effective doping control in Sm-doped $BiFeO_3$ thin films via deposition temperature. RSC Adv 10:40229–40233. https://doi.org/10.1039/D0RA06775J

124. Vagadia M, Ravalia A, Solanki PS, Choudhary RJ, Phase DM, Kuberkar DG (2013) Improvement in resistive switching of Ba-doped $BiFeO_3$ films. Appl Phys Lett 103:033504. https://doi.org/10.1063/1.4813551
125. Lin TK, Chang HW, Chen BA, Wei DH, Wang CR, Tu CS (2020) Effect of Pr substitution on the structure, nanomechanical and multiferroic characterizations of $Bi1\text{-}XPrxFeO_3$ polycrystalline films. Surf Coat Technol 393:125728. https://doi.org/10.1016/j.surfcoat.2020.125728
126. Agarwal R, Sharma Y, Hong S, Katiyar RS (2018) Modulation of oxygen vacancies assisted ferroelectric and photovoltaic properties of (Nd, V) Co-doped $BiFeO_3$ thin films. J Phys Appl Phys 51:275303. https://doi.org/10.1088/1361-6463/aac505
127. Manzoor S, Somvanshi A, Husain S (2018) Structural analysis of $LaFeO_3$ thin films grown on $SrTiO_3$ and $LaAlO_3$ substrates. AIP Conf Proc 1942:080011. https://doi.org/10.1063/1.5028845
128. Tsuchiya Y, Norota K, Watabe Y, Kuroda T, Iwata N, Hashimoto T, Yamamoto H (2012) Growth difference of $LaFeO_3$ thin films by pulsed laser deposition method using the targets prepared by pechini and conventional solid solution methods. Trans Mater Res Soc Jpn 37:369–372. https://doi.org/10.14723/tmrsj.37.369
129. Park J, Kim Y, Lee D, Song JH, Park J-H (2020) Twin-free epitaxial $LaFeO_3$ films grown on orthorhombic $GdScO_3$(110)o substrates. J Korean Phys Soc 76:273–276. https://doi.org/10.3938/jkps.76.273
130. Christiansen E, Nord M, Hallsteinsen I, Vullum PE, Tybell T, Holmestad R (2015) Structural investigation of epitaxial $LaFeO_3$ thin films on (111) oriented $SrTiO_3$ by transmission electron microscopy. J Phys Conf Ser 644:012002. https://doi.org/10.1088/1742-6596/644/1/012002
131. Cyza A, Cieniek Ł, Moskalewicz T, Maziarz W, Kusiński J, Kowalski K, Kopia A (2020) The effect of strontium doping on $LaFeO_3$ thin films deposited by the PLD method. Catalysts 10:954. https://doi.org/10.3390/catal10090954
132. Wang J (2003) Epitaxial $BiFeO_3$ multiferroic thin film heterostructures. Science 299:1719–1722. https://doi.org/10.1126/science.1080615
133. Rojac T, Kosec M, Budic B, Setter N, Damjanovic D (2010) Strong ferroelectric domain-wall pinning in $BiFeO_3$ ceramics. J Appl Phys 108:074107. https://doi.org/10.1063/1.3490249
134. Ederer C, Spaldin NA (2005) Weak ferromagnetism and magnetoelectric coupling in bismuth ferrite. Phys Rev B 71:060401. https://doi.org/10.1103/PhysRevB.71.060401
135. Ji W, Yao K, Lim Y-F, Liang YC, Suwardi A (2013) Epitaxial ferroelectric $BiFeO_3$ thin films for unassisted photocatalytic water splitting. Appl Phys Lett 103:062901. https://doi.org/10.1063/1.4817907
136. Haydous F, Scarisoreanu ND, Birjega R, Ion V, Lippert T, Dumitrescu N, Moldovan A, Andrei A, Teodorescu VS, Ghica C et al (2018) Rolling dopant and strain in Y-doped $BiFeO_3$ epitaxial thin films for photoelectrochemical water splitting. Sci Rep 8:15826. https://doi.org/10.1038/s41598-018-34010-9
137. Vavilapalli DS, Melvin AA, Kavita S, Yadav AK, Jha SN, Bhattacharyya D, Sarma SCh, Peter SC, Ramachandra Rao MS, Singh S (2019) Multifunctional brownmillerite $KBiFe_2O_5$: structural, magneto-dielectric, optical, photoelectrochemical studies and enhanced photocatalytic activity over perovskite $BiFeO_3$. Sol Energy Mater Sol Cells 200:109940. https://doi.org/10.1016/j.solmat.2019.109940
138. Salvador P (1985) Kinetic approach to the photocurrent transients in water photoelectrolysis at N-titanium dioxide electrodes. 1. Analysis of the ratio of the instantaneous to steady-state photocurrent. J Phys Chem 89:3863–3869. https://doi.org/10.1021/j100264a019

Chapter 15
Immobilization of Photocatalytic Material on the Suitable Substrate

Harshita Chawla, Seema Garg, Pravin P. Ingole, and Amrish Chandra

Abstract In the world of increasing industrialization and global population, environmental pollution has continued to rise over last few decade. Photocatalysis came forward as capable method in removal of various recalcitrant pollutants from atmosphere. The nano-photocatalytic semiconductors are majorly used in the form of slurry, and removal of these nano-photocatalytic materials turns out to be quite challenging and costly. Therefore, to resolve the problem of recollection of material, voluminous strategies have been executed for immobilising nano-photocatalyst on various substrates including carbon-based compounds, glass, zeolites, polymers, clay and ceramics and various natural fibres. The strategies including sol-gel, dip coating, polymer-assisted hydrothermal discharge, photo-etching, electrophoretic deposition, cold plasma discharge (CPD), RF magnetron sputtering and spray pyrolysis are discussed in this chapter. At last, characterization techniques used for studying various properties of immobilized catalyst are discussed in brief.

Keywords Photocatalyst immobilization · Immobilising strategies · Natural immobilizers · Sol-gel method · Carbonaceous substrate

15.1 Introduction

Over the passing few decades, problems regarding energy crisis and water contamination have imposed discrepancy in sustainable environment. Due to large-scale industrialization and heavy utilization of water in these activities, these

---

H. Chawla · S. Garg (✉)
Department of Chemistry, Amity Institute of Applied Sciences, Amity University, Noida, Uttar Pradesh, India
e-mail: sgarg2@amity.edu

P. P. Ingole
Department of Chemistry, Indian Institute of Technology, Delhi, India

A. Chandra
Amity Institute of Pharmacy, Amity University, Noida, Uttar Pradesh, India

S. Garg and A. Chandra (eds.), *Green Photocatalytic Semiconductors*,
Green Chemistry and Sustainable Technology,
https://doi.org/10.1007/978-3-030-77371-7_15

contaminants are released in various water bodies such as sewage water, surface water, ground water and drinking water. These contaminants include pharmaceutical wastes, pesticides, dyes, etc., which are water soluble. Till date, various wastewater treating methods including membrane filtration, sedimentation, coagulation and flocculation, filtration, reverse osmosis, chemical treatments, etc., were broadly employed to eliminate these impurities from water [1–4].

However, the techniques were not adequately effective for the treatment of wastewater consisting these harmful contaminants. In the recent past decade, the use of photocatalyst that have been implemented for the management of waste-water containing harmful effluents (such as agricultural waste, pharmaceutical waste, dyes etc.) has rapidly increased to a great extent. Now, researchers are mainly focussing on producing a photocatalyst which is highly stable, economically viable, non-toxic, and a catalyst resistant to corrosion as well. To the conventional methods used, the advanced oxidation processes (AOPs) have been demonstrated with highest success in regard with disintegration of these harmful pollutants. These AOPs are based on production of photo-induced charge carriers and formation of reactive species such as hydroxyl ions responsible for degradation of pollutants, and photocatalysis is one of these AOPs [5, 6].

Photocatalysis is not only useful in degradation of these harmful pollutants but also in production of clean energy as well as bacterial degradation. Various catalysts such as TiO_2, $BiVO_4$, BiOX (X=Cl, Br, I), Bi_2MO_6 (M=W, Mo, Cr), ZnO [7–10] have been employed for environmental remediation. These photocatalysts have been employed using slurry suspension system, i.e. suspension of fine powder into effluent water containing contaminants [11, 12]. Post-treatment, elimination of these photocatalysts have caused deduction in significant benefit caused by these photocatalysts as these processes are very costly and time-consuming as well as recovery and reuse of these photocatalyst at industrial scale are very difficult. As a result, it turned out to be highly challenging to use these NPs at industrial scale. These NPs if not removed after treatment of wastewater can exhibit cytotoxicity as well as genotoxicity to human as well as aquatic life [13–15].

Thus, in order to ease the recovery of photocatalyst and its reutilization, in 1993, immobilizing photocatalyst onto inert surface was widely accepted, and this technique has facilitated the reuse of the catalyst in eco-friendlier manner. Till date various strategies have been employed to immobilize catalyst on various substrates such as glass, zeolites, carbon nanotubes, ceramic fibres, clay, polymers, graphene oxide, photoelectrodes, wire mesh, cellulose, chitosan, *luffa cylindrica*, but usage of natural fibres is increasing due to their ease in availability, renewability, biodegradable, cost efficient as well as environmentally benevolent. These fibres provide a 3D support to the catalyst. But these photocatalysts often suffer inherent mass transfer limitations, as the effective surface area available for the reaction and irradiation decreases when compared to homogeneous catalytic systems. This chapter mainly summarizes materials and strategies used for immobilizing catalyst in 3D support system [16–22].

15.2 Photocatalyst Working Mechanism

Photocatalysis is an advanced oxidation process involving various intermediate steps. Preliminary step involves generation of electron–hole pair on irradiating light on surface of catalyst, where light source has wavelength equal or greater than that of band gap of semiconductor. This state is referred to as photo-excitation of semiconductor where charge separation takes place. Here, electrons on gaining sufficient energy cross band gap energy barrier and reach conduction band leaving holes behind in valance band. The holes created in valance band act as strong oxidizing agent, and electrons exited in conduction band act as strong reducing agent. The generated holes on surface of semiconductor oxidize electron donor, and exited electron reduces electron acceptor. The semiconductor photocatalyst therefore works accordingly as per particles present around them [23–28]. Diverse reactive oxygen species are generated involving hydroxyl ions (OH^-), superoxide radical ($O_2^{\cdot -}$) that are primarily responsible for degradation of pollutants. In case of photocatalysis, the effectiveness of the reaction is measured in terms of quantum yield [29]. It is a function of number of molecules degraded and the number of photons absorbed by the solution.

$$\text{Quantum Yeild} = \frac{\text{number of molecules undergoing dissosiation}}{\text{number of photons absorbed by the solution}}$$

The reaction below represents charge carrier reaction of TiO_2 photocatalyst.

$$TiO_2 + hv \xrightarrow{hvE_{BG}} h^+_{VB} + e^-_{CB}$$

If there are no scavengers available for electron trapping, then electrons will combine with holes present in VB. Therefore, to delay electron–hole recombination, the presence of electron quencher becomes vital. This is a restraining process in photocatalysis as it affects charge generation and reduces ability to reduce as well as oxidize harmful pollutants present in water [30, 31]. Also, in some cases, the pollutants may combine and form products which are more harmful than initial one. Figure 15.1 shows general mechanism of photocatalytic degradation of dye [32].

15.3 Various Substrates for Immobilization of Photocatalyst

Several substrates are available for supporting photocatalytic systems. These include activated carbon, glass, graphene oxide, silica, polymers, clay, zeolite, ceramics, alumina, quartz and various biodegradable materials such as cellulose, fly ash, coconut fibres, vycor glass, optical fibres, anodised iron, Raschig ring and glass wool. These materials have been widely implemented for immobilizing

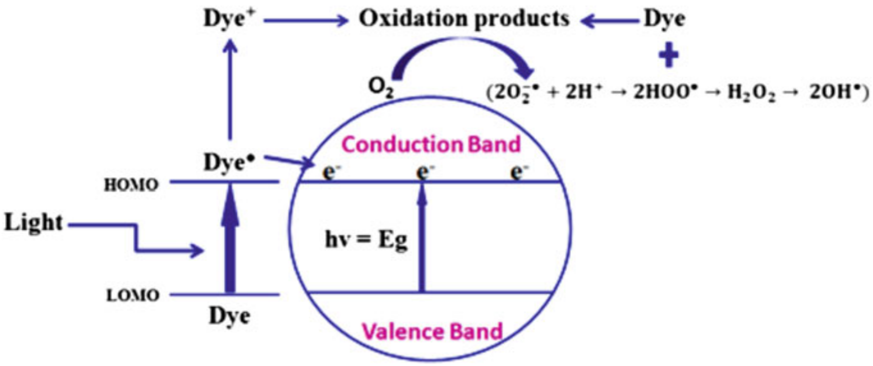

Fig. 15.1 Schematic diagram representing the photo-induced photocatalytic activity of photocatalyst (reprinted with permission from Ref. [32])

photocatalyst. Photocatalyst can be both optically transparent and opaque [18, 22, 33–35]. Though any support system can be chosen from above-listed materials but, it is essential that material possesses the following characteristics:

I The photocatalyst should be immobilised permanently and strongly in the entrapment medium.
II There should not be a great decrease in photo-activity of photocatalyst after immobilisation on suitable substrate.
III There should be noticeable increment in surface area of photocatalyst after immobilisation on substrate.
IV The substrate implemented as immobilizer should be capable of adsorbing contaminants on its surface for degrading pollutants effectively.
V The supporting material should contain an excellent stability against degrading activity of photocatalyst implemented, i.e. immobilizer should be resistant towards oxidoreduction power of photocatalyst.
VI It must provide a considerably large surface area.

The main feature while electing a significant support material is the ability of the photocatalyst to adhere to the photocatalytic material. We will hence try to illustrate some of the recently recounted entrapment media for the catalyst and the method adopted for the immobilisation process in the following sections of the chapter [36].

15.3.1 Carbonaceous Substrate

In last few decades, carbon-based immobilizing substrates such as activated carbon (AC), carbon nanotubes/nanofibers (CNTs), graphene oxide (rGO), fullerenes, carbon dots (CDs), carbon sponges/aerogels are majorly used. The literature reflects that these materials have gained quite high attention of researchers for immobilizing photocatalyst due to their excellent thermal, electronic, mechanical properties, high adsorption, highly inert to various chemicals and high stability. These carbonaceous substrates have shown a great increase in surface area as well increase in degrading efficiency of photocatalyst after immobilization. After broad range evaluation of immobilized photocatalyst on these carbonaceous materials, it was concluded that these materials especially nano-carbon substrates exhibit fascinating ability in enhancement of photocatalytic activity of immobilized photocatalyst [37–40]. Although there is difference in morphologies of listed carbonaceous materials, the working mechanism which increases the photocatalytic activity is proposed on following facets:

I With introduction of carbon as substrate, numerous heterojunctions were generated between catalyst and carbon which efficiently traps photo-generated electrons for longer interval of time and suppresses electron–hole recombination.

II These carbon-based materials are capable in incrementing adsorption capacity of visible light spectra and transportation of electron, and also, separation of charge carriers is enhanced due to good conductivity of these carbo compounds.

III In regard to higher surface area of immobilized photocatalyst on carbon-based substrate, more reaction sites are available, and the adsorption capacity of photocatalyst is significantly incremented. Therefore, more reactive sites are in contact with pollutant, and higher degradation is observed.

IV The excellent stability, inertness has ensured good utilization of carbon as substrate due to its unique physical and chemical properties.

Although researchers have achieved a great advancement in immobilizing photocatalysts on these carbonaceous materials, still there are many critical limitations which have to be resolved for promoting the practical applications and its industrialization. The major challenges faced on using these carbon-based substrates are as follows:

I In major cases, photocatalytic materials are loaded on surface of matrix of carbon, the interface formed between carbon substrate and photocatalytic material is not so intimate which further results in limited electron transfer ability and limited bond strength. Therefore, by improving the interaction forces between carbon matrix and photocatalytic semiconductor, properties such as photo-generated charge separation efficiency, band gap, light absorption efficiency can be further optimized accordingly.

II The nano-structured forms of carbon utilized for immobilization such as CNTs, CDs and graphene are highly efficient in enhancing the photocatalytic activity of these semiconductor photocatalyst, but due to their powder form, it is quite difficult to reobtain them after completion of reaction. Therefore, to resolve the collection problem, activated carbon is used in form of carbon block. Similarly, other carbonaceous compounds which are present in powder

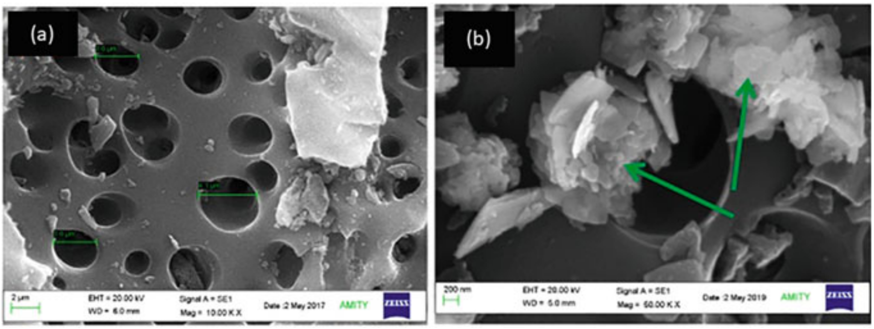

Fig. 15.2 SEM images **a** blank 2D block of activated carbon, **b** photocatalyst 1% BiOI-G loaded on carbon block (reprinted with permission from Ref. [41])

> form are converted into 2D/3D matrix so that there is no problem of recollecting material. Further, there is requirement for increasing stability of binding interactions of nano-catalyst on carbonaceous material and their mechanical strength. Figure 15.2a represents SEM image of 2D block of activated carbon, and 15.2b represents SEM image of photocatalyst loaded on carbon block [41].

Further development in these photocatalyst-carbonaceous materials can adequately help in commercialization and industrialization of photocatalytic water treatment, environment-friendly and clean energy production strategies [41, 42].

15.3.2 Glass

Even after many advancements in the field of photocatalyst immobilization over last decade, glass has still continued to be as a remarkable substrate for entrapment for most of photocatalytic applications. Glass has been employed as substrate in numerous physical forms such as beads, plates and rings. Most researchers instead of using external components such as rings and beads as anchoring agent have used glass for construction of photocatalytic reactor, and then, uniform layer of catalyst was coated on walls of reactor. With the inert nature of glass, in combination with its optical properties, its ability to withstand at high calcination temperature and cost-effectiveness, glass is still preferred as an efficient substrate for immobilization of photocatalyst. Previous studies have investigated degradation of HCHO, a recalcitrant pollutant using ZnO nano-photocatalyst which were immobilized on glass plate, on a bench-scale reactor, attached with peristaltic pump for mixing reacting mixture. A strong adherence of photocatalyst has been observed after calcination, and also, the presence of hydroxyl ions has been primarily observed. The use of glass beads has been observed as a versatile and convenient tool to increase surface area of photocatalyst. In this manner, photocatalyst surface is efficiently illuminated to light source leading towards excellent generation of charge carriers on the wall of photoreactor and beads. Researchers have shown 97% removal of ethylene using TiO_2 glass bead photoreactor. They pre-treated glass substrate using concentrated NaOH by dipping it for 24 h, and then, these substrates were dried at 350 °C for 3 h and were prepared using dip coating method [18, 19, 43–48]. Figure 15.3 shows TiO_2-coated glass beads filled in reactor and degrading pollutants in presence of solar light [19].

15.3.3 Zeolites

Zeolites are described as 3-D crystalline, microporous materials, with defined structural organization of channels and voids of discrete size which are accessible through well-defined pore and molecular dimension containing framework of silicon, alumina and oxygen atoms. These are naturally occurring compounds, formed during changes that occur in volcanic rock when it interacts with sea or freshwater. The 3D structure of zeolite contains aluminium ion in centre surrounded by silicon and four oxygen atoms containing minerals and overall charge is negative. Due to negative charge of complex, it can combine with various positively charged cations such as titanium, zinc, cadmium, lead, manganese and other transition metals. Generally, photocatalytic semiconductors contain transition metals that can form ionic interactions with zeolites. The most common use of zeolite is removal of

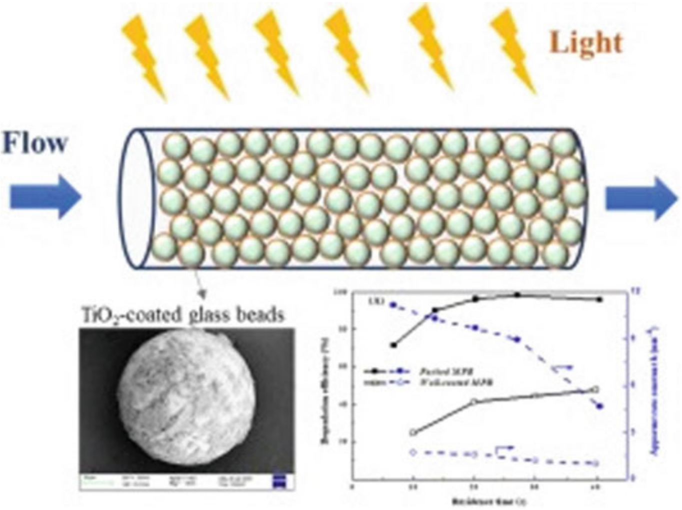

Fig. 15.3 Capillary micro-photoreactor packed with TiO_2-coated glass beads (reprinted with permission from Ref. [19])

heavy metals present in effluent water from industries. Few examples of types of zeolites used for immobilization of photocatalyst include phillipsite, stilbite, natrolite, etc. [49–53]. Figure 15.4 represents zeolite structure and zeolite loaded with catalyst [54]. Among the exclusive features of zeolites when compared to conventional catalyst support includes the following:

I Uniform diameter of pores.
II Pore width ranges with molecular dimension of zeolite. The diameter of pore is less than 2 nm.
III The nature of zeolite contains acidic sites which can form interactions with metals.
IV It is shape-selective, concentration-effective, the location of acidic sites in zeolite framework.

15.3.4 Clay and Ceramics

Clays are vital, naturally occurring, non-polluting material which have wide range of applications including water treatment, polymers, ceramics, cosmetics, paints, paper, pulp and pharmaceutical industries. Clays are referred to as naturally occurring fine-grained crystalline materials including carbonates, silicon oxides, metal oxides which turns hard on exposure to high heat. The components of clay are arranged in different structural layers and structural arrangement and are referred to as polytypism. Minerals forming clay are hydrous aluminium silicates in nature that retain large amount of water with other properties including swelling, colloidal behaviour and adsorption capacity. These minerals are classified as illite, kaolinite, bentonite, montmorillonite and chlorite. These minerals are commonly used for immobilizing photocatalyst as they have high stability, availability, high surface area and good structural characteristics. These minerals are naturally abundant,

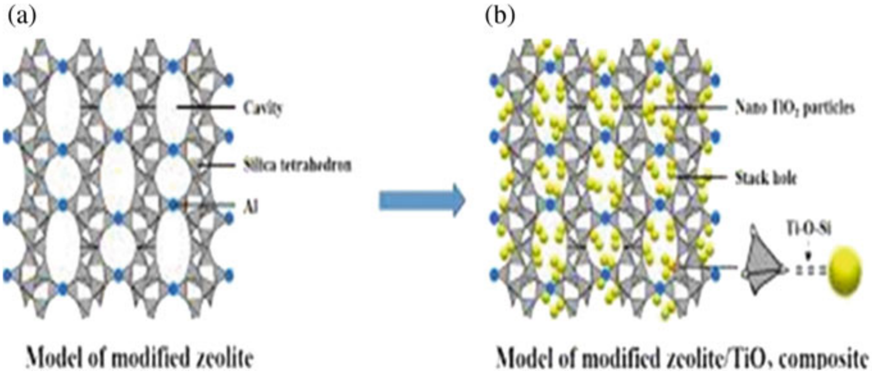

Fig. 15.4 **a** Blank zeolite, **b** zeolite pores loaded with photocatalyst (adapted from Ref. [54])

non-toxic, as well as play a significant role in scavenging pollutant in wastewater either using adsorption process and via ion exchange process or both. These minerals are basically used as depolluting agents. Studies have shown that degradation rate of pollutant depends on pore size of clay chosen. Higher the pore size, higher will be adsorption of pollutant on surface, more will be degradation [55–60].

Ceramics are solid materials comprising various non-metallic and inorganic components. These are found in both amorphous and crystalline forms. These materials during manufacturing process are subjected to temperatures above 500 ° C. These materials may be boride, metal oxides, carbides, nitrides or mixture of these compounds. These materials are present in the form of ions, and anions play a major role in depicting their morphological structure. Ceramics are used because of their insulation properties (including heat and electricity), higher hardness, brittleness, corrosion resistant and fracture properties without deformation in any structural arrangement. Ceramics in fibrous form have shown a great potential in immobilizing photocatalyst on its porous surface. These fibres are highly flexible, bear outstanding shape and size compatibility, large surface area, high tensile strength, high resistance toward acidic and alkali attack and temperature change. Due to its thermal conductivity, broader range of incident wavelength of solar light spectra is absorbed, more numbers of photo-generated charge carriers are formed that are further required for degradation activity. These fibres due to high flexibility and tensile strength can be given a variety of desired shapes [14]. Various studies have been carried out by immobilizing photocatalyst on surface of ceramic fibres. Figure 15.5 shows SEM images of blank (a) CerF, (b) BiOCl-CerF, (c) BiOBr-CerF and (d) BiOI-CerF [61].

15.3.5 Polymers

Monomers in a large number when combined with each other with chemical bonds give rise to macro molecules called polymers. The number of monomeric units may vary from polymer to polymer. They may be natural or synthetic. Synthesis of polymeric substances is easier compared to other substrate, enabling them to be utilized as an effective substrate for immobilization of photocatalyst. Numerous polymers have been used for immobilizing photocatalyst, namely polyvinyl chloride (PVC), polystyrene, polyaniline (PANi), expanded polystyrene, poly (methyl methacrylate) (PMMA), poly(styrene)-co poly(4-vinylpyridine), poly (tetrafluoro ethane), poly (3-hexylthiophene), low density polymer (LDP), high density polymer, polycaprolactam and carbon nitride polymer. Immobilization of photocatalyst on polymeric surface has shown that ability to adsorb naturally available solar light radiation had increased due to increase in surface area. Using biodegradable polymers for immobilization of photocatalyst has been promoted. The utilization of polymers for immobilization of photocatalyst has successfully developed at laboratory scale, but much studies are required for its commercialization [22, 62–68]. Figure 15.6 represents immobilized TiO_2 on polyethersulfone matrix [69].

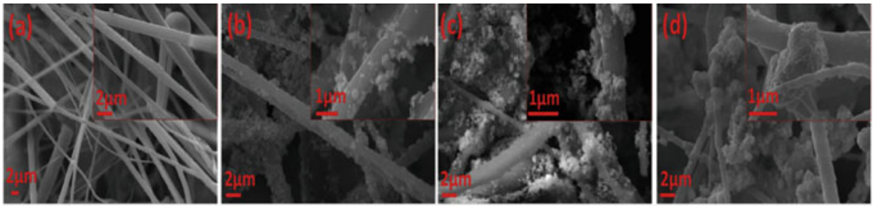

Fig. 15.5 SEM images of blank **a** CerF, **b** BiOCl-CerF, **c** BiOBr-CerF and **d** BiOI-CerF (reprinted with permission from Ref. [61])

Major advantages of using polymers as substrate for immobilization are as follows:

I These materials are chemically inert and mechanically stable, have high durability.

II They have hydrophobic nature which gives an advantage of concentrating organic pollutants on surface, thereby increasing efficiency of photocatalyst in degrading hydrophobic pollutants.

III These are generally inexpensive and readily available.

IV They have resistance toward UV and do not oxidized easily.

V Due to their thermoplastic nature, they bear softening properties, which further provide ease in coating catalyst over the surface of polymer.

VI They are available in density range of 0.9–2 g cm^{-1} and thus show penalty of advantages in developing buoyant photocatalyst

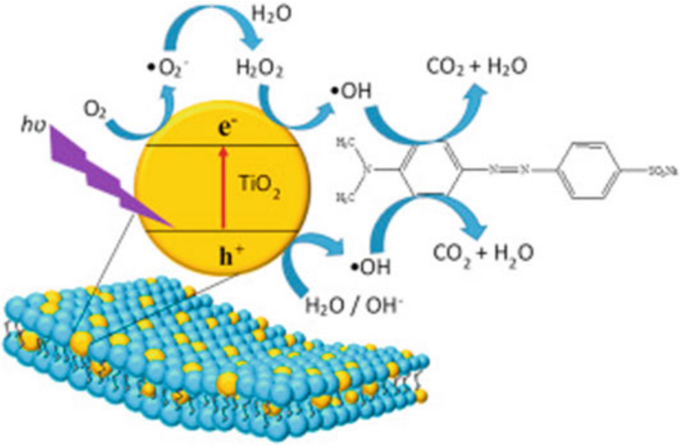

Fig. 15.6 Immobilization of TiO_2 on polyethersulfone matrix degrading Methyl orange dye (reprinted with permission from Ref. [69])

15.3.6 Additional Unusually Practiced Supports

Apart from above-listed substrates, many other substrates have been used for immobilizing catalyst including natural fibres such as luffa cylindrica, alginate beads and cellulose fibres. These materials due to their ease in availability of these substances and cost-effectiveness have advantage of being implemented at commercial scale. Recent studies have demonstrated that immobilizing photocatalyst for degradation of these pollutants have a higher photocatalytic activity then slurry reactor. Other than these many other biological fibres can be used for effective immobilization of photocatalyst [70].

15.4 Commonly Used Strategies for Immobilization of Photocatalyst

The strategies employed for immobilizing photocatalytic material on substrate play momentous role in defining the photocatalytic activity of the photocatalytic semiconductor. Hence, choosing the substrate for supporting photocatalyst depends on type of semiconductor and the targeted pollutant and by products formed after its degradation. Also, the strategies employed for deposition of photocatalyst should be such that it does not either decrease the activity of catalyst nor decrease the surface area but should increase both. Several strategies have been reported in the literature to achieve the same. These strategies include chemical vapour deposition, electrophoretic deposition, thermal treatment method, sol-spray method, cold plasma discharge, solvent casting, magnetic sputtering, polymer-assisted hydrothermal coating, photo-etching and sol-gel method consisting of dip coating. Many of these strategies are not widely employed as they require high temperature which can further decompose the substrate, and procedure is also highly expensive. From researcher’s point of view, sputtering method and sol-gel method are widely used strategies for immobilizing photocatalyst on inert support materials [71]. In this section, several photocatalyst immobilization strategies are reviewed and discussed.

15.4.1 Dip Coating

One of the most effective techniques being extensively used for research point of view is dip coating as it is very facile and convenient process of immobilizing photocatalyst on required approach. The photocatalyst is suspended in the solution in which catalyst is efficiently dispersed. Then, the chosen substrate is immersed in suspended photocatalyst slurry. Once photocatalyst is successfully loaded to the substrate, the solvent used for dispersing photocatalyst can be removed by oven drying. The forces responsible for coating of catalyst on surface of substrate are viscous drag, surface tension, inertial force and gravitational force [45, 72–76]. Generally, dip coating consists of following five steps:

I IMMERSION: The chosen substrate is dipped into photocatalytic slurry at constant speed. Based on the nature of substrate, pre-treatment of substrate is carried out so that it can hold catalyst on its surface or pores.

II START-UP: The substrate is immersed in slurry for a particular time interval such that a layer is deposited on its surface, and then, it is pulled out.

III DEPOSITION: When substrate is pulled out from slurry suspension, thin film of coated catalyst is visible. The thickness of coated catalyst depends on the speed by which substrate is pulled out from slurry and time interval for which it is dipped. Thickness is directly proportional to both speed and time interval.

IV DRAINAGE: This step involves drainage of excess solvent from substrate coated during deposition of catalyst.

V EVAPORATION: Solvent used to form slurry evaporates from the surface of substrate leading to formation of thin film of catalyst. If solvent used is volatile, it evaporates during deposition of photocatalyst (Fig. 15.7).

Because there is no requirement of any sophisticated equipment, this method is cost-effective, and thickness of catalyst can be easily adjusted. The drawback of this method is that it is quite slow process, and the coating produced may not be quality as required to hold catalyst for longer duration of time. This may affect the photocatalytic degradation efficiency. This method has shown good results when glass is used as substrate, but when graphene oxide is used as substrate, this may not produce sufficiently dense coating and cannot be applied to vast range of substrate. However, this method is used at large scale due to its cost-effectiveness but is effective from lab point of view [77–80].

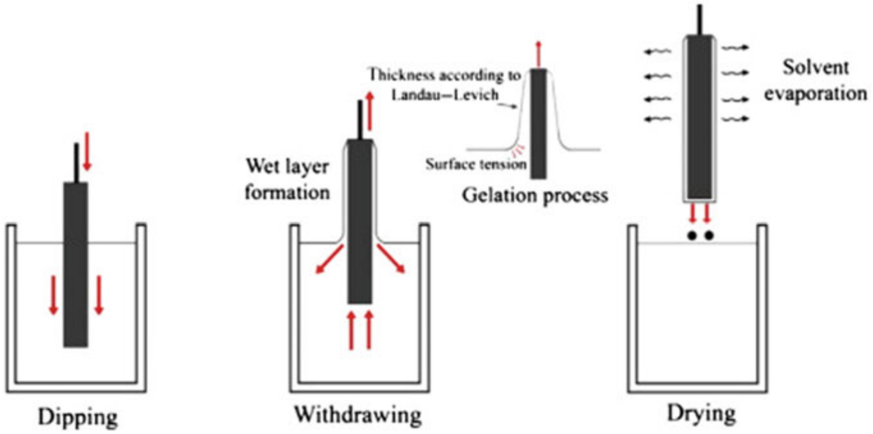

Fig. 15.7 Schematic view of dip coating method (reprinted with permission from Ref. [77])

15.4.2 Cold Plasma Discharge

This is an eco-friendly technique developed through which new polar functional groups can be introduced to surface of immobilising substrate, and this helps in facilitating attachment of photocatalyst on the surface and pores of substrate. Cold plasma refers to partially ionized gas consisting of electrons, ions, photons of UV range and reactive neutrals including exited and ground state molecules and radicals. These low energy molecular species and high energy electrons therefore initiate series of reaction which are responsible for production of energy and charges on substrate surface without production of any excessive heat. Studies have shown that using cold plasma discharge technique as pre-treatment of substrate helps in improving adhesion and hydrophilic properties of matrix used for immobilization of photocatalyst. This technique has shown various advantages over conventional method used for pre-treatment of substrate. The first and foremost reason is that this plasma-based treatment does not require allied reagents and water which in turn makes this process more economical and environment friendly. The prevalent advantage of implementing this strategy is that it has shown remarkable increment in degradation of pollutant present in industrial effluent as well as cost reduction in effluent treatment. Other merits of using this technique are that it increases tensile strength of fibres used as plasma treatment only occurs on surface leaving core unaffected and also it helps in eliminating surface cracks present on substrate. It also relaxes the stress accumulated in inner core of substrate created during coating of immobilized photocatalyst [81–87]. Figure 15.8 represents methods of plasma discharge [88].

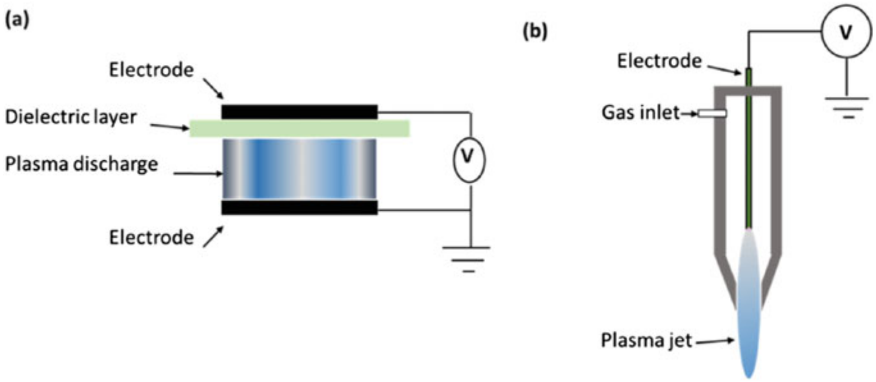

Fig. 15.8 Methods of discharge of plasma **a** dielectric discharge, **b** jet discharge (reprinted with permission from Ref. [89])

15.4.3 Polymer-Assisted Hydrothermal Decomposition (PAHD)

This is very commonly implemented strategy for immobilization of photocatalyst on polymeric substrate and is referred as polymer-assisted hydrothermal decomposition (PAHD). This strategy involves combination of hydrothermal approach of photocatalyst synthesis and its deposition on polymeric substrate simultaneously. This strategy is highly useful in case of water-soluble polymers, due to their ability with respect to control in viscosity of photocatalytic slurry and its bond formation with metallic ions and thus reduces ability of photocatalytic hydrolysis. Major advantages of implementing this strategy are that it avoids irregular morphology of particles, has broad particle size distribution, and the polymeric films formed are in range near to tens of microns [89].

15.4.4 RF Magnetron Sputtering

In addition to various methods which are in existence to prepare thin films of immobilised photocatalysts, magnetron sputtering using radio-frequency(rf) has come out as one of the most effective methods because of its inherent versatility and the capacity of homogenous surface coverage even at low temperatures under controlled processing conditions. The RF magnetron sputtering approach was found to be comparable to CPD technique. One of the main advantages of using magnetic RF sputtering is its ability in synthesis of metallic nanoparticles with better control over shape and size, alongside having smooth distribution of particles on oxide films with suitable technique of nanoparticle synthesis [90–92]. Figure 15.9 represents schematic representation of set-up used for immobilizing catalyst on substrate using this strategy [93]. Researchers have shown that using RF magnetron sputtering method TiO_2 was immobilised on ceramic fibres and degradation efficiency was increased by great extent. Also, it was concluded that with increase in sputtering time, degradation efficiency was also increased. It was also concluded that the sputtering time is directly related with thickness of film. When the film was thin, then irradiated light passes through, and lower radiations are absorbed by catalyst leading to decrement in photocatalytic efficiency, but as soon as optimum thickness is achieved, efficiency of light absorption with photo-generated charge carrier also increases [92, 94].

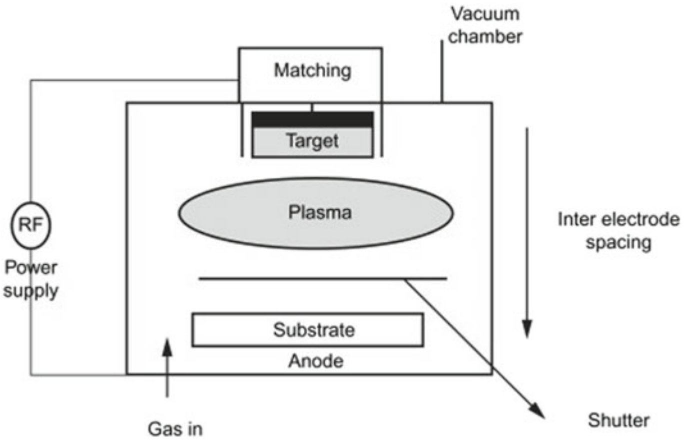

Fig. 15.9 Schematic representation of arrangement for RF magnetron sputtering (reprinted with permission from Ref. [93])

15.4.5 Photo-etching

Photo-etching process is based on principal of lithography. Lithography is a process which is mainly employed for fabricating micro molecules to form thin or thick layering for supporting any type of substance [95–98]. This phenomenon includes transfer of geometric pattern to photo-resist surface from photo-masking substances by usage of light irradiation. This process involves following steps:

I A substrate is chosen and is coated with thin uniform film of photo-resist over the substrate.
II A designed mask for forming pattern is placed over photo-resist layer.
III UV light is then irradiated over the arrangement formed; this irradiation of light leads to polymerization of photo-resist.
IV After the designed structure is obtained over the chosen substrate, mask and unpolymerized sections are removed using trichloroethylene solution, and excess section of substrate which are not covered using mask can be removed using HCl.

Figure 15.10 represents basic steps involved in photo-etching [99]. The major reason of using photo-itching is lowering of band gap of photocatalyst and formation of macropores. Formation of these pores acts as sensitizer and increases photo-activity of photocatalyst. The studies have shown that immobilized catalyst has a relative constant k value for up to 10 cycles. Therefore, photo-etching has come out as a promising strategy for immobilizing photocatalyst on any substrate [96].

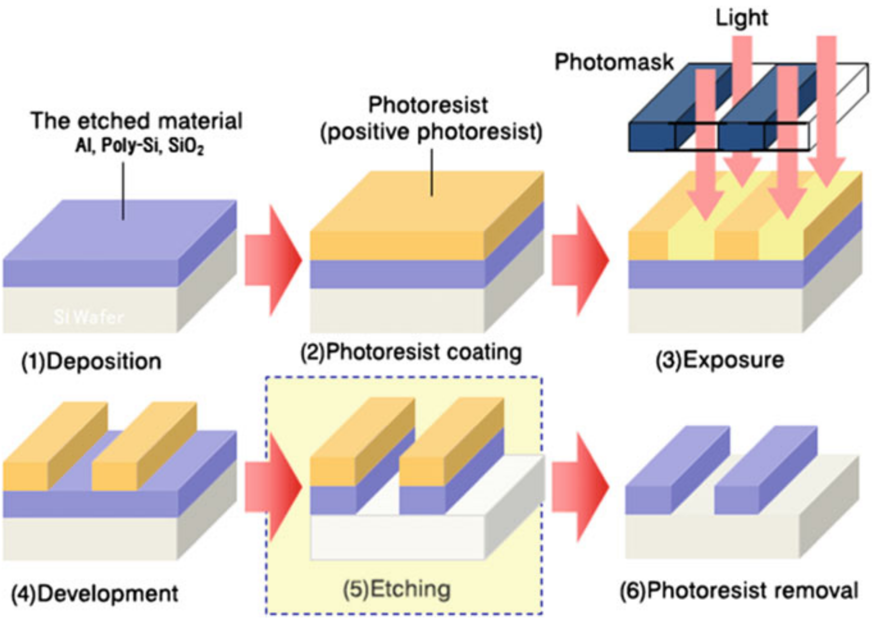

Fig. 15.10 Representation of flow diagram of photo-etching process (adapted from [99])

15.4.6 *Sol-Gel Method*

The sol-gel technique of immobilising photocatalyst is a wet-chemical strategy involving deposition of wet chemical solution in various steps. The steps include hydrolysis and polycondensation, gelation, ageing, drying, densification of solution and crystallization of solution and are followed in chronological order. This method is primarily applied for fabricating metal oxide using their corresponding metal ions as precursors. These primary materials have shown a vital role in determining the morphology of the immobilized photocatalyst. These precursors are capable of producing a gel-like integrated network of polymers or discrete particle [100–104]. This method includes following steps:

I The chosen metal oxides are dissolved in a solvent most commonly ethanol. On addition of little water hydrolyses material, polymeric form is formed. The solution turns little acidic, and the material thus formed is a loose-gel having liquid filled pores.

II To remove the liquid filled in pores and densifying the material, heat treatment of higher temperatures ranging from 100 °C to 1000 °C is provided.

Most commonly lower temperatures are implemented for maintaining structural morphologies and reducing the index of formed films. Even very minute quantities of dopants can be introduced while coating sol and the dopant are uniformly distributed in resulting product. These compounds are capable of undergoing a variety of reactions including hydrolysis and condensation reactions leading in production of inter-linked connections between metal centres (M) and oxo (MO–M) or hydroxy (M–OH–M) linkages. Presence of excess solvent is generally removed using drying process, which leads in densification and volume shrinkage of the photocatalyst immobilized on the film. The drying is further followed by a thermal treatment process, which further supports polycondensation and leads in enhancement of mechanical and structural properties of thus fabricated films by densification, sintering and grain growth. Major advantages of this technique include purity of deposited catalyst, homogeneity, lower temperature fabrication, control over morphology of fabricated material including shape, distribution, size and other properties, multilayer coatings, etc. Howsoever, production of multilayer coating can create a problem due to lack in drying efficiency between layers and may lead to heterogenous coating and further creating in decrement of photocatalytic activity [105].

15.4.7 Electrophoretic Deposition

Electrophoretic deposition has emerged out as remarkable electro-chemical method for coating and immobilizing semiconductors over various substrates mainly ceramics. This technique has become primary choice of researchers for preparation of thin as well multilayer film deposition of photocatalyst over chosen suitable substrate. The uniformity in films formed is comparatively high when compared to dip coating method. This method is capable in forming multilayer films of varying thickness. This method can be implemented commercially as thickness of film is controlled by electrically charged particles present between two electrodes, namely anode and cathode present in dielectric medium. The working principal regulating the deposition of powder photocatalyst involves following steps:

I The selected photocatalyst powder is dispersed in a solvent medium containing both electrodes where one electrode present is counter-electrode, and another electrode is of metallic substrate that is to be coated on.

II A net electric charge is developed on surface of powder particles dispersed due to electrostatic interactions with solvent molecules.

III As soon as external electric potential is applied, these suspended partially charged particles tend to move freely in suspension towards the electrode opposite to their polarity. This phenomenon of deposition of electrically charged particles over electrodes is referred to as electrophoresis. To enhance charge stabilization in suspension thus formed, additives such as acetylacetone and isopropanol are used. They increase durability and uniformity of coating.

IV The substrate is thus obtained with required coating of catalyst. Figure 15.11 represents schematic view of cathodic electrophoretic deposition cell.

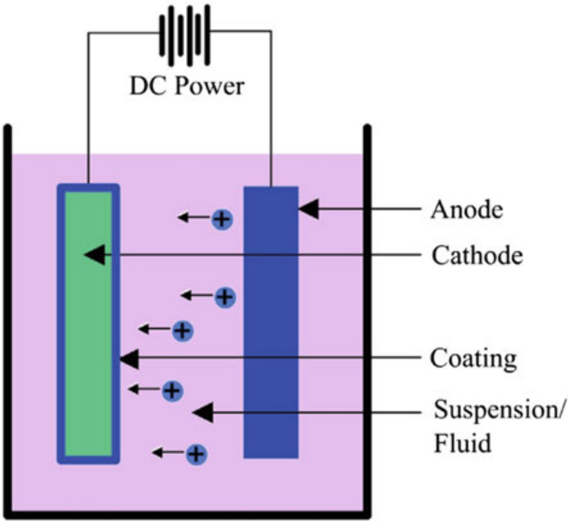

Fig. 15.11 Schematic representation of the cathodic electrophoretic deposition cell (reprinted with permission from Ref. [36])

This strategy has been employed in various industries for coating heavy equipment, automotive frames and large metal parts. This strategy is majorly applicable where substrate has irregular shape or object is quite complex, as this method leads to uniform coating. It is fast, cost-effective than many other listed strategies.

15.4.8 *Spray Pyrolysis*

Spray pyrolysis is a commonly implemented strategy for thin film deposition of photocatalyst over the surface of heated substrate, which includes formation of aerosols of photocatalyst. The solution formed is colloidal in nature [36, 106]. The formed aerosol is heated very rapidly at required high temperatures and is passed through several stages listed as follows:

I The solvent is evaporated from droplet surface.
II The droplets containing precipitated are then dried.
III Thermolysis is performed, i.e. annealing of precipitates at high temperature takes place.
IV Formation of microporous particles of desired phase composition takes place.
V As a result of above step, solid particles are formed.
VI At last, formed solid particles undergo sintering, i.e. particles get compacted under high pressure and temperature (Fig. 15.12).

This strategy leads to formation of uniform and fine deposition of photocatalyst over the surface of substrate. When compared to other strategies available, it holds

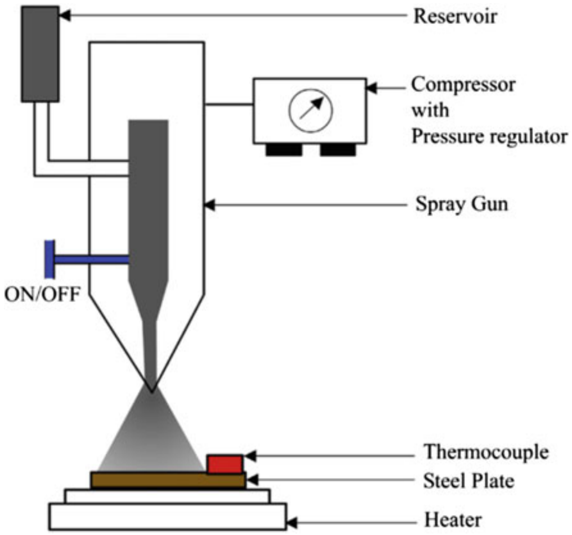

Fig. 15.12 Spray pyrolysis apparatus constituting of precursor solution, atomiser, temperature controller and substrate heater (reprinted with permission from Ref. [36])

numerous distinctive advantages. These advantages include its experimental set-up which does not require costly equipment and can be easily established at lab scale. It is very cost-effective method, and required chemicals and reagents are also easily available. The drop produced is of narrow size and thus has higher surface area leading to higher photocatalytic activity. The size and morphology of particles can be effectively controlled by variating preliminary condition, solvent, additives, concentration of reactant and flow rate in precursor solution. The resultant immobilized catalyst films have high density packing with higher uniformity. The resultant has high purity, nano structure, narrow size distribution, large surface area and high porosity resulting in better efficiency of photocatalyst [107–110].

15.4.9 Solvent Casting

Another most commonly implemented technique used for immobilizing photocatalyst in form of thin polymeric films of nanocomposite scaffold is solvent casting. The working principle of solvent casting is based on solvent containing uniform distribution of photocatalyst of specific size, and solution is kept in 3D mould for casting. This method is widely implemented due to its cost-effectiveness, ease in reaction variation and shorter preparation time interval. The solvent chosen for dispersion plays a key role in determining morphological properties including orientation of surface crystals, surface heterogenicity, swelling nature and rate of structural deformation of formed composite. CCl_4, methylene chloride and tetrahydrofuran are most commonly used solvents. These solvents are spread uniformly over teflon lined surface, and then, solvent is allowed to evaporate gradually

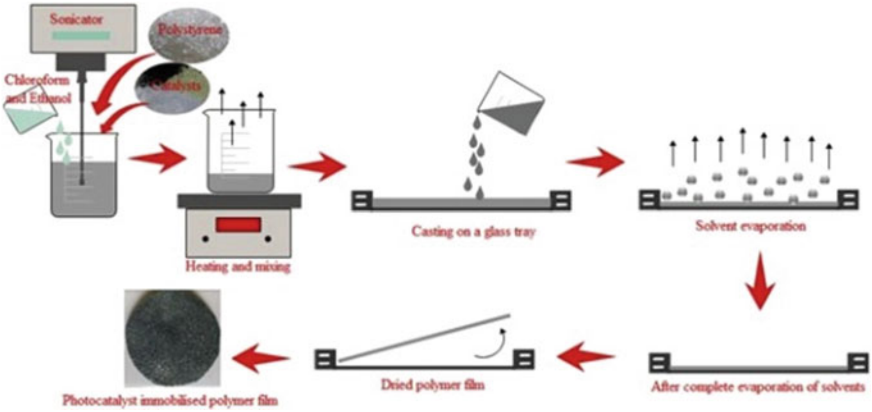

Fig. 15.13 Preparation of photocatalytic polymer film using solvent casting method (reprinted with permission from Ref. [117])

using continuous flow of dinitrogen stream. After complete evaporation of solvent, deposited films are dry casted using IR lamp. This method has shown excellent reusability and recyclability of photocatalyst for degrading environmental pollutants [111–116] (Fig. 15.13).

15.5 Surface Analysis of Impregnated Photocatalyst on Various Surface

It became essential to study the structural, morphological and physio-chemical properties of catalyst apart from their increment in photocatalytic activity after desired immobilization of photocatalyst on suitable substrate. This study can be achieved my means of various characterization techniques available. These techniques majorly include scanning electron microscopy (SEM), transmission electron microscopy (TEM), X-ray diffraction (XRD), X-ray photoelectron spectroscopy, thermal gravimetric analysis (TGA), dynamic light scattering (DLS), atomic force microscopy (AFM) and Brunauer–Emmett–Teller (BET) [117]. The brief information with their applications is listed as follows:

I Transmission Electron Microscopy: This technique is useful in determining anatomy of particles with size of particle in nm range. With help of electron beam, it determines crystal phase as well as crystal size.
II Scanning Electron microscopy: This technique produces image of surface of sample by means of electron beam. It helps in determining surface morphology including shape, measurement of sample size, analysis of sample composition using EDX, as well as study of micropores present on surface.

III X-Ray Diffraction: This technique helps in determination of type of crystal lattice, size, shape, edge length and phase analyzation of crystalline material.

IV Thermal Gravitation Analysis: This technique is used for determination of thermal properties of synthesised samples where change in mass of sample is measured over time with change in temperature. It helps in determination of composition of sample, degradation mechanism as well as kinetics of sample. It also helps in determination of ash contents of sample.

V X-Ray Photoelectron Spectroscopy: It is a surface-sensitive quantitative technique used for analysing surface elemental and chemical composition with complete electronic structure and density of electronic states of present material using photoelectric effect. Also, it helps in determination of bonding between elements present using line profiling across the surface of substrate containing immobilized photocatalyst. It provides empirical formula of sample and measures uniformity of elemental composition.

VI BET: This technique focuses on measurement of surface area including pore-size distribution over the surface of substrate and immobilized catalyst. The data thus obtained helps in prediction of rate of dissolution, and thus, specific surface area is predicted using area available for bio-activity. This analysis is also useful in evaluating performance of product as well consistency of manufacturing that product.

VII Dynamic Light Scattering: This is referred to as photon correlation spectroscopy or QLS which helps in deamination of particle size using suspension of particles in form of colloidal solution. This technique is helpful in measurement of hydrodynamic size of particles by means of laser light scattering by colloidal solution. The intensity of light scattered by these Brownian nanoparticles helps in correlation of hydrodynamic diameter. Smaller the particle, faster is the diffusion rate. As light hits and gets scattered by particle, it causes a Doppler shift. This Doppler shift helps in determining the particle size by means of change in wavelength. It is most appropriate technique listed till date for determination of particle sized.

VIII Atomic Force Microscopy (AFM): It is an influential technique used for analysing micro or nano coatings on various substrates. It uses probe for analysing surface structure. It helps in analysing surface adhesion, pores, friction, etching, polishing, lubricating as well as etching. In comparison with electron microscopy, it does not require any vacuum as it can work in air or liquid environment. It provides a true 3-D surface profiling without any requirement of pre-treatment of sample [118].

15.6 Summary

Photocatalysis has emerged out as green and highly potential technique among many AOPs for degrading recalcitrant pollutants including various organics, inorganics and bacterial disinfection with efficiency of producing clean energy fuels during degradation of these pollutants. Various reasons are present that hinders the implementation of photocatalyst for environmental remidiation at large scale.. Major factor governing is wavelength absorbed by photocatalyst for getting initiated for degradation of pollutant and second is cost-factor for its commercialization. In last decade, numerous studies have been carried out for immobilizing photocatalyst on various substrates to increase their reusability and recyclability, making the process more sustainable. In this chapter, we have tried to incorporate various substrates that have been implemented for immobilizing catalyst onto their surface. A large number of strategies have also been adapted for their immobilization, and few effective techniques are also listed with their processes for immobilizing catalyst. The research gap is present that the material immobilized should sustain for longer duration with recyclability of large number of cycles. It also includes that researchers should be encouraged for utilizing natural and biodegradable substrates for immobilizing catalyst on their surface. First and foremost, thinking of a researcher before choosing any substrate with suitable strategy for immobilizing photocatalyst should be that it should increase surface area of catalyst, secondly it should be held by substrate for longer duration, have inertness, it should not interfere the catalyst during its reaction with pollutant, should not be self-oxidizable, bear good conductivity and should increase absorption of visible light spectra. The major limitation that came across is inherent mass transfer of immobilized catalyst. A detailed emphasis is required for development of new immobilised photocatalysts that are not only capable of showing photocatalytic activity under visible and/ or solar light spectrum, but can also be recycled over many runs without significant loss in its photocatalytic activity. Nevertheless, it is worth to note that, a large-scale implementation of these types of immobilised catalysts can help in reducing a great stress on environment due to toxic effluents from industries, harmful organic compounds and pharmaceuticals from domestic sewage, etc.

References

1. Rezakazemi M, Khajeh A, Mesbah M (2018) Membrane filtration of wastewater from gas and oil production. ECL 16:367–388
2. Bratby J (2016) Coagulation and flocculation in water and wastewater treatment. IWA publishing
3. Cinperi NC, Ozturk E, Yigit NO, Kitis M (2019) Treatment of woolen textile wastewater using membrane bioreactor, nanofiltration and reverse osmosis for reuse in production processes. J Cleaner Prod 223:837–848
4. Kim J, Chung Y, Shin D et al (2003) Chlorination by-products in surface water treatment process. Desalination 151:1–9
5. Sharma K, Dutta V, Sharma S et al (2019) Recent advances in enhanced photocatalytic activity of bismuth oxyhalides for efficient photocatalysis of organic pollutants in water: a review

6. Garg S, Yadav M, Chandra A, Hernadi K (2019) A review on BiOX (X= Cl, Br and I) nano-/microstructures for their photocatalytic applications. J Nanosci Nanotechnol 19:280–294. https://doi.org/10.1166/jnn.2019.15771
7. Deepthi K, Suresh P, Umabala AM, Rao AVP (2017) Enhanced visible light assisted photo catalytic activity of Bi2MO6 (M= Mo, W) in presence of H2O2 for degradation of Rhodamine-B and methylene blue. Int J Appl Chem 13:773–785
8. Lee S-Y, Park S-J (2013) TiO_2 photocatalyst for water treatment applications. J Ind Eng Chem 19:1761–1769
9. Malathi A, Madhavan J, Ashokkumar M, Arunachalam P (2018) A review on $BiVO_4$ photocatalyst: activity enhancement methods for solar photocatalytic applications. Appl Catal A Gen 555:47–74
10. Singh S, Sharma R, Khanuja M (2018) A review and recent developments on strategies to improve the photocatalytic elimination of organic dye pollutants by BiOX (X= Cl, Br, I, F) nanostructures. Korean J Chem Eng 35:1955–1968
11. Pare B, Singh P, Jonnalgadda SB (2009) Degradation and mineralization of victoria blue B dye in a slurry photoreactor using advanced oxidation process
12. Pare B, Singh P, Jonnalgadda SB (2009) Artificial light assisted photocatalytic degradation of lissamine fast yellow dye in ZnO suspension in a slurry batch reactor
13. Reddy CV, Reddy KR, Harish VVN et al (2020) Metal-organic frameworks (MOFs)-based efficient heterogeneous photocatalysts: Synthesis, properties and its applications in photocatalytic hydrogen generation, CO_2 reduction and photodegradation of organic dyes. Int J Hydrogen Energy 45:7656–7679. https://doi.org/10.1016/j.ijhydene.2019.02.144
14. Yadav M, Garg S, Chandra A, Hernadi K %J CI (2019) Immobilization of green BiOX (X= Cl, Br and I) photocatalysts on ceramic fibers for enhanced photocatalytic degradation of recalcitrant organic pollutants and efficient regeneration process 45:17715–17722
15. Jung H, Min Cho K, Hwan Kim K et al (2018) Highly efficient and stable CO_2 reduction photocatalyst with a hierarchical structure of mesoporous TiO_2 on 3D graphene with few-layered MoS2. ACS Sustain Chem Eng 6:5718–5724. https://doi.org/10.1021/acssuschemeng.8b00002
16. Demir H, Top A, Balköse D, Ülkü S (2008) Dye adsorption behavior of Luffa cylindrica fibers. J Hazard Mater 153:389–394. https://doi.org/10.1016/j.jhazmat.2007.08.070
17. Shu Y, Aikebaier T, Quan X et al (2014) Selective catalytic reaction of NO_x with NH3 over Ce-Fe/TiO_2-loaded wire-mesh honeycomb: resistance to SO_2 poisoning. Appl Catal B 150–151:630–635. https://doi.org/10.1016/j.apcatb.2014.01.008
18. Serpone N, Borgarello E, Harris R et al (1986) Photocatalysis over TiO_2 supported on a glass substrate. Solar Energy Mater 14:121–127. https://doi.org/10.1016/0165-1633(86)90070-5
19. Zhang S, Zhang J, Sun J, Tang Z (2020) Capillary microphotoreactor packed with TiO2-coated glass beads: an efficient tool for photocatalytic reaction. Chem Eng Process Process Intensification 147: https://doi.org/10.1016/j.cep.2019.107746
20. Wang ZS, Kawauchi H, Kashima T, Arakawa H (2004) Significant influence of TiO_2 photoelectrode morphology on the energy conversion efficiency of N719 dye-sensitized solar cell. Coord Chem Rev 248:1381–1389
21. Yang J, Wang X, Zhao X et al (2015) Synthesis of uniform Bi2WO6-reduced graphene oxide nanocomposites with significantly enhanced photocatalytic reduction activity. J Phys Chem C 119:3068–3078
22. Etaiw SEH, Marie H (2018) Ultrasonic synthesis of 1D-Zn (II) and La (III) supramolecular coordination polymers nanoparticles, fluorescence, sensing and photocatalytic property. J Photochem Photobiol A 364:478–491
23. Wang J, Tang L, Zeng G, et al (2017) Plasmonic Bi metal deposition and g-C_3N_4 coating on Bi2WO6 microspheres for efficient visible-light photocatalysis. ACS Sustain Chem Eng 5:1062–1072
24. Venkatadri R, Peters RW (1993) Chemical oxidation technologies: ultraviolet light/hydrogen peroxide, Fenton's reagent, and titanium dioxide-assisted photocatalysis. Hazard Waste Hazard Mater 10:107–149

25. Yin HY, Wang L, Sun YF et al (2011) Enhancement of crystalization and photocatalysis of Bi2MoO6 nanoplates by SDS assisted hydrothermal method. In: Advanced materials research. Trans Tech Publ, pp 2091–2097
26. Zhang G, Song IY, Ahn KH et al (2011) Free radical polymerization initiated and controlled by visible light photocatalysis at ambient temperature. Macromolecules 44:7594–7599
27. Tyagi H, Chawla H, Bhandari H, Garg S (2021) Recent-enhancements in visible-light photocatalytic degradation of organochlorines pesticides: a review, materials today: proceedings. https://doi.org/10.1016/j.matpr.2020.12.1036
28. Singh (2021) Magnetic hybrid nanoparticles for drug delivery - Google Scholar, (n.d.). https://scholar.google.com/scholar?cluster=6557395070724245148&hl=en&oi=scholarr (accessed June 28, 2021)
29. Chawla H, Chandra A, Ingole PP, Garg S (2021) Recent advancements in enhancement of photocatalytic activity using bismuth-based metal oxides Bi2MO6 (M=W, Mo, Cr) for environmental remediation and clean energy production. J Ind Eng Chem
30. Gui M-S, Zhang W-D, Chang Y-Q, Yu Y-X (2012) One-step hydrothermal preparation strategy for nanostructured WO3/Bi2WO6 heterojunction with high visible light photocatalytic activity. Chem Eng J 197:283–288
31. Lei P, Wang F, Gao X et al (2012) Immobilization of TiO_2 nanoparticles in polymeric substrates by chemical bonding for multi-cycle photodegradation of organic pollutants. J Hazard Mater 227–228:185–194. https://doi.org/10.1016/j.jhazmat.2012.05.029
32. Chauhan I, Aggrawal S, Chandravati Mohanty P (2015) Metal oxide nanostructures incorporated/immobilized paper matrices and their applications: a review. RSC Adv 5:83036–83055
33. Li Z, Chen F, Yuan L et al (2012) Uranium (VI) adsorption on graphene oxide nanosheets from aqueous solutions. Chem Eng J 210:539–546
34. A. Rawool S, Samanta A, Ajithkumar T et al (2020) Photocatalytic hydrogen generation and CO_2 conversion using g-C_3N_4 decorated dendritic fibrous nanosilica: role of interfaces between silica and g-C_3N_4. ACS Appl Energy Mater 3:8150–8158. https://doi.org/10.1021/acsaem.0c01265
35. Kim J, van der Bruggen B (2010) The use of nanoparticles in polymeric and ceramic membrane structures: review of manufacturing procedures and performance improvement for water treatment. Environ Pollut 158:2335–2349
36. Srikanth B, Goutham R, Badri Narayan R et al (2017) Recent advancements in supporting materials for immobilised photocatalytic applications in waste water treatment. J Environ Manage 200:60–78
37. Pajootan E, Rahimdokht M, Arami M (2017) Carbon and CNT fabricated carbon substrates for TiO_2 nanoparticles immobilization with industrial perspective of continuous photocatalytic elimination of dye molecules. J Ind Eng Chem 55:149–163. https://doi.org/10.1016/j.jiec.2017.06.039
38. Wang H, Sun P, Cong S et al (2016) Nitrogen-doped carbon dots for “green” quantum dot solar cells. Nanoscale Res Lett 11:1–6
39. Li X, Cai W, Colombo L, Ruoff RS (2009) Evolution of graphene growth on Ni and Cu by carbon isotope labeling. Nano Lett 9:4268–4272
40. Zhang M, Shao C, Mu J et al (2012) Hierarchical heterostructures of Bi2MoO6 on carbon nanofibers: controllable solvothermal fabrication and enhanced visible photocatalytic properties. J Mater Chem 22:577–584
41. Yadav M, Garg S, Chandra A et al (2020) Green BiOI impregnated 2-dimensional cylindrical carbon block: a promising solution for environmental remediation and easy recovery of the photocatalyst. Sep Purif Technol 240:116628
42. Zhu D, Zhou Q (2020) Novel Bi2WO6 modified by N-doped graphitic carbon nitride photocatalyst for efficient photocatalytic degradation of phenol under visible light. Appl Catal B Environ 268:118426

43. Gavrilović Tv, Jovanović DJ, Dramićanin MD (2018) Synthesis of multifunctional inorganic materials: from micrometer to nanometer dimensions. In: Nanomaterials for green energy. Elsevier, pp 55–81
44. Qin M, Hou S, Wang LK et al (2007) Two methods for glass surface modification and their application in protein immobilization. Colloids Surf B 60:243–249. https://doi.org/10.1016/j.colsurfb.2007.06.018
45. Vaiano V, Iervolino G (2018) Facile method to immobilize ZnO particles on glass spheres for the photocatalytic treatment of tannery wastewater. J Colloid Interface Sci 518:192–199. https://doi.org/10.1016/j.jcis.2018.02.033
46. Behnajady MA, Modirshahla N, Daneshvar N, Rabbani M (2007) Photocatalytic degradation of C.I. Acid Red 27 by immobilized ZnO on glass plates in continuous-mode. J Hazard Mater 140:257–263. https://doi.org/10.1016/j.jhazmat.2006.07.054
47. Nawi MA, Sabar S, Jawad AH et al (2010) Adsorption of reactive red 4 by immobilized chitosan on glass plates: towards the design of immobilized TiO_2-chitosan synergistic photocatalyst-adsorption bilayer system. Biochem Eng J 49:317–325. https://doi.org/10.1016/j.bej.2010.01.006
48. Khataee AR, Pons MN, Zahraa O (2009) Photocatalytic degradation of three azo dyes using immobilized TiO_2 nanoparticles on glass plates activated by UV light irradiation: influence of dye molecular structure. J Hazard Mater 168:451–457. https://doi.org/10.1016/j.jhazmat.2009.02.052
49. Jansson I, Kobayashi K, Hori H et al (2017) Decahedral anatase titania particles immobilized on zeolitic materials for photocatalytic degradation of VOC. Catal Today 287:22–29. https://doi.org/10.1016/j.cattod.2016.11.041
50. Salaeh S, Juretic Perisic D, Biosic M et al (2016) Diclofenac removal by simulated solar assisted photocatalysis using TiO_2-based zeolite catalyst; mechanisms, pathways and environmental aspects. Chem Eng J 304:289–302. https://doi.org/10.1016/j.cej.2016.06.083
51. Yang L, Wang F, Hakki A et al (2017) The influence of zeolites fly ash bead/TiO_2 composite material surface morphologies on their adsorption and photocatalytic performance. Appl Surf Sci 392:687–696. https://doi.org/10.1016/j.apsusc.2016.09.023
52. Leal Marchena C, Lerici L, Renzini S et al (2016) Synthesis and characterization of a novel tungstosilicic acid immobilized on zeolites catalyst for the photodegradation of methyl orange. Appl Catal B 188:23–30. https://doi.org/10.1016/j.apcatb.2016.01.064
53. Mohamed RM, Mohamed MM (2008) Copper (II) phthalocyanines immobilized on alumina and encapsulated inside zeolite-X and their applications in photocatalytic degradation of cyanide: a comparative study. Appl Catal A 340:16–24. https://doi.org/10.1016/j.apcata.2008.01.029
54. Liao G, He W, He Y (2019) Investigation of microstructure and photocatalytic performance of a modified zeolite supported nanocrystal TiO_2 composite. Catalysts 9:502. https://doi.org/10.3390/catal9060502
55. Paul B, Martens WN, Frost RL (2012) Immobilised anatase on clay mineral particles as a photocatalyst for herbicides degradation. Appl Clay Sci 57:49–54. https://doi.org/10.1016/j.clay.2011.12.009
56. Hass Caetano Lacerda E, Monteiro FC, Kloss JR, Fujiwara ST (2020) Bentonite clay modified with Nb2O5: an efficient and reused photocatalyst for the degradation of reactive textile dye. J Photochem Photobiol A 388:112084. https://doi.org/10.1016/j.jphotochem.2019.112084
57. An T, Chen J, Li G et al (2008) Characterization and the photocatalytic activity of TiO_2 immobilized hydrophobic montmorillonite photocatalysts. Degradation of decabromodiphenyl ether (BDE 209). Catal Today 139:69–76. https://doi.org/10.1016/j.cattod.2008.08.024
58. Radeka M, Markov S, Lončar E et al (2014) Photocatalytic effects of TiO_2 mesoporous coating immobilized on clay roofing tiles. J Eur Ceram Soc 34:127–136. https://doi.org/10.1016/j.jeurceramsoc.2013.07.010

59. Sraw A, Kaur T, Pandey Y et al (2018) Fixed bed recirculation type photocatalytic reactor with TiO_2 immobilized clay beads for the degradation of pesticide polluted water. J Environ Chem Eng 6:7035–7043. https://doi.org/10.1016/j.jece.2018.10.062
60. Bel Hadjltaief H, ben Ameur S, da Costa P, et al (2018) Photocatalytic decolorization of cationic and anionic dyes over ZnO nanoparticle immobilized on natural Tunisian clay. Appl Clay Sci 152:148–157. https://doi.org/10.1016/j.clay.2017.11.008
61. Yadav M, Garg S, Chandra A, Hernadi K (2019) Immobilization of green BiOX (X= Cl, Br and I) photocatalysts on ceramic fibers for enhanced photocatalytic degradation of recalcitrant organic pollutants and efficient regeneration process. Ceram Int 45:17715–17722
62. Fakhri A, Gupta VK, Rabizadeh H et al (2018) Preparation and characterization of WS2 decorated and immobilized on chitosan and polycaprolactone as biodegradable polymers nanofibers: photocatalysis study and antibiotic-conjugated for antibacterial evaluation. Int J Biol Macromol 120:1789–1793. https://doi.org/10.1016/j.ijbiomac.2018.09.207
63. Das S, Mahalingam H (2019) Dye degradation studies using immobilized pristine and waste polystyrene-TiO_2/rGO/g-C_3N_4 nanocomposite photocatalytic film in a novel airlift reactor under solar light. J Environ Chem Eng 7: https://doi.org/10.1016/j.jece.2019.103289
64. Kasanen J, Salstela J, Suvanto M, Pakkanen TT (2011) Photocatalytic degradation of methylene blue in water solution by multilayer TiO_2 coating on HDPE. Appl Surf Sci 258:1738–1743. https://doi.org/10.1016/j.apsusc.2011.10.028
65. Matsuzawa S, Maneerat C, Hayata Y et al (2008) Immobilization of TiO_2 nanoparticles on polymeric substrates by using electrostatic interaction in the aqueous phase. Appl Catal B 83:39–45. https://doi.org/10.1016/j.apcatb.2008.01.036
66. Nawi RMA, Haitham K (2014) Fabrication, characterization and application of a reusableimmobilized TiO_2-PANI photocatalyst plate for the removal of reactive red 4 dyeS. Appl Surf Sci 319:90–98. https://doi.org/10.1016/j.apsusc.2014.07.049
67. Cantarella M, Sanz R, Buccheri MA et al (2016) Immobilization of nanomaterials in PMMA composites for photocatalytic removal of dyes, phenols and bacteria from water. J Photochem Photobiol A 321:1–11. https://doi.org/10.1016/j.jphotochem.2016.01.020
68. Das S, Mahalingam H (2020) Novel immobilized ternary photocatalytic polymer film based airlift reactor for efficient degradation of complex phthalocyanine dye wastewater. J Hazard Mater 383:121219. https://doi.org/10.1016/j.jhazmat.2019.121219
69. Hir ZAM, Moradihamedani P, Abdullah AH, Mohamed MA (2017) Immobilization of TiO_2 into polyethersulfone matrix as hybrid film photocatalyst for effective degradation of methyl orange dye. Mater Sci Semicond Process 57:157–165. https://doi.org/10.1016/j.mssp.2016.10.009
70. Khin MM, Nair AS, Babu VJ et al (2012) A review on nanomaterials for environmental remediation. Energy Environ Sci 5:8075–8109
71. Wood D, Shaw S, Cawte T et al (2020) An overview of photocatalyst immobilization methods for air pollution remediation. Chem Eng J 391:123490
72. Samy M, Ibrahim MG, Gar Alalm M, Fujii M (2020) Effective photocatalytic degradation of sulfamethazine by CNTs/LaVO4 in suspension and dip coating modes. Sep Purif Technol 235:116138. https://doi.org/10.1016/j.seppur.2019.116138
73. Samy M, Ibrahim MG, Gar Alalm M, Fujii M (2020) Effective photocatalytic degradation of sulfamethazine by CNTs/LaVO4 in suspension and dip coating modes. Sep Purif Technol 235: https://doi.org/10.1016/j.seppur.2019.116138
74. Bouarioua A, Zerdaoui M (2017) Photocatalytic activities of TiO_2 layers immobilized on glass substrates by dip-coating technique toward the decolorization of methyl orange as a model organic pollutant. J Environ Chem Eng 5:1565–1574. https://doi.org/10.1016/j.jece.2017.02.025
75. Kása Z, Orbán E, Pap Z et al Innovative and cost-efficient BiOI immobilization technique on ceramic paper-total coverage and high photocatalytic activity. https://doi.org/10.3390/nano10101959

76. Levchuk I, Guillard C, Dappozze F et al (2016) Photocatalytic activity of TiO_2 films immobilized on aluminum foam by atomic layer deposition technique. J Photochem Photobiol A 328:16–23. https://doi.org/10.1016/j.jphotochem.2016.03.034
77. Kakaei K, Esrafili MD, Ehsani A (2019) Graphene and anticorrosive properties. In: Interface science and technology. Elsevier B.V., pp 303–337
78. Ebnesajjad S, Landrock AH (2015) Adhesive applications and bonding processes. In: Adhesives technology handbook. Elsevier, pp 206–234
79. ten Elshof JE (2015) Chemical solution deposition techniques for epitaxial growth of complex oxides. In: Epitaxial growth of complex metal oxides. Elsevier, pp 69–93
80. Rane AV, Kanny K (2018) Manufacturing process-reinforced rubber sheet for rubber dam. In: Hydraulic rubber dam: an effective water management technology. Elsevier, pp 37–46
81. Zolfaghari P, Khaledian HR, Aliasgharlou N et al (2019) Facile surface modification of immobilized rutile nanoparticles by non-thermal glow discharge plasma: effect of treatment gases on photocatalytic process. Appl Surf Sci 490:266–277. https://doi.org/10.1016/j.apsusc.2019.06.077
82. Navaneetha Pandiyaraj K, Ram Kumar MC, Arun Kumar A et al (2016) Tailoring the surface properties of polypropylene films through cold atmospheric pressure plasma (CAPP) assisted polymerization and immobilization of biomolecules for enhancement of anti-coagulation activity. Appl Surf Sci 370:545–556. https://doi.org/10.1016/j.apsusc.2016.02.137
83. Ebrahimi S, Bordbar-Khiabani A, Yarmand B (2020) Immobilization of rGO/ZnO hybrid composites on the Zn substrate for enhanced photocatalytic activity and corrosion stability. J Alloy Compd 845: https://doi.org/10.1016/j.jallcom.2020.156219
84. de Rancourt de Mimérand Y, Li K, Zhou C et al (2020) Functional supported ZnO/Bi2MoO6 heterojunction photocatalysts with 3D-printed fractal polymer substrates and produced by innovative plasma-based immobilization methods. ACS Appl Mater Interfaces 12:43138–43151. https://doi.org/10.1021/acsami.0c12286
85. Li K, de Rancourt de Mimérand Y, Jin X et al (2020) Metal oxide (ZnO and TiO_2) and Fe-based metal–organic-framework nanoparticles on 3D-printed fractal polymer surfaces for photocatalytic degradation of organic pollutants. ACS Appl Nano Mater 3:2830–2845. https://doi.org/10.1021/acsanm.0c00096
86. Stojadinović S, Radić N, Tadić N et al (2020) Enhanced ultraviolet light driven photocatalytic activity of ZnO particles incorporated by plasma electrolytic oxidation into Al_2O_3 coatings co-doped with Ce3+. Opt Mater 101:109768. https://doi.org/10.1016/j.optmat.2020.109768
87. Ebrahimi S, Bordbar-Khiabani A, Yarmand B (2020) Immobilization of rGO/ZnO hybrid composites on the Zn substrate for enhanced photocatalytic activity and corrosion stability. J Alloy Compd 845:156219. https://doi.org/10.1016/j.jallcom.2020.156219
88. Chizoba Ekezie FG, Sun DW, Cheng JH (2017) A review on recent advances in cold plasma technology for the food industry: current applications and future trends. Trends Food Sci Technol 69:46–58
89. Jin C, Lu Y, Tong G et al (2020) Excellent microwave absorbing properties of ZnO/$ZnFe_2O_4$/Fe core-shell microrods prepared by a rapid microwave-assisted hydrothermal-chemical vapor decomposition method. Appl Surf Sci 531:147353. https://doi.org/10.1016/j.apsusc.2020.147353
90. Alfaro Cruz MR, Ceballos-Sanchez O, Luévano-Hipólito E, Torres-Martínez LM (2018) ZnO thin films deposited by RF magnetron sputtering: effects of the annealing and atmosphere conditions on the photocatalytic hydrogen production. Int J Hydrogen Energy 43:10301–10310. https://doi.org/10.1016/j.ijhydene.2018.04.054
91. Mahdhi H, Djessas K, ben Ayadi Z (2018) Synthesis and characteristics of Ca-doped ZnO thin films by rf magnetron sputtering at low temperature. Mater Lett 214:10–14. https://doi.org/10.1016/j.matlet.2017.11.108

92. Lelis M, Tuckute S, Varnagiris S et al (2019) Tailoring of TiO_2 film microstructure by pulsed-DC and RF magnetron co-sputtering. Surf Coat Technol 377:124906. https://doi.org/10.1016/j.surfcoat.2019.124906
93. Madhuri KV (2020) Thermal protection coatings of metal oxide powders. In: Metal oxide powder technologies. Elsevier, pp 209–231
94. Singh J, Khan SA, Shah J et al (2017) Nanostructured TiO_2 thin films prepared by RF magnetron sputtering for photocatalytic applications. Appl Surf Sci 422:953–961. https://doi.org/10.1016/j.apsusc.2017.06.068
95. Wang J, Zhang Z, Wang X et al (2018) Synthesis of novel p-n heterojunction m-Bi_2O_4/BiOCl nanocomposite with excellent photocatalytic activity through ion-etching method. Cuihua Xuebao/Chinese J Catal 39:1792–1803. https://doi.org/10.1016/S1872-2067(18)63142-0
96. Bo L, Liu H, Han H (2019) Photocatalytic degradation of trace carbamazepine in river water under solar irradiation. J Environ Manag 241:131–137. https://doi.org/10.1016/j.jenvman.2019.03.132
97. Pasikhani JV, Gilani N, Pirbazari AE (2018) Improvement the wastewater purification by TiO_2 nanotube arrays: the effect of etching-step on the photo-generated charge carriers and photocatalytic activity of anodic TiO_2 nanotubes. Solid State Sci 84:57–74. https://doi.org/10.1016/j.solidstatesciences.2018.08.003
98. Yin XL, Li LL, Liu ML et al (2019) MoSx/CdS nano-heterostructures accurately constructed on the defects of CdS for efficient photocatalytic H_2 evolution under visible light irradiation. Chem Eng J 370:305–313. https://doi.org/10.1016/j.cej.2019.03.231
99. Etch System—What is an Etch System? : Hitachi High-Tech GLOBAL. https://www.hitachi-hightech.com/global/products/device/semiconductor/etch.html. Accessed 17 Jan 2021
100. Demirci S, Yurddaskal M, Dikici T, Sarıoğlu C (2018) Fabrication and characterization of novel iodine doped hollow and mesoporous hematite (Fe2O3) particles derived from sol-gel method and their photocatalytic performances. J Hazard Mater 345:27–37. https://doi.org/10.1016/j.jhazmat.2017.11.009
101. Shafei A, Sheibani S (2019) Visible light photocatalytic activity of Cu doped TiO_2-CNT nanocomposite powder prepared by sol–gel method. Mater Res Bull 110:198–206. https://doi.org/10.1016/j.materresbull.2018.10.035
102. Zhang W, Liu Y, Pei X, Chen X (2017) Effects of indium doping on properties of xIn-0.1% Gd-TiO_2 photocatalyst synthesized by sol-gel method. J Phys Chem Solids 104:45–51. https://doi.org/10.1016/j.jpcs.2016.12.031
103. Mahdavi R, Ashraf Talesh SS (2017) The effect of ultrasonic irradiation on the structure, morphology and photocatalytic performance of ZnO nanoparticles by sol-gel method. Ultrason Sonochem 39:504–510. https://doi.org/10.1016/j.ultsonch.2017.05.012
104. Phin HY, Ong YT, Sin JC (2020) Effect of carbon nanotubes loading on the photocatalytic activity of zinc oxide/carbon nanotubes photocatalyst synthesized via a modified sol-gel method. J Environ Chem Eng 8: https://doi.org/10.1016/j.jece.2019.103222
105. Kaviyarasu K, Mariappan A, Neyvasagam K et al (2017) Photocatalytic performance and antimicrobial activities of HAp-TiO_2 nanocomposite thin films by sol-gel method. Surf Interfaces 6:247–255. https://doi.org/10.1016/j.surfin.2016.10.002
106. Spiridonova J, Mere A, Krunks M et al (2020) Enhanced visible and ultraviolet light-induced gas-phase photocatalytic activity of TiO_2 thin films modified by increased amount of acetylacetone in precursor solution for spray pyrolysis. Catalysts 10:1011. https://doi.org/10.3390/catal10091011
107. Abe Y, Laine RM (2020) Photocatalytic La4Ti3O12 nanoparticles fabricated by liquid-feed flame spray pyrolysis. Ceram Int 46:18656–18660. https://doi.org/10.1016/j.ceramint.2020.04.178
108. Gao F, Xu Z, Zhao H (2020) Flame spray pyrolysis made Pt/TiO_2 photocatalysts with ultralow platinum loading and high hydrogen production activity. Proc Combust Inst. https://doi.org/10.1016/j.proci.2020.06.330

109. Dundar I, Mere A, Mikli V et al (2020) Thickness effect on photocatalytic activity of TiO_2 thin films fabricated by ultrasonic spray pyrolysis. Catalysts 10:1058. https://doi.org/10.3390/catal10091058
110. Saito K, Yi E, Laine RM, Sugahara Y (2020) Preparation of Nb-doped TiO2 nanopowder by liquid-feed spray pyrolysis followed by ammonia annealing for tunable visible-light absorption and inhibition of photocatalytic activity. Ceram Int 46:1314–1322. https://doi.org/10.1016/j.ceramint.2019.09.094
111. Teixeira S, Martins PM, Lanceros-Méndez S et al (2016) Reusability of photocatalytic TiO_2 and ZnO nanoparticles immobilized in poly(vinylidene difluoride)-co-trifluoroethylene. Appl Surf Sci 384:497–504. https://doi.org/10.1016/j.apsusc.2016.05.073
112. Salazar H, Martins PM, Santos B et al (2020) Photocatalytic and antimicrobial multifunctional nanocomposite membranes for emerging pollutants water treatment applications. Chemosphere 250: https://doi.org/10.1016/j.chemosphere.2020.126299
113. Vaiano V, Sarno G, Sacco O, Sannino D (2017) Degradation of terephthalic acid in a photocatalytic system able to work also at high pressure. Chem Eng J 312:10–19. https://doi.org/10.1016/j.cej.2016.11.115
114. Nasir AM, Jaafar J, Aziz F et al (2020) A review on floating nanocomposite photocatalyst: fabrication and applications for wastewater treatment. J Water Process Eng 36:101300. https://doi.org/10.1016/j.jwpe.2020.101300
115. Sacco O, Vaiano V, Rizzo L, Sannino D (2018) Photocatalytic activity of a visible light active structured photocatalyst developed for municipal wastewater treatment. J Clean Prod 175:38–49. https://doi.org/10.1016/j.jclepro.2017.11.088
116. Wahid F, Khan T, Hussain Z, Ullah H (2018) Nanocomposite scaffolds for tissue engineering; properties, preparation and applications. In: Applications of nanocomposite materials in drug delivery. Elsevier, pp 701–735
117. Faraldos M, Bahamonde A (2018) Multifunctional photocatalytic coatings for construction materials. In: Nanotechnology in eco-efficient construction: materials, processes and applications. Elsevier, pp 557–589
118. Senthil Kumar P, Grace Pavithra K, Naushad M (2019) Characterization techniques for nanomaterials. In: Nanomaterials for solar cell applications. Elsevier, pp 97–124

Part IV
Environmental Remediation

Chapter 16
Photocatalytic and Other Similar Green Technologies for Reducing Environmental Impacts of Leather Industries

Hemen Dave, Mona Vajpayee, and Lalita Ledwani

Abstract This chapter reviews recent advancements in the photocatalytic process, along with other similar green technologies such as nanotechnology, nonthermal plasma treatment, ozone-based technologies, etc., with specific emphasis on reducing the environmental impacts of leather production and processing. Leather industries are among the most polluting industries worldwide, and to address the challenges leather industries are facing with respect to environmental pollution much scientific work has been carried out. Photocatalytical processes have been explored for treatment of wastewater from tanneries and leather dyeing and finishing. Green photocatalytic processes exhibit great potential for chromium removal from tanneries' wastewater, and degradation of dyes and other hazardous chemical compounds usually found in wastewater from leather industries. Nanomaterials and nanomaterial-based photocatalytic processes also provide leather and leather products with diverse types of surface functionalization and antimicrobial finish which is environmentally affable compared to conventional technology. Other similar technologies are nonthermal plasma and ozone technology which is principally based on nonthermal plasma. Nonthermal plasmas-ionized gases at low temperature have a potential for surface modification of leather which can render applications such as sterilization, improved uptake of dyes, chemicals, and natural products, varieties of finish including antimicrobial finish, etc. Being a dry technology the nonthermal plasma processing can significantly reduce environmental impacts compared to wet chemical processing. The ozone-based technologies are also similar in modes of action with that of the photocatalytic process. The ozone-based technologies are explored by contemporary researchers and are reported to have potential applications such as cleaner dehairing, cleaner preservation, treatment of tanneries' wastewater, hazardous chemicals used in leather

---

H. Dave
National Forensic Sciences University, Gandhinagar, Gujarat, India

M. Vajpayee · L. Ledwani (✉)
Department of Chemistry, Manipal University Jaipur, Rajasthan, India
e-mail: lalita.ledwani@jaipur.manipal.edu

S. Garg and A. Chandra (eds.), *Green Photocatalytic Semiconductors*,
Green Chemistry and Sustainable Technology,
https://doi.org/10.1007/978-3-030-77371-7_16

manufacturing, dye degradation, etc. The holistic overview provided in this chapter would be certainly useful to researchers working in these areas.

Keywords Leather · Pollution · Environmental impacts · Photocatalysis · Nonthermal plasma · Ozone · Waste treatment · Cr reduction · Dye degradation · Wastewater treatment

16.1 Introduction

Leather production is all about the transformation of proteinaceous skin/hide flayed from dead animals to a stable, economically important commodity with a wide variety of uses. Leather production involves pre-tanning, tanning and post-tanning operations; at each stage huge quantities of chemicals and water are required which give rise to massive loads of waste, both solid and liquid, with substantial environmental impacts [1]. As per a study, each year approximately 6.5 million tons of flayed animal skins and wet salted hides are processed worldwide, with around 4.8 billion square feet of leather production [1]. Other studies report 1.67×10^9 m^2 of leather manufactured every year with global sales of US$70 billion [2]. There are around 10,000 tanneries in the world with an estimated US$50 billion turnover; the largest supplier of leather is the European Union which exported 1163.1 thousand tons in the year 2014 [3]. The major production centres of leather are agroeconomic countries such as Argentina, Brazil, Mexico, China, South Korea, India and Pakistan [3]. South Asian leather industries comprise about 5000 tanneries which are small-scale, having a processing capacity of less than 2–3 tons of hides/skins per day, and are scattered all around the region [4]. For an agro-economy, local development can be enhanced by tanneries and leather processing industries but in time this can lead to serious pollution of the environment [3]. As per a statistical estimation, the world capacity of leather production is about 1.5×10^{10} kg hides/skins every year with a per day average discharge of more than 1.5×10^{10} kg of wastewater and an annual generation of 6×10^9 kg of solid waste [5]. India being a country with a huge livestock population, more than 3000 tanneries employing 2.5 million people are present in India, processing 80 million hides and 130 million skin pieces every year. Chrome tanning is commonly perceived in 80% of tanneries in India. India is a leading exporter of leather goods, having an export capacity of of $2.8 billion [6]. Leather production involves several stages/processes as described in Fig. 16.1. These stages/processes can be classified as pre-tanning or beamhouse operations followed by the tanning of pickled hide either by chrome tanning or vegetable tanning, and the associated stages/processes are called tanning yard operations. The leather thus produced is further provided with various finishes as per the product requirements [3].

At each stage of leather production and processing, huge amounts of water, chemicals and energy are required, and waste is produced at each stage which has significant environmental impacts as described in the next section. The challenge to

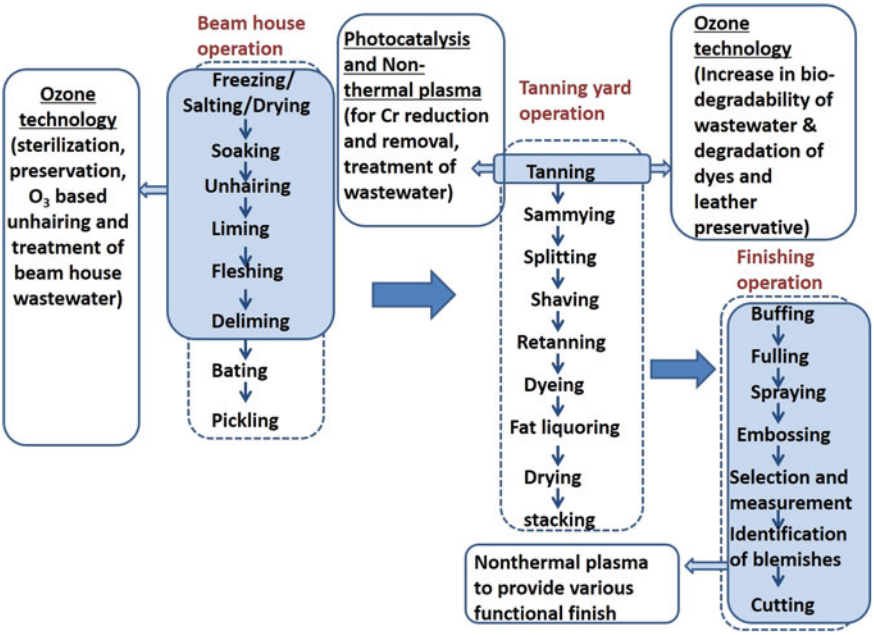

Fig. 16.1 Leather production/processing: pre-tanning, tanning and post-tanning operations

reduce the environmental impacts associated with leather production and processing has been addressed by various technological solutions [7]. In this chapter, we provide an overview for emerging photocatalytic, nonthermal plasma and ozone technology to reduce environmental impacts associated with leather production/processing. As seen in Fig. 16.1, the environmental impacts associated with beamhouse operations can be addressed by ozone technology; for effluent generated from the tanning process photocatalytic and nonthermal plasma-based treatment can provide an effective solution for chromium reduction and removal. All three technologies can be beneficially utilized in the treatment of tannery effluent; the ozonation explored widely for treatment of tannery effluent is described in the following sections.

16.2 Environmental Impacts Associated with Leather Production and Processing

The environmental impacts associated with leather production and processing are releases of pollutants to water, air and soil. Usage of electricity for rotation of drums/vessels is the main source of air pollution; use of fossil fuel for electricity generation can pollute air with oxide of sulphur, oxides of nitrogen, particulate matter and emission of heavy metals such as vanadium, manganese, nickel, etc. [3]. Air pollution resulting from leather processing includes emission of sulphides, thiols, VOCs and organic solvents, ammonia, powdered dyes, leather dust, etc., while polyaromatic hydrocarbons (PAHs) and halogenated organic compounds, PCDD/furans can be emitted when solid waste from leather production is incinerated for waste to energy combustion [3]. Huge quantities of chemicals and water usage for leather production and processing results in a significant portion converted to by-products and pollution. Nearly 100 different chemicals are used to convert raw hides/skins in to finished leather [8]. As per an estimate, every year 6.5 million tons of flayed animal skins and wet salted hides are processed, using 3.5 million tons of different chemicals for leather processing worldwide [1]. Furthermore, organic matter from flayed hides/skins are a major source of waste and by-products. For a bovine hide, about 20–25% weight of raw bovine hide is transformed into leather, with a further 65% transformed to sole leather, while the remaining material contributes to waste, partially being recovered as by-products [3]. When water is utilized in most leather production and processing operations, generally if 1 ton of raw hide is processed, it results in $\sim$250 kg leather with 15–50 kl of wastewater, 450–730 kg of solid waste and 500 kg of sludge generation [3]. The wastewater produced has an organic load of about 240 kg of chemical oxygen demand (COD), and 100 kg of bio-chemical-oxygen-demand (BOD), 150 kg of suspended solids (SS), 170 kg of sodium chloride (NaCl), 80 kg of sulphates and 5 kg of chromates [3]. Apart from the huge organic load that needs to be treated, tannery wastewater contains chromate, i.e., chromium (VI), oxidized from chromium (III) in tanning, which is of most concern because of its recognized carcinogenic, mutagenic and allergenic potential; for that 3 mg/kg (based on leather weight) is the current legislative limit [3]. With a worldwide emphasis now placed on production of chrome-free wet white leather, still 80–90% of tanneries are producing chrome-tanned wet blue leather, because the alternative treatments cannot produces the same quality leather as with chrome tanning [3]. The wastewater from leather production and processing also produces pollutants of significant concern such as the heavy metals copper, cobalt, barium, antimony, selenium, lead, zinc, mercury, nickel, cadmium compounds and arsenic, along with various toxic organic compound-azo dyes, polychlorinated biphenyl (PCB), formaldehyde resins, pesticide and biocide residues [3].

16.2.1 Liquid Waste from Leather Industries and Associated Impacts

As per an estimate, 57% of total water is consumed in pre-tanning and tanning processes while 35% of water is consumed for washing [1]. For one ton of raw hide processing 30–35 m^3 of wastewater gets produced, with a wide range of wastewater production from 10 to 100 m^3 per tons of raw hide depending on the type of hide, the production process and the quality of finished products required [9]. In a study related to the carbon and energy footprint analysis of tannery wastewater treatment it is reported that from 1 kg of raw material 0.3 to 0.4 kg of finished product is obtained with 25 to 45 l of water consumed per kg of raw material, being a water intensity of 0.13 m^3/m^2 of finished product [10]. Water consumption for leather production is estimated to be more than 5×10^7 m^3 per year for the five largest leather producing regions—Brazil, China, India, Italy and Russia, with the highest water footprint of 2.7×10^7 m^3 per year for China [10]. The global carbon footprint associated with tannery wastewater treatment is estimated to be 1.49×10^3 tCO_2, eq. d^{-1}; the energy intensity for tannery wastewater treatment is estimated to be 3.9 kWh kg^{-1} bCOD removed which is significantly higher compared to 1.4 kWh kg^{-1} bCOD for sewage treatment [10].

Preservation of hides by salt preservation can contribute 40% of Total Dissolved Solid (TDS) and 55% of chloride in effluent generated from leather production/processing. Dehairing of skins/hides by the liming process generates 40% and 50% of BOD and COD respectively, and contributes 60–70% to the total pollution load of leather processing [1]. The dehairing stage using sodium sulphide and lime contributes 84% of BOD, 75% of COD and 92% SS in wastewater generated from tannery industries [2, 11]. Conventional dehairing uses sodium sulphide which can affect the efficiency of effluent treatment and cause unfavourable environmental consequences [2]. Overall, wastewater generated from beamhouse operations contains a significantly high concentration of salts, because for the preservation of raw hide during this stage 300–400 kg of salts are required per ton of fresh flayed hide. Furthermore, unabsorbed sulphide and lime from the pelts in the liming process gets discharged in wastewater along with epidermis, broken hair, and non-structural proteins and other material which can increase COD and BOD if wastewater is produced in the soaking and liming stages. Amine additions to wastewater from beamhouse operations such as liming/deliming, and bating along with re-tanning operations can result in anaerobic conditions which are toxic for microorganisms playing an important role in wastewater treatment [3]. In subsequent tanning processes hides/skins after beamhouse operations are subjected to chrome tanning or natural tanning, which is processed with several stages that utilize huge variety of chemicals such as synthetic or natural tanning agent with acids, surfactants, salts, sulphonated oils, etc. Chromium tanning is the most used method; 90% of tanneries worldwide use this method in which chromium sulphate is applied at a concentration level of 8–10% [1].

In the most commonly used chrome tanning process only 60 to 80% of applied chromium salts are taken up by the hides/skins, thus the tannery effluent contains significant amounts of trivalent chromium along with other salts such as sulphide, sodium chloride and high concentration of organics with COD above 3000 mg/l [12]. Chromium is the pollutant of most concern; in order to prevent negative impacts to the environment upon discharge, the chromium concentration should not be more than 10 mg/l in the treated tannery effluent [12]. Cr(III) can be oxidized to Cr(VI) which is highly toxic, and the maximum permissible limit of Cr(VI) is 0.05 mg/l of $Cr_2O_7^{-2}$ [12]. Overall, 45–50 m^3 wastewater are generated per ton of raw hide processing, and 70% of total BOD, COD and total dissolved solids are resulting from the process [1]. A medium-sized tannery can produce over 300 million m^3 wastewater every day, which contain thousands of tons of chemicals along with solid waste [1]. In India, 4000 tons of chrome are salts used every year of which 60–70% are used in tanneries. Effluent generated from chrome tanning contains 1500–3000 mg/l chromium, with an average 30–40 l of effluent generated per kg of hide tanned, and an average 50 l of wastewater generated per kg of hide processed by leather finishing operations. Indian tanneries are discharging 9.42×10^6 l of wastewater every year [6]. In India, the river Ganga and its tributary has significantly affected tanneries situated in the surrounding area, with high concentrations of heavy metals in sediments of this riverine system. In Tamil Nadu state of South India, tanneries have contaminated 55,000 ha of land and 5 million people were affected by low quality drinking water due to salination of rivers, and also by ground water contamination from wastewater discharged from tanneries, which also leads to loss of agriculture productivity [2].

16.2.2 Solid Waste from Leather Industries and Associated Impacts

Leather production and processing generates a huge amount of solid waste disposal which is problematic for leather industries. As per the statistics, 650 kg of solid waste is produced from processing of 1 ton of wet salted hides [13]. As leather is made from proteinous hides/skins flayed from dead animals, various nonfibrous proteins or fibrous proteins other than collagen such as hair, fleshing wastes, etc., contribute to solid waste along with trimmings from raw hides/skins, chrome shavings and trimmings, buffering dust, strips, cuttings from leather along with chrome sludge, and effluent treatment plant (ETP) sludge generated from primary and secondary treatments [1]. The quantity of trimmings waste depends on the raw material; in general, it accounts for 5% weight by weight for hides and 12 to 15% weight by weight for skins. Every year about 418×10^3 tons of trimming waste are generated globally [13]. The contribution of beamhouse operations in total solid waste generation is 80%, whereas tanning operations contribute by 19% and finishing operations contribute by 1%. As per the scientific literature, 150 kg of finished leather is produced from one ton of raw hides/skins, whereas the remaining 850 kg contributes to solid waste, comprised of 450 kg of collagen waste and 400 kg of fleshing waste [1]. Apart from other solid waste produced from leather production and processing, sludge generated from effluent treatment can significantly impact the environment if not properly handled. Primary treatment of tannery effluent results in settled sludge generation which accounts for 5 to 10% of the total volume of effluent; further sludge quantity increases up to 20% for the case of biological treatment. The sludge has a solid content 3–5% which increases to 25–40% after dewatering [3]. As per an estimation, bovine tanneries in Europe are generating 4 × 10^5 tons of sludge and the same amount of other solid waste each year [3]. From the different types of solid waste generated from leather production and processing, the chrome shavings are of considerable concern due to the presence of heavy metal chromium, and the disposal of chrome shavings is quite challenging. As per an estimate, every year India is generating 0.2 million tons of chrome shavings whereas worldwide approximately 0.8 million tons of chrome shaving are generated which mostly get disposed of through landfill or incineration [14]. The chrome shavings are fibrous in nature, make up 3–5% of total proteinous waste, contain 30–40% moisture; though chrome shavings contain Cr(III) there is the possibility of its conversion to the 300 times more toxic Cr(VI) [14]. Landfilling of chrome shavings can liberate 40–50% methane gas which can be a significant contribution in global warming, Cr can be leached out from landfill sites and can contaminate ground water, making the soil unfit for cultivation [14]. Solid waste is also generated when leather goods, specially footwear, are manufactured; 15–20% of raw material used for manufacturing of leather goods gets converted to solid waste [11].

For disposal of waste generated from leather production and in processing operations; land filling, anaerobic digestion and thermal incineration are the conventional methods, but environmental impacts and inherent issues are associated with these methods. The presence of chromium in leather production/processing waste can causes severe ground water contamination in the case of ground co-disposal, and chronic air pollution with high concentration of trivalent chromium during thermal incineration [8, 15, 16]. In one study, the method in which tannery wastes were incinerated at 800 °C in a thermal incinerator of starved air under various oxygen flow rates to optimize the oxygen flow required to prevent the conversion of Cr from Cr(III) to Cr(VI) oxidation state is reported. The exploratory study of the incineration of waste under the external oxygen supply was conducted under various conditions. Using Portland cement and fine aggregate, the calcined waste has been effectively solidified/stabilized. The unconfined compressive strength of the blocks was within the range of 120–180 kg/cm whereas to determine the degree of leachate and metals, leachability research was conducted on solidified block through the toxicity characterization of leachate procedure (TCLP) which indicate 99.1–99.9% metal fixation and 55–66 mg/l was the dissolved organic concentration in the TCLP leachate [15].

16.3 Environment Friendly Technology for Leather Processing: Need of Hour

As described in the above sections, the large quantity of water required for production and processing of leather is converted to wastewater; a study of the United Nations Industrial Development Organization (UNIDO) highlights the huge water demand for leather production and processing as an area of environmental concern

[17]. For one ton of raw hides/skins, processing results in the generation of 30–40 m^3 of wastewater [4]. Fresh water requirements for leather production and processing can be reduced by proper treatment and reuse of tannery wastewater, but reuse of wastewater is not possible without its preliminary analysis, and due to the complexity of the matrix reuse of tannery wastewater is a real challenge. The ultimate quality of leather gets affected with changes in the pH or changes in formulation in cases of reuse and that is why reuse is not possible more than once [17]. Also, environmental impacts associated with discharge of tannery effluents comes under sharp criticism and that is why lots of research work has been carried out to find alternative treatments for leather production/processing wastewater and to improve conventional treatment processes by photocatalytic and other green treatments.

16.3.1 Photocatalytic Technology

Advanced oxidation by photocatalysis is one of the promising methods for wastewater treatment which is widely used for treatment of wastewater generated from various industrial activities, for degradation of organic pollutants present in wastewater [18]. Photocatalysis is all about the production of receptive oxygen species on acquaintance of a photocatalyst which is illuminated by UV or visible radiation. The produced reactive oxygen species have the capability for degradation and mineralization of a wide variety of synthetic organic contaminants and pollutants [7, 19]. The application of photocatalysis for treatment of wastewater and pollutant degradation may provide many advantages such as negligible generation of secondary pollution, harmless degradation products, with time and reaction requirements being less, etc., with some of the limitations such as band gap dependency and interfacial charge transfer [7]. Currently, extensive research work is under process for the synthesis of catalysts with higher performance and expansion of light response range of photocatalysts using a variety of approaches such as deposition of noble metal, ion modification, coupled semiconductor, optimization of energy band configuration of photocatalysts for specific applications [20]. Heterogenous photocatalysis involving transition metal ions for environmental applications [21], degradation of various organic pollutants [22], photocatalytic dye degradation [23], photocatalytic dye degradation by synergetic effect of adsorption [24], environmental applications of photo-electrocatalytic technologies [25], coupling of photocatalysis and biodegradation, etc., are major research areas. TiO_2 and ZNO are the most studied photocatalysts; apart from that layered double hydroxides-based photocatalysts [26], metal-doped TiO_2, non-metal doped/co-doped TiO_2 and TiO_2 nanostructured hybrids [27], MoS_2-based photocatalysis [28], metal oxide-cellulose nanocomposites-based photocatalysis [29], nanocomposites based on graphitic carbon nitride (g-C_3N_4), etc., are explored for environmental applications [30]. The major application of photocatalysis to reduce environmental impacts associated with leather production and processing is treatment of wastewater and reduction and removal of chromium [7, 31]. A reasonable photocatalytic reaction system can be developed for simultaneous treatment of two or more pollutants based on photocatalytic reactions with a redox reaction happening at the same time [31]. This approach can be beneficially utilized for treatment of tannery wastewater as described in the following section [7].

16.3.2 Nonthermal Plasma

Plasma is the fourth state of matter, it is ionized form of gases, though being a fourth state of matter, it necessarily has high temperature. The types of plasma which are called nonthermal plasmas or nonequilibrium plasmas are plasmas which do not have a high temperature. Nonthermal plasma technology is utilized as a dry, ecofriendly technology for surface modification of textiles and leather without altering the bulk properties. Nonthermal plasmas are of two types: low pressure plasma and atmospheric pressure plasma. Nonthermal plasma can be produced using a variety of gases as well as gas mixtures; it is an ionized gas which consists of charged particles/ions, energetic electrons, unionized gas molecules, reactive species such as hydroxyl radical, atomic oxygen, ozone, superoxide anion, hydrogen peroxide, reactive nitrogen species, gas molecules in ground and excited states and UV and visible photons. Leather being heat labile material, nonthermal plasma can be utilized for surface modification and eco-friendly processing of leather; atmospheric pressure plasmas are particularly suitable for leather processing. With inclusion of nonthermal plasmas the leather manufacturing process can be improved, less consumption of chemicals, water and energy savings can be achieved; thus nonthermal plasma has a huge potential in different areas of leather production and processing. Also, nonthermal plasmas can be utilized for wastewater treatment as described in subsequent section [32].

16.3.3 Ozone/Ozonation

Ozone is a trioxygen inorganic oxygen molecule with a chemical formula of O_3, an allotrope of oxygen with higher electrochemical oxidation potential, more reactivity and less stability compared to diatomic molecular oxygen. The electrochemical oxidation potential of ozone compared to other known oxidizing agents is as follows: fluorine, F_2 (3.06 V) > hydroxyl radical (2.80 V) > atomic oxygen O (2.42 V) > ozone (2.08 V) > hydrogen peroxide (1.78 V) > hypochlorite (1.49 V) > Cl_2 (1.36 V) > chlorine dioxide (1.27 V) > oxygen gas (1.23 V) [4]. Due to its powerful oxidation potential ozone/ozonation can be extensively utilized for removal of pollutants from industrial effluents. Pollutants present in industrial effluents can be degraded by direct attack of ozone or by free radicals which can a degrade wide variety of organic compounds [33]. There are three techniques for ozone production: (1) ultraviolet techniques in which oxygen exposed to UV radiation can produce ozone in concentrations of 0.0003 g/hour at 1/100 W each; (2) ozone can be produced by perchloric acid electrolysis; and (3) by electrical discharge—a nonthermal plasma-based technique [4].

The advantages of ozone/ozonation for leather production and processing can be summarized as follows: when ozone/ozonation is utilized for treatment of tannery effluent it results in removal of turbidity, colour, bacteria and viruses; also the odour problem in open air stages of effluent treatment plants can be eliminated even with a small capacity (5 g/h) ozone generator [4]. Ozone treatment can result in oxidation of secondary sludge (partial or complete), lysis and partial oxidation of bacterial biomass and other organics to increase availability of food when it recycled as activated sludge, and filamentous bacterial growth and other colloidal structures can be broken down and thus achieve easy dewatering of sludge [4]. For treatment of tannery wastewater when ozone/ozonation is applied with use of high concentration ozone generator in combination with biological treatment, it can decrease treatment time, required discharge standards can be achieved and floor space requirement for ETP can be reduced with properly designed colum/vessel for ozonation [4]. Ozone/ozonation treatment can be easily combined with other advanced oxidation treatments. Residual ozone can be easily destroyed by an UV radiation-based ozone destroyer [34]. Ozonation itself does not generate any sludge, unlike other treatments, and multiple pollution treatment goals can be achieved by a single application of ozonation [33].

16.4 Chromium Reduction and Removal by Photocatalytic and Nonthermal Plasma Technology

Chromium as basic chromium sulphate is applied for tanning in which processed hide gets converted to wet blue, which is a stable product not degraded further even by microbial action. It is a tanning agent which renders the best quality leather with many additional advantages such as low process cost at high speed, producing a light colour of tanned leather with good stability, all of which make it a most used tanning agent [12]; however, it is a pollutant which of major concern from the environmental point of view [17]. In chrome tanning around 60–80% of the chromium reacts with hides/skins and the rest lost to tannery process effluent [12]. When one ton of hides is converted to 200 kg of leather containing 3 kg of chromium, non-tanned solid waste of 250 kg and chromium-containing tanned solid waste is produced which contains 3 kg of chromium [14], and over the time 50,000 kg of wastewater is produced which contains 5 kg of chromium [8, 35]. In the chrome tanning process 20% of raw materials converts to leather and overall, 60% is chromium lost in solid and liquid waste with many associated environmental impacts such as conversion of Cr(III) to carcinogenic Cr(VI) and contamination of water resources, occupational diseases, potential threats due to skin penetration of Cr(VI) by use of leather products, and entry of chromium into the environment at the end of product life, etc. [35].

Conventionally, chromium is removed from tannery effluent by precipitation using alkalis such as NaOH, Na_2CO_3 or $Ca(OH)_2$; other methods for chromium removal are liquid–liquid extraction carried out by di(2,4,4trimethylpentyl) phosphonic acid and partially ammoniated di(2-ethylhexyl) phosphoric acid (D2EHPA), ion exchange, four stage extraction/re-extraction with mono(2-ethylhexyl) phosphoric acid (M2EHPA) or (D2EHPA), removal using high temperature and pressure, adsorption of suitable adsorbent such as kaolinite, flotation and removal by oleic acid surfactant and activated charcoal [3, 6]. In the most-used alkali precipitation method, chromium which is used as chromium sulphate for tanning/re-tanning is recovered by multiple washing and filtration. First, alkaline washing is carried out with hydrogen peroxide to oxidize Cr(III) to Cr(VI) to separate it from other metals, and next to that an acidic pH of solution is obtained after alkaline washing by H_2SO_4 and subsequently $FeSO_4$ and sodium bisulphite added to reduce Cr(VI) to Cr(III). From the reduced chromate solution with addition of NaOH a precipitation of $Cr(OH)_3$ is obtained and recovered by filtration [3]. Currently, many emerging techniques such as electrocoagulation, adsorption, biological treatment, membrane treatment and photocatalysis are explored for chromium removal from wastewater [7]. Significant environmental impacts associated with the most used precipitation and filtration method [12] due to usage of chemicals and usage of solvents in alternative techniques for chromium removal can be addressed by photocatalytic and nonthermal plasma-based treatment for tannery wastewater. Of the above-mentioned treatment the photocatalytic process is widely studied and is a more efficient treatment for chromium removal [36].

16.4.1 Application of Photocatalytic Process for Reduction and Removal of Chromium

In tanneries effluent chromium is present along with other organic pollutants; this co-existence of chromium with other pollutants creates difficulty in conventional treatment where chromium should be removed prior to any other treatment—otherwise Cr(III) can be converted to toxic Cr(VI). Photocatalysis can be advantageously used for simultaneous removal of chromium and other organic pollutants where toxic Cr(VI) can be reduced to Cr(III) and organic pollutants can be oxidized [7, 31, 37]. Various photocatalysts are studied for reduction and removal of chromium. Modified TiO_2 mediated photocatalysis is the most studied approach for the removal of chromium; this includes use of carbon-based advanced materials for TiO_2 modification, semiconductor-oxide-modified TiO_2, semiconductor sulfide-modified TiO_2, noble-metal-modified TiO_2, and dye-sensitized TiO_2 [38–40]. Other photocatalysts which are explored for Cr(VIII) reduction and removal by visible light or solar light are cerium-doped MoS_2 nanostructures [41], $LiMn_2O_4/SnO_2$ catalyst [42], α-Fe_2O_3 nanocrystals impregnated on g-C_3N_4-SO_3H [43], nonthermal plasma-vulcanized flower-like ZnS/Zn-Al composites for adsorptive photocatalysis [44], graphene nanocomposite photocatalysts [45], RGO/BiOI/ZnO composites [46], phosphorus-doped g-C_3N_4/SnS nanocomposite [47] $CaFe_2O_4$ [48], etc. 3-D hierarchical Ag/ZnO@CF photocatalyst reported for synergistic removal of Cr(VI) and phenol by heterogeneous and homogeneous catalysis [49]. Photocatalysis is reported for Cr(VI) reduction under LED visible light with simultaneous degradation of bisphenol A using S-TiO_2/UiO-66-NH_2 composite [50], methylene blue using mesoporous $BiVO_4$ photocatalyst using visible light [51], citric acid over TiO_2 particles under near UV irradiation [52], humic acid over TiO_2 particles under UV irradiation [53], etc. Photocatalytic reduction of Cr(VI) in the presence of polyethylene glycol (PEG), a water soluble non-ionic co-polymer is reported as an eco-friendly approach for removal of chromium from industrial wastewater [54]. Enhancement of Cr(VI) removal efficiency by photocatalysis can be improved via adsorption/photocatalysis synergy using electrospun chitosan/g-C_3N_4/TiO_2 nanofibres [55], or red peanut skin [56]. When Nb_2O_5 is explored as an alternative catalyst for reduction and removal of Cr(VI) from tannery wastewater, it proved to be 20% more efficient than TiO_2 and thus can be considered a promising alternative [57]. Bifunctional MOF/titanate nanotube composites have been studied for both photocatalysis and simultaneous adsorptive removal of formed Cr(III) [58].

Ti/TiO_2 photo anode with sodium sulphate was used to check the feasibility of UV irradiation-based photobleaching of leather dye acid red 151, anionic surfactant, and photo-electrocatalytic reduction of Cr(VI). With use of pH 2 and 0.1 mol l^{-1} sodium sulphate, 100% dye decolourization can be obtained with reduction of 98–100% of Cr(VI) and abatement of 95% of the original total organic carbon. The findings of this study indicate that photo-electrocatalytic oxidation can be considered as an exceptional alternative for treatment of tannery wastewater containing dyes, surfactants and toxic hexavalent chromium; at lower concentration of pollutants complete removal can be obtained [59]. In a similar study, parthenium weed activated carbon loaded with zinc oxide nanoparticles (ZnO-NPs-PWAC) was used for the simultaneous removal of methylene blue and Cr(VI), which was further studied with real tannery wastewater. In this study, detailed characterization was carried out to test photocatalytic activity of ZnO-NPs and ZnONPs-PWAC. ZnONPs alone provided more than 93% efficiency for decolourization of malachite green, congo red, and methylene blue under sunlight irradiation. PWAC provides more than 99% removal of Methylene Blue in 130 min where as ZnO-NPs-PWAC provides the same removal efficiency within 60 min. Similarly, PWAC provides more than 99% removal of Cr(VI) in 160 min, whereas ZnO-NPs-PWAC provides the same removal efficiency within 90 min. Combined reactions of photocatalysis and adsorption provides enhancement in removal efficiency; ZnO-NPs-PWAC also provided more than 92% removal efficiency for realistic tannery wastewater [60]. Other than TiO_2 and ZNO, silver chromate nanocrystals provided a fresh and feasible opportunity that can dispose of wastewater containing chromium and at the same time, producing a new visible-light catalyst that can degrade the organic pollutant in the wastewater. Ag_2CrO_4 nanocrystals were prepared by ultrasonic synthesis, template and hydrothermal. A comparative study of the product was investigated. Best results were reported with the product synthesized by the ultrasonic method (dye degradation within 8 min) than with the other two methods reported (dye degradation occurred in 42 min) [61]. Synthesis of spherical TiO_2 catalytic materials with hollow structure reported for photo-electrocatalytic reduction of Cr(VI); the result of the study indicates that a photocatalytical removal rate of Cr(VI) is 0.0126/min whereas the removal rate by photo-electrocatalysis is 0.0362/min which is three time faster than the former one. The spherical TiO_2 based photo-electrocatalysis studied for the actual tannery wastewater samples collected from three different tanning procedures, and excellent activity was also obtained with realistic tannery wastewater. This indicates the great potential of photocatalytic-based technology for Cr(VI) reduction and removal from tannery effluents [62]. Hydroxylated α-Fe_2O_3 was utilized for synergetic photocatalytic reduction of Cr(VI) and degradation of leather preservative 4-Chlorophenol under visible light. For one hour of visible light irradiation, Cr(VI) reduction was obtained in a range of 24.8% to 70.2%, while degradation of 4-Chlorophenol increased from 13.5 to 47.8%. The photocatalyst can be reused again and again; good degradation is obtained even after nine cycles of degradation [63].

16.4.2 Applications of Nonthermal Plasma for Chromium Reduction and Removal

Applications of nonthermal plasma are also reported for chromium reduction and removal. In a study, simultaneous Cr(VI) reduction and As(III) oxidation in aqueous solutions reported using a glow discharge plasma; experiments were carried out to study effects of input energy, pH value and concentrations for redox transformation of Cr(VI) and As(III). In the glow discharge treatment synergetic effect observed between Cr(VI) and As(III), the presence of Cr(VI) can significantly enhance As(III) oxidation. Increase in voltage inputs from 530 to 600 V can increase conversion of Cr(VI) from 96 to 100% and As (III) from 53 to 77%. In acidic pH reduction of Cr(VI) (96% reduction) proceeds rapidly compare to As(III); the optimum pH for As(III) is 7. The conversion is due to H_2O_2 generated in glow discharge which reduce Cr(VI) and hydroxyl radicals which can oxidize As(III). This has opened up a new possibility for treatment of chromium and arsenic containing wastewater [64]. In a similar study, removal of Cr(VI) and methylene blue was simultaneously carried out by atmospheric pressure argon plasma jet. In an acidic medium, the highest amount of hydrogen peroxide is formed which reduces Cr(VI) to Cr(III), and simultaneous removal of methylene blue and Cr(VI) is more beneficial than individual pollutants [65]. The same atmospheric pressure argon plasma jet was studied for simultaneous removal of As(III) and Cr(VI), where both the pollutants complement redox natura and simultaneous removal is beneficial

[66]. For Cr(VI) removal $CoFe_2O_4$/multiwalled carbon nanotubes (MWNTs)/sponge electrodes were prepared which enhances the performance of DBD. Cr(VI) and phenolic pollutants such as phenol, hydroquinone, nitrobenzene and *p*-nitrophenol were simultaneously removed using these plasma discharge systems. In this study optimum concentration of $CoFe_2O_4$ nanowires estimated 0.5 g/l and with that 98.52% degradation of phenol achieved [67]. In a similar study, simultaneous oxidation of phenol and reduction of Cr(VI) is studied with contact glow discharge electrolysis [68]. Simultaneous removal of Cr(VI) and an azo dye acid orange 7 has been studied; due to synergistic effects both pollutants improve degradation of each other. Under acidic condition 94% reduction of Cr(VI) is achieved; furthermore, with an increase in the input power from 80 to 120 V, Cr(VI) removal increased from 54 to 88% and removal of dye acid orange increased from 62 to 89% [69]. Atmospheric pressure argon glow discharge plasma at gas solution interface was explored for reduction of Cr(VI); here in the experiments a small quantity of ethanol was added as a hydroxyl radical scavenger. Further in the study, the same experiments were carried out using air glow discharge; 89% of Cr(VI) got removed from 25 ml 80 mg/l $K_2Cr_2O_7$ solution in presence of 2% v/v ethanol after a 15-min treatment with the air discharge [70]. In a similar study Cr(VI) reduction in aqueous solution was achieved in presence of ethanol as hydroxyl radical scavenger by micro-plasma [71]. In a study, Cr(VI) ion imprinted polypropylene (PP) fibres were fabricated by plasma mediated grafting which is effective and selective for Cr(VI) adsorption. The surfaces of PP fibres were activated by nonthermal RF plasma (argon and air) followed by gaseous phase acrylic acid grafting which is further amidated with triethylenetetramine and subjected to Cr(VI) template imprinting. It further explored for Cr(VI) removal in which highest adsorption capacity 167 mg/g obtained at pH 3. Adsorbed Cr(VI) eluate rapidly and effectively by 0.2% NaOH solution and adsorption efficiency maintained more than 80% even after ten regenerations [72].

16.5 Photocatalytic Process for Treatment of the Leather Industry's Wastewater and Other Applications

Various studies report application of TiO_2, and other nanoparticles used persuasively for photocatalytic dye degradation and the removal of organics and heavy metals from tannery wastewater. In a study, ITO (indium tin oxide coated glass) supported TiO_2 nanoparticles were utilized for photo-oxidation of dye released by leather industries. In the study, complete degradation and mineralization of dye into inorganic product is reported, while decolourization ratios of more than 90% were reported for the time of 480 min [73]. In another study, TiO_2 nanoparticles were prepared on alumina and glass beads; after that photocatalytic activity was studied for photo-oxidation of acid brown 14 leather dye in aqueous solution illuminated with solar light. Characterization techniques like HPLC and UV–Vis helps to keep track on changes in the concentration of acid brown 14 after photocatalytic degradation. The effectual results were reported for TiO_2 supported on alumina beads in an acidic condition [74]. Degradation of dermacid red (CAS: 6406-56-0), dermacid black RVE (CAS: 99576-15-5) and dermacid brown (CAS: 8011-86-7) leather dyes was carried out by photocatalysis with TiO_2 and a comparative study carried out for degradation of these dyes using ultrasound irradiation, photocatalysis with TiO_2, Fenton/photo Fenton and a combination of those techniques. For photocatalysis and photo Fenton UV illumination was used, whereas for ultrasound irradiation at low (20 kHz) and high frequencies (860 kHz) was utilized. Due to the different natures and structures of the azo dyes, each dye has a different optimization parameter of photocatalytic degradation by different combinations of advanced oxidation process; combination of these advanced oxidation processes has synergetic effects for dye decolourization. Maximum degradation of the chromophore group was reported in the first two hours of experiment [75]. Other than $TiO_{2,}$ silver chromate nanocrystals provided a fresh and feasible opportunity that can dispose of wastewater containing chromium and at the same time, produce a new visible-light catalyst that can degrade the organic pollutant in the wastewater. Ag_2CrO_4 nanocrystals were prepared by ultrasonic synthesis, template and hydrothermal methods and utilized for photocatalytic degradation of dye rhodamine B. In a comparative study of Ag_2CrO_4 nanocrystals prepared by the different methods, best results were obtained with the Ag_2CrO_4 nanocrystals synthesized by the ultrasonic method (dye degradation within 8 min) than with the other two methods reported (dye degradation occurred in 42 min) [61]. Apart from dye degradation, photocatalysis is explored for degradation of organic pollutants for wastewater. In a study, ZnO photocatalyst was also used to treat tannery wastewater, with 1gm/litre ZNO catalyst in effluent diluted by 1:200 proportion, which is irradiated by mercury vapour lamp irradiation (1850 μW cm^{-2}, Topcon UVR-2) for four hours at pH of 8.0. The treatment resulted in a reduction in physiochemical parameters—chemical oxygen demand (COD) from 15,023 to 350 mg/l, biochemical oxygen demand (BOD) from 4374 to 10 mg/l, total solids from 28,500 to 188 mg/l, total organic carbon from 4865 to 4.93 mg/l and turbidity from 331 to 1.15 NTU. The treatment also resulted in decrease in toxicity as tested by the lethality assay of microcrustacean *Artemia salina L*, with LC_{50} increasing from 14.90 to 56.82% [76]. In another study, ZnO-$ZnFe_2O_4$ composite photocatalyst supported by activated carbon studied for reduction in biochemical oxygen demand (BOD_5) of tannery wastewater under visible light irradiation. It is reported in the study that by adsorption only 9% of BOD_5 was removed while with the photocatalytic treatment 90% reduction in BOD_5 was obtained in a two-hour treatment [77]. The removal of residential tributyltin (TBT) from tannery wastewater was carried out by effective electro-field-assisted-photocatalytic technique using hierarchical TiO_2 microspheres. The rate removal 0.0052 min^{-1} was obtained with photocatalysis while 0.0488 min^{-1} was the rate of reaction by electro-field-assisted-photocatalytic removal of TBT which is nine times faster compared to photocatalysis [78]. In a study, immobilization of TiO_2 was carried out on macro-defect free cements to form photoactive polymer-cement composites which utilized for tannin degradation. Using MDF containing embedded TiO_2 nanoparticles 98% photodegradation of tannins obtained with six-hour irradiation with 254 nm [79]. Polyvinyl thiol (PVASH) assisted Ag NPs are reported for surface enhanced raman spectroscopy (SERS) detection and photocatalytic degradation of tannery waste landfill leachate with degradation rate of $0.0025\ \mathrm{min}^{-1}$ and $0.0039\ \mathrm{min}^{-1}$ for visible and UV light irradiation respectively [80]. Heterostructured $BiVO_4$-ZnO mixed oxide catalysts were utilized for sunlight-driven photocatalytic degradation of post-tanning wastewater. The photocatalyst has an optical band gap of 3.02 eV, which is suitable for sunlight-driven degradation; higher photocatalytic activity is observed for mixed oxide catalyst; 64% reduction in COD is achieved with this mixed oxide catalyst under optimal experimental conditions in the presence of sunlight for a six-hour treatment duration [81]. Various refractory organic compounds such as nonadec-1-ene, 2-phenylethanol, 2,4-di-tert-butylphenol and other organic compounds present in tannery effluent were identified and 2-phenylethanol photocatalytically degraded using standard Degussa P-25 TiO_2 (100 mg) under UV light. 2-phenylethanol was transformed into 2-tert-butyl-4,6-dimethylphenol, 2,6-di-tert-butyl-4-methylphenol by photocatalytic degradation and after prolong exposure of 30 h 100% degradation of 2-phenylethanol was achieved [82]. From leather skin waste carbonaceous *N*-containing materials are derived which are found to have photocatalytic activity due to crystalline species of $Cr_2O_3$and TiO_2 having degradation potential for contaminates such as phenol [83]. From collagen biowaste bi-functional iron embedded carbon nanostructures have been prepared which have photocatalytic activity and applications for lithium ion batteries [84].

16.6 Nonthermal Plasma and Ozone for Treatment of the Leather Industry's Wastewater

Both nonthermal plasma and ozone are advanced oxidation approaches, and as discussed in previous sections the most common and most efficient method for ozone generation is based on nonthermal plasma—specifically dialectic barrier discharge or silent discharge. The utilization of ozone for wastewater treatment is purely a chemical treatment owed to the higher oxidation potential of ozone [85], whereas the nonthermal plasma treatment of wastewater is based on advanced oxidation as well as physical treatment; either by nonthermal plasma discharge generated at the gas–liquid interface or within liquid [86]. The wastewater treatment and pollutant degradation by nonthermal plasma is associated with generation of powerful active species such as hydroxyl radical (·OH), super oxide, ozone and hydrogen peroxide, as well as pollution degradation by dissociation high energetic electrons, ultrasonic waves and UV radiation [86].

16.6.1 Nonthermal Plasma Treatment for Degradation of Leather Preservatives and Other Applications

Nonthermal plasma generated by dielectric barrier discharge (ceramic plate electrodes coupled with pulsed generator Minipuls 6, GBS Elektronic, Rossendrof, Germany) using different gas combinations such as argon, argon:oxygen (80:20) and air. These have been utilized for degradation of 2,4-dichlorophenol (2,4-DCP) (biocide used for leather preservation) [87] in aqueous solution; also the plasma treatment explored in combination of advanced oxidation such as the Fenton process. Plasma discharge created using Ar gas results in complete degradation of 2,4-DCP within 15 min; however, when 20% oxygen is added to Ar degradation of 2,4-DCP is delayed but mineralization improved due to accelerated oxidation of intermediate products by reactive species [86]. The addition of 10 mg/l ferrous ions to an aqueous solution of 2,4-DCP induced the Fenton process; better degradation and mineralization was achieved due to the fact that it resulted in the combination of two advanced oxidation processes—nonthermal plasma and the Fenton process [86]. Degradation of leather fungicide *p*-nitrophenol was carried out using microwave atmospheric plasma in aqueous solution; 100 mg/l of *p*-nitrophenol got removed completely with a 12-min treatment, and TOC removal of 57.6% was obtained. The pH of a solution has no significant impact on degradation; hydroxyl radical generated by plasma discharge playing a key role in degradation of *p*-nitrophenol [88]. Atmospheric pressure air DBD was reported for the sterilization of wastewater samples collected from leather processing plants. Aliquot of the wastewater sample was treated with air DBD for 75.5, 81.94, and 85.34 mA with a discharge current and exposure time of 30, 60 and 90 s. The plasma exposure at 75.5A can greatly change dominant bacterial groups at 30 and 60 s exposure, while 80% reduction in bacterial population is observed at 90 s exposure. The same trend is observed for plasma treatment at 81.94 A; the plasma treatment at 85.34 mA can eliminate all bacterial groups at 60 or 90 s exposure. This sterilization effect of the air DBD is conferred to active species such as NO, N_2^+, UV radiation; air DBD can be environmentally affable and a promising tool for wastewater treatment to eliminate microorganisms from treated wastewater without use of chlorine [89].

16.6.2 Ozone/Ozonation to Increase Biodegradability of Tannery Wastewater

Though ozone can be produced in three ways, nonthermal plasma-based silent discharge is the prevalent, most effective and economic method for ozone generation, which is greatly explored for treatment of wastewater [4, 90]. The ozone technique can be applicable for treatment of wastewater generated from beamhouse operations, and for treatment of tannery wastewater only after removal of chromium by precipitation using pre-alkalization [12]. Ozone has an electrochemical oxidation potential of 2.08 V, higher compared to molecular oxygen (1.23 V) from which it is produced, and thus it can be a preferred advanced oxidation method to improve performance of biological treatment of tannery wastewater [4, 36]. With bench scale experiments, ozone produced by silent discharge was explored as a tertiary treatment for tannery effluent collected from a CETP and ETP. Atmospheric air at a flow rate of 1.2 l/m was passed through silent discharge and ozone generated at a concentration of 0.5 g/m^3 purged through 1-l effluent sample for three hours using a diffuser having pore size of 160 μm. For the CETP effluent sample the ozone treatment resulted in 85% reduction in COD, the colour changed from dark brown to colourless and there was complete removal of odour. With the same method for ETP effluent sample, ozone treatment resulted in 81% reduction in COD, 40% reduction in BOD and more than 95% reduction in sulfides, with a colour change from dark green to colourless and complete elimination of odour [4]. In a field level experiment at tannery ETP a small ozone generator having capacity of 0.5 g/h, 1.5% w/w, 4 l/min utilized for injection of ozone with H_2O_2 in the ratio of H_2O_2/O_3 of 1:2 in a aeration tank (45 m^3) for 24 h. This resulted in a 25% reduction in BOD value and 20% reduction in COD value due to the production of perozone or hydroxyl radical having 60% more oxidation efficiency [4]. Strategic application of ozone as pre-treatment can increase the biodegradability of tannery effluent by anaerobic treatment due to simplification of complex and high molecular weight compounds. Pre-ozonation of tannery effluent can increase assimilable organic carbon in effluent by faction of 1:3 from 36 μg/l for raw effluent to 109 μg/l after ozonation; deoxygenation coefficient for BOD removal increased from 0.1/day to 0.25/day. Thus, treatment efficiency can be improved, treatment time can be reduced and with fewer problems of solid handling [4].

In another study, sequencing batch biofilter granular reactor (SBBGR) coupled with ozonation is explored for the treatment of tannery wastewater, where integration of ozonation is reported to improve efficiency of the biological treatment. In the study, wastewater from SBBGR flowed through the ozone reactor (0.25m^3) at a rate of 2 m^3/hour and recirculated again for final biological treatment. Due to high oxidation potential, ozone can degrade recalcitrant material present in tannery wastewater and thus a high removal rate is obtained for COD, BOD, TSS, TKN; colour and surfactant can be obtained with very less sludge production (0.1 kg dry sludge/m^3 of effluent treated). Without ozonation 91 ± 1% removal for COD, 99 ± 1% removal for BOD, 87 ± 2% removal for dissolved organic carbon (DOC), 88 ± 4% removal for TSS, 84 ± 4% removal for TKN, 93 ± 4% removal for surfactants and 24 ± 3% removal for colour is obtained by SBBGR. Whereas when ozonation integrated with the SBBGR 97.5 ± 0.5% removal for COD, 99 ± 1% removal for BOD, 93 ± 1% removal for dissolved organic carbon (DOC), 96 ± 1% removal for TSS, 91 ± 2% removal for TKN, 98 ± 5% removal for surfactant, 96 ± 2% removal for colour obtained, while 20 ± 2 mg/l ozone was consumed. The treatment cost after integration of ozonation with SBBGR is estimated at about 1€ per m^3 of wastewater which is four time lesser than the estimated cost without ozonation (about 4–5€ per m^3 of wastewater), whereas sludge generation (about 3 kg dry sludge/m^3 produced when the plant operated without ozonation) is 30 time less [34]. Ozonation has been applied for simultaneous removal of COD and colour from tannery effluent which resulted in enhanced biodegradability of tannery effluent and colour present in the removed material due to oxidative cleavage of chromophore groups of dyes and colour imparting substances. Effluent containing direct brown diazo dye and realistic effluent from wet tanning processes was treated with diffusion of ozone from an ozone generator at various process variables. For real tannery wastewater at optimum process condition 92% COD removal efficiency obtained, and BOD/COD ratio increase from 0.18 for without treatment to 0.49 after 30-min ozone treatment. For the both effluents, efficiency of ozonation depends upon the initial concentration of pollutants and ozone dosage, and pollution degradation follows pseudo first-order kinetics [33]. Ozonation combined with coagulation flocculation (CF-OZ) is studied to improve treatment of tannery wastewater and compared with coagulation flocculation and adsorption (CF-ADS). With CF-ADS 50.04% removal TOC, 53.13% removal of COD, 17.05% removal of Na^+, 61.13%, colour removal achieved and compared to that CF-OZ resulted in 46.50% removal TOC, 56.25%, removal of COD, 11.10% removal of Na^+, 85.34% colour removal. Further, ozonation decreases the COD/TOC ratio from 2.79 for untreated effluent to 2.66 for ozonated effluent and the BOD/COD ratio increased from 0.24 for untreated to 0.60 for CF-OZ and 0.47 for CF-ADS. Thus, both treatments facilitate further biological treatment of tannery effluent, ozonation being more beneficial compared to the other one [91]. Ozonation pre-treatment of two separated streams of wastewater generated from tanneries, i.e., beamhouse operation wastewater and tanning yard effluent were explored. The results of this study indicate that for both streams, ozonation prior to biological treatment breaks down refractory compounds. In the case of tanning yard effluent, pre-ozonation before aerobic treatment resulted in 95% COD removal and 91% DOC removal. For both the effluents, above-mentioned effect is found in the optimal range of ozone dose of 1 to 3 g per gram of DOC; further ozone dose is wasted in the destruction of already degradable compounds [92].

Advanced oxidation treatments, ozone and the Fenton process, were explored for treatment of tannery effluents at a central effluent treatment plant (CETP). The tannery effluents received at CETP has a BOD/COD ratio about 0.1 to 0.25 and even after physicochemical treatment the effluent has low biodegradability. The above-mentioned advanced oxidation treatments provided to effluent from primary settling tank of the CETP improved the biodegradability of effluents in subsequent activated sludge processes. Thirty to fifty percent COD removal was achieved by Fenton treatment and 15–20% COD removal obtained by ozonation at the primary stage; and after secondary treatment 60–70% COD removal obtained by ozonation and 50 to 60% COD obtained by the Fenton treatment. Ozonation was further explored for treatment of tannery effluents at CETP; coagulation and extended aeration followed ozonation considered as the best treatment which can provide 80–90% reduction in COD [93]. Ozonation as post-treatment is also found beneficial for treatment of tannery wastewater. In a study on the effect of ozonation, before, within and after biological treatment, it was found that application of ozone after biological treatment is most promising where the highest COD removal can be achieved by a low feeding time of five minute at a flow rate of 42.8 mg/l. Conversion of nonbiodegradables to readily biodegradable is possible due to ozonation and thus an improvement in biological degradation [94]. Catalytical ozonation using Mn-Cu/Al_2O_3 catalyst also explored for tertiary treatment of real tannery effluent which results in higher COD removal efficiency compared to ozonation alone. In catalytical ozonation COD removal increases with the quantity of catalyst from 0.5 to 3.0 g/l and ozone volume from 0.2 to 0.4 g/h. The highest 88.6% COD removal was obtained at 7pH, catalyst load of 2.0 g/l and ozone flow rate of 0.3 g/hour for treatment time of 60 min [95].

Ozone/ozonation as a chemical treatment/advanced oxidation treatment can be utilized for treatment of wastewater generated from chromium tanning after the removal chromium by pre-alkalization. The study was performed as a bench scale utilizing an ozone generator (COW-025, Afraz Mohit Sahand Ltd.) with a capability of 25 g/h ozone generation when the generator was fed with pure oxygen. The ozone generator connected with the ozone contactor (3-l cylinder), with a total reaction volume of 5 l including volume of the circulation loop. Ozonation as a chemical treatment/advanced oxidation treatment able to remove COD from 30 to 70% by providing treatment for 120 min with an ozone flowrate of 1 to 8 g/hour. From statistical analysis, an ozone dose of more than 15 g/h for 120 min predicated for complete COD removal. Colour removal by ozonation increased from 40 to 64% at a flowrate of 1 g/hour when pH decreased from 9 to 3; 85% colour removal obtained for ozonation at a flow rate of 8 g/hour at any pH. At optimum conditions with ozonation 88% COD removal and 93% colour removal was obtained, however when high concentration of ozone such as 8 g/hour is utilized, Cr(III) in wastewater can be converted to toxic Cr(VI) and therefore chromium removal by pre-alkalization is a necessity when ozone is directly applied for treatment of tannery wastewater [12]. Ozone/ozonation is reported to enhance biological treatment of wastewater generated from tanning processes utilizing plant-based polyphenols as natural tanning agents. Natural tanning is environmentally friendly compared to chrome tanning; however, poor biodegradability of tannins cause problems in biological treatment such as absorption of light and heat by tannins, reduction of efficiency of biological treatment due to persistent nature tannins remaining in effluent even after conventional treatment of tannery wastewater. In a study, a bubble column bench scale reactor attached with a ozone generator (Model No L6G, Faraday Instruments, India) was utilized for treatment of wastewater generated from natural tanning of leather. The ozone generator used in the study can produce ozone at 2 g/h by using oxygen as feed gas and produced ozone diffused through the wastewater by ceramic diffuser and treatment carried out for 30 min. Ozone due to its superior oxidation potential can degrade tannins, the BOD_5/COD ratio of untreated wastewater is 0.196 due to poor biodegradability of tannins which increased to 0.298 after the ozonation. Ozone pre-treatment resulted in a 20% reduction in COD and 49% removal of total phenols; improvement in subsequent biological treatment resulted in 60 mg/l BOD_5 and 350 mg/l COD in the treated effluent [96]. Ozonation has been explored for degradation of syntans used in leather tanning. Syntans are synthetic organic materials used for tanning, and like chrome tanning and natural tanning, syntans are not completely absorbed by hide and unreacted syntans are lost into effluent. Commercially available syntan which is aromatic sulfonic acid condensation product is degraded by a bench scale reactor connected with an ozone generator (Faraday Model No. L6G, India) which can produce 1–6 g/h ozone using oxygen as feed gas. Experiments were conducted using 100–700 ppm and ozone dose of 1 g/h. Tannin removal efficiency was found to be 98%, and 91% COD removal for syntan concentration of 100 ppm was obtained whereas 72% tannin removal and 48% COD reduction obtained for 700 ppm concentration [97]. Phenol sulfonic acid-syntan (PSAS) degraded by ozonation using a bench scale glass reactor of 3 l capacity connected with a lab-scale ozone generator (Faraday Instruments, Model No. L6G, India) which can generate 1–3 g/hour ozone using pure oxygen as feed gas. The optimum conditions for syntan degradation are found to be 7 pH, 5.2×10^{-3} mmol/l ozone concentration, 500 mg/l concentration of substrate. The ozonation treatment improved biodegradability of the syntan which was reflected as an increase in the BOD/COD ratio from 0.03 for untreated to 0.42; the degradation follows pseudo first order reactions, with increase in ozone dose maximum of 84.2% COD removal and 58% (dissolved organic carbon) DOC removal achieved at 7 pH [98].

16.6.3 Ozone/Ozonation for Dye Degradation

Ozone treatment, when applied to tannery wastewater treatment, can be advantageously utilized for degradation of dyes, preservatives/biocides applied during leather production and processing which would be otherwise difficult to degrade in conventional treatment due to its stable chemical structure and toxicity [85]. The advantages of ozonation for dye decolourization is no sludge generation, less cost and effective degradation. Degradation of sandopel brown BRR dye in aqueous solution carried out by ozone generated using ambient air by ozone generator (Model No-SA001, India) which can produce 3 g ozone/ hour. The dye decolourization by ozonation was carried out in a 5-l cylindrical glass reactor filled with various dye concentrations from 30 to 360 mg/l, pH 4 to 11 and through that ozone bubbled at a concentration of 1.6 mg/l for different times. Decolourization was faster at in alkaline pH; at pH 11 95% dye decolourization was achieved in 20 min whereas at pH of 4 the same results were obtained at 35 min. A maximum 97% dye decolourization obtained, decolourization decreased with an increase in initial dye concentration; for dye concentration of 30 mg/l, 97% decolourization was achieved in 30 min; where it took 170 min for dye concentration of 360 mg/l, dye decolourization by ozone follows first order kinetics [99]. In another study, ozonation and ozone along with hydrogen peroxide was explored for degradation of four leather dyes—direct black 168, acid black 241, acid brown 83 and acid brown 191 using a 1-l contact reactor connected to an ozone generator (Marca Iberozono, model 80). For dye degradation the contact reactor filled with 40 mg/l dye solution and ozonation was carried out at saturation for 60 min; the effect of pH was explored by adjusting pH 2 to 10. A similar experiment was performed for ozone + H_2O_2 treatment but adding 6 to 60 mg H_2O_2 (30% p/v) per 1 l of the dye solutions. Contact with ozone for a prolonged exposure time of 100 min resulted in complete decolourization of all the dyes; however, in the case of ozone treatment coupled with H_2O_2 greater colour reduction obtained at a shorter period of time in 4 to 5 min but afterwards no further improvement was observed [100]. Leather dye acid black 52 was degraded by ozonation using a packed bed reactor with different process variables such as pH, dye concentration, and contact time. One hundred per cent colour removal and 61% COD reduction was achieved at optimum conditions of 1.96 pH, 1159 mg/l dye concentration and 10.6 min contact time and 4.8 pH, 1159 mg/l dye concentration and 17 min contact time respectively [101]. In other similar studies three azo leather dyes, CI acid black 1 (AB1), CI acid yellow 19 (AY19) and CI acid orange 7 (AO7) degraded using a batch reactor of 500 ml volume connected with an ozone generator (model 1000 Nano Paak Sayyal, Iran). When experimental variables such as ozone dose, dye concentration, pH, temperature, etc., were studied; greater than 75% colour removal obtained under optimum conditions within the first five minutes of removal treatment, initial dye concentration and pH of dye solution are the most influential factors for dye degradation using ozonation [102]. Acid dye navitan bordeaux MB (C.I. acid violet 90), 100 ppm synthetic effluent sample was degraded by ozonation using a bubble column reactor and an experiment studied the influence of ozone dose, dye concentration and pH on the decolourization rate. The results of this study indicate that at a high ozone dose 90% removal can be achieved in 1–2 min, whereas at a low ozone dose of 90% removal can be achieved in 4–5 min, complete colour removal can be achieved in 5 min and 30 mg/l ozone concentration is required for 90% decolourization when pure oxygen gas is used for ozone generation. 50 mg/l ozone concentration required for 90% decolourization and complete decolourization achieved in 7 min when ozone is generated using ambient air [103]. In a study, ozonation was explored for decolourization of three leather dyes CI direct blue 1, CI green G and CI fast red B base and compared with electrocoagulation. The experimental set up was composed of a reactor (1100 l) connected with an ozone generator (Carbar—03A2-7 W). Molecular ozone is selective in dye degradation; in certain dye structures attached by ozone, dye degradation was carried out using a volume of 200 l of 50 mg/l dye solution. After 210 min 50% degradation was observed for CI direct blue 1 and 55% for CI fast red B base, and 61–89% for CI green G respectively [104]. Leather dye acid black 210 in aqueous solution degraded by ozonation and UV/ozonation; influence of pH, dye concentration, effect of UV radiation were studied, decolourization and mineralization studied by UV and TOC analysis. At optimum conditions 100% decolourization and 55% mineralization was achieved within a short time of 15 min [105].

16.6.4 Ozone/Ozonation for Degradation of Leather Preservatives

Chloro-substituted phenolic compounds are widely used as biocides/preservatives in leather production/processing [87], which can cause water pollution problems due to acute toxicity and poor biodegradability and the persistent nature of compounds [85]. These compounds are reported to have carcinogenic and mutagenic properties and are identified as priority pollutants by USEPA [85]. Ozonation is reported to be useful in degradation of 2,4-dichlorophenol (2,4-DCP), a commonly used biocide for preservation during leather production/processing. A laboratory scale study has been carried out using an ozone generator with different flowrates in the range of 100 to 400 mg ozone/hour with/without CuO/ZnO catalyst and ultrasound with 36 kHz frequency and output power of 150 W. The influence of different operation parameters such as temperature, catalysis loading rate, concentration of 2,4-dichlorophenol, etc., were studied to optimized degradation of 2,4-dichlorophenol. With ultrasound only, a maximum degradation of 28.85% was achieved, whereas combined treatment with ultrasound and ozonation gave maximum degradation of 95.66% when ZnO was used as the catalyst, and 97.03% when CuO was used as the catalyst for a 120-min treatment time. The degradation products for these combined ozonation processes are found to be nontoxic to microorganisms [85]. Another study reports the application of ozonation as pretreatment to improve the biodegradation of 2,4-dichlorophenol in wastewater along with other biodegradable organic matter. Ozonation provided to 2-l samples of various synthetic wastewaters containing 2,4-dichlorophenol using a ozone generator (oxygen feed) (WEDECO GSO30) having 6 g/h ozone flowrate, and treatment provided for 2, 5 and 10 min, the pH of wastewater samples adjusted to 9 and ozonated wastewater was further subjected to biological treatment. Ozone pretreatment results in a decreased concentration of 2,4-DCP and an increase in chloride concentration, which indicates conversion of 2,4-DCP to de-halogenated intermediates, the degradation of 2,4-DCP by ozonation follows pseudo first order kinetics, ozonation decrease toxicity of 2,4-DCP and further biodegradation is required for shorter time for degradation in case of the ozone pretreatment [106]. The further effect of ozonation as pretreatment for biodegradation of 2,4-DCP containing wastewater was explored using a pilot scale bioreactor where pre-ozonation results in improved sludge settleability and less sludge production; whereas in the case of non-ozonated 2,4-DCP containing wastewater sludge settleability was hampered [107]. In a study, ozonation is compared with photocatalysis (TiO_2 photocatalyst) based advanced oxidation process and nonthermal plasma-dielectric barrier discharge (DBD) in different gases using a planar falling film reactor for degradation of 2,4-DCP (100 mg/l, experimental volume 0.5 l). The outcome of the study indicates that ozone (ozone generator-Fischer, model OZ 502/10, Germany, 130 ± 5 mg/l ozone, feed gas-oxygen) is highly effective in degradation of 2,4-DCP; however, complete mineralization is not achieved as found by TOC analysis. When ozonation is coupled with photocatalysis, complete mineralization of 2,4-DCP was achieved after 60 min of treatment [86]. Ozonation as pretreatment can improve the biodegradability of 2,4-DCP; when 100 ppm solution of 2,4-DCP is treated with ozone dose of 0.12 g/l, the BOD_5/COD ratio increased from zero without treatment to 0.25 ($BOD_{21}/COD = 0.48$). With pre-ozonation, 80% of TOC removal can be achieved when the solution gets treated biologically by mixing with sewage and 70% TOC removal can be achieved when 100% of the pretreated solution was further treated biologically with short hydraulic retention time between 12 to 48 h [108].

Leather preservative chlorophene was degraded by ozone, UV and UV/ ozone-based advanced oxidation and studied with experimental variables such as pH, concentration of the pollutants, ozone dose and intensity of UV light. Of these, O_3 and UV/ O_3 can effectively degrade chlorophene. Maximum degradation can be achieved at pH of 8 and degradation increases with increase in ozone dose and intensity of UV. UV can enhance degradation of chlorophene, the pseudo-first-order rate constant found lowest, 9.8×10^{-4} min^{-1} for UV and 2.4×10^{-2} and 6.4×10^{-2} min^{-1} for ozonation and UV/Ozone treatment. The presence of another organic matter retarded degradation by 38% [109]. Biocide o-phenylphenol, a commonly used fungicide to prevent fungal attack of untanned and tanned hide and an endocrine disrupting compound degraded by ozonation and influence of pH tested. Degradation of o-phenylphenol by ozonation increases with the increase in pH, thus ozonation is an effective and quick method degradation of o-phenylphenol [110]. Leather antifungal agent 2-Mercaptobenzothiazole (MBT) was degraded by ozonation in pure water and tannery effluent in a fast and efficient manner. 2-Mercaptobenzothiazole (MBT) and its degradation products have a high affinity towards ozone, thus ozone treatment results in oxidation and partial mineralization; benzothiazole is an ozonation product which can form in concentrations of 60 mole per cent of the original concentration [111]. There are a few studies which deal with the toxicity of tannery effluent treated by ozonation. Ozonation of tannery effluent results into oxidation and partial mineralization of pollutants, and the destruction and improvement in biodegradability which can be measured by COD, BOD, TOC and DOC. The degradation of by-products can be formed which can be studied by separation and analytical techniques and toxicity of degradation products studied by biotoxicity testing. In a study, the toxicity of tannery wastewater before after ozonation was evaluated using *Daphnia magna Straus* and *Vibrio fischeri* bioassays. The study indicates a minor increase in the toxicity of effluent after ozonation for bacteria by *V. fischeri* bioassays, while no toxicity changed after ozonation against *Daphnia magna Straus* [112]. In other similar studies a slight decrease in the toxicity of tannery effluent was observed after ozonation and other treatments based on advanced oxidation [113]. A study viewed the generation of endocrine disruptive substances after ozone treatment of tannery wastewater which are qualitatively identified as nonylphenol ethoxylate (NPEO) degradation products: short chain NPEOs, nonylphenol carboxylates (NPECs) and nonylphenol (NP) by LC–MS. The study reports no increase in *V. fischeri* or *D. magna* toxicity but an increase in estrogenic potential after ozone treatment by enzyme-linked receptor assay (ELRA) [114].

16.7 Other Applications

16.7.1 Nonthermal Plasma Surface Modification of Leather for Ecofriendly Processing and Providing Functional Finish

Atmospheric pressure DBD plasma of air and ammonia gas was studied to provide surface functionalization and improvement in dyeing with natural dyes [115, 116]. Atmospheric pressure air DBD was utilized for the sterilization of goat hide, and thus the application of nonthermal plasma can be explored for leather preservation which can reduce the quantity of synthetic chemical-based antimicrobial agents [117]. Further treatment with air DBD results into better uptake of natural products; an antimicrobial finish was provided to hide/leather by treating it with bark extract of *Cassia renigera* and *Cassia fistula* [117]. Atmospheric pressure argon plasma was reported for inactivation of Syndrome coronavirus 2 (SARS-CoV-2) virus in leather and various other surfaces, thus atmospheric pressure plasma opens up new possibilities for control of COVID-19 as an efficient surface sterilization technique [118]. Antifungal properties that can be imparted to natural leather by surface modification with low temperature plasma treatment which was carried out with tetrafluoromethane (CF_4), hexafluoroethane (C_2F_6) and perfluoropropane (C_3F_8) [119].

Hydrophobic coating can be carried out on leather by plasma polymerization using different HMDSO/ toluene mixture, by the introduced silicon atoms on the natural leather surface [120]. Whereas superhydrophilicity and deformation resistance can be provided to natural leather by low pressure O_2/H_2O plasma treatment. This improvement in hydrophilicity is due to the incorporation of large numbers of hydrophilic groups such as hydroxyl, carboxyl, amines, etc. This groups increases reaction sites for binding of metal ions or dye molecules, etc., thus improvements in metal pickup, tanning or any other subsequent processing can be achieved [121]. In a study, the surface modification of pickled goat hides was carried out using low pressure oxygen plasma which increase in roughness due to the etching effect and the incorporation of oxygen containing functional groups and improvement in hydrophilicity. This results in improved uptake of chromium in chrome tanning and thus less chromium loss in wastewater. A 10-min treatment with low pressure oxygen plasma results in maximum chrome exhaustion, and surface chrome content increased from 1.09 to 1.31% [122]. Similar results were obtained by atmospheric pressure argon corona discharge for surface modification of crust sheep leather by different time durations from 3 to 9 s, which improved re-tanning and decreased the pollution load as studied by characterization of wastewater [123].

Low pressure plasma treatment with He/O_2 mixture as plasma forming gas was studied to control surface wettability, improve dyeability, and wet rubbing property, whereas a waterproof property to natural leather can be imparted by CF_4 plasma [124]. Atmospheric pressure diffuse ambient air plasma was utilized for surface modification of dyed natural leather to improve wettability and adhesion of glue

[125]. Surface modification of chrome tanned leather by atmospheric argon plasma improves surface wettability and improvement in dyeability of chrome tanned leather with acid and metal complex dyes [126]. Upholstery leather was provided flame retardant treatment using borax by atmospheric pressure argon plasma treatment; the plasma treatment results in the modification of surface and activation of surface by incorporating functional groups which results in better uptake of borax to impart the flame retardant property [127]. Dielectric barrier discharge was utilized to impart water repellency and flame retardant properties to leather and other materials [128]. Microwave excitation low pressure oxygen plasma is reported to enhance the adhesion of polyurethane coated leather and polyurethane foam [129]. Chrome shavings can be effectively disposed of with plasma pyro-gasification, and heavy metals from chrome shavings can be recovered by chemical pretreatment to precipitate out heavy metals from chrome shavings [130].

16.7.2 Ozone/Ozonation for Eco-friendly Preservation of Leather and Other Applications

Ozonation has been utilized as an eco-friendly alternative to conventional salts preservation [131] which requires 50 to 60% of common salt NaCl per unit weight of rawhide, which generates wastewater with salts concentration not less than 60,000 to 65,000 ppm. For the study, fresh goat skin was treated with ozone at a concentration of 2 g/h for 0.5 to 2 h in a specially designed reactor. The samples treated with ozone are kept in the open atmosphere and sealed bags at room temperature; ozone treatment for 30 min also can eliminate microorganisms present on raw skin, and samples could be preserved for more than two weeks. Thus, with ozonation flayed skins can be preserved for short periods, and the use of a high concentration of salts in conventional salt curing/preservation can be eliminated [132]. In a similar study, DBD-based ozone generation was utilized for preservation of goat skin; the generator was fed with oxygen gas to generate ozone at a concentration of 2 g/h and experimental goat skin was exposed to ozone for two hours. In this study, ozonation is also able to preserve the skin similarly with conventional salt curing [133]. Ozone can be utilized as ecofriendly biocides alternative for toxic and environmentally harmful chemical biocides which are added to beamhouse operations to prevent the microbial decomposition of hide. With 15-min ozonation per hour bacterial growth can be prevented, whereas 5-to-10-min ozonation is sufficient to keep the bacterial population under control where no damage to hide or skins is caused by bacteria [134]. Ozonation was also explored for sulphide-free dehairing of hides and skins; by using ozone complete dehairing can be achieved with significantly less environmental impacts compared to convention dehairing using sulphide [135]. With ozone-based dehairing, leather with similar characteristics obtained to that of conventional lime and sodium sulphide-based dehairing. The further benefits of ozone-based dehairing are more chromium absorption in tanning, more hair recovery and COD reduction in beamhouse effluents; plus reuse of effluent is possible [136].

Ozonation has been explored as an ecofriendly bleaching treatment for the decolourization of leather products. Bleaching is a necessary step for the removal of colour impurities; also for chrome tanned leather which is called wet-blue due to the blue colour imparted by chromium; conventional bleaching is a wet chemical process involving chemicals and thus environmental impacts associated with the process. Decolourization of chrome tanned leather and sheepskin dyed with black dye was carried out with ozonation using a laboratory-scale ozonator (Lundell Aquametrics, Inc.) having a 180 mg/h ozone generation capacity connected to the applicator. Ozone was produced using oxygen gas as feed, and with the ozone flowrate set to 3 l/min and treatment carried out from 3 to 30 min. An ozonation time of 30 min was found to be the optimum for decolourization of leather products [137]. Ozonation has been explored for chamois leather, which is one of the most popular and economically important leather articles, conventionally made from lamb or goat skin by the oil tanning technique. With ozonation of oil treated skins, leather products with similar characteristics to conventional chamois leather can be produced; ozonation can reduce the oxidation time to 60 min compared to an oxidation period of 10–12 days required in conventional methods [138].

16.8 Conclusion

The chapter provides an overview of photocatalysis, nonthermal plasma and ozonation-based technology for a reduction in the environmental impacts associated with leather production and processing. In this chapter, the leather production process was described, and the environmental impacts associated with leather production and processing were displayed. All three technologies are advanced oxidation processes with different mode of action. Photocatalysis and its variations as well as nonthermal plasma are considered as physicochemical treatments, whereas ozonation is considered as a purely chemical treatment, though the ozone generator is chiefly based on the nonthermal plasma silent discharge as air or oxygen. All three techniques were explored extensively for treatment and control of pollution from leather production and processing. As set forth in this chapter, photocatalysis, nonthermal plasma and ozonation all exhibit great potential for the control and treatment of pollution generated from leather industries. Thus, this chapter will certainly be useful to researchers and stockholders working in this field.

References

1. Kanagaraj J, Senthilvelan T, Panda RC, Kavitha S (2015) Eco-friendly waste management strategies for greener environment towards sustainable development in leather industry: a comprehensive review. J Clean Prod 89:1–17. https://doi.org/10.1016/j.jclepro.2014.11.013
2. Dixit S, Yadav A, Dwivedi PD, Das M (2015) Toxic hazards of leather industry and technologies to combat threat: a review. J Clean Prod 87:39–49. https://doi.org/10.1016/j.jclepro.2014.10.017
3. Tasca AL, Puccini M (2019) Leather tanning: life cycle assessment of retanning, fatliquoring and dyeing. J Clean Prod 226:720–729. https://doi.org/10.1016/j.jclepro.2019.03.335
4. Balakrishnan PA, Arunagiri A, Rao PG (2002) Ozone generation by silent electric discharge and its application in tertiary treatment of tannery effluent. J Electrostat 56:77–86. https://doi.org/10.1016/S0304-3886(02)00031-1
5. Hu J, Xiao Z, Zhou R et al (2011) Ecological utilization of leather tannery waste with circular economy model. J Clean Prod 19:221–228. https://doi.org/10.1016/j.jclepro.2010.09.018
6. Garg SK, Tripathi M, Srinath T (2012) Strategies for chromium bioremediation of tannery effluent. Rev Environ Contam Toxicol 217:75–140. https://doi.org/10.1007/978-1-4614-2329-4_2
7. GracePavithra K, Jaikumar V, Kumar PS, SundarRajan P (2019) A review on cleaner strategies for chromium industrial wastewater: present research and future perspective. J Clean Prod 228:580–593. https://doi.org/10.1016/j.jclepro.2019.04.117
8. Jiang H, Liu J, Han W (2016) The status and developments of leather solid waste treatment: a mini-review. Waste Manag Res 34:399–408. https://doi.org/10.1177/0734242X16633772
9. Lofrano G, Meriç S, Zengin GE, Orhon D (2013) Chemical and biological treatment technologies for leather tannery chemicals and wastewaters: a review. Sci Total Environ 461–462:265–281. https://doi.org/10.1016/j.scitotenv.2013.05.004
10. Giaccherini F, Munz G, Dockhorn T et al (2017) Carbon and energy footprint analysis of tannery wastewater treatment: a Global overview. Water Res Ind 17:43–52. https://doi.org/10.1016/j.wri.2017.03.001
11. Sivaram NM, Barik D (2019) Chapter 5—Toxic waste from leather industries. In: Barik D (ed) Energy from toxic organic waste for heat and power generation. Woodhead Publishing, pp 55–67
12. Houshyar Z, Khoshfetrat AB, Fatehifar E (2012) Influence of ozonation process on characteristics of pre-alkalized tannery effluents. Chem Eng J 191:59–65. https://doi.org/10.1016/j.cej.2012.02.053
13. Sathish M, Madhan B, Raghava Rao J (2019) Leather solid waste: an eco-benign raw material for leather chemical preparation—a circular economy example. Waste Manag 87:357–367. https://doi.org/10.1016/j.wasman.2019.02.026
14. Pati A, Chaudhary R, Subramani S (2014) A review on management of chrome-tanned leather shavings: a holistic paradigm to combat the environmental issues. Environ Sci Pollut Res Int 21:11266–11282. https://doi.org/10.1007/s11356-014-3055-9
15. Sekaran G, Swarnalatha S, Dandaiah S (2007) Solid waste management in leather sector. J Des Manuf Technol 1:47–52. https://doi.org/10.18000/ijodam.70008
16. Kanagaraj J, kandukalpatti chinnaraj V, Babu N, Sayeed S (2006) Solid wastes generation in the leather industry and its utilization for cleaner environment. J Sci Ind Res 65:541–548. https://doi.org/10.1002/chin.200649273
17. de Aquim PM, Hansen É, Gutterres M (2019) Water reuse: an alternative to minimize the environmental impact on the leather industry. J Environ Manag 230:456–463. https://doi.org/10.1016/j.jenvman.2018.09.077
18. Rueda-Marquez JJ, Levchuk I, Fernández Ibañez P, Sillanpää M (2020) A critical review on application of photocatalysis for toxicity reduction of real wastewaters. J Clean Prod 258:120694. https://doi.org/10.1016/j.jclepro.2020.120694

19. Gnanaprakasam A, Sivakumar VM, Thirumarimurugan M (2015) Influencing parameters in the photocatalytic degradation of organic effluent via nanometal oxide catalyst: a review. Ind J Mater Sci 2015:1–16. https://doi.org/10.1155/2015/601827
20. Jiang L, Wang Y, Feng C (2012) Application of photocatalytic technology in environmental safety. Proc Eng 45:993–997. https://doi.org/10.1016/j.proeng.2012.08.271
21. Litter MI (1999) Heterogeneous photocatalysis: transition metal ions in photocatalytic systems. Appl Catal B 23:89–114. https://doi.org/10.1016/S0926-3373(99)00069-7
22. Parul Kaur K, Badru R et al (2020) Photodegradation of organic pollutants using heterojunctions: a review. J Environ Chem Eng 8:103666. https://doi.org/10.1016/j.jece.2020.103666
23. Lau GE, Che Abdullah CA, Wan Ahmad WAN et al (2020) Eco-friendly photocatalysts for degradation of dyes. Catalysts 10:1129. https://doi.org/10.3390/catal10101129
24. Natarajan S, Bajaj HC, Tayade RJ (2018) Recent advances based on the synergetic effect of adsorption for removal of dyes from waste water using photocatalytic process. J Environ Sci 65:201–222. https://doi.org/10.1016/j.jes.2017.03.011
25. Daghrir R, Drogui P, Robert D (2012) Photoelectrocatalytic technologies for environmental applications. J Photochem Photobiol A 238:41–52. https://doi.org/10.1016/j.jphotochem.2012.04.009
26. Zhang G, Zhang X, Meng Y et al (2020) Layered double hydroxides-based photocatalysts and visible-light driven photodegradation of organic pollutants: a review. Chem Eng J 392:123684. https://doi.org/10.1016/j.cej.2019.123684
27. Basavarajappa PS, Patil SB, Ganganagappa N et al (2020) Recent progress in metal-doped TiO_2, non-metal doped/codoped TiO2 and TiO2 nanostructured hybrids for enhanced photocatalysis. Int J Hydrogen Energy 45:7764–7778. https://doi.org/10.1016/j.ijhydene.2019.07.241
28. Li Z, Meng X, Zhang Z (2018) Recent development on MoS2-based photocatalysis: a review. J Photochem Photobiol C 35:39–55. https://doi.org/10.1016/j.jphotochemrev.2017.12.002
29. Oyewo OA, Elemike EE, Onwudiwe DC, Onyango MS (2020) Metal oxide-cellulose nanocomposites for the removal of toxic metals and dyes from wastewater. Int J Biol Macromol 164:2477–2496. https://doi.org/10.1016/j.ijbiomac.2020.08.074
30. Ismael M (2020) A review on graphitic carbon nitride (g-C3N4) based nanocomposites: synthesis, categories, and their application in photocatalysis. J Alloy Compd 846:156446. https://doi.org/10.1016/j.jallcom.2020.156446
31. Ajiboye TO, Oyewo OA, Onwudiwe DC (2021) Simultaneous removal of organics and heavy metals from industrial wastewater: a review. Chemosphere 262:128379. https://doi.org/10.1016/j.chemosphere.2020.128379
32. Tudoran C, Roşu M-C, Coroş M (2020) A concise overview on plasma treatment for application on textile and leather materials. Plasma Process Polym 17:2000046. https://doi.org/10.1002/ppap.202000046
33. Preethi V, Parama Kalyani KS, Iyappan K et al (2009) Ozonation of tannery effluent for removal of cod and color. J Hazard Mater 166:150–154. https://doi.org/10.1016/j.jhazmat.2008.11.035
34. Di Iaconi C, Ramadori R, Lopez A (2009) The effect of ozone on tannery wastewater biological treatment at demonstrative scale. Biores Technol 100:6121–6124. https://doi.org/10.1016/j.biortech.2009.06.022
35. Kolomaznik K, Adamek M, Andel I, Uhlirova M (2008) Leather waste—potential threat to human health, and a new technology of its treatment. J Hazard Mater 160:514–520. https://doi.org/10.1016/j.jhazmat.2008.03.070
36. Rameshraja D, Suresh S (2011) Treatment of tannery wastewater by various oxidation and combined processes. Int J Environ Res 5:349–360. https://doi.org/10.22059/ijer.2011.320
37. Litter MI (2009) Treatment of chromium, mercury, lead, uranium, and arsenic in water by heterogeneous photocatalysis. In: de Lasa HI, Serrano Rosales B (eds) Advances in chemical engineering. Academic Press, pp 37–67

38. Athanasekou C, Romanos GEm, Papageorgiou SK et al (2017) Photocatalytic degradation of hexavalent chromium emerging contaminant via advanced titanium dioxide nanostructures. Chem Eng J 318:171–180. https://doi.org/10.1016/j.cej.2016.06.033
39. Acharya R, Naik B, Parida K (2018) Cr(VI) remediation from aqueous environment through modified-TiO_2-mediated photocatalytic reduction. Beilstein J Nanotechnol 9:1448–1470. https://doi.org/10.3762/bjnano.9.137
40. Litter MI (2017) Last advances on TiO_2-photocatalytic removal of chromium, uranium and arsenic. Curr Opin Green Sustain Chem 6:150–158. https://doi.org/10.1016/j.cogsc.2017.04.002
41. Wang H, Wen F, Li X et al (2016) Cerium-doped MoS_2 nanostructures: efficient visible photocatalysis for Cr(VI) removal. Sep Purif Technol 170:190–198. https://doi.org/10.1016/j.seppur.2016.06.049
42. Douafer S, Lahmar H, Benamira M et al (2019) Chromate reduction on the novel hetero-system $LiMn_2O_4/SnO_2$ catalyst under solar light irradiation. Surf Interfaces 17:100372. https://doi.org/10.1016/j.surfin.2019.100372
43. Balu S, Chen Y-L, Juang R-C et al (2020) Morphology-controlled synthesis of α–Fe_2O_3 nanocrystals impregnated on g-C_3N_4–SO_3H with ultrafast charge separation for photoreduction of Cr (VI) under visible light. Environ Pollut 267:115491. https://doi.org/10.1016/j.envpol.2020.115491
44. Zheng X, Liu D, Wen J, Lv S (2020) Nonthermal plasma-vulcanized flower-like ZnS/Zn-Al composites from Zn-Al layered double hydroxides for the adsorption-photo-reduction of Cr (VI). Sep Purif Technol 117934. https://doi.org/10.1016/j.seppur.2020.117934
45. Dakhinaray T, Dash BP, Sahoo PK et al (2020) Role of graphene nanocomposite photocatalysts in photo-reduction of Cr (VI) for wastewater treatment. Mater Today Proc. https://doi.org/10.1016/j.matpr.2020.09.335
46. Yang L, Xu C, Wan F et al (2019) Synthesis of RGO/BiOI/ZnO composites with efficient photocatalytic reduction of aqueous Cr(VI) under visible-light irradiation. Mater Res Bull 112:154–158. https://doi.org/10.1016/j.materresbull.2018.12.019
47. Sun H, Park S-J (2020) Phosphorus-doped g-C_3N_4/SnS nanocomposite for efficient photocatalytic reduction of aqueous Cr(VI) under visible light. Appl Surf Sci 531:147325. https://doi.org/10.1016/j.apsusc.2020.147325
48. Kenfoud H, Nasrallah N, Baaloudj O et al (2020) Photocatalytic reduction of Cr(VI) onto the spinel $CaFe_2O_4$ nanoparticles. Optik 223:165610. https://doi.org/10.1016/j.ijleo.2020.165610
49. Liang H, Li T, Zhang J et al (2020) 3-D hierarchical Ag/ZnO@CF for synergistically removing phenol and Cr(VI): heterogeneous vs. homogeneous photocatalysis. J Colloid Interface Sci 558:85–94. https://doi.org/10.1016/j.jcis.2019.09.105
50. Li Y-X, Wang X, Wang C-C et al (2020) S-TiO2/UiO-66-NH2 composite for boosted photocatalytic Cr(VI) reduction and bisphenol A degradation under LED visible light. J Hazard Mater 399:123085. https://doi.org/10.1016/j.jhazmat.2020.123085
51. Xie G, Wang H, Zhou Y et al (2020) Simultaneous remediation of methylene blue and Cr (VI) by mesoporous $BiVO_4$ photocatalyst under visible-light illumination. J Taiwan Inst Chem Eng 112:357–365. https://doi.org/10.1016/j.jtice.2020.05.014
52. Meichtry JM, Brusa M, Mailhot G et al (2007) Heterogeneous photocatalysis of Cr(VI) in the presence of citric acid over TiO_2 particles: relevance of Cr(V)–citrate complexes. Appl Catal B 71:101–107. https://doi.org/10.1016/j.apcatb.2006.09.002
53. Yang J-K, Lee S-M (2006) Removal of Cr(VI) and humic acid by using TiO_2 photocatalysis. Chemosphere 63:1677–1684. https://doi.org/10.1016/j.chemosphere.2005.10.005
54. Liu J, Huang K, Xie K et al (2016) An ecological new approach for treating Cr(VI)-containing industrial wastewater: photochemical reduction. Water Res 93:187–194. https://doi.org/10.1016/j.watres.2016.02.025
55. Li Q-H, Dong M, Li R et al (2021) Enhancement of Cr(VI) removal efficiency via adsorption/photocatalysis synergy using electrospun chitosan/g-C_3N_4/TiO_2 nanofibers. Carbohyd Polym 253:117200. https://doi.org/10.1016/j.carbpol.2020.117200

56. Kebir M, Chabani M, Nasrallah N et al (2011) Coupling adsorption with photocatalysis process for the Cr(VI) removal. Desalination 270:166–173. https://doi.org/10.1016/j.desal.2010.11.041
57. Josué TG, Almeida LNB, Lopes MF et al (2020) Cr (VI) reduction by photocatalyic process: Nb_2O_5 an alternative catalyst. J Environ Manag 268:110711. https://doi.org/10.1016/j.jenvman.2020.110711
58. Wang X, Liu W, Fu H et al (2019) Simultaneous Cr(VI) reduction and Cr(III) removal of bifunctional MOF/titanate nanotube composites. Environ Pollut 249:502–511. https://doi.org/10.1016/j.envpol.2019.03.096
59. Paschoal FMM, Anderson MA, Zanoni MVB (2009) Simultaneous removal of chromium and leather dye from simulated tannery effluent by photoelectrochemistry. J Hazard Mater 166:531–537. https://doi.org/10.1016/j.jhazmat.2008.11.058
60. Kamaraj M, Srinivasan NR, Assefa G et al (2020) Facile development of sunlit ZnO nanoparticles-activated carbon hybrid from pernicious weed as an operative nano-adsorbent for removal of methylene blue and chromium from aqueous solution: Extended application in tannery industrial wastewater. Environ Technol Innovation 17:100540. https://doi.org/10.1016/j.eti.2019.100540
61. Shen J, Lu Y, Liu J-K, Yang X-H (2016) Photocatalytic activity of silver chromate materials by various synthesis methods. J Exp Nanosci 11:650–659. https://doi.org/10.1080/17458080.2015.1110624
62. Zhao Y, Chang W, Huang Z et al (2017) Enhanced removal of toxic Cr(VI) in tannery wastewater by photoelectrocatalysis with synthetic TiO_2 hollow spheres. Appl Surf Sci 405:102–110. https://doi.org/10.1016/j.apsusc.2017.01.306
63. Wang J-C, Ren J, Yao H-C et al (2016) Synergistic photocatalysis of Cr(VI) reduction and 4-Chlorophenol degradation over hydroxylated α-Fe_2O_3 under visible light irradiation. J Hazard Mater 311:11–19. https://doi.org/10.1016/j.jhazmat.2016.02.055
64. Jiang B, Guo J, Wang Z et al (2015) A green approach towards simultaneous remediations of chromium(VI) and arsenic(III) in aqueous solution. Chem Eng J 262:1144–1151. https://doi.org/10.1016/j.cej.2014.10.064
65. Chandana L, Lakshminarayana B, Subrahmanyam Ch (2015) Influence of hydrogen peroxide on the simultaneous removal of Cr(VI) and methylene blue from aqueous medium under atmospheric pressure plasma jet. J Environ Chem Eng 3:2760–2767. https://doi.org/10.1016/j.jece.2015.09.030
66. Chandana L, Subrahmanyam Ch (2017) Non-thermal discharge plasma promoted redox transformation of arsenic(III) and chromium(VI) in an aqueous medium. Chem Eng J 329:211–219. https://doi.org/10.1016/j.cej.2017.05.114
67. Long Y, Nie J, Yuan C et al (2021) Preparation of CoFe2O4/MWNTs/sponge electrode to enhance dielectric barrier plasma discharge for degradation of phenylic pollutants and Cr(VI) reduction. Appl Catal B 283:119604. https://doi.org/10.1016/j.apcatb.2020.119604
68. Liu Y (2009) Simultaneous oxidation of phenol and reduction of Cr(VI) induced by contact glow discharge electrolysis. J Hazard Mater 168:992–996. https://doi.org/10.1016/j.jhazmat.2009.02.116
69. Zhang C, Sun Y, Yu Z et al (2018) Simultaneous removal of Cr(VI) and acid orange 7 from water solution by dielectric barrier discharge plasma. Chemosphere 191:527–536. https://doi.org/10.1016/j.chemosphere.2017.10.087
70. Ke Z, Huang Q, Zhang H, Yu Z (2011) Reduction and removal of aqueous Cr(VI) by glow discharge plasma at the gas-solution interface. Environ Sci Technol 45:7841–7847. https://doi.org/10.1021/es201680m
71. Du C, Yan J (2017) Reduction and removal of Cr(VI) from aqueous solution by microplasma. In: Du C, Yan J (eds) Plasma remediation technology for environmental protection. Springer, Singapore, pp 41–59
72. Luo Z, Xu J, Zhu D et al (2019) Ion-imprinted polypropylene fibers fabricated by the plasma-mediated grafting strategy for efficient and selective adsorption of Cr(VI). Polymers 11:1508. https://doi.org/10.3390/polym11091508

73. Macedo LC, Zaia DAM, Moore GJ, de Santana H (2007) Degradation of leather dye on TiO_2: a study of applied experimental parameters on photoelectrocatalysis. J Photochem Photobiol A 185:86–93. https://doi.org/10.1016/j.jphotochem.2006.05.016
74. Sakthivel S, Shankar MV, Palanichamy M et al (2002) Photocatalytic decomposition of leather dye: comparative study of TiO_2 supported on alumina and glass beads. J Photochem Photobiol A 148:153–159. https://doi.org/10.1016/S1010-6030(02)00085-0
75. Maroudas A, Pandis PK, Chatzopoulou A et al (2021) Synergetic decolorization of azo dyes using ultrasounds, photocatalysis and photo-fenton reaction. Ultrason Sonochem 71:105367. https://doi.org/10.1016/j.ultsonch.2020.105367
76. Hasegawa MC, de Daniel JFS, Takashima K et al (2014) COD removal and toxicity decrease from tannery wastewater by zinc oxide-assisted photocatalysis: a case study. Environ Technol 35:1589–1595. https://doi.org/10.1080/09593330.2013.874499
77. Mohammed A (2013) BOD5 removal from tannery wastewater over ZnO-$ZnFe_2O_4$ composite photocatalyst supported on activated carbon. J Chem Eng Mater Sci 4:80–86. https://doi.org/10.5897/JCEMS2013.0165
78. Zhao Y, Huang Z, Chang W et al (2017) Microwave-assisted solvothermal synthesis of hierarchical TiO_2 microspheres for efficient electro-field-assisted-photocatalytic removal of tributyltin in tannery wastewater. Chemosphere 179:75–83. https://doi.org/10.1016/j.chemosphere.2017.03.084
79. Baltes L, Patachia S, Tierean M et al (2018) Photoactive polymer-cement composites for tannins removal from wastewaters. J Environ Chem Eng 6:4357–4367. https://doi.org/10.1016/j.jece.2018.06.039
80. Aarthi A, Umadevi M, Parimaladevi R, Sathe GV (2019) Polyvinyl thiol assisted Ag NPs as an efficient SERS analyzer and visible light photocatalyst for tannery waste landfill leachate. Vacuum 161:125–129. https://doi.org/10.1016/j.vacuum.2018.12.022
81. Kumar ETD (2017) Solar light driven degradation of post tanning water at heterostructured $BiVO_4$-ZnO mixed oxide catalyst interface. Surf Interfaces 7
82. Natarajan TS, Natarajan K, Bajaj HC, Tayade RJ (2013) Study on identification of leather industry wastewater constituents and its photocatalytic treatment. Int J Environ Sci Technol 10:855–864. https://doi.org/10.1007/s13762-013-0200-9
83. Colmenares JC, Lisowski P, Bermudez JM et al (2014) Unprecedented photocatalytic activity of carbonized leather skin residues containing chromium oxide phases. Appl Catal B 150–151:432–437. https://doi.org/10.1016/j.apcatb.2013.12.038
84. Telay Mekonnen B, Meiyazhagan A, Ragothaman M et al (2019) Bi-functional iron embedded carbon nanostructures from collagen waste for photocatalysis and Li-ion battery applications: a waste to wealth approach. J Clean Prod 210:190–199. https://doi.org/10.1016/j.jclepro.2018.10.319
85. Barik AJ, Gogate PR (2017) Degradation of 2,4-dichlorophenol using combined approach based on ultrasound, ozone and catalyst. Ultrason Sonochem 36:517–526. https://doi.org/10.1016/j.ultsonch.2016.08.017
86. Hama Aziz KH, Miessner H, Mueller S et al (2018) Comparative study on 2,4-dichlorophenoxyacetic acid and 2,4-dichlorophenol removal from aqueous solutions via ozonation, photocatalysis and non-thermal plasma using a planar falling film reactor. J Hazard Mater 343:107–115. https://doi.org/10.1016/j.jhazmat.2017.09.025
87. Favaro G, De Leo D, Pastore P et al (2008) Quantitative determination of chlorophenols in leather by pressurized liquid extraction and liquid chromatography with diode-array detection. J Chromatogr A 1177:36–42. https://doi.org/10.1016/j.chroma.2007.10.106
88. Zhao C, Xue L, Zhou Y, et al (2020) A microwave atmospheric plasma strategy for fast and efficient degradation of aqueous p-nitrophenol. J Hazard Mater 124473. https://doi.org/10.1016/j.jhazmat.2020.124473
89. Ws E-S, Sa O, Aa M (2015) Deterioration to extinction of wastewater bacteria by non-thermal atmospheric pressure air plasma as assessed by 16S rDNA-DGGE fingerprinting. Front Microbiol 6:1098. https://doi.org/10.3389/fmicb.2015.01098

90. Rice RG (1996) Applications of ozone for industrial wastewater treatment—a review. Ozone: Sci Eng 18:477–515. https://doi.org/10.1080/01919512.1997.10382859
91. Mella B, Barcellos BS de C, Costa DE da S, Gutterres M (2018) Treatment of leather dyeing wastewater with associated process of coagulation-flocculation/adsorption/ozonation. Ozone Sci Eng 40:133–140. https://doi.org/10.1080/01919512.2017.1346464
92. Jochimsen JC, Schenk H, Jekel MR, Hegemann W (1997) Combined oxidative and biological treatment for separated streams of tannery wastewater. Water Sci Technol 36:209–216. https://doi.org/10.1016/S0273-1223(97)00389-2
93. Sivagami K, Sakthivel KP, Nambi IM (2018) Advanced oxidation processes for the treatment of tannery wastewater. J Environ Chem Eng 6:3656–3663. https://doi.org/10.1016/j.jece.2017.06.004
94. M.D SD, Genceli EA, Babuna FG, Orhon D (2004) Ozonation of nonbiodegradable organics in tannery wastewater. J Environ Sci Health Part A 39:1705–1715. https://doi.org/10.1081/ESE-120037871
95. Huang G, Pan F, Fan G, Liu G (2016) Application of heterogeneous catalytic ozonation as a tertiary treatment of effluent of biologically treated tannery wastewater. J Environ Sci Health Part A 51:626–633. https://doi.org/10.1080/10934529.2016.1159863
96. Kalyanaraman C, Kameswari KSB, Rao JR (2015) Studies on enhancing the biodegradation of tannins by ozonation and Fenton’s oxidation process. J Ind Eng Chem 25:329–337. https://doi.org/10.1016/j.jiec.2014.11.012
97. Rema T, Parivallal B, Ramanujam RA (2010) Studies on degradation of syntan used in leather tanning process using ozone. Int J Environ Sci Dev 1:264–267. https://doi.org/10.7763/IJESD.2010.V1.51
98. Thankappan R, Srinivasan SV, Suthanthararajan R, Sillanpää M (2018) Studies on removal of phenol sulfonic acid-syntan in aqueous medium using ozonation. Environ Technol 39:2434–2446. https://doi.org/10.1080/09593330.2017.1355936
99. Srinivasan SV, Rema T, Chitra K et al (2009) Decolourisation of leather dye by ozonation. Desalination 235:88–92. https://doi.org/10.1016/j.desal.2007.07.032
100. Prats D, Var P, Yagiie C (2003) Colour elimination through oxidation technologies in leather finishing industry waste waters. 65:10
101. Vedaraman N, Shamshath Begum S, Srinivasan SV (2013) Response surface methodology for decolourisation of leather dye using ozonation in a packed bed reactor. Clean Techn Environ Policy 15:607–616. https://doi.org/10.1007/s10098-012-0544-8
102. Kasiri MB, Modirshahla N, Mansouri H (2013) Decolorization of organic dye solution by ozonation; optimization with response surface methodology. Int J Ind Chem 4:3. https://doi.org/10.1186/2228-5547-4-3
103. Sekar ASS (2008) Removal of colour from tannery dye wastewater using ozone. Nat Environ Pollut Technol 7:4
104. Lambert JA, Vega MM, Isarain-Chávez E, Peralta-Hernández JM (2013) Ozone and electrocoagulation processes for treatment of dye in leather industry wastewater: a comparative study. Int J Emerg Technol Adv Eng 3:1–9
105. de Carvalho CB, de Franco ME, Souza FS, Féris LA (2018) Degradation of acid black 210 by advanced oxidative processes: O3 and O3/UV. Ozone Sci Eng 40:372–376. https://doi.org/10.1080/01919512.2018.1435258
106. Van Aken P, Van den Broeck R, Degrève J, Dewil R (2015) The effect of ozonation on the toxicity and biodegradability of 2,4-dichlorophenol-containing wastewater. Chem Eng J 280:728–736. https://doi.org/10.1016/j.cej.2015.06.019
107. Van Aken P, Van den Broeck R, Degrève J, Dewil R (2017) A pilot-scale coupling of ozonation and biodegradation of 2,4-dichlorophenol-containing wastewater: the effect of biomass acclimation towards chlorophenol and intermediate ozonation products. J Clean Prod 161:1432–1441. https://doi.org/10.1016/j.jclepro.2017.05.124
108. Contreras S, Rodríguez M, Momani FA et al (2003) Contribution of the ozonation pre-treatment to the biodegradation of aqueous solutions of 2,4-dichlorophenol. Water Res 37:3164–3171. https://doi.org/10.1016/S0043-1354(03)00167-2

109. He Z, Zhang A, Li Y et al (2011) Chlorophene degradation by combined ultraviolet irradiation and ozonation. J Environ Sci Health Part A 46:1–8. https://doi.org/10.1080/10934529.2011.526065
110. Olak-Kucharczyk M, Miller JS, Ledakowicz S (2012) Ozonation kinetics of o-phenylphenol in aqueous solutions. Ozone Sci Eng 34:300–305. https://doi.org/10.1080/01919512.2012.694339
111. Fiehn O, Wegener G, Jochimsen J, Jekel M (1998) Analysis of the ozonation of 2-mercaptobenzothiazole in water and tannery wastewater using sum parameters, liquid- and gas chromatography and capillary electrophoresis. Water Res 32:1075–1084. https://doi.org/10.1016/S0043-1354(97)00332-1
112. Schrank SG, Gebhardt W, José HJ et al (2017) Ozone treatment of tannery wastewater monitored by conventional and substance specific wastewater analyses. Ozone Sci Eng 39:159–187. https://doi.org/10.1080/01919512.2016.1273090
113. Schrank SG, José HJ, Moreira RFPM, Schröder HF (2004) Comparison of different advanced oxidation process to reduce toxicity and mineralisation of tannery wastewater. Water Sci Technol 50:329–334
114. Schrank SG, Bieling U, José HJ et al (2009) Generation of endocrine disruptor compounds during ozone treatment of tannery wastewater confirmed by biological effect analysis and substance specific analysis. Water Sci Technol 59:31–38. https://doi.org/10.2166/wst.2009.762
115. Dave H, Ledwani L, Nema SK (2016) Surface modification by atmospheric pressure air plasma treatment to improve dyeing with natural dyes: an environment friendly approach for leather processing. Plasma Chem Plasma Process 36:599–613. https://doi.org/10.1007/s11090-015-9687-9
116. Dave H, Ledwani L, Nema SK (2017) Improvement in natural dyeing with the aid of atmospheric pressure plasma treatment: a green solution for leather processing. Curr Environ Eng 4:140–149. https://doi.org/10.2174/2212717804666161208125652
117. Vajpayee M, Singh M, Dave H et al (2020) Antimicrobial finishing of hide/leather by atmospheric pressure plasma and extracts of Cassia renigera and Cassia fistula bark. Rend Fis Acc Lincei 31:1105–1116. https://doi.org/10.1007/s12210-020-00954-2
118. Chen Z(陈支通), Garcia G, Arumugaswami V, Wirz RE (2020) Cold atmospheric plasma for SARS-CoV-2 inactivation. Phys Fluids 32:111702. https://doi.org/10.1063/5.0031332
119. Ando H, Kataoka S, Kuwata M et al (1998) Low temperature fluorocarbon gas plasma treatment and fungal resistance on leather. J Japan Soc Colour Mater 71:91–99. https://doi.org/10.4011/shikizai1937.71.91
120. Kayaoğlu BK, Öztürk E (2013) Imparting hydrophobicity to natural leather through plasma polymerization for easy care effect. Fibers Polym 14:1706–1713. https://doi.org/10.1007/s12221-013-1706-y
121. You X, Gou L, Tong X (2016) Improvement in surface hydrophilicity and resistance to deformation of natural leather through O2/H2O low-temperature plasma treatment. Appl Surf Sci 360:398–402. https://doi.org/10.1016/j.apsusc.2015.11.030
122. Jiang Y, Li J, Liu F et al (2019) The effects of surface modification using O_2 low temperature plasma on chrome tanning properties of natural leather. J Ind Text 49:534–547. https://doi.org/10.1177/1528083718804205
123. Açıkel S, Çelik C, Kaygusuz M, Aslan A (2020) Effect of argon atmospheric pressure plasma (APP) treatment on the properties of sheep leathers and wastewater oft he retanning processes. J Soc Leather Technol Chem 104:120–129
124. Choi JH, Lee ES, Baik HK et al (2003) Surface modification of natural leather using low-pressure parallel plate plasma. Surf Coat Technol 171:257–263. https://doi.org/10.1016/S0257-8972(03)00282-2
125. Štěpánová V, Kelar J, Slavíček P et al (2017) Surface modification of natural leather using diffuse ambient air plasma. Int J Adhes Adhes 77:198–203. https://doi.org/10.1016/j.ijadhadh.2017.05.004

126. Acikel S, Aslan A, Oksuz L, Aktan T (2013) Effects of atmospheric pressure plasma treatments on various properties of leathers. J Am Leather Chem Ass 108:266–276
127. Açıkel S meriç (2019) Investigation of flame retardancy of Borax in upholstery leather modified with atmospheric pressure plasma. Eur J Sci Technol 17:844–851. https://doi.org/10.31590/ejosat.641656
128. Gaidau C, Surdu L, Niculescu M et al (2017) Research on cold plasma treatment of leather and fur based materials as ecological alternative. Industria textilă 68. https://doi.org/10.35530/IT.068.05.1365
129. Seul SD, Lim JM, Ha SH, Kim YH (2005) Adhesion enhancement of polyurethane coated leather and polyurethane foam with plasma treatment. Korean J Chem Eng 22:745–749. https://doi.org/10.1007/BF02705793
130. Pietrelli L, Ferro S, Reverberi AP, Vocciante M (2020) Removal and recovery of heavy metals from tannery sludge subjected to plasma pyro-gasification process. J Clean Prod 273:123166. https://doi.org/10.1016/j.jclepro.2020.123166
131. Wu J, Zhao L, Liu X et al (2017) Recent progress in cleaner preservation of hides and skins. J Clean Prod 148:158–173. https://doi.org/10.1016/j.jclepro.2017.01.113
132. Sivakumar V, Balakrishnan PA, Muralidharan C, Swaminathan G (2010) Use of ozone as a disinfectant for raw animal skins—application as short-term preservation in leather making. Ozone Sci Eng 32:449–455. https://doi.org/10.1080/01919512.2010.515524
133. Vaduganathan L (2017) The ozone treatment for elimination of toxic waste—an alternate for preservation of goat skins and enhancement of bleaching property of starch. 1 13:6005–6010. https://doi.org/10.24297/jac.v13i11.5883
134. MehmetM Mutlu, Cadircl BH, Ozgunay H et al (2009) Ozone as a biocide in soaking. J Soc Leather Technol Chem 93:18–20
135. Sundar VJ, Vedaraman N, Balakrishnan PA et al (2006) Sulphide free unhairing–studies on ozone based depilation. J Am Leather Chem Assoc 101:231–234
136. Balakrishnan PA, Vedaraman N, Rangasamy T, Muralidharan C (2006) An eco-benign approach for unhairing goat skin using ozone. Ozone Sci Eng 28:341–346. https://doi.org/10.1080/01919510600900274
137. Onem E, Yorgancioglu A, Namirti G et al (2017) Ozonation as an environmentally friendly method to decolorize the leather products. Ozone Sci Eng 39:454–461. https://doi.org/10.1080/01919512.2017.1322487
138. Sundar VJ, Muralidharan C, Sadulla S (2007) Research note: ozonation—an emerging inevitable option for chamois making. Ozone Sci Eng 29:405–409. https://doi.org/10.1080/01919510701573434

Chapter 17
Science and Technology Roadmap for Photocatalytic Membrane Separation: A Potential Route for Environmental Remediation and Fouling Mitigation

**Zaira Zaman Chowdhury, Ahmed Elsayid Ali, Khalisanni Khalid,
Rabia Ikram, Mahfujur Rahman, Shahjalal Md. Shibly,
Suresh Sagadevan, Rahman F. Rafique, and Arnab Barua**

Abstract The chapter presents an overview regarding the nanoenhanced photocatalytic membrane separation process. Photocatalytic membrane can exhibit better properties, such as permeability, water flux, and enhanced photodegradation ability with antifouling tendencies. Different types of photocatalyst along with their composites can be used for membrane fabrication process. Advantages and disadvantages of different types of membrane reactor along with their configuration are illustrated in this chapter. Fabrication process of photocatalytic membrane is also discussed in the subsequent section. Antifouling mechanism of photocatalytic membrane is also discussed in the concluding section of the chapter. This chapter outlines the importance of integration of nanophotocatalysts with the membrane

---

Z. Z. Chowdhury (✉) · A. E. Ali · S. Md. Shibly · S. Sagadevan · A. Barua
Nanotechnology and Catalysis Research Center (NANOCAT), University of Malaya,
50603 Kuala Lumpur, Malaysia

K. Khalid
Malaysian Agricultural Research and Development Institute (MARDI), Persiaran
Mardi-UPM, 43400 Serdang, Selangor, Malaysia

Biocomposite Technology Laboratory, Institute of Tropical Forestry and Forest Products
(INTROP), University Putra Malaysia (UPM), 43400 Serdang, Selangor, Malaysia

R. Ikram
Department of Chemical Engineering, University of Malaya, 50603 Kuala Lumpur, Malaysia

M. Rahman
Islamic Business School, Universiti Utara Malaysia, UUM, 06010 Sinto, Kedah, Malaysia

R. F. Rafique
John A. Reif, Jr. Department of Civil and Environmental Engineering, New Jersey Institute of
Technology (NJIT), 323 MLK Blvd., New York, NJ 07102, USA

S. Garg and A. Chandra (eds.), *Green Photocatalytic Semiconductors*,
Green Chemistry and Sustainable Technology,
https://doi.org/10.1007/978-3-030-77371-7_17

matrix to ensure higher photodegradation of pollutant, enhanced water flux with reduced fouling of the membrane.

Keywords Nanophotocatalyst · Membrane · Fouling · Photodegradation · Photocatalytic membrane reactors (PMRs) · Water flux

Abbreviation

Ag_3PO_4	Silver phosphate
Al_2O_3	Alumina
APS	Atmospheric plasma spraying
C_3N_4	Carbon nitride
CeO_2	Cerium oxide
CuO	Copper oxide
CVD	Chemical vapor deposition
FO	Forward osmosis
GO	Graphene oxide
GS	Gas separation
MD	Membrane distillation
MF	Microfiltration
NF	Nanofiltration
PA	Polyacrylonitrile
PEG	Polyethylene glycol
PES	Polyether sulfone
PMRs	Photocatalytic membrane reactors
PS	Polysulfone
PVC	Polyvinylchloride
PVDF	Polyvinylidene fluoride
rGO	Reduced graphene oxide
RO	Reverse osmosis
SnO_2	Tin oxide
TiO_2	Titanium oxide
UF	Ultrafiltration
VOCs	Volatile organic compounds
ZnO	Zinc oxide
ZrO_2	Zirconium oxide

17.1 Introduction

Rapid industrialization coupled with increasing number of population has initiated shortage of freshwater resources. Thus, necessary innovative approach should be undertaken to treat wastewater [1]. Recently, hybrid membrane separation process is gaining popularity worldwide due to its high efficiency, pronounced selectivity, less energy consumption, and easy operational features under room temperature [2, 3]. Membrane acts as a physical barrier which is porous and allows selective transportation of desired molecules with rejection of targeted pollutants up to greater extent. However, the efficiency of a membrane is subjected to numerous factors, including type of membrane, pore size distribution, hydrophilicity, polarity, surface roughness as well as chemo-mechanical properties [4, 5]. The membrane separation process is inhibited by deposition or adhesion of foulant over the surface of membrane which can form like a gel or cake and clog the pores to reduce the water transportation rate with time [6, 7]. Membrane separation efficiency is furthermore reduced by concentration polarization effect. The rejected solids or pollutants can accumulate over the surface of the membrane causing concentration polarization effect. The irreversible adhesion or deposition of suspended particles on the external surface of the membrane will decrease the overall performance. The foulant can be removed from the membrane surface using usually complex and expensive cleaning process. For reusing the membrane, back permeation, forward and reverse flushing, backwashing, air scouring need to be done. This inhibits the continuous operation of the membrane separation process leading to undesirable plant shut down. Even though membrane separation process needs higher establishment cost or operational expenses rather than the conventional processes (such as evaporation, use of activated carbon, deep-bed filtration, and coagulation, sedimentation, or chemical treatment), yet it is suitable to get high-quality purified water. Recently, physiochemical modification of traditional membrane is getting much more attention by the research community to develop fouling-resistant membrane. The physiochemical properties of the membrane can be improved using desired nanomaterials which can ensure separation of specific pollutant as well as can resist fouling tendency of the membrane [8].

The pollutant can be removed from aqueous effluents using other techniques like adsorption, coagulation by chemical agents, ion exchange on synthetic adsorbent resins, etc. [9–11]. Nevertheless, these techniques can generate secondary pollutants which need further treatment and regeneration. Recently nanophotocatalysts are widely used to make composite membrane for removal of organic compounds from wastewater. Mainly, photocatalysts can finally mineralize the targeted contaminants to produce harmless, simple compounds [12–14]. Photocatalysis can be regarded as a sustainable alternative technology which can ensure the degradation of organic and inorganic pollutants from aqueous effluents [15–18]. Semiconductor metal/metal oxide can act as photocatalyst, and it is usually suspended as a powder in aqueous medium. For industrial-scale application, recovery of these catalysts is somewhat difficult at the end of the process. It is necessary to prevent their wash out and leaching in the reactor medium. The photocatalysis process can be combined with the membrane separation process to overcome these limitations. Thus, photocatalytic membrane reactors (PMRs) can be used which can ensure catalyst separation, and the membrane process does not require any additional additives [19–21]. Presence of photocatalyst with membrane can also resist fouling [22]. Photocatalytic membrane was fabricated using titanium dioxide (TiO_2) over the polymeric support of the membrane [23]. In the presence of UV or visible light, the catalyst becomes active and generates hydroxyl radicals [24]. The hydroxyl radicals can disintegrate the organic foulants into harmless products. Until recently, a lot of initiatives were undertaken to fabricate photocatalytic membranes having self-cleaning, hydrophilicity, and antibacterial properties [3, 25–28]. The positive and negative impact of different types of membrane with photocatalytic membrane is summarized in Fig. 17.1.

In case of PMRs, some pressure-driven membrane like nanofiltration (NF), ultrafiltration (UF), and microfiltration (MF) membranes can act as selective barrier for the pollutant as well as separator for the photocatalyst [5]. To fabricate polymeric membrane, mainly polyethersulfone (PES) [29], polyvinylidene fluoride (PVDF) [30], polyethylene (PE) [31], etc., are used as they can provide high mechanical strength and resistance toward the chemicals. These types of membranes can be damaged under photocatalytic condition as the polymer chain can initiate hydroxyl radicals. Although inorganic membranes are expensive than the polymeric one, they are more promising alternative for PMRs due to their outstanding chemical and thermal stability. Thus, mixed matrix membrane having solid zeolite or nanophotocatalyst embedded inside the organic polymeric matrix is best option to mitigate fouling [32–35]. The unique properties of nanoparticles, specially large surface-to-volume ratio along with strong degradation efficiency of the nanoparticles make them suitable to be combined with the polymeric matrix for environmental remediation and fouling mitigation. Incorporation of nanoparticles can significantly alter the thermal, mechanical, magnetic, hydrophilicity, and morphological properties of the membrane to ensure better permeability of the membrane [36]. This chapter overviews the importance of using nanophotocatalysts

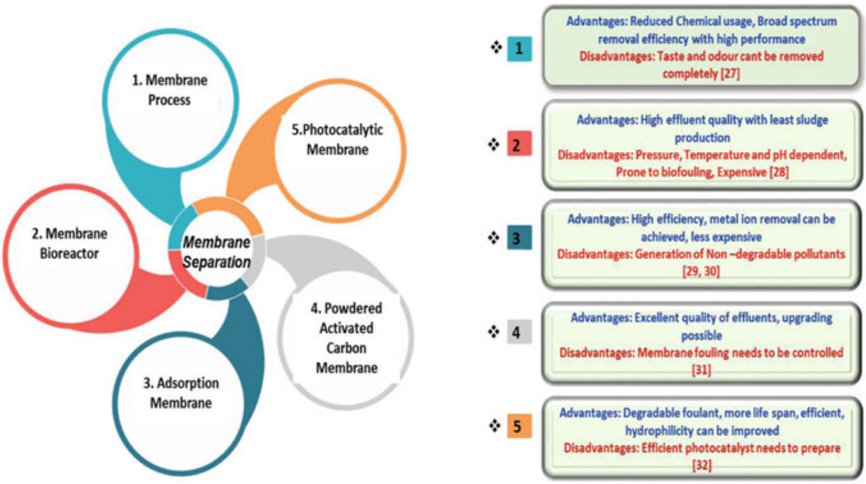

Fig. 17.1 **a** Photocatalytic separation layer over the non-photocatalytic support. **b** Non-photocatalytic separation layer over photoactive support

for water treatment. The fundamental of photocatalytic membrane, fabrication techniques, and types of photocatalytic membrane reactors (PMRs) are described in the subsequent section. The concluding part of the chapter explains about the foulant degradation mechanism of a hybrid membrane separation process.

17.2 Recent Roadmap for Photocatalytic Membrane Reactors (PMRs) in Water Treatment

17.2.1 PMRs with Photoactive Layer Over the Membrane Matrix

Photocatalytic membrane reactors (PMRs) are widely used for elimination of 4-nitrophenol [37], sodium dodecyl benzene sulfonate (SDBS) [38–41], phenols and chlorophenols [42, 43], organic dyes [44], herbicides [45], and several other chemicals from aqueous effluents. The set up and configuration of PMRs can be varied indifferent ways. The membrane can be decorated with a photoactive layer (Fig. 17.1a) which can act as a separation barrier in water treatment process. The second configuration contains no-photocatalytic layer deposited onto the porous surface of the membrane whereby the porous support act as active layer for separation (Fig. 17.1b). Based on membrane type, set up, configuration, and user requirement, the light source can be placed either on feed flow side or on the permeate side.

PMRs utilizing photocatalytic separation layer over the porous support layer of membrane are very popular in water treatment. The basic mechanism involves in this type of PMRs is illustrated by Fig. 17.2. The feed solution containing the organic pollutants is degraded in the presence of UV light where the light source is positioned on the feed side. The permeate contains purified water with non-degraded or some by-products after the photodegradation process. The final composition of the permeate, water quality depends on the physiochemical properties of the targeted pollutants and the efficiency of the applied photocatalytic layer placed over the membrane surface.

This type of PMRs configuration can provide purified water with increased permeate flux and the fouling can be restricted up to a certain level. In this process, humic and fulvic acids—which usually forms gel and cake over the surface of the membrane—are also decomposed [45]. The entrapment of TiO_2 nanoparticles inside the membrane matrix enhances hydrophilicity and reduces the fouling of the membrane [46].

During photocatalytic reactions in PMRs, all reactants along with aqueous effluents permeate through the pores of the photoactive layer where degradation of organic compounds is started initially. Presence of polymeric- or ceramic-based membrane support with photoactive layer ensures sufficient contact time to improve the reaction rate resulting higher water flux. The transportation of organic pollutants

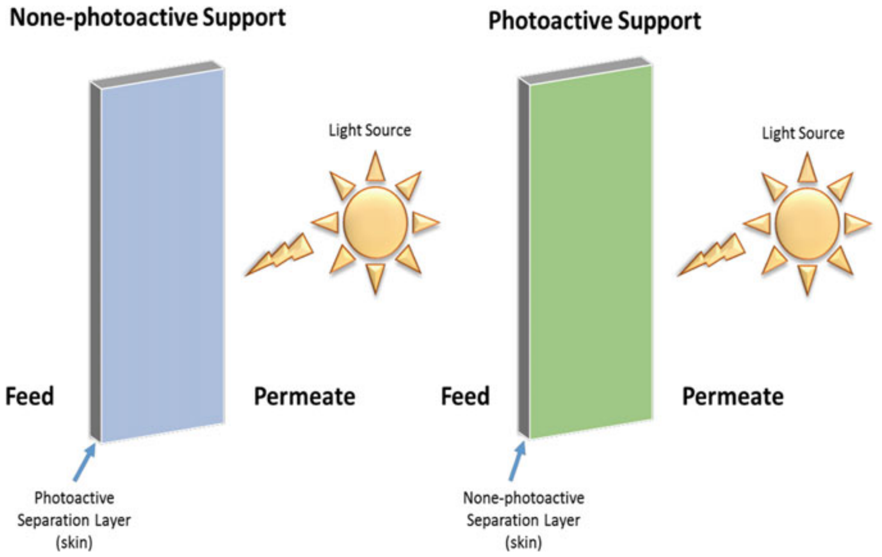

Fig. 17.2 Mechanism of photocatalytic membrane using photoactive separation layer for degradation of organic pollutants where pollutants are decomposed on the membrane surface and/or within its pores. The light source needs to be placed on feed side

through TiO_2 surface takes place by convection as well as diffusion process. Thus, larger area of the membrane along with photoactive layer will be favorable for the overall pollutant separation process.

The PMRs containing non-photoactive separation layer (Fig. 17.1b) is less widely used setup. Usually, in this type of configuration (Fig. 17.3), photocatalytic degradation process takes place on the permeate side. The pollutants along with aqueous solution are transported as permeate and the pollutants are degraded to form CO_2, water, and other degraded compounds based on the composition of the feed solution [47]. The main shortcoming of this process is the permeate composition where the membrane rejects the permeate along with the contaminants or its degraded products itself. Thus, the permeate is polluted in this setup (Fig. 17.2). The permeate is mineralized using the setup as illustrated by Fig. 17.3.

Gaseous phase oxidation of volatile organic compounds was earlier carried out using PMRs—the configuration of which is demonstrated by Fig. 17.4 [48]. The tubular photocatalytic membrane reactors were fabricated using a coating of TiO_2 layer over the alumina-based microfiltration (MF) membrane. Over the membrane cell, 4 or 8 UV light sources (4 W, λ max and 350 nm) were placed. The rate of air flow was kept at 50–500 cm^3/min, and it was fed inside the PMRs cell. The air was bubbled inside the methanol or ethanol solutions prior to diffusion inside the PMRs cell. The temperature of the volatile organic compounds (methanol or ethanol) was controlled, and the surface temperature of the TiO_2 membrane was around 100–120 °C. Rather than photocatalysis, faster decomposing of methanol was

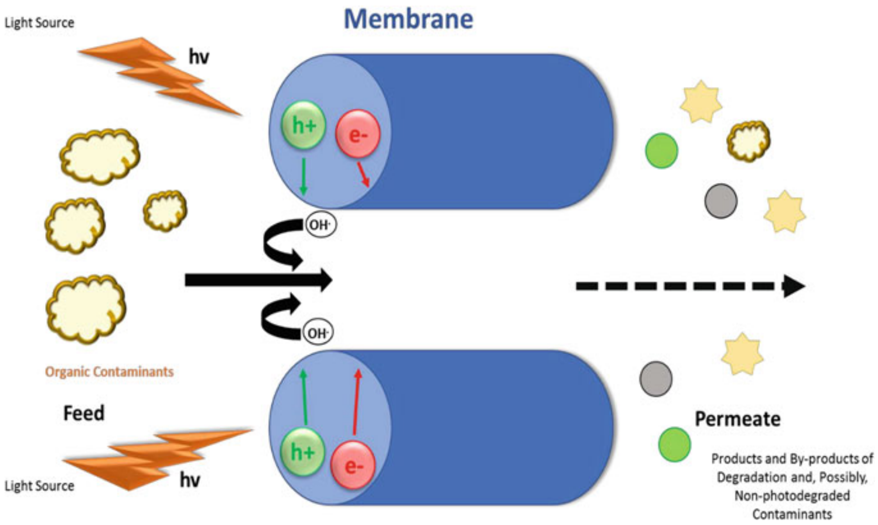

Fig. 17.3 Mechanism of photocatalytic membrane using non-photoactive separation layer for degradation of organic pollutants where pollutants are decomposed on the membrane surface and/or within its pores. The light source needs to be placed on permeate side

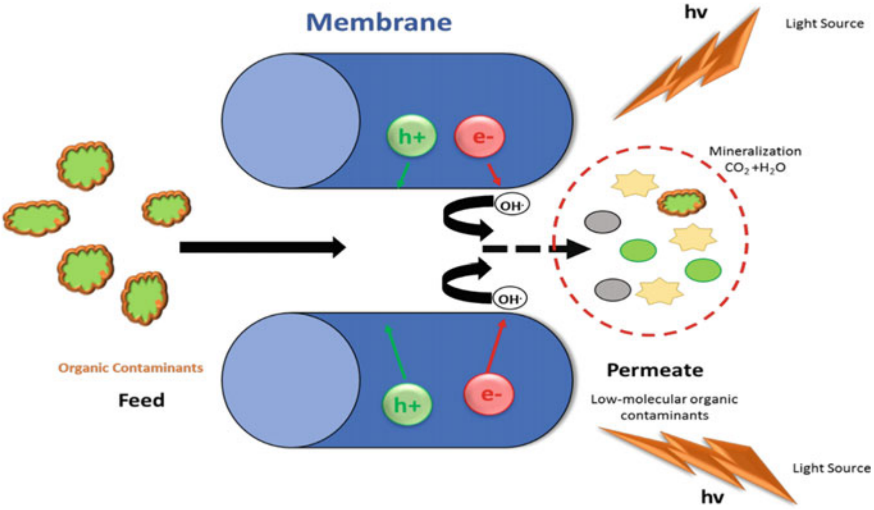

Fig. 17.4 Schematic representation of PMRs using $TiO_2/\alpha\text{-}Al_2O_3$ photocatalytic membrane for photocatalytic oxidation of methanol and ethanol in gaseous phase. *MFM* mass flow meter; *T* thermocouple; *GC* gas chromatograph; *BL* black light (modified and redrawn from Ref. [48])

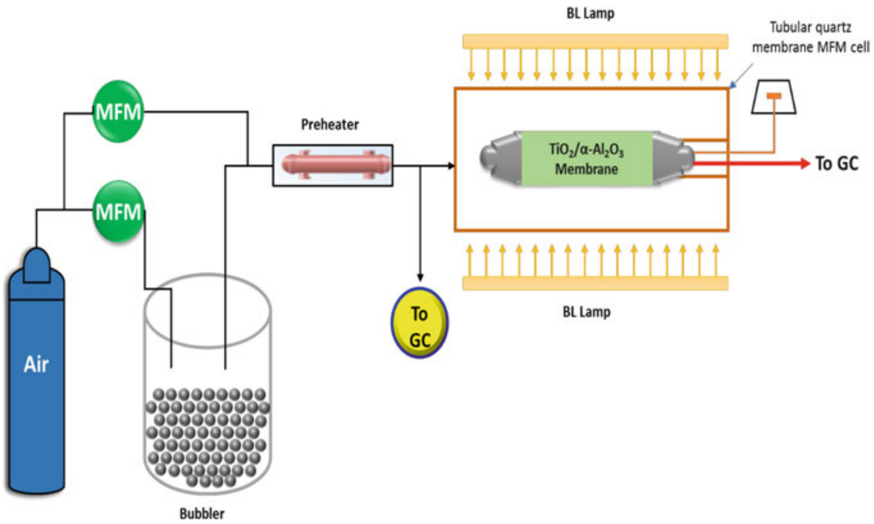

Fig. 17.5 Schematic representation of a PMRs using photocatalytic membrane for liquid phase process where *VP* vacuum pump; *Rp1* and *Rp2* permeate reservoirs (modified and redrawn from [38–40])

observed. Furthermore, the decomposition rate was dependent on the residence time of the volatile compounds inside the reactor chamber.

Photocatalytic decomposition of sodium dodecylbenzene sulfonate (SDBS) was carried out using silica/titania nanorods/nanotubes-based composite membranes (Fig. 17.5) [38–40].

The pollutant solution was placed inside the feed tank, and it was pumped inside the membrane cell using peristaltic pump (PP1). Recycling of permeate and feed solution was carried out. The UV light source contained a 300 W mercury lamp (λ max = 365 nm) which was equipped with cooling system. The lamp was mounted over the membrane cell. Air was bubbled inside the solution to initiate the decomposing of the organic compound studied here. Within 100 min, 89% of the targeted contaminants were degraded. Membrane fouling was reduced resulting higher water flux [38–40]. The pros and cons of using photocatalytic membrane reactors (PMRs) with photoactive layer are presented by Table 17.1.

17.2.2 PMRs with Suspended Photocatalyst Using Pressure-Driven Membranes

PMRs containing pressure-driven membrane can be used together with suspended photocatalyst in the medium. Suspended photocatalyst with microfiltration (MF) or ultrafiltration (UF) membranes is commonly used for degradation of organic contaminants like pharmaceuticals, humic and fulvic acids, trichloroethylene, bisphenol

Table 17.1 Advantages and drawbacks of PMRs using photocatalytic membranes

PMRs system	Membrane system	Advantages	Drawbacks
PMRs system using photocatalytic membrane	Pressure-driven/ depressurized membrane	1. Photocatalyst need not to be separated, the membrane can be used as long the photocatalysts have the activity	1. Degradation rate is slower
		2. No membrane fouling	2. Adjustment of photocatalyst loading is difficult
		3. Can exhibit enhanced hydrophilicity due to the presence of photocatalysts	3. Risk of damaging polymeric membrane due to UV lamp
		4. Contaminants can degrade both in feed or permeate section	4. Membrane replacement required frequently
		5. Degraded compounds form gel or cake layer over the membrane surface which can prevent microbial fouling	

A, chlorophenol, 4-nitrophenol, dyes, etc. It is used for treating the real wastewater generated from dye industry, gray water and surface aqueous stream, and synthetic waste effluents. Earlier, nanofiltration (NF) coupled with photocatalytic membrane was used for separation of dyes, 4-nitrophenol, and pharmaceuticals from wastewater [49]. Previous researchers suggested the use of photocatalytic membranes with reverse osmosis (RO) process for drinking water purification for fouling prevention [50, 51].

PMRs coupled with suspended photocatalyst can be classified into three major groups. In this regard, position of light source is a crucial factor. Thus, the light source can be placed [51]:

(a) Over/inside the feed tank,
(b) Over the membrane module,
(c) Over/inside a supplementary reservoir known as photoreactor positioned between the membrane module and the feed tank.

PMRs construction and design depends on the process type, mainly classified as dead end or cross-flow, batch or continuous flow process. The membrane type (MF, UF, NF) along with module of the membrane (flat sheet, hollow fiber, submerged, etc.), type, and position of the light source also influences the overall performance. The membrane module needs to design carefully so that the irradiation should strike the membrane surface to initiate the degradation. In case of PMRs with suspended photocatalyst, a photoreactive cell is equipped with the pressure-driven membrane unit. The pressurized membranes are submerged inside the photocatalytic slurry, and unit is efficient enough to operate under continuous and batch mode concurrently. Figures 17.6, 17.7, 17.8, 17.9, and 17.10 demonstrated various types of setup for PMRs using suspended photocatalyst and membranes.

Figure 17.6 illustrates the schematic setup for PMRs coupled with photocatalyst and NF membrane. This setup was used to remove dyes and 4-nitrophenol from water [50, 51]. NF membrane was placed inside the stainless steel cylindrical reactor, and the feed was pumped inside. Pressure regulating valve was used to monitor the pressure in feed inlet and retentate pipe lines. The photoreactor was set up in a annular way and a 125 W Hg lamp equipped axially inside the reactor with a jacket cooler over it. PMRs was working in batch or continuous mode where oxygen gas was bubbled through the reactor. In batch process, permeate was recycled several times and in continuous process, feed was pumped in continuously. The permeate in continuous process was removed repeatedly. In batch process, the concentration of pollutant decreased more quickly than the continuous process but the amount of retentate with time is more in continuous process.

Following design considerations should be carefully monitored for PMRs using NF technique [51]:

(a) Membrane Selection: The membrane should have desirable porosities to retain the catalyst and reject the pollutants under consideration. Process variables like pH, molecular weight and size of the pollutant, degradation by-products, pressure, etc., should be considered. If the NF membrane is selected carefully, then permeate quality can be improved due to Donnan exclusion theory [52].

(b) Light Source Type and Position: Light source immersed inside the reactors exhibited better performance than the light positioned externally.

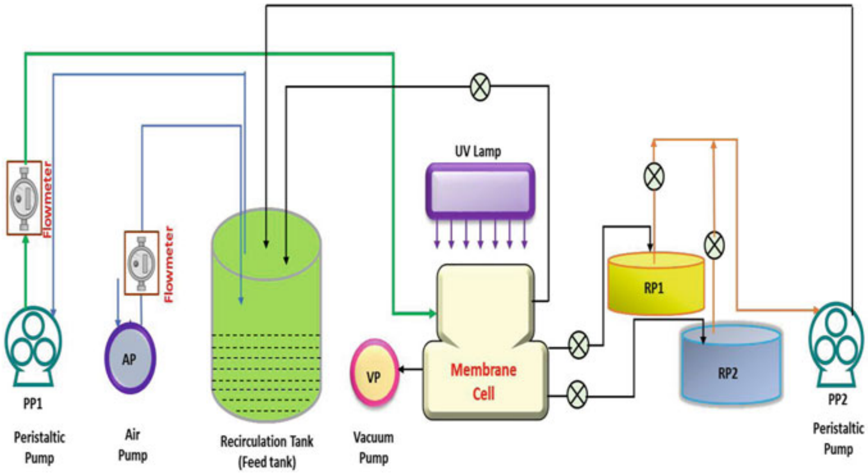

Fig. 17.6 Schematic representation of a PMRs setup using suspended photocatalyst and immersed UV light for liquid phase operation in batch or continuous process (modified and redrawn from Ref. [50])

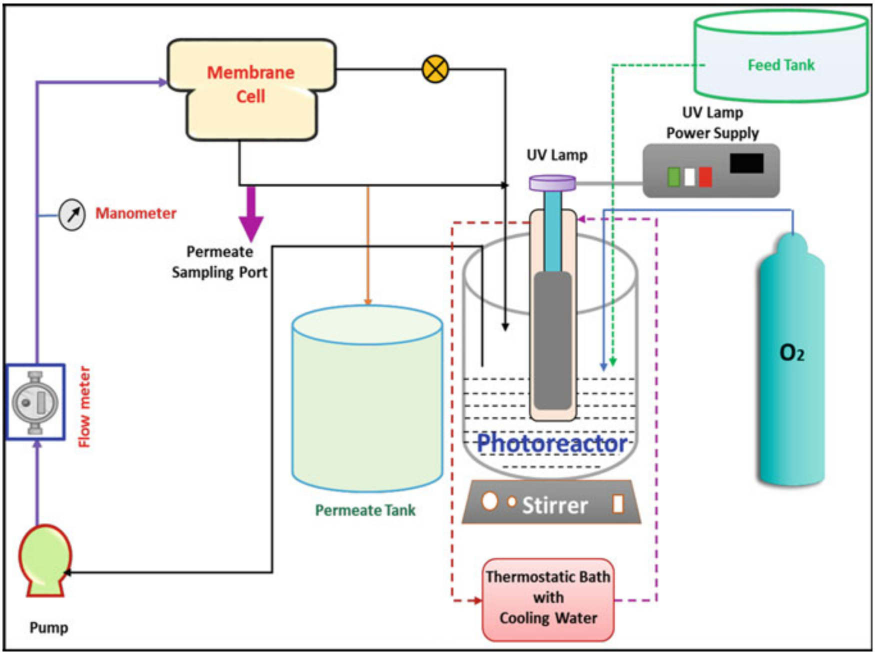

Fig. 17.7 Simplified layout of PMRs using suspended photocatalyst (modified and redrawn from Ref. [52])

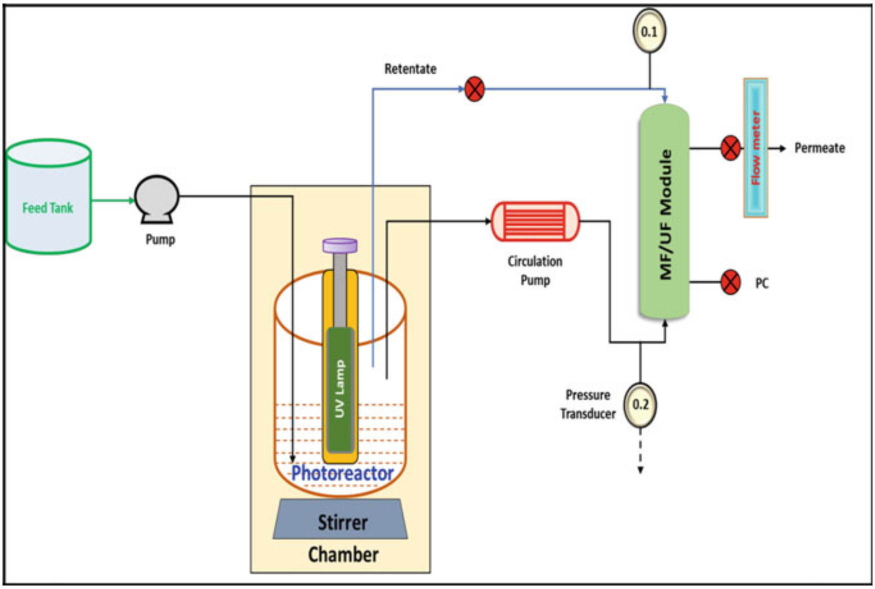

Fig. 17.8 Simplified process layout for pilot scale PMRs (modified and redrawn from Ref. [52])

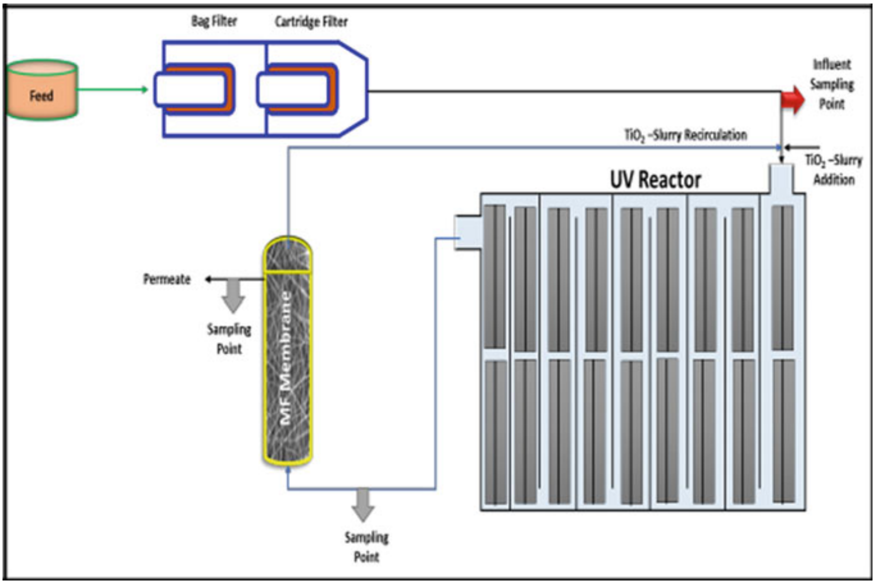

Fig. 17.9 Simple process layout of PMRs using submerged membrane with internal UV lamp (modified and redrawn from Ref. [53])

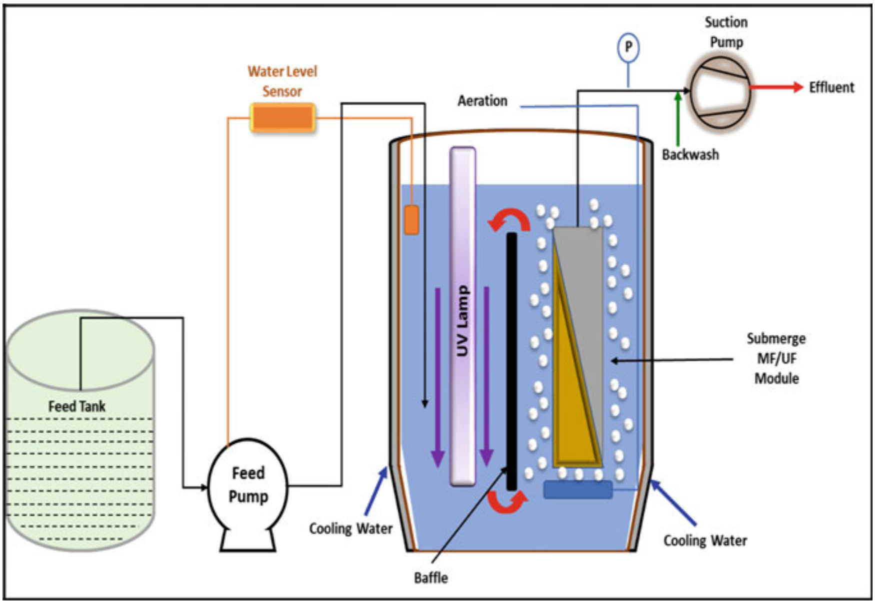

Fig. 17.10 Simple process layout of PMRs using submerged membrane with external UV lamp (modified and redrawn from Ref. [54])

(c) Concentration of Pollutant and Contact Time: The feed with pollutant can be diluted to get more photodegradation efficiencies. The residence time should be carefully observed.

PMRs were coupled with MF membrane to separate trichloroethylene (TCE) from aqueous solution (Fig. 17.7) [52]. A hollow fiber MF membrane was placed inside the photocatalytic reactor. The inner chamber of the reactor contained the UV light source. In the outer chamber, photocatalytic degradation was taking place. Both permeate and retentate were recycled inside the reactor after definite interval of time. The process was very efficient to remove TCE from water with 60% degradation rate in 2 h. Ceramic membrane-based MF unit was coupled with photocatalyst earlier for the elimination of endocrine disrupting compounds, pharmaceuticals, and estrogens from river water [52].

Turbulent flow conditions were maintained inside the reactor for homogeneous mixing. After leaving the UV reactor unit, the solution was passed to the membrane unit where TiO_2 was separated from the stream. The rejected nanoparticles of TiO_2 were passed again with the influent solution. Fouling was prevented by back-pulsed flow of air after every 1 min. 70% of the 29 targeted pollutants were removed. However, the process parameters of this system needed to be optimized to ensure less energy consumption [52].

Submerged membrane can be used with PMRs for better efficiency of the process and is illustrated by Fig. 17.8 [52, 53]. This system was used to separate fulvic acids from aqueous solution [53]. The reactor had two separate zones: one containing UV lamp which was regarded as oxidation zone and the other was considered as membrane separation zone. Both zones were interconnected to prevent membrane damages by UV light [53].

Bisophenol was also separated using submerged photocatalytic membrane as demonstrated by Figs. 17.9 and 17.10 [54, 55]. Inside the borosilicate glass reactor, the hollow fiber membrane was placed. The UV lamps were located outside of the reactor. Here, the membrane zone was not separated from the light source.

The advantages of depressurized system compared to pressurized PMRs are summarized below [53–55]:

(a) Flow of oxygen improved the mass transfer rate to enhance the photodegradation rate in this type of system.
(b) The intermittent permeation recovery can ensure high water flux and fouling resistance.

A solar photoreactor was earlier coupled with PMRs having suspended catalyst to degrade lincomycin from aqueous effluents in batch and continuous process (Fig. 17.11) [56]. The rejection rate for smaller molecular weight compounds in this process is relatively low—which is the major limitations of this process.

Above section provided a brief overview for PMRs working under different types of membrane system with some typical designs of the reactors. The summary of the advantages and disadvantages of PMRs using photocatalyst suspension is provided in Table 17.2.

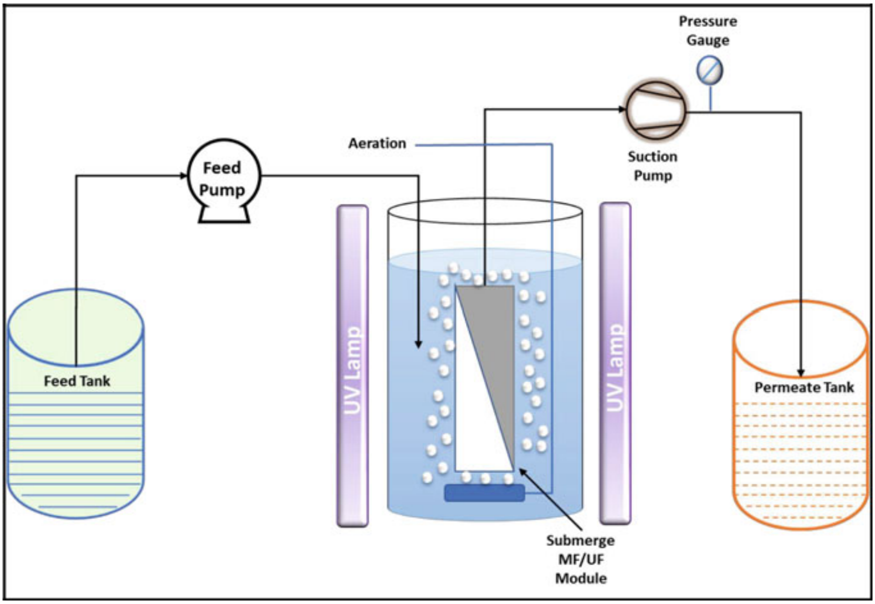

Fig. 17.11 **a** Batch system of PMRs, **b** continuous system of PMRs (A) switch valve; (B) thermocouple; (C) non-reacting tank; (D) pump; (E) regulation valve; (F) manometer; (G) membrane vessel; (H) line under pressure; (I) rotameter; (J) feed tank. *PFP* plug flow photoreactor (modified and redrawn from Ref. [56])

17.3 Fundamental of Photocatalytic Membrane Fabrication

The selected photocatalyst based on user requirement is introduced inside the polymeric or ceramic membrane to fabricate photocatalytic membrane. Figure 17.12 illustrates the basic layout of a photocatalytic membrane [57]. Over the porous membrane, a layer of photocatalyst can evidently show photocatalytic activity under visible light or UV irradiation [58]. Presence of Photocatalysts will initiate hydroxyl radicals formation which in turn will act as a strong oxidant and reluctant. This will lead degradation of pollutants into smaller and least toxic inorganic species without producing secondary pollutants [59]. Visible light, UV light, thermal treatment, and ultrasound-assisted treatment can generate reactive radicals. Immobilization of photocatalyst over the membrane enables it to act as a separation barrier within reaction products and aqueous effluents [60]. Thus, coupling of photocatalyst with the membrane can decrease the membrane fouling [61].

Photocatalysts can be immobilized over the membrane surface to form composite membrane for better performance, the summary of which is tabulated in Table 17.3.

Table 17.2 Major advantages and drawbacks of PMRs using suspended photocatalyst

PMRs system	Membrane system	Advantages	Drawbacks
PMRs system using suspended photocatalytic slurry	Pressure-driven/ depressurized membrane	1. Photocatalyst can be separated effectively	1. In pressurized system of using MF and UF, membrane fouling rate can be enhanced
		2. Without membrane replacement, the exhausted catalyst can be exchanged	2. Presence of by-products might degrade the quality of the permeate depending on the composition of the feed solution
		3. Adjustment of catalyst loading is easier	
		4. High degradation rate	
		5. Enhanced permeate flux due to application of submerged depressurized system	
		6. The light source can be positioned carefully to prevent polymeric membrane damage by free radicals and UV irradiation process	

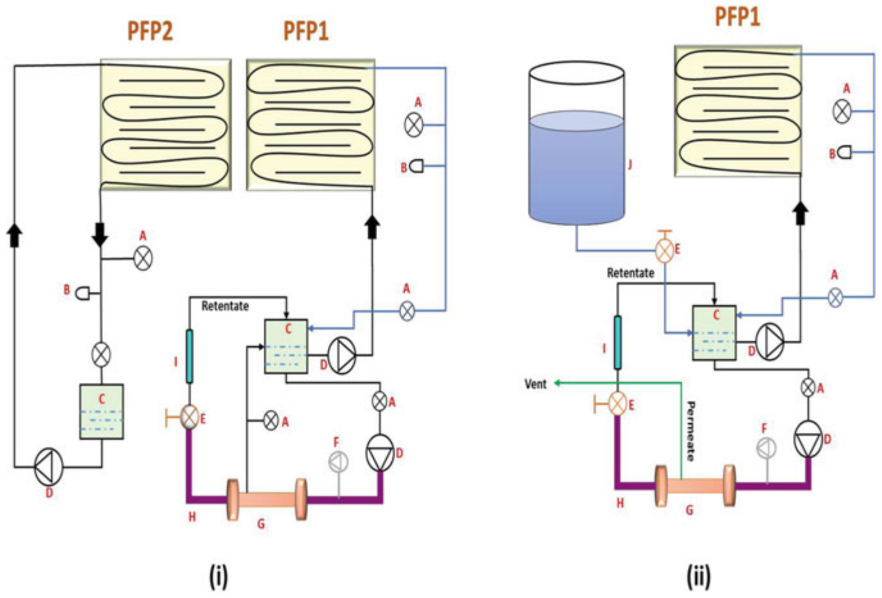

Fig. 17.12 Basic layout of photocatalytic membrane

Table 17.3 Photocatalytic composite membrane and its performance

Nanophotocatalyst and their composites	Types of membrane	Process variables	Research findings	References
TiO_2 nanoparticles doped with 1% graphitic carbon nitride having mesoporous structure (C_3N_4/TiO_2)	Ultrafiltration membrane (UF) made of polysulfone (PSF)	Pollutants: sulfamethoxazole (SMX) Source of light: UV Intensity of light: 300 W Wavelength: 270 nm	69% of pollutant degradation took place after 30 h under UV irradiation Hydrophilic membrane with lower contact angle of 58.1°	[62]
TiO_2 loaded over molecular imprinted polymer (MIP) (2 wt%)	Ultrafiltration membrane (UF) made of polysulfone (PSF)	Pollutants: methylene blue (MB) and methyl orange (MO) Source of light: UV Intensity of light: 10 W \Wavelength: <390 nm	In absence of UV, methylene blue (MB) percentage removal: 82.99 ± 8.61% Methyl orange (MO) percentage removal: 28.40 ± 2.91% In presence of UV – MB percentage removal: 96.90 ± 3.76% – MO percentage removal: 34.18 ± 7.45%	[63]
Crystals of zinc oxide (ZnO)	Polypropylene (PP) UF containing polymer-based membrane	Pollutants: methylene blue (MB) and humic acid pH: 3 and 6 (neutral) Source of light: UV for humic acid and white light for MB Intensity of light: – Wavelength: white light is 663 nm and UV is 254 nm	pH 3 The rate of MB degradation is 0.0214/min; Humic acid concentration lowered more than 50% pH 6 The rate of MB degradation is 0.0143/min; Humic acid concentration lowered less than 50%	[64]

(continued)

Table 17.3 (continued)

Nanophotocatalyst and their composites	Types of membrane	Process variables	Research findings	References
2% nanocrystals of AgNCs doped over the surface of polymeric graphitic carbon nitride (g-C_3N_4)	Nafion membrane	Pollutants: Rodamine B Source of light: visible light Intensity of light: 500 W Wavelength: $\geq$420 nm	AgNCs/g-C_3N_4/Nafion hybrid membrane demonstrated higher degradation percentages than g-C3N4 and g-C_3N_4/Nafion membrane The membrane was durable and was stable after recycling	[65]
Nitrogen-doped TiO_2 nanoparticles	Microfiltration (MF) ceramic-based Al_2O_3 membrane	Pollutants: antiepileptic drug, carbamazepine (CBZ) Source of light: UV light and visible light Intensity of light: 300 W Wavelength: 320–400 nm for UV light and 400–700 nm for visible light	Nitrogen doping over TiO_2/Al_2O_3 exhibited better photocatalytic activity than TiO_2/Al_2O_3 under both UV and visible light irradiation Increase in temperature increases degradation of CBZ while it was decreased with increased dissolved oxygen (DO) concentration	[66]

17.3.1 Photocatalytic Membrane Fabrication Techniques

Photocatalytic membrane can be classified based on constituent material of the membrane. Mainly it can be two types: inorganic membrane and hybrid organic/inorganic membrane [58]. The matrix of inorganic membrane can be ceramic, carbon, metal oxide, etc. The hybrid membrane contains polymers like polysulfone (PSF), polyethersulfone (PES), and polycarbonate with some inorganic materials incorporated with it.

Photocatalytic membrane can be synthesized using liquid phase deposition (LPD) method, sol–gel method, anodization, and concurrent application of electrospinning and electrospraying (SEE) technique. The low temperature deposition process (LPD) involves hydrolysis process followed by deposition of metal-fluoro complex directly over the surface without any thermal treatment [67]. The solution of 0.1 M ammonium hexafluorotitanate ($(NH_4)_2TiF_6$) and 0.3 M boric acid (H_3BO_3) was made using deionized water at temperature of 50 °C [68]. Oxygen plasma was used to heat silicon wafer. The heated wafer was immersed inside the solution at 50 °C. After certain time TiO_2 forms a layer over the Si support to yield Si/TiO_2 membrane. Titanium tetrafluoride (TiF_4) was mixed with ammonia and the mixture was hydrolyzed to produce thin film. It was grafted over Al_2O_3. Thus, photocatalytic Al_2O_3/TiO_2-based membrane was produced [69]. LPD method can generate membrane having high surface area, better selectivity as well as variable composition of the developed film.

There are two phases in sol–gel method—solution preparation and gelation of the synthesized solution. The colloidal suspension is known as solution and when the particles are interconnected after aging, then it is called gelation [70]. The process is inexpensive, chemically homogeneous and usually low calcination temperature is needed to produce the films [71]. Hydrolysis of TiO_2 was carried out to form sol, and later on, it was coated onto the porous support using dip-coating. At the end of the process, it was calcined to form anatase TiO_2 membrane [71].

Co-precipitation sol–gel method was used to produce TiO_2/Al_2O_3 composite [72]. The mixture was heated at 80–85 °C and nitric acid was refluxed with it to stabilize the mixture after certain time. To bind TiO_2 with Al_2O_3 matrix, a mixture of hydroxypropyl cellulose (HPC) and polyvinyl alcohol (PVC) was added with the above solution. Thus, the Al_2O_3 support was dip-coated by above mixture to produce photocatalytic membrane.

In the anodizing process, metal oxide base part ‘aluminum (Al), titanium (Ti), and zinc (Zn)’ which needs to be coated act as anode in the electrolytic cell. The photocatalytic reduction of CO_2 was improved using cadmium sulfide (CdS) photocatalyst over the surface of porous alumina (PAA) which was acting as anode inside the cell [73]. At first, the PAA surface was pretreated where annealing was carried out for 3 h at 400 °C under nitrogen atmosphere. Then, sulfuric acid (H_2SO_4) and phosphoric acid (H_3PO_4) acids were used for electropolishing. First step of anodizing was carried out followed by chemical etching process to take out the oxide layer. Second time anodizing was carried out and PAA membrane was produced. PAA membrane was sonicated to remove air bubbles. Then, cadmium nitrate ($CdNO_3$) solution was adsorbed over the surface of the PAA membrane. Sodium sulfide (Na_2S) was added to ensure precipitation of CdS particles inside the pores of the membrane.

Electrohydrodynamic atomization method involves electrospinning and electrospraying process concurrently. Solution of Nylon-6 was electrospinned and sprayed to form nanofibers [74] under electric field. Electrospinning involves evaporation of the polymer solution at preliminary stage. At secondary stage, solidification of polymer droplets takes place to yield nanofiber under electric field. The dispersed liquid can form charged particles during electrospraying process [75]. TiO_2 nanoparticles can be doped inside the electrospun nanofiber-based non-woven mesh to form three layers membrane [76]. Electrospun nylon-6 nanofibers were used to develop the base layer. The middle layer was fabricated by synchronized electrospinning and electrospraying process (SEE) both for doping anatase phase TiO_2 inside the Nylon-6 nanofiber matrix. The top layer of the membrane was also prepared by nylon-6 nanofiber. The layered structure of the membrane containing photocatalyst provides additional strength and unique physiochemical characteristics (Table 17.4).

Recently, photocatalytic membrane was fabricated by using a coating of rare-earth oxide-cerium (IV) oxide (CeO_2) over the stainless steel mesh having pore diameter around ~50 µm.

Table 17.4 Photocatalytic membrane fabrication methods, constituent photocatalyst, and their composites with performance analysis

References	Constituent photocatalytic nanomaterials and their composites	Fabrication technique	Pore diameter	Performance analysis
[72]	TiO_2 doped onto alumina (Al_2O_3) support	Sol–gel	1–3 µm	95% degradation of malachite green dye under UV light within 3 h
[68]	TiO_2 supported onto nickel	Anodizing	1 µm	After 6 h of nucleation by TiO_2, hardness and Young's modulus increased, showed better antibacterial activity
[73]	CdS-coated PAA	LPD	45–55 µm	Photocatalytic degradation of CO_2 to methanol
[76]	Nylon 6 nanofiber containing entrapped TiO_2 particles	Electrospinning and electrospraying	0.3–10 µm	Photocatalytic oxidation of 98% methylene blue dye within 2 h

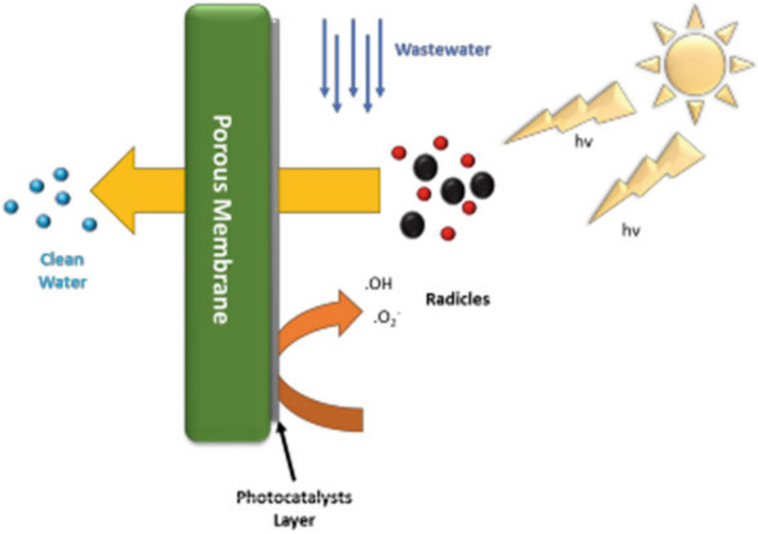

Fig. 17.13 Photocatalytic membrane fabrication using CeO_2 nanoparticles (modified and redrawn from Ref. [77])

At first, CeO_2 nanoparticles were dispersed in tetrahydrofuran and sonicated. Then it was sprayed (Fig. 17.13). The membrane was annealed for 4 h at 200 °C. CeO_2 nanoparticles having diameter of 50 nm were deposited over the membrane and the membrane exhibited significant photocatalytic as well as oily emulsion separation efficiency. As fabricated membrane showed both super-hydrophobic and super-lyophilic characteristics and could separate 99% oils from water, methylene blue dye was photocatalytically degraded using the membrane that was efficient enough to degrade 99.96% of the dye solution [77].

17.4 Functionalized Photocatalytic Composite Membrane and Its Modification Strategies

17.4.1 Photocatalyst/Polymer Membranes

Polymeric membranes [polyethylene terephthalate (PET), polysulfone (PSf), polyamide, polyvinylidene fluoride (PVDF), polyethersulfone (PES), polyvinylidene fluoride (PVDF), sulfonated polyethersulfone (SPES), polyethylene terephthalate (PET), polyurethane (PU), polyester, polyacrylonitrile (PAN), and polytetrafluoroethylene (PTFE)] were successfully incorporated with different types of catalyst to produce photocatalytic composite membranes for water treatment [78, 79]. The photocatalytic nanoparticles can be doped over the surface of the

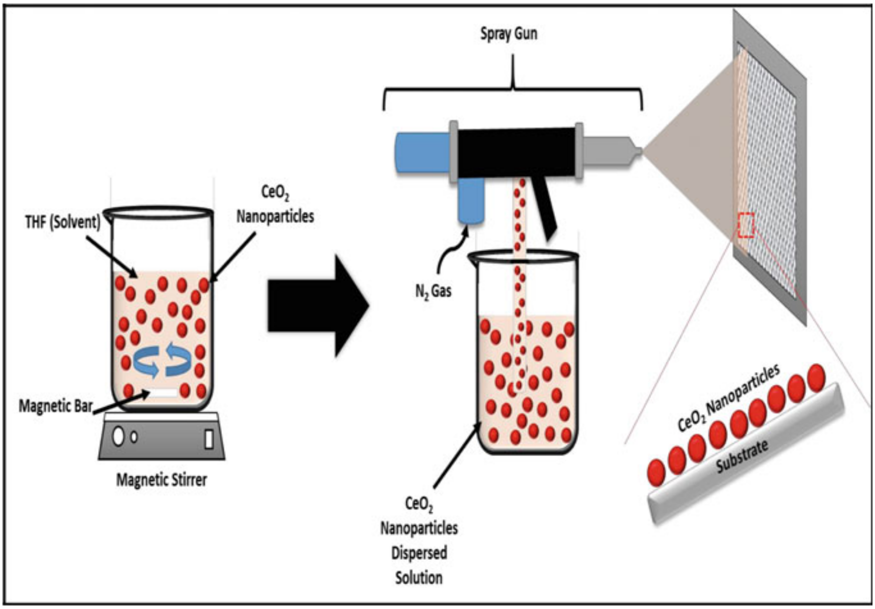

Fig. 17.14 Different types of photocatalytic membrane fabrication techniques

membrane or can be mixed with the polymeric solution before casting the membrane. The fabrication techniques used for photocatalytic membrane are shown in Fig. 17.14.

17.4.1.1 Surface Functionalized Photocatalytic Membrane

Dip-Coating by Photocatalyst

Surface-located TiO_2-based polymeric membranes can be fabricated by dip-coating or self-assembly [80], chemical grafting over the surface of the membrane, photoinduced polymerization [81] and ultrafiltration for deposition of a TiO_2 layer physically over the polymeric matrix [82]. The sol–gel process was used to produce TiO_2 slurry where polymeric membrane was dipped. Thus, TiO_2 nanoparticles were attached to the membrane surface by hydrogen bonding and complexation reactions with carbonyl or sulfone functional groups present on the membrane. The interaction between nanoparticles and –COOH functional groups also took place [83]. As fabricated membrane demonstrated photocatalytic as well as antimicrobial tendencies and was used to prevent biofouling of the membrane [83]. Earlier reverse osmosis (RO) membranes were coated using titanium dioxide (TiO_2) nanoparticles. The TFC polyamide membrane with TiO_2 nanoparticles showed its photocatalytic competence for the destruction of *Escherichia coli* (*E. coli*)—a bacterium cell in presence of UV light [84]. Commercially available polyethersulfone microfiltration (MF) membranes were coated with TiO_2-synthesized by sol–gel method [85] where TiO_2 anchored with the membrane surface by bonding with the sulfonic acid ($SO3^- H^+$) groups of the membrane surfaces during sulfonation. As fabricated membranes were used in membrane bioreactor (MBR) to observe its antifouling properties [85], membrane fouling was significantly reduced due to presence of photocatalysts. The phenomenon can be further attributed due to the hydrophilicity of the membranes [85]. The major limitations of this process are the leaching of nanoparticles with time which can cause ecotoxicological hazards for living organisms.

Photoinduced Polymerization and Chemical Grafting

In this process, the photocatalyst will be immobilized onto the surface of membrane surface in the presence of photoinitiator. Earlier amino propyl tri-ethoxy silane (APTES) was used as initiator to functionalize TiO_2 particles in the presence PES polymeric solution before casting to membrane. It was precipitated to form hollow fiber membranes having enhanced porosity, glass transition temperature, stiffness and hydrophilicity. The water flux and antifouling property also improved than the undoped sample. The composite photocatalytic membrane had less tensile strength and elongation at break [86].

TiO_2 was added to a suitable acrylic acid monomer was mixed with TiO_2 nanoparticles and sonicated for 20 min to ensure homogeneous dispersion. As a cross-linker ethylene glycol in the presence of photoinitiator-potassium-per-sulfate (1 wt%) was added with the above suspension. The PVDF membrane was dipped inside the above solution for 2 min and the mixture was placed over the glass plate. Finally, the membrane was irradiated using UV light for 15 min. TiO_2 nanoparticles were covalently attached with the membrane surface resulting enhanced antifouling properties. In the presence of hydrophilic functional groups, the membrane along with TiO_2 nanoparticles decreased the hydrophobic sorption between the whey protein and the surface of the photocatalytic membrane [87].

Physical Process

In this technique, the photocatalyst will be deposited onto the surface of the membrane physically. The slurry of photocatalyst will be filtered through pressure-driven membrane for physical attachment of photocatalyst with the membrane surface. The filtration time and pressure will be optimized to control the thickness of photocatalyst layer onto the surface of the membrane [88]. A dead-end filtration apparatus was used to modify cellulose acetate membrane by TiO_2 nanohorns physically [82], as fabricated photocatalytic membrane had porous, hierarchical texture, which increased the water flux and mitigate the fouling of the membrane [82].

17.4.1.2 Photocatalyst-Entrapped Polymeric Membranes

Phase Inversion

Phase inversion membrane can have different morphological structure, like flat sheets or hollow fibrous forms which is ideal for using under optimum hydrodynamic conditions (Fig. 17.15). It is most commonly used popular method.

Where nanoparticles can successfully be entrapped inside the membrane matrix. In this technique, the photocatalyst is mixed with the polymer solution homogeneously. After casting, the membrane is placed inside the coagulation bath for gelation [89], as fabricated TiO_2-based composite membrane exhibited enhanced permeability, porosity, wettability, and antifouling properties. However, photocatalytic membranes based on PES and PSF contain sulfone groups which under UV radiation deteriorates. PTFE and PVDF membranes are least affected by UV radiation [90]. Due to embedding the nanoparticles in membrane matrix by this method, the available surface area for water transportation is reduced, which is the major limitations of this process.

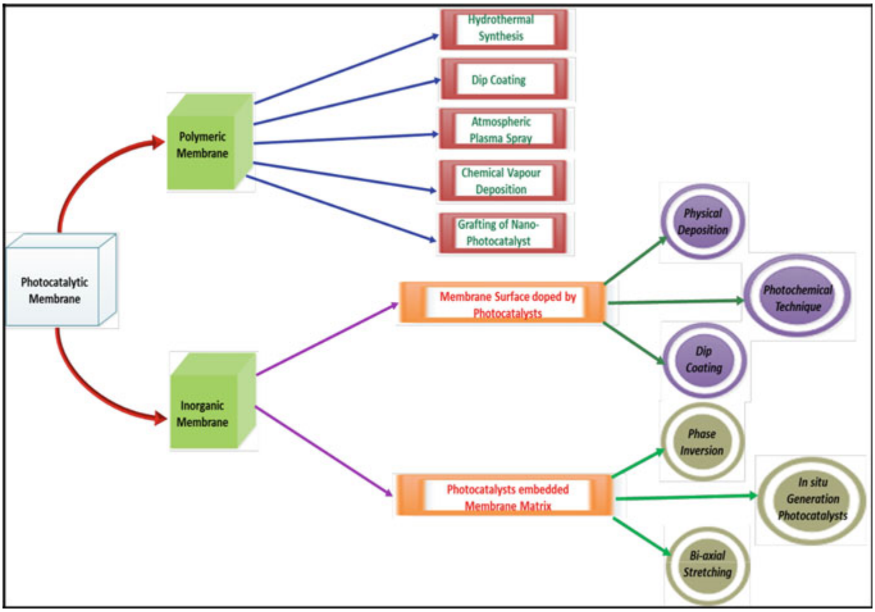

Fig. 17.15 Membrane fabrication using phase inversion technique (modified and redrawn from Ref. [89])

Stretching in Biaxial Condition

The physical method of biaxial stretching involves stretching membranes to modify their pore diameter. The process will permanently and significantly deform the porous texture but will improve overall performance of the membrane [91]. Earlier research used biaxial stretching of polytetrafluoroethylene (PTFE) membrane containing 2 wt% of anatase TiO_2 [92]. The photocatalysts were homogeneously distributed inside the membrane matrix resulting degradation of organic pollutants in ultra-pure water [93].

Application of In Situ Synthesized Photocatalysts

Application of in situ synthesized photocatalysts for membrane fabrication is comparatively modern, innovative approach. In this process, compatibility, loading of nanomaterial, water flux as well as selectivity can be optimized [93]. Earlier sulfonated poly(ether ether ketone) (SPEEK) nanocomposite membrane was fabricated using in situ mixed sol–gel process. In this method, titanium butoxide/2,4-pentanedione was mixed with DMAc and was added with the polymeric membrane solution. The solvents were evaporated at 120 °C. As synthesized membrane demonstrated better flexibility with transparent appearance, it also exhibited improved mechanical and thermal characteristics with better hydrolytic stability [94]. In situ polymerization of titanium isopropoxide was carried out using polyvinyl acetate (PVAc). PVAc was cross-linked with titanium alkoxide due to transesterification reaction. The strong chemical interaction prevents phase separation and was inhibited due to strong chemical bonding which in turn improves the dispersion of TiO_2 nanoparticles inside PVAc matrix. Presence of unreacted isopropyl groups and less crystalline TiO_2 particles inside the membrane matrix is the major limitations of this process [95].

17.4.2 Photocatalyst/Ceramic Membranes

Ceramic-based composite membranes are presently getting substantial importance due to their unique characteristics like—high thermal and mechanical stability, high water flux, higher life cycle, and greater resistance toward the corrosive chemicals. Based on the diameter of the pores, it can be classified as reverse osmosis (RO), ultrafiltration (UF), microfiltration (MF), gas separation (GS), pervaporation (PV), and ceramic membrane reactors (CMR). Ceramic membranes usually consist of different types of metal oxides or their composites including ZrO_2, TiO_2, SiO_2, and Al_2O_3 [96]. Ceramic membranes are fabricated using dip-coating method. A suitable photocatalyst or their composites is deposited over the surface of the ceramic layer (SiO_2, Al_2O_3, ZrO_2, $Al_2O_3/SiO_2/ZrO_2$, SiN/SiC, Al_2O_3/SiC).

Earlier TiO_2 photocatalyst was synthesized using hydrothermal process, dried and calcined at higher temperature before coating the ceramic membrane [96]. TiO_2 nanotubes were grafted inside the channels of the Al_2O_3-based ceramic membranes [97]. Photocatalyst/ceramic membranes were also fabricated using chemical vapor deposition (CVD) and atmospheric plasma spraying (APS) methods [98, 99].

17.4.3 Performance Evaluation: Photocatalytic, Organic-Polymeric Membrane, and Inorganic Photocatalytic Ceramic Membranes

Ceramic membranes are more thermally stable. It is more resistant toward the harsh chemicals compared to polymeric membrane. Due to extreme chemical condition, UV light, and temperature, polymeric membrane might have degradation. Membrane fouling is more pronounced in polymeric membrane. The surface of ceramic membranes is hydrophilic; thus, it is less likely to have fouling.

The uniform porous texture of ceramic membrane ensures higher water flux. The composition and physiochemical properties of the ceramic membranes can be easily analyzed compared to polymeric membrane. Ceramic membrane requires lower pressure to operate and can produce same volume of water under relatively less pressure compared to polymeric membrane. However, modification of ceramic membrane using nanophotocatalyst is somehow difficult as it needs suitable active sites to be attached with the photocatalysts [80]. Thus developing photocatalytic ceramic membranes are still restricted up to a certain extent.

17.5 Impact of Photocatalyst for Fouling Prevention

17.5.1 Influence of Photocatalyst Stacking/Entrapping on Membrane Fouling

Photocatalytic membrane separation process is considered as promising alternative for water treatment as in this method no additional sludge is produced [100, 101]. The active –OH radicals and O^{2-} species prevented the fouling of the membrane. The organic foulants deposited over the membrane surface were destroyed due to the photoinduced catalytic process. ZnO-PEG nanoparticles-based composite membrane was also efficient for mitigation of fouling and it was observed from unchanged texture SEM images of membrane surface compared to the bare one. This revealed that substantial photocatalytic degradation process had taken place to destroy the foulants over the membrane without any pore clogging or structural changes of the membrane surface [102]. The antifouling mechanism of photocatalyst-coated (TiO_2-coated) polymeric PVDF membrane can be illustrated by Fig. 17.16 [102].

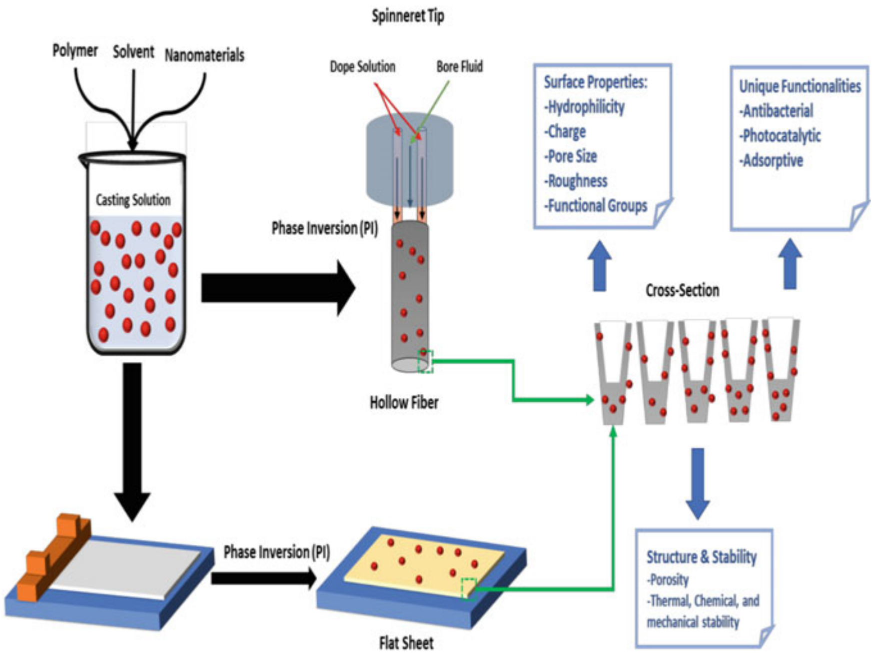

Fig. 17.16 Antifouling mechanism of TiO_2-doped PVDF membrane (modified and redrawn from Ref. [102])

17.5.2 *Influence of Hydrophilicity on Membrane Fouling*

Hydrophobic features of membrane surface can lead to the fouling phenomena up to a greater scale [103]. Hydrophobic membranes tend to adsorb organic foulants causing poor performance of the membrane [104]. Photocatalyst with oxygen containing groups can increase the hydrophilicity to reduce the fouling. Lot of research reports demonstrated that surface functionalized, modified membranes would degrade the foulant after optimum contact time under UV or visible light irradiation process [105, 106]. The increase in the hydrophilicity of membranes is proved by a decrease in the membrane contact angle. The summary of different types of modified membrane and their properties are enlisted in Table 17.5.

17.5.3 *Influence of Antibacterial Activity and Biofouling of Membrane*

In membrane bioreactors, biofouling takes place frequently [115]. Biofouling occurs due to accumulation of microorganisms, virus, and bacteria over the surface

Table 17.5 Modification of photocatalyst/polymeric membrane with research findings

Polymeric membrane	Process for modification	Type of photocatalyst and their composites	Contact angle (CA)	Brief research findings	References
Polysulfon (PS)	Blending	Nitrogen-infused GO/TiO_2	Contact angle decreased from 81° to 59.2°	Higher water flux and photocatalytic efficiencies	[57]
Polysulfon (PSF)	Blending	Mesoporous carbon nitride (C_3N_4)/TiO_2	Contact angle decreased from 70.8° to 58.1°	Pollutant removal by photocatalytic degradation, flexibility of design, highly stability	[107]
Polysulfon (PSF)	Blending	Copper oxide (Cu_2O)	Contact angle decreased from 75.5° to 45.3°	Higher drug removal with increased hydrophilicity of the membrane	[108]
Polysulfon (PSF)	Sol–gel	ZrO_2-SnO_2	Contact angle decreased from 62.9° to 45.97°	Degradation of pharmaceutical wastewater and fouling resistant	[109]
Polyether sulfone (PES)	Blending	CuO/ZnO	Contact angle decreased from 70.2° to 63.4°	Increased water flux, fouling resistant	[110]
Polyether sulfone (PES)	Blending	Boron-coated TiO_2–SiO_2/$CoFe_2O_4$	Contact angle decreased from 62.5° to 49.3°	Self-cleaning aptitude	[111]
Polyether sulfone (PES)	Blending	NH_2–Ag_3PO_4/g-C_3N_4	Contact angle decreased from 63.97° to 54.96°	Biofouling-resistant membrane	[112]
Polyvinylchloride (PVC)	Blending	TiO_2-doped halloysitenanotube	–	Improved photocatalytic properties	[105]
Polyvinylchloride (PVC)	Blending	Silver (Ag)/TiO_2	Contact angle decreased from 68° to ~62°	Highly hydrophilic and antibacterial properties	[113]
Polivinylidene fluoride (PVDF)	Coating	Polydopamine-coated reduced graphene oxide (rGO)/Ag_3PO_4	Contact angle decreased from 88.2° to 59.2°	Dye degradation in presence of UV and Vis light	[114]

of the membrane as depicted by Fig. 17.17 [115]. The extracellular polymeric substance (EPS) is produced by bacteria and causes biofouling. Currently, antibacterial membranes are fabricated which can ensure killing of bacteria and prevents their attachment with the membrane surface.

The photocatalytic membrane can exhibit bactericidal ability under irradiation using UV or visible light. The –OH radical can attack the cell membrane of the bacteria and biochemical reaction of lipid peroxidation takes place. TiO_2-coated hybrid polyamide membrane decreased the number of *E. coli* cell number due to presence of UV light [37]. It was concluded by previous researchers that the crystallinity index of nanocomposite can significantly enhance the antibacterial activity of the nanocomposite membrane. The outer skin layer of the membrane is more exposed to the UV radiation; thus, it can show more antibacterial activity. Interfacial polymerization of grafting method can be used to produce photocatalytic membrane. Highly viscous doping solution with photocatalyst synthesized by ex situ method can favorable decorate the nanoparticles over the skin layer [116]. On the contrary, viscous polymeric solution will inhibit the diffusion of photocatalyst inside the membrane matrix [117]. Photocatalytic membrane separation process can be integrated with biodegradation for efficient degradation of volatile organic compounds (VOCs) in a membrane bioreactor [118, 119]. The anti-biofouling properties of different types of membranes are listed in Table 17.6.

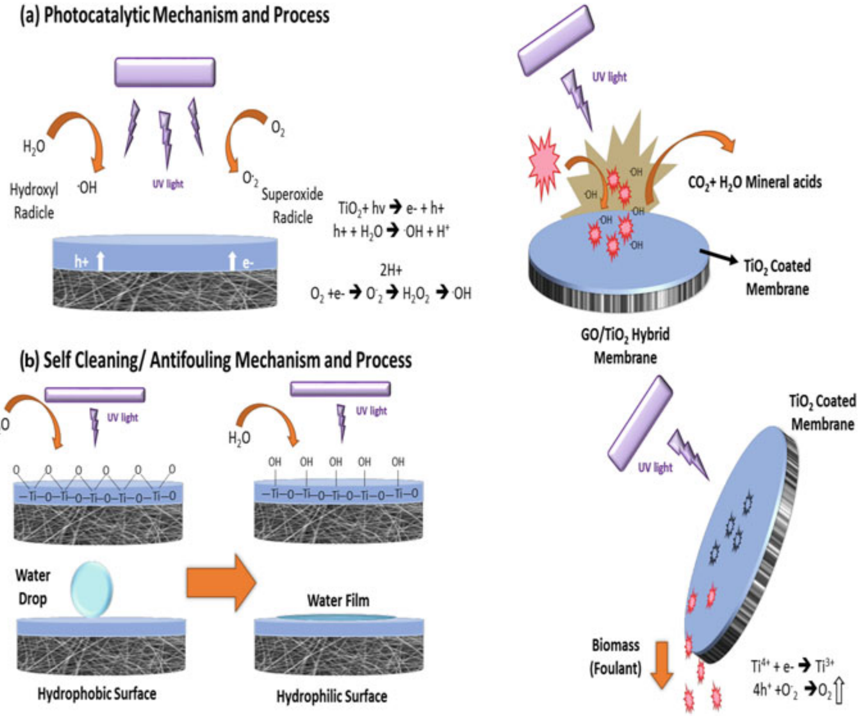

Fig. 17.17 Mechanism of biofouling (modified and redrawn from Ref. [115])

Table 17.6 Recent advances in photocatalytic fouling-resistant membranes

Type of membrane	Polymer matrix	Nanomaterials	Research findings	Type of bacteria	References
Microfiltration (MF)	Polyether sulfone (PES)	g-C_3N_4/NH_2-silver phosphate (Ag_3PO_4)	Enhanced flux Better hydrophilicity Antimicrobial	*Staphylococcus aureus* (Staph), Salmonella (Sal), and *E. coli*	[120]
Microfiltration (MF)	Polyethersulfone (PES)	g-C_3N_4/NH_2–Ag_3PO_4 Zn Al Cu-LDH/silver phosphate (Ag_3PO_4)	Superior permeability Biofouling resistant	Activated sludge	[105]
Ultrafiltration (UF)	Polivinylidene fluoride (PVDF)	TiO_2	Enhanced flux Better permeability Antibacterial	*E. coli*	[169]
Ultrafiltration (UF)	Polysulfone (PS)	Al_2O_3 LTL zeolite	Enhanced hydrophilicity Adhesionless membrane	*P. aeruginosa* and *E. coli*	[121]
Reverse osmosis (RO)	Polyacrylonitrile (PA)	GO	Biofouling Resistant Resistant to chlorine Higher flux Better permeability	–	[122]
Reverse osmosis (RO)	Polyacrylonitrile (PA)	TiO_2	Antibiofouling Better permeability	*E. coli*	[83]

17.6 Conclusion

Application of nanocatalyst for water treatment is becoming popular day by day. There is an emerging need to develop innovative process to purify the aqueous effluents suitable for safe consumption. Rapid industrialization in this era has generated lot of micro- and macro-pollutants which can cause serious threat for living organism. Present water treatment technologies can be modified using nanomaterials in a controlled way. Nanotechnology can help in water purification and can resolve the challenges associated with it [123–125].

Nanoadsorbent and nanocatalytic membrane separation process is very efficient, but these methods need to be applied carefully to prevent leaching in aqueous stream. Furthermore, the process is relatively expensive. Thus, until now it is not used for large-scale application. There is no digital monitoring system to ensure the trace amount of leached nanoparticles present inside the aqueous stream [126, 127]. Hybrid system using nanophotocatalyst with membrane separation process is comparatively new approach for treating wastewater. The synergistic effect of two processes makes the photocatalytic membrane reactor more efficient. Application of photocatalyst with membrane will disintegrate the organic compounds to harmless products. Furthermore membrane separation techniques will allow the separation and reuse of the catalyst up to a greater extent.

PMRs can directly use the photocatalytic membranes, or it can use suspended photocatalytic particles. For first type, membrane fouling can be prevented due to presence of photocatalyst. The photocatalytic degradation can take place either in feed side or permeate side. However, the photodegradation efficiency for these types of PMRs is lower. The nonporous support is loaded with suspended photocatalyst in another type of PMRs. PMRs having suspended catalyst show faster reactions for gaseous phase separation process. The presence of UV light or hydroxyl radicals can damage the membrane surface. Thus, the challenge of using polymeric membrane having photocatalyst needs to be carefully resolved. The fabricated membrane needs to be UV resistant, fouling resistant and has good separation efficiencies.

Suspended photocatalyst containing PMRs can ensure efficient separation of the used catalyst from the solution. Several membrane techniques, namely MF, UF, NF, PV, MD, and dialysis, can be coupled with photocatalysts to treat water. The phenomenon of fouling can be minimized using submerged membranes. To some extent, quality of permeate using pressure-driven membrane is lower as it cannot separate lower molecular weight compounds. To resolve this problem, PMRs can be utilized using membrane distillation (MD) process. Nevertheless, MD process is rather more complicated. Thus, PMRs applying pressure-driven membranes are more promising candidate for large-scale commercialization.

This chapter extensively focused on the importance of using photocatalytic membrane technology for water treatment. The mechanism of photocatalysis along with the advantages of using photocatalytic membrane has been illustrated. Presence of photocatalyst can mitigate the fouling problems and increase the overall performance of the membrane. Incorporation of photocatalyst with membrane can ensure hydrophilicity and enhance the antibacterial properties of the membrane. The contact angle of the composite membrane containing photocatalyst will be decreased. A thin hydrophilic layer will be formed using hydrogenase bond over the surface of the composite membrane which in turn will prevent the addition of foulants on the membrane surface. Due to presence of UV or visible light, the photocatalyst will generate reactive species which will destroy the bacterial cells. Still, further research is necessary in order to enhance the performance of the hybrid membrane separation processes to have greater permeate quality and flux.

Additionally, it is very essential to consider the real systems that is the purification of natural and real waste effluents containing multiple contaminants. Maximum experiments until now were concentrating to use model solution having single contaminants. All the same, the main complication for using hybrid photocatalytic membrane or PMRs is the type of light source. It is necessary to develop PMRs system, which can use inexpensive sunlight as a source of light for photodegradation of pollutants. Thus, band tuning is necessary for the photocatalyst to be active under solar radiation. This can be done by doping the photocatalyst using nonmetals or metals, nanocarbon, etc., which can shift the sorption edge toward the visible region. The leaching of entrapped nanoparticles in the permeate needs to be prevented during the filtration process. Careful measure should be undertaken to avoid discharge of hazardous nanocatalyst in the aqueous stream.

References

1. Luo J, Chen W, Song H, Liu J (2020) Fabrication of hierarchical layer-by-layer membrane as the photocatalytic degradation of foulants and effective mitigation of membrane fouling for wastewater treatment. Sci Total Environ 699: https://doi.org/10.1016/j.scitotenv.2019.134398
2. Chen W, Mo J, Du X, Zhang Z, Zhang W (2019) Biomimetic dynamic membrane for aquatic dye removal. Water Res 151:243–251. https://doi.org/10.1016/j.watres.2018.11.078
3. Ahmed FE, Lalia BS, Hashaikeh R (2015) A review on electrospinning for membrane fabrication: challenges and applications. Desalination 356:15–30. https://doi.org/10.1016/j.desal.2014.09.033
4. Meng S, Greenlee LF, Shen YR, Wang E (2015) Basic science of water: challenges and current status towards a molecular picture. Nano Res 8(10):3085–3110. https://doi.org/10.1007/s12274-015-0822-y
5. Meng S, Meng X, Fan W, Liang D, Wang L, Zhang W, Liu Y (2020) The role of transparent exopolymer particles (TEP) in membrane fouling: a critical review. Water Res 181: https://doi.org/10.1016/j.watres.2020.115930
6. Li R, Fan H, Shen L, Rao L, Tang J, Hu S, Lin H (2020) Inkjet printing assisted fabrication of polyphenol-based coating membranes for oil/water separation. Chemosphere 250: https://doi.org/10.1016/j.chemosphere.2020.126236
7. Rao L, Tang J, Hu S, Shen L, Xu Y, Li R, Lin H (2020) Inkjet printing assisted electroless Ni plating to fabricate nickel coated polypropylene membrane with improved performance. J Colloid Interface Sci 565:546–554. https://doi.org/10.1016/j.jcis.2020.01.069

8. Teng J, Wu M, Chen J, Lin H, He Y (2020) Different fouling propensities of loosely and tightly bound extracellular polymeric substances (EPSs) and the related fouling mechanisms in a membrane bioreactor. Chemosphere 255: https://doi.org/10.1016/j.chemosphere.2020.126953
9. Konstantinou IK, Albanis TA (2004) TiO2-assisted photocatalytic degradation of azo dyes in aqueous solution: kinetic and mechanistic investigations. Appl Catal B 49(1):1–14. https://doi.org/10.1016/j.apcatb.2003.11.010
10. Zollinger H (2003) Color chemistry: syntheses, properties, and applications of organic dyes and pigments. Wiley, Hoboken
11. Tang WZ, An Huren (1995) UV/TiO2 photocatalytic oxidation of commercial dyes in aqueous solutions. Chemosphere 31(9):4157–4170. https://doi.org/10.1016/0045-6535(95)80015-d
12. Wang T, Wang Z, Wang P, Tang Y (2019) An integration of photo-Fenton and membrane process for water treatment by a PVDF@$CuFe_2O_4$ catalytic membrane. J Membr Sci 572:419–427. https://doi.org/10.1016/j.memsci.2018.11.031
13. Khataee A, Sadeghi Rad T, Nikzat S, Hassani A, Aslan MH, Kobya M, Demirbaş E (2019) Fabrication of NiFe layered double hydroxide/reduced graphene oxide (NiFe-LDH/rGO) nanocomposite with enhanced sonophotocatalytic activity for the degradation of moxifloxacin. Chem Eng J 375: https://doi.org/10.1016/j.cej.2019.122102
14. Kıranşan M, Khataee A, Karaca S, Sheydaei M (2015) Artificial neural network modeling of photocatalytic removal of a disperse dye using synthesized of ZnO nanoparticles on montmorillonite. Spectrochim Acta Part A Mol Biomol Spectrosc 140:465–473. https://doi.org/10.1016/j.saa.2014.12.100
15. Rosman N, Salleh WNW, Mohamed MA, Jaafar J, Ismail AF, Harun Z (2018) Hybrid membrane filtration-advanced oxidation processes for removal of pharmaceutical residue. J Colloid Interface Sci 532:236–260. https://doi.org/10.1016/j.jcis.2018.07.118
16. Haddad Irani-nezhad M, Hassanzadeh J, Khataee A, Orooji Y (2019) A chemiluminescent method for the detection of H_2O_2 and glucose based on intrinsic peroxidase-like activity of WS2 quantum dots. Molecules 24(4):689. https://doi.org/10.3390/molecules24040689
17. Jalili R, Khataee A (2019) Aluminum(III) triggered aggregation-induced emission of glutathione-capped copper nanoclusters as a fluorescent probe for creatinine. Microchim Acta 186(1). https://doi.org/10.1007/s00604-018-3111-0
18. Darbandi M, Shaabani B, Schneider J, Bahnemann D, Gholami P, Khataee A, Yardani P, Hosseini MG (2019) TiO2 nanoparticles with superior hydrogen evolution and pollutant degradation performance. Int J Hydrogen Energy 44(44):24162–24173. https://doi.org/10.1016/j.ijhydene.2019.07.129
19. Vatanpour V, Karami A, Sheydaei M (2017) Central composite design optimization of Rhodamine B degradation using TiO_2 nanoparticles/UV/PVDF process in continuous submerged membrane photoreactor. Chem Eng Process 116:68–75. https://doi.org/10.1016/j.cep.2017.02.015
20. Khataee A, Arefi-Oskoui S, Abdollahi B, Hanifehpour Y, Joo SW (2015) Synthesis and characterization of Pr x Zn_{1-x} Se nanoparticles for photocatalysis of four textile dyes with different molecular structures. Res Chem Intermed 41(11):8425–8439. https://doi.org/10.1007/s11164-014-1901-5
21. Rajamanickam D, Shanthi M (2016) Photocatalytic degradation of an organic pollutant by zinc oxide—solar process. Arab J Chem 9:S1858–S1868. https://doi.org/10.1016/j.arabjc.2012.05.006
22. Peyravi M, Jahanshahi M, Mona Mirmousaei S, Lau W-J (2020) Dynamically coated photocatalytic zeolite–TiO_2 membrane for oil-in-water emulsion separation. Arab J Sci Eng. https://doi.org/10.1007/s13369-019-04335-2
23. Hir ZAM, Moradihamedani P, Abdullah AH, Mohamed MA (2017) Immobilization of TiO2 into polyethersulfone matrix as hybrid film photocatalyst for effective degradation of methyl orange dye. Mater Sci Semicond Process 57:157–165. https://doi.org/10.1016/j.mssp.2016.10.009

24. Hadnadjev-Kostic M, Vulic T, Marinkovic-Neducin R, Lončarević D, Dostanić J, Markov Sš, Jovanović Dš (2017) Photo-induced properties of photocatalysts: a study on the modified structural, optical and textural properties of TiO_2—ZnAl layered double hydroxide based materials. J Cleaner Prod 164:1–18. https://doi.org/10.1016/j.jclepro.2017.06.091
25. Iglesias O, Rivero MJ, Urtiaga AM, Ortiz I (2016) Membrane-based photocatalytic systems for process intensification. Chem Eng J 305:136–148. https://doi.org/10.1016/j.cej.2016.01.047
26. Molinari R, Lavorato C, Argurio P (2017) Recent progress of photocatalytic membrane reactors in water treatment and in synthesis of organic compounds. A review. Catal Today 281:144–164. https://doi.org/10.1016/j.cattod.2016.06.047
27. Sun T, Liu Y, Shen L, Xu Y, Li R, Huang L, Lin H (2020) Magnetic field assisted arrangement of photocatalytic TiO_2 particles on membrane surface to enhance membrane antifouling performance for water treatment. J Colloid Interface Sci 570:273–285. https://doi.org/10.1016/j.jcis.2020.03.008
28. Liu Y, Shen L, Lin H, Yu W, Xu Y, Li R, Sun T, He Y (2020) A novel strategy based on magnetic field assisted preparation of magnetic and photocatalytic membranes with improved performance. J Membr Sci 612: https://doi.org/10.1016/j.memsci.2020.118378
29. Xu Z-L, Alsalhy Qusay F (2004) Polyethersulfone (PES) hollow fiber ultrafiltration membranes prepared by PES/non-solvent/NMP solution. J Membr Sci 233(1–2):101–111. https://doi.org/10.1016/j.memsci.2004.01.005
30. Liberal J, Costa G, Carmo A, Vitorino R, Marques C, Domingues MR, Domingues P, Gonçalves AC, Alves R, Sarmento-Ribeiro AB, Girão H, Cruz MT, Batista MT (2015) Chemical characterization and cytotoxic potential of an ellagitannin-enriched fraction from *Fragaria vesca* leaves. Arab J Chem 12(8):3652–3666. https://doi.org/10.1016/j.arabjc.2015.11.014
31. Boubakri A, Hafiane A, Bouguecha SAT (2017) Direct contact membrane distillation: capability to desalt raw water. Arab J Chem 10:S3475–S3481. https://doi.org/10.1016/j.arabjc.2014.02.010
32. Yang T, Liu F, Xiong H, Yang Q, Chen F, Zhan C (2019) Fouling process and anti-fouling mechanisms of dynamic membrane assisted by photocatalytic oxidation under sub-critical fluxes. Chin J Chem Eng 27(8):1798–1806. https://doi.org/10.1016/j.cjche.2018.10.019
33. Ong CS, Goh PS, Lau WJ, Misdan N, Ismail AF (2016) Nanomaterials for biofouling and scaling mitigation of thin film composite membrane: a review. Desalination 393:2–15. https://doi.org/10.1016/j.desal.2016.01.007
34. Sidik DAB, Hairom NHH, Mohammad AW (2019) Performance and fouling assessment of different membrane types in a hybrid photocatalytic membrane reactor (PMR) for palm oil mill secondary effluent (POMSE) treatment. Process Saf Environ Prot 130:265–274. https://doi.org/10.1016/j.psep.2019.08.018
35. Kumari P, Bahadur N, Dumée LF (2020) Photo-catalytic membrane reactors for the remediation of persistent organic pollutants—a review. Sep Purif Technol 230: https://doi.org/10.1016/j.seppur.2019.115878
36. Vatanpour V, Madaeni SS, Rajabi L, Zinadini S, Derakhshan AA (2012) Boehmite nanoparticles as a new nanofiller for preparation of antifouling mixed matrix membranes. J Membr Sci 401–402:132–143. https://doi.org/10.1016/j.memsci.2012.01.040
37. Vatanpour V, Madaeni SS, Khataee AR, Salehi E, Zinadini S, Monfared HA (2012) TiO_2 embedded mixed matrix PES nanocomposite membranes: influence of different sizes and types of nanoparticles on antifouling and performance. Desalination 292:19–29. https://doi.org/10.1016/j.desal.2012.02.006
38. Soroko I, Livingston A (2009) Impact of TiO_2 nanoparticles on morphology and performance of crosslinked polyimide organic solvent nanofiltration (OSN) membranes. J Membr Sci 343(1–2):189–198. https://doi.org/10.1016/j.memsci.2009.07.026
39. Molinari R, Mungari M, Drioli E, Di Paola A, Loddo V, Palmisano L, Schiavello M (2000) Study on a photocatalytic membrane reactor for water purify cation. Catal Today 55:71–78

40. Zhang H, Quan X, Chen S, Zhao H (2006) The removal of sodium dodecylbenzene sulfonate surfactant from water using silica/titania nanorods/nanotubes composite membrane with photocatalytic capability. Appl Surf Sci 24:8598–8604
41. Zhang H, Quan X, Chen S, Zhao H, Zhao Y (2006) Fabrication of photocatalytic membrane and evaluation of its efficiency in removal of organic pollutants from water. Sep Purif Technol 50:147–155
42. Barni B, Cavicchioli A, Riva E, Zanoni L, Bignoli F, Bellobono IR, Gianturco F, De Giorgi A, Muntau H, Montanarella L, Facchetti S, Castellano L (1995) Laboratory-scale photodegradation of phenol in aqueous solution by photocatalytic membranes immobilizing titanium dioxides. Chemosphere 30:1847–1850
43. Bellobono IR, Morazzoni F, Bianchi R, Mangone ES, Stanescu R, Costache C, Tozzi PM (2005) Solar energy driven photocatalytic membrane modules for water reuse in agricultural and food industries. Pre-industrial experience using s-triazines as model molecules. Int J Photoenergy 7:87–94
44. Wang W-Y, Irawan A, Ku Y (2008) Photocatalytic degradation of Acid Red 4 using a titanium dioxide membrane supported on a porous ceramic tube. Water Res 42:4725–4732
45. Tsuru T, Toyosada T, Yoshioka T, Asaeda M (2001) Photocatalytic reactions in a filtration system through porous titanium dioxide membranes. J Chem Eng Jpn 34:844–847
46. Bae T-H, Tak T-M (2005) Effect of TiO_2 nanoparticles on fouling mitigation of ultrafiltration membranes for activated sludge filtration. J Membr Sci 249:1–8
47. Bosc F, Ayral A, Guizard C (2005) Mesoporous anatase coatings for coupling membrane separation and photocatalyzed reactions. J Membr Sci 265:13–19
48. Tsuru T, Kan-no T, Yoshioka T, Asaeda M (2006) A photocatalytic membrane reactor for VOC decomposition using Pt-modified titanium oxide porous membranes. J Membr Sci 280:156–162
49. Mozia S (2010) Photocatalytic membrane reactors (PMRs) in water and wastewater treatment. A review. Sep Purif Technol 73:71–91
50. Molinari R, Pirillo F, Falco M, Loddo V, Palmisano L (2004) Photocatalytic degradation of dyes by using a membrane reactor. Chem Eng Process 43:1103–1114
51. Molinari R, Palmisano L (2005) Photocatalytic membrane reactors in water purify cation'. In: Lehr J, Keeley J, Lehr J (eds) Water encyclopedia, domestic, municipal and industrial water supply and waste disposal, vol 1. Wiley, pp 791–797
52. Benotti MJ, Stanford BD, Wert EC, Snyder SA (2009) Evaluation of a photocatalytic reactor membrane pilot system for the removal of pharmaceuticals and endocrine disrupting compounds from water. Water Res 43:1513–1522
53. Fu J, Ji M, Wang Z, Jin L, An D (2006) A new submerged membrane photocatalysis reactor (SMPR) for fulvic acid removal using a nano-structured photocatalyst. J Hazard Mater 131:238–242
54. Chin SS, Lim TM, Chiang K, Fane AG (2007) Hybrid low-pressure submerged membrane photoreactor for the removal of bisphenol A. Desalination 202:253–261
55. Chin SS, Lim TM, Chiang K, Fane AG (2007) Factors affecting the performance of a low-pressure submerged membrane photocatalytic reactor. Chem Eng J 130:53–63
56. Augugliaro V, Garc í a-L ó pez E, Loddo V, Malato S, Maldonado I, Marc í G, Molinari R, Palmisano L (2005) Degradation of lincomycin in aqueous medium: coupling of solar photocatalysis and membrane separation. Solar Energy 79:402–408
57. Xu H, Ding M, Chen W et al (2018) Nitrogen–doped GO/TiO2 nanocomposite ultrafiltration membranes for improved photocatalytic performance. Sep Purif Technol 195:70–82
58. Zhang X, Wang DK, Diniz Da Costa JC (2014) Recent progresses on fabrication of photocatalytic membranes for water treatment. Catal Today 230:47–54
59. Leong S, Razmjou A, Wang K (2014) TiO_2 based photocatalytic membranes: a review. J Membr Sci 472:167–184
60. Ong CS, LauWJ Goh PS (2014) Investigation of submerged membrane photocatalytic reactor (sMPR) operating parameters during oily wastewater treatment process. Desalination 353:48–56

61. Starr BJ, Tarabara VV, Herrera-Robledo M (2016) Coating porous membranes with a photocatalyst: comparison of LbL self-assembly and plasma-enhanced CVD techniques. J Membr Sci 514:340–349
62. Yao X, Ma C, Huang H (2018) Solvothermal-assisted synthesis of biomass carbon quantum dots/bismuth oxyiodide microflower for enhanced photocatalytic activity. NANO 13:1850031
63. Melvin Ng HK, Leo CP, Abdullah AZ (2017) Selective removal of dyes by molecular imprinted TiO_2 nanoparticles in polysulfone ultrafiltration membrane. J Environ Chem Eng 5:3991–3998
64. Bojarska M, Nowak B, Skowroński J (2017) Growth of ZnO nanowires on polypropylene membrane surface—characterization and reactivity. Appl Surf Sci 391:457–467
65. Zhang H, Cao J, Kang P (2018) Ag nanocrystals decorated g-C_3N_4/Nafion hybrid membranes: one-step synthesis and photocatalytic performance. Mater Lett 213:218–221
66. Horovitz I, Avisar D, Baker MA (2016) Carbamazepine degradation using a N-doped TiO_2 coated photocatalytic membrane reactor: influence of physical parameters. J Hazard Mater 310:98–107
67. Lin C-C, Wuu D-S, Huang J-J (2018) Antireflection and passivation property of aluminium oxide thin film on silicon nanowire by liquid phase deposition. Surf Coat Technol 350:1058–1064
68. Park S, Park J, Heo J (2017) Growth behaviors and biocidal properties of titanium dioxide films depending on nucleation duration in liquid phase deposition. Appl Surf Sci 425:547–552
69. Huang J-J, Lin C-C, Wuu D-S (2017) Antireflection and passivation property of titanium oxide thin film on silicon nanowire by liquid phase deposition. Surf Coatings Technol 320:252–258
70. Owens GJ, Singh RK, Foroutan F (2016) Sol-gel based materials for biomedical applications. Prog Mater Sci 77:1–79
71. Salavati-Niasari M, Soofivand F, Sobhani-Nasab A (2016) Synthesis, characterization, and morphological control of $ZnTiO_3$ nanoparticles through sol-gel processes and its photocatalyst application. Adv Powder Technol 27:2066–2075
72. Habibpanah AA, Pourhashem S, Sarpoolaky H (2011) Preparation and characterization of photocatalytic titania-alumina composite membranes by sol-gel methods. J Eur Ceram Soc 31:2867–2875
73. Kandy MM, Gaikar VG (2018) Photocatalytic reduction of CO2 using CdS nanorods on porous anodic alumina support. Mater Res Bull 102:440–449
74. Zong H, Xia X, Liang Y (2018) Designing function-oriented artificial nanomaterials and membranes via electrospinning and electrospraying techniques. Mater Sci Eng C 92:1075–1091
75. Patil JV, Mali SS, Kamble AS (2017) Electrospinning: a versatile technique for making of 1D growth of nanostructured nanofibers and its applications: an experimental approach. Appl Surf Sci 423:641–674
76. Pahasup-anan T, Suwannahong K, Dechapanya W, Rangkupan R (2017) Fabrication and photocatalytic activity of TiO2 composite membranes via simultaneous electrospinning and electrospraying process. J Environ Sci 72:13–24
77. Baig U, Matin A, Gondal MA, Zubair SM (2019) Facile fabrication of superhydrophobic, superoleophilic photocatalytic membrane for efficient oil-water separation and removal of hazardous organic pollutants. J Clean Prod 208:904–915
78. Bet-moushoul E, Mansourpanah Y, Farhadi KH, Tabatabaei M (2016) TiO_2 nanocomposite based polymeric membranes: a review on performance improvement for various applications in chemical engineering processes. Chem Eng J 283:29–46. https://doi.org/10.1016/j.cej.2015.06.124
79. Leong S, Razmjou A, Wang K, Hapgood K, Zhang X, Wang H (2014) TiO_2 based photocatalytic membranes: a review. J Membr Sci 472:167–184. https://doi.org/10.1016/j.memsci.2014.08.016

80. Kim J, Van der Bruggen B (2010) The use of nanoparticles in polymeric and ceramic membrane structures: review. Environ Poll 158:2335–2349. https://doi.org/10.1016/j.envpol.2010.03.024
81. Barni B, Cavicchioli A, Riva E, Zanoni L, Bignoli F, Bellobono IR, Gianturco F, De Giorgi A, Muntau H, Montanarella L, Facchetti S, Castellano L (1995) Pilot-plant-scale photodegradation of phenol in aqueous solution by photocatalytic membranes immobilizing titanium dioxide (PHOTOPERM® process). Chemosphere 30:1861–1874. https://doi.org/10.1016/0045-6535(95)00067-I
82. Bai H, Liu Z, Sun DD (2010) Hierarchically multifunctional TiO2 nano-thorn membrane for water purification. Chem Commun 46:6542–6544. https://doi.org/10.1039/C0CC01143F
83. Kim SH, Kwak SY, Sohn BH, Park TH (2003) Design of TiO_2 nanoparticle self-assembled aromatic polyamide thin-film-composition (TFC) membrane as an approach to solve biofouling problem. J Membr Sci 211:157–165. https://doi.org/10.1016/S0376-7388(02)00418-0
84. Kwak SY, Kim SH (2001) Hybrid organic/inorganic reverse osmosis (RO) membrane for bactericidal anti-fouling 1. Preparation and characterization of TiO2 nanoparticle self-assembled aromatic polyamide thin-film-composite (TFC) membrane. Environ Sci Technol 35:2388–2394. https://doi.org/10.1021/es0017099
85. Bae TH, Tak TM (2005) Preparation of the TiO2 self-assembled polymeric nanocomposite membranes and examination of their fouling mitigation effects in a membrane bioreactor system. J Membr Sci 266:1–5. https://doi.org/10.1016/j.memsci.2005.08.014
86. Razmjou A, Holmes ARL, Li H, Mansouri J, Chen V (2012) The effect of modified TiO2 nanoparticles on polyethersulfone ultrafiltration hollow fiber membranes. Desalination 287:271–280. https://doi.org/10.1016/j.desal.2011.11.025
87. Madaeni SS, Zinadini S, Vatanpour V (2011) A new approach to improve antifouling property of PVDF membrane using in situ polymerization of PAA functionalized TiO_2 nanoparticles. J Membr Sci 380:155–162. https://doi.org/10.1016/j.memsci.2011.07.006
88. Molinari R, Palmisano L, Drioli E, Schiavello M (2002) Studies on various reactor configurations for coupling photocatalysis and membrane processes in water purification. J Membr Sci 206:399–415. https://doi.org/10.1016/S0376-7388(01)00785-2
89. Yin J, Deng B (2015) Polymer-matrix nanocomposite membranes for water treatment. J Membr Sci 479:256–275. https://doi.org/10.1016/j.memsci.2014.11.019
90. Chin SS, Chiang K, Fane AG (2006) The stability of polymeric membranes in a TiO2 photocatalysis process. J Membr Sci 275:202–211. https://doi.org/10.1016/j.memsci.2005.09.033
91. Morehouse JA, Taylor DL, Lloyd DR, Lawler DF, Freeman BD, Worrel LS (2006) The effect of uni-axial stretching on the roughness of microfiltration membranes. J Membr Sci 280:712–719. https://doi.org/10.1016/j.memsci.2006.02.027
92. Morris RE, Krikanova E, Shadman F (2004) Photocatalytic membrane for removal of organic contaminants during ultra-purification of water. Clean Technol Environ Policy 6:96–104. https://doi.org/10.1007/s10098-003-0198-7
93. Kotte MR, Choi M, Diallo MS (2014) A facile route to the preparation of mixed matrix polyvinylidene fluoride membranes with in-situ generated polyethyleneimine particles. J Membr Sci 450:93–102. https://doi.org/10.1016/j.memsci.2013.08.025
94. Luisa Di Vona M, Ahmed Z, Bellitto S, Lenci A, Traversa E, Licoccia S (2007) SPEEK-TiO_2 nanocomposite hybrid proton conductive membranes via in situ mixed sol–gel process. J Membr Sci 296:156–161. https://doi.org/10.1016/j.memsci.2007.03.037
95. Lantelme B, Dumon M, Mai C, Pascault JP (1996) In situ polymerization of titanium alkoxides in polyvinylacetate. J Non-Cryst Solids 194:63–71. https://doi.org/10.1016/0022-3093(95)00498
96. Xing W, Fan Y, Jin W (2013) Application of ceramic membranes in the treatment of water. In: Duke M, Zhao D, Semiat R (eds) Functional nanostructured materials and membranes for water treatment

97. Basile A (ed) (2013) Handbook of membrane reactors: volume 2 reactor types and industrial applications. Woodhead Publishing, Cambridge
98. Athanasekou CP, Romanos GE, Katsaros FK, Kordatosb K, Likodimos V, Falaras P (2012) Very efficient composite Titania membranes in hybrid ultrafiltration/photocatalysis water treatment processes. J Membr Sci 392–393:192–203. https://doi.org/10.1016/j.memsci.2011.12.028
99. Lin Y-F, Tung K-L, Tzeng Y-S, Chen J-H, Chang K-S (2012) Rapid atmospheric plasma spray coating preparation and photocatalytic activity of macroporous Titania nanocrystalline membranes. J Membr Sci 389:83–90. https://doi.org/10.1016/j.memsci.2011.10.018
100. Kumari P, Bahadur N, Dumée LF (2020) Photo-catalytic membrane reactors for the remediation of persistent organic pollutants—a review. Sep Purif Technol 230:
101. Ly QV, Kim H-C, Hur J (2018) Tracking fluorescent dissolved organic matter in hybrid ultrafiltration systems with TiO_2/UV oxidation via EEM-PARAFAC. J Membr Sci 549:275
102. Desa AL, Hairom NHH, Ng LY, Ng CY, Ahmad MK, Mohammad AW (2019) Industrial textile wastewater treatment via membrane photocatalytic reactor (MPR) in the presence of ZnO-PEG nanoparticles and tight ultrafiltration. J Water Process Eng 31:
103. Koulivand H, Shahbazi A, Vatanpour V, Rahmandoust M (2020) Separation and purification technology, vol 230, p 115895
104. Ng LY, Ahmad A, Mohammad AW (2017) Alteration of polyethersulphone membranes through UV-induced modification using various materials: a brief review. Arab J Chem 10: S1821
105. Ghalamchi L, Aber S, Vatanpour V, Kian M (2019) Comparison of NLDH and g-C_3N_4 nanoplates and formative Ag_3PO_4 nanoparticles in PES microfiltration membrane fouling: applications in MBR. Chem Eng Res Des 147:443
106. Ahmad R, Kim JK, Kim JH, Kim J (2017) Nanostructured ceramic photocatalytic membrane modified with a polymer template for textile wastewater treatment. Appl Sci 7:1284
107. Yu S, Wang Y, Sun F, Wang R, Zhou Y (2018) Novel mpg-C_3N_4/TiO_2 nanocomposite photocatalytic membrane reactor for sulfamethoxazole photodegradation. Chem Eng J 337:183
108. Zakeritabar SF, Jahanshahi M, Peyravi M (2018) Photocatalytic behavior of induced membrane by ZrO_2-SnO_2 nanocomposite for pharmaceutical wastewater treatment. Catal Lett 148:882–893
109. Nasrollahi N, Vatanpour V, Aber S, Mahmoodi NM (2018) Preparation and characterization of a novel polyethersulfone (PES) ultrafiltration membrane modified with a CuO/ZnO nanocomposite to improve permeability and antifouling properties. Sep Purif Technol 192:369
110. Singh R, Yadav V, Purkait MK (2019) Cu_2O photocatalyst modified antifouling polysulfone mixed matrix membrane for ultrafiltration of protein and visible light driven photocatalytic pharmaceutical removal. Sep Purif Technol 212:191
111. Zangeneh H, Zinatizadeh AA, Zinadini S, Feyzi M, Bahnemann DW (2019) Preparation and characterization of a novel photocatalytic self-cleaning PES nanofiltration membrane by embedding a visible-driven photocatalyst boron doped-TiO2SiO2/CoFe2O4 nanoparticles. Sep Purif Technol 209:764–775
112. Ghalamchi L, Aber, S, Vatanpour V, Kian M (2019) Comparison of NLDH and g-C3N4 nanoplates and formative Ag3PO4 nanoparticles in PESmicrofiltration membrane fouling: applications in MBR. Chem Eng Res Des 147:443–457
113. Mishra G, Mukhopadhyay M (2019) TiO_2 decorated functionalized halloysite nanotubes (TiO_2@HNTs) and photocatalytic PVC membranes synthesis, characterization and its application in water treatment. Sci Rep 9, 4345. https://doi.org/10.1038/s41598-019-40775-4
114. Nasrollahi N, Leila G, Vahid V, Alireza K (2020) Photocatalytic-membrane technology: a critical review for membrane fouling mitigation. J Ind Eng Chem 93:101–116
115. Yaqoob AA, Parveen T, Umar K, Nasir M, Ibrahim M Role of nanomaterials in the treatment of wastewater: a review. Water 12:1–30. https://doi.org/10.3390/w12020495

116. Sile-Yuksel M, Tas B, Koseoglu-Imer DY, Koyuncu I (2014) Effect of silver nanoparticle (AgNP) location in nanocomposite membrane matrix fabricated with different polymer type on antibacterial mechanism. Desalination 347:120
117. Wei Z, He Y, Huang Z, Xiao X, Li B, Ming S, Cheng X (2019) Photocatalytic membrane combined with biodegradation for toluene oxidation. Ecotoxicol Environ Saf 184:
118. Tufail A, Alharbi S, Alrifai J, Ansari A, Price WE, Hai FI (2021) Combining enzymatic membrane bioreactor and ultraviolet photolysis for enhancedremoval of trace organic contaminants: degradation efficiency and by-products formation. Process Safety Environ Protect 145:110–119. https://doi.org/10.1016/j.psep.2020.08.001
119. Rolewicz-Kalińska A, Lelicińska-Serafin K, Manczarski P (2021) Volatile organic compounds, ammonia and hydrogen sulphide removal using a two-stagemembrane biofiltration process. Chem Eng Res Design 165:69–80. https://doi.org/10.1016/j.cherd.2020.10.017
120. Ghalamchi L, Aber S, Vatanpour V, Kian M (2019) A novel antibacterial mixed matrixed PES membrane fabricated from embedding aminated Ag_3PO_4/g-C_3N_4 nanocomposite for use in the membrane bioreactor. J Ind Eng Chem 70:412
121. Dong L-x, Yang H-w, Liu S-t, Wang X-m, Xie YF (2015) Fabrication and anti-biofouling properties of alumina and zeolite nanoparticle embedded ultrafiltration membranes. Desalination 365:70
122. Chae H-R, Lee J, Lee C-H, Kim I-C, Park P-K (2015) Graphene oxide-embedded thin-film composite reverse osmosis membrane with high flux, anti-biofouling, and chlorine resistance. J Membr Sci 483:128
123. Damodar RA, You S-J, Chou H-H (2009) Study the self-cleaning, antibacterial and photocatalytic properties of TiO_2 entrapped PVDF membranes. J Hazard Mater 172:1321
124. Zhang M, Liu Z, Gao Y, Shu L (2017) Ag modified g-C_3N_4 composite entrapped PES UF membrane with visible-light-driven photocatalytic antifouling performance. RSC Adv 7:42919
125. Gunawan P, Guan C, Song X, Zhang Q, Leong SSJ, Tang C, Chen Y, Chan-Park MB, Chang MW, Wang K (2011) Hollow fiber membrane decorated with Ag/MWNTs: toward effective water disinfection and biofouling control. ACS Nano 5:10033
126. Schlosser D (2020) Biotechnologies for water treatment. In: Advanced nano-bio technologies for water and soil treatment, pp 335–343
127. Lu F, Astruc D (2020) Nanocatalysts and other nanomaterials for water remediation from organic pollutants. Coord Chem Rev 408:

Chapter 18
Photocatalysis Degradation of Dye Using P-Type Nanoparticles

A. Jegatha Christy, Preeti Singh, J. Anita Lett, and Suresh Sagadevan

Abstract People's demand for resources has risen dramatically, triggering energy shortages and environmental degradation, along with the growth of industry and the improvement of people's living standards. As a low-cost, environmentally friendly, and sustainable technology, photocatalytic technology has shown great potential in recent years and it has become a hot research subject. However, current photocatalytic technology is not able to meet industrial requirements. In the industrialization of photocatalyst technology, the greatest challenge is the development of an ideal photocatalyst that should have four characteristics, including high photocatalytic efficiency, a large specific surface area, full sunlight utilization, and recyclability. Therefore, the present chapter deals with the synthesis, characterization, and photocatalytic activity of nickel oxide (NiO) nanoparticles (NPs), where the solution combustion method makes use of nickel nitrate as an oxidizer and oxalic acid as fuel for the synthesis. From the X-ray diffraction (XRD) analysis, the NiO NPs are found to have formed in a cubic structure with an average crystallite size of 34 nm. The successful formation of the NiO particles was confirmed by the FTIR and UV-Vis spectroscopic analysis. The morphological analysis indicated the rod-like structure and EDX for the elemental composition. Further testing of the photocatalytic activity through the degradation of methyl orange (MO) dye confirmed an effective and potential catalytic nature of the synthesized NiO NPs.

A. Jegatha Christy
Research Center of Physics, Jayaraj Annapackiam College for Women (Autonomous),
Periyakulam, Theni District, Tamilnadu, India

P. Singh
Bio/Polymers Research Laboratory, Department of Chemistry, Jamia Millia Islamia,
New Delhi 110025, India

J. Anita Lett
Department of Physics, Sathyabama Institute of Science and Technology, Chennai,
Tamil Nadu, India

S. Sagadevan (✉)
Nanotechnology and Catalysis Research Centre, University of Malaya,
50603 Kuala Lumpur, Malaysia

S. Garg and A. Chandra (eds.), *Green Photocatalytic Semiconductors*,
Green Chemistry and Sustainable Technology,
https://doi.org/10.1007/978-3-030-77371-7_18

Keywords Photocatalysis · NiO nanoparticles · Oxalic acid fuel · Solution combustion method · Methyl orange · Cubic structure

18.1 Introduction

Water is an essential requirement of the ecosystem for a living and nonliving being for a healthy life. For living creatures, the accessibility of clean water is significant forever continuing exercises like drinking, cooking, cleaning, horticulture, and so on. Nature consists of its mechanism for recycling of water for providing an adequate quantity of freshwater which directly affects life sustainability and standard of the living beings. Current human being activities such as large deforestation, decreased agricultural lands, extensive use of chemical pesticides, industrial discharge of chemicals, etc. have disrupted the equilibrium between the usage and natural purification processes leading to a shortage of potable and filtered water. Most of the natural resources of drinking water are found to be contaminated with various poisonous materials and pathogenic microorganisms [1]. Water pollutants exist in various unsafe squander like pharmaceutical squanders, pesticides, herbicides, textiles, gums, and phenolic compounds. Eradicate pollutant from water has become a universal problem worldwide. In the current scenario, it becomes very essential to decrease this spectrum of a pollutant from water to maintain a high-quality eco-friendly nature has come up with the destruction of various forms of pollutions in the atmosphere due to environmental contamination which occurs in form of untreated hazardous dumped materials/organic matter which gets discharged into the water which disturbs the ecological safety affecting the quality of life [2].

Nanomaterials are the most rapidly used and lucrative approach to eradicate wastes from water. The application of nanotechnology provides cost-effective remediation techniques imposing a major challenge for the researchers for developing an adequate water remediation method for protecting the environment [3–8]. Synthesis of nanomaterial significantly concern in the remediation of heavy metals such as Hg, Pb, Cd, etc. from groundwater also undegradable organic compounds such as benzene, chlorinated solvents, toluene, etc. Precise control size and synthesis of nanomaterials at the molecular level are required to increase the affinity, capability, and selectivity for the removal of particulate pollutants. Thus, nanotechnology has a significant role in minimizing the exposure of harmful wastes to the water and provides safe water. Advanced oxidation processes (AOPs) termed "Photocatalysis" are a cost-effective approach to the treatment of organic effluent from contaminated water. AOPs can be classified into two forms Non-photochemical and Photochemical AOPs (homogeneous and heterogeneous photocatalytic processes). The photocatalyst is may be termed as a photoinduced reaction that is accelerated by the presence of a catalyst. These types of reactions are activated by absorption of a photon with sufficient energy which equals or higher than the bandgap energy (Eg) of the catalyst. Absorption of photons produces electron-hole pairs on the catalyst surface which in turn can reduce or oxidize the organic materials present in aqueous solutions. The main advantage of applying such a technique is its potential to convert the organic pollutants into nontoxic species (CO_2, H_2O) and no need to further separation processes. Researchers explore that AOPs dependent on Photocatalytic is an advanced strategy benefitting our atmospheric conditions by complete oxidation of natural organic molecules into non-harmful mixes CO_2 and H_2O. In addition to these AOPs, also generates hydroxyl free radicals (•OH). These •OH radicals are non-selective in nature act as strong oxidizing agents that readily react with contaminants to destroy and remove them from the water. Also, it completely degrades non-biodegradable organic compounds and makes water to be reusable [9]. Thus, photocatalytic phenomenon practices over the classical techniques, for example, quick oxidation, no development of polycyclic compounds, complete oxidation of contaminants, and high productivity. Hence, Photocatalytic degradation emerged as one of the foremost rich procedures for the treatment of toxic organic effluents by utilizing nanomaterial such as TiO_2, ZnO, ZnS, etc. which act as a catalyst [10]. In the past two decades, Nano metal oxides such as TiO_2, ZnO, NiO, Ag_2CrO_4, SnO_2, Cu_2O, and In_2O_3 has attracted public concern due to their high photocatalytic efficiency and stability, low cost and low toxicity, high physical and chemical stability, especially, strong ability to fully decomposing organic pollutant into harmless species (e.g., CO_2, H_2O, etc.). Most of the semiconducting oxides utilized for water decontamination are n-type among this nanostructure TiO_2 is the most seriously considered. Ongoing investigations on the photocatalytic movement of numerous p-type semiconducting progress metal oxides, for example, NiO, Cu_2O, FeO, and so on. The focus of this chapter is on the P-type NiO NPs are being tested for photocatalytic behavior using the degradation of methyl orange (MO) dye as a model drug under illumination conditions. NiO is a p-type semiconductor with a wide bandgap $\sim$(3.2 eV–4 eV) between valence and conduction band, making it specifically suitable as a photocatalyst and chemically stable with high electro-optical efficiency [11]. The studies on the use of nanostructure NiO as a photocatalyst for the degradation of organic dyes such as MB, RhB, Methyl Orange, Acid red has already been reported earlier [12].

In this chapter, we report the reaction mechanism involved in the degradation of MO dye using NiO which is a P-type nanomaterial, and its synthesis by solution combustion method and their physiochemical properties.

18.2 Materials and Methods

18.2.1 Materials

Nickel nitrate, oxalic acid, methyl orange (MO) dye of analytical grade were purchased from Sigma-Aldrich and are used without any further purifications.

18.2.2 Synthesis of NiO NPs

Solution combustion synthesis is a fast, easy, and less expensive method for the direct production of highly pure, homogeneous powders of metal oxide NPs [13–15]. Our interest in the production of NiO NPs' is that the method is surfactant-free and involves the combustion for the formation of any sized particles to study their thermal conductivity. This method uses metal nitrate as an oxidizing agent and an organic fuel as a reduction agent for the oxidation/reduction reactions. The preliminary supply of energy in the form of heat initiates the reaction and additionally generates the heat that helps to decompose the metal nitrate and salts. Thus the NiO NPs formed from nickel nitrate as an oxidizing agent and oxalic acid as the fuel were thoroughly characterized by various instrumental methods for the crystallinity and crystal structure, bonding, optical nature, morphology, elemental composition, etc. For the formation of NiO NPs, the stoichiometric ratio of nickel nitrate (as oxidizer) and oxalic acid (as fuel) were maintained to be unity, i.e., the stoichiometric amount of nickel(II) nitrate was first dissolved in deionized water, followed by the addition of fuel. The solution mixture was subjected to heating in a furnace maintained at 400 °C for 15 min and we see the release of enormous fumes from the combustion reaction. On cooling the reaction mixture to room temperature, we see the formation of NiO NPs in a black color powder; Reaction (18.1) is expected for the formation of NiO NPs from nickel nitrate precursor that makes use of oxalic acid fuel.

$$\mathrm{Ni(NO_3)_{2(c)}} + 0.05\mathrm{C_2H_2O_{4(c)}} + \mathrm{O_2} \rightarrow \mathrm{NiO_{(c)}} + \mathrm{N_{2(g)}} + (0.1\,\psi)2\mathrm{CO_{2(g)}} + 0.05\,\psi\mathrm{H_2O_{(g)}} \tag{18.1}$$

Here, the molar ratio of oxalic acid to nickel nitrate $\psi = 0.05$ corresponds to the total oxygen content of nickel nitrate that is used to completely oxidize oxalic acid. As a result, NiO NPs as the powdered product form and with the release of CO_2, N_2, and H_2O gasses are directly generated from the fuel-oxidizer reaction, where no additional supply of oxygen from outside is required.

18.2.3 Instrumental Analysis

The powder X-ray diffraction (XRD) patterns were recorded on the PANalytical X-ray diffractometer that works on 50 kV and 100 mA facility and use Cu Kα radiation ($\lambda = 0.1542$ nm), where the samples analyzed in the diffraction angle, 2θ of 20–80°. For the optical measurements, the UV-Vis spectroscopic analysis was performed on Shimadzu 1700 UV-Visible spectrophotometer, and similarly, to understand the nature of bonding, Shimadzu IRaffinity-1 Fourier Transform Infrared spectrometer was used. The size, composition, and atomic structure of NiO NPs were analyzed on a High-resolution transmission electron microscopy

(HRTEM; 200 keV JEOLJEM2100), Field emission scanning electron microscope (FESEM) (Carl Zeiss sigma) connected to the energy dispersive X-ray (EDX) detector were employed (respectively).

18.2.4 Photocatalytic Activity

To test the photocatalytic degradation efficiency of synthesized NiO NPs, the degradation studies were carried out in a 500 mL glass immersion photocatalytic reactor that uses an 8 W Xenon lamp as the light source and was placed axially in the vessel for the visible light irradiation. The lamp was inserted in a quartz tube to protect it from getting in contact with the aqueous solution. To maintain the dark conditions, the reactor setup was installed in a box and the reactor vessel was covered with aluminum foil to protect from the intrusion of ambient light. Also, to control the power supply of visible light, a timer circuit was used, and thus the on and off functions of the lamp works on its own after each irradiation. For the photocatalytic testing, MO dye at an initial concentration of 0.1 mM was reacted with 0.0125 mM of NiO NPs and with MO solution fully diluted and added. Now, the prepared dye solution was irradiated under visible light and the samples were collected at the specified intervals of time and recorded the changes in the absorption spectrum of MO dye. Since the MO dye exhibits the highest absorption spectrum in the visible region of 467 nm and so any changes to this absorbance value indicate the photocatalytic degradation of MO dye by the NiO NPs.

18.3 Results and Discussion

18.3.1 Physicochemical Characteristics

Figure 18.1 shows the powder XRD pattern of NiO NPs and from the figure, the peaks are observed at the 2θ of 37.3°, 43.4°, 62.9°, 75.4°, and 79.5° which can be linked to the diffraction planes of (111), (200), (220), (311), and (222), respectively (JCPDS: 78-0429). From the analysis of results, the diffraction peaks correspond to the formation of NiO NPs in cubic structure and the unit cell volume measured to be 72.82 $(\text{A}^\circ)^3$. Also, the NiO NPs average crystallite size was calculated using the Debye Scherrer equation (18.2),

$$D = K\lambda/\beta\cos\theta \tag{18.2}$$

where D corresponds to the crystallite size (nm), λ is the wavelength of X-ray source (0.15406 A°), β is the full width at half the maximum diffraction peak (FWHM) in radians, K the Scherrer constant having a value of 0.9–1 [16].

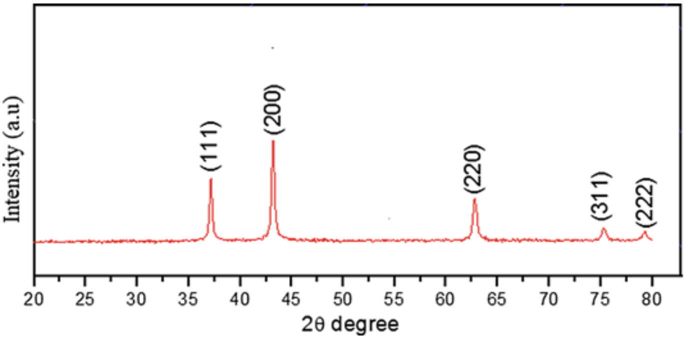

Fig. 18.1 Powder XRD pattern of the synthesized NiO NPs

The analysis provided a constant value of lattice where the standard data is very close to 4.177 A° and the average crystallite size of 34 nm.

Numerous experiments have shown that a special logarithmic series expansion of the Bragg reflection peak profiles. The Fourier coefficients can well describe the strain expansion caused due to the occurrence of dislocations.

W-H equation can be expressed as, $$\beta_{\mathrm{hkl}} \cos\theta = (\mathrm{k}\lambda/D) + (4\varepsilon \tan\theta) \quad (18.3)$$

Rearrangling this, generates Eq. (18.4), $$\beta_{\mathrm{hkl}} \cos\theta = (k\lambda/D) + (4\varepsilon \sin\theta) \quad (18.4)$$

The plot is drawn between $\beta \cos\theta$ and 4 sin θ, where the slope line provides the grain size (D) to the strain (ε), and intercept (k/D). The term $\beta \cos\theta$ was plotted for the orientation peaks of synthesized NiO NPs with respect to 4 sin θ, i.e., Figure 18.2 shows the results of the W-H analysis plot for the prepared NiO NPs and from the slope of line, the gran strain observed to have a positive value of

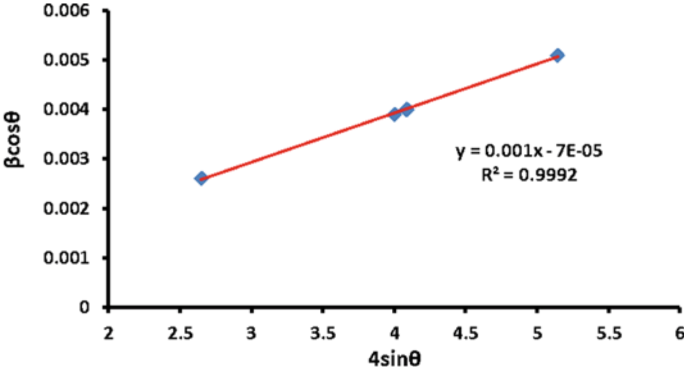

Fig. 18.2 W-H plot analysis of the synthesized NiO NPs

0.001. The observed value of lattice strain is very low and is due to the small size of crystallite and so has a negligible effect toward the peak expansion.

Figure 18.3 shows the FTIR analysis of NiO NPs in the wavenumber range of 500–4000 cm^{-1} and from the figure, the observation of broadbands in the range of 400–550 cm^{-1} can be assigned to the Ni–O stretching vibrations. Also, the observation of a characteristic band at 3442 cm^{-1} can be linked to the O–H stretching vibration and the band at 1614 cm^{-1} attributed to the H–O–H bending vibrations from the surface water/moisture that got adsorbed during the preparation of FTIR samples. The sharp band observed around 1365 cm^{-1} can be linked to the O–C=O symmetric and asymmetric stretching vibrations [17]. Thus, from the overall analysis of bands, it can be indicated for the successful formation of NiO NPs by the solution combustion method.

Figure 18.4 shows the UV-Vis absorption spectrum of NiO NPs and from the graph, the absorption maxima are observed around 245 nm. In the comparison of NiO NPs absorption maxima with that of the bulk NiO's absorption edge, a blue shift in the wavelength was observed [18]. The reflection of NiO NPs in a blue shift or lower wavelength side is due to the Burstein–Moss effect, which indicates for the quantum confinement effect resulted from the decreased size of particles [19].

Figure 18.5 shows the FESEM image of NiO NPs and from the figure, the particles appeared to have formed in the cubic shape which is joined to form a rod-like structure. The formation of such a rod-like structure can be linked to the

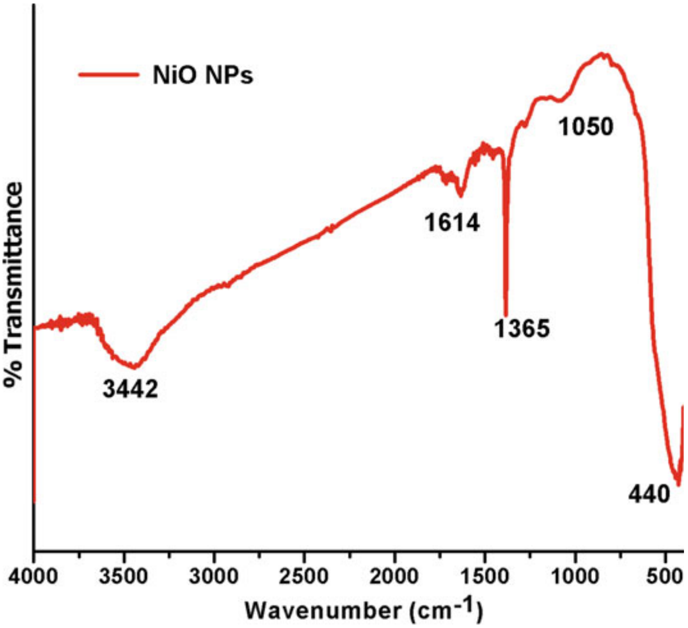

Fig. 18.3 FTIR spectrum of NiO NPs

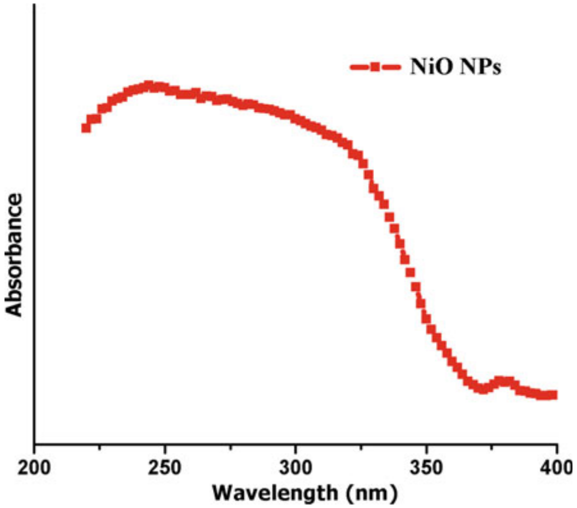

Fig. 18.4 Optical absorption spectra of NiO NPs

selective adsorption of fuel introduced during the synthesis. This has controlled the growth rate occurring in the atmosphere, vapor concentration, and oxygen atmospheric pressure resulting in low vapor supersaturation to attain the NiO NP's such a shape [20]. Also, the image shows the formation of several small particles and is due to the non-uniform distribution of heat and mass flow during the synthesis and thereby confirming the vital role played by the oxalic acid fuel towards the tailoring of surface morphology. Further, the EDX spectrum showed in Fig. 18.5 confirms the formation of NiO compounds by the observation of peaks for the O and Ni elements (at 1, 7, and 8 keV). However, the originated Cu signal is from the carbon-coated Cu grid used for the preparation of FESEM samples.

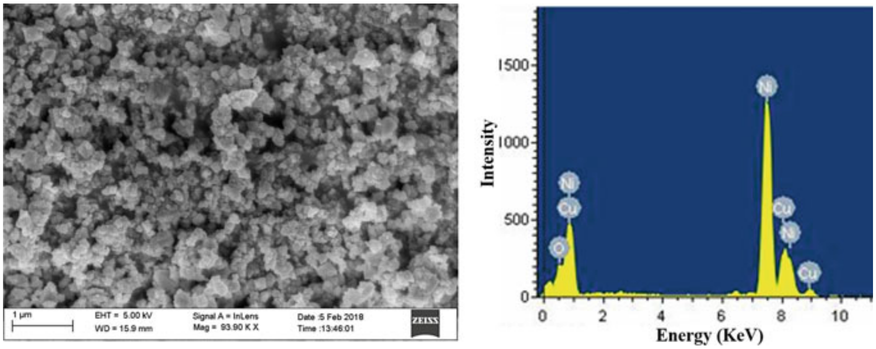

Fig. 18.5 FESEM image and EDX spectrum of NiO NPs

Figure 18.6(a–c) shows the HRTEM images of the NiO NPs at different magnifications and from the figure, the particles exhibit cubic structure with a width of about 100–200 nm. The lattice spacing of 0.147 nm was observed corresponding to the (220) planar cubic structure of NiO NPs and also, the interplanar distance between the (220) planes corresponds to the atomic fringe spacing. Also, the NiO NPs are providing information about the smooth surface of the particles and can be attributed to the enthalpy and flame temperature released during the combustion process, which in turn strongly influenced by the nature of the fuel and the oxidizer [21]. Based on the HRTEM results, it can be indicated that oxalic acid used in the form of fuel has a major role in deciding the formed NiO NP's shape, size, surface roughness, and crystallinity. Hence in the present study, oxalic acid played its role very well and helped to oxidize the nickel nitrate salt and formed the NiO NPs with a clear, smooth, and well-defined structure.

18.3.2 Photocatalytic Activity

Photocatalytic reactions are the chemical reaction that occurs due to close cooperation in-between light and photocatalyst. This technology has many benefits, including environmental safety, complete degradation of toxic substances without any harmful emissions thus, supporting the sustainability of the environment. Synthesized NiO NPs were subjected to determine their photocatalytic efficiency under the influence of visible light to degrade MO dye. Figure 18.7 shows the degrading curve of MO dye in the presence of NiO NPs recorded with the help of UV-V is spectroscopy over a 0–40 min time range. The decrease in the peak intensity of MO dye at 467 nm (Fig. 18.7) with an increase of time period shows the enhanced degrading efficiency or photocatalytic activity of NiO NPs under the impact of time. The reduction kinetic equation can be written as [22]:

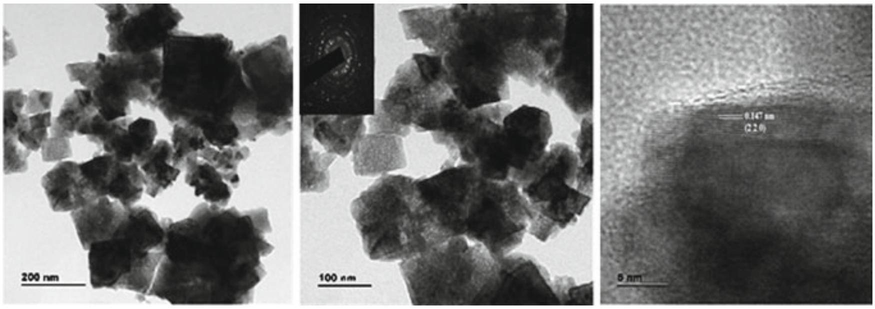

Fig. 18.6 HRTEM images NiO NPs at three different magnifications of 200, 100, and 5 nm

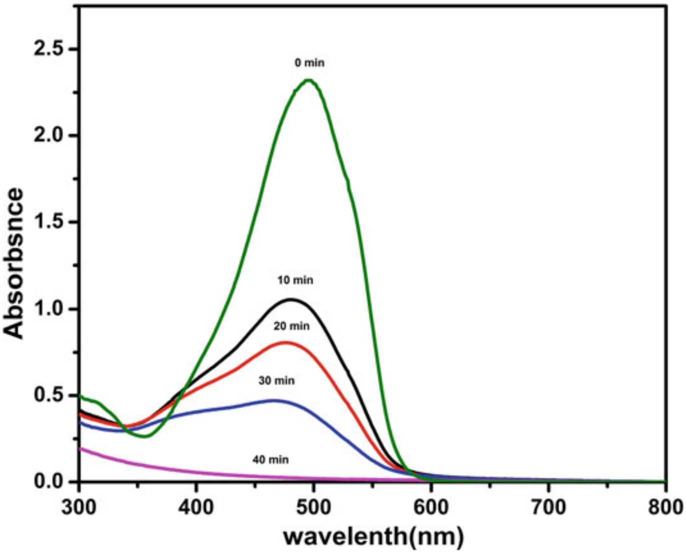

Fig. 18.7 UV-Vis absorbance spectrum of MO dye degradation catalyzed by the NiO NPs over different time intervals of light irradiation

$$\frac{\mathrm{d}C_t}{\mathrm{d}t} = \ln\frac{C_t}{C_0} = -k_{\mathrm{app}}C_t \tag{5}$$

where C_0 and C_t are the initial and final (at time t) MO dye concentrations, and k_{app} is the apparent rate constant and can be calculated by using the peak intensity value (467 nm) with respect to time. The calculated apparent rate constant, k_{app} is found to be $\sim$0.0239/min which is significantly high and the observed enhanced catalytic activity of NiO NPs can be related to its surface morphology.

Photocatalytic actions are induced by light causing the redox reaction of semiconductor material following the perspective of semiconductor photochemistry. A Forbidden energy bandgap exists in semiconductor distance between the low-energy valence band (VB) and a high-energy conduction band (CB). NiO nanoparticles have a strong tendency to get ionized easily due to their smooth surface as compared to rough surface nanoparticles. Figure 18.8 shows the schematic representation of the NiO catalyzed degradation mechanism of (any) dye. NiO catalyst forms most active species such as $\bullet O_2^-$ and H^+ under visible light for degradation of dye. This catalyst action is instigated by the transmission of electrons from VB (valence band) to the CB (conduction band) before the recombination with the hole. Also, this transfer of electrons (VB to CB) is intensely controlled by the surface properties of the catalyst used and dye molecules affecting their adsorption and interfacial wave function mixing [23, 24]. Also, the oxygen vacancies play an essential role in the degradation process, i.e., effectively utilizing the energy of the excited electron from the surface adsorbed oxygen or water (H_2O) molecule generating the highly active $\bullet O_2^-$ and $\bullet OH$ radicals species, respectively.

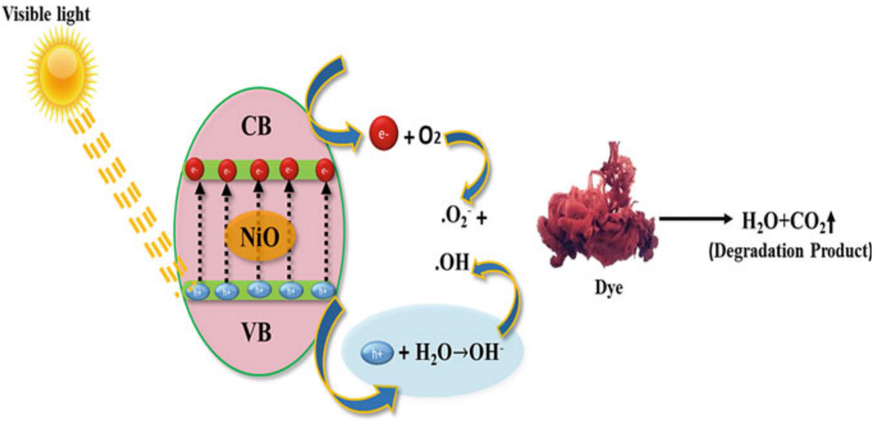

Fig. 18.8 Schematic representation of the photocatalytic dye degradation mediated by the NiO NPs

18.4 Conclusion

In conclusion, the present study deals with the photocatalytic activity testing of NiO NPs formed by making use of the solution combustion synthesis where oxalic acid fuel was used. The synthesized NiO NPs were characterized for the optical, structural, functional, and morphological properties. The XRD results confirmed the cubic structure of the formed NiO NPs and the average crystallite size of 34 nm was found. The UV-Vis absorption spectrum of NiO NPs showed a blue shift and is due to the quantum confinement effect and the FTIR spectrum confirmed the successful formation of the NiO material. The FESEM and HRTEM analysis confirmed the cubic and rod-like morphology of NiO NPs. Further tests of photocatalytic activity evaluated using MO dye degradation confirmed the catalytic efficiency of NiO NPs and the observed activity was explained based on the surface roughness associated with the particles.

Conflict of Interest The authors declare no conflict of interest with this work.

References

1. Sunandan B, Pal Samir K, Joydeep D (2010) Nanostructured zinc oxide for water treatment. Nanosci Nanotechnol Asia 2:90–102
2. Pelaez M, Nolan NT, Pillai SC, Seery MK, Falaras P, Kontos AG, Dunlop PS, Hamilton JW, Byrne J, O'Shea K, Entezari MH, Dionysiou DD (2012) A review on the visible light active titanium dioxide photocatalysts for environmental applications. Appl Catal B 125:331–349

3. Muthukumaran M et al (2020) Green synthesis of cuprous oxide nanoparticles for environmental remediation and enhanced visible-light photocatalytic activity. Optik Int J Light Electron Optics 214:164849
4. Sukhin Saravan R et al (2020) Evaluation of the photocatalytic efficiency of cobalt oxide nanoparticles towards the degradation of crystal violet and methylene violet dyes. Optik Int J Light Electron Optics 207:164428
5. Vidhya M, Raja Pandi P, Archana R et al (2020) Comparison of sunlight-driven photocatalytic activity of semiconductor metal oxides of tin oxide and cadmium oxide nanoparticles. Optik Int J Light Electron Optics 217:164878
6. Mathialagan A, Manavalan M, Venkatachalam K et al (2020) Fabrication and physicochemical characterization of g-C_3N_4/ZnO composite with enhanced photocatalytic activity under visible light. Opt Mater 100:109643
7. Priya R, Stanly S, Dhanalekshmi SB et al (2020) Comparative studies of crystal violet dye removal between semiconductor nanoparticles and natural adsorbents. Optik Int J Light Electron Optics 206:164281
8. Pradeev raj K, Sadaiyandi K, Kennedy A et al (2018) Influence of Mg doping on ZnO nanoparticles for enhanced photocatalytic evaluation and antibacterial analysis. Nanoscale Res Lett 13:229
9. Rehman S, Ullah R, Butt AM, Gohar ND (2009) Strategies of making TiO_2 and ZnO visible light active. J Hazard Mater 170(2–3):560–569
10. Motahari F, Mozdianfard MR, Soofivand F, Salavati-Niasari M (2014) NiO nanostructures: synthesis, characterization and photocatalyst application in dye wastewater treatment. RSC Adv 4(53):27654. https://doi.org/10.1039/c4ra02697g
11. Wan X et al (2013) Effects of catalyst characters on the photocatalytic activity and process of NiO nanoparticles in the degradation of methylene blue. Appl Surf Sci. https://doi.org/10.1016/j.apsusc.2013.03.126
12. Haider AJ, Al-Anbari R, Sami HM, Haider MJ (2019) Photocatalytic activity of nickel oxide. J Mater Res Technol 8:2802–2808
13. Sharma P, Lotey GS, Singh S, Verma NK (2011) Solution-combustion: the versatile route to synthesize silver nanoparticles. J Nanopart Res 13:2553–256
14. Sahoo P, Misra DK, Salvador J, Makongoa JPA, Chaubey GS, Takas NJ, Wiley JB, Poudeu PFP (2012) Microstructure and thermal conductivity of surfactant-free NiO nanostructures. J Solid State Chem 190:29–35
15. Niasari MS, Mohandes F, Davar F, Mazaheri M, Monemzadeh M, Yavarinia N (2009) Preparation of NiO nanoparticles from metal-organic frameworks via a solid-state decomposition route. Inorg Chim Acta 362:3691–3697
16. Umadevi M, Jegatha Christy A (2013) Optical, structural and morphological properties of silver nanoparticles and its influence on the photocatalytic activity of TiO_2. Spectrochim Acta Part A Mol Biomol Spectrosc 111:80–85
17. Mohseni Meybodi S, Hosseini SA, Rezaee M, Sadrnezhaad SK, Mohammadyani D (2012) Synthesis of wide band gap nanocrystalline NiO powder via a sonochemical method. Ultrason Sonochem 19:841–845
18. Barakat A, Al-Noaimi M, Suleiman M, Aldwayyan AS, Hammouti B, Hadda TB, Haddad SF, Boshaala A, Warad I (2013) Effect of calcination temperature on Cu doped NiO nanoparticles prepared via wet-chemical method: structural, optical and morphological studies. Int J Mol Sci 14:23941–23954
19. Al-Sehemi AG, Al-Sehemi AS, Du G, Ahmad T (2012) Synthesis and characterization of NiO nanoparticles by thermal decomposition of nickel linoleate and their optical properties. Mater Charact 68:77–81
20. Chen Da-Peng, Wang Xiao-Lin, Yi Du, Ni Song, Chen Zi-Bin, Liao Xiaozhou (2012) Growth mechanism and magnetic properties of highly crystalline NiO nanocubes and nanorods fabricated by evaporation. Cryst Growth Des 12:2842–2849

21. Jegatha Christy A, Umadevi M (2013) Novel combustion method to prepare octahedral NiO nanoparticles and its photocatalytic activity. Mater Res Bull 48:4248–4254
22. Alves CT, Oliveira A, Carneiro SAV, Silva AG, Andrade HMC, Vieira de Melo SAB, Torres EA (2013) Transesterification of waste frying oil using a zinc aluminate catalyst. Fuel Process Technol 106:102–107
23. Priya R, Stanly S, Anuradha R, Sagadevan S (2019) Evaluation of photocatalytic activity of copper ferrite nanoparticles. Mater Res Express 6:095014
24. Singh P, Abdullah MM, Sagadevan S, Kaur C, Ikram S (2019) Highly sensitive ethanol sensor based on TiO_2 nanoparticles and its photocatalyst activity. Optik Int J Light Electron Optics 182:512–518

Chapter 19

Nanoenhanced Photocatalytic Approach for Separation of Oily Emulsion from Aqueous Effluents: Recent Trends, Future Perspective and Challenges

Zaira Zaman Chowdhury, Ahmed Elsayid Ali, Arnab Barua, Rabia Ikram, Nisha Kumari Devaraj, Khalisanni Khalid, Mahfujur Rahman, Shahjalal Md. Shibly, Yasmin Abdul Wahab, Rahman F. Rafique, and Badrul Hisham Mohamad Jan

Abstract Supply of clean, freshwater for safe consumption has become a greatest challenge. Water resources are contaminated by anthropogenic as well as man-made activities day by day. Thus, it is required to utilize advanced wastewater treatment to ensure higher environmental protection and reuse the discharged water effectively. Oily wastewater is extremely toxic for aquatic organism as well as human being. Treating oil-contaminated water can be difficult because some of the microscopic compounds are hard to eliminate. The currently used methods are suitable for removing floating and suspended oily droplets from water. However, these conventional methods are not efficient for eliminating small, finely dispersed,

---

Z. Z. Chowdhury (✉) · A. Elsayid Ali · A. Barua · S. Md.Shibly · Y. A. Wahab
Nanotechnology and Catalysis Research Center (NANOCAT), University of Malaya, 50603 Kuala Lumpur, Malaysia

R. Ikram · B. Hisham Mohamad Jan
Department of Chemical Engineering, University of Malaya, 50603 Kuala Lumpur, Malaysia

N. K. Devaraj
Department of Electrical Engineering, Faculty of Engineering, Multimedia University, 63100 Cyberjaya, Malaysia

K. Khalid
Malaysian Agricultural Research and Development Institute (MARDI), Persiaran Mardi-UPM, 43400 Serdang, Selangor, Malaysia

K. Khalid
Biocomposite Technology Laboratory, Institute of Tropical Forestry and Forest Products (INTROP), University Putra Malaysia (UPM), 43400 Serdang, Selangor, Malaysia

M. Rahman
Islamic Business School, Universiti Utara Malaysia, UUM, 06010 Sinto, Kedah, Malaysia

R. F. Rafique
Department of Civil and Environmental Engineering, New Jersey Institute of Technology (NJIT), 323 MLK Blvd, New York, NJ 07102, USA

S. Garg and A. Chandra (eds.), *Green Photocatalytic Semiconductors*,
Green Chemistry and Sustainable Technology,
https://doi.org/10.1007/978-3-030-77371-7_19

colloidal oily particles. Application of membrane filtration is also restricted up to a certain extent due to fouling. In-depth research has been carried out to reduce membrane fouling. This chapter overviews the conventional techniques for elimination of oils from aqueous effluents. The chapter focuses the limitations of the conventional processes. The subsequent section of the chapter also illustrates the importance of using photocatalytic membrane. The concluding part of the chapter illustrates the future aspects of membrane technology and promising solutions associated with membrane modification methods using photocatalytic and/or hydrophilic nanomaterials and nanocomposite to enhance the permeate quality and water flux.

Keywords Nanomembrane · Oil separation · Permeate · Water flux · Photocatalyst · Hydrophilic nanocomposite

19.1 Introduction

Different industries namely petroleum, lubricant, oil refining and storage industries, transportation, food and metal industries are discharging large amount of oily pollutant in aquatic environment [1, 2]. This can adversely affect the quality of surface and groundwater. It can affect the quality of soil and can cause serious eco-toxicological hazards for environment [3, 4]. Thus, there is a crucial need for more advanced, efficient, and inexpensive water treatment and recycling techniques to separate oils from water. In order to develop these advanced techniques, it is necessary to consider different types of inorganic and organic contaminants that are dissolved into water with oily emulsions. These contaminants may involve dissolved minerals, industrial chemicals, gases, and polyaromatic hydrocarbons, dissolved organic materials mixed with oily wastewater [5, 6].

Presently, skimming [7, 8], flotation [9, 10], coagulation and flocculation [11, 12], electrocoagulation [7, 13, 14], centrifugation [4, 15], and biological methods [16] are used to eliminate oil from water. These conventional techniques are efficient for removing floating oil with a diameter greater than 150 μm or dispersed oil with a diameter greater than 20 μm. However, to remove minute dispersed, dissolved, and emulsified oily particles, it is necessary to adopt novel approaches such as membrane filtration process. Membrane separation can be combined with conventional treatment to remove oil from aqueous effluents effectively. Based on pore size, membranes can be classified into microfiltration (MF), ultrafiltration (UF), nanofiltration (NF), forward osmosis (FO) and reverse osmosis (RO), as shown in Fig. 19.1. For oil separation, mainly MD and UF are used widely.

The oily droplets will be rejected by the hydrophilic surface of the membrane and ensure water transportation to enhance the flux. The major limitations for membrane filtration process are fouling and flux reduction [18]. Membrane cleaning to eliminate the foulants is relatively an expensive process. Moreover, the membrane cleaning process can generate toxic chemicals and can reduce the lifespan of

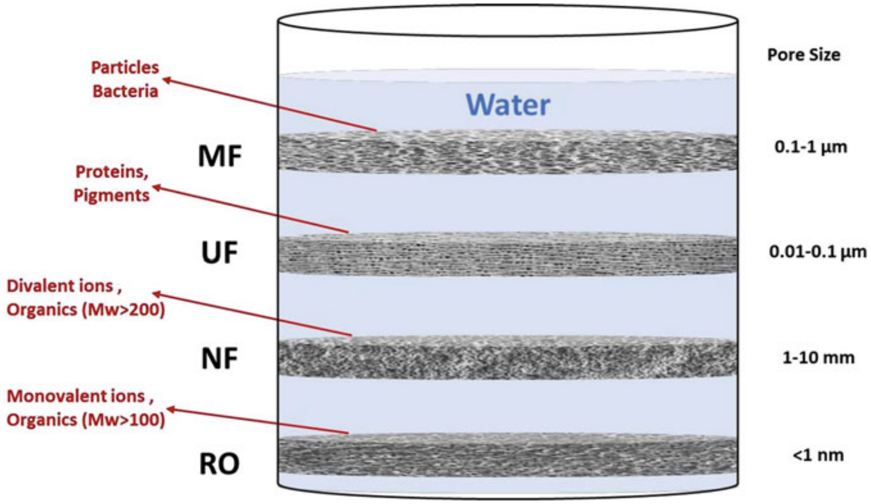

Fig. 19.1 Different types of membrane filtration process based on pore size distribution. Modified and redrawn from Ref. [17]

the membrane [19]. The aforementioned limitations can be resolved by increasing membrane hydrophilicity which in turn will reduce the fouling of membrane. Therefore, an ultra-hydrophilic membrane with nanoparticles is developed to separate oil particles from wastewater while preventing the attachment of oil droplets onto the surface of the membrane and stabilize the filtration process effectively [20, 21]. This revolutionizing approach can significantly reduce the fouling of membrane. Photocatalytic nanomaterials can be used to fabricate self-cleaning and highly hydrophilic membranes. Basically, the photocatalytic nanomaterials can decompose the organic compounds that are attached to the surface as foulants, when they are activated by natural or artificial light [22, 23].

It can convert the organic pollutants into less or nontoxic materials in presence of UV or visible light [23]. Solar light active super hydrophilic photocatalytic membranes can solve the issues related to fouling and can ensure self-cleaning of the membrane surface. Figure 19.2 illustrates the advantages and disadvantages of different types of traditional membrane filtration process, so far used for separation of oil from water.

The chapter provides brief overview on the conventional oil removal techniques. Additionally, this chapter also discusses the advantages and disadvantages of membrane filtration process for the elimination of oil from contaminated water. Mainly, the chapter focuses on the fouling issue and its connection with the flux reduction. The concluding part of the chapter describes about the future aspects of membrane technology and promising modification methods via photocatalytic and/or hydrophilic nanomaterials and nanocomposite for effective purification of oily contaminants from aqueous stream.

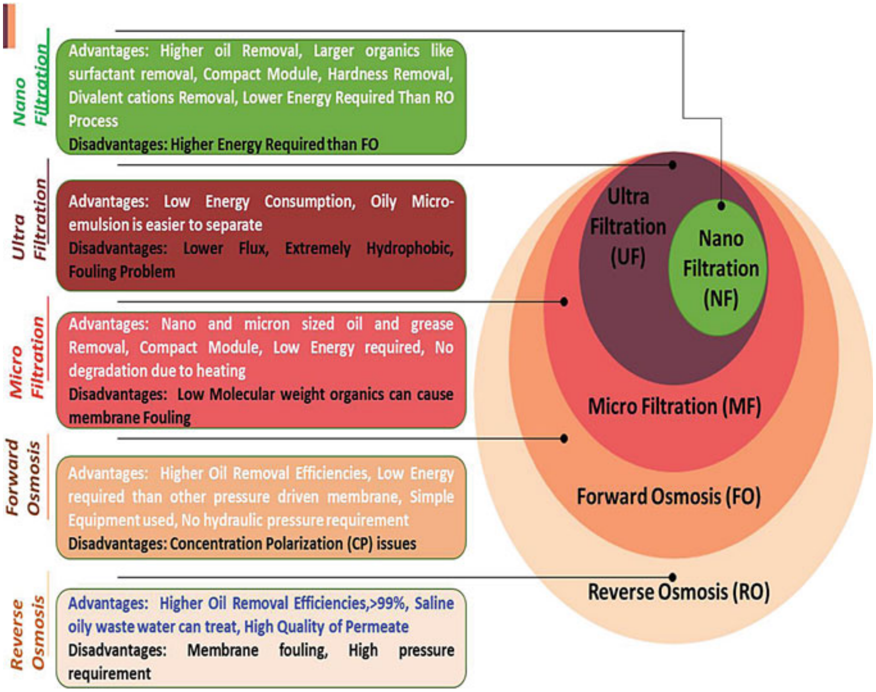

Fig. 19.2 Advantages and disadvantages of different types of membrane filtration process used for separation of oil from water

19.2 Significance of Eliminating Oily Emulsion from Aqueous Effluents

The complex mixture of oily emulsion contains droplets of oil, salts and surfactants. It also contains lot of straight chain, saturated and branched hydrocarbons, aromatic compounds, cyclic hydrocarbons, olifins, heavy metals and other sulfur and nitrogen containing compounds [6, 24, 25]. The extent of contamination of aqueous effluents by oil is dependent on the type, source, concentration, molecular weight and volume of the oil. Presence oil in water can adversely affect the fauna and flora of the aquatic environment [26]. The harmful impact of oily wastewater is caused by poisoning, coating and asphyxiation. It can cause sublethal damage and can reduce bacterial count, growth of plants, inhibit germination and root growth and can kill earthworms [27]. This affects the crop production and quality of groundwater [3, 4]. Oil contamination can affect human health and can cause damage of DNA chain. It is recognized as carcinogenic, genotoxic, and mutagenic agent which can cause autoimmune system disorder, allergies, breathing problems, natural abortion, or even cancer [24, 28, 29]. The mass population is exposed to crude oil contamination day by day. Thus, the amount of degenerative diseases was increased whereby decreased life expectancy rate was observed [24, 30–32]. The scenario highlights the importance of developing effective technique to treat oily wastewater.

Based on physical properties of the oil, it can be classified as:

(a) Free Floating Oil: The droplet size of free floating oil is around 150 μm and it can easily float over the surface water
(b) Dispersed oil: The droplet size of dispersed oil is around is 20–150 μm and they are electrically charged and form finer droplets. The constituents of dispersed oil are polyaromatic hydrocarbons and some selected alkylphenols and these types of oils are sparingly soluble in water [27].
(c) Oily Emulsion: Oily emulsion has droplet size around 20 μm and they are very stable compared to other forms [27].
(d) Dissolved oil: The transparent, water soluble oil is classified as dissolved oil and the droplet size is around 5 μm [27].

Thus, the treatment of oily wastewater needs advanced method or combination of techniques [31, 32]. Following section discusses about the treatment methods, so far used for purification of oily wastewater including pros and cons of different methods.

19.3 conventional Techniques Used for Oil Removal from Aqueous Effluents

Conventionally oil is removed from water using skimming, flotation, coagulation and flocculation, electrocoagulation, centrifugation, biological degradation, and destabilization using chemicals. Some of these techniques are explicitly used to reduce the chemical oxygen demand (COD) and biological oxygen demand (BOD) in oil-contaminated water. Biological degradation process uses anaerobic and aerobic bacteria to decompose the oily pollutants from water. These conventional techniques are not efficient enough to treat complex wastewater having multipollutants mixed with oils. The non-biodegradable organic pollutants present in oily wastewater need advanced water treatment techniques [4, 18]. On the other hand, the conventional methods have several advantages, such as the low operational cost and the relatively high efficiency in the case of biodegradation of floating and dispersed oil and biodegradable organic compounds. For effective removal, one or more conventional techniques can be combined together as a pretreatment step to deal with complex oil mixture separation from water [33]. Figure 19.3 demonstrates the pros and cons of using conventional methods for treating oily wastewater.

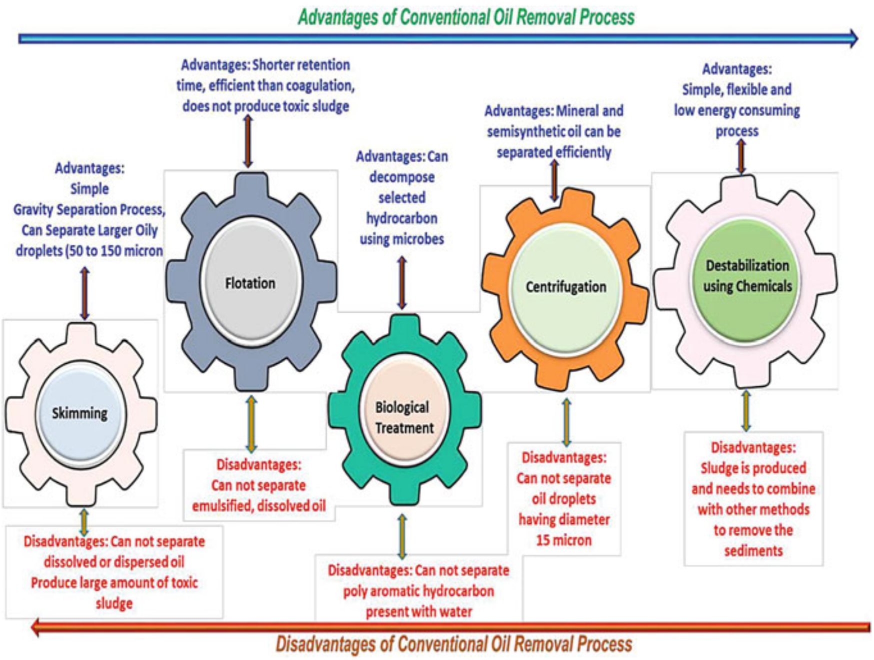

Fig. 19.3 Advantages and disadvantages of conventional oil removal process

19.3.1 Skimming

Skimming is a simple gravity separation technique that utilizes the density difference between water and oils. In this technique, oil rises at the top of the water and solid particles sink at the bottom [34]. In fact, skimming is the most adopted method to remove oil from water in different areas. American Petroleum Institute (API) uses a specifically designed separator tank which can efficiently separate oil droplets bigger than 150 μm [35]. Moreover, some separators contain parallel and/or corrugated plates, designed specially to remove droplets bigger than 50 μm [36]. The skimming technique is efficient for eliminating large oil droplets. However, this technique produces a large volume of toxic sludge at the end of the process. It is not efficient for removing smaller, dissolved/dispersed oily particles from contaminated water. Therefore, it is suggested to combine the skimming techniques with other methods to enhance the oil removal efficiency.

19.3.2 Flotation

Flotation is another method that utilizes the density difference to separate oil from water. However, the main working principle of flotation involves introducing air bubbles inside the water to adhere oil droplets with water and raise them to the surface. This occurs because of the density difference between the air bubbles and water. The conventional flotation methods are classified into three following types:

(a) Air Flotation (IAF) Process: In this process, a mechanical agitator is used to create air bubbles [9]. The high speed mechanical agitator can be combined with air injection system to enhance the bubble formation.
(b) Electro-Flotation (EF) Process: In this techniques, micro-bubbles are produced using direct current (DC) applied between two electrodes [29]. This will electrolyze the water to produce micro-bubbles.
(c) Dissolved Air Flotation (DAF) Process: In this technique, consecutively high pressure and low pressure are applied to generate bubbles inside the aqueous stream [29].

The flotation method requires shorter retention time and higher loading rate. It has higher efficiency compared to the conventional coagulation method. The flotation method does not produce toxic sludge and has a fast separation rate [9]. However, this method is not efficient enough to separate emulsified, sub-micro and nanoscale oily particles. The method requires extremely small bubbles, dormant hydrodynamic conditions, or the addition of emulsion breaking compounds before the flotation process. This will initiate discharging of extra chemicals and increase the complexity of the process. The process will be time-consuming and not cost-effective [8]. Hybrid systems are introduced to solve the challenges associated with the flotation methods. In hybrid system, coagulation and/or flocculation can be used together with IAF or DAF for effective separation of oils from water [37].

19.3.3 Centrifugation

Centrifugation is one of the oldest methods used to purify oil-contaminated water. The technique uses centrifugal forces to increase the flow rate and treatment efficiency. The centrifugation method has several advantages, such as the shorter retention time and utilization of small equipment [8, 12]. The basic principle of the centrifugation method is dependent on utilization of both buoyancy and drag forces. Briefly, the generated buoyancy force moves droplets toward the upward separator due to the density difference between the oil and water. Simultaneously, drag force (opposes buoyancy) uses terminal velocity to separate oil droplets according to size. The terminal velocity is generated when the drag force and buoyancy are equal [8].

It has been stated that centrifugation has excellent efficiency in purifying mineral and semi-synthetic oil from water [12]. The removal efficiency was above 90%

[12]. Nevertheless, the purified water can still contain up to 1500 mg/L of oil particles. Thus, it is necessary to increase the performance of the centrifugation method. Enhancing the separation efficiency of centrifugation can be achieved via enhancing the buoyancy force and/or increasing diameter of the oil droplet [8]. Therefore, other treatment methods, such as coagulation/flocculation and flotation are combined together to control the droplet diameter and increase the buoyancy force.

Hydrocyclones are also used to create centrifugal force. The structure of hydrocyclones contains simple cylindrical and conical parts and does not have any moving parts. Fluid is injected tangentially via an inlet in the upper side of the hydrocyclones. This creates a strong swirling motion and hence high centrifugal forces. During the movement of the fluid in a spiral way, dense particles are forced toward the inner wall and migrate toward the bottom of the device. Simultaneously, tiny or low-density particles move toward the upper part. Regardless of the simple structure and low cost of hydrocyclones, the process has very low removing efficiency for oil droplets with a diameter smaller than 15 μm [38]. Therefore, to enhance the separation performance, special hydrocyclones are designed in which bubbles are generated to collide with oil droplets [38].

19.3.4 Destabilization Using Chemicals

Chemical destabilization is one of the most commonly used water treatment methods that have been used for many years. The method involves the use of chemicals such as coagulants and flocculants to neutralize the surface of the particles and agglomerate them to form bulky particles known as sediments. Consequently, the larger particles can be easily removed via other techniques such as skimming or flotation. Generally, the chemical destabilization technique is preferred in many areas due to its simplicity, flexibility, and low-energy consumption [11, 39]. Some of the commonly used coagulants to remove oil from water are ferric chloride ($FeCl_3$), aluminum sulfate ($Al_2(SO_4)_3$), and polyaluminum chloride (PAC) [15, 40, 41]. These coagulants have low purification efficiency, and hence there is a need to develop more effective, low-cost coagulants. The researchers used a system where poly-zinc silicate and anionic polyacrylamide was mixed with oil-contaminated water prior to coagulation/flocculation method [42]. The system was very efficient to remove 99% of the oil [43]. It was stated that application of zinc silicate and anionic polyacrylamide will enhance the performance of coagulation/flocculation compared to conventional coagulants [43]. The presence of zinc in the system will neutralize the charges of colloidal particles in oily wastewater. Hence, it can reduce the turbidity, suspended solid contents and COD of oil-contaminated wastewater.

Electrocoagulation is introduced to reduce the amount of toxic chemicals discharged by the conventional coagulation method. In fact, the electrocoagulation method requires a minimal amount of reagent to operate, and it produces a small volume of sludge [13]. The basic principle of the method is based on in situ generations of coagulants via dissolving iron or aluminum ions electrically. These generated ions attract small particles and negatively charged droplets. Consequently, the droplets are separated by reducing the surface charges [42]. In this process, hydrogen gas is generated at the cathode while metal ions are generated at the anode. The generated hydrogen is used to float the flocculated light particles over the top of the water. Using aluminum in electrocoagulation will effectively remove oil from water and lower the energy consumption [14].

19.3.5 Biological Treatment

Biological treatment is considered as one of the best methods for water treatment. The method utilizes microbes to decompose organic contaminants and hydrocarbons in water. Examples of some microbes are genera *Nocardia Corynebacterium*, *Mycobacterium* and *Rhodococcus* [43]. The working principle of the microbes follows three processes, acetogenesis, fermentation, hydrolysis, and methanogenesis in aerobic or anaerobic conditions. During the process, the contaminants are partly and slowly converted into less harmful and stable substances [4, 44]. Although the biological treatment is a simple and cheap method, it is inefficient for removing oily pollutants. This is because oil pollutants are highly toxic materials and contain deficient nutrients and several organic substances such as aromatics, resins, asphaltenes, and saturated hydrocarbons. Consequently, the biological microbes cannot degrade all the contaminates efficiently. For instance, polycyclic aromatic hydrocarbons (PAHs) with high molecular weight are extremely difficult to decompose [16, 45].

Typically, biological treatment methods are not classified under conventional methods in different studies. Because several new technologies are conducted and published every year to develop biological treatment, especially in oily wastewater treatment. Some of the recently adopted technologies are up-flow anaerobic sludge blanket [16], membrane bioreactor [46], and biological aerated filter reactor [47]. Nevertheless, these technologies are new and cannot be used to fulfill the need for treating a large volume of oil-contaminated water for industrial scale.

19.4 Membrane Separation and Modification Process

Polymeric membranes are usually hydrophobic. The solids accumulate over the surface of the membrane which reduces the water flux [27, 48]. Different types of membrane modification were carried out to enhance the hydrophilicity of the membrane surface. Figure 19.4 illustrated different types of membrane modification process [49–51].

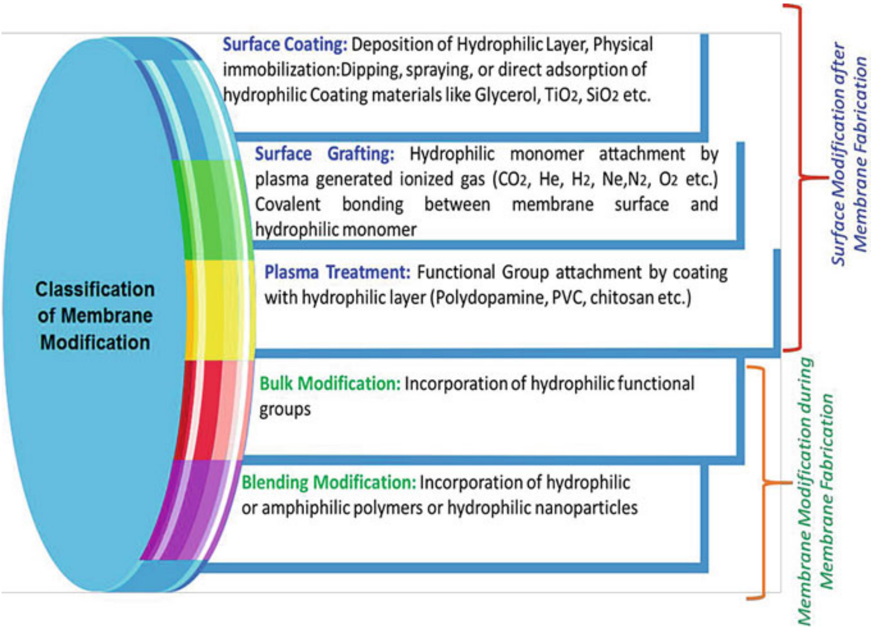

Fig. 19.4 Classification of membrane modification process

19.4.1 Membrane Surface Modification

Membrane surface can be modified via physical or chemical methods. There are several factors that are affecting the modification of the membrane surface. The major factor is the interaction between the modifiers and the membrane. Membrane modification can be carried out using coating the membrane with appropriate modifiers to enhance its overall performance. The coating materials need to be adsorbed over the surface of the membrane by electrostatic forces, van der Waals forces and hydrogen bonding. In general, the strength of these secondary forces which is responsible for adsorption is related to the characteristics of the polymer surface, and surface modifier.

Grafting and plasma treatment methods are widely used to modify the surface of the membrane as these two methods can modify the surface without affecting the bulk properties of the membrane [1, 28, 52]. Physical immobilization is a widely used technique to modify the membrane surface (Fig. 19.5a). This technique can be achieved by dipping the membrane into the colloidal solution of the modifier materials [52]. This form secondary interactions which strengthen the bonding between membrane and the modifier [52]. The surface coating process can be used to enhance the surface roughness besides the hydrophilicity of the membrane. Polyamide-based RO membrane was coated with polydopamine which reduces membrane roughness and fouling resistance during oily wastewater treatment [53].

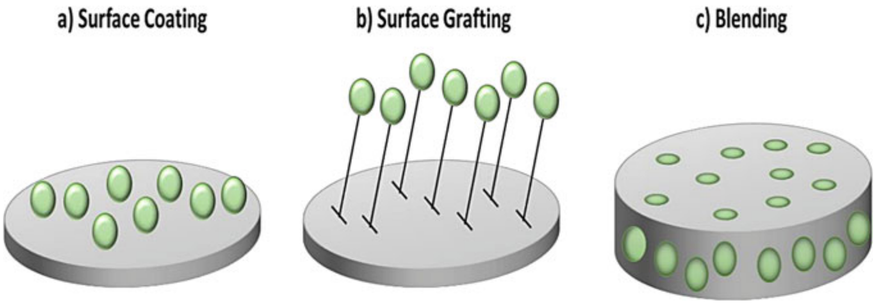

Fig. 19.5 Distribution of modifiers in membrane using different types of modification process **a** Surface coating. **b** Surface grafting. **c** Blending

Despite its significant advantages, physical adsorption and desorption have some limitations such as leaching over time [27, 28].

Surface grafting is another modification technique used to improve the performance of membrane filtration. The basic principle of surface grafting revolves around the immobilization of functional groups onto the membrane surface via covalent bonds (Fig. 19.5b, c). In comparison with physical immobilization, surface grafting enhances the stability of the membrane. PAN membrane was grafted with perfluoroalkyl groups and the flux reduction was decreased by 13% [54]. Ceramic supported polymeric UF membranes were grafted with zirconia [55, 56]. The oil rejection rate was between 45 and 65%. The system was free from irreversible fouling.

19.4.2 Blending Modification

Blending is the most preferred modification technique for enhancing membrane performance. In fact, blending modifications has some special characteristics over other techniques due to its low cost, simplicity, and versatility. Moreover, the blending method helps in controlling the desired properties of the produced membrane. Primarily, the blending technique is conducted during the phase inversion process where the polymers are transformed from liquid to solid phase. The modification materials are added to the polymer casting solution during the membrane fabrication process [20, 21].

Polyethylene glycol was blended with PSF membrane to enhance the filtration process [57]. Results revealed that the presence of polyethylene glycol had increased the membrane porosity significantly and the flux was also increased. Another research group blended the PSF membrane with other three types of polymeric materials including, PEI, PVP, and PES. The blended membranes are used to treat oil-contaminated water. The modified systems showed significant increase in flux, hydrophilicity and oil retention ratio. This is related to the obvious reduction in gel layer formation on the modified surface. PSF/PVP had exhibited the best removal performance among the different types of blended membranes.

PES membrane was blended with CA to remove oil contaminants from water. The researchers compared the performance of both pure PES and PES/CA blended membrane. The results showed that the pure PES has a stable flux of 27 L/m^2 after 60 min, meanwhile, the PES blended with CA has achieved a stable flux of 27 L/m^2 after 150 min. The increase in the flux is related to improved membrane hydrophilicity. Similar to other modification methods, blending has some drawbacks such as the limitation on the amount of particles remained on the membrane surface. This is because most of the particles are retained inside the bulk material which causes reduced efficiency of the membrane [58].

Many studies investigated the possible methods to enhance the performance and antifouling properties of the membrane in treating oily wastewater. Ceramic membranes are used lessly than the polymeric membranes. Ceramic membranes are difficult to modify to target certain contaminants from wastewater. Table 19.1 summarizes the list of polymeric membrane which has been used successfully used to eliminate oil from water.

Table 19.2 summarizes the list of inorganic membranes which have been used effectively for treating oily wastewater. Nanoenhanced membrane filtration process involves the application of certain nanomaterials for the membrane fabrication

Table 19.1 Removal of oil using polymeric membrane

Polymeric membrane	Modifiers	Initial concentration	Rejection % of oil (%)	Residual oil (mg/L)	Flux (L/m^{2}h)	Ref.
PS	Nil	1000	>99.9	<20	–	[59]
	Nil	300	87	30	–	[60]
	PVP & PEG[1]	–	>90	<10	–	[61]
		7	100		65 at 31°	[62]
PES	Pluronic F127	–	–	–	83	[63]
–	PVP	–	98.2–99.5	–	–	[64]
–	PVP	78	99.7	2	84.1	[65]
–	Cellulose acetate/PEG	–	88	–	27	[47]
Polyacrylonitrile	PDA/HPEI[2]	–	−98.5	–	1600	[66]
Polyamide	–	10–40	>96	–	624	[67]
PVDF	Nil	10,000	Permeate is oil 77	2300	–	[68]

Table 19.2 Removal of oil using inorganic membrane

Inorganic membrane	Initial concentration of oil (mg/L)	Rejection (%) of oil	Residual oil (mg/L)	Flux (L/m^{2}h)	Ref.
α-Al_2O_3	250	98–99	3–5	30–40	[69]
α-Al_2O_3	2000	96–98	40–80	163	[70–72]
α-Al_2O_3	75	95	4	–	[73]
γ- Al_2O_3 on α-Al_2O_3 support	Refinery waste	–	–	113	[74]
ZrO_3	6000	99.8	9–11	120–170	[75]
ZrO_2-TiO_2	10,000–24,000	79–91	–	–	[76]
TiO_2	32–5400	99.5	–	–	[77]
TiO_2	333	98	8.3	85 at 20 °C, 210 at 70 °C	[78]
TiO_2 on mullite support	200	92–97	6–16	–	[79]
α-Al_2O_3 and mullite	250–3000	84–94	–	58–105	[80]

process. It is assumed that nanomaterials will revolutionize the water treatment technologies, especially for purification of oil-contaminated water.

19.4.3 Nanoenhanced Membrane Modification

In the last years, nanomaterials have been employed intensively in water treatment, due to their unique physiochemical properties. Nanomaterials are also involved in the modification processes for a membrane to improve the filtration of oily contaminants [81–83]. Modification of membrane can change the porous texture of the membrane. Moreover, nanomaterials are used to ensure a uniform coating and control the fouling problem associated with the membrane via increasing the hydrophilicity as well as water flux and rejection rate of the contaminants. Incorporation of nanomaterials can enhance the stability, porosity and charge density of the membrane [84]. The type and amount of nanomaterials used for membrane modification need to be optimized carefully. Furthermore, the modification methods also can control the amount of added nanomaterials [84–86]. It was revealed that a small amount of nanomaterials can enhance the membrane hydrophilicity, but it can reduce the pore size. On the other hand, high content of nanomaterials can reduce the pore size dramatically and increase the agglomeration which results in blocked pores and lower treatment efficiency [55, 87–89]. Nanomaterials grafted or coated over the surface do not alter the membrane structure significantly. But blending with nanomaterials can increase the porous texture of the membrane [81, 84, 85, 90]. Oil separation was carried out using zirconium oxide coated Al_2O_3—ceramic membrane [91]. The study revealed that the thickness of the fouling layer was reduced due to the presence of ZrO_3 nanolayer. Moreover, the nano-coating has increased the oil repulsion which results in a simple washing process for oil droplets and improved the flux recovery. The hydrophilicity of membrane is also improved with the addition of nanoparticles.

SiO_2 nanoparticles were used to functionalize PSF membrane which improve the water flux during treating oil-contaminated water. In their system, the water flux has increased from 1.08 to 17.32 L/m^{2}h [92]. The antifouling properties increased with the amount of added SiO_2, which made the modified membrane easier to wash. To increase the oil removal performance of the membrane, the researchers blended CuO_2 nanoparticles with PES membrane, and they found that the permeability, pore diameter and antifouling properties increase with the increase in the amount of added nanoparticles [93]. Earlier, oleic acid solution was used to modify the surface of the blended PSF/ZnO membrane [94]. Their results indicated a significant increase in the hydrophilicity, flux rate, and permeability. However, increasing the amount of the nanoparticles above the optimum limit result in a sever agglomeration and reduce the membrane performance. Alumina nanoparticles were blended with PVDF membrane and the water flux was improved to 100% [95] (Table 19.3).

Table 19.3 Oil Removal results using nanoenhanced organic/inorganic hybrid membranes

Membrane structure	Modifiers	Feed oil concentration (mg/L)	Oil rejection (%)	Residual oil (mg/L)	Water flux (L/m^{2}h)	Ref.
PES	MnO_2	1000	−100	–	Good recovery	[96]
PVDF	Al_2O_3	15.5	98	<1	160	[97]
	TiO_2	–	98.8	–	82.5	[96]
	TiO_2 and PVP[1]	250	94	15	72	[98, 99]
	Silane/TiO_2	–	99	–	−350 to 600	[100]
	TiO_2/Al_2O_3	200	–	<50	70–160	[53, 101]
	SiO_2	–	–	–	2500	[102]
	Fluorinated SiO_2	Cooking wastewater	–	–	18–20	[103]
Cellulose acetate (CA)	Clay	200	93	14	–	[104]

PVP[1] is polyvinylpyrrolidone

19.5 Fouling Challenges for Eliminating Oils from Water Using Membrane Separation Process

Membrane fouling is the accumulation of solid contaminants on the surface and pores of the membrane during the filtration process. It is caused by inorganic solids, organic colloids and macromolecules, microorganisms, and soluble inorganic compounds [28, 52]. It is classified into organic fouling, inorganic fouling, scaling, and biofouling. Fouling is caused by the accumulation of oil droplets while scaling is caused via precipitation of salts, hydroxides over the surface during oil separation [45]. The concentration and physiochemical properties of the feed water can reduce or increase the fouling. Moreover, the membrane characteristics such as the hydrophilicity, the roughness of the surface, and charge properties also can alter the rate of fouling [22, 23]. The ambient conditions of the process can influence the formation of the fouling layer. This includes temperature, flow velocity, applied transmembrane pressure, and recovery rate [54, 56]. The mechanism of fouling is affected by the electrostatic and van der Waals forces between the contamination particles and the membrane surface.

Temperature, ionic strength, oil droplet size, pH value, and concentration of the oil can affect the interaction between the foulants and the membrane surface. In case of removing oily contaminants, oil droplets can easily form a hydrophobic layer on the surface of the membrane to reduce the water flux. This results in reducing the life span of the membrane and complicate the cleaning process. Economically, the flux reduction will result in higher energy consumption and increase the total treatment cost. Thus, enormous studies were conducted to eliminate the challenges using nanoenhanced photocatalytic membrane for removal of oils from water.

19.6 Significant Application of Photocatalytic Membrane, Degradation Mechanism and Performance Evaluation

The membrane separation process to filter oil from water has many limitations, such as the high operational cost, complexity, and the need for periodical cleaning processes. Usually, membranes are cleaned using chemicals that are discharged into the environment and cause secondary water pollution. The cleaning chemicals reduce the lifespan of the membrane and increases the total cost of the filtration process [19]. Therefore, researchers are adopting a new approach where hydrophilic photocatalytic nanomaterials are used to develop and enhance the self-cleaning and antifouling properties of the membranes. Photocatalytic membranes have great potential to decompose the fouling contaminates into nontoxic substances. Hence, it is an eco-friendly approach because it does not require any discharging of chemicals into the environment and it can use solar light irradiation after band gap modification to degrade the organic contaminants [22, 23].

Photocatalysts are synthesized from semiconductor metal/metal oxide that can be activated via photons interactions. In order to activate the photocatalyst, photons need to have sufficient energy to create holes (h+) and electrons (e-) [105]. The basic principle relies on the activation of electrons to jump from the valance band (VB) to the conduction band (CB). Due to presence of solar or UV light, electrons gain energy and transfer from VB to CB. Simultaneously, when electrons move to CB, positive charge holes are generated in the VB. Thus, the process creates electron/hole pairs. These photogenerated pairs are used to oxidize organic contaminants and reduce the electron acceptor like surface adsorbed molecular oxygen. Usually, the electron/hole pairs are recombined to produce heat within a very short period of time −10 to 100 ns [106]. The photocatalytic degradation will decompose the organic contaminants into nontoxic materials such as water, carbon dioxide, and inorganic ions like nitrate and sulfate. Photocatalysis mechanism of a semiconductor is illustrated by Fig. 19.6 [106].

In order to complete the photocatalytic reactions, the produced oxidative radicals ($\bullet OH/OH^-$, and $O_2/O_2\bullet^-$) must have a redox potential within the bandgap of the given photocatalyst ($E^o\bullet OH/OH- = 2.8$ eV, $E^o\bullet O_2/O_2- = -0.16$ eV). Nanomaterials with lower bandgap require less energy to transfer the electrons from VB to CB [107]. Therefore, it is necessary to choose a nanomaterial with good photocatalytic properties. It is preferred to use a material with modified bandgap using composite semiconductor-based photocatalyst having slower electron/hole pairs recombination rate (Fig. 19.7) [106].

Recently, photocatalytic nanocomposites are integrated with membrane separation process. Nanocomposites or hybrid photocatalysts are a combination of two or

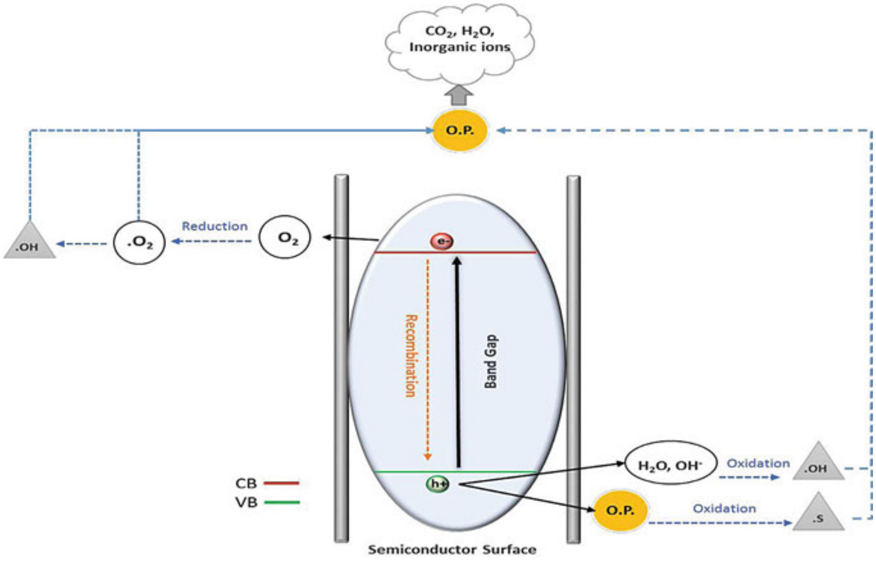

Fig. 19.6 Photocatalysis mechanism of a semiconductor photocatalyst

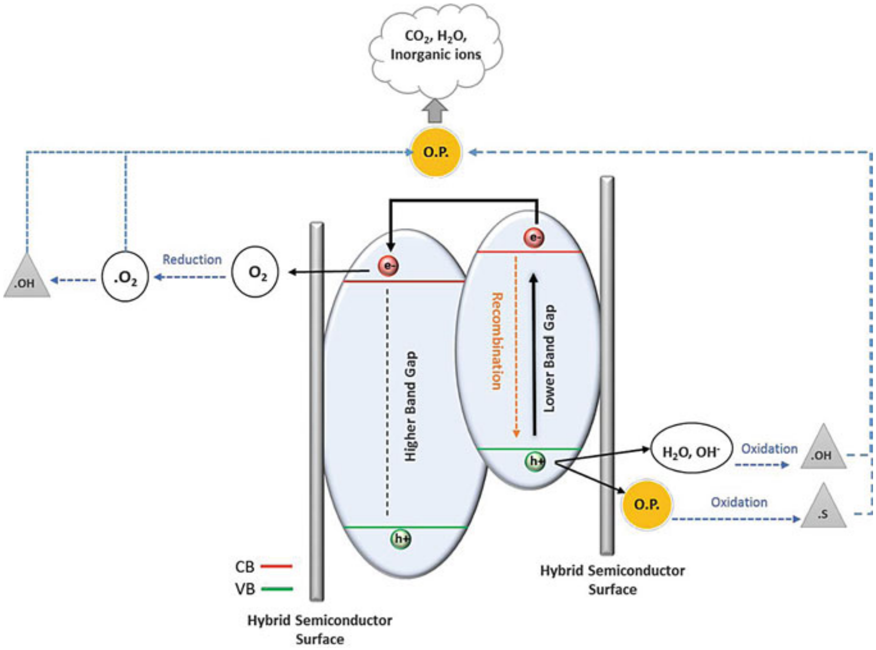

Fig. 19.7 Photocatalysis mechanism of a composite semiconductor photocatalyst

more semiconductor materials. The use of nanocomposites has enhanced the photocatalytic activity of the modified membrane-based treatment system. When photons interact with the composite, charge separation, only takes place inside the material with a lower bandgap. Consequently, the electrons from the material with lower bandgap transfers to the CB of the materials having higher bandgap. This reduces the number of electron acceptors, and oxidation occurs on the surface of the first nanomaterial [108]. Hybrid photocatalysts can be activated under wide range of wavelengths. Additionally, the system can separate the electron/hole pairs effectively. Integration of hybrid photocatalyst with the membrane can enhance the filtration process significantly [109].

As mentioned in the previous sections, photocatalytic wastewater treatments are considered as advanced oxidation processes (AOPs). In this regard, the use of photocatalysts in membrane reactors (photocatalytic membrane reactors) can be achieved in two different methods. The first method relies on the immobilization of photocatalysts onto the membrane surface (Fig. 19.8a), while the second method uses the suspension of photocatalysts [110] (Fig. 19.8b, c).

Both types of Photocatalytic membrane reactors are used for degradation of organic contaminants from water. However, the suspended photocatalysts have exhibited a greater active surface area and hence has high degradation efficiency compared to immobilized catalytic membrane reactor system. Nevertheless, the suspended photocatalysts reactor has several limitations, such as fouling and flux

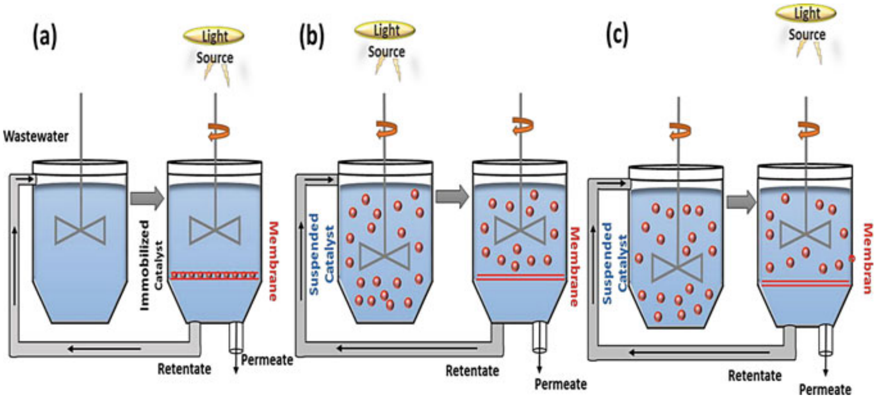

Fig. 19.8 Photocatalytic membrane reactor **a** The catalyst in immobilized in/on the membrane; **b** and **c** the catalyst in suspension form; in (**b**) light source over catalyst (**c**) light source is over membrane

reduction [106]. On the other hand, immobilized photocatalysts can show superior performance due to their high hydrophilicity. One of the main factors in selecting proper photocatalytic materials for membrane fabrication is its' stability. It is important to use a material with excellent stability when exposed to UV irradiation under harsh environment. Therefore, more studies focus on developing a UV-resistant photocatalytic polymeric and ceramic membrane [111].

Recently photothermal materials are used with membrane to enhance its' performance. Photothermal materials have two significant advantages. They can use light to adsorb photons, and they also can generate heat to enhance the decomposition rates. Compared to photocatalysts, photothermal materials can use a wider range of the solar spectrum, where photocatalysts are limited to their bandgap. Generally, the photothermal materials used in water treatment have higher solar absorption capability [112, 113]. CO_3O_4 and CuO are more frequently used photothermal catalyst to degrade the organic compounds [114]. Nanocarbons are frequently used as photothermal catalyst [115]. Photocatalyst or photothermal catalysts-based nanocarbon (Graphene, Graphene oxide, reduced Graphene oxide, carbon nanotubes) composites have different unique features such as the large surface area, high optical absorption rate, the ability to convert light to heat, great thermal and mechanical stability, and low density [115].

Different types of polymeric membranes (CA, PVDF, PTFE, PP, PES, PAN, PS, and PC) were modified using nanomaterials [116]. The results revealed that PAN, PTFE, PVDF-based composite membranes were stable under UV light for more than 30 days. The addition of nanomaterials improved the degradation performance of the membrane. The researchers found that the PVDF and PTFE membranes have higher stability under UV irradiation. The immobilization of photocatalyst over the membrane surface is dependent on several factors such as the type of membrane and reactor, filtration conditions, and the characteristics of the applied photocatalysts.

Several studies focus on membrane stability under UV light initiated oxidative conditions [117–119]. They examine the stability using different types of analyzing techniques, such as measuring the flux and rejection rate and observing the morphological features of the membrane using SEM, FTIR, or XRD analysis. ZnO blended PVDF membranes were used for water treatment [117–119]. The membrane exhibited great stability under UV light for several repeated cycles (15 cycles). Surface modified photocatalytic membranes were stirred with water and the turbidity was measured. Turbidity tests were carried out to confirm the stability of immobilized TiO_2 nanoparticles [118]. Blending modification causes leaching of nanoparticles during fabrication stage of the membrane. Thus, membrane modified by blending shows least leaching during the operation of the photocatalytic membrane. Compared to grafting and coating, blending modification is better as it is more stable during the cleaning process also [119].

The stability of photocatalytic membrane should be observed for longer period under UV light, oxidative environment, and in presence and adherence of oily droplets over the membrane surface. Until recently, different types of nanophotocatalysts including titanium dioxide (TiO_2), zinc oxide (ZnO), copper oxide (CuO_2), tin oxide (SnO_2), zinc sulfide (ZnS), tungsten trioxide (WO_3), and cadmium sulfide (CdS) were used for water treatment. Among these materials, TiO_2 is the most commonly used nanoparticles applied for membrane modification. This is due to its' low cost, high chemical stability, abundancy, and photocatalytic properties [106].

19.6.1 TiO_2-Based Photocatalytic Membrane

The special photocatalytic and hydrophilic properties of TiO_2 make it a good candidate for modifying membrane surface. Different researches examined the stability of the modified membrane under UV irradiation. Previously performance of ten types of polymeric membranes was compared. The results revealed that TiO_2 improve the UV resistance for PAN, PTFE, and PVDF membranes. Moreover, the authors analyzed the morphologies of TiO_2 coated membranes and studied the change in flux rate. Similarly, the stability of some commercial PSF + PP, fluoride + PP, and PAN-based membranes modified with TiO_2 was investigated under UV light. Blending TiO_2 with the PES membrane enhances the porous structure of the membrane and the membrane was fouling resistant [120].

Earlier TiO_2 was coated and blended with three different types of membranes polymeric (PAN, PSF, PVDF) membranes [121]. The researchers used the membrane in a bioreactor system to filter activated sludge. They found that presence of photocatalyst can enhance the antifouling properties to give better filtration performance. Moreover, the result revealed that TiO_2 deposition has better antifouling effects compared to blending TiO_2 with the membrane.

Earlier the performance of TiO_2 coated membrane was also investigated for separation of whey protein [19]. As fabricated membrane showed better photocatalytic and hydrophilic properties with enhanced flux. However, flux declination will take place if the loading of photocatalyst is not carefully monitored. TiO_2 modified membrane is used widely to treat different types of wastewater such as industrial waste, disinfection, dairy, textile, and agricultural wastewater. However, TiO_2 modified nanomembranes are introduced recently for purification of oil-contaminated wastewater.

The performance of TiO_2 coated ceramic membrane was observed for treating oily wastewater [122]. The hydrophilicity of the membrane enhanced the water flux to 150%. A further study used TiO_2 coated dynamic ceramic membrane to treat engine oil [123]. The physiochemical structure of the membrane inhibited pore blocking and thereby showed better antifouling properties. Three different types of glass fiber were coated with TiO_2 and were used for oil filtration [79]. Simple cleaning processes was used to clean the surface of the modified glass fiber, and it could be washed several times. The modified filtration membrane was highly hydrophilic and could reject oil efficiently. TiO_2 coated stainless-steel meshes was fabricated using a spray coating process [124]. The filtration process was driven by gravity. Thus, it was less energy-consuming process. They found that the oil removal is affected directly by the superhydrophilic and superoleophobic properties of the membrane.

TiO_2 was grafted onto PVDF membrane to fabricate hydrophilic membrane [122]. The contact angle of the membrane decreased from 123° to 32°. The modified membrane showed great antifouling properties. Certainly, the system required simple washing procedures to prevent flux declination. The stability of the membrane was examined under saline and acidic condition, but not under alkaline environment. Earlier TiO_2 coated PVDF membrane was used to treat oily water. Nevertheless, the membrane showed almost 100% water flux after washing the photocatalytic membrane with distilled water. The presence of salts affected the stability of the photocatalytic membrane. As the concentration of the salt was increasing, the photocatalytic coating was destabilizing which limits the application of the photocatalytic membrane. Same research group also prepared TiO_2-deposited PAN membrane to filter oily water. PVDF mixed matrix membrane was blended with 1D PANI/TiO_2 nanofibers for separation of oil from water [122]. The increase in the nanomaterials reduced the water contact angle. Meanwhile, the flux increased from 80 to 132 L/m^2L. The antifouling tendency of the membrane was increased with 99% oil rejection efficiencies. TiO_2-based photoreactor was used to oxidize the petroleum refinery wastewater [53]. The solution was later on filtered using PVDF membrane blended with a multiwalled carbon nanotube (MWCNTs) to separate oxidized particles and photocatalyst from water. The photoreactor decomposed over 80% of the contaminated water under UV light after six hours. The results of this research showed that photocatalytic membrane reactors have great potential in degrading oil containing hydrocarbon pollutants from wastewater.

TiO_2 nanoparticles are used for membrane modification due to their special characteristics such as the abundancy, low cost, eco-friendly and photocatalytic properties. Recently, many researchers have stated that TiO_2 also can be toxic for the environment if it is leached out from membrane surface. TiO_2, can be well activated under UV light to degrade the oil from water On the other hand, TiO_2 nanomaterials exhibit poor degradation efficiencies for crude hydrocarbon containing oil under solar irradiation [125]. Application of UV light source with membrane requires more operational cost. Therefore, attention has been drawn toward developing visible light active photocatalytic materials to be used for membrane modification [19] This can be achieved by doping TiO_2 with other nanocluster metal/metal oxides prior to blending with the membrane. The bright future of oil removal from the aqueous effluents is dependent on the development of solar light active superhydrophilic photocatalytic membrane. These types of membranes will have great antifouling properties, easier cleaning process, and will not require energy as it will use solar light irradiation.

19.6.2 Novel Metal/Metal Oxide-Based Composite Photocatalytic Membrane

In recent years, several studies have focused on the development of highly efficient photocatalysts for pollutants degradation. Generally, there are two approaches for developing photocatalysts; the first is to reduce the recombination rate of electrons and holes, and the second approach is to increase the visible light activity [106]. The first approach can be undertaken via preparation of composites materials, which will have high photon utilization efficiency. The second approach is to modify the photocatalyst to reduce its band gap value. In that case, it will be sensitive under solar light irradiation [106].

Halloysite nanotube (HNT) and/or CNTs are used as composites materials to improve the photocatalytic efficiency of TiO_2. Presence of HNTs and CNTs can block the recombination of electron and holes produced under UV light [1]. Incorporation of tungsten trioxide (WO_2) with TiO_2 can reduce the recombination rate of electrons/hole pairs and can improve the photocatalytic and visible light activity of TiO_2 [126, 127].

Recent studies stated the possibility of improving the photocatalytic properties and lifespan of TiO_2 by doping it with zeolite, silica (SiO_2), clay, and metals like copper (Cu), gold (Au), silver (Ag), platinum (Pt), and palladium (Pd) [108, 127–130]. Doping of TiO_2 with other metal oxide nanoparticles can also enhance the decomposition of organic contaminants under UV light. Some of the popular and widely used metal oxides are ZnO, SiO_2, CdS, and zirconium dioxide (ZrO_2) [185]. Recently bismuth vanadate (BiO_2) was used to synthesize Ti-free semiconductor photocatalyst which was efficiently used for water treatment [131].

As mentioned in the previous sections, carbon-based materials are used widely to improve the general performance of membrane filtration. Reduced graphene oxide (rGO) is recently used to enhance the light absorption and contaminates adsorption of the photothermal reactor. rGO has many advantages, such as the high photothermal activities and the ability to maintain and redirect photogenerated electrons. Moreover, rGO is also used with TiO_2 for composite fabrication. This can improve membrane stability, photocatalytic activity, optical properties, and hydrophilicity [132, 133]. The stability of TiO_2-based membrane is one of the main concerns during the modification process [134]. Despite the outstanding performance of the above-mentioned studies, there are still several disadvantages related to these modified membranes. It is essential to study the stability of the photocatalytic nanocomposites inside the membrane matrix. Furthermore, it is important to observe the durability of the membrane under UV irradiation.

19.7 Comparative Performance Evaluation for Using Different Types of Membrane

The performance shown by different types of polymric, inorganic and hybrid organic/inorganic membranes is discussed in previous section. The advantages and disadvantages of ceramic-based membranes are summarized in Fig. 19.9.

The performance of a ceramic-based (Al_2O_3/ZrO_2) membrane was compared with a polymeric membrane (poly(vinyl chloride) or PVC) for treating oily wastewater [135]. Fabrication of polymeric membrane involves less cost. However,

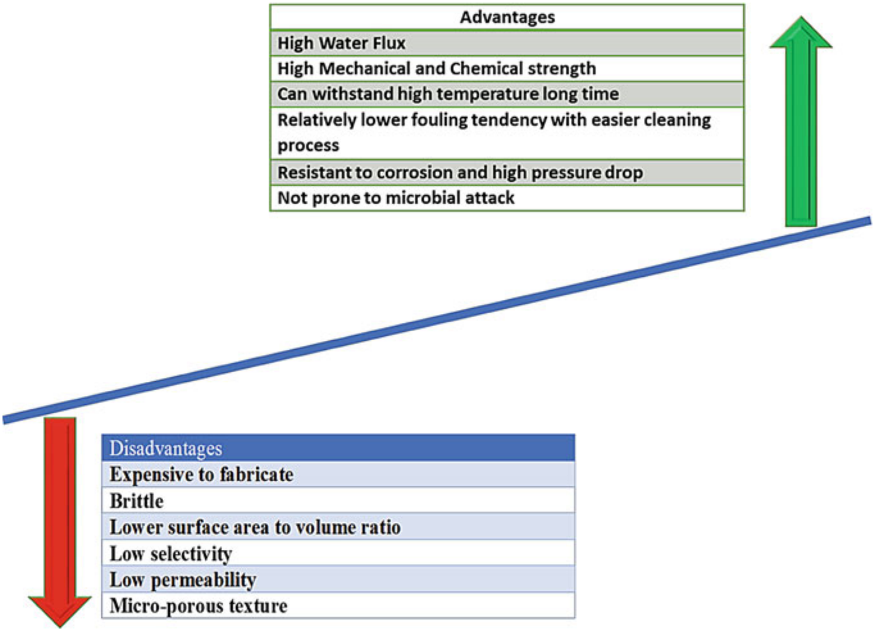

Advantages
High Water Flux
High Mechanical and Chemical strength
Can withstand high temperature long time
Relatively lower fouling tendency with easier cleaning process
Resistant to corrosion and high pressure drop
Not prone to microbial attack

Disadvantages
Expensive to fabricate
Brittle
Lower surface area to volume ratio
Low selectivity
Low permeability
Micro-porous texture

Fig. 19.9 Advantages and disadvantages of ceramic membranes

superior performance was exhibited by ceramic membrane as it showed higher oil removal efficiencies with fouling resistant properties [136].

Another study used four types of ceramic membrane (Al_2O_3, ZrO_2, TiO_2 and SiC) and compared their performance with polymeric PES/PVP-based microfiltration (MF) membrane [137]Fouling was reversible and showed the order PES/PVP $\sim$ Al_2O_3 $\sim$ $ZrO_2 > TiO_2 >$ SiC. Irreversible fouling tendencies were shown by following membranes in the order of: PES/PVP > $ZrO_2 > Al_2O_3 > TiO_2 >$ SiC. Fouling is a major limitations in membrane separation process. It was highlighted that very stable membrane structure is needed to resist fouling and withstand the cleaning procedure of the membrane [138]. The phenomenon of fouling would greatly reduce the percentage of oil removal [139].

Earlier fouling mechanism was discussed by researchers and it was concluded that fouling in MF membrane proceeds by four stages—initially standard blocking, secondly whole structure blocking, intermediary blocking, and lastly cake layer deposition (Fig. 19.10). The declining trend of the flux can be predicted using the cake filtration model [140]. Enhancement of pressure from 0.5 to 4 bar can significantly decrease the porous texture of the cake layer and it was decreased from 25.7 to 15.0% [140].

Polyamide thin film UF membrane was used for treating fuel oil and it was found that fouling mechanism followed cake filtration model. Multiple components are presents in oily feed and the colloidal features of the oil make the fouling process more complicated [141]. Four different process of fouling took place simultaneously and block the pores completely during the fuel oil treatment. The mechanism of fouling was well explained earlier using Polysulfone (PS) and cellulose-based UF membranes [137]. At the early stage, cake formation took place, later the growth of cake layer was increasing and the layer was compressible. In that case, high pressure was needed. Application of high pressure can enhance fouling rate [137]. For higher pressure, the flux was around 15 L/m^{2}h. If the operating pressure

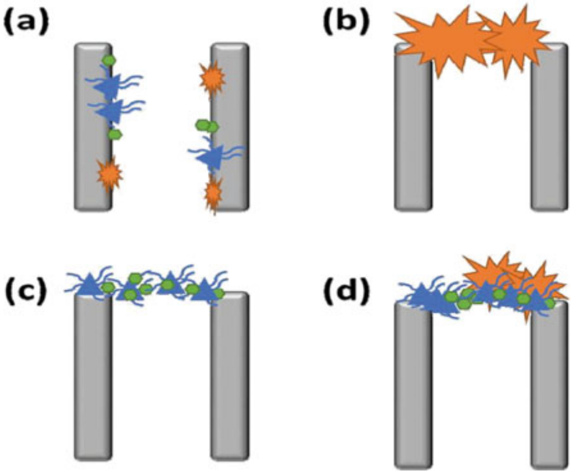

Fig. 19.10 Stages of Membrane Fouling **a** standard blocking, **b** complete blocking, **c** intermediate blocking and **d** cake layer formation

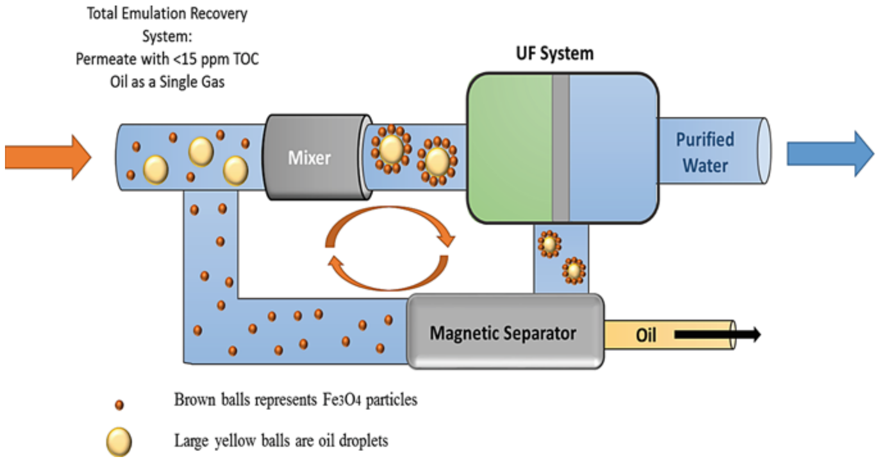

Fig. 19.11 Separation of oil using pickering solution to mitigate fouling. Redrawn from Ref. [142]

was kept at slightly lower level, then the fouling rate was relatively lower and in acceptable limit.

Application of pickering emulsion can decrease fouling during oil separation using UF membrane (Fig. 19.11) [142]. Magnetic nanoparticles having diameter less than 600 nm were mixed with poly wastewater to obtain pickering solution. Presence of nanoparticles over the oil droplets inhibited the contact of oily molecules with membrane surface. This will prevent fouling. The smaller pore size of UF will allow the transportation of water while rejecting the oils to pass through it.

19.8 Future Perspective and Challenges for Using Photocatalytic Membrane

Application of TiO_2 to some extent was not successful enough and the drawbacks are listed in Table 19.2. However, application of binary nanocomposites or some novel photocatalytic composites active under visible light can considerably increase the water flux, alleviate the fouling, and improve the rate of rejection and degradation ratios with time.

For using different types of photocatalytic membranes for treating oily wastewater, following crucial factors should be considered:

(a) Due to the interaction between the membrane surface and the nanocomposite, the properties of the fabricated membrane can be completely different in terms of their hydrophilic properties, distribution of pores and contact angle, etc.

(b) Before incorporating any types of photocatalyst with the membrane, the interaction mechanism between the membrane and the photocatalyst needs to be carefully analyzed. It was reported also that nanocomposites itself also can aid in fouling and affect membrane performance adversely.
(c) The size of oil droplets, ionic strength, concentration, properties of the oil can significantly affect the water flux, type of fouling and elimination rate of the pollutant.
(d) The final photocatalytic degradation and filtration efficiencies are dependent on process condition-like temperature, pH, contact time, transmembrane pressure, periodical cleaning and replacement of the membrane.
(e) The doping of photocatalyst with the membrane matrix needs to be optimized or else it can endanger the performance of the membrane by decreasing the hydrophilicity, widening pore size, reducing water flux and rejection rate, enhancing the depthness of the fouling layer, etc.
(f) Until now, in most of the studies; the performance of the photocatalytic membrane was characterized by using methylene blue dye, owing to its fairly fast degradation rate and it can be measured using a simple analytical tool-a spectrophotometer. In most of the studies, the dye degradation using photocatalytic membrane was around 90% [143, 144].
(g) Synergistic impact of photocatalysis and membrane separation process has some technical challenges associated with light type (UV or visible), distance between light and membrane surface, position of light source, wavelength, contact time for efficient degradation of organic pollutant, etc., which needs to be resolved before practical filtration operation [143, 144].
(h) Hydrophilicity and oleophobicity of the properties of the membrane need to be studied carefully for fouling mitigation

    (ii) Rejection of oil droplets by the membrane with high permeate quality,
    (ii) Selectivity in separation to separate oil from water and
    (iii) Prevents the accumulation or adhesion of the oily droplets over surface of the membrane to reduce the pore clogging and enhance the transportation of water [145]. The foulants particles from the dynamic membrane containing hydrophilic layer can be removed by back washing with water as illustrated by Fig. 19.12.

In most of the research, photocatalysis was carried out prior to membrane filtration or filtration by membrane followed by secondary stage of photocatalytic degradation and cleaning process [152]. In-depth research is needed which can combine photocatalytic degradation and self-cleaning of the membrane surface instantaneously.

(a) The stability of the membrane in case of treating oily wastewater under UV, visible light, state of oxidative environment, pressure drop and adherence of the oily particles needs to be considered in situ without making general conclusion about the applied constituent materials of the membrane and the nanomaterials itself.

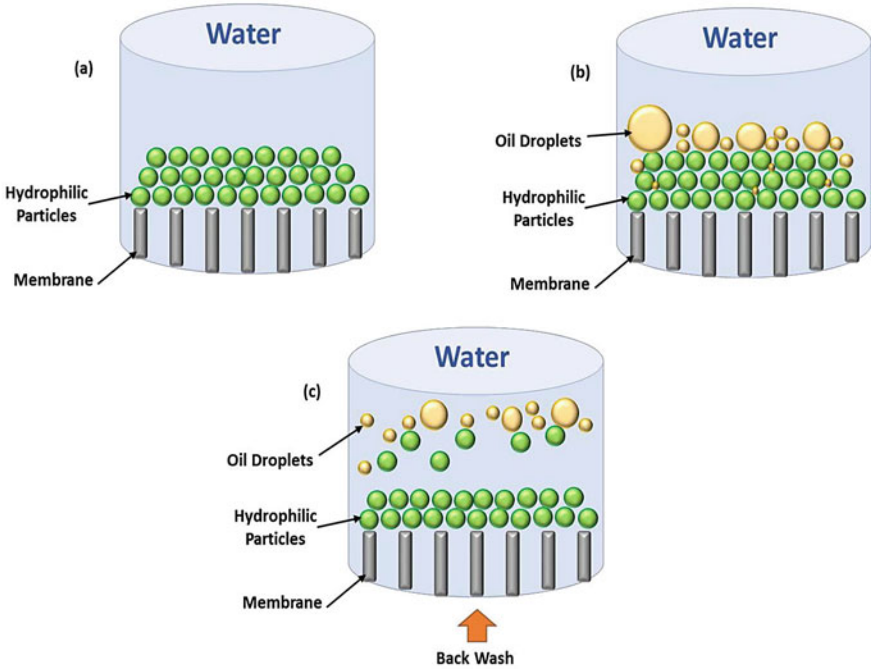

Fig. 19.12 **a** Dynamic membrane having hydrophilic layer. **b** Hydrophilic membrane trapping the oil accumulation and rejecting oily molecules. **c** Back washing using water to remove foulants

(b) The application of photocatalyst depends on the type of membrane matrix, type and design of the reactor, process conditions, etc.
(c) Earlier studies reported better antifouling and/or self-cleaning characteristics with desirable permeate quality and rate, enhanced photocatalytic activity (under UV and visible light), and superior stabilities under laboratory scale setup.

Nevertheless, even after several encouraging achievements; still lot of challenges required to be overcome for the large scale application of photocatalytic membrane for oil separation. Future studies need to emphasize these points and carefully considered to resolve those obstacles:

(a) Nanomaterial leakage of photocatalyst from the membrane surface after long-term operation needs to be investigated.
(b) For durability studies of the photocatalytic membrane, standardized protocols are necessary to make comparative evaluation of the process. Long-term stability tests need to be carried out under practical conditions.

(c) For successful implication of the method, cost analysis for membrane fabrication as well as operational expenses needs to be summarized for large scale application.
(d) Lastly, operational challenges associated with membrane cleaning needs to consider. Cleaning membrane surface with solar light can be a promising solution in that case.

19.9 Conclusion

Presence of oily emulsion in water can endanger aquatic organism and well as human beings. Careless discharge of oily wastewater can damage environment. Thus effective, advanced technique is needed to eliminate the oily emulsion from aqueous effluent. To comply with the stringent discharge limits, the conventional methods (skimming, centrifugation, chemical destabilization, flotation, and biological treatment) are not efficient enough, as those methods failed to eliminate submicron and nano-micron, colloidal, emulsified droplets of oils.

Compared to conventional methods, membrane filtration process is considered as a promising alternative to treat oily wastewater. Several types of membrane, mainly UF, NF, MF and RO has been utilized to remove oils from aqueous effluents. The constituent materials of the membrane were also varied from polymeric to inorganic-ceramic membrane to meet the required specifications. However, the phenomenon of fouling with reduced water flux is still a major limitation of membrane separation process.

In order to improve the membrane performance, surface modification or incorporation of photocatalytic nanoparticles in controlled about is necessary.

Integration of photocatalyst will enhance membrane hydrophilicity. This will enhance the water flux and degradation rate of pollutant. Photocatalytic membranes are fouling resistant and have self-cleaning aptitude which made them superior than the other conventional membranes. The synergistic effect of photodegradation and antifouling will reduce periodical replacement and cleaning of membrane resulting less expenses for membrane plants.

Until recently TiO_2 has been widely used as photocatalytic membrane for oil separation. However, it can operate under UV light effectively. This made the system somehow complicated up to certain extent. Prolonged contact time under UV irradiation can destroy polymeric network of the membrane. In this context, if visible/solar light active photocatalyst can be incorporated with membrane, then the process can be excellent and economically feasible. Visible light active photocatalytic membrane can have following advantages:

(a) Improvement of membrane performance due to antifouling properties
(b) Less Expensive and easy mode of operation, frequent replacement of membrane leading to undesirable plant shut down can be reduced making the process cost-effective

(c) Automatic self-cleaning of membrane is possible after certain interval of time
(d) Ecofriendly, cleaning without addition of chemical is possible
(e) Enhanced degradation with high water flux

The design and development of photocatalytic membrane for large scale application are also dependent on the stability of the membrane in presence of harsh physical or chemical-oxidative environment. Optimized incorporation of catalytic materials inside the membrane matrix is highly desirable to make the membrane leaching free. Otherwise, leaching of nanophotocatalyst can cause secondary pollution of aqueous stream which can pose serious threat for living organisms over time.

In-depth research is ongoing to overcome these challenges and ensure eco-friendly approach for separation of oils from water using membrane technology. Polymeric photocatalytic membranes have several advantages such as less fabrication cost, easier processability, and relatively less energy consumption. Have disadvantages of short lifetime making the overall process complicated. Ceramic-based inorganic membrane doped with photocatalyst can exhibit antifouling properties and higher oil removal efficiencies. However, the fabrication cost for ceramic-based photocatalytic membrane is higher. The major obstacle of ceramic-based photocatalytic membrane needs to be resolved. Thus, it is necessary that more research works should be carried out to analyze the fouling mechanism and provide innovative solution for designing cost-effective, antifouling membranes for commercial scale application in near future.

References

1. Padaki M, Surya Murali R, Abdullah MS, Misdan N, Moslehyani A, Kassim MA, Hilal N, Ismail AF (2015) Membrane technology enhancement in oil–water separation. A review. Desalination 357:197–207. https://doi.org/10.1016/j.desal.2014.11.023
2. Poulopoulos SG, Voutsas EC, Grigoropoulou HP, Philippopoulos CJ (2005) Stripping as a pretreatment process of industrial oily wastewater. J Hazard Mater 117(2–3):135–139. https://doi.org/10.1016/j.jhazmat.2004.08.033
3. Li C, Fu L, Stafford J, Belosevic M, Gamal El-Din M (2017) The toxicity of oil sands process-affected water (OSPW): a critical review. Sci Total Environ 601–602:1785–1802. https://doi.org/10.1016/j.scitotenv.2017.06.024
4. Yu L, Han M, He F (2013) A review of treating oily wastewater. Arab J Chem 10:S1913–S1922. https://doi.org/10.1016/j.arabjc.2013.07.020
5. Jaramillo-Gutiérrez MI, Rivero EP, Cruz-Díaz MR, Niño-Gómez ME, Pedraza-Avella JA (2016) Photoelectrocatalytic hydrogen production from oilfield-produced wastewater in a filter-press reactor using TiO2-based photoanodes. Catal Today 266:17–26. https://doi.org/10.1016/j.cattod.2015.12.008
6. Fakhru'l-Razi A, Pendashteh A, Abdullah LC, Biak DRA, Madaeni SS, Abidin ZZ (2009) Review of technologies for oil and gas produced water treatment. J Hazard Mater 170(2–3):530–551. https://doi.org/10.1016/j.jhazmat.2009.05.044
7. Singh MM, Szafran Z, Ibanez JG (1998) Laboratory experiments on the electrochemical remediation of environment. Part 4: color removal of simulated wastewater by

electrocoagulation-electroflotation. J Chem Edu 75(8):1040–1041. https://doi.org/10.1021/ed075p1040

8. Nordvik AB, Simmons JL, Bitting KR, Lewis A, Strøm-Kristiansen T (1996) Oil and water separation in marine oil spill clean-up operations. Spill Sci Technol Bull 3(3):107–122. https://doi.org/10.1016/s1353-2561(96)00021-7
9. Rubio J, Souza ML, Smith RW (2002) Overview of flotation as a wastewater treatment technique. Miner Eng 15(3):139–155. https://doi.org/10.1016/s0892-6875(01)00216-3
10. Painmanakul P, Sastaravet P, Lersjintanakarn S, Khaodhiar S (2010) Effect of bubble hydrodynamic and chemical dosage on treatment of oily wastewater by Induced Air Flotation (IAF) process. Chem Eng Res Des 88(5–6):693–702. https://doi.org/10.1016/j.cherd.2009.10.009
11. Zhou L, Wang W, Liu S, Zhang L, Xu H, Zhu W (2006) A sonochemical route to visible-light-driven high-activity BiVO4 photocatalyst. J Mol Catal A: Chem 252(1–2):120–124. https://doi.org/10.1016/j.molcata.2006.01.052
12. Benito JM, Ríos G, Ortea E, Fernández E, Cambiella A, Pazos C, Coca J (2002) Design and construction of a modular pilot plant for the treatment of oil-containing wastewaters. Desalination 147(1–3):5–10. https://doi.org/10.1016/s0011-9164(02)00563-5
13. Asselin M, Drogui P, Brar SK, Benmoussa H, Blais J-F (2008) Organics removal in oily bilgewater by electrocoagulation process. J Hazard Mater 151(2–3):446–455. https://doi.org/10.1016/j.jhazmat.2007.06.008
14. Ö_gütveren ÜB, Koparal S, Taylor P, Street M, Wt L (1997) Electrocoagulation for oil-water emulsion treatment. J Environ Sci Health. Part A Environ Sci Eng Toxicol 32(9–10):2507–2520. https://doi.org/10.1080/10934529709376699
15. Matos M, García CF, Suárez MA, Pazos C, Benito JM (2016) Treatment of oil-in-water emulsions by a destabilization/ultrafiltration hybrid process: Statistical analysis of operating parameters. J Taiwan Inst Chem Eng 59:295–302. https://doi.org/10.1016/j.jtice.2015.08.006
16. Liu G, Ye Z, Tong K, Zhang Y (2013) Biotreatment of heavy oil wastewater by combined upflow anaerobic sludge blanket and immobilized biological aerated filter in a pilot-scale test. Biochem Eng J 72:48–53. https://doi.org/10.1016/j.bej.2012.12.017
17. Kumar P, Sharma N, Ranjan R, Kumar S, Bhat Z, Jeong DK (2013) Perspective of membrane technology in dairy industry: a review Asian-Australas. J Anim Sci 26:1347
18. Ikhsan SNW, Yusof N, Aziz F (2017) A review of oilfield wastewater treatment using membrane filtration over conventional technology. Malays J Anal Sci 21(3):643–658. https://doi.org/10.17576/mjas-2017-2103-14
19. Madaeni SS, Ghaemi N (2007) Characterization of self-cleaning RO membranes coated with TiO2 particles under UV irradiation. J Membr Sci 303(1–2):221–233. https://doi.org/10.1016/j.memsci.2007.07.017
20. Kim J, Van der Bruggen B (2010) The use of nanoparticles in polymeric and ceramic membrane structures: review of manufacturing procedures and performance improvement for water treatment. Environ Pollut 158(7):2335–2349. https://doi.org/10.1016/j.envpol.2010.03.024
21. Liu F, Hashim NA, Liu Y, Abed MRM, Li K (2011) Progress in the production and modification of PVDF membranes. J Membr Sci 375(1–2):1–27. https://doi.org/10.1016/j.memsci.2011.03.014
22. Ulbricht M (2006) Advanced functional polymer membranes. Polymer 47(7):2217–2262. https://doi.org/10.1016/j.polymer.2006.01.084
23. Yu X, Ji Q, Zhang J, Nie Z, Yang H (2018) Photocatalytic degradation of diesel pollutants in seawater under visible light. Reg Stud Mar Sci 18:139–144. https://doi.org/10.1016/j.rsma.2018.02.006
24. Johnston JE, Lim E, Roh H (2019) Impact of upstream oil extraction and environmental public health: a review of the evidence. Sci Total Environ 657:187–199. https://doi.org/10.1016/j.scitotenv.2018.11.483

25. Han L, Tan YZ, Netke T, Fane AG, Chew JW (2017) Understanding oily wastewater treatment via membrane distillation. J Membr Sci 539:284–294. https://doi.org/10.1016/j.memsci.2017.06.012
26. Cote RP (1976) The effects of petroleum refinery liquid wastes on aquatic life, with special emphasis on the Canadian environment. Natl Res Counc Canada. K1A 0R6 (NRC Associate Committee on Scientific Criteria for Environmental Quality), 77
27. Tang J, Wang M, Wang F, Sun Q, Zhou Q (2011) Eco-toxicity of petroleum hydrocarbon contaminated soil. J Environ Sci 23(5):845–851. https://doi.org/10.1016/s1001-0742(10)60517-7
28. Tasker TL, Burgos WD, Piotrowski P, Castillo-Meza L, Blewett TA, Ganow KB, Stallworth A, Delompré PLM, Goss GG, Fowler LB, Vanden Heuvel JP, Dorman F, Warner NR (2018) Environmental and human health impacts of spreading oil and gas wastewater on roads. Environ Sci Technol 52(12):7081–7091. https://doi.org/10.1021/acs.est.8b00716
29. Abdel-Shafy HI, Mansour MSM (2016) A review on polycyclic aromatic hydrocarbons: source, environmental impact, effect on human health and remediation. Egypt J Pet 25 (1):107–123. https://doi.org/10.1016/j.ejpe.2015.03.011
30. Nwankwoala RNP, Gorgewill OA (2006) Analysis of the occurrence of cancer and other tumors in Rivers and Bayelsa States, Nigeria from December 1997–December 2000. Afr J Appl Zool Environ Biol 8:48–53
31. Coca J, Gutiérrez G, Benito J (2011) Treatment of Oily Wastewater. In: Coca-Prados J, Gutiérrez-Cervelló G (eds) Water purification and management. Springer, Dordrecht, The Netherlands, pp 1–55
32. Jiménez S, Micó MM, Arnaldos M, Medina F, Contreras S (2018) State of the art of produced water treatment. Chemosphere 192:186–208. https://doi.org/10.1016/j.chemosphere.2017.10.139
33. Gryta M (2001) Purification of oily wastewater by hybrid UF/MD. Water Res 35(15):3665–3669. https://doi.org/10.1016/s0043-1354(01)00083-5
34. Souza RS, Porto PSS, Pintor AMA, Ruphuy G, Costa MF, Boaventura RAR, Vilar VJP (2015) New insights on the removal of mineral oil from oil-in-water emulsions using cork by-products: effect of salt and surfactants content. Chem Eng J 285:709–717. https://doi.org/10.1016/j.cej.2015.10.007
35. Beychok MR (1967) Aqueous wastes from petroleum and petrochemical plants, 1st edn. Wiley, New York
36. Alzahrani S, Mohammad AW (2014) Challenges and trends in membrane technology implementation for produced water treatment: a review. J Water Process Eng 4:107–133. https://doi.org/10.1016/j.jwpe.2014.09.007
37. Edzwald JK (2010) Dissolved air flotation and me. Water Res 44(7):2077–2106. https://doi.org/10.1016/j.watres.2009.12.040
38. Kriipsalu M, Marques M, Nammari DR, Hogland W (2007) Bio-treatment of oily sludge: the contribution of amendment material to the content of target contaminants, and the biodegradation dynamics. J Hazard Mater 148(3):616–622. https://doi.org/10.1016/j.jhazmat.2007.03.017
39. Bai Z, Wang H, Tu ST (2011) Oil–water separation using hydrocyclones enhanced by air bubbles. Chem Eng Res Des 89(1):55–59. https://doi.org/10.1016/j.cherd.2010.04.012
40. Salahi A, Gheshlaghi A, Mohammadi T, Madaeni SS (2010) Experimental performance evaluation of polymeric membranes for treatment of an industrial oily wastewater. Desalination 262(1–3):235–242. https://doi.org/10.1016/j.desal.2010.06.021
41. Chen G (2004) Electrochemical technologies in wastewater treatment. Sep Purif Technol 38 (1):11–41. https://doi.org/10.1016/j.seppur.2003.10.006
42. Cañizares P, Martínez F, Jiménez C, Sáez C, Rodrigo MA (2008) Coagulation and electrocoagulation of oil-in-water emulsions. J Hazard Mater 151(1):44–51. https://doi.org/10.1016/j.jhazmat.2007.05.043

43. Zeng Y, Yang C, Zhang J, Pu W (2007) Feasibility investigation of oily wastewater treatment by combination of zinc and PAM in coagulation/flocculation. J Hazard Mater 147 (3):991–996. https://doi.org/10.1016/j.jhazmat.2007.01.129
44. Zeng Y, Park J (2009) Characterization and coagulation performance of a novel inorganic polymer coagulant—poly-zinc-silicate-sulfate. Colloids Surf A 334(1–3):147–154. https://doi.org/10.1016/j.colsurfa.2008.10.009
45. Kis Á, Laczi K, Zsíros S, Rákhely G, Perei K (2015) Biodegradation of animal fats and vegetable oils by Rhodococcus erythropolis PR4. Int Biodeterior Biodegradation 105:114–119. https://doi.org/10.1016/j.ibiod.2015.08.015
46. Brooijmans RJW, Pastink MI, Siezen RJ (2009) Hydrocarbon-degrading bacteria: the oil-spill clean-up crew. Microb Biotechnol 2(6):587–594. https://doi.org/10.1111/j.1751-7915.2009.00151.x
47. Mansourizadeh A, Javadi Azad A (2014) Preparation of blend polyethersulfone/cellulose acetate/polyethylene glycol asymmetric membranes for oil–water separation. J Polym Res 21 (3):1–9. https://doi.org/10.1007/s10965-014-0375-x
48. Zhao X, Wang Y, Ye Z, Borthwick AGL, Ni J (2006) Oil field wastewater treatment in Biological Aerated Filter by immobilized microorganisms. Process Biochem 41(7):1475–1483. https://doi.org/10.1016/j.procbio.2006.02.006
49. Van der Bruggen B (2009) Chemical modification of polyethersulfone nanofiltration membranes: a review. J Appl Polym Sci 114(1):630–642. https://doi.org/10.1002/app.30578
50. Zhu Y, Wang D, Jiang L, Jin J (2014) Recent progress in developing advanced membranes for emulsified oil/water separation. NPG Asia Mater 6(5):e101. https://doi.org/10.1038/am.2014.23
51. Rana D, Matsuura T (2010) Surface modifications for antifouling membranes. Chem Rev 110(4):2448–2471. https://doi.org/10.1021/cr800208y
52. Mittal P, Jana S, Mohanty K (2011) Synthesis of low-cost hydrophilic ceramic–polymeric composite membrane for treatment of oily wastewater. Desalination 282:54–62. https://doi.org/10.1016/j.desal.2011.06.071
53. Shi H, He Y, Pan Y, Di H, Zeng G, Zhang L, Zhang C (2016) A modified mussel-inspired method to fabricate TiO2 decorated superhydrophilic PVDF membrane for oil/water separation. J Membr Sci 506:60–70. https://doi.org/10.1016/j.memsci.2016.01.053
54. Kim MJ, Yoo GY, Yoo CK (2011) Development of combined fouling model in a membrane bioreactor. Asia-Pac J Chem Eng 6(3):423–432. https://doi.org/10.1002/apj.589
55. Zhang W, Ding L, Luo J, Jaffrin MY, Tang B (2016) Membrane fouling in photocatalytic membrane reactors (PMRs) for water and wastewater treatment: a critical review. Chem Eng J 302:446–458. https://doi.org/10.1016/j.cej.2016.05.071
56. Ebrahimi M, Ashaghi KS, Engel L, Willershausen D, Mund P, Bolduan P, Czermak P (2009) Characterization and application of different ceramic membranes for the oil-field produced water treatment. Desalination 245(1–3):533–540. https://doi.org/10.1016/j.desal.2009.02.017
57. Faibish RS, Cohen Y (2001) Fouling-resistant ceramic-supported polymer membranes for ultrafiltration of oil-in-water microemulsions. J Membr Sci 185(2):129–143. https://doi.org/https://doi.org/10.1016/S0376-7388(00)00595-0.
58. Arthanareeswaran G, Mohan D, Raajenthiren M (2010) Preparation, characterization and performance studies of ultrafiltration membranes with polymeric additive. J Membr Sci 350 (1–2):130–138. https://doi.org/10.1016/j.memsci.2009.12.020
59. Liang S, Kang Y, Tiraferri A, Giannelis EP, Huang X, Elimelech M (2013) Highly hydrophilic polyvinylidene fluoride (PVDF) ultrafiltration membranes via postfabrication grafting of surface-tailored silica nanoparticles. ACS Appl Mater Interfaces 5(14):6694–6703. https://doi.org/10.1021/am401462e
60. Lipp P, Lee CH, Fane AG, Fell CJD (1988) A fundamental study of the ultrafiltration of oil-water emulsions. J Membr Sci 36:161–177. https://doi.org/10.1016/0376-7388(88)80014-0

61. Chakrabarty B, Ghoshal AK, Purkait MK (2008) Ultrafiltration of stable oil-in-water emulsion by polysulfone membrane. J Membr Sci 325(1):427–437. https://doi.org/10.1016/j.memsci.2008.08.007
62. Al-Alawy AF, Al-Ameri MK (2017) Treatment of simulated oily wastewater by ultrafiltration and nanofiltration processes. Iraqi J Chem Pet Eng 18:71–85
63. Chen W, Peng J, Su Y, Zheng L, Wang L, Jiang Z (2009) Separation of oil/water emulsion using Pluronic F127 modified polyethersulfone ultrafiltration membranes. Sep Purif Technol 66(3):591–597. https://doi.org/10.1016/j.seppur.2009.01.009
64. Sadeghi I, Aroujalian A, Raisi A, Dabir B, Fathizadeh M (2013) Surface modification of polyethersulfone ultrafiltration membranes by corona air plasma for separation of oil/water emulsions. J Membr Sci 430:24–36. https://doi.org/10.1016/j.memsci.2012.11.051
65. Salahi A, Mohammadi T, Mosayebi Behbahani R, Hemmati M (2015) Asymmetric polyethersulfone ultrafiltration membranes for oily wastewater treatment: synthesis, characterization, ANFIS modeling, and performance. J Environ Chem Eng 3(1):170–178. https://doi.org/10.1016/j.jece.2014.10.021
66. Kong J, Li K (1999) Oil removal from oil-in-water emulsions using PVDF membranes. Sep Purif Technol 16(1):83–93. https://doi.org/10.1016/s1383-5866(98)00114-2
67. Zhai T-L, Du Q, Xu S, Wang Y, Zhang C (2017) Electrospun nanofibrous membrane of porous fluorine-containing triptycene-based polyimides for oil/water separation. RSC Adv 7 (36):22548–22552. https://doi.org/10.1039/c7ra01614j
68. Li H-J, Cao Y-M, Qin J-J, Jie X-M, Wang T-H, Liu J-H, Yuan Q (2006) Development and characterization of anti-fouling cellulose hollow fiber UF membranes for oil–water separation. J Membr Sci 279(1–2):328–335. https://doi.org/10.1016/j.memsci.2005.12.025
69. He Y, Jiang Z-W (2008) Technology review: Treating oilfield wastewater. Filtr Sep 45 (5):14–16. https://doi.org/10.1016/s0015-1882(08)70174-5
70. Mueller J, Cen Y, Davis RH (1997) Cross flow microfiltration of oily water. J Membr Sci 129:221–235
71. Hua F, Tsang YF, Wang Y, Chan S, Chua H, Sin S (2007) Performance study of ceramic microfiltration membrane for oily wastewater treatment. Chem Eng J 128:169–175. http://hdl.handle.net/10397/23698
72. Silalahi SH, Leiknes T (2011) High frequency back-pulsing for fouling development control in ceramic microfiltration for treatment of produced water. Desalin Water Treat 28:137–152. https://doi.org/10.5004/dwt.2011.2482
73. Reyhani A, Meighani HM (2016) Optimal operating conditions of micro-and ultra-filtration systems for produced-water purification: Taguchi method and economic investigation. Desalin Water Treat 57:19642–19654. https://doi.org/10.1080/19443994.2015.1101714
74. Abadi SRH, Sebzari MR, Hemati M, Rekabdar F, Mohammadi T (2011) Ceramic membrane performance in microfiltration of oily wastewater. Desalination 265:222–228. https://doi.org/10.1016/j.desal.2010.07.055
75. Bayat A, Mahdavi HR, Kazemimoghaddam M, Mohammadi T (2016) Preparation and characterization of-alumina ceramic ultrafiltration membranes for pretreatment of oily wastewater Desalin. Water Treat 57:24322–24332. https://doi.org/10.1080/19443994.2016.1146922
76. Zhong J, Sun X, Wang C (2003) Treatment of oily wastewater produced from refinery processes using flocculation and ceramic membrane filtration. Sep Purif Technol 32:93–98. https://doi.org/10.1016/j.arabjc.2013.07.020
77. Abdalla M, Nasser M, Fard AK, Qiblawey H, Benamor A, Judd S (2019) Impact of combined oil-in-water emulsions and particulate suspensions on ceramic membrane fouling and permeability recovery. Sep Purif Technol 212:215–222. https://doi.org/10.1016/j.seppur.2018.11.017
78. Ebrahimi M, Willershausen D, Ashaghi KS, Engel L, Placido L, Mund P, Bolduan P, Czermak P (2010) Investigations on the use of di_erent ceramic membranes for e_cient oil-field produced water treatment. Desalination 250:991–996

79. Pan Y, Wang T, Sun H, Wang W (2012) Preparation and application of titanium dioxide dynamic membranes in microfiltration of oil-in-water emulsions. Sep Purif Technol 89:78–83. https://doi.org/10.1016/j.seppur.2012.01.010
80. Zhu L, Chen M, Dong Y, Tang CY, Huang A, Li L (2016) A low-cost mullite-titania composite ceramic hollow fiber microfiltration membrane for highly e_cient separation of oil-in-water emulsion. Water Res 90:277–285. https://doi.org/10.1016/j.watres.2015.12.035
81. Abbasi M, Mirfendereski M, Nikbakht M, Golshenas M, Mohammadi T (2010) Performance study of mullite and mullite–alumina ceramic MF membranes for oily wastewaters treatment. Desalination 259:169–178. https://doi.org/10.1016/j.desal.2010.04.013
82. Kovács I, Veréb G, Kertész S, Beszédes S, Hodúr C, László Z (2018) Investigation of surface and filtration properties of TiO2 coated ultrafiltration polyacrylonitrile membranes. Water Sci Technol 77(4):931–938. https://doi.org/10.2166/wst.2017.610
83. Miller D, Dreyer D, Bielawski C, Paul D, Freeman B (2016) Surface modification of water purification membranes: a review autoren. Angewandte Chemie Int Edition 56(17):4662–4711. https://doi.org/10.1002/ange.201601509
84. Boshrouyeh Ghandashtani M, Tavangar T, Zokaee Ashtiani F, Karimi M, Fouladitajar A (2018) Experimental investigation and mathematical modeling of nano-composite membrane fabrication process: focus on the role of solvent type. Asia-Pac J Chem Eng 13(6): e2260. https://doi.org/10.1002/apj.2260
85. Yin J, Deng B (2015) Polymer-matrix nanocomposite membranes for water treatment. J Membr Sci 479:256–275. https://doi.org/10.1016/j.memsci.2014.11.019
86. Leong S, Razmjou A, Wang K, Hapgood K, Zhang X, Wang H (2014) TiO2 based photocatalytic membranes: a review. J Membr Sci 472:167–184. https://doi.org/10.1016/j.memsci.2014.08.016
87. Molinari R, Palmisano L, Drioli E, Schiavello M (2002) Studies on various reactor configurations for coupling photocatalysis and membrane processes in water purification. J Membr Sci 206(1–2):399–415. https://doi.org/10.1016/s0376-7388(01)00785-2
88. Zhang T, Wang X, Zhang X (2014) Recent progress in TiO2-mediated solar photocatalysis for industrial wastewater treatment. Int J Photoenergy 2014:1–12. https://doi.org/10.1155/2014/607954
89. Rahimpour A, Jahanshahi M, Rajaeian B, Rahimnejad M (2011) TiO2 entrapped nano-composite PVDF/SPES membranes: preparation, characterization, antifouling and antibacterial properties. Desalination 278(1–3):343–353. https://doi.org/10.1016/j.desal.2011.05.049
90. Venkatesh K, Arthanareeswaran G, Bose AC (2016) PVDF mixed matrix nano-filtration membranes integrated with 1D-PANI/TiO2 NFs for oil–water emulsion separation. RSC Adv 6(23):18899–18908. https://doi.org/10.1039/c5ra27022g
91. Rahimpour A, Madaeni SS, Taheri AH, Mansourpanah Y (2008) Coupling TiO2 nanoparticles with UV irradiation for modification of polyethersulfone ultrafiltration membranes. J Membr Sci 313(1–2):158–169. https://doi.org/10.1016/j.memsci.2007.12.075
92. Zhou J, Chang Q, Wang Y, Wang J, Meng G (2010) Separation of stable oil– water emulsion by the hydrophilic nano-sized ZrO2 modified Al2O3 microfiltration membrane. Sep Purif Technol 75(3):243–248. https://doi.org/10.1016/j.seppur.2010.08.008
93. Ahmad AL, Majid MA, Ooi BS (2011) Functionalized PSf/SiO2 nanocomposite membrane for oil-in-water emulsion separation. Desalination 268(1–3):266–269. https://doi.org/10.1016/j.desal.2010.10.017
94. Krishnamurthy PH, Yogarathinam LT, Gangasalam A, Ismail AF (2016) Influence of copper oxide nanomaterials in a poly(ether sulfone) membrane for improved humic acid and oil-water separation. J Appl Polym Sci 133(36):1–10. https://doi.org/10.1002/app.43873
95. Leo CP, Cathie Lee WP, Ahmad AL, Mohammad AW (2012) Polysulfone membranes blended with ZnO nanoparticles for reducing fouling by oleic acid. Sep Purif Technol 89:51–56. https://doi.org/10.1016/j.seppur.2012.01.002

96. Li YS, Yan L, Xiang CB, Hong LJ (2006) Treatment of oily wastewater by organic–inorganic composite tubular ultrafiltration (UF) membranes. Desalination 196(1–3):76–83. https://doi.org/10.1016/j.desal.2005.11.021
97. Jamshidi Gohari R, Halakoo E, Lau WJ, Kassim MA, Matsuura T, Ismail AF (2014) Novel polyethersulfone (PES)/hydrous manganese dioxide (HMO) mixed matrix membranes with improved anti-fouling properties for oily wastewater treatment process. RSC Adv 4 (34):17587–17596. https://doi.org/10.1039/c4ra00032c
98. Yuliwati E, Ismail AF (2011) Effect of additives concentration on the surface properties and performance of PVDF ultrafiltration membranes for refinery produced wastewater treatment. Desalination 273(1):226–234. https://doi.org/10.1016/j.desal.2010.11.023
99. Ong CS, Lau WJ, Goh PS, Ng BC, Matsuura T, Ismail AF (2014) Effect of PVP molecular weights on the properties of PVDF-TiO2 composite membrane for oily wastewater treatment process. Sep Sci Technol 49(15):2303–2314. https://doi.org/10.1080/01496395.2014.928323
100. Ong C, Lau W, Goh P, Ng B, Ismail A (2015) Preparation and characterization of PVDF–PVP–TiO2 composite hollow fiber membranes for oily wastewater treatment using submerged membrane system. Desalin Water Treat 53:1213–1223
101. Yi XS, Shi WX, Yu SL, Ma C, Sun N, Wang S, Jin LM, Sun LP (2011) Optimization of complex conditions by response surface methodology for APAM–oil/water emulsion removal from aqua solutions using nano-sized TiO2/Al2O3 PVDF ultrafiltration membrane. J Hazard Mater 193:37–44. https://doi.org/10.1016/j.jhazmat.2011.06.063
102. Yi XS, Yu SL, Shi WX, Wang S, Sun N, Jin LM, Ma C (2013) Estimation of fouling stages in separation of oil/water emulsion using nano-particles Al2O3/TiO2 modified PVDF UF membranes. Desalination 319:38–46. https://doi.org/10.1016/j.desal.2013.03.031
103. Ju J, Wang T, Wang Q (2015) A facile approach in fabricating superhydrophobic and superoleophilic poly (vinylidene fluoride) membranes for efficient water-oil separation. J Appl Polym Sci 132(24):n/a. https://doi.org/10.1002/app.42077
104. Li J, Guo S, Xu Z, Li J, Pan Z, Du Z, Cheng F (2019) Preparation of omniphobic PVDF membranes with silica nanoparticles for treating coking wastewater using direct contact membrane distillation: electrostatic adsorption vs. chemical bonding. J Membr Sci 574:349–357. https://doi.org/10.1016/j.memsci.2018.12.079
105. Tang CY, Chong TH, Fane AG (2011) Colloidal interactions and fouling of NF and RO membranes: a review. Adv Coll Interface Sci 164(1–2):126–143. https://doi.org/10.1016/j.cis.2010.10.007
106. Alfano OM, Bahnemann D, Cassano AE, Dillert R, Goslich R (2000) Photocatalysis in water environments using artificial and solar light. Catal Today 58(2–3):199–230. https://doi.org/10.1016/s0920-5861(00)00252-2
107. Molinari R, Lavorato C, Argurio P (2017) Recent progress of photocatalytic membrane reactors in water treatment and in synthesis of organic compounds . A review. Catal Today 281:144–164. https://doi.org/10.1016/j.cattod.2016.06.047
108. Ji Q, Yu X, Zhang J, Liu Y, Shang X, Qi X (2017) Photocatalytic degradation of diesel pollutants in seawater by using ZrO2 (Er3+)/TiO2 under visible light. J Environ Chem Eng 5 (2):1423–1428. https://doi.org/10.1016/j.jece.2017.01.011
109. Ong W-J, Tan L-L, Ng YH, Yong S-T, Chai S-P (2016) Graphitic carbon nitride (g-C3N4)-based photocatalysts for artificial photosynthesis and environmental remediation: are we a step closer to achieving sustainability? Chem Rev 116(12):7159–7329. https://doi.org/10.1021/acs.chemrev.6b00075
110. Ziolli RL, Jardim WF (2002) Photocatalytic decomposition of seawater-soluble crude-oil fractions using high surface area colloid nanoparticles of TiO2. J Photochem Photobiol A 147(3):205–212. https://doi.org/10.1016/s1010-6030(01)00600-1
111. Biniaz P, Makarem MA, Rahimpour MR (2020) Membrane reactor. In: Catalyst immobilization: methods and applications, vol 1. KGaA Boschstr. 12, 69469. Wiley-VCH Verlag GmbH & Co, Weinheim, Germany, pp 307–324

112. Kho ET, Tan TH, Lovell E, Wong RJ, Scott J, Amal R (2017) A review on photo-thermal catalytic conversion of carbon dioxide. Green Energy Environ 2(3):204–217. https://doi.org/10.1016/j.gee.2017.06.003
113. Li J, Ye Y, Ye L, Su F, Ma Z, Huang J, Xie H, Doronkin DE, Zimina A, Grunwaldt J-D, Zhou Y (2019) Sunlight induced photo-thermal synergistic catalytic CO2 conversion via localized surface plasmon resonance of MoO3−x. J Mater Chem A 7(6):2821–2830. https://doi.org/10.1039/c8ta10922b
114. Xu J, Li X, Wu X, Wang W, Fan R, Liu X, Xu H (2016) Hierarchical CuO colloidosomes and their structure enhanced photothermal catalytic activity. J Phys Chem C 120(23):12666–12672. https://doi.org/10.1021/acs.jpcc.6b03750
115. Gan Z, Wu X, Meng M, Zhu X, Yang L, Chu PK (2014) Photothermal contribution to enhanced photocatalytic performance of graphene-based nanocomposites. ACS Nano 8 (9):9304–9310. https://doi.org/10.1021/nn503249c
116. Chin SS, Chiang K, Fane AG (2006) The stability of polymeric membranes in a TiO2 photocatalysis process. J Membr Sci 275(1–2):202–211. https://doi.org/10.1016/j.memsci.2005.09.033
117. Wang Q, Cui J, Xie A, Lang J, Li C, Yan Y (2020) PVDF composite membrane with robust UV-induced self-cleaning performance for durable oil/water emulsions separation. J Taiwan Inst Chem Eng 110:130–139. https://doi.org/10.1016/j.jtice.2020.02.024
118. Du X-D, Yi X-H, Wang P, Zheng W, Deng J, Wang C-C (2019) Robust photocatalytic reduction of Cr(VI) on UiO-66-NH2(Zr/Hf) metal-organic framework membrane under sunlight irradiation. Chem Eng J 356:393–399. https://doi.org/10.1016/j.cej.2018.09.084
119. Liu L, Liu Z, Bai H, Sun DD (2012) Concurrent filtration and solar photocatalytic disinfection/degradation using high-performance Ag/TiO2 nanofiber membrane. Water Res 46(4):1101–1112. https://doi.org/10.1016/j.watres.2011.12.009
120. Li X, Janke A, Formanek P, Fery A, Stamm M, Tripathi BP (2018) One pot preparation of polysulfone-amino functionalized SiO2 nanoparticle ultrafiltration membranes for water purification. J Environ Chem Eng 6(4):4598–4604. https://doi.org/10.1016/j.jece.2018.06.045
121. Matthews RW, McEvoy SR (1992) A comparison of 254 nm and 350 nm excitation of TiO2 in simple photocatalytic reactors. J Photochem Photobiol A 66(3):355–366. https://doi.org/10.1016/1010-6030(92)80008-j
122. Gondal MA, Sadullah MS, Dastageer MA, McKinley GH, Panchanathan D, Varanasi KK (2014) Study of factors governing oil-water separation process using TiO2 films prepared by spray deposition of nanoparticle dispersions. ACS Appl Mater Interfaces 6(16):13422–13429. https://doi.org/10.1021/am501867b
123. Gupta SM, Tripathi M (2011) A review of TiO2 nanoparticles. Chin Sci Bull 56(16):1639–1657. https://doi.org/10.1007/s11434-011-4476-1
124. Tan BYL, Tai MH, Juay J, Liu Z, Sun D (2015) A study on the performance of self-cleaning oil–water separation membrane formed by various TiO2 nanostructures. Sep Purif Technol 156:942–951. https://doi.org/10.1016/j.seppur.2015.09.060
125. Moslehyani A, Ismail AF, Othman MHD, Matsuura T (2015) Design and performance study of hybrid photocatalytic reactor-PVDF/MWCNT nanocomposite membrane system for treatment of petroleum refinery wastewater. Desalination 363:99–111. https://doi.org/10.1016/j.desal.2015.01.044
126. Reijnders L (2009) The release of TiO2 and SiO2 nanoparticles from nanocomposites. Polym Degrad Stab 94(5):873–876. https://doi.org/10.1016/j.polymdegradstab.2009.02.005
127. Bárdos E, Kovács G, Gyulavári T, Németh K, Kecsenovity E, Berki P, Baia L, Pap Z, Hernádi K (2017) Novel synthesis approaches for WO3-TiO2/MWCNT composite photocatalysts- problematic issues of photoactivity enhancement factors. Catalysis Today 300:28–38. https://doi.org/10.1016/j.cattod.2017.03.019
128. Kovács G, Baia L, Vulpoi A, Radu T, Karácsonyi É, Dombi A, Hernádi K, Danciu V, Simon S, Pap Z (2014) TiO2/WO3/Au nanoarchitectures' photocatalytic activity, "from

degradation intermediates to catalysts' structural peculiarities", Part I: aeroxide P25 based composites. Appl Catal B 147:508–517. https://doi.org/10.1016/j.apcatb.2013.09.019

129. Mishra A, Mehta A, Sharma M, Basu S (2017) Impact of Ag nanoparticles on photomineralization of chlorobenzene by TiO 2 /bentonite nanocomposite. J Environ Chem Eng 5(1):644–651. https://doi.org/10.1016/j.jece.2016.12.042
130. Kalantari N, Vaezi MJ, Yadollahi M, Babaluo AA, Bayati B, Kazemzadeh A (2014) Synthesis of nanostructure hydroxy sodalite composite membranes via hydrothermal method: support surface modification and synthesis method effects. Asia-Pac J Chem Eng 10 (1):45–55. https://doi.org/10.1002/apj.1844
131. Dong S, Yu C, Li Y, Li Y, Sun J, Geng X (2014) Controlled synthesis of T-shaped BiVO4 and enhanced visible light responsive photocatalytic activity. J Solid State Chem 211:176–183. https://doi.org/10.1016/j.jssc.2013.12.027
132. Pan M, Shan C, Zhang X, Zhang Y, Zhu C, Gao G, Pan B (2018) Environmentally friendly in situ regeneration of graphene aerogel as a model conductive adsorbent. Environ Sci Technol 52(2):739–746. https://doi.org/10.1021/acs.est.7b02795
133. Neghi N, Kumar M, Burkhalov D (2019) Synthesis and application of stable, reusable TiO2 polymeric composites for photocatalytic removal of metronidazole: removal kinetics and density functional analysis. Chem Eng J 359:963–975. https://doi.org/10.1016/j.cej.2018.11.090
134. Wetchakun N, Chainet S, Phanichphant S, Wetchakun K (2015) Efficient photocatalytic degradation of methylene blue over BiVO4/TiO2 nanocomposites. Ceram Int 41(4):5999–6004. https://doi.org/10.1016/j.ceramint.2015.01.040
135. Xiao J-D, Jiang H-L (2019) Metal-organic frameworks for photocatalysis and photothermal catalysis. Acc Chem Res 52(2):356–366. https://doi.org/10.1021/acs.accounts.8b00521
136. Murić A, Petrinić I, Christensen ML (2014) Comparison of ceramic and polymeric ultrafiltration membranes for treating wastewater from metalworking industry. Chem Eng J 255:403–410. https://doi.org/10.1016/j.cej.2014.06.009
137. Dickhout JM, Moreno J, Biesheuvel PM, Boels L, Lammertink RGH, de Vos WM (2017) Produced water treatment by membranes: a review from a colloidal perspective. J Colloid Interface Sci 487:523–534. https://doi.org/10.1016/j.jcis.2016.10.013
138. Hofs B, Ogier J, Vries D, Beerendonk EF, Cornelissen ER (2011) Comparison of ceramic and polymeric membrane permeability and fouling using surface water. Sep Purif Technol 79(3):365–374. https://doi.org/10.1016/j.seppur.2011.03.025
139. Siagian UWR, Widodo S, Khoiruddin Wardani AK, Wenten IG (2018) Oilfield produced water reuse and reinjection with membrane. In: MATEC web of conferences, vol 156, 08005. https://doi.org/10.1051/matecconf/201815608005
140. Jepsen K, Bram M, Pedersen S, Yang Z (2018) Membrane fouling for produced water treatment: a review study from a process control perspective. Water 10(7):847. https://doi.org/10.3390/w10070847
141. Abbasi M, Sebzari MR, Salahi A, Mirza B (2012) Modeling of membrane fouling and flux decline in microfiltration of oily wastewater using ceramic membranes. Chem Eng Commun 199(1):78–93. https://doi.org/10.1080/00986445.2011.570391
142. Zhou J, Wandera D, Husson SM (2015) Mechanisms and control of fouling during ultrafiltration of high strength wastewater without pretreatment. J Membr Sci 488:103–110. https://doi.org/10.1016/j.memsci.2015.04.018
143. Dudchenko AV, Rolf J, Shi L, Olivas L, Duan W, Jassby D (2015) Coupling underwater superoleophobic membranes with magnetic pickering emulsions for fouling-free separation of crude oil/water mixtures: an experimental and theoretical study. ACS Nano 9:9930–9941. https://doi.org/10.1021/acsnano.5b04880
144. Li F, Yu Z, Shi H, Yang Q, Chen Q, Pan Y, Zeng G, Yan L (2017) A Mussel-inspired method to fabricate reduced graphene oxide/g-C 3 N 4 composites membranes for catalytic decomposition and oil-in-water emulsion separation. Chem Eng J 322:33–45. https://doi.org/10.1016/j.cej.2017.03.145

145. Chen Q, Yu Z, Li F, Yang Y, Pan Y, Peng Y, Yang X, Zeng G (2018) A novel photocatalytic membrane decorated with RGO-Ag-TiO 2 for dye degradation and oil– water emulsion separation. J Chem Technol Biotechnol 93(3):761–775. https://doi.org/10.1002/jctb.5426
146. Meng F, Chae S-R, Drews A, Kraume M, Shin H-S, Yang F (2008) Recent advances in membrane bioreactors (MBRs): membrane fouling and membrane material. Water Res 43 (6):1489–1512. https://doi.org/10.1016/j.watres.2008.12.044
147. Zare S, Kargari A (2018) Membrane properties in membrane distillation. Elsevier Inc. https://doi.org/10.1016/B978-0-12-815818-0.00004-7
148. Kang G, Cao Y (2012) Development of antifouling reverse osmosis membranes for water treatment: a review. Water Res 46(3):584–600. https://doi.org/10.1016/j.watres.2011.11.041
149. Zhao X, Su Y, Chen W, Peng J, Jiang Z (2012) Grafting perfluoroalkyl groups onto polyacrylonitrile membrane surface for improved fouling release property. J Membr Sci 415–416:824–834. https://doi.org/10.1016/j.memsci.2012.05.075
150. Bae T-H, Tak T-M (2005) Effect of TiO2 nanoparticles on fouling mitigation of ultrafiltration membranes for activated sludge filtration. J Membr Sci 249(1–2):1–8. https://doi.org/10.1016/j.memsci.2004.09.008
151. Caro J, Noack M, Kölsch P, Schäfer R (2000) Zeolite membranes—state of their development and perspective. Microporous Mesoporous Mater 38(1):3–24. https://doi.org/10.1016/s1387-1811(99)00295-4
152. Gondal MA, Sadullah MS, Qahtan TF, Dastageer MA, Baig U, McKinley GH (2017) Fabrication and wettability study of WO3 coated photocatalytic membrane for oil-water separation: a comparative study with ZnO coated membrane. Sci Rep 7(1):na. https://doi.org/10.1038/s41598-017-01959-y
153. Helali N, Rastgar M, Farhad Ismail M, Sadrzadeh M (2019) Development of underwater superoleophobic polyamide-imide (PAI) microfiltration membranes for oil/water emulsion separation. Sep Purif Technol 238:116451. https://doi.org/10.1016/j.seppur.2019.116451

Part V
Water Splitting and CO2 Reduction

Chapter 20
Photocatalytic CO_2 Reduction

András Sápi, Rajkumar Thangavel, Mohit Yadav, János Kiss, Ákos Kukovecz, and Zoltán Kónya

Abstract CO_2 emission is a problem and the world needs technologies using CO_2 as a fuel to produce important chemicals such as methanol or $C_{>2+}$ chemicals. Due to the high energy demand of the stable carbon dioxide molecule, thermocatalytic methods are using high-temperature or pressure for tangible yield and selectivity. One option to concentrate the energy input is to use alternative methods such as photochemistry, electrochemistry, etc. In this chapter, we will focus on the usage of heterogeneous photocatalytic methods for producing valuable products from CO_2 under UV and visible light irradiation. We focus on the main parts as electron structure of CO_2 and photoexcitation of such molecule; UV light and visible light assisted CO_2 photoactivation in the gas phase over TiO_2 based and other catalysts; Liquid phase CO_2 activation and the designing and upscaling techniques for CO_2 converting photoreactors.

Keywords Carbon dioxide · Thermocatalytic methods · Visible light · UV light · Methanol · $C_{>2+}$ chemicals

20.1 Introduction

Recently, the advancement in scientific developments have been increasingly rising to provide human society with ample conveniences and concurrently, instigating the reckless usage of the finite energy resources. By the year 2040, the growth in global energy demand is expected to increase by 27–28% [1]. At present, most of the energy needs are met by the burning of fossil fuels such as natural gas, oil, coal

---

A. Sápi (✉) · R. Thangavel · M. Yadav · J. Kiss · Á. Kukovecz · Z. Kónya
Interdisciplinary Excellence Centre, Department of Applied and Environmental Chemistry, University of Szeged, Rerrich Béla tér 1, Szeged 6720, Hungary
e-mail: sapia@chem.u-szeged.hu

Z. Kónya
MTA-SZTE Reaction Kinetics and Surface Chemistry Research Group, Rerrich Béla tér 1, Szeged 6720, Hungary

S. Garg and A. Chandra (eds.), *Green Photocatalytic Semiconductors*,
Green Chemistry and Sustainable Technology,
https://doi.org/10.1007/978-3-030-77371-7_20

and if this process continues the remaining fossil fuel reserves could be exhausted in the future [2, 3]. In addition, the excessive burning of fossil fuels leading to a rise in greenhouse gas (CO_2), which is the primary source of global warming and also a threat to the environment. At this rate the amount of CO_2 level in the atmosphere is predicted to increase from 400 to 750 ppm and the global temperature could possibly increase by 10–15 °F [4, 5]. Also, CO_2 being a thermodynamically stable compound resist absorbing the additional energy for its reduction. The incessant burning of non-renewable fossil fuels and the fast-diminishing rate of the current resources are escalating the need for development of an alternate sustainable energy solutions, which can directly combat and process the ever-increasing emissions of CO_2.

Until now, various techniques such as biological fixation, photoelectrochemical reduction, catalytic conversion, thermochemical and electrochemical conversion, carbon capturing and storage (CCS), etc., have been utilized for the CO_2 reduction [6, 7]. However, these techniques have suffered certain limitations, for instance, the biological fixation of CO_2 by microalgae leads to the formation and regeneration of enzymes [8]. Likewise, the electrochemical reduction of CO_2 requires high power electrical energy, therefore; the efficiency is lowered and there is instability of the electrode [9]. In addition, the CCS is one of the broadly researched technique with substantial efficacy, however; there is high environmental risk involved in the leakage from geological storages, and the high cost of transportation and compression also limits its practical applicability [10]. Similarly, the catalytic and thermal conversion is an efficient technique which utilizes transition metals as catalysts for the reduction of CO_2 into CO and CH_4. Nonetheless, due to the exothermic reaction with high-temperature and pressure, the economic viability of the process is low [11].

In recent times, photocatalytic reduction of CO_2 has been emerged as one of the most promising techniques owing to its economical and eco-friendly characteristics. This technique operates on the solar energy and water, which are abundantly available, and also, there is negligible emission of carbon [12, 13]. This technique is similar to an artificial photosynthesis process, which converts H_2O and CO_2 into useful solar fuels such as formic acid (HCOOH), formaldehyde (HCHO), methanol (CH_3OH), CO and CH_4 under solar light irradiations. Until now, various photocatalysts for instance graphitic carbon nitride (g-C_3N_4) [14], lead selenide (PbSe) [15], bismuth sulfide (Bi_2S_3) [16], cadmium sulfide (CdS) [17], zinc sulfide (ZnS) [18], zirconium oxide (ZrO_2) [19], gallium oxide (Ga_2O_3) [20], gallium phosphide (GaP) [21], tungsten oxide (WO_3) [22], zinc oxide (ZnO) [23], and titanium dioxide (TiO_2) [24] have been exploited for photocatalytic reduction of CO_2. Among the aforementioned photocatalysts, TiO_2 has been considered expansively owing to its exceptional characteristics such as non-toxicity, availability, and high chemical stability. Nonetheless, the photocatalytic execution of TiO_2 is efficient under UV light irradiations but it suffers from the fast-recombining tendency of the photoinduced charges [25–27]. In this regard, certain methodologies have been executed to boost its photocatalytic activity such as modulation and surface modifications in the morphology, development of heterojunction with other semiconductors for effectual charge transference, and effective parting of the photoinduced charges [28], surface plasmons and doping with nonmetals and metals, etc., to improve the activation of CO_2 [29–31].

This chapter provides current perspectives on the state of the art of photocatalytic hydrogenation of CO_2 over TiO_2-based and other photocatalysts, with a focus on reactor setups and material engineering. A comparative examination of existing systems, photoconversion rates, and the use of innovative designs to boost selectivity as well as new prospects for future growth, vital for photocatalytic reduction of CO_2 has been addressed. The effect of various operating and morphological parameters on the efficacy and selectivity of CO_2 photoreduction has been reviewed. Moreover, the outlooks in the advancement of the TiO_2-mediated photocatalysis for CO_2 photoreduction has been presented.

20.2 Structural Studies of CO_2 Adsorbates and Activation of CO_2

Before investigating the activation and transformations of CO_2 to valuable compounds, it is very desirable to summarize the bonding and structural characteristics of CO_2. CO_2 includes two equivalent C=O bond lengths that provide a linear geometry with bond angle of 180°. At the ground level, the electronic arrangement of O and C atoms are $1s^2 2s^2 2p^4$ and $1s^2 2s^2 2p^2$, respectively. The O and C atoms require 6 and 4 e^- to complete their octet. The CO_2 molecule shares 16 e^- in the molecular orbitals i.e. 8 e^- occupying 4 σ orbitals, and the remaining 8 are positioned in 2 π orbitals [32, 33]. The ground state molecule is expected to be linear with molecular orbitals as presented in Fig. 20.1.

From the diagram, it is clearly seen that the carbon dioxide molecule is very hard to bring in excited level. In the first excited level, the electron is generated to the $2\pi_u^*$ molecular orbital. The first important task in the CO_2 heterogenic catalysis, including the photoinduced process, is the activation of the linear CO_2 molecule by an electron donation to the lowest unoccupied (LUMO) molecular orbital from the substrate (catalysts) upon adsorption. In the formed anionic CO_2 (CO_2^-) molecule contains 17 electrons in the valence orbitals. This negatively charged anionic CO_2 exhibits a bent structure. The undistorted linear neutral and anionic CO_2 modes are displayed in Fig. 20.2.

Most of transition metal surfaces the CO_2 adsorbs molecularly and the physisorbed state does not convert to chemisorb state. Using a branch of surface science techniques (UPS, XPS, IR, XPS, NEXAFS, and HREELS) it was established that CO_2 adsorb reversible, it desorbs molecularly without any distortion of its molecular structure. The adsorption of CO_2 on a certain face of Ni, Fe, Cu chemisorption occurs and bent, negatively charged CO_2 is formed [34, 35]. Possible coordination sites of $CO_2^{\delta-}$ is represented in Fig. 20.3. However, it should be emphasized that electropositive adatom (especially alkali metals) may promote the

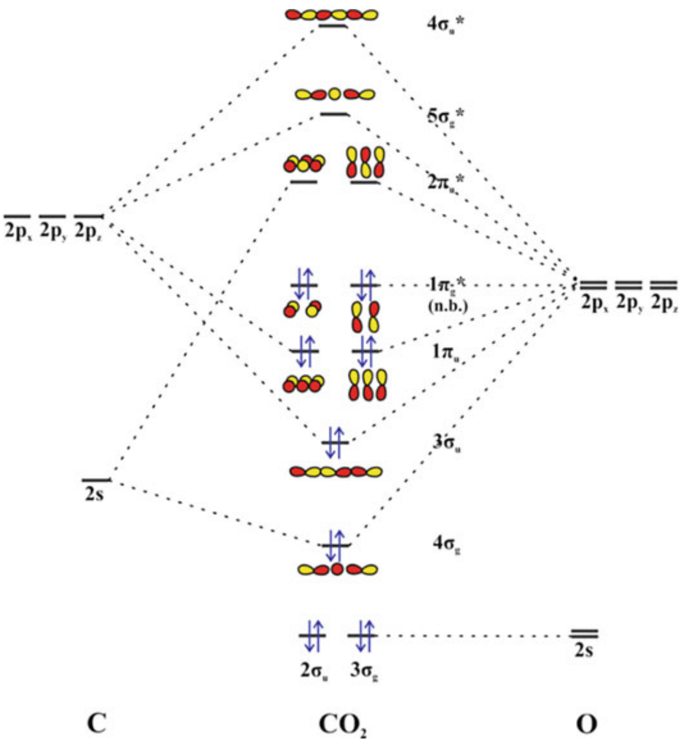

Fig. 20.1 Molecular orbital of linear CO_2. Reproduced from Ref. [32]

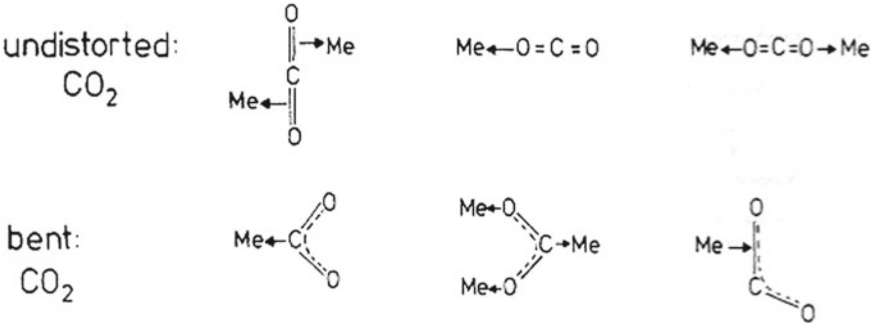

Fig. 20.2 Schematic illustration of coordination modes of neutral and anionic CO_2

activation of carbon dioxide and initiate the dissociation (C–O bond breaking). Alkali modification causes fundamental changes in the adsorption mode; electronegative alkali promotor induces electron transfer to the antibonding orbital of CO_2.

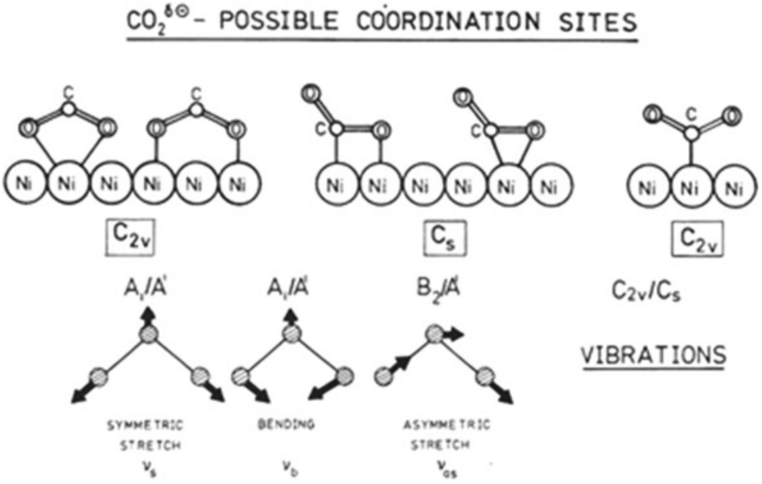

Fig. 20.3 Schematic presentation of the bending and stretching vibrations in bent CO_2^- coordination. Reproduced from Ref. [33]

Negatively charged CO_2 was detected on Rh(111) [36–38], on Pd(100) [39], on Pt(111) [40, 41] and on Ru(001) [42]. It was generally concluded, that the activated bent, negatively charged CO_2 transformed to oxalate and carbonate during heat treatment. The electronegative additives, like adsorbed oxygen results in a chemisorption of CO_2. Nice example for this adsorption is the Ni(111) surface, where the activated CO_2 and carbonates were identified by ARUPS and HREEL during coadsorption [43]. On $RuO_2(001)$ surface physisorbed CO_2, chemisorbed $CO_2^{\delta-}$, carbonate and dimerized form CO_{2*} $CO_2^{\delta-}$ were detected by HREEL [44].

Non-thermal, photo-assisted activation at adsorbate/metal interface may occur in many cases via substrate excitation with photon energy above 193 nm even at very low temperatures (90 K) [45–47]. In photochemistry, the incident photons in a certain way trigger the surface chemistry at the adsorbate/metal interfaces. The incident photons are absorbed by the metal surface to photogenerates the e^-–h^+ pairs which are delocalized and transported at the interface to trigger the chemical reactions at the surface. The mechanism of excitation is the central point in photoinduced chemical reactions at metal surfaces. White et al. divided the possible processes into three classes: (1) direct optical excitation of molecule (adsorbate/substrate complex) [48, 49], (2) optical excitation of substrate to produce photoelectrons above the vacuum level [50], and (3) optical excitation of the substrate to produce “hot” electrons below the vacuum level [51]. In the case of CO_2 the photochemistry attempts have not resulted in positive results on clean metal surfaces while the CO_2 has not unfilled orbital below the vacuum level and the first unfilled unoccupied $2\pi_u^*$ level is far above the vacuum level. However, the photoinduced activation of CO_2 was successful when the noble (transition) metal surfaces were modified with potassium [52, 53]. The potassium adatom decreased the work function of metals dramatically (by ~3.5 eV) [36, 37, 54–56]. In this way, the unfilled orbital of CO_2 upon adsorption moves just above the vacuum level and the ejected photoelectron could attach to the CO_2 molecules forming negatively charged molecules. An attempt was made to photolysis the adsorbed CO_2 in the presence of coadsorbed hydrogen or halogens. In contrast with the electropositive potassium adatoms, illumination of the coadsorbed system did not produce activated carbon dioxide. It is in harmony with the high work function of H- and halogen (Cl, I)-covered metals.

In surface photochemistry, one of the most important factors is the lifetime of generated excited molecules by light irradiation. In the case of metals this lifetime is rather low therefore the cross-section of photoinduced process also low, in the case of CO_2 the photochemistry cross-section is around 10^{-18}–10^{-20} cm^2. The quenching from the excited state to ground state occurs rapidly. In view of the sophisticated necessities that are required to be fulfilled by a photocatalyst (ample light-absorbing ability, suitable charge transference, instant charge migration stability and kinetics, etc.), it is evident that the semiconductors exhibit better characteristics, which are important in photocatalysis. The semiconductors have sufficient band gap energy ($E_g = E_c - E_v$) which allows excited e^- to migrate from the VBM to the CBM, thereby; creating an exciton upon light absorption $\geq$ the E_g of the semiconductor [57–59].

If the charge separation is large enough, charge transport can occur to the adsorbed molecule, including CO_2, and the formed $CO_2^{\delta-}$ has enough lifetime to generate further reaction paths. The electron transport from light irradiated semiconductor to CO_2 molecule is represented in Fig. 20.4. A direct IR spectroscopic evidence was found for the formation of chemisorbed CO_2 on pure TiO_2. An enhancement of intensity bands due to CO_2^- at 1640 and 1219 cm^{-1} was detected during illumination by the full arc of an Hg lamp [60].

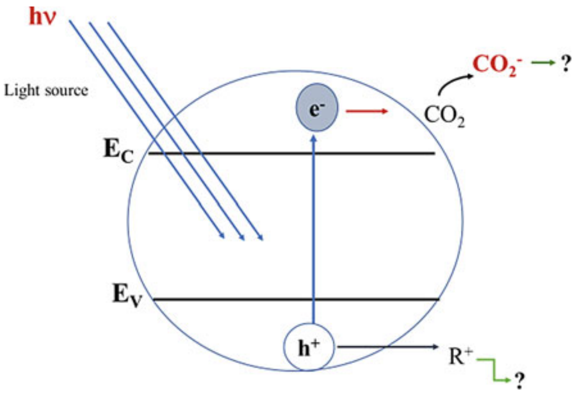

Fig. 20.4 Representation of CO_2^- formation on semiconductor due to light irradiation

20.3 UV Photo Activated Reactions of CO_2 on TiO_2 Type Catalysts

In the literature, the bulk optical characteristics of TiO_2 rutile and anatase phases are well-reported [61–63]. The photocatalytic execution of TiO_2 owing to its advantageous characteristics, such as economic viability, ready availability, chemical stability, high oxidation potential occurred as an expansive topic of research in comparison to other semiconductors. It is relatively cheap and readily available Similar to a typical semiconductor, TiO_2 gets activated under UV radiations to produced photoinduced charges, which results in high optical absorptivity due to strong redox entities on the surface as observed by photoacoustic and photoconductivity characteristics [64, 65]. The probability is large at the lowest photon energy to generate the charges, which can be appeared as the coupling of the highest DOS around the VBM and CBM. [66]. Both the TiO_2's polymorphs coexist at this point which occurs at $\sim$4.0 eV. It is very-well held that the E_g values of TiO_2 in rutile and anatase phases are direct and indirect, respectively. The recent observations are in agreement with the past evaluations that the E_g values for these transitions are 3.0 and 3.2 eV, respectively. [67]. This value offers hope that the TiO_2 can be widely used as photocatalyst in many reactions.

The suitable thermodynamic properties (including bandgaps) do not ensure satisfactory photocatalytic efficacy. The heterogeneous photocatalysis is usually governed on certain steps, which begins with the absorption of the incident light, then the charge excitation and parting is triggered followed by the charge migration, transference, recombination, and lastly utilization of the charges for the photocatalytic execution [68]. Moreover, the resulting photocatalytic efficacy is largely affected by the cumulative consequences of the aforementioned steps. Considering the sophisticated necessities, the active development of TiO_2 has intrigued our understanding with a novel category of TiO_2-based entities [69–79]. Owing to their large specific surface area, huge ion-exchange capacity, the TiO_2-based entities guarantee large dispersion of metal on/in their geometry and thereby; making them appropriate for catalytic applications.

The photochemical activity of TiO_2-like and other semiconductors is appreciably boosted by the deposition metal nps as dopants [59, 80, 81]. The photocatalytic fate of a semiconductor is scrutinized by the rate at which the photoinduced charges recombine. The presence of crystal defects, impurities, and the nature of the semiconductor can have a negative or positive influence on the recombining tendency of the e^-–h^+ pairs [82]. In addition, using noble metals as dopants in the semiconductor's matrix can substantially quench the recombining ability of the charges as they adequately sink the e^- [80–86]. The e^- sinking mechanism in n-type semiconductors for instance TiO_2 is analyzed by the Schottky barrier that restricts the e^- from moving backwards towards the semiconductors from the metal [87]. TiO_2-based entities have been listed in many reports for the CO_2 reduction [25, 27, 59, 88–95]. Three most important reactions should be discussed separately, which are outstanding in carbon dioxide transformations: (i) $CO_2 + H_2O$, (ii) $CO_2 + CH_4$, and (iii) $CO_2 + H_2$.

20.3.1 Photocatalytic $CO_2 + H_2O$ Reaction on Titania and Titania Derivates Catalysts

We summarize the CO_2's photoreduction with H_2O on TiO_2-like catalysts under UV light. The thermal driven chemistry is almost impossible from thermodynamic point of view. Not only the carbon dioxide photolysis but also the water splitting is an extremely important step in surface photochemistry. While the photosynthesis in biology is well-known and well-studied process, it is hardly reproducible in laboratory circumstances. Thanks to Fujishima and Honda, who have succeeded to photochemically decompose water on n-type TiO_2 by the light energy without any applied electric field in 1969 [96]. This finding offered the hope to study the photoinduced water splitting and the CO_2 + water reaction. From the end of the last century, a relatively large number of attempts and studies were published about this reaction obtained on pure and modified TiO_2 [19, 58, 97–108].

The photoinduced reaction between CO_2 and water resulted in CO and hydrocarbons using TiO_2-based catalysts have been widely studied [89, 93, 100, 102–109] implying that the reaction is primarily triggered by the production of two vital radicals, i.e.,$^{\cdot}CO_2^{-}$ and$^{\cdot}OH$. A varied series of products with the CO_2's photoreduction such as CO, CH_4, CH_3OH, H_2, C_2H_4, C_2H_5OH, CH_2O and $HCOOCH_3$ were detected on most of tested TiO_2-like catalysts [109]. The conversion and reaction products are depended on the modification of the titania. Until now, there is no general agreement on the reaction mechanism, however; numerous reports have implied the possibility of two reaction pathways, which rely on the CO_2 hydrogenation and dehydrogenation rates [93]. If the CO and CH_4 are produced, the deoxygenation is quicker in comparison to the addition of the H_2. The CO_2 photocatalytic reduction with water produces mainly CO on Fe/TiO_2 catalysts [105]. In this case, the deoxygenation is a favored path:

$$TiO_2 + h\nu \rightarrow h^+ + e^- \tag{20.1}$$

< Oxidization>

$$H_2O + h^+ \rightarrow OH^* + H^+ \tag{20.2}$$

$$\cdot OH^* + H_2O + h^+ \rightarrow O_2 + 3H^+ \tag{20.3}$$

<Reduction>

$$CO_2 + e^- \rightarrow CO_2^- \tag{20.4}$$

$$CO_2^- + 2H^+ + 2e^- \rightarrow CO + H_2O \tag{20.5}$$

Transiently formate may also form and it decomposes to CO product:

$$CO_2^- + H^+ + e^- \rightarrow HCOO^- \tag{20.6}$$

$$HCOO^- + H^+ \rightarrow CO + H_2O \tag{20.7}$$

The low-dimensional nano-TiO_2 photocatalysts produced CH_4, the yield on Pt/TiO_2 nanotubes were more remarkable [109]. It was assumed that photoexcited CO_2 is reduced to active carbon via formation of CO, and the active surface carbon is hydrogenated to alkyl radicals, which give methane. On decorated TiO_2 nanofibers with Pd or Pt particles formation of CH_3OH, HCOOH, and $HCOOCH_3$ (methylformate) photoproducts were observed. Sensitizing Pd/TiO_2 or Pt/TiO_2 with semiconductor CdSe quantum dots, gives two possibilities i.e. improved yield and positive influence on the reaction's selectivity [102]. Cu adatoms on TiO_2 resulted in a higher CH_3OH selectivity in photo-assisted reaction [107, 108]. Based on the experimentally detected products complex reaction steps were suggested supporting with DFT calculations [94, 102]:

$$HCOO + H \rightarrow HCOOH \tag{20.8}$$

$$HCOOH + H \rightarrow H_2COOH \tag{20.9}$$

$$H_2COOH \rightarrow CH_2O + OH^* \tag{20.10}$$

$$CH_2O + OH^* + H \rightarrow CH_2O + H_2O_{(g)} \tag{20.11}$$

$$CH_2O + H \rightarrow CH_3O \tag{20.12}$$

$$CH_3O + H \rightarrow CH_3OH_{(g)} \tag{20.13}$$

$$HCOOH + CH_3OH \rightarrow H_2O + HCOOCH_3 \tag{20.14}$$

The proposed reaction pathways in 20.8–20.14 steps have been formerly witnessed in similar reports over varied surface range [110]. Figure 20.5 displays the reaction pathway on an TiO_2 (anatase) based on fast hydrogenation mechanism.

The measured reaction energy for reduction of CO_2 is depicted in Fig. 20.5(b). The absorption of CO_2 at a Ti_{5f} spot on the anatase TiO_2(101) reveals a stable arrangement with $\Delta E_{ads} \sim -017$ eV, as reported previously [111]. The triggering force for CO_2 photoreduction with TiO_2 is observed to be the difference observed at the surface under irradiation between VBM of TiO_2 to the corresponding redox potential at the surface (−3.2 eV) [112].

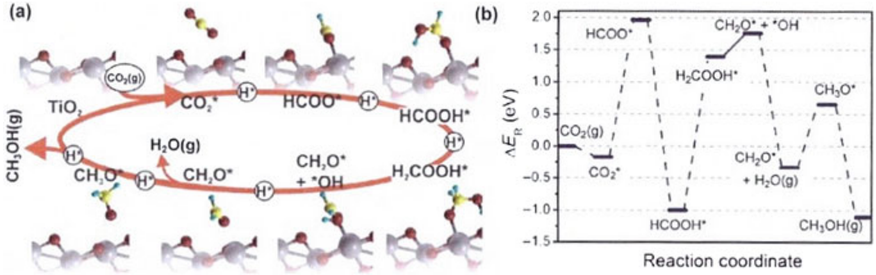

Fig. 20.5 **a** Geometrically optimized structures of the diverse range of intermediates along CO_2 reduction performed on the anatase $TiO_2(101)$ surface. **b** ΔE_R during CO_2 reduction, as described in 4–13 steps. In this case, the limiting step is the hydrogenation of HCOOH. Reproduced from Ref. [19]

20.3.2 *TiO_2 and TiO_2-based Catalysts for Photocatalytic Reduction of CO_2 with CH_4*

In the past few decades, the atmospheric concentration of the greenhouse gases, i.e., CH_4 and CO_2 have shown a monotonic increase, which along with other gaseous contaminants such as chlorofluorocarbons are contributing immensely to the global warming [113–116]. The valuable formation of syngas as a result of dry reformation reaction between CH_4 and CO_2 could be a possible solution to the problem. However, the process is not cost-effective to fulfill the energy demand, also, at the required temperature the catalysts are simply deactivated [117]. Photocatalysis shows an efficacious way remove the thermodynamic limitations of this endothermic process. The endless supply of solar energy can be stored in the form of the product's chemical bonds, which can be used for photoexcitation [94, 118].

There have been certain studies involving the usage of TiO_2-based entities for photocatalytic CO_2 reforming of CH_4. For instance, Shi et al. evaluated the photocatalytic execution of Cu/CdS–TiO_2/SiO_2 at 473 K under UV exposure [119]. At lower temperatures CO and ethane, while higher temperatures acetone was the dominant product. This innovative approach opened a new door for the application of varied TiO_2-based entities for CO_2 reforming with CH_4 at optimized temperatures. In another study, TiO_2 coated on stainless steel mesh adequately led to the photoreduction of CO_2 with CH_4 to generate HCOOH and CH_3COOH [120]. To obtain uniform distribution of particles and reduce the agglomeration of the catalyst, calcination can be employed, also; all TiO_2 samples that undergo calcination displayed a red shift in the light absorption in comparison to the TiO_2 (pure), primarily owing to the narrowing of E_g [121]. About 48.7 and 37.9% conversion of CH_4 and CO_2 were witnessed under optimized conditions. In addition to that, methyl formate and methyl acetate were observed to be the final products [122]. On pure TiO_2 the photocatalytic synthesis of formate and acetate derivatives from CO_2 and CH_4 may take place with the following reaction steps:

$$TiO_2 + h\nu \rightarrow h^+ + e^- \tag{20.15}$$

$$CH_4 + h^+ \rightarrow CH_3^* + H^+ \tag{20.16}$$

$$CO_2 + e^- \rightarrow CO_2^{-*} \tag{20.17}$$

$$CH_3^* + CH_3^* \rightarrow C_2H_6 \tag{20.18}$$

$$CH_4 + CO_2^{-*} \rightarrow CH_3COO^- + H^* \tag{20.19}$$

$$CH_3COO^- + H^+ \rightarrow CH_3COOH \tag{20.20}$$

$$CO_2^{-*} + H^* \rightarrow HCOO^- \tag{20.21}$$

$$CH_3COOH + CH_3^* \rightarrow HCOOCH_3 + H^* \tag{20.22}$$

Tahir et al. immobilized TiO_2 nps on a montmorillonite (MMT) clay particles as novel support system as MMT has the tendency to reduce the length of the charge transfer and assists TiO_2 in enhancing the adsorption of CH_4 and CO_2 within the interlayers and on the surface [123, 124]. The photocatalytic execution of as-fabricated support was witnessed to be 2.52 folds greater in comparison to the bare TiO_2. Along with CO, C_2H_5OH and CH_3OH were also obtained as byproducts with high selectivity of 0.19% and 19%, respectively.

The one-dimensional, layered titanates opened a new direction not only the in thermal chemistry, but in the photochemistry field. This TiO_2-like nanostructured system could increase the e^-–h^+ parting and facilitate the incorporation of nitrogen and lanthanum in the structure [94, 124, 125] and due cation exchange capacity ensure high metal dispersion creating new active sites for photo activations [69, 72–78]. Under UV light exposure, the formation of photoinduced charges was occurred on rhodium or gold promoted TNT, subsequently; the e^- and h^+ migrated to the energetically favorable locations. In addition, e^- possessed higher possibility to be appeared on the metal nps owing to the Fermi level equilibration (Eq. 20.24), which was witnessed between the oxide and metal [83].

$$TNT(e^-, h^+) \rightleftharpoons TNT(e^-) + TNT(h^+) \tag{20.23}$$

$$TNT(e^-) \rightleftharpoons M(e^-) \tag{20.24}$$

The hole (h^+) activates methane according to step (20.16) As it is well-demonstrated, that the hydrothermally prepared nanostructures (TNT) contain structural and surface water, which can be also photoexcited, and hydroxyl radical is produced. Higher activity was witnessed in the photocatalytic CH_4 conversion with the substantial addition H_2O to the system, which played a prime activity in the oxidation reaction [115]. The${}^{\cdot}$OH radicals are powerful oxidants that rapidly oxidized CH_4 in a radical-assisted reaction and the${}^{\cdot}CH_3$ radicals were adsorbed on the surface of the metal surface.

$$OH^{*} + CH_4 \rightarrow H_2O + CH^{*}_{3(M)} \tag{20.25}$$

The formed methyl radical can decompose or dimerize rely on the characteristics of the metal. The excited CO_2 radical may react with activated hydrogen according to steps (20.21) producing different products.

The TiO_2 along with titanate nanorods has been coupled with metal nps i.e. Au to take advantage of the LSPR phenomenon in photocatalytic activity [70, 81, 83]. It has been shown that the titanate nanotubes coupled with Au nps exhibited substantially improved photocatalytic efficacy in comparison to the Au/TiO_2 (anatase). However, the pristine titanate nanotubes did not show much activity solely. The plasmon absorption's intensity at 2.31 eV was witnessed to be greater with Au/TNT as compared to Au/TiO_2 [86, 116]. Meanwhile, the migration of e^- to the reactants from the metal was more advantageous. It was also witnessed that the LSPR-led photo effects substantially affected by the characteristics of TiO_2 for instance, crystallinity, surface area, shape, and size. It can be inferred that the TNT has a positive influence to disperse the metal nps in this context. In addition, the TNT can stabilize metal nps (Au and Rh) in the smaller range ($\sim$<3 nm) [72, 77, 86, 116]. The metal clusters in smaller molecular form for instance in Au_{25} can be attached firmly to the TNT's defect sites, which could directly participate in the photo-driven reactions. In some cases, the CO_2 in the dissolved carbonate form can work as h^+ sinks, subsequently boosting the parting of the e^-–h^+ pairs [126]. In addition, HCO_3^- trapped by the h^+ can produce${}^{\cdot}$OH radicals also (20.15) that can boost the activity. The Fig. 20.6 represents the proposed complex photochemical processes in CO_2–CH_4–H_2O system on nanostructured titanate modified with Rh and Au nps.

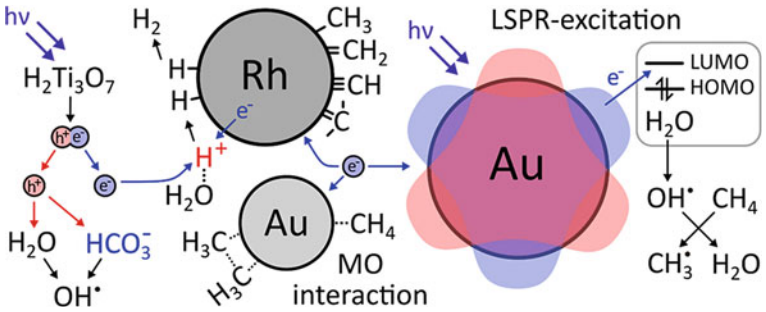

Fig. 20.6 Schematic representation of photochemical process in CO_2-CH_4-H_2O system on nanostructured titanate modified with Rh and Au nps. Reproduced from Ref. [116]

20.3.3 Photochemical Reduction of CO_2 with Hydrogen on TiO_2 Based Catalysts

Photocatalytic transformation of CO_2 with H_2 to beneficial resultants is a fascinating technique for obtaining the two-fold advantages of producing the solar fuels/chemicals and normalizing profuse atmospheric CO_2 heights. TiO_2 and TiO_2-based entities, precisely 1D (nanowires, nanotubes, etc.) and 2D (nanosheets, nanolayers) structures demonstrate good candidate for photocatalyst materials [19, 113, 127]. Fe and Pd decoration of TiO_2 enhanced the photochemical activity of TiO_2 [105, 106]. CO_2 photoreduction over various Rh/TiO_2 samples were studied [128]. The activity was witnessed to be lowered upon the reduction of Rh to be in a completely metallic state in Rh/TiO_2 and the resultant product varied from CO to CH_4. Cu deposition due to improved parting of the photoinduced charges had a positive effect on the formation of CO and CH_4 [129]. The combination of photo and thermal energy boosted the triggering force for photocatalysis, which led to the efficacious photo-thermo catalytic reduction of CO_2 with the as-optimized photocatalyst i.e. Ru/TiO_2 [130]. TiO_2 nanorods loaded Ag nps improved the photoreduction CO_2 to CH_4 under UV–visible light exposure [131]. Also, the formation of heterojunction Ag-NPs/TiO_2 NWs core–shell composite led to the efficacious photoinduced hydrogenation of CO_2 to CO under visible light exposure [132]. The photocatalytic evolution rates of CO were substantially boosted with the addition of Ag nps acting as a shell on TiO_2 NWs.

In another study, reverse water gas shift (RWGS) reaction has been used in a monolith photoreactor to reduce the CO_2 over TiO_2-modified with In and Au [133], and CO was witnessed as the key species with every photocatalyst, and along with CO some other products such as C_3H_6, C_2H_6, C_2H_4, and CH_4 were also identified. The quantum efficiency of CO with the Au-In/TiO_2 catalyst was observed to be 0.79%, which was 1.5, 5.64, and 105 times higher in comparison to Au/TiO_2, In-doped TiO_2 and un-doped TiO_2 catalyst, respectively. The generated induced h^+ and e^- resulted in breaking of O–C–O bond, development of C–O, C–H, and O–H bonds. According to thermodynamic scheme, CO_2 molecules requires 20, 18, 14, 12, 8, and 2 e^- to be transformed into C_3H_8, C_3H_6, C_2H_6, C_2H_4, CH_4, and CO, respectively (Fig. 20.7):

$$CO_2 + e - \rightarrow O \cdot CO- \tag{20.26}$$

$$H_2 + 2h^+ \rightarrow H^+ + H^+ \tag{20.27}$$

$$CO_2 + 2H^+ + 2e^- \rightarrow CO + H_2O \tag{20.28}$$

$$CO_2 + 8H^+ + 8e^- \rightarrow CH_4 + 2H_2O \tag{20.29}$$

$$2CO_2 + 12H^+ + 12e^- \rightarrow C_2H_4 + 4H_2O \tag{20.30}$$

$$2CO_2 + 14H^+ + 14e^- \rightarrow C_2H_6 + 4H_2O \tag{20.31}$$

$$3CO_2 + 18H^+ + 18e^- \rightarrow C_3H_6 + 6H_2O \tag{20.32}$$

$$3CO_2 + 20H^+ + 20e^- \rightarrow C_3H_8 + 6H_2O \tag{20.33}$$

The lower Fermi level of Au in comparison to TiO_2 allowed the transfer of photogenerated e^- from the excited states of TiO_2 to Au nps under UV light exposure, which resulted in the excess of e^- to get accumulated in the Fermi level of the metal that boosted the TiO_2's reductive potential. The positive and negative charged plasmas were parted because of the localized SPR of Au nps, and the lifetime of the charges prolonged as a result of redox mechanism enhancement [134].

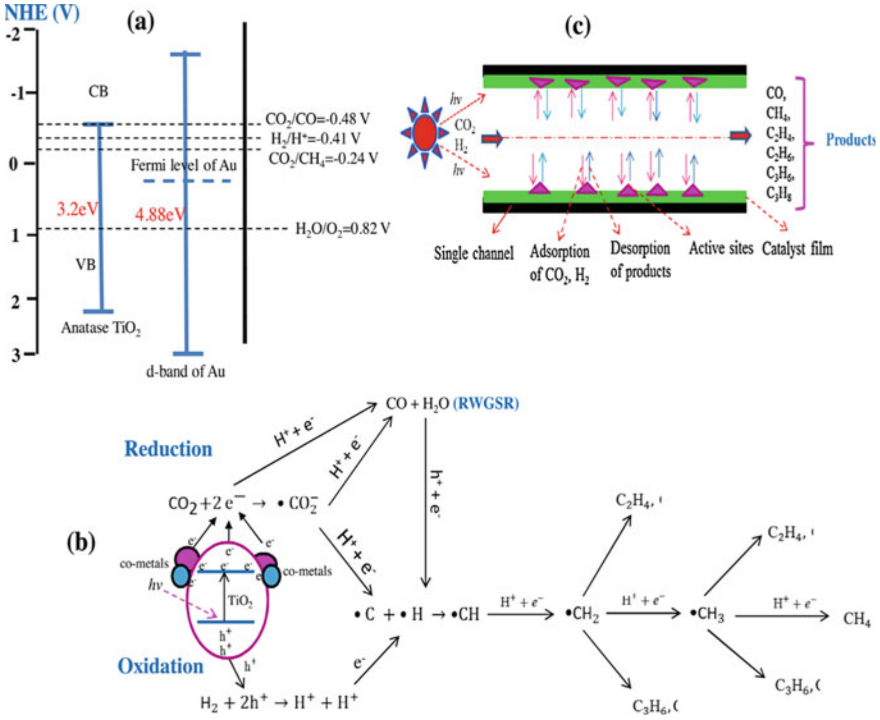

Fig. 20.7 **a** The related redox potential of CO_2 and energy band alignment of Au, TiO_2 (anatase) under 254 nm UV light exposure, **b** reaction representation for hydrogenation of CO_2 with oxidation–reduction mechanism and **c** adsorption–desorption mechanism in a monolith photoreactor. Reproduced from Ref. [133]

The gold decorated titania and titanates are an excellent examples for when the thermal and photoinduced chemistry can lead to very different products using the same reactant feed [90, 135]. It was observed that the size of Au nps on the surface had crucial effect on the resultant performance of the used catalysts that were activated thermally for the hydrogenation of CO_2 [135, 136]. During thermal catalytic reactions of $CO_2 + H_2$, mostly CO and water are the products, while in the photochemical process it is CH_4 to come to the forefront [90, 135]. As was pointed out that the nanostructured 1D titanates, titanate nanotubes (TNT) exhibit excellent properties, which are very useful in catalytic point of view due to its large surface area, and cation exchange properties [69–78]. The characterization techniques such as HRTEM, XPS, UV–visible spectroscopy revealed that the TNT samples comprised of Au clusters and Au ions i.e. Au^+ in much smaller sizes ($\sim d < 3$ nm) most possibly in Au_{25} form. The results implied that Au nps in the smaller size lost their electronic characteristics which can be witnessed in the bulk form. In addition, the plasmonic excitation properties were also found to be relatively larger in the Au nanocrystals. The exchanged gold ions and partially positive charged molecular-like Au_{25} can represent excess energy levels in TNT's band structure that helps in trapping of the photoinduced charges, thereby; prolonging the lifetime of the e^-–h^+ pairs. On the contrary, the presence of Au^+ ions as surface active sites boosted the reduction of CO_2 by synchronizing the e^- rich areas of the byproducts similarly to the O_2 vacancies.

The principle change in accordance with the thermally induced reaction was observed to attain CH_4 as the main product in all the cases. The Ch_4 formation is limited to the UV irradiation intervals. Based on the reaction products (CH_4 and water) and the intermediates which formed in the adsorption ($CO_2{}^{*-}$, $CO_3{}^{2-}$, $HCO_3{}^-$) and in the surface reaction (HCOO), it is proposed that the reduction of CO_2 via photocatalytic means occurs via surface formate [135]. The production of surface formates from carboxylate radical anions according to Eq. (20.34)

$$CO^{*-}_{2\left(Ti^{4+}\right)} + H^{+}_{(TNT)} + e^{-} \rightarrow HCOO^{-}_{\left(Ti^{4+}\right)} \tag{20.34}$$

The Au^+ weakens the C=O bond and coordinates the formate. The forming surface species are not relatively stable and can lead to further reduction (Fig. 20.8). Decisively, the formation of CH_4 occurs via short period of time methoxy intermediate. The intermediates obtained after the photo-hydrogenation after formate possess a short lifetime period as they were not identified via IR spectroscopy. The proposed photocatalytic transformation of formats on the Au/TNT displayed in Fig. 20.8.

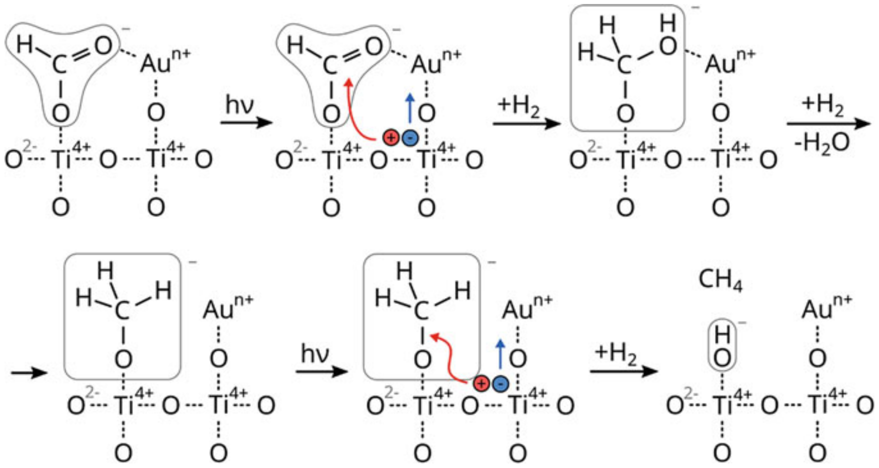

Fig. 20.8 Schematic representation of the photocatalytic conversion of formates on Au/TNT catalyst surface. The gold cation boosts the weakening of the C=O bond. Reproduced from Ref. [135]

20.4 Visible Light Driven Photoreduction of CO_2

The transformation of CO_2 via photocatalytic means to chemical feedstocks and fuels have been a fascinating approach to reduce CO2 emissions and meet the energy demands [137–140]. Semiconductor-based photocatalysis is a capable methodology to obtain chemical energy to solar energy. Various photocatalysts such as TiO_2 [141–143], ZnO [144] and $SrTiO_3$ [145] have been utilized. Moreover, the efficacy of the photocatalytic process is still quite low, due to the rapid electron-hole recombination rate, wide band gap which is unsuited for the lower efficacy of redox reactions and absorption of visible light. The photocatalytic process involves firstly, light absorption and the production of e^-–h^+ pairs by the photocatalyst, secondly, the parting and migration of photoinduced charges to the surface of the photocatalyst, and finally, CO_2 can be reduced into carbonaceous fuels by the photoinduced e^- in the CB, while H_2O would be oxidized into oxygen (O_2) by the photoinduced h^+ in the VB of a photocatalyst in the photocatalytic system of an aqueous solution or H_2O vapor [146].

Photocatalytic transformation of CO_2 relies firmly on the protons and e^- involved as summarized in Table 20.1 [147].

Visible light (VL) (~43%) in comparison to UV (~5%) of the incident solar light, thereby; producing VL-response photocatalysts is of great importance for efficacious solar energy conversion and utilization. In recent years, various VL-active photocatalysts have been produced for the transformation of CO_2 via photocatalytic means.

20.4.1 TiO_2 Based Photocatalysts

TiO_2 is most promising photocatalyst because it is chemically stable, economically viable, nonhazardous, and easily accessible. Moreover, the efficacy of TiO_2 for transformation of CO_2 is still very less because of its high E_g value of 3.2 eV, which bounds its applicability in UV region along with quick recombining tendency of the photoinduced carriers resulting in lower photocatalytic efficacy. Numerous methodologies such as E_g modulation, deposition of noble metals, and development of heterojunctions with other entities have been implemented to improve the VL absorption capability and the efficacious parting of the photoinduced carriers [148]. Asahi et al. studied the TiO_2 anatase's electronic band structure with varying doping entities such as S, P, F, N, C and observed that the doping of N narrowed the E_g and boosted the photocatalytic efficacy in the VL region probably owing to the mixing of O 2*p* valence band of TiO_2 with the N 2*p* level. This study is assumed as a revolution in VL photocatalysis [149]. Producing a distorted geometry by TiO_2's surface modification increased the VL-response. Chen et al. prepared black anatase TiO_2 nanoparticles through hydrogenation and showed photocatalytic H_2 production under near IR and VL absorption with a smaller E_g (1.0 eV). 0.2 mmol of H_2 per hour was generated on TiO_2 (black) loaded with 0.6 wt% Pt in a CH_3OH–H_2O solution that was about 2 times greater to various other semiconductor photocatalysts that have been reported earlier. The boosted photocatalytic efficacy was ascribed to the development of lower-energy midgap electronic states that delayed the recombining tendency of the photoinduced charges (Fig. 20.9) [150].

The oxygen vacancy sites in the TiO_2 makes it VL photocatalyst and also the activation sites for the CO_2 photoreduction [151–153]. TiO_2 nanocrystals deficit of O_2 with co-exposed (101) and (001) facets were reported with comparatively large quantum yield (0.134%) for the reduction of CO_2 to CO by H_2O vapor and 4 times higher efficacy in comparison to TiO_2(P25), TiO_2 (101) or (001) plane under VL exposure was witnessed [154]. Fang and coworkers prepared TiO_2 photocatalysts with increased amount of Ti^{3+} and co-exposed planes of (101) and (001) facets as e^-–h^+ sinks for efficacious parting of charges [155]. Zhao et al. prepared 4 wt% Cu coated black TiO_2. The photocatalytic activity reaches 1.7 folds higher to pure TiO_2 (black). The advanced photoactivity was due to the formation of oxygen vacancies in Cu encapsulated in TiO_2, CO_2 adsorption and increased parting of charges [156]. In addition, thermal treatment of the Cu/TiO_2 (P25) in H_2 atmosphere led to the production of Cu^+/Cu^0, Ti^{3+}, and oxygen vacancies, respectively. The advanced photoreduction can be attributed to the development of surface defect sites boosting CO_2 adsorption and following charge transmission to the adsorbed CO_2 and also, the presence of Cu^+/Cu^0 enable e^-–h_+ sink at varying sites [157]. V and Cu co-doped TiO_2 supported on polyurethane (Cu@VTiO_2/PU) and Cu and Ag co-doped TiO_2 supported on polyurethane (2Ag@4Cu-TiO_2/PU) were prepared for the transformation of CO_2 in reaction with H_2O vapor. The presence of Ti^{3+} increases the e^-–h^+ pair parting efficacy of TiO_2. New CO_2 adsorption sites were

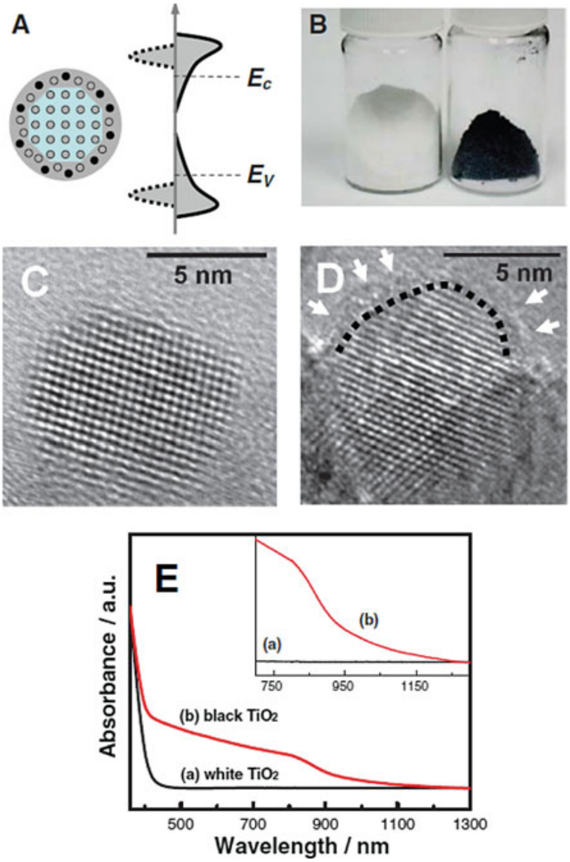

Fig. 20.9 **A** Representation of the scheme to yield black TiO_2. **B** Images of black and white TiO_2 nps. HR-TEM images of **D** black and **C** white TiO_2 nps **E** Optical absorption spectra of **a** white and **b** black TiO_2 nps. Reproduced from Ref. [150]

created due to the existence of O_2 vacancies on the photocatalyst's surface. CO and CH_4 were produced respectively attaining 588 and 933 mmol g^{-1} h^{-1} on 2Cu@4 V-TiO_2/PU 550 and 880 mmol $g_{cat}{}^{-1}$ on 2Ag@4Cu-TiO_2/PU under visible light [158, 159]. Various nonmetals such as N, S, and F used as dopants in TiO_2 have been scrutinized for their VL photocatalytic efficacy [149, 160–162]. Spirulina comprising of Chlorophyll loaded with N-doped TiO_2 catalysts (Sp/N-TiO_2) displayed heightened VL absorption. 0.5Sp/N-TiO_2 in the presence of H_2O photo-reduced CO_2 under VL to C_2H_6, C_2H_4, CH_4, and H_2 and with yields of 0.17, 0.12, 0.48, and 144.99 μmol g^{-1}, respectively. This increased execution in comparison to N-TiO_2 and pure TiO_2 can be ascribed to the boost in VL absorption, the synergistic effect between chlorophyll in Spirulina and N-TiO_2 and the surface oxygen vacancies [163]. I-TiO_2 was applied for the photocatalytic transformation of CO_2 with H_2O under VL exposure. It was observed that Ti^{4+} was substituted I^{5+} and consequently, Ti^{3+} was obtained to maintain neutrality. Under visible light, 10% I-doped TiO_2 was found to be highly active and yielded only CO with a formation rate of 2.4 μmol $g_{cat}{}^{-1}$ h^{-1} [164]. Using N as dopant in mesoporous TiO_2

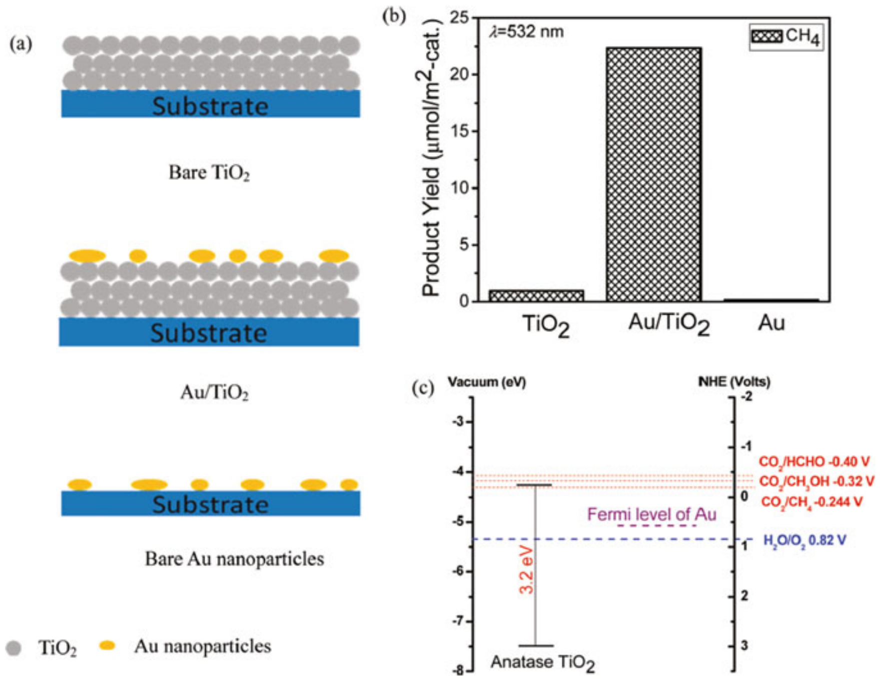

Fig. 20.10 **a** Representation of 3 photocatalysts types. **b** The products were obtained after 15 h of VL exposure after photocatalytic reaction on three varying catalytic surfaces. **c** Energy band alignment of Au, TiO_2 (anatase), and the suitable redox potentials of H_2O and CO_2 under VL exposure. Reproduced from Ref. [171]

with Ag, Au, and Pt as co-catalysts were employed for CO_2 photoreduction with water. It was observed that 0.2 wt% Pt loaded on N-doped mesoporous TiO_2 was more active with the CH_4 formation rate of 2.9 μmol g_{cat}^{-1} h^{-1} [165]. The TiO_2 incorporated with Ni^{2+} restricted the phase transformation and growth of the grain anatase crystallites. In the crystal lattice of TiO_2 the Ti atoms were observed to be replaced by the Ni^{2+} atoms, thereby; causing a shift towards the visible region. Furthermore, the recombining capability of photoinduced e^-–h^+ pairs were substantially quenched by the development of p–n junction in the NiO–TiO_2. It was observed that 1.5 wt% Ni^{2+} loaded catalyst exhibited highest CO_2 photoreduction with the CH_4 and CH_3OH formation rate of 7.71 and 19.51 μmol g_{cat}^{-1} h^{-1} respectively [166]. Ola's group have reported that Co, V, and Cr doped TiO_2 loaded on monolithic structures exhibit large CH_3CHO rate of 11.13 μmol g^{-1} h^{-1} in CO_2 transformation with H_2O in the vapor phase under VL exposure of 4 h with the 0.5 wt% V-TiO_2 monolith [167]. Fan et al. reported that nitrogen and nickel co-doped nano-TiO_2 (N–Ni–TiO_2) photocatalyst displayed a CH_3OH yield of 482 μmol/g-cat that was far more than that of nano-TiO_2 without doping (17.3 μmol/g-cat). The author attributed this increased execution to the synergistic influence of Ni^{2+} and N on nano-TiO_2 [168].

20.4.2 Metal Deposition on TiO_2

It was observed that the depositing plasmonic metal nps on TiO_2 increased the photocatalytic efficacy in the VL region because the metal nps could trigger the e^-–h^+ parting along with the surface e^- excitation due to their SPR effects [169, 170]. Hou and coworkers witnessed the enhancement in the photocatalytic efficacy, which was nearly 24-times greater than Au-deposited TiO_2 in comparison to TiO_2 (pristine) under VL exposure (532 nm) in the photo-transformation of CO_2 with H_2O vapor. This promoting effect is attributed to the sub-E_g absorption in the TiO_2 induced by powerful electromagnetic fields developed by the SP's of the Au nps, thereby; advancing the photocatalytic efficacy to form CH_4 in the VL region. However, in the UV region (254 nm), HCHO, CH_3OH, and C_2H_6 were also obtained alongside CH_4 as the photon energy was sufficient to carry out the d band electronic transitions in Au [171] (Fig. 20.10). TiO_2 nanowire films loaded with Ag NPs (Ag/TiO_2 NWFs) were used for photo-transformation of CO_2 in presence of H_2O. The photocatalyst exhibited visible light absorption properties due to the Ag nanoparticle's SPR and exceptional nanowire geometry of TiO_2 film. Ag NPs also effectually restricted the recombining capability of photoexcited e^-–h^+. The photocatalyst exhibited superior photocatalytic activity with the CH_3OH yield over 0.7 Ag /TiO_2 NWF which was superior in comparison to TiO_2 NWF (Pure) by a factor of 10 under VL and UV exposure [172].

Ang et al. synthesized reduced TiO_2 nanocrystals with co-exposure of [100] and [001] facets as e^- and h^+ sinks for effectual parting of carriers. Fang et al. synthesized reduced TiO_2 nanocrystals with co-exposure [100] and [001] facets as sinks for effectual parting of charges. Using different metals in the alloys can be beneficial to modulate their photocatalytic selectivity and efficacy. Zhang et al. showed that Pt and Au with sizes 5–12 nm co-decorated TiO_2 nanofibers can substantially increase the photo-execution for transformation of CO_2. This considerable boost can be ascribed to the Au nanoparticle's SPR and synergy of the electron-trap ability of Pt, which considerably advanced the charge parting in the TiO_2 [134]. Garcia and coworkers reported the Au-Cu loaded TiO_2 (P25) alloy, which led to the formation of CH_4 at a rate of 2000 μmol g^{-1} h^{-1} and selectivity of 97%. The ideal Cu-to-Au ratio was observed to be 2:1. In these alloy nanoparticles, Au induced VL absorption by SPR effect and Cu acts as bonding site to CO for further CH_4 generation[173].

20.4.3 TiO_2 Based Heterojunctions

Making heterostructures between narrow and wide E_g semiconductors can improve the photoactivity of photocatalysts. This strategy will lead to an increase in high absorption of incident photons in the VL region, boost the parting of e^-–h^+ pair and limit the oxidation and reduction sites. Reduced titania (RT)-Cu_2O heterostructure was reported for the transformation of CO_2 to CH_4. The optimal catalyst RT-$Cu_{0.75}$ displayed CH_4 yield of 462 nmol g^{-1}. The advanced execution can be ascribed to the inhibition of e^-–h^+ pair recombining capability by heterostructure and the presence of oxygen vacancy in the reduced titania that facilitated CO_2 activation and reduction [174]. TiO_2-Cu_2ZnSnS_4 nanocomposites reported for the transformation of CO_2 under VL exposure with a CH_4 and CO formation rates of 0.97 μmol h^{-1} g^{-1} and 14.53 μmol h^{-1} g^{-1}, respectively. In comparison to TiO_2, the maximum formation rates of CH_4 and CO over nanocomposite is 6 and 33 folds larger respectively with the seeming quantum yield of 0.431%. The increased photocatalytic efficacy can be credited to extended visible light absorption, close interfacial contact between TiO_2 and Cu_2ZnSnS_4 which facilitates the electron transference and inhibition of photoexcited charges recombining tendency [175]. In the presence of H_2O, the photocatalytic transformation of CO_2 has been reported using GaP/TiO_2 photocatalysts, in which CH_4 was identified as the key main product. The suitable GaP to TiO_2 ratio was found to be 1:10. The substantially increased efficacy can be credited to the effectual transference of charge between TiO_2 and GaP heterojunction [176]. Wang and coworkers reported CdSe/Pt/TiO_2 heterostructures for the transformation of CO_2 with H_2O under VL exposure. The products obtained were CH_3OH, and CH_4 with yield of 3.3 ppm g^{-1} h^{-1} and 48 ppm g^{-1} h^{-1}, respectively along with traces of H_2 and CO. The photogenerated e^- promoted into the CB of CdSe which were afterward injected into the CB of TiO_2. No activity was detected when CdSe or Pt/TiO_2 catalysts were used individually under identical reaction conditions [177]. The authors further used PbS quantum dots with varying sizes (3, 4 and 5 nm) to sensitize Cu-TiO_2 for CO_2 photoreduction. The CB edge of the smaller PbS was shifted to the higher energies due to the quantum confinement effect, which triggered the promotion of e^- into TiO_2's CB. The Cu/TiO_2 sensitized via 4 nm PbS quantum dot displayed $\sim$ 5 folds larger CO_2 photoreduction over non-sensitized Cu/TiO_2 owing to the synergetic influence of large charge parting and advanced light absorption [178]. Park and coworkers reported the photocatalytic transformation of CO_2 into CH_4 via TiO_2/CdS catalysts in the presence of water with isopropanol. They found that the production of CH_4 was $\sim$tenfold over TiO_2/CdS photocatalyst compared to that of TiO_2, however, the production of H_2 and CO were comparable [179]. Jing et al. reported TiO_2 with N-doped $LaFeO_3$ as VL photocatalyst that displayed advanced CO_2 transformation into O_2, CH_4, and CO as compared to the porous $LaFeO_3$. The substantial increase in efficacy was credited to the large SSA, effectual VL absorption, and charge transference in the interface formed between $LaFeO_3$-TiO_2 (Fig. 20.11) [180].

20.4.4 TiO_2 Combined with Carbon Materials

Graphene has received greater consideration owing to the exceptionally layered geometry, extraordinary physical, electronic, electrical, and optical characteristics

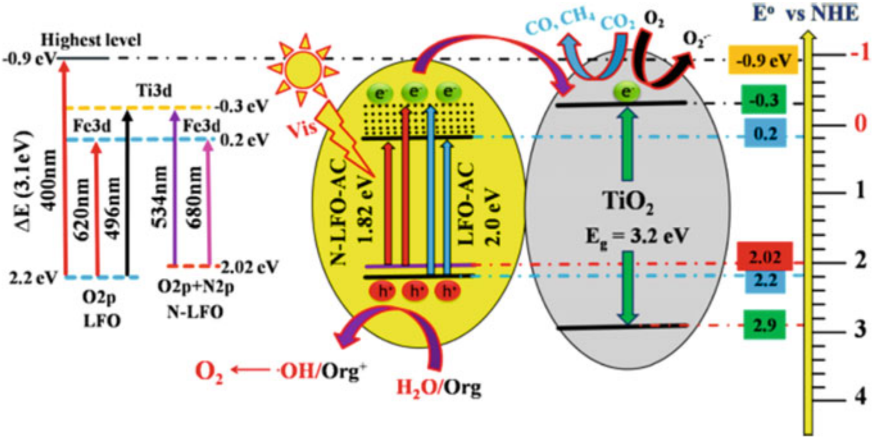

Fig. 20.11 Schematic representation of E_g of TiO_2, 6 N-LFO-AC, and LFO-AC, and the VL excited HLEEs migration in 6 T/6NLFO-AC samples along with the induced oxidation–reduction mechanism. Reproduced from Ref. [180]

[181]. Zhou et al. reported TiO_2/C@ZnCo-ZIF-L for the photocatalytic transformation of CO_2 with the improved CO production rate of 28.6 μmol h^{-1} g^{-1}, greater than those of bare TiO_2 (4.1 μmol h^{-1} g^{-1}), ZIF-L (0.36 μmol h^{-1} g^{-1}) and TiO_2/C (7.8 μmol h^{-1} g^{-1}). The increased photocatalytic efficacy can be credited to the effectual visible light-harvesting, higher e^{-}–h^{+} pairs partition and high CO_2 activation/adsorption capacity of MOF [182]. Recently, combining TiO_2 and graphene has attracted much attention owing to its improved performance. Williams and coworkers studied the GO reduction by photochemical reaction using TiO_2 under ultraviolet (UV) irradiation. Upon UV irradiation, charge separation occurs on the surface of TiO_2 and these formed electrons are accountable for functional group reduction on GO sheets. RGO/TiO_2 composite was formed via interaction of the surface hydroxyl group of TiO_2 with the carboxyl group of GO sheets by charge transfer [183]. Tan and coworkers reported the photo-transformation of CO_2 to CO, CH_4, C_2H_6 and C_2H_4 over 5wt%GO oxygen-rich TiO_2 (5wt%GO-OTiO_2) photocatalyst under VL exposure with H_2O. CH_4 was the main product with the yield of 3.45 μmol g_{cat}^{-1} after reaction period of 8 h over 5wt%GO-OTiO_2 [184]. Tu et al. prepared $Ti_{0.91}O_2$/graphene hollow spheres by epitaxial technique (layer-by-layer). The photo-transformation of CO_2 using $Ti_{0.91}O_2$/graphene hollow spheres exhibited CH_4 and CO formation rates of 1.14 and 8.91 μmolg^{-1} h^{-1} respectively. This photocatalyst exhibited 9- and 5-folds higher efficacy in comparison to P25 and pure $Ti_{0.91}O_2$ hollow spheres, respectively. The substantial increase in the photocatalytic efficacy was credited to the quick transference of charge, prolonged parting of carriers, and advanced absorption of light [185]. TNT arrays incorporated reduced GO (TNT-rGO) was reported for the photo-transformation of CO_2 to methane. TNT-rGO displayed 4.4 times higher CH_4 formation rate in comparison to TNT (pure sample). The advanced execution was credited to the effectual charge

partition triggered by the rGO and superior light absorption [186]. Single-layer graphene was produced from the graphite by liquid-phase exfoliation [187]. Liang et al. prepared graphene-TiO_2 composite by two different solution-led approaches, solvent exfoliation (SEG-TiO_2) and oxidation–reduction (RGO-TiO_2). SEG-TiO_2 displayed greater photocatalytic efficacy for CO_2 transformation to CH_4 in comparison to RGO-TiO_2 owing to increased electron mobility and lesser SEG density defect in comparison to that of RGO, which advanced higher effectual diffusion of photoinduced e^- to the photocatalyst's reactive sites. Compared to bare TiO_2, the SEG-TiO_2 displayed 7.2-fold enhancement under visible light illumination [188]. Moreover, Liang and coworkers also studied the photocatalytic execution of 2D-2D graphene/TiO_2 and 1D-2D SWCNT/TiO_2 nanosheets for the transformation of CO_2. The graphene/TiO_2 nanosheets produced 73.5% more CH_4 than SWCNT-TiO_2 under ultraviolet irradiation. The substantial increase in the photocatalytic execution can be credited to the large contact surface between TiO_2 and graphene than between SWCNT and TiO_2 which facilitates better separation of photogenerated charge carriers and CO_2 photoreduction efficiency. However, SWCNT are more effectual titania photosensitizers, resulting in superior efficacy improvement parameters under VL exposure [189]. Cu_2O/graphene/Titania Nanotube Array (TNA) composite was applied for the photo-transformation of CO_2. The methanol generation rate of 45 μmol cm^{-2} h^{-1} was attained under VL exposure with the seeming quantum efficacy at 420 nm of 5.71%. The superior efficacy was credited to the improved absorption of light, effectual quenching of e^-–h^+ recombining tendency and boosted the transference of e^- across interfaces [190].

20.4.5 Other Metal Oxide Based Photocatalysts

As alternatives to TiO_2, investigation of certain other VL reactive semiconductors for instance metal oxide and mixed metal oxide entities has also been carried out [191]. GO was functionalized by PTCDAAAA (perylenetetracarboxylic dianhydride aspartic acid modified anhydride) with COOH groups to form A-GO, which was then decorated by CdS nanoparticles to construct CdS/A-GO for the transformation of CO_2 with H_2O. CdS/A-GO displayed an increased photocatalytic efficacy in comparison to CdS/P-GO (GO functionalized PTCDA, perylenetetracarboxylic dianhydride) and CdS/GO. CdS/A-GO produced methanol as main product while CdS/P-GO and CdS/GO produced mainly CO. CO formation on CdS/GO, CdS/P-GO, and CdS/A-GO are 0.6, 12.7, and 2.2 μmol h^{-1} respectively. Methanol formation on CdS/GO, CdS/P-GO and CdS/A-GO are 0.1, 1.3, and 26.5 μmol h^{-1} respectively. CdS nanoparticles are responsible for absorbing VL to produce e^-–h^+ pairs while A-GO is responsible for efficient electron–hole separation, CO_2 adsorption and H_2O dissociation. The hydrogen atoms generated from H_2O dissociation and the COOH groups of PTCDAAA leads to the conversion from CO_2 to CH_3OH [192]. Huo et al. reported double-shelled Cu_2O/MnO_x

mesoporous hollow structure to boost the stability and efficacy of Cu_2O-based photocatalytic entities. The CO and H_2 formation rates of 5.71 and 4.11 μmol h^{-1} respectively which was 7.1 times higher in activity compared with Cu_2O nanoparticles. The enhanced activity can be ascribed to multi reflection and scattering of incident light duo to the presence of double-shelled structure, efficacious parting of charges, and easy transference of charge to the photocatalyst's surface [193]. Wang et al. prepared α-Fe_2O_3/Cu_2O photocatalyst with introduction of Z-scheme for CO_2 photo-transformation under VL exposure. The α-Fe_2O_3/Cu_2O hybrid possessing 1:1 molar ratio displayed advanced photocatalytic capability and after 3 h of activity yielded 5.0 μmol ${g_{cat}}^{-1}$ of CO. The substantial increase in the photocatalytic capacity was credited to the higher parting of e^-–h^+ owing to the development of p–n junction as a result of Z-scheme developed between Cu_2O and α-Fe_2O_3 [194]. ZnGaNO nanotubes exhibited improved photocatalytic execution in CO_2 transformation with VL formation rate of 0.072 μmol g^{-1} h^{-1} for ZnGaNO nanotubes which were about 2 times higher than 0.033 μmol g^{-1} h^{-1} for ZnGaNO nanotubes fabricated via solid-state reaction. The increased photocatalytic capability was credited to the large SSA and less recombining tendency of carriers [195]. ZnO/ZnTe hierarchical superstructures were introduced for the photo-transformation of CO_2 into CH_4 under VL exposure. The development of heterojunction increases the activity and facilitated the transference of charge between ZnO and ZnTe and as well as sharing common cations for the heterostructure [196]. CuZnO@Fe_3O_4 core–shell microspheres loaded with rGO was applied as photocatalyst for the photoreduction of CO_2 to methanol under VL exposure. The advanced catalytic execution was credited to the improved migration of e^- and effectual parting of charge via sp^2 hybridized delocalized arrangement in rGO[197]. WO_3 with the E_g of 2.6 eV displayed strong VL absorption. However, the quick recombining ability of the charges restricted its photocatalytic execution. The photocatalytic execution of the WO_3 was improved by tuning its electronic structure [198]. Ultrathin WO_3 nanosheet with thickness of 4–5 nm was prepared for the photo-transformation of CO_2 with vapor of H_2O under VL exposure. The WO_3 nanosheet yielded 1.14 μmol g^{-1} h^{-1} of CH_4. The quantum confinement effect of WO_3 nanosheet exhibits a tuning in the band structure that enabled the photo-transformation of CO_2 that is not possible in the bulk WO_3 [199]. Crystal facets hold a substantial part in determining the specific catalytic performances. WO_3 with rectangular sheet-like crystal geometry with exposed (002) facet produced CH_4 from rCO_2 with H_2O vapor, on the other hand; WO_3 cubes having equal concentrations of (002), (020), and (200) facets were observed to be inactive. It was anticipated that (002) facet comprised of an increasing CB of 0.3 eV as compared to bulk WO_3 which is sufficient to reduce CO_2 to CH_4 [200]. Pt/In_2O_3 coated with a thick carbon layer of 5 nm displayed increased photo-transformation of CO_2 to CH_4 and CO with the evolution rate of 27.9 and 126.6 μmol/h. The considerable increase in the photocatalytic capacity can be accredited to advanced VL absorption, endorsed e^-–h^+ parting and improved chemisorption of CO_2 [201]. Chen et al. reported $Ni(OH)_2$/TaON composite and obtained hydrogen yield of 3.15 μmol h^{-1} which was 2 folds greater in comparison to obtained on 0.5 wt% Pt/TaON

(1.48 μmol h^{-1}) [202]. Porous TaON microspheres were reported for the photo-transformation of CO_2 to CH_3CHO and C_2H_5OH with the formation rate of 0.52 and 2.03 μmol h^{-1} g^{-1} under VL exposure. The considerable increased photocatalytic capacity in comparison to the commercial TaON accredited to the porous spherical geometry, which effectually trapped the incident light and provides more reaction sites [203]. $SnNb_2O_6$ is a layered niobate reported as a VL sensitive photocatalysts for splitting of water and the decontamination of organic pollutants [204–206]. $SnNb_2O_6$ 2D nanosheets displayed advanced photocatalytic execution for the photo-transformation of CO_2 in presence of H_2O to CH_4 with the evolution rate of 110.9 μL h^{-1} g^{-1} under VL exposure. The photocatalytic capability of $SnNb_2O_6$ nanosheets were witnessed to be ~4 and 45 folds greater in comparison to the common N-doped TiO_2 and layered $SnNb_2O_6$, respectively. The increased efficacy was credited to the higher adsorption of CO_2 on $SnNb_2O_6$ nanosheets [207]. $SrTiO_3$ with a bandgap of 3.2 eV were used as photocatalyst in decontamination of contaminants and splitting of water [208]. $SrTiO_3$ doped with Co, Ni and Fe displayed increased photocatalytic capability for transformation of CO_2 with VL exposure. Among which, $SrTiO_3$ doped with Co ions displayed the advanced photocatalytic execution and Pt-$SrTi_{0.98}Co_{0.02}O_3$ yielded 63.6 ppm h^{-1} of CH_4 that was ~ 3 folds greater than that of Pt-TiO_2/N [209]. $SrTiO_3$ co-doped with Au and Rh was evaluated for syngas photosynthesis from and H_2O and CO_2 in VL exposure. The synergistic effect of Rh and Au on $SrTiO_3$ produced advanced syngas that was 153 and 22 times greater to Rh@$SrTiO_3$ and Au@$SrTiO_3$, respectively [210].

20.4.6 Copper-Based Photocatalysts

CuO possessing a narrow E_g value of (1.2–1.5 eV) and being a p-type semiconductor can be incorporated with semiconductors to form heterojunctions and promoting the parting of photo-produced charges. Kim et al. have synthesized Cu_2O/S-doped TiO_2 p-n-p heterojunction for the photo-transformation of CO_2 to CH_4. The photocatalyst produced 2.31 μmol m^{-2} h^{-1} CH_4 that is ~10 times greater in comparison to TiO_2 nanotube. The improved execution of the photocatalyst can be credited to the large light absorption and effectual parting of the e^-–h^+ couples [211]. Wang and coworkers introduced ZnO/CuO nanocomposites for the photo-transformation of CO_2 into CO, where the surface of the CuO nanowires was engineered with large quantity of ZnO islands with the application of atomic layer deposition (pulsed cycles). The nanocomposite displayed the maximum efficacy and yielded 1.98 mmol $g_{cat}{}^{-1}$ h^{-1} of CO. The mechanism for the CO_2 photoreduction involves concurrent CO_2 reduction and H_2O oxidation in the active perimeter area between ZnO islands and CuO nanowire [212]. Gusain et al. reported rGO-copper oxide (CuO and Cu_2O) nanophotocatalysts for the photo-transformation of CO2 into CH_3OH in VL exposure. The rGO-CuO and rGO-Cu_2O composites displayed advanced photocatalytic execution and resulted in

7 (1228 μmol g^{-1}) folds methanol than bare CuO nanorods (175 μmol g^{-1}). The increased photocatalytic execution of CuO was credited to effectual parting of charges and migration of photo-produced e^{-} over the rGO geometry [213]. Wang and coworkers introduced CuO/Cu_2O NWAs@rGO towards photocatalytic transformation of CO_2 to CO in VL exposure. The CuO/Cu_2O NWAs@rGO displayed greater CO yield of 0.31 μmol cm^{-2} than CuO/Cu_2O NWAs (0.2 μmol cm^{-2}). The delay in the recombining capability of e^{-}–h^{+} pair and efficacious migration of photo-produced e^{-} through rGO nanosheets was main the key reason for high photocatalytic execution [214].

20.4.7 Bismuth-Based Photocatalysts

Bi_2WO_6 with narrower E_g value of 2.8 eV can be applied as VL sensitive photocatalyst [215]. Oxygen deficient $Bi_2Sn_2O_7$ nanoparticles were reported for the photo-transformation of CO_2 to CO in VL exposure. The rate at which CO was formed was witnessed to be 14.88 μmolg^{-1} h^{-1} over $Bi_2Sn_2O_7$ that was ~8.1 folds greater in comparison to bulk $Bi_2Sn_2O_7$ which yielded 1.83 μmolg^{-1} h^{-1} of CO. The increased efficacy was accredited to the quick transmission of charges and existence of profuse oxygen vacancies [216]. Ultrathin square nanoplates of Bi_2WO_6 with ~9.5 nm thickness was reported for CO_2 photo-transformation in VL exposure. The photocatalyst displayed improved efficacy and yielded 1.1 μmol g^{-1} h^{-1} of CH_4, which was observed to be superior in comparison to Bi_2WO_6 that yielded 0.045 μmol g^{-1} $h^{-1}$of CH_4 via solid-state reaction. The increased efficacy is because of the presence of preferentially exposed (001) surface. The nanoplates ultrathin geometry promoted quick mobility of the charges that advanced the parting of the photo-produced e^{-}–h^{+} [217]. Hierarchical flower-like Bi_2MoO_6 was scrutinized for the photo-transformation of CO_2 in VL exposure and yielded 18.8 and 24.8 μmol $g_{cat}{}^{-}1$ of C_2H_5OH and CH_3OH, respectively, much greater in comparison to those produced with Bi_2WO_6 hollow microspheres [218]. Ball-flower-like Bi_2WO_6 was reported for photo-transformation of CO_2 in VL exposure. CO was the main product and competitive adsorption between H_2O and CO_2 was observed which decreases the yield of CO [219].

20.4.8 C_3N_4 Based Photocatalysts

Graphitic carbon nitride (g-C_3N_4) with optimal band-edge positions and a moderate E_g value (2.7 eV) can be witnessed to be potential photocatalyst for the obtaining H_2 from splitting of H_2O [220, 221]. Nevertheless, the photocatalytic capacity of pure g-C_3N_4 is somehow less because of quick recombining capability of e^{-}–h^{+} pairs, lower SSA and lower level of light absorption in the VL area [222]. Numerous methodologies for examples, modulating electronic structure, designing nanostructures, engineering crystal-structure, and formation of heterojunctions with other suitable semiconducting entities have been employed to advance the photocatalytic execution of bare g-C_3N_4. Zhang and Dong probably first reported the photo-transformation of CO_2 into CO via bare g-C_3N_4 comprising of porous structure in the presence of vapor in VL exposure [223]. Cu_2ZnSnS_4/Pt-g-C_3N_4 heterojunction was introduced for the transformation of CO_2 into CH_4 and CO in VL exposure. The photocatalyst showed greater CO_2 transformation yielding 17.351/7.961 μmolg^{-1} h^{-}1, which is considered to be an average formation rate for CO/CH_4 and nearly 5.56 and 3.31 folds greater in comparison to pure g-C_3N_4. The considerable increase in the efficacy was credited to the higher SSA, efficacious harvesting tendency of photons via Cu_2ZnSnS_4 and multiple interfacial migrations of photoinduced charges, LSPR, and e^{-} capturing capacity of Pt, which triggered an effectual interfacial charge parting [224]. Zhu et al. reported sheet-like ZnO/$ZnWO_4$/g-C_3N_4 heterojunction for the photocatalytic transformation of CO_2 to C_2H_5OH, CH_3OH, CH_4, and CO with the formation rate of 1.98, 3.85, 6.24, and 1.12 μmol h^{-1} g^{-1}, respectively. The improved efficacy can be credited to the efficacious parting of the photo-produced charges and large capacity for light-harvesting via heterojunction [225]. Precursor dependent photocatalytic activity and product selectivity was observed on g-C_3N_4. The porosity in g-C_3N_4 prepared from urea produced CH_3OH and C_2H_5OH whereas g-C_3N_4 prepared from melamine produced selectively C_2H_5OH for the photo-transformation of CO_2 in VL exposure. The production of different product from different precursors is possibly because of the disparities in the microstructure and crystallinity of g-C_3N_4 [226]. By altering g-C_3N_4's band structure, the selectivity of the CO_2 photo-transformation reaction can be controlled. Niu and coworkers reported that g-C_3N_4 nanosheets and bulk g-C_3N_4 with E_g values of 2.97 and 2.77 eV produced two different products i.e. CH_4 and CH_3CHO [227]. Photocatalyst deposited with noble metals such as Pt, Ag, and Au can considerably improve the photocatalytic transformation of CO_2. Yu and coworkers deposited Pt on g-C_3N_4 in 0–2.0 wt%, which displayed considerable influence on the photocatalytic transformation of CO_2 into HCHO, CH_3OH and CH_4 in VL exposure. The production of CH_4 improved with increase in the Pt loading from 0 to 1 wt% and concurrently, the production of CH_3OH and HCHO were also elevated for Pt loading (0–0.75 wt%). The increased execution was credited to the existence of Pt that boosted the migration and improvement of photo-produced e^{-} to the Pt surface from g-C_3N_4 [228]. Bai and coworkers loaded g-C_3N_4 with varying facets of Pd and it was witnessed that the CO_2 transformation was more likely on Pd (111) facets as compared to Pd with (100) facets [229]. Establishing heterojunction between g-C_3N_4 with other semiconducting entities allows the transmission of charge and thereby, improved the CO_2 photo-transformation mechanism. Jiang and coworkers introduced direct Z-scheme hierarchical α-Fe_2O_3/g-C_3N_4 hybrid system for the photo-transformation of CO_2 to CO, and yielding 27.2 μmol g^{-1} h^{-1} of CO that was observed to be 2.2 folds greater in comparison to (10.3 μmol g^{-1} h^{-1}) generated by pure g-C_3N_4. The results obtained were extraordinary as these were acquired in the absence of sacrifice reagent and cocatalyst [230]. Li et al. reported m-CeO_2/g-C_3N_4 photocatalyst prepared applying silica as hard template. The photo-transformation of CO_2 with vapor (H_2O) resulted in the production of CH_4 and CO. The increased activity was accredited to the synergic influence developed between g-C_3N_4 and CeO_2, which promoted efficacious parting of charges and activation of CeO_2 via the reduction of Ce^{4+} to Ce^{3+} through the captured e^- [231]. He and coworkers fabricated a Z-scheme driven SnO_{2-x}/g-C_3N_4 composite and the SnO_{2-x} with the ideal loading of 42.2 wt% exhibited CO_2 transformation rate of 22.7 μmol g^{-1} h^{-1} which was observed to be 5 and 4.3 folds greater in comparison to P25 and g-C_3N_4, respectively. The increased activity was credited to the development of heterojunction between g-C_3N_4 and SnO_{2-x} which efficaciously triggered the parting of photo-produced charges via direct Z-scheme process [232]. Zhou and coworkers fabricated a heterojunction by synthesizing g-C_3N_4-N-TiO_2 for the photocatalytic transformation of CO_2. It was witnessed that g-C_3N_4-N-TiO_2 produced only one product i.e., CO, whereas, N-TiO_2 produced two products i.e., CH_4 and CO, respectively. The CO was obtained at a rate of 12.2 μmol g^{-1} h^{-1} which was 4 folds greater in comparison to TiO_2(P25) [233]. Wang and coworkers synthesized 2D-2D MnO_2/g-C_3N_4 heterojunction for the photocatalytic transformation of CO_2 to CO and much-advanced efficacy was witnessed in comparison to pristine g-C_3N_4 and MnO_2 which was as a result of well-oriented band positions of g-C_3N_4 and MnO_2 which efficaciously parting the charges [234]. Ye and coworkers fabricated hybrid nanosheets of UiO-66/g-C_3N_4 via electrostatic self-assembly approach for the photo-transformation of CO_2. The resulting nanocomposite displayed increased photocatalytic efficacy for CO_2 transformation to CO in VL exposure in comparison to bulk g-C_3N_4, and g-C_3N_4 bare nanosheets. The improved capability was credited to the efficacious parting of e^-–h^+ pair by the transmission of photo-produced e^- to UiO-66 from the CB of g-C_3N_4 nanosheets [235]. Liu and coworkers introduced hybrid tubular g-C_3N_4/ZIF-8 geometry for the photocatalytic transformation of CO_2 into CH_3OH. The methanol production rate reached 0.75 μmol h^{-1} g^{-1} which was observed to be 3 folds greater to pure g-C_3N_4 [236]. Ong et al. synthesized a heterojunction photocatalysts involving metal-free 0D/2D carbon nanodot/protonated g-C_3N_4 (pCN) (CND/pCN) for the photo-transformation of CO_2 to CO and CH_4. The 3 wt% CND displayed the greatest execution and yielded 29.23 μmol $g_{catalyst}{}^{-1}$ of CH_4 and 29.23 μmol $g_{catalyst}{}^{-1}$ of CO in 10 h of VL exposure, which were 2.28 and 3.6 folds greater in comparison to the pure pCN. The increased efficacy was credited to the multiple advantages that occurred after the between CNDs and pCN. This synergistic influence allowed the quick transmission of photo-produced e^- to CNDs from pCN and delayed the charge recombining tendency [237]. Ong et al. reported a heterojunction formed between the rGO and protonated g-C_3N_4 (pCN) 2D/2D hybrid for the photo-transformation of CO_2 to CH_4. The optimized 15 wt% rGO/pCN displayed the maximum CH_4 generation of 13.93 μmol $g_{catalyst}{}^{-1}$ which were 1.7 and 5.4 folds greater in comparison to 15rGO/CN (pure g-C_3N_4 w/o protonation treatment) and pCN, respectively. The increased efficacy was credited to the exceptional interfacial interaction between 2D/2D rGO/pCN heterojunction that efficaciously migrated photo-produced charges and limits charge recombining ability [238].

20.5 Liquid Phase CO_2 Activation and the Designing and the Upscaling Techniques for CO_2 Converting Photoreactors

Design and development of a photoreactors is crucial in the efficient reduction of CO_2. A photoreactor is usually a chamber in which the reaction products are produced when the incident photons, reactants, and the photocatalyst come in contact with each other. There are three major factors that regulate the overall efficiency of a photoreactor used in photoreduction of CO_2 i.e., operational mode (viz., continuous, batch or semi-batch), configuration of the photocatalyst and the phases of the reactant involved in the reaction (viz., liquid–solid, gas–solid, gas–liquid–solid, etc.) [239, 240]. As shown in Fig. 20.12, the photocatalysts can typically be applied in reactor setups either in the suspended form or after immobilization on a substrate. In order to obtain optimal results, an effective and efficient photoreactor must have a uniform distribution of the incident light throughout the whole system [59]. At present, the comparative study of the product yield and the configuration of the reactors in the photo-transformation of CO_2 is mostly stated in accordance with the quantum efficiency.

20.5.1 Slurry Reactor Systems

When the photocatalyst is dispersed in an aqueous matrix, the rate of the reaction can be examined based on certain factors such as the absorption characteristics of the reactants in the medium, intensity of the incident light on the photocatalyst surface, and quantum efficiency of the photocatalyst. The slurry systems have a key certain advantage in which the photocatalyst with small size and high specific surface area can be uniformly distributed in the aqueous medium, thereby; the incident light can illuminate the entire external surface of the photocatalyst without any phase segregation [239]. Tahir et al. [28] designed and fabricated 3D Ti_3AlC_2 MAX/TiO_2 composite supported on a monolithic substrate with high level of light absorption and charge transfer efficiency via sol–gel method. The photocatalytic reduction of CO_2 was performed in varying reaction systems i.e., methane bi-reforming (MBR), methane dry reforming (MDR), and methane steam reforming (MSR). The Ti_3AlC_2 MAX/TiO_2 showed 6.8 times higher photoreduction efficiency for CO_2 as compared to pristine TiO_2 and yielded 1566 µmol g-cat^{-1} of CO. In another study, Moradi et al. [241] reported Pt@Bi-TiO_2 photocatalysts with varying Bi (0–5 wt%) and Pt (0–2 wt%) dopant concentration using photo-deposition and a two-step sol–gel methodology for photoreduction of CO_2. The results revealed that the TiO_2 modified with 1.5 wt% of Pt and 3 wt% of Bi yielded 20.6 µmol/g of CH_4, which was approximately 6.2 times higher over the pure TiO_2. The increasing doping concentration of Pt and Bi substantially allowed efficient charge transfer that subsequently enhanced the conversion of CO_2 into

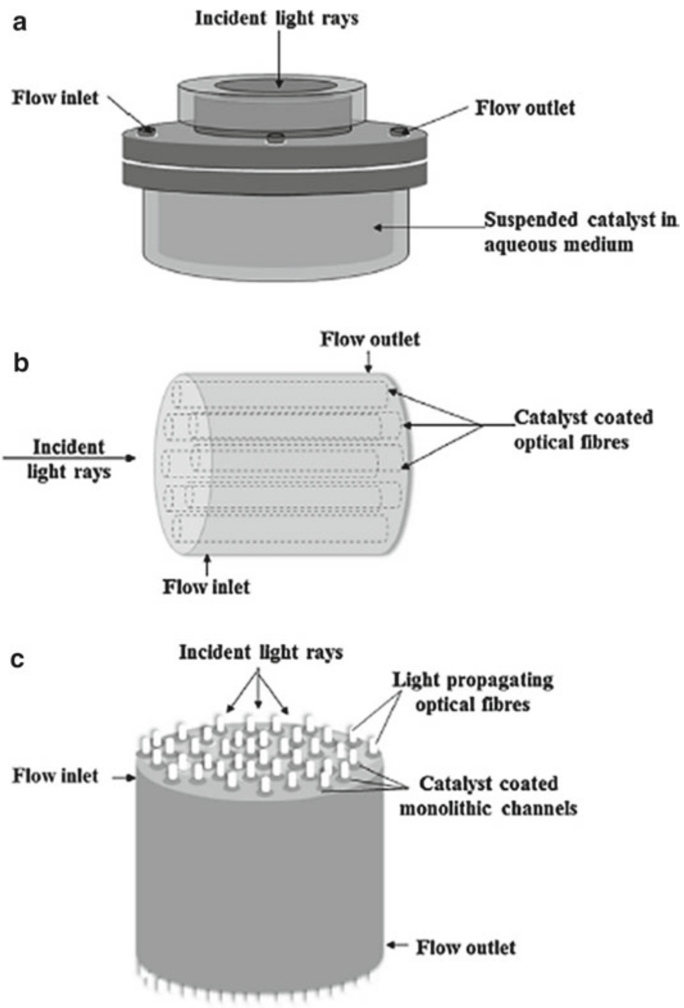

Fig. 20.12 Schematic of **a** slurry reactor design with top illumination, **b** optical fiber reactor design with side illumination and **c** internally illuminated reactor with top illumination. Reproduced from Ref. [59]

CH_4. Muhammad et al. [242] developed a template-free synthesis of lanthanum modified graphitic carbon nitride nanotubes (La/g-CNT) for photoreduction of CO_2. CO with yield of 491 μmole g-cat^{-1} h^{-1} was obtained using 5 wt% La/g-CNT, which was about 5.9 and 3.6 folds greater in comparison to g-CN and g-CNS samples. In addition, La/g-CNT also produced higher amount of H_2 which was almost 5.1 and 2.95 times higher than that of g-CN and g-CNT, respectively. The TiO_2 immobilized ZSM-5 integrated with copper or cobalt catalysts were investigated in a slurry photoreactor, in which $NaHCO_3$ (0.1 M) was used as a reductive agent. The quantum efficiency of CH_3OH with Cu–TiO_2/ZSM-5 resulted in 10.11% after 12 h of reaction time, which was due to the high absorption potential of ZSM-5 that positively influenced the photoconversion rates [243]. Despite the fact that there is ease of operation in the slurry systems and the photocatalyst can be loaded in the higher concentration, however; the removal of the powder photocatalyst from the aqueous medium is still challenging, as the process is time consuming and there is loss of photocatalyst particles during the separation and regeneration process [244–246]. In addition, the incident light travels through the bulk liquid phase and a major part of photocatalyst surface area might remain inactive because of low photon absorption [240, 247].

20.5.2 Immobilized Photocatalyst-Based Fixed Bed Reactor System

The limitations of the photocatalyst recovery from the aqueous medium can be overcome by fixed bed reactor systems, which allow the immobilization of the photocatalysts onto a fixed substrate such as monoliths, fibers, beads, plates, porous carbon, etc. In these designs, the immobilized sample is placed inside the reactor chamber and the light is irradiated directly on it from the light source. However, light distribution in these kinds of reactor designs becomes a major drawback, which is affected by the spatial distance between the photocatalyst and the geometry of the incident light source [248]. Moreover, when choosing the support of choice, the gas phase allows higher flexibility as compared to slurry systems considering the spatial relationship between the light source and the reactor. Tahir et al., [249] reported the Ni and montmorillonite (MMT) immobilized TiO_2 composite, in fixed bed photoreactors system for CO_2 reduction. CO was detected as the main product using photocatalytic RWGS. In addition, the photoreduction of CO_2 with Ni-MMT/TiO_2 composite was significantly higher as compared to TiO_2 and MMT/TiO_2 photocatalysts because of the better MMT dispersion and Ni which offered higher surface area and successfully inhibited the charges recombination rate. Jia et al. [250] in their study rationally designed a novel Ni–Co bimetallic photocatalyst immobilized on a TiO_2-coated SiO_2 spheres (NiCo/TiO2@SiO_2) and examined in fluidized bed reactor for methanation of CO_2. High-level conversion of CO_2 was observed with more than 95% of CH_4 selectivity by the NiCo/TiO_2@SiO_2. Nevertheless, the improved photoreduction execution was constant for over 100 h in the fluidized bed reactor, which confirmed the stability and reproducibility of the immobilized photocatalyst in the long-run. In another study, Liu et al. [251] designed a series of Ni/FDU-12 catalysts via impregnation route with location-controlled Ni particle size. Also, an ethylene glycol solution of trehalose was employed as a sacrificial carbon template and delivery conveyor. The impregnated sample exhibited excellent stability and photocatalytic methanation of CO_2. The carbonization of residual ethylene glycol and trehalose offered a physical barrier between the carbon species inside the pores and the in-situ immobilized Ni nanoparticles, which delayed the charge transfer throughout high-temperature transformation of CO_2. Chen et al. [252] displayed a VL hybrid photocatalytic system for the transformation of CO_2. A simple approach was adopted for the immobilization of $[Ni(terpy)_2]^{2+}$ (Ni(tpy)) on inorganic ligand-capped $CsPbBr_3$ nanocomposite. After the analysis, it was found that the Ni(tpy) boosted the specific catalytic sites and effectually trapped the e^- to prohibit the regrouping of photo-produced charges in the $CsPbBr_3$ nanocomposite. A high yield of 1724 μmol/g in the photoreduction of CO_2 to CH_4/CO was acquired with the $CsPbBr_3$-Ni(tpy) catalytic system, which is ~26 folds greater to $CsPbBr_3$ nanocomposite. Sharma et al. [253] used activated carbon fibers (ACF) for the immobilization of Ni-loaded TiO_2, which offered large illuminated surface area that efficiently boosted the transformation of CO_2 in the aqueous phase (H_2O) to yield CH_3OH under UV and VL exposure. The introduction of Ni in the TiO_2 matrix inhibited the phase transformation and efficiently controlled the grain size of anatase crystallites. The results revealed that after 2 h of VL and UV exposure 986.3 and 755.1 μmol g^{-1} yield of CH_3OH was obtained over NiO–TiO_2/ACF after the photoreduction of CO_2. The immobilized sample was easily separated from the aqueous medium and showed good stability after n-number of cycles.

20.5.3 Gas-Phase Reactor Designs

The conversion into a transportable and storable fuel is a challenging process. The gas-phase CO_2 photoreduction under natural sunlight concentration is the most effective path to setup a feasible CO_2 to fuel translation technology. Until now, numerous investigations have been carried out which have utilized slurry or liquid-based reactor designs for the photoreduction of CO_2. Such designs even under alkaline conditions and high partial pressures suffer poor solubility of CO_2 in the aqueous medium, which is expensive, complex, and the resultant toxic solutions seem to bring no substantial improvement in activity [254, 255]. Accordingly, Hamdy et al. [256] designed a variant mixture containing C_3H_8, C_3H_6, C_2H_6, C_2H_4, and CH_4 set of hydrocarbons, respectively. The hydrocarbon mixture was tested in a photoreactor with water vapor and different photocatalysts under UV illumination. As a result, CH_4 was obtained to be relatively stable as compared to the other hydrocarbons after 2 h of UV illumination, with substantial reduction of CO_2 detected for some photocatalysts. The study of Hamdy et al. certain other researchers [257–259], establish an integral appeal of flow-through photoreactors, in which hydrocarbon products are obtained that can potentially be oxidized in the photoreactor. A descriptive flow-through photocatalytic design can be seen in Fig. 20.13 [260]; where the photocatalyst is suspended over a nanoporous disk that comprised of spun glass which allows the flow of the reactants under AM 1.5 irradiation.

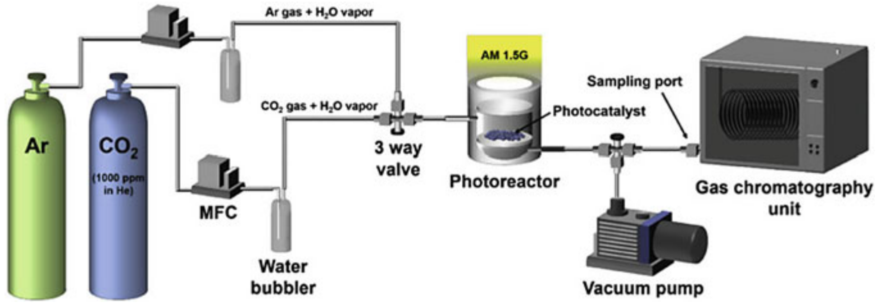

Fig. 20.13 Illustration of experimental layout for flow-through photocatalytic CO_2 to fuel conversion experiments, including online gas chromatography system for dynamic analysis of gaseous products. Reproduced from Ref. [260]

With regard to a marketable photocatalytic design, the photocatalyst as a non-porous substrate or loose powder is impractical for large scale utilization. For an optimum photocatalyst configuration, the usage of engineering it in the form of thick gas-permeable wafers, which are dense enough for high-level absorption of incident light, and possess an adequate degree of mechanical association to empower handling is desirable. The capability to considerably improve the product rate production by photoreactor system allows a stirring outlook. Pipelzadeh et al. [261] in their study reported a standard photoreactor with planar photocatalytic support for gas flows, adapted to handle dynamic pressure swings. The photocatalytic process ($CO_2 + H_2O + AM1.5 \rightarrow CH_4$) was initiated to imitate breathing during the procedure under either of the two conditions i.e., with dynamic pressure swings (PS, 5–3 bar) or constant pressure (CP, 5 bar, flow rates of 50 or 100 ml/min). The described pressure swings and the rate of gas flow were monitored by a Teledyne ISCO D260 syringe pump. Under the gas flow rates of 100 ml/min and 50 ml/min, the rate of change of pressure was found to be 0.8 bar/min and 0.4 bar/min, respectively. The photoreduction of CO_2 by P25 TiO_2 and ZIF-8/P25 TiO_2 nanocomposite samples were tested using the variable/constant pressure photoreactor. The photocatalyst used in the examination under constant and variable pressure swings led to comparable rates of formation of CH_4, and with the increase photocatalyst stability, there was an increase in the flow rates of CH_4 of $\sim 3\times$ to $20\times$, respectively. Brusa and coworkers [262] examined the photocatalytic oxidation of cyclohexane over TiO_2 for the yield and product selectivity of cyclohexanone and cyclohexanol generation under light irradiation ($\lambda \sim$ 254–366 nm) and photon flux (0.3 Einstein cm^2/s 5.0). Working at fixed temperature, it was observed that both the light intensity and irradiation wavelength had a positive influence on the cyclohexanone/cyclohexanol product ratios. However, at certain wavelength, it was observed that the product ratio was directly proportional to the intensity of light irradiation. In concordance from these results, Niu et al. [227] used the fixed graphitic-C_3N_4 and photocatalyst configuration, however, changed the physical structure to vary the bandgap of the composition. In VL exposure, the photoreduction of CO_2 was examined and the major products were observed to be CH_4 and CH_3CHO with graphite-C_3N_4 nanosheets ($E_g \sim 2.97$ eV) and bulk graphitic-C_3N_4 ($E_g \sim 2.77$ eV), respectively. The results implied that the absorption of reactant was found to be dependent on the photocatalyst's atomic structure, which was found to be similar for both the samples, thereby; the initial pathway and the adsorption state of the reactant species were also identical. Hence, the difference in the products obtained will be attributed to variations in the transmission rates of photoinduced charges, which imply the value of being able to distinguish photogenerated exciton efficiently over a prolonged duration of operation. Therefore, it can be inferred that an increase in the level of hindrance around the surface of the photocatalyst confines the mass transfer film resistance, with weakening returns as other rate restrictions such as reaction or diffusion kinetics become dominant. In the end, it can be noted that all reported photoreactor systems have one thing in common i.e., the reaction occurs at the photocatalyst's surface. In other words, a semiconducting entity is irradiated and subsequently treated with $CO_2 + H_2O$, in which the reactants undergo random adsorption and desorption to produce the photogenerated induced charges with the modification in the rate of gas flow, configuration of undergoing reactants, and subsequently, photocatalyst structure and composition [263].

20.6 Summary

In terms of the IPCC (Intergovernmental Panel on Climate Change), Carbon Dioxide Removal alternatives are required to compensate residual emissions from a likely climate overshoot of the goals set at the Paris Agreement. At the industrial level, three strategies are favorable: reduced GHG (greenhouse gas) emissions, CO_2 Capture and Storage (CCS), and CO_2 utilization. In CO_2 utilization processes, the CO_2 molecule activation could be difficult due to the stability of the CO_2 molecule. Beside several thermal methods, the usage of photo-energy can accumulate energy towards better C–O bonding cleavage. With photocatalysis, we can use solar energy, as well as reducing the temperature of reactions of $CO_{2,}$ as well as finding new ways for producing fuels from such carbon source. We believe that the usage of heterogeneous photocatalytic methods for producing valuable products from CO_2 under UV and VL exposure can be an option for further carbon dioxide utilization. For doing so, we focused on the main parts as electron structure of CO_2 and photoexcitation of such molecule; UV light and visible light assisted CO_2 photoactivation in the gas stage over TiO_2 based and other catalysts; Liquid phase CO_2 activation and the designing and upscaling techniques for CO_2 converting photoreactors.

Table 20.1 Photocatalytic CO_2 reduction primary products with their corresponding values of reduction potential (pH = 7)

List of equation	Reaction mechanism	Final products	*E*° (V) versus NHE (pH = 7)
1	$CO_2 + e^- \rightarrow CO_2^{\cdot -}$	Anion radical $CO_2^{\cdot -}$	−1.90
2	$CO_2 + 2\,H^+ + 2mathrme^- \rightarrow CO + H_2O$	CO	−0.53
3	$CO_2 + 2H^+ + 2mathrme^- \rightarrow HCOOH$	HCOOH	−0.61
4	$CO_2 + 8H^+ + 8e^- \rightarrow CH_4 + 2H_2O$	CH_4	−0.24
5	$CO_2 + 4\,H^+ + 4e^- \rightarrow HCHO + H_2O$	HCHO	−0.48
6	$CO_2 + 6\,H^+ + 6e^- \rightarrow CH_3OH + H_2O$	CH_3OH	−0.38
7	$H_2O + 2h^+ \rightarrow 1/2O_2 + 2H^+$	O_2	0.82
8	$2H^+ + 2e^- \rightarrow H_2$	H_2	−0.42

Acknowledgements AS gratefully acknowledges the support of the Bolyai Janos Research Fellowship of the Hungarian Academy of Science and the “UNKP-20-5-SZTE-663” New National Excellence Program of the Ministry for Innovation and Technology. ÁK, and KZ is grateful for the fund of NKFIH (OTKA) K112531 & NN110676 and K120115, respectively. The financial support of the Hungarian National Research, Development, and Innovation Office through the GINOP-2.3.2-15-2016-00013 project “Intelligent materials based on functional surfaces—from syntheses to applications” and the Ministry of Human Capacities through the EFOP-3.6.1-16-2016-00014 project and the 20391-3/2018/FEKUSTRAT are acknowledged.

References

1. Schirone L, Pellitteri F (2017) Sustainability 9:2321
2. Gustavsson L, Haus S, Lundblad M, Lundström A, Ortiz CA, Sathre R, Le Truong N, Wikberg P-E (2017) Renew Sustain Energy Rev 67:612–624
3. Höök M, Tang X (2013) Energy Policy 52:797–809
4. Santos J, Cesarin A, Sales C, Triano M, Martins P, Braga A, Neto N, Barroso A, Alves P, Huaman C (2017) world academy of science EaT. Int J Biol Biomol Agric Food Biotechnol Eng 11:419–426
5. Hussain J, Khan A, Zhou K (2020) Energy 117409
6. Muratori M, Kheshgi H, Mignone B, Clarke L, McJeon H, Edmonds J (2017) Int J Greenhouse Gas Control 57:34–41
7. Nguyen V-H, Nguyen B-S, Jin Z, Shokouhimehr M, Jang HW, Hu C, Singh P, Raizada P, Peng W, Lam SS (2020) Chem Eng J 126184
8. Razzak SA, Ali SAM, Hossain MM, deLasa H (2017) Renew Sustain Energy Rev 76:379–390
9. Yin Z, Palmore GTR, Sun S (2019) Trends Chem 1:739–750
10. Huaman RNE, Jun TX (2014) Renew Sustain Energy Rev 31:368–385
11. Hossain MN, Chen S, Chen A (2019) Appl Catal B: Environ 259:118096

12. Wang X, Wang Y, Gao M, Shen J, Pu X, Zhang Z, Lin H, Wang X (2020) Appl Catal B: Environ 270:118876
13. Qin D, Zhou Y, Wang W, Zhang C, Zeng G, Huang D, Wang L, Wang H, Yang Y, Lei L (2020) J Mater Chem A
14. Ohno T, Murakami N, Koyanagi T, Yang Y (2014) J CO2 Utilization 6:17–25
15. Ali A, Oh W-C (2017) Fullerenes. Nanotubes Carbon Nanostruct 25:449–458
16. Wang Y, Xin F, Chen J, Xiang T, Yin X (2017) J Nanosci Nanotechnol 17:1863–1869
17. Kočí K, Praus P, Edelmannová M, Ambrožová N, Troppová I, Fridrichová D, Słowik G, Ryczkowski J (2017) J Nanosci Nanotechnol 17:4041–4047
18. Zhou R, Guzman MI (2014) J Phys Chem C 118:11649–11656
19. Lo C-C, Hung C-H, Yuan C-S, Wu J-F (2007) Sol Energy Mater Sol Cells 91:1765–1774
20. Pan Y-X, Sun Z-Q, Cong H-P, Men Y-L, Xin S, Song J, Yu S-H (2016) Nano Res 9:1689–1700
21. Senftle TP, Lessio M, Carter EA (2016) Chem Mater 28:5799–5810
22. Yang Y, Zhan F, Li H, Liu W, Yu S (2017) J Solid State Electrochem 21:2231–2240
23. Xiong Z, Lei Z, Xu Z, Chen X, Gong B, Zhao Y, Zhao H, Zhang J, Zheng C (2017) J CO2 Utilization 18:53–61
24. Reli M, Kobielusz M, Daniš S, Macyk W, Obalová L, Kuśtrowski P, Rokicińska A, Kočí K (2017) Appl Surf Sci 391:282–287
25. Tahir M, Amin NS (2013) Energy Convers Manage 76:194–214
26. Nahar S, Zain M, Kadhum AAH, Hasan HA, Hasan M (2017) Materials 10:629
27. Habisreutinger SN, Schmidt-Mende L, Stolarczyk JK (2013) Angew Chem Int Ed 52:7372–7408
28. Tahir M (2020) J CO2 Utilization 38:99–112
29. Sohn Y, Huang W, Taghipour F (2017) Appl Surf Sci 396:1696–1711
30. Pei D, Luan J (2011) Int J Photoenergy 2012
31. White JL, Baruch MF, Pander JE III, Hu Y, Fortmeyer IC, Park JE, Zhang T, Liao K, Gu J, Yan Y (2015) Chem Rev 115:12888–12935
32. Taifan W, Boily J-F, Baltrusaitis J (2016) Surf Sci Rep 71:595–671
33. Freund H-J, Roberts MW (1996) Surf Sci Rep 25:225–273
34. Eischens R, Pliskin W (1957) Advances in Catalysis. Elsevier, pp 662–668
35. Copperthwaite R, Davies P, Morris M, Roberts M, Ryder R (1988) Catal Lett 1:11–19
36. Solymosi F, Bugyi L (1987) J Chem Soc Faraday Trans 1: Phys Chem Condens Phases 83:2015–2033
37. Kiss J, Révész K, Solymosi F (1988) Surf Sci 207:36–54
38. Solymosi F, Klivényi G (1994) Surf Sci 315:255–268
39. Solymosi F, Berkó A (1986) J Catal 101:458–472
40. Liu Z, Zhou Y, Solymosi F, White J (1989) J Phys Chem 93:4383–4385
41. Liu Z, Zhou Y, Solymosi F, White J (1991) Surf Sci 245:289–304
42. Hoffmann F, Weisel M, Paul J (1994) Surf Sci 316:277–293
43. Bartos B, Freund H-J, Kuhlenbeck H, Neumann M, Lindner H, Müller K (1987) Surf Sci 179:59–89
44. Wang Y, Lafosse A, Jacobi K (2002) J Phys Chem B 106:5476–5482
45. Zhou X-L, Zhu X-Y, White J (1991) Surf Sci Rep 13:73–220
46. Ho W (1992) Res Chem Intermed 17:27–38
47. Zhu X (1994) Annu Rev Phys Chem 45:113–144
48. Zhu X-Y (1997) Surf Sci 390:224–236
49. Wolf M, Nettesheim S, White J, Hasselbrink E, Ertl G (1990) J Chem Phys 92:1509–1510
50. Jo SK, Zhu X-Y, Lennon D, White J (1991) Surf Sci 241:231–243
51. Kiss J, Lennon D, Jo S, White J (1991) J Phys Chem 95:8054–8059
52. Solymosi F, Klivényi G (1993) Catal Lett 22:337–342
53. Solymosi F, Klivenyi G (1994) J Phys Chem 98:8061–8066
54. Solymosi F, Kiss J, Kovacs I (1988) J Phys Chem 92:796–803
55. Solymosi F, Kiss J, Révész K (1991) J Chem Phys 94:8510–8519

56. Kovács I, Kiss J, Kónya Z (2020) Catalysts 10:675
57. Diebold U (2003) Surf Sci Rep 48:53–229
58. Henderson MA (2011) Surf Sci Rep 66:185–297
59. Ola O, Maroto-Valer MM (2015) J Photochem Photobiol C 24:16–42
60. Rasko J, Solymosi F (1994) J Phys Chem 98:7147–7152
61. Mo S-D, Ching W (1995) Phys Rev B 51:13023
62. Sekiya T, Igarashi M, Kurita S, Takekawa S, Fujisawa M (1998) J Electron Spectrosc Relat Phenom 92:247–250
63. Murakami M, Matsumoto Y, Nakajima K, Makino T, Segawa Y, Chikyow T, Ahmet P, Kawasaki M, Koinuma H (2001) Appl Phys Lett 78:2664–2666
64. Sumita T, Yamaki T, Yamamoto S, Miyashita A (2002) Appl Surf Sci 200:21–26
65. Toyoda T, Tsuboya I (2003) Rev Sci Instrum 74:782–784
66. Tang H, Berger H, Schmid P, Levy F (1994) Solid State Commun 92:267–271
67. Kavan L, Grätzel M, Gilbert S, Klemenz C, Scheel H (1996) J Am Chem Soc 118:6716–6723
68. Li X, Yu J, Low J, Fang Y, Xiao J, Chen X (2015) J Mater Chem A 3:2485–2534
69. Kukovecz Á, Kordás K, Kiss J, Kónya Z (2016) Surf Sci Rep 71:473–546
70. Dosado AG, Chen W-T, Chan A, Sun-Waterhouse D, Waterhouse GI (2015) J Catal 330:238–254
71. Kasuga T, Hiramatsu M, Hoson A, Sekino T, Niihara K (1998) Langmuir 14:3160–3163
72. Kukovecz Á, Pótári G, Oszkó A, Kónya Z, Erdőhelyi A, Kiss J (2011) Surf Sci 605:1048–1055
73. Bavykin DV, Friedrich JM, Walsh FC (2006) Adv Mater 18:2807–2824
74. Sun X, Li Y (2003) Chem A Eur J 9:2229–2238.
75. Cesano F, Bertarione S, Uddin MJ, Agostini G, Scarano D, Zecchina A (2010) J Phys Chem C 114:169–178
76. Madarász D, Pótári G, Sápi A, László B, Csudai C, Oszkó A, Kukovecz Á, Erdőhelyi A, Kónya Z, Kiss J (2013) Phys Chem Chem Phys 15:15917–15925
77. Pótári G, Madarász D, Nagy L, László B, Sápi A, Oszkó A, Kukovecz A, Erdohelyi A, Kónya Z, Kiss J (2013) Langmuir 29:3061–3072
78. Pusztai P, Puskás R, Varga E, Erdőhelyi A, Kukovecz A, Kónya Z, Kiss J (2014) Phys Chem Chem Phys 16:26786–26797
79. Kumar SG, Devi LG (2011) J Phys Chem A 115:13211–13241
80. Wu MC, Hiltunen J, Sápi A, Avila A, Larsson W, Liao HC, Huuhtanen M, Tóth G, Shchukarev A, Laufer N, Kukovecz A, Kónya Z, Mikkola JP, Keiski R, Su WF, Chen YF, Jantunen H, Ajayan PM, Vajtai R, Kordás K (2011) ACS Nano 5:5025–5030
81. Park H, Park Y, Kim W, Choi W (2013) J Photochem Photobiol C 15:1–20
82. Linsebigler AL, Lu G, Yates JT Jr (1995) Chem Rev 95:735–758
83. Subramanian V, Wolf EE, Kamat PV (2004) J Am Chem Soc 126:4943–4950
84. Jakob M, Levanon H, Kamat PV (2003) Nano Lett 3:353–358
85. Bowker M, Morton C, Kennedy J, Bahruji H, Greves J, Jones W, Davies PR, Brookes C, Wells PP, Dimitratos N (2014) J Catal 310:10–15
86. László B, Baán K, Varga E, Oszkó A, Erdőhelyi A, Kónya Z, Kiss J (2016) Appl Catal B 199:473–484
87. Ioannides T, Verykios XE (1996) J Catal 161:560–569
88. Lan Y, Lu Y, Ren Z (2013) Nano Energy 2:1031–1045
89. Izumi Y (2013) Coord Chem Rev 257:171–186
90. Halasi G, Gazsi A, Bánsági T, Solymosi F (2015) Appl Catal A 506:85–90
91. Yuan L, Xu Y-J (2015) Appl Surf Sci 342:154–167
92. Roy SC, Varghese OK, Paulose M, Grimes CA (2010) ACS Nano 4:1259–1278
93. Dhakshinamoorthy A, Navalon S, Corma A, Garcia H (2012) Energy Environ Sci 5:9217–9233
94. Kulandaivalu T, Mohamed AR, Ali KA, Mohammadi M (2020) Renew Sustain Energy Rev 134:110363

95. Nguyen TP, Nguyen DLT, Nguyen V-H, Le T-H, Vo D-VN, Trinh QT, Bae S-R, Chae SY, Kim SY, Le QV (2020) Nanomaterials 10:337
96. Fujishima A, Honda K (1972) Nature 238:37–38
97. Hemminger J, Carr R, Somorjai G (1978) Chem Phys Lett 57:100–104
98. Anpo M, Chiba K (1992) J Mol Catal 74:207–212
99. Yamashita H, Fujii Y, Ichihashi Y, Zhang SG, Ikeue K, Park DR, Koyano K, Tatsumi T, Anpo M (1998) Catal Today 45:221–227
100. Solymosi F, Tombacz I (1994) Catal Lett 27:61–65
101. Kwak BS, Kang M (2015) Appl Surf Sci 337:138–144
102. Sarkar A, Gracia-Espino E, Wågberg T, Shchukarev A, Mohl M, Rautio A-R, Pitkänen O, Sharifi T, Kordas K, Mikkola J-P (2016) Nano Res 9:1956–1968
103. Liu L, Li Y (2013) Aerosol Qual Res 14:453–469
104. Liu Y, Zhou S, Li J, Wang Y, Jiang G, Zhao Z, Liu B, Gong X, Duan A, Liu J (2015) Appl Catal B 168:125–131
105. Nishimura A, Tatematsu D, Toyoda R, Hirota M, Koshio A, Kokai F, Hu E (2019) MOJ Solar Photoen Syst 3:1–8
106. Nishimura A, Inoue T, Sakakibara Y, Hirota M, Koshio A, Kokai F, Hu E, Mater AIMS (2019) Science 6:464–483
107. Liu L, Zhao C, Miller JT, Li Y (2017) J Phys Chem C 121:490–499
108. Nishimura A (2020) Photochem Photophy Recent Adv IntechOpen
109. Zhang Q-H, Han W-D, Hong Y-J, Yu J-G (2009) Catal Today 148:335–340
110. Grabow L, Mavrikakis M (2011) ACS Catal 1:365–384
111. He H, Zapol P, Curtiss LA (2010) J Phys Chem C 114:21474–21481
112. Valdés Á, Qu Z-W, Kroes G-J, Rossmeisl J, Nørskov JK (2008) J Phys Chem C 112:9872–9879
113. Mikkelsen M, Jørgensen M, Krebs FC (2010) Energy Environ Sci 3:43–81
114. Mahmodi G, Sharifnia S, Rahimpour F, Hosseini S (2013) Sol Energy Mater Sol Cells 111:31–40
115. Kiss J, Alberas DJ, White J (1992) Surf Sci 275:82–91
116. László B, Baán K, Oszkó A, Erdőhelyi A, Kiss J, Kónya Z (2018) Top Catal 61:875–888
117. Ferencz Z, Baán K, Oszkó A, Kónya Z, Kecskés T, Erdőhelyi A (2014) Catal Today 228:123–130
118. Narayanan H, Viswanathan B, Yesodharan S (2016) Current Catal 5:79–107
119. Shi D, Feng Y, Zhong S (2004) Catal Today 98:505–509
120. Merajin MT, Sharifnia S, Hosseini S, Yazdanpour N (2013) J Taiwan Inst Chem Eng 44:239–246
121. Delavari S, Amin NAS (2016) Appl Energy 162:1171–1185
122. Tahir M, Amin NS (2013) Appl Catal B 142:512–522
123. Tahir M, Tahir B, Amin NS (2015) Mater Res Bull 63:13–23
124. Delavari S, Amin NAS, Ghaedi M (2016) J Clean Prod 111:143–154
125. Tahir B, Tahir M, Amin NAS (2018) Energy Convers Manage 159:284–298
126. Dimitrijevic NM, Vijayan BK, Poluektov OG, Rajh T, Gray KA, He H, Zapol P (2011) J Am Chem Soc 133:3964–3971
127. Razzaq A, In S-I (2019) Micromachines 10:326
128. Kohno Y, Hayashi H, Takenaka S, Tanaka T, Funabiki T, Yoshida S (1999) J Photochem Photobiol A 126:117–123
129. Edelmannová M, Lin K-Y, Wu JCS, Troppová I, Čapek L, Kočí K (2018) Appl Surf Sci 454:313–318
130. Wang C, Fang S, Xie S, Zheng Y, Hu YH (2020) J Mater Chem A 8:7390–7394
131. Kong D, Tan JZY, Yang F, Zeng J, Zhang X (2013) Appl Surf Sci 277:105–110
132. Tahir M, Tahir B, Amin NAS, Zakaria ZY (2017) J CO_2 Utilization 18:250–260
133. Tahir B, Tahir M, Amin NS (2015) Appl Surf Sci 338:1–14
134. Zhang Z, Wang Z, Cao S-W, Xue C (2013) J Phys Chem C 117:25939–25947
135. Kiss J, Kukovecz Á, Kónya Z (2019) Catal Lett 149:1441–1454

136. Laszlo B, Baan K, Ferencz Z, Galbacs G, Oszko A, Konya Z, Kiss J, Erdohelyi A (2019) J Nanosci Nanotechnol 19:470–477
137. Rao H, Schmidt LC, Bonin J, Robert M (2017) Nature 548:74–77
138. Voiry D, Shin HS, Loh KP, Chhowalla M (2018) Nat Rev Chem 2:0105
139. Yu J, Low J, Xiao W, Zhou P, Jaroniec M (2014) J Am Chem Soc 136:8839–8842
140. Wang S, Guan BY, Lou XWD (2018) Energy Environ Sci 11:306–310
141. Xu F, Zhang J, Zhu B, Yu J, Xu J (2018) Appl Catal B 230:194–202
142. Miyoshi A, Nishioka S, Maeda K (2018) Chem Eur J 24:18204–18219
143. Xiong Z, Lei Z, Li Y, Dong L, Zhao Y, Zhang J (2018) J Photochem Photobiol C 36:24–47
144. Xin C, Hu M, Wang K, Wang X (2017) Langmuir 33:6667–6676
145. Luo C, Zhao J, Li Y, Zhao W, Zeng Y, Wang C (2018) Appl Surf Sci 447:627–635
146. Schneider J, Matsuoka M, Takeuchi M, Zhang J, Horiuchi Y, Anpo M, Bahnemann DW (2014) Chem Rev 114:9919–9986
147. Fung C-M, Tang J-Y, Tan L-L, Mohamed AR, Chai S-P (2020) Mater Today Sustain 100037
148. Chen X, Mao SS (2007) Chem Rev 107:2891–2959
149. Asahi R, Morikawa T, Ohwaki T, Aoki K, Taga Y (2001) Science 293:269–271
150. Chen X, Liu L, Peter YY, Mao SS (2011) Science 331:746–750
151. Yaghoubi H, Li Z, Chen Y, Ngo HT, Bhethanabotla VR, Joseph B, Ma S, Schlaf R, Takshi A (2015) ACS Catal 5:327–335
152. Indrakanti VP, Schobert HH, Kubicki JD (2009) Energy Fuels 23:5247–5256
153. Indrakanti VP, Kubicki JD, Schobert HH (2011) Fuel Process Technol 92:805–811
154. Liu L, Jiang Y, Zhao H, Chen J, Cheng J, Yang K, Li Y (2016) ACS Catal 6:1097–1108
155. Fang W, Khrouz L, Zhou Y, Shen B, Dong C, Xing M, Mishra S, Daniele S, Zhang J (2017) Phys Chem Chem Phys 19:13875–13881
156. Zhao J, Li Y, Zhu Y, Wang Y, Wang C (2016) Appl Catal A 510:34–41
157. Liu L, Gao F, Zhao H, Li Y (2013) Appl Catal B 134:349–358
158. Pham T-D, Lee B-K (2017) J Catal 345:87–95
159. Pham T-D, Lee B-K (2017) Appl Catal A 529:40–48
160. Yu JC, Ho W, Yu J, Yip H, Wong PK, Zhao J (2005) Environ Sci Technol 39:1175–1179
161. Xu J, Ao Y, Fu D, Yuan C (2008) Appl Surf Sci 254:3033–3038
162. Li D, Haneda H, Hishita S, Ohashi N (2005) Chem Mater 17:2596–2602
163. Phongamwong T, Chareonpanich M, Limtrakul J (2015) Appl Catal B 168:114–124
164. Zhang Q, Li Y, Ackerman EA, Gajdardziska-Josifovska M, Li H (2011) Appl Catal A 400:195–202
165. Li X, Zhuang Z, Li W, Pan H (2012) Appl Catal A 429:31–38
166. Ola O, Maroto-Valer MM (2014) J Catal 309:300–308
167. Ola O, Maroto-Valer MM (2016) Chem Eng J 283:1244–1253
168. Fan J, Liu E-Z, Tian L, Hu X-Y, He Q, Sun T (2011) J Environ Eng 137:171–176
169. Ye W, Long R, Huang H, Xiong Y (2017) J Mater Chem C 5:1008–1021
170. Zheng X, Zhang L (2016) Energy Environ Sci 9:2511–2532
171. Hou W, Hung WH, Pavaskar P, Goeppert A, Aykol M, Cronin SB (2011) ACS Catal 1:929–936
172. Liu E, Hu Y, Li H, Tang C, Hu X, Fan J, Chen Y, Bian J (2015) Ceram Int 41:1049–1057
173. Neaţu ST, Maciá-Agulló JA, Concepción P, Garcia H (2014) J Am Chem Soc 136:15969–15976
174. Ali S, Lee J, Kim H, Hwang Y, Razzaq A, Jung J-W, Cho C-H, In S-I (2020) Appl Catal B Environ 279:119344
175. Raza A, Shen H, Haidry AA, Shahzad MK, Sun L (2020) Appl Surface Sci 529:147005
176. Marcì G, García-López EI, Palmisano L (2014) Catal Commun 53:38–41
177. Wang C, Thompson RL, Baltrus J, Matranga C (2010) The Journal of Physical Chemistry Letters 1:48–53
178. Wang C, Thompson RL, Ohodnicki P, Baltrus J, Matranga C (2011) J Mater Chem 21:13452–13457

179. Park H, Ou H-H, Kang U, Choi J, Hoffmann MR (2016) Catal Today 266:153–159
180. Humayun M, Qu Y, Raziq F, Yan R, Li Z, Zhang X, Jing L (2016) Environ Sci Technol 50:13600–13610
181. Novoselov KS, Geim AK, Morozov SV, Jiang D, Zhang Y, Dubonos SV, Grigorieva IV, Firsov AA (2004) Science 306:666–669
182. Zhou A, Dou Y, Zhao C, Zhou J, Wu X-Q, Li J-R (2020) Appl Catal B: Environ 264:118519
183. Williams G, Seger B, Kamat PV (2008) ACS Nano 2:1487–1491
184. Tan L-L, Ong W-J, Chai S-P, Mohamed AR (2017) Chem Eng J 308:248–255
185. Tu W, Zhou Y, Liu Q, Tian Z, Gao J, Chen X, Zhang H, Liu J, Zou Z (2012) Adv Func Mater 22:1215–1221
186. Razzaq A, Grimes CA, In S-I (2016) Carbon 98:537–544
187. Hernandez Y, Nicolosi V, Lotya M, Blighe FM, Sun Z, De S, McGovern I, Holland B, Byrne M, Gun'Ko YK (2008) Nat Nanotechnol 3:563–568
188. Liang YT, Vijayan BK, Gray KA, Hersam MC (2011) Nano Lett 11:2865–2870
189. Liang YT, Vijayan BK, Lyandres O, Gray KA, Hersam MC (2012) J Phys Chem Lett 3:1760–1765
190. Li F, Zhang L, Tong J, Liu Y, Xu S, Cao Y, Cao S (2016) Nano Energy 27:320–329
191. Nikokavoura A, Trapalis C (2017) Appl Surf Sci 391:149–174
192. Zhu L, Liu Y, Peng X, Li Y, Men Y-L, Liu P, Pan Y-X (2020) ACS Appl Mater Interfaces 12:12892–12900
193. Huo H, Liu D, Feng H, Tian Z, Liu X, Li A (2020) Nanoscale
194. Wang J-C, Zhang L, Fang W-X, Ren J, Li Y-Y, Yao H-C, Wang J-S, Li Z-J (2015) ACS Appl Mater Interfaces 7:8631–8639
195. Zhou P, Gao H, Yan S, Zou Z (2016) Dalton Trans 45:3480–3485
196. Ehsan MF, He T (2015) Appl Catal B 166:345–352
197. Kumar P, Joshi C, Barras A, Sieber B, Addad A, Boussekey L, Szunerits S, Boukherroub R, Jain SL (2017) Appl Catal B 205:654–665
198. Dong P, Hou G, Xi X, Shao R, Dong F (2017) Environ Sci Nano 4:539–557
199. Chen X, Zhou Y, Liu Q, Li Z, Liu J, Zou Z (2012) ACS Appl Mater Interfaces 4:3372–3377
200. Xie YP, Liu G, Yin L, Cheng H-M (2012) J Mater Chem 22:6746–6751
201. Pan Y-X, You Y, Xin S, Li Y, Fu G, Cui Z, Men Y-L, Cao F-F, Yu S-H, Goodenough JB (2017) J Am Chem Soc 139:4123–4129
202. Chen W, Chu M, Gao L, Mao L, Yuan J, Shangguan W (2015) Appl Surf Sci 324:432–437
203. Han Q, Zhou Y, Tang L, Li P, Tu W, Li L, Li H, Zou Z (2016) RSC Adv 6:90792–90796
204. Hosogi Y, Shimodaira Y, Kato H, Kobayashi H, Kudo A (2008) Chem Mater 20:1299–1307
205. Liang S, Zhu S, Chen Y, Wu W, Wang X, Wu L (2012) J Mater Chem 22:2670–2678
206. Liang S, Liang R, Wen L, Yuan R, Wu L, Fu X (2012) Appl Catal B 125:103–110
207. Zhu S, Liang S, Bi J, Liu M, Zhou L, Wu L, Wang X (2016) Green Chem 18:1355–1363
208. Patial S, Hasija V, Raizada P, Singh P, Singh AAPK, Asiri AM (2020) J Environ Chem Eng 103791
209. Kou J, Gao J, Li Z, Yu H, Zhou Y, Zou Z (2015) Catal Lett 145:640–646
210. Li D, Ouyang S, Xu H, Lu D, Zhao M, Zhang X, Ye J (2016) Chem Commun 52:5989–5992
211. Kim HR, Razzaq A, Grimes CA, In S-I (2017) J CO2 Utilization 20:91–96
212. Wang W-N, Wu F, Myung Y, Niedzwiedzki DM, Im HS, Park J, Banerjee P, Biswas P (2015) ACS Appl Mater Interfaces 7:5685–5692
213. Gusain R, Kumar P, Sharma OP, Jain SL, Khatri OP (2016) Appl Catal B 181:352–362
214. Zhang Q, Huang L, Kang S, Yin C, Ma Z, Cui L, Wang Y (2017) RSC Adv 7:43642–43647
215. Zhang L, Zhu Y (2012) Catal Sci Technol 2:694–706
216. Guo S, Di J, Chen C, Zhu C, Duan M, Lian C, Ji M, Zhou W, Xu M, Song P, Long R, Cao X, Gu K, Xia J, Liu H, Zhao Y, Song L, Xiong Y, Li S, Liu Z (2020) Appl Catal B: Environ 276:119156
217. Zhou Y, Tian Z, Zhao Z, Liu Q, Kou J, Chen X, Gao J, Yan S, Zou Z (2011) ACS Appl Mater Interfaces 3:3594–3601
218. Dai W, Yu J, Xu H, Hu X, Luo X, Yang L, Tu X (2016) CrystEngComm 18:3472–3480

219. Sun Z, Yang Z, Liu H, Wang H, Wu Z (2014) Appl Surf Sci 315:360–367
220. Naseri A, Samadi M, Pourjavadi A, Moshfegh AZ, Ramakrishna S (2017) J Mater Chem A 5:23406–23433
221. Yin S, Han J, Zhou T, Xu R (2015) Catal Sci Technol 5:5048–5061
222. Zheng Y, Lin L, Wang B, Wang X (2015) Angew Chem Int Ed 54:12868–12884
223. Dong G, Zhang L (2012) J Mater Chem 22:1160–1166
224. Raza A, Shen H, Haidry AA (2020) Appl Catal B: Environ 277:119239
225. Zhu L, Li H, Xu Q, Xiong D, Xia P (2020) J Colloid Interface Sci 564:303–312
226. Mao J, Peng T, Zhang X, Li K, Ye L, Zan L (2013) Catal Sci Technol 3:1253–1260
227. Niu P, Yang Y, Jimmy CY, Liu G, Cheng H-M (2014) Chem Commun 50:10837–10840
228. Yu J, Wang K, Xiao W, Cheng B (2014) Phys Chem Chem Phys 16:11492–11501
229. Bai S, Wang X, Hu C, Xie M, Jiang J, Xiong Y (2014) Chem Commun 50:6094–6097
230. Jiang Z, Wan W, Li H, Yuan S, Zhao H, Wong PK (2018) Adv Mater 30:1706108
231. Li M, Zhang L, Wu M, Du Y, Fan X, Wang M, Zhang L, Kong Q, Shi J (2016) Nano Energy 19:145–155
232. He Y, Zhang L, Fan M, Wang X, Walbridge ML, Nong Q, Wu Y, Zhao L (2015) Sol Energy Mater Sol Cells 137:175–184
233. Zhou S, Liu Y, Li J, Wang Y, Jiang G, Zhao Z, Wang D, Duan A, Liu J, Wei Y (2014) Appl Catal B 158:20–29
234. Wang M, Shen M, Zhang L, Tian J, Jin X, Zhou Y, Shi J (2017) Carbon 120:23–31
235. Shi L, Wang T, Zhang H, Chang K, Ye J (2015) Adv Func Mater 25:5360–5367
236. Liu S, Chen F, Li S, Peng X, Xiong Y (2017) Appl Catal B 211:1–10
237. Ong W-J, Putri LK, Tan Y-C, Tan L-L, Li N, Ng YH, Wen X, Chai S-P (2017) Nano Res 10:1673–1696
238. Ong W-J, Tan L-L, Chai S-P, Yong S-T, Mohamed AR (2015) Nano Energy 13:757–770
239. Bideau M, Claudel B, Dubien C, Faure L, Kazouan H (1995) J Photochem Photobiol A 91:137–144
240. Ray AK (1999) Chem Eng Sci 54:3113–3125
241. Moradi M, Khorasheh F, Larimi A (2020) Sol Energy 211:100–110
242. Muhammad A, Tahir M, Al-Shahrani SS, Ali AM, Rather SU (2020) Appl Surface Sci 504:144177
243. Wang J-J, Jing Y-H, Ouyang T, Zhang Q, Chang C-T (2015) Catal Commun 59:69–72
244. Palmisano G, García-López E, Marci G, Loddo V, Yurdakal S, Augugliaro V, Palmisano L (2010) Chem Commun 46:7074–7089
245. Guczi L, Erdôhelyi A (2012) Catalysis for alternative energy generation. Springer Science & Business Media
246. Bouchy M, Zahraa O (2003) Int J Photoenergy 5
247. Mukherjee PS, Ray AK (1999) Chem Eng Technol Ind Chem Plant Equipment-Process Eng Biotechnol 22:253–260
248. Howe R (1998) Dev Chem Eng Miner Process 6:55–84
249. Tahir M, Tahir B, Zakaria ZY, Muhammad A (2019) J Clean Prod 213:451–461
250. Jia C, Dai Y, Yang Y, Chew JW (2019) Int J Hydrogen Energy 44:13443–13455
251. Liu Q, Dong H (2020) ACS Sustain Chem Eng 8:2093–2105
252. Chen Z, Hu Y, Wang J, Shen Q, Zhang Y, Ding C, Bai Y, Jiang G, Li Z, Gaponik N (2020) Chem Mater 32:1517–1525
253. Sharma A, Lee B-K (2017) Catal Today 298:158–167
254. Gattrell M, Gupta N, Co A (2006) J Electroanal Chem 594:1–19
255. Hoffmann MR, Moss JA, Baum MM (2011) Dalton Trans 40:5151–5158
256. Hamdy MS, Amrollahi R, Sinev I, Mei B, Mul G (2014) J Am Chem Soc 136:594–597
257. Yang C-C, Vernimmen J, Meynen V, Cool P, Mul G (2011) J Catal 284:1–8
258. Kamegawa T, Shudo T, Yamashita H (2010) Top Catal 53:555–559

259. Ai Z, Lee S, Huang Y, Ho W, Zhang L (2010) J Hazard Mater 179:141–150
260. Sorcar S, Hwang Y, Grimes CA, In S-I (2017) Mater Today 20:507–515
261. Pipelzadeh E, Rudolph V, Hanson G, Noble C, Wang L (2017) Appl Catal B 218:672–678
262. Brusa MA, Grela MA (2005) J Phys Chem B 109:1914–1918
263. Sorcar S, Yoriya S, Lee H, Grimes C, Feng S (2020) Mater Today Chem 16:100264

Chapter 21
Emerging Photocatalysts for Hydrogen Production

Priyanka Pandey and Pravin P. Ingole

Abstract Hydrogen has an enormous potential to become the ideal and promising energy source as it is a green, renewable and high energy density resource. It is efficiently storable and highly abundant in nature. Different approaches have been used to produce hydrogen; however, clean hydrogen production is not always green; i.e. only a few of these methods are environment-friendly. The photo-electrochemical water splitting for hydrogen production got great attention to reduce dependency on a non-renewable resource with waste minimization for clean hydrogen generation. This chapter gives a comprehensive view of different production methods and electrode materials for photocatalytic water splitting towards hydrogen production. The covered topics include different metal oxides (MOs), metal chalcogenides (MSs) and different shapes of nanocomposites, which are used for photoelectrocatalytic hydrogen production. Also, the advantages and disadvantages of the selected materials and methods for hydrogen evolution from water splitting are discussed along with their challenges and prospects.

Keywords H_2 production · Green chemistry · Photocatalyst · Metal oxide (MOs) · Metal chalcogenides · Photoelectrochemical water splitting

21.1 Introduction

Energy is the key source for modern economic growth and social development. The increased industrial energy consumption and demand are global issues due to climate change [1, 2]. The renewable energy (RE) sources offer noticeable solutions towards reduced greenhouse gas (GHG) effects and alternative energy for the long-term economic development [1–3]. Therefore, different techniques providing RE are necessary for developing decarbonized energy sources, which are

---

P. Pandey · P. P. Ingole (✉)
Department of Chemistry, Indian Institute of Technology Delhi, Hauz Khas, New Delhi 110016, India
e-mail: ppingole@chemistry.iitd.ac.in

S. Garg and A. Chandra (eds.), *Green Photocatalytic Semiconductors*,
Green Chemistry and Sustainable Technology,
https://doi.org/10.1007/978-3-030-77371-7_21

low-carbon, safe, and price reliable for the society [2–6]. However, the complete decarbonization of different industry and transport sectors required high energy, challenging through electrification. The same challenge could be addressed by hydrogen fuel from renewables, which allows vast amounts of renewable energy to benefit the power sectors [5–7]. Additionally, the energy storage capacity and high heating value of hydrogen make it excellent fuel than other energy sources [8, 9]. Thus, hydrogen gas (H_2) has been accepted as one of the cleanest energy carriers and environment-friendly compared to fossil fuels [7, 10, 11].

Hydrogen is the most abundant, lightest, simplest and fundamental element in the universe [12]. It has the simplest atomic structure, which consisted of one proton and one electron to easily allow making a bond with various organic and inorganic elements to produce several stable chemical compounds [12, 13]. In the environment, it is found in different forms (water, living materials and fossil fuel) in combination with oxygen, carbon and nitrogen. However, the pair of hydrogen atom constitutes of H_2 molecule and acts as a gas at standard condition while at very low temperature and high pressure, it becomes liquid or solid. It is not a primary source of energy but assumed as a secondary form of energy [12–14]. The way to produce hydrogen needs to assure their environmental impact and energy efficiency on society.

Generally, the existing hydrogen production technologies are thermolysis, steam reforming, auto-thermal reforming, gasification, thermochemical water splitting, plasma arc decomposition, proton exchange membrane and biological methods, and used different feedstocks like natural gas, water, biomass and coal to convert into hydrogen fuel [15–18]. Annually, around 55 million tons of hydrogen produced per year with 6% of consuming rate [16, 17]. Nearly, 50% of global demand for hydrogen emanates from steam methane reforming, rest 28% from oil/naphtha reforming, coal gasification cover 18%, electrolysis of water 3.9% and remaining 0.1% from other sources [16–18]. These applied methods have substantial disadvantages due to the emission of carbon monoxide (CO), carbon dioxide (CO_2), greenhouse gases causative of ozone layer depletion [19–21]. The electrolytic process (plasma arc decomposition, alkaline hydrolysis and water proton exchange membrane) exhibits maximum energy efficiency for hydrogen production. Simultaneously, these processes drawback demands more energy and is a non-sustainable process [20, 21].

Several projects are under process to decrease the production costs and decarbonization associated with sustainable energy [19, 20]. The analytical approach should follow green chemistry principle, namely (i) reduced unnecessary derivatization, (ii) prohibiting waste production, (iii) termination of non-hazardous chemical synthesis, (iv) utilization of renewable feedstocks, (v) energy-efficient approach, (vi) suitable catalyst, (vii) degradable reactant and product and (viii) real-time monitoring of hazardous substance formation [21–24]. Towards this end, the photocatalytic and photo-electrochemical (PEC) water splitting approaches have been extensively used for hydrogen production [23–25]. However, its efficiency in industrial use needs more attention.

Alternatively, the PEC water splitting method is a favourable way to produce hydrogen fuel [22–24]. A PEC cell is a three-electrode system where semiconductor-based photoelectrode absorbs solar energy converted into chemical energy to solve the current energy demand based on green chemistry principle [23–25]. The semiconductors, essential components of a PEC cell, are known as photocatalytic material. It absorbs incident photons and converts it into electron–hole pairs at the surface of nanostructured materials [15]. These photogenerated charge carriers directly take part in splitting water into hydrogen and oxygen [24]. Till date, numerous semiconductors (metal oxides, chalcogenides, nitrides, phosphides, carbides and many more) have been explored due to their different shape, size (1D/2D morphology), atomic arrangements and electrode potential to reduce hydrogen with their high production efficiency [22–24]. Moreover, the selection of semiconductor material for water splitting depends on electrode potential (>1.23 V), bandgap energy, large surface area, fast charge carrier separation, high electronic mobility, suitable morphology, photostable, recyclable and high current density [14, 15].

Several metal oxides (MOs)-based photocatalysts have been studied [24, 25] for water splitting due to their intrinsic properties [14, 15]. Especially those MOs having d0 and d10 electronic configured metal cations showed high quantum efficiencies [26, 27]. Amongst them, TiO_2, Cu_2O, V_2O_5, WO_3, Fe_2O_3, SnO_2 and ZrO_2 have been broadly investigated photocatalyst for water splitting with an applied bias voltage [15, 26–29]. These photo-active materials are only active for ultraviolet (<400 nm) and visible light (400–800 nm) under solar illumination [27]. Although MOs are accomplishing many of the excellent photocatalytic conditions, recombination of electrons–hole pair, probability of reverse reaction and only response for UV and visible light are the major drawback [27–29]. Therefore, the efficiency of MOs is still inadequate for the solar light absorption that can be tuned for more hydrogen production [14, 22–30]. Further, there is a need of advanced materials for PEC investigation to justify the oxidation of organic substrates under UV-Vis-NIR region to enhance their quantum efficiency [31].

Additionally, the earth-abundant transition metal chalcogenides (MoS_2, WS_2, $MoSe_2$, WSe_2, FeS_2, $CoSe_2$, CoS_2, NiS_2, $NiSe_2$, TaS_2, TiS_2, CdS and CdSe) are the emerging photocatalyst for hydrogen production [32–34]. Remarkably, the two-dimensional (2D) metal chalcogenides have gained consideration because of their nanosheet or nanoplates like morphology. It provides a large surface area, different surface states, tunable electrical properties and atomic thickness [33]. These 2D-layered nanosheets showed significant physical, chemical and electronic properties compared to their bulk counterparts [33. 34]. The metal sulphides are the appropriate photocatalysts due to their high carrier mobility, small bandgap, Vis-NIR active and better absorption response compare to the MOs. It has a high conduction band (CB) position and electrode potential for hydrogen production [34]. Moreover, ternary, quaternary or penternary chalcogenides are a new class of alternative catalytic materials because they can offer high flexibility for tuning the bandgap without relying on toxic elements [35]. However, metal sulphides would undergo photo-corrosion in the absence of sacrificial electron donors and protective layering [33–35]. It can be controlled using doping in the metal chalcogenides lattice with impurity atoms (Ni, Cu and O) or compounds (TixOy, NixOy, etc.). It creates structural defects and designed proper Z-scheme heterojunction to inhibit the photo-corrosion [36, 37]. Additionally, the photocatalyst charge transfer path and their mechanism are not well-explained, and it needs progressive research [37]. Theoretical and experimental studies confirmed that metal sulphide-based catalysts' performance is efficient for more hydrogen evolution [35–38]. Furthermore, a successful sustainable, clean and economical energy strategy must be addressed as feasible solutions for all different challenges. This chapter summarizes an overview of emerging photocatalyst and advanced hydrogenation technology with their pros and cons.

21.2 Different Methods of Hydrogen Production

Power of hydrogen is to decrease our dependency on fossil fuel. It reduces the CO_2 emission from the environment and is an encouraging solution for storing variable RE to achieve a 100% renewable and sustainable hydrogen economy. The hydrogen economy consisted of four main steps like fabrication, packaging, security and consumption, interlinked and interdependent. The way to produce hydrogen and their selection of suitable technologies are based on the type of available renewable energy resources that must be clean during the whole process. Hydrogen production method from renewable and non-renewable energy sources has been classified based on "Green Chemistry" principles with their advantages and disadvantages observations. Thus, the five main categories exist for the production of hydrogen associated with their input energy resources, which is given in Table 21.1. This chapter is dedicated to emerging photocatalyst for hydrogen production from photo-electrochemical water splitting techniques.

At the laboratory scale, the first-time hydrogen is produced from "Red-hot Iron filings". It is derived from metal–water hydrogen production methods. It is a primitive method and uses in a hot air balloon. But at large scale for economical purpose, different techniques are developed; out of them, some are explained in this section with their advantages and disadvantages.

21.2.1 Steam Methane Reforming (SMR)

The steam methane reforming (SMR) is a catalytic and energy-efficient profitable technology for producing hydrogen from light hydrocarbons (methane, gasoline, methanol, or ethanol) [4, 6, 11]. Natural gas evolution is an advanced and developed process for near-term hydrogen production [6, 18]. Usually, it uses high-temperature steam (700–1000 °C) to produce hydrogen from natural gas. The SMR is an endothermic reaction in which methane reacts with steam (3–25 bar

Table 21.1 Classification of hydrogen production methods and procedure with their advantage and disadvantage

S. No.	Methods	Procedures	Advantage	Disadvantage	Ref.
1.	Chemical	Red-hot iron filings metal–water hydrogen production	Laboratory scale production (primitive method)	Hydrogen produced at small scale. Energy efficiency is 32%	[39]
2.	Thermal	Thermolysis	Required high thermal (>2500 K) energy to dissociate water into H_2 and O_2 Single-step procedure Using renewable feedstock, reducing derivatives	System requires extreme high temperatures, incompatible with energy efficiency	[40]
		Thermochemical water splitting	Thermochemical water spitting requires moderate temperature ranges (600–1200 K) to split water into H_2 and O_2 No need of separator between H_2 and O_2 evolution. Electricity input is very low	Used H_2SO_4 as hazardous solvent, needs high temperature, multi-steps required	[41]
		Biomass conversion	Crops, agricultural, forestry, industrial and municipal waste used as feedstock	Complex reaction, CO_2 and Tar emit as a by-product, energy efficiency is questionable	[6, 10]
		Steam reforming (a) Steam methane reforming (SMR) (b) Partial oxidation (POX) (c) Auto-thermal Reforming (ATR)	Using biogas or Natural gas as renewable resources. Reduced derivatives Use of catalyst increases the energy efficiency and yield of synthesis Inexpensive and most industrialized method	CO is waste product, Reversible reaction Required high amount of reactant Less energy efficient	[4, 6, 11, 18]
		Gasification	Coal and biomasses use as Solid feedstock At high temperature and pressure, solid fuel reacts with O_2 and steam to produce H_2	Tar and CO/CO_2 as by-product, lower energy efficiency	[19–21]

(continued)

Table 21.1 (continued)

S. No.	Methods	Procedures	Advantage	Disadvantage	Ref.
3.	Electrical	Plasma arc decomposition	CH_4 decomposed into H_2 and CO_2 via plasma arc at high voltage	Uses high voltage, carbon black as by-product	[17, 18]
		Electrolysis (a) Alkaline hydrolysis (b) Proton exchange membrane (c) Solid oxide electrolysis cell	Industrial method, use of renewable energy resources (wind, solar, geothermal) to convert chemical energy into electrical energy Less derivatives	Hazardous by-product, not easily degraded	[11, 15, 16]
4.	Photolytic	Photo-electrochemical water splitting	No waste production, minimum reagent input, uses alkaline electrolyte, working under normal temperature and pressure condition, uses renewable energy resource, single-step reaction and photo catalysts are employed	System components biodegradability and safety information are questionable	[1, 9, 13, 16]
		Hybrid thermo-chemical water splitting cycles	Thermally driven chemical reaction, use of renewable energy, no secondary pollutant	Required multistep reaction, energy efficiency is slow	[16, 24–27]
		High-temperature electrolysis	Steam separated into H_2 and O_2 at high temperature and low heat, use of renewable energy resources (solar, wind or geothermal), as heat sources. Avoids KOH in reaction	Required higher temperature, energy efficiency is less	[26–35]

(continued)

Table 21.1 (continued)

S. No.	Methods	Procedures	Advantage	Disadvantage	Ref.
5.	Biological	Dark Fermentation	Biological route, i.e. in the presence of anaerobic bacteria under dark condition and in the absence of molecular O_2 Reaction drives at room temperature and pressure	CO_2 as a product, maximum use of reagents oppose atom economy, and complex biological mechanisms, create more derivatives	[42]
		Bio-photolysis	Photolysis of water in the presence of anaerobic condition —cyanobacteria or microalgae under presence of solar light. Water is only resource, biological catalysed reaction	Complex biological route	[43]
		Photo-fermentation	Solar light driven biochemical production of H_2 from water	Multistep reaction system, CO_2 as secondary product and other derivatives	[44]
		Artificial photosynthesis	Produces O_2 from capturing CO_2 of air, photo-sensitive catalyst as artificial pigment	Less derivatives and unknown biodegradability of components	[45]

pressure) to produce hydrogen, carbon monoxide (CO) and carbon dioxide (CO_2) [10, 12, 40]. Similarly, in “water–gas shift reaction”, the CO and steam are reacted to produce CO_2 and more hydrogen. Further, the pressure swing adsorption method is used to remove CO_2 and other impurities from the gas stream to get pure hydrogen [39, 40], including other fuels (ethanol, propane or even gasoline) [18–20].

Steam methane reforming reaction

$$CH_4 + H_2O\ (+\text{heat}) \leftrightharpoons CO + 3H_2 \tag{21.1}$$

Water–gas shift reaction

$$CO + H_2O \leftrightharpoons CO_2 + H_2\ (+\text{small amount of heat}) \tag{21.2}$$

This method's significance is the use of renewable feedstocks rather than depleting resources, i.e. minimization of unnecessary secondary product. However, the drawback is the production of the secondary pollutant (CO and CO_2). Since it is a reversible reaction, it required more reagents to convert into a product, i.e. to maximize the incorporation of all reagents used into the final product which opposes the atom economy.

21.2.2 Partial Oxidation (POX)

Partial oxidation (POX) is a non-catalytic technology that utilizes heavy hydrocarbon feedstock to produce CO-rich syngas at high temperatures (between 1100 and 1500 °C). It has been recommended for hydrogen fuel production towards automobile and commercial application [41, 42]. A partial amount of oxygen reacts with the hydrocarbons in POX, which is completely not enough to oxidize the hydrocarbons to CO_2 and H_2O [43]. In the presence of atmospheric oxygen (small amount), the reaction produces hydrogen, CO and a small amount of CO_2, primarily. Also, it produces nitrogen when the reaction has occurred with air rather than pure oxygen. The catalytic partial oxidation (CPOX) system operates at the lower operating temperatures, whereas, due to exothermic nature, it is very tough to control the temperature of reaction [40–43]. Generally, for natural gas conversion, nickel- (Ni) or rhodium (Rh)-based catalysts are required but, Ni has a strong ability to yield coke and Rh make it more costly [42]. Krummenacher and his group [43] have successfully utilized the CPOX process to oxidate decane, hexadecane and diesel fuel. Usually, POX reactors thermal efficiencies with methane fuel estimated 60–75% of heating values [41]. The process requires a smaller reactor vessel and is much faster than steam reforming. However, the produced hydrogen is less compared to the steam reforming process. Moreover, for pure hydrogen production, two separate units must oxidize the methane as air separation and oxygen purification.

$$CH_4 + \frac{1}{2}O_2 + H_2O = 3H_2 + CO_2\,(+\text{heat}) \tag{21.3}$$

This production method is similar to the steam reforming method. The primary modification is that it produces CO_2 instead of CO. This modification does not affect the assessment of partial oxidation and is difficult to control the reaction selectivity towards total combustion of hydrocarbon [43].

21.2.3 Auto-thermal Reforming (ATR)

The auto-thermal reforming (ATR) method is additions of steam into the CPOX system. It consists of a thermal zone where POX and CPOX are used to generate heat that needs to drive the downstream steam reforming reactions in a catalytic zone of the single reactor [44]. Hence, the reactor's temperature profile showed a sharp increase in the thermal zone due to the POX exothermic nature [45]. A significant advantage of this process over SMR is that it can be stopped and started at any time rapidly. It can produce a large amount of hydrogen, lowering the process temperature [46]. In ATR operation, the proportion of oxygen to fuel and steam versus carbon must be accurately controlled at every stage of the temperature reaction and gas production [46–48]. Thus, the ATR method having advantages in relative compactness, lower capital cost and potential at economic scale [48]. The ATR thermal efficiency is comparatively high to that of POX reactors and fewer than that of steam methane reforming [46, 47]. The disadvantage is that it requires air or oxygen, which is not a green approach. It has limited commercial experience in terms of controlling wastes and energy efficiency [21].

21.2.4 Gasification of Coal and Other Hydrocarbons

Gasification is another thermal hydrogen production method. It is a commercially used process to convert biomass and coal liquid into H_2 gas. In this process, the fossil fuel sources react with oxygen and steam at high temperature and pressure. The resulting synthesis gas contains H_2 and CO. In the second step, it reacts with steam to separate the hydrogen [47]. This complex reaction mechanism consists of multiple steps to produce CO and CO_2 [48, 49] as below.

$$C_s + H_2O \rightleftharpoons CO + H_2 \tag{21.4}$$

The gasification process is performed in a fixed bed reactor with or without a catalyst for better performance [50, 51]. The products formed are syngas stream (H_2 to CO) which later used as the feedstock to a Fischer–Tropsch synthesis to produce higher hydrocarbons or in a water–gas shift reaction for the production of hydrogen [50, 52]. However, the gasification process delivers substantial amounts of "tars" as a product at an operational temperature of 800–1000 °C range. Therefore, the ancillary reactor uses calcined dolomite or nickel catalysts to clean and promote product gas [51]. The water–gas shift reaction process can get a pure and increased hydrogen concentration at the separation procedure [53]. Usually, gasification reactors are manufactured at large scale, requiring large amounts of material to be constantly fed to them. Its estimated energy efficiencies 35–50% calculated based on the lower heating value [53]. The major drawback is providing a large amount of resources, which must be collected from the large amounts of biomass increases its logistics costs. This limit of the gasification plants lowers the commercialization of biomass-based hydrogen production.

21.2.5 Electrical Method of Hydrogen Production

Alternatively, an electrical method is an eco-friendly technology of H_2 production through electrolysis of H_2O. It consisted of an electrolytic cell, electrolyte and electrodes system (anode and cathode) interconnected with external bias/potential. When applying an external voltage, an electric current passes through two electrodes and reduces H_2O or hydrocarbon into H_2 (as below equation) [16].

Water electrolysis:

$$H_2O \overset{(\text{electricity})}{\rightarrow} H_2 + \frac{1}{2}O_2 \ \Delta H = -288 \text{ kJ mol}^{-1} \tag{21.5}$$

At anode:

$$4OH^- = O_2 + 2H_2O + 4e^- \tag{21.6}$$

At cathode:

$$2H_2O + 2e^- = H_2 + 2OH^- \tag{21.7}$$

The required electricity is dependent on renewable energy resources such as biomass, geothermal, wind and solar energy [18, 54]. Electrical energy is converted into chemical energy in H_2 and O_2 as an advantageous product in an electrolytic cell. In an alkaline cell, water is introduced at the cathode, which decomposed into H_2 and OH^-. Simultaneously, the OH^- travels through the electrolyte to the anode, where O_2 is formed [55]. During the process, hydrogen is left in the alkaline solution, separated outside in a gas–liquid separations unit of the electrolyzer [55]. It showed 100–300 mA cm^{-2} current density with their energy efficiency of ~50–60%. It is the most common advanced and extensively used electrolysis technology in the industry [56]. The alkaline commercial electrolyzers use 30% KOH for electrolysis that can be reproduced again. Alternatively, the proton exchange membrane (PEM) electrolysis and solid oxide electrolysis cells (SOEC) have also gained significant attention for hydrogenation [56, 57]. In PEM electrolyzers, water electrolysis occurs at the anode where it split into H_2 and O_2 without any separation unit to get pure H_2 [56–58]. In PEM electrolyzer, the following reactions occurred at the anode and cathode.

Water electrolysis:

$$H_2O \overset{(\text{electricity})}{\rightarrow} H_2 + \frac{1}{2}O_2 \ \Delta H = -288 \text{ kJ mol}^{-1} \tag{21.8}$$

At anode:

$$2H_2O \rightarrow O_2 + 4H^+ + 4e^- \tag{21.9}$$

At cathode:

$$4H^+ + 4e^- \rightarrow 2H_2 \tag{21.10}$$

The SOEC electrolyzers are also one of the most electrically efficient solid oxide fuel cells, but less advanced technology compared to PEM. It uses thermal energy in place of the electrical energy to split water into H_2/O_2 [11]. The use of higher temperature increases the electrolyzer efficiency by reducing the anode and cathode overpotentials at high power consumption [15, 16]. SOEC technology is having corrosion problems during the electrolyzing process. Its mechanism is similar to alkaline electrolysis system, where anion travels through the electrolyte and leaving the hydrogen ion in the unreacted steam [59]. The SOEC process requires high temperature, precious materials for fabrication. It makes an additional heat source cost, which makes it more sensitive and expensive [58–60]. Therefore, several studies are going on towards lowering the cost of renewable energy for electrolysis.

21.2.6 Photo-Electrochemical Method

The photo-electrochemical (PEC) water splitting is a photoelectrolysis process, where photoelectrodes are exposed under photonic energies which produce chemical energy at the end of reaction [61, 62]. The hydrogen production follows the sequences as (i) incident photon energy should be greater than the semiconductors bandgap energy to produce electron–hole pair, (ii) fast migration of electron from anode to cathode to produce electrical current, (iii) reduce H^+ and OH^- at cathode and anode, respectively, (iv) gaseous H_2 and O_2 are separated and stored in two different chambers. The photoelectrolysis of H_2O could be understood via the following steps:

Photon absorption

$$4h\nu \rightarrow 4h^+ + 4e^- \tag{21.11}$$

At anode

$$2H_2O + 4h^+ \rightarrow 4H^+ + O_2 \tag{21.12}$$

At cathode

$$4H^+ + 4e^- \rightarrow 2H_2 \tag{21.13}$$

Overall reaction

$$2H_2O + 4hv \rightarrow 2H_2 + O_2 \tag{21.14}$$

The above chemical equation shows that the generation of electron–hole pairs depends upon the number of absorbed photons. The hydrogenation method's advantage is entirely dependent upon renewable energy resources (sunlight) without waste production. Also, it is a single-step photocatalytic reaction at room temperature and pressure. The photo-corrosion is a disadvantage of PEC reaction, which can be controlled using emerging photocatalyst optimization. Chapter 22 discusses the fundamentals and experimental aspects of PEC water, splitting in more essential details. The emerging photocatalysts are specially designed on the physical, chemical and electrical properties (Please see details in Sect. 21.3).

21.3 Emerging Photocatalytic Materials

A wide range of semiconducting materials has been developed as a photocatalyst for hydrogen evolution. It should absorb a sufficient amount of incident radiation to generate electron–hole pair to reduce proton (H^+) into hydrogen (H_2) molecule. Universally, the thermodynamic reduction potential of H^+ to H_2 is 0.0 V versus NHE at pH = 0. Therefore, semiconductor's conduction band (CB) bottom position should have placed at more negative potential than the H^+ reduction potential (shown in Fig. 21.1). Therefore, the synthesized photocatalyst should have a small bandgap, photo and thermally stability, chemically non-reactive, earth-abundant, low cost, and nontoxic [63].

Commonly, three types of photocatalyst have been developed: metal oxides, metal chalcogenides and metal-free photocatalyst from the last few decades [59–63]. But issues due to large bandgap (metal oxides—only absorb UV light), heavy metal toxicity, fast charge recombination, improper band position, costly and eroding nature need to be addressed for further improvement in photocatalyst [64]. In this viewpoint, the two-dimensional (2D) materials, transition metal oxide, MXene (chalcogenide, carbides, nitrides and carbonitrides), oxynitrides, oxysulphide, phosphides, z-scheme heterocatalyst, co-catalyst, metal–organic framework (MOF) and pervoskites have recently attracted much attention as emerging photocatalyst [64–68]. The 2D generation of nanocrystal is having plates or sheet-like

Fig. 21.1 Schematic illustration of photocatalytic hydrogen generation through H^+ reduction reaction

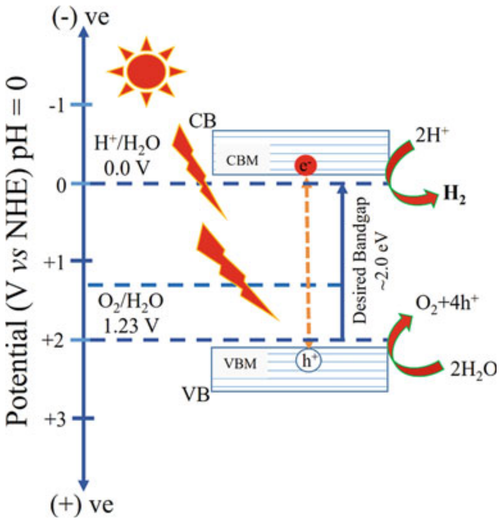

structure with the lateral size 100 nm to few micrometres and the thickness <50 nanometres. It provides a high surface area, excellent physiochemical, electronic and optical properties for photocatalytic hydrogenation [69].

The 2D nanoplates (Fig. 21.2) are arranged in a layer that showed strong covalent bonding in-plane, which offers more active binding sites to establish more heterojunctions. The lateral side of these nanoplates layers is connected with weak van der Waals force [70]. Hence, 2D nanostructure has aroused broad interests as favourable photocatalysts with their advantageous feature. The bandgap and the

Fig. 21.2 Prototypical of 2D nameplates showing in-plane and lateral side bonding that accelerate the activity of photocatalyst for H^+ reduction into H_2

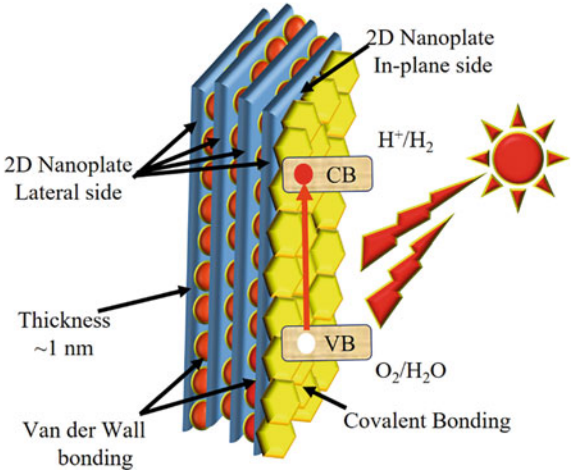

light absorption of the 2D semiconductor can be adjusted by tuning the number of ultrathin layers, reducing the recombination of electrons and holes. Additionally, semiconductors' specific surface area is enhanced and get involved in the photocatalytic reaction [71–73].

21.3.1 Two-Dimensional Transition Metal Chalcogenides

Development of 2D transition metal chalcogenide (2D-TMCs) has gained great attention in recent years. The 2D-TMCs are layered compounds with the general chemical formula of MC2, (M = Fe, Cd, Co, Cu, Mo, W, etc., and C = S and Se) [74]. Amongst them, the 2D-MSs are prepared with hexagonal layers of metal atoms that are sandwiched between two layers of sulphide atoms (S-M-S). In nanosheet plane, sulphides and metal (S-M-S) are attached with covalent bonds, while at the lateral side of the layered sheets are bonded via van der Waals interactions. Several 2D-MS_2 (MoS_2, CuS_2, CoS_2, NiS_2, WS_2, CdS_2 and FeS_2) got attention due to promising visible light active photocatalyst [33, 70–76]. The ultrathin nanolayers of 2D-MoS_2 (thickness $\sim$0.65 nm) are more stable than bulk MoS_2. The synthesized 2D-MoS_2 nanosheet exhibits a direct bandgap of 1.96 eV compared to bulk MoS_2 indirect bandgap of 1.2 eV, and due to that, bulk MoS_2 not able to activate the photocatalytic reaction [70]. In another study, Zhang's group suggested a 10 wt% of WS_2, 2D heterostructured CdS/WS_2 composed of 2D CdS and 2D WS_2 nanosheets exhibited the largest H_2 evolution. The WS_2 functioning as an electron-trapping site, and consequently, it emits H_2 in visible light irradiation, which was greater than that of pure CdS [77, 78]. Giovanni and group synthesized new type of iron sulphide (2D-FeS, pyrrhotite) nanoparticle for water electrolysis towards hydrogen evolution at low overpotentials and gave high current densities [79]. Thus, the studies suggested that MS_2 having noticeable perspective as an economically feasible and capable photocatalyst for water splitting.

21.3.2 Two-Dimensional Transition Metal Oxides (2D TMO)

The 2D transition metal oxides (TiO_2, Co_3O_4, NiO, CuO, MoO_3, m-$BiVO_4$, V_2O_5, Fe_2O_3 and Fe_3O_4) are highly stable and energized towards PEC water splitting applications [74–84]. The 2D nanoplates morphology of anatase TiO_2 provides enhanced active sites on the basal plane side. It catalyses the splitting reaction and yields four times more H_2 than traditional anatase nanocrystals [80]. Chen et al. proposed efficient 2D WO_3 nanoplatelets of larger bandgap than the bulk crystal due to positive shifting in both CB and VB edges for evaluating CH_4 [81]. Also, other n-type 2D MoO_3 (wide bandgap) nanoplates are introduced as an emerging photocatalyst for H_2 evolution. It degrades methylene blue (MB) and rhodamine B (RhB) dyes under the irradiation of sunlight [82]. Additionally, the orthorhombic crystal structure of 2D V_2O_5 ($\sim$80 nm lateral size) makes zigzag double chains of VO_5 pyramids and shares the corners with the oxygen atom bridge. It provides an enhanced surface area for a significant evolution of the H_2 molecule compared to the commercial counterpart [83, 84]. Therefore, the current synthetic approach may reveal a new brand pathway to prepare shape-controlled transition metal oxides nanomaterial for water splitting.

21.3.3 MXenes and Novel Composites

MXenes (Ti_2C, Nb_2C, V_2C, Mo_2C, $(Ti0.5Nb0.5)_2C$, $(V0.5Cr0.5)_3C_2$, Ti_3CN, Ti_3C_2 and Nb_4C_3) are new inventive photocatalyst series of 2D nanomaterials with common formula $M_{n+1}X_nT_x$ ($n = 1 - 3$), where M is a transition metal (Mo, V, Nb or Ti), X is carbide, nitride, carboxynitride, and T_x represents the surface functional groups [76, 86]. The synthesized MXenes are strong photocatalyst with enhanced electrical conductivity and energy efficiency. Yuan et al. synthesized Ti_3C_2 by applying laminated defect-controlled, and carbon-supported sulphur-doped TiO_2 junction photocatalyst (LDC-S-TiO_2/C) exhibited a high rate of H_2 generation [87]. Also, Sun et al. described the improvement of $Ti_3C_2T_x$ composite with carbon nitride. However, MXenes showed both metallic and hydrophilic nature, which can transform into a semi-conductive state using terminal O and F groups' surface adsorption for better catalytic properties [87, 88]. While Su and his group reported that different MXene-Niobium pentoxide/carbon/niobium carbide hybrid photocatalyst exhibited four times higher efficiency than the pure niobium pentoxide [89]. In another study, a CdS composite structure with Ti_3C_2 exhibited a proficient co-catalyst efficiency (14,342 μmol h^{-1} g^{-1}) of H_2 evolution and apparent quantum efficiency of 40.1% at 420 nm irradiation of photons [90]. Hence, the resultant 2D MXene demonstrates an efficient emerging photocatalyst of hydrogen production.

21.3.4 Metal–Organic Frameworks

The metal–organic frameworks (MOFs) materials and their photocatalytic behaviour have been widely reported in different energy storage applications [76]. Their porous structure and the high surface area along with linking ability towards the metal/organic linkers or cages make them promising materials for further applications. Silva et al. evaluated the photocatalytic behaviour of UiO-66 and found a high yield of H_2 in the presence of methanol [91]. A synthesized amino-functionalized titanium (IV) MOF and 2-amino-benzene dicarboxylic acid as organic linker used in H_2 production in an additional study. The resulted hybrid materials exhibited the photon harvesting capability of organic linker towards H_2 evolution [92]. Yan and co-workers produced a CdS-doped MOF composite for evaluation of H_2 production. It exhibited high stability of the catalytic material under solar light irradiation (up to 5 h) [93]. Similarly, Shen et al. reported Au, Pd and Pt metal-doped MOFs' catalytic productivity for H_2 production. They found that in the absence of Pt, the yield is very low related to the doped materials [94]. Significantly, MOF offers strong structural stability along with trading sufficient surface sites to attach more water molecule and resultant H_2 evolution [95]. In a recent study, Gao et al. reported the effect of $Co_xNi_{4-x}S_4$ on the surface of MIL-101 and demonstrated the importance of surface atomic structures for photocatalytic H_2 production. Remarkably, the adsorption is the primary step in the H_2 evolution, and metal sulphide ($Co2Ni_2S_4$@MIL-101) displayed the utmost activity [96].

21.3.5 Z-Scheme Heterostructure Photocatalyst

Newly developed direct Z-scheme-based heterostructure is one of the emerging photocatalytic systems to convert solar energy into H_2 fuel. This system has consisted of two photocatalysts: first acts as hydrogen evolution photocatalyst (HEP) and second acts as oxygen evolution photocatalyst (OEP) [97]. On illumination, the photogenerated electrons of HEP (CB) and hole of OEP (VB) split water into H_2 and O_2, respectively, at two separate photocatalysts. The photoexcited electron in the CB of OEP directly jumps into VB of HEP to combine with photo-holes to provide more electron to reduce H^+ into H_2. The travelling of the electron from HEP CB to OEP VB through a shuttle completing the cycle using "Z-pattern" as shown in Fig. 21.3 [98, 99]. It is also known as artificial photosynthesis motivated via the photosystem II/I (PSII/PSI) coupling from natural

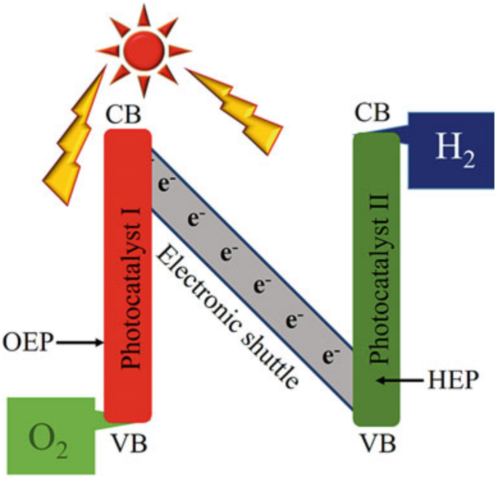

Fig. 21.3 Schematics of 2D Nanoplates based Z-scheme heterostructure photocatalyst system consisted with hydrogen and Oxygen evolution photocatalysts

photosynthesis. Generally, before coupling the HEP and OEP photocatalysts for the Z-scheme system are first examined in half-reactions to test HEP and OEP catalytic activity. The scavenger, namely methanol, sodium sulphide and triethanolamine, is used for H_2 production. It consumed the photogenerated holes, and the remaining photoexcited electrons applied to reduce H^+ efficiently [99]. This system is more efficient than a single photocatalyst, allowing restrictions on the conduction and valence band potentials of semiconductor photocatalysts to be widened [100].

The scientific groups are continually working on "Z-scheme" system towards industrially efficient system by altering the morphology of the semiconductors (shape & size), tuning bandgap, stable redox couples and photostable cocatalysts [99, 100]. Guo's group recently reported ZnO_{1-x}(10 wt%)/$Zn_{0.2}Cd_{0.8}S$ Z-scheme photocatalyst for H_2 production with a high quantum yield (49.5% at 420 nm), which is higher than bare ($Zn_{0.2}Cd_{0.8}S$ and ZnO_{1-x}) sample [97]. In another study, Ta_3N_5 was used to form a direct Z-scheme ZnO@Ta_3N_5 heterostructure that exhibited much higher hydrogen evolution (~500 μmol/g-h) than indirect Z-scheme photocatalyst (Ta_3N_5 and ZnO) [101]. Similarly, direct Z-scheme of C_3N_4-TiO_2, WO_3/g-C_3N_4, and hexagonal boron carbon nitride (BCN)—TiO_2 nanocomposites photocatalysts give new insights on enhancing the photocatalytic H_2 production ability [102, 103]. Thus, the entire Z-scheme system's charge transfer dynamics is more profound to understand the mechanism; i.e. it minimizes the undesirable reversible reaction. This reversible reaction is poorly understood, and it is one of the limiting factors towards the progress of the Z-scheme system, which needs further attention. Thus, the Z-scheme having potentials to convert maximum solar light into fuel energy (~40%) than a single photocatalyst system (~30%), which is a leading energetic force for development.

21.4 Hydrogen Production Mechanism of Photoelectrocatalyst

Photocatalytic water splitting and hydrogen evolution have proven to be an excellent solution to maintain natural resource, and answers economic and social problems [13]. Generally, the photocatalysis process is centred on a semiconducting catalyst material and their conversion efficiency from sunlight to H_2 energy [15]. In PEC water splitting mechanism, the photons absorb light energy, and it should be higher or equal than semiconductor bandgap energy. Consequently, it produces photogenerated charge carriers known as electron–hole pair. Thus, the exciting electrons jump from valence band maximum (VBM) to the conduction band minimum (CBM), leaving holes in the valence band. This phenomenon is known as bandgap photoexcitation [23]. After the initial photoexcitation process, there is a lifetime in the nanosecond regime for the photo-induced electrons. Further, it migrates on the surface of photocatalysts, which participate in the redox reaction. Overall, there is a need for a positive Gibbs free energy (237.13 kJ/mol) to complete the water splitting process; i.e. it cannot occur spontaneously [24]. It directs that the CB potential should be more negative or comparably higher than the redox potential of the lowest unoccupied molecular orbital (LUMO) of the acceptor molecule. For the oxidation reaction, VB potential required more positive than the redox potential of the highest occupied molecular orbital (HOMO) of the donor molecule. This rule directs the property of acceptor/donor molecules to be reduced or oxidized and directly suggests the probability of H_2 and O_2 production. Hence, for efficient H_2 and O_2 evolution, CB potential of the photocatalyst must be more negative than H_2 production level. On the other hand, VB potential has to be more positive than the water oxidation level [75–78].

Overall water splitting:

$$2H_2O \rightarrow 2H_2 + O_2 \quad \Delta G^0 = 237.2\text{kJ mol}^{-1} \tag{21.15}$$

Hydrogen evolution reaction:

$$2H^+ + 2e^- \rightarrow H_2 \tag{21.16}$$

Oxygen evolution reaction:

$$2H_2O + 4h^+ = O_2 + 4H^+ \tag{21.17}$$

Therefore, the water splitting requires two electrons and four holes (as shown in equation) to evolve one molecule of H_2 or O_2, respectively. Hence, overall water splitting depends (Fig. 21.1) on the CBM and VBM positions, bandgap and size [85, 88, 97]. Therefore, 1.23 eV minimum activation energy is required to cross the energy barrier as well as to split water into H_2 and O_2. This is possible if semiconducting material absorbs approximately 1000 nm wavelength of the light near-infrared region [98–100]. The photocatalyst energy bandgap should be approximately 2.0 eV towards efficient splitting. It can absorb a maximum portion of the solar spectrum with a minimum required overpotential [100, 104]. The major disadvantages of PEC reaction are the recombination of the electron–hole pair. It should be very less in competition with the charge transfer process, which otherwise impedes the PEC efficiency [97–99]. The PEC reaction efficiency completely integrated with semiconductor electronic structure and their reaction ability at the electrode/electrolyte interface [104, 105]. The photocatalytic water splitting having two different ways to get desired H_2 molecule, i.e. single semiconductor photocatalyst system (SSPS) and two semiconductor photocatalyst system (TSPS). The SSPS required one-step photoexcitation and photoexcited electron directly jump from VB to CB of the same photocatalyst. There are no other trapping sates available, which may increase the recombination rate of electron and hole pair [104, 105]. Whereas, in the TSPS process, photoexcitation induces electrons and holes at two different places (one electron-rich and another hole-rich). The first semiconductor photoexcited electron trapped by the second semiconductor VB (following Z-pattern) and minimizes the recombination rate of electron and hole [15, 104]. The TSPS system has a better competency in facilitating charge separation and redox ability. Therefore, it is assuming that as addressed aforementioned, emerging photocatalysts should have broad light absorption range, efficient charge separation and strong redox ability to govern efficient photocatalytic water splitting reaction.

21.5 Summary

Several methods and techniques have been explored for the generation of H_2 fuel. Alternatively, significant development towards H_2 production is going on from renewable resources to lower the dependency on fossil fuels and reduce carbonization. H_2 generation technologies from several resources such as natural gas, biomass, petroleum and water are being done. Table 21.1 summarizes different methods, which utilizes a green chemistry approach along with their applied feedstocks, advantages, disadvantages and energy efficiencies. Amongst, the popular technologies SMR, POX, ATR and gasification methods, they can generate a significant amount of H_2. Overall, the H_2 production and its efficiency depend on technology resources, reaction condition and semiconducting material cost. Also, these methods are compromising green chemistry principle somewhere. The noteworthy progress has been made in the improvement of H_2 production. It is technologically more advance and cost-effective compared to the traditional approach. In PEC method, water splits to produce H_2 using emerging photocatalyst in the presence of sunlight, i.e. renewable energy source. These 2D nanostructured emerging photocatalysts are extensively used due to high surface area, small bandgap, lower recombination of electron–hole pair and high efficiency of quick charge separation and transfer. Further, optimization of these emerging photocatalyst may provide new insights into their use in low-cost renewable energy application.

Acknowledgements Priyanka Pandey is thankful to DST, New Delhi, India, for the funded project (SR/WOS-A/CS-90/2016) under the WOS-A scheme. Pravin P. Ingole is thankful to SERB-DST for the funded projects (SB/FT/CS-047/2014 and SB/EMEQ-339/2014).

References

1. Muhammad R, Mubashar R, Irshad M, Gillani SSA, Tahir MBilal, Khalid NR, Yasmin A, Shehzad MA (2020) A comprehensive study on methods and materials for photocatalytic water splitting and hydrogen production as a renewable energy resource. J Inorg Organomet Polym Mater 30:3837–3861. https://doi.org/10.1007/s10904-020-01611-9
2. Stambouli AB, Traversa E (2002) Fuel cells, an alternative to standard sources of energy. Renew Sustain Energy Rev 6:295–304. https://doi.org/10.1016/S1364-0321(01)00015-6

3. Kumar A, Kumar K, Kaushik N, Sharma S, Mishra S (2010) Renewable energy in India: current status and future potentials. Renew Sustain Energy Rev 14:2434–2442. https://doi.org/10.1016/j.rser.2010.04.003
4. Holladay JD, Hu J, King DL, Wang Y (2009) An overview of hydrogen production technologies. Catal Today 139:244–260. https://doi.org/10.1016/j.cattod.2008.08.039
5. Nilsson M (2007) Red light for green paper: the EU policy on energy efficiency. Energy Policy 35:540–547. https://doi.org/10.1016/j.enpol.2005.12.023
6. Singh S, Jain S, Venkateswaran PS, Tiwari AK, Nouni MR, Pandey JK, Goel S (2015) Hydrogen: a sustainable fuel for future of the transport sector. Renew Sustain Energy Rev 51:623–633. https://doi.org/10.1016/j.rser.2015.06.040
7. Sanderson K (2011) It's not easy being green. Nature 469:18–23. https://doi.org/10.1038/469018a
8. Pudukudy M, Yaakob Z, Mohammad M, Narayanan B, Sopian K (2014) Renewable hydrogen economy in Asia-opportunities and challenges: an overview. Renew Sustain Energy Rev 30:743–757. https://doi.org/10.1016/j.rser.2013.11.015
9. Yao Y, Gao X, Li Z, Meng X (2020) Photocatalytic reforming for hydrogen evolution: a review. Catalysts 10:335–352. https://doi.org/10.3390/catal10030335
10. Sobrino FH, Monroy CR, Perez JLH (2010) Critical analysis on hydrogen as an alternative to fossil fuels and biofuels for vehicles in Europe. Renew Sustain Energy Rev 14:772–780. https://doi.org/10.1016/j.rser.2009.10.021
11. Dincer I, Acar C (2015) Review and evaluation of hydrogen production methods for better sustainability. Int J Hydrogen Energy 40:11094e117. https://doi.org/10.1016/j.ijhydene.2014.12.035
12. Momirlan M, Veziroglu TN (2005) The properties of hydrogen as fuel tomorrow in sustainable energy system for a cleaner planet. Int J Hydrogen Energy 30:795–802. https://doi.org/10.1016/j.ijhydene.2004.10.011
13. Dey KK, Gahlawat S, Ingole PP (2019) $BiVO_4$ optimized to nano-worm morphology for enhanced activity towards photoelectrochemical water splitting. J Mater Chem A 7:21207–21221. https://doi.org/10.1039/c9ta07353a
14. García N, Mori K, Kuwahara Y, Yamashita H (2018) Recent strategies targeting efficient hydrogen production from chemical hydrogen storage materials over carbon-supported catalysts. NPG Asia Mater 10:277–292. https://doi.org/10.1038/s41427-018-0025-6
15. Fujishima A, Honda K (1972) Electrochemical photolysis of water at a semiconductor electrode. Nature 238:37–38. https://doi.org/10.1038/238037a0
16. Hosseini SE, Wahid MA (2016) Hydrogen production from renewable and sustainable energy resources: promising green energy carrier for clean development. Renew Sust Energy Rev 57:850–866. https://doi.org/10.1016/j.rser.2015.12.112
17. Balat H, Kırtay E (2010) Hydrogen from biomass-Present scenario and future prospects. Int J Hydrogen Energy 35:7416–7426. https://doi.org/10.1016/j.ijhydene.2010.04.137
18. Ehteshami SMM, Chan SH (2014) The role of hydrogen and fuel cells to store renewable energy in the future energy network-potentials and challenges. Energy Policy 73:103–109. https://doi.org/10.1016/j.enpol.2014.04.046
19. Abdalla AM, Hossain S, Nisfindy OB, Azad AT, Dawood M, Azad AK (2018) Hydrogen production, storage, transportation and key challenges with applications: a review. Energy Convers Manag 165:602–627. https://doi.org/10.1016/j.enconman.2018.03.088
20. Rosen MA, Koohi-Fayegh S (2016) The prospects for hydrogen as an energy carrier:an overview of hydrogen energy and hydrogen energy systems. Energ Ecol Environ 1:10–29. https://doi.org/10.1007/s40974-016-0005-z
21. Celik D, Yıldız M (2017) Investigation of hydrogen production methods in accordance with green chemistry principles. Int J Hydrog Energy 42:23395–23401. https://doi.org/10.1016/j.ijhydene.2017.03.104
22. Kunturu PP, Huskens J (2019) Efficient solar water splitting photocathodes comprising a copper oxide heterostructure protected by a thin carbon layer. ACS Appl Energy Mater 2:7850–7860. https://doi.org/10.1021/acsaem.9b01290

23. Fu CF, Wu X, Yang J (2018) Material design for photocatalytic water splitting from a theoretical perspective. Adv Mater 30:1802106–1802111. https://doi.org/10.1002/adma.201802106
24. Cao S, Piao L, Chen X (2020) Emerging photocatalysts for hydrogen evolution. Trends Chem 2:57–70. https://doi.org/10.1016/j.trechm.2019.06.009
25. Hisatomi T, Kubota J, Domen K (2014) Recent advances in semiconductors for photocatalytic and photoelectrochemical water splitting. Chem Soc Rev 43:7520–7535. https://doi.org/10.1039/C3CS60378D
26. Chen YC, Huang YS, Huang H, Su PJ, Perng TP, Chen LJ (2020) Photocatalytic enhancement of hydrogen production in water splitting under simulated solar light by band gap engineering and localized surface plasmon resonance of ZnxCd1-xS nanowires decorated by Au nanoparticles. Nano Energy 67:104225–110431. https://doi.org/10.1016/j.nanoen.2019.104225
27. Tee SY, Win KY, Teo WS, Koh LD, Liu S, Teng CP, Han MY (2017) Recent progress in energy-driven water splitting. Adv Sci 13:1600337. 10.1002/advs.2016.00337
28. Hussain M (2010) Synthesis, characterization, and photocatalytic application of novel TiO_2 nanoparticles. Chem Eng J 157:45–51. https://doi.org/10.1016/j.cej.2009.10.043
29. Tamirat AG, John Rick, Dubale AA, Su WN, Hwang BJ (2016) Using hematite for photoelectrochemical water splitting: a review of current progress and challenges. Nanoscale Horiz 1:243–267. https://doi.org/10.1039/c5nh00098j
30. Wang H, Rogach AL (2013) Hierarchical SnO_2 nanostructures: recent advances in design, synthesis, and applications. Chem Mater 26:123–133. https://doi.org/10.1021/cm4018248
31. Khan MM, Adil SF, Mayouf AA (2015) Metal oxides as photocatalysts. J Saudi Chem Soc 19:462–464. https://doi.org/10.1016/j.jscs.2015.04.003
32. Wang F, Shifa TA, Zhan X, Huang Y, Liu K, Cheng Z, Jiang C, He J (2015) Recent advances in transition-metal dichalcogenide based nanomaterials for water splitting. Nanoscale 7:19764–19788. https://doi.org/10.1039/C5NR06718A
33. Pandey P, Gahlawat S, Ingole Pravin P (2020) Physical barricading at the nanoscale: protecting pyrite from weathering toward efficient and stable electrocatalysis of the oxygen evolution reaction. ACS Sustain Chem Eng 8:15584–15594. 10.1021/acssuschemeng.0c04756
34. Di T, Xu Q, Ho WK, Tang H, Xiang Q, Yu J (2019) Review on metal sulphide-based Z-scheme photocatalysts. Chem Cat Chem 11:1394–1411. https://doi.org/10.1002/cctc.201802024
35. Yin J, Jin J, Lin H, Yin Z, Li J, Lu M, Guo L, Xi Pin, Yu Tang, Yan CH (2020) Optimized metal chalcogenides for boosting water splitting. Adv Sci 7:1903070–1903100. https://doi.org/10.1002/advs.201903070
36. Zhang K, Guo L (2013) Metal sulphide semiconductors for photocatalytic hydrogen production. Catal Sci Technol 3:1672–1690. https://doi.org/10.1039/C3CY00018D
37. Kato T, Hakari Y, Ikeda S, Jia Q, Iwase A, Kudo A (2015) Utilization of metal sulfide material of $(CuGa)_{1-x}Zn_2xS_2$ solid solution with visible light response in photocatalytic and photoelectrochemical solar water splitting systems. J Phys Chem Lett 6:1042–1047. https://doi.org/10.1021/acs.jpclett.5b00137
38. Hassan MS, Jana A, Gahlawat S, Bhandary N, S Bera, Ingole PP, Sapra S (2019) Colloidally synthesized defect-rich $MoSe_2$ nanosheets for superior catalytic activity. Bull Mater Sci 42:74–85. https://doi.org/10.1007/s12034-019-1774-8
39. Shuo XU, Jing LIU (2019) Metal-based direct hydrogen generation as unconventional high density energy. Front Energy 13:27–53. https://doi.org/10.1007/s11708-018-0603-x
40. Konieczny A, Mondal K, Wiltowski T, Dydo P (2008) Catalyst development for thermocatalytic decomposition of methane to hydrogen. Inte J Hydrog Energy 33:264–272. https://doi.org/10.1016/j.ijhydene.2007.07.054
41. Farid S, Dincer I (2020) A review and comparative evaluation of thermochemical water splitting cycles for hydrogen production. Energy Convers Managem 205: https://doi.org/10.1016/j.enconman.2019.112182

42. Lukajtis R, Holowacz I, Kucharska K, Glinka M, Rybarczyk P, Przyjazny A, Kaminski Marian (2018) Hydrogen production from biomass using dark fermentation. Renew Sustain Energy Rev 91:665–694. https://doi.org/10.1016/j.rser.2018.04.043
43. Krummenacher JJ, West K, Schmidt LD (2003) Catalytic partial oxidation of higher hydrocarbons at millisecond contact times: decane, hexadecane, and diesel fuel. J Catal 215:332–343. https://doi.org/10.1016/S0021-9517(03)00011-3
44. Yan Y, Guo H, Zhang L, Zhu J, Yang Z, Tang Q, Xin J (2014) Effect of catalytic cylinders on autothermal reforming of methane for hydrogen production in a microchamber reactor. Scie World J 2014:451919–451928. https://doi.org/10.1155/2014/451919
45. Geissler K, Newson E, Vogel F, Truong TB, Hottingera P, Wokaun A (2001) Autothermal methanolreforming for hydrogen production in fuel cell applications. Phys Chem Chem Phys 3:289–293. https://doi.org/10.1039/B004881J
46. Vita A, Pino L, Italiano C, Palella A (2019) Steam reforming, partial oxidation, and autothermal reforming of ethanol for hydrogen production in conventional reactors. Ethanol Sci Eng Chapter 6:159–191. https://doi.org/10.1016/B978-0-12-811458-2.00006-7
47. Maqbool W, Lee ES (2014) Syngas production process development and economic evaluation for gas-to-liquid applications. Chem Eng Technol 37:995–1001. https://doi.org/10.1002/ceat.201300579
48. Castro JD, Tinoco RR, Bouallou C (2010) Hydrogen production from natural gas: auto-thermal reforming and CO_2 capture. Chem Eng Trans 21:163–168. https://doi.org/10.3303/CET1021028
49. Voldsund M, Jordal K, Anantharaman R (2016) Hydrogen production with CO_2 capture. Int J Hydrogen Energy 41:4969–4992. https://doi.org/10.1016/j.ijhydene.2016.01.009
50. Menendez M, Herguido J, Berard A, Patience GS (2019) Experimental methods in chemical engineering: reactors-fluidized beds. Can J Chem Eng 97:2383–2394. https://doi.org/10.1002/cjce.23517
51. Gnanapragasam NV, Rosen MA (2017) A review of hydrogen production using coal, biomass and other solid fuels. Biofuels 8:725–745. https://doi.org/10.1080/17597269.2017.1302662
52. Ail SS, Dasappa S (2016) Biomass to liquid transportation fuel via Fischer Tropsch synthesis—technology review and current scenario. Renew Sust Energ Rev 58:267–286. https://doi.org/10.1016/j.rser.2015.12.143
53. Singh SV, Zhao M, Paul SF, Shah N, Anthony EJ (2017) Progress in biofuel production from gasification. Prog Energy Combust Sci 61:189–248. https://doi.org/10.1016/j.pecs.2017.04.001
54. Liu X, Zhang S, Dong J, Xu X (2016) A short-term analysis of hydrogen demand and refueling station cost in Shenzhen China. Energy Procedia 104:317–322. https://doi.org/10.1016/j.egypro.2016.12.054
55. Chen L, Dong X, Wang Y, Xia Y (2016) Separating hydrogen and oxygen evolution in alkaline water electrolysis using nickel hydroxide. Nat Commun 7:11741–11748. https://doi.org/10.1038/ncomms11741
56. Dincer I, Acar C (2015) Review and evaluation of hydrogen production methods for better sustainability. Int J Hydrogen Energy 40:11094–11111. https://doi.org/10.1016/j.ijhydene.2014.12.035
57. Hosseini SE, Wahid MA (2016) Hydrogen production from renewable and sustainable energy resources: promising green energy carrier for clean development. Renew Sustain Energy Rev 57:850–866. https://doi.org/10.1016/j.rser.2015.12.112
58. Sapountzia FM, Gracia JM, Weststrate CJ, Fredriksson HOA, Niemantsverdriet JW (2017) Electrocatalysts for the generation of hydrogen, oxygen and synthesis gas. Prog Energy Combust Sci 58:1–35. https://doi.org/10.1016/j.pecs.2016.09.001
59. Dhruba JD, Seval G, Jaesung K, Taylor F, Yingjie S, Anne CC, Umit SO (2019) Hydrogen production from water in a solid oxide electrolysis cell: effect of Ni doping on lanthanum strontium ferrite perovskite cathodes. Ind Eng Chem Res 58:22497–22505. https://doi.org/10.1021/acs.iecr.9b03731

60. Peneva M, Zuboy J, Hunter C (2019) Economic analysis of a high-pressure urban pipeline concept (HyLine) for delivering hydrogen to retail fueling stations. Transp Res D Transp Environ 77:92–105. https://doi.org/10.1016/j.trd.2019.10.005
61. Zhang Y, Heo YJ, Lee JW, Lee JH, Bajgai J, Lee KJ, Park SJ (2018) Photocatalytic hydrogen evolution via water splitting: a short review. Catalysts 8:655. https://doi.org/10.3390/catal8120655
62. Hsieh PY, Wu JY, Chang TFMark, Chen CY, Sone M, Hsu YJ (2020) Near infrared-driven photoelectrochemical water splitting: review and future prospects. Arabian J Chem 13:8372–8387. https://doi.org/10.1016/j.arabjc.2020.05.025
63. Ibhadon AO, Fitzpatrick P (2013) Heterogeneous photocatalysis: recent advances and applications. Catalysts 3:189–218. https://doi.org/10.3390/catal3010189
64. Serpone N, Emeline AV (2012) Semiconductor photocatalysis-past, present, and future outlook. J Phys Chem Lett 3:673–677. https://doi.org/10.1021/jz300071j
65. Babu VJ, Vempati S, Uyar T, Ramakrishna S (2015) Review of one-dimensional and two-dimensional nanostructured materials for hydrogen generation. Phys Chem Chem Phys 17:2960–2986. https://doi.org/10.1039/c4cp04245j
66. Salcedo-Abraira P, Sergio MFV, Babaryk AA, Cabrero-Antonino M, Gregorio P, Salles F, Navalon S, Garcia H, Horcajada P (2020) Nickel phosphonate MOF as efficient water splitting photocatalyst. Nano Res 14:450–457. https://doi.org/10.1007/s12274-020-3056-6
67. Guerrero A, Bisquert J (2017) Perovskite semiconductors for photoelectrochemical water splitting applications. Curr Opin Electrochem 2:144–147. https://doi.org/10.1016/j.coelec.2017.04.003
68. Yang J, Yan H, Zong X, Wen F, Liu M, Li C (2013) Roles of cocatalysts in semiconductor-based photocatalytic hydrogen production. Phil Trans R Soc A 371:20110430–20110445. https://doi.org/10.1098/rsta.2011.0430
69. Tan C, Cao X, Wu XJ, He Q, Yang J, Zhang X, Chen J, Zhao W, Han S, Nam GH, Sindoro M, Zhang H (2017) Recent advances in ultrathin two-dimensional nanomaterials. Chem Rev 117:6225–6331. https://doi.org/10.1021/acs.chemrev.6b00558
70. Low J, Cao S, Yu J, Wageh S (2014) Two-dimensional layered composite photocatalysts. Chem Commun 50:10768–10777. https://doi.org/10.1039/c4cc02553a
71. Kouser S, Thannikoth A, Gupta U, Waghmare UV, Rao CNR (2015) 2D-GaS as a photocatalyst for water splitting to produce H2. Small 11:4723–4730. https://doi.org/10.1002/smll.2015.01077
72. Dong F, Li Y, Wang Z, Ho, Ho WK (2015) Enhanced visible light photocatalytic activity and oxidation ability of porous graphene-like g-C_3N_4 nanosheets via thermal exfoliation. Appl Surf Sci 358:393–403. https://doi.org/10.1016/j.apsusc.2015.04.034
73. Yu T, Hu Z, Wang H, Tan X (2020) Enhanced visible-light-driven hydrogen evolution of ultrathin narrow-band-gap g-C_3N_4 nanosheets. J Mater Sci 55:2118–2128. https://doi.org/10.1007/s10853-019-04082-7
74. Haque F, Daeneke T, Kalantar-zadeh K, Ou JZ (2018) Two-dimensional transition metal oxide and chalcogenide-based photocatalysts. Nano Micro Lett 10:23–50. https://doi.org/10.1007/s40820-017-0176-y
75. Rufino M. Yerga N, Galvan MCA, lvarez, del Valle F, Jose A. de la Mano Villoria, Fierro JLG (2009) Water splitting on semiconductor catalysts under visible-light irradiation. ChemSusChem 2:471–485. https://doi.org/10.1002/cssc.200900018
76. Ganguly P, Harb M, Cao Z, Cavallo L, Breen A, Dervin S, Dionysiou DD, Pillai SC (2019) 2D nanomaterials for photocatalytic hydrogen production. ACS Energy Lett 4:1687–1709. https://doi.org/10.1021/acsenergylett.9b00940
77. Zhang K, Fujitsuka M, Du Y, Majima T (2018) 2D/2D Heterostructured CdS/WS_2 with efficient charge separation improving H_2 evolution under visible light irradiation. ACS Appl Mater Interfaces 10:20458–20466. https://doi.org/10.1021/acsami.8b04080
78. Heift D (2019) Iron sulfide materials: catalysts for electrochemical hydrogen evolution. Inorganics 7:75–94. https://doi.org/10.3390/inorganics7060075

79. Giovanni D, Wang C, Nowak WA, Greneche S, Lecoq JM, Mouton H, Giraud L, Tard MC (2014) Bioinspired iron sulfide nanoparticles for cheap and long-lived electrocatalytic molecular hydrogen evolution in neutral water. ACS Catal 4:681–687. https://doi.org/10.1021/cs4011698
80. Xu H, Ouyang S, Li P, Kako T, Ye J (2013) High-active anatase TiO_2 nanosheets exposed with 95% 100 facets toward efficient H_2 evolution and CO_2 photoreduction. ACS Appl Mater Interfaces 5:1348–1354. https://doi.org/10.1021/am302631b
81. Chen X, Zhou Y, Liu Q, Li Z, Liu J, Zou Z (2012) Ultrathin, single-crystal WO_3 nanosheets by two-dimensional oriented attachment toward enhanced photocatalystic reduction of CO_2 into hydrocarbon fuels under visible light. ACS Appl Mater Interfaces 4:3372–3377. https://doi.org/10.1021/am300661s
82. Alsaif MM, Latham K, Field MR, Yao DD, Medehkar NV, Beane GA, Kaner RB. Russo SP, Ou JZ, Kalantar-zadeh K (2014) Tunable plasmon resonances in two-dimensional molybdenum oxide nanoflakes. Adv Mater 26:3931–3937. https://doi.org/10.1002/adma.201306097
83. Bhandari C, Lambrecht WR, van Schilfgaarde M (2015) Quasiparticle self-consistent GW calculations of the electronic band structure of bulk and monolayer V_2O_5. Phys Rev B 91 (12):125116. https://doi.org/10.1103/PhysRevB.91.125116
84. Puangpetch T, Chavadej S, Sreethawong T (2011) Mesoporous assembled V_2O_5 nanosheet synthesized via a surfactant-modified sol-gel technique and its photocatalytic H_2 production activity under visible light irradiation. Powder Technol 208:37–41. https://doi.org/10.1016/j.powtec.2010.11.039
85. Jasion D, Barforoush JM, Qiao Q, Zhu Y, Ren S, Leonard KC (2015) Low-dimensional hyperthin FeS_2 nanostructures for efficient and stable hydrogen evolution electrocatalysis. ACS Catal 5:66536657. https://doi.org/10.1021/acscatal.5b01637
86. Pang J, Mendes RG, Bachmatiuk A, Zhao L, Ta HQ, Gemming T, Liu H, Liu Z, Rummeli MH (2019) Applications of 2D MXenes in energy conversion and storage systems. Chem Soc Rev 48:72–133. https://doi.org/10.1039/c8cs00324f
87. Guo Z, Zhou J, Zhua L, Sun Z (2016) MXene: a promising photocatalyst for water splitting. J Mater Chem A 4:11446–11452. https://doi.org/10.1039/c6ta04414j
88. Yuan W, Cheng L, An Y, Lv S, Wu H, Fan X, Zhang Y, Guo X, Tang J (2018) Laminated hybrid junction of sulfur-doped TiO_2 and a carbon substrate derived from Ti_3C_2 MXenes: toward highly visible light-driven photocatalytic hydrogen evolution. Adv Sci 5:1700870–1700880. https://doi.org/10.1002/advs.201700870
89. Su T, Peng R, Hood Z, Naguib M, Ivanov I, Keum J, Qin Z, Guo Z, Wu Z (2017) One-step synthesis of Nb_2O_5/C/Nb_2C (MXene) composites and their use as photocatalysts for hydrogen evolution. Chem Sus Chem 11:688–699. https://doi.org/10.1002/cssc.201702317
90. Ran J, Gao G, Li FT, Ma TY, Du A, Qiao SZ (2017) Ti_3C_2 MXene co-catalyst on metal sulfide photo-absorbers for enhanced visible-light photocatalytic hydrogen production. Nat Commun 8:13907–139017. 10.1038/ncomms13907
91. Silva GC, Luz I, Xamena LFX, Corma A, Garcia H (2010) Water stable Zr-benzenedicarboxylate metal-organic frameworks as photocatalysts for hydrogen generation. Chemistry 16:11133–11138. https://doi.org/10.1002/chem.200903526
92. Horiuchi Y, Toyao T, Saito M, Mochizuki K, Iwata M, Higashimura H, Anpo M, Matsuoka M (2012) Visible-light-promoted photocatalytic hydrogen production by using an amino-functionalized Ti(IV) metal-organic framework. J Phys Chem C 116:20848–20853. https://doi.org/10.1021/jp3046005
93. He J, Yan Z, Wang J, Xie J, Jiang L, Shi Y, Yuan F, Yu F, Sun Y (2013) Significantly enhanced photocatalytic hydrogen evolution under visible light over CdS embedded on metal-organic frameworks. Chem Commun 49:6761–6763. https://doi.org/10.1039/C3CC43218A
94. Shen L, Luo M, Huang L, Feng P, Wu L (2015) A clean and general strategy to decorate a titanium metal organic framework with noble-metal nanoparticles for versatile photocatalytic applications. Inorg Chem 54:1191–1193. https://doi.org/10.1021/ic502609a

95. Tilgner D, Kempe R (2017) A plasmonic colloidal photocatalyst composed of a metal-organic framework core and a gold/anatase shell for visible-light-driven wastewater purification from antibiotics and hydrogen evolution. Chem Eur J 23:3184–3190. https://doi.org/10.1002/chem.201605473
96. Gao H, Zhen W, Ma J, Lu G (2017) High efficient solar hydrogen generation by modulation of Co-Ni sulfide (220) surface structure and adjusting adsorption hydrogen energy. Appl Catal B 206:353–363. https://doi.org/10.1016/j.apcatb.2017.01.048
97. Guo HL, Du H, Jiang YF, Jiang N, Shen CC, Zhou X, Liu YN, Xu AW ()2017 Artificial photosynthetic Z scheme photocatalyst for hydrogen evolution with high quantum efficiency. J Phys Chem C 121:107–114. https://doi.org/10.1021/acs.jpcc.6b10013
98. Yugo M, Fujiyoshi S, Gunji T, Sayama K (2017) Photocatalytic Z scheme water splitting for independent H_2/O_2 production via a stepwise operation employing a vanadate redox mediator under visible light. J Phys Chem C 121:9691–9697. https://doi.org/10.1021/acs.jpcc.7b00905
99. Jones W, Martin DJ, Caravaca A, Beale AM, Bowker M, Maschmeyer T, Hartley G, Masters A (2019) A comparison of photocatalytic reforming reactions of methanol and triethanolamine with Pd supported on titania and graphitic carbon nitride. Appl Catal B Environ 240:373–379. https://doi.org/10.1016/j.apcatb.2017.01.042
100. Wang Y, Suzuki H, Xie J, Tomita O, Martin DJ, Higashi M, Kong D, Abe R, Tang J (2018) Mimicking natural photosynthesis: solar to renewable H2 fuel synthesis by Z-scheme water splitting systems. Chem Rev 118:5201–5241. https://doi.org/10.1021/acs.chemrev.7b00286
101. Liang YH, Liao MW, Mishra M, Perng TP (2019) Fabrication of Ta3N5eZnO direct Z-scheme photocatalyst for hydrogen generation. Inter J Hydro Energy 44:19162–19167. https://doi.org/10.1016/j.ijhydene.2018.07.117
102. Yu J, Wang S, Low J, Xiao W (2013) Enhanced photocatalytic performance of direct Z-scheme g-C_3N_4-TiO_2 photocatalysts for the decomposition of formaldehyde in air. Phys Chem Chem Phys 15:16883–16890. https://doi.org/10.1039/c3cp53131g
103. Xing X, Zhang M, Hou L, Xiao L, Li Q, Yang J (2017) Z-scheme BCN-TiO_2 nanocomposites with oxygen vacancy for hydrogen production. Int J Hydrogen Energy 42:28434–28444. https://doi.org/10.1016/j.ijhydene.2017.09.125
104. Ng BJ, Putri LK, Kong XY, Teh YW, Pasbakhsh P, Chai SP (2020) Z-scheme photocatalytic systems for solar water splitting. Adv Sci 7:1903171–1903213. https://doi.org/10.1002/advs.201903171
105. Deshpande A, Shah P, Gholap RS, Gupta NM (2009) Interfacial and physico-chemical properties of polymer-supported CdSZnS nanocomposites and their role in the visible-light mediated photocatalytic splitting of water. J Colloid Interface Scie. 333:263–268. https://doi.org/10.1016/j.jcis.2009.01.037

Chapter 22
Electrocatalytic and Photo-catalytic Water Splitting

Preeti Chaudhary and Pravin P. Ingole

Abstract In the present time where our renewable energy sources are depleting, and sooth from industries and coal burning is making air poisonous to breathe, the need for a switch into a sustainable energy system has become a necessity. One fruitful solution to the problem is photo-electrochemical (PEC) water splitting. Implementing PEC for the power generation reduces the burden on fossil fuels for solar energy storage. The Sun being a natural and the most abundant energy source, a dilemma is how to most effectively capture that energy and store it but at the lowest cost; we would try to discuss this in the present chapter. Designing photo-electrocatalyst is one of the main challenge, keeping all the perspective of PEC in mind. Fabricating heterojunction using different functional and suitable material for PEC in a single catalyst enables to enlarge the area of light harvesting properties and enhancing water splitting efficiency by improving the photo-excited charge separation and increasing the chemical stability of the catalyst to make it viable. The chapter gives an overview on the designing of heterojunctions for enhancing PEC water splitting performance. Along with the heterojunction synthesis, recent progress in the heterojunction-based PEC system and the working mechanism behind the charge separation is also discussed in the chapter. The chapter also provides the future directions for PEC water splitting.

Keywords Photo-electrochemical water splitting · Photo-electrocatalysts · Heterojunctions · Charge transfer mechanism and kinetics

22.1 Introduction and Scope

Due to the rapidly growing energy demand and depletion of fossil fuels and sources of energy, the world in the present century is on the edge of energy crises. According to International Energy Outlook 2016 (IEO 2016) [1] report, total

---

P. Chaudhary · P. P. Ingole (✉)
Department of Chemistry, Indian Institute of Technology, Delhi, New Delhi 110016, India
e-mail: ppingole@chemistry.iitd.ac.in

S. Garg and A. Chandra (eds.), *Green Photocatalytic Semiconductors*,
Green Chemistry and Sustainable Technology,
https://doi.org/10.1007/978-3-030-77371-7_22

consumption of energy would increase from 549 quadrillion Btu in 2012 to 815 quadrillion Btu in 2040. It is the time to lay down the foundation of a sustainable society which would reduce the dependency on fossil fuels and also the amount of environmental pollution, because the depletion is leading to global climate change and environmental deterioration. Thus, it is the need of the time to increase the use of renewable energy sources as they are the fastest growing energy sources and are good replacement to fossil fuels.

Among the various sources of renewable energy such as solar, biomass, biofuel, geothermal, wind and tidal, the solar energy has gained a lot of attention as it is the largest and one of the most promising sources for sustainable development without having any compromise with the quality of environment. The energy from Sun is by far the largest natural resource as the Sun irradiating the surface of the Earth (1.3×10^5 TW) but a jump has been found in a global energy consumption (1.6×10^1 TW in 2010) [2]. Solar water splitting can be accomplished by three methods: photo-catalysis, photovoltaics and photo-electrochemical (PEC) water splitting. Photovoltaic electrolysis is high in both cost and efficiency, but the main quandary is between efficiency and cost. The cost problem can be sorted out by using photo-catalysis, but at the same time, the consumption of energy reduces the overall water splitting efficiency. PEC water splitting demonstrated for the first time by Fujishima and Honda [3] takes over the high potential efficiency up to >30% and is also cost effective. It efficiently converts solar energy to storable and transportable hydrogen fuel because of its potential high efficiency and other advantages of low cost and environmental friendliness. The solar energy conversion efficiency can be improved by solar water splitting techniques [4]. Thus, considering all the points, PEC came out to be an attractive and excellent technological solution to tackle the present environment and energy related issue.

In this chapter, nano-heterostructured materials are discussed for PEC cell application. Some of the nanostructure materials came out with multifunctional electrocatalytic activity. The following part presents brief introduction to PEC water splitting cells, PEC cell apparatus, PEC set up, reactions involved, thermodynamic and kinetic aspects, major breakthrough and advances in the field of PEC. The latter part covers the developed materials and their application in PEC cell followed by the future perspective effective in the field of PEC.

22.2 Concept of Photo-Electrochemical Water Splitting

Photo-electrochemical water splitting, i.e. for the evolution of hydrogen and oxygen, being one of the effective techniques for the utilization of solar energy [5] has drawn great interest. A basic design for a PEC water splitting cell is such that it consists of two electrodes dipped in aqueous electrolyte as shown in Fig. 22.1. One is the working electrode (p-type or n-type semiconductor or a heterostructure) an active photo-electrode for the initiation of water splitting and another one is counter electrode, and water-based electrolyte. The third electrode is reference electrode;

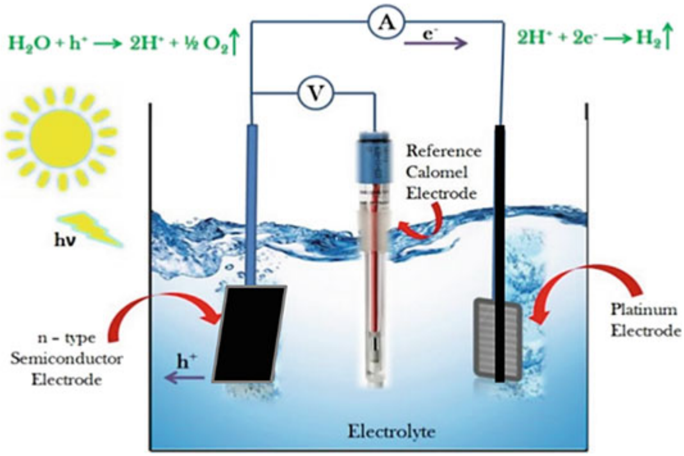

Fig. 22.1 Basic configuration of PEC cell consisting of three electrodes and an electrolyte. The reactions at anode and cathode are also shown

generally, Ag/AgCl/saturated KCl, Hg/HgO or saturated calomel electrode (SCE) is used that monitors the voltage applied on working electrode. For the working electrode to be illuminated with light, the PEC cell should consist of an optically transparent (quartz) window.

Construction of working electrode involves the drop casting (as shown in Fig. 22.2) of dispersed catalyst on the conductive side of the substrate. For making its connection feasible in PEC cell, thin copper wire is glued with the substrate using silver paste for electrical contact, and the corners and backside of the substrate were blocked using the epoxy resin. The free copper wire was sealed in glass tube to avoid its contact with electrolyte and assure that only the front side of electrodes comes in contact with the electrolyte otherwise the electrochemical reactions associated with Cu wire may interfere with the redox features from PEC water splitting.

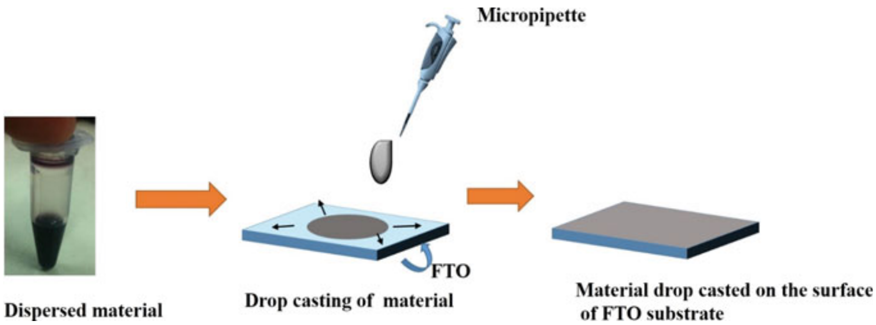

Fig. 22.2 Steps involved in fabrication of working electrode for PEC water splitting

Fig. 22.3 Basic principle of PEC water splitting cell representing the generation of electron and hole in the presence of light

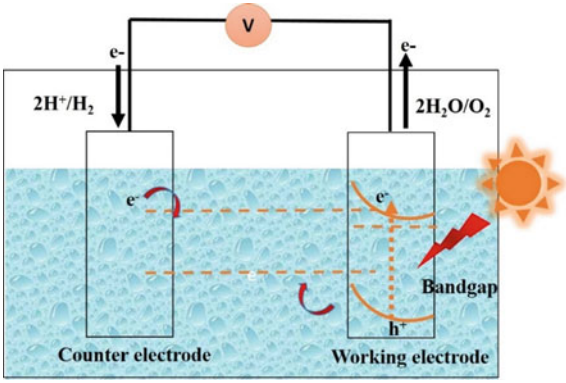

Figure 22.3 represents the basic principle of PEC water splitting. Under the illumination of light, electrons (e-) get excited from the valence band (VB) to the conduction band (CB) of a semiconductor photo-anode, where holes are left behind in the VB, thus generation of electron–hole pair takes place at photo-electrode.

The generated electrons move to the counter electrode and are utilized for hydrogen evolution reaction (HER). The holes get transferred to the surface of working electrode and are involved in a process of oxygen evolution reaction (OER), the other half-reaction.

Components of Photo-electrochemical (PEC) cell:

In all types of photo-electrochemical systems, the basic mechanism is same as that of generation of photo-excited electron–hole pair. The transfer of electrons at the interface continues until the Fermi level of the electrode and electrolyte are in the same position. In general, PEC cells are composed of a photo-electrode (photo-cathode or photo-anode) [6] with a counter electrode (as represented in Fig. 22.4) or in some cases, two photo-electrodes (photo-anode and photo-cathode) without external counter electrode. Using photo-anode as photo-electrode, the

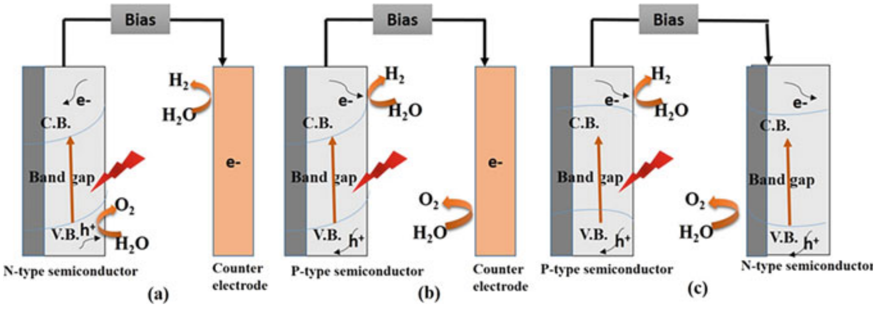

Fig. 22.4 Different types of photo-electrochemical cells, **a** counter electrode with photo-anode, **b** counter electrode with photo-cathode and **c** both photo-anode and photo-cathode without counter electrode. Reprinted with permission from Ref. [7]

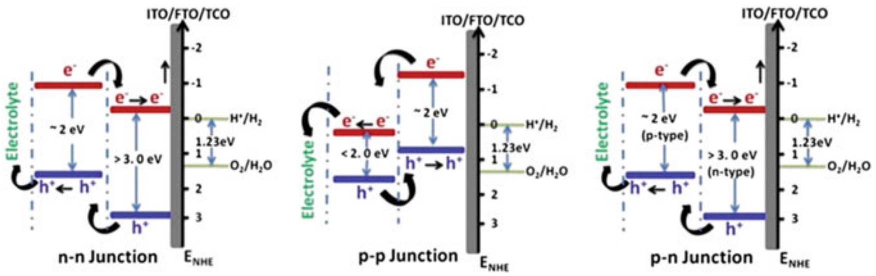

Fig. 22.5 Different types of heterojunctions with their band positions and water splitting charge transfer mechanisms. Reprinted with permission from Ref. [7]

transfer of electrons takes place to the counter electrode from the conduction band of a photo-anode. These electrons take part in HER whereas the holes left behind are utilized in the OER. In a p-type photo-cathode, OER takes place at the counter electrode and hydrogen generation occurs by utilizing electrons directly from the electrolyte. Moreover, the heterostructures between two semiconductors with varying electronic properties are also used. These are discussed below and depicted in Fig. 22.5.

1. **n-n type:**

   Photo-anode constructed of heterojunction having both semiconductors of n-type, thus called n-n type [7]. In this heterostructure, semiconductors are chosen such that the conduction band position of semiconductor attached to the conductive layer should be lower than that of the conduction band position of the semiconductor lying on the electrolyte side. In the presence of light, photo-excited electrons travel to the counter electrode through external circuit for the reduction and the holes are accumulated on semiconductor electrode/electrolyte interface for water oxidation.

2. **p-p type:**

   Here, a designed heterostructured photo-cathode has both the semiconductors of p-type. Photo-excited electrons are transferred directly to the semiconductor electrode/electrolyte interface and water is reduced to hydrogen. Figure 22.5 shows different types of heterojunctions with their band positions and charge transfer mechanism.

3. **p-n type:**

   p-n type heterojunctions can be used either as photo-cathode or as a photo-anode. In both cases, holes and electrons move in opposite directions and an efficient charge separation takes place in comparison to single (n or p type) semiconductor electrode.

Photo-electrode Materials:

TiO_2 was the first photo-anode material for PEC that was illustrated by Fujishima and Honda [8] in 1972. Then, Bard and co-workers illustrated the basics behind PEC cells using the materials like TiO_2, $Ni(OH)_2$, etc. But by the 2005, the number of published work on photo-electrochemical water splitting reflected the rapid interest of scientist in this field. Currently, the research on exploring more efficient semiconductor materials for PEC is still on. As TiO_2 is effective as a photo-catalyst only under the presence of UV light due to wider band gap of ca. 3.4 eV, scientists have tried to develop non-TiO_2 catalyst and had even succeeded in it by inventing some novel photo-catalysts such as α-Fe_2O_3, ZnO, $BiVO_4$, WO_3 and NiO. Other than metal oxides, their carbides, nitrides, sulphides, phosphides and selenides are also frequently indulged in PEC water splitting. Some semiconductors such as CuO and CdS show excellent light absorption but are not effective for driving water splitting due to their inappropriate band edge positions. Thus, the performance of a PEC cell depends mainly on the activity and features of the chosen semiconductor photo-electrode. There are a number of requirements related to material for effective PEC water splitting, and the most critical aspect among these is to design a catalyst for PEC water splitting. The material to be an ideal candidate for PEC activity should have some of the basic characteristics as discussed below.

Suitable band gap and appropriate band edge positions:

The band gap of a material defines the light absorbing region for the photo-anode material. The lower band gap reflects the absorbance in wider light spectrum. The conduction and valence band edge positions should match with the electrochemical redox potentials for HER and OER, respectively, to drive the water splitting reactions and to maintain material stability. The water splitting reaction takes place at a potential difference of 1.23 eV, thus for a material to be useful for water splitting, it should have band gap energy greater than 1.23 eV. The band gap of the semiconductor should be greater than 1.23 eV for water oxidation. Some of the semiconductor materials with band gap values and band edge positions are shown in Fig. 22.6.

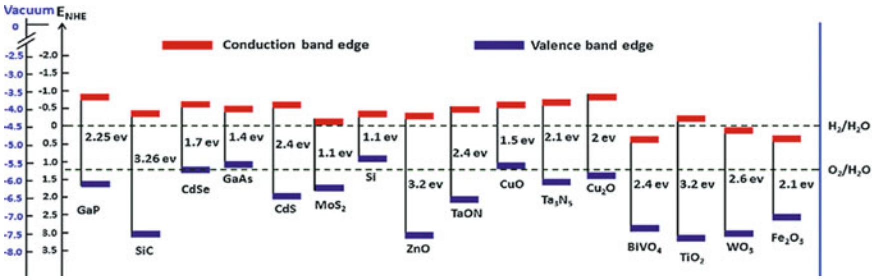

Fig. 22.6 Band gap values and band edge positions of some of the well-known semiconductors. Reprinted with permission from Ref. [7]

Appropriate band edge positions:

Apart from having a perfect band gap for water splitting, appropriate valence and conduction band edge positions are a crucial requirement for water oxidation and reduction reactions of water. Figure 22.7 depicts the suitable band edge positions for water splitting. Conduction band minimum should hold a position at more negative energy than the redox position of H_2O/O_2 level of water and its valence band maximum must be positioned at more positive than redox position of H_2O/O_2. The discussed positions of VBM and CBM ensure that the water splitting reaction is energetically favourable without bias voltage. Thus, to design an efficient catalyst for PEC, the knowledge of semiconductors electronic band structure parameters, viz. VBM and CBM positions especially relative to redox potential of H_2O/O_2 is a scalable approach.

High crystallinity and greater surface area:

Crystallinity and greater surface area are also an important parameter for the efficient PEC activity. The greater crystalline nature of the catalyst owes the ability to inhibit the photo-excited charge carriers. Improvement in crystallinity has the ability to repair the crystal defects. The presence of crystal defects decelerates the charge carrier recombination rate. Thus, with the improvement in crystallinity, these crystal defects get repaired up, lowering down the speed of charge carrier recombination. Another factor that triggers the activity of PEC catalyst is the higher surface area. Greater surface area creates more number of active sites that facilitate the semiconductors contact with reactant molecules/species or we can say that it provides the more opportunities for the catalyst activity to take place thus promoting the catalytic activity of water oxidation at a rapid rate. Thus, to prevent the recombination phenomenon for better charge separation and mobility, catalyst should possess high crystallinity and larger surface area.

Stability:

Years long work has been done in the field of PEC but for making this technology to be up scaled, the stability is a key factor. Though there has been a significant number of publications in this field, the main focus has been put with various ideas

Fig. 22.7 Ideal straddling condition of conduction and valence band edges of a semiconductor

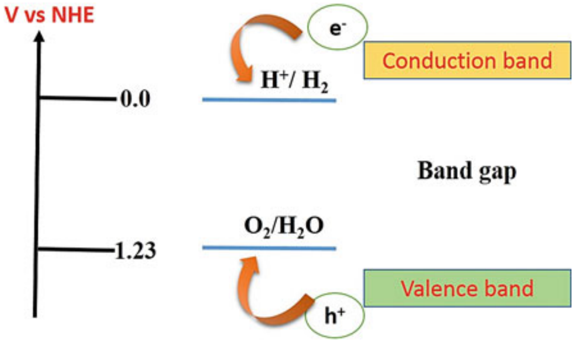

in having the efficiency and stability of the catalyst especially for the cost effective materials. The stability of a material can be explained in various ways especially for PEC catalyst; stability in the presence of light, withstanding the reaction for a longer time and maintaining its identity even after completion of the reaction, the reusability of the material, and stability in different pH conditions. Electrochemical material has to be thermodynamically stable when in contact with the electrolyte and should be kinetically stable while being indulge in faradic reactions. Corrosion stability should also be taken into consideration that is after coming in contact or after keeping dipped in the electrolyte for long hour, the material should not be corroded or oxidized. Sometimes the dissolution of the certain material is also being noticed when applied potential is varied or while in contact with the electrolyte. Stability in the presence of light is also important for PEC study. It has been noticed many a times that the catalyst is stable electrochemically but once it is illuminated with the light either the dissolution or the decrement in the activity is observed. Another stability that is of prerequisite is stability in the varied pH electrolyte, that is the catalyst showing a good performance should be stable in acidic, basic and neutral medium.

After being aware of the necessity and the types of stability, the several steps have been implied for forming the stable semiconductors: (a) implementation of thin metallic film or layer that would even work as a catalyst and helps in forming the Schottky junctions and (b) sustain the stability even in the harsh conditions a few nanometer thick oxide layers are implemented that can easily tunnel the charge carriers. Oxide layer should be chosen such that it avoids the electrolyte permeability, possibility of cracks and reduction of pinholes. Thus, stability and sustainability are an important parameters for a catalyst to be applicable in industry.

Low cost:

It is important to keep in mind the abundance and cost of the material while designing the catalyst, especially for commercial application. The production of hydrogen by different techniques is compared [9] in Table 22.1 accompanied with their capital cost and the efficiencies. Thus, to bring the material in commercial application, the low cost is another critical consideration. Besides this, for the large-scale implementation, the materials should be non-toxic.

PEC mechanism:

Increasing interest to store solar energy in the form of alcohols and hydrogen inspires the photo-oxidation of water. It is generally followed by two methods as represented in Fig. 22.8: one is natural photosynthesis, that represents the approach in the direction of hydrogen production, and another is water splitting. PEC splitting of water is an artificial photosynthesis mechanism. It is an uphill reaction, thus requires an external bias as photo-voltage to drive water splitting reaction. This generates an interest in the generation of charge carriers for the two half reactions.

Table 22.1 Comparison of the installed capital cost and production cost for different hydrogen production technologies

Production technology	Efficiency (%)	Installed capital cost	Production cost
Steam methane reforming (SMR)	80	\$138.9 Million	6.73 \$/GJ
Partial oxidation (POX)	89	\$307.1 Million	12.02 \$/GJ
Gasification of coal	48	\$490.5 Million	16.89 \$/GJ
Electrolysis grid power	95	\$331.3 Million	23.49 \$/GJ
Electrolysis PV power	95	\$389.2 Million[3]	53.73 \$/GJ
Electrolysis solar thermal power	95	\$360.3 Million[3]	38.61 \$/GJ

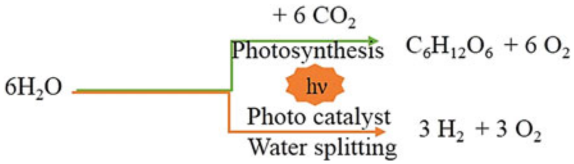

Fig. 22.8 Representation of two complimentary reaction of water splitting into their respective constituents

Photo-anode as a Photo-electrode:

Figure 22.9 represents the PEC water splitting mechanism based on photo-anode as a photo-electrode. In the presence of light, electrons get excited from the valence band (VB) of the photo-anode to the conduction band (CB), and holes remain behind in the VB. On the application of external bias, the upward bending of CB and VB at the interface takes place. At the interface in a direction from photo-electrode to electrolyte, an electric field is built up due to which the separated photo-generated holes migrate towards electrolyte and electrons stays back in the photo-anode. These electrons transferred to the conductive substrate through the nanostructured material which further gets conducted to the cathode surface where they reduce the protons for the generation of hydrogen gas. In this scenario, the holes which are left behind in the VB of the photo-anode travel from within the surface and oxidizes water for oxygen production. Some photo-generated holes and electrons which fail to reach the photo-electrode surface during transfer process get recombine and neutralize.

Photo-cathode as a Photo-electrode:

Prerequisite for the photo-cathode is that it should be a p-type semiconductor as represented in Fig. 22.10. When the p-type semiconductor is irradiated by light, electrons get excited from the VB to the CB leaving holes behind in the VB. At the interface of the electrolyte and photo-cathode, a downward bending of the VB and CB occurs which directs the electric field from electrolyte to the photo-cathode. In this case, electrons in the CB of photo-cathode travels to the surface of electrode for the HER and holes to the anode for the OER. As similar to the photo-anode, in

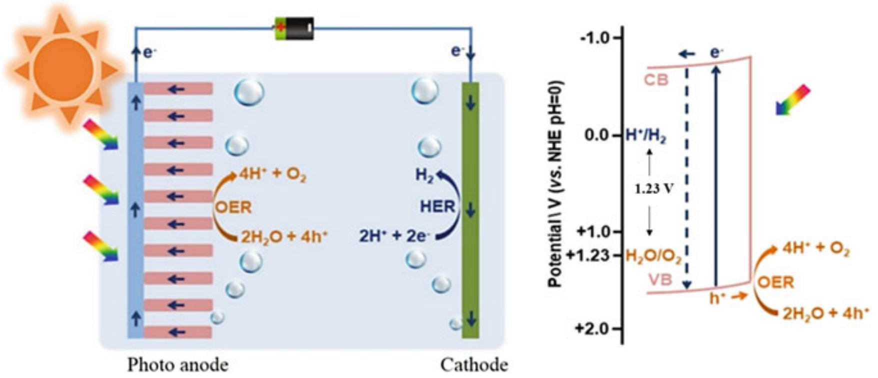

Fig. 22.9 Representation of PEC water splitting mechanism using photo-anode as a photo-electrode. Modified image adapted from Ref. [9]

photo-cathode, neutralization of the left behind electrons and holes takes place (Fig. 22.11).

Fundamental steps involved in photo-electrochemical water splitting:

PEC water splitting involves multiple steps as discussed below.

(a) **Light–matter interaction**

When the material is confronted to light, the light can be absorbed, reflected or transmitted depending on the media used. Generally, shortened propagation distance in the electrolyte media is profitable to avoid some of the necessary losses. When the light strikes the semiconductor, photons get absorbed if the

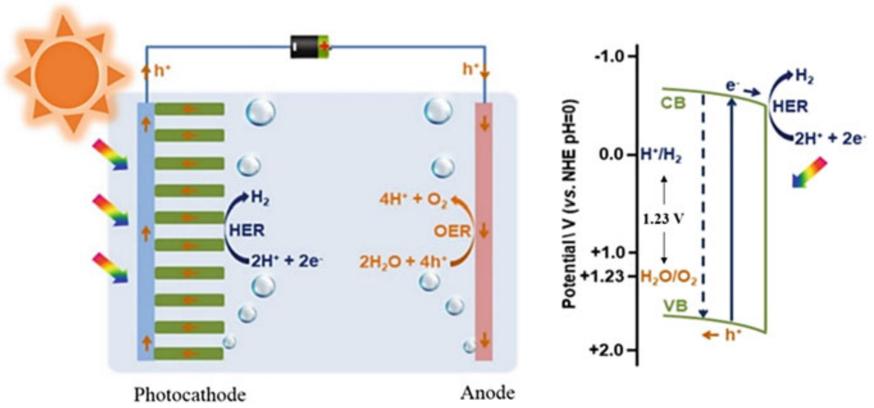

Fig. 22.10 Representation of PEC water splitting mechanism using photo-cathode as a photo-electrode. Modified image adapted from Ref. [9] with permission

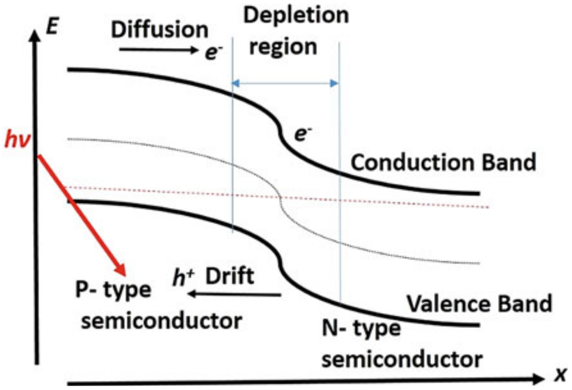

Fig. 22.11 Energy band diagram for p–n junction presenting generation of photo-electrons and their movement

band gap energy of the semiconductor is lower than the energy of photon. Absorbed energy is conducted to the electrons in the VB thus leading to the generation of electron–hole pair [11].

(b) **Photo-generation of charge:**

Electronic states of the atoms combine to form valence band and conduction band in the semiconductor that are apart by a band gap called forbidden gap. If a material absorbs the photon from the incident light, the electrons get excited to the conduction band and vacancies are created in the valence band, called as holes. The kind of the majority charge carriers generated is either free electrons or holes and determines the nature of semiconductor whether n or p-type. Position of Fermi level also contributes to the opto-electronic properties of the materials. In the n-type semiconductor, the position of Fermi level is near to conduction band and majority charge carriers are electrons, but in the p-type semiconductor, the majority carriers are holes and the Fermi level is next to the valence band.

(c) **Separation of charge and transport:**

After the generation of charge carriers, the next crucial point is to avoid their recombination because due to this recombination, the free electrons and holes are not available for the further reactions. The separation of charges can be carried out in two ways either by external potential or by an internal potential. External potential can be applied via electrochemical instrument but many a times internal built-in potential is required to overcome the recombination. There are many ways for creating a built-in electric fields.

- p-n heterojunction:

  p-n heterojunction is formed by bringing in contact the p-type and n-type semiconductor which are of totally different character. Due to the different nature of two materials, the diffusion of charges takes place thus forming a space charge layer on the junction of electrode and electrolyte which gives rise to the strong internal electric field.

- Schottky junction:

  Equilibration of the free electrons at Fermi level takes place thus leading to the bending of the valence and conduction band edges when in contact with metals.
- Semiconductor–liquid junction:
- Formation of the Helmholtz double layer tales place at semiconductor–liquid junction. Again, an equilibration of Fermi level would result into bending of band edges.
- Catalysis:

  Catalyst also plays a crucial role in the efficiency of the water splitting reaction. Catalyst promotes the reaction in many ways like via providing alternate pathways, lowering the barrier of activation energy, etc. After the generation of charge carriers, the electrons/holes move to the surface for electrochemical reaction.
- Water splitting:

Water splitting drives two half reactions, HER and OER. The complete water splitting reaction requires a thermodynamic potential of 1.23 V. The variation in this potential value can be explained by the Nernst equation. The variation in potential value is also seen with the change in solution pH.

HER:

$$\mathrm{pH} = 0 \quad 4\mathrm{H}^+ + 4\mathrm{e}^+ = 2\mathrm{H}_2, \quad \mathrm{E}^0 = 0\,\mathrm{V\,versus\,NHE} \tag{22.1}$$

$$\mathrm{pH} = 14 \quad 4\mathrm{H}_2\mathrm{O} + 4\mathrm{e}^- = 2\mathrm{H}_2 + 4\mathrm{OH}^-, \quad \mathrm{E}^0 = 0.83\,\mathrm{V\,versus\,NHE} \tag{22.2}$$

OER:

$$\mathrm{pH} = 0 \quad 2\mathrm{H}_2\mathrm{O} = \mathrm{O}_2 + 4\mathrm{H}^+ + 4\mathrm{e}^-, \quad \mathrm{E}^0 = 1.23\,\mathrm{V\,versus\,NHE} \tag{22.3}$$

$$\mathrm{pH} = 14 \quad 4\mathrm{OH}^- = \mathrm{O}_2 + 2\mathrm{H}_2\mathrm{O} + 4\mathrm{e}^-, \quad \mathrm{E}^0 = 0.4\,\mathrm{V\,versus\,NHE} \tag{22.4}$$

To drive these reactions effectively, we need overpotentials called η_{HER} and η_{OER}. The value of this overpotential that requires for water splitting decided by many factor like the electrocatalyst and pH value of the electrolyte. [12].

(f) **Photo-electrochemical Water Splitting:**

In PEC water splitting, generation of electron–hole pair takes place which are separated by the external or internal electric fields. Helmholtz double layer is formed at the interface due to the diffusion of charges, and Fermi level equilibration also takes place. Further continuing the process, the band bending also takes place which maintains the electric neutrality. The separation of the electron–hole pairs takes place due to the built-in electric field.

22.3 Experimental Methodology

Electrode fabrication:

The designing of proper electrodes has an important role in electrochemical measurements. Powdered material is dispersed in suitable solvent as shown in Fig. 22.12a and then drop casted on the working electrode surface. For HER study, the glassy carbon electrode as represented in Fig. 22.12b is used as the working electrode (in general). The dispersed material is drop casted on the glassy carbon surface and dried under the lamp for further use. For PEC study, a smooth film of the dispersed material is drop casted on ITO/FTO either manually or by using spin coating. For the electrical contacts, these substrates are connected by a copper wire using a silver paste. The uncovered conducting substrate is covered by the epoxy resin.

For the study of PEC measurements, the prepared electrodes are dipped in electrolyte in electrochemical cell. The cell constitutes of three electrodes: working electrode, counter electrode and reference electrode, all together dipped in an electrolyte. Quartz allows the light to reach the working electrode. After all the connections, WE is confronted to light and PEC study is done.

Cyclic Voltammetry:

Cyclic voltammetry is an electrochemical technique that helps in studying the redox property of an analyte and is also used for studying the qualitative information about the catalyst, like electrochemical response of the catalysts, catalytic activity of the catalyst, etc. This technique finds an important application in OER, HER and oxygen reduction reaction (ORR). All these cyclic voltammetry studies are done under the varied potential window. In cyclic voltammetry study, a fix potential window is decided with fixed initial and final potential points. We apply the

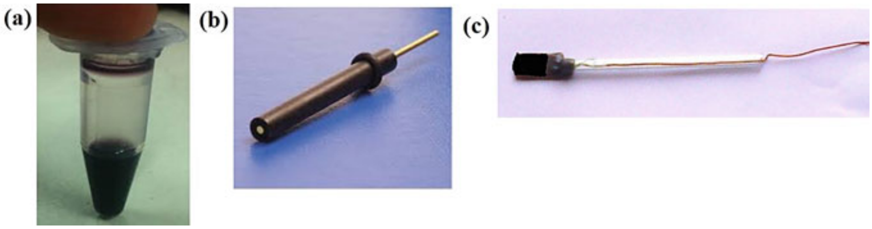

Fig. 22.12 **a** Sample dispersion ready for drop cast, **b** fabricated working electrode for HER and **c** fabricated working electrode for PEC

potential and study the current feature with respect to the potential. Thus, we plot a current recorded at the working electrode versus applied potential.

In the cyclic voltammetry study, we get a redox peak for the ions/molecules present in the analyte as well adsorbed on the electrode surface depending upon the nature of the analyte under study. The materials' oxidation and reduction potential can be found. In cyclic voltammetry, we study both the forward (positive) and backward scan (negative). In a way, we can say that it is the cyclic study, ends up at the point where it has been started. We can carry out the cyclic voltammetry study either by as single or multiple cycle. A reversible cyclic voltammetry is represented in Fig. 22.13 describing the various parts labelled. In the given figure, scan starts at the −0.4 V and sweep in a forward direction. Portion (a) of the fig represents the initial potential region where the potential is not sufficient for the redox process to take place and the observed current is due to the non-Faradaic processes. Part (b) shows the next step where the onset of oxidation has started and the current increases exponentially with the increasing voltage. This process is studied when the analyte is within the diffuse double layer near the electrode. The current reaches a maximum point (c), an anodic peak current (i_{pa}) for oxidation. After this, the current starts decreasing as the analyte has almost depleted and the diffuse double layer increases in size. In the portion (d), the current starts decreasing exponentially as the current is limited by the mass transport. The potential is scanned in a more positive direction till the point steady state is reached and further increase in potential has no effect on the current. In the next step (e), the scan reverses to the negative potential and the reductive scan continues until the oxidized analyte which has accumulated on the electrode can be reduced. The last portion (f) is labelled for the cathodic peak current (i_{pc}) scans in opposite direction at the cathodic current peak (E_{pc}). The obtained peak current for the anodic and cathodic should be reversed in sign and equal in magnitude, provided we are studying the reversible process.

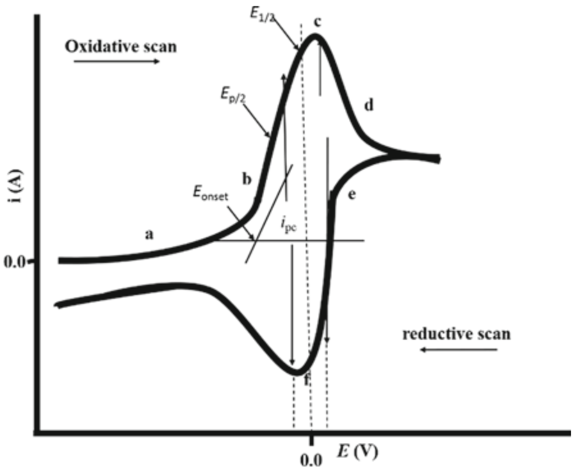

Fig. 22.13 Pictorial representation of CV curve for a reversible electron transfer system

Linear Sweep Voltammetry (LSV):

LSV is a voltammetry technique similar to cyclic voltammetry except that the scanning of the potential takes place in a single direction. The potential is varied at a constant rate and the current is produced by the electrode as a function of applied potential. The increased current is recorded which flows between the working and counter electrode.

Chronoamperometry:

The electrochemical stability of the catalyst is recorded using the chronoamperometry at a particular potential. In this technique, current is recorded as a function of potential. Before running the chronoamperometry, cyclic voltammetry scans are run to find out the fixed potential for the study of chronoamperometry. In chronoamperometry, fixed area electrodes are used to study the electrode processes. This technique is used for the analysis of diffusion coefficient of the electroactive species and for mechanistic investigations of the electrode process. The relation between the current and time is explained by the Cottrell equation [13].

$$i\,(t) = \frac{nFACD^{1/2}}{\pi^{1/2}t^{1/2}} = kt^{-1/2} \tag{22.5}$$

The current versus $t^{-1/2}$ gives a straight line and their slope provides the diffusion coefficient (D), surface area (A) and concentration of the species.

Transient Photocurrent:

Transient photocurrent study is employed to study the time-dependent extraction of charges in the presence of light and functioning of current with time in the presence and absence of light. To further study about the photo-generated electron–hole pairs response v/s time, the transient photocurrent is studied. When a semiconductor film is exposed to light, the photo-generation of charges takes place. These charges are extracted on the electrodes resulting in a current as photocurrent. Photocurrent curves are recorded for certain number of ON–OFF cycles under white light illumination (i.e. under light chopping). During repeated ON–OFF irradiation cycles, the reproducible current responses are recorded. A prompt and reproducible photocurrent under each illumination is observed and quickly returns to zero when the irradiation was interrupted, the photocurrent rapidly dropped to almost zero (steady-state value), and reverted to the original value once light was switched on back again. Greater value of photocurrent for a material is regarded as a best candidate. This also notifies the efficient charge separation and longer life span.

Mott–Schottky:

Mott–Schottky (M-S) analysis is an important tool to study semiconductor heterostructure behaviour, properties and to gain the idea about the fundamental mechanism for comparative PEC performance including the onset and increment in photocurrent density. It is the measurement of interfacial capacitance of electrode with voltage. Two important parameters, flat band potential and the charge carrier density of the semiconductor material, can be calculated from Mott–Schottky plot. The n-type and p-type nature of the material is verified by the nature of the slope of M-S plot. If the slope is positive, it is n-type, and if the slope is negative, it is p-type semiconductor. When no band bending takes place even after the application of the voltage is called flat band potential, this flat band potential can be obtained from the Mott–Schottky equation.

$$\frac{1}{C^2} = \left(\frac{2}{q \in 0 \in Nd}\right)\left(V_{\text{app}} - V_{\text{fb}} - \frac{kT}{q}\right) \tag{22.6}$$

The Mott–Schottky curves ($1/C^2$ vs electrode potential, where C is the space charge layer capacitance) were plotted to estimate the donor density (N_d), flat band potential (V_fb) and depletion layer width of thin films. Here, e is the electronic charge, ε is the dielectric constant of the semiconductor, ε_0 is the permittivity of the vacuum, V_app is the applied potential, q is the electric charge and kT/q is the temperature-dependent term. We can obtain flat band potential extrapolating linear plot at $1/C^2 = 0$.

22.3.1 Strategies for Modifying Semiconductor for Enhanced Photocurrent and Stability

PEC water splitting makes the best use of semiconductor properties such as excited electron–hole pair, their separation and charge transfer due to them. But, in most of the cases, even after the well-aligned positions of valence band/conduction band edges for HER and OER, the kinetics of the reactions results out to be sluggish. The enhancement for the kinetics accounts for the overpotential. Hence, to enhance the PEC activity at the lower overpotential, the various strategies are being taken into account such as band gap engineering via doping, nanostructuring, making heterojunctions, usage of co-catalyst and surface passivation.

Doping:

The practical efficiency of the catalyst sometimes comes out to be lesser than the theoretical value because of some factors such as short hole diffusion length, poor conductivity and slow kinetics. Among the various strategies, doping is an effective approach to improve the efficiency of a PEC semiconductor catalyst as it tailors the electronic and optical properties. Insertion of a heteroatom with diverse atomic radii and varied electronic configuration into a semiconductor lattice proved to be a most exportable approach. Since years, various metal and non-metal elements such as Cr, Ti, Sn, S, P and N have been doped in the semiconductor to improve the overall PEC activity. The effect of doping: (1) increases the range of light absorption, (2) increases the concentration of charge carriers, thus improving the electrical conductivity, (3) acts as an electron traps thus facilitating the separation of electron hole, (4) The inclusion of the foreign element by in situ doping also alters the morphology of the semiconductor.

When a doping is done in a semiconductor, the formation of intermediate band states takes place which efficiently harvests the solar light and thus enhances the PEC activity. Doping strategies enhance the optical and electrical properties even for small band gap semiconductors [14, 15] specially in metal oxide due to polar-on-hopping conduction mechanism (charge carriers in metal oxides tends to localize as small polar-on) [16]. Non-metal dopants like B, C, N, P, S and halogen lead to improved photo-activity and better charge transport properties. Using metal ions as a dopant such as Fe^{3+}, V^{4+}, Mo^{5+} in wider band gap semiconductors such as TiO_2 leads to enhancement in photo-electrochemical performances. Metal doping leads to a donor or acceptor energy level in a semiconductor band gap, which leads to extension of the range of absorption. It can be seen from Fig. 22.14 that the acceptor level or the donor level can effectively shorten the semiconductor band gap so that it can effectively absorb and utilize the visible light.

Generally, neither very low level of doping can sufficiently increase the conductivity nor too high level increases the efficiency. An adequate amount of doping alters the optical and electrical properties, mobility, diffusion length, and charge carrier concentration thus resulting in increased photocurrent, and shifts in onset potential is also observed due to alteration of band gap. Given below is Table 22.2 that shows the comparison of variant dopants with current value achieved.

Nanostructuring:

Nanostructuring of materials represents an effective strategy to reach the goal of efficient PEC. One-dimensional (1 D) nanostructures such as nanowires, nanotubes and nanorods enhance photo-electrochemical activity as compared to corresponding planar structures. Discovery of carbon nanotube with variety of interesting properties motivated the research focus in the field of nanostructured materials. Among the various nanotube materials, titanium dioxide nanotube arrays are of particular

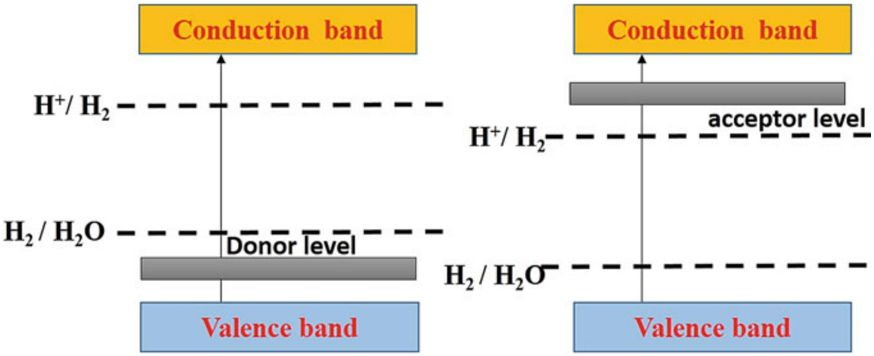

Fig. 22.14 Schematic representing the donor and acceptor level due to the metal doping

Table 22.2 Table showing the comparison of various dopants with achieved current density value in a particular electrolyte using AM 1.5 light source and a potential of 1.23 V versus RHE

S.N.	Base material	Dopant	Electrolyte used	Current density	Ref.
1.	Fe_2O_3	La	1 M KOH	0.11 mA/cm^2	[17]
2.	CN_x	Ni	0.1 M KOH	75.6 μA/cm^2	[18]
3.	g-C_3N_4	B	0.1 M Na_2SO_4	103.2 μA/cm^2	[19]
4.	$BiVO_4$	Mo	0.5 M Na_2SO_4	4.98 mA/cm^2	[20]
5.	WO_3	Bi	1 M NaOH	1.511 mA/cm^2	[21]
6.	Fe_2O_3	S	1 M NaOH	1.44 mA/cm^2	[22]
7.	Fe_2O_3	Sn, Zr	1 M NaOH	1.34 mA/cm^2	[23]
8.	Fe_2O_3	Mn	1 M NaOH	1.60 mA/cm^2	[24]
9.	Fe_2O_3	Si	1 M NaOH	1.45 mA/cm^2	[25]
10.	Fe_2O_3	Ti	0.1 M KOH	0.42 mA/cm^2	[26]
11.	Fe_2O_3	Sn	0.1 M KOH	1 mA/cm^2	[27]

interest. Moreover, the branched or dendritic-shaped nanostructure semiconductor grown vertically on the substrate proves to be more efficient for PEC [17]. Vertically aligned nanostructure materials provides a large surface area thus enabling the greater amount of photo-generated charge carriers to diffuse in the electrode–electrolyte interface thus preventing the charge recombination and supporting charge separation. Nanostructures could also reduce the surface light reflection thus increasing the light absorption efficiency.

The 2D nanostructures have greater surface area, and also their small thickness reduces the travelling distance for the photo-generated holes to reach to the surface. Among them, NiO as a 2D nanostructured material is particularly the most promising one because of its appropriate valence band edge positions for the OER [29] and other examples are ZnO nanorods, TiO_2 nanotubes [30] and nanoflowers [31]. Similarly, nanostructured branched or dendritic [32] semiconductors are also proved effective for water splitting.

Some of the nanostructured materials with current density in different electrolyte are discussed in Table 22.3. Nanostructured materials have low charge carrier recombination as small radial dimension enables a greater fraction of photo-generated minority carriers to diffuse to the electrode–electrolyte interface; due to the direct growth of the photoactive material over the substrate, an electron transfer between the material and substrate is improved. The nanostructuring of the semiconductors also enhances the visible light absorption extent. Some types of nanostructures are being compared in a Table 22.4 with different features and current density value.

Surface Passivation

OER is a slow kinetic reaction but the passivation of the surface has proved out to be an effective strategy to reduce the energy barrier for water splitting and thus

Table 22.3 Table showing the comparison of nanostructure catalyst with achieved current density value in a particular electrolyte using AM 1.5 light source at a given applied potential

S. N.	Nanostructured catalyst	Electrolyte	Potential, V versus RHE	Current density (mA/cm^2)	Ref.
1.	TiO_2 nanotubes	1 M KOH	1.23	0.90	[29]
2.	TiO nanotubes array	1 M KOH	1.23	0.065	[30]
3.	TiO nanotubes array with other semiconductors	1 M KOH	1.23	1.5	[31]
4.	Hydrogen-treated TiO_2 Nanowire	1 M NaOH	0.40	1.9	[32]
5.	Ni/Si-doped TiO_2 nanostructure	1 M KOH	1.23	2.28	[33]
6.	PtO/ZnO nanowires	0.2 M Na_2SO_4	1.23	2.3	[34]
7.	CuO nanowires	1 M Na_2SO_4	−0.30	1.4	[35]
8.	Cu_2O nanowire	0.5 M Na_2SO_4	0.00	10	[36]

lowering the onset potential. Initially, the passivating layers were mainly employed to overcome corrosion and increase the photochemical stability. Some semiconductors have large surface area for water oxidation, but this needs to be compensated with greater overpotential or external application of bias. Surface passivation came out as a strategy to reduce the large overpotential for catalytic activity of water oxidation or reduction. In other words, suppressing the overpotential for catalytic activity also helps in preventing the self-oxidation and reduction thus improving the stability.

Table 22.5 summarizes surface passivation approach to enhance the water oxidation. Grazel et al. reported surface modification of hematite with IrOx to attain the PEC current value of 3 mA/cm^2 [53]. Some mixed transition metal oxides are also investigated such as NiO and NiFeOx which lead to a cathodic shift in onset potential. Generally, a passivating layer is a surface layer that inhibits the consumption of photo-generated charges by the side reactions and thus increases the Faradic efficiency and voltage. The designing of passivating layers has paved a greater interest as it prevents charge transfer inhibition and can be easily incorporated onto a high surface area nanostructure. A few examples of surface passivating OER catalyst are $Ni(OH)_2$, FeOOH and NiOOH.

Surface Plasmon Resonance (SPR):

Combination of surface plasmon with exciton such as Ag [29] and Au [54] decorating on the surface of hematite is studied to help in water splitting activity. Generally, surface plasmons are studied as the conduction electrons oscillations of the conductive material. Metal nanoparticles being irradiated by the incident light

Table 22.4 Table showing the comparison of nanostructure catalyst with achieved current density value with different synthesis method

S. N.	Morphology	Features	Synthesis method	J (mA/cm^2)	Ref.
1.	Bulk	Dense, high e–h recombination and high photon absorption	Electrodeposition	No photo-response	[37]
2.	Dendrites	Dense, poor light absorption, long electron path and high e–h recombination	Electrodeposition	0.018	[38]
3.	Nanoparticles	More surface area than bulk, long electron path and low electrode/electrolyte interaction	Anodization	0.05	[39]
4.	Mesoporous	More surface area than bulk and higher electrode/electrolyte interaction than nanoparticles	Colloidal Synthesis	1.1	[40]
5.	Nanowires	Strong anisotropic conductivity and low grain boundaries	Hydrothermal	1.24	[41]
6.		Nanowalls of 5–6 nm thick and high aspect ratio	Sono-electroanodization	1.41	[42]
7.	Nanocones	Large surface area and enhanced light trapping	Template-assisted ultrasonic spray pyrolysis	2.42	[43]

The current density is measured at 1.23 V versus RHE

generate electric field at the surface of nanoparticles. Photo-anodes decorated with plasmonic metals increase the light absorption. Plasmonic nanoparticles show the interaction with photons via excitation of surface plasmon resonance. By using

Table 22.5 Table showing the comparison of surface passivation layer with achieved current density value, onset values and with different synthesis ways

S. N.	Passivation layer	E_{Onset} shift (mV)	E_{Onset}, V versus RHE	Electrolyte	Synthesis method	Ref.
1.	IrO_2	200	0.80	1 M NaOH	Controlled potential electroflocculation	[44]
2.	Co-Pi	100	0.60	1 M KOH and 0.2 M KCl supporting	Photo-electrodeposition	[45]
3.	Co–Pi	170	0.90	1 M NaOH	Photo-electrodeposition	[46]
4.	$Ni(OH)_2$	300	0.80	1 M KOH	ALD	[47]
5.	Co_3O_4	40	0.66	1 M NaOH	In situ hydrothermal	[48]
6.	Al_2O_3	100	0.80	1 M NaOH	ALD	[49]
7.	TiO_2	100	0.88	1 M NaOH	ALD	[50]
8.	Ga_2O_3	220	0.80	1 M NaOH	Chemical bath deposition	[51]

different composition, size and shape of plasmonic nanostructures, we can design the catalyst that can enhance the light absorption to the full solar spectrum. So far, several mechanisms are being studied to improve the PEC water splitting such as plasmon resonance energy transfer (PRET), plasmon induced heating, hot electron transfer and photon scattering and reflection reduction at the interface [55].

Quantum dot Sensitization:

Quantum dot (QD) sensitization is an efficient tool for effective PEC due to following reasons:

(i) Extend the material absorption from UV visible to NIR region.
(ii) Tuning of the band gap across the absorption spectra.
(iii) Resistance to photo-bleaching.
(iv) Generation of excitons and energy transfer-assisted charge collection.

Working with metal oxide/QD facilitates charge separation and inhibits recombination via generating a potential difference at the interface. Further, Table 22.6 represents the summary of quantum dot sensitization with photocurrent densities.

Controlling surface states and electronic structure:

To minimize the superficial electronic states, the trap states play an important role in solving the problems of inefficient charge separation thus enhancing PEC efficiency. This can be done if we control the synthesis and post-synthesis treatments

Table 22.6 Table showing the summary of quantum dot sensitization with photocurrent densities

S. N.	Semiconductor	Sensitizer	Morphology	Photocurrent density (mA/cm^2)	Ref.
1.	TiO_2	PbS/CdS with Al_2O_3 over coating	Nanotube array	5.19 at − 0.25 V versus SCE IPCE	[55]
2.	TiO_2	PbS	Nanofilm	1.9 at 0 V versus SCE	[56]
3.	$BaSnO_3$	CdS	NWs	4.8 at 0 V versus SCE	[57]
4.	α-Fe_2O_3	CdSe	Nanoporous film	0.55 at 1.0 V versus SCE	[58]
5.	N-doped ZnO	CdTe	NWs array	0.46 at 0.5 V versus Ag/AgCl	[59]
6.	ZnO	CdS and CdSe modified with IrO_x	NWs on silicon microwires	1.64 at 0 V versus Ag/AgCl	[60]
7.	ZnO	CdSe	Nanotubes	5.10 at 0 V versus SCE	[61]
8.	ZnO	CdSe	Nanorods	2.48 at 0 V versus SCE	[62]
9.	WO_3	PbS	Nanoflower	1.8 at 1 V versus Ag/AgCl	[63]

or if we incorporate other metals on the surface of the semiconductor which can both fill the traps and acts as an OER catalyst.

Heterostructure:

Enhancement in the PEC performance can be achieved by analysing the charge transfer process at the interface. Different junctions or interfaces among the different materials or with electrolyte enable the charge separation. This practice paved a new pathway for the designing of heterostructures. This approach allows the varied suitable properties from participating semiconductor and overcoming a single photo-catalysts' drawback such as limited absorption range and the electron hole recombination. Heterostructure of the functional materials is designed such as that the energy levels of the materials have matched or overlapped band structures. This overlapping of the band structures facilitates the charge migration from one material to another and thus enhancing the oxidation and reduction ability.

Types of heterostructure on the basis of band alignment:

Generally, for the study of photo-generated charge separation, there are mainly four types heterojunctions named as type I, type II, type III and Z-scheme as described in Fig. 22.15. Among these structures, type II and Z-scheme play the most important

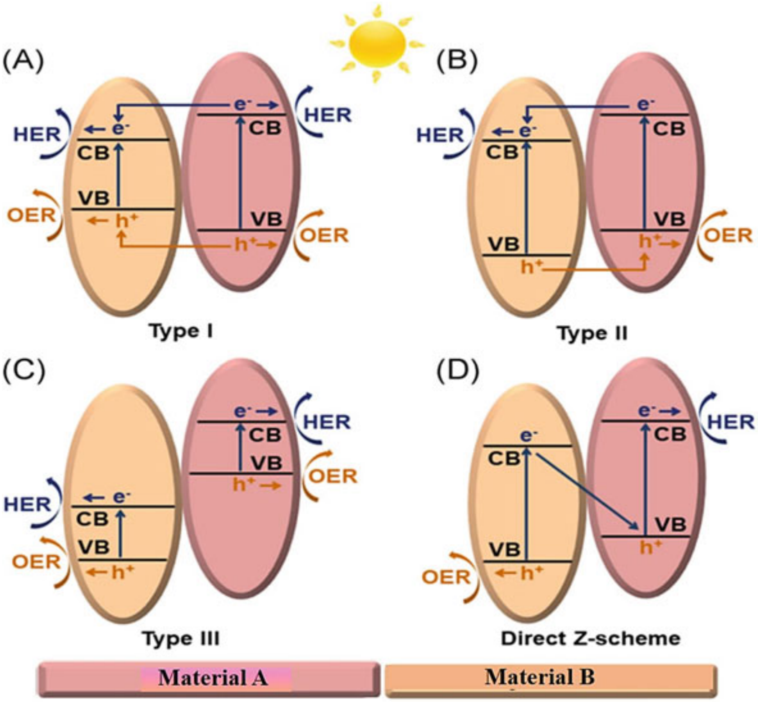

Fig. 22.15 Band alignment and charge transfer mechanism of **(A)** type I, **(B)** type II, **(C)** type III, and **(D)** direct Z-scheme. VB is valence band; CB is conduction band; HER is hydrogen evolution reaction; OER is oxygen evolution reaction. Modified image [8] adapted from Ref. [9]

role in preventing the recombination of photo-generated electrons/holes, as will be discussed below.

Type I:

In type I heterojunction, the VB and CB of the material A are within the band gap region of material B. When the hybrid is irradiated by the incident light, the holes and electrons are transferred from material B to material A in a single direction. This one-way movement of electrons and holes is also facilitated due to more negative CB and more positive VB of material B than that of material A.

Type II:

In this type of heterostructure, the band edge positions of material A and material B are staggered between them such that the VB position of material A is more positive than B and the CB position of material B is more negative than that of material A, thus the electrons and holes flow in opposite directions. When the heterostructure is exposed to light, the electrons get transferred from B to A and holes from A to B.

This kind of double charge transfer plays significant role in charge separation and thus improving the PEC activity.

Type III:

In this type of heterostructure, the difference between the VB and CB edges is larger. The VB and CB of material A and B do not overlap with each other; as a result, they require a higher driving force for charge transfer. When the hybrid is excited by light, the photo-generated electrons from material A combine with the holes of material B, thus the holes from material A and electrons from material B are free to participate in the oxidation and reduction process of water, respectively.

Z-type:

Though the type II alignment is quite effective for charge separation, it is limited by its drawback of reducing the redox ability of the photo-electrodes. The transfer of electrons from the CB of material A to the CB of material B and the flow of holes from the VB of material A to the less positive VB of material B reduce the redox ability of the photo-electrodes. To overcome this shortcoming, direct Z-scheme heterojunction has been reported. In this scheme, the electrons from the CB of material A combine directly with the holes in the VB of material B. Thus, the oxidation of water occurs in material A, and the left behind electrons in the material B contributes to water reduction.

Carbon nitride and metal oxide-based Heterojunction:

Among the carbon-based semiconductors, graphitic carbon nitride (g-C_3N_4) semiconductor with a suitable band gap of 2.7 eV is one of the most important catalysts for PEC reactions. Many efforts have been done to enhance its activity among which coupling with other semiconductors has proven to be an effective approach. Choosing the other semiconductor with g-C_3N_4, metal oxides came out with a fruit full strategy. Suitable band gap, low cost, ease of synthesis and low electric resistance make them the potential candidate for PEC. Further, the improvement of optical properties and charge separation is sort out via heterojunction [64]. Due to the suitable alignment of the g-C_3N_4 and metal oxide, their heterostructures were designed and have proved out to be the best candidates. Graphitic carbon nitride selectively forms type (II) heterojunctions, thus a better charge separation is achieved in the heterostructure.

22.4 Summary and Future Outlook

PEC water splitting has proved in itself to be the unique way for utilizing solar energy conversion into fuels. Since the pioneered time, a keen attention has been paid for the designing of efficient and active photo-anode. However, even after the many efforts, the photo-anode suffers from various intrinsic limitations which result in charge recombination and sluggish water oxidation kinetics. Still, a long way has to go to achieve the benchmark in this field. In this chapter, we have discussed different aspects for a material to be an active photo-anode and the different modification strategies in the semiconductor to make them more reliable and efficient for PEC. These strategies include the modification of the surface by different methods and intrinsically. Among all the strategies described above, the formation of heterostructure has proved to be the most efficient. Especially, the type II and Z-type heterostructured has gained a great fame in the field of PEC due to the efficiently active approach for charge separation. These type of heterostructure can be formed between the two metal oxide semiconductors. Due to the suitable alignment of the g-C_3N_4 and metal oxide, their heterostructures were also designed and are proved out to be one of the best candidates.

References

1. Li Y, Li W, Ke T, Zhang P, Ren X, Deng L (2016) Electrochem Commun 69:68–71
2. Hisatomi T, Kubota J, Domen K (2014) Chem Soc Rev
3. Fujishima A, Honda K (1972) Nature 238:37–38
4. Liu Q, Zhang J (2013) Langmuir 29:3821–3828
5. Jukk K, Kongi N, Tammeveski K, Solla-Gullón J, Feliu JM (2015) Electrochem Commun 56:11–15
6. Li Z, Luo W, Zhang M, Feng J, Zou Z (2013) Energy Environ Sci 6:347–370
7. Choudhary S, Upadhyay S, Kumar P, singh N, Satasangi VR, Shrivastav R, Das S (2012) Int J Hydrogen Energy 37:18713–18730
8. Acar C, Dincer I (2014) Int J Hydrogen Energy 39:1–12
9. Wang L, Si W, Tong Y, Hou F, Pergolesi D, Hou J, Lipert T, Dou SX, liang J (2020) Carbon Energy 2:223–250
10. Pandey T, Nissimagoudar AS, Mishra A, Singh AKJ (2020) Mater Chem A 8:13812–13819
11. Trasatti S (1986) Pure Appl Chem 58:955–966
12. Bard A, Faulkner L (2001) Electrochemical methods fundamentals and applications. Wiley. 0-471-04372-9
13. Tamirat AG, Rick J, Dubale AA, Su W-N, Hwang B (2016) J Nanoscale Horiz 1:243–267
14. Kim JH, Lee JS (2019) Adv Mater 1806938
15. Jang JW, Friedrich D, Muller S, Lampers M, Hempel H, Lardhi S, Cao Z, Harb M, Cavallo L, Heller R, Eichberger R, krol R, Abdi F (2017) Adv Energy Mater 7:1701536
16. Baxter JB, Aydil ES (2005) Appl Phys Lett 86:053114
17. Jayaraman L, Tee S, Kumar Y, Lee PS, Liew CJJ, Chi SL, Hor D, Ramakrishna TSA, Luo S (2014) Mater Chem A 2:19290–19297
18. Zhang W, albero J, Xi Lange KM, Garcia H, Wang X, Shalom M (2017) ACS Appl Mater Interfaces 38:32667–32677
19. Ruan Q, Luo W, Xie J, Wang Y, Liu X, Bai Z, Carmalt CJ, Tang J (2017) Angew Chem 129:8333–8337
20. Ye K, Li H, Huang D, Xia S, Qiu W, Li M, Hu Y, Mai W, Ji H, Yang S (2019) Nat Commun 10:3687
21. Kalanur SS, Yoo I, Eom K, Seo H (2018) J Catal 357:127–137
22. Zhang R, Wang Y, Chen T, Qu F, Liu Z, Du G, Asir AM, Gao T, Sun X (2017) ACS Sustain Chem Eng 9:7502–7506
23. Tamirat AG, Su W-N, Dubale AA, Chena H-M, Hwang B-J (2015) J Mater Chem A 3:5949–5961

24. Huang J, Hu G, Ding Y, Pang M, Ma B (2016) J Catal 340:261–269
25. Cesar I, Kay A, Martinez JAG, Grätzel M (2006) J Am Chem Soc 128:4582–4583
26. Yan D, Tao J, Kisslinger K, Cen J, Wu Q, Orlovb A, Liu M (2015) Nanoscale 7:18515–18523
27. Annamalai A, Lee HH, Choi SH, Lee SY, Gracia-Espino E, Subramanian A, Park J, Kong K, Jang JS (2016) Sn/Be Sci Rep 6:28183
28. Chaudhary P, Ingole PP (2020) Int J Hydrog Energy 45:16060–16070
29. Kim HI, Monllor-Satoca D, Kim W, Choi W (2015) Energy Environ Sci 8:247–257
30. Cui H, Zhao W, Yang C, Yin H, Lin T, Shan Y, Xie Y, Gua H, Huang FJ (2014) Mater Chem A 2:8612–8616
31. Lin CJ, Lu YT, Hsieh CH, Chien SH (2009) Appl Phys Lett 94:113102
32. Wang G, Wang H, Ling Y, Tang Y, Yang X, Fitzmorris RC et al (2011) Nano Lett 11 (7):3026–3033
33. Kusior A, Wnuk A, Trenczek-Zajac A, Zakrzewska K, Radecka M (2015) Int J Hydrogen Energy 40:4936–4944
34. Fu S, Zhang B, Hu H, Zhang Y, Bi Y (2018) Catal Sci Technol 8:2789–2793
35. Lia J, Jina X, Lib R, Zhaob Y, Wanga X, Liua X, Hang Jiaoa H (2019) Appl Catal B 1–8:240
36. Luo J, Steier L, Son MK, Schreier M, Mayer MT, Gratzel M (2016) Nano Lett 16(3):1848–1857
37. Chou J-C, Lin S-A, Lee C-Y, Gan J-Y (2013) J Mater Chem A 1:5908–5914
38. Zheng JY, Kang MJ, Song G, Son SI, Suh SP, Kim CW, Kang YS (2012) CrystEngComm 14:6957–6961
39. Fu L, Yu H, Li Y, Zhang C, Wang X, Shao Z, Yi B (2014) Phys Chem Chem Phys 16:4284–4290
40. Gonçalves RH, Lima BHR, Leite ER (2011) J Am Chem Soc 133:6012–6019
41. Ling Y, Wang G, Wheeler DA, Zhang JZ, Li Y (2011) Nano Lett 11:2119–2125
42. Liu J, Cai YY, Tian ZF, Ruan GS, Ye YX, Liang CH, Shao GS (2014) Nano Energy 9:282–290
43. Mohapatra SK, John SE, Banerjee S, Misra M (2009) Chem Mater 21:3048–3055
44. Qiu Y, Leung SF, Zhang Q, Hua B, Lin Q, Wei Z, Tsui K-H, Zhang Y, Yang S, Fan Z (2014) Nano Lett:14:2123–2129
45. Tilley SD, Cornuz M, Sivula K, Grätzel M (2010) Angew Chem 49:6405–6408
46. Zandi O, Hamann TW (2014) J Phys Chem Lett 5:1522–1526
47. Zhong DK, Cornuz M, Sivula K, Gratzel M, Gamelin DR (2011) Energy Environ Sci 4:1759–1764
48. Young KMH, Hamann TW (2014) Chem Commun 50:8727–8730
49. Xi L, Tran PD, Chiam SY, Bassi PS, Mak WF, Mulmudi HK, Batabyal SK, Barber J, Loo JSC, Wong LH (2012) J Phys Chem C 116*:*13884–13889
50. Formal F, Tetreault L, Cornuz N, Moehl M, Gratzel M, Sivula K (2011) Chem Sci 2:737–743
51. Yang X, Liu R, Du C, Dai P, Zheng Z, Wang D (2014) ACS Appl Mater Interfaces 6:12005–12011
52. Hisatomi T, Formal FL, Cornuz M, Brillet J, Tetreault N, Sivula K, Gratzel M (2011) Energy Environ Sci 4:2512–2515
53. Chaudhary P, Ingole PP (2018) Int J Hydrogen Energy 43:1344–1354
54. Du C, Yang X, Mayer MT, Hoyt H, Xie J, McMahon G (2013) Angew Chem Int Ed 52:12692–12705
55. Zeng M, Peng X, Liao J, Wang G, Li Y, Li J Phys Chem Chem Phys 18:17404–17413
56. Ikram A, Sahai S, Rai S, Dass S, Shrivastav R, Satsangi VR (2016) Phys Chem Chem Phys 18:5815–5821
57. Zhang Z, Li X, Gao C, Teng F, Wang Y, Chen L (2015) J Mat Chem A 3:12769–12776
58. Sahai S, Ikram A, Rai S, Dass S, Shrivastav R, Satsangi VR (2014) Int J Hydrog Energy 39:11860–11866
59. Chen CK, Shen YP, Chen HM, Chen C-J, Chan T-S, Lee J-F, Liu R-S (2014) Eur J Inorg Chem 773–779

60. Sheng W, Sun B, Shi T, Tan X, Peng Z, Liao G (2014) ACS Nano 8(7):7163–7169
61. Chouhan N, Yeh CL, Hu SF, Huang JH, Tsai CW, Liu RS (2010) J Electrochem Soc 157:1430–1433
62. Chouhan N, Yeh CL, Hu S-F, Liu R-S, Chang W-S, Chen K-H (2011) Chem Commun 47:3493–3495
63. Su F, Lu J, Tian Y, Ma X, Gong J (2013) Phys Chem Chem Phys 15:12026–12032
64. Baek JH, Kim BJ, Han GS, Hwang SW, Kim DR, Cho IS, Jung HS (2017) ACS Appl. Mater Interfaces 9(2):1479–1487

Chapter 23
Bandgap Engineering of Heterostructures for Visible Light-Driven Water Splitting

Susmita Bera and Srabanti Ghosh

Abstract Interfacial bandgap engineering of semiconductor-based heterojunction provides a propitious route to improve solar energy conversion in energy-related applications due to the synergistic effects of fast charge transfer, band bending and suitable oxidation and reduction potentials. In the last decades, a great number of studies on heterostructures have been implemented in environmental remediation, water splitting and CO_2 reduction under solar light. This chapter provides the bandgap engineering of semiconductor photocatalysts through atomic doping, alloying and hybridization to alter electronic structures and enhance the light absorption, charge transfer, surface reactions in the photocatalytic processes. Furthermore, the current progresses in the band gap engineering of quantum dots, metal oxides, organic semiconductors, 2D-hybrid materials for photocatalytic and photoelectrocatalytic (PEC) water splitting has been discussed and summarized. Finally, the challenges and perspectives for future research to develop highly efficient bandgap engineered heterostructures for water splitting have been proposed.

Keywords Bandgap engineering · Semiconductor · Heterostructure · Water splitting

23.1 Introduction

Photocatalytic water splitting becomes a promising and ecofriendly route for the solar energy conversion into chemical energy for alleviating the energy crisis [1, 2]. Recently, various photocatalysts, mainly semiconductor-based materials have been developed and showed significant results in wastewater treatment, photocatalytic H_2 generation, water splitting and CO_2 reduction [3, 4]. However, application of

---

S. Bera · S. Ghosh (✉)
Energy Materials and Devices Division, CSIR—Central Glass and Ceramic Research Institute, 196, Raja S. C. Mullick Road, Kolkata 700032, India
e-mail: srabanti@cgcri.res.in

S. Garg and A. Chandra (eds.), *Green Photocatalytic Semiconductors*,
Green Chemistry and Sustainable Technology,
https://doi.org/10.1007/978-3-030-77371-7_23

traditional semiconductor-based photocatalysts in water splitting still faces many challenges such as fast charge recombination, low photo-conversion efficiency and poor stability [5]. In an attempt to enhance the photocatalytic efficiency and address these drawbacks, numerous strategies have been developed including surface modification, defect engineering, crystal faces design, bandgap engineering, etc. [6, 7]. Among these, bandgap engineering has been considered as a favorable way to control the electronic band structure and charge carrier migration route of a photocatalysts which in turn influences the overall catalytic activity. Theoretically, the band gap (E_g) of a semiconductor should be greater than 1.23 eV for visible light absorption, and however practically, it must be higher (>2.0 eV) due to the presence of over potentials. Simultaneously, the photocatalyst must have a narrow bandgap to absorb the large wavelength light of solar spectrum. The kinetics of the photogenerated charge carrier separation and transfer should be faster to efficiently drive charge migration. Moreover, the band edge potentials of the semiconductor should be closely located near the desired redox potentials of the catalytic reaction, so that excited electrons and photo-induced holes can easily engage into the surface reactions. Hence, the overall mechanistic approach should favor the lower recombination rate and improvement of the stability of the catalytic system [8, 9]. This is challenging task for a single semiconductor photocatalysts to meet all the requirements at a time.

The development of heterostructures or hybrid catalysts using combination of semiconductors with highly matched band alignments has been attracted enormous research interest [5, 10]. Heterostructured photocatalyst has several potential benefits like improved light absorption, effective charge separation, reduced overpotential and stability for photocatalytic and PEC water splitting applications. For example, formation of nano-heterojunction between low band gap Bi_2S_3($\sim$1.47 eV) and a high band gap BiOCl ($\sim$3.10 eV) effectively reduce the band gap and extend the absorption range upto near-IR region [11]. Similarly, when a heterostructure formed between a low band gap semiconductors having high absorption coefficient with a large band gaps, then surface functionalization or sensitization will occur which influences catalytic activity. As example, low band gap Ag_2S (1.42 eV) showed high H_2 evolution reaction (HER) activity after deposition of Ag nanoparticles on its surface [12]. In case of p–n junction (semiconductor/semiconductor) or the Schottky junction (metal/semiconductor), an internal electrical potential can be formed at the interface which may drive the charge separation and transport to the surface efficiently [13–15]. However, the integration of semiconductor with a suitable co-catalyst can lower the redox overpotential at the respective active sites [16]. Depending on the charge separation mechanism, heterostructures are divided into different categories, such as type-I, type-II, surface, Z-scheme and S-scheme heterojunction [8, 17]. Such various heterostructures showed high efficiency for solar light conversion into storable energy resources.

This book chapter describes the bandgap engineering of semiconductor-based materials through doping, alloying and hybridization to improve the light absorption, charge transfer, surface reaction rate. The current status of the band gap engineering of quantum dots, metal oxides, organic semiconductors, 2D-hybrid materials for water splitting has been discussed in this chapter with recent literature examples and mechanistic details, as well as perspectives in hydrogen generation.

23.2 Photocatalytic and PEC Water Splitting

Primarily, the photocatalytic water splitting involves three basic reactions, firstly, photon absorption and generation of charge carriers with high energy than the band gap of the semiconducting material, then photogenerated electron–hole separation and transfer to the surface of the photocatalyst, and finally, oxidation/reduction reaction occurred on the surface of the material. Thermodynamically, it is an uphill reaction process which requires minimum 1.23 eV energy as the change of Gibbs free energy for this reaction is $\Delta G^\circ = 237.2$ kJ/mol but practically requires higher energy than 1.23 eV due to the over potentials of the reactions [8, 9]. Basically, the water splitting process may consist of two half reactions, (i) water oxidation by the photo-induced holes and (ii) proton reduction by the photogenerated electrons to H_2 (Scheme 23.1a). Most of the semiconductor-based photocatalyts are able to perform half reaction, either water reduction or oxidation because of their band edge potentials [7, 8]. Although few materials are reported for both the oxidation and reduction reactions with limited efficiency. To promote the H_2/O_2 evolution reaction, generally scavengers have been used to hinder the electron–hole recombination and increase the water oxidation/reduction rate kinetics. In case of photoelectrochemical (PEC) cell, both the oxidation and reduction reaction may occur simultaneously, where oxidation takes place on anode and reduction on the counter electrode to generate H_2 under the applied potential. In fact, the applied potential may help photogenerated electrons to drive from the anode to the counter electrode. However, the solar to hydrogen (STH) conversion efficiency of PEC cells is relatively low for large scale water splitting. Thus, a specific engineering for material design is required to improve the STH efficiency of the photoelectrochemical cells.

23.3 Types of Heterostructures

Heterostructure is an integrated structure of two or more semiconductors, where charge carriers are generated and transfer from one semiconductor to the other semiconductor and thus prolong the lifetime of charge carriers by lowering the fast recombination rate [7]. Formation of heterojunction facilitates the design of advanced photocatalysts due to effective spatial charge separation [10]. Moreover, it helps the excited carriers to be available for the redox reactions and consequently results an enhanced photocatalytic activity. The other parameters, including diffusion length, mobility and position of apparent fermi level, etc. influence the overall

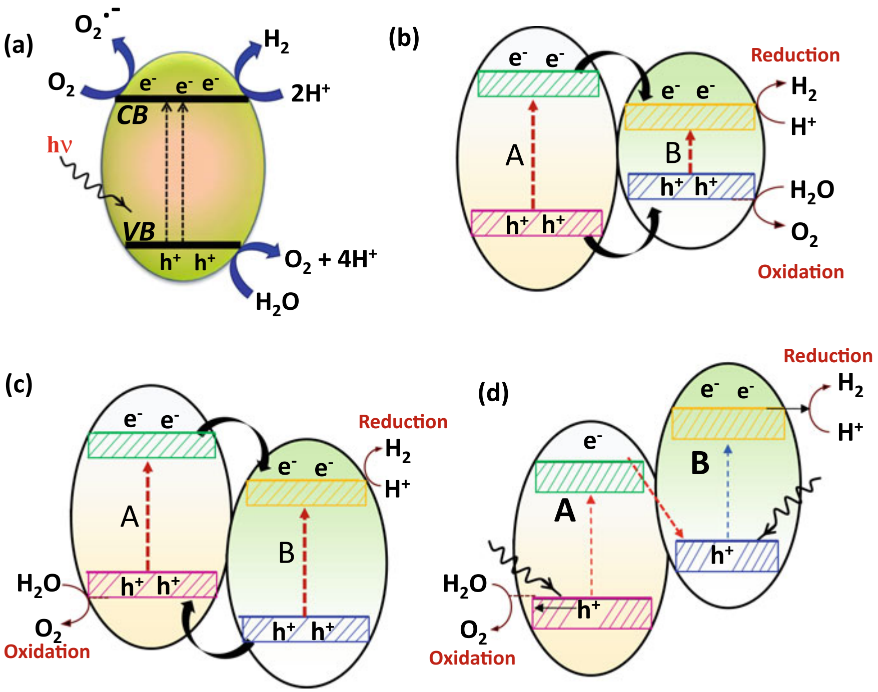

Scheme 23.1 **a** Mechanism of water splitting on a photocatalyst. Schematic band diagram and charge separation on **b** Type-I, **c** Type-II and **d** Z-scheme heterostructures

photocatalytic activity of a heterostructure. In case of Type-I heterojunction, the CB of semiconductor A is higher than the CB of semiconductor B, and the VB is lower than the corresponding VB of semiconductor B. Under light illumination, the excited electrons of A will transfer to the CB of B due to lower CB potential energy and simultaneously holes of A will transfer to the VB of B because of low VB potential energy relative to semiconductor A. Thus, efficient electron–hole separation cannot possible for the Type-I heterojunction photocatalyst due to the accumulation of charge carriers on the semiconductor B (Scheme 23.1b). Type-II heterojunction formed when the CB potential of semiconductor A is higher than the corresponding CB of the semiconductor B and the VB potential of A is lower than the semiconductor B. Under excited condition, the electrons of A will transfer to CB of B, while holes of B will migrate to the VB of A, ensuing facile charge separation [18–20]. Thus, from the above energy band configurations, it is obvious that the Type-II heterojunction has the most effective structure for spatial separation, however the redox ability is not satisfactory as the reduction and oxidation reactions occur at the lower potentials. To overcome this problem and to develop a stable, scalable and efficient photocatalytic system Bard et al. [21] proposed the idea of Z-scheme system in 1979. Z-scheme photocatalytic system is composed of two semiconductors, where electrons of one semiconductor directly recombine with the holes of the other semiconductor through an ionic or solid conductor, or by developing Ohmic contact directly (Scheme 23.1d). As a result, electrons of semiconductor B (with more negative potential) and holes of semiconductor A (with more positive potential) becomes free for catalytic reactions. Thus, both the charge separation and suitable potentials for the redox reactions have been achieved by this Z-scheme heterostructure system [8, 22–24]. Recently, development of direct Z-scheme has attracted enormous attention as it is mediator free system with lower backward reaction rate.

23.4 Bandgap Engineering in Semiconductors

One of the key limiting factors that greatly hinder the efficiency of a photocatalytic system is the fast charge carrier recombination, which can be suppressed by the specific bandgap engineering strategies through introduction of defects, variation of morphology, use of co-catalyst, development of heterostructures, etc.

23.4.1 Defect Engineering

Defect played important roles in semiconductors by offering active sites for the desire reactions as well as it served as recombination centers for charge carriers [25–27]. The commonly observed defects in semiconductors can be classified into three types; bulk defect, surface defect and interfacial defect [27]. The three types of defects are schematically presented in Scheme 23.2 considering TiO_2 as a representative photocatalyst. Bulk defects are formed within a crystal when vacancy created by the displacement of some atoms or due to the formation of interstices. Bulk defects influence the bond energy, bond length, band bending, electron affinity, apparent position of Fermi level, charge and energy density, interface charge density of states, etc. of semiconductor photocatalyst [28]. The bulk defects are commonly observed in TiO_2 due to the presence of Ti^{3+} through self-doping and oxygen vacancy via escape of lattice oxygen from the bulk crystal (Scheme 23.2a). Notably, oxygen vacancy defects may create electro-positivity within the bulk, which promote electron–hole separation [29]. The surface of semiconductor nanomaterials possesses numerous superior properties with the large area, high energy and abundant exposed atoms. Metal and oxygen vacancies both can be present on the surface of semiconductor (Scheme 23.2b).

In case of metal oxide semiconductor, surface oxygen vacancy can provide co-ordinatively unsaturated sites for molecule adsorption and activation, which resulted a localized electron clouds at the surface. The surface metal defects may enhance the stability against photocorrosion and charge separation in the photocatalysis. Notably, the controlling parameters such as the concentration,

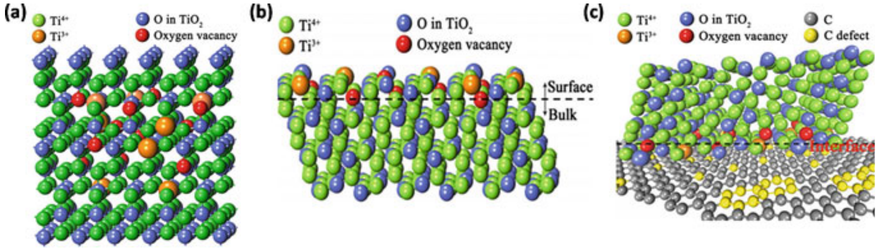

Scheme 23.2 Schematic presentation of **a** bulk defect, **b** surface defect and **c** interface defect considering TiO_2 as a representative photocatalyst. (Reproduced from Ref. [6] with permission from The Royal Society of Chemistry, 2015)

distribution, mobility and controllable creation of surface defects may form a defect bridge through defect-strain coupling, defect-electron or defect-defect interactions, which improve the conductivity and charge separation [29]. Additionally, interface defects exist at the interfacial contact between metal–semiconductor or semiconductor–semiconductor heterostructures. It is important to note that both surface and bulk defects can exist at the interface. Scheme 23.2c represents the carbon-TiO_2 heterostructure where metal, oxygen and carbon vacancies are present at the interface area as well as carbon surface. The interface defects can enhance the interaction between different components and promote the surface reactions. For example, Huang et al. [30] developed monolayer Bi_2WO_6 with interior W-vacancies and investigated the influence of vacancy for surface catalytic reactions under visible light illumination. The schematic diagram of sandwich-like single unit-cell Bi_2WO_6 with vacancy in the interior WO_4 layer has been presented in Fig. 23.1a. The W-vacancies in the defective monolayers was identified by the high-angle annular dark-field scanning transmission electron microscope (HAADF-STEM) imaging (Fig. 23.1b). In the dark field, Bi-atoms appears brighter than W-atoms due to the relatively heavier atomic weight and in the intensity analysis pronounced dip has been observed at a W-site, which suggests the presence of a W-vacancy at the atomic arrangement (Inset of Fig. 23.1b). This interior surface W-vacancy is beneficial to promote the light absorption, charge transport to the surface, etc. via formation of W-vacancy-related mid-gap states, which resulted in 1.4 times and 3 times improved benzylic alcohol oxidation under solar light compared to the monolayers and the bulk system, respectively.

Very recently, Ruan et al. [31] described the role of fluoride ions in stabilizing anatase TiO_2 where fluoride ions are bonded with Ti-vacancies on the (100) facets. Ultrathin nanosheets were prepared by hydrothermal method with a tunable thickness (2.9–13.5 nm). Figure 23.1c shows the TEM images of TiO_2 nanosheets of thickness 2.9 nm which are well crystalline. The lattice spacings of 3.79 Å and 3.76 Å are well matched with (100) and (010) planes of anatase TiO_2, respectively (Fig. 23.1d). The as-prepared TiO_2 nanosheets (NS-5) demonstrates the maximum H_2 generation rate of $\sim$41.04 mmol h^{-1} g^{-1} with quantum efficiency of 41.6% under UV light. The enhanced catalytic activity has been achieved due to the

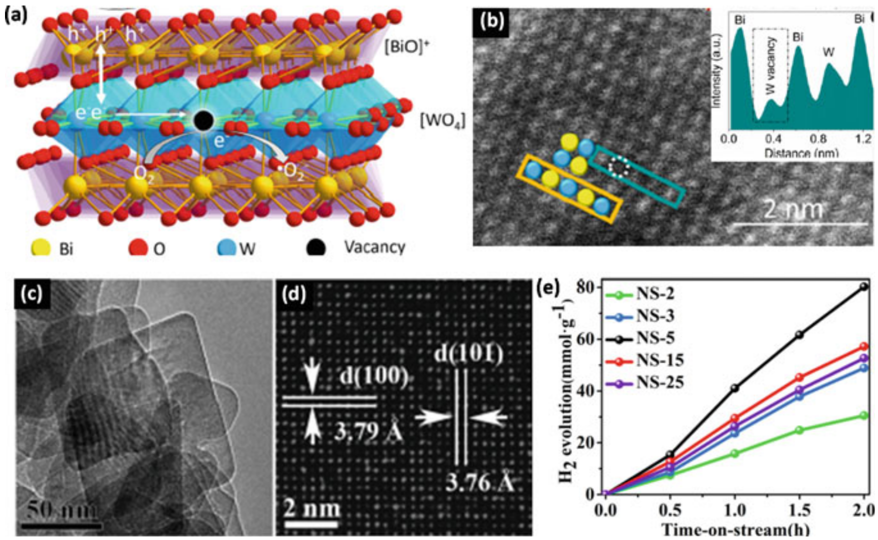

Fig. 23.1 **a** The schematic atomic structures of defect-rich Bi_2WO_6. **b** HAADF-STEM image of defect-rich Bi_2WO_6 with the intensity profile (Inset). **c** TEM image and **d** HRTEM image of TiO_2 NSs using 5 mL ethanol during synthesis (NS-5). **e** Time courses photocatalytic H_2 generation through water splitting under ultraviolet light using as-synthesized TiO_2 NSs as catalyst (Reproduced from Refs. [30] and [31] with permission from American Chemical Society, 2020 and 2019, respectively)

bonding of fluoride ions with Ti-vacancies on the (100) surface which further improve the electron−hole separation as well as stability of (100) surfaces. Hence, it can be concluded that defect engineering is a potential strategy to functionalize the crystal surface and electronic structure. However, the roles of defects specifically location, density, bulk to surface relative concentration ratio of defects, etc. in photocatalytic H_2 generation appear to be complicated and not fully understood. Thus, specific experimental and theoretical studies on defect engineering may get more attention in near future.

23.4.2 Structural Engineering

Structural engineering via fabrication of multicomponent semiconductors is another approach for developing visible light active photocatalysts and band gap can be tuned by varying the composition and stoichiometry of the elements [6]. A series of multicomponent photocatalysts through solid-state reaction have been reported for various photocatalytic applications. For example, $La_5Ti_2MS_5O_7$ (M=Ag, Cu) [32], $Sm_2Ti_2S_2O_5$ [33], $(Ga_{1-x}Zn_x)(N_{1-x}O_x)$ [34], $BaTaO_2N$ [35], $LaTiO_2N$ [36], $(Ag_{0.75}Sr_{0.25})(Nb_{0.75}Ti_{0.25})O_3$, $Cu_xNa_{1-x}Nb_{13}O_{33}$ [37], etc. have been successfully used as photocatalysts for pollutant degradation, H_2 generation, CO_2 reduction, etc. under UV and visible light. J. C. Hill and his co-workers [38] fabricated solid solution of Mo-rich $CuW_{1\text{-}x}Mo_xO_4$ thin film and investigated the effects of M on band structure. The top view SEM images of pure $CuWO_4$, $CuW_{0.55}Mo_{0.45}O_4$ and $CuW_{0.35}Mo_{0.65}O_4$ films have been shown in Fig. 23.2(a–c), where $CuWO_4$ surface has nodular features and it becomes smoother with the increase of Mo. The change of morphology occurs due to differential growth of $CuWO_4$ which effectively reduce the bandgap from 2.3 eV (for $CuWO_4$) to 2 eV (for $CuW_{0.35}Mo_{0.65}O_4$).

Similar kind of bang gap engineering was also reported for $Zn_{1-x}Cd_xS$ (x = 0, 0.1–1.0) solid solution by Li et al. [39]. A significant shift of the absorption edges with the increasing Cd content has been observed in UV–Vis absorption spectra (Fig. 23.2d) and consequently the color of the powder samples changed from white to yellow with band gap reduced from 1.9 eV to 1.14 eV. It is clear from Fig. 23.2e that, incorporation of Cd enhances the H_2 generation rate up to a certain concentration then decreases. The $Zn_{0.5}Cd_{0.5}S$ composite exhibits the highest rate of H_2 generation ~7.42 mmol h^{-1} g^{-1}, which is 54 times higher than that of pure ZnS (~0.14 mmol h^{-1} g^{-1}) due to the balance between band gap and band edge potentials. Further, DFT calculation demonstrated that the charge redistribution between Zn and Cd atoms in $Zn_{0.5}Cd_{0.5}S$ composite leads to a chemical shift for the

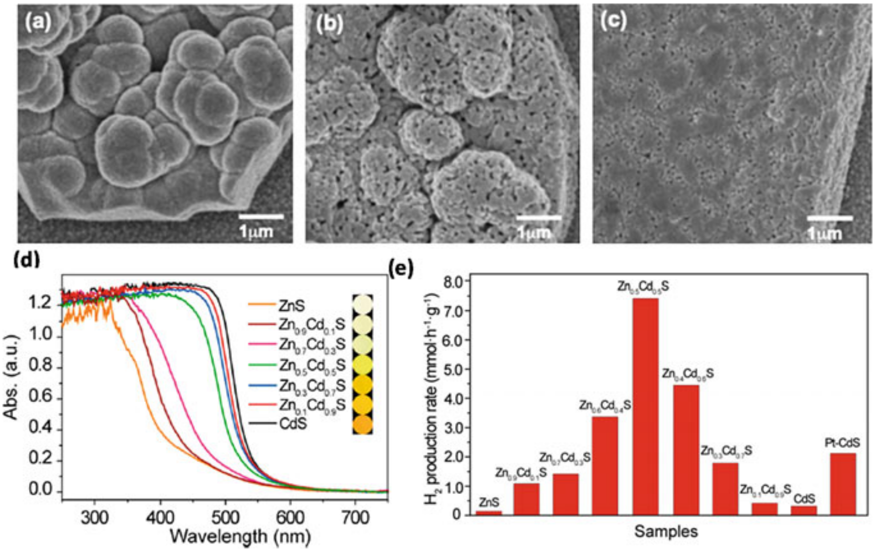

Fig. 23.2 SEM images of the **a** $CuWO_4$, **b** $CuW_{0.55}Mo_{0.45}O_4$, and **c** $CuW_{0.35}Mo_{0.65}O_4$ thin films. **d** UV−Vis diffuse reflection spectra of the $Zn_{1-x}Cd_xS$ composites. **e** Photocatalytic H_2 generation rate of $Zn_{1-x}Cd_xS$ (x = 0, 0.1, 0.3, 0.4, 0.5, 0.6, 0.7, 0.9, and 1.0) composites using mixed aqueous electrolyte (Na_2S/Na_2SO_3) under visible light (≥400 nm). For comparison, Pt loaded CdS (Pt −CdS, 0.9 wt % loading of Pt) has been prepared and tested. (Reproduced from Refs. [38] and [39] with permission from The Royal Society of Chemistry and The American Chemical Society, 2013)

binding energies of elements, which accelerates the charge separation and photocatalytic activity.

However, most of the multicomponent semiconductors are prepared by high temperature solid-state reaction which leads to formation of low surface area, limited catalytic activity. To improve the photocatalytic activity, mesoporous structures with high surface area and crystallinity are required.

23.4.3 Tuning the Size and Shape of the Nanostructure

Besides varying the components of semiconductor, tuning the size and morphology of the nanostructures considered as a very simple and effective way to control the electrical, optical and redox properties. Due to the unique size and shape dependent optical properties, semiconductor-based nanostructures have attracted intense research focus for the last couple of decades.

23.4.3.1 Quantum Confined Structures

When the size of a material becomes too small, the electrons-holes pairs can be confined by a potential barrier within a small region which is comparable to the wavelength of electrons, i.e., de-Broglie wavelength, then a pronounced quantization in the energy states will occur within a ranges from 5 to 25 nm for typical semiconductors (Groups IV, III–V, II–VI), results in enhancement in bandgap compared to the bulk one [40]. Generally, the charge carriers in semiconductors are confined in one, two or three spatial dimensions which are termed as quantum films, quantum wires and quantum dots, respectively. Semiconductor quantum dots (QDs) have been considered as an excellent light harvesting system for photocatalytic H_2 generation because of multiple exciton generation ability with large extinction coefficients, high surface to volume ratio and enhanced photostability [41, 42]. The QDs can exhibit quantum confinement effect which enhances the charge carrier density at the surfaces for light-induced catalytic reactions. In this contest, chalcogenide-based semiconductor QDs, like CdS, CdSe, CdTe, etc. have been extensively examined as efficient photosensitizers for H_2 generation as reduction site, however, the large scale application of these QDs are limited due to high toxicity and unstable under long time irradiation [43–45]. Therefore, development of Cd-free and tunable bandgap QDs photosensitizers are highly desirable for photocatalytic water splitting application. To overcome this issue, multicomponent QDs have been developed by various research groups and tested for photocatalytic H_2 generation [44, 46]. For example, Yuan et al. [47] prepared $(AgIn)_xZn_{2(1-x)}S_2$QDs which showed band gap tunability with variation of chemical compositions. From the UV–Visible absorption spectra it is clearly evident that $(AgIn)_xZn_{2(1-x)}S_2$ QDs have strong absorption in visible region along with a tail in the near-IR region, whereas ZnS QDs shows absorption in UV region (Fig. 23.3a).

The bandgaps of $(AgIn)_xZn_{2(1-x)}S_2$ QDs are 2.78, 2.56, 2.34, 2.21 and 2.02 eV ($x = 0.1, 0.3, 0.5, 0.7$ and 0.9) respectively.

Thus, bandgaps are decreased with the increase of x value which may well consistent with the colors of the as-synthesized QDs in CH_2Cl_2 solutions (Fig. 23.3b). Interestingly, $(AgIn)_xZn_{2(1-x)}S_2$ QDs display size dependent strong luminescence under visible and near-IR light (Fig. 23.5c). Moreover, a red shift has been observed in emission maxima with the increase of x value, which implies reduced bandgap. Initially, the photocatalytic H_2 generation activities increase remarkably for a certain x value and then decreases. The $(AgIn)_{0.5}ZnS_2$QDs system shows highest activity (~276 mmol h^{-1} g^{-1}) after 12 h of visible light illumination. They proposed that the lower activity of $(AgIn)_xZn_{2(1-x)}S_2$QDs with higher x value owing to the modification of CB energy level (Fig. 23.3d). The CB edge potentials become more negative with the decrease of x value, indicating that ZnS-dominant QDs ($\Delta G1 > \Delta G2 > \Delta G3$) can strongly reduce the water molecule compared to the $AgInS_2$-dominant QDs. Whereas, the $AgInS_2$-dominant QDs allowed desirable longer wavelength light absorption in $(AgIn)_xZn_{2(1-x)}S_2$ QDs.

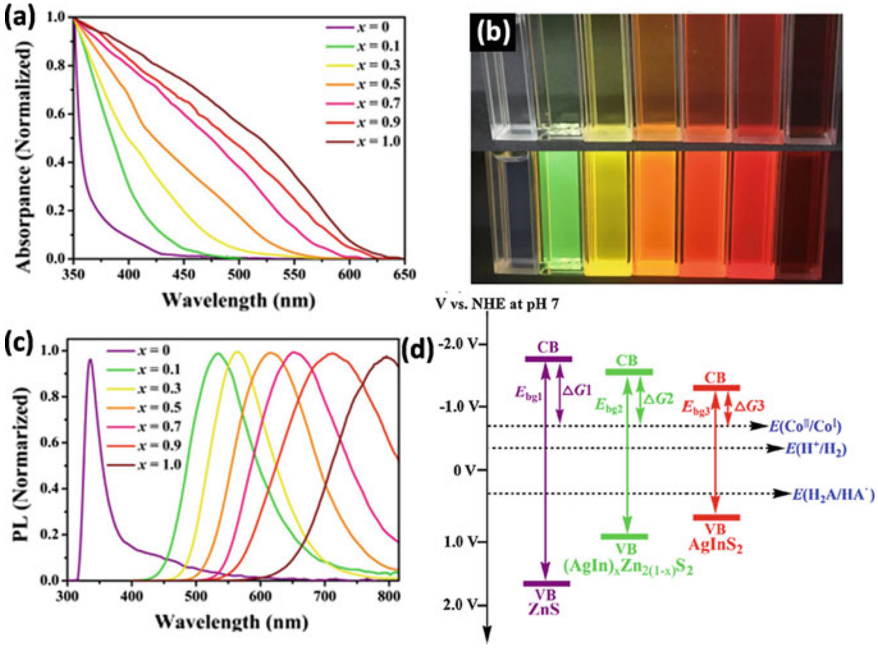

Fig. 23.3 **a** Absorption spectra of bare ZnS, bare $AgInS_2$ and $(AgIn)_xZn_{2(1-x)}S_2$ QDs in CH_2Cl_2 solution. **b** The photograph of as-prepared QDs under 365 nm UV light excitation in CH_2Cl_2 solution (5 mg ml^{-1}), from left to right: bare ZnS, $(AgIn)_xZn_{2(1-x)}S_2$ QDs, $x = 0.1, 0.3, 0.5, 0.7, 0.9$ and then bare $AgInS_2$. **c** The emission spectra of the synthesized QDs upon excitation at 350 nm, however ZnS at 280 nm. **d** Schematic presentation of calculated CB minima and VB maxima of bare ZnS, $(AgIn)_xZn_{2(1-x)}S_2$ composite QDs and bare $AgInS_2$. (Reproduced from Ref. [47] with permission from Elsevier 2017)

Thus, a balance between strong absorption contents and charge carrier separation for $(AgIn)_{0.5}ZnS_2$QDs leads to the higher photocatalytic H_2 generation.

23.4.3.2 1D Nanostructures

One-dimensional (1D) nanostructures such as nanowires, nanotubes, nanorods, nanofibers, and nanobelts have been played an integral role in the design and construction of photocatalytic applications [48]. 1D nanostructure showed distinct structural behavior with more chemical reactivity because of large surface to volume ratio and 1D confinement. In case of photocatalysis, 1D geometry is beneficial because of long distance fast electron transport and high length to diameter ratio which promote the light absorption and scattering properties [49]. Various nanostructures like nanoparticles, quantum dot, nanorods, nanosheets, hierarchical nanostructures of semiconductor have been developed and used in diverse fields such as optoelectronics, photovoltaic devices, and photocatalysis. For example, 1D TiO_2 nanostructures displayed higher photocatalytic and photoelectrocatalytic water splitting than that of bulk and nanomaterials due to large specific surface area which promote photogenerated charge carrier transfer along the axial direction [50]. However, 1D TiO_2 nanostructures have limitation in visible light absorption because of wideband gap of 3.2 eV, fast recombination of electron–hole pairs which lower the photocatalytic efficiency. Further, 1D semiconductor nanostructures like ZnO, Ta_3N_5, CdS, CdSe, Bi_2S_3, Ni_3S_2, InGaN, In_2S_3, Ag_2WO_4, Fe_2O_3, etc. have been developed which exhibited high efficiency in water oxidation/ reduction due to short charge transfer distance [50–53]. Interestingly, 1D core–shell-like structures have gained much more research interest due to their potential in solar to chemical energy conversion [54]. Thus, the fabrication of controlled diameter, length, crystallinity as well as the suitable band gap with band edge potentials of 1D nanostructures are challenging to gain maximum photocatalytic H_2 generation.

23.4.3.3 2D Nanostructures

Two-dimensional (2D) materials at nanoscale have fascinated consideration for photocatalytic applications due to their tunable thickness dependent physical and chemical properties such as high specific surface area, good crystallinity, facile functionalization, improved charge separation, and rich surface active sites. For example, Yu et al. [55] developed TiO_2 semiconductor with varied morphologies, such as nanoparticles, nanotubes and nanosheets and showed morphology dependent band gap change. The TEM images of three types of TiO_2 morphology are shown in Fig. 23.4a–c, where nanoparticles are of average diameter about ~ 15 nm, nanotubes are of diameter about ~ 8 nm with length hundreds of nanometers and nanosheets are of ~ 50 nm in size. The selected area electron diffraction pattern implies that all the synthesized nanostructures are highly crystalline (Inset of Fig. 23.4a–c).

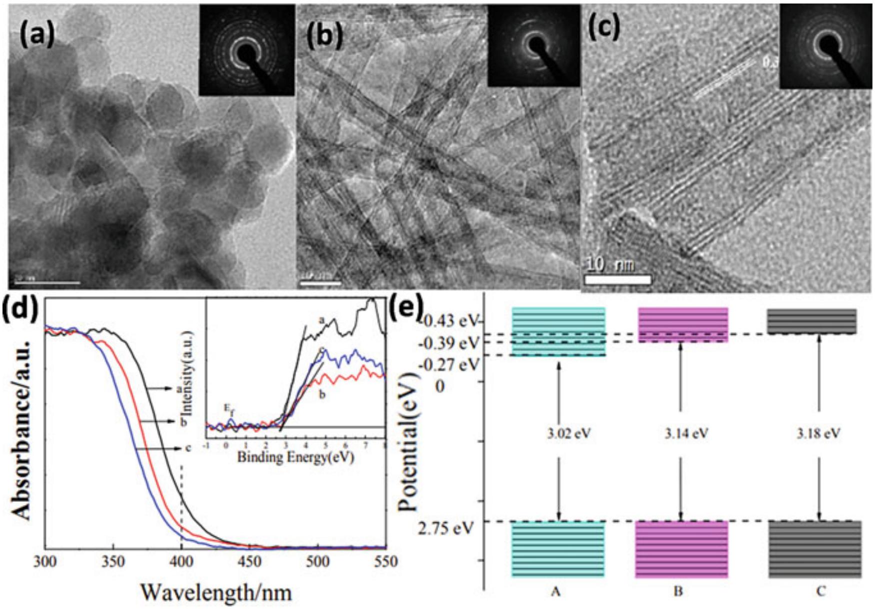

Fig. 23.4 TEM images of TiO_2 **a** nanoparticles, **b** nanotube and **c** nanosheets, Inset: SAED patterns of corresponding TEM images. **d** UV–Vis DRS spectra of TiO_2 nanostructures, Inset: Valance band XPS spectra. **e** Schematic presentation of the calculated band gap and band edge potentials of the TiO_2 nanostructures. (Reproduced from Ref. [55] permission from The Royal Society of Chemistry, 2014)

A morphology dependent blue shifting has been observed in absorption spectra and band gap changes from ~3.02 eV (for nanoparticles) to ~3.18 eV (for nanosheets). Further, the valence band maximum of TiO_2 nanostructures are calculated from the valance band XPS spectra which is ~2.75 eV. Therefore, the conduction band minimum for TiO_2 nanostructures is determined as −0.27 eV, −0.39 eV and −0.43 eV for nanoparticle, nanotube and nanosheets, respectively (Fig. 23.4e). Moreover, experimental results are well supported with the DFT calculations of energy states. Due to the quantum confinement effect, the band gap increases for which lifetime of the charge carriers has been prolonged.

The crystal phase engineering of 2D semiconductors is a potential way to improve the photocatalytic performance either by enhancing the absorption range or facile charge transfer and separation ability. For example, Lu and his co-workers [56] first reported TiO_2 nanosheets with 47% (001) facets which showed higher photoactivity under visible Light. In case of TiO_2, it has been widely recognized that the (101) facets are more reductive than (001) facets and the (001) face act as excited electron reservoir [57, 58]. Besides TiO_2, ultrathin CdS, graphene, g-C_3N_4, $BiVO_4$, WO_3, Bi_2WO_6, BiOX (X = Cl, Br, I), layered perovskites, layered double hydroxide, dichalcogenides like MoS_2, $MoSe_2$, $MoTe_2$, WS_2, WSe_2, MXenes like Zr_2C, Fe_2C, Ti_2N, Ti_3N_2, Ti_3CN, Ti_4C_3, Cr_2C and Zr_3C_2, hexagonal boron nitride,

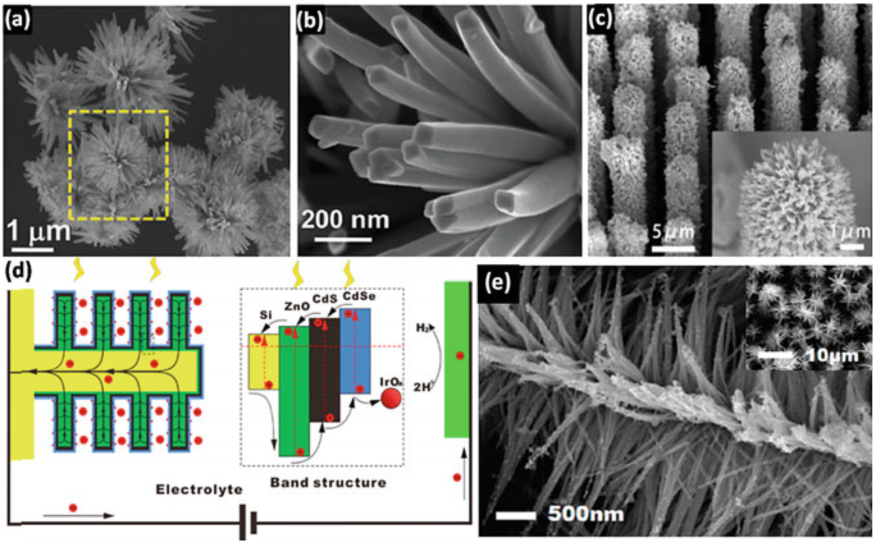

Fig. 23.5 FESEM images of Bi_2S_3 at **a** low and **b** high magnification. **c** SEM image of quantum dot-sensitized (CdS, CdSe and IrO_xQDs) hierarchical ZnO wires, Inset: high magnification SEM image. **d** Schematic of PEC water splitting along with charge generation, separation in a hierarchical nanostructure, Inset: the energy level distribution of the different components of hierarchical structure has been presented. **e** SEM image of the CdS, CdSe sensitized ZnO/WO3 array, Inset: top view of the material. (Reproduced from Refs. [61, 63] and [64] with permission from The Royal Society of Chemistry, The American Chemical Society, 2018, 2014 and 2011, respectively)

black phosphorus, etc. have been also developed successfully, which showed high photocatalytic H_2 generation under visible light compared to their bulk counterpart [59, 60].

23.4.3.4 Hierarchical Nanostructures

Recently, three dimensional (3D) hierarchical nanostructures which are assembled by nanorord, nanoplates or other type of nanoscale building blocks, are gaining much interest in the field of photocatalysis. Significant efforts have been made to develop advanced inorganic semiconductor-based 3D nanostructures due to interesting anisotropic properties, high surface area and more available catalytic active sites. The 3D hierarchical structures are also favorable for the charge separation and transfer to surface active sites. Metal sulfide like Bi_2S_3, $CuInS_2$, $ZnIn_2S_4$, Cu_3SnS_4, ZnS, etc. are very familiar to form 3D nanoflower like hierarchical structure and displayed superior photocatalytic H_2 generation through water reduction. For example, flower like 3D microstructure of Bi_2S_3 have been prepared by our group through a simple hydrothermal method using mercaptosuccinic acid as S-source

[61]. Figure 23.5a, b represents the low and high magnification Field Emission SEM(FESEM) images of flower like Bi_2S_3 microstructure, consists of 1D solid rods which are radiated from a common center and stacked uniformly to form a flower like morphology. Inorganic oxide-based semiconductors, such as TiO_2, ZnO, Bi_2WO_6, and Cu_2O also formed 3D hierarchical structure and showed enhanced activity for photoelectrochemical water splitting under solar light [62]. As example, Sheng et al. [63] develop ZnO nanowires array on silicon microwires by vapor–liquid-solid method and used as a photoanode for PEC water splitting. The hierarchical structure was further sensitized with CdS, CdSe and IrO_x quantum dots. The SEM image of the sensitized array structure has been shown in Fig. 23.5c, where hierarchical ZnO wires are fully covered by the layer of colloid QDs. They demonstrated that the tree-like structure promotes the photoelectrochemical reactions because of large surface area with proper contact of electrode and electrolyte. The schematic of charge separation and transfer has been presented in Fig. 23.5d, where the core–shell structure of ZnO nanowire branches may help in charge separation and collection, and the Si-nanowire used as the carrier transfer channel. As a result, 23-fold enhancement has been obtained for Si/ZnO hierarchical structure compared to pure ZnO nanowires and improves the stability of the as-prepared photoanode.

Similar kind of hierarchical structure has been reported by Kim et al. [64] for PEC H_2 generation. They fabricated branched 3D arrays of WO_3/ZnO via the epitaxial growth of the ZnO nanowires on the WO_3 nanorods, which exhibited dramatically increase light scattering capacity. The SEM image of the WO_3/ZnO arrays is represented in Fig. 23.5e, where it has been clearly shown that all of the ZnO nanowires are well covered and decorated on the WO_3 nanorods and formed a hierarchical structure. The top view of the WO_3/ZnO arrays has been shown in the inset of Fig. 23.5e, which displays a beautiful flower like structure of ZnO nanodiscs which are surround WO_3 nanorod from all directions. This branched structure increases the surface area for more light utilization, faster the charge transport through the brunches, which leads to enhancement in the photocurrent via PEC water splitting. In addition, the needle like ZnO structure reduce the charge recombination due to the availability of the large number of active sides and the nanorods decrease the external potential bias which is required for PEC water splitting by offering exposed polar facets compared to bare WO_3 nanorods. Consequently, five times higher power conversion efficiency has been achieved for hierarchical structure compared to bare WO_3 nanorods. It can be concluded that the 3D hierarchical morphology is suitable for high photocatalytic activity owing to large surface areas, the existence of mesopores and suitable band gap.

23.4.4 *Surface Engineering*

Beside the size, shape and composition of a semiconducting catalyst, surface has a great role in controlling the photocatalytic activity as the oxidation/reduction is mostly occurred on the surface of the catalyst. Thus, surface engineering is very crucial to obtain the highest performance of a photocatalyst. Moreover, surface modification would not change the crystal structure of catalyst and helps in improving the conductivity and stability of the semiconductor counterparts. Furthermore, the electronic properties can be regulated by the formation of intermediate state which may enhance the light harvesting activity. Thus, for photocatalytic or electrocatalytic water splitting to generate H_2 or O_2, surface engineering via modification or sensitization have attracted a great interest recently. For example, Coelho et al. [65] modify the surface of WO_3 thin film by the deposition of metallic Bi to developed dendritic $BiVO_4/WO_3$ heterostructure. Figure 23.6a shows the top view SEM image of $BiVO_4/WO_3$ photoanode. Interestingly, the band gap has been reduced to 2.45 eV from 2.78 eV after formation of $BiVO_4$ on the WO_3 surface (Fig. 23.6b). Very recently, A. Tofanello's group [66] reported that modification of the surface of the hematite photoanode by gold nanoparticles promote visible light absorption and enhance the PEC performance. They also investigated the changes of hematite surface with the concentration change of Au nanoparticles and demonstrated that the lower Au amount leads to a higher photocurrent response (1.20 mA cm^{-2}) at 1.23 Vs RHE. In presence of alkaline electrolyte, a hydrated/oxidized gold phase has been formed at the electrode/electrolyte interface for higher concentrations loading of Au nanoparticles on hematite, which may decrease the charge transfer efficiency. The PEC water splitting process and the limitation of high concentration of Au nanoparticle have been schematically presented in Fig. 23.6c. In presence of light illumination, the photogenerated electrons of Au nanoparticle directly transfer to the CB of hematite's surface and the photo-induced holes of semiconductor can be trapped at the Au—hematite interface. Although, some electrons of Au nanoparticles can be transferred to the electrolyte, which create an oxidized resistive surface around the nanoparticles and accelerates the charge recombination rate, thereby reduce the PEC activity. Therefore, suitable loading of metal nanoparticles is fruitful to enhance the catalytic activity of semiconductor photocatalysts. Similarly, the metal loading on the conjugated polymer or other carbon-based nanostructures enhances the photocatalytic activity as well as stability [67]. As example, gold-based multimetallic nanoalloys ($Au_{50}Pt_{24}Pd_{26}$/PPy) decorated polypyrrol (PPy) nanofibers showed enhanced light absorption under visible and near-IR region because of the surface plasmonic effect of Au. Moreover, the alloy formation with Pd or Pt may increase the active sites for catalysis which results in almost six-fold enhanced H_2 generation rate compared to pure PPy [68]. Therefore, it can be concluded that surface modification has a very crucial role in improving the photocatalytic activity as well as stability of the catalyst.

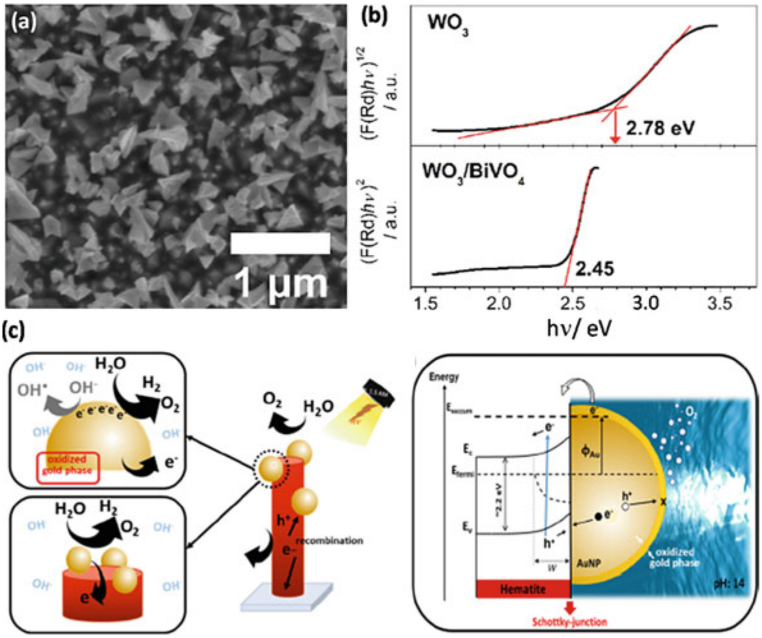

Fig. 23.6 **a** Top view SEM image of metallic Bi modified WO_3 photoanode. **b** The Tauc plot of pure WO_3 and $WO_3/BiVO_4$ photoanodes. **c** Schematic representation of the Au decorated hematite electrode and 1 M NaOH electrolyte interface during the PEC reactions and the band diagram at the Schottky junction. (Reproduced from Refs. [65] and [66] with permission from Elsevier and The Royal Society of Chemistry, 2020)

23.4.5 Heterostructure Formation

Heterostructure architecture between two semiconductors can reduce the charge diffusion length and the fast recombination rate and improve the overall photocatalytic efficiency by separating the charge carriers and transfer to the redox reaction center. In addition, an internal electric field created at the interface between two semiconductors when equilibrium of Fermi levels happened which resulted in band bending and promote the charge separation ability, thus leading improved photocatalytic and PEC activity toward H_2 generation. The formation of heterostructure further changes the electronic properties of the semiconductors via changing the effective band gap and band edge potentials. Therefore, development of heterostructures has been regarded as most effective way to enhance the electron–hole pair separation as well as make a balance between light absorption and redox reactions. Conventionally, type-II heterostructures are considered as efficient system for photocatalytic water splitting because of suitable band alignments. For example, Khan et al. [20] fabricated conventional type-II heterostructures between graphitic carbon nitrides (g-C_3N_4) and Nb_2O_5, which effectively lower the bandgap

(2.82 eV) compared to bare Nb_2O_5 (3.25 eV) with substantial redshift and enhancement in visible light absorption (Fig 23.7a). Further, Mott − Schottky analysis confirms a significant shifting of flat band potential toward lower hydrogen evolution reaction. As a result, three-fold enhancement in PEC photocurrent has been achieved for g-C_3N_4/Nb_2O_5 heterojunctions (−0.17 mA/cm^{-1} at a potential 1.0 V vs RHE) compared to bare oxide. The photocatalytic water splitting mechanism has been presented in Fig 23.7b. Due to the large band gap (3.25 eV), Nb_2O_5 is unable to generate excited electron and holes under visible light. Thus, photoexcited electrons from the CB of g-C_3N_4 may transfer to the CB of Nb_2O_5 via interface of the heterojunction, which further take part in water reduction to generate H_2. The effective charge separation in Type-II configuration suppresses the fast recombination rate and significantly enhances the PEC efficiency. However, due to the charge transfer to the lower potential, the redox ability of the electrons may reduce in Type-II heterostructures. Thus, an advanced type photocatalytic system is needed which can satisfy both the requirements of fast charge separation and strong thermodynamic driving force for oxidation/reduction simultaneously.

Recently, significant attention has been paid to develop Z-scheme architecture due to unique electronic band alignments which can meets the aforesaid requirements of high redox potentials with effective charge separation. However, liquid phase and all-solid-state Z-scheme systems have some limitations, including long term stability and availability of redox mediator, cost-effectiveness, energy loss due to backward reaction. Therefore, development of direct Z-scheme system has been attracted recent research focus, where no electron mediator is required for charge transfer. Moreover, lower energy electrons and holes are directly recombine with each other through the junction interface to make free the higher energetic electrons and holes for oxidation/reduction reactions. In this way, the effective band gap of the system also tuned to harness more solar light under visible region. For example, Zou et al. [69] fabricated direct Z-scheme CdS/$BiVO_4$ heterostructures, where ~20 nm CdS nanoparticles are homogeneously deposited on the $BiVO_4$ nanosheets (Fig. 23.8a).

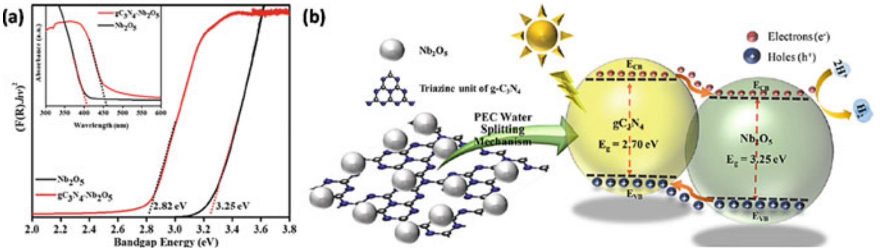

Fig. 23.7 **a** Tauc's plots of g-C_3N_4 and g-C_3N_4/Nb_2O_5 Type-II heterostructures from UV−Vis DRS spectra, Inset: DRS spectra of the synthesized materials. **b** Proposed Type-II charge transfer mechanism over g-C_3N_4/Nb_2O_5 heterostructures for PEC water splitting. (Reproduced from Ref. [20] with permission from The American Chemical Society, 2019)

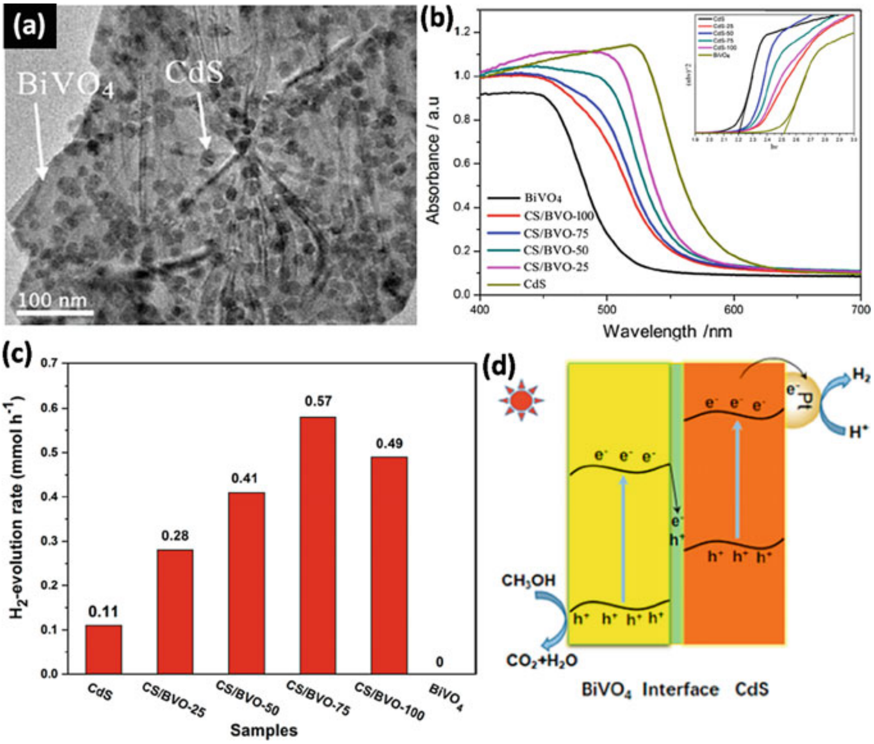

Fig. 23.8 **a** TEM image of CdS/BiVO$_4$ heterostructure. **b** UV–Vis DRS spectra of bare CdS, bare BiVO$_4$ and the CdS/BiVO$_4$ with different loading concentration of CdS. **c** The comparison of photocatalytic H$_2$ generation under visible light. **d** The schematic band alignment and direct Z-scheme charge transfer mechanism for CdS/BiVO$_4$ heterostructures. (Reproduced from Ref. [69] with permission from The American Chemical Society, 2019)

The formation of Z-scheme heterostructure promotes the visible light absorption compared to bare BiVO$_4$ (Fig. 23.8b). Notably, the bang gaps of the heterostructures change with the loading of more CdS on the BiVO$_4$. The H$_2$ generation rate has been enhanced with the increase of CdS loading and CSBVO-75 exhibits highest rate of ~0.57 mmol h^{-1} which is almost 5.2 times of pure CdS (Fig. 23.8c). However, H$_2$ generation rate decreases further loading of CdS because of agglomeration. A direct Z-scheme charge transfer mechanism has been proposed to demonstrate the higher photocatalytic activity of CdS/BiVO$_4$ heterostructures as shown in Fig. 23.8d. Under the visible light, both CdS and BiVO$_4$ can generate electron–hole pairs due to the band gaps <3 eV. The photoexcited electrons of CdS may transfer to the co-catalyst Pt and react with the adsorbed H$^+$ ions to form H$_2$. At the same time, the photo-induced holes of BiVO$_4$ would be engaged in oxidation of methanol. Now, the CB electrons of BiVO$_4$ and the VB holes of CdS could not occur reduction or oxidation of water molecules because of insufficient potentials. Meanwhile, an Ohmic contact is formed at the CdS/BiVO$_4$ which can act as electron mediator. Thus, effective charge separations as well as suitable potential for the redox reactions have been achieved by this direct Z-scheme system. However, stability remains an issue for the Cd-based heterostructures. Therefore, more attention has been paid on development of Cd-free heterostructures, such as Bi-based, TiO_2-based, and ferrite-based with other semiconductor or carbon structures.

23.5 Conclusion and Future Prospect

Semiconductor-based heterostructures have been widely used to enhance the light absorption range, charge separation ability and catalytic activity for H_2 generation, PEC water splitting, etc. However, the quantum efficiency of the conventional heterostructures is not satisfactory for large scale applications. Thus, various types of engineering have been deliberated to overcome the limitations of single semiconductors, such as poor light absorption ability, low active sites and stability. In this chapter, band gap engineering of heterostructures has been thoroughly discussed via atomic doping, alloying, and hybridization, structural and morphological modification. Further, the effect of band gap engineering for visible light-driven photocatalytic H_2 generation has been summarized. The tunable band structure can be achieved by structural engineering method which can effectively promote the photoexcited charge separation, reduce the undesirable recombination rate, accelerates the redox ability of excited electrons and holes with prolong lifetime. Moreover, surface engineering benefits the availability of active sites with large surface to volume ratio, which is critical for achieving the high photocatalytic efficiency. However, the comprehensive thermodynamics and kinetics of charge transfer at the interface of heterostructures are not clear. So, future efforts should be focused on understanding of photocatalytic mechanisms at fundamental level. At the same time, the characterization techniques for charge separations and transfer have to be explored in future. Moreover, the effect of band bending and position of the apparent Fermi level at the junction interface as well as electrode–electrolyte interface is not properly considered during explaining the proposed mechanism. Thus, there are lots of challenges and scopes to explore the band gap engineering and its effect in photocatalytic water splitting.

Acknowledgements One of the authors (SB) is thankful to the Department of Science & Technology (DST), India, for providing the INSPIRE fellowship award.

References

1. Abe R (2010) Recent progress on photocatalytic and photoelectrochemical water splitting under visible light irradiation. J Photochem Photobio C Photochem Rev 11:179–209
2. Takanabe K (2017) Photocatalytic water splitting: quantitative approaches toward photocatalyst by design. ACS Catal 7:8006–8022
3. Ahmad H et al (2015) Hydrogen from photo-catalytic water splitting process: a review. Renew Suss Energy Rev 43:599–610
4. Jian J et al (2018) Recent advances in rational engineering of multinary semiconductors for photoelectrochemical hydrogen generation. Nano Energy 51:457–480
5. Wang Z et al (2019) Recent developments in heterogeneous photocatalysts for solar-driven overall water splitting. Chem Soc Rev 7:2109–2125
6. Ghosh S (ed) (2018) Visible-Light-Active photocatalysis: nanostructured catalyst design, mechanisms and applications. Wiley-VCH VerlagGmbh & Co. KGaA, April, 2018, pp 227–252. ISBN: 978–3–527–34293–8
7. Li X et al (2015) Engineering heterogeneous semiconductors for solar water splitting. J Mater Chem A 3:2485–2534
8. Ghosh S (ed) (2020) Heterostructured photocatalysts for solar energy conversion. Elsevier Inc., 1 Oct 2020. ISBN: 97801282007281
9. Qu Y et al (2013) Challenge and perspective of heterogeneous photocatalysts. Chem Soc Rev 42:2568–2580
10. Afroz K et al (2018) A heterojunction strategy to improve the visible light sensitive water splitting performance of photocatalytic materials. J Mater Chem A 6:21696–21718
11. Wang Y et al (2018) Synergistic effect of charge generation and separation in epitaxially grown $BiOCl/Bi_2S_3$ nano-heterostructure. ACS Appl Mater Interfaces 10:15304–15313
12. Basu M et al (2017) Ag_2S/Ag heterostructure: a promising electrocatalyst for hydrogen evolution reaction. Langmuir 33:3178–3186
13. Bera S et al (2019) Photocatalytic hydrogen generation using gold decorated $BiFeO_3$ heterostructures as an efficient catalyst under visible light irradiation. Sol Energy Mater Sol Cells 194:195–206
14. PeiL et al (2019) Schottky junction effect enhanced plasmonic photocatalysis by TaON@Ni NP heterostructures. Chem Commun 55:11754–11757
15. Xiao JD et al (2017) Integration of plasmonic effects and schottky junctions into metal-organic framework composites: steering charge flow for enhanced visible-light photocatalysis. Angew Chem Int Ed 57:1103–1107
16. Bai S et al (2016) Surface and interface design in cocatalysts for photocatalytic water splitting and CO_2 reduction. RSC Adv 6:57446–57463
17. Wang Z et al (2019) Recent developments in heterogeneous photocatalysts for solar-driven overall water splitting. Chem Soc Rev 48:2109–2125
18. Wang Y et al (2013) Visible light driven type II heterostructures and their enhanced photocatalysis properties: a review. Nanoscale 5:8326–8339
19. Jeon D et al (2018) WO_3/conducting polymer heterojunction photoanodes for efficient and stable photoelectrochemical water splitting. ACS Appl Mater Interfaces 10:8036–8044
20. Khan I et al (2019) Graphitic carbon nitride impregnated niobium oxide ($g\text{-}C_3N_4/Nb_2O_5$) type (II) heterojunctions and its synergetic solar-driven hydrogen generation. ACS Appl Energy Mater 2:607–615
21. Bard AJ (1979) Photoelectrochemistry and heterogeneous photo-catalysis at semiconductors. J Photochem 10:59–75
22. Li H et al (2016) Z-scheme photocatalytic systems for promoting photocatalytic performance: recent progress and future challenges. Adv Sci 3:1500389–1500401
23. Zhou P et al (2014) All-solid-state Z-scheme photocatalytic systems. AdvMater 26:4920–4935

24. Bera S et al (2020) Silver as solid-state electron mediator in MoS_2/Ag–$AgVO_3$ Z-Scheme heterostructures for photocatalytic H_2 generation. J Alloys Compd 830(25):154527–154539
25. Nowotny J et al (2015) Defect chemistry and defect engineering ofTiO_2-based semiconductors for solar energy conversion. Chem Soc Rev 44:8424–8442
26. Bai S et al (2018) Defect engineering in photocatalytic materials. Nano Energy 53:296–336
27. Zhou W, Fu H (2018) Defect-mediated electron−hole separation in semiconductor photocatalysis. Inorg Chem Front 5:1240–1254
28. Wang X et al (2016) Topological defects in liquid crystals as templates for molecular self-assembly. Nat Mater 15:106–112
29. Pala RS, Metiu H (2007) The structure and energy of oxygen vacancy formation in clean and doped, very thin films of ZnO. J Phys Chem C 111:12715–12722
30. Huang H et al (2020) Subsurface defect engineering in single-unit-cell Bi_2WO_6 monolayers boosts solar-driven photocatalytic performance. ACS Catal 10:1439–1443
31. Ruan L et al (2019) Surface defect-controlled growth and high photocatalytic H_2 production efficiency of anatase TiO_2 nanosheets. ACS Appl Mater Interface 11:37256–37262
32. Suzuki T et al (2012) A titanium-based oxysulfide photocatalyst: $La_5Ti_2MS_5O_7$ (M = Ag, Cu) for water reduction and oxidation. Phys Chem Chem Phys 14:15475–15481
33. Ishikawa A et al (2002) Oxysulfide $Sm_2Ti_2S_2O_5$ as a stable photocatalyst for water oxidation and reduction under visible light irradiation ($\lambda \leq 650$ nm). J Am Chem Soc 124:13547–13553
34. Maeda K et al (2006) Photocatalyst releasing hydrogen from water. Nature 440:295
35. Higashi M et al (2013) Fabrication of an efficient $BaTaO_2N$ photoanode harvesting a wide range of visible light for water splitting. J Am Chem Soc 135:10238–10241
36. Zhang F et al (2012) Cobalt-modified porous single-crystalline $LaTiO_2N$ for highly efficient water oxidation under visible light. J Am Chem Soc 134:8348–8351
37. Joshi UA et al (2010) Semiconducting oxides to facilitate the conversion of solar energy to chemical fuels. J Phys Chem Lett 1:2719–2726
38. Hill JC et al (2013) Synthesis, photoelectrochemical properties, and first principles study of n-type $CuW_{1\text{-}x}Mo_xO_4$ electrodes showing enhanced visible light absorption. Energy Environ Sci 6:2440–2446
39. Li Q et al (2013) $Zn_{1-x}Cd_xS$ solid solutions with controlled bandgap and enhanced visible-light photocatalytic H_2-production activity. ACS Catal 3:882–889
40. Wu K, Lian T (2016) Quantum confined colloidal nanorod heterostructures for solar-to-fuel conversion. Chem Soc Rev 45:3781–3810
41. Martindale BCM et al (2015) Solar hydrogen production using carbon quantum dots and a molecular nickel catalyst. J Am Chem Soc 137:6018–6025
42. Das A et al (2015) A cobalt-dithiolene complex for the photocatalytic and electrocatalytic reduction of protons. ACS Catal 5:1397–1406
43. Cheng L et al (2018) CdS-Based photocatalysts. Energy Environ Sci 11:1362–1391
44. Yuan YJ et al (2018) Cadmium sulfide-based nanomaterials for photocatalytic hydrogen production. J Mater Chem A 6:11606–11630
45. Kershaw SV et al (2013) Narrow bandgap colloidal metal chalcogenide quantum dots: synthetic methods, heterostructures, assemblies, electronic and infrared optical properties. Chem Soc Rev 42:3033–3087
46. Yue S et al (2019) Metal chalcogenide quantum dot-sensitized 1D-based semiconducting heterostructures for optical-related applications. Energy Environ Sci 12:1454–1494
47. Yuan YJ et al (2017) Bandgap engineering of $(AgIn)_xZn_{2(1-x)}S_2$ quantum dot photosensitizers for photocatalytic H_2 generation. Appl Catal B 204:58–66
48. Xiao FX et al (2015) One-dimensional hybrid nanostructures for heterogeneous photocatalysis and photoelectrocatalysis. Small 11:1–17
49. Weng B et al (2014) One-dimensional nanostructure based materials for versatile photocatalytic applications. RSC Adv 4:12685–12700
50. Ge M et al (2016) A review of one-dimensional TiO_2 nanostructured materials for environmental and energy applications. J Mater Chem A 4:6772–6801

51. Khanchandani S et al (2013) Band gap tuning of ZnO/In_2S_3 core/shell nanorod arrays for enhanced visible-light-driven photocatalysis. J Phys Chem C 117:5558–5567
52. Lin Z et al (2015) Electronic reconstruction of α-Ag_2WO_4 nanorods for visible-light photocatalysis. ACS Nano 9:7256–7265
53. Pradhan GK et al (2013) Fabrication of α-Fe_2O_3 Nanorod/RGO composite: a novel hybrid photocatalyst for phenol degradation. ACS Appl Mater Interfaces 5:9101–9110
54. Mondal K, Sharma A (2016) Recent advances in the synthesis and application of photocatalytic metal–metal oxide core–shell nanoparticles for environmental remediation and their recycling process. RSC Adv 6:83589–83612
55. Yu Y et al (2014) The design of TiO_2 nanostructure (nanoparticle, nanotube and nanosheet) and their photocatalytic activity. J Phys Chem C 118:12727–12733
56. Yang HG et al (2008) Anatase TiO_2 single crystals with a large percentage of reactive facets. Nature 453:638–641
57. Pan J et al (2011) On the true photoreactivity order of {001}, {010}, and {101} facets of anatase TiO_2 crystals. Angew Chem Int Ed 50:2133–2137
58. Yu J et al (2014) Enhanced photocatalytic CO_2-reduction activity of anatase TiO_2 by coexposed {001} and {101} facets. J Am Chem Soc 136:8839–8842
59. Lu Q et al (2016) 2D transition-metal-dichalcogenide-nanosheet-based composites for photocatalytic and electrocatalytic hydrogen evolution reactions. Adv Mater 28:1917–1933
60. Khan AH et al (2017) Two-dimensional (2D) nanomaterials towards electrochemical nanoarchitectonics in energy-related applications. Bull Chem Soc Jpn 90:627–648
61. Bera S et al (2018) Fabrication of Bi_2S_3/ZnO heterostructures: an excellent photocatalyst for visible-light-driven hydrogen generation and photoelectrochemical properties. New J Chem 42:541–554
62. Li G et al (2019) Facile synthesis of oriented feather-like TiO_2 bundle catalysts for efficient photocatalytic water splitting. Cryst Growth Des 19:3584–3591
63. Sheng W et al (2014) Quantum dot-sensitized hierarchical micro/nanowire architecture for photoelectrochemical water splitting. ACS Nano 8:7163–7169
64. KimH et al (2011) Highly efficient photoelectrochemical hydrogen generation using hierarchical ZnO/WO_x nanowires cosensitized with CdSe/CdS. J Phys Chem C 115:25429–25436
65. Coelho D et al (2020) Bi electrodeposition on WO_3 photoanode to improve the photoactivity of the WO_3/$BiVO_4$ heterostructure to water splitting. Chem Eng J 399:125836
66. Tofanello A et al (2020) Hematite surface modification toward efficient sunlight-driven water splitting activity: the role of gold nanoparticle addition. J Phys Chem C 124:6171–6179
67. Ghosh S et al (2020) Enhanced solar hydrogen generation using Cu-Cu_2O integrated polypyrrole nanofibers as heterostructured catalysts. Int J Hydrog Energy 45:6159–6173
68. Ghosh S et al (2019) Functionalized conjugated polymer with plasmonic Au nanoalloy for photocatalytic hydrogen generation under visible-NIR. Int J Hydrog Energy 44:13262–13272
69. Zou L et al (2017) High efficient photodegradation and photocatalytic hydrogen production of CdS/$BiVO_4$ heterostructure through Z-scheme process. ACS Sustain Chem Eng 5:303–309

Chapter 24
Novel Solid Photocatalysts for Hydrogen Generation from Aqueous Phases

Eike S. Welter and Roger Gläser

Abstract A sustainable economy requires technologies and materials for conversion and storage of renewable energy, ideally from sunlight. Photocatalytic hydrogen production offers an attractive solution for the transformation of sunlight into chemical energy and, thus, the simultaneous energy storage in the form of hydrogen. The efficiency of photocatalytic hydrogen production not only depends on technological factors but on the choice of suitable photocatalysts. In this chapter, key aspects of materials used as solid photocatalysts for hydrogen evolution from aqueous phases including metal oxides, metal sulfides, and carbon-based semiconductors, are treated. With respect to the multitude of existing principles for the enhancement of the photocatalytic material properties, the specific manipulation, and introduction of defects as well as the combination of semiconductors to form Z-schemes is discussed. Finally, an overview of the mechanisms and reaction pathways of hydrogen formation by heterogeneous photocatalysis, both for photoreforming of organic substrates and water splitting, is given.

Keywords Solar energy · Hydrogen evolution · Water splitting · Heterogeneous photocatalysis · Semiconductor photocatalysts · Defect engineering · Z-scheme · Aqueous phase

24.1 Introduction and Scope

Hydrogen is considered a promising (carbon-free) energy carrier to satisfy the ever-growing energy demand of the world. Simultaneously it could help replace the use of conventional fossil fuels for the energy generation and transportation. Furthermore, in view of concepts to avoid the use of fossil resources for carbon–neutral synthesis of chemicals, it could be utilized together with CO_2 and N_2 as a feedstock to obtain the vast majority of the currently used chemicals in a renewable

---

E. S. Welter · R. Gläser (✉)
Universität Leipzig, Leipzig, Germany
e-mail: roger.glaeser@uni-leipzig.de

S. Garg and A. Chandra (eds.), *Green Photocatalytic Semiconductors*,
Green Chemistry and Sustainable Technology,
https://doi.org/10.1007/978-3-030-77371-7_24

way. For hydrogen to be truly sustainable, it needs to be produced from environmentally friendly sources like water, biomass, or other organic compounds from renewable sources. Today a handful of different approaches exist, to supply H_2 directly from water or aqueous organic solutions as a feedstock. These can be divided, according to the form of energy input, into thermal, electrical, biochemical, and photonic hydrogen production.

Since neither water, nor most of the organic compounds used for the purpose of hydrogen production directly interact with radiation in the infrared, visible or near ultraviolet region to a sufficient degree, typically the use of a photocatalyst is required. Both homogenous and heterogeneous photocatalysts are studied to an extensive degree. However, in this book chapter, only solid semiconductors for purely photocatalytic hydrogen formation in form of particulate suspension reaction systems are discussed. Also, photoelectrocatalytic systems, which are often linked to photocatalytic systems, are not covered, as these are part of another Chap. 22.

Despite the fact, that a multitude of semiconductors exists that are capable of the hydrogen evolution from both water and aqueous solutions containing organic compounds, the observed activities fall behind the expectations of technical application. That is especially the case for semiconductors utilized without additional modifications or extensions to enhance the photocatalytic activity. By now a great number of modifications has been developed ranging from doping with different cations (Chaps. 9 and 11), formation of composites (Chaps. 4, 5, 6 and 8), loading with sensitizers (Chap. 11) or co-catalysts to crystal facet and defect engineering (Chap. 12). Along with these, a multitude of different working principles exist, which include the extension of the light absorption (Chaps. 9 and 10), the improvement of charge carrier transportation and recombination, as well as the introduction of new active sites.

In the present Chapter, the main focus is placed on the use of defect-modified photocatalysts as well as direct Z-scheme photocatalysts from the material classes of metal oxides, metal sulfides, and carbon-based semiconductors, mainly in the form of graphitic carbon nitride (g-C_3N_4), for purely photocatalytic hydrogen production from aqueous phases. The chapter is divided into three sections. In the first section, key properties of photocatalytic active materials are briefly presented, with a focus on the electronic properties and charge carrier processes (trapping, recombination, interfacial charge transfer). In the following section, the two selected design strategies for the enhancement of the activity, i.e., defect engineering and Z-scheme construction, are presented. First, defect engineering is treated with respect to the classification of defects, their synthesis, and the implications for photocatalytic conversions. This is followed by Z-scheme construction, starting with an overview of the different types and developments of Z-scheme systems. Then, direct Z-schemes are discussed in more detail with focus on the advantages and the role of the interface. The section is finished by looking into the role of defects and the most recent developments in the field of Z-scheme photocatalysts. The final part of the Chapter deals with the formation of hydrogen from aqueous phases. In this section, first, the two basic forms of hydrogen generation, i.e., photoreforming using sacrificial agents (SAs) and overall water splitting, are introduced. Then, the mechanism of overall water splitting and the performance of solid photocatalysts presented in section two in this reaction are dealt with. This is followed by a discussion of the available types of sacrificial agents for hydrogen generation from aqueous phases, with a focus on alcohols and biomass-derived molecules. For the decomposition of pollutants from aqueous phase, which can also be applied for hydrogen production, the reader is referred to another Chap. 21. The section concludes by comparing the performance of the different design strategies for the enhancement of hydrogen generation by photoreforming.

24.2 Key Aspects of Photocatalytically Active Materials

The materials applied in heterogeneous photocatalysis depend on a variety of properties. Since the basic principles and most important material properties have already been discussed in detail in introductory chapters, only selected material characteristics with particular relevance for the further topics of this chapter will be discussed here. The focus of this section is on the electronic properties, the importance of which becomes clear, when looking at the processes occurring during a photocatalytic reaction. The typical steps of a photocatalytic reaction over a solid semiconductor are displayed in Fig. 24.1 together with the superordinate processes described below. In short, light is absorbed in a first step, and an exciton (electron–hole pair) is generated. This exciton is separated, and the individual charge carriers are transferred to the semiconductor-co-catalyst interface or to the semiconductor-solution interface, where the chemical reaction takes place. According to Takanabe [1] a photocatalytic reaction can be divided into six superordinate processes:

1 Photon absorption,
2 Exciton separation,
3 Carrier diffusion,
4 Carrier transportation,
5 Catalytic efficiency,
6 Mass transfer of reactants.

The steps one to four mainly depend on the electronic properties of the semiconductor. Also in step five, the electronic properties in form of the exchange current density and charge transfer resistance partially govern the process. Evidently, the electronic processes such as excitation, exciton separation, and charge carrier transfer in the semiconductor and at interfaces precede the classical mass transfer processes of reactants. As a consequence charge transfer processes are major limitations for the photocatalytic activity of a given material [2]. However, a photocatalyst is only highly active if all the processes displayed above occur at a high rate.

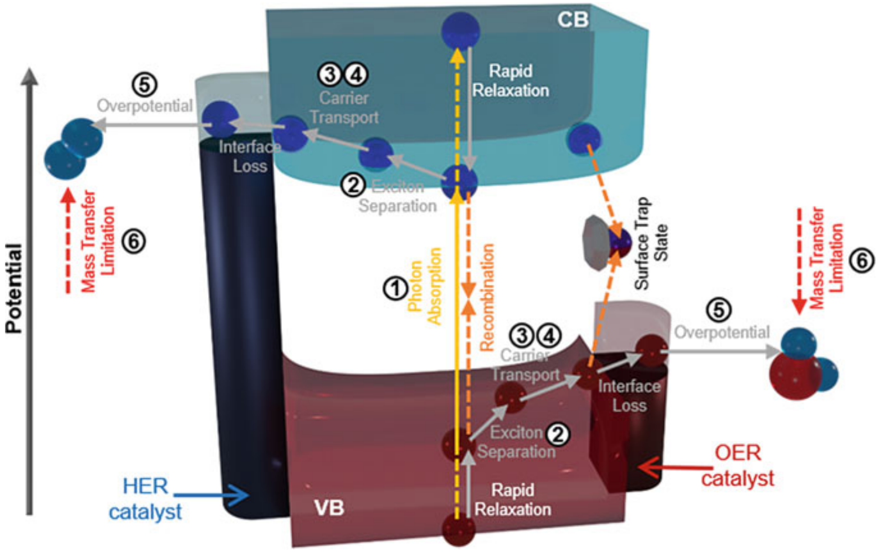

Fig. 24.1 Schematic display of the processes occurring during heterogeneous photocatalysis over a semiconductor. The assigned numbers refer to the superordinate processes, which are given in the text according to [2, 3]

Among the many ways to modify a solid photocatalyst towards specific processes and properties to enhance the efficiency of energy utilization within the semiconductor, the first and most apparent is the elemental composition of the material. The periodic table of the elements shown in Fig. 24.2 visualizes the roles of different elements, and how they can be used to construct the electronic structure of a semiconductor. Typically, elements from groups 15 to 17 are used as a foundation for the valence band (VB) with the main contribution being the p-orbitals. The groups four to six and 12 to 14 are primarily used for the electronic structure of the conduction band (CB) with either d^0- or d^{10}-configuration. Other elements like the alkaline, earth alkaline, and many of the lanthanides typically do not contribute directly to the band structure of the semiconductor, but are important in composing the crystal structure of non-binary metal oxides and metal sulfides which in return directly influences the band structure and band edge positions [4, 5]. Furthermore, many elements throughout the periodic table are used as dopants to modify the electronic structure or co-catalysts to enhance the charge transfer and separation. However, for these aspects the reader may refer to Chaps. 9 and 11.

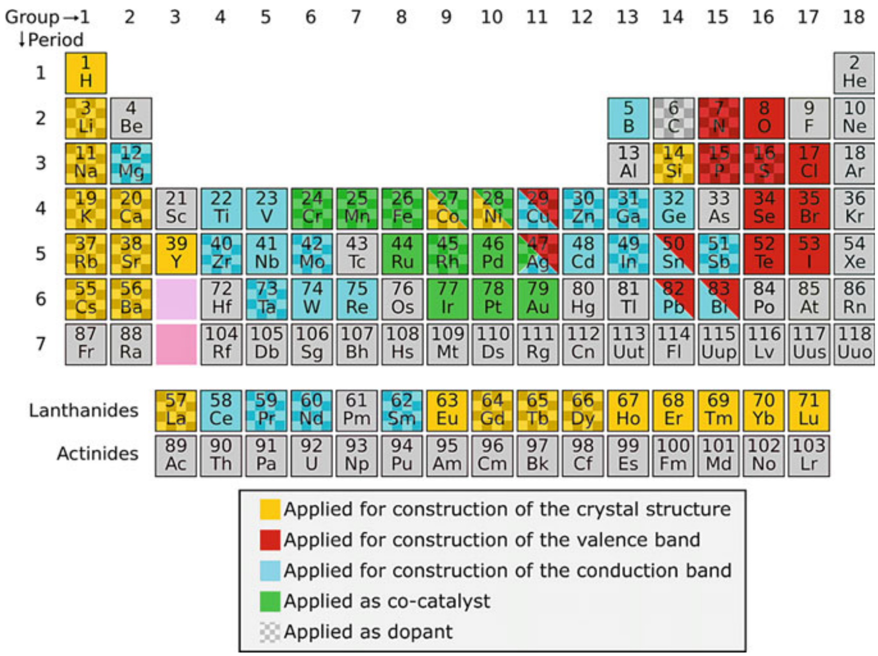

Fig. 24.2 Elements used in the construction of photocatalysts with application for photocatalytic water splitting and their respective purpose according to [6] and [4]

24.2.1 The Impact of the Electronic Structure

The electronic structure of a given semiconductor originates from the interactions of the orbitals of the different atoms in the semiconductor and the periodic arrangement in the given crystal structure. The resulting electronic energy bands, the sum of which corresponds to the electronic structure, are typically determined using a combination of different experimental techniques [7] and the calculation with different theories and approximations. The electronic structure of a semiconductor is therefore often referred to as the electronic band structure, which is the basis for the categorization into metal, semiconductor, and insulator. In this respect, semiconductors have their highest occupied band completely filled and the energy distance to the next band can be overcome by thermal excitation of electrons (band gap < 5 eV).

The band structure has implications for several material properties when used in photocatalytic reactions. Above all, the energetic position of the band edges of VB and CB determines the thermodynamic driving force of the charge carriers for a given reaction. Figure 24.3 shows the band edge positions for several different semiconductors in comparison to the redox potentials needed for the hydrogen evolution reaction (HER) and the oxygen evolution reaction (OER). It becomes clear, that without any adjustments or modifications of the semiconductors not all of them are capable to carry out both reactions. For example, the reductive potential of the CB of α-Fe_2O_3, WO_3, $BiVO_4$, Ag_3PO_4 or BiOI is too low with respect to the redox potential needed for H_2 formation from water at pH = 0. On the other side, the oxidative potential of the VB of CuO, $CuFe_2O_4$ or $CuInS_2$ is not suitable to catalyze the OER and form O_2 from H_2O [8]. However, as will be pointed out in later sections (Sects. 24.4.1.2 and 24.4.2.4) these kinds of materials can, through modifications, still be applied for photocatalytic hydrogen generation.

Furthermore, the mobility of the charge carriers in a semiconductor is dependent on the band structure. The charge carrier mobility and the effective mass of the charge carrier are inversely proportional to each other, meaning a high effective mass leads to a small charge carrier mobility and vice versa. Since the effective mass of the charge carrier depends, according to the effective mass theory, on the curvature of the bands, also the charge carrier mobility is directly related to the band curvature. Narrow or flat bands (energy wise) have a small curvature and thus a low carrier mobility (high effective mass), while wide or disperse bands have a stronger curvature and thus a high carrier mobility (low effective mass). This can also be seen as the result of stronger interactions of adjacent orbitals in the more dispersed bands [10]. Typically, a high charge carrier mobility is beneficial for photocatalytic reactions, as this results in a higher diffusion length of charge carriers before they recombine. For example, α-Fe_2O_3 has a charge carrier mobility of $\sim$0.1 $cm^2\ V^{-1}\ s^{-1}$ and a charge carrier diffusion length of $\sim$4 nm, while WO_3 has a charge carrier mobility of up to 10 $cm^2\ V^{-1}\ s^{-1}$ resulting in a diffusion length of up to 700 nm. However, this generalization is not valid for all systems. For instance, $BiVO_4$ has a charge carrier mobility of $\sim$0.2 $cm^2\ V^{-1}$ s similar to that of α-Fe_2O_3, but a diffusion length of 70 nm due to the higher charge carrier lifetime [11]. Table 24.1 gives an overview of the range of charge carrier mobility, lifetime, and diffusion length in some selected semiconductors to illustrate typical ranges of these properties in semiconductors relevant for hydrogen generation.

In addition, light absorption is largely governed by the electronic structure. The band gap, resulting from the distance of VB and CB position, determines the part of the light spectrum that can be absorbed by a semiconductor. Figure 24.3 includes the band gap energies for a set of different semiconductors that are used in photocatalysis. As a result of the band gap energy the wide band gap semiconductors (>3.0 eV) in Fig. 24.3a are either not capable at all to absorb visible light or can only utilize a minor part of the visible spectrum. This is typical for metal oxides containing only metal cations in electron configuration d^0 (Ti^4, V^{5+}, Zr^{5+}, Nb^{5+}, Ta^{5+}, W^{6+}) or d^{10} (Zn^{2+}, In^{3+}, Ga^{3+}, Sn^{4+}, Sb^{5+}), because, in this case, the VB is merely formed by the O 2p orbitals positioned around +3 eV against NHE [10]. In the case of semiconductors consisting of multiple different cations or anions, other orbitals come into play and the contributions become more complex [5]. Figure 24.4 illustrates the effect of the band gap for the utilization of solar light, based on the AM 1.5G solar spectrum [42]. It becomes clear, that with a band gap of 3.2 eV, which is typical for the most widely applied photocatalyst TiO_2 (anatase), less than 2.6% of the introduced energy can be utilized at best to generate charge carriers for the photocatalytic reaction.

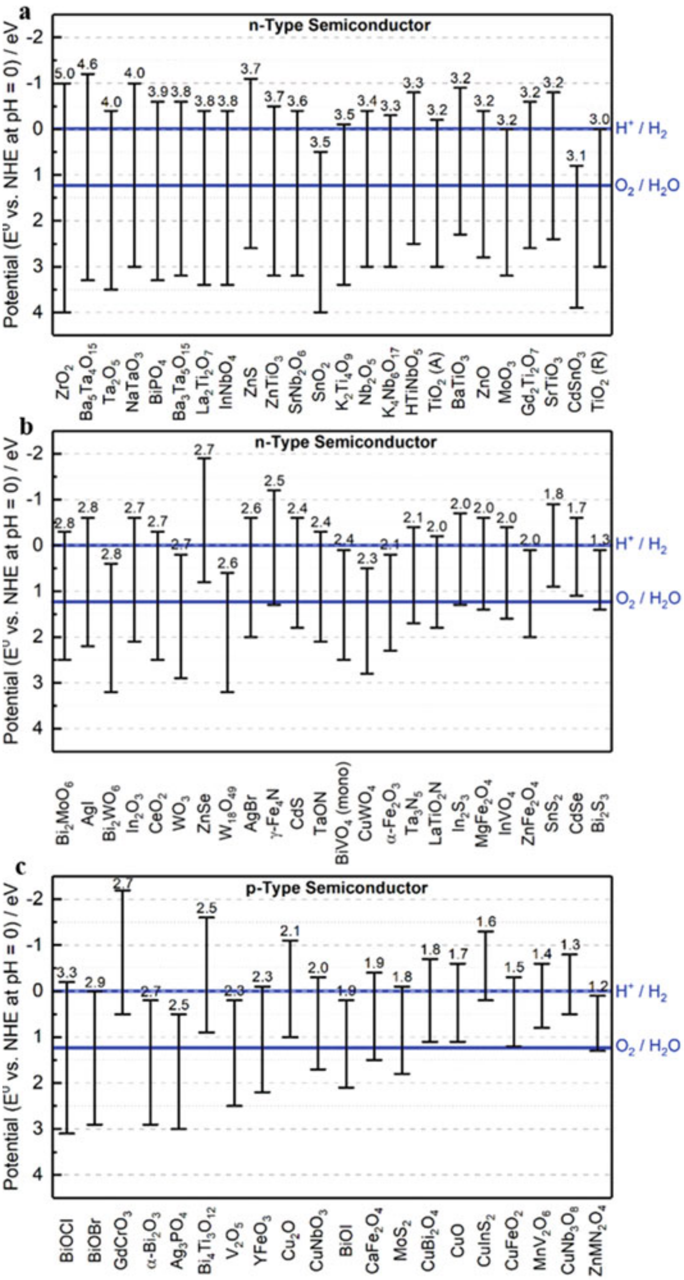

Fig. 24.3 Band gap values and band edge positions of **a** wide band gap ($E_g > 3.0$ eV) n-type; **b** narrow band gap ($E_g < 3.0$ eV) n-type and **c** p-type semiconductors used as photocatalysts, according to [6, 9]

Table 24.1 Charge carrier mobility (μ), lifetime (τ), and diffusion length of selected semiconductors

Semiconductor	μ/cm^2 V^{-1} s^{-1}	τ/ns	Diffusion length/nm
Ta_2O_5	0.00001 [12]	–	–
TaON	0.01 [12]	1.83 ns [13]	–
α-Fe_2O_3	0.01–0.1 [14, 15]	0.36–4.3 ps [16]	2–4 [17]
Ta_3N_5	0.1–4.4 [12, 18]	3.1–8.7 ps [18]	–
$BiVO_4$	0.04–0.2 [11, 19]	40 ns [11]	70–147 [11, 20]
TiO_2 (rutile)	0.5 [21]	24–28 ns [22, 23]	100 [23]
$SrTiO_3$	1–8 [24]	50 ns [25]	300–600 [26]
WO_3	3–10 [27, 28]	1.62 ns [29]	530–700 [20]
TiO_2 (anatase)	17 [30]	1000 ns [23]	10,000 [23]
ZnS	80–160 [31]	18 ns [32]	–
CdS	15–265 [33, 34]	3.6 ns [35]	60–440 [36]
ZnO	111–440 [37, 38]	2.8 ns [32, 39]	200–438 [40, 41]

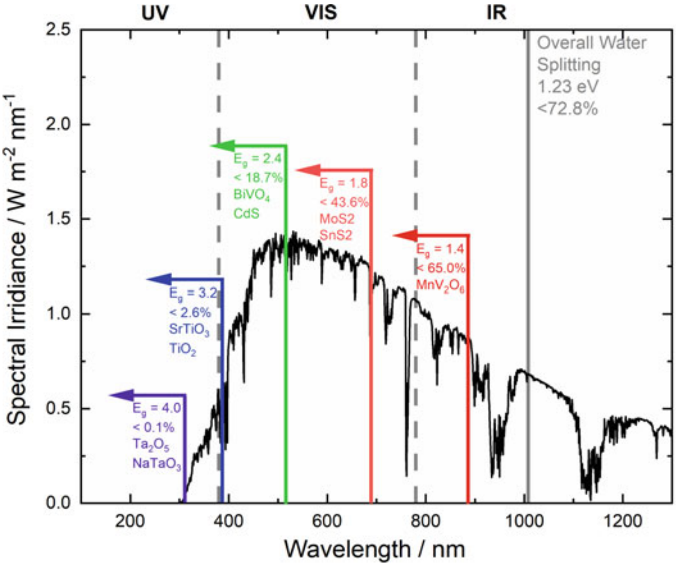

Fig. 24.4 AM 1.5G solar spectrum based on the SMARTS2 model [42]. The vertical lines indicate the band gap position of selected semiconductors used in photocatalysis to visualize the usable part of the solar spectrum for a given semiconductor in dependence of the band gap

Likewise, the mode of light absorption is defined by the position of VB maximum and CB minimum. If these two positions have the same k-value (crystal momentum), meaning they are directly above each other in the electronic band structure diagram, the band gap is considered as “direct”. In the other case, when the position of VB maximum and CB minimum are not aligned, the semiconductor has an “indirect” band gap [43]. This fact has implications on both light absorption and charge carrier recombination. In an indirect band gap, the transition from VB to CB and vice versa requires the change of crystal momentum, which cannot be provided by a photon itself. Therefore, either a phonon or a defect has to participate in these processes, making them less likely to occur. This also causes light to penetrate deeper into the semiconductor before it is absorbed. In turn, the charge carriers have to travel a longer distance through the semiconductor, eventually not being able to reach the external surface.

24.2.2 The Fate of Charge Carriers

After the initial generation of charge carriers through excitation with light, their fate depends on the competition between several reactions. To understand the efficiency and limitations of semiconductor photocatalysts as well as the mechanisms behind semiconductor photocatalysis, it is essential to consider these fundamental reactions. As these phenomena occur on a timescale of femto- to microseconds, the work that has been done so far in the investigation of particulate semiconductors is in large parts limited to TiO_2.

Figure 24.5 shows the timescale of the reactions that follow charge carrier excitation in TiO_2 starting from trapping at shallow and deep trapping sites and the recombination of charge carriers in different positions to the interfacial charge transfer. The process of charge carrier recombination competes on two different timescales with the other two processes. Initially, on the timescale of pico- to nanoseconds trapping and recombination compete against each other. This is followed by the competition of the interfacial charge transfer of the initially trapped charge carriers and the recombination, in range of nano- to microseconds.

The relationships discussed here can in most parts be applied to other semiconducting materials, although it should be noted that the exact nature of the reaction states and the equilibrium of the individual reactions can differ from that for TiO_2 as shown in several studies, e.g., for g-C_3N_4 [44], $BiVO_4$ [45–47], Fe_2O_3 [48].

24.2.2.1 Recombination

The recombination of charge carriers is mainly responsible for poor energy utilization. For example, in TiO_2 typically only 10% of the generated charge carriers are utilized for the redox reaction, while the rest is lost to recombination processes. Recombination can be categorized into three types, which are visualized in Fig. 24.6. An extensive description of the processes can be found in [51].

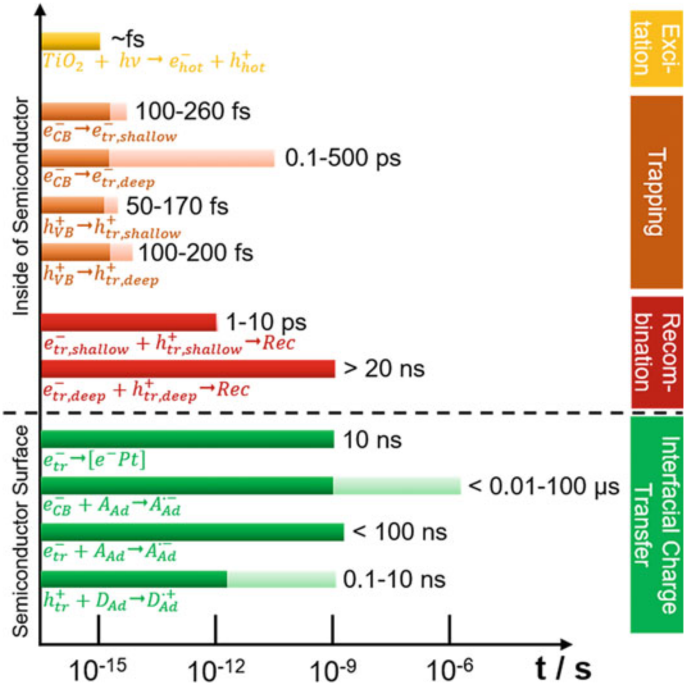

Fig. 24.5 Time scale of photoinduced processes in TiO_2 according to [49, 50]

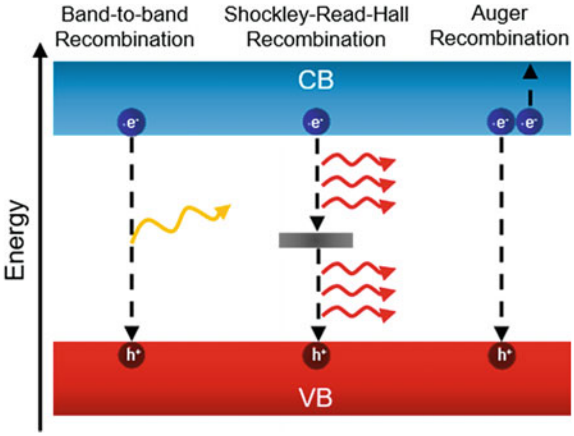

Fig. 24.6 Illustration of charge carrier recombination types in semiconductor materials

- Band-to-band recombination
- Auger recombination [52]
- Shockley–Read–Hall recombination [53, 54].

Band-to-band recombination occurs when an electron in the CB falls back into an empty state (hole) in the VB. This transition is usually a radiative process and dominating in direct band gap semiconductors (see Sect. 24.2.1), while in indirect band gap semiconductors, the necessary participation of a phonon makes this type of recombination negligible. Similarly, the Auger recombination requires the participation of a third particle (electron or hole), thus making it only likely to occur in semiconductors with a high charge carrier density. In contrast to the other types of recombination the Shockley–Read–Hall recombination occurs only in the presence of defect levels (both in the bulk and on the surface) and is, therefore, most important in heavily defective semiconductors. It can be envisioned in two ways, either as the annihilation of electron and hole that meet at the defect state or as the stepwise transition of the electron to a trap state followed by the transition into the VB.

24.2.2.2 Trapping

Trapping describes the (partial) localization of charge carriers in a semiconductor at disordered or defective positions in the semiconductor framework (for the different defect types see Sect. 24.3.1.1). A visualization of this charge carrier localization is given in Fig. 24.7. The corresponding positions are called trap states and can be divided into shallow and deep trap states. The shallow traps are energetically close to the characteristic energy of CB (electrons) or VB (holes), while the energetic position of the deep traps differs much more than the thermal energy of electrons and holes (~26 meV at 300 K) from CB and VB [55].

Fig. 24.7 Illustration of the energetic effect of defects (trap states) on the charge carrier localization according to [56]

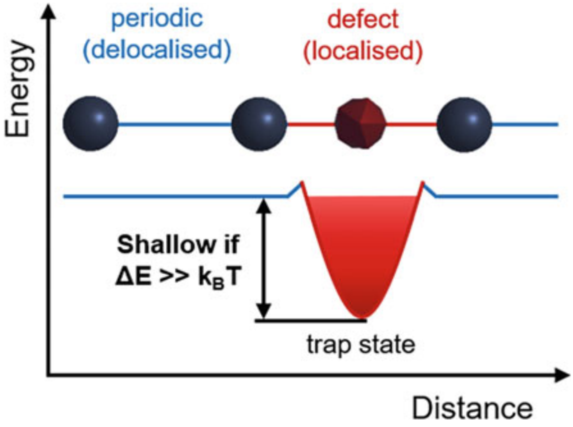

For TiO_2 different groups were experimentally identified which can act as trap states or correspond to the trapped charge carriers, using techniques like transient absorption spectroscopy or electron paramagnetic resonance spectroscopy. The holes are most likely trapped close to the surface at bridging O^{2-} or OH^- groups at the surface, while the electrons are trapped at Ti^{3+} both at the surface and in the bulk [49].

Similar to TiO_2, trapping of holes in hydroxyl groups close to the surface was reported for ZnO [57]. In g-C_3N_4 heteroatoms and dangling bonds act as shallow traps, while interstitial atoms and vacancies act as deep traps [44]. For $BiVO_4$ the presence of shallow and deep traps has been reported, even though no specific groups or structures were identified so far [45, 58]. Generally, the existence of certain trap states is material and even crystal phase-dependent, thus, materials need to be studied individually [59]. However, it should be noted that typically the presence of crystal defects and lattice imperfections is responsible for the presence of trap states.

As already discussed in Sect. 24.2.2.1, charge carrier trapping influences recombination, as it allows the Shockley–Read–Hall recombination mode. Besides, charge carrier trapping also has an impact on charge carrier migration, lifetime, and reactivity. The former is affected, as trapped charge carriers cannot move freely through the semiconductor. In case of deep trap states, the charge carriers tend to stay in the trapped position. However, in shallow traps, two possible migration mechanisms are known. Either the trapped charge carriers are excited by thermal energy or light back into the band and become free charge carriers again or they move from trap to trap state, which is called polaronic hopping [60]. The impact on the charge carrier migration can also be expressed as the change of the carrier mobility of the free charge carriers without trapping (μ_0) corrected for the fraction of the average time (τ) they spent in the trapped or free state, as expressed in Eq. (24.1). The result is the effective charge carrier mobility (μ_{eff}) [56].

$$\mu_{\text{eff}} = \mu_0 \left(\frac{\tau(\text{free})}{\tau(\text{free}) + \tau(\text{trap})} \right) \tag{24.1}$$

Even though the charge carrier mobility might be reduced due to trapping, the lifetime is drastically increased by several orders of magnitude compared to free charge carriers in VB and CB (micro- to milliseconds for trapped electrons vs. pico- to nanoseconds for free electrons) (see Fig. 24.5). Directly connected to the charge carrier lifetime, trapping can also affect the reactivity of charge carriers, as charge carriers trapped close to the surface are more likely to participate in the subsequent redox reactions. Due to the increased lifetime, the trapped charge carriers might even facilitate reactions that require the participation of multiple charge carriers at once, like in water oxidation [61, 62]. However, deeply trapped charge carriers are considered to be lost for the reaction, thus reducing the photocatalytic activity [49, 55]. Therefore, in general, active photocatalysts require a high density of shallow traps, while the density of deep traps is kept to a minimum.

24.2.2.3 Interfacial Charge Transfer

The behavior of the interfacial charge transfer is related to the interactions of the components involved at the interface. The components that have to be considered in photocatalysis depend on the composition of the photocatalyst and the reaction to be investigated and can range from metals and semiconductors to various molecules [63, 64] and even cells. This concept is therefore of special importance for sensitizers (Chap. 11), any form of junctions (Chaps. 6 and 11) and surface interactions. Since interface engineering is already covered in the previous chapter, interfacial charge transfer for semiconductor–semiconductor junctions is only briefly discussed here. Furthermore, charge transfer processes connected to reactions involved in photocatalytic hydrogen evolution are discussed in Sect. 24.4.

Since the most relevant semiconductor–semiconductor interactions to facilitate charge transfer are of either type-II or direct Z-scheme, the focus will be put on these two. As can be seen from Fig. 24.8, the main difference between type-II heterojunction and direct Z-scheme is the band bending that occurs upon contact of the semiconductor interfaces. This band bending is the result of the difference in the chemical potential of semiconductor one and two and leads to the formation of an in-built electric field, which is the driving force for the interfacial charge transfer. In both cases, this also results in the spatial separation of charge carriers [65]. However, the band bending in a type-II heterojunction causes both CBs of semiconductor one and two as well as the VBs to be closer in terms of their energetic potential, leading to the migration of charge carriers to the respective band with the lower potential. This results in a lower reduction and oxidation potential that can be utilized for the reaction. In contrast, in a Z-Scheme the charge carriers in the band with the higher potential stay, while the electrons in the semiconductor with the lower CB and the holes in the semiconductor with the higher VB migrate to recombine and prevent photodegradation. The advantage of this charge transfer is that the higher redox potential of both semiconductors can be utilized. However, in this process, half of the charge carriers are lost to recombination. It should be mentioned, that the charge transfer in a Z-scheme can also be facilitated by metals [66] through the formation of as a Schottky junction that acts a channel for the electrons, or trap states [67] in between the bands of both semiconductors that allow for a trap assisted charge carrier transfer.

24.3 Design Strategies to Enhance Photocatalytic Activity for Hydrogen Generation

The previous section has highlighted the implications of selected properties for photocatalytic reactions. Often a given semiconductor has disadvantages in certain areas, like the light absorption or redox potential. However, through modifications, these drawbacks might be overcome and, thus, the photocatalytic activity can be

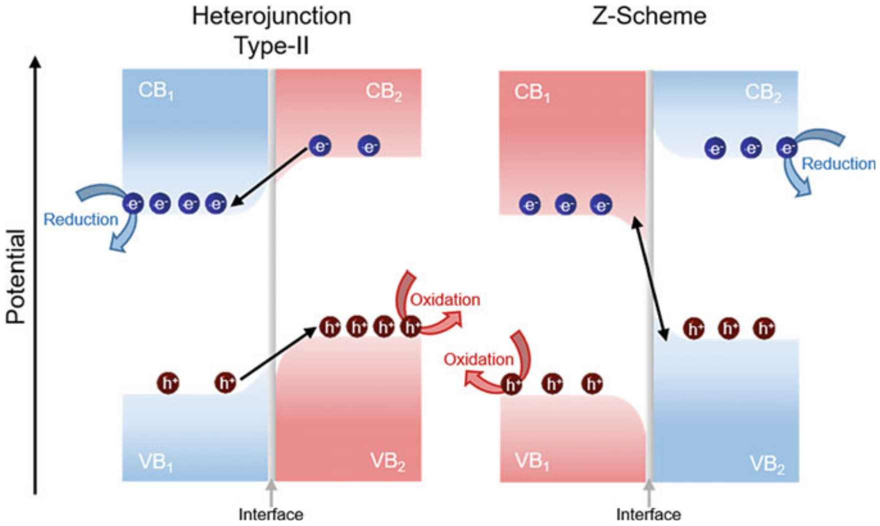

Fig. 24.8 Schematic energy diagram of type-II heterojunctions (left) and Z-schemes (right) during band alignment. The black arrows indicate the direction of charge carrier transportation from one semiconductor to another

improved. In this respect, a multitude of strategies exists that can be utilized to enhance the photocatalytic activity ranging from changes in the material composition and construction of heterostructures to the control of particle morphologies and crystal facets. The first part of this section will be limited to the design strategy of defect introduction with a focus on point defects. The second part deals with the well-known construction of Z-schemes in its newest form as direct Z-schemes.

24.3.1 Defect Engineering

Defects are the imperfections within crystalline solids, that interrupt the periodic arrangement of a crystal structure. For a long time, defects were considered to be only detrimental to photocatalytic reactions. This is because defects can act as trap states and increase the charge carrier recombination. Additionally, defects lead to scattering of charge carriers and thus reduce the charge carrier mobility. Eventually, the positive effects of defects on photocatalytic reactions were recognized leading to the development of controlled defect introduction into photocatalysts and the investigation of the operating principle and more profound mechanisms of the involvement of defects in photocatalysis [68]. In this respect, a multitude of different types of defects exist, which will be introduced in the following section. The more detailed discussion will be focused on the most frequently reported point defects. An overview of common methods of defect generation will be given and the influence on aspects of photocatalytic processes like light absorption, electronic properties, and surface interactions will be discussed.

24.3.1.1 Classification of Defect Types

Defects in crystals can be divided according to their dimensionality and structure, to their position in the material, or whether they are of intrinsic or extrinsic nature [68–70]. For the former, four different types can be distinguished, with further sub-division into particular types, which are listed in the following:

- 0D: Point defects (vacancy, interstitial, doping),
- 1D: Line defects (screw dislocation, edge dislocation),
- 2D: Planar defects (grain boundary, twin boundary),
- 3D: Volume defects (lattice disorder, void).

These types can also be sorted according to their position, which is of importance to the actual effect a defect will have in a photocatalyst, as we will see in Sect. 24.3.1.5. Point (0D) and volume (3D) defects can both exist at the external surface or in the bulk, while line (1D) and planar (2D) defects tend to originate in the bulk, but terminate at the surface, thus they can also be considered surface defects. For an illustration, the different types of defects are visualized in Fig. 24.9.

For the formal description of defects, the widely known Kröger-Vink valence notation is frequently used, which is helpful to specify the exact framework position and nature of a defect. However, this notation is only useful for point-defects and requires the knowledge of the position and relative charge of the defect [72].

The defect types have different origins. Point defects result from the replacement, insertion, or removal of atoms in the framework and are often accompanied by the change of the material stoichiometry. Line defects result from a plastic deformation of the crystal lattice, while planar defects are caused by stacking or antiphase boundaries corresponding to a full inversion of the atom arrangement in the framework. Both line and planar defects do not cause a change in the material composition. Volume defects are the result of a clustering of multiple defects and are typically accompanied by the presence of point defects [68, 73]. Furthermore, multiple defect types can co-exist in a single material.

In addition, special types of defects exist, like Frenkel- or Schottky-defects. However, as the defects in photocatalysts are generally not further investigated regarding these special defect-types, a detailed discussion of these defects will not be provided here. For further information on this matter, the interested reader is referred to textbooks on the chemistry of solids, e.g., Refs. [74, 75].

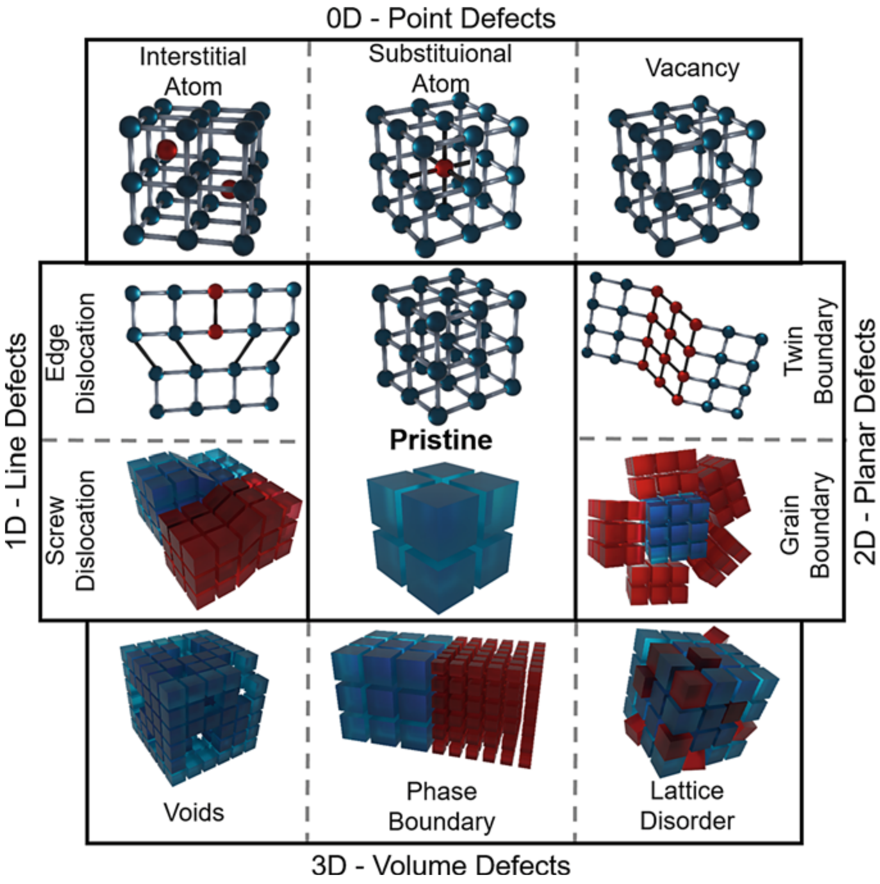

Fig. 24.9 Schematic overview of defect types according to [70, 71]

24.3.1.2 Synthesis Approaches for Defect Introduction

To understand and effectively utilize defects, methods are necessary to introduce them in a controlled fashion into solid photocatalysts. By now a vast number of different synthesis routes have been developed, which are summarized in Fig. 24.10. Additionally, Table 24.2 gives an overview of the resulting defects and their role in photocatalytic hydrogen evolution. The influence of the synthesis route on the resulting defects and their properties has been reviewed by Yang et al. [76] for black TiO_2. This review points out that the influence of the synthesis route itself and the experimental parameters applied are often neglected and, thus, can be hardly understood. However, a quantitative approach regarding defect concentration and distribution, which is so far often missing, might be helpful to compare defective materials and to understand the impact of defects in more depth.

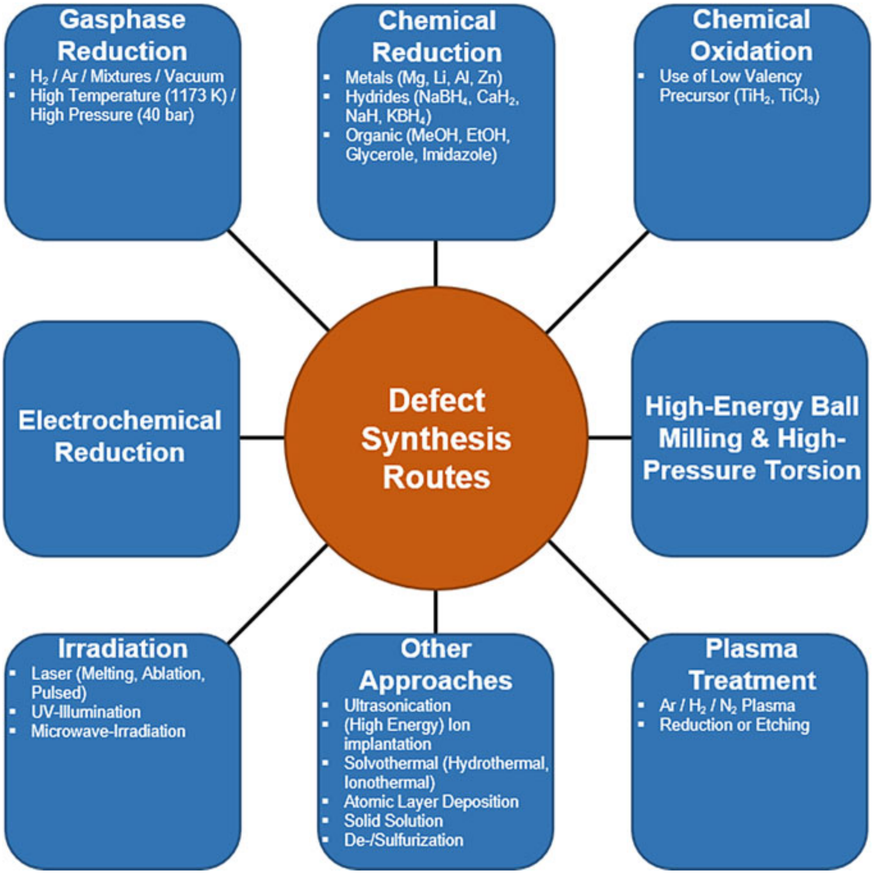

Fig. 24.10 Schematic overview of typical synthesis routes for the introduction of defects into semiconductors

The synthesis routes can be divided according to their nature into chemical and physical methods or whether the defects are introduced during the synthesis of the material or as a post-treatment step. The main difference is that the post-treatment typically leads to a preferential defect introduction at or close to the surface. The different synthesis approaches have been summarized and described in several reviews. In this respect, the reviews of Bai et al. [68], which gives insight by which synthesis routes certain defects can be obtained, and that of Su et al. [72], who focus on TiO_2 and black TiO_2, but give a broad overview of the present synthesis routes in the field, should be highlighted.

Table 24.2 Synthesis methods for defect engineering, resulting defects and their location, operating principle in enhancing the photocatalytic activity, and the reaction conditions for photoreforming or overall water splitting with the resulting hydrogen evolution

Material	Co-catalyst	Synthesis approach	Defect/ Location	Role of defect	H_2 evolution rate/mmol g^{-1} h^{-1}	Reaction conditions	Refs.
Bi_3O_4Br	Pt (1.0 wt.-%)	Surfactant assisted self-assembly	Bi-vacancy, O-vacancy	Light absorption (mid gap level, CB shift), charge transfer and separation	0.380	50 mg catalyst, 50 mL CH_3OH (10 vol.-%), 300 W Xe lamp	[77]
BiOCl	None	Hydrothermal synthesis	O-vacancy, low valence Bi/surface and sub-surface	Active site, charge transfer and separation, light absorption	Water splitting 8.4 μmol in 24 h (0.035 mmol h^{-1} g^{-1})[a)]	10 mg catalyst, 100 mL H_2O, 500 W Xe lamp	[78]
Black TiO_2	Pt (0.5 wt.-%)	Chemical reduction (Al) + high-temperature Ar-treatment	O-vacancy, Ti^{3+}, lattice disorder/ sub-surface or bulk	Light absorption, charge transfer	6.4—UV 0.140—Vis	100 mg catalyst, 120 mL CH_3OH (25 vol.-%), UV—300 W Hg lamp, Vis—AM 1.5G	[79]
Black TiO_2	Pt (1 wt.-%)	High-temperature H_2 treatment	Low valence Ti	Light absorption (VB shift)	0.136 mmol h^{-1} (1.36)[a]	100 mg catalyst, 100 mL CH_3OH (20 vol.-%), AM 1.5G (100 mW cm^{-2})	[80]
Black TiO_2	None	High-temperature H_2 treatment	O-vacancy, Ti^{3+}, lattice disorder	Light absorption, charge separation and transportation and trapping	0.133	20 mg catalyst, 40 ml CH_3OH (25 vol.-%), 300 W Xe lamp ($\lambda > 420$ nm)	[81]
Black TiO_2	Pt (2 wt.-%)	High-temperature H_2 treatment	O-vacancy, Ti^{3+}/surface	Light absorption (mid-gap states),	6.5	100 mg catalyst, 100 mL CH_3OH (20	[82]

(continued)

Table 24.2 (continued)

Material	Co-catalyst	Synthesis approach	Defect/ Location	Role of defect	H_2 evolution rate/mmol g^{-1} h^{-1}	Reaction conditions	Refs.
				carrier separation and recombination supression		vol.-%), AM 1.5G (100 mW cm^{-2})	
Black TiO_2	Pt (1 wt.-%)	High pressure H_2 treatment	Ti^{3+}, lattice disorder, surface	Light absorption	3.94	500 mg catalyst, 200 mL CH_3OH (20 vol.-%), 300 W Xe lamp	[83]
Black TiO_2	Pt (0.5 wt.-%)	High-temperature H_2 treatment	Ti^{3+}, lattice disorder/ surface and bulk	Light absorption, carrier separation and transportation	3.30[a]	50 mg catalyst, 100 mL CH_3OH (20 vol.-%), AM 1.5G (100 mW cm^{-2})	[84]
Black TiO_2	Pt (1 wt.-%)	Chemical reduction (Mg) + gasphase reduction (Ar)	Ti^{3+}, O-vacancy/ surface	Light absorption (VB and CB tail), suppression of recombination	43.2—UV 0.440—Vis	10 mg, 50 mL CH_3OH (20 vol.-%), 400 W Xe lamp (IR filter) and visible light filter ($\lambda = 400$–780 nm)	[85]
Black TiO_2	Pt (0.5 wt.-%)	H_2-Plasma treatment	O-vacancy, Ti^{3+}, lattice disorder/ surface	Light absorption (mid-gap states), carrier density, suppression of recombination	8.2	100 mg catalyst, 120 mL CH_3OH (25 vol.-%), AM 1.5G	[86]
Black TiO_2	Pt (1.0 wt.-%)	Chemical reduction ($NaBH_4$) + gasphase reduction (Ar)	O-vacancy, Ti^{3+}/surface	Light absorption, carrier density and separation	UV—6.5 Vis—0.18 (UV—325 μmol h^{-1}) (Vis 9 μmol h^{-1})	50 mg catalyst, 120 mL CH_3OH (25 vol.-%), 300 W Xe lamp ($\lambda > 400$ nm)	[87]

(continued)

Table 24.2 (continued)

Material	Co-catalyst	Synthesis approach	Defect/ Location	Role of defect	H_2 evolution rate/mmol g^{-1} h^{-1}	Reaction conditions	Refs.
				and transportation			
Black TiO_2	Pt (1 wt.-%)	Chemical oxidation ($TiCl_3$) and Zn reduction	O-vacancy, Ti^{3+}/bulk	Light absorption	UV—6[a] Vis—0.08[a] (UV—0.6 mmol h^{-1}) (Vis—8 μmol h^{-1})	100 mg catalyst, 120 mL CH_3OH (30 vol.-%), 300 W Xe lamp without and with filter ($\lambda > 420$ nm)	[88]
Black TiO_2	Pt (1 wt.%)	Chemical reduction ($NaBH_4$) + Ar-treatment	O-vacancy, Ti^{3+}, lattice disorder, surface	Light absorption	7.02	50 mg catalyst, 100 mL CH_3OH (20 vol.-%), 350 W Xe lamp (λ = 350–750 nm)	[89]
Black TiO_2	None	High energy proton implantation	Ti^{3+}, lattice disorder surface and sub-surface	Active sites	15 μL h^{-1} cm^{-2} (0.336 mmol h^{-1} cm^{-2})[a)]	2 mg catalyst, 10 ml CH_3OH (50 vol.-%), AM 1.5G (100 mW cm^{-2})	[90]
Black TiO_2	Pt (0.6 wt.-%)	High pressure hydrogenation	Lattice disorder/ surface	Light absorption (CB tail, mid-gap states)	10 (0.1 Vis only)	20 mg catalyst, CH_3OH (50 vol.-%), AM 1.5G (1 sun)	[91]
$CaTiO_3$	Pt (1 wt.-%)	Pt-assisted hydrogenation	O-vacancy/ surface	Light absorption (VB tail), active site	2.296 mmol g^{-1} h^{-1}	20 mg catalyst, 100 mL CH_3OH (50 vol.-%) AM 1.5G	[92]
g-C_3N_4	Pt (1.0 wt.-%)	Alkaline treatment	N-vacancy	Light absorption (CB shift), charge carrier separation	6.9	10 mg catalyst, 30 mL lactic acid (25 vol.-%), 300 W Xe lamp ($\lambda > 420$ nm)	[93]

(continued)

Table 24.2 (continued)

Material	Co-catalyst	Synthesis approach	Defect/ Location	Role of defect	H_2 evolution rate/mmol g^{-1} h^{-1}	Reaction conditions	Refs.
g-C_3N_4	Pt (6 wt.-%)	High-temperature Ar-treatment	Lattice disorder	Light absorption (VB and CB tail), suppression of recombination	157.9 μmol h^{-1} (3.158)[a]	50 mg catalyst, 300 mL triethanolamine (10 vol.-%), 300 W Xe lamp (λ > 440 nm)	[94]
$K_4Nb_6O_{17}$	None	Chemical reduction (KBH_4)	O-vacancy	Charge separation and trapping	1.661	10 mg catalyst, 200 ml CH_3OH (20 vol.-%), 300 W Xe lamp	[95]
CdS@ g-C_3N_4	None	Hydrothermal treatment + high-temperature Ar-treatment	S-vacancy	Light absorption (red shift), charge separation	19.88	30 mg catalyst, 60 mL lactic acid (10 vol.-%), 300 W Xe lamp (λ > 420 nm)	[96]
NiS@ g-C_3N_4	None	Hydrothermal treatment + High-temperature Ar-treatment	S-vacancy	Light absorption, charge transfer and separation	31.3	20 mg catalyst, 60 mL lactic acid (10 vol.-%), 300 W Xe lamp (λ > 420 nm)	[97]
$SrTiO_3$	Pt (1.0 wt.-%)	Chemical reduction ($NaBH_4$)	O-vacancy/ surface	Light absorption, charge transfer and separation	2.2 (112 μmol h^{-1})	50 mg catalyst, 120 mL CH_3OH (25 vol.-%)	[98]
$SrTiO_3$	Pt (1 wt.-%)	Laser melting	O-vacancy	Light absorption (VB and CB tail)	0.00246	100 mg catalyst, 100 mL CH_3OH (50 vol.-%), 300 W Xe lamp (λ > 400 nm, 200 mW cm^{-2})	[99]
TiO_2	None	UV illumination in presence of MeOH (during reaction)	O-vacancy, Ti^{3+}	Active sites	0.172	2 mg catalyst, 10 mL CH_3OH (50 vol.-%),	[100]

(continued)

Table 24.2 (continued)

Material	Co-catalyst	Synthesis approach	Defect/ Location	Role of defect	H_2 evolution rate/mmol g^{-1} h^{-1}	Reaction conditions	Refs.
						365 nm LED (90 mW cm^{-2})	
TiO_2	Pt (1.0 wt.-%)	Solverthermal (glycerol)	Ti-vacancy/ bulk	Carrier density and mobility	29.8	10 mg catalyst, 120 mL CH_3OH (30 vol.-%)	[101]
TiO_2	Pt (1.0 wt.-%)	Solvothermal (glycerol)	Ti^{3+}, Ti- and O-vacancies	Light absorption (mid-gap states), carrier density and separation	50.3	10 mg catalyst, 120 mL CH_3OH (30 vol.-%), 300 W Xe lamp	[102]
TiO_2	Pt (1.0 wt.-%)	Chemical reduction (imidazole)	O-vacancy	Light absorption (mid-gap states), charge separation	0.115	100 mg catalyst, CH_3OH (25 vol.-%), 300 W Xe lamp ($\lambda > 400$ nm, 195 mW cm^{-2})	[103]
TiO_2	Pt (1.0 wt.-%)	Chemical reduction ($NaBH_4$)	O-vacancy, Ti^{3+}/bulk and/or surface	Light absorption, charge transfer and separation, carrier density	2.139	50 mg catalyst, 120 mL CH_3OH (30 vol.-%), AM 1.5G or 300 W Xe lamp ($\lambda > 420$ nm)	[104]
ZnS	None	Solvothermal (phase-transition)	S-vacancy	Light absorption, charge separation and trapping, active sites	~0.018	50 mg catalyst, 100 mL lactic acid (5 vol.-%), 300 W Xe lamp ($\lambda > 410$ nm)	[105]
ZnS	None	Hydrothermal	Zn-vacancy/ surface and sub-surface	Light absorption, photostability	0.337^1	50 mg catalyst, 400 mL Na_2S/ Na_2SO_3, 300 W Xe lamp ($\lambda > 420$ nm)	[106]

(continued)

Table 24.2 (continued)

Material	Co-catalyst	Synthesis approach	Defect/ Location	Role of defect	H_2 evolution rate/mmol g^{-1} h^{-1}	Reaction conditions	Refs.
Zn_mCd_nS	None	Hydrazine hydrothermal synthesis	S-Vacancy, low valence Cd, interstitial metal/ surface	Light absorption	11.4 (571 μmol h^{-1})	50 mg catalyst, 80 mL Na_2SO_3/Na_2S (each 0.35 M), 300 W Xe lamp (λ > 420 nm)	[107]
Zn_mCd_nS	None	Hydrazine hydrothermal synthesis	Low valence Zn and Cd, S-vacancy	Light absorption (mid gap states), carrier trapping,	0.353	10 mg catalyst, 100 mL Na_2S/Na_2SO_3 (each 0.35 M), 300 W Xe lamp (λ > 420 nm)	[108]
$Zn_{1-x}Cd_xS$/ SiO_2	None	Sulfurization	Cd-vacancy, low valence Cd/surface	Carrier trapping, active sites	1.323 mmol h^{-1} (13.23 mmol h^{-1} g^{-1})$^{a)}$	100 mg catalyst, 100 mL Na_2S (0.35 M), Na_2SO_3 (0.25 M), 300 W Xe lamp (λ > 420 nm)	[109]
ZrO_2	Pt (1.0 wt.-%)	Chemical reduction (Mg) + high-temperature H_2/ Ar-treatment	Zr^{3+}, O-Vacancy/ surface	Light absorption (mid-gap states), carrier recombination (reduced)	0.505 mmol g^{-1} h^{-1}	50 mg catalyst, 50 mL CH_3OH (20 vol.-%), AM 1.5G (1 sun)	[110]

Values for hydrogen evolution rate marked with ^{a} were calculated based on data given in the corresponding reference

24.3.1.3 Defects for Enhancing Semiconductor Properties for Photocatalytic Reactions

The presence of defects will alter the material properties, especially if they are present in high density. Using the concept of defect engineering, the density of defects, and to some extent their physical appearance, e.g. point or volume defects, can be controlled. This in return provides the possibility to control different properties of a photocatalyst and increase its photocatalytic performance. As can directly be seen from Table 24.2, depending on the type of defect and the position inside the material the light absorption, charge transfer, separation, and recombination behavior as well as active sites on the photocatalyst surface can be affected. In many cases, more than one property is affected simultaneously.

In this respect, the most often reported defects in the field of photocatalysis are either vacancies (Chap. 12) low valence cations or dopants (Chaps. 9 and 11), all belonging into the group of point defects. In this Chapter, the focus is placed on the effects of vacancies and low valence cations, as these are known from metal oxides and sulfides, but can also occur in carbonaceous materials like g-C_3N_4 (see Table 24.2).

Besides the defect type, the concentration or density of defects inside a photocatalyst plays a crucial role. In many studies, the negative effects of too high defect concentrations are mentioned, which is often ascribed to the recombination of charge carriers at the defect sites. This shows that for defects to be useful in photocatalysis the balance of the different charge carrier processes (excitation, separation, transport, and recombination) needs to be kept.

24.3.1.4 Light Absorption

One of the key aspects of semiconductors that is changed by the introduction of defects is light absorption. This may occur by either sub-band gap states leading to the formation of a band-tail or the development of mid-gap states not directly connected to VB or CB. The two effects are schematically illustrated in Fig. 24.11. While the band-tails simply decrease the band gap, the mid-gap states allow for transitions into the band gap to newly formed defect levels. The resulting effect of either band-tail or defect-states is the extension of the absorption to larger wavelengths.

Both anion and cation defects can lead to the formation of mid-gap states and band tailing, often even acting together due to hybridization. For example, in black TiO_2, it is widely accepted that the presence of Ti^{3+} cations lead to the formation of mid-gap states with a transition of 0.75 eV to 1.64 eV. Additionally, the Ti^{3+} cations can form a CB tail in combination with oxygen vacancies. [111, 112] It should be noted that the formation of the VB tail in black TiO_2 is typically due to hydrogen doping. In other materials (Zn_mCd_nS—S-vacancies [108], Bi_3O_4Br—O-vacancies [77], g-C_3N_4—N-vacancies [93]), the presence of mid-gap states or the shift of the VB due to the formation of anion vacancies are reported as well.

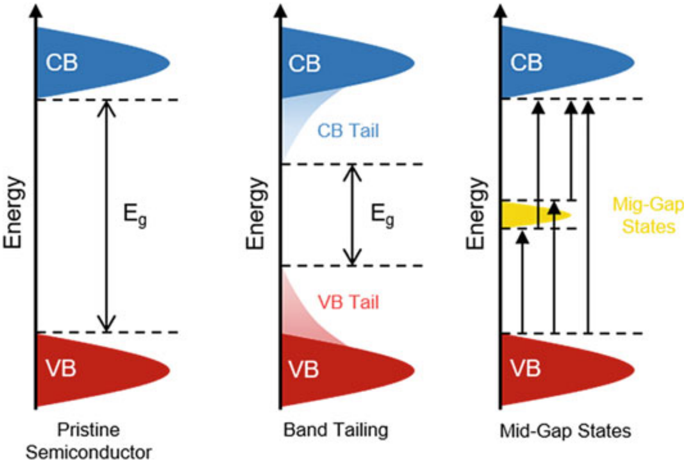

Fig. 24.11 Illustration of changes in the density of states due to defect introduction

The example of ZrO_2 illustrates the effectiveness of defects for light absorption. Pristine ZrO_2 has a band gap of around 5 eV and is, thus, on the edge of being a semiconductor. Sinhamahapatra et al. [110] used chemical reduction with Mg to introduce both O-vacancies and low valent Zr. The presence of these vacancies lowered the band gap to 1.52 eV due to the formation of VB and CB tails, which allowed for visible light photocatalytic hydrogen evolution (see Sect. 24.4.2.4).

The position and thus the extent of the increased light absorption can be tuned by the location and density of defect states inside the semiconductor. However, as discussed in Sect. 24.2.2.1, the presence of defects allows for Shockley–Read–Hall recombination and as a consequence with an increased concentration of defects the probability of recombination increases, eventually leading to prevailing recombination [68]. Furthermore, the increased light absorption due to the presence of defects is spatially limited. Thus, effective light absorption in the whole photocatalyst can only happen in the presence of bulk defects, otherwise the extended light absorption is limited to the surface region. However, the distribution of defects has additional implications, which will be discussed in the next section.

24.3.1.5 Charge Carrier Dynamics and the Influence of Defect Location

Following charge carrier generation through light absorption, the charge carriers need to be separated to prevent immediate recombination. Table 24.2 shows that this separation is often affected by the introduction of defects. Experimentally, the improvement of charge carrier separation is often observed in form of an increased charge carrier lifetime, for example by transient absorption spectroscopy. Further information on characterization techniques suitable to investigate the changes discussed here may be found in the reviews of Rajaraman et al. [113] and Qian et al. [61].

The enhancement of charge separation can be explained in several ways and strongly depends on the location of the defect. Defects in the bulk tend to act as recombination centers, as they trap charge carriers inside the photocatalyst, without the possibility for a reaction, eventually leading to recombination. On the other side, the defects on the surface and sub-surface can act as traps that facilitate the reaction. As reacted charge carriers cannot recombine this leads to an increased charge carrier separation. Therefore, in this case, the efficiency to facilitate the charge transfer depends on whether the charge carriers are consumed by adsorbed reactants. If the trapped charge carriers do not react fast enough, the surface defects become recombination centers like their counterparts in the bulk. In this respect, the defects show similarities to metal and metal oxide co-catalysts, that act as charge carrier sinks [68, 114].

Another possibility is the formation of a “built-in” electric field. This is especially the case, if oxygen is removed, as the remaining vacancies are charged positively due to the high electron negativity of the surrounding oxygen atoms. Due to the local charge imbalance, electrons are attracted, while holes are repelled, leading to charge carrier separation on the atomic scale [87, 115]. This built-in electrical field simultaneously enhances the migration of the charge carriers within the semiconductor [68].

Interestingly, vacancies can even lead to the formation of heterojunctions inside a material, like in the solid solution of Zn_mCd_nS. In this material, the presence of S-vacancies leads to the formation of two defects states which are either close to the VB or to the CB. As the S-vacancies are located at the surface, inside the bulk no such defect states exist resulting in a type-I heterojunction between bulk and surface [107]. As shortly discussed in Sect. 24.2.2.3, heterojunctions facilitate both charge carrier separation and migration.

Another aspect that can affect charge carrier separation is a change in the Fermi level, which leads to a shift of the built-in electric field of semiconductors. For example, anion vacancies act as electron donors and, thus, shift the Fermi level closer to the CB to fulfill charge neutrality, while, vice versa, low valence cations or cation vacancies act as electron acceptors shifting the Fermi level in the direction of the VB. Directly linked to that, there is also a change in the charge carrier density [84, 87]. The effects on the location of the Fermi level in both n-type and p-type semiconductors are displayed in Fig. 24.12.

However, changes in the Fermi level in metal oxide, metal sulfide, and organic semiconductors are limited by polaron formation, which in case of an excessive increase or decrease of the electron density prevents a further shift of the Fermi level, leading to Fermi level pinning. This topic has been summarized very well by Lohaus et al. [116] and will not be discussed in detail here. It should just be mentioned that also in this case the location of defects has a large impact, as the crystal periodicity near the surface is broken and, thus, the band gap no longer exists, instead many discrete energy levels are formed. In this case, the Fermi level becomes even more important, as it directly governs the occupation of these states.

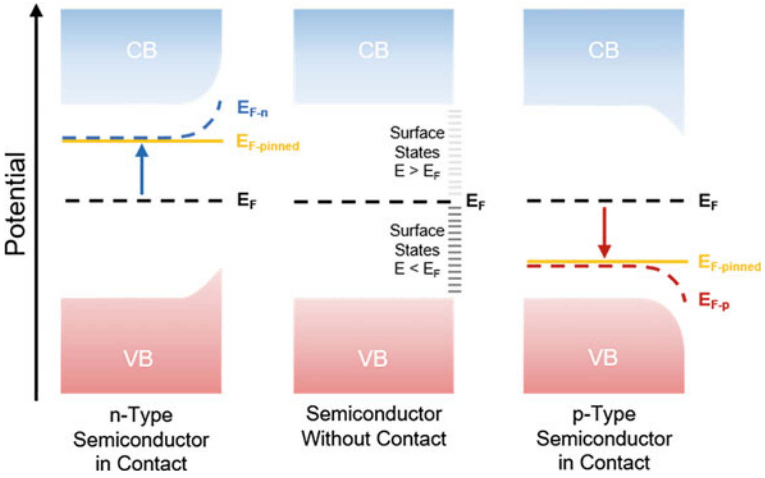

Fig. 24.12 Changes in the Fermi level position (E_F) due to electron donors ($E_{F\text{-}n}$) and electron acceptors ($E_{F\text{-}p}$) and the effect of Fermi level pinning ($E_{F\text{-pinned}}$) in both cases

Therefore, in some cases, the position of the Fermi level can explain the drop in activity above a certain defect concentration in a material, due to increased charge carrier recombination. With respect to the question “how much is too much”, we want to refer the reader to the review of Maarisetty and Bara [73], who have discussed this in detail.

Furthermore, the defect location can also affect the interaction between photocatalyst and reactants. However, this requires, that the defects are positioned at the external (accessible) semiconductor surface. The effects of defects on these interactions will be discussed in the next section.

24.3.1.6 Photocatalyst Reactant Interactions

Many studies have shown the importance of defects for the interaction of solids with molecules. In this respect, the sorption process of reactants and, upon contact, the structure of the adsorbed reactants are affected, but also the transfer of charge carriers can be influenced. Here, the main focus lies on the adsorption and activation of water and alcohols on TiO_2. For the interaction of oxygenates with other materials, the reader may refer to the excellent review of Vohs [117].

Upon contact, the photocatalyst can affect the reactant and change, for instance, the bond length or angle and deform the structure of the molecule, ultimately leading to bond cleavage. This process is called dissociative adsorption and is one of the major contributions of defects to the reactant activation on (photo)catalyst surfaces, as it is typically absent on defect-free surfaces [120]. In fact, Schaub et al. [118] have shown for rutile that dissociative adsorption of water is only possible on oxygen vacancies, leading to the formation of two hydroxyl groups due to the interaction with neighboring oxygen atoms (Fig. 24.13a). In addition, Das et al. [121] could demonstrate that O-vacancies in TiO_2 lower the change in the free energy for both HER and OER, thus making the reactions more likely to proceed. Nowotny et al. [119] proposed that Ti-vacancies can interact with H_2O molecules and form stabilized adsorbate-complexes, that allow surrounding oxygen ions to transfer holes to split water into protons and an adsorbed oxygen atom (Fig. 24.13b). For both O- and Ti-vacancies, it is likely that surface dipoles are formed due to the difference in electron density of defects and the surrounding atoms. These dipoles can reduce the steric exclusion between H_2O and the photocatalyst surface by altering the surface potential, thus drastically increasing the water adsorption capability [73].

Besides TiO_2, the effects of defects on the interaction of photocatalyst and reactant have also been investigated for other materials. One of the most interesting material in this respect is BiOCl. It is one of the few examples for overall photocatalytic water splitting on a semiconductor with defects not introduced by doping. The study of Zhang et al. [78] shows by means of density functional theory (DFT) calculations that a surface with oxygen vacancies has a higher adsorption energy for water adsorption and therefore is favorable. The reaction of the adsorbed water on surface oxygen vacancies proceeds then similar to the description of Schaub et al. [118] for TiO_2.

The interaction of alcohols (mainly methanol and ethanol) with TiO_2 has been studied by many groups [122–124] both experimentally and theoretically. Guo et al. [125] have published an extensive review on this topic, which also covers the interaction of TiO_2 with a broader range of molecules. Therefore, in the present Chapter, the discussion will be limited to the interactions of TiO_2 with methanol. Lang et al. [122] have calculated the behavior of methanol on anatase with DFT and reached the conclusion that methanol adsorbs molecularly on defect-free surfaces, whereas in the presence of oxygen surface and sub-surface vacancies, dissociative adsorption occurs leading to the formation of an alkoxide and a hydroxyl group. Additionally, the resulting alkoxides were found to be more reactive, thus helping to scavenge the holes from the photocatalyst [120].

24.3.2 Z-Scheme Photocatalysts

The conceptual idea of Z-scheme photocatalytic systems is already more than 40 years old. It is based on the photosynthesis mechanism known from plants [126]. The history, developments, and principles of Z-scheme systems have been recently reviewed in detail by Ng et al. [127], while the photocatalyst synthesis approaches were reviewed by Xu et al. [128]. Therefore, only the general properties of Z-scheme systems will be covered followed by an overview of the newest generation of Z-schemes, i.e., direct Z-schemes.

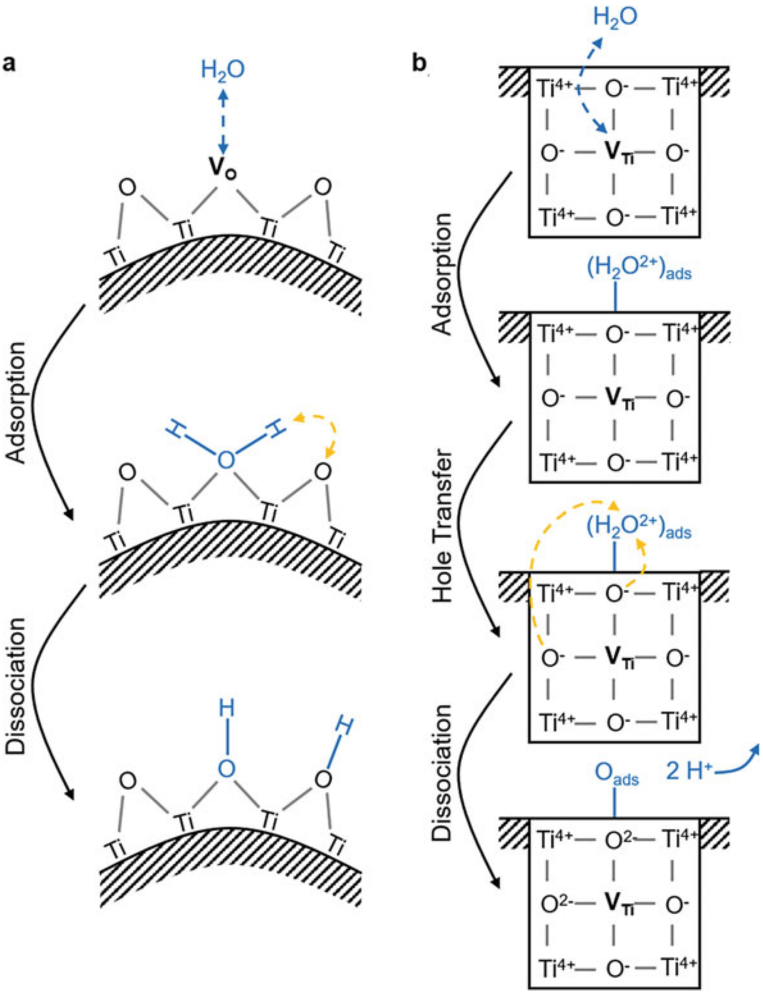

Fig. 24.13 **a** Interaction of oxygen vacancies (V_O) and **b** titanium vacancies (V_{Ti}) with water on TiO_2 leading to dissociative adsorption according to [118, 119]

Z-scheme systems are comprised of a combination of two semiconductors, each catalyzing one half-reaction (oxidation or reduction). These two semiconductors are often connected via a redox mediator. The typical arrangement in a Z-scheme is shown in Fig. 24.14. From here on, the semiconductor with the higher reduction potential will be referred to as PC-I. Likewise, the semiconductor with the higher oxidation potential will be referred to as PC-II. The role of the redox mediator is to enable a pathway for electron transfer from PC-II to PC-I and to prevent photo-corrosion or the formation of a heterojunction.

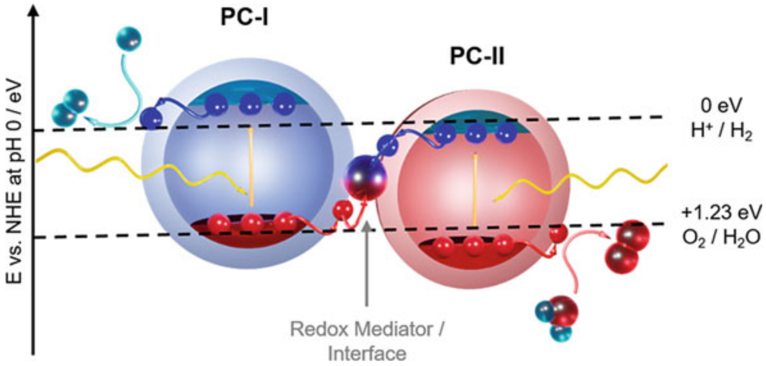

Fig. 24.14 Schematic band energy diagram of a Z-scheme system for photocatalytic water splitting

In the first Z-scheme generation, liquid redox mediators in form of ion redox couples such as IO_3^-/I^-, Fe^{3+}/Fe^{2+} or $[Co(bpy)_3]^{3+/2+}$ were used. However, these redox mediators were limited in their efficiency to transfer charge carriers and susceptible to the photocatalytic backreaction. Furthermore, they were prone to changes in the pH-value and had a tendency to absorb part of the visible light spectrum [127]. In the second generation of Z-schemes, the all-solid-state Z-schemes, the redox couple was substituted for a conducting material like a noble metal or a conductive carbon resulting in an Ohmic contact between semiconductors. These Z-scheme types have a reduced susceptibility for the backward reaction and a less intense light-shielding effect. However, even with all-solid-state Z-schemes several drawbacks (backwards reaction, light-shielding, photo-corrosion) remained, as the conductor is still exposed to the reaction environment. This led to the development of direct Z-schemes, which omit the use of an additional redox mediator or conductive material. Instead, the built-in electric field of semiconductor interfaces is utilized as shown in Fig. 24.8 [129].

Nevertheless, all the above-mentioned Z-scheme variations come with several advantages for photocatalytic reactions, which make them promising systems in the field of photocatalytic hydrogen generation. These advantages include, but are not limited to

1. simultaneous preservation of the higher reduction and oxidation potential,
2. high efficiency for charge carrier separation,
3. spatial separation of active sites of half reactions,
4. extended light absorption range,
5. wide spectrum of photocatalyst combinations.

It should be emphasized here that a careful evaluation of the Z-scheme mechanism of semiconductor composites is necessary as these can easily be confused with type II heterojunctions. Typical approaches to differentiate between the Z-schemes and type II heterojunctions include radical species trapping experiments, metal loading tests, XPS characterization under illumination, as well as DFT simulations of the internal electric field. For further details, the reader may refer to the review of Low et al. [130].

24.3.2.1 Direct Z-Scheme Systems

In contrast to first- and second-generation Z-schemes, the third-generation direct Z-schemes exclusively rely on the built-in electric field of the semiconductors, making them the first binary Z-scheme systems. This latest generation further improves the resistance towards the backwards reaction and photo-corrosion and significantly reduces the light-shielding as no additional component on or around the photocatalyst is present. Furthermore, the effort and costs to synthesize such systems can be reduced [129].

In the case of direct Z-schemes, the electron flow from PC-II to PC-I can be understood as the accumulation of opposite charge carriers near the interface of both semiconductors, which leads to strong electrostatic attraction. Simultaneously, electrostatic repulsion prevents the formation of a type II heterojunction and, thus, the transfer of electrons from the CB of PC-I to PC-II and holes from the VB of PC-II to PC-I [127]. This behavior originates from a difference in the Fermi level of the semiconductors that are brought together. Upon contact electrons will flow from PC-I to PC-II until the Fermi levels are in thermodynamic equilibrium. This leads to an electric charge at the interface. PC-I will be positively charged, while PC-II will be negatively charged, resulting in an electric field acting as the driving force for the Z-scheme charge carrier recombination mode [128].

Even though synthesis methods for Z-scheme construction will not be discussed here, it should be highlighted that the synthesis procedure can affect the mode of charge carrier transfer between two semiconductors. The work of Jiang et al. [131] demonstrates this clearly. In this work, a composite of CdS and g-C_3N_4 was prepared in two different ways. Using chemical-deposition to place CdS on g-C_3N_4 resulted in the formation of a Z-scheme, while the photo-deposition of CdS resulted in a type II heterojunction. The reason for this different behavior was that the photo-deposition led to a selective growth of CdS on g-C_3N_4 at electron transfer sites, as the S^{2-} needed for CdS formation had to be formed by reduction of elemental sulfur. The main geometrical configurations for Z-scheme construction and their respective advantages and disadvantages are treated in a review of Xu et al. [128].

(i) Defect-Free Direct Z-Scheme Photocatalyst Systems

In the previous section, the example of CdS on g-C_3N_4 was discussed to show the importance of the interface formation and mode of contact between PC-I and PC-II. Even though physical formation of the interface is possible, especially in systems with opposite surface charge, most often the chemical formation of the interface is used as can be seen in Table 24.3. This is due to the more stable interface as a result of chemical bond formation compared to their counterparts derived from physical interaction. Furthermore, chemical synthesis strategies allow for improved control of the distribution of the semiconductors.

Another important point to consider for the synthesis of direct Z-schemes is the choice of semiconductors to be combined. As the charge recombination pathway is governed by the internal electric field that is generated upon contact of PC-I and PC-II, besides the staggered band gap typical for Z-schemes, the semiconductors require proper Fermi levels. Only if the Fermi level of PC-I is above the Fermi level of PC-II the alignment of the work functions upon contact can lead to the accumulation of electrons in PC-I and holes in PC-II [132]. It should be noted that coupling of p- and n-type semiconductors can result in the formation of p–n junction, which induces an electric field opposite to that needed for the electron flow in Z-scheme mode.

Despite these additional restrictions the advantage of a multitude of semiconductor combinations also remains for the third-generation Z-scheme systems as evident from Table 24.3. Among these are many semiconductors that are not capable of performing overall photocatalytic water splitting alone due to their unsuitable redox potential, e.g.,WO_3, α-Fe_2O_3, $BiVO_4$, or semiconductors that are prone to photo-corrosion, e.g., CdS, ZnS, $ZnIn_2S_4$. This shows the remarkable capabilities of Z-Scheme photocatalytic systems for overcoming material limitations. The respective performance for hydrogen generation will be discussed in Sects. 24.4.1.2 and 24.4.2.4.

(ii) Defects in Direct Z-Scheme Photocatalyst Systems

The utilization of defects to construct redox mediator free Z-schemes, which utilize the electric field that is created when two semiconductors are brought into contact, was recently reported for the first time [151]. Since for the electron transfer in a Z-scheme-like manner, the semiconductor interface is vital, mainly surface, and sub-surface defects play a role for the Z-scheme formation. Besides, the presence of defects of course also influence other properties that were discussed in Sect. 24.3.1.3 as well. This section will, therefore, focus on the role of defects as redox mediator substitutes.

Table 24.4 gives an overview of the reported Z-scheme combinations, whose mode of charge transfer involves the presence of defects. Additionally, the synthesis approach for the interface formation is given and their respective performance for hydrogen evolution. Again, the latter will be discussed in Sects. 24.4.1.2 and 24.4.2.4. It should be mentioned that all photocatalysts displayed in Table 24.4 were investigated according to the Z-scheme mechanism and can, thus, be clearly distinguished from heterojunctions.

The main role of the defects is the adjustment of the position of either VB [153, 154, 160] or CB [152, 157, 158] by the insertion of mid-gap defect levels. The defect levels are closer in energy to their corresponding counterpart, which facilitates the transfer between these bands. The other two possible modes of action are the formation of a redox couple [156, 159] quite similar to the first generation

Table 24.3 Direct Z-scheme photocatalytic systems including the applied co-catalysts, the method used for interface formation and confirmation of the Z-scheme charge transfer mode. In addition, the performance of the Z-scheme systems for H_2-evolution (as H_2 evolution rate) via photoreforming and overall photocatalytic water splitting together with the respective reaction conditions are given

PC-I	PC-II	Co-catalyst	Interface formation	Confirmation of Z-scheme transfer mode	H_2-Evolution rate/mmol g^{-1} h^{-1}	Reaction condition	Refs.
Overall Photocatalytic Water Splitting							
Black Phosphorus	$BiVO_4$	None	Physical (ultrasonication)	Single semiconductor activity, redox potential determination	0.160	5 mg catalyst, 8 mL H_2O, 320 W Xe lamp (λ > 420 nm, 400 mW cm^{-2})	[133]
CdS	$BiFeO_3$	None	Chemical (precipitation)	Redox potential determination	UV 0.6002 Vis 0.4214	100 mL H_2O, 125 W high-pressure Hg lamp	[134]
$Cd_{0.5}Zn_{0.5}S$	$BiVO_4$	Pt (3 wt.-%)	Chemical (chemical bath deposition)	Radical trapping (DMPO)	Water splitting 0.0456 Photoreforming 2.35	100 mL H_2O (or Na_2S (0.35 m) and Na_2SO_3 (0.25 M), 300 W Xe lamp (λ > 420 nm)	[135]
Cu_3P	Bi_2WO_6	None	Physical (ball milling)	Single semiconductor activity, redox potential determination	9.3 µmol g^{-1} (0.00465)$^{\mathbf{a}}$	100 mg catalyst, 80 mL Na_2HPO_4/ NaH_2PO_4 (0.5 M) AM 1.5G (100 mW cm^{-2})	[136]
Cu_7S_4	γ-MnS	MnO_x (0.6 wt.-%)	Chemical (cation exchange)	Single semiconductor activity, redox potential determination	Water splitting 0.209 Photoreforming 0.718	1 mg catalyst, 6 mL H_2O (or Na_2S (0.35 M) and Na_2SO_3 (0.25 m) for photoreforming), 300 W Xe lamp	[137]
g-C_3N_4	α-Fe_2O_3	RuO_2 (0.1 wt.-%)	Chemical (calcination)	Radical trapping (DMPO)	Water splitting 0.0382 Photoreforming 31.4	50 mg catalyst, H_2O, 300 W Xe lamp (λ > 400 nm) or for photoreforming 10 mg catalyst, 100 mL triethanolamine (TEOA) (10 vol.%)),	[138]
g-C_3N_4	$BiFeO_3$	None	Chemical (calcination)	Redox potential determination	UV 0.161 Vis 0.023	40 mg catalyst, 100 mL H_2O, 125 W medium pressure Hg lamp (5 mW cm^{-2})	[139]

(continued)

Table 24.3 (continued)

PC-I	PC-II	Co-catalyst	Interface formation	Confirmation of Z-scheme transfer mode	H_2-Evolution rate/mmol g^{-1} h^{-1}	Reaction condition	Refs.
g-C_3N_4	$BiVO_4$	Pt (3 wt.-%)	Chemical (calcination)	Identification of reactive oxygen species, radical trapping (DMPO)	15.6 μmol h^{-1} $(0.156)^{\mathbf{a}}$	100 mg catalyst, 100 ml H_2O, 300 W Xe lamp ($\lambda > 420$ nm)	[140]
g-C_3N_4	WO_3 H_2O	None	Chemical (hydrothermal)	Carrier lifetime investigation, single semiconductor activity	0.482	100 mg catalyst, 100 mL H_2O, 300 W Xe lampg ($\lambda > 420$ nm, 180 mW cm^{-2})	[141]
$ZnIn_2S_4$	WO_3	PtS (0.5 wt.-%) and MnO_2 (3.0 wt.-%)	Chemical (precipitation)	Redox potential determination	15.5 μmol in 8 h $(0.0194)^{\mathbf{a}}$	100 mg catalyst, 100 mL H_2O, 300 W Xe lamp (420 nm < λ < 800 nm)	[66]
Photoreforming							
Ag_2S	WO_3	None	Chemical (precipitation)	Radical trapping (terephthalic acid)	32.9 μmol h^{-1} $(0.219)^{\mathbf{a}}$	15 mg catalyst, 10 mL lactic acid (10 vol.-%), 300 W Xe lamp	[142]
CdS	WO_3	Pt	Chemical (hydrothermal)	DFT calculation	15.522	50 mg catalyst, 100 mL Na_2SO_3 (0.25 M) and Na_2S (0.35 M), 300 W Xe lamp ($\lambda > 400$ nm)	[143]
CdS	ZnS	None	Chemical (chemical bath deposition)	In-situ XPS, DFT calculation	4.134	50 mg catalyst, 80 mL Na_2SO_3 (0.25 M) and Na_2S (0.35 M), 350 W Xe lamp	[144]
$CuInS_2$	g-C_3N_4	Pt (1 wt.-%)	Chemical (hydrothermal)	Noble metal deposition (Pt), photoluminescence lifetime	1.29	50 mg catalyst, 100 mL Na_2SO_3 (0.2 M) and Na_2S (0.25 M), 300 W Xe lamp ($\lambda > 420$ nm)	[145]
g-C_3N_4	CdS				56.9 μmol h^{-1}		[131]

(continued)

Table 24.3 (continued)

PC-I	PC-II	Co-catalyst	Interface formation	Confirmation of Z-scheme transfer mode	H_2-Evolution rate/mmol g^{-1} h^{-1}	Reaction condition	Refs.
		Pt (1 wt.-%)	Chemical (chemical deposition)	Charge carrier transfer via photoluminescence, metal photodeposition (Pt, PbO_2)	(5.69)[a]	10 mg catalyst, 100 mL Na_2SO_3 (0.1 M) and Na_2S (0.05 M), 300 W Xe lamp (λ > 420 nm)	
g-C_3N_4	WO_3	Pt (1 wt.-%)	Chemical (calcination)	DFT calculation	3.12	50 mg catalyst, 80 mL TEOA (10 vol.-%), 300 W Xe lamp	[146]
g-C_3N_4	$W_{18}O_{49}$	Pt (3 wt.-%)	Chemical (hydrothermal)	Metal photo-deposition (Au, PbO_2), DFT calculation	8.597	50 mg catalyst, 120 mL triethanolamine (TEOA) (10 vol.-%), 300 W Xe lamp (λ > 420 nm)	[147]
$Zn_{0.67}Cd_{0.33}S$	ZnO	None	Chemical (solid-state reaction)	DFT calculation	38.93	25 mg catalyst, 100 mL Na_2SO_3 (0.1 M) and Na_2S (0.1 M), 300 W Xe lamp (λ > 420 nm)	[148]
$ZnIn_2S_4$	$LaNiO_3$	None	Chemical (precipitation)	Single semiconductor activity, redox potential determination	1.6	20 mg catalyst, 100 ml TEOA (10 vol.-%), 300 W Xe lamp (λ > 420 nm)	[149]
$ZnIn_2S_4$	WO_3	None	Physical (electrostatic adsorption)	Single semiconductor activity, redox potential determination	2.2029	20 mg catalyst, 100 mL Na_2SO_3 (0.25 M) and Na_2S (0.35 M), 300 W Xe lamp (λ > 420 nm)	[150]

Values for the H_2-evolution rate for entries marked with[a] were calculated from data given in the corresponding reference

Table 24.4 Combination of PC-I and PC-II in defect-based direct Z-scheme photocatalytic systems including the applied co-catalysts, the role of the defects for Z-scheme construction, and the method used for interface formation and confirmation of the Z-scheme charge transfer mode. H_2-evolution rate and reaction conditions for hydrogen evolution via photoreforming and overall photocatalytic water splitting are given

PC-I	PC-II	Co-Catalyst	Interface Formation	Role of Defect	Confirmation of Z-Scheme Transfer Mode	H_2-Evolution rate/mmol g^{-1} h^{-1}	Reaction Conditions	Refs.
$AgIn_5S_8$	ZnS	None	Chemical (hydrothermal)	Zn-vacancies acting as CB in ZnS and enable transfer pathway to $AgIn_5S_8$	Radical trapping (DMPO)	0.9328	20 mg catalyst, 100 mL Na_2S (0.35 m) and Na_2SO_3 (0.25 m), 300 W Xe lamp ($\lambda > 420$ nm)	[152]
CdS	$CdWO_{4-x}$	Pt (0.5 wt.-%)	Chemical (solvothermal)	Formation of ohmic contact due to surface O-vacancies in $CdWO_{4-x}$	Single semiconductor activity, radical trapping	$\sim 14^{a}$	20 mg catalyst, 100 mL lactic acid (10 vol.-%), 300 W Xe lamp ($\lambda > 420$ nm)	[151]
CdS	WO_{3-x}	MoS_2 (0.1 wt.-%)	Chemical (microwave-assisted hydrothermal synthesis)	O-vacancies in WO_{3-x} act as VB	Single semiconductors activity	2.8525	100 mg catalyst, 100 mL lactic acid (10 vol.-%), 350 W Xe lamp ($\lambda = 400$–800 nm)	[153]
CdS	WO_{3-x}	None	Chemical (wet chemical precipitation)	O-vacancies in WO_{3-x} capture electrons and enable transfer pathway	Single semiconductors activity	6.5453	50 mg catalyst, 80 mL lactic acid (10 vol.-%), $\lambda = 400$–800 nm	[154]
Cu_2O	TiO_{2-x}	Pt				32.6		[155]

(continued)

Table 24.4 (continued)

PC-I	PC-II	Co-Catalyst	Interface Formation	Role of Defect	Confirmation of Z-Scheme Transfer Mode	H_2-Evolution rate/mmol g^{-1} h^{-1}	Reaction Conditions	Refs.
		(1 wt.-%)	Chemical (photo-deposition)	Ti^{3+} mid-gap states lead to band alignment	DFT calculations		20 mg catalyst, 100 mL CH_3OH (10 vol.-%), AM 1.5G	
g-C_3N_4	MnO_2	Pt (3 wt.-$)	Chemical (hydrothermal)	Mn^{3+} prevents charge carrier recombination through Mn^{3+}/Mn^{4+} redox cycle	Single semiconductor activity, identification of reactive oxygen species	Photoreforming 28.0 Water Splitting 0.0606	Triethanolamine or pure water, λ > 400 nm	[156]
g-C_3N_4	TiO_2	Pt	Chemical (calcination)	Ti^{3+} mid-gap states act as CB and enable transfer pathway to g-C_3N_4	Single semiconductor activity, product selectivity	AM 1.5G 1.938 Vis 0.287	100 mg catalyst, 100 mL CH_3OH (10 vol.-%), 300 W Xe lamp (λ > 400 nm–260 mW cm^{-2}/AM 1.5G–300 mW cm^{-2})	[157]
g-C_3N_4	ZnO	Pt (1 wt.-%)	Physical	O-vacancies act as CB and enable transfer pathway to g-C_3N_4	Radical trapping (DMPO)	0.322	100 mg catalyst, 100 mL TEOA (10 vol.-%), 300 W Xe lamp (λ > 420 nm)	[158]
MoS_2	Bi_2O_3	None	Chemical (solvothermall)	O-vacancies in Bi_2O_3 act as interface	Identification of reactive oxygen species	3.0752	25 mg catalyst, 50 mL TEOA	[159]

(continued)

Table 24.4 (continued)

PC-I	PC-II	Co-Catalyst	Interface Formation	Role of Defect	Confirmation of Z-Scheme Transfer Mode	H_2-Evolution rate/mmol g^{-1} h^{-1}	Reaction Conditions	Refs.
				charge mediator			(0.25 m), AM 1.5G	
$ZnIn_2S_4$	g-C_3N_4	Pt (1 wt.-%)	Chemical (hydrothermal)	Defective functional groups in g-C_3N_4 shift the VB (staggered bands)	Radical trapping experiments (DMPO)	1.65	100 mg catalyst, 100 mL triethanolamine (TEOA) (20 vol.-%), 300 W Xe ($\lambda > 420$ nm)	[160]

Values for H_2-evolution rate for entries marked with ^{a} were obtained from a graph of evolved H_2 in the given reference through the presence of defects and the formation of an Ohmic contact due to the generation of quasi-continuous states at the interface [151]. It should be mentioned that most of the studies included in Table 24.4 do not specifically mention the formation of an Ohmic contact. Still, it is likely that this is also the case in these works, as defects near the surface promote the formation of continuous states at the surface. Note also that in all studies reported so far, the defects were only introduced into PC-II.

Even though defects can enable the formation of direct Z-schemes that function without an additional redox mediator, the control of the defect distribution in the semiconductor is difficult. This is even more true, since the local distribution for the formation of the interface needs to be controlled in addition to the bulk-surface distribution to keep the balance between the inner charge transfer of the weak charge carriers and the outer charge transfer of the strong charge carriers to the reactants of the photocatalytic conversion [129].

24.3.2.2 Recent Developments

Numerous Z-scheme photocatalysts are already known. However, it is time-consuming to unambiguously assess experimentally whether a given semiconductor combination will lead to the successful formation of Z-scheme charge transfer. In this respect, the trend to investigate material combinations via computational approaches is emerging to predict the material properties and the preferred charge-transfer modes in order to select promising semiconductors for novel Z-scheme-based photocatalysts [161, 162].

Another emerging trend is the expansion of Z-schemes towards multi-component systems including heterojunctions and Z-schemes in one photocatalytic system [163, 164] or dual Z-scheme charge transfer [165, 166]. These new photocatalysts allow to further improve the utilization of charge carriers and the expansion of light absorption. For example, Hezam et al. [163] used Cs_2O–Bi_2O_3–ZnO in overall photocatalytic water splitting, combining a type II heterojunction between Bi_2O_3 and ZnO and the Z-scheme mode between Cs_2O and Bi_2O_3 as well as Cs_2O and ZnO. The three-component system reached a H_2 evolution rate of 149.5 μmol g^{-1} h^{-1}, while without Cs_2O no activity was observed. This concept is therefore promising for new generations of Z-scheme photocatalysts.

24.3.3 Other Design Strategies

Apart from defect engineering and Z-scheme construction dealt with above, many other design strategies for the enhancement of the photocatalytic activity of particulate photocatalysts have been investigated. These include, inter alia, crystal-facet engineering [167], dye sensitization [168], doping [169], nanostructuring [170], heterostructure and composite formation [171], and surface plasmon resonance [172]. Among these design strategies, co-catalyst deposition is especially worth mentioning as it is a universal tool to enhance the photocatalytic activity of semiconductors and as it can be combined with most other design strategies. In this context, the reviews of Bai et al. [173, 174] are recommended that explain in detail the peculiarities of co-catalysts and the corresponding interface design, also for the more recent and complex hybrid co-catalysts consisting of several components.

24.4 Photocatalytic Hydrogen Generation from Aqueous Media

The formation of hydrogen from aqueous media can be categorized by the presence or absence of components in the aqueous phase that are consumed during the photocatalytic reaction. A more sophisticated view would consider the products of the photocatalytic conversion and divide the systems according to the origin of the hydrogen atoms formed. In this respect true photocatalytic water splitting, also called overall photocatalytic water splitting, would require that all the hydrogen and oxygen is formed from water, resulting in a stoichiometric molar ratio of 2:1 (n_{H2}: n_{O2}). If this is not the case, the reaction should be referred to as photoreforming or sacrificial agent-assisted water splitting. Figure 24.15 illustrates the half reactions taking place in the case of overall photocatalytic water splitting and photoreforming.

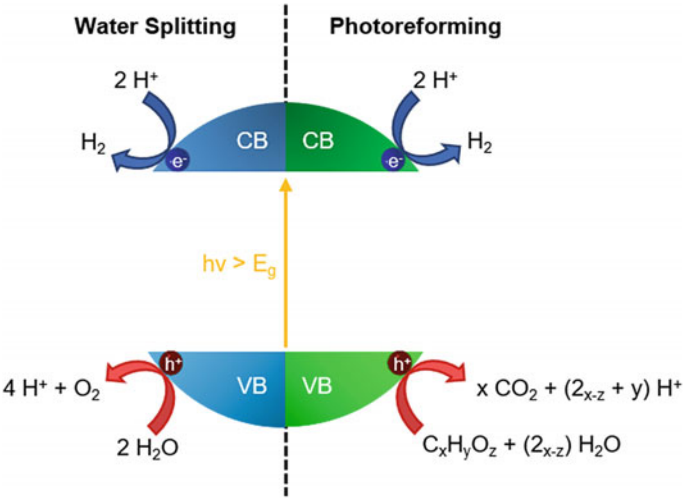

Fig. 24.15 Representation of the redox reactions occurring on photocatalyst surfaces in the case of overall photocatalytic water splitting (left) and photoreforming (right)

Typical additives that are used to generate hydrogen via photoreforming from aqueous media are organic substances like alcohols (CH_3OH, C_2H_5OH), carboxylic acids, amines, or biomass-derived chemicals (glucose, cellulose, glycerole). Especially for metal sulfides, inorganic substances like Na_2S or Na_2SO_3 are used as well. The purpose of sacrificial agents is to act as hole scavengers, to reduce the potential of the oxidative reaction, and utilize semiconductors with an otherwise unsuitable VB. Additionally, these additives can prevent photo-corrosion due to charge carrier accumulation.

In this section, both overall photocatalytic water splitting and photoreforming will be treated. Therefore, first the reactions are introduced and, if possible, the mechanisms for the reactions are mentioned. In case of photoreforming, only alcohols and biomass-derived sacrificial agents are included. The utilization of wastewater and organic contaminants for the purpose of hydrogen evolution is discussed in a separate Chap. 21 and will, therefore, not be covered here.

24.4.1 Hydrogen Generation from Water

Overall photocatalytic water splitting is a multi-electron transfer process that requires the transfer of two electrons per molecule of water, as we can see from Eqs. (24.2) and (24.3). The overall reaction requires a potential of 1.23 V (Eq. 24.4) and an energy of 2.458 eV per molecule of H_2 and is thus an endothermic reaction [175].

$$2H^+ + 2e^- \rightarrow H_2 \quad E^{\emptyset}_{\mathrm{red}} = 0\ \mathrm{eV} \tag{24.2}$$

$$H_2O \rightarrow 2H^+ + 2e^- + \frac{1}{2}O_2 \quad E^{\emptyset}_{\mathrm{ox}} = 1.23\ \mathrm{eV} \tag{24.3}$$

$$H_2O \rightarrow \frac{1}{2}O_2 + H_2 \quad \begin{array}{l} E^{\emptyset} = 1.23\ \mathrm{eV} \\ \Delta G^{\emptyset} = +237\ \mathrm{kJ\ mol^{-1}} \end{array} \tag{24.4}$$

Resulting from the potential of water splitting two thermodynamic requirements arise. First, the band gap in case of single photocatalyst systems cannot be smaller than 1.23 eV resulting in a maximum utilizable wavelength of 1008 nm. Second, the band positions need to be at or above +1.23 eV against NHE at pH = 0 for the VB and at or below 0 eV against NHE at pH = 0 for the CB to provide the necessary redox potential. However, often the reaction is kinetically hindered and therefore requires a higher oxidation and reduction potential [6].

The driving force for a reaction of electrons and hole inside a semiconductor under light irradiation with energy greater than the band gap can be calculated from the position of the quasi Fermi levels (F_n—electrons—Eq. (24.5), F_p—holes—Eq. (24.6)) according to Eq. (24.7), with E_{CB} and E_{VB} being the minimum and maximum of CB and VB respectively, k_B the Boltzmann constant, T the absolute temperature, N_{CB} and N_{VB} the effective densities of states in CB and VB, n and p the carrier concentration of electrons and holes [176].

$$F_n = E_{\mathrm{CB}} + k_B T \ \ln \frac{n}{N_{\mathrm{CB}}} \tag{24.5}$$

$$F_p = E_{\mathrm{VB}} + k_B T \ \ln \frac{p}{N_{\mathrm{VB}}} \tag{24.6}$$

$$nG = -\left|F_n - F_p\right| = -E_g - k_B T \ \ln \frac{np}{N_{\mathrm{CB}} N_{\mathrm{VB}}} \tag{24.7}$$

24.4.1.1 Reaction Mechanism

Numerous studies were devoted to investigate the reaction mechanism for overall photocatalytic water splitting. However, the mechanism has not yet been fully elucidated. Therefore, the most widely accepted mechanisms for both HER and OER will be presented here.

Meanwhile, it is generally accepted that the overall photocatalytic water splitting, not only over TiO_2, but also over other solid photocatalysts, is limited by the OER, as this reaction requires the transfer of four electrons to generate one O_2 molecule compared to the two electrons required in HER for the evolution of one H_2 molecule. HER is assumed to proceed similar to the reaction mechanisms, either the Volmer-Heyrovsky mechanism or the Volmer-Tafel mechanism, found for purely electrocatalytic hydrogen generation [177]. Both reactions mechanisms are shown in Fig. 24.16. The main difference between the two is the reduction of the second proton and subsequent bond formation [178]. However, often the actually occurring reaction mechanism is not clear and just the reduction step of a single proton is considered [179].

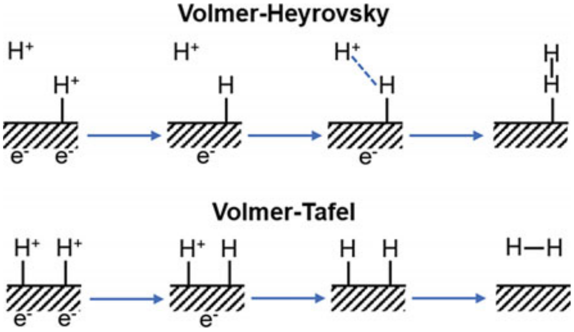

Fig. 24.16 Volmer-Heyrovsky and Volmer-Tafel reaction mechanism of the hydrogen evolution reaction, according to [178]

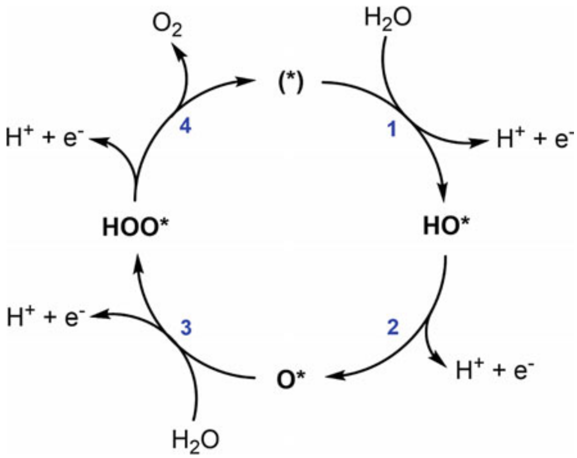

Fig. 24.17 Oxygen evolution reaction mechanism according to [185]

As the OER is considered the rate-limiting reaction in overall photocatalytic water splitting, numerous studies are focused on the investigation of the reaction mechanism of water oxidation. In many reports, it is assumed that the reaction proceeds in four steps, which can be connected to form a catalytic cycle like that exemplified in Fig. 24.17 [180–182]. However, other mechanisms are suggested as well. For example Durran et al. [183] put forward two OER mechanisms on Fe_2O_3 under alkaline conditions, which require the simultaneous accumulation of three holes for the rate-determining step (oxygen–oxygen bond formation). Hu et al. [184] proposed a dual pathway reaction mechanism on TiO_2, which involves two catalytic cycles on different active sites that are connected.

Important for both HER and OER is the fact, that the rate-limiting step varies, depending on the photocatalyst used for the reaction [180], the crystal structure [181], crystal facet [182] and coordination of the active site in case of a co-catalyst [186].

24.4.1.2 Semiconductor Performance in Hydrogen Generation from Water

The evaluation of the photocatalytic performance can be done using a broad set of different figures of merit. For the most often used quantities and their meaning, together with the implications of the experimental procedure, the reader may refer to the detailed review of Muhammad and Takanabe [187]. Here, the discussion will be predominantly based on the reaction rate and the apparent quantum efficiency (AQE). It should be mentioned that a direct comparison of different photocatalytic systems is often difficult due to the variety of reaction conditions applied and experimental setups used. Furthermore, only photocatalysts who have been shown to produce hydrogen and oxygen simultaneously in a stoichiometric ratio close to

2:1 will be considered, photocatalysts that do not meet these conditions are dealt with in Sect. 24.4.2.4.

Although defect engineering is a powerful tool to enhance the photocatalytic activity, only few defects engineered photocatalysts have been reported to be active for overall photocatalytic water splitting, even in combination with other design strategies like Z-scheme construction (compare Tables 24.2 and 24.4). For example, Zhang et al. [78] prepared nanosheets of BiOCl with low valence Bi-atoms and O-vacancies. The authors have shown that the nanostructuring of the BiOCl promotes O-vacancy formation. Simultaneously, the nanostructure enforces a surface or sub-surface position of the defects, which reduces the recombination induced by bulk defects. Furthermore, they investigated the presence of defects on the reaction experimentally via loading of NiO_x co-catalyst and theoretically via DFT calculation. The DFT calculation showed, that the presence of O-vacancies reduces the energy needed to split water. The photocatalytic water splitting with NiO_x co-catalyst supported this, as the presence of the co-catalyst reduced the photocatalytic activity from 35 μmol h^{-1} g^{-1} (8.4 μmol in 24 h) to 10 μmol h^{-1} g^{-1} (2.4 μmol in 24 h). In another example Mo et al. [156] deposited MnO_2 on g-C_3N_4 to form a Z-scheme photocatalyst that utilizes defects for the charge transfer. In this case low valence Mn cations in the MnO_2 allowed for transfer of the charge carriers between MnO_2 and g-C_3N_4. The material was capable of overall photocatalytic water splitting using visible light with a hydrogen evolution rate of 60.6 μmol h^{-1} g^{-1}.

In contrast to the defect photocatalysts, the direct Z-scheme photocatalysts show a higher performance for overall photocatalytic water splitting. Correspondingly more reports on the use of direct Z-schemes for photocatalytic water splitting can be found in the literature (see Table 24.3). The reported photocatalytic reaction rates range over two orders of magnitude making a direct comparison difficult. For example, She et al. [138] combined α-Fe_2O_3, a semiconductor known for its high recombination rate (see Table 24.1), with g-C_3N_4 to form a Z-scheme photocatalyst. In their work, they could not detect any activity towards hydrogen evolution for pure α-Fe_2O_3 even in the presence of triethanolamine as sacrificial agent. However, the Z-scheme photocatalyst showed activity for overall photocatalytic water splitting with a reaction rate of 38.2 μmol h^{-1} g^{-1}. This shows how Z-scheme catalysts can enhance the performance of semiconductors by facilitating charge carrier separation and thus lowering recombination. In another work, Yuan et al. [137] used Cu_7S_4 and γ-MnS as a Z-scheme photocatalyst. The material exhibits a photocatalytic activity of 209 μmol h^{-1} g^{-1} under full light spectrum and an AQE of 5.5% at 420 nm. With a band gap of 0.77 eV Cu_7S_4 absorbs a large part of the light spectrum, but is not capable for overall water splitting as the reaction would require a potential of 1.23 eV. This example demonstrates the capability of Z-schemes to overcome the restrictions for the light absorption in single semiconductor-based photocatalysts. Yang et al. [141] report an even higher photocatalytic activity using $WO_3 \cdot H_2O$/g-C_3N_4. The photocatalytic system reached a hydrogen evolution rate of 482 μmol h^{-1} g^{-1} under visible light ($\lambda > 420$ nm) and an AQE of 6.2% at 420 nm. The activity for hydrogen evolution is 4.4 times higher than that of pure g-C_3N_4 and the amount of evolved oxygen is fourfold that of pure $WO_3 \cdot H_2O$.

24.4.2 Hydrogen Generation from Sacrificial Agents

The photocatalytic activity for overall water splitting is often low compared to other photocatalytic reactions. Some catalysts are even inactive for this reaction, which can be due to a mismatch in the band position and the potential needed for the reaction (see Fig. 24.3), or high recombination rates and slow charge carrier transfer (see Table 24.1). Therefore, the photoreforming of inorganic and organic substances can be a viable alternative for the photocatalytic generation of hydrogen, as the oxidation reaction requires a lower potential and can, thus, more readily consume holes and prevents charge carrier recombination. Furthermore, in the conversion of sacrificial agents, a process called "current doubling" can occur in which unstable radicals are formed that can inject additional electrons into the CB of the photocatalyst. This effect results in an increased hydrogen evolution. However, this is not due to the action of electrons generated by light absorption of the semiconductor, but by the reaction of holes with the sacrificial agent. Therefore, the evolved hydrogen only originates in part from water while a considerable fraction of hydrogen is directly or indirectly formed from the sacrificial agent. Hence, the resulting activities should not be mistaken for water splitting [188, 189].

The reactions of sacrificial agents with an excited photocatalyst system can be categorized based on whether the sacrificial agent functions as an electron donor (ED), i.e., as oxidative quenching (Eq. 24.8), or as an electron acceptor (EA), i.e., as reductive quenching (Eq. 24.9). In the case of hydrogen evolution, only the oxidative quenching has to be considered, as the generation of hydrogen is a reductive process and consumers electrons. Typical reactions occurring in the presence of various sacrificial agents were recently reviewed by Kumaravel et al. [190].

$$\text{Oxidative Quenching} \quad PC^* + ED \rightarrow PC^- + ED^+ \tag{24.8}$$

$$\text{Reductive Quenching} \quad PC^* + EA \rightarrow PC^+ + EA^- \tag{24.9}$$

In consideration of the vast amount of sacrificial agents available, it should be noted that the suitability of sacrificial agents for a given photocatalyst may vary. For example, metal oxide photocatalysts tend to work well with alcohols, while metal sulfides often require Na_2S or Na_2SO_3 to prevent photo-corrosion, and g-C_3N_4 shows the highest activity in the presence of amines. The results of Wang et al. [191] indicate that the presence of similar functional groups in the photocatalyst and the sacrificial agent enhance the resulting photocatalytic activity for hydrogen evolution. In this respect, the following discussion will focus on alcohols and biomass-derived substrates as sacrificial agents.

24.4.2.1 Alcohols as Sacrificial Agents

When sacrificial agents are used, the photocatalytic activity strongly depends on the nature of the sacrificial agent. As Christoforidis and Fornasiero [192] pointed out, the structure and complexity of the sacrificial agents play an important role for the photocatalytic activity. In this regard, the presence of OH-groups in the sacrificial agent molecule may be beneficial due to enhanced chemical adsorption and transfer of holes. With respect to the complexity in the case of alcohols as sacrificial agents, it was observed that at high sacrificial agent concentrations the reactivity drops in the order primary > secondary > tertiary [193]. However, at low concentrations the trend is inverted [194]. This behavior was linked to the polarity of the different alcohols, the acidity of the respective OH-groups in the alcohols, and steric hindrance due to the size of the molecules.

However, it needs to be mentioned that the activity for hydrogen generation form sacrificial agents depends in addition on other factors like the pH-value, reactant concentration, and utilized co-catalyst. Often this is due to the formation of intermediate products that differ in their reactivity. Shiragami et al. [195] have shown that the molecular structure is highly important when using alcohols as the products of polyols with discontinuous hydroxyl groups along the carbon chain and longer-chain alcohols carrying only one hydroxyl group were often stable and did not lead to the formation of CO_2 and H_2, thus limiting the photocatalytic hydrogen evolution. This fact led to the development of a different process strategy in which the photocatalytic generation of hydrogen is linked to the formation of value-adding chemicals by selective oxidation of organic compounds. This strategy will be addressed in Sect. 24.4.2.2, as it is more relevant for the conversion of biomass-derived molecules.

The most often used alcohol in photocatalytic hydrogen evolution is methanol. From an economic perspective, methanol currently offers the lowest cost per consumed hole [196]. The reaction of methanol can, in principle, occur via two pathways either involving the direct transfer of a hole to methanol or the indirect oxidation via $^{\bullet}OH$ formed by the oxidation of adsorbed water molecules. Guzman et al. [197] investigated the reaction on TiO_2 (S-doped with Cu co-catalyst) with the help of isotope labeling experiments, from which they concluded that the indirect oxidation via $^{\bullet}OH$ shown in Eqs. (24.10–24.15) dominates the photocatalytic conversion of methanol [].

$$H_2O + h^+ \rightarrow {}^{\bullet}OH + H^+ \tag{24.10}$$

$$CH_3OH + {}^{\bullet}OH \rightarrow {}^{\bullet}CH_2OH + H_2O \tag{24.11}$$

$$^{\bullet}CH_2OH \rightarrow HCHO + H^+ + e^- \tag{24.12}$$

$$2H^+ + 2e^- \rightarrow H_2 \tag{24.13}$$

$$HCHO + H_2O \rightarrow HCOOH + H_2 \tag{24.14}$$

$$HCOOH \rightarrow CO_2 + H_2 \tag{24.15}$$

The conversion of methanol proceeds via formaldehyde and formic acid as intermediate products to CO_2 and H_2. It is important to notice that for TiO_2 in the absence of oxygen, the reaction only proceeds to HCHO and no electron injection into the CB occurs [189].

$$CH_3OH \rightarrow HCHO + H_2 \quad \Delta G^{\emptyset} = +64.1\ \text{kJ mol}^{-1} \tag{24.16}$$

$$HCHO + H_2O \rightarrow HCOOH + H_2 \quad \Delta G^{\emptyset} = +47.8\ \text{kJ mol}^{-1} \tag{24.17}$$

$$HCOOH \rightarrow CO_2 + H_2 \quad \Delta G^{\emptyset} = -95.8\ \text{kJ mol}^{-1} \tag{24.18}$$

$$CH_3OH + H_2O \rightarrow CO_2 + 3H_2 \quad \Delta G^{\emptyset} = +16.1\ \text{kJ mol}^{-1} \tag{24.19}$$

From the viewpoint of energy storage of light in form of chemical energy, the overall process (Eq. 24.19) can only store 16.1 kJ mol^{-1} which is an order of magnitude lower than in overall photocatalytic water splitting (237 kJ mol^{-1}). While the formation of intermediate reaction products (Eqs. 24.16 and 24.17) requires energy, the final conversion to CO_2 (Eq. 24.18) is a thermodynamically favorable reaction with a large negative Gibbs energy. On the other side, the formation of CO_2 as an energy sink acts as a barrier for the undesired backwards reaction [189].

24.4.2.2 Biomass-Derived Substrates as Sacrificial Agents

Biomass is regarded as a promising and abundant resource for the production of renewable energy and chemicals. Its conversion and upgrading are expected to play an important role in the transition of the current chemical and energy-producing industries towards a more sustainable future. Recently, biomass has also found its way into the field of photochemistry. With respect to hydrogen generation, two routes have been established. This is, on the one side, photoreforming similar to the already presented use of alcohols as sacrificial agents (Sect. 24.4.2.1), and on the other side the so-called photobiorefinery approach in which biomass-derived chemicals are selectively converted to value-added products.

Looking at photoreforming of biomass, both raw biomass and already refined feedstocks have been used to generate hydrogen photocatalytically. Huang et al. [198] have summarized the different compounds used so far and noted that with refined feedstocks higher rates for hydrogen generation due to the higher solubility compared to raw biomass are achieved. However, as most biomass-derived substrates are valuable chemicals themselves, the use of crude feedstocks or even raw biomass should be preferred, if only used for hydrogen generation. In this respect, the further discussion will focus on selected results dealing with the conversion of glycerol and lignocellulose. For the conversion of raw biomass, the reader may refer to the reviews of Kuehnel and Reisner [199] and Huang et al. [198].

In contrast to other biomass-derived substrates, glycerol is a by-product of biodiesel and vegetable oil production with limited use and thus available in vast amounts making it an ideal candidate for use as sacrificial agent. Lakshmana Reddy et al. [200] have summarized the most important studies available on glycerol photoreforming. The reaction follows a mechanism similar to that of other alcohols and proceeds via the formation of radical species leading to the formation of glyceraldehyde as an intermediate product, which is then converted to a CO radical before finally resulting in the formation of CO_2. The overall reaction can be summarized according to Eq. (24.20). Reddy et al. [201] have compared glycerol with other sacrificial agents (methanol, ethanol, ethylene glycol) and have shown that the use of activity drops in the order glycerol > ethylene glycol > ethanol > methanol, which was attributed to the polarity of the different molecules. Additionally, they also used crude glycerol for photoreforming, which resulted in a three times lower hydrogen evolution rate (H_2 from crude glycerol 15.5 mmol g^{-1} h^{-1}; H_2 from glycerol 48.0 mmol g^{-1} h^{-1}). This observation is likely due to residues of the industrial process like long-chain fatty acids. However, the activity is still comparable to the use of methanol (16.1 mmol h^{-1} g^{-1}), which makes glycerol a promising sacrificial agent for hydrogen generation.

$$C_3H_8O_3 + 3H_2O \rightarrow 7H_2 + 3CO_2 \quad \Delta G^{\emptyset} = +5.3\ \text{kJ mol}^{-1} \tag{24.20}$$

The most abundant form of biomass is lignocellulose, which is like glycerol mostly a waste product and therefore an interesting compound for photoreforming in the aqueous phase. The use of lignocellulose in photocatalysis has been recently reviewed in depth by Liu et al. [202] and with the focus on hydrogen generation by Kuehnel and Reisner [199]. As lignocellulose is a complex mixture of cellulose, hemicellulose, and lignin, the full conversion to CO_2 and H_2 is difficult and has so far not been achieved. In this context, especially the complex chemical structure of the feedstock poses a particular challenge for the photoreforming process. Therefore, lignocellulose is the ideal candidate for the photobiorefinery concept, which has just recently been reviewed in great detail by Butburee et al. [203]. In this concept, biomass is converted photocatalytically to useful products including a wide range from aromatic compounds, carbonyl compounds, and alcohols to H_2 and CO. Often the lignocellulose is digested in a pretreatment step into its major compounds, which are then further converted via photocatalytic reaction. While lignin and hemicellulose typically results in the formation of a wide spectrum of aromatic compounds, cellulose can be converted fully or partially into hydrogen [202]. In this regard the work of Wakerley et al. [204] needs to be highlighted. They converted unprocessed lignocellulose from different sources into H_2 using a CdS/CdO_x photocatalyst under AM 1.5G irradiation with a photocatalytic activity of up to ~5.3 mmol g^{-1} h^{-1}. They explain these results with a combination of the employed in-situ digestion via basic treatment, the wide light absorption of the CdS core and the protection against photocatalyst degradation by the CdO_x shell. Their results show, that even unprocessed lignocellulose might be an effective sacrificial agent for a sustainable photocatalytic hydrogen generation.

24.4.2.3 Other Sacrificial Agents

In the discussion of photoreforming for hydrogen generation, other sacrificial agents besides the already discussed alcohols and biomass-derived substrates must be considered as well. Pellegrin and Odobel [205] have extensively reviewed the already investigated organic compounds that are used in the context of solar fuel production. A detailed discussion on the photocatalytic hydrogen evolution using Na_2S and Na_2SO_3, the most commonly used inorganic sacrificial agents, can be found in the work of Li et al. [206].

24.4.2.4 Semiconductor Performance in Hydrogen Generation from Sacrificial Agents

In a previous Sect. (24.4.1.2) the performance of photocatalysts capable of overall photocatalytic water splitting was already discussed. Thus, this section is concerned with photocatalytic systems that are used for hydrogen generation in combination with an additional compound other than water and the photocatalyst itself. We will again mainly rely on the reaction rate and the AQE to compare different photocatalytic systems. An overview of the performance of defect engineered photocatalysts (Table 24.2, Sect. 24.3.1.3), direct Z-schemes (Table 24.3, Sect. (i)), or a combination of both (Table 24.4, Sect. (ii)) can be found in the tables presented in the respective sections.

In contrast to overall photocatalytic water splitting the reported photocatalytic hydrogen evolution rates in photoreforming cover a range of several orders of magnitude from the lower micromolar range up to tens of millimoles. Due to differences in experimental conditions a direct comparison is however difficult. Nevertheless, it shows that the presence of co-catalysts in addition to the presented design strategies often remains necessary to obtain H_2 evolution rates above 1 mmol h^{-1} g^{-1}. Interestingly, many of the studies referred to in Tables 24.2–24.4 use visible or simulated solar light for their photocatalytic reactions with the highest reported activity, both for defect engineered and Z-scheme-based materials, for photocatalysts without an additional co-catalyst. In this respect, the highest reported H_2 evolution rate we found for defect containing photocatalysts and Z-scheme-based photocatalysts were 31.3 mmol g^{-1} h^{-1} for a NiS@g-C_3N_4 photocatalyst [97] and 38.93 mmol g^{-1} h^{-1} for $Zn_{0.67}Cd_{0.33}S$/ZnO photocatalyst [148] respectively. In this respect, both design strategies seem to be comparable in terms of enhancing photocatalytic activity of photoreforming for hydrogen generation.

Even though many studies focus on the utilization of visible or solar light, occasionally lamps without restriction of the light spectrum are used. This can enhance the observed photocatalytic activity, as more photons with suitable energy are introduced into the system. For example Pan et al. [102] used defective TiO_2 with a Pt co-catalyst in combination with a 300 W Xe-arc lamp. They reported a photocatalytic reaction rate for methanol photoreforming of 50.3 mmol h^{-1} g^{-1}.

Closely connected to the pure amount of hydrogen evolved is the utilization of the incident light, often expressed in terms of AQE, which gives the ratio of the number of reacted electrons over the number of incident photons. One of the main advantages of both defects engineered and Z-scheme-based photocatalysts are the extension of the usable light spectrum and the efficient use of the generated charge carriers for a given photocatalytic reaction. This can be seen for example in the work of She et al. [148]. The Z-scheme comprised of $Zn_{0.67}Cd_{0.33}S$ solid solution and ZnO nanoparticles reached an AQE of 40.97% at 420 nm, which was 2.2 times higher than of the pure solid solution. In another example She et al. [138] demonstrated for α-Fe_2O_3/g-C_3N_4 an AQE of 44.35% at 420 nm. Considering the limitations of low charge carrier lifetime and diffusion length (see Table 24.1) typically present in α-Fe_2O_3 this work shows the capabilities of Z-scheme construction for the enhancement of the photocatalytic activity. On a side note it should be mentioned that due to the charge carrier transfer mode in Z-scheme systems half of the electrons are lost due to recombination, thus theoretically limiting the AQE to 50%, if effects like current doubling are neglected.

Likewise, Yu et al. [109] reported for defect engineered $Zn_{1-x}Cd_xS$ on SiO_2 containing sulfur vacancies an AQE of 48.6% at 420 nm. In addition, Li et al. [82] reported an AQE of 76.2% at 365 nm for mesoporous black TiO_2 containing O-vacancies and Ti^{3+}-cations. However, at 420 nm the AQE dropped to 8.4%, correlating with the band gap shift to 2.93 eV (423 nm) induced by the defects present within the material. Another example showing the capabilities to increase or even induce photocatalytic activity using defect engineering was published by Sinhamahapatra et al. [110] on ZrO_2. They introduced O-vacancies and Zr^{3+}-cation point defects by Mg-treatment in combination with high-temperature Ar/H_2-treatment. The resulting material had a band gap of 1.52 eV and was active for hydrogen evolution (0.505 mmol g^{-1} h^{-1}) under simulated solar light by photoreforming of methanol due to the extension of light absorption.

In contrast, several studies [85, 87, 88] based on defect-engineered black TiO_2 for photoreforming of methanol show that the extension of the light absorption to the whole visible range induced by the increased defect density does not correlate with the visible light photocatalytic activity. For example, Sinhamahapatra et al. [85] obtained a remarkable activity of 43 mmol g^{-1} h^{-1} using the full solar spectrum, while the activity dropped to 0.440 mmol h^{-1} g^{-1} when the lamp spectrum was limited to the range of 400–780 nm. This behavior was attributed to increased charge carrier recombination. Similar, Tan et al. [87] reported a decrease in activity in black TiO_2 from 6.5 mmol g^{-1} h^{-1} under UV/visible light irradiation with a

300 W Xe lamp to 0.180 mmol g^{-1} h^{-1} when the light spectrum was cut off below 400 nm. These studies illustrate the importance of the balance between activity increase and recombination in defect engineering. But they also show the limitations for enhancement of the photocatalytic activity by extension of the light absorption, especially in materials with high defect concentration.

24.5 Conclusions and Perspectives

Hydrogen is a valuable option for the contemporary challenge of energy transition and a sustainable, carbon–neutral chemical industry. In this respect, photocatalysis might play a vital role, as it allows to utilize light as an energy source. In contrast to conventional heterogeneous catalysis, the efficiency, both from the economic and the reaction perspective, remains a major challenge in photocatalyzed reactions. As a result, semiconductor photocatalysts are now available in a large variety of compositions to overcome major obstacles like limited stability and activity. Over time and driven by the desire to create more active photocatalysts, large parts of the scientific work has focused on the development and continuous improvement of a wide range of design strategies for solid photocatalysts. A major point of most material design strategies is to enhance light absorption for increasing the density of generated excited charge carriers and to prevent their recombination. As the trend goes to multi-component photocatalysts, design strategies can be expected to become more complex and include a combination of approaches towards the preparation of new types of photocatalysts. The design strategies introduced in this chapter provide examples, how such combinations might be achieved. Certainly, however, other strategy combinations, like the connection of Z-schemes or defects to heterojunctions hold promise for future developments.

Also, the comparison of different catalysts remains difficult, as the conditions for photocatalytic reactions are often not comparable and existing figures of merit can only partly represent the differences of the photocatalysts. An agreement on how to reliably carry out and report photocatalytic data would help in this respect.

Despite the large number of studies dedicated to the overall photocatalytic water splitting reaction, the reported activity towards hydrogen generation is so far still rather low and falls significantly behind those of photoreforming. However, a direct comparison reveals that the oxygen evolution reaction (OER) is typically the limiting reaction step for the photocatalytic water splitting reaction. Therefore, the OER has to move closer into the focus of current research efforts and should receive more attention in the further development of solid photocatalysts.

One of the key challenges remaining in photoreforming for hydrogen generation from aqueous phases is the cost, availability, and sustainability of converted substrates, as these are major driving factors for the economical supply of hydrogen via this process. However, this also provides an opportunity for new concepts such as the photo-biorefinery, which target the conversion of chemicals available from renewable feedstocks like biomass in its various forms or waste from the food or paper processing industry.

Moreover, the number of tools available to study photocatalytic reactions has increased. New techniques like the (time-resolved) transient absorption spectroscopy or in-situ and operando spectroscopy have been developed. But also, the growing use of computational methods to study aspects like the formation of electric fields inside solid photocatalysts, which are hardly explored by experimental techniques, will contribute to a deeper understanding of photocatalysts and photocatalytic reactions.

In addition, biocatalysts like living cells or enzymes, as well as hybrid materials combining semiconductors with bio-based materials are an emerging field for photocatalytic hydrogen generation from aqueous media. Also, other interdisciplinary processes like photo-electrochemical hydrogen generation will be important in the future of this research field and will likely contribute to the understanding of existing and the development of new photocatalysts. Vice versa the implementation of photocatalysts as electrode materials should be considered in the fields of electro- and photo-electrocatalysis. Without doubt, hydrogen generation via photocatalysis may develop into a sustainable pathway in addition to those based on direct application of electro(cata)lytic water splitting, if (and when) more active catalysts can be identified and prepared.

References

1. Takanabe K (2016) Solar water splitting using semiconductor photocatalyst powders. Top Curr Chem 371:73–103. https://doi.org/10.1007/128_2015_646
2. Takanabe K (2017) Photocatalytic water splitting: quantitative approaches toward photocatalyst by design. ACS Catal 7:8006–8022. https://doi.org/10.1021/acscatal.7b02662
3. Nurlaela E, Ziani A, Takanabe K (2016) Tantalum nitride for photocatalytic water splitting: concept and applications. Mater Renew Sustain Energy 5:1–21. https://doi.org/10.1007/s40243-016-0083-z
4. Kudo A, Miseki Y (2009) Heterogeneous photocatalyst materials for water splitting. Chem Soc Rev 38:253–278. https://doi.org/10.1039/b800489g
5. Inoue Y (2009) Photocatalytic water splitting by RuO_2-loaded metal oxides and nitrides with d0- and d10 -related electronic configurations. Energy Environ Sci 2:364. https://doi.org/10.1039/B816677N
6. Wang Q, Domen K (2020) Particulate Photocatalysts for Light-Driven Water Splitting: Mechanisms, Challenges, and Design Strategies. Chem Rev 120:919–985. https://doi.org/10.1021/acs.chemrev.9b00201
7. Zhang L, Ran J, Qiao S-Z et al (2019) Characterization of semiconductor photocatalysts. Chem Soc Rev 48:5184–5206. https://doi.org/10.1039/c9cs00172g
8. Li J, Wu N (2015) Semiconductor-based photocatalysts and photoelectrochemical cells for solar fuel generation: a review. Catal Sci Technol 5:1360–1384. https://doi.org/10.1039/C4CY00974F
9. Marschall R (2014) Semiconductor composites: strategies for enhancing charge carrier separation to improve photocatalytic activity. Adv Funct Mater 24:2421–2440. https://doi.org/10.1002/ADFM.201303214

10. Grundmann M (2016) The physics of semiconductors: an introduction including nanophysics and applications, Third edn. Graduate Texts in Physics. Springer, Cham, Heidelberg, New York, Dordrecht, London
11. Abdi FF, Savenije TJ, May MM et al (2013) The origin of slow carrier transport in $BiVO_4$ thin film photoanodes: a time-resolved microwave conductivity study. J Phys Chem Lett 4:2752–2757. https://doi.org/10.1021/JZ4013257
12. de Respinis M, Fravventura M, Abdi FF et al (2015) Oxynitrogenography: controlled synthesis of single-phase tantalum oxynitride photoabsorbers. Chem Mater 27:7091–7099. https://doi.org/10.1021/acs.chemmater.5b02938
13. Zhou Y, Chen G, Liu Y et al (2016) Surface natrotantite phase induced efficient charge carrier separation and highly active surface of TaON for superior enhanced photocatalytic performance. Adv Mater Interfaces 3:1600429. https://doi.org/10.1002/admi.201600429
14. Gardner RFG, Sweett F, Tanner DW (1963) The electrical properties of alpha ferric oxide—II. J Phys Chem Solids 24:1183–1196. https://doi.org/10.1016/0022-3697(63)90235-X
15. Morin FJ (1954) Electrical properties of α-Fe_2O_3. Phys Rev 93:1195–1199. https://doi.org/10.1103/PHYSREV.93.1195
16. Joly AG, Williams JR, Chambers SA et al (2006) Carrier dynamics in α-Fe_2O_3 (0001) thin films and single crystals probed by femtosecond transient absorption and reflectivity. J Appl Phys 99:53521. https://doi.org/10.1063/1.2177426
17. Mulmudi HK, Mathews N, Dou XC et al (2011) Controlled growth of hematite (α-Fe_2O_3) nanorod array on fluorine doped tin oxide: synthesis and photoelectrochemical properties. Electrochem commun 13:951–954. https://doi.org/10.1016/j.elecom.2011.06.008
18. Ziani A, Nurlaela E, Dhawale DS et al (2015) Carrier dynamics of a visible-light-responsive Ta_3N_5 photoanode for water oxidation. Phys Chem Chem Phys 17:2670–2677. https://doi.org/10.1039/c4cp05616g
19. Rettie AJE, Lee HC, Marshall LG et al (2013) Combined charge carrier transport and photoelectrochemical characterization of $BiVO_4$ single crystals: intrinsic behavior of a complex metal oxide. J Am Chem Soc 135:11389–11396. https://doi.org/10.1021/ja405550k
20. Pala RA, Leenheer AJ, Lichterman M et al (2014) Measurement of minority-carrier diffusion lengths using wedge-shaped semiconductor photoelectrodes. Energy Environ Sci 7:3424–3430. https://doi.org/10.1039/C4EE01580K
21. Henderson MA (2011) A surface science perspective on TiO_2 photocatalysis. Surf Sci Rep 66:185–297. https://doi.org/10.1016/J.SURFREP.2011.01.001
22. Kato M, Kohama K, Ichikawa Y et al (2015) Carrier lifetime measurements on various crystal faces of rutile TiO single crystals. Mater Lett 160:397–399. https://doi.org/10.1016/j.matlet.2015.08.018
23. Yamada Y, Kanemitsu Y (2012) Determination of electron and hole lifetimes of rutile and anatase TiO_2 single crystals. Appl Phys Lett 101:133907. https://doi.org/10.1063/1.4754831
24. Trier F, Christensen DV, Pryds N (2018) Electron mobility in oxide heterostructures. J Phys D Appl Phys 51:293002. https://doi.org/10.1088/1361-6463/AAC9AA
25. Yamakata A, Vequizo JJM, Kawaguchi M (2015) Behavior and energy state of photogenerated charge carriers in single-crystalline and polycrystalline powder $SrTiO_3$ studied by time-resolved absorption spectroscopy in the visible to mid-infrared region. J Phys Chem C 119:1880–1885. https://doi.org/10.1021/jp510647b
26. Kennedy JH, Frese KW (1978) Photooxidation of water at α-Fe_2O_3 electrodes. J Electrochem Soc 125:709–714. https://doi.org/10.1149/1.2131532
27. Butler MA (1977) Photoelectrolysis and physical properties of the semiconducting electrode WO_2. J Appl Phys 48:1914–1920. https://doi.org/10.1063/1.323948
28. Lin R, Wan J, Xiong Y et al (2018) Quantitative study of charge carrier dynamics in well-defined WO_3 nanowires and nanosheets: insight into the crystal facet effect in photocatalysis. J Am Chem Soc 140:9078–9082. https://doi.org/10.1021/jacs.8b05293
29. Xiao T, Tang Z, Yang Y et al (2018) In situ construction of hierarchical WO_3/g-C_3N_4 composite hollow microspheres as a Z-scheme photocatalyst for the degradation of

antibiotics. Appl Catal B (Applied Catalysis B: Environmental) 220:417–428. https://doi.org/10.1016/j.apcatb.2017.08.070

30. Forro L, Chauvet O, Emin D et al (1994) High mobility n-type charge carriers in large single crystals of anatase (TiO_2). J Appl Phys 75:633–635. https://doi.org/10.1063/1.355801
31. Era K, Katayama H, Shionoya S (1968) Drift mobilities of electrons and holes in ZnS crystals. J Phys Soc Jpn 24:1180–1181. https://doi.org/10.1143/JPSJ.24.1180
32. Zhang X, Fang H, Tang S et al (1997) Determination of two-photon-generated free-carrier lifetime in semiconductors by a single-beam Z-scan technique. Appl Phys B 65:549–554. https://doi.org/10.1007/s003400050312
33. Spear WE, Mort J (1963) Electron and hole transport in CdS crystals. Proc Phys Soc 81:130–140. https://doi.org/10.1088/0370-1328/81/1/319
34. Bradberry GW, Spear WE (1964) Electron mobility and edge emission in CdS crystals. Br J Appl Phys 15:1127–1129. https://doi.org/10.1088/0508-3443/15/9/419
35. Li HP, Kam CH, Lam YL et al (2001) Optical nonlinearities and photo-excited carrier lifetime in CdS at 532 nm. Opt Commun 190:351–356. https://doi.org/10.1016/S0030-4018(01)01066-5
36. Oakes JJ, Greenfield IG, Partain LD (1977) Diffusion length determination in thin-film CuxS/CdS solar cells by scanning electron microscopy. J Appl Phys 48:2548–2555. https://doi.org/10.1063/1.323971
37. Özgür Ü, Alivov YI, Liu C et al (2005) A comprehensive review of ZnO materials and devices. J Appl Phys 98:41301. https://doi.org/10.1063/1.1992666
38. Yang X, Xu C, Giles NC (2008) Intrinsic electron mobilities in CdSe, CdS, ZnO, and ZnS and their use in analysis of temperature-dependent Hall measurements. J Appl Phys 104:73727. https://doi.org/10.1063/1.2996032
39. Zhang XJ, Ji W, Tang SH (1997) Determination of optical nonlinearities and carrier lifetime in ZnO. J Opt Soc Am B 14:1951. https://doi.org/10.1364/JOSAB.14.001951
40. Hwang J-S, Donatini F, Pernot J et al (2011) Carrier depletion and exciton diffusion in a single ZnO nanowire. Nanotechnology 22:475704. https://doi.org/10.1088/0957-4484/22/47/475704
41. Lopatiuk O, Chernyak L, Osinsky A et al (2005) Electron-beam-induced current and cathodoluminescence studies of thermally activated increase for carrier diffusion length and lifetime in n-type ZnO. Appl Phys Lett 87:162103. https://doi.org/10.1063/1.2106001
42. Gueymard C (1995) SMARTS2, a simple model of the atmospheric radiative transfer of sunshine: algorithms and performance assessment. Florida Solar Energy Center, Florida
43. López R, Gómez R (2012) Band-gap energy estimation from diffuse reflectance measurements on sol-gel and commercial TiO_2: a comparative study. J Sol-Gel Sci Technol 61:1–7. https://doi.org/10.1007/s10971-011-2582-9
44. Rahman MZ, Mullins CB (2019) Understanding charge transport in carbon nitride for enhanced photocatalytic solar fuel production. Acc Chem Res 52:248–257. https://doi.org/10.1021/acs.accounts.8b00542
45. Ravensbergen J, Abdi FF, van Santen JH et al (2014) Unraveling the carrier dynamics of $BiVO_4$: a femtosecond to microsecond transient absorption study. J Phys Chem C 118:27793–27800. https://doi.org/10.1021/jp509930s
46. Suzuki Y, Murthy DHK, Matsuzaki H et al (2017) Rational interpretation of correlated kinetics of mobile and trapped charge carriers: analysis of ultrafast carrier dynamics in $BiVO_4$. J Phys Chem C 121:19044–19052. https://doi.org/10.1021/acs.jpcc.7b05574
47. Selim S, Pastor E, García-Tecedor M et al (2019) Impact of oxygen vacancy occupancy on charge carrier dynamics in $BiVO_4$ photoanodes. J Am Chem Soc 141:18791–18798. https://doi.org/10.1021/jacs.9b09056
48. Wheeler DA, Wang G, Ling Y et al (2012) Nanostructured hematite: synthesis, characterization, charge carrier dynamics, and photoelectrochemical properties. Energy Environ Sci 5:6682. https://doi.org/10.1039/C2EE00001F
49. Schneider J, Matsuoka M, Takeuchi M et al (2014) Understanding TiO_2 photocatalysis: mechanisms and materials. Chem Rev 114:9919–9986. https://doi.org/10.1021/cr5001892

50. Kohtani S, Kawashima A, Miyabe H (2017) Reactivity of trapped and accumulated electrons in titanium dioxide photocatalysis. Catalysts 7:303. https://doi.org/10.3390/catal7100303
51. Böer KW, Pohl UW (eds) (2019) Semiconductor physics. Springer International Publishing, Cham
52. Kao KC (2004) Optical and electro-optic processes. In: Dielectric phenomena in solids. Elsevier, pp 115–212
53. Shockley W, Read WT (1952) Statistics of the recombinations of holes and electrons. Phys Rev 87:835–842. https://doi.org/10.1103/PHYSREV.87.835
54. Hall RN (1952) Electron-hole recombination in Germanium. Phys Rev 87:387. https://doi.org/10.1103/PHYSREV.87.387
55. Ohtani B (2013) Titania photocatalysis beyond recombination: a critical review. Catalysts 3:942–953. https://doi.org/10.3390/catal3040942
56. Jin H, Debroye E, Keshavarz M et al (2020) It's a trap! On the nature of localised states and charge trapping in lead halide perovskites. Mater Horiz 7:397–410. https://doi.org/10.1039/C9MH00500E
57. Micic OI, Zhang Y, Cromack KR et al (1993) Trapped holes on titania colloids studied by electron paramagnetic resonance. J Phys Chem 97:7277–7283. https://doi.org/10.1021/j100130a026
58. Pattengale B, Huang J (2017) Implicating the contributions of surface and bulk states on carrier trapping and photocurrent performance of $BiVO_4$ photoanodes. Phys Chem Chem Phys 19:6831–6837. https://doi.org/10.1039/c6cp08564d
59. Wang X, Feng Z, Shi J et al (2010) Trap states and carrier dynamics of TiO_2 studied by photoluminescence spectroscopy under weak excitation condition. Phys Chem Chem Phys 12:7083–7090. https://doi.org/10.1039/b925277k
60. Guo Q, Zhou C, Ma Z et al (2019) Fundamentals of TiO_2 photocatalysis: concepts, mechanisms, and challenges. Adv Mater 31:e1901997. https://doi.org/10.1002/adma.201901997
61. Qian R, Zong H, Schneider J et al (2019) Charge carrier trapping, recombination and transfer during TiO_2 photocatalysis: an overview. Catal Today 335:78–90. https://doi.org/10.1016/j.cattod.2018.10.053
62. Tang J, Durrant JR, Klug DR (2008) Mechanism of photocatalytic water splitting in TiO_2. Reaction of water with photoholes, importance of charge carrier dynamics, and evidence for four-hole chemistry. J Am Chem Soc 130:13885–13891. https://doi.org/10.1021/ja8034637
63. Creutz C, Brunschwig BS, Sutin N (2006) Interfacial charge-transfer absorption: 3. Application to semiconductor-molecule assemblies. J Phys Chem B 110:25181–25190. https://doi.org/10.1021/jp063953d
64. Bertoluzzi L, Lopez-Varo P, Jiménez Tejada JA et al (2016) Charge transfer processes at the semiconductor/electrolyte interface for solar fuel production: insight from impedance spectroscopy. J Mater Chem A 4:2873–2879. https://doi.org/10.1039/C5TA03210E
65. Wang Y, Wang Q, Zhan X et al (2013) Visible light driven type II heterostructures and their enhanced photocatalysis properties: a review. Nanoscale 5:8326–8339. https://doi.org/10.1039/c3nr01577g
66. Ding Y, Wei D, He R et al (2019) Rational design of Z-scheme PtS-$ZnIn_2S_4$/WO_3-MnO_2 for overall photo-catalytic water splitting under visible light. Appl Catal B (Applied Catalysis B: Environmental) 258:117948. https://doi.org/10.1016/j.apcatb.2019.117948
67. Liu Y, Zhou Y, Yu S et al (2020) Defect state assisted Z-scheme charge recombination in $Bi_2O_2CO_3$/graphene quantum dot composites for photocatalytic oxidation of NO. ACS Appl Nano Mater 3:772–781. https://doi.org/10.1021/ACSANM.9B02276
68. Bai S, Zhang N, Gao C et al (2018) Defect engineering in photocatalytic materials. Nano Energy 53:296–336. https://doi.org/10.1016/j.nanoen.2018.08.058
69. Dong B, Liu T, Li C et al (2018) Species, engineering and characterizations of defects in TiO_2-based photocatalyst. Chin Chem Lett 29:671–680. https://doi.org/10.1016/j.cclet.2017.12.002

70. Ran L, Hou J, Cao S et al (2020) Defect engineering of photocatalysts for solar energy conversion. Sol RRL 2241:1900487. https://doi.org/10.1002/solr.201900487
71. Liu J, Wei Z, Shangguan W (2019) Defects engineering in photocatalytic water splitting materials. ChemCatChem 11:6177–6189. https://doi.org/10.1002/cctc.201901579
72. Su Z, Liu J, Li M et al (2020) Defect engineering in titanium-based oxides for electrochemical energy storage devices. Electrochem Energ Rev 7:321. https://doi.org/10.1007/s41918-020-00064-5
73. Maarisetty D, Baral SS (2020) Defect engineering in photocatalysis: formation, chemistry, optoelectronics, and interface studies. J Mater Chem A 8:18560–18604. https://doi.org/10.1039/D0TA04297H
74. Tilley RJD (2013) Understanding solids: the science of materials, 2nd edn. John Wiley & Sons Inc., Chichester, West Sussex, United Kingdom
75. Ibach H, Lüth H (2009) Solid-state physics: an introduction to principles of materials science, 4, extensively updated and enl. ed. Physics and astronomy online library. Springer, Dordrecht
76. Yang Q, Dong L, Su R et al (2019) Nanostructured heterogeneous photo-catalysts for hydrogen production and water splitting: a comprehensive insight. Appl Mater Today 17:159–182. https://doi.org/10.1016/j.apmt.2019.07.016
77. Di J, Xia J, Chisholm MF et al (2019) Defect-tailoring mediated electron-hole separation in single-unit-cell Bi_3O_4Br nanosheets for boosting photocatalytic hydrogen evolution and nitrogen fixation. Adv Mater 31:e1807576. https://doi.org/10.1002/adma.201807576
78. Zhang L, Han Z, Wang W et al (2015) Solar-light-driven pure water splitting with ultrathin BiOCl nanosheets. Chemistry 21:18089–18094. https://doi.org/10.1002/chem.201503778
79. Wang Z, Yang C, Lin T et al (2013) Visible-light photocatalytic, solar thermal and photoelectrochemical properties of aluminium-reduced black titania. Energy Environ Sci 6:3007. https://doi.org/10.1039/c3ee41817k
80. Zhou W, Li W, Wang J-Q et al (2014) Ordered mesoporous black TiO(2) as highly efficient hydrogen evolution photocatalyst. J Am Chem Soc 136:9280–9283. https://doi.org/10.1021/ja504802q
81. Negi SS (2019) Enhanced light harvesting and charge separation over wormhole mesoporous $TiO_2{-}X$ nanocrystallites towards efficient hydrogen generation. Sustain Energy Fuels 3:1191–1200. https://doi.org/10.1039/C8SE00580J
82. Li H, Sun B, Yang F et al (2019) Homojunction and defect synergy-mediated electron–hole separation for solar-driven mesoporous rutile/anatase TiO_2 microsphere photocatalysts. RSC Adv 9:7870–7877. https://doi.org/10.1039/C9RA00633H
83. Lu H, Zhao B, Pan R et al (2014) Safe and facile hydrogenation of commercial Degussa P25 at room temperature with enhanced photocatalytic activity. RSC Adv 4:1128–1132. https://doi.org/10.1039/C3RA44493G
84. Zhang K, Zhou W, Zhang X et al (2016) Large-scale synthesis of stable mesoporous black TiO_2 nanosheets for efficient solar-driven photocatalytic hydrogen evolution via an earth-abundant low-cost biotemplate. RSC Adv 6:50506–50512. https://doi.org/10.1039/C6RA06751D
85. Sinhamahapatra A, Jeon J-P, Yu J-S (2015) A new approach to prepare highly active and stable black titania for visible light-assisted hydrogen production. Energy Environ Sci 8:3539–3544. https://doi.org/10.1039/C5EE02443A
86. Wang Z, Yang C, Lin T et al (2013) H-Doped black titania with very high solar absorption and excellent photocatalysis enhanced by localized surface plasmon resonance. Adv Funct Mater 23:5444–5450. https://doi.org/10.1002/adfm.201300486
87. Tan H, Zhao Z, Niu M et al (2014) A facile and versatile method for preparation of colored TiO_2 with enhanced solar-driven photocatalytic activity. Nanoscale 6:10216–10223. https://doi.org/10.1039/c4nr02677b
88. Zhao Z, Tan H, Zhao H et al (2014) Reduced TiO_2 rutile nanorods with well-defined facets and their visible-light photocatalytic activity. Chem Commun 50:2755–2757. https://doi.org/10.1039/c3cc49182j

89. Tian J, Hu X, Yang H et al (2016) High yield production of reduced TiO_2 with enhanced photocatalytic activity. Appl Surf Sci 360:738–743. https://doi.org/10.1016/j.apsusc.2015.11.056
90. Liu N, Häublein V, Zhou X et al (2015) "Black" TiO_2 nanotubes formed by high-energy proton implantation show Noble-Metal-co-Catalyst free photocatalytic H_2-evolution. Nano Lett 15:6815–6820. https://doi.org/10.1021/acs.nanolett.5b02663
91. Chen X, Liu L, Yu PY et al (2011) Increasing solar absorption for photocatalysis with black hydrogenated titanium dioxide nanocrystals. Science 331:746–750. https://doi.org/10.1126/science.1200448
92. Cai J, Cao A, Huang J et al (2020) Understanding oxygen vacancies in disorder-engineered surface and subsurface of $CaTiO_3$ nanosheets on photocatalytic hydrogen evolution. Appl Catal B (Applied Catalysis B: Environmental) 267:118378. https://doi.org/10.1016/j.apcatb.2019.118378
93. Yu H, Shi R, Zhao Y et al (2017) Alkali-assisted synthesis of nitrogen deficient graphitic carbon nitride with tunable band structures for efficient Visible-Light-Driven hydrogen evolution. Adv Mater 29. https://doi.org/10.1002/adma.201605148
94. Kang Y, Yang Y, Yin L-C et al (2015) An amorphous carbon nitride photocatalyst with greatly extended visible-light-responsive range for photocatalytic hydrogen generation. Adv Mater 27:4572–4577. https://doi.org/10.1002/adma.201501939
95. Bi W, Ye C, Xiao C et al (2014) Spatial location engineering of oxygen vacancies for optimized photocatalytic H_2 evolution activity. Small 10(2820–5):2742. https://doi.org/10.1002/smll.201303548
96. Wang Y, Xu X, Lu W et al (2018) A sulfur vacancy rich CdS based composite photocatalyst with g-C_3N_4 as a matrix derived from a Cd-S cluster assembled supramolecular network for H_2 production and VOC removal. Dalton Trans 47:4219–4227. https://doi.org/10.1039/c7dt04912a
97. Lu L, Xu X, An K et al (2018) Coordination polymer derived NiS@g-C_3N_4 composite photocatalyst for sulfur vacancy and photothermal effect synergistic enhanced H_2 production. ACS Sustain Chem Eng 6:11869–11876. https://doi.org/10.1021/ACSSUSCHEMENG.8B02153
98. Tan H, Zhao Z, Zhu W-B et al (2014) Oxygen vacancy enhanced photocatalytic activity of pervoskite SrTiO(3). ACS Appl Mater Interfaces 6:19184–19190. https://doi.org/10.1021/am5051907
99. Gu L, Wei H, Peng Z et al (2017) Defects enhanced photocatalytic performances in $SrTiO_3$ using laser-melting treatment. J Mater Res 32:748–756. https://doi.org/10.1557/jmr.2016.461
100. Wierzbicka E, Zhou X, Denisov N et al (2019) Self-Enhancing H_2 Evolution from TiO_2 nanostructures under Illumination. Chemsuschem 12:1900–1905. https://doi.org/10.1002/cssc.201900192
101. Wang S, Pan L, Song J-J et al (2015) Titanium-defected undoped anatase TiO_2 with p-type conductivity, room-temperature ferromagnetism, and remarkable photocatalytic performance. J Am Chem Soc 137:2975–2983. https://doi.org/10.1021/ja512047k
102. Pan L, Wang S, Xie J et al (2016) Constructing TiO_2 p-n homojunction for photoelectrochemical and photocatalytic hydrogen generation. Nano Energy 28:296–303. https://doi.org/10.1016/J.NANOEN.2016.08.054
103. Zou X, Liu J, Su J et al (2013) Facile synthesis of thermal- and photostable titania with paramagnetic oxygen vacancies for visible-light photocatalysis. Chemistry 19:2866–2873. https://doi.org/10.1002/chem.201202833
104. Zhao Z, Zhang X, Zhang G et al (2015) Effect of defects on photocatalytic activity of rutile TiO_2 nanorods. Nano Res 8:4061–4071. https://doi.org/10.1007/S12274-015-0917-5
105. Fang Z, Weng S, Ye X et al (2015) Defect engineering and phase junction architecture of wide-bandgap ZnS for conflicting visible light activity in photocatalytic H_2 evolution. ACS Appl Mater Interfaces 7:13915–13924. https://doi.org/10.1021/acsami.5b02641

106. Hao X, Wang Y, Zhou J et al (2018) Zinc vacancy-promoted photocatalytic activity and photostability of ZnS for efficient visible-light-driven hydrogen evolution. Appl Catal B (Applied Catalysis B: Environmental) 221:302–311. https://doi.org/10.1016/j.apcatb.2017.09.006
107. Zhang X, Zhao Z, Zhang W et al (2016) Surface defects enhanced visible light photocatalytic H_2 production for Zn-Cd-S solid solution. Small 12:793–801. https://doi.org/10.1002/smll.201503067
108. Zhang G, Ling X, Liu G et al (2020) Construction of defective Zinc-Cadmium-Sulfur nanorods for Visible-Light-Driven hydrogen evolution without the use of sacrificial agents or cocatalysts. Chemsuschem 13:756–762. https://doi.org/10.1002/cssc.201902889
109. Yu G, Zhang W, Sun Y et al (2016) A highly active cocatalyst-free semiconductor photocatalyst for visible-light-driven hydrogen evolution: synergistic effect of surface defects and spatial bandgap engineering. J Mater Chem A 4:13803–13808. https://doi.org/10.1039/C6TA03803D
110. Sinhamahapatra A, Jeon J-P, Kang J et al (2016) Oxygen-deficient Zirconia (ZrO2-x): a new material for solar light absorption. Sci Rep 6:27218. https://doi.org/10.1038/srep27218
111. Ullattil SG, Narendranath SB, Pillai SC et al (2018) Black TiO_2 nanomaterials: a review of recent advances. Chem Eng J 343:708–736. https://doi.org/10.1016/j.cej.2018.01.069
112. Fang W, Xing M, Zhang J (2017) Modifications on reduced titanium dioxide photocatalysts: a review. J Photochem Photobiol C 32:21–39. https://doi.org/10.1016/j.jphotochemrev.2017.05.003
113. Rajaraman TS, Parikh SP, Gandhi VG (2019) Black TiO_2: a review of its properties and conflicting trends. Chem Eng J 123918. https://doi.org/10.1016/j.cej.2019.123918
114. Zhang Y-C, Afzal N, Pan L et al (2019) Structure-activity relationship of defective metal-based photocatalysts for water splitting: experimental and theoretical perspectives. Adv Sci 6:1900053. https://doi.org/10.1002/advs.201900053
115. Zhou W, Fu H (2018) Defect-mediated electron–hole separation in semiconductor photocatalysis. Inorg Chem Front 5:1240–1254. https://doi.org/10.1039/C8QI00122G
116. Lohaus C, Klein A, Jaegermann W (2018) Limitation of Fermi level shifts by polaron defect states in hematite photoelectrodes. Nat Commun 9:4309. https://doi.org/10.1038/s41467-018-06838-2
117. Vohs JM (2013) Site requirements for the adsorption and reaction of oxygenates on metal oxide surfaces. Chem Rev 113:4136–4163. https://doi.org/10.1021/cr300328u
118. Schaub R, Thostrup P, Lopez N et al (2001) Oxygen vacancies as active sites for water dissociation on rutile TiO_2(110). Phys Rev Lett 87:266104. https://doi.org/10.1103/PhysRevLett.87.266104
119. Nowotny J, Bak T, Nowotny MK et al (2006) TiO_2 surface active sites for water splitting. J Phys Chem B 110:18492–18495. https://doi.org/10.1021/jp063699p
120. Pan X, Yang M-Q, Fu X et al (2013) Defective TiO_2 with oxygen vacancies: synthesis, properties and photocatalytic applications. Nanoscale 5:3601–3614. https://doi.org/10.1039/c3nr00476g
121. Das T, Chakraborty S, Ahuja R et al (2019) Functionalization and defect-driven water splitting mechanism on a quasi-two-dimensional TiO_2 hexagonal nanosheet. ACS Appl Energy Mater 2:5074–5082. https://doi.org/10.1021/acsaem.9b00745
122. Lang X, Liang Y, Sun L et al (2017) Interplay between methanol and anatase TiO_2 (101) surface: the effect of subsurface oxygen vacancy. J Phys Chem C 121:6072–6080. https://doi.org/10.1021/acs.jpcc.6b11356
123. Guo Q, Xu C, Ren Z et al (2012) Stepwise photocatalytic dissociation of methanol and water on TiO_2 (110). J Am Chem Soc 134:13366–13373. https://doi.org/10.1021/ja304049x
124. Zhou C, Ren Z, Tan S et al (2010) Site-specific photocatalytic splitting of methanol on TiO_2 (110). Chem Sci 1:575. https://doi.org/10.1039/c0sc00316f
125. Guo Q, Zhou C, Ma Z et al (2016) Elementary photocatalytic chemistry on TiO_2 surfaces. Chem Soc Rev 45:3701–3730. https://doi.org/10.1039/c5cs00448a

126. Bard AJ (1979) Photoelectrochemistry and heterogeneous photo-catalysis at semiconductors. J Photochem 10:59–75. https://doi.org/10.1016/0047-2670(79)80037-4
127. Ng B-J, Putri LK, Kong XY et al (2020) Z-scheme photocatalytic systems for solar water splitting. Adv Sci 7:1903171. https://doi.org/10.1002/advs.201903171
128. Xu Q, Zhang L, Yu J et al (2018) Direct Z-scheme photocatalysts: Principles, synthesis, and applications. Mater Today 21:1042–1063. https://doi.org/10.1016/j.mattod.2018.04.008
129. Xia X, Song M, Wang H et al (2019) Latest progress in constructing solid-state Z scheme photocatalysts for water splitting. Nanoscale 11:11071–11082. https://doi.org/10.1039/c9nr03218e
130. Low J, Jiang C, Cheng B et al (2017) A review of direct Z-scheme photocatalysts. Small Methods 1:1700080. https://doi.org/10.1002/smtd.201700080
131. Jiang W, Zong X, An L et al (2018) Consciously constructing heterojunction or direct Z-scheme photocatalysts by regulating electron flow direction. ACS Catal 8:2209–2217. https://doi.org/10.1021/acscatal.7b04323
132. Di T, Xu Q, Ho W et al (2019) Review on metal sulphide-based Z-scheme photocatalysts. ChemCatChem 11:1394–1411. https://doi.org/10.1002/cctc.201802024
133. Zhu M, Sun Z, Fujitsuka M et al (2018) Z-scheme photocatalytic water splitting on a 2D heterostructure of black phosphorus/bismuth vanadate using visible light. Angew Chem Int Ed 57:2160–2164. https://doi.org/10.1002/anie.201711357
134. Kolivand A, Sharifnia S (2020) Enhanced photocatalytic hydrogen evolution from water splitting by Z-scheme CdS/$BiFeO_3$ heterojunction without using sacrificial agent. Int J Energy Res. https://doi.org/10.1002/er.5966
135. Zeng C, Hu Y, Zhang T et al (2018) A core–satellite structured Z-scheme catalyst Cd0.5Zn0.5S/$BiVO_4$ for highly efficient and stable photocatalytic water splitting. J. Mater. Chem. A 6:16932–16942. https://doi.org/10.1039/C8TA04258F
136. Rauf A, Ma M, Kim S et al (2018) Mediator- and co-catalyst-free direct Z-scheme composites of Bi_2WO_6-Cu_3P for solar-water splitting. Nanoscale 10:3026–3036. https://doi.org/10.1039/c7nr07952d
137. Yuan Q, Liu D, Zhang N et al (2017) Noble-metal-free Janus-like structures by cation exchange for Z-scheme photocatalytic water splitting under broadband light irradiation. Angew Chem 129:4270–4274. https://doi.org/10.1002/ange.201700150
138. She X, Wu J, Xu H et al (2017) High efficiency photocatalytic water splitting using 2D α-Fe_2O_3/g-C_3N_4 Z-scheme catalysts. Adv Energy Mater 7:1700025. https://doi.org/10.1002/aenm.201700025
139. Sepahvand H, Sharifnia S (2019) Photocatalytic overall water splitting by Z-scheme g-C_3N_4/$BiFeO_3$ heterojunction. Int J Hydrogen Energy 44:23658–23668. https://doi.org/10.1016/j.ijhydene.2019.07.078
140. Xie H, Zhao Y, Li H et al (2019) 2D $BiVO_4$/g-C_3N_4 Z-scheme photocatalyst for enhanced overall water splitting. J Mater Sci 54:10836–10845. https://doi.org/10.1007/s10853-019-03664-9
141. Yang Y, Qiu M, Li L et al (2018) A direct Z-scheme Van Der Waals heterojunction ($WO_3 \cdot H_2O$/g-C_3N_4) for high efficient overall water splitting under visible-light. Sol RRL 2:1800148. https://doi.org/10.1002/solr.201800148
142. Zhang S, Wang J, Chen S et al (2019) Construction of Ag_2S/WO_3 direct Z-scheme photocatalyst for enhanced charge separation efficiency and H_2 generation activity. Ind Eng Chem Res 58:14802–14813. https://doi.org/10.1021/acs.iecr.9b02335
143. Hu T, Li P, Zhang J et al (2018) Highly efficient direct Z-scheme WO_3/CdS-diethylenetriamine photocatalyst and its enhanced photocatalytic H_2 evolution under visible light irradiation. Appl Surf Sci 442:20–29. https://doi.org/10.1016/j.apsusc.2018.02.146
144. Wang S, Zhu B, Liu M et al (2019) Direct Z-scheme ZnO/CdS hierarchical photocatalyst for enhanced photocatalytic H_2-production activity. Appl Catal B (Applied Catalysis B: Environmental) 243:19–26. https://doi.org/10.1016/j.apcatb.2018.10.019

145. Li X, Xie K, Song L et al (2017) Enhanced photocarrier separation in hierarchical graphitic-C_3N_4-supported $CuInS_2$ for Noble-Metal-Free Z-scheme photocatalytic water splitting. ACS Appl Mater Interfaces 9:24577–24583. https://doi.org/10.1021/acsami.7b06030
146. Yu W, Chen J, Shang T et al (2017) Direct Z-scheme g-C_3N_4/WO_3 photocatalyst with atomically defined junction for H_2 production. Appl Catal B (Applied Catalysis B: Environmental) 219:693–704. https://doi.org/10.1016/j.apcatb.2017.08.018
147. Huang Z-F, Song J, Wang X et al (2017) Switching charge transfer of C_3N_4/W18O49 from type-II to Z-scheme by interfacial band bending for highly efficient photocatalytic hydrogen evolution. Nano Energy 40:308–316. https://doi.org/10.1016/j.nanoen.2017.08.032
148. Shi J, Li S, Wang F et al (2018) In situ topotactic fabrication of direct Z-scheme 2D/2D ZnO/$Zn_xCd_{1-x}S$ single crystal nanosheet heterojunction for efficient photocatalytic water splitting. Catal Sci Technol 8:6458–6467. https://doi.org/10.1039/C8CY01884G
149. Wang Z, Su B, Xu J et al (2020) Direct Z-scheme $ZnIn_2S_4$/$LaNiO_3$ nanohybrid with enhanced photocatalytic performance for H_2 evolution. Int J Hydrogen Energy 45:4113–4121. https://doi.org/10.1016/j.ijhydene.2019.12.077
150. Tan P, Zhu A, Qiao L et al (2019) Constructing a direct Z-scheme photocatalytic system based on 2D/2D WO_3/$ZnIn_2S_4$ nanocomposite for efficient hydrogen evolution under visible light. Inorg Chem Front 6:929–939. https://doi.org/10.1039/C8QI01359D
151. Jia X, Tahir M, Pan L et al (2016) Direct Z-scheme composite of CdS and oxygen-defected $CdWO_4$: An efficient visible-light-driven photocatalyst for hydrogen evolution. Appl Catal B (Applied Catalysis B: Environmental) 198:154–161. https://doi.org/10.1016/j.apcatb.2016.05.046
152. Zhu S, Zhang Y, Qian X et al (2020) Zn defect-mediated Z-scheme electron-hole separation in $AgIn_5S_8$/ZnS heterojunction for enhanced visible-light photocatalytic hydrogen evolution. Appl Surf Sci 504:144396. https://doi.org/10.1016/j.apsusc.2019.144396
153. Li F, Hou Y, Yu Z et al (2019) Oxygen deficiency introduced to Z-scheme CdS/WO_{3-x} nanomaterials with MoS_2 as the cocatalyst towards enhancing visible-light-driven hydrogen evolution. Nanoscale 11:10884–10895. https://doi.org/10.1039/c8nr10230a
154. Ran Q, Zhong T, Li F et al (2020) CdS nanoparticles grown in situ on oxygen deficiency-rich WO_{3-x} nanosheets: direct Z-scheme heterojunction towards enhancing visible light-driven hydrogen evolution. CrystEngComm 22:5818–5827. https://doi.org/10.1039/D0CE00966K
155. Wei T, Zhu Y-N, An X et al (2019) Defect modulation of Z-scheme TiO_2/Cu_2O photocatalysts for durable water splitting. ACS Catal 9:8346–8354. https://doi.org/10.1021/acscatal.9b01786
156. Mo Z, Xu H, Chen Z et al (2019) Construction of MnO_2/Monolayer g-C_3N_4 with Mn vacancies for Z-scheme overall water splitting. Appl Catal B (Applied Catalysis B: Environmental) 241:452–460. https://doi.org/10.1016/j.apcatb.2018.08.073
157. Kong L, Zhang X, Wang C et al (2018) Ti3+ defect mediated g-C_3N_4/TiO_2 Z-scheme system for enhanced photocatalytic redox performance. Appl Surf Sci 448:288–296. https://doi.org/10.1016/j.apsusc.2018.04.011
158. Wang J, Xia Y, Zhao H et al (2017) Oxygen defects-mediated Z-scheme charge separation in g-C_3N_4/ZnO photocatalysts for enhanced visible-light degradation of 4-chlorophenol and hydrogen evolution. Appl Catal B (Applied Catalysis B: Environmental) 206:406–416. https://doi.org/10.1016/j.apcatb.2017.01.067
159. Goud BS, Koyyada G, Jung JH et al (2020) Surface oxygen vacancy facilitated Z-scheme MoS_2/Bi_2O_3 heterojunction for enhanced visible-light driven photocatalysis-pollutant degradation and hydrogen production. Int J Hydrogen Energy 45:18961–18975. https://doi.org/10.1016/j.ijhydene.2020.05.073
160. Wang M, Huang S, Pang X et al (2019) Switching charge kinetics from type-I to Z-scheme for g-C_3N_4 and $ZnIn_2S_4$ by defective engineering for efficient and durable hydrogen evolution. Sustain Energy Fuels 3:3422–3429. https://doi.org/10.1039/C9SE00639G

161. Fu C-F, Zhang R, Luo Q et al (2019) Construction of direct Z-Scheme photocatalysts for overall water splitting using two-dimensional van der waals heterojunctions of metal dichalcogenides. J Comput Chem 40:980–987. https://doi.org/10.1002/jcc.25540
162. Niu X, Bai X, Zhou Z et al (2020) Rational design and characterization of direct Z-scheme photocatalyst for overall water splitting from excited state dynamics simulations. ACS Catal 10:1976–1983. https://doi.org/10.1021/acscatal.9b04753
163. Hezam A, Namratha K, Drmosh QA et al (2018) Direct Z-scheme Cs_2O–Bi_2O_3–ZnO heterostructures for photocatalytic overall water splitting. J Mater Chem A 6:21379–21388. https://doi.org/10.1039/C8TA08033J
164. Xue C, Zhang P, Shao G et al (2020) Effective promotion of spacial charge separation in direct Z-scheme WO_3/CdS/WS_2 tandem heterojunction with enhanced visible-light-driven photocatalytic H_2 evolution. Chem Eng J 398:125602. https://doi.org/10.1016/j.cej.2020.125602
165. Wang N, Wu L, Li J et al (2020) Construction of hierarchical Fe_2O_3@MnO_2 core/shell nanocube supported C_3N_4 for dual Z-scheme photocatalytic water splitting. Sol Energy Mater Sol Cells 215:110624. https://doi.org/10.1016/j.solmat.2020.110624
166. Subha N, Mahalakshmi M, Myilsamy M et al (2018) Direct Z-scheme heterojunction nanocomposite for the enhanced solar H_2 production. Appl Catal A 553:43–51. https://doi.org/10.1016/j.apcata.2018.01.009
167. Tu W, Guo W, Hu J et al (2020) State-of-the-art advancements of crystal facet-exposed photocatalysts beyond TiO_2: design and dependent performance for solar energy conversion and environment applications. Mater Today 33:75–86. https://doi.org/10.1016/j.mattod.2019.09.003
168. Reginato G, Zani L, Calamante M et al (2020) Dye-sensitized heterogeneous photocatalysts for green redox reactions. Eur J Inorg Chem 2020:899–917. https://doi.org/10.1002/ejic.201901174
169. Shao W, Wang H, Zhang X (2018) Elemental doping for optimizing photocatalysis in semiconductors. Dalton Trans 47:12642–12646. https://doi.org/10.1039/c8dt02613k
170. Xu C, Ravi Anusuyadevi P, Aymonier C et al (2019) Nanostructured materials for photocatalysis. Chem Soc Rev 48:3868–3902. https://doi.org/10.1039/c9cs00102f
171. Low J, Yu J, Jaroniec M et al (2017) Heterojunction photocatalysts. Adv Mater 29. https://doi.org/10.1002/adma.201601694
172. Reddy NL, Rao VN, Vijayakumar M et al (2019) A review on frontiers in plasmonic nano-photocatalysts for hydrogen production. Int J Hydrogen Energy 44:10453–10472. https://doi.org/10.1016/j.ijhydene.2019.02.120
173. Zhong S, Xi Y, Wu S et al (2020) Hybrid cocatalysts in semiconductor-based photocatalysis and photoelectrocatalysis. J Mater Chem A 8:14863–14894. https://doi.org/10.1039/D0TA04977H
174. Bai S, Yin W, Wang L et al (2016) Surface and interface design in cocatalysts for photocatalytic water splitting and CO_2 reduction. RSC Adv 6:57446–57463. https://doi.org/10.1039/C6RA10539D
175. Pan H (2016) Principles on design and fabrication of nanomaterials as photocatalysts for water-splitting. Renew Sust Energ Rev 57:584–601. https://doi.org/10.1016/j.rser.2015.12.117
176. Fajrina N, Tahir M (2019) A critical review in strategies to improve photocatalytic water splitting towards hydrogen production. Int J Hydrogen Energy 44:540–577. https://doi.org/10.1016/j.ijhydene.2018.10.200
177. Chen Y, Ji S, Sun W et al (2020) Engineering the atomic interface with single platinum atoms for enhanced photocatalytic hydrogen production. Angew Chem Int Ed 59:1295–1301. https://doi.org/10.1002/anie.201912439
178. Ho Lee C, Uck Lee S (2018) Theoretical basis of electrocatalysis. In: Pati RK, Mukhopadhyay I, Ray A (eds) Electrocatalysts for fuel cells and hydrogen evolution—theory to design. IntechOpen

179. Park K-W, Kolpak AM (2019) Mechanism for spontaneous oxygen and hydrogen evolution reactions on CoO nanoparticles. J Mater Chem A 7:6708–6719. https://doi.org/10.1039/C8TA11087E
180. Xu S-M, Yan H, Wei M (2017) Band structure engineering of transition-metal-based layered double hydroxides toward photocatalytic oxygen evolution from water: a theoretical-experimental combination study. J Phys Chem C 121:2683–2695. https://doi.org/10.1021/acs.jpcc.6b10159
181. Zhou X, Dong H, Ren A-M (2016) Exploring the mechanism of water-splitting reaction in NiOx/β-Ga_2O_3 photocatalysts by first-principles calculations. Phys Chem Chem Phys 18:11111–11119. https://doi.org/10.1039/c5cp07260c
182. Muuronen M, Parker SM, Berardo E et al (2017) Mechanism of photocatalytic water oxidation on small TiO_2 nanoparticles. Chem Sci 8:2179–2183. https://doi.org/10.1039/c6sc04378j
183. Le Formal F, Pastor E, Tilley SD et al (2015) Rate law analysis of water oxidation on a hematite surface. J Am Chem Soc 137:6629–6637. https://doi.org/10.1021/jacs.5b02576
184. Wang D, Sheng T, Chen J et al (2018) Identifying the key obstacle in photocatalytic oxygen evolution on rutile TiO_2. Nat Catal 1:291–299. https://doi.org/10.1038/s41929-018-0055-z
185. Ma Z, Lin S, Sa R et al (2017) A comprehensive understanding of water photooxidation on Ag_3PO_4 surfaces. RSC Adv 7:23994–24003. https://doi.org/10.1039/C7RA02853A
186. Gao G, Bottle S, Du A (2018) Understanding the activity and selectivity of single atom catalysts for hydrogen and oxygen evolution via ab initial study. Catal Sci Technol 8:996–1001. https://doi.org/10.1039/c7cy02463k
187. Qureshi M, Takanabe K (2017) Insights on measuring and reporting heterogeneous photocatalysis: efficiency definitions and setup examples. Chem Mater 29:158–167. https://doi.org/10.1021/acs.chemmater.6b02907
188. Kalamaras E, Lianos P (2015) Current doubling effect revisited: current multiplication in a PhotoFuelCell. J Electroanal Chem 751:37–42. https://doi.org/10.1016/j.jelechem.2015.05.029
189. Schneider J, Bahnemann DW (2013) Undesired role of sacrificial reagents in photocatalysis. J Phys Chem Lett 4:3479–3483. https://doi.org/10.1021/jz4018199
190. Kumaravel V, Imam M, Badreldin A et al (2019) Photocatalytic hydrogen production: role of sacrificial reagents on the activity of oxide, carbon, and sulfide catalysts. Catalysts 9:276. https://doi.org/10.3390/catal9030276
191. Wang M, Shen S, Li L et al (2017) Effects of sacrificial reagents on photocatalytic hydrogen evolution over different photocatalysts. J Mater Sci 52:5155–5164. https://doi.org/10.1007/s10853-017-0752-z
192. Christoforidis KC, Fornasiero P (2017) Photocatalytic hydrogen production: a rift into the future energy supply. ChemCatChem 9:1523–1544. https://doi.org/10.1002/cctc.201601659
193. Bowker M, Morton C, Kennedy J et al (2014) Hydrogen production by photoreforming of biofuels using Au, Pd and Au–Pd/TiO_2 photocatalysts. J Catal 310:10–15. https://doi.org/10.1016/j.jcat.2013.04.005
194. Strataki N, Bekiari V, Kondarides DI et al (2007) Hydrogen production by photocatalytic alcohol reforming employing highly efficient nanocrystalline titania films. Appl Catal B (Applied Catalysis B: Environmental) 77:184–189. https://doi.org/10.1016/j.apcatb.2007.07.015
195. Shiragami T, Tomo T, Matsumoto T et al (2013) Structural dependence of alcoholic sacrificial agents on TiO_2-photocatalytic hydrogen evolution. Bull Chem Soc Jpn 86:382–389. https://doi.org/10.1246/bcsj.20120274
196. Zhao J, Shi R, Li Z et al (2020) How to make use of methanol in green catalytic hydrogen production? Nano Select 1:12–29. https://doi.org/10.1002/nano.202000010
197. Guzman F, Chuang SSC, Yang C (2013) Role of methanol sacrificing reagent in the photocatalytic evolution of hydrogen. Ind Eng Chem Res 52:61–65. https://doi.org/10.1021/ie301177s

198. Huang C-W, Nguyen B-S, Wu JC-S et al (2020) A current perspective for photocatalysis towards the hydrogen production from biomass-derived organic substances and water. Int J Hydrogen Energy 45:18144–18159. https://doi.org/10.1016/j.ijhydene.2019.08.121
199. Kuehnel MF, Reisner E (2018) Solar hydrogen generation from lignocellulose. Angew Chem Int Ed 57:3290–3296. https://doi.org/10.1002/anie.201710133
200. Lakshmana Reddy N, Navakoteswara Rao V, Mamatha Kumari M et al (2018) Nanostructured semiconducting materials for efficient hydrogen generation. Environ Chem Lett 16:765–796. https://doi.org/10.1007/s10311-018-0722-y
201. Reddy NL, Kumar S, Krishnan V et al (2017) Multifunctional Cu/Ag quantum dots on TiO_2 nanotubes as highly efficient photocatalysts for enhanced solar hydrogen evolution. J Catal 350:226–239. https://doi.org/10.1016/j.jcat.2017.02.032
202. Liu X, Duan X, Wei W et al (2019) Photocatalytic conversion of lignocellulosic biomass to valuable products. Green Chem 21:4266–4289. https://doi.org/10.1039/C9GC01728C
203. Butburee T, Chakthranont P, Phawa C et al (2020) Beyond artificial photosynthesis: prospects on photobiorefinery. ChemCatChem 34:26. https://doi.org/10.1002/cctc.201901856
204. Wakerley DW, Kuehnel MF, Orchard KL et al (2017) Solar-driven reforming of lignocellulose to H_2 with a CdS/CdOx photocatalyst. Nat Energy 2. https://doi.org/10.1038/nenergy.2017.21
205. Pellegrin Y, Odobel F (2017) Sacrificial electron donor reagents for solar fuel production. C R Chim 20:283–295. https://doi.org/10.1016/j.crci.2015.11.026
206. Li C, Hu P, Meng H et al (2016) Role of sulfites in the water splitting reaction. J Solution Chem 45:67–80. https://doi.org/10.1007/s10953-015-0422-1

Chapter 25
Visible Range Activated Metal Oxide Photocatalysts in New and Emerging Energy Applications

Cigdem Sahin and Canan Varlikli

Abstract Metal oxide semiconductors are known to provide adequate activity in most of the photocatalytic processes. Among them, visible active or activated ones gain the highest attention because of their wide range of application areas induced by light absorption and followed by charge transport. In this chapter, the focus of potential application areas is limited to solar fuels and solar cells as they represent two of the most studied fields of green photocatalytic semiconductors.

Keywords Photocatalyst · Metal oxide · Visible light · Solar fuel · Solar cell

25.1 Introduction

Worldwide energy consumption is rapidly increasing due to industrial developments and population growth. Over 80% of energy demand is derived from fossil fuels which can cause environmental pollutions [94, 105, 114]. Solar energy is an ideal source of clean and renewable energy. Photocatalysis has great interest due to its potential for solar energy and environmental applications [42, 54].

Photocatalysis is mainly used in the fields of hydrogen production, solar cells, self-cleaning surfaces, antibacterial agents, air and water purifications [26, 57, 89]. Although there are many efforts on photocatalyst materials and photocatalytic applications, the development of visible light-activated photocatalyst materials is still needed for commercial applications [21]. The photocatalytic process is initiated by the light absorption, following the formation of electron–hole pairs in a semiconductor. Sunlight contains about 4% UV light and 43% visible light [86]. With

---

C. Sahin (✉)
Chemistry Department, Art and Science Faculty, Pamukkale University, Denizli 20160, Turkey
e-mail: csahin@pau.edu.tr

C. Varlikli
Department of Photonics, Izmir Institute of Technology, Urla, Izmir 35430, Turkey
e-mail: cananvarlikli@iyte.edu.tr

S. Garg and A. Chandra (eds.), *Green Photocatalytic Semiconductors*,
Green Chemistry and Sustainable Technology,
https://doi.org/10.1007/978-3-030-77371-7_25

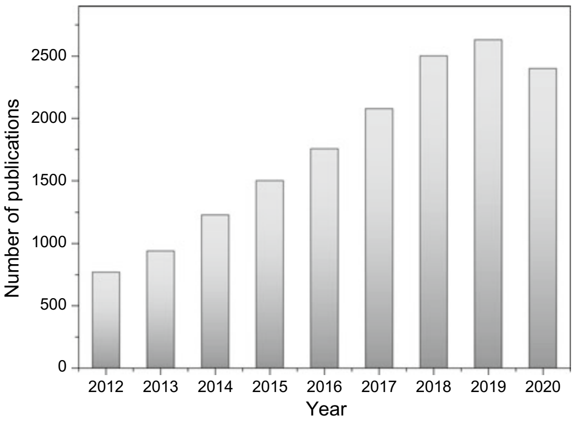

Fig. 25.1 The number of publications versus years for the keyword of "visible photocatalysis" according to Web of Science

the aim of the maximum use of solar light, a growing interest is observed in search of visible light-activated photocatalysts. A search in Web of Science for the keywords of "visible photocatalysis" have resulted over 18.000 publications since 2012 (Fig. 25.1).

Among photocatalytic materials, visible range activated metal oxide photocatalysts have attracted attention due to their light absorption, charge separation, and transport properties. The visible light response of a metal oxide can be tuned through many doping processes including metal doping, non-metal doping, dye sensitization, etc. [8, 78]. In this chapter, the focus is on the visible range activated metal oxides and their potential application areas which are limited to solar fuels and solar cells.

25.2 Development/Preparation of Visible Active Metal Oxide Photocatalysts

Metal oxides such as TiO_2, ZnO, ZrO_2 and SnO_2 with wide band gap show photocatalytic activity under UV light for solar fuels and environmental applications. For effective utilization of solar light, UV active metal oxides can be tuned to visible range active metal oxides by using metal doping, non-metal doping, various co-doped systems, dye sensitization, and composite semiconductors [8, 84, 99, 109, 127]. These approaches can also provide the optimization of morphology, surface area, crystallinity, porosity, and energy levels of metal oxides which can improve photocatalytic activity.

Non-metal doping of metal oxides with N, C, S, and F atoms can extend the absorption response to visible range and improve photocatalytic activity. Nitrogen is one of the most promising dopants for visible light active photocatalysts due to its comparable atomic size with oxygen, small ionization energy, and stability [20, 24, 99]. Titanium dioxide (TiO_2) is the most widely used metal oxide for photocatalytic applications due to its unique material properties; nontoxic, stabile, and low cost [15, 30, 109]. Doping of TiO_2 with the nitrogen sources can form a new N 2p band above the O 2p valance band of TiO_2 and lead to optical absorption in the visible light region (Fig. 25.2) [3, 4, 23, 145]. Additionally, the formation of the oxygen vacancies can be observed due to N-doping which also play an important role in the red-shifted absorption band edge [49, 117, 145].

There are various physical and chemical techniques such as sputtering, ion implantation, sol–gel, solvothermal, and hydrothermal methods for the preparation of N-doped TiO_2 [49, 79, 95, 136]. Diker et al. have prepared, N-doped TiO_2 nanoparticles by using 1° and 2° alkyl and alcohol amines [n-propylamine (nPRYL), ethanolamine (ETOH), propanolamine (PROH), diethylamine (DETYL), dipropylamine (DPRYL), diethanolamine (DETOH), and ammonium hydroxide (NH4OH)] as nitrogen sources through microwave and hydrothermal growth methods. Their study showed that the nitrogen doping into the TiO_2 lattice depends on the preparation conditions and nature of nitrogen source; alkyl chain length differences of amine sources did not make a significant effect on the doping process [18]. Some of the other nitrogen sources used for N-doped TiO_2 are ammonium chloride, ammonium hydroxide, urea, and hydrazine [14, 49, 68, 145]. These studies showed that the morphology and crystallinity of TiO_2 with anatase/brookite structure can be improved with N-doping method using solvothermal process by hydrazine as nitrogen source. While SEM image of the undoped TiO_2 shows quasi-spherical nanoparticles, the formation of uniform TiO_2 nanorods are observed by nitrogen doping in TiO_2 (Fig. 25.3). The high crystallinity of N-doped TiO_2 nanorods can decrease charge recombination, resulting in higher photocatalytic activity under visible light compared to undoped TiO_2 [31].

One of the other non-metals utilized in doping of TiO_2 is fluorine which causes oxygen vacancies due to the reduction of Ti^{4+} to Ti^{3} $^{+}$by charge compensation between F^{-} and Ti^{4+}. These Ti^{3+} donor surface states can place close the conduction band of TiO_2 which might result in visible light absorption [63, 99, 109, 137]. S-doping is also one of the useful strategies for improving the visible light

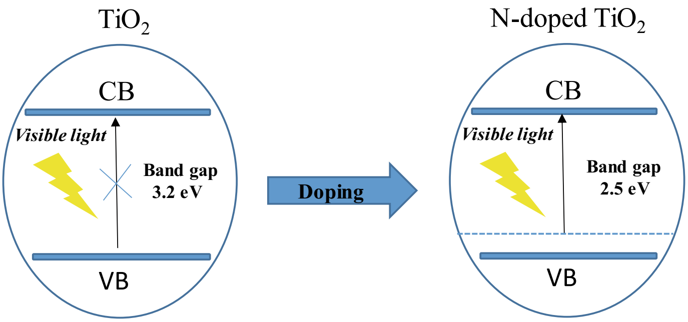

Fig. 25.2 Energy level diagrams for undoped and N-doped TiO_2

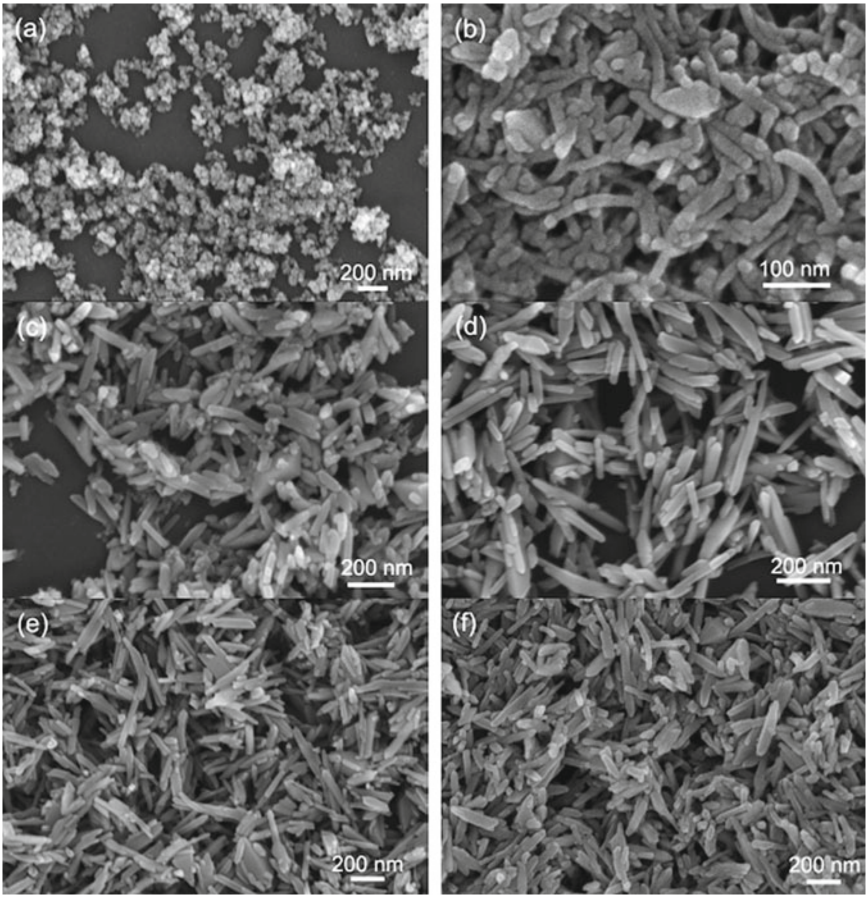

Fig. 25.3 SEM images of the samples: undoped TiO_2 (**a**); N-doped TiO_2, $N_2H_4 \cdot H_2O$ concentration 12.3 mol/L (**b**); 10.3 mol/L (**c**); 8.2 mol/L (**d**); 6.2 mol/L (**e**); 4.1 mol/L (**f**) (Reprinted from Ref. [31] with permission from Royal Society of Chemistry)

photocatalytic activity of TiO_2. S-doping TiO_2 can also provide small crystallite size, high porosity, and uniform surface [38, 99].

An important improvement was observed with the use of B/N co-doping which resulted in red anatase TiO_2 microspheres. Formation of red TiO_2 is attributed to the synergetic effect of both B and N atoms in co-doped titania. In this process, substitution of oxygen by nitrogen is facilitated through the pre-doping of TiO_2 with boron to weaken the Ti–O bonds. The absorption edge of the red anatase TiO_2 has been extended up to 700 nm [70]. Figure 25.4 shows the absorption and Raman spectra of the white TiO_2 and red TiO_2.

The doping of metal oxides with transition metals such as Fe, Cu, Co, Cr, Ru, Pt, and Au may form a new energy level between valance and conduction bands,

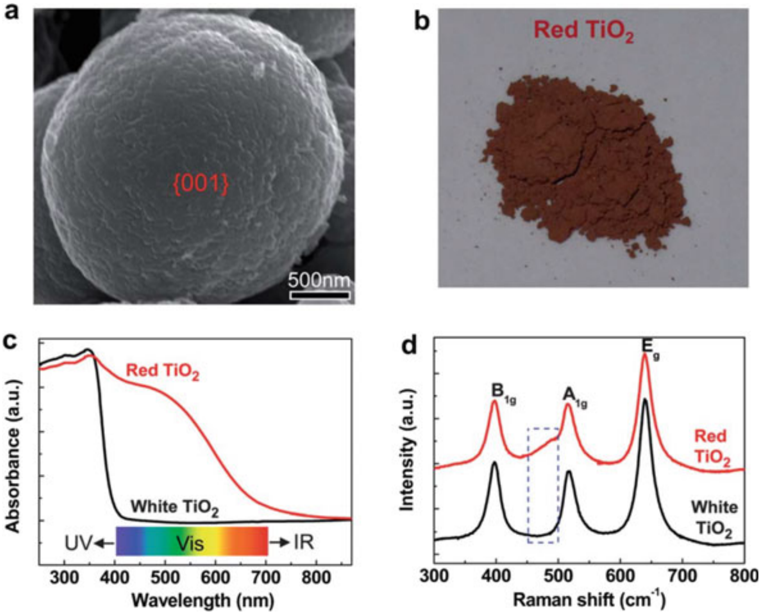

Fig. 25.4 **a** SEM image of a red TiO_2 microsphere; **b** optical photograph of the prepared red TiO_2 sample; **c** and **d** UV–visible absorption and Raman spectra of the white TiO_2 and red TiO_2 (Reprinted from Ref. [70] with permission from Royal Society of Chemistry)

resulting in a red shift in the absorption edge of metal oxide [16, 133, 151, 152]. It is showed that Co transition metal doping in ZnO significantly enhances visible light-responsive of the photocatalyst. Smaller ionic radius of Co^{2+} than Zn^{2+} facilitated the incorporation of Co^{2+} in ZnO and lead to the s-d and p-d interactions between the localized d electrons of the Co^{2+} ions and ZnO band electrons, resulting in the formation of new charge-transfer bands in visible-light region [41, 66, 102, 106, 114]

The adsorption of dye molecules such as organic or organometallic compounds to metal oxides such as TiO_2 and ZnO enhances photoresponse in visible light region as well. Under visible light, the excited electrons are transferred from the LUMO energy level of the dyes to the conduction band of metal oxide. In this system, electron injection in a femtosecond scale forms faster than the recombination of electron–hole pairs in nanoseconds to milliseconds scale which may reduce recombination rate [25, 39, 80]. The higher surface area of the photocatalyts is desired for the high amount of dye adsorption on metal oxide which may improve photocatalytic activity [25].

To extend the light absorption to the visible range, another effective strategy is the formation of composite semiconductors. This can be achieved by the coupling metal oxide such as TiO_2, ZnO and CeO_2 with large band gap and a semiconductor of narrow band gap such as CdS, Bi_2S_3 and V_2O_5 [5, 88, 115]. In electron transfer mechanism of composite semiconductor, electron is injected from the conduction band of semiconductor with small band gap to the large band gap semiconductor [25]. Samal et al. have demonstrated that UV light active ZnO and CeO_2 semiconductors with wide band gap (3.2 eV) can be tuned to visible light active photocatalyst by combining reduced graphene oxide (rGO) (band gap 2.5 eV) [115]. Sivasakthi et al. have reported that the morphology of g-C_3N_4–CuO/ZnO composite semiconductor play an important role in visible light absorption [120]. The combination of micron-size flower-like CuO/ZnO with g-C_3N_4 thin sheets can lead to broad absorption peak in the range of 300 and 570 nm (Fig. 25.5). Formation of composite semiconductor using CoO with narrow band gap and TiO_2 can enhance visible light absorption and charge-transfer for photocatalytic applications [27].

The use of any of the above-mentioned strategies makes significant contributions on the development of visible active metal oxide photocatalysts by either chaining the electronic band structure or by acting as co-light absorbers.

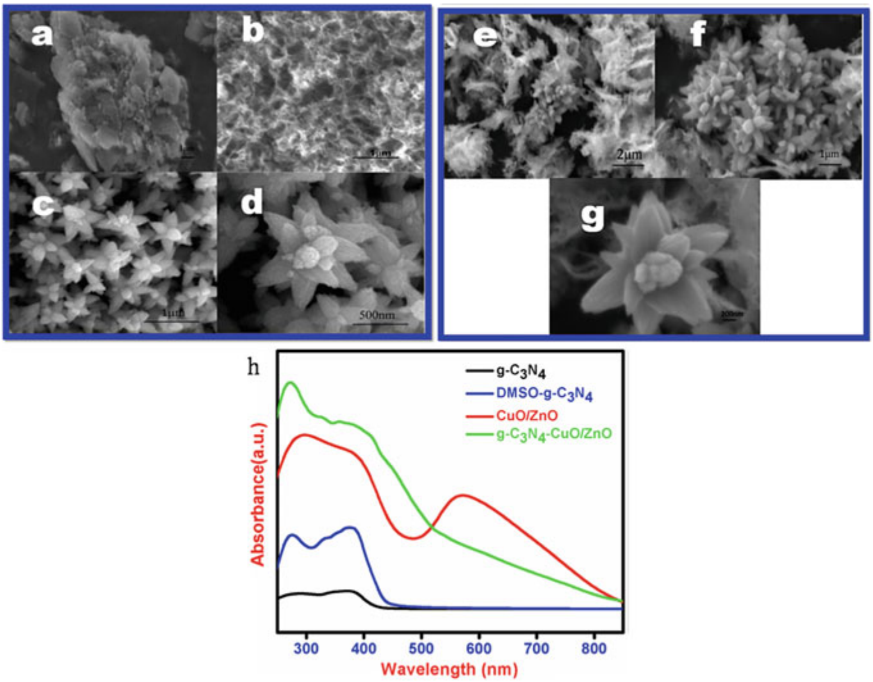

Fig. 25.5 FESEM images of **a** bulk g-C_3N_4, **b** DMSO-g-C_3N_4, **c** and **d** CuO/ZnO, **e–g** g-C_3N_4–CuO, **f** UV–VIS spectra of g-C_3N_4, DMSO-g-C_3N_4, CuO/ZnO and g-C_3N_4–CuO/ZnO (Adapted from Ref. [120], Copyright (2020), with permission from Elsevier)

25.3 Solar Fuel Applications

Photocatalytic H_2 production and CO_2 reduction processes have attracted attention in solar fuel applications for clean energy [121, 141]. After [29] discovered semiconductor-based photocatalytic water-splitting in a photoelectrochemical cell, there are many efforts on the synthesis of photocatalytic materials for H_2 production as clean energy fuel [29, 90, 105]. Among photocatalytic materials, visible range activated metal oxide photocatalysts have gained importance as photoanode in H_2 production technology [160]. Metal oxides can allow the optimization of their properties such as the morphology, surface area, crystallinity, and particle size by modifications using metal doping, non-metal doping, various co-doped systems, dye sensitization, and composite semiconductors [42, 78]. For the use of metal oxides in H_2 production, it is desirable that metal oxides have certain properties such as suitable band gap, suitable energy levels for H_2 generation, high quantum yield, corrosion-resistant, and stability [78, 90]. The basic mechanism of photocatalytic water-splitting for hydrogen production involves the following steps; the generation of electron–hole pairs under light irradiation, charge separation, and surface chemical reactions between generated carriers with water (Fig. 25.6) [146].

TiO_2 is widely studied as photocatalyst for H_2 production due to its chemical stability, nontoxic, and corrosion-resistant. It is known that N-doped TiO_2 can generally show high crystallinity and small particle size which can improve the H_2 generation efficiency [72, 92, 128]. Recently, Kong et al. have reported a nanolayered heterostructure based on N-doped TiO_2 and N-doped carbon (N–TiO_2/NC) by using both doping and compositing in TiO_2 for hydrogen evolution [59]. The obtained N–TiO_2/NC nanocomposite exhibits enhanced visible light absorption, superior charge separation and transport ability due to N-doping of TiO_2 and superior conductivity due to N-doped carbon. Furthermore, the use of both doping and compositing in TiO_2 can increase the surface area and affect the morphology of TiO_2 (Fig. 25.7). Therefore, the nanolayered N–TiO_2/NC heterostructure shows

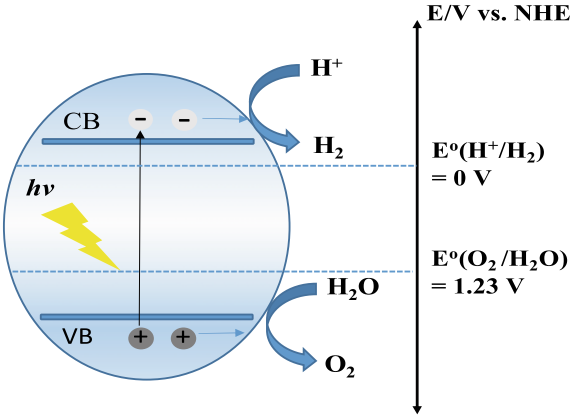

Fig. 25.6 Mechanism of photocatalytic water-splitting for hydrogen production

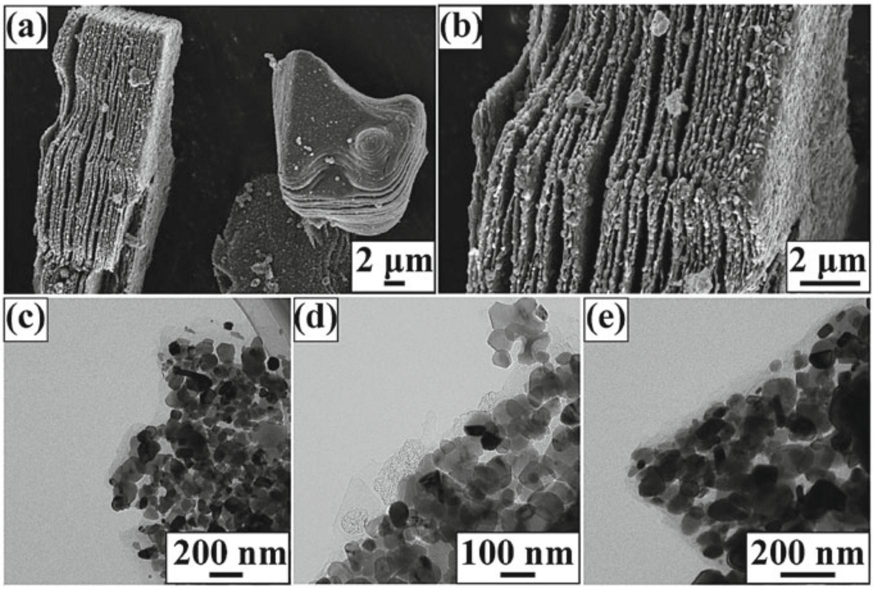

Fig. 25.7 **a**, **b** SEM images, and **c**–**e** TEM images of N–TiO_2/NC Reprinted with permission from Ref. [59]. Copyright (2020) American Chemical Society

effective water-splitting under visible light with H_2 evolution rate up to 102.6 µmol g^{-1} h^{-1} [59].

Park et al. have shown that doping Ag ions on TiO_2 surface affects hydrogen production by photocatalytic water-splitting using liquid phase plasma (LPP) [98]. Ag-doped TiO_2 exhibits small crystal size and uniform surface which can increase visible light absorption and hydrogen evolution rate. In this process, the use of LLP method and CH_3OH as a sacrificial reagent shows an increase in hydrogen evolution rate [98]. To increase the efficiency of hydrogen production, one of other strategies is synthesis of reduced graphene oxide (rGO) supported $InVO_4$–TiO_2 nanocomposite by the hydrothermal method. rGO/$InVO_4$–TiO_2 nanocomposites show high surface area, small particle size, strong Ti–C band interaction. The loading of $InVO_4$ and rGO to TiO_2 can provide high electron mobility, efficient charge carrier separation, and transportation, resulting in high H_2 evolution rate of 1699 µmol h^{-1} (Fig. 25.8) [150].

CuO is considered a photocatalyst for H_2 production due to narrow band gap and earth abundance [28, 45, 138]. However, the use of CuO as photocatalyst may cause rapid recombination of charge carriers, photocorrosion, low water adsorption capacity and large intrinsic over-potential for water reduction which may limit photocatalytic hydrogen evolution application [130]. Recently, a variety of strategies have been developed to overcome these shortcomings [17, 130, 147]. Wang et al. have reported the synthesis of C-doped CuO hollow spheres to increase water adsorption capability and efficiency of photocatalytic hydrogen evolution. The

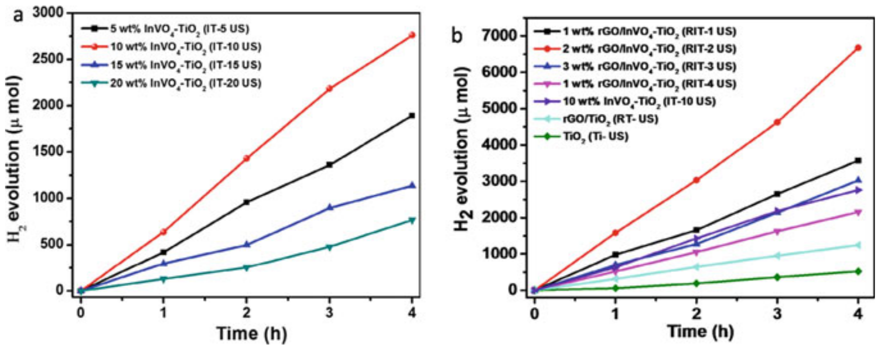

Fig. 25.8 Photocatalytic H_2 production of as-prepared **a** 5 wt% $InVO_4$–TiO_2 (IT-5US), 10 wt% $InVO_4$–TiO_2 (IT-10 US), 15 wt% $InVO_4$–TiO_2 (IT-15 US) and 20 wt% $InVO_4$–TiO_2 (IT-20 US) nanocomposite. **b** Photocatalytic H_2 production of as-prepared 1.0 wt% rGO/$InVO_4$–TiO_2 (RIT-1 US), 2 wt% rGO/$InVO_4$–TiO_2 (RIT-2 US), 3 wt% rGO/$InVO_4$–TiO_2 (RIT-3 US), 4 wt% rGO/$InVO_4$–TiO_2 (RIT-4 US), 10 wt% $InVO_4$–TiO_2 (IT-10 US), rGO/TiO_2 (RT–US) nanocomposites and TiO_2 (Ti–US) (Adapted from Ref. [150], Copyright (2020), with permission from Elsevier)

hollow and porous structure of C-doped CuO can provide large surface area which results in good water adsorption capability and abundant reactive sites. The presence of single-phase and highly crystalline CuO was observed in the as-prepared C–CuO hollow spheres (Fig. 25.9) which can affect charge separation and transportation. Doping C atoms to CuO can decrease the reaction energy barrier for H_2 production. In this approach, C-doped CuO hollow spheres show efficient hydrogen production under visible light with the H_2 evolution rate of 67.3 mmol/g/h [130]. Cots et al. have shown that the addition of iron by impregnation method facilitates the external conversion of the CuO nanowires into a ternary copper iron oxide which can decrease the corrosion of the CuO as photocathodes [17].

ZnO is a good candidate for hydrogen production due to its low cost and chemical stability. The light absorption, charge carriers mobility, and recombination processes of ZnO can be tuned by using metal doping, non-metal doping, and composite semiconductors [10, 46, 77]. Many successful methods have been reported to improve the efficiency of hydrogen production. One of strategies is the doping ZnO with Cu and Ni transition metals. In this strategy, there is no important change in the morphologies of ZnO:Cu and ZnO:Ni (Fig. 25.10). However, the formation of oxygen vacancies was observed in ZnO:Cu and ZnO:Ni which improves the charge separation and reduces recombination of electron and hole pairs compared to pure ZnO. This results in the H_2 evolution rate of 67.3 mmol/g/h [46]. Bilal et al. have reported the effect of incorporation of MoS_2 with a different concentration in ZnO on composite size, surface area, recombination rate, and H_2 evolution efficiency. 3 wt % of MoS_2 in ZnO showed the enhanced surface area and decreased particle size, resulting in H_2 evolution efficiency with 165 $\mu molh^{-1}$ g^{-1} [10]. Hydrogen production efficiencies and morphologies of some metal oxides are given in Table 25.1 from recent literature reports. These studies show that metal

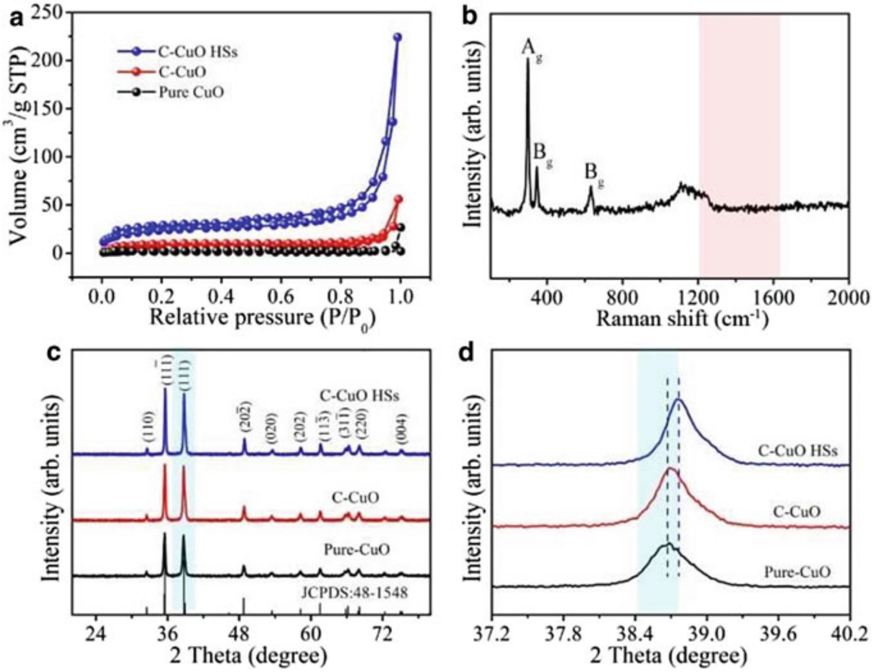

Fig. 25.9 **A** N_2 adsorption/desorption isotherms of pure-CuO, C–CuO, and C–CuO hollow spheres **B** Raman spectra of C–CuO hollow spheres. **C**, **D** XRD patterns of Pure-CuO, C–CuO, and C–CuO hollow spheres (Reprinted with permission from Ref. [130] Copyright (2020) John Wiley and Sons)

oxides can be promising photocatalysts for the evolution of hydrogen under visible light illumination.

Recently, the conversion of CO_2 to valuable fuels have gained to resolve global warming problem. Photocatalytic CO_2 reduction is one of promising processes to obtain solar fuels such as methane and methanol [139, 144]. In 1979, Inoue et al. reported for first time that the photoelectrocatalytic reduction of CO_2 to methyl alcohol, formaldehyde, and formic acid using TiO_2, ZnO, CdS, WO_3, GaP and SiC semiconductors [48]. Although significant advances in the photocatalytic reduction of CO_2 have been obtained since 1979, it is still needed that new photocatalytic materials have high visible light absorption, high conversion efficiency, and high selectivity of products for commercial applications. In recent years, an increasing interest was observed in the use of visible range activated metal oxide for photocatalytic CO_2 reduction.

Visible active or activated metal oxide and their composites such as Au/TiO_2, TiO_2/CdS, $\alpha\text{-}Fe_2O_3/g\text{-}C_3N_4$, CuO/Cu_2O, Ni/ZnO have generally been used as photoanode in CO_2 reduction process [46, 52, 73, 107, 126]. For effective CO_2 reduction process, it is needed from photocatalysts to meet the following

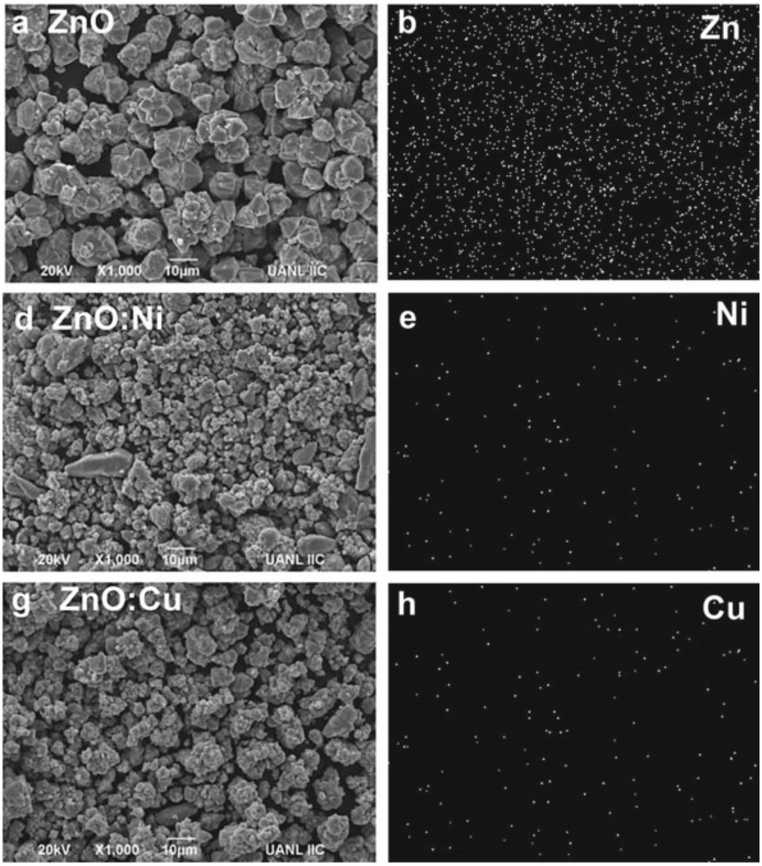

Fig. 25.10 SEM images and elemental mapping of **a**–**b** ZnO, **d**–**e** ZnO:Ni, and **g**–**h** ZnO:Cu samples (Reprinted by permission from [Springer Nature] [Journal of Materials Science: Materials in Electronics] [Ref. 46], COPYRIGHT (2020))

requirements; high visible light absorption, more negative potential than the redox potential of CO_2 reduction, high CO_2 adsorption on photocatalysts and effective charge separation and low recombination rate [100, 119]. The modifications of metal oxides by using metal doping, dye sensitization, and composite semiconductors can provide increased visible light absorption, high surface area, high mobility, enhanced selectivity of products, and high CO_2 adsorption on photocatalysts [46, 64, 100, 144]. Recently, Wang et al. have reported α-Fe_2O_3–ZnO/rGO heterostructure for effective photoreduction of CO_2 that resulted in CH_3OH generation rate of 1.8 μmolg^{-1} h^{-1} under visible light [134]. In this system, while the introduction of α-Fe_2O_3 to the heterostructure can decrease the carrier recombination rate, rGO with high surface area can inhibit the aggregation of Zn spheres. Furthermore, the high mobility and conductivity of rGO can increase carrier

Table 25.1 Metal oxides for photocatalytic water-splitting for hydrogen production

Photocatalyst	Preparation method	Morphology	Particle size (nm)	SSA (m^2/g)	Hydrogen production	Refs.
Black TiO_2	Nanocasting	Mesoporous	5–6 (pore size)	158	188 $\mu molh^{-1}$	[142]
Au/TiO_2	Photodeposition	Nanoparticles	9.1–13	–	5.5 $\mu molh^{-1}$	[123]
$Cu–TiO_2$	Sol immobilization	Nanoparticles	15–25	–	150 $\mu molJ^{-1}\ g^{-1}$	[91]
$g\text{-}C_3N_4/TiO_2$	Vapor deposition	Nanoparticles	20	67.1	513	[122]
CuS/TiO_2	Hydrothermal	Nanoflakes and Nanospindles	–	35	1262	[13]
$rGO/InVO_4–TiO_2$	Hydrothermal	Nanoparticles	–	148.7	1699 $\mu molh^{-1}$	[150]
MoS_2/TiO_2	Anodization, PVD, CVD	Nanoflakes and nanocavity	–	–	181 $\mu molh^{-1}\ cm^{-2}$	[37]
$MoS_2/CdS/TiO_2$	Sol–gel, calcination, hydrothermal	Porous monolith	500 (pore size)	63.39	4146 $\mu molh^{-1}\ g^{-1}$	[22]
MoS2/ZnO	Hydrothermal	Nanoparticles	–	–	1410 $\mu molh^{-1}\ g^{-1}$	[154]
Ni/ZnO	Nital-solution	Hexagonal truncated-pyramid	93	<8	224 $\mu molh^{-1}\ g^{-1}$	[46]
$ZnO/Fe_2O_3/g\text{-}C_3N_4$	Impregnation, calcination	Particles	–	23.5	25 $\mu molh^{-1}$	[77]
$CuO/g\text{-}C_3N_4$	Wet impregnation	Layered structure	–	–	50.1 $\mu molg^{-1}$	[55]
C/CuO	Facile one-step pyrolysis strategy	Hollow spheres	–	72.8	67.3 $\mu molh^{-1}\ g^{-1}$	[130]
Co_3O_4	Hydrothermal	Microflower	–	74.439	132.2 $\mu molh^{-1}\ g^{-1}$	[140]

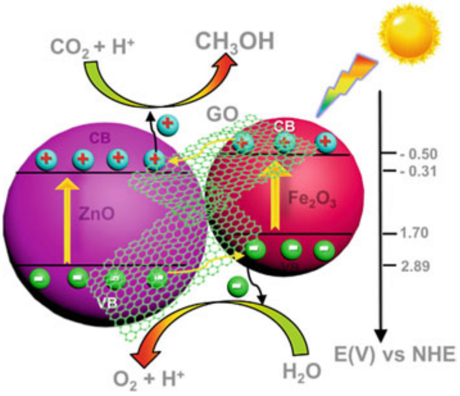

Fig. 25.11 Schematic illustration of a proposed photocatalytic mechanism in the α-Fe_2O_3–ZnO/rGO (Reprinted from Ref. [134], Copyright (2020), with permission from Elsevier)

transport rate of ZnO. The mechanism of CO_2 reduction to CH_3OH in α-Fe_2O_3–ZnO/rGO is presented in Fig. 25.11.

Wang et al. have developed a new porous Copper/Zinc Bimetallic Oxides Derived from novel metal-organic framework (MOF) for conversion CO_2 to methanol with rate of 3.71 mmol g_{cat}^{-1} h^{-1} [135]. This strategy can enhance surface area of photocatalyst which can facilitate adsorption of CO_2 and the release of CH_3OH. Low et al. have reported that highly-efficient recyclable TiO_2/CdS composite for the conversion CO_2 to CH_4 [73]. The loading CdS on TiO_2 can enhance visible light absorption, stability, and CH_4 production rate compared to TiO_2 and CdS. The conversion efficiencies and morphologies of some metal oxides for photocatalytic CO_2 reduction are given in Table 25.2 from recent literature reports. Many researchers have presented new strategies to increase the conversion efficiency of CO_2 to valuable fuels. Although significant achievements have been obtained, it needed to improve conversion efficiency for photocatalytic CO_2 reduction.

25.4 Solar Cell Applications

Solar cell is one of promising technologies to meet world energy demand using solar energy. Silicon-based solar cells are the most popular in photovoltaic market. Recently, dye-sensitized solar cells (DSSCs) have gained great interest for the conversion of sunlight into electricity due to low manufacturing cost and high efficiency in comparison with silicon-based solar cells [58, 155]. DSSC is a new generation of solar cell known as 3rd generation solar cell which the efficiency could reach to 12–14% [53, 148]. The structure of DSSC consists of photoanode with sensitizer, electrolyte, and counter electrode and the working principle is based on photoelectrochemical process (Fig. 25.12). Metal oxides such as TiO_2, ZnO and SnO_2 are used as photoanode in DSSC applications. For the use of metal oxides as

Table 25.2 Some metal oxides for photocatalytic CO_2 reduction

Photocatalyst	Preparation method	Morphology	Particle size (nm)	SSA (m2/g)	Performance	Refs.
TiO_2/CdS	Anodization-calcination	Nanoring	–	–	CH_4: 11.9 mmolh^{-1} m^{-2}	[73]
Au–TiO_2	Hydrothermal	Yolk-shell hollow spheres	–	149.6	CH_4: 2.52 μmolg^{-1} h^{-1}	[126]
TiO_2/MoS_2	Hydrothermal transformation	Microspheres	11.4 *d*	35	CH_4: 2.86 μmolg^{-1} h^{-1} CH_3OH:2.55 μmolg^{-1} h^{-1}	[143]
Ni/ZnO	Nital-solution	Hexagonal truncated-pyramid	93	<8	CH_3OH: 29 μmolg^{-1} h^{-1}	[46]
C–In_2O_3	Hydrothermal	Nanobelt	–	61.3	CH_4: 27.9 μmol h^{-1}	[97]
α-Fe_2O_3/g-C_3N_4	Hydrothermal	Microscale rods	~1 μm l ~0.1 μm *d*	–	CH_3OH:5.63 μmolg^{-1} h^{-1}	[36]
Cu_2O/rGO	Hummer's	Rhombic dodecahedral	400–700	–	CH_3OH:355.3μmolg$_{cat}$$^{-1}$ after 20 h	[71]
NiO/Ni-Graphene	Incipient wetness impregnation	Nanoparticles	8.5	–	CH_4: 642 μmolg$_{Ni}$$^{-1}$ h^{-1}	[81]

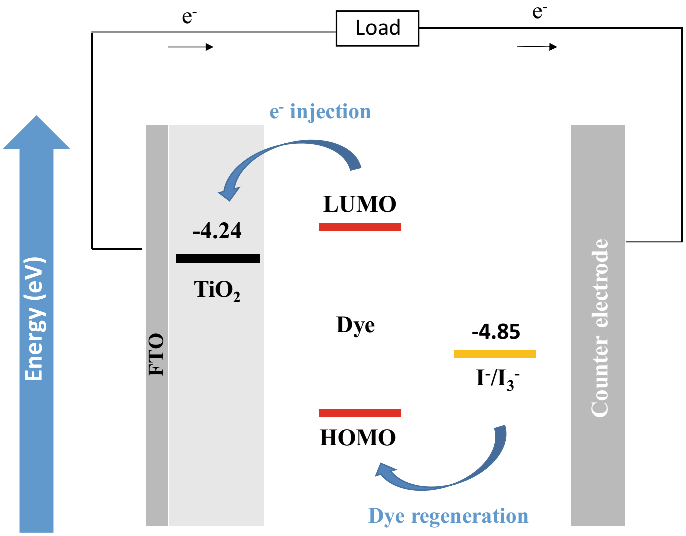

Fig. 25.12 The working principle of DSSC

photoanode, it is required that metal oxides have large surface area, suitable energy levels, rapid electron transport, and low electron recombination for high efficiency of DSSC [2, 7, 19, 47, 118].

TiO_2 is one of the most widely used photoanode materials in DSSCs due to its stability, electron-transport property, and electron diffusion length [35, 56]. The morphology, surface area, and particle size of TiO_2 play an important role in the efficiency of DSSCs. It was shown the small particle size and large pore size of TiO_2 can provide better electron transport and high current efficiency. The high surface area can increase the adsorption of dye molecules on TiO_2, resulting in an improvement in the efficiency of DSSCs [33, 35, 43, 62]. The modification of TiO_2 by using dye sensitization, metal and non-metal doping approaches can provide wide absorption range in visible region and improvement in DSSC efficiency [32, 87, 110, 113]. Kumar et al. have reported the synthesis of the aromatic amines (aniline and o-phenylenediamine) capped TiO_2 composites as scattering layer for DSSC with the maximum photo-conversion efficiency of 9.84% [61]. Aromatic amine capped TiO_2 shows uniform particle size and homogeneous amine distribution over TiO_2 (Fig. 25.13), leading to high light scattering ability and high visible light absorption. This can provide higher photocurrent density and fill factor, resulting in higher cell efficiency compare to pristine TiO_2. Sahu et al. have demonstrated that Cu-doped TiO_2 as photoanode increases the efficiency of DSSC with improved open-circuit voltage [112]. The incorporation of Cu^{2+} ions into TiO_2 shifts the Fermi level towards the conduction band edge and an important increase in open-circuit voltage (V_{oc}) was observed. Furthermore, the high surface area of Cu-doped TiO_2 improves the adsorption of N719 ruthenium dye molecules with

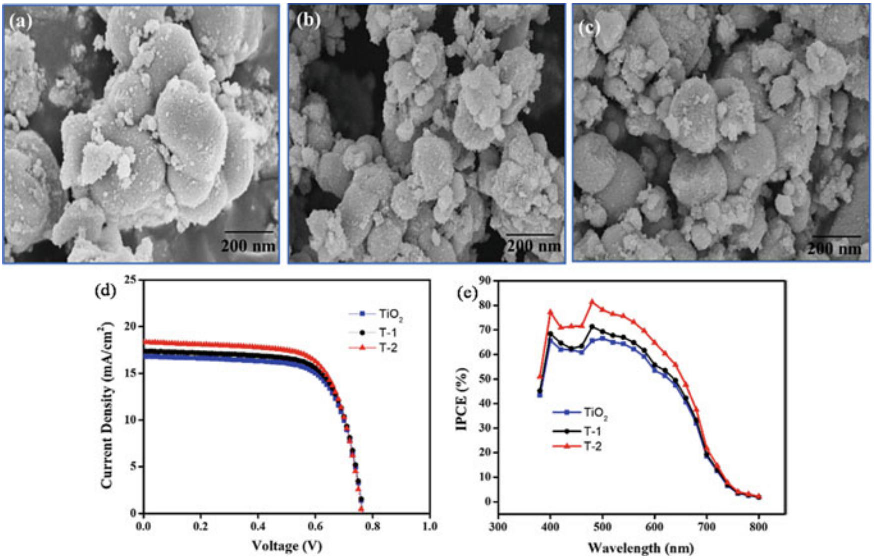

Fig. 25.13 **a**–**c** FE-SEM images of TiO_2, T-1 (aniline capped TiO_2) and T-2 (o-phenylenediamine capped TiO_2) composite, **d** Photocurrent density–voltage curves of TiO_2, T-1 and T-2 composite as scattering layer. **e** IPCE spectra of TiO_2, T-1 and T-2 composite (Adapted from Ref. [61], Copyright (2020), with permission from Elsevier)

high short circuit current density (J_{sc}). Kakiage et al. have reported that highly-efficient dye-sensitized solar cells using collaborative sensitization by an alkoxysilyl-anchor and carboxy-anchor organic dyes to TiO_2 [53]. This approach enhances the electron injection from dye molecules to TiO_2, achieving over 14% conversion efficiency in the cells.

In DSSC applications, ZnO is one of the photoanodic materials seen as an alternative to TiO_2 due to higher electron mobility and longer electron lifetime. However, ZnO still exhibits lower cell efficiency and lower stability compared to TiO_2 [2, 104, 125, 129]. There are many efforts to improve the performance of ZnO-based DSSCs. The doping with Mn, Ca, Cu, or Sr is one of the important strategies improving the optical and electrical properties of ZnO. It was shown that electrical conductivity and optical transmission of ZnO films in visible regions were improved using doping with Mn. Ca or Cu elements [44, 82, 83, 124]. The formation of semiconductor composites is used as photoanode in DSSC. Banik et al., have reported the effect of mesoporous ZnO hollow spheres loading on SnO_2 for DSSC application [7]. It is seen that the addition of ZnO hollow spheres increases surface area with good light-harvesting ability and improves transport properties. Thus SnO_2–ZnO hollow spheres composite exhibits higher cell efficiency of 4.37% compared to that of SnO_2 (1.15%).

Recently, Li et al. have reported that the synthesis of $Co_3O_4@Co_3S_4$ by a facile in-situ sulfurization method and used as counter electrode for flexible dye-sensitized solar cells [65]. The introduction of Co_3S_4 to Co_3O_4 can provide high conductivity, faster charge transfer and high electrocatalytic activity of the counter electrode which can results the improvement of cell efficiency of 5.30% compared to cell with a sputtered Pt counter alectrode (5.23%).

The use of liquid electrolyte systems in DSSCs limits long-term stability of cell due to iodine sublimation and solvent evaporation in electrolyte. Solid-state dye-sensitized solar cells (ss-DSSC) can overcome this problem by replacement of the liquid electrolyte with a solid-state hole transporting material (HTM) or polymer electrolyte [9, 50, 69]. However, ss-DSSC still exhibit lower efficiency due to lower hole conductivity and poor pore filling of HTMs than DSSC with liquid electrolyte [1, 6, 9, 153]. The morphology, particle size, and surface area of metal oxides have an important effect on electron transport and recombination properties of ss-DSSCs. The solid-state electrolyte can improve stability of devices. Recently, Cao et al. have obtained a solid-state DSSC with an efficiency of 11.3% using mesoscopic TiO_2 and copper(II/I) hole transport materials [11].

Recently, organic photovoltaics (OPV) have attracted interest due to their lightweight and flexible properties in photovoltaic technology which the power conversion efficiency could reach to 17.5% [93, 116]. The general structure of OPV consists of an electron donor material and an electron acceptor material between two electrodes. Metal oxides can act as electron-accepting material, active material, electron transport layer, charge blocking layer, optical spacer, charge collector in OPV [34, 67]. The use of doping methods can affect the power conversion efficiency of devices. Sn-doped TiO_2 as ETL shows effective charge separation and improved electrical properties due to the replacement of Ti^{4+} with Sn^{4+} which can result in higher J_{sc} and cell efficiency in comparison with TiO_2 [108]. It was found that the doping ZnO with Mg or Li elements can shift the energy levels of ZnO and increase V_{oc} value which can lead to improvement in cell efficiency [75, 96]. Jiang et al. have reported that organic solar cells with triethanolamine passivated ZnO exhibit higher electron mobility, and longer charge carrier recombination lifetime in comparision with the devices based on as-cast ZnO [51]. Triethanolamine passivated ZnO can improve the stability of devices with efficiency of 15.61%. the mechanism of organic solar cells with triethanolamine passivated ZnO was shown in Fig. 25.14.

Perovskite solar cells (PSCs) are promising candidates for next-generation photovoltaic technology which the power conversion efficiency could reach to 25.5% [93, 60, 159]. The high power conversion efficiency of PSCs are related to their high visible light absorption ability, high carrier mobility, and long carrier diffusion length [12, 76, 103]. In general, the structure of PSC consists of electron transport layer (ETL), perovskite material, hole transport layer (HTL), and metal electrode. Metal oxides such as TiO_2, SnO_2 and ZnO have been widely used as electron transport layer (ETL) in PSCs [40, 85, 111]. For ideal ETL, there are some desired properties from metal oxide such as a good contact with perovskite layer, proper band alignment with perovskite layer, and high carrier mobility [12, 132]. The optimization of metal oxide for ETL can be made using elemental doping, combining different semiconductors and surface modifications. It is found that the

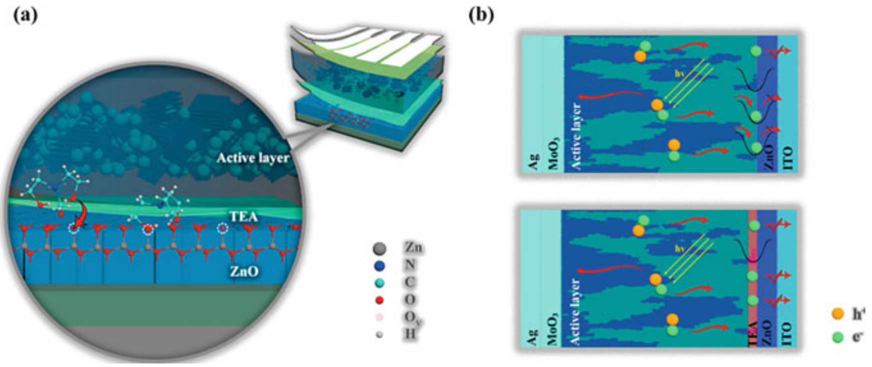

Fig. 25.14 **a** Experimental mechanism schematic of triethanolamine passivating ZnO. **b** Experimental mechanism schematic of the charge transporting process of OSCs based on as-cast ZnO and triethanolamine-capped ZnO (Reprinted with permission from Ref. [51]. Copyright (2020) American Chemical Society)

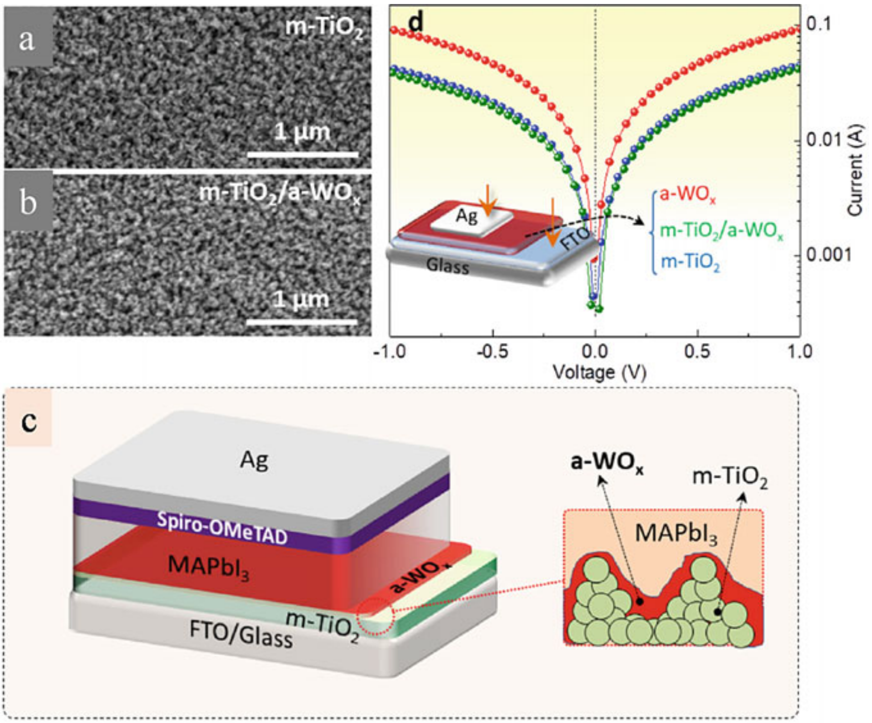

Fig. 25.15 **a** Top-view SEM images of the m-TiO_2 and **b** m-TiO_2/a-WO_x layers on ITO glass, respectively. **c** The structure of the perovskite solar cells. **d** The illuminated J–V curves of the cells with an architecture of Ag/m–TiO_2/FTO glass and Ag/a–WO_x/FTO glass layers, respectively. The inset shows the architecture (Reprinted from Ref. [131], Copyright (2020), with permission from Elsevier)

doping TiO_2 with Zn, Mg, N, or Sn elements can increase J_{sc} and V_{oc}, resulting enhancement in power conversion efficiency of PSCs [74, 157, 158]. The use of mesoporous TiO_2/amorphous WO_x composite as ETL enhances interfacial charge transfer in PSC and results in high power conversion efficiency of 20.98% [131]. The deposition of a-WO_x on TiO_2 can provide smoother surface compared to TiO_2 (Fig. 25.15) and improve the crystallization of the perovskite films. This can provide the higher electron mobility and reduced defect density in perovskite films which can improve charge transfer and performance of the devices.

ZnO is n-type semiconductor as an electron transport layer in PSCs. ZnO has various morphologies such as nanorods, nanowires, nanotubes, nanosheets, and nanowalls [12, 156]. Among these nanostructures, ZnO nanorod has attracted in PSCs due to its highly visible transmittance and high contact area. Yun et al. have demonstrated the effect of length of ZnO nanorod on the power conversion efficiency of PSC [149]. The optimum length of ZnO nanorod can provide good crystalline quality of the films which can reduce charge recombination and increase the efficiency of cell (14.22%). In_2O_3 is another n-type semiconductor material for PSC application due to well-tuned band gap, high mobilty, and electron selective capacity. Oin et al. have reported low-temperature solution-processed In_2O_3 nanocrystalline film as an electron selective layer (ESL) for PSC [101]. The power conversion efficiency of 14.83% was obtained by introducing phenyl-C61-butyric acid methyl ester (PCBM) layer between the In_2O_3 ESL and the perovskite layer.

25.5 Conclusion

In this chapter recent progress on visible range activated metal oxide semiconductors in green photocatalytic applications of solar fuels and solar cells is summarized. TiO_2 and ZnO are chosen as the model semiconductors as they represent the most widely utilized ones. No matter in what crystalline structure or morphology, doped and undoped metal oxides have become one of the essential components of solar energy conversion to fuels and/or current. In those applications, metal oxides standout with their chemical and thermal stability, morphology variety, position of conduction and valance band energy levels, optical properties, and cost. It is obvious that whenever the durability and efficiency problems are solved, its economy will increasing grow.

References

1. Abate A, Leijtens T, Pathak S, Teuscher J, Avolio R, Errico ME et al (2013) Lithium salts as "redox active" p-type dopants for organic semiconductors and their impact in solid-state dye-sensitized solar cells. Phys Chem Chem Phys 15(7):2572–2579. https://doi.org/10.1039/C2CP44397J
2. Akman E (2020) Enhanced photovoltaic performance and stability of dye-sensitized solar cells by utilizing manganese-doped ZnO photoanode with europium compact layer. J Mol Liq 317:114223. https://doi.org/10.1016/j.molliq.2020.114223
3. Ansari SA, Khan MM, Ansari MO, Cho MH (2016) Nitrogen-doped titanium dioxide (N-doped TiO_2) for visible light photocatalysis. New J Chem 40(4):3000–3009. https://doi.org/10.1039/C5NJ03478G
4. Asahi R, Morikawa T, Irie H, Ohwaki T (2014) Nitrogen-doped titanium dioxide as visible-light-sensitive photocatalyst: designs, developments, and prospects. Chem Rev 114 (19):9824–9852. https://doi.org/10.1021/cr5000738
5. Bai S, Li H, Guan Y, Jiang S (2011) The enhanced photocatalytic activity of CdS/TiO_2 nanocomposites by controlling CdS dispersion on TiO_2 nanotubes. Appl Surf Sci 257 (15):6406–6409. https://doi.org/10.1016/j.apsusc.2011.02.007
6. Bailie CD, Unger EL, Zakeeruddin SM, Grätzel M, McGehee MD (2014) Melt-infiltration of spiro-OMeTAD and thermal instability of solid-state dye-sensitized solar cells. Phys Chem Chem Phys 16(10):4864–4870. https://doi.org/10.1039/C4CP00116H
7. Banik A, Ansari MS, Qureshi M (2018) Efficient energy harvesting in SnO_2-based dye-sensitized solar cells utilizing nano-amassed mesoporous zinc oxide hollow microspheres as synergy boosters. ACS Omega 3(10):14482–14493. https://doi.org/10.1021/acsomega.8b02520
8. Basavarajappa PS, Patil SB, Ganganagappa N, Raghava K, Raghu AV, Venkata C (2019) Sciencedirect recent progress in metal-doped TiO_2, non-metal doped/codoped TiO_2 and TiO_2 nanostructured hybrids for enhanced photocatalysis, 5. https://doi.org/10.1016/j.ijhydene.2019.07.241
9. Benesperi I, Michaels H, Freitag M (2018) The researcher's guide to solid-state dye-sensitized solar cells. J Mater Chem C 6(44):11903–11942. https://doi.org/10.1039/C8TC03542C
10. Bilal M, Muhammad T, Muhammad S, Muhammad R, Najeeb S, Rehman U, Muhammad S (2020) Visible light responsive photocatalytic hydrogen evolution using MoS_2 incorporated ZnO. Appl Nanosci 10(10):3925–3931. https://doi.org/10.1007/s13204-020-01476-x
11. Cao Y, Saygili Y, Ummadisingu A, Teuscher J, Luo J, Pellet N et al (2017) 11% efficiency solid-state dye-sensitized solar cells with copper(II/I) hole transport materials. Nat Commun 8(1):15390. https://doi.org/10.1038/ncomms15390
12. Cao Z, Li C, Deng X, Wang S, Yuan Y, Chen Y et al (2020) Metal oxide alternatives for efficient electron transport in perovskite solar cells: beyond TiO_2 and SnO_2. J Mater Chem A 8(38):19768–19787. https://doi.org/10.1039/D0TA07282F
13. Chandra M, Bhunia K, Pradhan D (2018) Controlled synthesis of CuS/TiO_2 heterostructured nanocomposites for enhanced photocatalytic hydrogen generation through water splitting. Inorg Chem 57(8):4524–4533. https://doi.org/10.1021/acs.inorgchem.8b00283
14. Cheng X, Yu X, Xing Z, Yang L (2016) Synthesis and characterization of N-doped TiO_2 and its enhanced visible-light photocatalytic activity. Arab J Chem 9:S1706–S1711. https://doi.org/10.1016/j.arabjc.2012.04.052
15. Cherni D, Ayedi S, Jaouali I, Moussa N, Nsib MF (2020) Preparation of solar/visible-light active TiO_2 photocatalysts with carboxylic acids for the degradation of phenol. React Kinet Mech Catal 129(2):1091–1102. https://doi.org/10.1007/s11144-020-01756-1
16. Choi W, Termin A, Hoffmann MR (1994) The Role of Metal Ion Dopants in quantum-sized TiO_2: correlation between photoreactivity and charge carrier recombination dynamics. J Phys Chem 98(51):13669–13679. https://doi.org/10.1021/j100102a038

17. Cots A, Bonete P (2018) Improving the stability and efficiency of CuO photocathodes for solar hydrogen production through modification with iron´. ACS Appl Mater Interfaces 10:26348–26356. https://doi.org/10.1021/acsami.8b09892
18. Diker H, Varlikli C, Mizrak K, Dana A (2011) Characterizations and photocatalytic activity comparisons of N-doped nc-TiO_2 depending on synthetic conditions and structural differences of amine sources. Energy 36(2):1243–1254. https://doi.org/10.1016/j.energy.2010.11.020
19. Diker H, Varlikli C, Stathatos E (2014) N-doped titania powders prepared by different nitrogen sources and their application in quasi-solid state dye-sensitized solar cells. Int J Energy Res 908–917. https://doi.org/10.1002/er.3091s
20. Diwald O, Thompson TL, Zubkov T, Walck SD, Yates JT (2004) Photochemical activity of nitrogen-doped rutile TiO_2(110) in visible light. J Phys Chem B 108(19):6004–6008. https://doi.org/10.1021/jp031267y
21. Djurišić AB, He Y, Ng AMC (2020) Visible-light photocatalysts: prospects and challenges. APL Mater 8(3). https://doi.org/10.1063/1.5140497
22. Du J, Wang H, Yang M, Zhang F, Wu H, Cheng X et al (2018) ScienceDirect highly efficient hydrogen evolution catalysis based on MoS_2/CdS/TiO_2 porous composites 3:3–11. https://doi.org/10.1016/j.ijhydene.2018.03.208
23. Dunnill CW, Parkin IP (2011) Nitrogen-doped TiO_2 thin films: photocatalytic applications for healthcare environments. Dalton Trans 40(8):1635–1640. https://doi.org/10.1039/C0DT00494D
24. Emeline AV, Kuznetsov VN, Rybchuk VK, Serpone N (2008) Visible-light-active titania photocatalysts: the case of N-doped <svg style="vertical-align:-4.32007pt; width:42.637501px;" id="M1" height="20.637501" version="1.1" viewBox="0 0 42.637501 20.637501" width="42.637501" xmlns:xlink="http://www.w3.org/1999/xli. Int J Photoenergy, 2008:258394. https://doi.org/10.1155/2008/258394
25. Etacheri V, Di Valentin C, Schneider J, Bahnemann D, Pillai SC (2015) Visible-light activation of TiO_2 photocatalysts: advances in theory and experiments. J Photochem Photobiol C 25:1–29. https://doi.org/10.1016/j.jphotochemrev.2015.08.003
26. Fagan R, McCormack DE, Dionysiou DD, Pillai SC (2016) A review of solar and visible light active TiO_2 photocatalysis for treating bacteria, cyanotoxins and contaminants of emerging concern. Mater Sci Semicond Process 42:2–14. https://doi.org/10.1016/j.mssp.2015.07.052
27. Favet T, Cottineau T, Keller V, El Khakani MA (2020) Comparative study of the photocatalytic effects of pulsed laser deposited CoO and NiO nanoparticles onto TiO_2 nanotubes for the photoelectrochemical water splitting. Solar Energy Mater Solar Cells 217. https://doi.org/10.1016/j.solmat.2020.110703
28. Fishman ZS, Rudshteyn B, He Y, Liu B, Chaudhuri S, Askerka M et al (2016) Fundamental role of oxygen stoichiometry in controlling the band gap and reactivity of cupric oxide nanosheets. J Am Chem Soc 138(34):10978–10985. https://doi.org/10.1021/jacs.6b05332
29. Fujishima A, Honda K (1972) Electrochemical photolysis of water at a semiconductor electrode. Nature 238(5358):37–38. https://doi.org/10.1038/238037a0
30. Fujishima A, Rao TN, Tryk DA (2000) Titanium dioxide photocatalysis. J Photochem Photobiol C Photochem Rev 1(1):1–21. https://doi.org/10.1016/S1389-5567(00)00002-2
31. Gai L, Duan X, Jiang H, Mei Q, Zhou G, Tian Y, Liu H (2012) One-pot synthesis of nitrogen-doped TiO_2 nanorods with anatase/brookite structures and enhanced photocatalytic activity. CrystEngComm 14(22):7662–7671. https://doi.org/10.1039/C2CE25563D
32. Gao N, Wan T, Xu Z, Ma L, Ramakrishna S, Liu Y (2020) Nitrogen doped TiO2/Graphene nanofibers as DSSCs photoanode. Mater Chem Phys 255:123542. https://doi.org/10.1016/j.matchemphys.2020.123542
33. Ge Z, Wang C, Chen Z, Wang T, Chen T, Shi R et al (2021) Investigation of the TiO_2 nanoparticles aggregation with high light harvesting for high-efficiency dye-sensitized solar cells. Mater Res Bull 135:111148. https://doi.org/10.1016/j.materresbull.2020.111148

34. Gershon T (2011) Metal oxide applications in organic-based photovoltaics. Mater Sci Technol 27(9):1357–1371. https://doi.org/10.1179/026708311X13081465539809
35. González-Verjan VA, Trujillo-Navarrete B, Félix-Navarro RM, de León JND, Romo-Herrera JM, Calva-Yáñez JC et al (2020) Effect of TiO_2 particle and pore size on DSSC efficiency. Mater Renew Sustain Energy 9(2):13. https://doi.org/10.1007/s40243-020-00173-7
36. Guo H, Chen M, Zhong Q, Wang Y, Ma W, Ding J (2019) Synthesis of Z-scheme α-Fe_2O_3/g-C_3N_4 composite with enhanced visible-light photocatalytic reduction of CO_2 to CH_3OH. J CO_2 Util 33:233–241. https://doi.org/10.1016/j.jcou.2019.05.016
37. Guo L, Yang Z, Marcus K, Li Z, Luo B, Zhou L et al (2018). MoS_2/TiO_2 heterostructures as nonmetal plasmonic photocatalysts for highly efficient hydrogen evolution. Energy Environ Sci 11(1):106–114. https://doi.org/10.1039/C7EE02464A
38. Han C, Pelaez M, Likodimos V, Kontos AG, Falaras P, O'Shea K, Dionysiou DD (2011) Innovative visible light-activated sulfur doped TiO_2 films for water treatment. Appl Catal B Environ 107(1):77–87. https://doi.org/10.1016/j.apcatb.2011.06.039
39. Hannappel T, Burfeindt B, Storck W, Willig F (1997) Measurement of ultrafast photoinduced electron transfer from chemically anchored Ru-Dye molecules into empty electronic states in a colloidal anatase TiO_2 film. J Phys Chem B 101(35):6799–6802. https://doi.org/10.1021/jp971581q
40. Hashmi SG, Martineau D, Li X, Ozkan M, Tiihonen A, Dar MI et al (2017) Air processed inkjet infiltrated carbon based printed perovskite solar cells with high stability and reproducibility. Adv Mater Technol 2(1):1600183. https://doi.org/10.1002/admt.201600183
41. He R, Hocking RK, Tsuzuki T (2012) Co-doped ZnO nanopowders: location of cobalt and reduction in photocatalytic activity. Mater Chem Phys 132(2):1035–1040. https://doi.org/10.1016/j.matchemphys.2011.12.061
42. He Y, Ng AMC (2020) Visible-light photocatalysts: prospects and challenges. APL Mater 8:030903. https://doi.org/10.1063/1.5140497
43. Hou X, Aitola K, Lund PD (2020). TiO_2 nanotubes for dye-sensitized solar cells—a review. Energy Sci Eng 00:1–17. https://doi.org/10.1002/ese3.831
44. Hu D, Liu X, Deng S, Liu Y, Feng Z, Han B et al (2014) Structural and optical properties of Mn-doped ZnO nanocrystalline thin films with the different dopant concentrations. Physica E Low-Dimens Syst Nanostruct 61:14–22. https://doi.org/10.1016/j.physe.2014.03.007
45. Huan TN, Rousse G, Zanna S, Lucas IT, Xu X, Menguy N et al (2017) A dendritic nanostructured copper oxide electrocatalyst for the oxygen evolution reaction. Angew Chemie Int Edn 56(17):4792–4796. https://doi.org/10.1002/anie.201700388
46. Huerta AM, Luévano FE, Leticia H, Martínez MT, Sánchez AT (2019) Photocatalytic—H_2 production and—CO_2 reduction on Cu, Ni—doped ZnO: effect of metal doping and oxygen vacancies. J Mater Sci Mater Electron 30(20):18506–18518. https://doi.org/10.1007/s10854-019-02204-0
47. Ibrayev N, Serikov T, Zavgorodniy A, Sadykova A (2018) The effect of the DSSC photoanode area based on TiO_2/Ag on the conversion efficiency of solar energy into electrical energy. IOP Conference Series: Materials Science and Engineering 289(1).https://doi.org/10.1088/1757-899X/289/1/012024
48. Inoue T, Fujishima A, Konishi S, Honda K (1979) Photoelectrocatalytic reduction of carbon dioxide in aqueous suspensions of semiconductor powders. Nature 277(5698):637–638. https://doi.org/10.1038/277637a0
49. Jagadale TC, Takale SP, Sonawane RS, Joshi HM, Patil SI, Kale BB, Ogale SB (2008) N-doped TiO_2 nanoparticle based visible light photocatalyst by modified peroxide Sol−Gel method. J Phys Chem C 112(37):14595–14602. https://doi.org/10.1021/jp803567f
50. Jang YJ, Thogiti S, Lee K, Kim JH (2019) Hole-Transporting Material. Curr Comput-Aided Drug Des 9:452

51. Jiang H, Li T, Han X, Guo X, Jia B, Liu K, Cao H, Lin Y, Zhang M, Li Y, Zhan X (2020) Passivated metal oxide n-Type contacts for efficient and stable organic solar cells. ACS Appl Energy Mater 3(1):1111–1118. https://doi.org/10.1021/acsaem.9b02158
52. Jiang Z, Wan W, Li H, Yuan S, Zhao H, Wong PK (2018) A hierarchical Z scheme α-Fe_2O_3/g-C_3N_4 hybrid for enhanced photocatalytic CO_2 reduction. Adv Mater 30(10):1706108. https://doi.org/10.1002/adma.201706108
53. Kakiage K, Aoyama Y, Yano T, Oya K, Fujisawa J, Hanaya M (2015) Highly-efficient dye-sensitized solar cells with collaborative sensitization by silyl-anchor and carboxy-anchor dyes. Chem Commun 51(88):15894–15897. https://doi.org/10.1039/C5CC06759F
54. Kanhere P, Chen Z (2014) A review on visible light active perovskite-based photocatalysts. Molecules 19(12):19995–20022. https://doi.org/10.3390/molecules191219995
55. Karthik P, Kumar TRN, Neppolian B (2020) ScienceDirect redox couple mediated charge carrier separation in g-C_3N_4/CuO photocatalyst for enhanced photocatalytic H_2 production, 45:7541–7551. https://doi.org/10.1016/j.ijhydene.2019.06.045
56. Khan J, Gu J, Meng Y, Chai Z, He S, Wu Q et al (2017) Anatase TiO_2 single crystal hollow nanoparticles: their facile synthesis and high-performance in dye-sensitized solar cells. CrystEngComm 19(2):325–334. https://doi.org/10.1039/C6CE02062C
57. Khan MM, Adil SF, Al-Mayouf A (2015) Metal oxides as photocatalysts. J Saudi Chem Soc 19(5):462–464. https://doi.org/10.1016/j.jscs.2015.04.003
58. Kishore Kumar D, Kříž J, Bennett N, Chen B, Upadhayaya H, Reddy KR, Sadhu V (2020) Functionalized metal oxide nanoparticles for efficient dye-sensitized solar cells (DSSCs): a review. Mater Sci Energy Technol 3:472–481. https://doi.org/10.1016/j.mset.2020.03.003
59. Kong X, Peng Z, Jiang R, Jia P, Feng J, Yang P et al (2020) Nanolayered heterostructures of N—doped TiO_2 and N—doped carbon for hydrogen evolution. https://doi.org/10.1021/acsanm.9b02217
60. Kothandaraman RK, Jiang Y, Feurer T, Tiwari AN, Fu F (2020) Near-infrared-transparent perovskite solar cells and perovskite-based tandem photovoltaics. Small Methods 4 (10):2000395. https://doi.org/10.1002/smtd.202000395
61. Kumar TRN, Yuvaraj S, Kavitha P, Sudhakar V (2020) Aromatic amine passivated TiO_2 for dye-sensitized solar cells (DSSC) with $\sim$ 9. 8 % efficiency. Sol Energy 201:965–971. https://doi.org/10.1016/j.solener.2020.03.077
62. Lee K, Suryanarayanan V, Ho K (2006) The influence of surface morphology of TiO_2 coating on the performance of dye-sensitized solar cells $, vol 90, pp 2398–2404. https://doi.org/10.1016/j.solmat.2006.03.034
63. Li D, Haneda H, Labhsetwar NK, Hishita S, Ohashi N (2005) Visible-light-driven photocatalysis on fluorine-doped TiO_2 powders by the creation of surface oxygen vacancies. Chem Phys Lett 401(4):579–584.https://doi.org/10.1016/j.cplett.2004.11.126
64. Li X, Wen J, Low J, Fang Y, Yu J (2014) Design and fabrication of semiconductor photocatalyst for photocatalytic reduction of CO_2 to solar fuel, vol 57. https://doi.org/10.1007/s40843-014-0003-1
65. Li Z, Chen L, Yang Q, Yang H, Zhou Y (2021) Applied Surface science compacted stainless steel mesh-supported Co_3O_4 porous nanobelts for HCHO catalytic oxidation and Co_3O_4 @ Co_3S_4 via in situ sulfurization as platinum-free counter electrode for flexible dye-sensitized solar cells. Appl Surf Sci 536:147815. https://doi.org/10.1016/j.apsusc.2020.147815
66. Lima MK, Fernandes DM, Silva MF, Baesso ML, Neto AM, de Morais GR et al (2014) Co-doped ZnO nanoparticles synthesized by an adapted sol–gel method: effects on the structural, optical, photocatalytic and antibacterial properties. J Sol-Gel Sci Technol 72 (2):301–309. https://doi.org/10.1007/s10971-014-3310-z
67. Lin Z, Jiang C, Zhu C, Zhang J (2013) Development of inverted organic solar cells with TiO_2 interface layer by using low-temperature atomic layer deposition. ACS Appl Mater Interfaces 5(3):713–718. https://doi.org/10.1021/am302252p
68. Lin Y-H, Weng C-H, Srivastav AL, Lin Y-T, Tzeng J-H (2015) Facile synthesis and characterization of N-Doped $\mathbf{TiO_2}$ photocatalyst and its visible-light activity for

photo-oxidation of ethylene. J Nanomater 2015:807394. https://doi.org/10.1155/2015/807394

69. Liu B, Li X, Liu M, Ning Z, Zhang Q, Li C et al (2012) Photovoltaic performance of solid-state DSSCs sensitized with organic isophorone dyes: effect of dye-loaded amount and dipole moment. Dyes Pigm 94(1):23–27. https://doi.org/10.1016/j.dyepig.2011.11.005
70. Liu G, Yin L-C, Wang J, Niu P, Zhen C, Xie Y, Cheng H-M (2012) A red anatase TiO_2 photocatalyst for solar energy conversion. Energy Environ Sci 5(11):9603–9610. https://doi.org/10.1039/C2EE22930G
71. Liu S-H, Lu J-S, Pu Y-C, Fan H-C (2019) Enhanced photoreduction of CO_2 into methanol by facet-dependent Cu_2O/reduce graphene oxide. J CO_2 Util 33:171–178. https://doi.org/10.1016/j.jcou.2019.05.020
72. Liu S-H, Syu H-R (2012) One-step fabrication of N-doped mesoporous TiO_2 nanoparticles by self-assembly for photocatalytic water splitting under visible light. Appl Energy 100:148–154. https://doi.org/10.1016/j.apenergy.2012.03.063
73. Low J, Dai B, Tong T, Jiang C, Yu J (2019) In Situ irradiated X-ray photoelectron spectroscopy investigation on a direct Z-Scheme TiO_2/CdS composite film photocatalyst. Adv Mater 31(6):1802981. https://doi.org/10.1002/adma.201802981
74. Lv Y, Tong H, Cai W, Zhang Z, Chen H, Zhou X (2021) Boosting the efficiency of commercial available carbon-based perovskite solar cells using Zinc-doped TiO_2 nanorod arrays as electron transport layer. J Alloy Compd 851:156785. https://doi.org/10.1016/j.jallcom.2020.156785
75. Lloyd MT, Lee Y-J, Davis RJ, Fang E, Fleming RM, Hsu JWP, Kline RJ, Toney MF (2009) Improved efficiency in Poly(3-hexylthiophene)/zinc oxide solar cells via lithium incorporation. J Phys Chem C 113(41):17608–17612. https://doi.org/10.1021/jp907758s
76. Ma L, Hao F, Stoumpos CC, Phelan BT, Wasielewski MR, Kanatzidis MG (2016) Carrier diffusion lengths of over 500 nm in lead-free perovskite $CH_3NH_3SnI_3$ films. J Am Chem Soc 138(44):14750–14755. https://doi.org/10.1021/jacs.6b09257
77. Mao N (2019) Investigating the heteronjunction between ZnO/Fe_2O_3 and g-C_3N_4 for an enhanced photocatalytic H_2 production under visible-light irradiation. Sci Rep 9:12383. https://doi.org/10.1038/s41598-019-48730-z
78. Martha S, Sahoo PC, Parida KM (2015) RSC advances an overview on visible light responsive metal oxide based photocatalysts for hydrogen energy production. RSC Adv 5:61535–61553. https://doi.org/10.1039/C5RA11682A
79. Martínez-Ferrero E, Sakatani Y, Boissière C, Grosso D, Fuertes A, Fraxedas J, Sanchez C (2007) Nanostructured titanium oxynitride porous thin films as efficient visible-active photocatalysts. Adv Func Mater 17(16):3348–3354. https://doi.org/10.1002/adfm.200700396
80. Martini I, Hodak JH, Hartland GV (1998) Effect of water on the electron transfer dynamics of 9-Anthracenecarboxylic acid bound to TiO_2 nanoparticles: demonstration of the marcus inverted region. J Phys Chem B 102(3):607–614. https://doi.org/10.1021/jp972925f
81. Mateo D, Albero J, García H (2018) Graphene supported NiO/Ni nanoparticles as efficient photocatalyst for gas phase CO_2 reduction with hydrogen. Appl Catal B 224:563–571. https://doi.org/10.1016/j.apcatb.2017.10.071
82. Mehmood B, Khan MI, Iqbal M, Mahmood A, Al-Masry W (2020) Structural and optical properties of Ti and Cu co-doped ZnO thin films for photovoltaic applications of dye sensitized solar cells. Int J Energy Res 1–15. https://doi.org/10.1002/er.5939
83. Mimouni R, Kamoun O, Yumak A, Mhamdi A, Boubaker K, Petkova P, Amlouk M (2015) Effect of Mn content on structural, optical, opto-thermal and electrical properties of ZnO: Mn sprayed thin films compounds. J Alloy Compd 645:100–111. https://doi.org/10.1016/j.jallcom.2015.05.012
84. Modanlu S, Shafiekhani A (2019) Synthesis of pure and C/S/N co-doped Titania on Al mesh and their photocatalytic usage in Benzene degradation. Sci Rep 9(1):16648. https://doi.org/10.1038/s41598-019-53189-z

85. Mohamad Noh MF, Teh CH, Daik R, Lim EL, Yap CC, Ibrahim MA et al (2018) The architecture of the electron transport layer for a perovskite solar cell. J Mater Chem C 6 (4):682–712. https://doi.org/10.1039/C7TC04649A
86. Mohapatra L, Parida K (2017) A review of solar and visible light active oxo-bridged materials for energy and environment. Catal Sci Technol 7(11):2153–2164. https://doi.org/10.1039/C7CY00116A
87. Mousa MA, Khairy M, Mohamed HM (2018) Dye-sensitized solar cells based on an N-Doped TiO_2 and TiO_2-graphene composite electrode. J Electron Mater 47(10):6241–6250. https://doi.org/10.1007/s11664-018-6530-0
88. Mu J, Chen B, Zhang M, Guo Z, Zhang P, Zhang Z et al (2012) Enhancement of the visible-light photocatalytic activity of In_2O_3–TiO_2 nanofiber heteroarchitectures. ACS Appl Mater Interfaces 4(1):424–430. https://doi.org/10.1021/am201499r
89. Nakata K, Fujishima A (2012) TiO_2 photocatalysis: design and applications. J Photochem Photobiol C 13(3):169–189. https://doi.org/10.1016/j.jphotochemrev.2012.06.001
90. Navlani-garcía M, Mori K, Kuwahara Y, Yamashita H (2018) Recent strategies targeting efficient hydrogen production from chemical hydrogen storage materials over carbon-supported catalysts, pp 277–292. https://doi.org/10.1038/s41427-018-0025-6
91. Nie J, Patrocinio AOT, Hamid S, Sieland F, Sann J, Xia S et al (2018) New insights into the plasmonic enhancement for photocatalytic H_2 production by Cu–TiO_2 upon visible light illumination. Phys Chem Chem Phys 20(7):5264–5273. https://doi.org/10.1039/C7CP07762A
92. Nishijima K, Kamai T, Murakami N, Tsubota T, Ohno T (2008) Photocatalytic hydrogen or oxygen evolution from water over S- or N-doped TiO_2 under visible light. Int J Photoenergy 2008:173943. https://doi.org/10.1155/2008/173943
93. NREL (2020) Best Research-Cell Efficiency Chart. https://www.nrel.gov/pv/cell-efficiency.html. Accessed Dec 2020
94. Nolan M, Iwaszuk A, Lucid AK, Carey JJ, Fronzi M (2016) Design of novel visible light active photocatalyst materials: surface modified TiO_2. Adv Mater 28(27):5425–5446. https://doi.org/10.1002/adma.201504894
95. Nolan NT, Synnott DW, Seery MK, Hinder SJ, Van Wassenhoven A, Pillai SC (2012) Effect of N-doping on the photocatalytic activity of sol–gel TiO_2. J Hazard Mater 211–212:88–94. https://doi.org/10.1016/j.jhazmat.2011.08.074
96. Olson DC, Shaheen SE, White MS, Mitchell WJ, van Hest MFAM, Collins RT, Ginley DS (2007) Band-offset engineering for enhanced open-circuit voltage in polymer–oxide hybrid solar cells. Adv Funct Mater 17(2):264–269. https://doi.org/10.1002/adfm.200600215
97. Pan Y-X, You Y, Xin S, Li Y, Fu G, Cui Z et al (2017) Photocatalytic CO_2 reduction by carbon-coated indium-oxide nanobelts. J Am Chem Soc 139(11):4123–4129. https://doi.org/10.1021/jacs.7b00266
98. Park Y, Kim B, Jeong S, Jeon K, Chung K, Jung S (2020) Characteristics of hydrogen production by photocatalytic water splitting using liquid phase plasma over Ag-doped TiO_2 photocatalysts. Environ Res 188(January):109630. https://doi.org/10.1016/j.envres.2020.109630
99. Pelaez M, Nolan NT, Pillai SC, Seery MK, Falaras P, Kontos AG et al (2012) A review on the visible light active titanium dioxide photocatalysts for environmental applications. Appl Catal B 125:331–349. https://doi.org/10.1016/j.apcatb.2012.05.036
100. Qin D, Zhou Y, Wang W, Zhang C, Zeng G, Huang D et al (2020) Recent advances in two-dimensional nanomaterials for photocatalytic reduction of CO_2: insights into performance, theories and perspective. J Mater Chem A 8(37):19156–19195. https://doi.org/10.1039/D0TA07460H
101. Qin M, Ma J, Ke W, Qin P, Lei H, Tao H et al (2016) Perovskite solar cells based on low-temperature processed indium oxide electron selective layers. ACS Appl Mater Interfaces 8(13):8460–8466. https://doi.org/10.1021/acsami.5b12849

102. Qiu X, Li G, Sun X, Li L, Fu X (2008) Doping effects of Co_2+ ions on ZnO nanorods and their photocatalytic properties. Nanotechnology 19(21):215703. https://doi.org/10.1088/0957-4484/19/21/215703
103. Quan LN, Rand BP, Friend RH, Mhaisalkar SG, Lee T-W, Sargent EH (2019) Perovskites for next-generation optical sources. Chem Rev 119(12):7444–7477. https://doi.org/10.1021/acs.chemrev.9b00107
104. Quintana M, Edvinsson T, Hagfeldt A, Boschloo G (2007) Comparison of dye-sensitized ZnO and TiO_2 solar cells: studies of charge transport and carrier lifetime. J Phys Chem C 111(2):1035–1041. https://doi.org/10.1021/jp065948f
105. Rafique M, Mubashar R, Irshad M, Gillani SSA, Tahir MB, Khalid NR et al (2020) A comprehensive study on methods and materials for photocatalytic water splitting and hydrogen production as a renewable energy resource. J Inorg Organomet Polym Mater 30 (10):3837–3861. https://doi.org/10.1007/s10904-020-01611-9
106. Rajbongshi BM, Samdarshi SK (2014) ZnO and Co-ZnO nanorods—Complementary role of oxygen vacancy in photocatalytic activity of under UV and visible radiation flux. Mater Sci Eng B 182:21–28. https://doi.org/10.1016/j.mseb.2013.11.013
107. Rajeshwar K, de Tacconi NR, Ghadimkhani G, Chanmanee W, Janáky C (2013) Tailoring copper oxide semiconductor nanorod arrays for photoelectrochemical reduction of carbon dioxide to methanol. ChemPhysChem 14(10):2251–2259. https://doi.org/10.1002/cphc.201300080
108. Ranjitha A, Thambidurai M, Shini F, Muthukumarasamy N, Velauthapillai D (2019) Effect of doped TiO_2 film as electron transport layer for inverted organic solar cell. Mater Sci Energy Technol 2(3):385–388. https://doi.org/10.1016/j.mset.2019.02.006
109. Rehman S, Ullah R, Butt AM, Gohar ND (2009) Strategies of making TiO_2 and ZnO visible light active. J Hazard Mater 170(2–3):560–569. https://doi.org/10.1016/j.jhazmat.2009.05.064
110. Şahin Ç, Apostolopoulou A, Stathatos E (2018) New bipyridine ruthenium dye complexes with amide based ancillary ligands as sensitizers in semitransparent quasi-solid-state dye sensitized solar cells. Inorg Chim Acta 478:130–138. https://doi.org/10.1016/j.ica.2018.04.009
111. Şahin Ç, Diker H, Sygkridou D, Varlikli C, Stathatos E (2020) Enhancing the efficiency of mixed halide mesoporous perovskite solar cells by introducing amine modified graphene oxide buffer layer. Renew Energy 146:1659–1666. https://doi.org/10.1016/j.renene.2019.07.162
112. Sahu K, Dhonde M (2020) Microwave-assisted hydrothermal synthesis of Cu-doped TiO_2 nanoparticles for efficient dye-sensitized solar cell with improved open-circuit voltage. Int J Energy Res 1–10. https://doi.org/10.1002/er.6169
113. Sakthivel T, Ashok Kumar K, Ramanathan R, Senthilselvan J, Jagannathan K (2017) Silver doped TiO_2 nano crystallites for dye-sensitized solar cell (DSSC) applications. Mater Res Express 4(12):126310. https://doi.org/10.1088/2053-1591/aa9e36
114. Samadi M, Zirak M, Naseri A, Khorashadizade E, Moshfegh AZ (2016) Recent progress on doped ZnO nanostructures for visible-light photocatalysis. Thin Solid Films 605:2–19. https://doi.org/10.1016/j.tsf.2015.12.064
115. Samal A, Das DP (2018) Transfiguring UV light active "metal oxides" to visible light active photocatayst by reduced graphene oxide hypostatization. Catal Today 300:124–135. https://doi.org/10.1016/j.cattod.2017.03.052
116. Sariciftci NS, Smilowitz L, Heeger AJ, Wudl F (1992) Photoinduced electron transfer from a conducting polymer to buckminsterfullerene. Science 258(5087):1474 LP–1476. https://doi.org/10.1126/science.258.5087.1474
117. Serpone N (2006) Is the band gap of pristine TiO_2 narrowed by anion- and cation-doping of titanium dioxide in second-generation photocatalysts? J Phys Chem B 110(48):24287–24293. https://doi.org/10.1021/jp065659r
118. Shakeel Ahmad M, Pandey AK, Abd Rahim N (2017) Advancements in the development of TiO_2 photoanodes and its fabrication methods for dye sensitized solar cell (DSSC)

applications. A review. Renew Sustain Energy Rev 77:89–108. https://doi.org/10.1016/j.rser.2017.03.129

119. Shi H, Long S, Hu S, Hou J, Ni W, Song C, Li K (2019) Applied catalysis B: environmental interfacial charge transfer in 0D/2D defect-rich heterostructures for efficient solar-driven CO_2 reduction. Appl Catal B 245:760–769. https://doi.org/10.1016/j.apcatb.2019.01.036
120. Sivasakthi S, Gurunathan K (2020) Graphitic carbon nitride bedecked with CuO/ZnO hetero-interface microflower towards high photocatalytic performance. Renew Energy 159:786–800. https://doi.org/10.1016/j.renene.2020.06.027
121. Sivula K (2013) Metal oxide photoelectrodes for solar fuel production, surface traps, and catalysis. J Phys Chem Lett 4(10):1624–1633. https://doi.org/10.1021/jz4002983
122. Tan Y, Shu Z, Zhou J, Li T, Wang W, Zhao Z (2018) One-step synthesis of nanostructured g-C_3N_4/TiO_2 composite for highly enhanced visible-light photocatalytic H_2 evolution. Appl Catal B 230:260–268. https://doi.org/10.1016/j.apcatb.2018.02.056
123. Tanaka A, Teramura K, Hosokawa S, Kominami H, Tanaka T (2017) Chemical science visible light-induced water splitting in an aqueous suspension of a plasmonic Au/TiO_2 photocatalyst with metal co-catalysts. Chem Sci 8:2574–2580. https://doi.org/10.1039/C6SC05135A
124. Tayyaba S, Ashraf MW, Tariq MI, Akhlaq M, Balas VE, Wang N, Balas MM (2020) Simulation, analysis, and characterization of calcium-doped ZnO nanostructures for dye-sensitized solar cells. Energies 13:4863
125. Tiwana P, Docampo P, Johnston MB, Snaith HJ, Herz LM (2011) Electron mobility and injection dynamics in mesoporous ZnO, SnO2, and TiO_2 films used in dye-sensitized solar cells. ACS Nano 5(6):5158–5166. https://doi.org/10.1021/nn201243y
126. Tu W, Zhou Y, Li H, Li P, Zou Z (2015) Au@TiO2 yolk–shell hollow spheres for plasmon-induced photocatalytic reduction of CO2 to solar fuel via a local electromagnetic field. Nanoscale 7(34):14232–14236. https://doi.org/10.1039/C5NR02943K
127. Varlikli C, Diker H (2014) Aliofkhazraei M (ed) Titanium dioxide nanostructures in new and emerging energy technologies (Chapter 1 of Handbook of Functional Nanomaterials, vol 3). Nova Science Publishers, Inc.
128. Villa K, Black A, Domènech X, Peral J (2012) Nitrogen doped TiO_2 for hydrogen production under visible light irradiation. Solar Energy 86(1):558–566. https://doi.org/10.1016/j.solener.2011.10.029
129. Vittal R, Ho K-C (2017) Zinc oxide based dye-sensitized solar cells: a review. Renew Sustain Energy Rev 70:920–935. https://doi.org/10.1016/j.rser.2016.11.273
130. Wang F, Xiao L, Chen J, Chen L, Fang R (2020) Regulating the electronic structure and water adsorption capability by constructing carbon-doped CuO hollow spheres for efficient photocatalytic hydrogen evolution. Chemsuschem 13:5711–5721. https://doi.org/10.1002/cssc.202001884
131. Wang F, Yang M, Zhang Y, Du J, Han D, Yang L et al (2020) Constructing m-TiO_2/a-WOx hybrid electron transport layer to boost interfacial charge transfer for efficient perovskite solar cells. Chem Eng J 402:126303. https://doi.org/10.1016/j.cej.2020.126303
132. Wang S, Wang A, Deng X, Xie L, Xiao A, Li C et al (2020) Lewis acid/base approach for efficacious defect passivation in perovskite solar cells. J Mater Chem A 8(25):12201–12225. https://doi.org/10.1039/D0TA03957H
133. Wang W, Zhang J, Chen F, He D, Anpo M (2008) Preparation and photocatalytic properties of Fe_3+-doped Ag@TiO_2 core–shell nanoparticles. J Coll Interface Sci 323(1):182–186. https://doi.org/10.1016/j.jcis.2008.03.043
134. Wang X, Li Q, Zhou C, Cao Z, Zhang R (2019) ZnO rod/reduced graphene oxide sensitized by a -Fe_2O_3 nanoparticles for effective visible-light photoreduction of CO_2. J Coll Interface Sci 554:335–343. https://doi.org/10.1016/j.jcis.2019.07.014
135. Wang Z, Jiao X, Chen D, Li C (2020) Porous Copper/Zinc bimetallic oxides derived from MOFs for efficient photocatalytic reduction of CO_2 to methanol. Catalysts 10:1127

136. Wu D, Long M, Cai W, Chen C, Wu Y (2010) Low temperature hydrothermal synthesis of N-doped TiO_2 photocatalyst with high visible-light activity. J Alloys Compd 502(2):289–294. https://doi.org/10.1016/j.jallcom.2010.04.189
137. Wu G, Chen A (2008) Direct growth of F-doped TiO_2 particulate thin films with high photocatalytic activity for environmental applications. J Photochem Photobiol A Chem 195 (1):47–53. https://doi.org/10.1016/j.jphotochem.2007.09.005
138. Wu J, Bollinger AT, He X, Božović I (2017) Spontaneous breaking of rotational symmetry in copper oxide superconductors. Nature 547(7664):432–435. https://doi.org/10.1038/nature23290
139. Wu J, Huang Y, Ye W, Li Y (2017) CO_2 reduction: from the electrochemical to photochemical approach. Adv Sci 4:1700194. https://doi.org/10.1002/advs.201700194
140. Wu M, Ke S, Chen W, Zhang S, Zhu M, Zhang Y et al (2020) Optimization of the facet structure of cobalt oxide catalysts for enhanced hydrogen evolution reaction. Catal Sci Technol 10(4):1040–1047. https://doi.org/10.1039/C9CY01900F
141. Xiang Q, Cheng B, Yu J (2015) Graphene-Based photocatalysts for solar-fuel generation. Angew Chemie Int Edn 54(39):11350–11366. https://doi.org/10.1002/anie.201411096
142. Xiong Y, Gu D, Deng X, Tüysüz H, Gastel M Van, Schüth F, Marlow F (2018) High surface area black TiO_2 templated from ordered mesoporous carbon for solar driven hydrogen evolution. Microporous Mesoporous Mater 268:162–169. https://doi.org/10.1016/j.micromeso.2018.04.018
143. Xu F, Zhu B, Cheng B, Yu J, Xu J (2018) 1D/2D TiO_2/MoS_2 hybrid nanostructures for enhanced photocatalytic CO_2 reduction. Adv Opt Mater 6(23):1800911. https://doi.org/10.1002/adom.201800911
144. Xu L, Xiu Y, Liu F, Liang Y, Wang S (2020) Research progress in conversion of CO_2 to valuable fuels. Molecules 25:3653
145. Yang G, Jiang Z, Shi H, Xiao T, Yan Z (2010) Preparation of highly visible-light active N-doped TiO_2 photocatalyst. J Mater Chem 20(25):5301–5309. https://doi.org/10.1039/C0JM00376J
146. Yang L, Zhou H, Fan T, Zhang D (2014) Semiconductor photocatalysts for water oxidation: current status and challenges. Phys Chem Chem Phys 16(15):6810–6826. https://doi.org/10.1039/C4CP00246F
147. Yang Y, Xu D, Wu Q, Diao P (2016) Cu_2O/CuO bilayered composite as a high-efficiency photocathode for photoelectrochemical hydrogen evolution reaction. Sci Rep 6:35158. https://doi.org/10.1038/srep35158
148. Yella A, Lee H-W, Tsao HN, Yi C, Chandiran AK, Nazeeruddin MK et al (2011) Porphyrin-sensitized solar cells with cobalt (II/III)–based redox electrolyte exceed 12 percent efficiency. Science 334(6056):629–634. https://doi.org/10.1126/science.1209688
149. Yun S, Guo T, Li Y, Gao X, Huang A, Kang L (2020) Well-ordered vertically aligned ZnO nanorods arrays for high-performance perovskite solar cells. Mater Res Bull 130:110935. https://doi.org/10.1016/j.materresbull.2020.110935
150. Yusuf H, Kumar S, Ashokkumar M (2019) Ultrasound assisted synthesis of reduced graphene oxide (rGO) supported $InVO_4$-TiO_2 nanocomposite for efficient hydrogen production. Ultrason Sonochem 53:1–10. https://doi.org/10.1016/j.ultsonch.2018.12.009
151. Zada A, Qu Y, Ali S, Sun N, Lu H, Yan R et al (2018) Improved visible-light activities for degrading pollutants on TiO_2/g-C_3N_4 nanocomposites by decorating SPR Au nanoparticles and 2,4-dichlorophenol decomposition path. J Hazard. Mater. 342:715–723. https://doi.org/10.1016/j.jhazmat.2017.09.005
152. Zeng Y, Wu W, Lee S, Gao J (2007) Photocatalytic performance of plasma sprayed Pt-modified TiO_2 coatings under visible light irradiation. Catal Commun 8(6):906–912. https://doi.org/10.1016/j.catcom.2006.09.023
153. Zhang J, Vlachopoulos N, Jouini M (2016) Efficient solid-state dye sensitized solar cells: the influence of dye molecular structures for the in-situ photoelectrochemically polymerized PEDOT as hole transporting material. Nano Energy 19:455–470. https://doi.org/10.1016/j.nanoen.2015.09.010

154. Zhang S, Tang F, Liu J, Che W, Su H, Liu W et al (2017) MoS_2-coated ZnO nanocomposite as an active heterostructure photocatalyst for hydrogen evolution. Radiat Phys Chem 137:104–107. https://doi.org/10.1016/j.radphyschem.2016.09.026
155. Zhang S, Jin J, Li D, Fu Z, Gao S, Cheng S et al (2019) Increased power conversion efficiency of dye-sensitized solar cells with counter electrodes based on carbon materials. RSC Adv 9(38):22092–22100. https://doi.org/10.1039/c9ra03344k
156. Zhang Y, Zhai G, Gao L, Chen Q, Ren J, Yu J et al (2020) Improving performance of perovskite solar cells based on ZnO nanorods via rod-length control and sulfidation treatment. Mater Sci Semicond Process 117:105205. doi.org/https://doi.org/10.1016/j.mssp.2020.105205
157. Zhang Z-L, Li J-F, Wang X-L, Qin J-Q, Shi W-J, Liu Y-F et al (2017) Enhancement of perovskite solar cells efficiency using N-doped TiO_2 nanorod arrays as electron transfer layer. Nanoscale Res Lett 12(1):43. https://doi.org/10.1186/s11671-016-1811-0
158. Zheng J, Deng X, Zhou X, Yu M, Xia Z, Chen X, Huang S (2019) Efficient formamidinium–methylammonium lead halide perovskite solar cells using Mg and Er co-modified TiO2 nanorods. J Mater Sci Mater Electron 30(12):11043–11053. https://doi.org/10.1007/s10854-019-01446-2
159. Zheng L, Wang J, Xuan Y, Yan M, Yu X, Peng Y, Cheng Y-B (2019) A perovskite/silicon hybrid system with a solar-to-electric power conversion efficiency of 25.5%. J. Mater. Chem. A 7(46):26479–26489. https://doi.org/10.1039/C9TA10712F
160. Zhou L, Shinde A, Guevarra D, Haber JA, Persson KA, Neaton JB, Gregoire JM (2020) Successes and opportunities for discovery of metal oxide photoanodes for solar fuels generators. ACS Energy Lett 5(5):1413–1421. https://doi.org/10.1021/acsenergylett.0c00067

Chapter 26
Hybridized Nanomaterials for Enhancing Photocatalytic Activity in Solar Fuel Production

Özlem Kap, Nesrin Horzum, and Canan Varlikli

Abstract Meeting the increasing demand for energy and clean water, access to these resources has become an essential requirement of modern human life. Nanohybrid material engineering is significant for the development of functional materials which can be used as photocatalyst. By optimizing the size, shape, and surface properties of such nanostructures, the photocatalytic process in terms of ensuring sustainable resource supply can be improved. The hybrid nanomaterials aim to obtain a high visible light absorption and low charge recombination resulting in a superior efficiency of photocatalytic reactions. The application areas which benefit from such nanohybrid materials are the filtration and degradation of organic pollutants and the photochemical hydrogen production for solar water splitting. This chapter describes in detail the nanohybrid materials including metal oxides, carbon-based materials, metal sulfides, metal–organic frameworks, and transition metal phosphides as well as bandgap tuning based on these structures, which affect the efficiency of photocatalysis.

Keywords Photocatalytic activity · Energy conversion · Photocatalytic degradation · Nanohybrid materials · Heterostructure · Solar fuel

---

Ö. Kap (✉) · N. Horzum
Engineering Sciences Department, İzmir Katip Çelebi University, İzmir 35620, Turkey
e-mail: ozlem.kap@ikc.edu.tr

N. Horzum
e-mail: nesrin.horzum.polat@ikc.edu.tr

Ö. Kap
Physics of Complex Fluids, Faculty of Science and Technology, MESA+ Institute for Nanotechnology, University of Twente, Enschede 7500AE, The Netherlands

C. Varlikli
Department of Photonics, İzmir Institute of Technology, Urla, İzmir 35430, Turkey
e-mail: cananvarlikli@iyte.edu.tr

S. Garg and A. Chandra (eds.), *Green Photocatalytic Semiconductors*,
Green Chemistry and Sustainable Technology,
https://doi.org/10.1007/978-3-030-77371-7_26

26.1 Introduction

The non-renewable energy resources reserve mainly constituted of fossil fuels have a limited source and might be run out in the near future, causing an energy crisis [121]. Besides, the pollutant gases have produced by these fossil resources threaten global life due to contamination of air and climate change [38, 159]. Therefore, it has become important to improve the use of renewable resources which can supply the energy demand of the world. While the sources such as wind, biomass, hydro, geothermal, which have all renewable energy potential, have a strong production performance, the solar energy potential is relatively high, and it differs from the others remarkably given the capacity [193].

In recent years, the production of fuels such as hydrogen, methanol, and methane produced by converting solar energy into chemical energy has become a very rational approach to meet the energy demand and to cope with the environmental challenges. Photoelectrochemical (PEC) water splitting and CO_2 reduction is performed by using different semiconductor nanostructures as a photocatalyst to perform the solar-to-fuel conversion. Figure 26.1a shows the primary mechanism of water splitting by using a semiconductor photocatalyst. This mechanism works as follows: when a photocatalyst exposed the light which is greater or equal to its bandgap energy, absorbs the photons. Thus electrons and holes are formed bounded by Coulomb forces on the valance band and conduction band, respectively [233]. The semiconductor utilizes a proton to excite an electron from valance band to the conduction band in an excited state. The exposed light excites the electrons into the conduction band by leaving behind the holes in the valance band, as seen in Fig. 26.1b. An oxidation–reduction reaction proceeds during the exposure of the light. The charge carriers dissociate in a catalyst-liquid interface to produce hydrogen and oxygen from water molecules. However, one of the challenges during

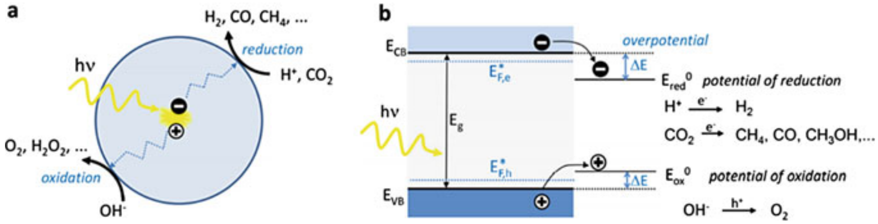

Fig. 26.1 **a** Photocatalytic processes on semiconductor nanomaterial involving photoexcitation and formation of electron−hole pair in the nanomaterial. The charges separately diffuse to the surface, where they can participate in reduction and oxidation reactions, respectively; **b** Energy diagram of the same process for a semiconductor with conduction band minimum located at E_{CB} and valence band maximum at E_{VB}, separated by a bandgap E_g. The overpotentials, ΔE, shown in blue, provide the driving force for the transfer of the charges to the electron acceptor (reduction) and donor (oxidation) molecules. the Fermi levels of the electrons and the holes are elevated to so-called quasi-Fermi levels, corresponding to Fermi levels under illumination (from Ref. [233] with permission from American Chemical Society)

the reaction is that the electrons and holes recombine on the catalyst surface, which resulted in low conversion efficiency.

In order to increase the photoconversion efficiency of the semiconductor nanomaterials, some methods used have led to the emergence of different strategies. These strategies may involve changing the shape, size, composition, and thus the active surface sites of the semiconductor photocatalysis [15]. It may involve doping method, surface functionalization, or forming a new interface with different nanomaterials as a heterostructure [190]. Therefore, the electronic band structure of the material would differ, and the solar-to-fuel efficiency would result in various efficiency depending on the bandgap engineering of the material. The required minimum energy transfer to achieve water splitting should be 1.23 eV per electron, according to Nernst's equation [254]. Thus, the photocatalyst to be used must absorb solar light photon energy greater than 1.23 eV. In a photoanode to conduct the oxygen evolution reaction (OER), the valence band must be more positive than the O_2/H_2O potential. In contrast, in a photocathode, the hydrogen evolution reaction (HER) would be conducted with more negative potential than the H^+/H_2 potential [227]. The band edge positions of different materials are shown in Fig. 26.2.

The requirement to perform an effective PEC water splitting and to commercialize it is to increase light-to-energy conversion efficiency. Until today, studies have been carried out on the development of low-priced, non-toxic, stable, and efficient semiconductor materials that can absorb the light in the visible region of the electromagnetic spectrum. It should be noted that the solar light, which is a green energy source by itself, is also included in the scope of green energy in the many synthesis methods of photocatalysts used to harvest it.

Many literature studies, in which all configurable and hybrid combinations of nanomaterials have been investigated using as a photocathode or photoanode in overall solar water splitting reaction to increase efficiency as a photocatalyst. This book chapter focuses on recent studies on solar-to-fuel conversion because of the

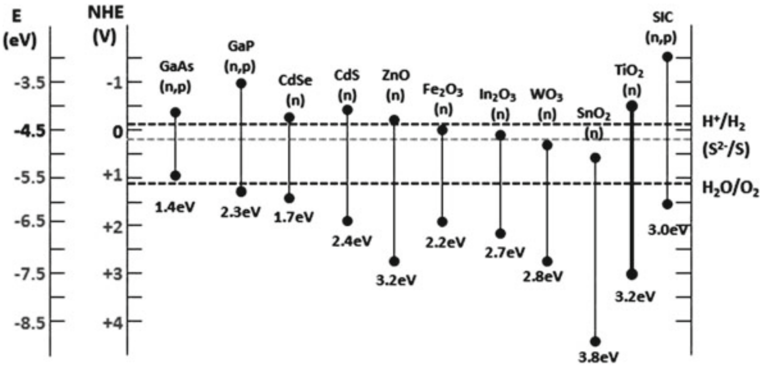

Fig. 26.2 Band edge positions of semiconductors and their relevance with photocatalytic H_2 generation

highly efficient nanomaterials such as metal oxides, metal–organic frameworks, carbon-based materials, metal sulphides, and phosphides which have been used mostly for photoelectrochemical water splitting applications. The factors which reduce the efficiency of solar conversion will be discussed based on the electron–hole recombination, limited photon absorption, and charge separation efficiency for the mentioned nanomaterials. This chapter has been evaluated for water splitting and CO_2 reduction application of the nanomaterials, however, it should be noted that the same structures can also be used for photocatalytic degradation application.

26.2 Metal Oxides

In this section, we aim to focus on the use of hybridized metal oxide nanomaterials in the study of photocatalysis for hydrogen generation from water splitting, pollutant degradation, and greenhouse gas reduction. Nanostructured metal oxides are ideal photocatalysts due to their high surface area, reactive sites, bandgap, and morphology [116, 213]. The metal oxide first remembered as a photocatalyst is titanium dioxide (TiO_2) with its non-toxicity, chemical stability, and high photocatalytic activity. However, one disadvantage is the wide bandgap (3.2 eV) that makes TiO_2 only sensitive to the ultraviolet (UV) region [48]. Another disadvantage is the fast electron–hole recombination and its relatively poor charge-carrying ability, resulting in low quantum efficiencies [96, 169]. Several approaches have been used to modify TiO_2 materials to overcome these disadvantages. Not only morphological modifications such as the production of TiO_2 nanomaterials with larger surface area, but also chemical modifications which include metal, non-metal, metal- non-metal, metal oxide doping, immobilization of TiO_2 on secondary substrates, and the use of nanomaterials as TiO_2 support, composite fabrication with semi-conductors have been applied to increase photocatalytic activity. In this context, some studies which have been conducted in recent years are classified in Table 26.1.

Doping is one of the frequently used methods to increase the photocatalytic activity of TiO_2 by reducing the bandgap and constructing new energy levels. The proper amount of doping will reduce the recombination of photogenerated charges, but when used excessively, they act as a recombination center [5]. One of the favorite metal doping for TiO_2 semiconductor is iron which is non-toxic, inexpensive, and earth-abundant element. Because the ionic radius of iron is very close to the TiO_2 lattice parameter [306], in this case, it can also be doped easily. However, the iron doping process requires precise control during synthesis. Xu et al. showed that the photocatalytic performance of Fe-doped TiO_2 varies depending on the method of synthesis, iron precursor, and iron concentration which cause the changes in porosity, particle size, and morphology [291]. The CH_4 formation yield was 0.23 $\mu mol\ g^{-1}\ h^{-1}$ under visible light illumination for Fe-doped TiO_2. Its specific surface area and bandgap were 275 $m^2\ g^{-1}$, 2.75 eV, respectively. Fe-TiO_2-500 was synthesized via one-step hydrothermal method at 500 °C. BET

Table 26.1 The chemical modification classification for TiO_2

Chemical modifications			
Metal doping	Bimetal doping	Metal oxide doping	Metal/non-metal doping
Silver (Ag) [69], Aluminium (Al) [191] Cobalt (Co) [307] Chromium (Cr) [170] Copper (Cu) [41] Erbium (Er) [226] Gallium (Ga) [152] Lanthanum (La) [145] Magnesium (Mg) [179] Molybdenum (Mo) [115] Manganese (Mn) [236] Nickel (Ni) [110] Niobium (Nb) [173] Palladium (Pd) [212] Platinum (Pt) [39] Rhodium (Rh) [108] Ruthenium (Ru) [4] Antimony (Sb) [133] Tin (Sn) [228] Strontium (Sr) [326] Terbium (Tb) [274] Vanadium (V) [194] Tungsten (W) [137] Ytterbium (Y) [14] Zinc (Zn) [104] Zirconium (Zr) [46]	Au–Ag [304] Bi–Y [76] Cu–Ni [160] Cu–Zn [160] Fe–Ni [240] Ni–Bi [183] Ni–Cr [218] Ni–Si [129] Mn–Zn [276] Er–W [113] La–Nb [75] Rh–Sb [106] Sn–La [343] Sr–Rh [184] Zr–Ag [180] Zr–Pd [46]	Cu_2O [296] Fe_2O_3 [177] MoO_3 [109] NiO [112] PdO [105] PtO [174] SnO_2 [83] WO_3 [66] V_2O_5 [198] ZnO [189] ZrO_2 [157]	Fe–N [54] Ag–N [316] K–Na–Cl [45]
	Nanomaterials supported on TiO_2	**Hybrid TiO_2 nanostructures**	**Non-metal doping**
	Ag nanoparticles [332] Au nanoparticles [187] Au–Pd nanoparticles [42] Bi nanoparticles [333] Cu nanoparticles [210] CuO nanoparticles [312] Pd–Au nanoparticles [224] PdCoNi nanoparticles [24] Pt nanoparticles [234] Pt–Pb nanoparticles [9] SnO_2 nanostructures [256]	Graphitic carbon nitride ($g\text{-}C_3N_4$)–Pt–TiO_2 [313] TiO_2 supported MOF-199 derived Cu–Cu_2O nanoparticles [158] $g\text{-}C_3N_4$ nanosheet hybridized N-doped TiO_2 nanofibers [77] TiO_2/FeMnP core/shell nanorod [216] Pd-decorated hierarchical TiO_2 constructed from the MOFs NH_2-MIL-125(Ti) [300] $Cu/TiO_2/Ti_3C_2T_x$ [192] NH_2-MIL-125(Ti)/TiO_2 [309] Cu/TiO_2 core−shell heterostructures derived from Cu-MOF [176] TiO_2 nanorod mats surface sensitized by cobalt ZIF-67 [56] Fe_2TiO_5–TiO_2 [321] MOF-derived TiO_2 photoanodes sensitized with quantum dots (CdSe@CdS) [221] Ru species supported on MOF-derived N-doped TiO_2/C hybrids [299]	Carbon (C) [130] Nitrogen (N) [107] Phosphorus (P) [171] Sulfur (S) [197] Selenium (Se) [287] Fluorine (F) [17] Chlorine (Cl) [270] Bromine (Br) [265] Iodine (I) [215] N–S [58] C–N–S [51]
			TiO_2 supported on secondary substances
			Activated carbon fibers (ACFs) [64] Carbon nanotubes (CNTs) [10] Graphitic carbon nitride ($g\text{-}C_3N_4$) [229] Graphene [79] Graphene oxide [249] Silica [196] Aluminium silicate [95] Zeolite [315] Biochar [317] Poly(methyl methacrylate) nanofibers [134] Poly(styrene-co-vinylphosphonic acid) fibers [88]

specific surface area was 202 m^2, and the bandgap was of 2.42 eV. The bandgap and porosity reduced by the chancing the synthesis condition, which results in an increase of the CH_4 formation rate as 0.47 μmol g^{-1} h^{-1}.

The concentration of metal doping affects the photocatalytic activity of doped-TiO_2 since the metal doping may tune the anatase–rutile transformation during the synthesis [5]. Anatase is the indirect bandgap semiconductor, whereas rutile is direct bandgap semiconductor. Indirect bandgap anatase exhibits a longer lifetime of photoexcited electrons and holes. It has been shown that anatase has the lightest effective mass, which helps the fastest migration of photogenerated electrons and holes from the inside to surface of anatase TiO_2 by lowering the recombination rate of photogenerated charge carriers. Therefore, anatase TiO_2 has a higher photocatalytic activity than rutile TiO_2 [319].

Rutile and anatase have a band of 3.0 and 3.2 eV, respectively. Ding et al. have formed a heterojunction with these two phases, and the internal electric field has been built with two different work functions of anatase and rutile. They showed that the heterophase junction constructed by using TiO_2 nanobelt increases photocatalytic activity [49]. Figure 26.3 is a schematic illustration of the photocatalytic mechanism owing to the heterophase junction. Moreover, the O_2 production rate was investigated with increasing calcination temperature. The highest O_2 evolution rate of 0.352 mmol h^{-1} g^{-1} was obtained due to the formation of anatase/rutile heterophase junctions connections at 900 °C. TiO_2 nanobelt calcinated at 600, 700, 800 °C were pure anatase, at 1000 °C was of pure rutile, and the O_2 evolution rate is 0.09, 0.124, 0.16 and 0.198 mmol h^{-1} g^{-1}, respectively. Thus, constructed anatase/rutile heterophase junctions enhanced carrier separation efficiency and carrier recombination suppress.

Some non-metallic element dopings which are most commonly used in the literature have been listed in Table 26.1. Non-metallic doping increases the light absorption in the visible region of TiO_2, enhancing the electron–hole separation, but again they act as recombination centers due to the formed oxygen vacancies [5]. However, it was stated that the performance of the non-metallic doping could not enhance the photocatalytic activity as much as metallic doping [96]. The advantage

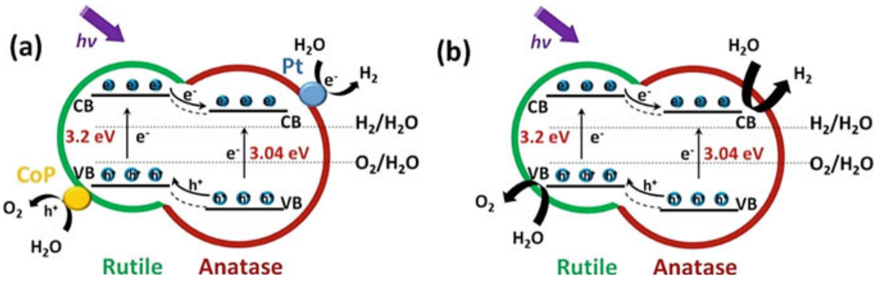

Fig. 26.3 Schematic illustration of the photocatalytic mechanism of the rutile/anatase heterophase junction **a** with and without Pt/CoP cocatalysts (Reprinted from Ref. [49] with permission from Elsevier)

of the non-metallic doping to metals does not act as electron traps, and they have been used to improve photocatalytic activity by using this feature [298].

The p-states of the non-metallic elements mix with the O-2p states of TiO_2 which causes redshift on the valance band and the bandgap decreases. Nitrogen is one of the most frequently used as dopants for TiO_2. Likewise, C doped TiO_2 also enables the formation of new energy levels above the valence band, so the lower absorption spectrum shifts to the higher wavelengths [12]. F-doped TiO_2 is another non-metal doping element, and they occupy the oxygen vacancies which are in the lattice rather than doping into the TiO_2. Thus, electron–hole recombination sites are reduced by fluorine. Moreover, Du et al. stated that the reason why F doping decreases photocatalytic activity is that element F causes surface fluorination, not doping [55]. A very high photocatalytic activity has been obtained by the F doping method by using Mesoporous mesocellular foams as support for fluorine atoms in a study. In order to increase the substitution of these atoms, the vacuum activation method was used to boost the oxygen vacancies in TiO_2, thus yielding Ti^{3+}-F lattice structures.

The F-doped catalyst exhibits high photocatalytic activity and stability for H_2 evolution under solar light irradiation with an AM 1.5 air mass filter. The success of the technique attributed to the decrease of recombination sites by high concentration F doping and the synergistic effect between lattice Ti^{3+}-F and surface Ti^{3+}-F [289]. Other single metal oxides used for photocatalytic applications other than TiO_2 include ZnO [57, 87, 93], CeO_2 [85], CuO [203], Cu_2O [283], SnO_2 [186, 225], Fe_2O_3 [82], NiO [139], MoO_3 [205, 344], WO_3 [217], ZrO_2 [68], Ag_2O [268], Bi_2O_3 [266], In_2O_3 [90]. Besides defect engineering strategies such as surface hydrogenation, metal reduction, and thermal treatment to create oxygen vacancies, heterostructure engineering is considered to be another effective way of obtaining photocatalysts with improved efficiencies [11]. For example, metal catalysts (Au, Pt, Pd, Cu) and bimetallic catalysts (Au–M (M=La, Ni, Cu, Fe, Cr, Y), Pt–Cu, Pd–Cu) are supported on various single and dual metal oxides to enhance the light absorption capacity under UV light due to the Schottky barrier and SPR [40]. The photocatalytic activity of the metal oxides can be improved by not only changing the morphology (i.e., obtaining nanostructures with a core/shell structure) but also using binary metal oxides (ZnO/V_2O_5 [8], ZnO/In_2O_3 [43], CeO_2 supported on SiO_2 fibers [89], Fe_2O_3/TiO_2 [16], Fe_2O_3/WO_3 [178], ZnO Nanorod/α-Fe_2O_3 [251], NiO/V_2O_5 [175], Bi_2O_3–$BiFeO_3$ [163], SnO_2/ZnO [341], WO_3–$BiVO_4$ nanostructures [120]) with higher oxygen mobility over the surface, visible light activity. Besides precious metals decorated binary metal oxides, ternary metal oxide nano-photocatalysts ($CuO/CeO_2/ZnO$ [151] $Bi_2O_3/Bi_2SiO_5/SiO_2$ microspheres [320]) with more efficient photocatalytic performance have been studied. Moreover, QDs, carbon nanotubes, g-C_3N_4 are used as sensitizers for photocatalytic metal oxide structures such as ZnO/CdS [3], ZnO/CdTe [156], MoO_3-MWCNT [219] ZrO_2/g-C_3N_4 [94], etc. An important class of metal oxide catalysts in green energy production is perovskite oxides (such as titanate-based perovskites; $ATiO_3$ (A=Ba, Ca, Co, Cu, Fe, Mg, Mn, Ni, Pb, Sr, Zn), tantalite-based; $KTaO_3$, $NaTaO_3$, and other-metal-based perovskite oxide photocatalysts like $BaZrO_3$, $LaFeO_3$, and $LaMnO_3$ because of their excellent absorption, bandgap tunability, and water splitting [185].

26.3 Carbon-Based Nanomaterials

26.3.1 Graphene-Based Nanomaterials

Graphene (G) consists of a single layer of sp^2 hybridized carbon atoms, arranged in a 2D honeycomb lattice. In addition to being the thinnest material known, it is also the most robust material with a 1GPa Young' modulus [117]. Graphene synthesis can be carried out either by the top-down approach via mechanical, chemical, or electrochemical exfoliation methods or by the bottom–up approach via chemical vapor deposition and chemical synthesis methods [20]. In Table 26.2, the methods used to synthesize graphene-based structures are summarized, additively, the synthesis methods of composite structures have also been shown.

Graphene has drawn attention in solar fuel applications due to excellent properties such as high stability, large specific surface area, the strong adsorption capacity, high thermal and electrical conductivity [6]. The high surface area contributes to the stabilization of the metal NPs, metal oxide, and quantum dot structures because the expanded π orbitals of G overlap with the d orbitals of the metallic structures [6]. Thus, it can be seen from the literature studies shown in Table 26.2; the formed heterojunction contributes to the photocatalytic conversion efficiently.

A well-known structure among various graphene derivatives is graphene oxide (GO) which is obtained by the oxidation of graphene. Contrary to the hydrophobic nature of graphene, GO containing hydrophilic functional groups (hydroxyl, carbonyl, carboxyl, epoxide) eliminates the problem of aggregation in aqueous solutions [47]. GO has low electrical conductivity; however, it is increased by the reduction of GO [21]. In a study, Zhu et al. used Ag NPs, CdS NRs, and reduced graphene oxide(rGO) composite material as photocatalyst for CO_2 reduction [345]. According to the result, it was determined that CO_2 adsorption capacity of CdS was 5.01 $cm^3\ g^{-1}$, while rGO–CdS and Ag–rGO–CdS were 6.60 and 6.02 $cm^3\ g^{-1}$, respectively. Increased adsorption indicates the positive contribution of RGO's high electrical conductivity, p–p conjugation between the rGO and CO_2, higher surface area (46.2 m^2g^{-1}) and large surface active sites. Moreover, both Ag and RGO act as the electron acceptor, which expedite in the CO_2 reduction reaction.

The degree of the reduction of GO can change the bandgap of the material, which is essential in the photocatalytic applications [2]. The optical band gap obtained by incorporation of G/GO into different materials is shown in Table 26.2. It has been reported in the studies the existence of G or GO resulted in narrowed the bandgap [74, 102, 141, 201, 220, 231, 242, 269, 335]. As a result of the bandgap calculation with the Tauc plot analysis, Sorcar et al. found that doped GO amount with 0.25, 0.50, or 0.75 ml to the reduced blue titania (RBT) reduced the bandgap to 2.61, 2.41, 2.22 eV, respectively, which was 2.68 eV for pure RBT [231]. While the produced C_2H_6 and CH_4 amount increased for 0.25 and 0.50 doping, and it decreased compared to the two for 0.75 doping. Similarly, Wang et al. detected CH_4

Table 26.2 Typical photocatalytic H_2-production systems of graphene-based nanomaterials

Catalyst	Synthesize-preparation method	Optical bandgap (eV)	Application	Products/Activity ($\mu mol \cdot g^{-1} \cdot h^{-1}$)	References
Graphene/TiO_2/Mo	Sol–gel for composite	2.62	Decomposition of methylene blue	–	[102]
Graphene/TiO_2	Drop-casting for graphene film on FTO-glass/magnetron sputtering, thermal treatment for composite	–	Photoelectrochemical (PEC) water splitting	–	[252]
$PbBiO_2Br$/GO	Hydrothermal synthesis for composite	2.40	Removal of CO_2, crystal violet dye and 2-hydroxybenzoic acid	CH_4/1.193	[141]
TiO_2/GO/rGO	Electrochemical anodization for TiO_2, UV-A radiation for reduction of GO, reflux process for GO and rGO functionalization	–	Photocatalytic reduction of CO_2	CO_2/760 μmol g^{-1}	[204]
Defective Graphene/NiO/Ni NPs	Pyrolysis for graphene, thermal treatment for composite	–	Photoassisted CO_2 reduction by H_2	CH_4/642.66	[165]
Graphene/UIO-66-NH_2	Hydrothermal synthesis and microwave-irradiation induced solvothermal synthesis for composite	2.64	CO_2 photo-reduction under visible-light	CO_2/42.6 μmol	[269]
rGO/CdS/ZnO	In-situ growth	2.12	Synthesis of the efficient hybrids for photocatalytic or PEC hydrogen generation	H_2/ 0.79 μmol cm^{-2} h^{-1}	[335]
N-doped defective graphene/RhCrOx /STO:Al	Pyrolysis for graphene, impregnation for composite	–	Produce a hybrid material for efficient photocatalyst	H_2/6375 O_2/3080	[167]

(continued)

Table 26.2 (continued)

Catalyst	Synthesize-preparation method	Optical bandgap (eV)	Application	Products/Activity (μmol·g^{-1}·h^{-1})	References
rGO/Rh_2O_3/Rh NPs	Hummers method for GO, Hydrothermal, thermal treatment for composite	–	CO_2 photoreduction	CH_4/814.38	[101]
Graphene/Cu_2O	Pyrolysis for graphene	–	CO_2 reduction	H_2/ 2031 μmol cm^{-2} h^{-1}	[91]
rGO/TiO_2	Reflux and vacuum thermal treatment for composite	2.36	Photocatalytic reduction of CO_2 into solar fuel	CH_4/12.75	[220]
N-doped rGO/ TiO_2/$ZnFe_2O_4$	Hummers method for graphene oxide, hydrothermal synthesis for composite	2.98	Degradation of reactive Yellow 86 and methanol oxidation	H_2/2481	[242]
Graphene/CeO_2/ CuO/QDs	Calcination for graphene	1.75 (CuO–G) 2.70 (CeO_2 –G)	Synthesis highly efficient material for solar-driven hydrogen production	–	[201]
rGO/$CoFe_2O_4$/ TiO_2	Hummers method for GO, Ultrasound-assisted wet impregnation for composite	3.20 (TiO_2–G) 1.38 ($CoFe_2O$–G)	Synthesis stable photocatalyst for high production of hydrogen	H_2/76559	[74]
N- and Co-doped graphene/TiO_2	Hydrothermal synthesis for TiO_2, sonochemical and calcination methods for composite	–	Photocatalytic generation of H_2O_2 within the visible light range	H_2/677.44	[307]
Graphene/Cu_2O	Pyrolysis for graphene	–	Photoassisted methanation	CH_4/14930	[164]
Graphene/ reduced blue titania/Pt NPs	Annealing the mixture of graphene and RBT, Pt photo deposited composite	2.22	Photoconversion of CO_2 to CH_4 and C_2H_6	CH_4/37 C_2H_6/11	[231]

(continued)

Table 26.2 (continued)

Catalyst	Synthesize-preparation method	Optical bandgap (eV)	Application	Products/Activity (μmol·g^{-1}·h^{-1})	References
Graphene/ chlorophyll Cu	Film preparation method	2.66	Conversion of CO_2 to C_2H_6	C_2H_6/68.23	[282]
GO/Benzidine	Hummers' method for graphene, hydrothermal synthesis for composite	–		H_2/690	[339]
Multilayer Graphene/Gold nanoplatelets	Pyrolysis for composite	–	Synthesize an efficient photocatalyst for water splitting	H_2/1200000	[166]
Graphene nanoribbon/CdS	Solvothermal method for composite	2.17	H_2 evolution under visible-light illumination	H_2/1890	[285]

evolution for G-doped UIO-66-NH_2, and the evolution decreased for UIO-66-NH_2/3.0GR compared to UIO-66-NH_2/2.0GR [269]. The reason for the reduction is attributed to the excessive graphene which covers the active regions of the MOF structure. It is understood from the results that the optimum amount of G/GO doped materials increase the CH_4/H_2 evolution.

Any other G-doped nanostructure is bismuth oxyhalides, which are materials that may be the candidates for third-generation solar cell, can provide photocatalytic activity with visible light [305]. Recently, $PbBiO_2Br$/GO composite was produced via hydrothermal method as a new novel material with different grams of GO [141]. The morphology can be seen in Fig. 26.4. The bandgap energy of the composite was to 2.40 eV, which was lower compared to 2.47 eV bandgap energy of $PbBiO_2Br$. Thus, the composite material increased the photocatalytic conversion rate from CO_2 to CH_4. This change has been attributed to the double-bond resonant structure of GO which transports photo-generated electrons and suppresses the electron–hole recombination of the photocatalyst. Although the conversion of CO_2 to CH_4 is thermodynamically favorite, the requirement of 8 electrons makes this process kinetically complicated this process compared to the CO conversion, which requires 2 electrons transfer. In a study in which CO_2 conversion to CO was carried out by using multi-leg TiO_2 nanotubes wrapped with GO and rGO layer [204].

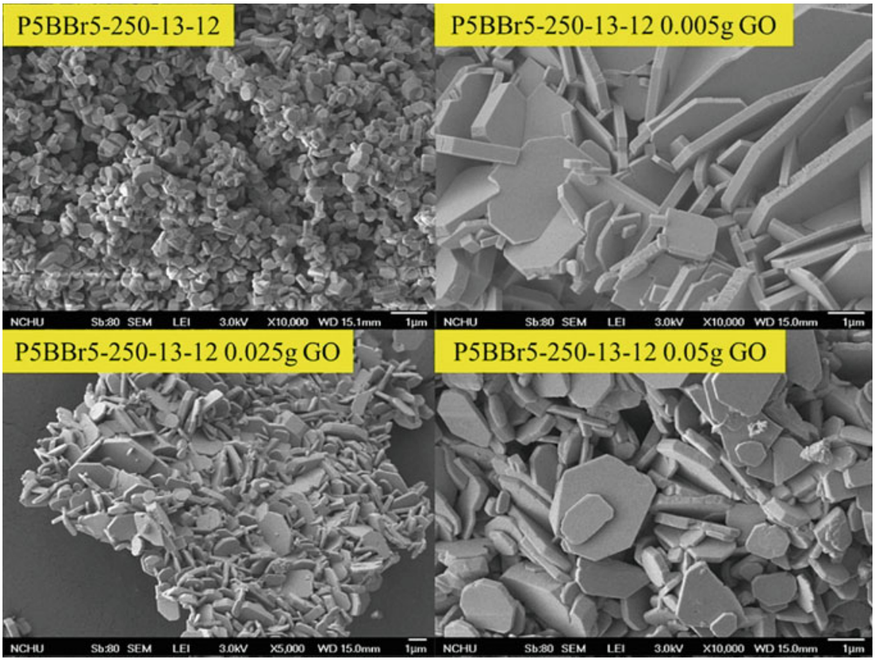

Fig. 26.4 SEM images of as-prepared samples by the hydrothermal autoclave method at different grams of GO (Molar ratio Pb:Br = 5:5, temp = 250 °C, time = 12 h) (Reprinted from Ref. [141] with permission from Elsevier)

Multi-leg TiO_2 nanotubes wrapped with GO and rGO were exposed to CO_2 for different periods. The rate of CO formation was observed to remain at the highest level (760 μmol g^{-1}) after 120 min for rGO wrapped nanotubes when compared to GO wrapped and bare multi-leg TiO_2 nanotubes. The high CO formation has been attributed to the electrical conductivity of GO/rGO layers connecting adjacent nanotubes which increased interaction between adsorbed CO_2 and photo-generated electrons.

The most important advantage of using graphene-based nanomaterials is that it increases the energy conversion by enhancing the photoabsorption and electron–hole separation with its high surface area. Moreover, the absorption spectrum of doped graphene and graphene with layer stacking defects extends from UV to NIR, which makes them an important class of material candidates for photocatalysis solar light [6].

26.3.2 Graphitic Carbon–Nitride

Two-dimensional (2-D) graphitic carbon nitride (g-C_3N_4) has become interested due to its unique properties such as its metal-free structure, easy preparation, high thermal and chemical stability, low cost [146, 161, 181]. The g-C_3N_4 has the photocatalytic activity under the visible-light with the bandgap of 2.7 eV [334]. However the photocatalytic performance of pure g-C_3N_4 is low, due to the rapid recombination rate of the photo-generated electron–hole pair and low specific surface area, but a growing number of studies exist about improvement in the lifetime of charge carriers in the literature [62, 325].

In order to enhance the photocatalytic performance, heterostructures are formed by combining with another semiconductor suitable for the band structure of g-C_3N_4 [62]. Li et al. classified the g-C_3N_4 heterojunction structures based on the charge transfer routes and the characteristics of g-C_3N_4 as type-II, Z-scheme, S-scheme, p-n heterojunctions and Schottky heterojunctions [135]. Type II heterojunctions are constructed with metal oxides (TiO_2 [7, 278, 284, 301, 336], CuO [301], ZnO [18, 100, 281] SnO [34, 263], Fe_2O_3 [200, 244, 294], CeO_2 [154, 232], WO_3 [28, 255], metal sulfides (CdS [33, 73, 81, 132, 257, 340]), SnS_2 [324], MoS_2 [131, 260], $ZnIn_2S_4$ [131, 202, 250]), metal telluride (ZnTe [264]) which have a more positive valence band than g-C_3N_4. While type II heterojunctions are successful in improvement of the charge carriers separation, the redox activity would be weakened due to the migration of the electrons and holes to the lower level of CB and VB, respectively [209]. For this reason, the charge transfer model inspired from the green plants, g-C_3N_4 based Z-scheme heterojunctions systems have been developed to ensure efficient separation of the charge carriers and to advance the redox activity of the charges in the liquid phase [123]. The system, called the direct Z-scheme, has been developed to perform electron transfer via solid materials instead of the liquid medium [293]. One of the drawbacks of the Z-scheme heterojunction systems is that the conductor material also absorbs light, and the light-harvesting efficiency of both photocatalysts is reduced. In another drawback is; if the Fermi level of the solid conductor material which transfers the electron from the higher CB of one photocatalyst to the lower VB of the other photocatalyst is lower than the photocatalysts, a Schottky barrier forms causing the suppression of the electron flow. Besides, if the solid conductor during the synthesis is not precisely embedded between the photocatalysts, it only acts as a co-catalyst instead of charge transfer carrier [209, 292]. In order to eliminate these shortcomings, reduction photocatalyst (RP) and oxidation photocatalyst (OP) is used in g-C_3N_4 based S-scheme heterojunction systems. The internal electric field, band bending, and Coulombic attraction ensure the driving force for the charge transfer [292].

Various methods such as heat treatment, photo deposition, pyrolysis, ion exchange method, solvothermal and hydrothermal method, electrospinning method, deposition–precipitation method have been used in order to synthesize of g-C_3N_4 based materials with controllable morphology. The photocatalytic activities of the structures are summarized in Table 26.3 depending on the specific types of heterojunction with particular application, bandgap, and synthesis method for the composites.

Visible light responsive g-C_3N_4 material, which is an alternative to TiO_2 due to its unique properties, is being studied water splitting application for the efficient H_2 evolution. In order to improve the drawbacks mentioned above, type II, Z-scheme, and S-scheme heterojunction structures were developed to ensure high charges redox ability and efficient charge separation, especially in S-scheme heterojunctions, resulting in higher photocatalytic performance.

26.3.3 Carbon Quantum Dots (CQDs)

CQDs, which are zero-dimensional (0D) nanoparticles with sizes below 10 nm, are attractive because of their many unique and novel properties [295]. Their optical properties, fluorescence emissions, tunable bandgaps, and good chemical stability make it a great candidate for solar fuel applications [149]. Top-down synthesis approach with laser ablation, arc-discharge, and electrochemical oxidation, and bottom-up approach hydrothermal/solvothermal, microwave pyrolysis methods are known for the CQDs [13, 273]. During the synthesis process, the core structure of the CQDs can be functionalized with rich oxygen-containing functional groups such as carboxyl and hydroxyl [13]. That functional groups provide hybridization between CQDs and noble metals (NMs), which are turning up superior properties [65].

In solar fuel applications, CQDs increase the number of electron–hole pairs; thus, the enhancing charge transfer promotes photocatalytic activity. The hydrogen production mechanism has been depicted in four steps by using the carbon dots, as shown in Fig. 26.5. First, light irradiation and photon absorption occur; secondly, the electron in stimulated from the VB to the CB. Thirdly, the photo-produced electrons pass to the semiconductor surface, and finally, the resulting electrons and holes conduct the water-splitting process.

Table 26.3 The photocatalytic activities of the g-C_3N_4 based heterojunction type structures

g-C_3N_4 based heterojunction type	Catalyst	Synthesis method	Application	Products/activity (μmol·g^{-1}·h^{-1})	Optical bandgap (eV)	References
Type II	Ag_2S/K	Deposition	H_2 evolution	H_2/895	2.65	[323]
	r-TiO_2	Theoretical study	H_2S splitting	–	2.40	[278]
	SiC	Theoretical study	H_2 production	–	2.0	[290]
	$KNbO_3$ (100)	Theoretical study	Enhancing the photocatalytic performance	–	2.11	[155]
	ZnTe	Hydrothermal	CO_2 reduction	CH_3CH_2OH/ 17.1 μmol cm^{-2} h^{-1}	2.22	[264]
	Nb_2O_5	Pulse sonication	PEC water splitting	–	2.82	[103]
	MoS_2 QDs/ g-C_3N_4	Calcination under Ar/H_2	Degradation of methyl orange and phenol	–	2.52	[222]
	rGO/Fe_2O_3	Hydrothermal	H_2 production	H_2/6607	1.9	[244]
Z-scheme	$Bi_4O_5Br_2$	Water-induced self-assembled	H_2O_2 production of	H_2O_2/ 300 μmol cm^{-2} h^{-1} g^{-1}	2.39	[331]
	SWCNT	Two-step air etching	H_2 evolution	H_2/1346	–	[275]
	$NiMoO_4$	Calcination	CO_2 conversion	CH_4/635, CO/432, O_2/ 1853, HCOOH/647	2.31	[248]
	Cu_2O	Calcination	CO_2 conversion	CH_3OH/2.83	2.1	[330]
	ZnO/$ZnWO_4$	Calcination	CO_2 conversion		–	[342]

(continued)

Table 26.3 (continued)

$g\text{-}C_3N_4$ based heterojunction type	Catalyst	Synthesis method	Application	Products/activity (μmol·g^{-1}·h^{-1})	Optical bandgap (eV)	References
				CO/1.12, CH_4/6.24, CH_3OH/3.85, CH_3CH_2OH/1.98		
	$SnFe_2O_4$	Hydrothermal	CO_2 conversion	CO/7.56	–	[98]
	Nb-doped TiO_2	Calcination	CO_2 reduction	CH_4/562 CO/420 O_2/1702 HCOOH/698	~2.79	[247]
S-scheme	WO_3	Electrostatic self-assembly	H_2 production	H_2/982	WO_3/2.68	[61]
	$Zn_{0.2}Cd_{0.8}S$/diethylenetriamine	Solvothermal	H_2 production	H_2/6.69	$Zn_{0.2}Cd_{0.8}S$-DETA/2.48	[168]
	CdS	Calcination and hydrothermal	H_2 production	H_2/15.3	CdS/2.30	[207]
	$CuInS_2$	Hydrothermal	H_2 production	H_2/373	$CuInS_2$/1.20	[150]

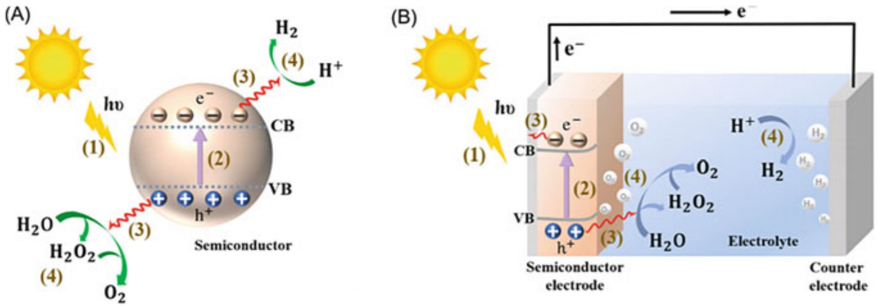

Fig. 26.5 Schematic illustration of the mechanisms for **A** photocatalytic and **B** photoelectrochemical hydrogen evolution (Reprinted from Ref. [71] with permission from Elsevier)

Sun et al. coated the Ag NPs with the CQDs to investigate the photocatalytic activity of the composite in which the highest photocatalytic obtained for AgNPs with 16% CQDs. The methanol (CH_3OH) formed as the main product by reduction of CO_2 in this reaction as 17.82 μmol after 10 h of illumination. The produced CH_3OH was three times more than the pure Ag catalyst [238]. Additionally, the dispersion effects of the CQDs prevents the NPs from the aggregation, thus increasing surface area is another crucial reason for the boosted photocatalytic activity [65]. Cobalt monoxide (CoO), which also has an aggregation problem during the synthesis, has high photocatalytic activity with 5% solar—to hydrogen efficiency (STH) [138]. Since the conversion efficiency obtained as a result of CoO/g-C_3N_4 type II heterojunction systems were not optimal [261], this system was combined with CQDs. The ternary CoO/g-C_3N_4/CQDs system showed higher photocatalytic activity with the optimum H_2 conversion rate of 987.4 μmol g^{-1} h^{-1} compare to $BiVO_4$/CQDs/CdS with 1.24 μmol/h and NiO/CQDs/$BiVO_4$ with 1.21 μmol h^{-1} [223]. The highly efficient photocatalytic activities of the carbon dots can be attributed to their electron-donating and accepting abilities, and possible active surface sites [124].

Some limiting factors to use of CQDs are the low absorption for long-wavelength, rapid decay in the initial excited state, long-term stability problem, and the weak interfacial interaction between carbon dots [149]. It is recommended that the chemical structure of the CQDs should be investigated to enhance charge transfer properties. Moreover, the future composite structures should be formed with biomaterials and copper chalcogenide structures other than metal, oxides, bismuth-based metal compounds, and carbon materials composite structures which already exist in the literature [30].

26.4 Metal Sulfide-Based Nanomaterials

Metal sulfides are one of the class of the semiconductor structures that are widely used in photocatalytic reactions for the conversion of water into hydrogen fuel using solar energy. The outstanding features; low cost, promising photocatalytic activity, long lifetime, high absorption in the visible spectrum with great mobilities of electrons and holes are the main reasons for their popularity [182]. Until today, there are various heterogeneous and hybrid structures produced with metal sulfides with superior properties for energy conversion [80].

The most commonly used structures in PEC applications of metal sulphides are CdS, ZnS, FeS_2, MoS_2, CuS, Bi_2S_3 and Sb_2S_3. Top–down and bottom–up approaches are used to synthesize these nanostructures. While the top–down approaches consist of sputtering, electrospinning, lithography, exfoliation, and milling; the bottom–up approaches have consisted of chemical vapor deposition, atomic layer deposition, pyrolysis, thermal deposition, pulsed laser deposition, micro-emulsion, precipitation, hydrothermal and solvothermal synthesis, electrodeposition, and microwave irradiation techniques [27, 36].

Especially CdS have drawn attention with the narrower direct band gap of 2.42 eV compared to TiO_2 which has 3.2 eV bandgap. Moreover, among the other sulfide structures, CdS have favorable photocatalytic performance due to the absorption wavelength, which is shorter 516 nm. This wavelength corresponds to a broader absorption spectrum, again compared with $TiO_{2,}$ which absorbs the ultraviolet light with a wavelength of less than 387 nm [36]. However, the main issue that limits the use of CdS as photocatalyst is photocorrosion, lack of active sites, the high photo-generated electron–hole recombination rate [329]. Different types of heterostructures [243], co-catalysts incorporation [148], sacrificial reagents addition [72], metallic/non-metallic catalysts coupling [308] have been utilized to overcome the limitations.

Recently, Ren et al. have synthesized CdS coupled with a 2D Cu_7S_4 co-catalyst nanosheets, which increase the active sites and electron transfer yield, for photocatalytic hydrogen generation application [206]. It will be useful to consider the most striking aspects of this study based on the fundamental mechanism. The electron–hole pair of CdS nanosheets (NSs) easily recombined under irradiation, and H_2 evolution rate is lower. Efficient separation of electron–hole pairs was achieved by the presence of large contact areas, which is also shown by PL measurements between CdS/Cu_7S_4 NSs. The H_2 production for pure CdS increased from 2.6 mmol g^{-1} h^{-1} to 27.8 mmol g^{-1} h^{-1} for CdS-2% Cu_7S_4 composite. Moreover, the apparent quantum efficiency value of the composite decreased with increasing light wavelength at 420, 450, 500, and 550 nm resulted in 14.7%, 12.3%, 9.6%, and 7.2%, respectively. Light absorption wavelength of the heterostructure has affected the H_2 evolution. As another literature study, the 10 wt % CdS/g-C_3N_4 nanocomposite structure enabled the increase in the surface area and the improvement of charge separation. The H_2 evolution rate was increased to 216.48 μmol h^{-1} g^{-1}, which is four times higher compared to pure CdS [97].

However, it was found that the photocatalytic activity obtained with 20% CdS/g-C_3N_4 nanocomposite was lower than pure CdS. This situation is attributed to the fact that the number of electrons generated electrons from g-C_3N_4 may be decreased by the shielding effect of CdS. The H_2 production rate, experimental conditions, and bandgap values of the composites which were obtained with high efficiency by using sulphide-based nanostructures including CdS and MoS_2 are shown in Table 26.4.

Zinc sulfide, which belongs to II–VI group semiconductor, has been worked as a photocatalyst due to the remarkable features such as thermal stability, nontoxicity, and lower cost [118]. It has cubic zinc blende and hexagonal wurtzite crystalline forms with the bandgap 3.72 eV and 3.77 eV, respectively [60]. As a result of this wide-bandgap, UV light absorption for electron–hole separation occurs at $\lambda < 340$ nm wavelength. In order to use the advantages of ZnS in accordance with solar fuel applications, efforts have been made to expand the light absorption in the visible wave spectrum [118].

One of the attempts to decrease the bandgap of ZnS is the use of the proper amount of dopant. For this purpose, Pang et al. modulated the electronic band structure of ZnS using Ni dopant, which is a non-toxic metal [188]. They showed that the photocatalytic CO_2 reduction activity decreased as a result of the diminishment in sulfur vacancies with the increasing amount of Ni doping. The obtained H_2 evolution was almost nine times higher with 0.1wt% Ni dopant by using full Xe arc lamp compare to pure ZnS.

The heterostructure formed by ZnS/ZnO, which has common anion, has been synthesized for increased solar fuel production [127]. The lattice mismatch (15%) between these two structures, the proposed Z-scheme system, and different annealing time for in-situ growth of ZnO directly on the ZnS enabled this structure to result in high H_2 evolution compared to pure ZnS. These results show that the particle size, shape, crystal structure, and degree of crystallinity which changes via the thermal treatment, affect the charge separation of the nanostructures alike the using various heterostructure and dopant materials.

MoS_2, a 2D structure of transition-metal dichalcogenides (TMDCs), has been widely used for solar fuel application to enhance hydrogen evolution. Its tunable bandgap within the 1.2–1.9 eV depending on the number of the sheet layers, high surface area, and abundant active sites are the advantages that make it able to be modified to increase photocatalytic activity [280]. Methods such as mechanical and chemical exfoliation, chemical vapor deposition are used in their synthesis [111]. While producing in large quantities is a drawback of mechanical exfoliation; chemical exfoliation may result in a low yield due to the wild control of the intercalation process with liquid and lithium intercalation. Besides, the toxicity of the solvents used for intercalation and long reaction time for chemical exfoliation are the other drawbacks for production of the MoS_2 [280]. CVD is the ideal method for large scale production, and it can provide high-quality MOS_2 production by controlling morphology, crystallinity, and defects [114].

MoS_2 has been used to obtain different heterostructures with other semiconductor materials which resulted in efficient solar energy conversion by changing

Table 26.4 Typical photocatalytic H_2-production systems of metal sulfides

Catalyst	Synthesis method	Products/activity (μmol·g^{-1}·h^{-1})	AQY (%)/ Wavelength (nm)	Light source	Optical bandgap (eV)	References
CdS/TiO_2	Hydrothermal	CH_4/27.85 μmol g^{-1}	–	350 W Xe lamp	CdS/2.27 TiO_2/3.04	[267]
L-Cys/CdS/NiCoP	Self-assembly	H_2/218000	76.3/420 nm	300 W Xe lamp	2.65	[92]
CdS/Ru	Deposition/precipitation	CH_4/2.585	–	0.71 W cm^{-2}	2.17	[22]
CdS/Nb_2O_5/SnS_2	Ultrasonication	H_2/43198 μmol g^{-1}	0.65/425	300 W Xe lamp	1.96	[162]
CdS frame-in-cage	Solution reaction	H_2/13.6	3.2/400	300 W Xe lamp	~2.3	[322]
CdS/InP	Wet impregnation	CO/216	0.44 /425	150 W Xe lamp	CdS/2.34 InP/2.20	[50]
CdS/Bi_2MoO_6	Solvothermal	H_2/6830	5.9/420	150 W Xe lamp	2.40	[29]
ZnS/CdS/ $Cd_{0.5}Zn_{0.5}S$/MoS_2	Template-assisted ion-exchange/ electrostatic assembly	H_2/50650	13.7/420	300 W Xe lamp	2.49	[237]
CoOx/N, S-C/CdS	Reflux process	H_2/40100	57.6/420	300 W Xe lamp	3.6	[258]
$Cs_{0.33}WO_3$/CdS	Precipitation	H_2/2648	–	300 W Xe lamp	2.78	[126]
CoP QDs/CdS NRs	Ultrasound	H_2/104947	32.16/420	300 W Xe lamp	CdS/2.37	[239]
CdS/$Cd_{0.5}Zn_{0.5}S$/ ZnS-Ni$(OH)_2$	Photodeposition	H_2/86790	22.8/420	300 W xenon lamp	CdS/2.42 $Cd_{0.5}Zn_{0.5}S$/ 2.52 ZnS/3.32	[211]

interfacial charge transfer properties [37]. Cho et al. obtained a few layered MoS_2/CdS QD. It was stated that the catalytic activity of the system in the hydrogen formation reaction (HER) would increase due to the enhanced carrier concentrations [37, 119, 329]. According to the results of transient absorption spectroscopy, ultrafast charge separation and long-lasting charge-separated states in heterostructures were obtained compared to bare MoS_2. In the other study, MoS_2 had been used as a co-catalyst in the heterostructure which was produced by in situ sulfidation of $CdMoO_4$ nanooctahedrons for the production of CdS/MoS_2 nanooctahedrons [329]. The pure CdS exhibited poor HER activity, and lower photocurrent density compares to bare MoS_2. Moreover, the heterostructure of CdS/MoS_2 showed highest HER activity photocurrent density. The results revealed that the heterostructure was promoting the electron transfer across the interface with the longest lifetime of photoinduced electron–hole pairs. The optimum H_2 production rate was in 27.16 mmol h^{-1} g^{-1} under visible light.

In an outstanding study in which MoS_2 was used as a co-catalyst, the H_2 production rate was obtained as 275 mmol h^{-1} g^{-1} [119]. Co-doped MoS_2/CdS structure is obtained firstly, by producing the Co crystals via pulsed laser ablation in liquid; secondly, Co dopped into a few layers of MoS_2 by ultrasonication and lastly, integrated with CdS. The synthesize steps can be seen on Fig. 26.6. The reasons to be achieved the high H_2 evolution rate by the system are; activation of the MoS_2 basal plane with the appropriate size (3.1 nm) and concentration of dopant, enhancement of the optical and electronic properties due to the crystal size of the dopant, and the exfoliation of MoS_2. Moreover, the heterostructure has demonstrated superior stability up to 5 cycles successfully for the long-term stability test.

The H_2 production rate, experimental conditions, and bandgap values of the composites which were obtained with high efficiency by using sulphide-based nanostructures except MoS_2 and CdS are shown in Table 26.5.

A novel structure, Z-scheme WO_3/CdS/WS_2 tandem heterostructure has been synthesized first embedding the WO_3 nanocrystals into WS2 nanoplate via the in-situ sulfurization of bulk WO_3 [297]. Afterwards the monodispersed CdS nanograins anchored on the ultrathin WO_3/WS_2 nanoplate. WO_3 has higher oxidation potential in the valence band, and CdS has a higher reduction potential in the conduction band. This situation makes the direct Z-scheme heterojunction possible to form between WO_3 and CdS. Additionally, WS_2 has been used as a co-catalyst which has a direct band on 1.9 eV. Its large surface area makes it easier to couple with photo absorber across the entire surface and WS_2 is the origin of the unsaturated sulfur atoms at the edges. This system efficient spatial charge separation resulted in highly efficient H_2 evolution of 14.34 mmoL h^{-1} g^{-1} with 22.96% quantum efficiency. Figure 26.7a and b shows the H_2 evolution of the pure and heterostructures for WS_2/CdS/WO_3. The pure WO_3 does not have hydrogen production because of the unsuitable conduction band potential. WO_3/WS_2 nanoplate composite, also, does not generate the H_2 due to the rapid recombination of photo-generated electrons and holes. The CW-3 (WS_2/CdS/WO_3) heterostructure

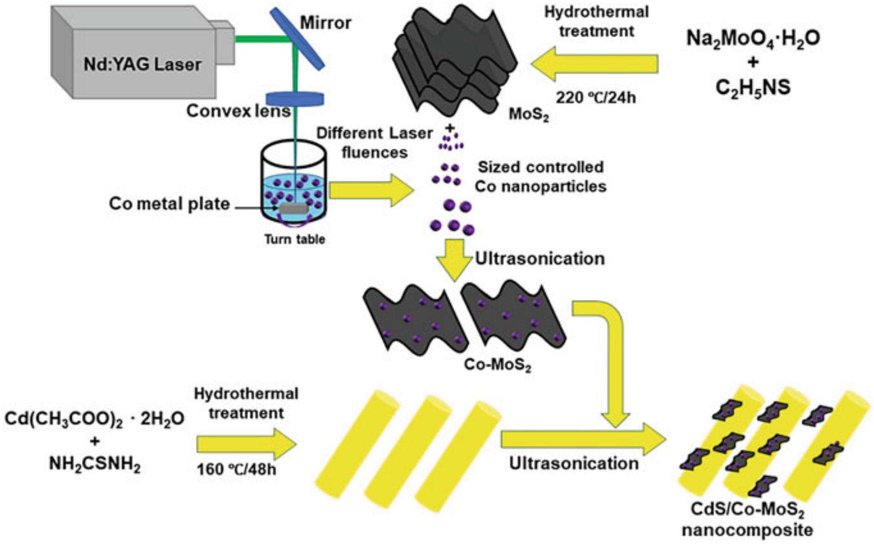

Fig. 26.6 Schematic illustration of the synthesis of CdS/Co–MoS_2 nanocomposites. Step I: Size-controlled cobalt nanocrystal synthesis via PLAL using 532-nm Nd:YAG laser with different laser fluence (0.32, 0.64, 0.96, 1.91, 2.86 and 3.82 J/cm^2). Step II: Formation of bulk MoS_2 nanosheets through hydrothermal synthesis. Step III: Formation of few-layer Co–MoS_2 nanocomposites using ultrasonication. Step IV: Integration of ultrathin Co–MoS_2 nanosheets on 1D–CdS nanorods by ultrasonication and long-time magnetic stirring to generate interfacial contact between CdS and Co–MoS_2 nanostructures (Reprinted from Ref. [119] with permission from Elsevier)

has the highest H_2 evolution rate. As well, the dosage of the 2D ultrathin WO_3/WS_2 nanoplate matrix also has a control on the photocatalytic H_2 production. As shown in Fig. 26.7c, the stability of the CW-3 composite did not decrease after six cycles, and AQE was found as 0.88% at 700 nm (Fig. 26.7d).

26.5 Transition Metal Phosphides (TMPs)

Metal transition phosphites are the superior materials that can be an alternative to noble metals with good photocatalytic performance and are even cheaper, abundant, and highly stable [279]. The photocatalytic performance increases due to the electronic structure of the phosphorus in the TMP structure [199], besides the types of different metals and the metal/phosphorus ratio also contribute to the photocatalytic activity. Other types of metal phosphites were produced for solar fuel application such as BP [246], CoP [143], Co_2P [122], Ni_2P [328], MoP [144], Cu_3P [241], FeP [53], RuP_2 [230], WP_2 [195], NbP [70] and NiCoP [92]. The electronegative nature of P atoms limits the electron delocalization of metals, which

Table 26.5 Typical photocatalytic H_2-production systems of metal sulfides

Catalyst	Synthesis method	H_2 production rate (μmol g^{-1} h^{-1})	AQY (%)/ Wavelength (nm)	Light source	Optical bandgap (eV)	References
NiS/ g-C_3N_4	Photodeposition	244	–	LED lamps	g-C_3N_4/ 2.7	[259]
ZnS/Cu	Ion-exchange	1000	17.6/ 410 ± 10	150 W Xe lamp	3.36	[44]
$Zn_{1-x}Cu_xS$	Hydrothermal	1296	2.48/365	Xe arc lamp	~3.5	[153]
WS_2/CdS/ WO_3	Hydrothermal	14,340	22.96/435	300 W Xe lamp	2.32	[297]
SnS_2/ CdS/ Nb_2O_5	Ultrasonication	55,887 μmol g^{-1}	0.65/425	300 W Xe lamp	~1.96	[162]
$CuSbS_2$	Hot-injection	2140	–		1.46	[214]
$FeCoS_2$/ CoS_2	Solvothermal	28.1 μmol h^{-1} (per o.5 mg catalyst)	–	300 W Xe lamp	–	[272]

decreases conductivity. As the P content increases, the structure can be a semiconductor or even insulator. Electronegative P atoms trap protons and stabilize the activation of H_2 atoms attached to the surface [208]. Thus, it is known that the obtained hydrogen evolution activity is greater in CoP than Co_2P and MoP than Mo_3P [23, 286].

TMPs have relatively high photocatalytic conversion rate results in the literature studies. A heterostructure, CoxP/CdS, which has the H_2 evolution of 500 mmol g^{-1} h^{-1} was formed by the photochemical method for illumination time up to 50 min [52]. It has been observed that the conversion activity increased by 85 times compared to pure CdS with increasing illumination time. After the 50th minute, the surplus amount of Co_XP caused lowering in oxidation reaction sites on the CdS surface, resulting in lower hydrogen evolution. This indicates that composition optimization has a crucial role in modifying photocatalytic activity.

The synthesis methods of TMP nanostructures can be classified according to organic and inorganic phosphorus sources [25, 52]. The organophosphorus, tri-n-octylphosphine (TOP), and triphenylphosphine (TPP), have been used as phosphorus sources by breaking the C–P bond with high-boiling organic solvents at temperatures up to 300 °C. Thus, replacement with a metal precursor can be achieved for TMP synthesis [25]. Hypophosphites are used as inorganic P sources which are decomposed above 250 °C and following by the reaction between metal precursor and PH3 via CVD method. Alternative methods such as hydrothermal synthesis, a gas–solid response, phosphorization take place under high temperatures. Considering the scope of green synthesis, microwave-assisted and PH3

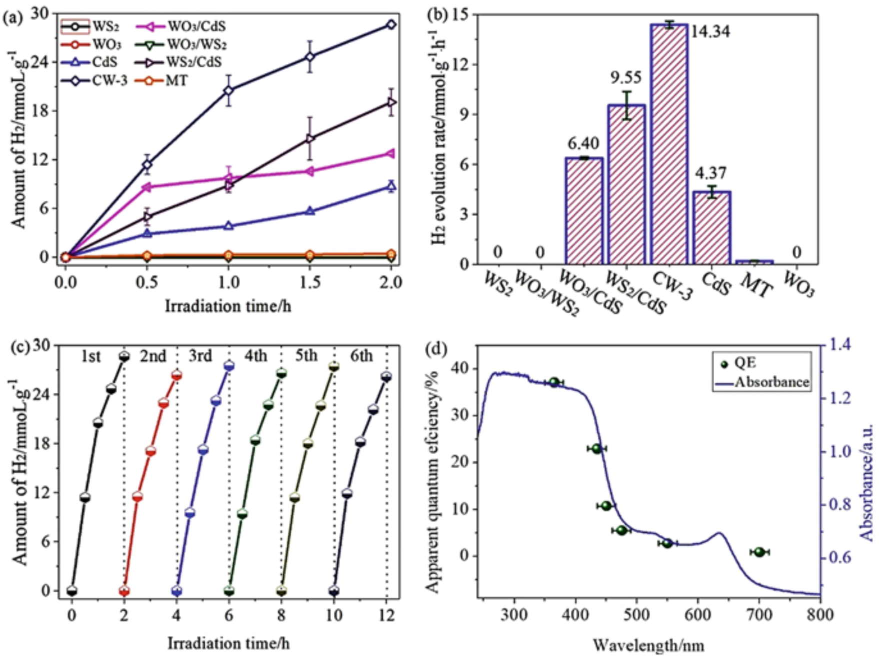

Fig. 26.7 **a** Time-dependent amounts and **b** the rates of H_2 evolution over different samples under visible light irradiation ($\lambda > 420$ nm); **c** Recycling H_2 evolution and **d** wavelength-dependent AQE of H_2 evolution from the CW-3 composite (Reprinted from Ref. [297] with permission from Elsevier)

plasma methods seem more suitable to conduct the synthesis for shorter reaction times by avoiding the high-temperature conditions [25].

The MoP is another TMP structure that draws attention with its similar electronic structure of Pt and its high conductivity [311]. In a study, it was used as a cocatalyst with CdS to construct a heterostructure [302]. The first drawback of the synthesis is the agglomeration which results due to the high-temperature phosphorization process. The second drawback originates from the TOP route due to its the toxicity, low yield, and complex operation [271]. These problems were solved by synthesizing freestanding ultra-small MoP quantum dots at low temperatures. The pyrolysis of ammonium molybdate and subsequent calcination steps at different temperatures were used for the synthesis of MoP, and then it has been dispersed with commercial CdS. The photocatalytic H_2 evolution rate of 0.60 mmol h^{-1} g^{-1} and 13.88 mmol h^{-1} g^{-1} were obtained for the pure CdS and MoP/CdS, respectively. This highly stable photocatalytic performance obtained is 1.44 times higher than Pt cocatalyst with AQY (420 nm) 66.7%.

Table 26.6 shows the synthesis methods of different TMP composite structures with high-performance hydrogen evolution rates, the conditions in which the experiments performed based on the recent literature studies.

Table 26.6 Typical photocatalytic H_2-production systems of transition metal phosphides

Catalyst	Synthesis method	H_2 production rate (μmol g^{-1} h^{-1})	AQY (%)/Wavelength (nm)	Light source	Optical bandgap (eV)	Phosphorus source	References
Cu_3P-Ni_2P/ g-C_3N_4	Hydrothermal	6526.7	18.5/400	300 W Xe lamp	1.66	Red P	[241]
MoP/g-C_3N_4	Self-assembly	327.5	10.2/420	300 W Xe lamp	–	$(NH_4)_2HPO_4$	[144]
BP/g-C_3N_4	Calcination	31.5	0.03/400	300 W Xe lamp	1.51/MoP 2.74/ g-C3N4	Red P	[246]
$Fe_xCo_{1-x}P$/CdS	Stirring	18,270	50.6/420	Visible light	1.59/ $Fe_{0.4}Co_{0.6}P$	$NaH_2PO_2{\cdot}H_2O$	[318]
NixP/CuS/CdS	Photochemical deposition	18,160	0.38/420	300 W Xe lamp	–	NaH_2PO_2	[136]
InP/CdS	Wet impregnation	216	0.44 /425	150 W Xe lamp	2.34/CdS 2.20/InP	Tris(diethylamino) phosphine	[50]
$Ni_{12}P_5$/S/ $Cd_{0.5}Zn_{0.5}S$	Evaporation/deposition/ precipitation	525.5	15/420	300 W Xe lamp	2.31/ $Cd_{0.5}Zn_{0.5}S$ 2.67/S	Red P	[71]
FeP/CdS	Solvothermal	37,920	31.50/420	300 W Xe lamp	2.32/CdS	Red P	[53]
Ni_2P/MoP/ g-C_3N_4	Photodeposition	517	5.9/420	300 W Xe lamp	2.75/ g-C_3N_4	$NaH_2PO_2{\cdot}H_2O$	[328]
CoP/TiO_2	Hydrothermal	604	–	300 W Xe lamp	3.11/TiO_2	$NaH_2PO_2{\cdot}H_2O$	[143]
CoP QDs/CdS NRs	Ultrasound	104,947	32.16/420	300 W Xe lamp	2.37/CdS	$NaH_2PO_2{\cdot}H_2O$	[239]
Co_2P/RB	Hydrothermal	5997.5	–	300 W Xe lamp	1.78/RP	Red P	[122]

26.6 Metal Oxide Frameworks (MOFs)

MOFs are the crystalline hybrid materials consisting of metal ions as inorganic metal centers connected by organic ligands [86]. Metal-organic frameworks (MOFs) materials have attracted photocatalytic H_2 generation application due to high surface area, high porosity, superior visible light absorbance, tunable bandgap, designable structure, good thermal and chemical stability [338]. However, the low conductivity of the MOFs limits their photocatalytic efficiency. The coordinatively unsaturated metal sites and the active groups on the organic linkers in MOF structures provide catalytic activity. The limits of the catalytic activity can be changed by functionalizing the metal sites, organic linkers and confining the pores [99, 142]. As an advantage, the high porosity of MOFs minimizes electron–hole recombination due to their short transport distance. The charge separation and photocatalytic activity will be increased by the addition of the electronegative structures to the MOFs [99].

MOF nanostructures can be synthesized by several methods, including solvothermal [59], layer by layer growth [1], electrochemical deposition [147], chemical vapor deposition [310], atomic/molecular layer deposition methods [172].

The incorporation of noble metals (Au [327], Ag [26], Pd [35], Pt [288], Rh [19], Ru), non-noble metals (Co [140], Cu [67], Fe [235], Ni [32]) has been carried out in previous studies in which the photocatalytic activity increased via the functionalization of the MOFs. The large pores of the MOFs provide an ideal host for nanoparticles (NPs) and single atoms (SAs). Taking advantage of this feature, NPs and/or SAs of Ru^{3+} incorporated NH_2-MIL-125/N-doped TiO_2/C was produced by using NH_2-functionalized MOF, which provides stabilization of metal cations [299]. The highest rate of H_2 evolution reached 100.0 μmol h^{-1} for NPs/SAs Ru^{3+} incorporated MOF. The evolution rate is higher than 58.3 μmol h^{-1} for Ru^{3+} composite structure where the only single atom is used, and it is higher than 83.9 μmol h^{-1}, which belongs to Pt/N-doped TiO_2 MOF material. The obtained performance has been attributed to the synergistic coupling between Ru nanoparticles and single atoms.

Nanoparticles (NPs) of noble metals (i.e. Ag, Au, Pt) which are active reaction sites can powerfully harness their surface plasmon resonance (SPR), accordingly, they absorb the visible light [262]. However, due to the high cost of the novel metals, non-noble-metal MOF analogues have been developed for high-performance catalytic activity. Moreover, the mixture of the different species of MOF heterostructures with carbon [128, 245], metal oxides [63], metal sulfides [245] covalent organic frameworks (COF) [84], phosphide [125] based materials have been produced for high photocatalytic performance. The recent studies are summarized in Table 26.7 based on the high photocatalytic performance of MOF systems.

MOFs have tunable porosity, metal centers, and organic ligands which provide advantages in their use. These properties render them the right candidate in catalytic applications such as CO_2 capture and H_2 evolution. In recent years, the studies

Table 26.7 Typical photocatalytic H_2-production systems of MOFs

Catalyst	Synthesis method	H_2 production rate (mmol g^{-1} h^{-1})	Light source	Optical bandgap (eV)	References
NH_2-UiO-66-MOF/TpPa-1-COF	One-pot synthesis	23.41	300 W Xe lamp	2.02/TpPa-1-COF 2.88/NH_2-UiO-66	[314]
MOF-Cu(I)	Solvothermal	4.21	500 W Xe lamp	2.13	[31]
Pt/MIL-125-(SCH_3)	Solvothermal	3.8	350 W Xe lamp	2.69	[78]
MIL-125/g-C_3N_4/TiO_2	Calcination	0.606	300 W Xe lamp	3.04	[277]
UIO-67/Ru/Pt	Solvothermal	1.13	150 W Xe Lamp	–	[303]
NH_2-MIL-125 (Ti)/benzoic acid-functionalized g-C_3N_4	Solvothermal	1.123	300 W Xe lamp	2.60/NH_2-MIL-125	[337]

resulted in high conversion efficiencies by using the MOF structures. While it is an advantage to be produced especially with low cost, MOFs may have stability problems due to factors such as pH and temperature due to organic linkers [253]. Besides, material production on the industrial scale is still another limiting factor.

26.7 Summary

Today, it is known that among the usage of energy resources, renewable energy sources are in demand due to the environmental effects of non-renewable fossil fuels. Solar energy has a greater potential than the total energy of all renewable energy sources. It is quite reasonable to use H_2 as a solar fuel in order to realize the energy generation of fuels obtained from the sun, and photocatalysts are used to achieve this conversion. Nanomaterials have been used in different types and structures to understand its advantages and disadvantages, to provide high H_2 conversion, and to carry out the conversion both efficient and stable. In this chapter of the book, the semiconductor nanomaterials as metal oxides, metal–organic frameworks, carbon-based materials, metal sulfides, and phosphides have been summarized in view of their usage in photocatalytic conversion. The synthesis and design of the materials and their hybridized structures, doping, heterostructures with each other for the enhanced photocatalytic conversion were discussed in each section. It has been emphasized that each combination performs uniquely depending on both bandgaps and synergetic effects of combination with each other and also the contributions of morphology, crystallinity, composition ratios to this efficiency. The literature studies prove that the different designs of these structures and their stability, performance, and reproducibility can be changed. It can be said that in the near future, for the efficient use of solar fuels, nanomaterial engineering will proceed in the direction of structures that allow industrial production with different interfaces, morphology, and compositions.

References

1. Abbasi AR, Akhbari K, Morsali A (2012) Dense coating of surface mounted CuBTC metal–organic framework nanostructures on silk fibers, prepared by layer-by-layer method under ultrasound irradiation with antibacterial activity. Ultrason Sonochem 19(4):846–852
2. Acik M, Chabal YJ (2013) A review on thermal exfoliation of graphene oxide. J Mater Sci Res 2(1):101
3. Adegoke KA, Iqbal M, Louis H et al (2019) Synthesis, characterization and application of CdS/ZnO nanorod heterostructure for the photodegradation of Rhodamine B dye. Mater Sci Energy Technol 2(2):329–336
4. Al-Shomar SM (2020) Investigation the effect of doping concentration in Ruthenium-doped TiO_2 thin films for solar cells and sensors applications. Mater Res Express 7(3):12
5. Al Jitan S, Palmisano G, Garlisi C (2020) Synthesis and surface modification of TiO_2-based photocatalysts for the conversion of CO_2. Catalysts 10(2):30
6. Albero J, Mateo D, Garcia H (2019) Graphene-based materials as efficient photocatalysts for water splitting. Molecules 24(5):21
7. Alcudia-Ramos MA, Fuentez-Torres MO, Ortiz-Chi F et al (2020) Fabrication of g-C_3N_4/TiO_2 heterojunction composite for enhanced photocatalytic hydrogen production. Ceram Int 46(1):38–45
8. Aliaga J, Cifuentes N, Gonzalez G et al (2018) Enhancement photocatalytic activity of the heterojunction of two-dimensional hybrid semiconductors ZnO/V_2O_5. Catalysts 8(9):13
9. Ando F, Tanabe T, Gunji T et al (2018) Effect of the d-Band center on the oxygen reduction reaction activity of electrochemically dealloyed ordered intermetallic platinum-lead (PtPb) nanoparticles supported on TiO_2-deposited cup-stacked carbon nanotubes. ACS Appl Nano Mater 1(6):2844–2850
10. Ashkarran AA, Fakhari M, Hamidinezhad H et al (2015) TiO_2 nanoparticles immobilized on carbon nanotubes for enhanced visible-light photo-induced activity. J Mater Res Technol JMRT 4(2):126–132
11. Bai S, Zhang N, Gao C et al (2018) Defect engineering in photocatalytic materials. Nano Energy 53:296–336
12. Bakbolat B, Daulbayev C, Sultanov F et al (2020) Recent developments of TiO_2-based photocatalysis in the hydrogen evolution and photodegradation: a review. Nanomaterials 10 (9):16
13. Baker SN, Baker GA (2010) Luminescent carbon nanodots: emergent nanolights. Angew Chem Int Edn 49(38):6726–6744

14. Bang HJ, Lee H, Park YK et al (2020) Fabrication of Yb-doped TiO_2 using liquid phase plasma process and its photocatalytic degradation activity of naproxen. J Mater Sci 55 (23):9665–9675
15. Banin U, Waiskopf N, Hammarstrom L et al (2021) Nanotechnology for catalysis and solar energy conversion. Nanotechnology 32(4):28
16. Barreca D, Carraro G, Gasparotto A et al (2015) Fe_2O_3-TiO_2 Nano-heterostructure photoanodes for highly efficient solar water oxidation. Adv Mater Interfaces 2(17):11
17. Bayan EM, Lupeiko TG, Kolupaeva EV et al (2017) Fluorine-doped titanium dioxide: synthesis, structure, morphology, size and photocatalytic activity. In: Parinov IA, Chang SH, Jani MA (ed) Advanced materials: techniques, physics, mechanics and applications, vol 193. Springer-Verlag Berlin, Berlin, pp 17–24
18. Bayan S, Gogurla N, Midya A et al (2016) White light emission characteristics of two dimensional graphitic carbon nitride and ZnO nanorod hybrid heterojunctions. Carbon 108:335–342
19. Benseghir Y, Lemarchand A, Duguet M et al (2020) Co-immobilization of a Rh catalyst and a keggin polyoxometalate in the UiO-67 Zr-based metal-organic framework: in depth structural characterization and photocatalytic properties for CO_2 reduction. J Am Chem Soc 142(20):9428–9438
20. Bhuyan MSA, Uddin MN, Islam MM et al (2016) Synthesis of graphene. Int Nano Lett 6 (2):65–83
21. Bozkurt H, Diker H, Varlikli C Fabrication and characterization of a solution processed flexible thermal sensor by using chemically synthesized GO and rGO. In: 2019 innovations in intelligent systems and applications conference (ASYU), IEEE
22. Cai SC, Zhang M, Li JJ et al Anchoring single-atom Ru on CdS with enhanced CO_2 capture and charge accumulation for high selectivity of photothermocatalytic CO_2 reduction to solar fuels. Sol. RRL: 10
23. Callejas JF, Read CG, Popczun EJ et al (2015) Nanostructured Co_2P electrocatalyst for the hydrogen evolution reaction and direct comparison with morphologically equivalent CoP. Chem Mater 27(10):3769–3774
24. Caner N, Bulut A, Yurderi M et al (2017) Atomic layer deposition-SiO_2 layers protected PdCoNi nanoparticles supported on TiO_2 nanopowders: exceptionally stable nanocatalyst for the dehydrogenation of formic acid. Appl Catal B Environ 210:470–483
25. Cao S, Wang CJ, Fu WF et al (2017) Metal phosphides as co-catalysts for photocatalytic and photoelectrocatalytic water splitting. Chemsuschem 10(22):4306–4323
26. Chandra R, Nath M (2020) Facile synthesis of metal-organic framework (ZIF-11) and Ag NPs encapsulated-ZIF-11 composite as an effective heterogeneous catalyst for photodegradation of methylene blue. Appl Organomet Chem 34(11):19
27. Chandrasekaran S, Yao L, Deng LB et al (2019) Recent advances in metal sulfides: from controlled fabrication to electrocatalytic, photocatalytic and photoelectrochemical water splitting and beyond. Chem Soc Rev 48(15):4178–4280
28. Chang F, Zheng JJ, Wu FY et al (2019) Binary composites WO_3/g-C_3N_4 in porous morphology: facile construction, characterization, and reinforced visible light photocatalytic activity. Colloid Surf A-Physicochem Eng Asp 563:11–21
29. Chava RK, Son N, Kim YS et al (2020) Integration of perovskite type Bi(2)MoO (6)nanosheets onto one dimensional CdS: a type-II heterostructured photocatalytic system for efficient charge separation in the hydrogen evolution reaction. Inorg Chem Front 7 (15):2818–2832
30. Chen BB, Liu ML, Huang CZ (2020) Carbon dot-based composites for catalytic applications. Green Chem 22(13):4034–4054
31. Chen D-M, Sun C-X, Liu C-S et al (2018) Stable layered semiconductive Cu (I)–organic framework for efficient visible-light-driven Cr (VI) reduction and H_2 evolution. Inorg Chem 57(13):7975–7981

32. Chen JX, Xing Z, Han J et al (2020) Enhanced degradation of dyes by Cu-Co-Ni nanoparticles loaded on amino-modified octahedral metal-organic framework. J Alloy Compd 834:14
33. Chen L, Xu YM, Chen B (2019) In situ photochemical fabrication of CdS/g-C_3N_4 nanocomposites with high performance for hydrogen evolution under visible light. Appl Catal B Environ 256:8
34. Chen YF, Tang D, Wang ZH et al (2020) Sn-bridge type-II PCN/Sn/SnO heterojunction with enhanced photocatalytic activity. Semicond Sci Technol 35(11):15
35. Cheng HM, Long XY, Bian FX et al (2020) Efficient photocatalytic one-pot hydrogenation and N-alkylation of nitrobenzenes/benzonitriles with alcohols over Pd/MOFs: effect of the crystal morphology & “quasi-MOF” structure. J Catal 389:121–131
36. Cheng L, Xiang QJ, Liao YL et al (2018) CdS-Based photocatalysts. Energy Environ Sci 11 (6):1362–1391
37. Cho JS, Suwandaratne NS, Razek S et al (2020) Elucidating the mechanistic origins of photocatalytic hydrogen evolution mediated by MoS_2/CdS quantum-dot heterostructures. ACS Appl Mater Interfaces 12(39):43728–43740
38. Chowdhury MS, Rahman KS, Selvanathan V et al Current trends and prospects of tidal energy technology. Environ Dev Sustain 16
39. Chung YH, Han K, Lin CY et al (2020) Photocatalytic hydrogen production by photo-reforming of methanol with one-pot synthesized Pt-containing TiO_2 photocatalysts. Catal Today 356:95–100
40. Cifuentes B, Bustamante F, Cobo M (2019) Single and dual metal oxides as promising supports for carbon monoxide removal from an actual syngas: the crucial role of support on the selectivity of the Au-Cu system. Catalysts 9(10):25
41. Clarizia L, Andreozzi R, Apuzzo J et al (2020) Efficient acetaldehyde production and recovery upon selective Cu/TiO_2-photocatalytic oxidation of ethanol in aqueous solution. Chem Eng J 393:7
42. Cybula A, Priebe JB, Pohl MM et al (2014) The effect of calcination temperature on structure and photocatalytic properties of Au/Pd nanoparticles supported on TiO_2. Appl Catal B Environ 152:202–211
43. Das A, Patra M, Hazarika M et al (2019) ZnO-In(2)O(3)nanocomposite: an efficient solar photocatalyst. In: Kaurav N, Choudhary KK, Dixit RC, Mishra A (eds) Prof. Dinesh Varshney memorial national conference on physics and chemistry of materials, 2100. Amer Inst Physics, Melville
44. Daskalakis I, Vamvasakis I, Papadas IT et al (2020) Surface defect engineering of mesoporous Cu/ZnS nanocrystal-linked networks for improved visible-light photocatalytic hydrogen production. Inorg Chem Front 7(23):4687–4700
45. Diao W, He J, Wang Q et al (2020) K, Na and Cl co-doped TiO_2 nanorod arrays on carbon cloth for efficient photocatalytic degradation of formaldehyde under UV/visible LED irradiation. Catal Sci Technol
46. Didi A, Gomez-Calcerrada LM, Benhamou A et al (2018) Versatility in the catalytic and photocatalytic reactions of composites based on Zr- and Zr-Pd-doped titania nanoparticles. Ceram Int 44(14):17266–17276
47. Diker H, Bozkurt H, Varlikli C (2020) Dispersion stability of amine modified graphene oxides and their utilization in solution processed blue OLED. Chem Eng J 381:122716
48. Diker H, Varlikli C, Mizrak K et al (2011) Characterizations and photocatalytic activity comparisons of N-doped nc-TiO_2 depending on synthetic conditions and structural differences of amine sources. Energy 36(2):1243–1254
49. Ding L, Yang SR, Liang ZQ et al (2020) TiO_2 nanobelts with anatase/rutile heterophase junctions for highly efficient photocatalytic overall water splitting. J Colloid Interface Sci 567:181–189
50. Do KH, Kumar DP, Rangappa AP et al (2020) Indium phosphide quantum dots integrated with cadmium sulfide nanorods for photocatalytic carbon dioxide reduction. ChemCatChem 12(18):4550–4557

51. Dong F, Zhao WR, Wu ZB (2008) Characterization and photocatalytic activities of C, N and S co-doped TiO_2 with 1D nanostructure prepared by the nano-confinement effect. Nanotechnology 19(36):10
52. Dong Y, Kong L, Wang G et al (2017) Photochemical synthesis of CoxP as cocatalyst for boosting photocatalytic H_2 production via spatial charge separation. Appl Catal B 211:245–251
53. Dou M-Y, Han S-R, Du X-X et al (2020) Well-defined FeP/CdS heterostructure construction with the assistance of amine for the efficient H_2 evolution under visible light irradiation. Int J Hydrog Energy 45(56):32039–32049
54. Douven S, Mahy JG, Wolfs C et al (2020) Efficient N, Fe Co-Doped TiO_2 active under cost-effective visible LED light: from powders to films. Catalysts 10(5):22
55. Du MM, Qiu BC, Zhu QH et al (2019) Fluorine doped TiO_2/mesocellular foams with an efficient photocatalytic activity. Catal Today 327:340–346
56. El Rouby WMA, Antuch M, You SM et al (2019) Novel nano-architectured water splitting photoanodes based on TiO_2-nanorod mats surface sensitized by ZIF-67 coatings. Int J Hydrog Energy 44(59):30949–30964
57. Elhousseini MH, Isik T, Kap O et al (2020) Dual remediation of waste waters from methylene blue and chromium (VI) using thermally induced ZnO nanofibers. Appl Surf Sci 514:10
58. Eslami A, Amini MM, Yazdanbakhsh AR et al (2016) N, S co-doped TiO_2 nanoparticles and nanosheets in simulated solar light for photocatalytic degradation of non-steroidal anti-inflammatory drugs in water: a comparative study. J Chem Technol Biotechnol 91 (10):2693–2704
59. Esrafili L, Tehrani AA, Morsali A et al (2019) Ultrasound and solvothermal synthesis of a new urea-based metal-organic framework as a precursor for fabrication of cadmium (II) oxide nanostructures. Inorg Chim Acta 484:386–393
60. Fang XS, Zhai TY, Gautam UK et al (2011) ZnS nanostructures: from synthesis to applications. Prog Mater Sci 56(2):175–287
61. Fu JW, Xu QL, Low JX et al (2019) Ultrathin 2D/2D WO_3/g-C_3N_4 step-scheme H-2-production photocatalyst. Appl Catal B Environ 243:556–565
62. Fu JW, Yu JG, Jiang CJ et al (2018) g-C_3N_4-based heterostructured photocatalysts. Adv Energy Mater 8(3):31
63. Fu N, Ren XC (2020) Synthesis of double-shell hollow TiO_2@ZIF-8 nanoparticles with enhanced photocatalytic activities. Front Chem 8:10
64. Fu PF, Luan Y, Dai XG (2004) Preparation of activated carbon fibers supported TiO_2 photocatalyst and evaluation of its photocatalytic reactivity. J Mol Catal A Chem 221(1–2):81–88
65. Fu YK, Zeng GM, Lai C et al (2020) Hybrid architectures based on noble metals and carbon-based dots nanomaterials: a review of recent progress in synthesis and applications. Chem Eng J 399:22
66. Gao LK, Gan WT, Qiu Z et al (2017) Preparation of heterostructured WO_3/TiO_2 catalysts from wood fibers and its versatile photodegradation abilities. Sci Rep 7:13
67. Gao YJ, Zhang L, Gu YM et al (2020) Formation of a mixed-valence Cu(i)/Cu(ii) metal-organic framework with the full light spectrum and high selectivity of CO(2) photoreduction into CH4. Chem Sci 11(37):10143–10148
68. Garcia-Lopez E, Marci G, Pomilla FR et al (2018) ZrO_2 Based materials as photocatalysts for 2-propanol oxidation by using UV and solar light irradiation and tests for CO_2 reduction. Catal Today 313:100–105
69. Gogoi D, Namdeo A, Golder AK et al (2020) Ag-doped TiO_2 photocatalysts with effective charge transfer for highly efficient hydrogen production through water splitting. Int J Hydrog Energy 45(4):2729–2744
70. Gujt J, Zimmer P, Zysk F et al (2020) Water structure near the surface of Weyl semimetals as catalysts in photocatalytic proton reduction. Struct Dyn US 7(3):6

71. Guo M, Guo X, Lin H et al (2020) Novel noble-metal free S/Ni12P5/Cd0. 5Zn0. 5S composite with enhanced H_2 evolution activity under visible light. Int J Hydrog Energy
72. Guo Q, Liang F, Li XB et al (2019) Efficient and selective CO_2 reduction integrated with organic synthesis by solar energy. Chem 5(10):2605–2616
73. Guy N (2020) Directional transfer of photocarriers on CdS/g-C_3N_4 heterojunction modified with Pd as a cocatalyst for synergistically enhanced photocatalytic hydrogen production. Appl Surf Sci 522:12
74. Hafeez HY, Lakhera SK, Narayanan N et al (2019) Environmentally sustainable synthesis of a $CoFe_2O_4$-TiO_2/rGO ternary photocatalyst: a highly efficient and stable photocatalyst for high production of hydrogen (Solar Fuel). ACS Omega 4(1):880–891
75. Hajizadeh-Oghaz M (2019) Synthesis and characterization of Nb-La co-doped TiO_2 nanoparticles by sol-gel process for dye-sensitized solar cells. Ceram Int 45(6):6994–7000
76. Hamdi A, Ferraria AM, do Rego AMB et al (2013) Bi-Y doped and co-doped TiO_2 nanoparticles: characterization and photocatalytic activity under visible light irradiation. J Mol Catal A Chem 380:34-42
77. Han C, Wang YD, Lei YP et al (2015) In situ synthesis of graphitic-C_3N_4 nanosheet hybridized N-doped TiO_2 nanofibers for efficient photocatalytic H-2 production and degradation. Nano Res 8(4):1199–1209
78. Han SY, Pan DL, Chen H et al (2018) A Methylthio-Functionalized-MOF Photocatalyst with High Performance for Visible-Light-Driven H_2 Evolution. Angew Chem Int Ed 57 (31):9864–9869
79. Han WJ, Ren L, Zhang Z et al (2015) Graphene-supported flocculent-like TiO_2 nanostructures for enhanced photoelectrochemical activity and photodegradation performance. Ceram Int 41(6):7471–7477
80. Hao HM, Lang XJ (2019) Metal sulfide photocatalysis: visible-light-induced organic transformations. ChemCatChem 11(5):1378–1393
81. Hao XQ, Hu Y, Cui ZW et al (2019) Self-constructed facet junctions on hexagonal CdS single crystals with high photoactivity and photostability for water splitting. Appl Catal B Environ 244:694–703
82. Hasan M, Hadzifejzovi E, Rohan JF et al (2018) Electrochemcial synthesis of nanoporous hematite (α-Fe_2O_3) and their applications towards photocatalytic water oxidation. The Electrochemical Society, Glasgow, Scotland, Meeting Abstracts
83. Hassan SM, Ahmed AI, Mannaa MA (2019) Preparation and characterization of SnO_2 doped TiO_2 nanoparticles: effect of phase changes on the photocatalytic and catalytic activity. J Sci 4(3):400–412
84. He SJ, Rong QF, Niu HY et al (2019) Platform for molecular-material dual regulation: a direct Z-scheme MOF/COF heterojunction with enhanced visible-light photocatalytic activity. Appl Catal B Environ 247:49–56
85. Hezam A, Namratha K, Drmosh QA et al (2020) CeO_2 nanostructures enriched with oxygen vacancies for photocatalytic CO_2 reduction. ACS Appl Nano Mater 3(1):138–148
86. Hilal ME, Aboulouard A, Akbar AR et al (2020) Progress of MOF-derived functional materials toward industrialization in solar cells and metal-air batteries. Catalysts 10(8):31
87. Horzum N, Hilal ME, Isik T (2018) Enhanced bactericidal and photocatalytic activities of ZnO nanostructures by changing the cooling route. New J Chem 42(14):11831–11838
88. Horzum N, Mari M, Wagner M et al (2015) Controlled surface mineralization of metal oxides on nanofibers. RSC Adv 5(47):37340–37345
89. Horzum N, Munoz-Espi R, Glasser G et al (2012) Hierarchically structured metal oxide/silica nanofibers by colloid electrospinning. ACS Appl Mater Interfaces 4(11):6338–6345
90. Hu BB, Guo Q, Wang K et al (2019) Enhanced photocatalytic activity of porous In_2O_3 for reduction of CO_2 with H_2O. J Mater Sci Mater Electron 30(8):7950–7962
91. Hurtado L, Natividad R, Garcia H (2016) Photocatalytic activity of Cu_2O supported on multi layers graphene for CO_2 reduction by water under batch and continuous flow. Catal Commun 84:30–35

92. Iqbal S (2020) Spatial charge separation and transfer in L-cysteine capped NiCoP/CdS nano-heterojunction activated with intimate covalent bonding for high-quantum-yield photocatalytic hydrogen evolution. Appl Catal B Environ 274:10
93. Isık T, Hilal ME, Horzum N (2019) Green synthesis of zinc oxide nanostructures. In: Zinc oxide based nano materials and devices. IntechOpen
94. Ismael M, Wu Y, Wark M (2019) Photocatalytic activity of ZrO_2 composites with graphitic carbon nitride for hydrogen production under visible light. New J Chem 43(11):4455–4462
95. Jayasree P, Remya N (2020) Photocatalytic degradation of paracetamol using aluminosilicate supported TiO_2. Water Sci Technol 82(10):2114–2124
96. Jeon JP, Kweon DH, Jang BJ et al Enhancing the photocatalytic activity of TiO_2 catalysts. Adv Sustain Syst 19
97. Ji C, Du C, Steinkruger JD et al (2019) In-situ hydrothermal fabrication of CdS/g-C_3N_4 nanocomposites for enhanced photocatalytic water splitting. Mater Lett 240:128–131
98. Jia YF, Ma HX, Zhang WB et al (2020) Z-scheme $SnFe_2O_4$-graphitic carbon nitride: reusable, magnetic catalysts for enhanced photocatalytic CO_2 reduction. Chem Eng J 383:11
99. Jiao L, Wang Y, Jiang HL et al (2018) Metal-organic frameworks as platforms for catalytic applications. Adv Mater 30(37):23
100. Jin C, Li W, Chen YS et al (2020) Efficient photocatalytic degradation and adsorption of tetracycline over type-II heterojunctions consisting of ZnO nanorods and K-Doped exfoliated g-C_3N_4 nanosheets. Ind Eng Chem Res 59(7):2860–2873
101. Karachi N, Hosseini M, Parsaee Z et al (2018) Novel high performance reduced graphene oxide based nanocatalyst decorated with Rh_2O_3/Rh-NPs for CO_2 photoreduction. J Photochem Photobiol A Chem 364:344–354
102. Khan H, Jiang ZR, Berk D (2018) Molybdenum doped graphene/TiO_2 hybrid photocatalyst for UV/visible photocatalytic applications. Sol Energy 162:420–430
103. Khan I, Baig N, Qurashi A (2019) Graphitic carbon nitride impregnated niobium oxide (g-C3N4/Nb2O5) type (II) heterojunctions and its synergetic solar-driven hydrogen generation. ACS Appl Energy Mater 2(1):607–615
104. Khan MI, Sabir M, Mustafa GM et al (2020) 300 keV cobalt ions irradiations effect on the structural, morphological, optical and photovolatic properties of Zn doped TiO_2 thin films based dye sensitized solar cells. Ceram Int 46(10):16813–16819
105. Khojasteh H, Salavati-Niasari M, Abbasi A et al (2016) Synthesis, characterization and photocatalytic activity of PdO/TiO_2 and Pd/TiO_2 nanocomposites. J Mater Sci Mater Electron 27(2):1261–1269
106. Kim SG, Dhandole LK, Seo YS et al (2018) Active composite photocatalyst synthesized from inactive Rh & Sb doped TiO_2 nanorods: enhanced degradation of organic pollutants & antibacterial activity under visible light irradiation. Appl Catal A Gen 564:43–55
107. Kim TH, Go GM, Cho HB et al (2018) A novel synthetic method for N doped Tio(2) nanoparticles through plasma-assisted electrolysis and photocatalytic activity in the visible region. Front Chem 6:10
108. Kiss J, Sapi A, Toth M et al (2020) Rh-induced support transformation and Rh incorporation in titanate structures and their influence on catalytic activity. Catalysts 10(2):29
109. Kokorin AI, Sviridova TV, Konstantinova EA et al (2020) Dynamics of photogenerated charge carriers in TiO_2/MoO_3, TiO_2/WO_3 and TiO_2/V_2O_5 photocatalysts with mosaic structure. Catalysts 10(9):14
110. Kongsong P, Jantaporn W, Masae M (2020) Enhanced photocatalytic activity of Ni doped TiO(2)nanowire-nanoparticle hetero-structured films prepared by hydrothermal and sol-gel methods. Surf Interface Anal 52(8):486–492
111. Krishnan U, Kaur M, Singh K et al (2019) A synoptic review of MoS_2: synthesis to applications. Superlattices Microstruct 128:274–297
112. Ku Y, Lin CN, Hou WM (2011) Characterization of coupled NiO/TiO_2 photocatalyst for the photocatalytic reduction of Cr(VI) in aqueous solution. J Mol Catal A Chem 349(1–2):20–27

113. Kubacka A, Munoz-Batista MJ, Ferrer M et al (2018) Er-W codoping of TiO_2-anatase: structural and electronic characterization and disinfection capability under UV-vis, and near-IR excitation. Appl Catal B Environ 228:113–129
114. Kumar R, Sahoo S, Joanni E et al (2019) A review on synthesis of graphene, h-BN and MoS_2 for energy storage applications: recent progress and perspectives. Nano Res 12 (11):2655–2694
115. Kumaravel V, Rhatigan S, Mathew S et al (2020) Mo doped TiO_2: impact on oxygen vacancies, anatase phase stability and photocatalytic activity. J Phys Mater 3(2):15
116. Kus M, Hakli Ö, Zafer C et al (2008) Optical and electrochemical properties of polyether derivatives of perylenediimides adsorbed on nanocrystalline metal oxide films. Org Electron 9(5):757–766
117. Lee C, Wei XD, Kysar JW et al (2008) Measurement of the elastic properties and intrinsic strength of monolayer graphene. Science 321(5887):385–388
118. Lee GJ, Wu JJ (2017) Recent developments in ZnS photocatalysts from synthesis to photocatalytic applications—a review. Powder Technol 318:8–22
119. Lee H, Reddy DA, Kumar DP et al (2019) Ultra-small cobalt nanocrystals embedded in 2D-MoS_2 nano-sheets as efficient co-catalyst for solar-driven hydrogen production: study of evolution rate dependence on cobalt nanocrystal size. Appl Surf Sci 494:239–248
120. Lee MG, Kim DH, Sohn W et al (2016) Conformally coated $BiVO_4$ nanodots on porosity-controlled WO_3 nanorods as highly efficient type II heterojunction photoanodes for water oxidation. Nano Energy 28:250–260
121. Lewandowska-Bernat A, Desideri U (2018) Opportunities of power-to-gas technology in different energy systems architectures. Appl Energy 228:57–67
122. Li CY, Fu M, Wang Y et al (2020) In situ synthesis of Co_2P-decorated red phosphorus nanosheets for efficient photocatalytic H-2 evolution. Catal Sci Technol 10(7):2221–2230
123. Li HJ, Tu WG, Zhou Y et al (2016) Z-Scheme photocatalytic systems for promoting photocatalytic performance: recent progress and future challenges. Adv Sci 3(11):12
124. Li HT, Liu RH, Lian SY et al (2013) Near-infrared light controlled photocatalytic activity of carbon quantum dots for highly selective oxidation reaction. Nanoscale 5(8):3289–3297
125. Li K, Zhang Y, Lin YZ et al (2019) Versatile functional porous cobalt-nickel phosphide-carbon cocatalyst derived from a metal-organic framework for boosting the photocatalytic activity of graphitic carbon nitride. ACS Appl Mater Interfaces 11 (32):28918–28927
126. Li N, Fan HK, Dai YJ et al (2020) Insight into the solar utilization of a novel Z-scheme Cs0.33WO3/CdS heterostructure for UV-Vis-NIR driven photocatalytic hydrogen evolution. Appl Surf Sci 508:9
127. Li P, He T (2018) Common-cation based Z-scheme ZnS@ZnO core-shell nanostructure for efficient solar-fuel production. Appl Catal B-Environ 238:518–524
128. Li S, Ji K, Zhang M et al (2020) Boosting the photocatalytic CO_2 reduction of metal–organic frameworks by encapsulating carbon dots. Nanoscale 12(17):9533–9540
129. Li T, Ding DY (2020) Photoelectrochemical water splitting with black Ni/Si-doped TiO_2 nanostructures. Int J Hydrog Energy 45(41):20983–20992
130. Li WJ, Liang R, Zhou NY et al (2020) Carbon black-doped anatase TiO_2 nanorods for solar light-induced photocatalytic degradation of methylene blue. ACS Omega 5(17):10042–10051
131. Li WJ, Lin ZY, Yang GW (2017) A 2D self-assembled $MoS_2/ZnIn_2S_4$ heterostructure for efficient photocatalytic hydrogen evolution. Nanoscale 9(46):18290–18298
132. Li X, Edelmannova M, Huo PW et al (2020) Fabrication of highly stable CdS/g-C_3N_4 composite for enhanced photocatalytic degradation of RhB and reduction of CO_2. J Mater Sci 55(8):3299–3313
133. Li X, Qian JH, Xu JS et al (2018) Synthesis, characterization and electrical properties of TiO_2 modified with SiO_2 and antimony-doped tin oxide. J Mater Sci Mater Electron 29 (14):12100–12108

134. Li Y, Zhao HJ, Yang MJ (2017) TiO_2 nanoparticles supported on PMMA nanofibers for photocatalytic degradation of methyl orange. J Colloid Interface Sci 508:500–507
135. Li YF, Zhou MH, Cheng B et al (2020) Recent advances in g-C_3N_4-based heterojunction photocatalysts. J Mater Sci Technol 56:1–17
136. Li YH, Yi MY, Li JY et al (2019) Noble metal free CdS@CuS-NixP hybrid with modulated charge transfer for enhanced photocatalytic performance. Appl Catal B Environ 257:6
137. Li YY, Walsh AG, Li DS et al (2020) W-Doped TiO(2)for photothermocatalytic CO(2) reduction. Nanoscale 12(33):17245–17252
138. Liao LB, Zhang QH, Su ZH et al (2014) Efficient solar water-splitting using a nanocrystalline CoO photocatalyst. Nat Nanotechnol 9(1):69–73
139. Lin ZY, Du C, Yan B et al (2018) Two-dimensional amorphous NiO as a plasmonic photocatalyst for solar H-2 evolution. Nat Commun 9:11
140. Liu F, Cao J, Yang ZH et al (2021) Heterogeneous activation of peroxymonosulfate by cobalt-doped MIL-53 (Al) for efficient tetracycline degradation in water: coexistence of radical and non-radical reactions. J Colloid Interface Sci 581:195–204
141. Liu FY, Dai YM, Chen FH et al (2020) Lead bismuth oxybromide/graphene oxide: synthesis, characterization, and photocatalytic activity for removal of carbon dioxide, crystal violet dye, and 2-hydroxybenzoic acid. J Colloid Interface Sci 562:112–124
142. Liu M, Wu J, Hou H (2019) Metal–Organic Framework (MOF)-based materials as heterogeneous catalysts for C−H bond activation. Chem Eur J 25(12):2935–2948
143. Liu Q, Huang J, Tang H et al (2020) Construction 0D TiO_2 nanoparticles/2D CoP nanosheets heterojunctions for enhanced photocatalytic H_2 evolution activity. J Mater Sci Technol
144. Liu W, Shen J, Liu QQ et al (2018) Porous MoP network structure as co-catalyst for H-2 evolution over g-C_3N_4 nanosheets. Appl Surf Sci 462:822–830
145. Liu X, Yang J, Hu LQ et al {001}/{101} facets co-exposed TiO(2) microsheet arrays with Lanthanum doping for enhancing photocatalytic CO(2) reduction. J Mater Sci Mater Electron 11
146. Liu XL, Ma R, Zhuang L et al Recent developments of doped g-C_3N_4 photocatalysts for the degradation of organic pollutants. Crit Rev Environ Sci Technol 40
147. Liu Y, Xu N, Chen W et al (2018) Supercapacitor with high cycling stability through electrochemical deposition of metal–organic frameworks/polypyrrole positive electrode. Dalton Trans 47(38):13472–13478
148. Lu XX, Toe CY, Ji F et al (2020) Light-induced formation of MoOxSy clusters on CdS nanorods as cocatalyst for enhanced hydrogen evolution. ACS Appl Mater Interfaces 12 (7):8324–8332
149. Luo H, Guo Q, Szilagyi PA et al (2020) Carbon dots in solar-to-hydrogen conversion. Trends Chem 2(7):623–637
150. Luo JH, Lin ZX, Zhao Y et al (2020) The embedded $CuInS_2$ into hollow-concave carbon nitride for photocatalytic H_2O splitting into H-2 with S-scheme principle. Chin J Catal 41 (1):122–130
151. Luo KY, Li J, Hu WY et al (2020) Synthesizing CuO/CeO_2/ZnO ternary nano-photocatalyst with highly effective utilization of photo-excited carriers under sunlight. Nanomaterials 10 (10):13
152. Luo S, Nguyen-Phan TD, Vovchok D et al (2018) Enhanced, robust light-driven H-2 generation by gallium-doped titania nanoparticles. Phys Chem Chem Phys 20(3):2104–2112
153. Lv PW, Xu CS, Huang JJ et al (2020) Reversible photochromism for the enhancement of carrier separation in Zn1-xCuxS. J Alloy Compd 844:8
154. Ma R, Zhang S, Li L et al (2019) Enhanced visible-light-induced photoactivity of type-II CeO_2/g-C_3N_4 nanosheet toward organic pollutants degradation. ACS Sustain Chem Eng 7 (10):9699–9708
155. Ma YY, Shen YQ, Gao X et al (2019) First-principles investigation on hydrogen evolution reaction in $KNbO_3$ (100)/g-C_3N_4 heterojunction. Appl Catal A Gen 582:7

156. Macdonald TJ, Nann T (2011) Quantum dot sensitized photoelectrodes. Nanomaterials 1 (1):79–88
157. Mahy JG, Lambert SD, Tilkin RG et al (2019) Ambient temperature ZrO_2-doped TiO_2 crystalline photocatalysts: highly efficient powders and films for water depollution. Mater Today Energy 13:312–322
158. Majeed I, Nadeem MA, Badshah A et al (2017) Titania supported MOF-199 derived Cu-Cu_2O nanoparticles: highly efficient non-noble metal photocatalysts for hydrogen production from alcohol-water mixtures. Catal Sci Technol 7(3):677–686
159. Malik P, Awasthi M, Sinha S Biomass-based gaseous fuel for hybrid renewable energy systems: an overview and future research opportunities. Int J Energy Res 31
160. Malika M, Rao CV, Das RK et al (2016) Evaluation of bimetal doped TiO_2 in dye fragmentation and its comparison to mono-metal doped and bare catalysts. Appl Surf Sci 368:316–324
161. Mamba G, Mishra AK (2016) Graphitic carbon nitride (g-C_3N_4) nanocomposites: a new and exciting generation of visible light driven photocatalysts for environmental pollution remediation. Appl Catal B Environ 198:347–377
162. Mandari KK, Son N, Pandey S et al (2020) Nb_2O_5-SnS_2-CdS heteronanostructures as efficient visible-light-harvesting materials for production of H-2 under solar light irradiation. J Alloy Compd 835:15
163. Margha FH, Radwan EK, Badawy MI et al (2020) Bi2O3-$BiFeO_3$ glass-ceramic: controllable beta/gamma-Bi_2O_3 transformation and application as magnetic solar-driven photocatalyst for water decontamination. ACS Omega 5(24):14625–14634
164. Mateo D, Albero J, Garcia H (2017) Photoassisted methanation using Cu_2O nanoparticles supported on graphene as a photocatalyst. Energy Environ Sci 10(11):2392–2400
165. Mateo D, Albero J, Garcia H (2018) Graphene supported NiO/Ni nanoparticles as efficient photocatalyst for gas phase CO_2 reduction with hydrogen. Appl Catal B Environ 224:563–571
166. Mateo D, Esteve-Adell I, Albero J et al (2016) 111 oriented gold nanoplatelets on multilayer graphene as visible light photocatalyst for overall water splitting. Nat Commun 7:8
167. Mateo D, Garcia-Mulero A, Albero J et al (2019) N-doped defective graphene decorated by strontium titanate as efficient photocatalyst for overall water splitting. Appl Catal B Environ 252:111–119
168. Mei FF, Li Z, Dai K et al (2020) Step-scheme porous g-C_3N_4/Zn0.2Cd0.8S-DETA composites for efficient and stable photocatalytic H-2 production. Chin J Catal 41(1):41–49
169. Memisoglu G, Varlikli C, Diker H (2013) Solution-processed polyfluorene: naphthalenediimide–N-doped TiO_2 hybrids for ultraviolet photodetector applications. J Electron Mater 42(12):3502–3511
170. Mendiola-Alvarez SY, Guzman-Mar JL, Turnes-Palomino G et al (2019) Synthesis of Cr3+-doped TiO_2 nanoparticles: characterization and evaluation of their visible photocatalytic performance and stability. Environ Technol 40(2):144–153
171. Mendiola-Alvarez SY, Hernandez-Ramirez MA, Guzman-Mar JL et al (2019) Phosphorous-doped TiO_2 nanoparticles: synthesis, characterization, and visible photocatalytic evaluation on sulfamethazine degradation. Environ Sci Pollut Res 26(5):4180–4191
172. Meng X (2017) An overview of molecular layer deposition for organic and organic–inorganic hybrid materials: mechanisms, growth characteristics, and promising applications. J Mater Chem A 5(35):18326–18378
173. Min YX, Yang XY, Wang DW et al (2019) Tuning mixed-phase Nb-doped titania films for high-performance photocatalysts with enhanced whole-spectrum light absorption. Catal Sci Technol 9(21):6027–6036
174. Mkhalid IA, Fierro JLG, Mohamed RM et al (2020) Impact of the PtO loading on mesoporous TiO_2 nanoparticles for enhanced photodegradation of Imazapyr herbicide under simulated solar light. J Nanopart Res 22(11):14
175. Mohammed SA, Al Amouri L, Yousif E et al (2018) Synthesis of NiO:V_2O_5 nanocomposite and its photocatalytic efficiency for methyl orange degradation. Heliyon 4(3):12

176. Mondal I, Gonuguntla S, Pal U (2019) Photoinduced fabrication of Cu/TiO_2 core-shell heterostructures derived from Cu-MOF for solar hydrogen generation: the size of the Cu nanoparticle matters. J Phys Chem C 123(43):26073–26081
177. Moniz SJA, Shevlin SA, An XQ et al (2014) Fe_2O_3-TiO_2 nanocomposites for enhanced charge separation and photocatalytic activity. Chem Eur J 20(47):15571–15579
178. Muller A, Kondofersky I, Folger A et al (2017) Dual absorber Fe_2O_3/WO_3 host-guest architectures for improved charge generation and transfer in photoelectrochemical applications. Mater Res Express 4(1):9
179. Nair SB, John KA, Joseph JA et al (2020) Role of magnesium doping for ultrafast room temperature crystallization and improved photocatalytic behavior of TiO_2 nanotubes. Mater Today Proc 25:203–207
180. Naraginti S, Stephen FB, Radhakrishnan A et al (2015) Zirconium and silver co-doped TiO_2 nanoparticles as visible light catalyst for reduction of 4-nitrophenol, degradation of methyl orange and methylene blue. Spectroc Acta Pt A Molec Biomolec Spectr 135:814–819
181. Naseri A, Samadi M, Pourjavadi A et al (2017) Graphitic carbon nitride (g-C_3N_4)-based photocatalysts for solar hydrogen generation: recent advances and future development directions. J Mater Chem A 5(45):23406–23433
182. Nasir JA, Rehman ZU, Shah SNA et al (2020) Recent developments and perspectives in CdS-based photocatalysts for water splitting. J Mater Chem A 8(40):20752–20780
183. Nematollahi R, Ghotbi C, Khorasheh F et al (2020) Ni-Bi co-doped TiO_2 as highly visible light response nano-photocatalyst for CO_2 photo-reduction in a batch photo-reactor. J CO_2 Util 41:101289
184. Nguyen CC, Dinh CT, Do TO (2017) Hollow Sr/Rh-codoped TiO_2 photocatalyst for efficient sunlight-driven organic compound degradation. RSC Adv 7(6):3480–3487
185. Nguyen VH, Do HH, Nguyen TV et al (2020) Perovskite oxide-based photocatalysts for solar-driven hydrogen production: progress and perspectives. Sol Energy 211:584–599
186. Osuntokun J, Onwudiwe DC, Ebenso EE (2017) Biosynthesis and photocatalytic properties of SnO_2 nanoparticles prepared using aqueous extract of cauliflower. J Clust Sci 28(4):1883–1896
187. Panayotov DA, Yates JT (2007) Spectroscopic detection of hydrogen atom spillover from au nanoparticles supported on TiO_2: use of conduction band electrons. J Phys Chem C 111 (7):2959–2964
188. Pang H, Meng XG, Song H et al (2019) Probing the role of nickel dopant in aqueous colloidal ZnS nanocrystals for efficient solar-driven CO_2 reduction. Appl Catal B Environ 244:1013–1020
189. Pant B, Ojha GP, Kuk YS et al (2020) Synthesis and characterization of ZnO-TiO_2/carbon fiber composite with enhanced photocatalytic properties. Nanomaterials 10(10):11
190. Parrino F, Bellardita M, Garcia-Lopez EI et al (2018) Heterogeneous photocatalysis for selective formation of high-value-added molecules: some chemical and engineering aspects. ACS Catal 8(12):11191–11225
191. Paulauskas IE, Modeshia DR, Ali TT et al (2013) Photocatalytic activity of doped and undoped titanium dioxide nanoparticles synthesised by flame spray pyrolysis platinum-doped TiO_2 composites show improved activity compared to commercially available product. Platin Met Rev 57(1):32–43
192. Peng C, Wei P, Li XY et al (2018) High efficiency photocatalytic hydrogen production over ternary Cu/TiO_2@Ti_3C_2Tx enabled by low-work-function 2D titanium carbide. Nano Energy 53:97–107
193. Perez R, Perez M (2009) A fundamental look at energy reserves for the planet. The IEA SHC solar update 50(2)
194. Pham TD, Lee BK (2017) Novel photocatalytic activity of Cu@V co-doped TiO_2/PU for CO_2 reduction with H_2O vapor to produce solar fuels under visible light. J Catal 345:87–95
195. Pi MY, Wu TL, Zhang DK et al (2016) Facile preparation of semimetallic WP2 as a novel photocatalyst with high photoactivity. RSC Adv 6(19):15724–15730

196. Pierpaoli M, Zheng X, Bondarenko V et al (2019) Paving the way for a sustainable and efficient SiO_2/TiO_2 photocatalytic composite. Environments 6(8):12
197. Pillai VV, Lonkar SP, Alhassan SM (2020) Template-free, solid-state synthesis of hierarchically macroporous S-Doped TiO_2 nano-photocatalysts for efficient water remediation. ACS Omega 5(14):7969–7978
198. Pooseekheaw P, Thongpan W, Panthawan A et al (2020) Porous V_2O_5/TiO(2) nanoheterostructure films with enhanced visible-light photocatalytic performance prepared by the sparking method. Molecules 25(15):11
199. Pu Z, Liu T, Amiinu IS et al (2020) Transition-metal phosphides: activity origin, energy-related electrocatalysis applications, and synthetic strategies. Adv Funct Mater 2004009
200. Qi YH, Xu JX, Fu YL et al (2019) Metal-organic framework templated synthesis ofg-C_3N_4/Fe_2O_3@FeP composites for enhanced hydrogen production. ChemCatChem 11(15):3465–3473
201. Qian JC, Chen ZG, Chen F et al (2018) Exploration of CeO_2-CuO quantum dots in situ grown on graphene under hypha assistance for highly efficient solar-driven hydrogen production. Inorg Chem 57(23):14532–14541
202. Qin YY, Li H, Lu J et al (2020) Synergy between van der waals heterojunction and vacancy in $ZnIn_2S_4$/g-C_3N_4 2D/2D photocatalysts for enhanced photocatalytic hydrogen evolution. Appl Catal B Environ 277:10
203. Raizada P, Sudhaik A, Patial S et al (2020) Engineering nanostructures of CuO-based photocatalysts for water treatment: current progress and future challenges. Arab J Chem 13 (11):8424–8457
204. Rambabu Y, Kumar U, Singhal N et al (2019) Photocatalytic reduction of carbon dioxide using graphene oxide wrapped TiO_2 nanotubes. Appl Surf Sci 485:48–55
205. Razmyar S, Sheng T, Akter M et al (2019) Low-temperature photocatalytic hydrogen addition to two-dimensional MoO_3 nanoflakes from isopropyl alcohol for enhancing solar energy harvesting and conversion. ACS Appl Nano Mater 2(7):4180–4192
206. Ren DD, Shen RC, Jiang ZM et al (2020) Highly efficient visible-light photocatalytic H-2 evolution over 2D–2D CdS/Cu_7S_4 layered heterojunctions. Chin J Catal 41(1):31–40
207. Ren DD, Zhang WN, Ding YN et al (2020) In situ fabrication of robust cocatalyst-free CdS/g-C_3N_4 2D–2D step-scheme heterojunctions for highly active H-2 evolution. Sol RRL 4 (8):11
208. Ren XH, Philo D, Li YX et al (2020) Recent advances of low-dimensional phosphorus-based nanomaterials for solar-driven photocatalytic reactions. Coord Chem Rev 424:34
209. Rhimi B, Wang CY, Bahnemann DW (2020) Latest progress in g-C(3)N(4) based heterojunctions for hydrogen production via photocatalytic water splitting: a mini review. J Phys Energy 2(4):16
210. Rodriguez JA, Evans J, Graciani J et al (2009) High water-gas shift activity in TiO_2(110) supported Cu and Au nanoparticles: role of the oxide and metal particle size. J Phys Chem C 113(17):7364–7370
211. Ruan QQ, Ma XW, Li YY et al (2020) One-dimensional CdS@Cd0.5Zn0.5S@ZnS-Ni(OH)(2) nano-hybrids with epitaxial heterointerfaces and spatially separated photo-redox sites enabling highly-efficient visible-light-driven H(2) evolution. Nanoscale 12(39):20522–20535
212. Rusinque B, Escobedo S, de Lasa H (2020) Photoreduction of a Pd-doped mesoporous TiO_2 photocatalyst for hydrogen production under visible light. Catalysts 10(1):24
213. Sahin C, Dittrich T, Varlikli C et al (2010) Role of side groups in pyridine and bipyridine ruthenium dye complexes for modulated surface photovoltage in nanoporous TiO_2. Sol Energy Mater Sol Cells 94(4):686–690
214. Sarilmaz A, Genc E, Aslan E et al (2020) Photocatalytic hydrogen evolution via solar-driven Water splitting by $CuSbS_2$ with different shapes. J Photochem Photobiol A Chem 400:6

215. Saroj S, Singh L, Singh SV (2020) Solution-combustion synthesis of anion (iodine) doped TiO_2 nanoparticles for photocatalytic degradation of Direct Blue 199 dye and regeneration of used photocatalyst. J Photochem Photobiol A Chem 396:13
216. Schiper DE, Zhao ZH, Leitner AP et al (2017) A TiO_2/FeMnP Core/Shell nanorod array photoanode for efficient photoelectrochemical oxygen evolution. ACS Nano 11(4):4051–4059
217. Shabdan Y, Markhabayeva A, Bakranov N et al (2020) Photoactive Tungsten-Oxide Nanomaterials for Water-Splitting. Nanomaterials 10(9):37
218. Shahan M, Ahmed AM, Shehata N et al (2019) Ni-doped and Ni/Cr co-doped TiO_2 nanotubes for enhancement of photocatalytic degradation of methylene blue. J Colloid Interface Sci 555:31–41
219. Shakir I, Choi JH, Shahid M et al (2012) MoO_3-MWCNT nanocomposite photocatalyst with control of light-harvesting under visible light and natural sunlight irradiation. J Mater Chem 22(38):20549–20553
220. Shehzad N, Tahir M, Johari K et al (2018) Improved interfacial bonding of graphene-TiO_2 with enhanced photocatalytic reduction of CO_2 into solar fuel. J Environ Chem Eng 6 (6):6947–6957
221. Shi L, Benetti D, Li FY et al (2020) Phase-junction design of MOF-derived TiO_2 photoanodes sensitized with quantum dots for efficient hydrogen generation. Appl Catal B Environ 263:10
222. Shi L, He Z, Liu SQ (2018) MoS_2 quantum dots embedded in g-C_3N_4 frameworks: a hybrid 0D–2D heterojunction as an efficient visible-light driven photocatalyst. Appl Surf Sci 457:30–40
223. Shi WL, Wang JB, Yang S et al (2020) Fabrication of a ternary carbon dots/CoO/g-C_3N_4 nanocomposite photocatalyst with enhanced visible-light-driven photocatalytic hydrogen production. J Chem Technol Biotechnol 95(8):2129–2138
224. Shin HU, Lolla D, Nikolov Z et al (2016) Pd-Au nanoparticles supported by TiO_2 fibers for catalytic NO decomposition by CO. J Ind Eng Chem 33:91–98
225. Singh J, Kaur H, Kukkar D et al (2019) Green synthesis of SnO_2 NPs for solar light induced photocatalytic applications. Mater Res Express 6(11):8
226. Singh K, Harish S, Kristy AP et al (2018) Erbium doped TiO_2 interconnected mesoporous spheres as an efficient visible light catalyst for photocatalytic applications. Appl Surf Sci 449:755–763
227. Smith WA, Sharp ID, Strandwitz NC et al (2015) Interfacial band-edge energetics for solar fuels production. Energy Environ Sci 8(10):2851–2862
228. Sohail M, Baig N, Sher M et al (2020) A novel tin-doped titanium oxide nanocomposite for efficient photo-anodic water splitting. ACS Omega 5(12):6405–6413
229. Song GX, Chu ZY, Jin WQ et al (2015) Enhanced performance of g-C_3N_4/TiO_2 photocatalysts for degradation of organic pollutants under visible light. Chin J Chem Eng 23(8):1326–1334
230. Song LM, Zhang SJ (2018) RuP2/CdS photocatalysts for enhanced hydrogen evolution in water spitting and mechanism of enhancement. Powder Technol 339:479–486
231. Sorcar S, Thompson J, Hwang Y et al (2018) High-rate solar-light photoconversion of CO_2 to fuel: controllable transformation from C-1 to C-2 products. Energy Environ Sci 11 (11):3183–3193
232. Sreekanth TVM, Nagajyothi PC, Dillip GR et al (2017) Determination of band alignment in the synergistic catalyst of electronic structure-modified graphitic carbon nitride-integrated ceria quantum-dot heterojunctions for rapid degradation of organic pollutants. J Phys Chem C 121(45):25229–25242
233. Stolarczyk JK, Bhattacharyya S, Polavarapu L et al (2018) Challenges and prospects in solar water splitting and CO_2 reduction with inorganic and hybrid nanostructures. ACS Catal 8 (4):3602–3635
234. Su N, Hu XL, Zhang JB et al (2017) Plasma-induced synthesis of Pt nanoparticles supported on TiO_2 nanotubes for enhanced methanol electro-oxidation. Appl Surf Sci 399:403–410

235. Su SY, Xing ZP, Zhang SY et al (2021) Ultrathin mesoporous g-C_3N_4/NH_2-MIL-101(Fe) octahedron heterojunctions as efficient photo-Fenton-like system for enhanced photo-thermal effect and promoted visible-light-driven photocatalytic performance. Appl Surf Sci 537:11
236. Sudrajat H, Babel S, Ta AT et al (2020) Mn-doped TiO_2 photocatalysts: Role, chemical identity, and local structure of dopant. J Phys Chem Solids 144:9
237. Sun BW, Wang H, Wu JK et al (2020) Designed synthesis of unique ZnS@CdS@Cd0.5Zn0.5S-MoS_2 hollow nanospheres for efficient visible-light-driven H-2 evolution. Crystengcomm 22(16):2743–2755
238. Sun FC, Maimaiti H, Liu YE et al (2018) Preparation and photocatalytic CO_2 reduction performance of silver nanoparticles coated with coal-based carbon dots. Int J Energy Res 42 (14):4458–4469
239. Sun QQ, Yu ZB, Jiang RH et al (2020) CoP QD anchored carbon skeleton modified CdS nanorods as a co-catalyst for photocatalytic hydrogen production. Nanoscale 12(37):19203–19212
240. Sun T, Fan J, Liu EZ et al (2012) Fe and Ni co-doped TiO_2 nanoparticles prepared by alcohol-thermal method: application in hydrogen evolution by water splitting under visible light irradiation. Powder Technol 228:210–218
241. Sun WJ, Fu ZY, Shi HX et al (2020) Cu(3)P and Ni(2)P co-modified g-C(3)N(4) nanosheet with excellent photocatalytic H(2) evolution activities. J Chem Technol Biotechnol 95 (12):3117–3125
242. Suppuraja P, Parthiban S, Swaminathan M et al (2019) Hydrothermal fabrication of ternary NrGO-TiO_2/$ZnFe_2O_4$ nanocomposites for effective photocatalytic and fuel cell applications. Mater Today Proc 15:429–437
243. Teixeira IF, Quiroz J, Homsi MS et al (2020) An overview of the photocatalytic H-2 evolution by semiconductor-based materials for nonspecialists. J Braz Chem Soc 31(2):211–229
244. Thangavel N, Bellamkonda S, Arulraj AD et al (2018) Visible light induced efficient hydrogen production through semiconductor-conductor-semiconductor (S-C-S) interfaces formed between g-C_3N_4 and rGO/Fe_2O_3 core-shell composites. Catal Sci Technol 8 (19):5081–5090
245. Thi QV, Tamboli MS, Ta QTH et al (2020) A nanostructured MOF/reduced graphene oxide hybrid for enhanced photocatalytic efficiency under solar light. Mater Sci Eng B 261:114678
246. Tian B, Wu YQ, Lu GX (2021) Metal-free plasmonic boron phosphide/graphitic carbon nitride with core-shell structure photocatalysts for overall water splitting. Appl Catal B Environ 280:9
247. Truc NTT, Bach LG, Hanh NT et al (2019) The superior photocatalytic activity of Nb doped TiO_2/g-C_3N_4 direct Z-scheme system for efficient conversion of CO_2 into valuable fuels. J Colloid Interface Sci 540:1–8
248. Truc NTT, Pham TD, Nguyen MV et al (2020) Advanced $NiMoO_4$/g-C_3N_4 Z-scheme heterojunction photocatalyst for efficient conversion of CO_2 to valuable products. J Alloy Compd 842:8
249. Tseng IH, Sung YM, Chang PY et al (2017) Photocatalytic performance of titania nanosheets templated by graphene oxide. J Photochem Photobiol A Chem 339:1–11
250. Uddin A, Muhmood T, Guo ZC et al (2020) Hydrothermal synthesis of 3D/2D heterojunctions of $ZnIn_2S_4$/oxygen doped g-C_3N_4 nanosheet for visible light driven photocatalysis of 2,4-dichlorophenoxyacetic acid degradation. J Alloy Compd 845:11
251. Uma K, Muniranthinam E, Chong SH et al (2020) Fabrication of hybrid catalyst ZnO nanorod/alpha-Fe_2O_3 composites for hydrogen evolution reaction. Curr Comput Aided Drug Des 10(5):12
252. Van CN, Hai NT, Olejnicek J et al (2018) Preparation and photoelectrochemical performance of porous TiO_2/graphene nanocomposite films. Mater Lett 213:109–113
253. Verma P, Stewart DJ, Raja R (2020) Recent advances in photocatalytic CO_2 utilisation over multifunctional metal–organic frameworks. Catalysts 10(10):1176

254. Walter MG, Warren EL, McKone JR et al (2010) Solar water splitting cells. Chem Rev 110 (11):6446–6473
255. Wang CH, Qin DD, Shan DL et al (2017) Assembly of g-C_3N_4-based type II and Z-scheme heterojunction anodes with improved charge separation for photoelectrojunction water oxidation. Phys Chem Chem Phys 19(6):4507–4515
256. Wang CH, Shao CL, Zhang XT et al (2009) SnO_2 nanostructures-TiO_2 nanofibers heterostructures: controlled fabrication and high photocatalytic properties. Inorg Chem 48 (15):7261–7268
257. Wang GZ, Zhou F, Yuan BF et al (2019) Strain-tunable visible-light-responsive photocatalytic properties of two-dimensional CdS/g-C_3N_4: a hybrid density functional study. Nanomaterials 9(2):10
258. Wang JM, Xu QC, Liu ML et al (2020) The synergetic effect of N, S-codoped carbon and CoOx nanodots derived from ZIF-67 as a highly efficient cocatalyst over CdS nanorods. Sustain Energ Fuels 4(4):1954–1962
259. Wang M, Cheng JJ, Wang XF et al (2021) Sulfur-mediated photodeposition synthesis of NiS cocatalyst for boosting H-2-evolution performance of g-C_3N_4 photocatalyst. Chin J Catal 42 (1):37–45
260. Wang M, Ju P, Li JJ et al (2017) Facile synthesis of MoS_2/g-C_3N_4/GO ternary heterojunction with enhanced photocatalytic activity for water splitting. ACS Sustain Chem Eng 5(9):7878–7886
261. Wang N, Li XJ (2018) Facile synthesis of CoO nanorod/C_3N_4 heterostructure photocatalyst for an enhanced pure water splitting activity. Inorg Chem Commun 92:14–17
262. Wang P, Huang BB, Dai Y et al (2012) Plasmonic photocatalysts: harvesting visible light with noble metal nanoparticles. Phys Chem Chem Phys 14(28):9813–9825
263. Wang Q, Chen X, Tian J et al The preparation of S-SnO_2/g-C(3)N(4)heterojunction and its photocatalytic degradation of phenol and trichlorophenol. J Mater Sci Mater Electron 12
264. Wang QL, Wang XK, Yu ZH et al (2019) Artificial photosynthesis of ethanol using type-II g-C_3N_4/ZnTe heterojunction in photoelectrochemical CO_2 reduction system. Nano Energy 60:827–835
265. Wang QQ, Zhu SL, Liang YQ et al (2017) One-step synthesis of size-controlled Br-doped TiO_2 nanoparticles with enhanced visible-light photocatalytic activity. Mater Res Bull 86:248–256
266. Wang S, Wang L, Huang W (2020) Bismuth-based photocatalysts for solar energy conversion. J Mater Chem A
267. Wang SJ, Chen L, Zhao XL et al (2020) Efficient photocatalytic overall water splitting on metal-free 1D SWCNT/2D ultrathin C_3N_4 heterojunctions via novel non-resonant plasmonic effect. Appl Catal B-Environ 278:8
268. Wang XF, Li SF, Yu HG et al (2011) Ag_2O as a new visible-light photocatalyst: self-stability and high photocatalytic activity. Chem Eur J 17(28):7777–7780
269. Wang XJ, Zhao XL, Zhang DQ et al (2018) Microwave irradiation induced UIO-66-NH_2 anchored on graphene with high activity for photocatalytic reduction of CO_2. Appl Catal B-Environ 228:47–53
270. Wang XK, Wang C, Jiang WQ et al (2012) Sonochemical synthesis and characterization of Cl-doped TiO_2 and its application in the photodegradation of phthalate ester under visible light irradiation. Chem Eng J 189:288–294
271. Wang Y, Kong B, Zhao D et al (2017) Strategies for developing transition metal phosphides as heterogeneous electrocatalysts for water splitting. Nano Today 15:26–55
272. Wang Y, Wang S, Zhang SL et al (2020) Formation of hierarchical $FeCoS_2$–CoS_2 double-shelled nanotubes with enhanced performance for photocatalytic reduction of CO_2. Angew Chem
273. Wang YF, Hu AG (2014) Carbon quantum dots: synthesis, properties and applications. J Mater Chem C 2(34):6921–6939

274. Wang ZC, Song YC, Cai XF et al (2019) Rapid preparation of terbium-doped titanium dioxide nanoparticles and their enhanced photocatalytic performance. R Soc Open Sci 6 (10):14
275. Wang ZL, Chen YF, Zhang LY et al (2020) Step-scheme CdS/TiO_2 nanocomposite hollow microsphere with enhanced photocatalytic CO_2 reduction activity. J Mater Sci Technol 56:143–150
276. Wattanawikkam C, Pecharapa W (2020) Structural studies and photocatalytic properties of Mn and Zn co-doping on TiO_2 prepared by single step sonochemical method. Radiat Phys Chem 171:8
277. Wei C, Zhang W, Wang X et al (2020) MOF-derived mesoporous gC_3N_4/TiO_2 heterojunction with enhanced photocatalytic activity. Catal Lett 1–15
278. Wei SQ, Wang F, Yan P et al (2019) Interfacial coupling promoting hydrogen sulfide splitting on the staggered type II g-C_3N_4/r-TiO_2 heterojunction. J Catal 377:122–132
279. Weng C-C, Ren J-T and Yuan Z-Y (2020) Transition metal phosphide-based materials for efficient electrochemical hydrogen evolution: a critical review. ChemSusChem
280. Wu C, Zhang J, Tong X et al (2019) A critical review on enhancement of photocatalytic hydrogen production by molybdenum disulfide: from growth to interfacial activities. Small 15(35):25
281. Wu SJ, Zhao HJ, Li CF et al (2019) Type II heterojunction in hierarchically porous zinc oxide/graphitic carbon nitride microspheres promoting photocatalytic activity. J Colloid Interface Sci 538:99–107
282. Wu TS, Zhu C, Han DX et al (2019) Highly selective conversion of CO_2 to C_2H_6 on graphene modified chlorophyll Cu through multi-electron process for artificial photosynthesis. Nanoscale 11(47):22980–22988
283. Wu YA, McNulty I, Liu C et al (2019) Facet-dependent active sites of a single Cu_2O particle photocatalyst for CO_2 reduction to methanol. Nat Energy 4(11):957–968
284. Wu YX, Liu LM, An XQ et al (2019) New insights into interfacial photocharge transfer in TiO_2/C_3N_4 heterostructures: effects of facets and defects. New J Chem 43(11):4511–4517
285. Xia Y, Cheng B, Fan JJ et al (2019) Unraveling photoexcited charge transfer pathway and process of CdS/graphene nanoribbon composites toward visible-light photocatalytic hydrogen evolution. Small 15(34):9
286. Xiao Z, Bi C, Shao Y et al (2014) Efficient, high yield perovskite photovoltaic devices grown by interdiffusion of solution-processed precursor stacking layers. Energy Environ Sci 7(8):2619–2623
287. Xie W, Li R, Xu QY (2018) Enhanced photocatalytic activity of Se-doped TiO_2 under visible light irradiation. Sci Rep 8:10
288. Xing HM, Teng SY, Xing ZH et al (2020) Effect of Pt cocatalyst on visible light driven hydrogen evolution of anthracene-based zirconium metal-organic framework. Appl Surf Sci 532:7
289. Xing M, Zhang J, Qiu B et al (2015) A brown mesoporous TiO_2-x/MCF composite with an extremely high quantum yield of solar energy photocatalysis for H_2 evolution. Small 11 (16):1920–1929
290. Xu L, Li Q, Li XF et al (2019) Rationally designed 2D/2DSiC/g-C_3N_4 photocatalysts for hydrogen production. Catal Sci Technol 9(15):3896–3906
291. Xu M, Wu H, Tang YW et al (2020) One-step in-situ synthesis of porous Fe3+-doped TiO_2 octahedra toward visible-light photocatalytic conversion of CO_2 into solar fuel. Microporous Mesoporous Mat 309:7
292. Xu QL, Zhang LY, Cheng B et al (2020) S-Scheme Heterojunction Photocatalyst. Chem 6 (7):1543–1559
293. Xu QL, Zhang LY, Yu JG et al (2018) Direct Z-scheme photocatalysts: principles, synthesis, and applications. Mater Today 21(10):1042–1063
294. Xu QL, Zhu BC, Jiang CJ et al (2018) Constructing 2D/2D Fe_2O_3/g-C_3N_4 direct Z-scheme photocatalysts with enhanced H-2 generation performance. Sol RRL 2(3):10

295. Xu XY, Ray R, Gu YL et al (2004) Electrophoretic analysis and purification of fluorescent single-walled carbon nanotube fragments. J Am Chem Soc 126(40):12736–12737
296. Xu YH, Liang DH, Liu ML et al (2008) Preparation and characterization of Cu_2O-TiO_2: Efficient photocatalytic degradation of methylene blue. Mater Res Bull 43(12):3474–3482
297. Xue C, Zhang P, Shao GS et al (2020) Effective promotion of spacial charge separation in direct Z-scheme WO3/CdS/WS2 tandem heterojunction with enhanced visible-light-driven photocatalytic H-2 evolution. Chem Eng J 398:10
298. Yadav V, Verma P, Sharma H et al (2020) Photodegradation of 4-nitrophenol over B-doped TiO_2 nanostructure: effect of dopant concentration, kinetics, and mechanism. Environ Sci Pollut Res 27(10):10966–10980
299. Yan BL, Liu DP, Feng XL et al (2020) Ru species supported on MOF-derived N-doped TiO_2/C hybrids as efficient electrocatalytic/photocatalytic hydrogen evolution reaction catalysts. Adv Func Mater 30(31):9
300. Yan BL, Zhang LJ, Tang ZY et al (2017) Palladium-decorated hierarchical titania constructed from the metal-organic frameworks NH_2-MIL-125(Ti) as a robust photocatalyst for hydrogen evolution. Appl Catal B-Environ 218:743–750
301. Yan MY, Jiang ZY, Zheng JM et al (2020) Theoretical study on transport-scheme conversion of g-C_3N_4/TiO_2 heterojunctions by oxygen vacancies. Appl Surf Sci 531:7
302. Yang F, Liu D, Li Y, et al Solid-state synthesis of ultra-small freestanding amorphous MoP quantum dots for highly efficient photocatalytic H_2 production. Chem Eng J 406:126838
303. Yang S, Fan D, Hu W et al (2018) Elucidating charge separation dynamics in a hybrid metal-organic framework photocatalyst for light-driven H_2 evolution. J Phys Chem C 122 (6):3305–3311
304. Yang XH, Wang Y, Zhang LT et al (2020) The use of tunable optical absorption plasmonic Au and Ag decorated TiO_2 structures as efficient visible light photocatalysts. Catalysts 10 (1):14
305. Yang Y, Zhang C, Lai C et al (2018) BiOX (X = Cl, Br, I) photocatalytic nanomaterials: applications for fuels and environmental management. Adv Colloid Interface Sci 254:76–93
306. Yang YJ, Yu YL, Wang JS et al (2017) Doping and transformation mechanisms of Fe_3+ ions in Fe-doped TiO_2. CrystEngComm 19(7):1100–1105
307. Yi LH, Lan FJ, Li JE et al (2018) Efficient noble-metal-free Co-NG/TiO_2 photocatalyst for H-2 evolution: synergistic effect between single-atom Co and N-doped graphene for enhanced photocatalytic activity. ACS Sustain Chem Eng 6(10):12766–12775
308. Yi SS, Zhang XB, Wulan BR et al (2018) Non-noble metals applied to solar water splitting. Energy Environ Sci 11(11):3128–3156
309. Yoon JW, Kim DH, Kim JH et al (2019) NH_2-MIL-125(Ti)/TiO_2 nanorod heterojunction photoanodes for efficient photoelectrochemical water splitting. Appl Catal B-Environ 244:511–518
310. Young C, Wang J, Kim J et al (2018) Controlled chemical vapor deposition for synthesis of nanowire arrays of metal–organic frameworks and their thermal conversion to carbon/metal oxide hybrid materials. Chem Mater 30(10):3379–3386
311. Yu P, Wang F, Shifa TA et al (2019) Earth abundant materials beyond transition metal dichalcogenides: a focus on electrocatalyzing hydrogen evolution reaction. Nano Energy 58:244–276
312. Yuan J, Zhang JJ, Yang MP et al (2018) CuO nanoparticles supported on TiO_2 with high efficiency for CO_2 electrochemical reduction to ethanol. Catalysts 8(4):11
313. Zang YP, Li LP, Xu YS et al (2014) Hybridization of brookite TiO_2 with g-C_3N_4: a visible-light-driven photocatalyst for As_3+ oxidation, MO degradation and water splitting for hydrogen evolution. J Mater Chem A 2(38):15774–15780
314. Zhang FM, Sheng JL, Yang ZD et al (2018) Rational design of MOF/COF hybrid materials for photocatalytic H_2 evolution in the presence of sacrificial electron donors. Angew Chem Int Edn 57(37):12106–12110

315. Zhang GX, Song AK, Duan YW et al (2018) Enhanced photocatalytic activity of TiO_2/zeolite composite for abatement of pollutants. Microporous Mesoporous Mat 255:61–68
316. Zhang H, Tang Q, Li QS et al (2020) Enhanced photocatalytic properties of PET filaments coated with Ag-N Co-doped TiO_2 nanoparticles sensitized with disperse blue dyes. Nanomaterials 10(5):24
317. Zhang HY, Wang ZW, Li RN et al (2017) TiO_2 supported on reed straw biochar as an adsorptive and photocatalytic composite for the efficient degradation of sulfamethoxazole in aqueous matrices. Chemosphere 185:351–360
318. Zhang J, Zhao Q, Zhang JX et al (2020) Highly active FexCo1-xP cocatalysts modified CdS for photocatalytic hydrogen production. Int J Hydrog Energy 45(43):22722–22731
319. Zhang JF, Zhou P, Liu JJ et al (2014) New understanding of the difference of photocatalytic activity among anatase, rutile and brookite TiO_2. Phys Chem Chem Phys 16(38):20382–20386
320. Zhang L, Wang WZ, Sun SM et al (2013) Solar light photocatalysis using Bi_2O_3/Bi_2SiO_5 nanoheterostructures formed in mesoporous SiO_2 microspheres. CrystEngComm 15 (46):10043–10048
321. Zhang P, Lu XF, Luan D et al (2020) Fabrication of heterostructured Fe_2TiO_5–TiO_2 nanocages with enhanced photoelectrochemical performance for solar energy conversion. Angew Chem 132(21):8205–8209
322. Zhang P, Luan DY, Lou XW (2020) Fabrication of CdS frame-in-cage particles for efficient photocatalytic hydrogen generation under visible-light irradiation. Adv Mater 32(39):6
323. Zhang QL, Chen PF, Chen L et al (2020) Facile fabrication of novel Ag_2S/K-g-C_3N_4 composite and its enhanced performance in photocatalytic H-2 evolution. J Colloid Interface Sci 568:117–129
324. Zhang R, Bi LL, Wang DJ et al (2020) Investigation on various photo-generated carrier transfer processes of SnS_2/g-C_3N_4 heterojunction photocatalysts for hydrogen evolution. J Colloid Interface Sci 578:431–440
325. Zhang S, Gu PC, Ma R et al (2019) Recent developments in fabrication and structure regulation of visible-light-driven g-C_3N_4-based photocatalysts towards water purification: a critical review. Catal Today 335:65–77
326. Zhang XY, Li L, Zhou QL et al (2019) Facile synthesis of novel gully-like double-sized mesoporous structural Sr-doped ZrO_2-TiO_2 composites with improved photocatalytic efficiency. J Solid State Chem 269:375–385
327. Zhang YM, Song J, Shao WH et al (2021) Au@NH2-MIL-125(Ti) heterostructure as light-responsive oxidase-like mimic for colorimetric sensing of cysteine. Microporous Mesoporous Mat 310:9
328. Zhao J, Fu B, Li X et al (2020) Construction of the Ni_2P/MoP heterostructure as a high-performance cocatalyst for visible-light-driven hydrogen production. ACS Appl Energy Mater
329. Zhao L, Dong T, Du J et al (2020) Synthesis of CdS/MoS_2 nanooctahedrons heterostructure with a tight interface for enhanced photocatalytic H_2 evolution and biomass upgrading. Sol. RRL: 2000415
330. Zhao X, Fan YY, Zhang WS et al (2020) Nanoengineering construction of Cu_2O nanowire arrays encapsulated with g-C_3N_4 as 3D spatial reticulation all-solid-state direct Z-Scheme photocatalysts for photocatalytic reduction of carbon dioxide. ACS Catal 10(11):6367–6376
331. Zhao XS, You YY, Huang SB et al (2020) Z-scheme photocatalytic production of hydrogen peroxide over $Bi_4O_5Br_2$/g-C_3N_4 heterostructure under visible light. Appl Catal B-Environ 278:11
332. Zhao YX, Yang BF, Xu J et al (2012) Facile synthesis of Ag nanoparticles supported on TiO_2 inverse opal with enhanced visible-light photocatalytic activity. Thin Solid Films 520 (9):3515–3522
333. Zhao ZW, Zhang WD, Lv XS et al (2016) Noble metal-free Bi nanoparticles supported on TiO_2 with plasmon-enhanced visible light photocatalytic air purification. Environ Sci Nano 3 (6):1306–1317

334. Zheng Y, Liu J, Liang J et al (2012) Graphitic carbon nitride materials: controllable synthesis and applications in fuel cells and photocatalysis. Energy Environ Sci 5(5):6717–6731
335. Zhong YM, Yang SY, Cai X et al (2020) Bio-inspired multilayered graphene-directed assembly of monolithic photo-membrane for full-visible light response and efficient charge separation. Appl Catal B-Environ 263:13
336. Zhou BX, Ding SS, Wang Y et al (2020) Type-II/type-II band alignment to boost spatial charge separation: a case study of g-C_3N_4 quantum dots/a-TiO_2/r-TiO_2 for highly efficient photocatalytic hydrogen and oxygen evolution. Nanoscale 12(10):6037–6046
337. Zhou G, Wu M-F, Xing Q-J et al (2018) Synthesis and characterizations of metal-free semiconductor/MOFs with good stability and high photocatalytic activity for H_2 evolution: a novel Z-scheme heterostructured photocatalyst formed by covalent bonds. Appl Catal B 220:607–614
338. Zhou H-C, Long JR, Yaghi OM (2012) Introduction to metal–organic frameworks, ACS Publications
339. Zhou X, Cui SC, Liu JG (2020) Three-dimensional graphene oxide cross-linked by benzidine as an efficient metal-free photocatalyst for hydrogen evolution. RSC Adv 10 (25):14725–14732
340. Zhou XF, Fang YX, Cai X et al (2020) In situ photodeposited construction of Pt-CdS/g-C3N4-MnOx composite photocatalyst for efficient visible-light-driven overall water splitting. ACS Appl Mater Interfaces 12(18):20579–20588
341. Zhu LL, Hong MH, Ho GW (2015) Hierarchical assembly of SnO_2/ZnO nanostructures for enhanced photocatalytic performance. Sci Rep 5:11
342. Zhu LY, Li H, Xu QL et al (2020) High-efficient separation of photoinduced carriers on double Z-scheme heterojunction for superior photocatalytic CO_2 reduction. J Colloid Interface Sci 564:303–312
343. Zhu XD, Pei LX, Zhu RR et al (2018) Preparation and characterization of Sn/La co-doped TiO_2 nanomaterials and their phase transformation and photocatalytic activity. Sci Rep 8:14
344. Zhu YH, Yao Y, Luo Z et al (2020) Nanostructured MoO_3 for efficient energy and environmental catalysis. Molecules 25(1):26
345. Zhu ZZ, Han Y, Chen CP et al (2018) Reduced graphene oxide-cadmium sulfide nanorods decorated with silver nanoparticles for efficient photocatalytic reduction carbon dioxide under visible light. ChemCatChem 10(7):1627–1634